



Southern African Universities Power Engineering Conference

SAUPEC 2014

30 - 31 January 2014

University of KwaZulu-Natal and Durban University of Technology

Durban, South Africa



**UNIVERSITY OF
KWAZULU-NATAL™**
**INYUVESI
YAKWAZULU-NATALI**

**PROCEEDINGS OF THE 22ND
SOUTHERN AFRICAN UNIVERSITIES POWER
ENGINEERING CONFERENCE – DIGITAL EDITION**

SAUPEC 2014

30 - 31 January 2014

University of KwaZulu-Natal and Durban University of Technology

Durban, South Africa

Review: Authors were invited to submit full papers to the broad subject “Electrical engineering”. Each paper was peer reviewed by at least two specialist reviewers. In the case where the reviewers did not agree, a third review was done to decide the outcome. Final acceptance was based on the contribution, scientific and technical merit of the paper.

Disclaimer: Authors are responsible for the contents of their papers.

Published by Southern African Universities Power Engineering Conference

School of Engineering, Howard College Campus, University of KwaZulu-Natal
Durban, South Africa

Tel: +27 31 260 2725

ISBN 978-1-86840-619-7

Acknowledgements

Organising Committee:

Chair – AK Saha, Co-chair – A Swanson, R Tiako, RP Carpanen, GF d'Almaine

Web site:

H.J. Vermeulen (Stellenbosch University)

Welcome address:

Prof. Trois, Dean and Head of School of Engineering, University of KwaZulu-Natal

Keynote address:

Mr Ntsokolo Divisional Executive Transmission, ESKOM Holdings SoC Limited

Technical Reviewers:

Cape Peninsula University of Technology

M Adonis, G Atkinson - Hope

Nelson Mandela Metropolitan University

W Phipps,

Stellenbosch University

HJ Vermeulen, MJ Kamper, JP Holtzhausen, PJ Randewijk, T Mouton, R J-Wang, N Gule

University of Cape Town

P. S. Barendse, C de Beer, KA Folly, R Herman, K Awodele, J de la Bat, D Oyedokun

North-West University

J de Kock, K Uren, AJ Grobler, T Seiphetlho, J Rens, J Van Schoor

University of Johannesburg

AM Bapubiandi, DC Pentz,

University of KwaZulu-Natal

A Swanson, AK Saha, JR Tapamo, R Tiako, OA Mafimidiwo, BO Mkandawire

University of the Witwatersrand

J Van Coller, I Hofsajer, W Cronje, C Nyamupangedengu, J Braid, M Shuma-Iwisi

Foreword

It is a privilege to welcome you to the 22nd Southern African Universities Power Engineering Conference, to be hosted by University of KwaZulu-Natal and Durban University of Technology at the University of KwaZulu-Natal, Howard College Campus. We hope that the papers presented will generate some stimulating conversations and that all involved will experience some academic growth.

We would like to thank all the reviewers for their huge contribution to the success of the conference. Thank you for the excellent feedback you gave the authors as well as the timely fashion in which you completed the reviews. Your time and efforts are greatly appreciated. Only papers that were accepted by two reviewers are published in the proceedings. Discussion papers were not reviewed and are used to present work in progress. Digital copies are included on the compact disc included in the conference kits.

The welcome address by Professor C. Trois Dean and Head of School of School of Engineering, of the University of KwaZulu-Natal is definitely a highlight. Your support for this conference and engineering at the NWU is greatly appreciated. We would also like to thank Mr Ntsokolo for delivering the keynote address as the Divisional Executive Transmission, ESKOM Holdings SoC Limited. The organising committee would also like to thank the University of KwaZulu-Natal for making their facilities available.

Enjoy Durban and SAUPEC 2014!

SAUPEC 2014 Organising Committee

Table of contents

Topic A: Control and Applications

1. DEVELOPMENT OF A QUADCOPTER FOR POWER LINE INSPECTION -
N.J. WILKEN AND R. GOUWS 2
2. AERIAL POWER LINE MONITORING STUDIES FOR SKA - M. GROCH,
H.C. READER, P. PIETERSE 9
3. FIELD EXPERIENCES WITH THE UKZN POWER LINE INSPECTION ROBOT -
T. LORIMER AND T. ROWELL 13
4. IMPLEMENTATION OF A ROTOR ANGLE MEASUREMENT TECHNIQUE USING
SYNCHROPHASOR TECHNIQUES - PRELIMINARY INVESTIGATIONS -
B.W.D. BERRY, M.A. EDWARDS AND K.J. NIXON 19
5. OPTIMIZING THE PROPERTIES OF THE OPTICAL CURRENT TRANSFORMER
WITH SPECIAL REFERENCE TO FASTER TRANSIENT RESPONSE -
N.J. OOSTHUYSEN AND J.J. WALKER 26
6. DESIGN AND IMPLEMENTATION OF HYBRID POWER SYSTEM CONTROLLER
FOR SOLAR-WIND SYSTEM - M. MANEVELD, M. NTHONTHO
AND S. CHOWDHURY 31
7. AN INVESTIGATION INTO GAIT GENERATION FOR MICROCONTROLLER-BASED
QUADRUPED ROBOTS WITH THREE DEGREE OF FREEDOM APPENDAGES -
M. G. HEYDENRYCH AND G. PHILLIPS 37
8. DESIGN OF A TRANSMISSION LINE MONITORING SOLUTION FOR AN
UNMANNED QUADCOPTER - T. VAN ROOYEN, R. GOUWS 44

Topic B: High Voltage

9. CORONA MEASUREMENT IN AN INVERTED COAXIAL GEOMETRY TO
EVALUATE THE EFFECT OF CONDUCTOR TEMPERATURE - P. J. PIETERSE 51
10. CHARACTERISING ELECTRICAL TREES IN MGO/EPOXY NANOCOMPOSITE
INSULATION THROUGH PD - D. R. CORNISH AND C. NYAMUPANGADENGU 57
11. DESIGN, TESTING AND IMPLEMENTATION OF A DATA ACQUISITION SYSTEM
FOR LIGHTNING ELECTRIC FIELD MEASUREMENTS - J.H. LANGE, H.G.P. HUNT
AND K.J. NIXON 63
12. A FREQUENCY-DOMAIN ANALYSIS OF VARISTOR CURRENT UNDER
DISTORTED SUPPLY VOLTAGE - P. BOKORO, I. JANDRELL AND M. HOVE 69

13. PARTIAL DISCHARGE EVALUATION OF A HIGH VOLTAGE TRANSFORMER - I.K. KYERE AND J.J. WALKER	73
14. OPTIMIZATION OF LOSS REDUCTION THROUGH A CONVERTED HVAC TRANSMISSION LINE INTO HVDC MODEL IN DIGSILENT - M J MUSHAGALA AND PROF G ATKINSON-HOPE	78
15. A STUDY ON THE FEASIBILITY OF TAPPING POWER OFF AN OVERHEAD HVDC TRANSMISSION LINE - S.M. MTAKATI, A.G. ROBERTS, W. PHIPPS AND R.T. HARRIS	83
16. NANOCOMPOSITE DIELECTRICS: SMART INSULATION TECHNOLOGY? - C. NYAMUPANGEDENGU	89
17. LIGHTNING SAFETY GAME - D T SADIE, A G DREYER AND E TRENGOVE	95
18. DESIGN, CONSTRUCTION, TESTING AND COMMISSIONING OF A 20KA 10/350MS CURRENT IMPULSE GENERATOR - S. MUZOKA, T. GORA, K.J. NIXON AND I.R. JANDRELL	101
19. INVESTIGATION INTO LIGHTNING SHIELDING FAILURE FOR HVDC LINES BASED ON INITIATION OF INDUCED LEADERS FROM THE POLE CONDUCTORS - G J STRELEC AND KJ NIXON	107
20. EFFECT OF TEMPERATURE VARIATIONS ON WAVE PROPAGATION CHARACTERISTICS IN XLPE MV POWER CABLES - G D MLANGENI, M SOTSAKA AND C NYAMUPANGEDENGU	111
21. THE CONVERGENCE OF HVDC CABLE AND VOLTAGE SOURCE CONVERTER TECHNOLOGIES: NEW SCOPE FOR HVDC TRANSMISSION – A C BRITTEN	117
22. INFLUENCE OF THE PERMITTIVITY AND RESISTIVITY ON THE ELECTRICAL STRESS IN MULTI-LAYER INSULATION SYSTEMS AT DIFFERENT FREQUENCIES - T. JOUBERT AND J.J. WALKER	123
23. ASPECTS OF THE ELECTROMAGNETIC ENVIRONMENT IN TRACTION SYSTEMS - J. CLAY AND I. HOFSAJER	128
24. THE SCOPE OF EPPEI-SPONSORED RESEARCH INTO HVDC AT UKZN: A PERSONAL VIEW – A C BRITTEN	136

Topic C: Power Systems

25. AN IMAGE PROCESSING METHODOLOGY FOR INSULATOR HYDROPHOBICITY CLASSIFICATION USING FLASH PHOTOGRAPHY - G. W. BLIGNAULT AND H.J. VERMEULEN	140
26. MODELLING IMPACT OF TRANSFORMER ASSET MANAGEMENT STRATEGIES ON COSTS USING SYSTEMS TYPOLOGIES AND PROBABILISTIC INFERENCES - B.O. MKANDAWIRE, A.K. SAHA AND N.M. IJUMBA	147

27. IDENTIFICATION OF POWER SYSTEM OSCILLATION PATHS IN POWER SYSTEM NETWORKS - S MVUYANA, DR J VAN COLLER AND T MODISANE	153
28. CAMEL NETWORK UPGRADE - K JIKIJA AND P. LAZANAS	159
29. DEVELOPMENT OF AN INSTALLATION AND COMMISSIONING PROCESS FOR MV OPEN RACK HARMONIC FILTERS FOR DISTRIBUTION NETWORKS - A M MERU AND G ATKINSON-HOPE	165
30. MITIGATING THE SYSTEM AVERAGE INTERRUPTION FREQUENCY INDEX (SAIFI) AND THE SYSTEM AVERAGE INTERRUPTION DURATION INDEX (SAIDI) ON THE ESKOM <i>KLEVEBANK 88/44/11KV</i> SUBSTATION - Q E LOUW AND P LAZANAS	171
31. COMPARISON OF LOW VOLTAGE RIDE THROUGH CAPABILITIES OF SYNCHRONOUS GENERATOR WITH STATCOM AND DFIG BASED WIND FARMS - W APPADOO AND S CHOWDHURY	176
32. IMPACT OF PHASOR MEASUREMENT UNITS ON DISTRIBUTION SYSTEM STATE ESTIMATION - A. E. KAHUNZIRE, K. O. AWODELE	182
33. EVALUATION OF THE POTENTIAL RISK OF VOLTAGE COLLAPSE IN THE CAPE NETWORK AS A RESULT OF GIC - A. JAKOET, A. K. SAHA AND ALL JARVIS	188
34. THE USE OF DIGSILENT POWERFACTORY SOFTWARE FOR POWER SYSTEM EFFICIENCY CALCULATIONS UNDER DISTORTED CONDITIONS - H AMUSHEMBE AND G ATKINSON-HOPE	194
35. ALLOCATING ENERGY WHEELING COST IN A DEREGULATED ENVIRONMENT - K T. AKINDEJI	200
36. ASSESSMENT OF THE HARMONIC ENVIRONMENT OF A POWER STATION'S MV AUXILIARY POWER SYSTEM - M MAKHETHA, J VAN COLLER AND M MANYAGE	205
37. COMPARISON OF EVOLUTIONARY OPTIMIZATION TECHNIQUES ON ECONOMIC LOAD DISPATCH WITH TRANSMISSION LINE CONSTRAINTS - A GOUDARZI AND AK SAHA	212
38. COMPARISON OF DIFFERENT REACTIVE POWER COMPENSATION METHODS IN A POWER DISTRIBUTION SYSTEM - J. NYANGOMA, K. AWODELE	218

Topic D: Machines

39. DESIGN AND EVALUATION OF A 1 KW ROTARY TRANSFORMER - NL ZIETSMAN, N GULE 225
40. INTERPRETATION AND SIGNIFICANCE OF SHAFT VOLTAGES IN ROTATING ELECTRICAL MACHINES - W. DOORSAMY AND W. A. CRONJE 230
41. STATOR DESIGN FOR A 4KW AXIAL FLUX PERMANENT MAGNET GENERATOR - G.L. CLASEN AND A.J. GROBLER 235
42. GEAR RATIO SELECTION OF AN OUTER-STATOR MAGNETICALLY GEARED MACHINE - P.M. TLALI, S. GERBER AND R-J. WANG 242
43. IMPLEMENTATION OF A MOVING BAND SOLVER FOR FINITE ELEMENT ANALYSIS OF ELECTRICAL MACHINES - S. GERBER AND R-J. WANG 249
44. SIMULATION OF DELTA MODULATED PWM-FED BDCE CONTROLLED NINE PHASE INDUCTION MACHINE DRIVE - L GUNDA AND N GULE 255
45. TESTING AND CHARACTERIZING THE MOTOR AND DRIVE SYSTEM OF A SOLAR VEHICLE (OCTOBER 2013) - F SMAL AND A J GROBLER 261
46. TAN DELTA TESTING OF MV MOTOR STATOR COIL INSULATION - G. LEBESE, G SIKHAKHANE, Y LEKALAKALA AND J VAN COLLER 267
47. THE EFFECT OF STRESS GRADING LENGTH ON TAN-DELTA AND CAPACITANCE MEASUREMENTS ON MV MOTOR COILS - Y.L LEKALAKALA AND J.M VAN COLLER 273
48. INVESTIGATION OF CORRELATION BETWEEN THERMAL AGEING PREDICTIONS AND MEASURED FURAN LEVELS FOR GENERATOR TRANSFORMERS - MT. METEBE, J. VAN COLLER AND R CORMACK 279
49. A STUDY OF ROTOR TOPOLOGIES OF LINE-START PM MOTORS FOR COOLING FAN APPLICATIONS - J'EAN-PIERRE ELS, ALBERT SORGDRAGER AND RONG-JIE WANG 284
50. PERFORMANCE COMPARISON FOR MOTORING AND GENERATING MODES OF A RELUCTANCE SYNCHRONOUS MACHINE - J. DU PLOOY AND N. GULE 290
51. DEVELOPMENT OF A SINGLE PHASE INDUCTION MOTOR VARIABLE SPEED DRIVE - A.J. McLAREN AND P.J. RANDEWIJK 296
52. SIMULATING SURGE PROPAGATION IN A ROTOR COIL FOR ROTOR SHORTED TURN DETECTION - T. MASHAU, D. TARRANT, J. VAN COLLER 302
53. DESIGN PROCEDURE OF A LINE-START PERMANENT MAGNET SYNCHRONOUS MACHINE - A.J SORGDRAGER, A.J GROBLER AND R-J WANG 307

Topic E: Energy and Energy Storage

54. DEVELOPMENT OF A VALVE REGULATED LEAD ACID (VRLA) BATTERY MODEL TO AID IN BATTERY EQUALIZATION DESIGN - J.P A ALMEIDA 316
55. SIMULATION AND PERFORMANCE ANALYSIS OF DIFFERENT BATTERY MODELS FOR ENERGY STORAGE - L RALIKHWATHA, G MACHINDA AND S CHOWDHURY 323
56. THE IMPACT OF DEMAND SIDE MANAGEMENT ON UTILITIES: ESKOM - M. TABIRI, K. AWODELE 329
57. ENERGY SAVINGS IN HIGHER EDUCATION INSTITUTIONS: SOLAR WATER HEATER IMPACT ANALYSIS - O.M. POPOOLA AND C. BURNIER 335
58. ANALYTICAL EVALUATION OF THE ENERGY LOSSES OF AN AIR SOURCE HEAT PUMP WATER HEATER: A RETROFIT TYPE - STEPHEN L. TANGWE, MICHAEL SIMON AND EDSON L. MEYER 341
59. ENERGY MONITORING DEVICE FOR SUSTAINABLE USER CENTRED SMART ENERGY SYSTEMS - D. WOLSKY, H. HUNT AND K. J. NIXON 347
60. BATTERY POWERED ELECTRIC VINEYARD TRACTORS: A FEASIBILITY STUDY - M M GULDENPFENNIG AND M J KAMPER 352
61. DESIGN AND DEVELOPMENT OF A PROTOTYPE SUPER CAPACITOR POWERED ELECTRIC BICYCLE - K. MALAN, M. COUTLAKIS AND J. BRAID 358

Topic F: Renewables and Alternative Energy

62. RETROSPECTIVE ANALYSIS OF BIOFUEL PRODUCTION IN AFRICA - C. NYAMWENA-MUKONZA 366
63. OVERVIEW OF ENERGY EFFICIENCY CHARACTERISATION AND MEASUREMENT OF A SOLAR-PV WATER PUMP FOR THE PURPOSE OF IDENTIFYING SYSTEM COMPONENT MATCHING PROBLEMS - T.A. HOOGENBOEZEM AND D.C. PENTZ 372
64. IMPROVING SOLAR ENERGY GENERATION THROUGH THE USE OF THREE DIMENSIONAL PHOTOVOLTAICS TECHNOLOGY - O A MAFIMIDIWO, A K SAHA 378
65. VOLTAGE DIP MITIGATION WITH DISTRIBUTED GENERATION IN RENEWABLE BASED MICROGRIDS - N MARARAKANYE, J FADIRAN AND I S CHOWDHURY 384
66. HARDWARE SOLAR POWER EMULATOR FOR EXPERIMENTAL MICRO-GRID STUDIES - A. EL-HADDAD, F. BELLIM, N. HORONGA, W. CRONJE 390
67. PERFORMANCE EVALUATION OF A SOLAR CAR'S PHOTOVOLTAIC ARRAY - R A LOTRIET AND A J GROBLER 397

68. THE DEVELOPMENT OF A PASSIVELY CONTROLLED SEGMENTED VARIABLE PITCH SMALL-SCALE HORIZONTAL AXIS WIND TURBINE - S N POOLE, R PHILLIPS 404
69. DEVELOPMENT OF AN INTEGRATED LABORATORY TEST SETUP FOR HIGH TEMPERATURE PEM FUEL CELL PERFORMANCE STUDIES - C. DE BEER, P. BARENDSE, P. PILLAY, B. BULLECKS AND R. RENGASWAMY 409

Topic G: Power Generation and Education

70. DELIVERING PRACTICAL INSTRUCTION TO POWER ENGINEERING UNDERGRADUATE STUDENTS AT AN OPEN DISTANCE LEARNING INSTITUTE - A.J. SWART AND P.T.A MAHLARE 416
71. MULTIVARIATE ANALYSIS OF DATA AS A DECISION MAKING AND DESIGN PREDICTION TOOL: COAL ABRASIVENESS INDEX DETERMINATION - T F NDLOVU, A F MULABA-BAFUBIANDI, T N MKHWANAZI 421
72. INVESTIGATION OF FINES GENERATION BASED ON ROM COAL PHYSICAL AND CHEMICAL PROPERTIES - R.S. TSHIPA, A.F. MULABA-BAFUBIANDI, N. TSHIONGO-MAKGWE AND M. BAGOPI 425
73. PREDICTION OF CLEAN COAL PRODUCT USING MATHEMATICAL MODELS - R.S. TSHIPA, A.F. MULABA-BAFUBIANDI, N. TSHIONGO-MAKGWE 430
74. ASSESSING THE ACCURACY OF A PROTECTION CURRENT TRANSFORMER USED IN A WIDE AREA MONITORING SYSTEM - C.M. MABOTHA, M.M. MASHABA AND K.J NIXON 435
75. DEVELOPMENT OF ALTERNATIVE ELECTRICAL STRESS MONITORING TRANSDUCERS APPLICABLE TO MV/LV DISTRIBUTION TRANSFORMERS - F. A. NETSHIONGOLWE, R. CORMACK, J. M. VAN COLLER 441

Topic H: Power Electronics

76. COUPLING OF GATE DRIVER EMI IN A BOOST CONVERTER - G.N. WOODING, A.S. DE BEER AND J.D. VAN WYK 448
77. PERFORMANCE OF PASSIVE AC/DC FILTERS AND DC SMOOTHING REACTORS IN UHVDC POWER SYSTEMS - F M KASANGALA, G ATKINSON-HOPE 453
78. CLASS D AUDIO AMPLIFIER THEORY INCLUDING A SIMPLE FEEDBACK LOOP EXAMPLE - S. NIENABER AND H.D.T. MOUTON 459
79. SOME ASPECTS ON INTEGRATED CURRENT SHUNTS FOR HIGH FREQUENCY SWITCHING POWER ELECTRONIC CONVERTERS - A.L.J. JOANNOU D.C. PENTZ J.D. VAN WYK 465
80. REDUCTION IN EMI FOR AN LED BUCK CONVERTER - L.L.T. LAM A.S. DE BEER 471
81. HIGH BANDWIDTH HIGH POWER INVERTER FOR FACT DEVICES - M.LOOI 477

82. A HIGH-FREQUENCY CMOS BASED DRIVER FOR HIGH-POWER MOSFET APPLICATIONS - A.J. SWART 483

Topic I: Condition Monitoring and Systems Automation

83. HOUSEHOLD ELECTRICITY AND WATER MONITOR AND CONTROL WITH CELLULAR COMMUNICATIONS AND WEB INTERFACE - R.I. MÜLLER AND M.J. BOOYSEN 489
84. TRANSIENT RESPONSE OF EQUIPMENT TO FAST TRANSFER - C VAN RENSBURG AND AJ GROBLER 494
85. EFFICIENT LIGHTING DESIGN FOR BUILDINGS AND OFFICES: A CASE FOR THE CHANCELLOR OPPENHEIMER LIBRARY UNIVERSITY OF CAPE TOWN - R BOADZO, S CHOWDHURY 500
86. POWER LINE COMMUNICATION CHANNEL MODELLING: ESTABLISHING THE CHANNEL CHARACTERISTICS - F. ZWANE AND T. J.O. AFULLO 505
87. INVESTIGATING COMMON SCADA SECURITY VULNERABILITIES USING PENETRATION TESTING - S G RALETHE AND K J NIXON 510
88. IMPLEMENTATION OF A REMOTE MONITORING AND CONTROL SYSTEM USING A CELLULAR NETWORK - I VAN NIEKERK AND G PHILLIPS 517
89. DESIGN AND IMPLEMENTATION OF A SUB-METRE ACCURACY POSITIONING SYSTEM USING A CONSUMER GRADE GPS RECEIVER - D. HINCH, J. PENN, K. J. NIXON, G. J. GIBBON 523

Topic A

Control and Applications

DEVELOPMENT OF A QUADCOPTER FOR POWER LINE INSPECTION

N J Wilken and R Gouws*

North West University, School of Electrical and Computer Engineering, Potchefstroom South-Africa, njwilken@gmail.com

**North West University, School of Electrical and Computer Engineering, Potchefstroom South-Africa, rupert.gouws@nwu.ac.za*

Abstract. The inspection of transmission lines is to be done annually. It is proposed that a quadcopter is used to do the inspection of these transmission lines. The modelling of the quadcopter was done by studying its physical characteristics and ultimately a mathematical model could be presented with the use of the Newton equations. The control strategy suitable of this project is the use of PD control, which will consist of four control loops combined as one. The prototype quadcopter is able to do transmission line inspections, is equipped with a monitoring system, move smoothly and have special features like stabilizing mode and altitude hold.

Key Words. Quadcopter; PD Controller; Altitude Controller; Arduino and Controller simulation.

1. INTRODUCTION

A constant supply of energy is a necessity for a country that wants an ever growing economy. To meet this demand, reliable electrical networks that consist of power lines are essential.

Eskom is a power supplying company that have generated and sold over 225 000 Giga-Watt-hour in the year of 2011 and 2012, providing 45% of all the electricity used in Africa and 95% of all the electricity used in South-Africa [1]. In order to supply these enormous amounts of electricity thousands of kilometres of transmission lines is needed and is found all over Africa.

1.1 Problem Background

The inspection of transmission lines are done annually in the form of line patrol, this is when a team from Eskom walk the line with the help of a motor vehicle to do a visual inspection on the condition of the transmission lines. Due to the vast amount of time needed to do this and the accessibility constrains due to rough terrain and obstacles, some of the inspections are done by a helicopter. According to an Eskom financial report of 2010 the expenses for these inspections run up to R36 million per year [2]. The use of a helicopter is a costly method to inspect transmission lines and thus an alternative solution to this problem needs to be found.

It is proposed that a transmission line inspecting quadcopter needs to be developed that is more effective than the conventional methods of inspecting power transmission lines, in terms of time, safety and the costs involved.

1.2 Existing Solutions to the Problem

Transmission lines are not an unfamiliar sight and ever since these lines made their appearance it was needed to be monitor by means of inspection. Over the years different solutions have been found to do this task.

Transmission lines have been inspected on foot for a very long time as there was no better method available to perform this task. Power networks consist of thousands of kilometres of transmission lines and take a vast amount of time to inspect on foot if inspection is done thoroughly. Furthermore power lines are sometimes built in rough terrain that

is difficult to access due to mountains, new development and height constrains.

A method used with more success is to inspect the power lines with the help from a helicopter. This technique is very accurate because it can overcome the height constrains involved with power lines. Using a robot is the most recent solution and method of inspecting power transmission lines. This robot is developed to run on the earth wire of the line and with a camera in attached to the frame of the robot, photos and even videos can be recorded of the transmission line [3].

2. PROPOSED SOLUTION

In order to obtain a general feel and knowledge of what to expect during the design of this project, proper research had to be done on similar projects with roughly the same scope. The research revealed some important aspects that need more planning and time than other, stumbling stones to avoid, crucial approaches for success and risks involved in completing this project.

The quadcopter needs to be able to fly along a power line for inspection purposes and should consist of an autopilot function. This function should provide the ability that the quadcopter can hover, do auto take-off and landing on command of the operator. The physical construction should be able to house and supply power to a monitoring system for the inspection purpose. The following key components were acknowledged to guarantee that the project is a success:

- Custom development of a controller to achieve the desired features that the quadcopter should consist of.
- Construction/Assembling of an appropriate frame/chassis.
- Achieving lift-off, flying and movement of the quadcopter, by means of motors, propellers and speed control.
- Design a monitoring system to do a visual inspection on the power lines.
- Establish a remote communication system between quadcopter and operator.
- Supplying power to all the components on the quadcopter.

These components listed are only high level and require a lot more detail to incorporate correctly into the quadcopter for complete success.

3. DYNAMIC QUADCOPTER MODEL

In order to design a controller for the quadcopter it is first of all necessary to develop a dynamic model that accurately describes the quadcopter in terms of its movements and principal characteristics.

3.1 Physical and Mathematical Model

The axis and structure orientation of the quadcopter that will be used to do the modelling is in Fig. 1 [4], where x, y and z is the coordinates of the quadcopters centre of gravity. The Φ represents the roll angle; θ represents the pitch angle and Ψ the yaw angle.

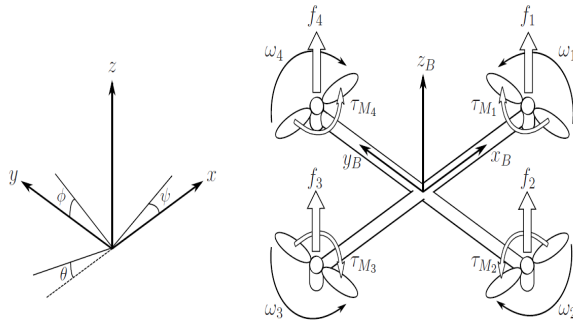


Fig. 1: Quadcopter body and inertia frames used for modeling.

From Fig. 1 it can be seen that the rolling moment takes places around the y-axis, the pitching moment around the x-axis and the yawing moment around the z-axis. The linear position (ξ) and the Euler angles (η) are defined as

$$\xi = \begin{bmatrix} x \\ y \\ z \end{bmatrix}, \eta = \begin{bmatrix} \phi \\ \theta \\ \psi \end{bmatrix} \quad (1)$$

A transformation matrix is required to switch between the body and inertial frames. This matrix, denoted by R, is called the rotation matrix [4].

$$\bar{R} = \begin{bmatrix} C_\psi C_\theta & C_\psi S_\theta S_\phi - S_\psi C_\phi & C_\psi S_\theta C_\phi + S_\psi S_\phi \\ S_\psi C_\theta & S_\psi S_\theta S_\phi + C_\psi C_\phi & S_\psi S_\theta C_\phi - C_\psi S_\phi \\ -S_\theta & C_\theta S_\phi & C_\theta C_\phi \end{bmatrix} \quad (2)$$

In the rotation matrix C_ψ represents $\cos(\Psi)$, S_θ represents $\sin(\theta)$ and so forward. The assumption is made that the body of the quadcopter is rigid and symmetrical, and in an X configuration in the x-axis and y-axis as seen in Fig. 1. The inertia matrix is then given by

$$\bar{I} = \begin{bmatrix} I_{xx} & 0 & 0 \\ 0 & I_{yy} & 0 \\ 0 & 0 & I_{zz} \end{bmatrix} \quad (3)$$

The fact that the structure is symmetrical yields the result that $I_{xx} = I_{yy}$ for the diagonal matrix of the inertia. The next step is to conceptualize the force

from each motor (f_i) that is created by its angular velocity ($\dot{\omega}_i$).

$$f_i = k\omega_i^2 \quad (4)$$

The i denote the motor number and k is a certain lift constant of that motor. Similarly a torque (τ_{M_i}) is created around the axis of that motor and is given by

$$\tau_{M_i} = b\omega_i + I_M \quad (5)$$

where I_M is the moment of inertia and b is the drag constant. A thrust (T) is created as a result of the collective forces of all four motor that will act in the direction of the z-axis [4].

$$T = \sum_{i=1}^4 f_i = k(\omega_1^2 + \omega_2^2 + \omega_3^2 + \omega_4^2) \quad (6)$$

The torques (τ) that corresponds with roll, pitch and yaw in the body frame is then given as

$$\bar{\tau}_B = \begin{bmatrix} k(-\omega_2^2 + \omega_4^2)l \\ k(-\omega_1^2 + \omega_3^2)l \\ k(\omega_1^2 - \omega_2^2 + \omega_3^2 - \omega_4^2)l \end{bmatrix} = \begin{bmatrix} \tau_\phi \\ \tau_\theta \\ \tau_\psi \end{bmatrix} \quad (7)$$

provided that the rotation of the motors is chosen as in Fig. 1 and that the length (l) from the motor to the centre of gravity is the same for all the motors. The Newton-Euler equations can now be used to describe the dynamics of the quadcopter from the equations obtained already. This then yields

$$\begin{bmatrix} \ddot{x} \\ \ddot{y} \\ \ddot{z} \end{bmatrix} = -g \begin{bmatrix} 0 \\ 0 \\ 1 \end{bmatrix} + \frac{T}{m} \begin{bmatrix} C_\psi S_\theta C_\phi + S_\psi S_\phi \\ S_\psi S_\theta C_\phi - C_\psi S_\phi \\ C_\theta C_\phi \end{bmatrix} \quad (8)$$

which can be used to get the expressions for acceleration in the x-axis, y-axis and z-axis. In the equation above, the g denote gravitation and m the mass of the entire quadcopter. The Euler-Lagrange equations can now be used to get a matrix system in terms of the acceleration in the Euler angles [4].

$$\begin{bmatrix} \ddot{\phi} \\ \ddot{\theta} \\ \ddot{\psi} \end{bmatrix} = \begin{bmatrix} \tau_\phi / I_{xx} \\ \tau_\theta / I_{yy} \\ \tau_\psi / I_{zz} \end{bmatrix} \quad (9)$$

This equation for the acceleration in the Euler angles is only valid if the Coriolis Effect is ignored. Since this is a small scale project and will not be traveling fast over long distances, this effect can be ignored in the dynamic model.

3.2 Simulation of Dynamic Model

The matrix systems and equations from the previous section should now be rearranged in such a way that a state space model can be determined, which will aid the student when trying to simulate the model. The following equations are obtained

$$\begin{aligned}
 \ddot{x} &= T/m (C_\psi S_\theta C_\phi + S_\psi S_\phi) \\
 \ddot{y} &= T/m (S_\psi S_\theta C_\phi - C_\psi S_\phi) \\
 \ddot{z} &= T/m (C_\theta C_\phi) - g \\
 \ddot{\phi} &= \tau_\phi / I_{xx} \\
 \ddot{\theta} &= \tau_\theta / I_{yy} \\
 \ddot{\psi} &= \tau_\psi / I_{zz}
 \end{aligned} \quad (10)$$

From these equations [4] it can easily be seen that all of the movement is as a consequence of the lifting force from the rotating motors. It can also be seen that the thrust is responsible for the displacement in position and torque is responsible for the acceleration in the Euler angles.

It was found that the easiest way to model the system is to decouple the inputs, thus the quadcopter will be modelled with three different models. When the three models have been developed they can just be added together to form the overall model of the quadcopter. The three models are one for the altitude and yaw, the second for the roll and the third for the pitch angle.

The state space model for each of these models has been generated using manipulation of the equations and then the three models were combined once again to produce the entire model required. The model simplification technique used in [5] has been implemented on the model. The state space model is presented in the form of

$$\begin{aligned}
 \dot{X} &= AX + BU \\
 Y &= CX + DU
 \end{aligned} \quad (11)$$

where the X is the state matrix, U is the input matrix and Y is output matrix.

$$\begin{aligned}
 X &= [x \ y \ z \ \phi \ \theta \ \psi \ \dot{x} \ \dot{y} \ \dot{z} \ \dot{\phi} \ \dot{\theta} \ \dot{\psi}]^T \\
 U &= [T \ \tau_\phi \ \tau_\theta \ \tau_\psi]^T \\
 Y &= [x \ y \ z \ \phi \ \theta \ \psi]^T
 \end{aligned} \quad (12)$$

The A, B, C and D matrix were obtained by using the unique equations formulated earlier. The resultant state space model has been simulated in MATLAB® Simulink®.

The aim of this simulation is to verify that the dynamic quadcopter model acts in a similar manner to a real life quadcopter. To test this behaviour a step input was used to simulate a change the total thrust, roll angle, pitch angle and yaw angle. The output of the model is then measured on oscilloscopes, to see what effect each input has on the position of x, y and z and the Euler angles roll, pitch and yaw.

4. DETAIL CONTROL

During the simulation of the derived model of the quadcopter it was seen that some effects of the quadcopter model in not desirable. Since this model proved to be accurate the only method to get rid of these effects is by means of proper control.

The derived state space model of the quadcopter that has been simulated in Simulink® was used to obtain equations for each of the inputs to the model. From the MATLAB® equations a controller can be devolved that would control the quadcopter to make it useful.

4.1 Controller Design

The controller of the quadcopter will consist of four major control loops that would ultimately be combined to create the controller. The controller type that will be used for all four of the control loops is PD controllers. The control loops will be designed to control the thrust provide by the motors, the rolling moment around the x-axis, the pitching moment around the y-axis and the yawing moment around the z-axis.

The PD control loop for the total thrust provided from the four motors will have the following balance

$$\frac{z}{T} = \frac{K_A}{s^2} \quad (13)$$

where z is the output position, T is the total thrust of the motors and K_A a certain constant determine by the quadcopter characteristics. Since thrust is the input, for a PD controller, it can be written as

$$T = (k_{p,z}(z_d - z) + k_{d,z}(z_d - z)s) \frac{m}{C_\phi C_\theta} \quad (14)$$

where $k_{p,z}$ and $k_{d,z}$ are the PD constants and z_d is the input to the thrust control loop, indicating the desired altitude. Using the equations above the transfer function can be obtained

$$T_z(s) = \frac{z}{z_d} = \frac{\frac{m}{C_\phi C_\theta} (K_A k_{d,z} s + K_A k_{p,z})}{s^2 + \frac{m}{C_\phi C_\theta} (K_A k_{d,z} s + K_A k_{p,z})} \quad (15)$$

The transfer function can now be used to implement the control loop to control the thrust, given that the constants of the quadcopter are known. The propagation and derivative constants of the altitude control loop can now be calculated for a certain settling time and percentage overshoot. After careful consideration and reviewing literature a suitable settling time would be less than one second while any percentage less than 5% would be an acceptable overshoot for the controllers.

A similar approach has been followed to calculate the transfer functions of the rolling moment around the x-axis control loop, the pitching moment around the y-axis control loop and the yawing moment around the z-axis control loop. The transfer function for the rolling moment around the x-axis is

$$T_\phi(s) = \frac{\phi}{\phi_d} = \frac{I_{xx} (K_B k_{d,\phi} s + K_B k_{p,\phi})}{s^2 + I_{xx} (K_B k_{d,\phi} s + K_B k_{p,\phi})} \quad (16)$$

where ϕ is the output roll angle, ϕ_d is the desired roll angle and $K_B, k_{p,\phi}$ and $k_{d,\phi}$ is constants associated with the roll control loop. The propagation and derivative constants of the roll moment control loop can now be calculated for the specified settling

time and percentage overshoot. The transfer function for the pitching moment around the y-axis is

$$T_{\theta}(s) = \frac{\theta}{\theta_d} = \frac{I_{yy} (K_C k_{D,\theta} s + K_C k_{P,\theta})}{s^2 + I_{yy} (K_C k_{D,\theta} s + K_C k_{P,\theta})} \quad (17)$$

where θ is the output pitch angle, θ_d is the desired pitch angle and $K_C, k_{P,\theta}$ and $k_{D,\theta}$ is constants associated with the pitch control loop. The transfer function for the yawing moment around the z-axis is

$$T_{\psi}(s) = \frac{\psi}{\psi_d} = \frac{I_{zz} (K_D k_{D,\psi} s + K_D k_{P,\psi})}{s^2 + I_{zz} (K_D k_{D,\psi} s + K_D k_{P,\psi})} \quad (18)$$

where ψ is the output yaw angle, ψ_d is the desired yaw angle and $K_D, k_{P,\psi}$ and $k_{D,\psi}$ is constants associated with the yaw control loop. The four control loops designed above should yield the required controller, once they are combined and all the constants are known and calculated, to control the quadcopter. The control scheme of the quadcopter will be in the form of Fig. 2.

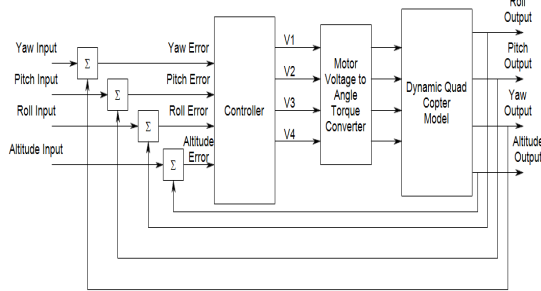


Fig.2: Quadcopter Control Scheme.

The controller of the quadcopter is only able to change one thing in order to control it and that is the voltage of the four motors (V_1, V_2, V_3, V_4). As the motor voltage varies the speed and direction of the angular velocity will also vary. It is for this reason that a converter is added to calculate the voltages required at each motor to achieve the thrust and torques needed at the output. The controller in Fig. 2 is the combination of the four control loop designed above.

4.2 Controller Simulation

In order to verify that the controllers designed in the previous section yield the required response with the calculated values for the propagation and derivative constants, it must first be simulated in Simulink®. The four controllers have been constructed and simulations could begin using the known and calculated constants. The resultant altitude controller can be seen in Fig. 3.

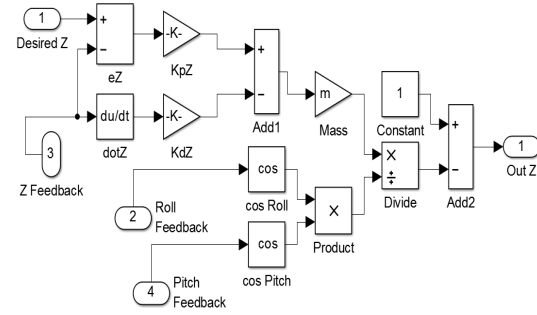


Fig.3: Altitude control loop.

The controller makes use of three summing nodes, a multiplication and division function to present the control of a desired altitude as input to the actual altitude. To be able to deliver the desired altitude the controller makes use of the feedback from the actual altitude, roll angle and pitch angle. This feedback is used to compute an error to continuously check that the desired movement is achieved. The step response yield the requirement in terms of the settling time and maximum overshoot.

The control loop for the roll controller can be seen in Fig. 4, where a desired roll angle is given as input and the output is the actual roll angle. The controller uses only the actual roll angle as feedback to compute the error and stabilize the quadcopter.

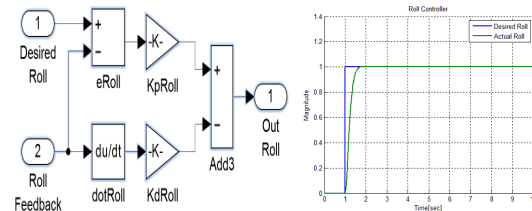


Fig.4: Roll control loop and step response result.

The results of the step response of the roll controller is shown in the right of Fig. 4 where it can be seen that it delivers a stable response with minimal overshoot in an acceptable settling time. From the simulation it is also seen that the coordinate of x is change while the rolling moment occurs. The pitch control loop is almost identical to the roll controller, the only difference being the input desired pitch angle and the output of the actual pitching angle. The pitch control loop is shown in the left side of Fig. 5 with its step response on the right.

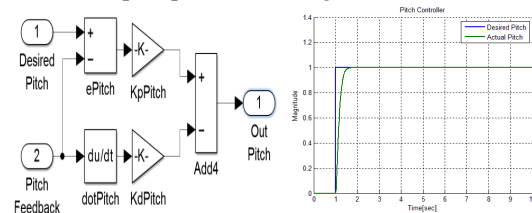


Fig.5: Pitch control loop and step response result.

When the controller is connected to the derived quadcopter model and given a step input the result can be seen in the right half of Fig. 5. The output of this response deliver all the required objectives stated in the beginning of this section. From the simulation

it is also seen that the coordinate of y is change while the pitching moment occurs. The yaw controller was designed and simulate in a similar manner and the control loop is shown is the left side of Fig. 6.

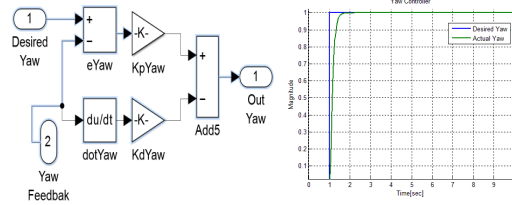


Fig.6: Yaw control loop and step response results.

The right side of Fig. 6 show the result of when a step input is given to the desired yaw vs. the output of the controller. The overshoot and the settling time are easily adjusted to the desired maximums by tweaking the gains of the propagation and derivative constants of the controller. This tuning action will ensure for a quadcopter that is stable and delivers excellent results in terms of inspection quality.

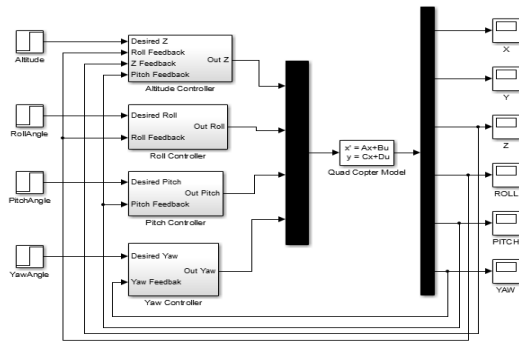


Fig.7: Simulate quadcopter model and controllers.

The four controllers designed and simulated in this section can now be joined together to form the quadcopter controller. The quadcopter controller is then joined to the derived dynamical model of the quadcopter to simulate the entire movement of the quadcopter. This simulated quadcopter model with its controllers can be seen in Fig. 7. The results of the entire quadcopter system remain the same as already mentioned in this section.

5. RESULTS

During the results section all the findings obtained from various tests will be stated and the do's as well as the don'ts will be discussed. The results will be compared with the simulations done in the previous chapter and will be the indication whether the project is successful in delivering the required objectives.

5.1 Motor and Battery Test

A motor test was done to determine the current it would draw when the motor is in different states. Measurements were taken while the motor had no load and then again with load connected to the shaft of the motor. The load used for this test was two different propellers sizes namely a 12X4.5 and 10X4.5 propeller. The results of the motor test can be seen in Fig. 8.

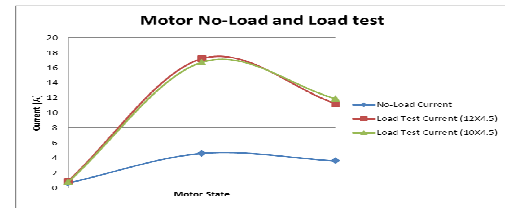


Fig.8: Motor Current curves under various loads.

The power needed to keep the motor rotating is then calculate as 166W for the 12X4.5 propeller and 175.8W for the 10X4.5 propeller. From the power results one can see that the bigger propeller will be more effective to use, given that it can lift the entire weight of the quadcopter. These power consumptions can now be used to calculate how much power will be used when flying.

Although a low voltage Li-Po alarm will be used to warn the operator when the battery is nearing its end to give power to the quadcopter, it is essential that one has a predetermined figure of what operating time would be available. The motor running current, as determined above, is used to calculate the total operating time the battery would be able to supply power to the quadcopter. The results can be seen in Fig. 9.

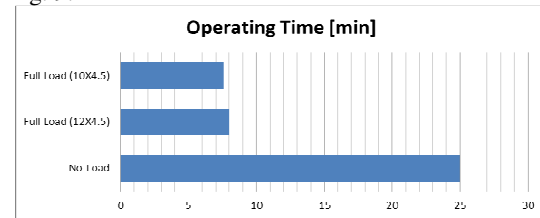


Fig.9: Results for battery discharge test.

The results in terms of operating time, in minutes, give the same figure as the operating currents of the motor under certain loads. As the operating current of the motor increases the time that the battery will be able to supply power will decrease. With propellers connected to the motors shaft the best operating time a single battery would deliver is about 9 minutes.

5.2 Quadcopter controller results

In order to ensure safe operation the roll and pitch controllers of the quadcopter where given saturation values. The values used are a lower limit of -45° and an upper limit of $+45^\circ$. The impact of this is that the quadcopter is only allowed to rotate 45° around the x- and y-axis in both directions.

The roll, pitch, yaw and altitude controller has been tested individually by means of data logging using the flight controller board, while the quadcopter were in flight.

The result for both the roll and pitch controller revealed that the required change in roll and pitch angle, given by the operator, could be achieved by the controllers while compensating for external interferences like the changing wind speed. From the data obtain, the yaw controller appeared to be extremely sensitive. When given a small required change in the yaw angle, as an input, the actual

change in the yaw angle were considerable larger. The reason for this is due to the fact that the motors provide twice as much thrust that the actually needed for the specific quadcopter. When the altitude controller was tested the observation has been made that the altitude proved to very difficult to be maintained, varying about 5 to 6 meters. It is for this precise reason that the student implemented a special altitude hold function that keeps the altitude within a range of less than one meter when activated.

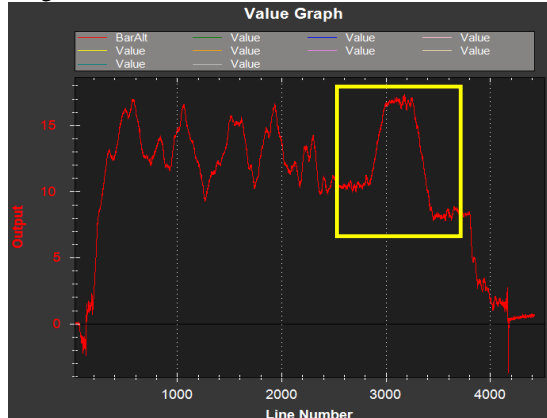


Fig.10: Attitude of Quadcopter measured by barometer
In Fig. 10 the results of the on-board barometer can be seen, where the altitude is measured in meters. The altitude hold function was activated while the quadcopter was in flight between samples 2400 and 3800, as indicated by the yellow frames. When the input throttle is altered while in the quadcopter is in altitude hold mode, the required altitude for the hold function is adjusted up or down. As one can see, the altitude remain extremely stable when the desired altitude is achieved varying by less than a meter. The results thus verify that the simulated controller constants that were programmed into the actual control delivered an excellent starting point to achieve the fast response and stability that is required from the quadcopter.

5.3 Integrated system line inspection

The goal of this project is deliver a product or method that Eskom can use to do their line inspection with, while reducing the costs and improving the quality of the inspection results. Thus the quadcopter without the monitoring system are merely a toy and of no use to Eskom. The monitoring system were attached to the quadcopter and the result can be seen in Fig. 11.

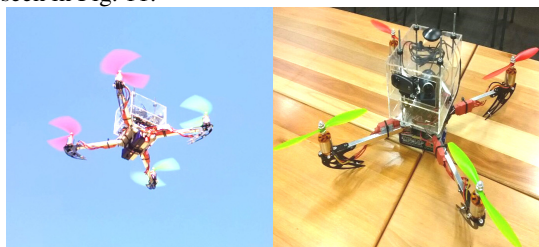


Fig.11: Final quadcopter with monitoring system.

The integrated quadcopter executed all required movements smoothly while remaining completely stable. To verify that the quadcopter could indeed deliver the required performance to do a power transmission line inspection and yield the results as needed to declare the project a success, the quadcopter has been tested on such an inspection. The image in Fig. 12 shows the quadcopter while flying close to a transmission line.

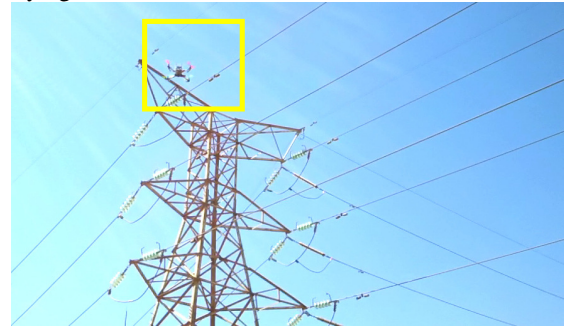


Fig.12: Quadcopter doing a transmission line inspection.

The integrated transmission line test was done while there was a breeze at an altitude of about 16 to 18 meters. All of the controllers together with the altitude hold function were used during this field test with great success. The quadcopter could be flown at a distance of about 4 meters from the transmission line. The on-board inspection results can be seen in Fig. 13.

On the left hand side of Fig. 13 a snapshot using the normal camera were taken with the quadcopter about 4 meters from the transmission line and on the right hand side is a snapshot using the concept thermal imaging camera.



Fig.13: On-board inspection results from quadcopter

The images are good enough to identify faults on the line. This means that the quadcopter provides the required stability to obtain the inspection results as required by Eskom.

6. CONCLUSION

The modelling of the quadcopter was done by studying its physical characteristics and ultimately a mathematical model could be presented with the use of the Newton equations of motion. The state space model had to be extracted to simulate the derived model in Simulink®.

The control strategy suitable of this project is the use of PD control, which will consist of four control loops combined as one. The overshoot and the settling time are easily adjusted to the desired maximums by tweaking the gains of the propagation

and derivative constants of the controller. This tuning action ensures for a quadcopter that is stable and delivers excellent results in terms of inspection quality.

The simulated PD constants were programmed onto the controller. These constants proved to be an excellent starting point and only required a small amount of alteration to deliver a smooth and stable response. The altitude hold function delivered extremely accurate results varying by less than a meter while maintaining a constant altitude. This feature proved to be very useful when the transmission line inspection test was done to obtain good quality inspection results.

From all the results it is however evident that due to the limitations of the quadcopter, in terms of the operating time, it cannot yet be used as an alternative to the line inspections. Since a detailed air inspection is to be done at 15km/h the quadcopter will only be able to cover 2.25km of transmission line per battery. It is recommended that the power source of the quadcopter be improved or replaced by a more efficient energy source and weigh reduction be done on the quadcopter components. Given the improvements the quadcopter could be used when conducting a transmission line inspection.

REFERENCES

- [1] Eskom, "Eskom: Our business," Eskom, [Online]. Available: <http://www.eskom.co.za/c/40/company-information/>. [Accessed 15 01 2013].
- [2] Eskom, "financialresults," 2010. [Online]. Available: http://financialresults.co.za/2010/eskom_ar2010/eskom_abridged-ar2010/flippingbook.swf?pageNumber=. [Accessed 15 01 2013].
- [3] A. Burger, "Chapter 3: Overhead line inspections," in *The fundamentals and practice of overhead line maintenance*, Johannesburg, Crown Publications, 2006, pp. 34-49.
- [4] L. Teppo, "Modelling and control of quadpoter," Aalto University, Espoo, 2011.
- [5] P. Castillo, R. Lozano and A. E. Dzul, "The Quad-rotor Rotorcraft," in *Modelling and Control of Mini-Flying Machines*, Compiegne, France, Springer, 2004, pp. 39-60.

AERIAL POWER LINE MONITORING STUDIES FOR SKA

M. Groch, H.C. Reader, P. Pieterse

Dept. EE Engineering, University of Stellenbosch, South Africa, Email: hcreader@sun.ac.za

Abstract: A method to determine radiating characteristics of sparking on sub-132 kV power lines using an unmanned aerial vehicle (UAV) is presented. Minimum air insulation distances (MAID) for the effective UAV's floating conductive properties are determined through laboratory, computational electromagnetic and empirical techniques. A 22 kV test line incorporating an artificial spark generator is studied using the UAV.

Keywords: Air insulation, power line sparking, high voltage metrology, unmanned aerial vehicles.

1. INTRODUCTION

South Africa continues to develop the Karoo Array Telescope (KAT) in the form of MeerKAT, located in the Northern Cape of South Africa. This forms a subset of the Square Kilometre Array (SKA). This will ultimately be the most sensitive, contemporary radio astronomy telescope in the world. Our research contributes to the strategies used to minimise environmental radio frequency interference (RFI) due to power provision on 33 kV, and probably 132 kV, transmission lines. We are interested here in the use of an unmanned aerial vehicle (UAV) to study line sparking behaviour. To do this, we have to be certain of safe-fly zones for the vehicle around the proposed lines.

Breakdown testing under transient conditions, using laboratory, computational electromagnetic (CEM) and empirical techniques will be shown. Finally, the UAV will demonstrate a sparking line radiation pattern.

2. HV BREAKDOWN TESTING

2.1 Test Configuration and Procedure

To arrive at an accurate computational model and develop confidence in a test configuration, a study to measure the floating potentials of a conductive UAV alongside a high voltage test line was initiated. These measurements were compared to a CEM solution. Discrepancies between the measurements and modelling were reduced through careful definition of the system ground, and ensuring sufficient clearances to the laboratory walls and equipment. The CEM modelling was refined along with the test configuration until confidence was gained in both through equivalence. The resulting test setup, with a well-defined electromagnetic boundary, is shown in Figure 1.

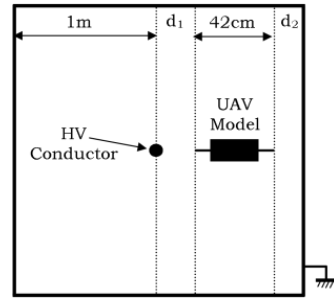


Figure 1: UAV switching impulse testing configuration

An electrically equivalent 1:1 scale model of our commercially-available UAV was used as the test object in the breakdown measurements. This model is designed with galvanic connectivity throughout to replicate an EMC-hardened UAV (Figure 2).

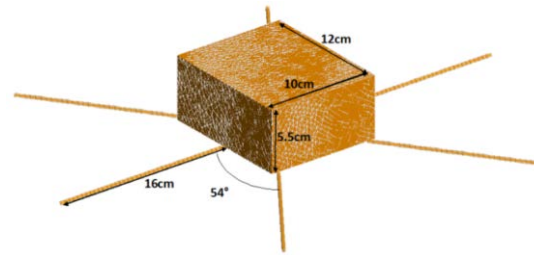


Figure 2: The 1:1 scale model of the EMC-shielded UAV.

The hull and motor control cables of the UAV are modelled with a solid metal enclosure and copper brazing rods, respectively. Minimum air insulation distances (MAID) are determined through switching impulse testing with our UAV model suspended alongside the test line, as in Figure 1.

2.2 Switching Impulse Testing

A Marx bank generator is used to produce a switching impulse test voltage. An external wave-shaping network ensures that the impulses injected on to the line adhere to IEC 60071-2 specifications [1] for impulse rise and fall times (250/2500 μ s). Breakdown tests are undertaken with positive switching impulses. The probability of flashover is determined at multiple primary gap distances, d_1 . The critical flashover (CFO; 50 % probability of breakdown) and standard deviation, σ , are determined at each distance d_1 by plotting the breakdown values on log-normal probability paper. Interpolation and extrapolation beyond the measured range yield the CFO and σ value. These two factors may be used to describe fully the air gap performance.

Due to the limitations of our test setup and scale, Rizk's empirical model [2] for streamer breakdown is coupled to our measured results to describe MAIDs alongside phase conductors. Breakdown due to the leader mechanism was ignored. Two inputs are required by Rizk's equations, namely a critical streamer field gradient and a geometric factor. These are determined in section 3.

3. DERIVING THE INPUT PARAMETERS FOR RIZK'S EMPIRICAL MODEL

With the test configuration established, a CEM model is calibrated to the measurement environment. The CEM model is then used to determine the geometric factor, which accounts for the potential of the UAV at breakdown.

The suitability of a method-of-moments (MOM) software package, FEKO [3], was investigated for our test configuration. Corroboration was demonstrated under quasi-static conditions through AC breakdown tests (Figure 3).

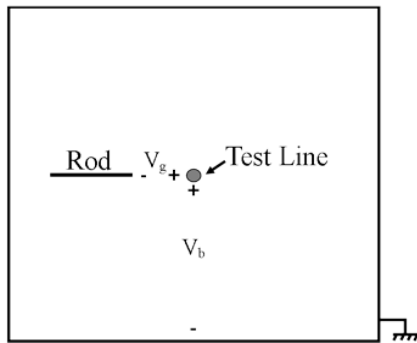


Figure 3: Test environment to calibrate FEKO, the CEM package.

The conductor potential and the conductor-UAV air gap potential at the instant of breakdown are determined through two tests. The conductor potential, V_b , is determined by inducing flashover in the primary gap for the setup in Figure 3. To determine the primary gap potential, V_g , at the instant of breakdown, the rod is

electrically connected to ground and the AC flashover is induced once again.

To establish confidence in the CEM package, the relationship between V_b and V_g is examined under full-scale conditions. The breakdown voltage, V_b , is injected onto the test line with a voltage port in FEKO. The gap voltage, V_g , is then checked with a near-field request. The results documented in Table 1 show agreement to within 2 %.

TABLE I
CEM AND MEASUREMENT COMPARISON OF POTENTIALS
FOR OUR SETUP IN FIGURE 3

	Measured	FEKO Prediction
V_b [kV _{pk}]	210	210
V_g [kV _{pk}]	161	164

The verified FEKO model may now be used to predict the UAV's potential in space. The ratio of the UAV's potential to the conductor potential gives the geometric factor. Figure 4 shows the geometric factor as a function of distance in the primary gap.

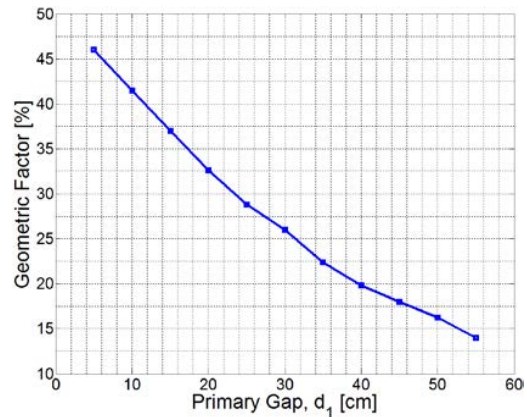


Figure 4: Derived geometric factor for the UAV in our setup.

The geometric factor (Figure 4) is used as an input into Rizk's model for streamer breakdown. The critical streamer field gradient, E_{crit} , may now be determined by fitting Rizk's predicted CFO to our measured CFO values. A combination of the primary, d_1 , and secondary, d_2 , gap breakdown voltages are used in Rizk's model to determine the minimum breakdown voltage of the system. Streamer breakdown in the primary air gap, U_{S1} , is given as [2]

$$U_{S1} = (E_{crit1} \cdot d_1) / (1 - k_0) \quad (1)$$

The geometric factor, k_0 , is taken from Figure 4 in Section 3 at each sampled primary gap distance, d_1 . The breakdown of the secondary gap, U_{S2} , occurs at [2]

$$U_{S2} = E_{crit2} \cdot d_2 \quad (2)$$

A comparison of (1) and (2) is made to determine the minimum breakdown voltage, U_b , as a function of the

primary gap distance. This is shown in Figure 5. The CFO is found three standard deviations above U_b due to the normal distribution of the phenomenon:

$$CFO = U_b / (1 - 3\sigma) \quad (3)$$

It is suggested in [2] that a 5 % standard deviation be used for switching impulse breakdown.

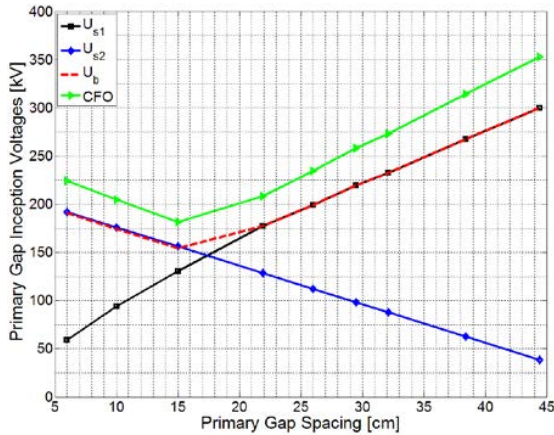


Figure 5: The CFO is derived from consideration of the breakdown in both air gaps.

The E_{crit} values in (1) and (2) are determined by fitting the CFO prediction in Figure 5 to our measured CFO values (Figure 6).

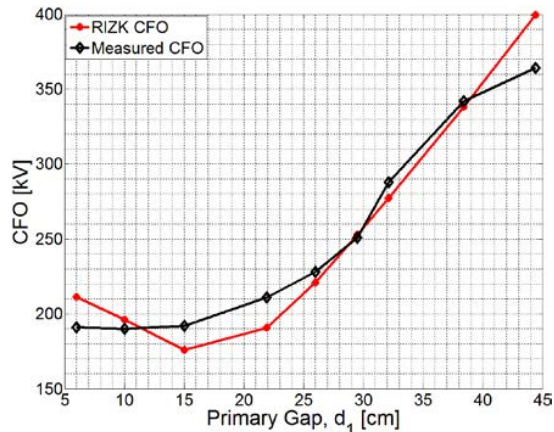


Figure 6: E_{crit} is derived by fitting Rizk's model to our measurements.

Rizk's streamer prediction model is fitted with an $E_{crit1} = 550$ kV/m and an $E_{crit2} = 430$ kV/m. Only E_{crit1} is pertinent moving forward, as only the primary gap is of interest. With the input parameters defined, MAIDS alongside a 132 kV OHTL may now be described.

4. 132 kV MAID PREDICTION

After redefining the geometric factor for a single air gap (conductor-UAV), the methodology in Section 4 is followed to determine U_b for the UAV alongside a 132 kV phase conductor. The breakdown voltage prediction

for a switching impulse with a critical front time is depicted in Figure 7.

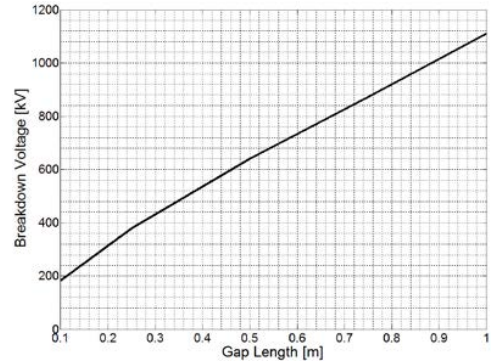


Figure 7: Predicted breakdown voltage alongside a phase conductor of a 132 kV OHTL.

The basic switching level (BSL) of a 132 kV OHTL is specified as 650 kV in [4]. This is the maximum expected switching transient on a 132 kV line. The streamer breakdown prediction in Figure 7 shows that a clearance of approximately 0.6 m is required near a 132 kV OHTL at the BSL. A safety factor (left to the user to determine) should also be included to account for inadvertent positional drift of the UAV. Consequently, the clearance is not a concern for our measurements on the 33 kV OHTL, and is rather governed by our confidence in the UAV positioning.

5. LINE RADIATION AND MEASUREMENT SYSTEM

To induce OHTL radiation, a spark gap was attached to a live line. The spark gap is set to 2 mm which leads to approximately 3 sparking pulses per 50 Hz half cycle. The spark gap was clamped onto the centre phase conductor of a short test line at the SKA support base near Klerefontein (Figure 8). The 1.5 km line is supported by wooden poles at a height of approximately 12 m.

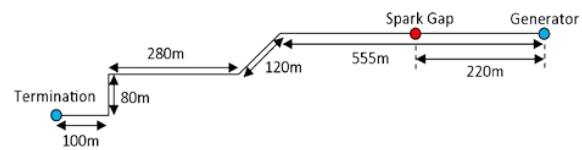


Figure 8: The 22 kV power line schematic.

Currents are injected onto the line by the sparking action, which then radiate as they propagate. A UAV with an on-board measurement system (Figure 9) is used to monitor the OHTL radiation.

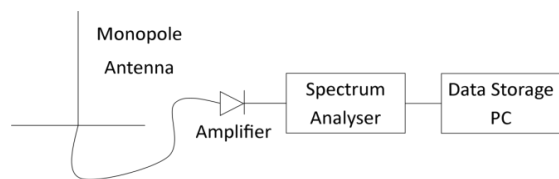


Figure 9: On-bard aerial measurement system

A 239 MHz stub antenna was used to detect the power line radiation. The antenna was orientated at 45° to capture horizontal and vertical polarization components. The measured signal was passed through a low noise amplifier to increase the dynamic range of the system. The measured signal is then sampled by a commercially-available spectrum analyser and stored on a data storage computer.

6. MEASUREMENTS AND SIMULATIONS

Aerial measurements were taken with flights alongside the power line for comparison to FEKO [3], a computational code. The measured electric field (E-field) profile was obtained by removing the antenna pattern gain in post-processing steps. This resulting E-field profile was compared to normalised FEKO predictions along these sampled flight paths (Figure 10).

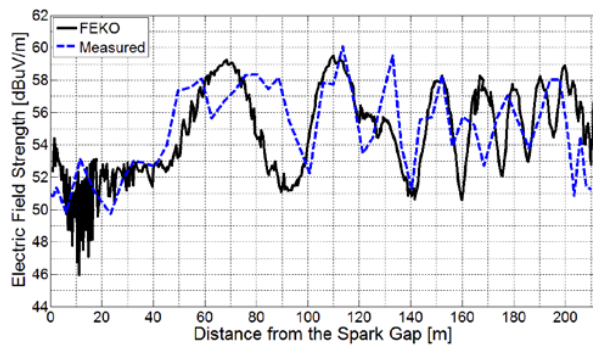


Figure 10: Comparison of the measured and CEM prediction of the E-field profiles.

Good agreement in Figure 11 instils confidence in the CEM model. We now use our FEKO model to examine the radiation characteristics of our test line. A far-field polar pattern is generated at the measured frequency (239 MHz) in Figure 11.

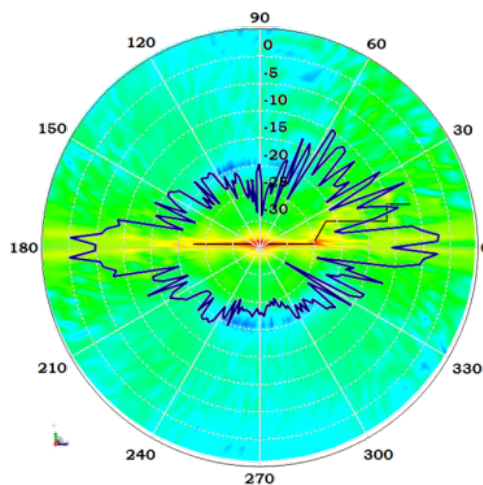


Figure 11: The far field polar pattern at 239 MHz shows end-fire radiation.

It is seen that the power line radiates in end-fire mode. This is consequential for power line layout near radio-quiet zones as well as for inspection techniques.

7. CONCLUSIONS

UAV-specific safe-fly zones were determined for sub-132kV power lines. This aligns with our measurement campaign, as well as future requirements for live-line monitoring. The safe-fly zones were determined through high voltage switching impulse testing and empirical techniques. These techniques serve as a simplified method of predicting MAIDs, as opposed to the resource-intensive testing usually required.

With confidence in UAV minimum approach distances established, aerial sparking measurements were undertaken. A CEM package, FEKO, was validated against these measurements and then used to describe power line radiation characteristics. It was confirmed that power lines radiate in end-fire mode.

ACKNOWLEDGEMENT

The authors would like to thank:

- Omicron Electronics GmbH and Eskom TESP for funding the project.
- Ls Telcom of South Africa for lending us their UAVs and equipment, and for assisting in the aerial measurement campaign.
- Mr. W Croukamp and the workshop staff at the EE Engineering Dept., Stellenbosch, for constructing the cage.

REFERENCES

- [1] *Insulation Co-ordination – Part 2: Application Guide*, IEC 60071-2, 1996.
- [2] F. Rizk, "Effect of Floating Conducting Objects on Critical Switching Impulse Breakdown of Air Insulation", *IEEE Trans. Power Del.*, Vol. 10, No. 3, pp. 1360-1370, July, 1995.
- [3] FEKO Suite 6.2 (www.feko.info), EM Software & Systems – S.A. (Pty) Ltd, PO Box 1354, Stellenbosch, 7599, South Africa.
- [4] *Overhead Electrical Lines Exceeding AC 45kV – Part 3: Set of National Normative Aspects*, EN 50341-3-9, 2001.

FIELD EXPERIENCES WITH THE UKZN POWER LINE INSPECTION ROBOT

T. Lorimer* and T Rowell*

* Dept. of Electrical, Electronic & Computer Engineering, King George V Avenue, University of KwaZulu-Natal, Durban, South Africa E-mail: Lorimer@ukzn.ac.za, Rowell@ukzn.ac.za

Abstract: Thousands of kilometres of overhead power lines are inspected for damage, so that maintenance may be carried out on that damage before faults occur. In an attempt to make the inspection process more efficient, a number of research teams around the world have designed and built power line inspection robots. Many of these machines do not progress beyond the laboratory prototype phase. A team at The University of KwaZulu-Natal has been developing such a robot, but has progressed to the level of field testing their device. This paper describes those tests and some of the practical challenges involved.

Keywords: Mobile Robotics, Field Robotics, Overhead power line inspection

1. INTRODUCTION

Existing methods of overhead power line inspection involve the inspector moving along the line, either by ground (foot) or by air (helicopter). As a result of the time taken and fuel used, these methods of inspection are expensive. It is also sometimes physically and logistically difficult to traverse the terrain along the right-of-way.

The cost and inconvenience of sending out personnel to inspect the lines may be reduced by using unmanned inspection vehicles designed to travel along the lines. The last decade has seen a large increase in research and development around these power line inspection machines.

Flying alongside, or rolling on the line, are the two reasonable methods of locomotion for a power line inspection machine. The University of KwaZulu-Natal's (UKZN's) power line robot was chosen to be of the rolling type, since rolling along the line offers several advantages over flying: greater efficiency, larger payload capacity, and a wider scope for inspection (due to being in direct contact with the line).

There are two major technological challenges for rolling machines to overcome. One is negotiating the obstacles they encounter, such as spacers, dampers, suspension clamps, and jumper cables (jumpers are slack cables that connect two tensioned spans on either side of a strain tower). The other challenge is to ensure robustness in the presence of strong electromagnetic fields around live lines.

The purpose of this paper is to discuss the testing that the power line inspection robot has undergone in the face of these two challenges. Most importantly, the experiences in field testing have revealed many smaller challenges around operability and robustness, and these practical difficulties are also described. Whilst they are not difficult engineering challenges, these minor problems

together can render a complex system almost unusable, and therefore must be considered.

2. DESCRIPTION AND PURPOSE OF TECHNOLOGY

To overcome obstacles, the machine must have sufficient degrees of freedom. UKZN's power line robot has two arms connected together serially by a set of three joints. On the unconnected end of each arm there is a gripper that the power line may fit into. The gripper uses a set of wheels as jaws to clamp the line. The robot is capable of holding the line with one gripper and manoeuvring the other gripper around in space with the arm joints. In this way, the robot may reach around, and grip the line beyond an obstacle. A full description of the robot is provided in [1].

At this stage, UKZN's power line robot is actually a remotely operated vehicle, capable of executing predefined motions. Chiefly, however, it is the task of a ground-based operator to control the robot. He does this through a base-station connected wirelessly to the robot, which receives telemetry from, and transmits commands to, the robot. There are a number of cameras on the robot directed at the line the robot is on, and the feeds of these cameras are also relayed to the base-station so that the operator may be aware of the robot's surroundings.

Overall, the mass of the robot is 20 kg, and it may be relatively easily handled by linemen. The small mass is operationally beneficial, since the robot may be deployed without the need for heavy machinery. Indeed, as shown in [4], it is possible to deploy an inspection vehicle onto a live line using an arrangement of insulated rods and rope directly from a tower. A variation of this method of deployment has been adopted by the UKZN team, as shown in Figure 1, where a hot stick is used as a bridge between the tower and the line, on which the robot may traverse.



Figure 1: Insulated rod used as bridge for deployment

An early strategic decision was taken to design the robot exclusively for inspection tasks (as opposed to physical maintenance performed by such machines as in [2]), and the main payload is to be the CoroCAM multispectral camera as described in [3]. The CoroCAM enables views of infrared, visual, and ultraviolet spectra, and weighs 2.5 kg.

The robot is required to match and improve on the inspection detail achievable by current inspection methods. In addition to using the situational awareness cameras for navigation as described above, they allow for a detailed view of the conductor and line hardware. There are cameras mounted to each gripper, and these are particularly useful, as when a gripper is detached from the line, its camera may be moved around to attain different views of hardware, similar to the multipurpose arm described in [2]. Due to the cameras' proximity with the line, more detail is acquired than is possible when viewing from a helicopter or from the ground.

3. HIGH VOLTAGE EXPERIMENTS

The robot would be most useful if it is possible to deploy on live power lines. To this end, high voltage (HV) experiments have been carried out in laboratories at the University of Witwatersrand and at the University of KwaZulu-Natal. Two types of experiments were carried out: the first with the robot placed on an insulated rod that was attached perpendicular to the energised conductor, with the robot driving towards the conductor as shown in Figure 2, and the second with the robot placed on the conductor, with the conductor then energised.

The two setups simulated the situations that the robot encounters in the field, namely the deployment from the tower onto a line (as shown in Figure 1), and driving along a line. For both experiments the conductor voltage was 100 kV.

The team at UKZN has developed two prototype line inspection robots, the first being a proof of concept, and

the second being a field-ready machine. Prototype 1 was used for initial HV testing.

For the tests, several minor changes were made to the electronics on the robot to ensure that it would function in the HV environment. Firstly, varistors were connected between the terminals of the motors, as well as from the terminals to ground. A varistor was also placed between the supply rails. Should arcing have occurred to the windings of the motors, the connected varistors would clamp the winding voltage to safe levels in order to protect the drive electronics. Secondly, high-value resistors were placed between the motors' terminals and ground to prevent arcing when a motor was not switched on (the terminals would be otherwise floating). Finally, the ground of the electronic system on the robot was tied to the all-conductive structure of the robot so that there would be no potential difference between the structure and electronics.

A high-resistance probe was fitted to the front gripper of the robot to provide a definite arcing point when approaching the conductor for the first experiment, shown in Figure 2. The resistance of the probe was to limit the inrush current during arcing. AN arc length of approximately 200 mm was recorded when the conductor was at 100 kV. The low break-down was attributed to the sharpness of the end of the probe, together with the experiment being done at altitude (in Witwatersrand).

In terms of managing the electrical field, the electronics and wiring were electrically shielded, using conductive enclosures that were rounded on the outer edges, as well as conductive mesh. For the most part, the rounded edges on the enclosures limited the electric field strength and so limited corona discharge. It was evident, however, that even small seams in the structure of such enclosures would generate corona if they were in the outer limits of the field, as shown in Figure 3.

The robot functioned normally during both experiments.



Figure 2: Prototype 1 during conductor approach

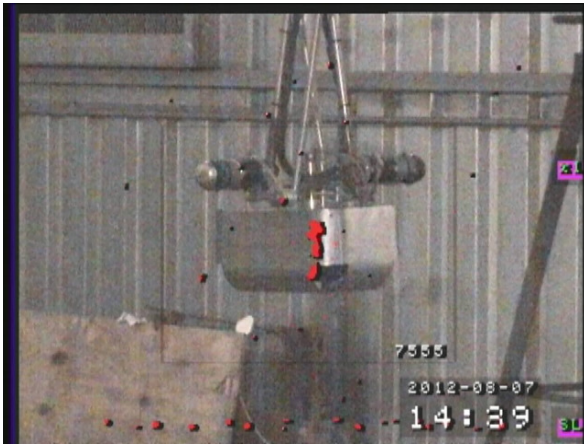


Figure 3: Corona discharge around edges of plate join

Experiments similar to those described above have been carried out at UKZN, using Prototype 2. For several of the conductor approach carried out, the resistive probe was left off the machine while arcing occurred. This caused malfunctions in the electronics and in the communication link between the robot and the ground station, although no permanent damage occurred. The robot functioned correctly with the probe fitted during arcing, which indicated that inrush current indeed needed to be limited. Tests on Prototype 2 are on-going.

4. FIELD EXPERIENCES

Deeper understanding of the challenges around using remotely operated technology on high voltage power lines has been gained through experiences in testing the inspection robot on real power lines. Field work has thus far been limited to out-of-service lines to limit risk. Two tests of the technology are described here: the first on 132 kV structures in Durban, South Africa, and the second on 220 kV structures in Drury, New Zealand. The Durban test took place on 18-12-2012, and the Drury test took place from 17-09-2013 to 20-09-2013. Between tests, the robot underwent significant changes that improved robustness and usability. The authors feel that field testing has increased technology's maturity much faster than what would have been possible from lab testing.

8.1 Durban, South Africa

The Durban field test of the robot took place on the Ottawa-Parlock 132 kV line along the N2 highway in Durban. The line is a double circuit with twin bundle Elm conductors.

A number of logistical and technical problems were experienced during the test. Nevertheless the test was partially successful in terms of validating the fundamental systems of the robot. The test included deployment, negotiating obstacles, and driving along a span. The test

was most useful in highlighting the inadequacies of the robot as-built at the time.

For deployment, the preferred plan was to use a hot stick as a bridge between the tower and the line, where the robot rolled along the stick from the tower to the line, as described above in Section 2. The deployment was poorly coordinated by the UKZN team due to a lack of field experience, and eventually the linemen were instructed to place the robot directly onto the dead conductor.

In terms of the robot itself, two of the three on board cameras were over-exposed outdoors (auto-iris did not work reliably on these cameras), so the operator had limited situational awareness from on-board sensors, and he did not have direct sight of the robot. This made the negotiation of obstacles, such as that shown in Figure 4, extremely difficult. The operator received assistance through a spotter who watched the robot through binoculars, relaying its configuration and suggesting movements.

The wireless communications from the base-station to the robot driving along the line performed adequately: the built-in wireless module in the robot's on-board computer was used, and this was connected to by Ubiquiti SR71 USB modules installed on the ground-station laptop.

One lesson learned from the field experience was that while the inadequacies of the robot during lab testing were quite manageable, in the field they could be nearly crippling. Most of the improvements in the technology came from a number of fairly straightforward hardware and software upgrades, several of which are discussed here.

In order to reduce the chances of a fall from the conductor, safety hooks were built onto the grippers of the robot. The hooks fit around the line and may be engaged in both holding and hanging gripper positions. In software, it is ensured that at least one safety hook is engaged at all times. This small addition to the robot, which was initially overlooked, improves safety in both obstacle negotiations and during line traversal.



Figure 4: Robot during negotiation of a vibration damper

Four new and improved-quality cameras were installed for situational awareness. The positions of those cameras were changed to improve visibility. A camera is mounted to each arm, pointed toward the parent gripper, and a camera is mounted to each gripper, pointed toward the line. The layout provides the operator with sufficient sensing to triangulate the position of the line. The cameras are fitted with high field of view lenses, which provide the operator with both close views of the line, as well as far ahead of the robot so that obstacles may be spotted.

In terms of electronics, a new version of the board that drives the joint servos was designed and fabricated. Much of the work focussed on consolidating the modifications made to the original boards in order to improve robustness. One of the improvements worth mentioning was to increase the reliability of the joint measurements. At the time, joint measurements only came from absolute encoders attached to the output shafts at each joint. If an encoder were to fail (dirt on the encoder disk, loose connection, etc.), it would disable the robot, and this could become critical when on a power line. It was known that a measurement of the joint position was possible by recording the number of hall-effect pulses from the brushless motors driving each joint. Thus, by making the necessary changes in the design, two joint position measurements are now made to increase reliability.

One area that was overlooked due to time constraints ahead of the Durban test was the exposed electronics around the bottom of the robot. A composite box was designed and built for the purpose of protecting the electronics both mechanically and electrically. The structure was built using epoxy resin and woven glass fibre laid up on a balsa core. Aluminium mounting points were epoxied into the box. To provide shielding from the electric field in future deployments, conductive paint was applied to the box. The paint connected the surface of the box to the metal mounting points, which in turn connected to the robot structure.

The box also provided strong mounting points for batteries and inspection cameras. Fans mounted to the inside of the box, with filtered vents on the opposite side of the box, provided cooling for the on board computer, power distribution board, and batteries.

Disassembly of the robot during troubleshooting was difficult due to the wiring loom routing through joints on the robot. While the original routing was most efficient in terms of space, it effectively tied the robot structure together. The wiring layout was redesigned, such that the loom exited out of the robot structure ahead of each joint, and was routed through a flexible external conduit (that was electrically shielded with braiding). Strategic points in the wiring loom were made pluggable, such that the major structural components on the robot could be

detached mechanically and electrically from the rest of the robot, when needed. The robot complete with upgrades, is shown in Figure 5.



Figure 5: The upgraded robot being winched to the line

8.2 Drury, New Zealand

Operations over the 4 days in Drury took place on the lowest phase of the Huntly-Otahuhu circuit 220 kV line. The line is a double circuit with twin bundle Zebra conductors. The circuit used for deployment was out of service at the time. The neighbouring circuit was live.

The initial work on site involved the linemen familiarising themselves with the technology, the hot stick set up, and an attempt at deploying the robot onto a jumper cable. The live line team were well prepared to deploy the robot, due to their tasks being clearly laid out by a user manual that was prepared ahead of the test, as well as the instructions provided on the day. The linemen performed professionally and they successfully set up the hot stick between the tower and jumper cable as planned, as was shown in Figure 1.

There were several unknowns in deploying the robot onto the jumper cable (and not onto the main line as was originally intended for the deployment scheme), and these unknowns would only be realised in the field. Unfortunately, the level of slack in the jumper cable was too great for the robot to grip the line adequately and the method had to be abandoned for the remainder of the test. (Relocating to the suspension tower downrange, where the main line was accessible, was not possible.)

From then, deployment onto the dead line was carried out by two linemen in a bucket truck. A hoist attached to the main line was used to pull the robot up to the awaiting linemen, who would then hook the robot onto the line.

Much time was spent finding and fixing minor faults on the robot over the first two days. These included such things as shorting drive motor wires damaged during transit, and interference in the camera feed caused by lack of shielding.

At the test, the reliability and robustness was adequate for carrying out a jumper cable negotiation: the most difficult operation that the robot would have to perform. This involved climbing onto, driving down and up, and then climbing off of, a jumper. The operation of climbing onto the jumper is shown in Figure 6. A safety tether was connected from the robot to the main line during the manoeuvre. To the author's knowledge, the UKZN robot is only the second of its kind to perform such a manoeuvre. Climbing the jumper proved that perhaps the greatest technical challenge that a rolling power line inspection robot would encounter, may be overcome.

The situational awareness cameras were of utmost importance in controlling the robot during obstacle negotiations. The cameras relayed the necessary information, as shown in Figure 7, to the ground-station, which the operator could then use to navigate the robot. They also provided a close view of the line and hardware, which may be used for visual inspections in future deployments.

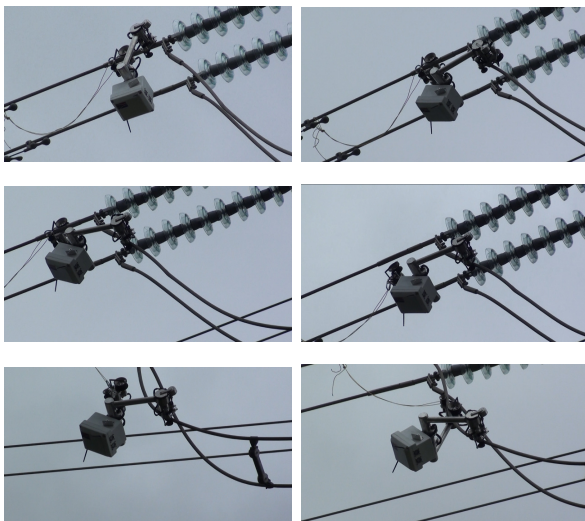


Figure 6: Sequence for climbing onto jumper cable

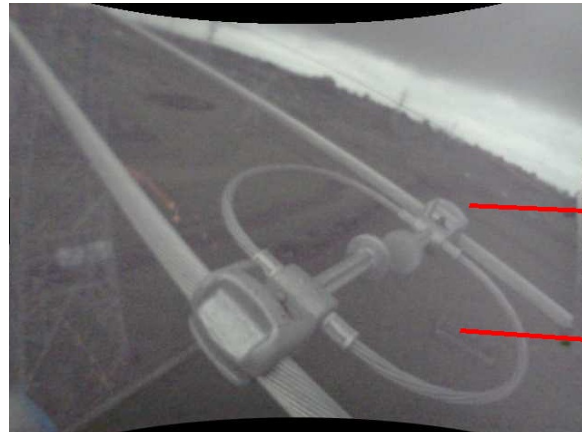


Figure 7: Camera feeds from gripper camera (above) and arm camera (below).

15. CONCLUSION

The objective of testing the power line inspection robot was to find any shortcomings in the system. It was also proved during those tests that it is possible for a rolling robot to overcome the greatest technical challenges: of negotiating all obstacles types, and of surviving in the high voltage (HV) environment. The field tests on overhead lines were particularly useful as they revealed the largest areas in which development was/is required.

The paper described HV testing and the changes made to the robot in order to survive those tests. It went on to discuss two tests on real overhead power lines, as well as the updates necessary on the robot to improve robustness and operability.

16. ACKNOWLEDGEMENTS

This project was partially funded through Eskom Contract 4600011734 and the Eskom Tertiary Education Support programme. The UKZN team is extremely grateful for the support of Nishal Mahatho of Eskom since the inception of the project.

Duma Mhaule of Ethekewini Electricity organised the field testing in Durban, and Andrew Renton organised the demonstration in Drury, New Zealand. The people and the organisations involved in making the field deployments possible, brought great value to the project, which the UKZN team is deeply thankful for.

Hugh Hunt and Ken Nixon of Wits University, as well as Andrew Swanson of UKZN, provided expertise in carrying out high voltage tests, and this is greatly appreciated by the UKZN team.

17. REFERENCES

- [1] T. Lorimer and E. Boje: "A simple robot manipulator able to negotiate power line hardware", *Proceedings: 2nd International conference on applied robotics for the Power Industry*, Zurich, pp. 120-125, September 2012.
- [2] N. Pouliot and S. Montambault: "LineScout Technology: From Inspection to Robotic Maintenance on Live Transmission Power Lines", *Proceedings: International conference on Robotics and Automation*, Kobe, pp. 1034-1040, May 2009.
- [3] R. Stolper, J. Hart, and N. Mahatho: "The Design and Evaluation of a Multi-Spectral Imaging Camera for the Inspection of Transmission Lines and Substation Equipment", *Proceedings: Insulator News & Market Report Conference*, Hong Kong, 2005.
- [4] P. Debenest and M. Guarnieri: "Expliner - From Prototype Towards a Practical Robot for Inspection of High-Voltage Lines", *Proceedings: 1st International Conference on Applied Robotics for the Power Industry*, Montréal, October 2010.

IMPLEMENTATION OF A ROTOR ANGLE MEASUREMENT TECHNIQUE USING SYNCHROPHASOR TECHNIQUES – PRELIMINARY INVESTIGATIONS

BWD Berry*,**, MA Edwards* and KJ Nixon**

* Operations Planning, Eskom Transmission, Corner of Lake and Power Roads, Germiston, 1400, South Africa E-mail: brian.berry@eskom.co.za, armien.edwards@eskom.co.za

** School of Electrical and Information Engineering, Private Bag 3, Wits 2050, South Africa E-mail: ken.nixon@wits.ac.za

Abstract: All power systems are prone to electromechanical oscillations between generators which can become unstable under certain conditions. This instability can have catastrophic consequences such as plant damage or partial blackouts. It is therefore important to monitor these oscillations and ensure that the risks are mitigated through corrective operational actions done by the power system operators. Whilst this behaviour can be observed in the generators' terminal voltage phase and magnitude, the internal rotor angle (load angle) of a synchronous machine is useful for understanding the true severity and interaction of electromechanical oscillations in a power system. There is a proposed method of measuring the rotor angle using both a Phasor Measurement Unit (PMU) on the machine voltage terminals and a KeyPhasor which is a standard installation on most large generators. This research aims to determine the accuracy of such a method within a laboratory environment. The importance of monitoring rotor angle over wide areas is explored and the test environment is discussed in detail including the use of a PMU model constructed in Simulink and the results of various tests are presented and analysed.

Keywords: Phasor Measurement Unit (PMU), Wide Area Monitoring System (WAMS), synchrophasor, power system stability, IEEE C37.118, rotor-angle, Simulink, KeyPhasor

1. INTRODUCTION

The modern era of power delivery is faced with many challenges due to decreased reserves, increased use of renewable generation, Flexible Alternating Current Transmission System (FACTS) devices, and changes in customer/load behaviour. In order to manage the risks introduced by these challenges, it is important to have near real time observability of the health of the power system [1]. Synchrophasor technology provides high resolution, accurate measurement techniques which are useful for power system monitoring. Whilst Phasor Measurement Unit (PMU) metrics used over a wide area can show the interactions between synchronous machines, a direct rotor angle measurement could show these phenomena in a more reliable and quantifiable manner. Both the PMU standard of China and the current IEEE standard refer to a method of measuring the rotor angle by means of a KeyPhasor [2,3,4]. Whilst this is mentioned, it has not been explored or documented adequately in practice. This paper details how the rotor angle is measured and tested using a PMU model created in Simulink to monitor a miniature synchronous generator under several operating conditions.

The structure of this paper is as follows: a brief overview of synchrophasor technology and rotor angle measurement techniques is presented then the general approach to this research is described. This is followed by an overview of the test environments, the methodology used and preliminary results. Finally, recommendations for further work are listed and conclusions are provided.

2. PMU MEASUREMENT TECHNOLOGY BACKGROUND

One of the key benefits of PMU measurement technology is the use of highly accurate GPS timing to measure phase angle which can be compared over a wide area. This is done in the following way: the GPS time is used to construct a time reference (this is essentially the same over a wide area due to the high accuracy of GPS timing). This time reference is transmitted to the PMU via a 1 Pulse per Second (PPS) signal which is used to define the start of each second. The phase angle is then measured as the angle difference between the start of the second and the peak of the wave as shown in Figure 1 [1].

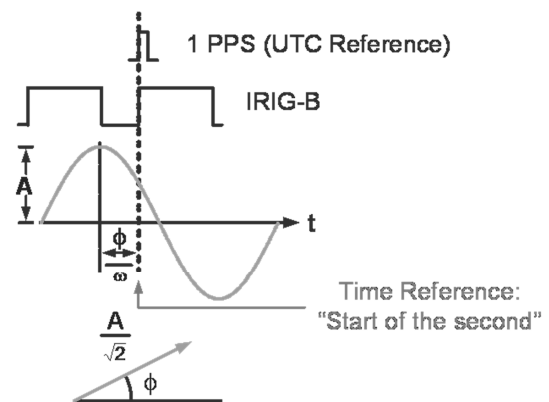


Figure 1: Phase angle measurement using a GPS time reference via the 1 PPS signal

This time reference can then be replicated over each sample so that a relative angle can be calculated per frame. Therefore if the voltage is at synchronous frequency (i.e. 50 Hz) and the frame rate is a factor of this frequency (i.e. 10, 25 or 50 Hz) then the phasor would remain stationary. However if the frequency of the voltage signal is off nominal, the phasor would then rotate at a speed of $f_m - f_n$ where f_m is the measured frequency and f_n is nominal frequency [1,4].

This technique of phase angle measurement allows for the comparison of angles of a wide area since all PMUs share the same time reference. Combining this measurement with high resolution reporting (up to 50 frames a second), makes this data extremely useful for observing a power system's dynamic health [1].

4. ROTOR ANGLE AS A POWER SYSTEM METRIC

4.1. Benefits of the Rotor Angle Metric

Angular stability in a power system refers to the system's ability to return to equilibrium (synchronism) after large disturbances (transient stability) or oscillatory behaviour (small-signal stability). These phenomena are excited by deficits between electrical and mechanical power which inherently alter the rotor angle. Rotor angle is therefore a metric that is fundamental to understanding power system stability [5].

Whilst the terminal voltage angle of the synchronous machine is strongly related to the rotor angle, this changes under disturbed conditions and is also dependent on the voltage support surrounding the machine. Rotor angle which is determined from the physical position of the rotor represents a more mechanical metric and therefore shows the stability phenomena in a more fundamental, independent and predictable manner hence the desire to measure and use it directly in Wide Area Monitoring System (WAMS) applications.

4.2. Rotor Angle Measurement

There are two common methods for measuring rotor angle: the first method estimates the rotor angle position from the terminal voltage and an equivalent model of the generator, the second method is done via physical measurement of the rotor relative to space. The preference is to use the physical measurement since models inherently contain errors due to the assumptions used. These errors are particularly evident under dynamic conditions [2,4].

As per Annex F of IEEE C37.118.1-2011 standard and other sources, there is a method for determining the rotor angle of a synchronous machine by using what is known as a KeyPhasor pulse [2,3,4]. A KeyPhasor pulse is simply a pulse which is sent once per electrical revolution of a synchronous machine's rotor. This is typically measured using a stationary electromagnetic sensor on the stator

which pulses each time a slot (or ridge) on the rotor passes it. The number of slots is equal to the amount of poles on the machine therefore allowing for one pulse per electrical revolution, i.e. ± 50 PPS for a 50 Hz system [6]. When aligning this pulse with the 1 PPS signal from the GPS used to synchronise Phasor Measurement Units (PMU), the rotor position relative to time can be determined (angle α in Figure 2). By first observing the behavior of the generator under no load conditions, angle γ can be measured because at these conditions the terminal voltage is approximately equal to the excitation voltage. As seen in the bottom chart of Figure 2, once the machine is loaded, the rotor angle ($\delta = \alpha - \gamma - \beta$) can be determined since β is measured by the PMU and the other angles were determined during the no load condition.

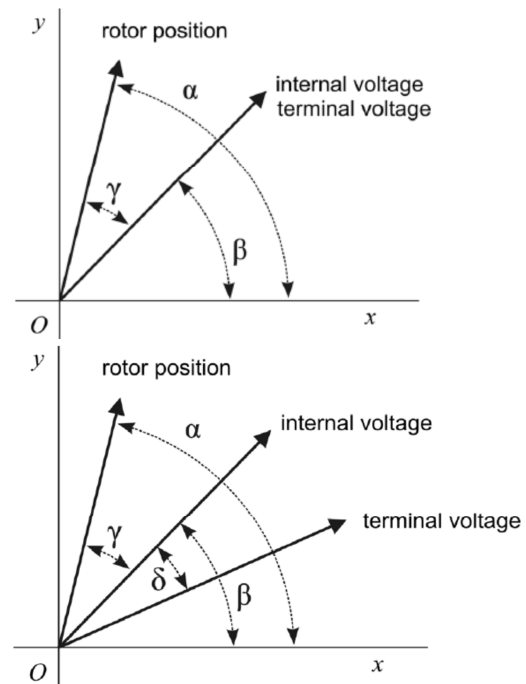


Figure 2: Top: Rotor position phasor diagram under no-load conditions, Bottom: Rotor position phasor diagram under loaded conditions [4]

5. PMU PERFORMANCE

The standard which defines PMU performance, known as IEEE C37.118, was revised in 2011 and is divided into two parts, the first (C37.118.1) dealing with PMU measurements and performance and the second (C37.118.2) focusing on the protocol for data transmission [4,7].

The C37.118.1 standard defines an error measurement metric which encompasses both the magnitude and phase error. This is known as the Total Vector Error and is defined as follows.

$$TVE = \sqrt{\frac{(X_r(n) - X_r)^2 + (X_i(n) - X_i)^2}{X_r^2 + X_i^2}}$$

Where $X_r(n)$ and $X_i(n)$ are the measured values, given by the measuring device, and X_r and X_i are the theoretical values of the input signal at the instant of time of measurement [4]. To elaborate, TVE is shown graphically in Figure 3. 1% TVE equates to an operational area within the circle which is contained by a $\pm 1\%$ magnitude and $\pm 0.573^\circ$ angle error tolerance [4].

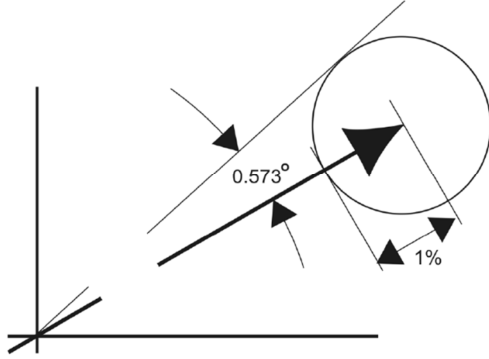


Figure 3: Total Vector Error (TVE) shown visually as an operational area of 1% magnitude and 0.573° angle tolerance [4]

The C37.118.1 also specifies an error calculation for both frequency and rate-of-change of frequency (ROCOF):

Frequency Measurement Error:

$$FE = |f_{true} - f_{measured}| = |\Delta f_{true} - \Delta f_{measured}|$$

ROCOF Measurement Error:

$$RFE = |(df/dt)_{true} - (df/dt)_{measured}|$$

The C37.118-1 standard defines performance in two parts: steady state and dynamic performance. These are clarified further below.

5.1. Steady State Performance

The steady state performance requirements are listed below:

1. Frequency accuracy
2. Magnitude accuracy (voltage and current)
3. Phase angle accuracy (voltage and current)
4. Harmonic rejection
5. Out-of-band interference (0-100 Hz oscillation acceptance/rejection)

5.2. Dynamic Performance

The dynamic performance requirements are listed below:

1. Modulation tests (amplitude and phase)
2. Frequency ramp test
3. Step tests (amplitude and phase)
4. Reporting latency test

6. APPROACH TAKEN

The aim of this research is to define and test an algorithm for measuring rotor angle on large synchronous machines. Since this cannot be done directly on a large machine without having proven the concept, this is first

attempted in controlled conditions. The approach taken is therefore to measure the rotor angle of a miniature synchronous machine using this method under several operating conditions. However, in order to determine the accuracy of this measurement, the true value of the rotor angle must be known. Rotor angle is difficult to measure since it is defined by the relationship between the electrical and mechanical angles. This algorithm is therefore first tested using simulated results from an Electromagnetic Transient (EMT) calculation program (DIgSILENT PowerFactory). In order to do this a full PMU model is created in Simulink as it is necessary to measure both the electric and mechanical angles. Once proven in this theoretical environment, the model is tested in a laboratory environment by using a dSPACE system to read physical measurements from the synchronous generator into Simulink. Whilst rotor angle is not directly measured, the terminal voltages and currents are simultaneously measured by a commercial PMU (which has been tested to comply with the IEEE C37.118.1 standard) [8,9]. The commercial PMU values are then used as the accuracy reference and it can therefore be deduced that the rotor angle measurement is relatively accurate under real conditions. Whilst this is not the best case, it is sufficient to draw conclusions and move to the next phase of testing, which is to implement this system on large generators which have rotor angle measurements that can be used as accuracy references.

7. TEST ENVIRONMENT OVERVIEW ⁽³⁾

7.1. Simulation Environment

DIgSILENT PowerFactory was used to do EMT studies for a small network. Two large synchronous generators were connected via long lines to represent a synchronous machine-infinite bus type system. The instantaneous voltage and current were measured on the generator terminals and the data exported to textfiles. The KeyPhasor pulse was created by monitoring the instantaneous angle between the rotor's d-axis and a stationary reference. Events can then be simulated on this grid, i.e. tripping of lines, step changes to generators/load, etc. The data is then simply imported into Simulink in a format that is readable to the model. An integration step of 0.1 ms is used to mimic the 10 kHz sampling frequency used in the laboratory environment.

7.2. Laboratory Environment

The laboratory environment consists of a 20 kW, 2-pole, synchronous machine rotated by a drive-controlled induction machine. As shown in Figure 4, the stator voltages and currents are monitored by a commercial PMU via voltage and current transformers (CTs and VTs). The commercial PMU is also supplied with an accurate GPS unit which provides a 1 pulse-per-second (1 PPS) signal used to define its highly accurate time reference.

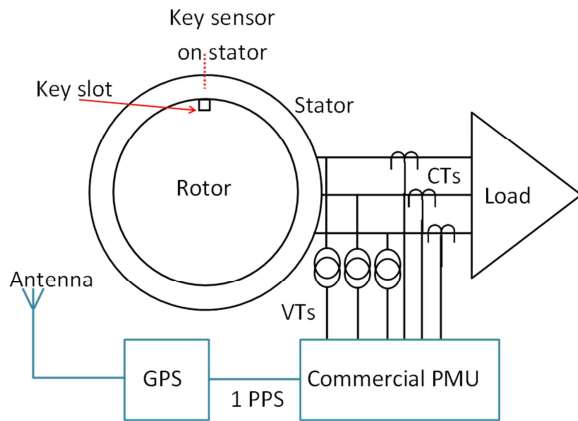


Figure 4: Physical connections from the synchronous machine to the commercial PMU used for accuracy validation

As shown in Figure 5, the PMU model mimics the commercial PMU setup using different CTs and VTs due to the lower input rating of the dSPACE system. The PMU model also uses the 1 PPS supplied from the commercial GPS unit via a fibre to copper converter. Rotor measurements are taken by measuring the field current via a Hall-effect transducer (since it is DC) and the KeyPhasor pulse. The KeyPhasor pulse is created by an electromagnetic sensor whose output changes significantly when a slot on the shaft passes by. In practice there would be a slot for each electrical pole pair, but since this is a 2-pole machine there is only one slot. Figure 6 shows a photograph of the physical KeyPhasor sensor that was made for this experiment.

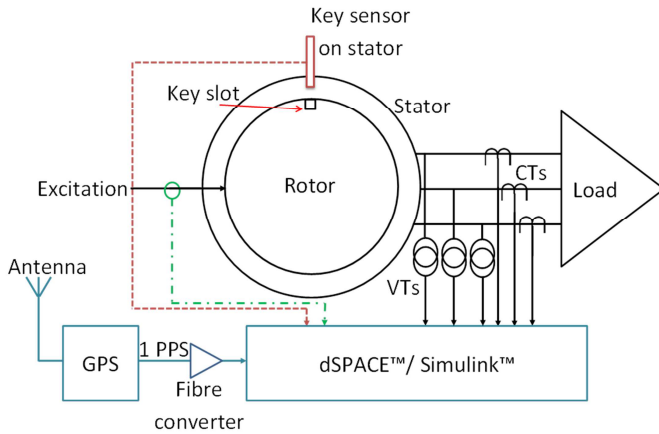


Figure 5: Physical connections from the synchronous machine to the dSPACE system

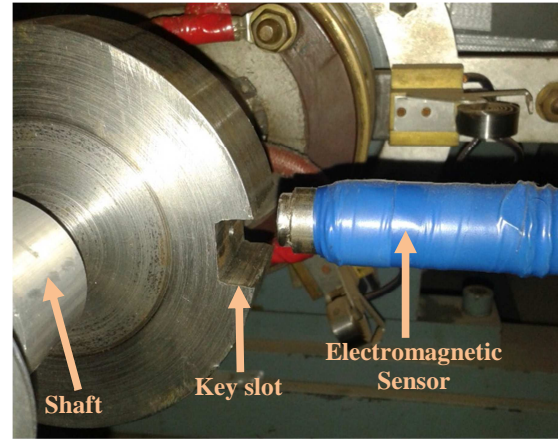


Figure 6: Photo of the KeyPhasor measurement system used on the laboratory synchronous machine

8. PMU MODEL

The PMU model is constructed in Simulink and is made up of functional blocks. Figure 7 shows an overview of the complete PMU model. Five inputs from the synchronous generator are injected into the model via the dSPACE system, namely the 1 PPS signal, instantaneous voltage and current waveforms, DC field current and the key pulse. The input data is scaled to the appropriate primary values and the field voltage (E') is determined based on the open circuit test results. The time module creates a time signal based on the 1 PPS signal (which is used to time stamp the data packets) and also subdivides the 1 PPS signal into a pulse per 20 ms (PP20ms). The PP20ms signal is used as an interrupt to trigger the capturing of the phasor angle, magnitude and frequency. The rotor angle is calculated by subtracting the key angle from the voltage angle. The reason that this is not done internally is because WAMS software allows this to be done over wide areas which means that the physical angles between two different generators can be monitored without the erroneous effect of the terminal voltage angle.

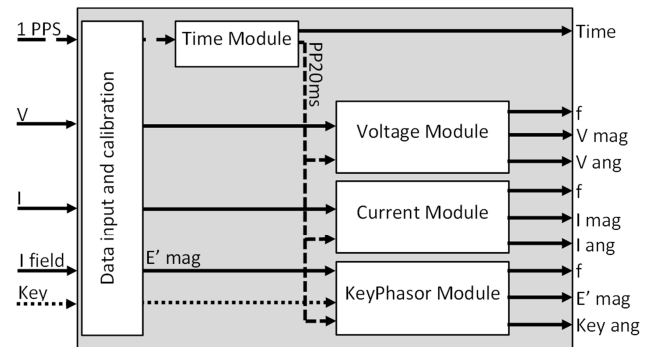


Figure 7: Overview of complete PMU model

Figure 8 shows a high-level breakdown of each phasor module. Whilst this example is shown for the voltage module, the module is almost identical for both the current module. The KeyPhasor has the same components except that the magnitude is simply passed through since it is a DC value. A phase-locked loop is used to track the

frequency and produce an instantaneous angle (ωt). The frequency, angle and magnitude metrics are then compensated because of errors caused from various sources (these errors are explained in the next section). The results are also time shifted to coincide with the correct time stamp since the frequency tracking causes delays to the output signal. The instantaneous values are then captured on the rising edge of each 20 ms pulse. This produces a phasor quantity which is based on the nominal frequency of 50 Hz.

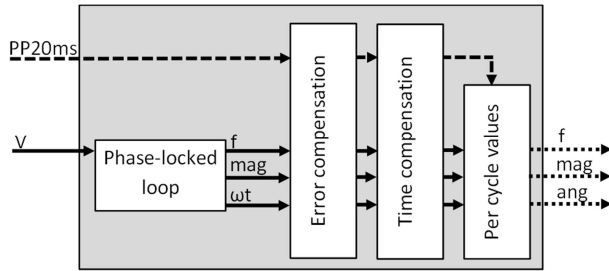


Figure 8: Phasor module breakdown

The time module is shown in Figure 9. The 1 PPS signal is used to create an accurate pulse every 20 ms. However, since the internal clock of the dSPACE unit drifts in time, this error must be compensated. The pulse generator is supplied by a clock source which is created by integrating to a value which is the sum of one and the time drift error per second. This essentially creates a new clock with little drift error. The time formatting block simply formats the clock signal into seconds and fractions of a second which is then directly usable for time stamping the phasor data packets.

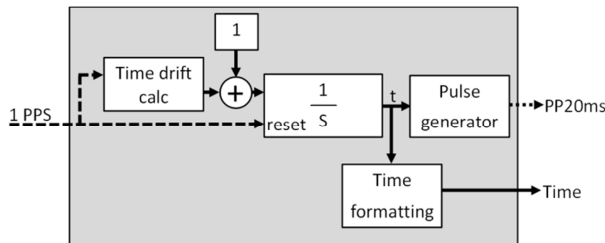


Figure 9: Time module breakdown

9. ERROR COMPENSATION

9.1. Error due to Changing Frequency

When the frequency signal is off-nominal, a static error occurs on the angle. This is compensated by offsetting the angle value a constant value multiplied by the frequency deviation. The constant value is determined by injecting the model with steady state off-nominal frequencies and observing the output error.

Another error occurs when the frequency is changing, i.e. this error is dependent on the rate at which the frequency changes. This error is compensated by determining the rate of change of frequency over half a cycle and correcting with a constant value. This value is found using the same method as the frequency error mentioned above.

9.2. Error due to dSPACE Time Drift

The dSPACE system's internal clock is prone to drift (as with any uncompensated electronic system) which causes inherent angle and frequency errors. This error is determined by counting the amount of samples between each 1 PPS pulse. The sampling frequency is 10 kHz but typically 10006 samples are observed between each 1PPS pulse. This 0.6 ms error equates to an error of approximately 0.03 Hz which is calculated in real time and directly added to the frequency output. The angle is compensated by adjusting the PP20ms pulse to be exactly every 20 ms (based on GPS time).

9.3. Error due to Sampling Resolution

Unfortunately, protection relays typically do not sample at high frequencies since this is unnecessary for their typical applications [10]. This leads to errors because whilst the time drift error can be compensated for every 20 ms, the value is rounded off to the nearest sample. i.e. the dSPACE drifts 0.6 ms every second which equates to a $0.6/50 = 0.012$ ms offset on each PP20ms pulse, if the sample period is 0.1 ms then this error will only be compensated every 10 samples or so. This means that the angle error due to low sampling must be calculated and compensated for in the periods when the error is rounded off.

9.4. Error due to Calculation Delays

The tracking of frequency and angle takes time since a buffer is used in the phase-locked loop. This delay is compensated for by delaying the time stamp value by the buffer length. It is tested by applying a step change to the input and ensuring that the response is not delayed.

10. PRELIMINARY RESULTS

An EMT simulation was executed where no events occur for 5 seconds and then the measured generator's power is stepped by 10 %. This leads to a step change in the rotor angle and a ramp change in frequency.

Figure 10 shows the PMU model's performance for the EMT simulated inputs. The top graph shows that the voltage (blue) and KeyPhasor (green) track the simulated frequency (red) fairly well. The middle graph shows the measured voltage (blue) and KeyPhasor (green) angles and the bottom chart shows the measured (blue) and simulated (green) rotor angle. It is evident from these charts that the algorithm works but is currently very noisy. The initial oscillations shown on the angles are due to the phase-locked loop settling after start-up of the algorithm. Providing more steady state time would eliminate this error.

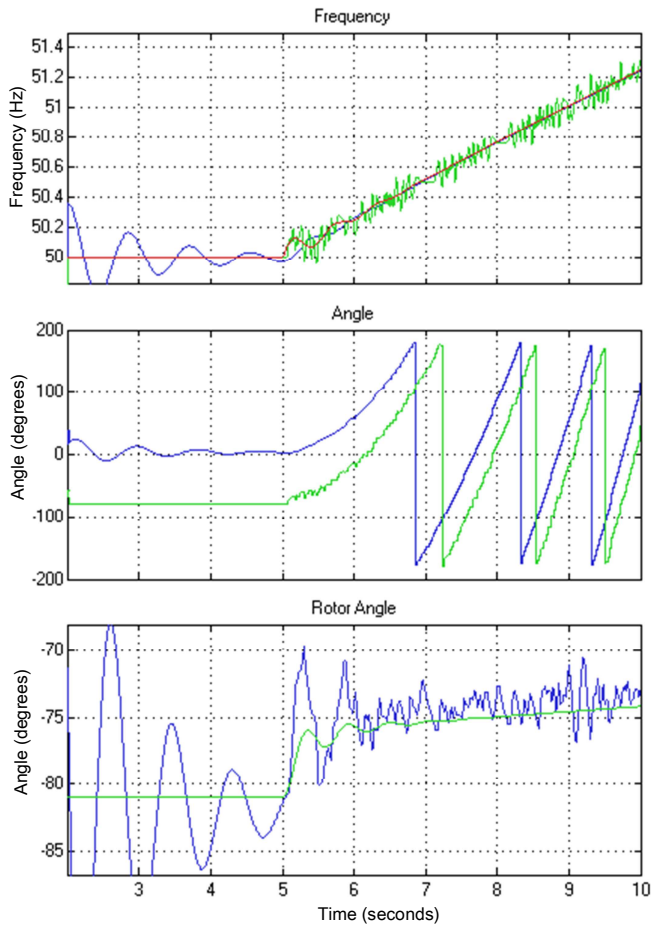


Figure 10: PMU model results from EMT simulation inputs

The PMU model was then moved to the laboratory environment where the miniature synchronous generator was monitored whilst increasing the stator current to approximately 15 A which is around half of the rated output of the machine. Figure 11 shows the errors on the terminal metrics when comparing the commercial PMU and the PMU model. The frequency error is between ± 25 mHz, the magnitude error between ± 0.7 V and the angle error is between 0° and 4° . These equate to a Total Vector Error (TVE) of less than 8% which is much higher than the C37.118-1 requirement.

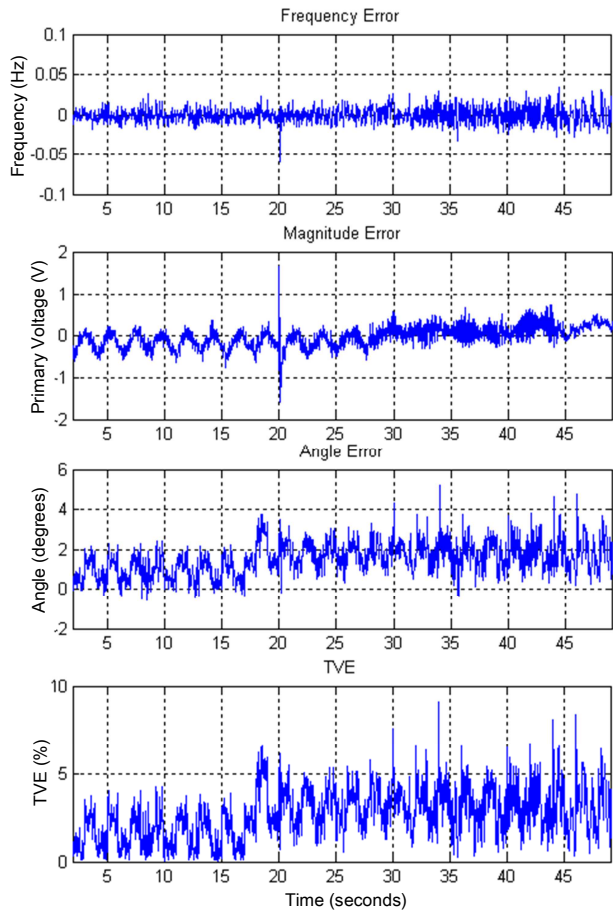


Figure 11: Errors between commercial PMU and PMU model.

Figure 12 shows the test results for when the miniature generator was loaded to ≈ 15 A. The frequency chart shows that both the rotor (green) and voltage (blue) frequencies coincide fairly well. Since the terminal metrics tie up with the commercial PMU, this provides confidence in the rotor angle measurement (shown in the bottom chart). The rotor angle measurement shows an increase of approximately 5° when the machine is loaded to 15 A. Once again these metrics are noisy and therefore require filtering.

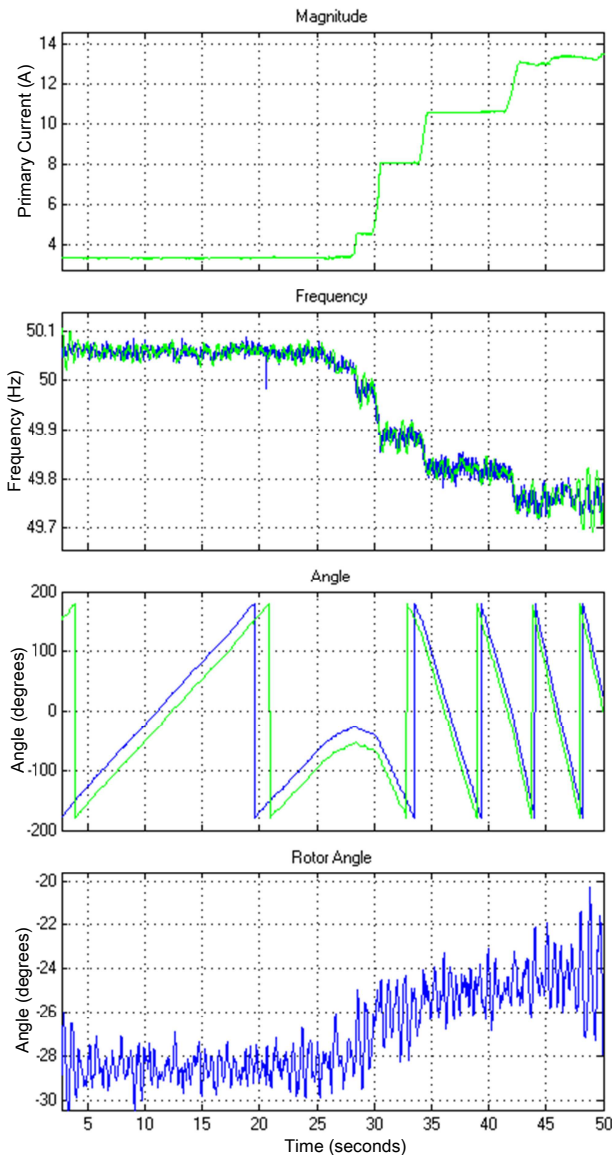


Figure 12: PMU model results from the miniature synchronous machine.

11. FURTHER WORK

It is clear from the results that whilst the algorithm is tracking the metrics, there is much work to be done in terms of improving its performance. The work to be done on the model is broken down as follows:

- *Improve PMU model accuracy*

Attempt to improve accuracy to within 1% TVE for steady state at least. These errors are largely due to low sampling resolution and lack of filtering. A phase-locked loop that functions over several cycles would lead to better steady state performance.

- *Test further with the EMT simulations*

Create more events which have predictable outcomes and off-nominal values. i.e. simulate impedance changes and scenarios with off-nominal frequencies.

- *Test dynamic conditions*

Test the miniature synchronous generator under various conditions particularly dynamic conditions, i.e. step change in load.

- *Implement on large scale generator with a PMU vendor*

The final steps of this project would be to work with a vendor to get this algorithm implemented on a commercial PMU. During development, tests should be done on the relay by connecting it to a physical large synchronous machine.

12. CONCLUSION

The benefits of measuring the rotor angle of synchronous machines have proven this to be a useful metric for power system stability applications. A method for measuring the rotor angle via a KeyPhasor pulse is described and successfully tested in both a simulation and laboratory environment. The work done here reveals the challenges presented when attempting to create a Phasor Measurement Unit (PMU) in practise. Errors due to low sampling frequencies and time drift cause much noise in the resultant signals but these errors can typically be compensated for. The results presented here are somewhat noisy but will be improved with filters and a phase-locked loop with a longer sampling window in future work.

13. REFERENCES

- [1] JS Thorp AG Phadke, *Synchronized Phasor Measurements and Their Applications*, 1st ed., A Stankovic MA Pai, Ed.: Springer Science+Business Media, LLC, 2008.
- [2] ZHOU Jie et al., "Rotor Position Measurement Method for Generator Power Angles," in *The International Conference on Advanced Power System Automation and Protection*, 2011, pp. 2196-2200.
- [3] Jingtao Wu, Ji Zhou, Daonong Zhang, Zhaojia Wang, and ShiMing Xu, "PMU Standard of China," IEEE, 2008.
- [4] Power System Relaying Committee, "IEEE Standard for Synchrophasor Measurements for Power Systems," IEEE Power & Energy Society, IEEE Std C37.118.1™-2011, Dec 2011.
- [5] P Kundur, *Power System Stability and Control*, 1st ed., MG Lauby NJ Balu, Ed.: McGraw-Hill, Inc., 1994.
- [6] Bently Nevada, "Specifications and Ordering Information - 3500/25 Enhanced Keyphasor Module," 2003.
- [7] Power System Relaying Committee, "IEEE Standard for Synchrophasor Data Transfer for Power Systems," IEEE Power & Energy Society, IEEE Std C37.118.2™-2011, Dec 2011.
- [8] B Berry, "Eskom Verification of the WAMS PMU FAT of the 72B Firmware – Steady State Results," Eskom, Oct 2012.
- [9] B Berry, "Eskom Verification of Dynamic Results of the WAMS PMU FAT for the 72B Firmware," Eskom, Oct 2012.
- [10] Bogdan Kasztenny and Mark Adamiak, "Implementation and Performance of Synchrophasor Function within Microprocessor Based Relays," in *Power Systems 2008 Conference*, Clemson, USA, 2008.

OPTIMIZING THE PROPERTIES OF THE OPTICAL CURRENT TRANSFORMER WITH SPECIAL REFERENCE TO FASTER TRANSIENT RESPONSE

N.J. Oosthuysen* and J.J. Walker**

* Department of Power Engineering, Faculty of Engineering and Technology, Vaal University of Technology, Vanderbijlpark, RSA. E-mail: nico@vut.ac.za

** Visiting Professor at VUT and Director – Walmet Technologies (Pty) LTD, Vereeniging, RSA. E-mail: jerryw@vut.ac.za

Abstract: A current transformer is a means of measuring a very large electrical current, converting it to a much smaller current, requiring low power electronics in the display system. The traditional method was based on the electromagnetic principle of an iron ring around the current conductor, supplied with a secondary transformer winding. The latter will deliver a small current directly proportional to the large current, to be displayed by an electronic system. An optical current transformer (OCT) is constructed only by winding an optical fibre cable around the current conductor. The phenomenon where the angle of a polarized light beam, propagating through the optical cable, is deflected when the magnetic flux lines, generated by the large current, are appearing longitudinal in the said cable, are utilized to determine the main current. OCT's are already well developed, but lack to observe a very fast changing transient impulse. This paper describes a research and developing process to solve this problem.

Keywords: Optical current transformer, transient, Faraday Effect, angle of deflection.

1. INTRODUCTION

The basic principle of the electromagnetic current transformer (EMCT) is shown below in figure 1:

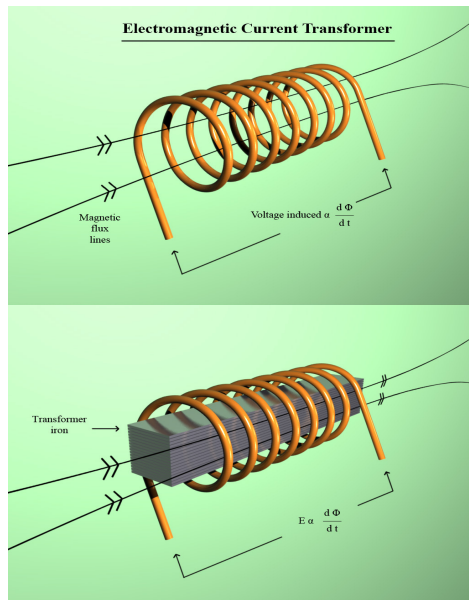


Figure 1: Electromagnetic current transformer in basic form

In principle, the magnetic flux lines are cutting the copper wire at 90°, on condition that the strength of the flux must be busy changing. This means that the EMCT can only operate in an AC environment. The presence of a suitable core, like in the second case in figure 1, makes the coupling factor extremely more effective.

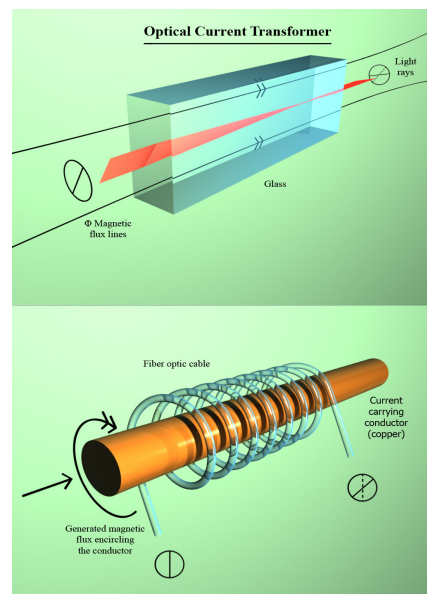


Figure 2: Optical current transformer in basic form

A basic optical current transformer is shown in figure 2. In the top part of figure 2, a polarized light ray is propagating through a piece of glass, and when magnetic flux lines are appearing longitudinal to it, the angle of polarization is being deflected. This phenomenon is known as the Faraday effect.

In the second part of figure 2, it can be seen that the Faraday effect can be utilized as a CT by winding a fibre optic cable around the current carrying conductor, supply the polarized light ray, and detect the angle of deflection at the end of the said optic cable. Note that no core/iron core is required. This is an advantage, and an even more important advantage is that an OCT also detects DC.

2. DETECTING THE ANGLE OF DEFLECTION

The angle of deflection is determined by passing the exiting light ray through a polarized filter, and then detecting the change in intensity.

The normal method is to start zero current with an angle of 90° between the light ray and the polarized filter. Zero current equals zero intensity, and an increasing current means increasing intensity. This method benefits the measurement of large currents, as will come clear in the following explanation.

The purpose of this research and development is to enhance reaction speed on detecting fast impulse disturbance. Therefore, the following alternative method will be evaluated. See figure 3.

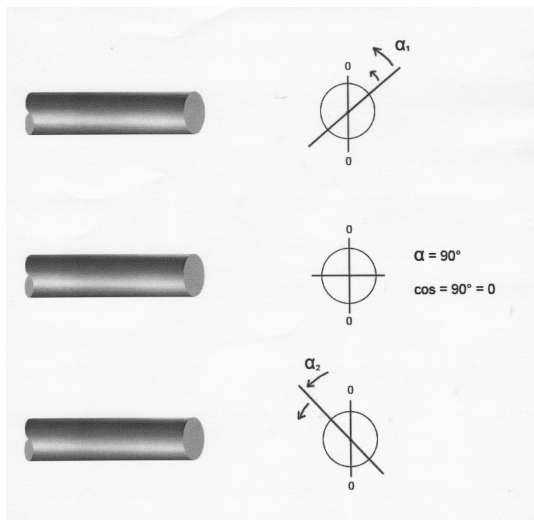


Figure 3: Different methods of detecting angle deflection

Using the principle of maximum brightness for zero current and decaying brightness for increasing current, means faster change in brightness on initial current change, resulting in a quicker detection of an impulse. The electronic system can easily be adapted for this kind of measurement.

3. COMPLETE OCT IN CONVENTIONAL FORMAT

An operating OCT consists of the optical section creating the polarized light ray, the fibre optic cable coil wound around the current carrying conductor, optical sensing, electronic measuring, linearizing section, and digital display, as well as data logging if required.

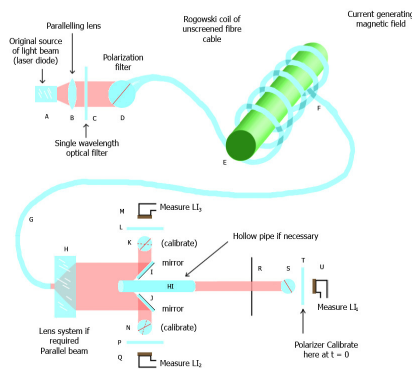


Figure 4: Complete OCT system

There are many ways to create a complete OCT. The researcher compiled the system shown in figure 4.

It is not feasible to give a comprehensive and detailed description of the working of the system in figure 4 in a paper like this. However, the following principles will be implemented to improve sensitivity, as sensitivity is also associated with reaction speed:

3.1: LOSSLESS DIODE

A diode in conjunction with an OpAmp can deliver a perfect diode with zero voltage drop during the conducting phase. A suggested circuit diagram is shown in figure 5:

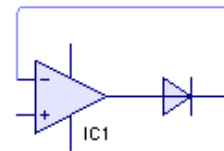


Figure 5: Lossless diode assembly

In figure 4, sections M and Q are actually utilized to determine the “direction” of the angle deflection, whereas section U is the original brightness detector. M and Q will oppose each other, but by preceding the sensors at M and Q by the circuit shown in figure 6, the resulting change in brightness at all points M, Q and U, can be added together, resulting in maximum possible sensitivity.

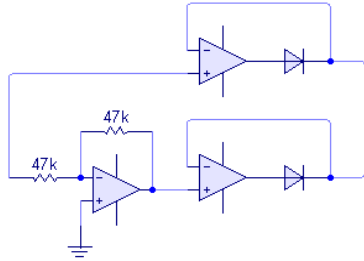


Figure 6: The output of this ideal diode setup will deliver a positive output going out, regardless the polarity of the changing input signal.

3.2: COMPLETE ELECTRONIC SECTION

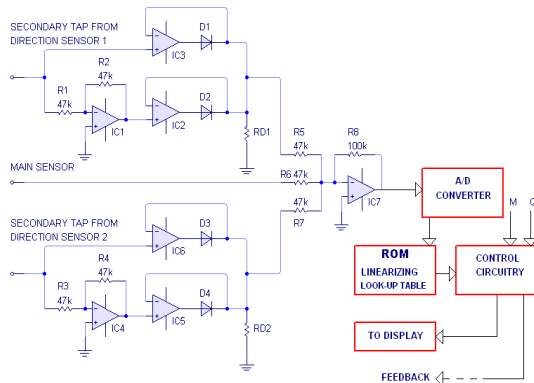


Figure 7: The complete electronic section at the final output

Referring to figure 4, the readings coming from U, M and Q are added together in the summer of IC7 (figure 7 now), and then fed to an Analogue-to-digital converter. Since the output will be proportional to $\cos(\theta)$ to the power a certain number, a linearizing look-up table will be created in a ROM-memory to obtain the final reading. The electronic control can also be seen in figure 7, including the display. A “feedback output” can be used to maintain a preset constant current, in stead of measuring it.

4. ENHANCING THE REACTION TIME IN ANGLE DEFLECTION

“Reaction time on angle deflection in the Faraday effect can be improved by negative feedback, similar in principle as found in analogue electronic amplifiers”.

This is a claim made by the researcher of this project.

A motivation to make this claim, is to refer to “analogy” between analogue electronics and several other disciplines in the engineering world. Two examples will now be discussed:

• Shock absorber of a vehicle

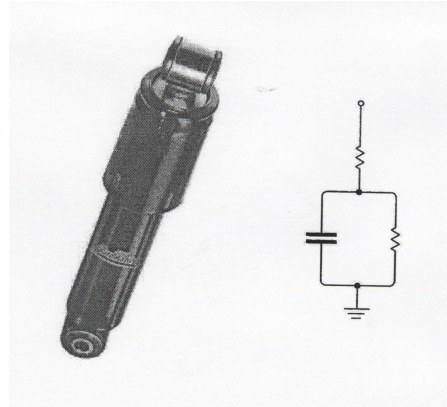


Figure 8: An electronic circuit equivalent of a vehicle shock absorber

In mechanical/electronic analogy, a shock absorber can be converted to a small resistor, in series with a very big capacitor. A very large resistor may be included in parallel to the capacitor.

A transfer function is now developed for the electronic circuit. Sophisticated mathematical methods can now be used to determine values for the components to obtain the correct response to impulses, slow and fast load changes, and any kind of desired properties.

The electronic components are transferred back to mechanical values to design the shock absorber.

• The acoustic world

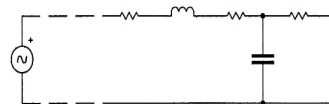
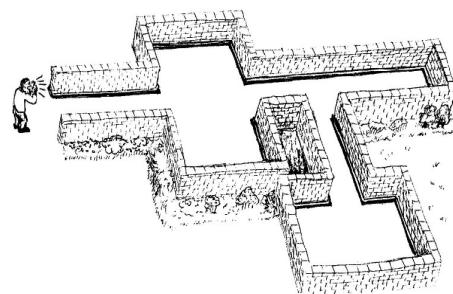


Figure 9: The electronic equivalent of an acoustic setup

In figure 9, a man screams at a certain frequency into a building. Suppose this sound must be reflected much more powerful; than the other frequencies of his voice.

An acoustic expert can convert the setup into an electronic circuit diagram. The passage is a series

resistor, the broadening part of the passage is a series inductor, the room running out of the passage is a capacitor parallel to ground, and similar the passage ends as an external load resistor.

The electronic expert can adapt the values of the components to obtain resonance at the specific frequency, and the new electronic values can be converted back to the acoustic model the make some modifications.

The purpose of all this background will come clear in the following sections.

4.1: NEGATIVE FEEDBACK IN ELECTRONIC AMPLIFIERS

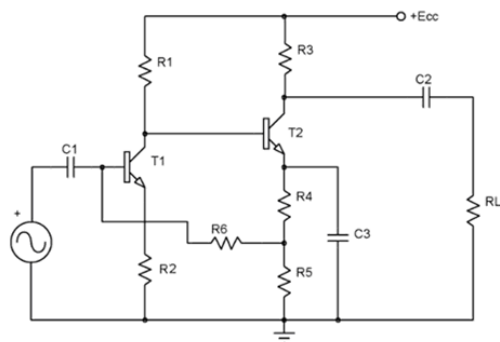


Figure 10: An open loop electronic amplifier

The two transistor amplifier in figure 10 is in open loop configuration. The total voltage gain on the input signal is equal to the product of the gains of each transistor stage. This will be quite a large number, but properties like frequency response and harmonic distortion will be poor.

Suppose the designer consider good specifications as higher priority than gain.

The designer will now apply negative feedback:

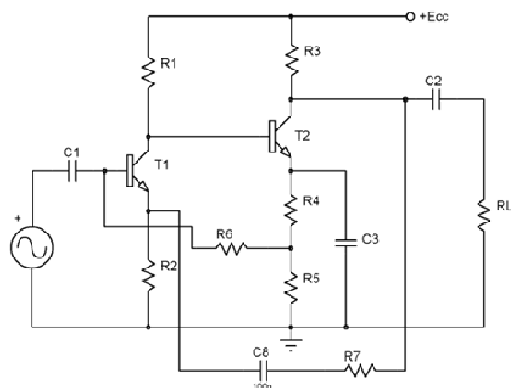


Figure 11: The same amplifier than in figure 10, but equipped with dynamic negative feedback

The voltage gain is now given by (R_7/R_2) . Suppose the original gain, divided by this new gain, is a factor 20. This is called the feedback factor D. Although gain is being sacrificed, properties like distortion and bandwidth (reaction time!) is improved by this factor D.

4.2: THE PHILOSOPHY OF ANALOGY

The researcher will now implement all these foregoing background into his postulation of the possibility of the existence of analogy between the optical world and analogue electronics as well.

There are two ways to make a signal, which is too big for the involved application, smaller:

The first method is to attenuate it, meaning dissipating a certain amount of its energy in a series load resistor;

The second method is to oppose it with an electronic derived signal, with zero energy losses in the process:

► In this second method, certain properties are improved by the so-called feedback factor as mentioned earlier; some properties may be draw-backed; the designer must just choose the correct methods.

► The researcher's philosophy on analogy between any discipline and analogue electronics, is that certain properties can be improved by applying negative feedback to create the "opposing" signal as stated in the second method above, and that includes optical technology.

Such technology has been applied to the measurement of light intensity, but till to date, the researcher could not find any attempt to apply negative feedback in an optical system to enhance the reaction time on the angle of deflection in a Faraday-effect system; researching and developing such technology forms the main part of this thesis; on the contrary, the outcome of intense research and evaluation may prove that it is not possible to accomplish improvement as expected.

Since this research project is in its beginning stage, it is not known how negative feedback on the reaction time in angle deflection in the Faraday effect can be accomplished.

It can be expected that it will require high level technology, and a high degree of meditating, testing, and evaluation.

A final representation of such an optimized OCT is shown in figure 12.

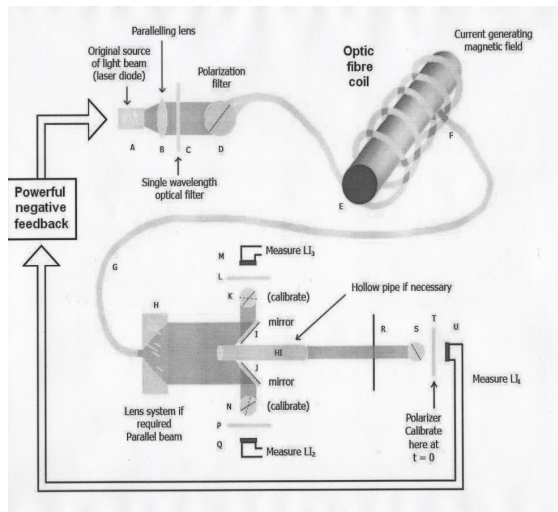


Figure 12: Representation of negative feedback in the optical system

How the negative feedback will be implemented in the system of figure 12, is the research, developing, constructing, testing and evaluating work for 2014. Communication and consulting with manufacturers and users of existing OCT's will be a high priority.

5. OUTCOME OF RESEARCH PROJECT

It will deliver a great feeling of thankfulness if the a positive outcome on this project can make a contribution to the development of optical current transformers, especially in applications where high speed data logging is implemented to assist in investigations where high amplitude short duration impulses caused serious damage in high voltage networks.

6. REFERENCES

- [1] Liehr, Sasha: "Optical Measurement of Current in Power Converters", *M.Sc. Dissertation, University of Stockholm, Sweden*. 2006.
- [2] Mansuripur, M: "The Faraday Effect", published in: *Optics & Photonics News*, 1999.
- [3] Instrument transformers, *Application Guide*, by the manufacturers ABB. Editor: Knut Sjøvall.

DESIGN AND IMPLEMENTATION OF HYBRID POWER SYSTEM CONTROLLER FOR SOLAR-WIND SYSTEM

M Maneveld*, M Nthontho* and S Chowdhury*

**University of Cape Town, Department of Electrical Engineering, Cape Town, South Africa.*

Abstract. Investigating alternatives to energy generation methods which can offer remote areas a source of supply in a cost-effective and efficient manner is crucial for South Africa's citizens. Renewable energy, although unreliable with the unpredictable nature of the weather, is an alternative worth pursuing due to its auspicious results when implemented in a suitable area. On a global scale, with the increase in greenhouse gas emissions, coal-fired power stations which South Africa depends on for energy are seen as a threat to the economy. In order to develop an efficient renewable energy system, the concept of integrating various renewable energy sources with a battery storage unit, forming a hybrid power system, is very popular. This paper investigates the following: wind turbine models, PV model designs and battery storage units. Matlab Simulink is used to model the hybrid power system (HPS). PV, wind and battery models are built and simulated on Simulink. Eight cases were used to test the controller's operation within the HPS. The designed controller was able to select between the most effective resource depending on the weather conditions.

Key Words. Solar PV System; Wind Energy System; Controller.

1. INTRODUCTION

Renewable energy is generally deemed a clean form of energy generation. With the increase in greenhouse gas emissions on a global scale, it is only logical that a solution to this crisis is sought after. Renewable energy, although unreliable with the unpredictable nature of weather conditions, is a plausible alternative. The integration of various renewable energy schemes such as PV and wind energy, prove to be more reliable as a renewable energy scheme, especially with the inclusion of a battery storage unit. With the extension of the grid for remote areas deemed as costly, the idea of implementing a hybrid power system looks more appealing.

This paper investigates how a load can be constantly supplied from a hybrid power system (HPS). That is the task being studied was to find out how to achieve a constant supply from a HPS with the aid of an intelligent controller. The purpose of the study was to design a controller that would monitor the behaviour of the developed HPS model and decide, based on various weather conditions, which source would sufficiently supply the load. The objectives of this paper are therefore to:

- Model and simulate the PV, wind battery hybrid power system in MATLAB Simulink
- Develop a controller in MATLAB Simulink for the HPS that will analyse the hybrid power system and delegate the roles of each resource at any given time with respect to the weather conditions and
- Test the performance of the aforementioned HPS with the aforementioned controller for the different cases that encompasses the availability/unavailability of each energy resource.

The study considered in this paper only focuses on PV and wind energy renewable energy sources. Cell

batteries were the only type of energy storage devices studied for the integration of the HPS. The area in which the HPS is meant to be implemented is generalized based on the cases deduced for the weather conditions. Specific areas were not considered for the cases. In general, the HPS considered was implemented in relatively sunny and windy areas that are not prone to severely stormy weather conditions. All models were built on Matlab Simulink. Technical and Economic viability of HPS is not considered in this paper. This paper focuses on control of the HPS, assuming the system is economically and technically viable for a chosen load and climatic conditions of a chosen area.

2. AN OVERVIEW ON RENEWABLE ENERGY

In a report released by the Energy Information Administration in 2009, it was stated that in 2006, 41% of the world's electricity supply could be accounted for by the generation of energy via the burning of coal [1]. Several government agencies worldwide are currently fixated on promoting the use of alternative methods of energy generation, such as renewable energy schemes, to reduce the quantity of carbon emissions on a global scale [1].

According to [2], in 2008 South Africa faced a dilemma where the current energy generation capacity, at the time, was incapable of meeting the load demand. The country went under a series of scheduled blackouts in the form of load-shedding. As it stands, the country's current state of affairs do not look entirely auspicious. An alternative means of generating electricity would only serve as a promising option for South Africa if it could contest the amount of energy produced by our coal power plants. According to [2], South Africa possesses the wind resources that could account for 5-6% of South Africa's load demand.

By starting small, renewable energy could serve to supply remote areas and then branch out as the technology incorporated in current renewable energy schemes advances. By adopting this approach, many of the under-privileged population will have a chance at a better lifestyle.

3. ENVIRONMENTAL IMPACT OF RENEWABLE ENERGY

There is a great need for an alternative method of power generation because burning fossil fuels increases greenhouse gas emissions. The future of power generation lies with renewable energy given that renewable energy offers a cleaner form of energy generation and will decrease the rate at which fossil fuels are utilized in the process of generating electric energy.

South Africa also faces a problem where rural or remote areas do not have access to electricity. Extending the grid, with the aim of supplying areas in need of electricity, is not seen as a favourable endeavour, due the steep costs associated with the extension [3]. Consequently, distance and the high costs associated with extending the grid are two factors which have limited the access of many peripheral rural areas to electricity. HPSs are seen as plausible solution to connect these areas.

4. HYBRID POWER SYSTEMS – HPS

Renewable energy can be seen as the best solution in theory. Unfortunately, with the implementation of this scheme, it has been found that this solution is not as reliable as we would like it to be – renewable energy is dependent on weather conditions and the nature of weather changes is unpredictable. The need for a hybrid power system stems from the fact that implementing only one type of renewable energy source in a power system offers a fairly unreliable means of generating energy [3]. Combining renewable energy sources enhances the power system's reliability [3]. This implies that the likelihood of hybrid power systems ensuring a consistent source of supply is far more probable – in contrast to individual renewable energy schemes working independently – which is a result of having stability in the system [4]. Before delving further into the task at hand, below is a description of the solar and wind energy which form the HPS.

4.1 Solar Energy System

The abundance of solar power that is available to be harnessed makes it appealing. It is a known fact that the implementation of this form of renewable energy entails high installation costs. The appealing aspect of PV generation schemes is its cost-effectiveness in small-scale setups in contrast with larger systems [5]. The image below shows a schematic structure of a solar system. The system consists of: a solar panel,

battery charge controller, battery bank and an inverter system.

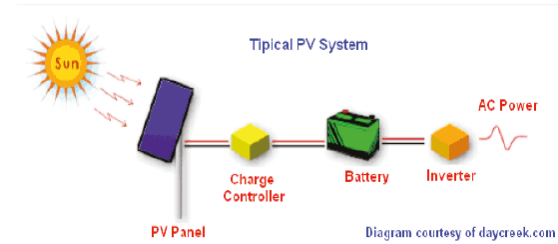


Fig. 1: Solar System Configuration

The solar system as modeled in Simulink. The figure below illustrates the model.

As shown in the figure below, the inputs to the PV model were designed as follows: Irradiance (varies from 0.2kW/m² to 1kW/m²) and Temperature (varies from 25 degrees C to 70 degrees C).

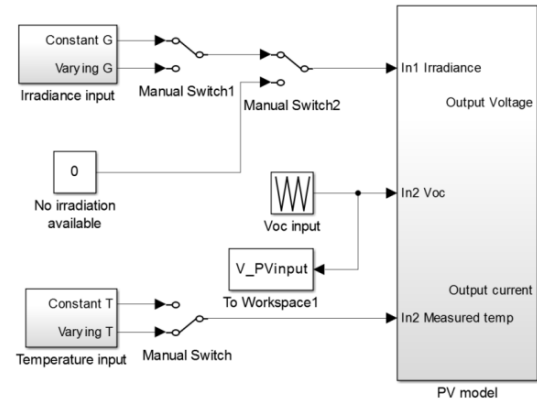


Fig. 2: Solar System Configuration in Simulink

For the purpose of this paper, the following assumptions were made when the solar system was designed: 1. The PV system operates at maximum power point tracking (MPPT) where the input takes in a constant “1” which represent the MPP when the PV source is available. A “0” logic represents solar resources below the MPP threshold. That is, irradiance below 0.2kW/m² threshold. 2. The PV source generates enough energy to supply the load when this source is detected as “available” by the controller. 3. The AC source, step-down transformer and rectifier combination is considered to be the PV model equivalent which can be implemented in the HPS. 4. The PV model supplies enough energy to meet the load demand. 5. The PV model operates under steady-state conditions.

The HPS is also made of wind power systems. Below is a description of development of the wind energy system model.

4.2 Wind Energy System

In [3] it is said that wind energy is considered to be the fastest growing form of renewable energy. Although there are CO₂ emissions attributed to the

construction and maintenance associated with wind energy, but these emissions are considerably small compared to CO₂ emissions caused by the usage of fossil fuels in power plants [6].

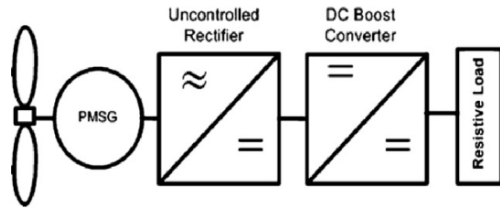


Fig. 3: Wind Energy System Configuration

The wind energy system was modelled in Simulink as a doubly-fed induction generator (DFIG). This design consists of a wound rotor induction generator and the rotor in this design is fed from the wind variable frequency [7]. The speed was maintained at 1.2 p.u. via a torque controller [7].

The following assumptions were made during the design of the wind energy system: 1. The output power is sufficient to assume an optimal performance of the wind system, 2. The output of the wind system is sufficient to supply the load demand, and 3. The generator operates at a value just above synchronous speed.

Similarly, with wind power, when the wind resources are below a set threshold, it is represented with logic "0". Above this threshold, wind resource is considered available and represented with logic "1".

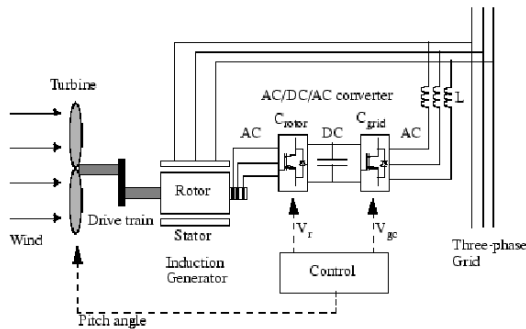


Fig. 4: DFIG Modelling Wind Energy System

5. DEVELOPMENT OF AVAILABILITY CONTROLLER FOR HPS

A controller is necessary for an HPS system in order to ensure that the system performs supplies the load effectively. It is crucial that the controller analyses the system's behaviour and guarantee that only one energy reliable source supplies the load at any given time.

The HPS controller analyses the input given from the PV, Wind and Battery storage unit and evaluates the inputs before arriving at the result which states the scenario the system is dealing with. The scenarios that the HPS is anticipated to encounter correspond to certain cases and these cases are discussed below.

The controller is expected to operate in accordance with and cater for the following cases:

CASE 1: Zero supply

This is the 000 scenario where none of the renewable energy resources are available to supply the load and the battery storage unit is depleted. In this instance we can consider the network to be facing a "blackout". The load cannot be supplied via the HPS.

CASE 2: No sun, no wind, only battery storage

This is the 001 scenario where there is an inadequate amount solar irradiation available for the PV, and there is lack of wind energy available to be harnessed. The load is supplied from the battery bank.

CASE 3: No sun, only wind energy, battery depleted

This is the 010 scenario where the battery storage unit is depleted. The load is supplied from the wind turbines and excess will be used to charge the battery bank.

CASE 4: No sun, only wind energy and battery charged

This is the 011 scenario where either the wind energy scheme or battery storage unit can be used to supply the load.

CASE 5: PV available, No wind, battery depleted

This is the 100 scenario where only the PV system is available to supply the load. The battery is depleted and there is no wind.

CASE 6: PV available, No wind, and battery charged

This is the 101 scenario where there is insufficient amount of wind energy available. The battery bank is fully charged and there is enough solar radiation.

CASE 7: PV available, wind available, battery depleted

This is the 110 scenario where both the PV and Wind energy systems can harness enough solar irradiation and wind energy, respectively. The battery bank is depleted.

CASE 8: PV, wind and battery storage available

This is the 111 scenario where all three resources are available to supply the load.

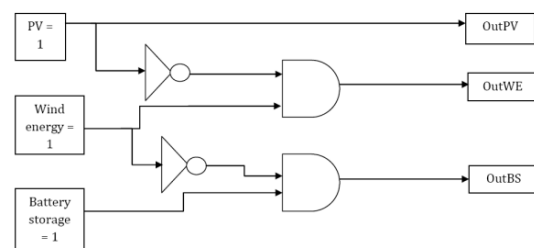


Fig. 5: Boolean Expression of the Relationship between the Anticipated Inputs and Outputs of the HPS Controller

6. RESULTS OF THE PV PERFORMANCE IN THE HPS

The following results are attained via the controller when the HPS is in operation. Achieving the expected results for each case demonstrates the controller's ability to operate with accuracy for the required task. The cases were preset before running the simulations so that the controller's operation could be tested. The displays indicate a "1" for the following eight cases when the controller has both detected that the source is available to supply the load and selected the source to supply the load.

The table below shows how the controller delegated the roles of each source for each of the eight cases that were set up for the HPS to operate under.

Table 1: Inputs and Outputs to the Controller

CASES	INPUTS (SCENARIOS)			OUTPUTS (AVAILABILITY)		
	PV	WE	BS	PV	WE	BS
CASE 1	0	0	0	0	0	0
CASE 2	0	0	1	0	0	1
CASE 3	0	1	0	0	1	0
CASE 4	0	1	1	0	1	0
CASE 5	1	0	0	1	0	0
CASE 6	1	0	1	1	0	0
CASE 7	1	1	0	1	0	0
CASE 8	1	1	1	1	0	0

CASE 1: Zero supply (scenario 000)

As aforementioned, this case renders the load demand unmet. The zeros in the first three displays indicate that all the three-phase circuit breakers remain open and as a result the load is not supplied.

CASE 2: No sun, no wind, only battery storage (scenario 001)

The case indicates that the battery is available for discharge and the PV and wind energy schemes cannot meet the load demand. Figure 6 below shows the controller's results display.

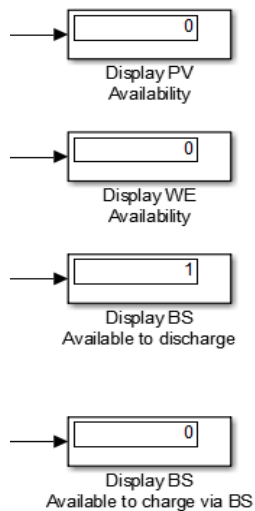


Fig. 6: Display of Controller Signals for Case 2

In this scenario, the battery bank is discharging. It is therefore crucial for the controller to keep track of the battery status. The controller, keeping track of the battery status, displays the following result when the battery is discharged. The Figure 7 below shows the results from the controller.

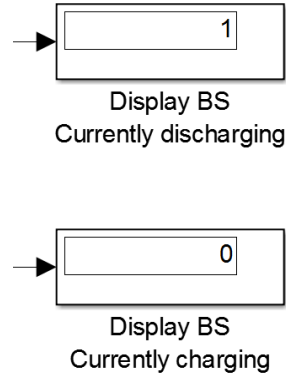


Fig. 7: Battery Status Display for Case 2

CASE 3: No sun, no battery storage, only wind energy (scenario 010)

In this case the controller has deduced that the wind energy scheme is available to supply the load. The controller sends a signal to the three-phase circuit breaker responsible for completing the connection between the wind energy scheme and load. The breaker then closes the circuit, enabling the load to be supplied via the wind energy scheme.

CASE 4: No sun, only wind energy and battery storage available (scenario 011)

For this scenario it was decided that although the battery storage unit is available for discharge, the wind energy scheme will be selected to supply the load in an attempt to preserve the stored energy that the battery contains. The resulting signal is sent to the three-phase circuit breaker responsible for connecting the wind energy scheme and load. Consequently, the circuit breaker closes thus enabling the supplying of the load via the wind energy scheme.

CASE 5: No wind, no battery, PV available (scenario 100)

This is the case where the PV system supplies the load. The output signal is sent to the circuit breaker responsible for completing the connection between the load and PV system, enabling the supplying of the load via the PV system. If in fact the circuit breakers for the wind energy or battery storage scheme are closed, the result on the display will be sent to the respective circuit breakers enabling the "opening" of the circuit breakers.

CASE 6: No wind, only battery storage and PV available (scenario 101)

For this case the controller decides that, although the battery storage unit is capable of supplying the load, the PV system will in fact supply so that the available solar energy does not go to waste.

The load demand will then be met by the PV system. The circuit breakers for the wind energy or battery storage scheme are closed, the result on the display will be sent to the respective circuit breakers enabling the opening of the three-phase circuit breakers.

CASE 7: No battery storage, only PV and wind available (scenario 110)

In this case, not only is there a means to supply the load via the PV system, but the wind energy scheme is also available to supply the load. The battery storage is depleted in this scenario. Given that there are two readily available sources of supply, the wind energy scheme will be allocated to supply the battery, enabling it to charge, whilst the PV system supplies the load. The Figure 8 below shows the display of the model controller signals. The PV system feeds the load and the wind system charges the battery bank.

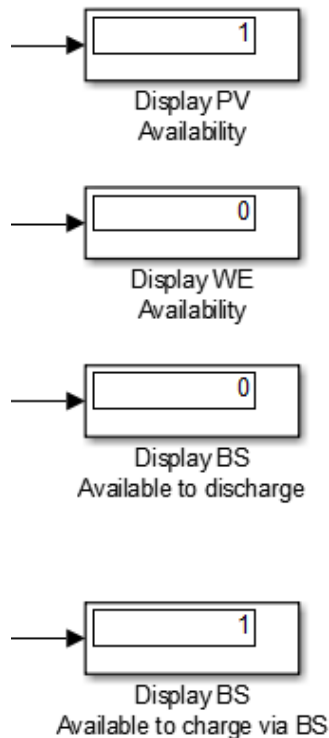


Fig. 8: Display of Controller Signals for Case 7

In the case 7 (Figure 9) the battery is deemed depleted and the wind system is available to supply the load whilst the PV system supplies the load. In practice circuit breakers will be implemented connecting the battery and wind system such that the battery can charge via the energy generated by the wind system. The controller displays the following during this process.

CASE 8: All three resources are available (scenario 111)

This case essentially presents a scenario where all three resources are available to supply the load. The Figure 10 below illustrates that the controller has chosen the PV system to supply the load.

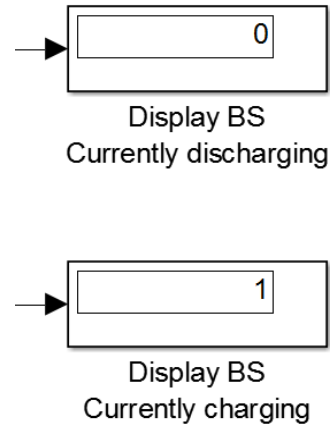


Fig. 9: Battery Status Display for Case 7

It becomes apparent that this case creates a wasteful scenario where the wind energy available for capture goes to waste.

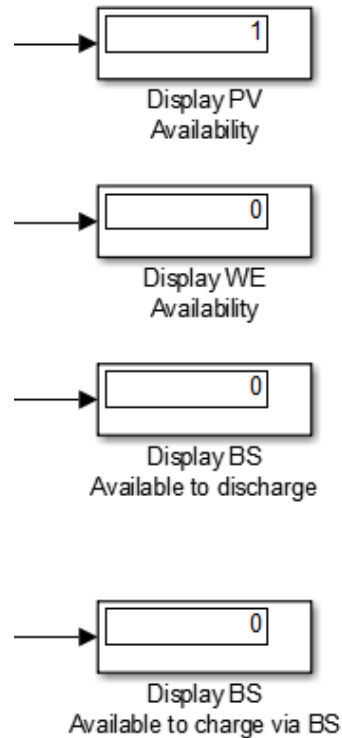


Fig. 10: Display of Controller Signals for Case 8

7. CONCLUSIONS

The controller operated successfully within the HPS. It functioned as expected under the various cases i.e. weather conditions and presented the expected outputs for the various test cases. The results presented above indicate the successful operation of the controller to be implemented in an HPS.

The results indicate that the controller delegated the roles of each source for each of the eight cases that were set up for the HPS to operate under. The availability of the sources were correctly determined

in each case and the load was supplied when possible, the available sources that were not meant to supply the load at any given time was kept at bay whilst the desired supply for the scenario feed the load.

The controller illustrated that the charging occurred during case 7 where the wind system would essentially need to supply the battery so that it can charge. It was tested for an overcharge of the battery and displayed the result which indicated that an alert, in practice, would be sent out so that it can be known that the battery is malfunctioning. The discharging of the battery was correctly depicted on the controller displayed. All in all, the performance of the controller was satisfactory.

ACKNOWLEDGEMENTS

The authors gratefully acknowledge the support, and research infrastructure provided by Eskom Holdings Ltd. and Electrical Engineering Department at the University of Cape Town in carrying out this research work.

REFERENCES

- [1] N.K.C Nair and N. Garimella, "Battery energy storage systems: Assessment for small-scale renewable energy integration," *Energy and Buildings*, vol. 2124-2130, no. 11, p. 42, November 2010.
- [2] J. Krupa and S. Burch, "A new energy future for South Africa: The political ecology of South African renewable energy," *Energy Policy*, vol. 39, no. 10, pp. 6524-6261, October 2011.
- [3] T. Mtshali, G. Coppez, S. Chowdhury and S.P. Chowdhury, "Simulation and Modelling of PV-Wind-Battery Hybrid Power System," in *PESGM*, San Diego, 2011, pp. 1-7.
- [4] G. Coppez, S. Chowdhury and S.P. Chowdhury, "The Importance of Energy Storage in Renewable Power Generation: A Review," in *UPEC*, Cardiff, 2010, pp. 1 - 5.
- [5] S. Chowdhury, S.P. Chowdhury and P. Crossley, *Microgrids and Active Distribution Networks*. London, United Kingdom: The Institution of Engineering and Technology, 2009.
- [6] R. Saidur, N.A. Rahim, M.R. Islam and K. H. Solangi, "Environmental impact of wind energy," *Renewable and Sustainable Energy Reviews*, vol. 15, no. 5, pp. 2423-2430, June 2011.
- [7] MATLAB Simulink (R2013a). (2013) Help, SimPowerSystems, FACTS and Renewable Energy Systems, Renewable Energy Systems, Wind Turbine Doubly-Fed Induction Generator (phasor type). Manual.

AN INVESTIGATION INTO GAIT GENERATION FOR MICROCONTROLLER-BASED QUADRUPEL ROBOTS WITH THREE DEGREE OF FREEDOM APPENDAGES

M. G. Heydenrych* and G. Phillips**

*S4 Integration, Project Management, Unit 5, Pogson Park, Pogson Road, Sydenham, Port Elizabeth, 6001, South Africa. Email: heydenrych.martin@gmail.com

**Nelson Mandela Metropolitan University, Faculty of Engineering, the Built Environment and Information Technology, Gardham Avenue, Summerstrand, Port Elizabeth, 6001, South Africa. Email: Grant.Phillips@nmmu.ac.za

Abstract. This paper introduces the AntereQuad, a four-legged robot with three linkages per appendage for which locomotion is investigated. Gait generation is the formulation and selection of a sequence of coordinated appendage and body motions to propel a quadruped robot along a desired path. The nucleus of this study, and a fundamental part of gait generation, is the control strategy used to determine the joint parameters that provide the desired position of each of the appendage tips. Inverse kinematics (IK) is proposed as a methodology for the development of such a control strategy which facilitates gait generation. Trigonometry and rotation matrices are then discussed as valuable ways to mathematically represent structural relationships in kinematic manipulators. Additionally, the study describes mechanical and electronic aspects of the design which directly or indirectly impact gait generation. The algorithms presented are simple to implement, computationally cheap, and stable for every joint configuration. Furthermore, the resulting quadruped gaits are steady, smooth and accurate.

Key Words. Robotics; inverse kinematics; quadrupeds; creep gait; trot gait; rotation matrices; Cartesian coordinate system; analytical trigonometry; Euclidean geometry; electronics.

1. INTRODUCTION

Less than half the earth's landmass is accessible to wheeled and tracked vehicles, yet, people live and access almost any place on earth [1]. Consequently, modern machinery and robots are required to be able to achieve effective mobility on terrains which are too difficult for existing vehicles to navigate. The benefits and significance of legged robots may be realized in applications such as forestry where terrain is severely demanding or in land reclamation projects in waterways where significant wading depths are required [2]. Furthermore, modern farming operations are characterized by large farm equipment with sizable axle loads which improve production efficiency. Legged machinery make far less frequent contact with topsoil compared to the rolling contact of wheeled vehicles. In this manner legged robots such as quadrupeds may reduce soil compaction which negatively impacts soil productivity [3].

There have been four distinct research thrusts in terms of design models for quadruped robot locomotion [4]. The first of these models employed a very complicated mechanical design which was based on the anatomy of a dog. This design consisted of twenty-eight joints. These were very simple, rotational, one degree of freedom (DOF) linkages [5]. The second research line opted for fewer joints, but joints which provided complex degrees of freedom [6]. This model resulted in a significant increase in cost as it required additional sensor equipment, a complex leg mechanism, and a high performance controller. The third research thrust opposed the first and second in that the model reduced design complexity. This was achieved by reduced degrees of freedom and the implementation of fewer linkages. Each leg had only one actuator activating two degrees of freedom [7]. According to Hoang, *et al.* [4], this minimalist design did not achieve effective nor efficient locomotion. The final research line is that of the entertainment quadruped robot. These complex designs have 20 degrees of freedom and a large variety of sensors [4]. Robots based on this model are vastly cheaper than conventional robots because they utilise a standard interface, and integrate components which are mass-produced.

This paper combines various characteristics from each of the abovementioned design models and presents a robot with twelve simple, rotational joints. The complexity of walking-pattern generation is greatly reduced while effective locomotion is achieved. Quadruped robots are complex systems of motion. Is it thus difficult to create and optimise walking patterns in order to produce accurately governable locomotion. Quadrupedal gaits require that the robot's centre of gravity be projected inside the polygon formed by the supporting legs at all times. The research considers various kinematic approaches for their viability as control models to be used to construct gaits. Kinematics, otherwise known as classical mechanics, is described as the geometry of motion and is used to describe the motion of systems composed of joined parts [8]. Such kinematic equations are divided into two fundamental approaches. The first, forward kinematics (FK) requires joint parameters of a robot's limbs to be known. This method then describes the position and movement of the appendage tip based on all the joint parameters of the appendage. Inverse kinematics (IK), on the other hand, uses the known coordinate of the appendage tip to determine each of the joint parameters for the appendage. The latter option has experienced a great evolution in the last twenty years and is significantly more useful for quadrupedal gait generation. This is because it is more practical to feed quantifiable appendage-tip coordinates into

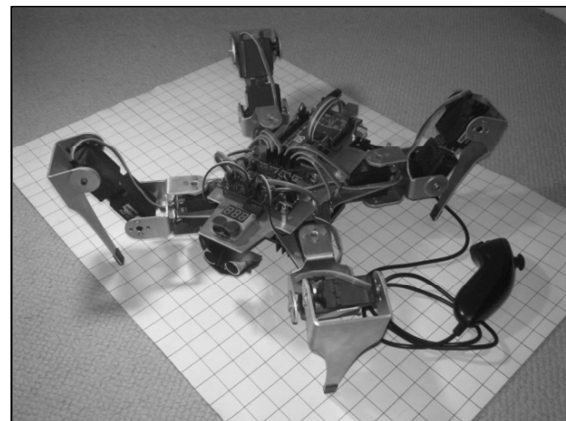


Fig. 1: The AntereQuad.

algorithms than multiple joint angles which are problematic to measure [8]. This paper proposes an analytical IK method which is not only fast but also accurate and robust for various joint configurations. Finally, the study describes the development of two quadrupedal gaits: the creep gait and the trot gait.

2. CHASSIS DESIGN

The primary aim during the construction of the prototype chassis was to optimise the robot's dimensions. Quadruped chassis dimensions impact gait efficiency, chassis balance, and kinematic limits.

2.1 Prototype Chassis Design and Construction

AntereQuad adopts a reptilian stance (as represented in Fig. 2) in its frontal joint arrangement. Each leg consists of two segments and three joints. This design model is preferred due to the versatility it offers, although it escalates gait complexity. This configuration provides a wide, stable base which keeps the centre of gravity of the robot low, so allowing for improved stability [9]. Furthermore, the chassis is characterized by coxae servos equidistant of each other so as to reduce chassis balance complexity. Quadrupedal leg-joint anatomies are similar for each individual leg, ensuring that the algorithm developed to control one appendage may control all appendages in the same manner. The servo motors forming the hip joints experience greater torque than the other two actuators on each limb and are of a higher torque specification [9]. The quadruped's appendage proportions imbue the chassis with the ability to hold a fixed standing position when not under power because the femur is suspended from the tibia. The AntereQuad's tibia is approximately 80 percent longer than its femur so as to promote gait efficiency. Appendage lengths are kept short as this has a direct impact on the size and cost of actuators, thus impacting power consumption for the system. Significantly, the ratio between the area defined by the coxae servo positions, and the area between the leg tips has an impact on gait stability. As the size of a quadruped's base increases so also the distance each appendage is required to travel in order to cause a shift in centre of gravity increases. The prototype construction process assisted in establishing the following final chassis' dimensions: 127 millimeter distance between coxae joints, 52 millimeter coxa length, 70 millimeter femur length, 126 millimeter tibia length.

2.2 Chassis Construction

Chassis rigidity, weight distribution, and symmetry are characteristics which are paramount for purposes of maintaining balance during gaits. Besides purely geometrical considerations, an unbalanced chassis will cause balance

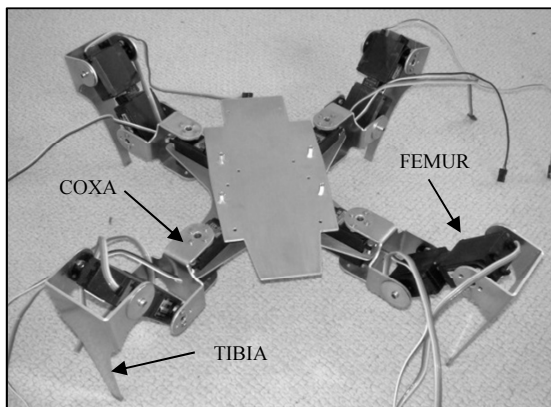


Fig. 2: Completed Quadruped Chassis.

issues during gaits. Chassis rigidity is impacted by three factors: material rigidity, joint flex and servo gear play. These factors contribute to chassis flex which permits the robot's centre of mass to shift, opposing body translation during gaits. As a result of this, the robot loses gait stability. Furthermore, servo vibrations are intensified when chassis flex occurs. This reduces the efficiency of the system by increasing the dynamic forces acting on the structure and placing the servos under unnecessary strain.

2.3 Actuator Torque Calculations

Statics is concerned with how a mechanical system would act if everything is perfectly motionless and rigid [10]. Both static and dynamic forces act on a robot chassis during various gaits. Dynamic forces were deemed negligible during the slow-moving creep gait. Dynamic forces, however, must be calculated for the trot gait. A critical consideration is the maximum hip servo moment of force required to be generated during gaits. Moment arms were used to undertake basic force calculations for the quadruped chassis. This is shown by:

$$\tau = \frac{w}{d} \times d \quad (1)$$

Where: τ = maximum torque required at hip servo

W = gross chassis weight

L = number of legs on ground during gait

D = distance between coxa and perpendicularly applied force.

Servo torque calculations were based on a projected maximum chassis weight. The calculated minimum torque at both the femur joints during trot and creep gaits, respectively, served as a benchmark when making servo motor selection choices to power the AntereQuad for any gait.

3. ELECTRONICS SYSTEMS DESIGN

A critical part of this study is the seamless integration of streamlined control algorithms with sound chassis design by means of cost effective hobby electronics. This is due to the time-sensitive nature of gait sequences and delicate chassis-balance requirements.

3.1 Microcontroller

The Arduino Mega 2560 provides a low-cost solution while offering reasonable performance. The computational power of the Mega 2560, however, does not handle pure floating point IK calculations. The Arduino Mega platform greatly reduces development time since available resources aid low-level computing. Furthermore, higher-level project objectives are well supported by Arduino's functions and libraries. Fig. 3 provides an overview of the AntereQuad's electronics.

3.2 Servo Controller

The SSC32 offers 32 channels of one microsecond resolution servo control. Of particular interest and relevance for this study is the SSC32's ability to facilitate synchronized or "group" servo moves with a single instruction set. This greatly reduces the low-level servo control functions because the SSC32 permits velocity computation for multiple servos so that servos travelling the same distance at differing speeds end their movement operations simultaneously.

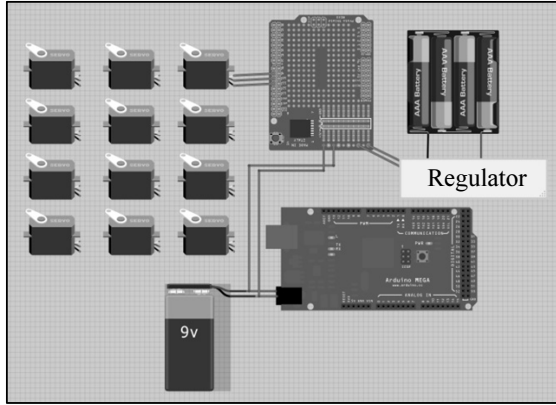


Fig. 3: Electronic Hardware and Actuator Integration.

3.3 Servo Specification

The following guidelines were established to ensure appropriate actuator selection:

- Metal-gearred servos should be sourced since these improve chassis robustness and accuracy of gait control.
- The operating current of each servo option has major implications for regulator design and battery selection.
- The ideal hip and knee servos are required to generate the established benchmark moment of force.
- Due to minimal force along their axis of rotation the coxae servos may be of a lesser specification than the hip and knee servos.

The trot gait is considered to be the most demanding gait in terms of power consumption [7]. Dynamic forces acting on the chassis are the reason for this due to the speed at which a quadruped trots, which ensures that at any given time two downward-accelerating legs have the entire chassis weight resting on them. Subsequently, total servo current consumption for the trot gait is taken as the worst-case scenario for regulator and battery specification. Since the coxae servos experience no true load as they traverse along a horizontal axis, the total coxa servo current drawn is calculated by:

$$I_{total (coxa servo)} = N \times I_{running (no load)} \quad (2)$$

Where: N = number of coxae servos

Due to the rate at which interchange occurs between the stepping of diagonally opposite leg pairs, the total current drawn for the hip servo servos sees four servos incorporated into the calculation. Moreover, since the maximum hip servo moment of force required for this gait is approximately 60 percent of the hip servos' rated torque, total hip servo current is calculated from:

$$I_{total (hip-servo)} = N \times (0.6 \times I_{stall}) \quad (3)$$

During the trot gait the knee servos experience minimal loading. For this reason total knee current may be calculated as follows:

$$I_{total (knee-servo)} = N \times I_{running (no load)} \quad (4)$$

The proposed maximum current consumption for the system during trot gaits is calculated from:

$$I_{total} = I_{total (coxa servo)} + I_{total (hip servo)} + I_{total (knee-servo)} \quad (5)$$

3.4 Regulator Configuration

Quadruped robots which execute static gaits are typically not efficient. The total current required for the AntereQuad's gaits is substantial. In addition to this, servo power consumption varies significantly during gaits. Hence, the electrical power system is required to be robust in order that the specified current drain requirements are met regardless of these factors. Typically regulators are not able to offer low dropout voltages while satisfying demanding current requirements. The LM338 regulator is a five amp adjustable three-terminal positive voltage regulator with low dropout capabilities [11]. In order to provide reliable operation without sustaining damage the LM338 regulators were placed in a parallel configuration as shown in Fig. 4.

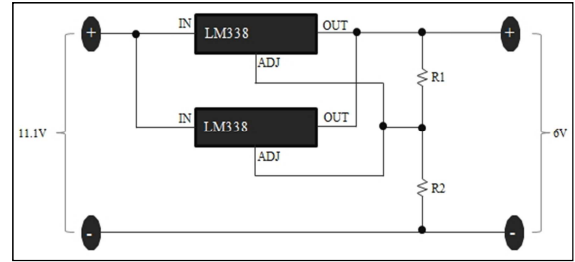


Fig. 4: Parallel LM338 Regulator Configuration.

3.5 Battery Specification

Crucial considerations in the battery selection process include suitable capacity (Ah) for robot run-time, and appropriate voltage for regulator operation so as to meet drop-out voltage requirements. A lithium polymer (Li-Po) battery is utilized to minimize chassis weight since it displays high energy density properties and offers a suitably high discharge rate. Another property of the Li-Po battery which renders it suitable for reliable operation is its constant characteristics over many cycles [12].

4. GAIT GENERATION

Legged robots such as quadrupeds are uniquely advantageous to traverse extreme terrain. This is because of their ability to isolate their body from terrain irregularities, avoid undesirable footholds, regulate their stability, and achieve energy efficiency [13]. The difficulty has been to generate gaits that demonstrate these characteristics.

4.1 Creep Gait

There are six different step-sequences for the creep gait of which only one step-sequence provides good stability during all phases of the gait [14]. This happens to be the same step-sequence that animals use. The chief criterion necessary in order to obtain a stable slow-speed walk is that only one leg is ever lifted at a time to take a step, while the centre-of-gravity of the robot body or chassis must lie within the triangle drawn through the three grounded feet. Imbalance and tipping will occur if the centre of gravity is outside the stability-triangle, and stability will be marginal when the centre of gravity lies along, or close to, one of the edges of the stability-triangle. Animals use back-and-forth movements of their heads or tails to adjust their balance during locomotion. Since a quadruped robot is unable to do this, the chassis needs to translate from side to side during the creep gait. The creep gait achieved by AntereQuad is shown in Fig. 5 for purposes of result validation.

Creep Gait Sequence: For gait position one, the left rear (LR) leg supports while the right rear (RR) leg is stepping. Similarly, positions two and four of the step-sequence gain stability from translating diagonally onto the lifted leg after

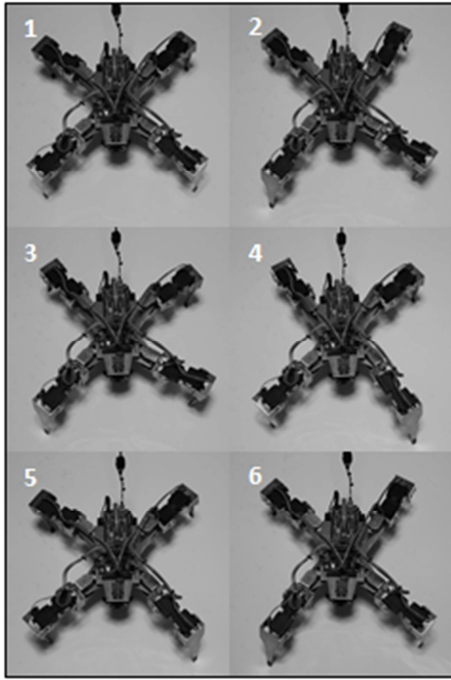


Fig. 5: Creep Gait Sequence.

it has been placed. This may be seen for position two since the leg (RR) which is on the same side as the lifted-leg (RF) is moved forward to a position near the midline. The opposite leg (LF) to the lifted leg (RF) is vertical and directly supports the front-end of the frame. Again, a stable tripod is formed from the three grounded legs in position three. Position four is simply a mirror-image of position two.

4.2 Trot Gait

During the trot gait a quadruped lifts two diagonal legs simultaneously. The robot balances on the other two diagonal legs which remain grounded.

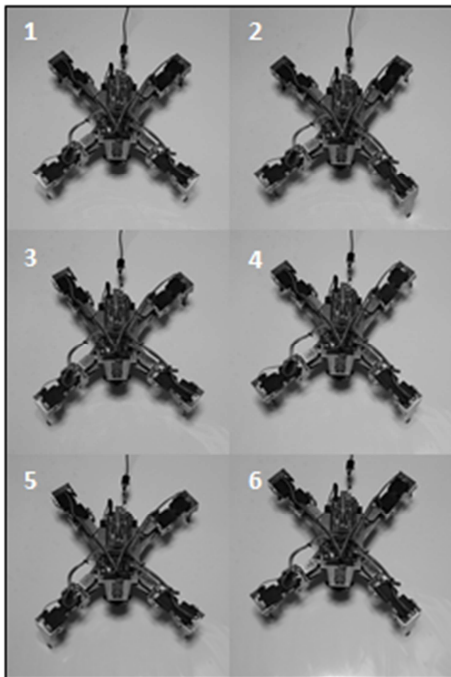


Fig. 6: Trot Gait Sequence.

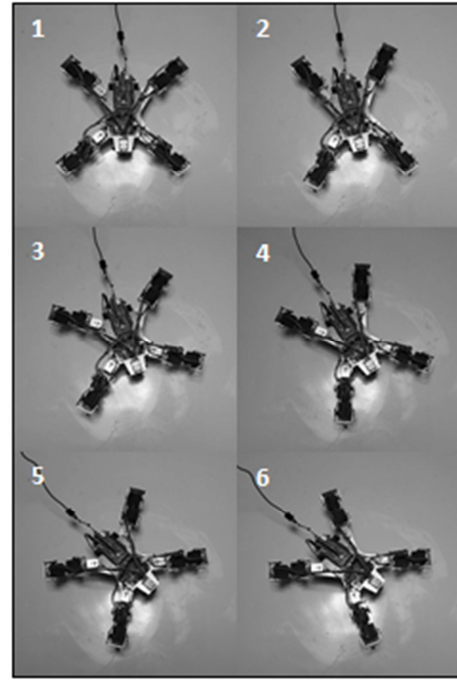


Fig. 7: Rotation Gait Sequence.

The chassis is projected forward on these two diagonally grounded legs while the other legs lift, swing forward, and become grounded in new forward positions. This alternating sequence is repeated at high frequency so as to reduce the period for which appendages are in the air. Additionally, the duty cycle may be altered to improve stability. Fig. 6 displays the trot gait performed by AntereQuad for purposes of results validation. Additionally, Fig. 7 shows another form of the trot gait, named the rotation gait, used for trot gait direction changes.

4.3 Gait Implementation in Code

Gaits are implemented in code using a class so that each leg's x, y- and z-coordinates are modified in turn in a gait sequence function which is executed in the order determined by the following arrays [15]:

Creep Gait (twenty steps in gait):

```
StepNr [LF] = 1;
StepNr [LR] = 6;
StepNr [RR] = 11;
StepNr [RF] = 16;
```

Trot Gait (fourteen steps in gait):

```
StepNr [LF] = 1;
StepNr [LR] = 8;
StepNr [RR] = 1;
StepNr [RF] = 8;
```

All the grounded legs shift in the opposite direction to the appendage simultaneously taking steps. The *StrideLength* variable determines the step distance while *LegLiftHeight* represents the stepping height of each stepping appendage. The *RotY* is the variable which determines the amount by which the robots turns with each step. The *BodyShift* variable is the amount by which the *StrideLength* is divided so as to control the distance the grounded legs are translated between every step. The following gait-sequence function calculates gait positions:

```
for (int LegNo = 0; LegNo < 4; LegNo++){
    if (GaitStep == StepNr[LegNo]) {
```

```

GaitState[LegNo].X = -StrideLength.X/2;
GaitState[LegNo].Z = -StrideLength.Z/2;
GaitState[LegNo].Y = LegLiftHeight/2;
GaitState[LegNo].RotY=StrideLength.RotY/2;
} // Appendage tip rising for step
else if (GaitStep=StepNr[LegNo]+1) {
    GaitState[LegNo].Z = 0;
    GaitState[LegNo].X = 0;
    GaitState[LegNo].Y = LegLiftHeight;
    GaitState[LegNo].RotY = 0;
} // Appendage raised to full height
else if (GaitStep=StepNr[LegNo]+2) {
    GaitState[LegNo].Z = StrideLength.Z/2;
    GaitState[LegNo].Z = StrideLength.Z/2;
    GaitState[LegNo].Y = LegLiftHeight/2;
    GaitState[LegNo].RotY=StrideLength.RotY/2;
} // Appendage tip lowering to position
else if (GaitStep=StepNr[LegNo]+3) {
    GaitState[LegNo].Z = StrideLength.Z/2;
    GaitState[LegNo].Z = StrideLength.Z/2;
    GaitState[LegNo].Y = 0;
    GaitState[LegNo].RotY=StrideLength.RotY/2;
} // Place appendage tip down
else {
    GaitState[LegNo].X = GaitState[LegNo].X -
        (StrideLength.X/BodyShift);
    GaitState[LegNo].Z = GaitState[LegNo].Z -
        (StrideLength.Z/BodyShift);
    GaitState[LegNo].Y = 0;
    GaitState[LegNo].RotY=GaitState[LegNo].RotY -
        (StrideLength.RotY/BodyShift);
} // Move robot chassis forward
    
```

Another component of the creep gait sequence which is not indicated is the body translation away from the appendage which is about to step. In this manner the chassis' centre of gravity is projected within the tripod formed by the grounded appendages.

5. SOFTWARE AND ALGORITHM DEVELOPMENT

In this study the robot chassis is modeled kinematically using a two-dimensional Cartesian coordinate system. Steps are proposed for the derivation of simple IK equations using analytical trigonometry, permitting generation of leg motions exclusive to three degree-of-freedom robots. Rotation matrices are employed for the purpose of coordinate transformation between various frames of reference in three-dimensional Euclidean space.

5.1 Body Inverse Kinematics Algorithms

The first aspect to consider for body IK development is the physical dimensions of the robot. This imbues the algorithm with intelligence regarding the physical properties of the chassis. There are four dimensions to consider: coxa length, femur length, tibia length, and the distance between the four coxae. The dimension parameters are superimposed on a two-dimensional Cartesian plane [15] as shown in Fig. 8.

In doing so, the centre of the chassis takes on the x- and z-coordinates, $F_G(0,0)$. This Cartesian plane will be referred to as the global reference frame. The four coxae are each positioned on their own set of coordinates. These coordinates are established by adding or subtracting an x- or z-offset value from the $F_G(0,0)$ set of coordinates at the

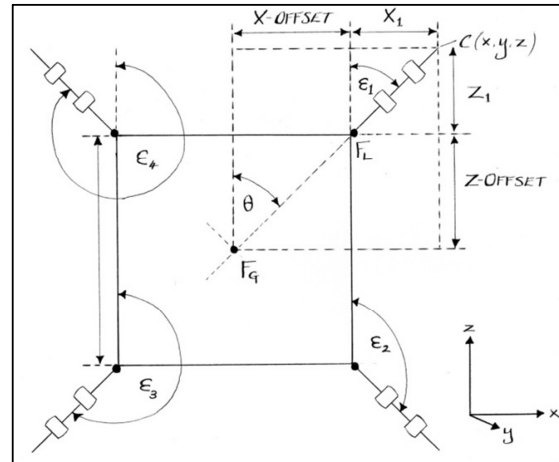


Fig. 8: Body Inverse Kinematics Model.

centre of the chassis. Thus, four unique coxae coordinates are established with respect to the chassis centre $C(x,y,z)$.

For purposes of leg IK calculations the end effector coordinates are not only required to be known with respect to the chassis centre, but also with respect to the coxae coordinates. For this reason the four previously established coxae coordinates are each superimposed within the centre of their own Cartesian planes. These four offset Cartesian planes will be referred to as local frames, shown as $F_L(0,0)$.

These frames should be seen as individual sets of Cartesian planes for each appendage. Each coxa's x- and z-offset distance represents its position within the global frame. In order to further develop the identity of each the four local frames, and orientate the coxae Cartesian planes, coxae offset angles are established. If the vertical z-axis of the front right local frame is viewed, in an initial quadruped start-up position, the leg will be offset 45 degrees in a clockwise direction from this axis. Shifting to the right rear frame, the appendage will be offset 135 degrees from the vertical z-axis in a similar manner. The left rear and left front coxae positions will have offsets of 225 degrees and 315 degrees, respectively. These angles are inputs for the rotation matrix responsible for coordinate transformation from the global frame to any of the four local frames. At this point the framework for the body IK algorithm has been established. Hence, it is now possible to describe the body IK algorithm, which is always executed within the global frame which is constructed by the addition of coordinate inputs from the local frame for each appendage:

```

posIO.X = CurPos[LegNo].X + BodyPos.X +
    GaitState[LegNo].X + coxaOffset.X;
posIO.Z = CurPos[LegNo].Z + BodyPos.Z +
    GaitState[LegNo].Z + coxaOffset.Z
posIO.Y = CurPos[LegNo].Y + BodyPos.Y +
    GaitState[LegNo].Y;
    
```

Body Rotations: The following basic rotation matrices may be implemented in code in order to rotate the vectors - body coordinates in this case - about the x, y, or z axis, in three dimensions. Each of these basic vector rotations appears counter-clockwise when the axis about which they occur points toward the observer. The coordinate system is right-handed, and the angle θ is positive. Rz, for instance, would rotate toward the y-axis a vector aligned with the x-axis.

$$R_x(\theta) = \begin{bmatrix} 1 & 0 & 0 \\ 0 & \cos\theta & -\sin\theta \\ 0 & \sin\theta & \cos\theta \end{bmatrix} \quad (6)$$

$$R_y(\theta) = \begin{bmatrix} \cos\theta & 0 & \sin\theta \\ 0 & 1 & 0 \\ -\sin\theta & 0 & \cos\theta \end{bmatrix} \quad (7)$$

$$R_z(\theta) = \begin{bmatrix} \cos\theta & -\sin\theta & 0 \\ \sin\theta & \cos\theta & 0 \\ 0 & 0 & 1 \end{bmatrix} \quad (8)$$

One rotation matrix may now be obtained from these three using matrix multiplication which represents rotations around each axis. For example, the product represents a rotation whose yaw, pitch, and roll angles are α , β , and γ , respectively:

$$R' = R_x(\gamma) \times R_y(\beta) \times R_z(\alpha) \quad (9)$$

The matrix product above may be used to represent modifications to the coordinates of the end effector with respect to the robot chassis' centre of mass. The matrix product above may also be used to represent changes to the coordinates of the end effector with respect to each of the four respective coxae of the quadruped. A methodology, however, is required in order to move from the global frame of the chassis' centre to the local frame with the horizontal hip joint servo forming the origin.

Coordinate Transformation: A rotation matrix is once again used to perform this coordinate transformation from the chassis frame to the coxa frame [15]. The offset angle may be 45, 135, 225, or 315 degrees depending on which local frame is being shifted to.

$$\begin{aligned} FL_FeetPos.X &= FG_FeetPos.X * \cos(\text{angleOffset}) - \\ &\quad FG_FeetPos.Z * \sin(\text{angleOffset}); \\ FL_FeetPos.Z &= FG_FeetPos.X * \sin(\text{angleOffset}) + \\ &\quad FG_FeetPos.Z * \cos(\text{angleOffset}); \\ FL_FeetPos.Y &= FG_FeetPos.Y; \end{aligned}$$

Once this has been completed it is possible to use the coordinates on which coordinate transformation have been performed on as inputs to the leg IK algorithms to be translated into joint angles.

Servo Output Functions: A linear function is used to transform the joint angles into suitably scaled and constrained servo pulse width values:

$$y = ax + b \quad (10)$$

Where: b = upper servo pulsewidth limit

$$a = \pi$$

x = offset value which, when subtracted from the upper servo pulsewidth limit, gives the lower pulsewidth limit.

The Arduino constrain function is used to constrain the joint angle within a pre-established range so as to establish kinematic limits:

$$\text{int mSecond} = \text{constrain}(\text{CurrentAngle}[i] + \text{servoOffset}[i], \text{jointMin}[i\%3], \text{jointMax}[i\%3]);$$

5.2 Leg Inverse Kinematics Algorithms

If a quadruped is to balance itself dynamically then it is critical for the system to be aware of where its feet currently are, and where they will be required to be. This is the objective when developing algorithms for AntereQuad's leg movements. The structure of each limb is modeled kinematically, and then derived and implemented in the form of basic trigonometry. The deliverable of this section is an algorithm which permits a set of x -, y - and z -coordinates to

act as inputs for which corresponding servo angle outputs are produced.

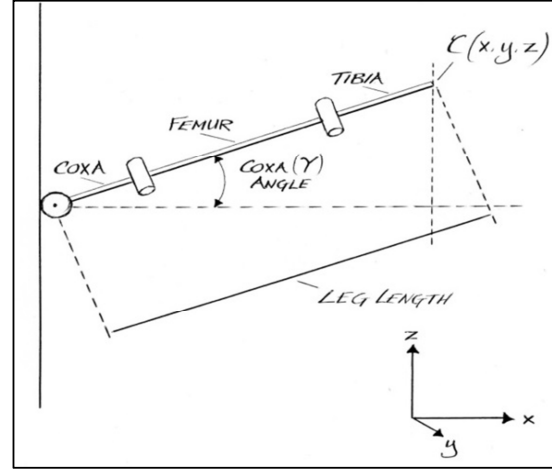


Fig. 9: Leg IK Model Top View.

In order to reduce the problem's complexity it is broken down from a three-dimensional problem into two two-dimensional problems as seen in Fig. 9 and Fig. 10. The objective is to solve for alpha (α), beta (β) and gamma (γ). The x - and z -coordinates of the appendage tip with respect to the coxa joint are known: $C(x, y, z)$. Hence, it is possible to derive the following formula from a top view of the quadruped's limb by calculating the hypotenuse formed by the x - and z -plane coordinates in Fig. 9:

$$LL = \sqrt{x^2 + z^2} \quad (11)$$

Where: LL = Leg Length

Moving to the side-view of the appendage, as represented in Fig. 10, it is possible to calculate the hypotenuse of the triangle "A" formed by the height of the chassis and the width of the quadruped's stance:

$$\text{Hyp} = \sqrt{(LL - CL)^2 + y^2} \quad (12)$$

Where: CL = Coxa Length

The following trigonometry function is used to find α_1 :

$$\alpha_1 = \tan^{-1}((LL - CL) / y) \quad (13)$$

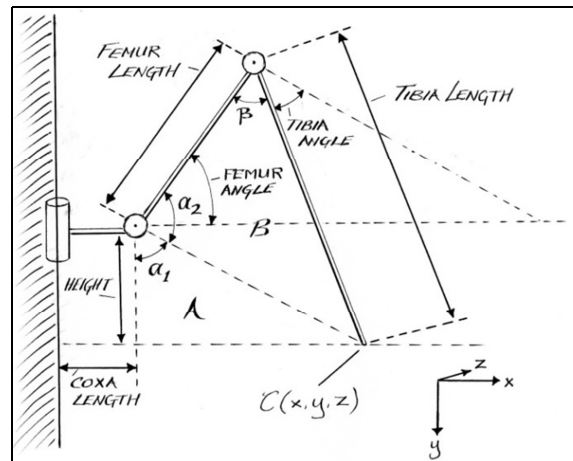


Fig. 10: Leg IK Model Side View.

The Law of Cosines, which states that one may calculate the angles of a triangle if the lengths of all three sides are known, is used to determine α_2 :

$$\alpha_2 = \cos^{-1}((TL^2 - FL^2 + hyp^2)/(-2 \times FL \times hyp)) \quad (17)$$

Where: FL = Femur Length

TL = Tibia Length

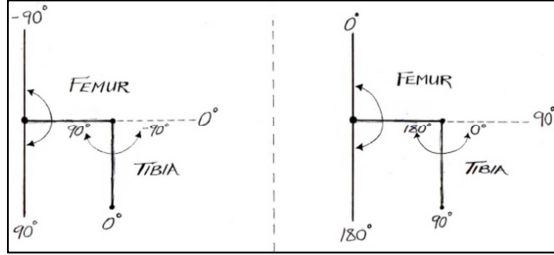


Fig. 11: True Servo Angles (L) and Calculation Angles (R).

In order to simplify calculations, the reference axis for the femur and tibia joints are different (as represented in Fig 11). The femur servo angle is given with respect to the horizontal x-axis, while the tibia angle is always given with respect to the dynamic axis formed by drawing a line through the vertical hip joint and the knee joint. Consequently, the femur angle with respect to the x-axis is shown as:

$$\text{Femur angle} = 90^\circ - (\alpha_1 + \alpha_2) \quad (14)$$

The quadruped's femur length, tibia length, and the hypotenuse of triangle "A" (which forms the third side of the triangle "B") are all known. Thus, the law of cosines is used once again to develop a solution for β :

$$\beta = \cos^{-1}((hyp^2 - TL^2 - FL^2)/(-2 \times FL \times TL)) \quad (15)$$

Now the tibia angle is adjusted to always have a value of zero degrees when perpendicular to the femur of the appendage:

$$\text{Tibia angle} = 90^\circ - \beta \quad (16)$$

Now, shifting from a side-view back to a top-view, the following trigonometry function is used to develop a solution for the coxa angle by utilising the known x- and z-coordinates of the leg tip:

$$\text{Coxa angle} = \tan^{-1}\left(\frac{z}{x}\right) \quad (17)$$

6. CONCLUSION

The purpose of the construction of the AntereQuad was to provide a platform for an investigation into the development of walking patterns for four-legged robots with three degree of freedom appendages. Two gait types, namely, the trot gait and the creep gait were developed. Based on the research performed, it may be concluded that inverse kinematics provides a suitable methodology whereby quantifiable appendage-tip coordinates are input into control algorithms. The combination of analytical trigonometry and rotation matrices form a simple, fast, yet accurate control algorithm for mathematically representing structural relationships in kinematic manipulators. The application of inverse kinematics methodologies to the development of this study's control algorithms yields a control strategy which is simple to implement, computationally cheap, and stable for every joint configuration. Furthermore, the resulting quadruped gaits are steady, smooth and accurate. Future studies are to

ensure that the robot chassis for which gaits are being generated be symmetrical, evenly weighted, and rigid. Additionally, subsequent research should carefully consider actuator performance since it is paramount for the achievement of chassis rigidity and appendage movement accuracy. In future studies integer values may be replaced by pure floating point values for inverse kinematics calculations. This would improve appendage movement accuracy, thereby causing the quadruped's movements to become increasingly stable during gaits.

ACKNOWLEDGEMENTS

M. G. H. thanks Grant Phillips for his enthusiastic support relating to the technical aspects of this study. M. G. H. also thanks Oscar Liang for his input regarding IK implementation, which proved to be an invaluable resource for the algorithm development process. Finally, due credit must be given to Gareth Greenwood and Crystal Rowe who tirelessly and meticulously reviewed numerous drafts of this paper.

REFERENCES

- [1] M. Raibert, K. Blankespoor, G. Nelson and R. Playter, "BigDog, the Rough Terrain Quadruped Robot," Seoul, 2008.
- [2] H. Hwang and Y. Youm, *Advanced Robotics - Steady Crawl Gait Generation Algorithm for Quadruped Robots*, London: Taylor & Francis, 2012.
- [3] S. Duiker, "Avoiding Soil Compaction," in *Avoiding Soil Compaction*, Pennsylvania, Pennsylvania State College of Agricultural Sciences, 2004, pp. 1-8.
- [4] V. D. Hoang, N. T. Phuong, S. M. Yoon, H. K. Kim and S. B. Kim, "A New Approach for Designing Quadruped Robots," Kumamoto, 2007.
- [5] G. A. Bekey, "Autonomous Robots - From Biological Inspiration to Implementation and Control," MIT Press, 2005.
- [6] Y. Fukuoka, H. Kimura and A. H. Cohen, "Adaptive dynamic walking of a quadruped robot on irregular terrain based on biological concepts," *Int J. Robt. Rese.*, vol. 22, pp. 187-202, 2003.
- [7] I. Poulakakis, E. Papadopoulos and M. Buehler, "On the stable passive dynamics of quadruped running," *Proc. IEEE Robo. Auto.*, pp. 1368-1373, 2003.
- [8] B. Baxter, "Fast Numerical Methods for Inverse Kinematics," 21 February 2000. [Online]. Available: <http://www.billbaxter.com/courses/290/html/img0.htm>. [Accessed 23 February 2013].
- [9] T. Tee, K. Low, H. Ng and Y. Fredrick, "Mechatronics Design and Gait Implementation of a Quadruped Legged Robot," in *Seventh International Conference on Control, Automation, Robotics and Vision (ICARCV)*, Singapore, 2002.
- [10] Society of Robots, "Robot Statics," 2013. [Online]. Available: http://www.societyofrobots.com/mechanics_statics.shtml. [Accessed 2 June 2013].
- [11] Texas Instruments Incorporated, "LM138/LM338 5-Amp Adjustable Regulators (Datasheet)," Dallas, 2013.
- [12] J. Ewing, "Introduction to Batteries," Great Hobbies Inc., 2013. [Online]. Available: http://www.greathobbies.com/technical/tech_batteries_3.php. [Accessed 5 Oct 2013].
- [13] D. Wettergreen and C. Thorpe, "Gait Generation for Legged Robots," in *IEEE International Conference on Intelligent Robots and Systems*, Pittsburgh, 1992.
- [14] Oricom Technologies, "Stability Analysis of the Creep Gait," December 2004. [Online]. Available: <http://oricomtech.com/projects/proj2/crp-stab.htm>. [Accessed 12 June 2013].
- [15] O. Liang, "OscarLiang.net," 2013. [Online]. Available: <http://blog.oscarliang.net/inverse-kinematics-and-trigonometry-basics/>. [Accessed 23 July 2013].

DESIGN OF A TRANSMISSION LINE MONITORING SOLUTION FOR AN UNMANNED QUADCOPTER

T van Rooyen*, R Gouws**

*North West University, School of Electrical, Electronic and Computer Engineering, Potchefstroom Campus, tianvnr00y@gmail.com

**North West University, School of Electrical, Electronic and Computer Engineering, Potchefstroom Campus, rupert.gouws@nwu.ac.za

Abstract. Eskom owns thousands of kilometres of transmission lines that need to be inspected in order to plan maintenance. Current methods of inspection are costly and ineffective and could pose safety risks. Systems already developed for inspection purposes do not meet the specifications as determined by Eskom for transmission line inspection. A solution is proposed by the design and construction of a monitoring system consisting of a single board computer (SBC), USB video and infrared cameras, and a GPS unit. The system is attached to a quadcopter that flies along the transmission line to collect data. Software is developed that stream the video and GPS data to a monitoring station and provide logging capability.

Key Words. Eskom; transmission line monitoring; quadcopter.

1. INTRODUCTION

Eskom's Transmission department spends a vast amount of money per year to perform transmission line inspections. Current methods are costly and ineffective. The monitoring system design presented in this paper is aimed at providing a system that provides the same level of functionality as current methods used by Eskom at a reduced cost. High quality inspection data must be acquired in order to plan maintenance activities.

The remainder of this paper is structured as follows: First, a brief background of current inspection methods and existing technologies are presented. Then, the system analysis, functional analysis, monitoring system design, monitoring system operation, results and future work are discussed. Finally, a conclusion is drawn.

2. BACKGROUND

This section provides background on current methods of inspection and existing monitoring solutions.

2.1 Current methods of inspection

Eskom makes use of two types of inspections, namely air inspections done by helicopter and ground inspections done by patrolmen. Three types of air inspections are done: detailed air inspection, fast air inspection and fire risk air inspections. Detailed air inspections are done every three years to evaluate the condition of the line hardware, conductors, conductor spacers, insulators, earth wire and tower structures from as close as is possible using a helicopter. Fast air inspections are conducted annually. The purpose of this inspection is to establish the general condition of the transmission line and servitude [1]. It must be ensured that the transmission line and servitude complies with all the minimum legal, safety and environmental requirements. Fire risk air inspections are done in areas where veld fires are experienced on a regular basis. The purpose of this inspection is to evaluate the potential fire risk in an area before the annual fire season. Ground inspections are conducted once every twelve months. Ground inspections are done to identify obvious defects on

the line. All findings for an inspection must be recorded and supported with photos and video. When crews are conducting an aerial inspection, defects with regards to the following aspects needs to be inspected and noted [1]:

- Broken or damaged insulators.
- Pollution that negatively impacts the performance of the transmission line. Types of pollution to be noted include industrial, mine/dust, marine or bird pollution.
- Birds' nests on structures and damaged or missing bird guards.
- Moved or missing vibration dampers.
- Broken or missing spacer.
- Trees, reeds, grass or other natural products impairing servitude.
- Defect regarding general hardware including anti-climb devices, tower members, tower labels, stays and other general hardware concerns.
- Damaged conductors.
- Damaged shield wire.

2.2 Existing monitoring solutions

Systems have been developed for the purpose of transmission line inspection. The LineScout is a robot developed by Hydro Québec to be used for inspecting live transmission lines [2]. The LineScout uses two wheels to run on top of a live line. The LineScout is equipped with a three-axis robotic arm. The arm is equipped with a camera and has the ability to grip a variety of tools. The robotic arm grants the ability to carry a variety of sensors to be used for inspection, such as visual-, infrared- and electrical resistance inspections [3].

The Expliner is a robot developed by HiBot to be used to perform inspection tasks on high-voltage lines [4]. The Expliner moves along the transmission line by means of four wheels mounted on two axles. The robot is equipped with four sets of laser sensors to perform detail measurements of the transmission line conductor. The robot also houses a high-

definition, high-zoom camera to be used for detail visual inspection of the line.

All of the systems considered above attach to the transmission lines by means of wheels or rollers. These systems thus have difficulty in moving past obstacles such as vibration dampers or visibility markers. Further, these systems focus on the acquisition of specialized data or general repair. Eskom inspections do not require such specialised data or repair functionality. These systems are thus not suited to perform Eskom transmission line inspections.

3. SYSTEM ANALYSIS

This section contains the system analysis of the monitoring system.

3.1 Project Objective

Conceptualise and design a monitoring system that will be placed inside a quad-copter type unmanned aerial vehicle. The monitoring system should provide the same level of functionality as current methods for inspection. Data collected should be of such quality that it could effectively be used to plan maintenance activities [1], [5].

3.2 Requirements Analysis

The design of the system presented in this paper was done according to a set of specifications in order to satisfy the design problem. These specifications are:

- Live video streaming must be achieved to provide real-time monitoring capabilities.
- The system must be equipped with a mobile network connection. The system will be mounted on a quadcopter and a wireless network connection is thus needed. It must be ensured that the wireless network connection has sufficient bandwidth to enable live streaming of data from the monitoring system.
- The system must have locational awareness. Locational data must be captured in order to plan maintenance activities.
- The system must be lightweight as it must be mounted to a quadcopter. Excess weight will impact negatively on the flight characteristics of the quadcopter.
- The system will run from battery power and must thus have low power consumption. Low power consumption will mean longer flight times.
- The system must be compact as limited space is available on the quadcopter.
- The system must be reliable.
- The system must be designed with future improvement in mind.

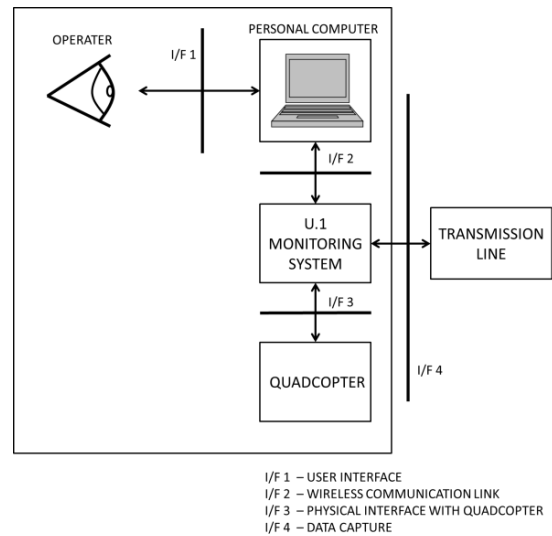


Figure 1: Operational architecture

3.3 Operational Analysis

Figure 1 shows the operational analysis of the system. The operator will interact with the system via a computer running the correct software (I/F 1). This computer will act as a remote control station. A wireless network connection will be established between the computer and the monitoring system (I/F 2). This interface will allow controlling the system and facilitate the transfer of data to and from the monitoring system. The monitoring system will be attached to a quadcopter via I/F 3. Finally, the monitoring system will acquire data from the transmission line via I/F 4.

4. MONITORING SYSTEM FUNCTIONAL ANALYSIS

Figure 2 shows the functional architecture of the monitoring system. High level functional units are identified. The system will have a central processing platform to which all other components will connect (F/U 1). Software to control the system will run on this functional unit. Hardware will be added that will acquire data from the transmission line (F/U 2). A locational sensor will be added to log the position of the system (F/U 3). F/U 2 and F/U 3 will both interface with the transmission line via I/F 4. Wireless communication (F/U 4) is added to the system to enable networking functionality between the remote control station and the monitoring system via I/F 2. The system will contain a power source (F/U 5) to power the system. A housing is designed to contain the system (F/U 6).

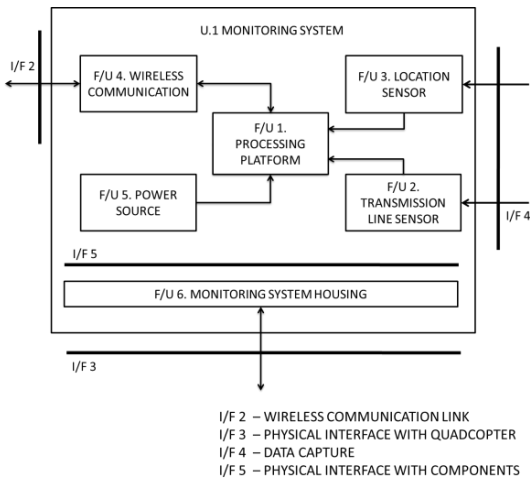


Figure 2: Monitoring system functional architecture

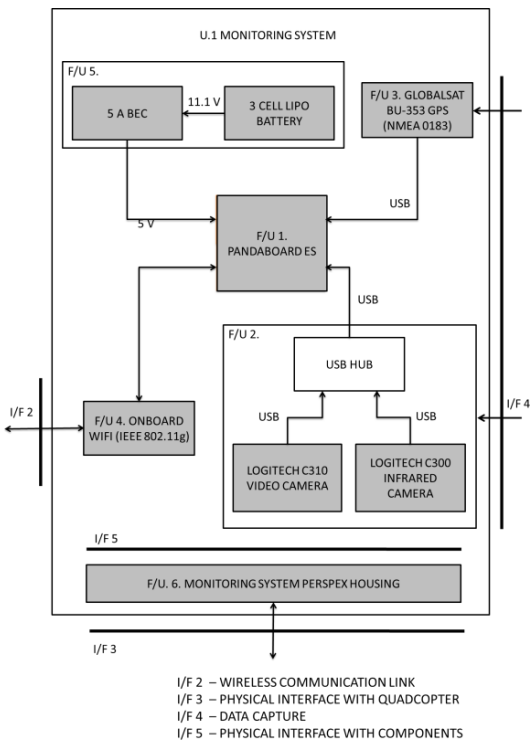


Figure 3: Monitoring system design

5. MONITORING SYSTEM DESIGN

This section contains the details of the design of the monitoring system. The design of each of the functional units present in Figure 2 is considered. The software to run on the monitoring system is also described. Figure 3 shows the detail design as discussed in this section.

5.1 Processing Platform

It was chosen to use the single board computer (SBC) architecture for the processing platform. Its compact size and low power consumption have made SBC's a popular choice for embedded systems [6]. The Pandaboard is used. The Pandaboard is the most

powerful SBC available. It features a 1.2 GHz ARM A9 dual core processor, 1 GB of RAM, two USB ports and onboard Wifi. The Pandaboard is well suited to the task at hand and is the choice SBC in many video processing applications [7], [8], [9]. The features setting it apart from other SBC's are its processor and large amount of RAM. The availability of these resources made the Pandaboard an attractive option when also considering future development. The Pandaboard uses a SD card as storage. A 16 GB SD card is used for this purpose. The Pandaboard runs from a regulated 5 V source and draws a maximum of 4 A. Figure 4 shows the Pandaboard used. Important aspects of the board are marked on the figure.

5.2 Transmission Line Sensor

USB cameras were chosen to use to capture visual data of the transmission line. A USB webcam design was chosen as it is inexpensive and it will be easily integrated with the SBC platform. The camera must be able to provide a level of detail that will enable effective inspection and maintenance planning. Cameras considered were high-definition cameras. The Logitech C310 camera was chosen to use as the video camera for the system. The camera is capable of 5 MP image and 720p video capture. This will be sufficient quality to perform inspection.

Equipping the system with an infrared camera will enable the temperature of the transmission line to be monitored. It was found that all photo sensors in digital cameras are susceptible to light in the near-infrared spectrum. Manufacturers add an infrared filter to keep infrared light from reaching the photo sensor. If this sensor is to be removed the camera will be able to capture the near-infrared light. A filter can then be added to filter out the visible light so that the camera only sees infrared light. A USB camera can be used and modified for this purpose. A Logitech C300 camera was used and modified into serving as an infrared camera.

5.3 Location Sensor

GPS units were considered to provide locational data for the monitoring system. GPS modules that provide a USB interface were selected as they would integrate easily with the SBC configuration. The Globalsat BU-353 GPS module was selected to be used on the system. The GPS uses the SIRF Star 3 chipset and the manufacturers claim an accuracy of 10 meters. The GPS takes at most 42 seconds to get a fix on its location in the case of a cold start. The module is certified to be waterproof to the IPX6 standard and features a magnetic mount. The data sent from the GPS is sent in the NMEA 0183 protocol at 4800 baud.

5.4 Wireless Communication

Wifi was selected to be used for the wireless network connection between the monitoring system and the remote control station. To enable Wifi connectivity, both the monitoring system and the remote control station needs to have access to the Wifi network.

The Pandaboard features an onboard Wifi module. This is convenient as no extra hardware is needed to connect the monitoring system to the Wifi network. To connect the remote control station to the Wifi network, a Wifi access point will be used. A local Wifi network will be hosted from the remote control station to which the monitoring station will connect. A local Wifi network will have sufficient bandwidth for the purposes of the system and to demonstrate the concept.

5.5 Power source

It was chosen to use a Lithium Polymer (LiPo) battery to provide power to the monitoring system. A three cell 3300 mAh battery was used for the purpose. However, a three cell battery has a nominal voltage of 11.1 V, which is not suitable for the Pandaboard, which runs of a 5 V supply. A 5 A battery eliminator circuit (BEC) was used to regulate the voltage from the battery to 5 V. A BEC is a switch mode regulator popular for use in the radio control hobby community.

5.6 Software

Ubuntu 12.04 LTS was loaded onto the SD card used by the Pandaboard. Using Linux as an operating system abstracts the developer from the technical aspects of using the Pandaboard as the operating system takes care of the technical details. Using connected hardware components become easier as drivers for the hardware are packaged with most Linux distributions. Custom C++ software was developed to run on the Linux platform. The software controls the operation of the system and enables communication between the monitoring system and the remote control station. An open source multimedia framework, Gstreamer, was used in conjunction with the C++ software to simplify the process of video streaming and camera control.

6. MONITORING SYSTEM OPERATION

The software on the monitoring system was configured to run as soon as the Pandaboard starts up. As soon as the system is active, a signal is sent to the remote control station to indicate the system is online. Figure 5 shows the user interface from which the system is operated. The user has the ability to select one of the two cameras and switch the video feed on or off. A separate screen shows the video feed. The coordinates and time as recorded on the monitoring system is sent to the remote control station every three seconds. The software has the functionality to log issues that is identified during an inspection. Comments are typed into a textbox and saved to text file with the current time and coordinates.

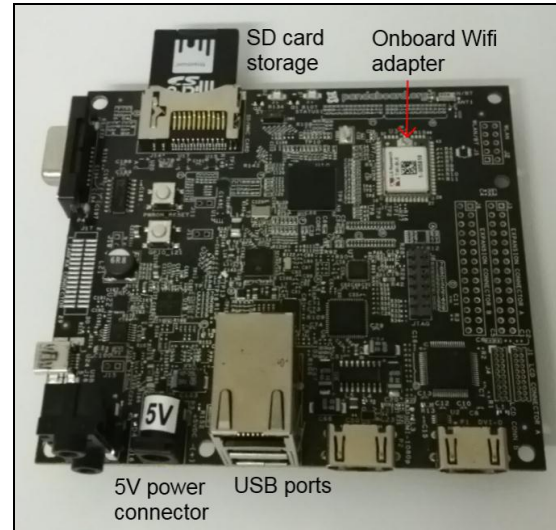


Figure 4: Pandaboard SBC

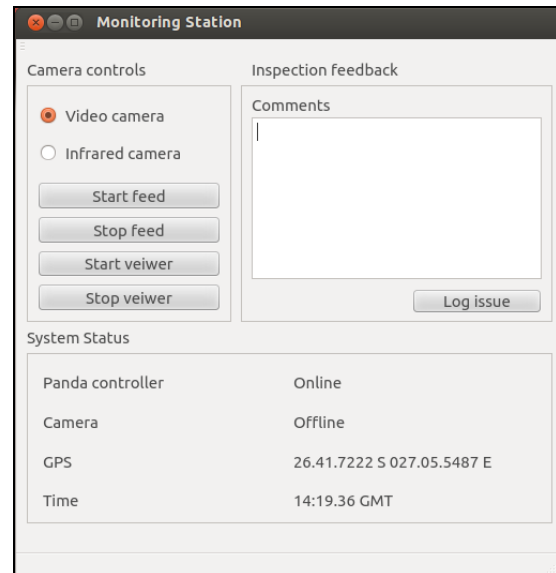


Figure 5: Remote control station user interface

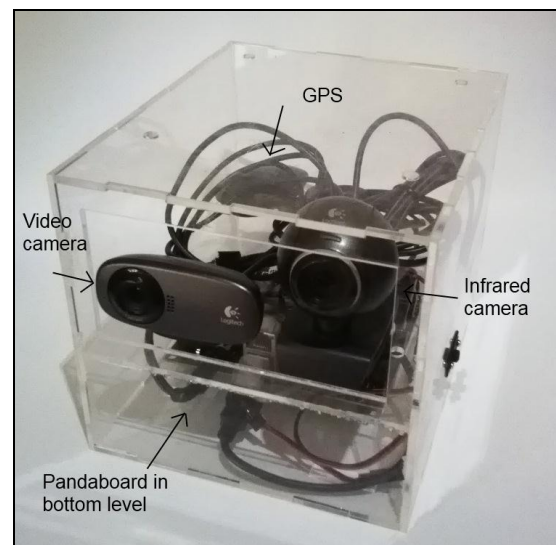


Figure 6: Monitoring system in Perspex housing

7. RESULTS

Results found while testing the system will be included in this section. Figure 6 shows the system without the power source contained in the Perspex housing before being attached to the quadcopter.

7.1 Power consumption

The power draw was measured at various times in the operation of the system. Figure 7 shows the power draw at the various stages of operation. The system draws mainly between 2 W and 4.5 W on startup. When the system is in idle, it draws an average of 4 W of power. When the cameras are enabled, the system draws up to 5.5 W. The system draws approximately 5 W of power during normal operation.

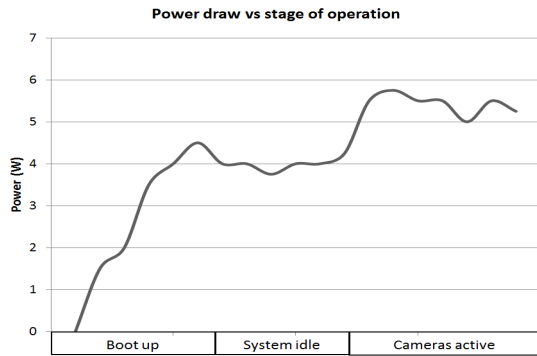


Figure 7: Power draw vs stage of operation

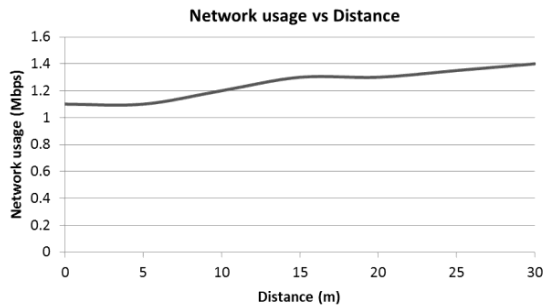


Figure 8: Network usage versus distance



Figure 9: Integrated system

7.2 Network usage

The network usage of the system was measured. It was found that when the monitoring system is moved further away from the Wifi router, the network usage increased. Figure 8 shows the network usage at different distances away from the Wifi router. The system uses between 1.1 Mbps when closer than 10 m and up to 1.4 Mbps at the limit of the range for the local Wifi network.

7.3 GPS accuracy testing

The accuracy of the GPS used on the monitoring system was tested. The GPS coordinates extracted from the GPS module can be seen displayed on the graphical user interface shown in Figure 5. A commercial Garmin GPS was enabled at the same location and the coordinates noted. Figure 10 shows the coordinates as recorded by the Garmin GPS.



Figure 10: Garmin GPS coordinates

The coordinates captured by the monitoring system are S 26°41.722' E 027°05.546'. This is almost identical to the coordinates measured by the Garmin GPS.

7.4 Integrated testing

The monitoring system was integrated with the quadcopter. Figure 9 shows the monitoring system installed on the quadcopter. The monitoring system can be seen mounted on top of the quadcopter between the propeller blades. The system was tested in a realistic environment as what it would be used in. The integrated system was flown next to a substation and transmission lines. Video from both the video camera and infrared camera was recorded. Figure 11 and Figure 12 show images taken from the video and infrared cameras respectively.



Figure 11: Image taken from video camera stream



Figure 12: Image taken from infrared camera stream

It can be seen from Figure 11 that the quality of the video is such that details of the transmission line and associated hardware can clearly be seen. The quality of the video enables transmission line inspection to be performed. Although the concept of a thermal imaging camera was proved, the infrared camera was not sensitive enough to infrared light to effectively be used as an alternative to a thermal imaging camera.

8. FUTURE WORK

This section will detail work that will be done in the future. The system as designed is aimed at proving the concept of a monitoring system attached to a quadcopter to perform transmission line inspection. Further work needs to be done to improve the quality of inspection data or add other types of sensors to the monitoring system. High quality thermal imaging will be added to the system. This will enable the system to accurately gauge the temperature of the transmission line to detect failing hardware. Lidar sensors will be added with which the system can form a 3D map of the surroundings. Servo operated camera gimbals will be added to enable smoother operation of the cameras.

Further work also needs to be done on the networking capabilities of the system. This system used a local Wifi network to prove the concept. Adjustments to the system will be made to incorporate technologies such as cellular networks for long range communication and data streaming.

9. CONCLUSION

In this paper, a monitoring system was designed for transmission line inspection. The monitoring system attaches to a quadcopter that flies along the transmission line. The monitoring system is capable of real-time video streaming to a remote control station from where the system is operated. GPS coordinates accompany the video feed. Fault logging capabilities are provided. High quality inspection results were obtained that can successfully be used as a cost effective alternative to current methods of inspection.

REFERENCES

- [1] Eskom, "Supporting Clauses," in *Routine Inspection and Maintenance of Transmission Lines*, Johannesburg, 2008, pp. 4-7.
- [2] Hydro Québec, "LineScout - A Robot for Inspecting Live Transmission Lines," Hydro Québec, Varennes, Pamphlet 2010.
- [3] N. Pouliot S. Montambault, "Design and validation of a mobile robot for power line inspection and maintenance," in *Field and Service Robotics*, Chamonix, 2007, pp. 3970-3977.
- [4] HiBot, *Expliner Robot for Inspection of Very-High Voltage Transmission Lines*. Tokyo, 2009, p. 1.
- [5] Eskom Holdings Ltd., in *Fundamentals and practice of overhead line maintenance*, Johannesburg, Crown Publications, 2004, pp. 37-56.
- [6] C.B., Altug, E. Yigit, "Visual attitude stabilization of an unmanned helicopter in unknown environments with an embedded single board computer," in *Robotic and Sensor Environments*, Magdeburg, 2012, pp. 49-54.
- [7] Paolo Di Giamberardino, Daniela Iacoviello, and R. M. Natal Jorge, "A New Approach," in *Computational Modelling of Objects Represented in Images III: Fundamentals, Methods and Applications*. Rome: CRC Press, 2012, p. 46.
- [8] Xin Li, Zhan Ma, and F. C. A. Fernandes, "Unified complexity model for H.264/AVC video processing on mobile platform," in *Image Processings (ICIP)*, Orlando, FL, 2012, pp. 2937-2940.
- [9] H. O. Uhan and A. Akbas, "Designing a system allowing high-definition video transfer with minimum latency and multi-use access to projection device by wireless," in *Complex Systems (ICCS)*, Agadir, 2012, pp. 1-6.

Topic B

High Voltage

CORONA MEASUREMENT IN AN INVERTED COAXIAL GEOMETRY TO EVALUATE THE EFFECT OF CONDUCTOR TEMPERATURE

P. J. Pieterse

Electrical and Electronic Engineering, Stellenbosch University, Private Bag X1, Matieland 7602, South Africa, Email: petrus@sun.ac.za

Abstract: The effect of conductor temperature on the corona performance of power lines has been evaluated. Initial tests were performed on a preheated (live) conductor as it cools down with regular, intermittent temperature measurements taken after each momentary disruption of the HV supply. An inverted test topology, with the centre conductor grounded, was developed and used for further studies. This allows precise temperature control of the conductor whilst energised at HV. This arrangement however sets new challenges with regards to the electrical measurement as traditional methods using screen electrodes cannot be used. An inverted test cage topology is presented and various test methods evaluated. Furthermore; the selection of coupling capacitor and matching / decoupling circuit is discussed. The data for both methods using different conductors is finally compared.

Keywords: Power Line Corona, Corona cage, Inverted corona cage, partial discharge, coupling capacitor, effect of conductor current.

1. INTRODUCTION

Corona cages have been used in the past to study the effect of power line design on the corona performance of overhead power line conductors. This is achieved by simulating the local field using a set of coaxially arranged conductors. When ignoring the effects due to space charge formation, the electric field reduces at a rate of $1/r$ for a coaxial system. The applied voltage is adjusted in order to attain the desired field strength at the conductor for a given electrode geometry in correlation with the actual system design.

The effect of conductor current on power line corona performance has been studied by F.W. Peek [1] using small diameter conductors (2.6 mm – 4 mm). Peek evaluated the effect of both AC and DC current flowing in the wire. Using the wire temperature to calculate the air density surrounding the wire, Peek found this correction to be too large. No direct correlation was found, possibly due to inaccuracies concerning temperature measurement.

A study was initiated in the form of a graduate project in 2010 and the work was reported in [2, 3]. It was found in [3] that the corona inception could be predicted by using Peek's formula [1] using the conductor temperature to calculate the relative air density and a surface factor of 0.965 (smooth rod). This initial test results were obtained using intermittent heating, energising and measuring intervals as both the heating and the high voltage supply had to be connected to the centre conductor in turn. This

method was very cumbersome and unreliable. In 2011 alternate measuring techniques using bridge circuits were evaluated for AC and positive DC [4]. Later trials [5] utilised an inverted cage topology in order to precisely control and measure the conductor temperature. This topology as shown in figure 1 is used for further study with the conductor now being at zero potential.

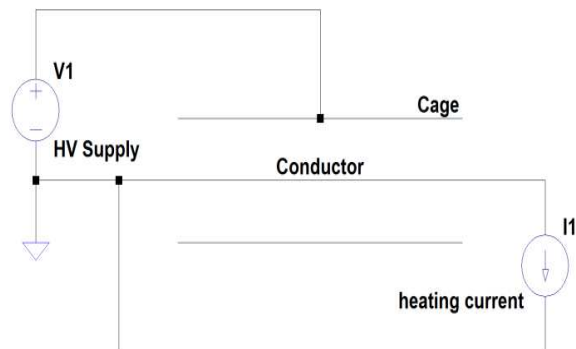


Figure 1: Inverted corona cage

This topology, having the outer cage at high voltage, prohibits the use of an external screen or shield electrodes at the ends. Furthermore, the corona current has to now be measured on the wire or by means of a high voltage coupling capacitor and cannot be measured between the outer cage and ground as in the usual manner.

2. TEST ARRANGEMENT

2.1 Test cage design

Using a conductor range of 10 – 25 mm and a maximum test voltage of 100 kV, the outer cage (extruded mesh) was dimensioned so that the maximum outer diameter was used that would allow a high enough E-field on the conductor to cause stable corona without flashover. The outer conductor (cage) has an inner diameter of 800 mm and is 1 250 mm in length. A 27 mm diameter tube is welded to each end of the cage to control the E-field at the edges. The completed test cage is shown in figure 2.

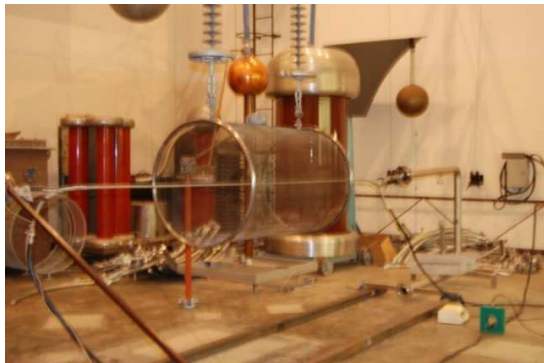


Figure 2: Test cage

2.2 Heating circuit

Each end of the centre conductor of the coaxial conductor arrangement is connected to a low voltage, high current transformer. The conductor temperature is controlled by varying the current circulated through it using an auto-transformer as a regulator. The temperature of the conductor was allowed to stabilise before experiments were performed.

3. CORONA DETECTION TECHNIQUES

Initial results [4, 5] were obtained visually using a Corocam MK I camera with photomultiplier optimised for the UV spectrum. Identification criteria [5] were established to evaluate the extent of the discharges as given in appendix A. In an attempt to better quantify the results obtained, electrical detection techniques had to be developed for this special (inverted) case.

3.1 Electrical parameters

An electrical discharge due to ionisation causes the movement of charge. This charge movement creates a current and voltage wave within the circuit which is determined by the characteristic impedance of the system as well as the circuit impedance. The measured current is derived from the original discharge site and therefore the integral of the current is referred to as the apparent charge.

Using the dimensions of the cage the electrical parameters are obtained as follows:

<i>Cage capacitance</i>	$C = 17.2 \text{ pF}$
<i>Cage Inductance</i>	$L = 1.01 \text{ } \mu\text{H}$
<i>Characteristic impedance</i>	$Z_0 = 242.5 \Omega$
<i>Wave transition time</i>	$t_{trans} = 5.213 \text{ ns}$

Conductor corona can be expected to contain a broad spectrum of noise up to 3 MHz with typical frequency content between 0.5 to 1.6 MHz [6]. Measurements conducted on a small corona cage at SU [7] showed this range to extend up to roughly 30 MHz

Using the propagation velocity of the line, the wavelength at 30 MHz is 7.2 m. Even though the cage is much shorter, system reflections may occur, which distort the measured corona current pulses. These reflections are caused by the impedance mismatch between the ends of the coaxial system and that of the test section.

3.2 Impedance matching and decoupling network

A simple lumped resistive matching element can be used as the system is assumed to be lossless and is much shorter than the shortest wavelength of the signal. The high test voltage however, requires the use of a coupling capacitor in series. Similar techniques have been used in [7, 8]. Satisfactory results were obtained with a matching T network, (240Ω:50Ω) that was constructed and is shown in figure 3, when injecting a voltage pulse into the test section. The self-inductance of the coupling capacitor and the loop inductance created by the physical connections create a slower response as well as modifying the system impedance, which affects the current pulse shape of the corona pulses [9].



Figure 3: Matching network

A common decoupling technique, employed in corona measurement circuits, is through the use of a coupling capacitor in series with measuring impedance R connected across the test sample. Should the capacitor be considered as a short circuit at high frequencies, the resistor R may serve as a measuring as well as matching impedance. Figure 4 shows an example of a typical decoupling circuit commonly referred to as straight detection with sample capacitance C_A , coupling capacitor C_K and current transducer CD. An alternate connection,

with the measuring impedance connected between the outer cage and ground is often applied in corona cage measurement techniques.

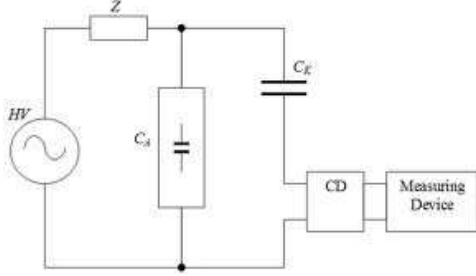


Figure 4: Typical corona detection scheme

Since this is not possible with the inverted (cage at High voltage) topology, the current has to be measured via a coupling capacitor or on the line.

3.3 Coupling capacitor and filter design

A corona discharge creates a displacement current pulse i travelling in both directions away or toward the discharge site. The magnitude of the incident potential wave is:

$$v_i = -\frac{1}{2} i Z_0 \quad (1)$$

With Z_0 the characteristic impedance of the coaxial system. Integrating both sides yield,

$$\int_0^t v_i dt = -\frac{Z_0}{2} \int_0^t i dt \quad (2)$$

And since, $q = \int i dt$ it is evident that the integral of the voltage is proportional to the charge.

$$\left| \int_0^t v_i dt \right| = \frac{Z_0}{2} \cdot q \quad (3)$$

Assuming the discharge wave to have a double exponential shape with a relatively short rise time, the incident voltage wave may be approximated as:

$$v_i = V_p e^{-t/\tau_s} \quad (4)$$

The measured output v_t is a function of both the pulse time constant τ_s as well as the circuit time constant τ_m :

$$v_t = V_p e^{-t\left(\frac{1}{\tau_s} + \frac{1}{\tau_m}\right)} \quad (5)$$

If the conversion accuracy h is expressed as the ratio between the measured charge and the charge displaced at the discharge site,

$$h = \frac{q_{measured}}{q_{actual}} \quad (6)$$

And since q is proportional to the integral of the voltage wave for fixed characteristic impedance Z_0 , as in (3), the conversion factor h may be found by integration of (4) & (5) and then evaluating (6).

$$h = \frac{\int v_t dt}{\int v_i dt} = \frac{\tau_m}{\tau_s + \tau_m} \quad (7)$$

When this response is given in terms of the ratio of circuit and pulse time constants $a = \frac{\tau_m}{\tau_s}$ the response is:

$$h = \frac{q_{measured}}{q_{actual}} = \frac{a}{1+a}$$

This yields reproduction accuracies as follows:

Time constant ratio a	Reproduction accuracy h
5	0.83
10	0.91
15	0.94
20	0.95
40	0.97

It is proposed [10] that the time constant of the measuring circuit be 5 times the length of the wave or,

$$\tau_m = C_m R_m \geq 5t_0$$

C_m and R_m are the measuring circuit capacitance and resistance and t_0 the expected length of the pulse. If t_0 is expressed in terms of τ_0 , assuming a pulse length of $t_0 \approx 5\tau$, then $\tau_m \geq 25\tau_0$. These values will yield a conversion accuracy of at least 96%.

A coupling capacitor of 1200 pF was used. When terminating the system into 240 Ω , the longest pulse that can be measured accurately is 58 ns, using 480 Ω allows measurement of 115 ns pulses. Positive corona pulses may have a pulse length of 250 μs [6] which implies that much larger measuring time constants are to be considered. It is notable that 300 Ω resistive elements are combined in series with capacitors of 500 pF or less in practice.

A compromise has to be afforded between the measurement bandwidth and distortion of the signal due to reflections. Narrowband measurements according to IEC, Nema and CISPR are normally preferred as the system can be calibrated using a calibrator with the correct pulse shape.

A simple band-pass filter with its response, shown in figure 5, was constructed so as to remove the power frequency components from the measured signal. The Pass band is roughly between 100 kHz and 100 MHz.

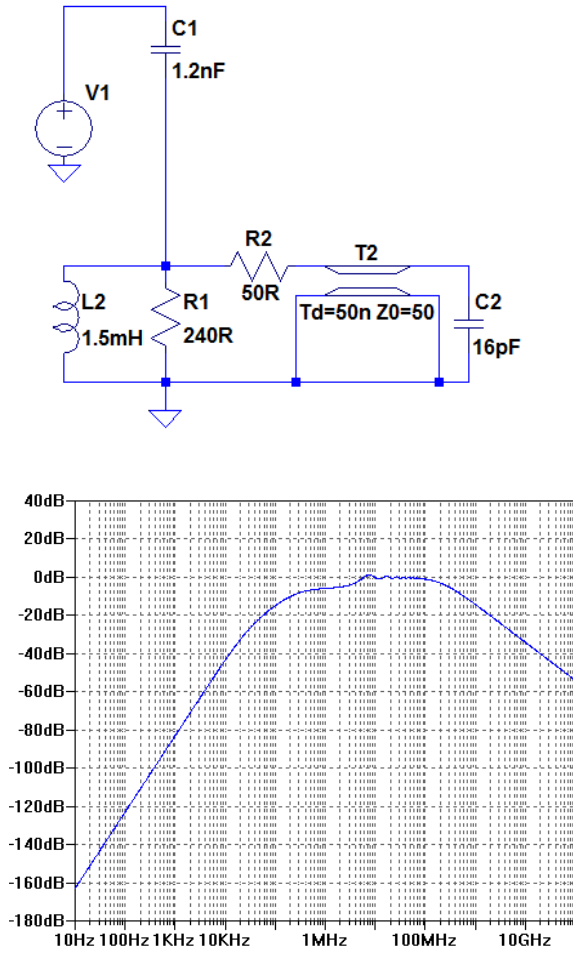


Figure 5: Band-pass filter schematic and freq. response

4. TEST RESULTS

Tests were initially performed using optical detection techniques. Tests conducted by Duze [4] were performed using a non-inverted cage. The test cage was 800 mm wide with a stranded conductor of 27 mm diameter (0.795 GMR ratio). These tests were conducted for both AC and DC+ with a pre-heated conductor in the cooling phase. Regular temperature test intervals interrupted the process of corona inception voltage determination. The data points were time stamped and the trend created by interpolating the temperature data.

Tests conducted by Hector [5] were conducted using an inverted cage with current through the centre conductor regulated to obtain temperature stability. These tests were performed using a smooth conductor of 17.4mm diameter with an outer cage diameter of 800 mm (which was connected to the HV supply).

Figure 6 shows the Inception field magnitude (full corona, as per appendix A) versus the conductor temperature for individual studies using different methods. The predicted inception field strength

magnitude according to Peek is calculated for each geometric structure with Peek* referring to the geometry used by Duze, and Peek** that used by Hector. The conductor temperature is used to calculate the relative air density and the final value for E obtained is multiplied by 0.66. Another study [3] determined this factor to be 0.96. Further work is under way to resolve these discrepancies.

5. CONCLUSIONS

In order to control the conductor temperature accurately, a method was adopted whereby the normal test cage arrangement was reversed. This eliminated the need for a large and costly heating transformer insulated to 100 kV. Initial work conducted with the inverted cage agrees well with previous studies using the normal topology.

The test pulse is modified by a number of circuit factors and this makes it very difficult to determine the exact shape of the trace, further work is required.

The choice of coupling capacitor is normally not given enough attention however it has been shown that the choice of capacitor greatly influences the measured output current.

The effect of impedance matching could not be adequately studied due to the inherent difficulties met when using an inverted cage. It is postulated that the reflection / distortions of the test signal are insignificant especially when studying corona activity for multiple sources. These would lead to superposition errors which may be resolved by means of integration to find the total power dissipated. Statistical techniques may as well be implemented.

The effect of conductor temperature has been studied and found to be significant. Peek's formula may be applied to determine the expected corona inception level using the conductor temperature to determine the relative air density in the zone surrounding the conductor as well as including a constant multiplier factor (0.66) to the final value of E obtained. This scaling factor is similar to the roughness factor m. A new set of constants may have to be defined to remove possible ambiguities.

6. ACKNOWLEDGEMENTS

The author would like to thank H.J. Vermeulen and J.P. Holtzhausen, for their valuable inputs.

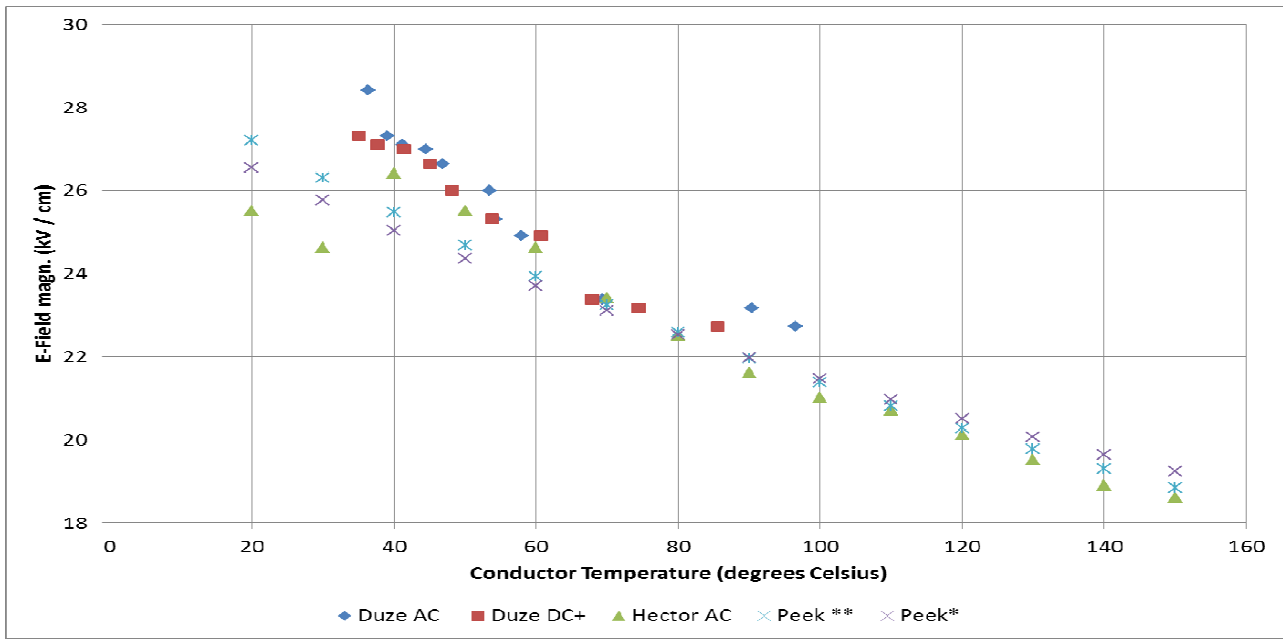






Figure 6: Band-pass filter schematic and freq. response

7. REFERENCES

- [1] FW Peek, "Dielectric phenomena in high voltage engineering" McGraw-Hill, 1929
- [2] JP Holtzhausen, PL Buckle, PJ Pieterse, HJ Vermeulen. "An experimental Investigation into the effect of conductor temperature on AC Power line corona." Southern African Universities Power Engineering Conference, SAUPEC 2010, Johannesburg, January 2010: pp. 300-304.
- [3] JP Holtzhausen, PJ Pieterse, HJ Vermeulen, "Investigation of the Effect of Conductor Temperature on AC Power Line Corona", International Conference on High Voltage Engineering and Application, New Orleans, ICHVE2010, 11 – 14 October 2010.
- [4] A Duze, "An experimental investigation into the effect of conductor temperature on AC and DC corona", Graduate project (E) 448, Stellenbosch University, 2011
- [5] RK Hector, "Design and evaluation of an inverted corona cage for high temperature conductor corona measurements" Graduate project (E) 448, Stellenbosch University, 2011
- [6] P Sarma Maruvada, "Corona performance of high voltage transmission" Research studies press, 2000
- [7] RG Urban, "Modeling corona noise on high voltage transmission lines" Master's Thesis, Stellenbosch University, 2001.
- [8] AJ Otto, "Direct current conductor corona modeling and metrology", PHD Thesis Stellenbosch University, 2009.
- [9] S El-Debeiky, M Khalifa, "Calculating the corona pulse characteristics and its radio interference", IEEE Trans PAS, Vol 90, 1971.
- [10] FH Kreuger, "Partial discharge detection in high voltage equipment", Butterworth and Co., 1989

APENDIX A

CRITERION USED TO EVALUATE CORONA DISCHARGES	
Corocam Image	Visual Description
	<p><u><i>First Glow Discharge</i></u></p> <p>The visual corona that was observed with a corocam, is the first glow discharge observed on the conductor</p>
	<p><u><i>Corona Inception Voltage (CIV)</i></u></p> <p>The corona inception voltage was documented when three or more possible glow discharges was observed on the surface of the conductor.</p>
	<p><u><i>Full Corona</i></u></p> <p>The rms voltage is documented when the corona activity on the conductor is very high and glow discharges are visible on the conductor within the region of the cage.</p>
	<p><u><i>Streamer Development</i></u></p> <p>This stage of corona activity is documented when a discontinuous streamer occur at least once in a 10 second interval.</p>

CHARACTERISING ELECTRICAL TREES IN MGO/EPOXY NANOCOMPOSITE INSULATION THROUGH PD MEASUREMENTS

D. R. Cornish* and C. Nyamupangadengu*

*School of Electrical & Information Engineering, University of the Witwatersrand, Johannesburg,
Private Bag 3, Wits 2050, Johannesburg, South Africa

Abstract: Nanocomposite insulation provides a new possibility for enhancing the quality of conventional insulations. This is desirable as most solid insulation is vulnerable to the phenomenon of electrical treeing. Any technology that can retard electrical trees would be beneficial. The effect on electrical treeing of varying levels of MgO nanofiller in an epoxy host material is tested using PD detection techniques. From the results of the experiments, a model is proposed that to add value to the recent models in the literature. Furthermore the data is analysed in an attempt to detect trends between filler levels, which can be tested on other nanofiller materials.

Key words: Nanocomposite, Electrical Tree, Partial Discharge, MgO Epoxy

1. INTRODUCTION

With the advent of solid insulation material, many of the biggest problems in cable insulation were solved: mainly with regards to ease of repair, weight and flexibility concerns. Susceptibility to electrical treeing is however still a problem. This has caused a concerted push in research concerning nanocomposite insulations which is currently occurring throughout the world. The success of first microcomposite materials and nanocomposite technology in construction materials have shown promising possibilities in material properties modification [1]. A major focus for the research community is electrical treeing: either its eradication or at least significant reduction in effects through nanocomposite technology. Nanocomposite insulation technology is however still in its infancy, with the actual electrical treeing mechanism still not fully understood [2]. Furthermore multiple nanoparticle materials are under investigation. Nanocomposite research also serves as a platform to re-evaluate the electrical tree models with a view towards conformation of both conventional insulation and the newer nanocomposite insulation. In that regard, an investigation into the effects seen with differing nanofiller levels of MgO in a host epoxy resin has been undertaken. This is done through electrical tree characterisation using Partial Discharge (PD) time evolution graphs and Phase Resolved PD Patterns (PRPDs). This information is then analysed for trend data and a model for the time evolution of the electrical tree is proposed and contrasted with existing models.

2. BACKGROUND

Of the modern solid insulation materials, Cross Linked PolyEthylene (XLPE) has proven to be tough, flexible, relatively light and a strong dielectric material compared to other options. The reasons for its strength, the cross linking between polymer chains, is also its greatest weakness in some ways. These cross-links are highly susceptible to damage from high electric field stress. This results in XLPE failing mere hours after an electrical tree has been initiated. It is a weakness almost

all rubber based solid insulation face due to the way the polymer chains interact. It has also been found that electrical treeing is essentially the final failure mode of all insulation in some form or another [2].

Nanocomposite insulations may be a relatively new field but it has attracted the attention of many researchers worldwide. Most researchers are currently working with epoxy resin as the host material for several reasons such as simple manufacture procedure and it is still used throughout industry for jointings, motor and generators to name a few. Once the behaviours have been fully understood, the effects should correlate to more complex host materials such as XLPE.

2.1 Interface models

There are several models that have been developed to explain the modifications seen with nanocomposite material but the most recent and appropriate models are the Polymer Chain Alignment Model (PCAM) [3] and the recently proposed failure model proposed by Tanaka [4].

In the PCAM model, the nanoparticles act as anchor points which cause an interface region to be formed [3]. The interface region can be regarded as polymer strands radiating out from the nanoparticle due to the oxide hydroxide bonds that form. This interface region is also posited to exist around microparticles in microcomposite insulation and is thought to be the reason for the beneficial effects seen in composite insulations. Lewis has further modelled the interface region for both microcomposites and nanocomposites and shown that the interfacial volume of a nanoparticle is much greater than the microparticle interface volume [5]. This interface region is also hypothesised to act as a hole-electron recombination point [3], which may explain many of the beneficial effects. These long polymer strands that are not roughly parallel to the general growth direction of the electrical tree would cause an impediment to the electrical tree growth. This may also force the electrical tree to form around the interface region rather

than through it, further delaying the growth rate and allowing the insulation to survive for longer. The much greater interface volume is thought to be what causes the unexpected and stronger effects than is seen in microcomposites [5].

Tanaka recently discovered that an electrical tree can fully bridge the insulation between the electrodes without failure occurring for many hours afterwards [6]. He has further hypothesised with more experimental data that the important aspect to the electrical tree is the width of the microtubules [4]. The electrical tree may breach the insulation but is not yet wide enough to allow for a short circuit to occur. This also implies that the spread rate of the microtubules can be greater than the microtubule widening rate.

In previous work by the authors, the PD time evolution plots were examined for nanocomposite epoxy samples. A PD time evolution plot in this case is the average PD magnitude plotted over entire life of the sample. The patterns displayed common as well as unusual characteristics such as corona-like PRPDs. The parameter metrics of interest have been chosen as: the time to failure; the peak average PD magnitude; and the mean average PD magnitude. Such data allows detection of trends. The information generated enables the possible explanations of how nanoparticles improve the host material.

3. EXPERIMENTAL PROCEDURE

The samples used for this work were manufactured at TU Delft in the Netherlands. The production procedure is detailed in [7] and summarised as follows. Huntsman™ type CY231 epoxy with hardener type HY925 were used for the host epoxy and precautions were taken to ensure uniform dispersion of the MgO nano-filler. The test samples were specifically designed with Ogura™ needles that have a well defined $5\ \mu\text{m}$ tip allowing for accurate electric field descriptions to be calculated. The gap distance between the base of the sample and the needle tip was set to 3 mm. This gap was chosen as representative of the distance between two conductors in a cable. Finally to ensure a smooth surface on the plane electrode, a silver conductive paint was applied to the bottom of the samples. A diagram of the general sample construction is shown in Figure 1.

The experiment was designed in accordance with the IEC 60270 standard's PD measurement circuit. The PD data is logged continuously using a computer throughout the process. The sample was connected to the test circuit using a customised connector to smooth all sharp points and avoid all possible corona and PDs except those inside the sample. As a final countermeasure to spurious PDs outside the area of interest, the sample is submerged in transformer oil. The voltage applied to the sample was slowly increased to the applied voltage, $V_{app} = 20\ \text{kV}_{RMS}$ and maintained until breakdown oc-

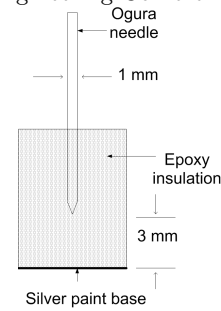


Figure 1 : Diagram of test sample structure.

curred. It is noted that the noise level within the testing environment is approximately 0.3 pC.

4. RESULTS AND OBSERVATIONS

As the focus of this paper is on the characteristics of varying levels of MgO nanofiller in epoxy, there are several parameters that need to be analysed. Firstly, each nanofiller level will be analysed using a categorisation system. This will be done using PD time evolution graphs correlated with the recorded PRPDs. Secondly the data will be quantified, compared and contrasted between different nanofiller levels to allow for analysis of any possible trends that may occur. From this analysis a refinement of the previously mentioned model is presented based on the new data and information.

4.1 Categorisation of electrical tree PD data

The nanofiller levels of the MgO used in the experiment were 0 % (clean or neat epoxy), 0.5 % by weight (%wt), 2 %wt and 5 %wt.

In a previous paper by the authors, a categorisation scheme was developed for the PD time evolution plots [8]. A brief description of this categorisation scheme is given below. It is noted that the PD time evolution behaviour is correlated with the PRPD to further categorise the system.

4.1.1 Clean Epoxy: An example of a PD time evolution graph of clean epoxy is shown in Figure 2a. The plot is separated into categories A and B, which are further discussed as follows;

- **Category A:** This category represents the initiation phase of the electrical tree and is characterised by a slow, approximately linear increase in the average PD magnitude. This is believed to be due to the intense electric field stress causing an electrical bush tree to form. A typical PRPD of this category is shown in Figure 3. At around 0.3 hours however, a rapid rise in average PD magnitude presents itself, prompting another category.
- **Category B:** As the electrical bush tree has grown,

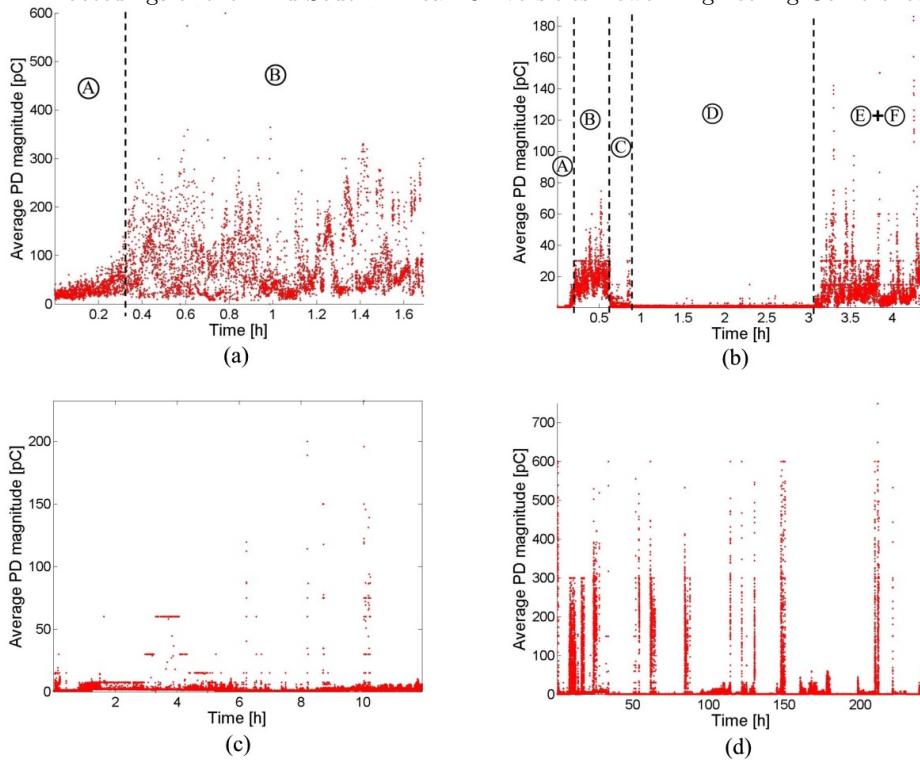


Figure 2 : PD time evolution plots for (a) clean epoxy, (b) 0.5 %wt MgO/Epoxy, (c) 2 %wt MgO/Epoxy and (d) 5 %wt MgO/Epoxy

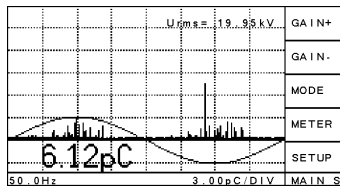


Figure 3 : Example PRPDP for category A.

it is theorised that an electrical branch tree has developed allowing larger PDs to occur. This phase is characterised by a rapid increase in the large PD magnitude. It should be noted that the small PD magnitudes are still present but are averaged out by the occurrence of so many large PDs. This can be seen from the PRPDPs for this time period as shown in Figure 4. This can be explained by the bush trees still experiencing PDs.

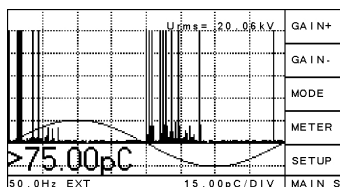


Figure 4 : Example PRPDP for category B.

Once the electrical branch tree has grown large enough, category B PD behaviour continues to occur until failure of the sample is reached. The PRPDPs are as expected for typical PDs in both categories, with the PDs occurring on the rising and falling edges of the sinusoid.

4.1.2 0.5 %wt MgO/Epoxy: The plot of PD time evolution for a 0.5 %wt filler level of MgO is shown in Figure 2b. As can be seen in Figure 2b, the categorisation marks, categories A and B still occur. This appears to remain true for all the clean epoxy and nanocomposite epoxy samples. This is accounted for by the model that is being developed as the nano-particles are unlikely to affect the initiation of the electrical tree as an electrical bush tree is a necessary first step. The cascade into an electrical branch tree is further unavoidable due to the stress induced by the needle. From that point onwards however nanocomposite insulation differs from standard clean epoxy due to the additional categories that occur.

- **Category C:** This additional category is characterised by a sudden drop to relatively small partial discharges. This loss of the large average PD magnitudes can only occur if the longer tubules of the electrical branch tree, that allow the large magnitudes, have at least partially carbonised. Some of these tubules may also have encountered nanoparticles or the interface region around it which im-

pede progress. Whilst the nanoparticles are much smaller than the tubules, the leading edge of the tubule where propagation occurs is relatively small and may be interrupted by the nano-particle or the dense radial polymer strands close to it. A typical category C PRPDP is shown in Figure 5.

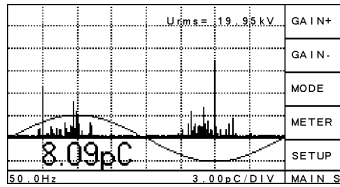


Figure 5 : Example PRPDP for category C.

- **Category D:** This category shows a complete cessation of all partial discharge activity above the noise level. This can only occur if all the tubules have completely carbonised or terminated due to the nanofiller. Figure 6 shows a typical PRPDP for category D.

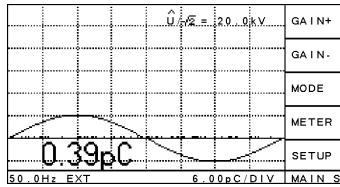


Figure 6 : Example PRPDP for category D.

- **Category E+F:** After category D has started, the stress may be actually increased in the regions where electrical trees have been terminated. This will be discussed further in the next section. As can be seen, no real clustering of data points occurs in the figure implying the spread of average PD magnitudes is more even. The reason for this can be deduced by looking at the PRPDP of the category in Figure 7. The PDPRP displays both PD patterns, that is activity on the rising and falling edges of the sinusoidal voltage, but with typical corona patterns. Corona PDPRPs show most of the activity occurring on the peaks and troughs of the sinusoid. This points to 2 events occurring simultaneously. As the micro-tubules have spread, the nanoparticles and their interfaces may protrude into the micro-tubule along it's length. Due to the protrusions having a different permittivity, as well as possible carbonisation, these protrusions will cause an electric field stress. The stress would cause corona to occur, resulting in widening of the tubule as well as promoting propagation as depicted in Figure 8. This widening causes PD activity to initiate again but with noticeably larger PD magnitudes due to the micro-tubules being wider.

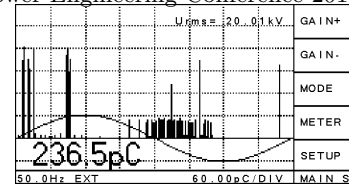


Figure 7 : Example PRPDP for categories E and F.

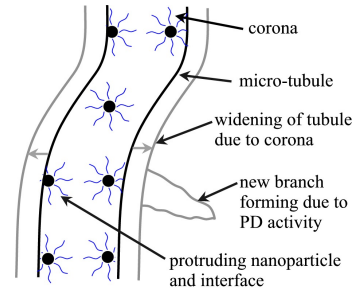


Figure 8 : Model for behaviour in categories E and F with grey depicting effects of corona. Not to scale.

4.1.3 2 %wt MgO/Epoxy: With the 2 %wt samples, similar behaviour was observed. This correlates to the previous paper where 2 %wt of both Al_2O_3 and Si_2O were investigated [8]. As in the previous 0.5 %wt samples, there is a clear pattern in the PD time evolution plot. Categories A and B are present as expected although a rapid drop in magnitude is seen at around 20 minutes before the large PDs start to occur. This can happen if the bush electrical tree carbonises before the branch electrical tree can gain sufficient length. This may also indicate nanoparticles close to the tip of the needle interfering with the growth of the electrical trees. Multiple cycles of categories C through F are visible in Figure 2c. This figure has not been demarcated as the widths are too small to easily mark them out but categories C to F can be seen by applying the system above.

4.1.4 5 %wt MgO/Epoxy: An example of a PD time evolution for the 5 %wt MgO/Epoxy samples is shown in Figure 2d. The 5 %wt sample behaves similar to other nanofiller levels but it is quite clear that more than one cycle of categories C to F can occur. The much longer duration compresses the categories making it difficult to demarcate but the amount of cycles makes the cyclical pattern quite apparent. This correlates with the model described in Section 4.1.2 as categories C to F occur when the electrical tree has encountered nanoparticles. This can be viewed as the electrical tree encountering a 3 dimensional shell layer of nanoparticles. This encounter can happen multiple times as the electrical tree passes the previous nanoparticles and encounters the next layer of nanoparticles. The much longer time to failure is notable for the 5 %wt sample lasted over 10 consecutive days. These observation correlate with

Table 1 : Table of metrics extracted from PD data.

Filler Material	Amount of Filler (% weight)	Sample	Time to failure (h)	Peak average PD magnitude (pC)	Mean average PD magnitude (pC)
Clean Epoxy	0.0	1	1.69	600.00	75.11
MgO	0.5	1	1.21	300.00	19.50
MgO	0.5	2	4.40	186.20	6.70
MgO	0.5	3	0.72	750.00	197.01
MgO	2.0	1	6.66	411.20	106.36
MgO	2.0	2	5.98	445.10	7.22
MgO	2.0	3	11.90	232.40	1.98
MgO	5.0	2	243.37	750.00	2.50

the data presented by colleagues at TU Delft [9].

5. DISCUSSION

Trends can be extracted from categorisations of the PD time evolution, PRPDP behaviours and statistical data from the samples. Table 1 shows the relevant statistical information extracted: time to failure; peak average PD magnitude; mean average PD magnitude; and the standard deviation of the average PD magnitude.

The clean epoxy sample is included here for comparison purposes. Other clean epoxy samples were only tested for time to failure, which when combined with this sixth sample, gives a mean time to failure of 8.74 hours. This is shown in Table 2. The 0.5 %wt samples have a significantly shorter lifespan than the clean epoxy. This may indicate that at these low filler levels, the nanoparticles act as electric field stress enhancements more than impedance to electrical tree growth.

Another interesting trend is the inverse relationship between time to failure and peak average PD magnitude. Most show that larger peaks in the average PD magnitudes give smaller time to failures. This is a small sample size but given the uniformity in behaviour exhibited with categorisation as well as correlation with other literature [8, 9], the behaviour cannot be ignored. More experiments are needed to validate these observations and expand them to other nanofiller materials. Furthermore clean epoxy samples will need to undergo the same experiments to give a firmer control samples to work from.

The 2 %wt samples show a similar time to failure but the 5 %wt show a significant increase from around 9 hours to 10 days before the sample failed. This value is also in keeping with other time to failures of 5 %wt Al_2O_3 and 5 %wt Si_2O from colleagues at TU Delft [9]. More nanofiller levels will need to be investigated to achieve an optimization graph for filler levels and this may vary according to both nanofiller material and the host material.

Table 2 : Table with time to failures of all six clean epoxy samples.

Sample	Time to failure (h)
1	12.0
2	15.5
3	7.0
4	11.0
5	5.26
6	1.69

5.1 Hypothesised electrical treeing model in nanocomposites

The background models point to the reason nanocomposites may be effective in retarding electrical tree formation. In neat or clean epoxy, the electrical tree can easily form between the polymer strands as only the weak Van der Waal's forces between polymer strands needs to be overcome. This is not in conflict with the proposed model as this model may be the underlying micro-model that explains the macro-model behaviour described in this paper.

This categorisation system prompted a model to be developed as delineated in a previous publication by the authors [8]. The most interesting portion of the categorisation section is categories E and F, where corona occurs in an insulation which is beyond expectations. This may be due to the nanoparticles protruding into the micro-tubule acting as a electric field stress enhancement feature. This stress enhancement in the tubule could cause corona which would lead to the micro-tubules widening and propagating further, as the grey depicts in Figure 8, explaining the PD behaviour that occurs simultaneously. This model has however been slightly updated to include Tanaka's conclusions. The model has been delineated above by slowly going through each of the categories and proposing the physical causes behind the recorded behaviour. The behaviour exhibited by the samples is primarily a factor of the interface region, which can impede the widening of the tubules slowing down breakdown. This model also works to explain the cyclical nature of the categories C to F, with each cycle representing a different layer

Proceedings of the 22nd South African Universities Power Engineering Conference 2014

of nano-particles. This also implies that the denser the nanoparticle dispersion, the more pronounced the effects such as increase in time to failure. There would be a turning point however where the interface regions start to overlap and interfere with each other causing gaps through which the electrical trees can spread and clumping of the polymer strands, possibly causing further electric field stress enhancement.

6. FUTURE WORK

Nanocomposite insulation can be considered to only just be entering its adolescence if not still in its infancy. This implies that there are multiple avenues still left unexplored without even considering possible new nanofiller materials. Several avenues of research are of interest to the authors. The two immediate avenues will be on further quantifying the behaviour over multiple filler levels of various materials. An imaging methodology is also still a major area of interest as this would allow at least partial verification of the proposed model. Beyond these focuses, different nanofiller materials outside the current standard materials are continuously being investigated.

7. CONCLUSION

Experiments monitoring the PD behaviour of MgO/Epoxy nanocomposite insulation have yielded very similar results when compared to the same experiments carried out on Al_2O_3 and Si_2O . This shows similar treeing mechanisms occurring between materials. Furthermore this behaviour can be categorised and used to model the current stage of the electrical trees. This model does not contradict recently developed micro-models in literature lending credence to it. Trends are visible between different filler levels with the categories being the most obvious. Beyond that, there is a definite variation in time to failure with nanofiller levels. Furthermore once more experiments have been concluded the investigation into the link between peak average PD magnitudes and the associated time to failure may yield interesting developments in the model.

ACKNOWLEDGEMENTS

The authors would like to acknowledge Eskom for their support of the High Voltage Engineering Research Group through TESP. The authors would also like to

express gratitude to the Department of Trade and Industry (DTI) for THRIP funding and to thank the National Research Foundation (NRF) for direct funding of the research group. Finally thanks must be given to the Technical University of Delft for their aid and resources in producing the test samples used in the experiments.

REFERENCES

- [1] W. Zhu, P. Bartos, and A. Porro. "Application of nanotechnology in construction." *Materials and Structures*, vol. 37, pp. 649–658, 2004.
- [2] L. A. Dissado. "Understanding Electrical Trees in Solids: From Experiment to Theory." *IEEE Transactions on Dielectrics and Electrical Insulation*, vol. 9, pp. 483–497, 2002.
- [3] T. Andritsch. *Epoxy Based Nanocomposites for High Voltage DC Application - Synthesis, Dielectric Properties and Space Charge Dynamics*. Ph.D. thesis, Technical University of Delft, 2010.
- [4] T. Tanaka. "Mechanisms of crossover phenomenon in tree length vs. applied voltage characteristics between base epoxy and its nanocomposites." In *18th International Symposium on High Voltage Engineering*. 2013.
- [5] T. Lewis. "Interfaces are the dominant feature of dielectric at the nanometric level." *IEEE Transactions on Dielectrics and Electrical Insulation*, vol. 11, pp. 739–753, 2004.
- [6] T. Tanaka. "Comprehensive understanding of treeing V-t characteristics of epoxy nanocomposites." In *Proceedings of the 17th International Symposium on High Voltage Engineering (ISH), Hannover, Germany*. 2011.
- [7] C. Nyamupangedengu, R. Kochetov, P. H. F. Morshuis, and J. J. Smit. "A Study of Electrical Tree Partial Discharges in Nanocomposite Epoxy." *2012 Annual Report Conference on Electrical Insulation and Dielectric Phenomena (CEIDP)*, vol. 1, pp. 912–915, 2012.
- [8] D. Cornish and C. Nyamupangedengu. "Electrical tree partial discharge characteristics in nanocomposites." In *18th Symposium on High Voltage Engineering*. 2013.
- [9] R. Kochetov, T. Andritsch, U. Lafont, P. Morshuis, and J. Smit. "Electrical tree propagation time to breakdown for epoxy resin composites containing alumina and silica nanoparticles." In *18th Symposium on High Voltage Engineering*. 2013.

DESIGN, TESTING AND IMPLEMENTATION OF A DATA ACQUISITION SYSTEM FOR LIGHTNING ELECTRIC FIELD MEASUREMENTS

J.H. Lange*, H.G.P. Hunt* and K.J. Nixon*

* School of Electrical & Information Engineering, University of the Witwatersrand, Private Bag 3, 2050, Johannesburg, South Africa

Abstract: Understanding how lightning damages equipment, by studying the electric fields measured during a lightning event, allows for the better design of lightning protection systems. Existing electric field measurement systems require external power and intervention and thus cannot be used where desired. A design for a battery powered autonomous measurement system was completed, prototyped and tested. This system, tested up to sampling frequencies of 15 MHz, has 8 million points of sample memory at 12 bits per sample and can operate autonomously on battery power for extended periods of time. The system has an input range of $\pm 1\text{V}$, a resolution of $488\mu\text{V}$ and a 3% measurement error.

Key words: lightning, electric fields, data acquisition system.

1. INTRODUCTION

Most lightning research setups are too costly and complex to be effectively used where or as desired. Shunt and Rogowski coil based measurement systems are intrusive and therefore may not be implemented where desired. Measuring the electric fields during a lightning strike is less invasive than these methods and can thus be used to infer lightning current. The data acquisition system utilized must sample fast enough to capture as much information during the $100\mu\text{s}$ flash duration, while having sufficient memory to sample at those sampling rates for the 1100 ms flash duration. Existing oscilloscopes that meet these requirements may not be used effectively. It is therefore desirable to build a system with a 4 MSps sample rate and 8 million sample memory. This system must also store the samples to non-volatile memory for later retrieval, while being battery powered.

A background to lightning and the properties thereof are presented leading to the requirements of the design. This is then followed by the design of the sensor and system. The results obtained from a prototype of the design built are then presented. Finally future development of the system and other possible applications of the system designed are considered.

2. BACKGROUND

Lightning can cause damage to sensitive and critical hardware, causing financial and bodily harm [1]. Understanding the manner by which lightning causes damage is key to designing protection systems. There are four basic mechanisms of cloud-to-ground lightning damage: physical damage, secondary damage, electromagnetic effect damage and damage due to changes in ground reference potential [2]. The culmination of the damage

from these mechanisms, results in expensive property damage each year [1]. Lightning accounts for 24% of Eskom Transmission's total line faults [3]. Core to understanding how lightning damages equipment is understanding how the energy from a lightning strike is delivered [1]. Of particular interest is the current waveform of a lightning strike which can be inferred from the changes in an electric field during a lightning strike [4,5].

In order to understand the requirements of the system, it is important to understand some of the fundamental aspects of lightning physics. This is covered in the following section.

2.1 Cloud-to-Ground lightning

Negative cloud-to-ground lightning is the most common of cloud to ground lightning [2, 6]. Lightning originates from a build up of charge within a cloud forming various charge centers, resulting in electric fields formed between these charge centers and the cloud and ground [2, 7]. When the electric field, or collection of charges reaches a critical value the discharge process is initiated. Stepped leaders begin traveling towards the ground. When these negative stepped leaders attach to a positive leader from the ground, a large flow of charge travels through the path of ionized air created. The duration of the initial discharge is approximately $100\mu\text{s}$. This is the initial strike and may be followed by several subsequent discharges to ground [2,6]. The majority of these subsequent discharges ($\approx 95\%$) occur within the following 1100ms after the initial strike [6]. These discharges result in a decrease of the electric field to ground [4]. By measuring the change in the vertical electric fields, it is possible to infer the change in charge in a lightning strike [5,7].

2.2 Existing measurement systems

Existing systems very often rely on an array of oscilloscopes or data acquisition tools housed in a central location. These systems require additional support hardware or human interference and a reliable supply of power. Furthermore these systems need to be properly isolated from the sensor equipment. This isolation may further distort the signal, and add cost. Furthermore these systems are expensive, by means of an example the Multiple Station Experiment in Florida, used Yokogawa DL716 oscilloscopes and the Lecroy LT344. Other installations may rely on rocket triggered lightning, which differs both in magnitude and waveform [6].

Due to the mains power requirement of these oscilloscopes, permits may not be obtained to place the system where desired. These requirements and limitations often mean that these systems rely on artificially triggered lightning to provide data to study. These systems may not capture the naturally occurring lightning, if someone is not available to control the system and reset it after each strike.

Shunt vs field measurement: When inferring the lightning current transferred during attachment of a lightning event to a tower, there are generally two techniques that can be used. The first one utilizes a shunt resistor or a Rogowski coil placed on a conductive core through which lightning current will flow. This relies on a direct strike to the tower, with all the current flowing through a central location. Very often rocket triggered lightning is used in these applications. The issue thereof is that rocket triggered lightning has different properties to that of naturally occurring lightning [6]. Implementation thereof is challenging as access is required to the top of the tower. Another technique measures the changes in the electric fields associated with a lightning strike. This technique does not require lightning to strike the tower directly or have a single termination point. It does however require knowledge of the lightning attachment point.

3. IMPLEMENTATION

The measurement system is designed to

- Sample a lightning impulse fast enough to capture all relevant information. It is assumed that 4 MSps is fast enough.
- Sample a lightning event for long enough to capture as many pre- and post- strike events as possible.
- Use as little power as possible, such that it may run autonomously for extended periods on battery power alone
- Have large non-volatile storage capability to which it can store the information from multiple strikes.

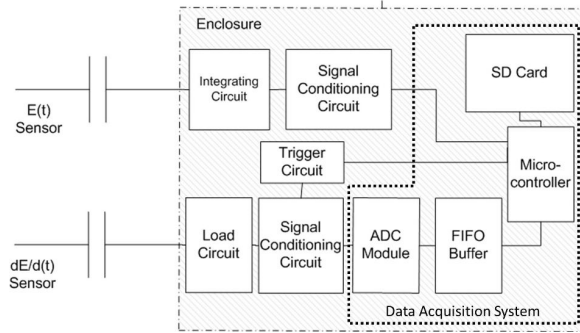


Figure 1: Block diagram of electric field sensors and data acquisition system.

Two electric field sensors were connected to a measurement system, for verification of measurements. The field derivative sensor is sampled with a high speed Analogue to Digital Converter (ADC) and the samples temporarily stored in a First-In First-Out (FIFO) memory unit. The samples are then copied from the memory using an ARM micro controller onto a Secure Digital (SD) memory card as shown in Figure 1.

3.1 Electric field sensor

For this implementation the sensor used is a capacitive sensor comprising of two circular aluminum plates, placed a distance of 8 cm parallel to each other, forming a floating electric field sensor that can be modeled as a field derivative dependent current source [6]. By placing a known load on the sensor, the field derivative, or integral thereof (the electric field) can be measured [6, 8]. By adjusting the load, the gain of the sensor can be manipulated to provide the correct output range. The output of the sensor is put through various filtering and conditioning stages. Any further amplification or reduction of the signal levels is provided by this conditioning stage.

In order to verify correct operation of the sensors, a test setup was created to apply various known fields to the sensors. Using a pair of plates at least three times larger in dimension as the sensors, placed parallel to each other, a known electric field was created, and could be inferred by measuring the voltage over the plates. In order to simulate the electric fields experienced during a waveform an RC decay voltage was applied to the field setup [6].

3.2 Data acquisition system

Existing oscilloscopes and data acquisition systems are designed with quick refresh rates. The data acquisition system does not need to update as quickly. Therefore the post-data-capture-processing requirements are significantly lower.

Data from the ADC is continuously recorded to the FIFO

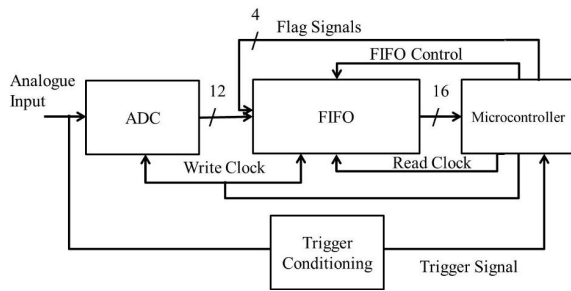


Figure 2: Block diagram of data acquisition system.

memory at the sampling frequency. Once the trigger event has occurred, the sampling continues for a set period of time and then stops. The micro-controller then pulls the data off the FIFO memory at its own slower rate [9]. The basics of this design are shown in Figure 2. Using an external ADC as opposed to the onboard ADC's was chosen as it allows for faster and higher resolution ADC's than may be available within a microcontroller.

FIFO memory: Before the other system components could be considered, the properties of the memory available from local suppliers had to be investigated. It was preferable to use SDRAM due to the large memory density, high speeds and low cost. However the use of SDRAM requires additional hardware to control the memory that can operate at the speeds required. It was therefore decided to use a FIFO integrated circuit. The FIFO chip used, the AL460 from Averlogic, has a density of 128 Mbit arranged in 16 bit words (8 million words) operating up to speeds of 150 MHz at low power levels. Additionally this FIFO also allows for the output pins to be tri-stated to high impedance. This means that the output of multiple FIFO memory chips could be connected to a single input of the micro-controller. As a result, time interleaving and multiple channels can be added to the design, with relatively little additional system design or hardware.

Analogue to Digital Converter: Since the ADC was to be put into a potentially noisy environment, it was desirable that the input to the ADC be differential [10]. The Analog Devices AD9235 which was chosen for its high 12-bit resolution, low power consumption, parallel output and low cost [11]. The ADC can sample at high frequencies up to 60 MSps. The ADC has a 1% accurate internal voltage reference thereby reducing system component count and complexity. This reference can be replaced with an external reference in order to ensure consistent performance if multiple ADC's are used.

ADC signal processing: Since the ADC samples a differential signal the input to the acquisition system needs

to be processed appropriately. In order to provide the ADC with the required differential input, a single pole 100 Hz high pass filter was used [11]. DC coupling is not required as the sensors do not record DC or electrostatic fields.

Post-capture processing and system control: The micro-controller chosen for this design is a STM32F407-VGT6. This ARM based micro-controller operates at 168 MHz, has 1 MB of flash memory and 192 kB of RAM. The micro-controller also has an SDIO module allowing for fast write speeds to an SD card. Furthermore this microprocessor has a real time clock which is imperative in synchronizing lightning measurements. The micro-controller also has external interrupt pins, allowing the micro-controller to interrupt on digital signals less than 50 ns long [12].

Firmware: The firmware was written to start the sampler after a set period of time after the reset event. It would then wait for the trigger, before continuing sampling for a set period and then stopping the recording process. After recording the firmware would copy the data from the FIFO to either the serial communication port or the SD card in a comma-delimited (.csv) format.

SD card: The use of an SD card as a non-volatile storage system is ideal for a lightning measurement application. Its small size and high memory density means that the information from multiple strikes can be stored on the device. It also allows researchers to exchange storage devices from the system quickly and easily. The SD card used in testing was a Toshiba 8 GB HC Micro SD card.

The large program memory available on the micro-controller allows for the implementation of a FAT file system library. This allows the data to be read by nearly all computing systems should the SD card be removed from this system. The FAT file system library was implemented using a modified version of the FatFs library. A write speed of over 300 kB/s was achieved. This allows for the 8 million samples to be written in a comma-delimited format in under 3 minutes. It may be possible to reduce this time significantly by using a faster SD card to increase write speeds.

4. TESTING

The test setup uses a signal generator as input signals to the acquisition system and an oscilloscope, a RIGOL DS1102E as a transfer standard as shown in Figure 3. A complete set of samples are then obtained from both the data acquisition system and the oscilloscope and compared.

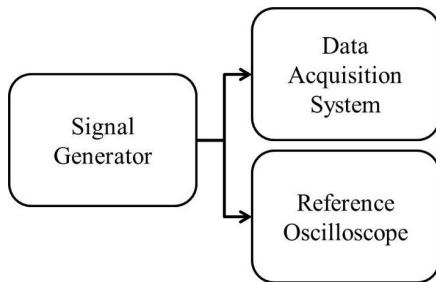


Figure 3: Block diagram of test setup used for the testing of the measurement system.

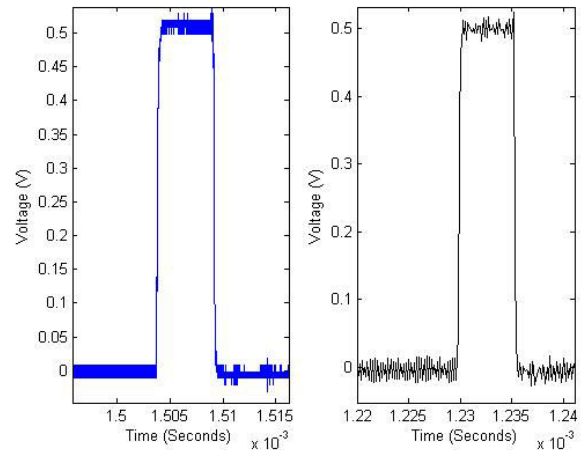


Figure 6: Comparison of test impulse captured with the reference oscilloscope at 100 MSps (left) and the data acquisition system at 8 MSps (right)

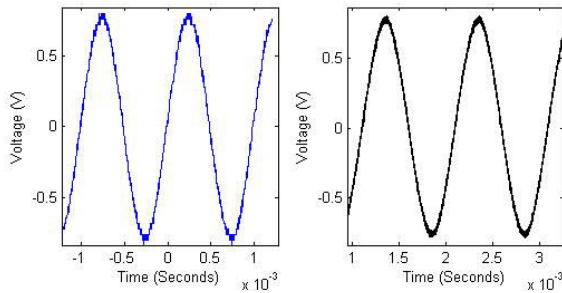


Figure 4: Comparison of a 1 kHz sine wave captured with the reference oscilloscope at 100 MSps (left) and the data acquisition system at 8 MSps (right)

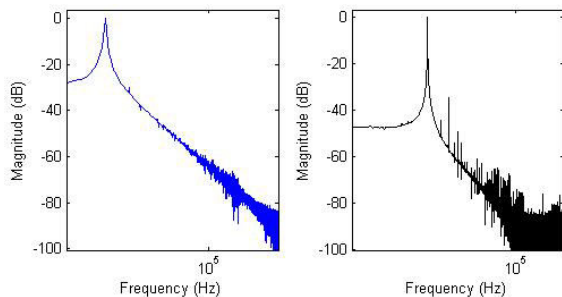


Figure 5: Comparison of a normalized FFT of 1 Mpts of a 1 kHz sine wave captured with the reference oscilloscope at 250 kSps (left) and the data acquisition system at 8 MSps (right)

4.1 1 kHz sinusoid test

In order to verify correct operation of the measurement system in a controlled environment the analogue input to the ADC from a signal generator was conditioned through a 100 Hz single pole high pass filter. Once correct operation of the measurement system was obtained, further tests were conducted to evaluate the accuracy, precision and fidelity of the measurement system compared to other measurement systems that were available.

With a sampling rate of 8 MSps, the sampling system recorded 8 million samples of a 1 kHz sine wave. These samples were compared to the input of, the ADC as measured with a Rigol DS1102E oscilloscope captured at roughly the same time as shown in Figure 3. The results of these tests are shown in Figures 4 and 5. The RMS magnitudes of the waveforms obtained from both the oscilloscope (566 mV) and the measurement system (551 mV) were compared to those obtained from a Fluke 115 multimeter (570 mV). The accuracy of the voltage measurements can be confirmed accurate to approximately 3% error. The range of the measurement system was confirmed to be $\pm 1V$, resulting in a resolution of $488\mu V$.

The signal to noise ratio of the acquisition system was verified to be approximately 50 dB. From Figure 5, this is higher than that measured by the oscilloscope used. Thus it is uncertain whether this noise is from the acquisition system used or the signal generator.

4.2 Impulse test

An impulse lasting $5.4\mu s$, recurring every $800\mu s$ was generated using the signal generator. The waveforms are shown in Figure 6 and 7. The fidelity, compared to an

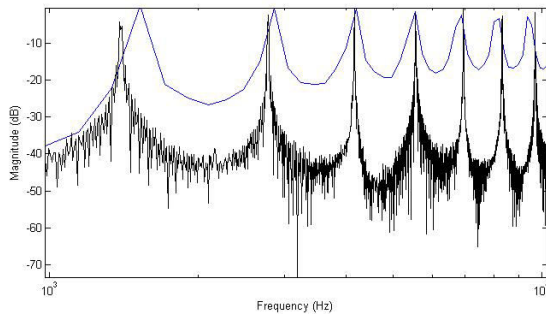


Figure 7: Comparison of a normalized FFT performed on 1 MPts of the test impulse captured with the reference oscilloscope at 100 MSps (left) and the data acquisition system at 8 MSps (right)

established oscilloscope, of the measurement system when measuring an impulse can be confirmed. It is noted that the rise time of the ADC cannot be measured from this test, which is to be expected due to the ADC's 500 MHz analogue bandwidth [11]. It can be deduced from the shift in frequencies of the harmonics in Figure 7 that there is some error in the sampling rates of either the acquisition system or the oscilloscope or both. However it is more likely that the difference in sampling frequencies of the measurement system and the scope resulted in a lower resolution at the lower frequencies for the FFT performed on the oscilloscope's samples.

5. DISCUSSION

It was noted that there was significant noise issues created by undershoot or overshoot clamped via diodes (used for input protection) to the power rails. This noise was reduced by adding shunt resistors between the digital outputs and inputs thereby dampening the undershoot or overshoot. These resistors of 150Ω are much larger than those recommended in the data sheets of approximately 15Ω largely due to the larger inductance of the breadboard prototype compared to the ideal printed circuit boards.

Due to power supply related difficulties experienced the integrated circuits used for the signal preconditioning for the ADC, obtained stopped functioning correctly. These devices DC coupled the signals and were impedance matched to the ADC. Thus in order to continue development, the differential signal was provided using a high pass filter [11]. The filter implemented had a bandwidth of 100 Hz and most importantly allowed the AC signal to be DC shifted to the required levels for the ADC. This setup was used in all the tests performed on the system.

The architecture used for the measurement system has the advantage of providing a easily scalable system that can operate at high sampling frequencies that are limited only

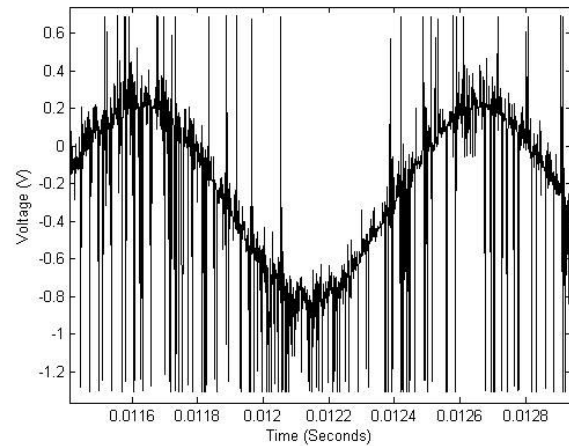


Figure 8: Signal measured of a 1 kHz sin waveform sampled at 1 MSps using the acquisition system before timing corrections were implemented.

by the FIFO memory and ADC. This means that it is not necessary to use a processor that operates fast enough to fetch the data and store it to memory. It also allows for multiple channels to be added without any additional processing hardware allowing for time interleaving to be easily implemented to increase memory and sampling rate on a single channel. It does however introduce a limitation in copying the data from the FIFO, resulting in slower update rates. Thus if two lightning strikes occur shortly one after another, the second strike may not be recorded by the measurement system.

At sampling frequencies of over 1 MHz, digital errors were present in the results as shown in Figure 8. These errors were a result of the timing delays present in the parallel buses. The ADC outputs data and the FIFO memory samples the data on the rising edge of the clock, thus with the delays present in the clock signal and the parallel bus, a large majority of the output from the ADC was lost. By delaying the clock to the FIFO memory, achieved using the complementary clock output provided by the micro-controller or the FIFO, the digital data loss was reduced to negligible levels.

During testing the acquisition system was powered from a laboratory power supply and the current measured with a Fluke 115 multimeter. Sampling at 15 MHz, the micro-controller, FIFO and ADC, required 400 mA at 3.1 V. This power consumption of 1.2 W allows the system to run on a 12 V 7 AH battery for 56 hours (2 days, 8 hours), assuming a DC-DC converter efficiency of 80% [13]. Under sleep or low power conditions, the system required 80 mA at 3.1 V. This is a power consumption of 250 mW. Under these conditions the system can operate on the aforementioned battery (12 V 7 AH) for 250 hours

(10 days).

It should be noted that these power consumption values were for a system made using demonstration boards, which consisted of unused peripherals, LEDs and linear regulators and as such are not designed for optimal power usage.

5.1 Future development and possible applications

This project can be further extended by using GPS for time synchronization, solar panels to extend battery life, wireless communication and directionality sensing. Since the system is independent many can be used to obtain two dimensional waveforms of the electric fields during a lightning strike. The applications of this project are not just limited to lightning research. The measurement system may find applications in high voltage measurements where sufficient isolation is often hard to obtain.

6. CONCLUSION

The 100 μ S flash duration, and 1100 ms duration of a lightning event defines the requirements of a measurement system required to measure and record the electric fields during a lightning event. A data acquisition system for the measurement of the output from the electric field sensor has been designed and tested. Designed specifically for measuring the waveforms that occur during a lightning strike and subsequent strikes, the system can run autonomously for extended periods on battery power. It displays fidelity with existing acquisition systems, and has a resolution of 488 μ V (12 bits) on a input range of ± 1 V accurate to 3%. It has a memory depth of 8 million samples, has been tested to 15 MHz sampling frequency.

ACKNOWLEDGMENTS

The authors would like to thank CBI-electric for funding the Chair of Lightning at the University of the Witwatersrand and for direct support of the Research Group. They would also like to thank Eskom for the support of the Lightning/EMC Research Group through the TESP programme. Thanks are extended to the department of Trade and Industry (DTI) for THRIP funding as well as to the National Research Foundation (NRF) for direct funding of the Research Group.

REFERENCES

- [1] A. Barwise. "Lightning and surge protection for PV systems on solar panel." *Electricity and Control*, Crown Publications, pp. 41–42, Oct. 2013.
- [2] E. Kuffel, W. S. Zaengl, and J. Kuffel. *High Voltage Engineering Fundamentals*. Butterworth-Heinemann, 2000.
- [3] L. Peter and F. Mokhonoana. "Lightning Detection Improvement FALLS Brought to Eskom's Transmission Line Design and Fault Analysis." In *21st International Lightning Detection Conference*, p. 6. Midrand, South Africa: Eskom - Trans Africa Projects, 2010.
- [4] J. Rai, D. K. Sharma, R. Chand, K. Kumar, and M. Israil. "Horizontally and Vertically Polarized Components of Lightning Electric Fields." In *19th International Lightning Detection Conference*, pp. 1–8. Tucson Arizona, USA, 2006.
- [5] C. Schumann and M. M. F. Saba. "Continuing Current Intensity in Positive Ground Flashes." In *2012 International Conference on Lightning Protection (ICLP)*, 1996, pp. 1–5. Vienna, Austria, 2012.
- [6] J. E. Jerauld. *Properties of Natural Cloud-to-Ground Lightning Inferred from a Multiple-Station Measurements of Close Electric and Magnetic Fields and Field Derivatives*. Ph.D. thesis, University of Florida, 2007.
- [7] M. A. Uman. *The Lightning Discharge*. Courier Dover Publications, 2001.
- [8] W. Ibrahim, M. Ghazali, and S. Ghani. "Measurement of Vertical Electric Fields from Lightning Flashes using Parallel Plate Antenna." *International Conference on Electrical, Control and Computer Engineering 2011 (InECCE)*, pp. 466–471, Jun. 2011.
- [9] Online communication with members of the EEVblog Electronics Community Forum. "High Speed Analogue Logger, Last Accessed: 24/10/2013." URL <http://www.eevblog.com/forum/>.
- [10] C. Calvo. "Improve system performance with differential signal chains." *EE Times-Asia*, pp. 1–3, 2010.
- [11] Analog Devices. "AD9235 Datasheet.", 2004.
- [12] ST-Microelectronics. "STM32F405xx Datasheet.", 2013.
- [13] Murata Power Solutions. "OKR-T / 3 Series DC-DC converters Data sheet.", 2009.

A FREQUENCY-DOMAIN ANALYSIS OF VARISTOR CURRENT UNDER DISTORTED SUPPLY VOLTAGE

P. Bokoro*, I. Jandrell* and M. Hove**

* School of Electrical and Information Engineering, University of the Witwatersrand, Private Bag 3, Wits 2050, South Africa, E-mail: 688331@students.wits.ac.za, E-mail: ian.jandrell@wits.ac.za

** Dept. of Electrical and Electronic Engineering Science, University of Johannesburg, Private Bag 524, Auckland Park, South Africa, E-mail: mhove@uj.ac.za

Abstract: In this paper, the impact of supply voltage harmonics on the third harmonic current-based condition assessment of varistor is experimentally verified. Therefore, time-domain current and voltage waveforms, measured from ten identical varistor samples, are decomposed in frequency-domain. The flattop window of the FFT technique is used to determine the rms values and subsequently the third harmonic amplitude of the varistor current, before and after injection of harmonics. The harmonic-generating load consists of a triac-based ac voltage controller driving a resistive load unit at fixed firing angle of 10 degrees. All varistor devices used in this work were subjected to rated ac operating voltage. However, the results obtained indicated that the operation of a harmonic source connected across the varistor arrester has the effect of increasing the magnitude of the third harmonic component of the varistor current.

Keywords: Varistor arresters, third harmonic current, harmonics injection, time-domain waveform, frequency-domain waveform.

1. INTRODUCTION

The third harmonic component of the varistor current provides critical information relative to the condition of varistor devices [1, 2]. The key role of arresters in modern electrical or data circuits [3], justifies the recommended removal of degraded or aged arresters from service, in a bid to curb any chances of reduced protection or catastrophic failure of sensitive equipment. The third harmonic current (THC)-based assessment is often relied upon to monitor signs of degradation or ageing [4, 5]. Based on time-domain waveforms obtained mainly from Matlab simulation works, Jaroszewsky et al reported the negative influence of voltage harmonics on the leakage current measurement [6]. This finding is experimentally verified in this work with low voltage varistor units operating under harmonics distorted supply voltage. The time-domain current and voltage measured before and after harmonics injection, are decomposed in the frequency-domain using fast fourier transform (FFT) methodology. The frequency components obtained are analysed using the Flattop window technique of the FFT. For the purpose of this work, varistor samples and a triac-based ac voltage controller, are both connected in parallel to an ac voltage source. The voltage controller, which is driving a fixed resistive load across its output, is used as a harmonic source with third harmonic being the predominant component [7]. The supply voltage is set to operate at normal continuous rated voltage of varistor devices.

The flattop window analysis of the current spectra obtained before and after harmonics injection suggests that the injection of third harmonics on the system voltage causes the third harmonic component to be inflated without necessarily indicating the ageing of

arresters, and therefore renders the THC-based condition assessment of varistor arresters misleading.

2. METHODOLOGY

2.1 Description of the Test Regime

To meet the objectives of this work, a test regime enabling varistor arresters to be sequentially subjected to distorted and clean ac voltage was built. The test system consisted of a 0-250 V, 50 Hz variable ac voltage source supplying a triac-based ac voltage controller and a low voltage varistor unit. The voltage controller drives a fixed resistive load. For measurement and display purposes of scaled down time-domain current and voltage waveforms, the 2.5 VA stromwandler 4NA1104-OCB20 10/1 A current transformer (CT) with a 10W/1k Ω resistor connected across its output, is used to monitor the varistor current. The voltage across the varistor is measured through a 14 VA 220/24 V transformer. The waveforms thus obtained are captured using the TDS 1001B Tektronix digital scope. Channel 1 of the scope is used to display the current signal whereas channel 2 is dedicated to the voltage signal. The rms readings of the current flowing through and the voltage across the varistor are also obtained with the aid of the Fluke 289 and the Escort-EDM 82 digital meters respectively. The supply voltage is monitored using the YF-3120 digital meter. The test set up is depicted in figure 1.

2.2 Harmonic Source

The switching element of the ac voltage controller consists of 600 V, insulated TO-220 general purpose triac, which in fact is a combination of two thyristors mounted in antiparallel. To effect harmonic distortion in

the set up described above, the triac is preferentially fired at 10 degrees mark to enable distorted current to be drawn through, and thus distorting the voltage across the varistor. The voltage across the resistive load, which is directly proportional to the current through the load, is also measured through a 14 VA 220/24 V transformer. The waveforms of the voltage appearing across the varistor samples before and after harmonics injection are given in figure 2.

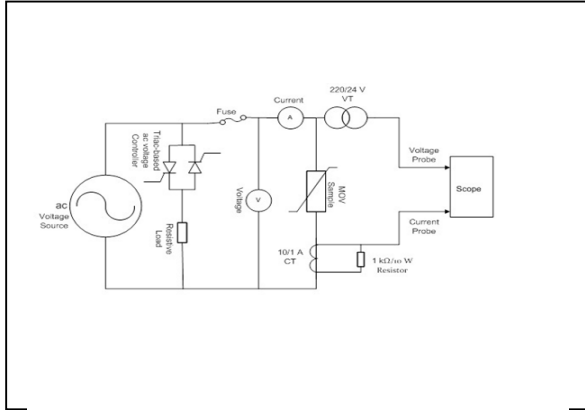


Figure 1: Experimental set up

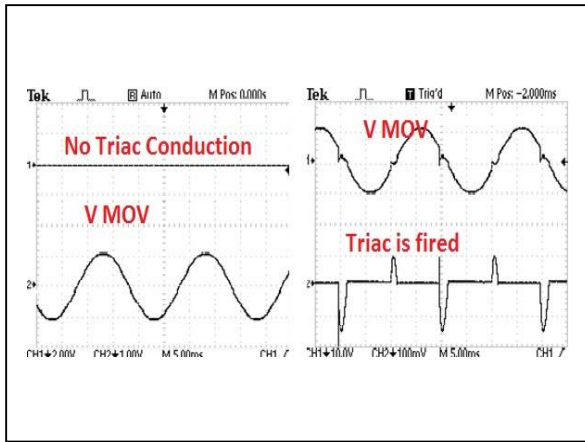


Figure 2: Varistor voltage before and after harmonics injection

3. FAST FOURIER TRANSFORM TECHNIQUE

Computer programs and digital instrumentation are continuously used in data acquisition or waveform recording and analysis. This justifies the need for discrete fourier transform (DFT) algorithms. The most preferred and utilised DFT approach is the FFT calculation which provides reduced amount of computation time involved. The FFT technique firstly decomposes n points of a time-domain waveform into single points, and calculates the n frequency spectra corresponding to n time-domain waveforms [8]. The last step of the FFT approach is to

synthesize the n frequency spectra into a single frequency spectrum of the waveform. The time-domain current and voltage waveforms obtained before and after harmonics injection are given in figures 3 and 4 respectively. These waveforms are subjected to the FFT process of the TDS 1001B digital scope to obtain the frequency-domain waveforms.

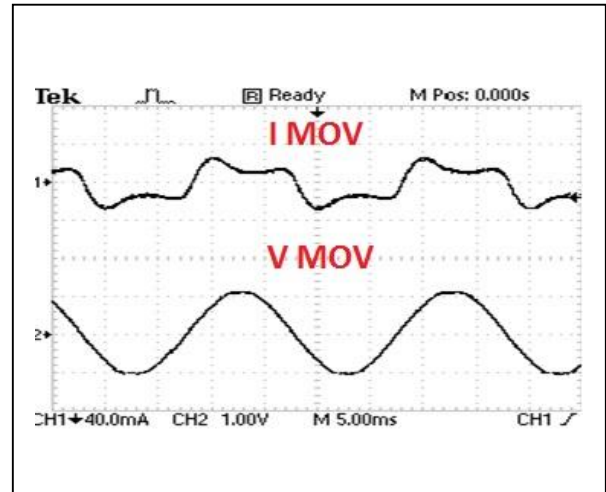


Figure 3: Time-domain current and voltage waveforms before supply distortion

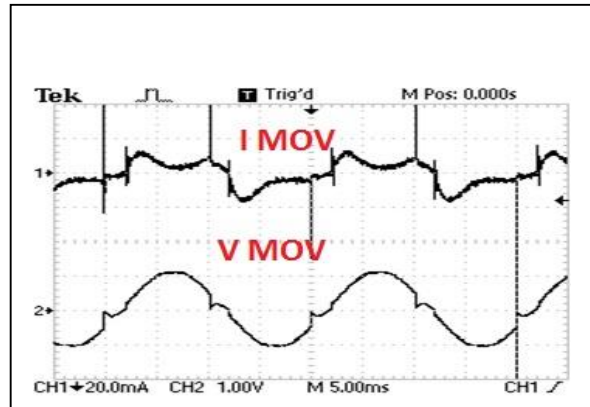


Figure 4: Time-domain current and voltage waveforms after supply distortion

4. AMPLITUDE OF THE THC

To estimate the percentage increase of the THC after harmonics injection, the amplitudes of the third harmonic components were measured in the frequency-domain of the current waveforms before and after harmonics injection conditions. Therefore, the flattop window was suitably selected on the FFT screen display of the scope. This enabled spectral leakage to be reasonably minimised in order to improve the accuracy of the amplitudes of the measured current components. Equation 1 enables the conversion from the frequency gain expressed in decibel (dB) into the rms value.

$$I_0 = I_i \cdot 10^{\frac{dB}{20}} \quad (1)$$

Where:

I_0 = the rms magnitude of output current

I_i = the rms magnitude of input current

dB = the current gain in decibel

The difference between the THC amplitudes obtained before and after distortion, which in fact indicates the change in terms of the external operating condition (switching of triac), is expected to be quite significant. Equation 2 enables the difference margin of the THC amplitudes to be quantified.

$$\Delta I = (I_A - I_B) \quad (2)$$

Where:

I_A = the rms magnitude of current after harmonics injection

I_B = the rms magnitude of current before harmonics injection

ΔI = change between the rms currents

5. RESULTS AND DISCUSSION

The typical time-domain waveforms of the varistor samples obtained before and after harmonics injection are given in figures 3 and 4 respectively. In the frequency-domain, the varistor waveforms before supply voltage distortion are depicted in figure 5.

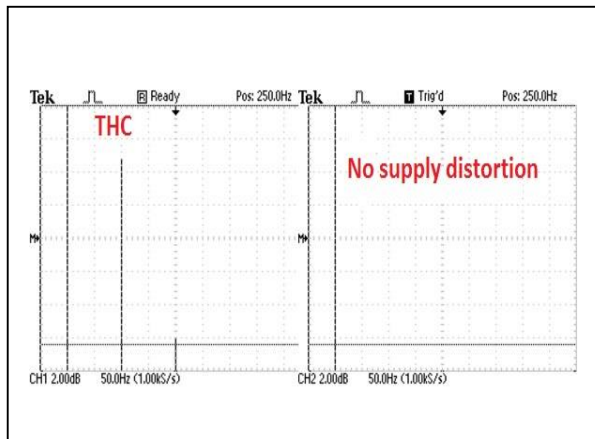


Figure 5: Frequency-domain waveforms before supply distortion

Under distortion conditions, the typical frequency-domain waveforms of the samples involved are given in figure 6.

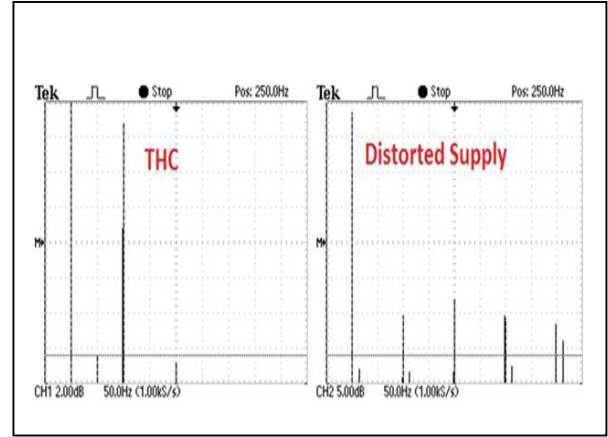


Figure 6: Frequency-domain waveforms after supply distortion

The time-domain waveform of the varistor current obtained before harmonics injection appears to be distorted. This is confirmed by the existence of harmonic frequencies in the frequency-domain spectrum of the current under the same experimental condition. After harmonics injection, the increase of the third harmonic amplitude is visible in the frequency spectrum. Out of the ten varistor devices used in the experiment, the increase in the THC amplitude is observed in nine samples while only one sample displayed no THC amplitude growth whatsoever after harmonics injection. On average the THC amplitude variation between the two experimental conditions is averaged at 28.2 %.

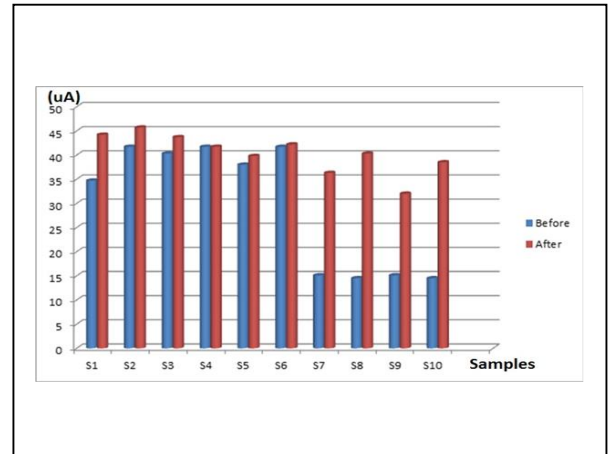


Figure 7: THC amplitudes before and after harmonics injection

It could also be noticed that 60 % of the samples studied showed marginal THC amplitude difference between the two experimental conditions. These samples could actually be degraded. The trend of the THC amplitudes for the samples before and after harmonics injection is shown in figure 7.

6. CONCLUSION

The time-domain waveform of the varistor leakage current, measured before and after harmonics injection, is decomposed in frequency-domain in order to verify the negative impact of distorted supply voltage on the THC-based condition assessment of varistor arresters. This study has demonstrated that a harmonic source, with predominant third harmonic components, providing distortion to the voltage across varistor units, causes the THC amplitude to increase. This increase in the THC is not necessarily indicative of the varistor condition.

REFERENCES

- [1] V. Larsen and K. Lien: "In-service Testing and diagnosis of gapless metal oxide surge arresters", Proceedings: *9th International Symposium on Lightning Protection*, Foz do Iguacu, November 2007.
- [2] F. Mahmood, M. Nadeem and U. Jamail: "A Comprehensive need of zinc oxide varistors in electronics technology", *Science Research Journal*, Vol. 18 No. 3, pp. 185-195, July 2007.
- [3] J. Woodworth: "Arrester condition monitors-A state of the art review", Arrester Facts 036, www.arresterworks.com.
- [4] A. Karim, S. Begum and M. Hashmi: "Performance and failure during energy testing of zinc oxide varistor processed from different size fraction and passivation thickness", *International Journal of Mechanical and Materials Engineering*, Vol. 5 No. 2, pp. 175-181, October 2010.
- [5] M. Wang, Q. Tang and C. Yao: "AC degradation characteristics of low voltage zno varistors doped with Nd₂O₃", *Ceramics International*, Vol. 33 No. 2, pp. 1095-1099, November 2010.
- [6] M. Jaroszewsky, P. Kostyla and K. Wieczorek: "Effect of voltage harmonics content on arrester diagnostic result", *International Conference on Solid Dielectrics*, Toulouse, July 2004.
- [7] R. Herrera, P. Salmeron and S. Litran: "Assessment of harmonic distortion sources in power networks with capacitor banks", Proceedings: *11th International Conference on Renewable Energies and Power Quality*, Las Palmas de Gran Canary, April 2011.
- [8] S.W. Smith: *The scientist and engineer's guide to digital signal processing*, pp. 141-241, www.dspguide.com.

Partial Discharge Evaluation of a High Voltage Transformer

I.K. Kyere* and J.J. Walker**

* Vaal University of Technology, Dept. of Power Engineering, Private Bag X021, Vanderbijlpark, 1900, South Africa E-mail: isaack@vut.ac.za

** Walmet Technologies (Pty) Ltd. E-mail: jerrywalker@walmet.co.za

Abstract: This paper describes the procedures followed to evaluate the condition of the insulation of a 11 kV Voltage transformer (VT) in the High Voltage Laboratory at Vaal University of Technology through measurement of partial discharges. This is the second part of the evaluation of the insulation of the 300 kV transformer in the high voltage laboratory. The method employed in this evaluation to detect the partial discharge signals, namely, the use of Capacitive Coupling by means of a Coupling Capacitor. The partial discharge evaluation methodology followed consists of measurement of the partial discharge magnitude and Phase Resolved Partial Discharge Measurements. The results from the measurement of partial discharge signal detection method are discussed.

Keywords: Partial Discharge, Voltage Transformers, Coupling Capacitor, Evaluation, Insulation.

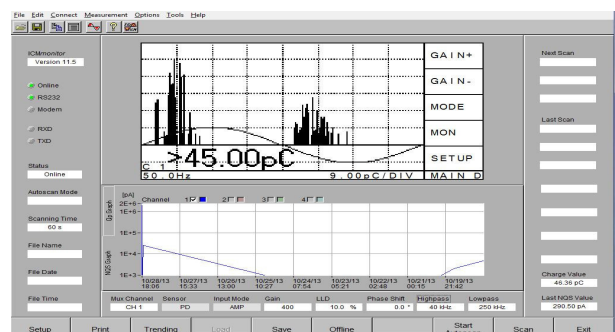
1. INTRODUCTION

The circumstances surrounding the evaluation of high voltage (HV) insulation system to decrease the danger and to prevent breakdown of the insulation of key units like transformers is a motivation to the utility Companies to use such evaluation techniques [6, 7]. An increase demand as well as bulk power dealings increase the rate of transformer ageing due to escalating rate of the operating stresses [7]. The failure of HV transformers are due to insulation breakdown caused by mechanical, thermal and electrical ageing [9]. It is therefore, important to have a well documented diagnostic method, so that potential insulation problems can be attended to during scheduled outage time.

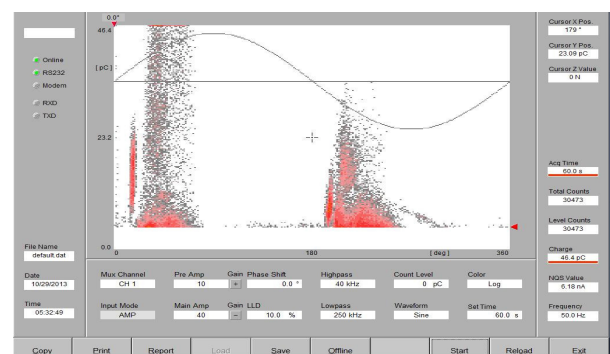
The high voltage transformer 400 / 300 000 V transformer in the high voltage laboratory was manufactured in 1967 and it is necessary to evaluate the condition of the insulation to ensure a safe environment when experiments are done in the laboratory. The measurements done on the 11 kV voltage transformer forms the basis to prove the validity of the evaluation methods on a 300 kV transformer.

The methodology followed in this paper is made up of Phase Resolved Partial Discharge (PRPD) Measurements and Evaluation. PRPD evaluation is a method that displays the PD activity in a three-dimensional (3D) way to identify the phase relationship, the magnitude of the PD activity and finally the discharge rate and is well-suited for on-line measurements [3]. Figure 1(a) and 1(b) shows the different

between the traditional and the 3D PRPD patterns for the same defect.



(a)



(b)

Figure 1: (a) Traditional PRPD pattern (b) 3D PRPD pattern

The measurements were done using an ICMmonitor (from Power Diagnostix) which fully complies with the requirements of IEC 60270 methods to measure partial discharges. PRPD patterns help to identify the behaviour of PD, its defect geometry and the intensity of the defect [10]. The experimental results from PRPD measurements using a Coupling Capacitor are discussed.

2. PD DIAGNOSTIC ON TRANSFORMERS

2.1 PD measurement using coupling capacitor

The circuit arrangement shown in Figure 2 consisting of HV power supply, the test object, the Coupling Capacitor Cc, the measuring impedance Zm, and the PD measuring device which consist of the ICMmonitor from Power Diagnostix and personal computer with software to evaluate and save the data. The HV side of the voltage transformer were connected to the coupling capacitor and energized. The LV side and the insulation were grounded as an attempt to measure PD activity and also identify the type of PD. Acquired PD patterns were measured at different voltage levels.

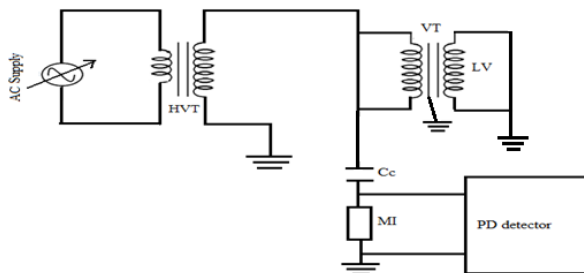
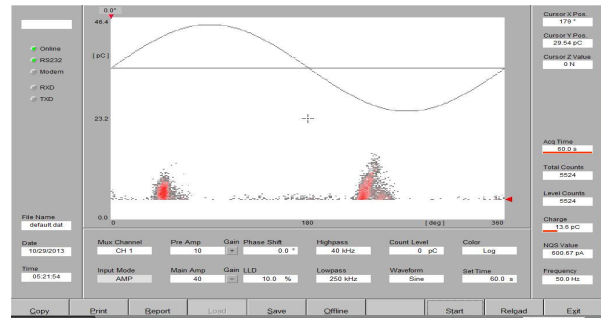
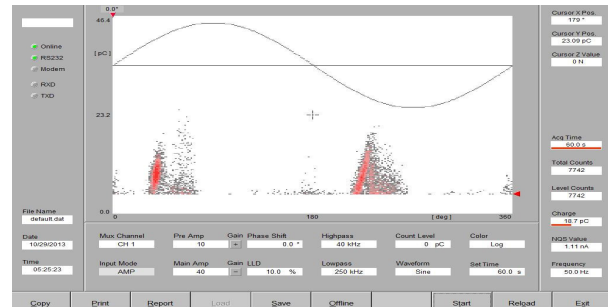


Figure 2: Partial discharge measuring circuit

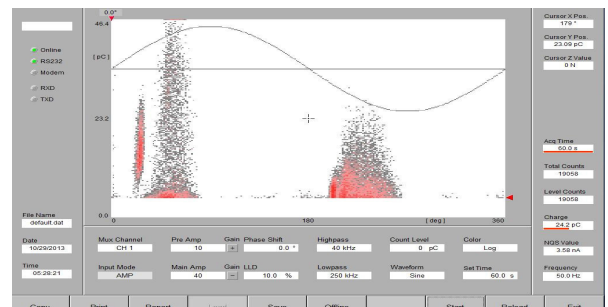
Figure 3 shows the results of the measurements with different applied voltages with the coupling capacitor as detection device. The system was calibrated using a calibration pulse magnitude of 5 pico Coulomb (pC).



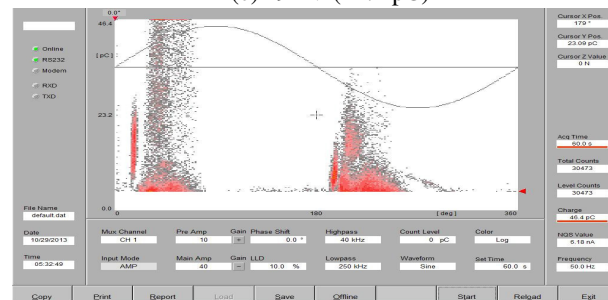
(a) 7.5 kV (13.6 pC)



(b) 8 kV (18.7 pC)



(c) 9 kV (24.2 pC)



(d) 10 kV (46.4 pC)

Figure 3: PRPD pattern measured on an 11 kV VT

3. MEASUREMENT WITH ONE SIDE OF HV CONNECTED TO CC AND ONE OF THE LV SIDE GROUNDED

Figure 4 shows the conventional PD test circuit in accordance with IEC 60270 [5] and 60073-3 [6]. Figure 5 shows the PRPD pattern obtained from the 11 kV voltage transformers. The acquired PD was measured at 7.5 kV and 10 kV, 15 kV and 16 kV. The knee-point voltage of the transformer was measured at 12 kV with the last two measurements when the transformer core was saturated.

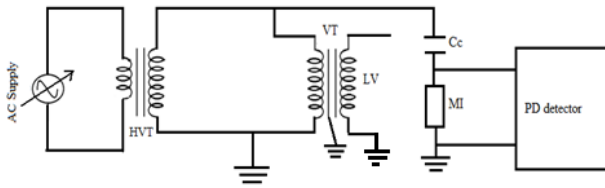
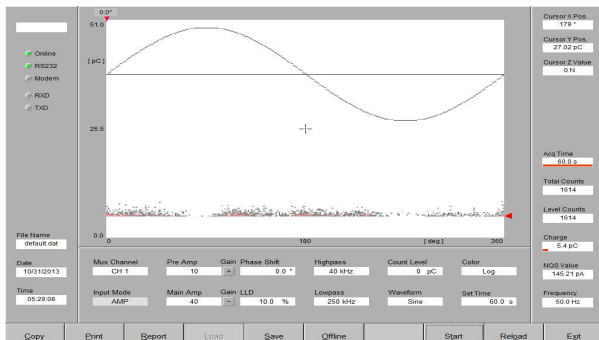
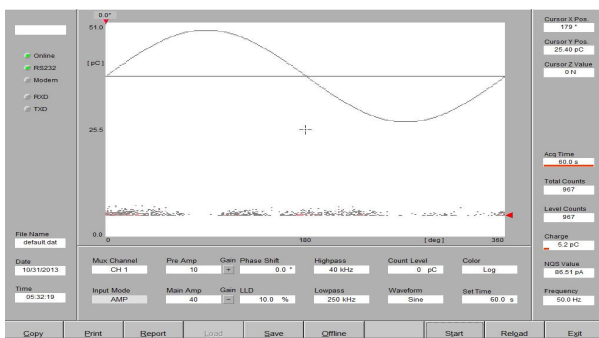


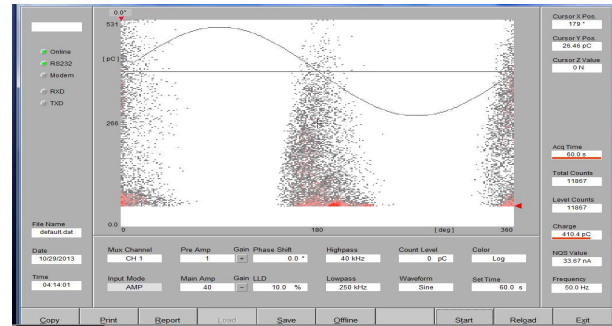
Figure 4: Partial discharge measuring circuit



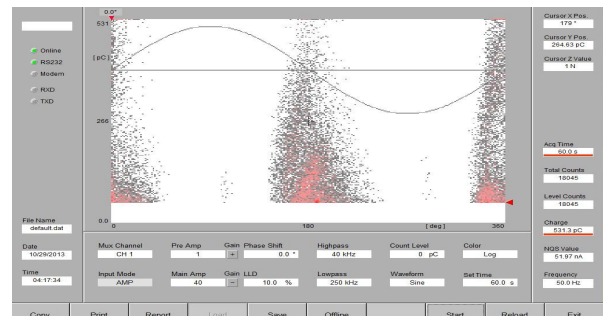
(a)7.5 kV (5.4 pC)



(b)10 kV (5.2 pC)



(c)15 kV (410.4 pC)



(d)16 kV (531.3 pC)

Figure 5: PRPD pattern measured on an 11 kV VT

4. EXPLANATION OF RESULTS

Figure 3 shows PRPD patterns of cavity discharge in the insulation of the high voltage winding when the low voltage winding and core are grounded and HV side are connected to the coupling capacitor as shown in Figure 2. When the applied voltage is higher, the numbers of PDs per cycle, total charge per cycle and the maximum magnitude of the cavity discharge are higher. A partial discharge normally occurs in the cavity when the electric field in the cavity is higher than the inception field and there is an initial free electron to start an avalanche process. Since the process of having a free electron is random, the occurrence of a cavity discharge is also random [2].

When the applied voltage is increased, the maximum discharge magnitude is larger because the maximum electric field in the cavity is higher. At higher applied voltage, the electric field in the void increases faster towards the inception field. This results in more discharges in one applied voltage cycle. When the void is located in the middle of the material, the electric field on the surface

of the void is symmetrical and the discharge patterns of cavity discharge at positive and negative cycles of the applied voltage will also be symmetrical [2]. The magnitudes of the discharges at the different applied voltages are shown in Figure 3.

Figure 5 shows the discharge patterns when the transformer is excited from the high voltage winding as shown in Figure 4. There were no discharges recorded below the knee point voltage of 12 kV as shown in Figure 5(a) and 5(b). Partial discharge activity was only recorded above the knee point voltage as shown in Figure 5(c) and 5(d). The discharges occur at the zero crossings of the applied voltage. One of the possible reasons for the discharges only occurring above the knee-point voltage can be the distortion of the induced voltage when the core is saturated. The peak of the distorted induced voltage will increase as the core goes deeper into saturation. The PRPD pattern seen also indicates that the discharges are not due to a cavity in the insulation but can rather be attributed to surface discharges [2].

The reason why the discharges occurring when the connection as in Figure 2 did not appear during the second test (Figure 4) can be that the defect is in the high voltage insulation at the end of the winding connected to earth during the second test. The defects were therefore not stressed enough for discharges to occur. This postulate was not tested and will be investigated during further tests.

5. CONCLUSION

This paper presented two methods to evaluate the condition of a 11 kV voltage transformer using the electrical method of partial discharge detection [5]. Two types of discharges have been evaluated in this paper using PRPD technique. From the results obtained both connection systems resulted in discharge activity not detected by the other system. When using the connection proposed in the standards [5] defects appearing in the section of the high voltage winding insulation connected to earth will possibly not be detected while the magnitude of the applied voltage (above the knee-point) can cause the core to saturate resulting in discharge activity.

6. REFERENCE

- [1] O. Bergius: *Implementation of On-Line Partial Discharge Measurements in Medium Voltage Cable network*. Master thesis, Tampere University of Technology, pp.33-34. 2012.
- [2] H. ILLIAS, T. S. YUAN, AB H. ABU. BAKAR, H. MOKHLIS, G. CHEN and P. L. LEWIN: "Partial Discharge Patterns in High Voltage Insulation". *In proceedings of IEEE International Conference on Power and Energy (PECon)*, Kota Kinabalu Sabah, Malaysia, pp. 751-755. 2-5 December 2012.
- [3] A.S., Kumar, R.P. Gupta, K. Udayakumar and A. Venkatasami: "Online Partial Discharge Detection and Location Techniques for Condition Monitoring of Power Transformers". A review. *In proceedings of International Conference on Condition Monitoring and Diagnosis*, Beijing, China, pp. 927 – 931. 21-24 April, 2008.
- [4] G. Luo and, D. Zhang: "Study on Performance of HFCT and UHF Sensors in Partial Discharge Detection". *In proceedings of IPEC 2010 conference*, Singapore, pp. 630-635. 27-29 October 2010.
- [5] IEC60270: "Standard. High – Voltage Test Techniques – Partial Discharge Measurements". 2000.
- [6] IEC60073-3: "Standard. Power transformers – Part 3: Insulation levels, dielectric tests and external clearances in air". 2000.
- [7] A. Mehta, R.N. Sharma, S. Chauhan and S.D. Agnihotri: "Study the Insulation System of Power Transformer Bushing". *International Journal of Computer and Electrical Engineering*, Vol.3, No.4; pp. 544-547. August 2011.
- [8] I.A. Metwally: "Failures, Monitoring and New Trends of Power Transformers". *Digital Object Identifier 10.1109/MPOT.2011. 940233. IEEE POTENTIALS*, pp. 36 - 43. 2011.
- [9] M.G. Niasar: *Partial Discharge Signatures of Defects in Insulation Systems consisting of oil and Oil – impregnated Paper*. Licentiate thesis, Stockholm, Sweden, pp.33 - 35. 2012.
- [10] H.M. Ryan: *High Voltage Engineering and Testing, Second Edition*. The Institution of Electrical Engineers,

London, United Kingdom, pp. 405 – 417 and 533 – 546. 2001.

- [11] S.M. Strachan, S. Rudd, S.D.J. McArthur and M.D. Judd: “Knowledge-Based Diagnosis of Partial

discharges in Power Transformers”. *IEEE Transactions on Dielectrics and electrical Insulation*, Vol. 15, No.1; pp. 259 – 267. February 2008.

OPTIMIZATION OF LOSS REDUCTION THROUGH A CONVERTED HVAC TRANSMISSION LINE INTO HVDC MODEL IN DIGSILENT SOFTWARE

M J. Mushagala* and G. Atkinson-Hope**

**Cape Peninsula University of Technology, Centre of Power System Research Laboratory in Department of Electrical Engineering, Keizersgracht, Tennant Street. Cape Town- South Africa
E-mail: MushagalaM@cput.ac.za/jigomm@yahoo.fr*

***Cape Peninsula University of Technology, Technology Transfer and Industrial Linkages, Centre of Power System Research Laboratory in Department of Electrical Engineering Keizersgracht, Tennant Street. Cape Town- South Africa.
E-mail: atkinsonhopeg@cput.ac.za*

Abstract: Losses are an important parameter of consideration for mitigation and thereby enhancing the Available Transfer Capability of Power Systems. Loss mitigation is a two stage process the first stage is the Planning phase and the second stage is the Operational phase. This paper discusses briefly the Planning phase activities. The various methods of mitigating the losses in the Operational phase have been presented in this paper with emphasis on one technique whereby a converted existing HVAC transmission line has to carry direct current (DC). The contribution of this paper is the combination of HVAC and converted DC transmission line working in parallel to monitor their operations. These results obtained through decision making factors will demonstrate that a combination of HVAC and converted DC transmission line could be a solution enhancing power transfer. The method is tested with an HVAC working parallel with a converted DC transmission line modelled in DIGSILENT and validated. Results have been presented and analysed in this paper.

Key Words: Current carrying capacity; HVDC; Power transfer capacity; DIGSILENT.

1 INTRODUCTION

Due to the problems associated with constructing new overhead lines, it is important to examine the possible options for increasing the transmission capacity on present existing infrastructures and making maximum use of existing transmission systems through upgrading power transfer. When feasible, upgrades are an attractive alternative, because the costs and lead-times are less than those for constructing new lines.

The constraints limit a system's ability to transmit power and lower the use rates of the existing transmission network. The paper describes the constraints on a system's capacity to transmit power from one area to another [1].

The paper also discusses the upgrade possibilities to increase the transmission capacity of the existing transmission lines so that additional power can be transmitted reliably from one area of a system to another or from one entire system to another. Some of the potential remedies for these constraints through upgrades are presented along with a comparison of the power increase that can be achieved on an existing network [1].

2 RESEARCH AIMS AND OBJECTIVES

The aim of this paper is to investigate and analyse a conventional HVAC transmission line performance

operating in parallel with a converted DC line and still supplying AC to the end users.

The percentage power upgraded and percentage power losses would be evaluated for both converted DC line and AC line when operating together to determine if both lines could reliably operate together.

3 LITERATURE REVIEW

The primary objective of power systems designer is to operate the systems economically at maximum efficiency and supply power on demand to various load centres with high reliability. The rising electric power demand in the 21st century, has called for restructuring of the electric Power System. The restructuring is on the technical aspect. As regards the technical aspect the Power Systems are expanding in size to meet the huge power demand and are complex due to advancement of technology. In addition to modern Power Systems being highly interconnected over long distances to carry power from the sources to the loads, there is an economic reason also. The interconnected systems benefit by (a) exploiting load diversity (b) sharing of generation reserves and (c) economy gained from the use of large efficient units without sacrificing reliability. Under the above condition, it becomes more and more important to enhance the reliability of the Power System. An aspect of interest here is quantifying the loss accurately and adopting measures

to minimize the loss, thereby resulting in improved power transfer capability.

In 2012, South Africa's utility power supplier, Eskom, had a loss of 7686 GWh on their 132 kV to 765 kV transmission lines [2]. These losses were 3.08% of Eskom reserve capacity. Hence, Losses have always been a subject of interest to study.

This paper presents the interest of the authors in discussing some Planning techniques and determining the losses in AC transmission system under various conditions before being converted to DC. It presents an effective method of mitigating losses to enhance Available Transfer Capability when existing AC transmission line once converted to carry direct current (DC) could optimised these transmission lines operation.

3.1 Losses in Power System

Losses in simple terms may be stated as the difference between the power generated and the power received.

$$P_{loss} = P_G - P_R \quad (1)$$

Where:

$$\begin{aligned} P_{loss} &= \text{Total Losses,} \\ P_G &= \text{Power Generated} \\ P_R &= \text{Power Received} \end{aligned}$$

3.2 Technical Losses

The technical losses are internal to the Power system and occur due to the components in the system. They occur naturally and consist mainly of power dissipation in electrical system components such as transmission lines, etc. Technical losses are a function of the system design parameters and the dynamic state of the power system.

By proper design of the system parameters such as diameter of the conductor, length of the conductor, selection of the right material, operation voltage and loss can be controlled. This is an activity of the Planning Stage. Research by [2] has stated that an alternative to the long-distance HVAC transmission system that may decrease high energy losses is a converted HVAC line to a HVDC transmission line. The reactance of the line $jX = j\omega L$ is not present in direct current systems as $\omega = 0$, only the series resistance R of the transmission line causes losses, which means that the transport of active power through a converted HVDC transmission line will not require any reactive power or any specific load angle δ .

3.3 Planning to minimize losses.

The Technical losses can be calculated based on the natural properties of components in the power system: resistance, reactance, capacitance, voltage, current, and power, which are routinely calculated by Power Engineer planners as a way to specify what components can be added to the system, in order to reduce losses and improve the voltage levels and efficiency. Transmission

losses in the network constitute economic loss providing no benefits. Transmission losses are construed as a loss of revenue by the utility. The magnitude of each of these losses needs to be accurately estimated and practical steps taken to minimize them to their optimal level. Before we begin to discuss the various steps in the planning of designing a Power System that should operate with minimum losses, here are major reasons for technical losses in Power System as stated by [2]; it is due to inadequate planning: there is inadequate investment on transmission and distribution (T&D). While the desired investment ratio between generation and T&D should be 1:1, it has decreased to 1:0.45 [1]. To overcome the above drawback, various technologies could be developed on a long transmission line operating below their power transfer capability and implemented. One of those developed technology could be conversion of existing HVAC transmission line to DC. The phase to phase clearance, phase to ground clearance required would be smaller for DC transmission as compared to equivalent AC transmission.

4 APPLICATION TO A PRACTICAL SYSTEM.

The analytical methodology and conversion effectiveness is applied to investigate the possibility of increasing the PTC of the existing 400 kV AC transmission line by conversion to DC, where by Power losses of existing transmission line would be reduced.

4.1 Transmission Line Network Data

The 400 kV AC High Voltage transmission system (shown in Fig. 1) has the following data:

Two circuits (on two separate towers, 150 m apart) of a three bundles per phase with 0.38m spacing. Each circuit has horizontal spacing with 18.8 m between adjacent phases. The line has 1200km of a length.

$$\begin{aligned} R_{AC} = R_{DC} &= 0.0437 \text{ ohm/km} \\ \text{Internal Inductance} &= 0.04231713 \text{ mH/km} \\ \text{Outer Diameter} &= 35.94 \text{ mm} \end{aligned}$$

5 AC NETWORK PARAMETERS

From figure 1, T1 is a star-star-star connected three winding transformer with 132 kV (L-L) voltage on its low voltage side connected to Bus 1 and 400 kV L-L voltage on its high and medium voltage side connected to Bus 2. T1 has a Z% of 6.98% on high and medium voltage side and 7.18% on low voltage side with copper losses of 0 kW on high and medium as well on low voltage side. The rating of the transformer is 1250 MVA on high and medium voltage side with 2500 MVA on low voltage side. The double HVAC transmission lines (from Line 1, line to line3) are 1200 km long each at 400 kV L-L. The Line 1, 2 and 3 are modelled as an equivalent- π model [4].

T2, T3 and T4 are star-star connected transformers with 400 kV/24 kV voltage ratings.

Bus 7 is modelled as a voltage controlled bus with a fixed real power P and a fixed voltage magnitude $|V|$. The variables are the reactive power Q and the voltage angle δ . In this study the fixed P is 2x900MW. The voltage at Bus 1 and 7 will be checked against their limit when loads are varied. Transformers 2, 3, 4 and 5 are for tapping loads 1, 2, 3 and 4. The load connected at Bus 2, 3, 5 and 8 represents the localised area of the national grid. They are modelled as a fixed PQ load.

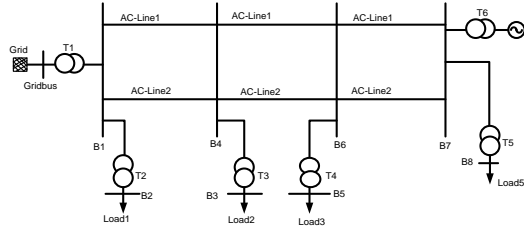


Figure 1: 400kV HVAC Network system configuration

6 RESULTS OF POSSIBLE CONVERSION SCHEME

The conversion scheme is to increase the power transfer capability of the existing 400 kV double-circuit transmission, whereby one AC transmission line would be converted to DC and the other line would remain AC for load tapping. The performance of this network would be analysed. The DC line will have two terminals (point to point DC line): The rectifier terminal will be connected to one of the 400 kV bus and the inverter terminal will be connected to the other 132kV bus.

Figure 2 shows a sketch of system configuration for scheme 1 with one AC transmission line converted to DC.

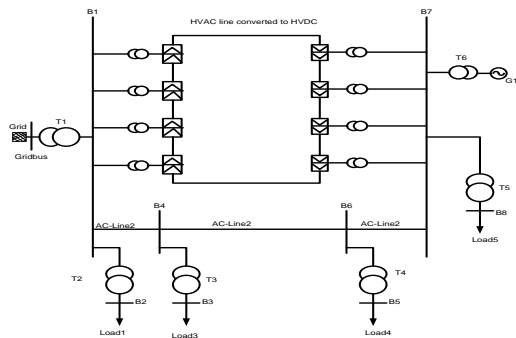


Figure 2: HVAC Transmission line converted to HVDC working together with HVAC

Comparing with the surge impedance loading (SIL) of one circuit of the 400 kV AC transmission system, which is estimated to be 827 MW one can conclude that a substantial power transfer capability can be obtained by converting it to DC.

6.1 Transmission Capacity Upgraded when an AC line converted to DC

The fast development of power electronics based on new and powerful semiconductor devices has led to innovative

technologies, such as HVDC, which can be applied to transmission line. The technical and economical benefits of this technology represent an alternative to the application in AC systems. Some aspects, such as increasing the capacity of transmission of the existing lines are creating additional requirements for the operation of Power Systems. HVDC offer major advantages in meeting these requirements.

The HVDC transmission systems are point-to-point configurations where a large amount of energy is transmitted between two regions.

To determine the percentage Power being upgraded by the converted DC line would be to divide the difference of Power Transfer of the DC line and the AC line with the one of AC line, as shown in (2):

$$\% \text{ Power Upgrade} = \left(\frac{P_{DC} - P_{AC}}{P_{AC}} \right) \times 100 \% \quad (2).$$

$$\% \text{ Power loss decreased} = \left(\frac{P_{actloss} - P_{DCloss}}{P_{actloss}} \right) \times 100 \% \quad (3)$$

By using equations 2 and 3 into our network results, it is found that the converted DC network is being operated at an upgrade power of 179.172% and the percentage (%) power loss has decreased to 42.56 %. By upgrading power transfer and decreasing power loss the total life cycle of cost (LCC) could be reduced whereby the objective of conductor optimisation process could be met when total cost of operation is reduced (TCO) through power loss. The total life cycle cost (LCC) is then the sum of the initial capital investment cost (CIC) and total cost of operation (TCO) as described in equation (4):

$$LCC = CIC + TCO \quad (4)$$

The Capital Investment Cost (CIC) which is the cost of line erection and is based on the cost of material and the cost of labour. The total cost of operation (TCO) is related to the cost of losses and the cost of maintenance over the life cycle of the line [5].

Under different case studies performed, this paper analysed both converted DC line and HVAC operating together by monitoring power losses in both lines and what could be their performance and adaptation when both are connected on the same bus- bar by monitoring their power transfer, current and voltage.

6.2 HVAC parallel with Converted DC Transmission line

The converted link is a bipolar, with current control for rectifier set at 1.45176 kA. The DC link is modelled with 12 pulse converter bridges which are made up of two six pulse bridges. Each of the six pulse converter bridges has four series converters with two star-to-star transformers, and two in star-to-delta transformers for harmonic cancellation. Figure 3 is a one line diagram model in DIGSILENT of the converted network working together with a parallel HVAC transmission line.

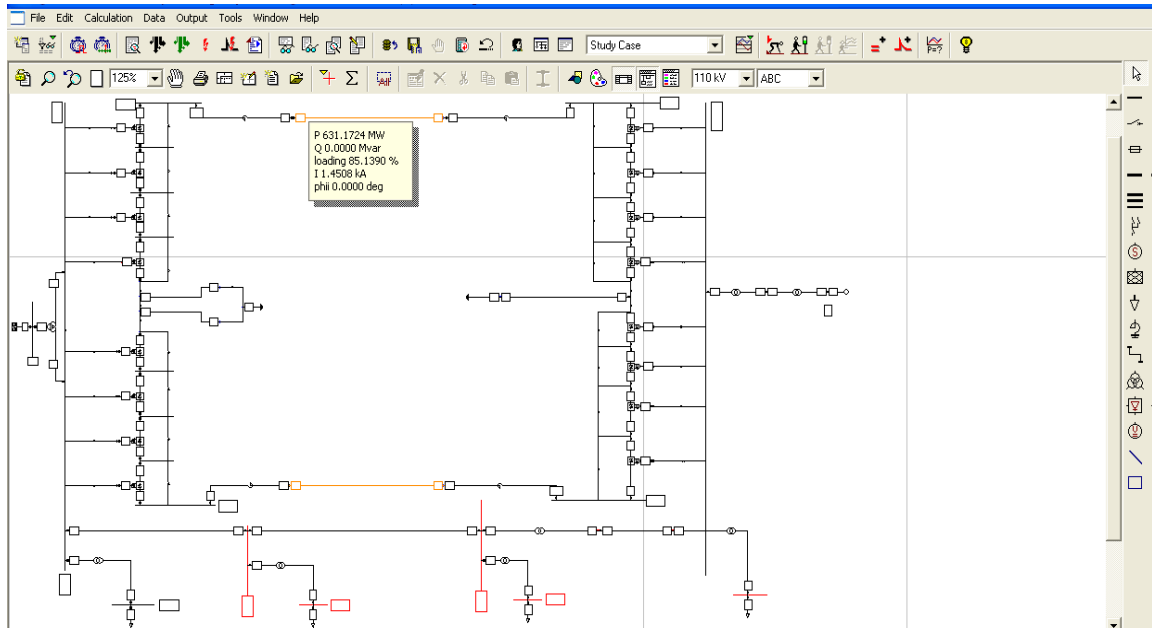


Figure 3: Converted bipolar DC line in parallel with HVAC transmission line

7 CASE RESULTS

7.1 HVAC Transmission network results.

These results are obtained for load flows to investigate when there is a growth on load demand which varied from 100MVA to 250MVA to monitor the performance of both parallel AC transmission lines. The power flow, power losses and voltage deviation are summarized in table 1 and 2.

7.1.1 Case Study 1: Parallel HVAC transmission line

Table 1: Case study 1: Power and Voltage results

Elements	$S_{Load} = 4 \times 100 \text{MVA}$		$S_{Load} = 4 \times 200 \text{MVA}$		$S_{Load} = 4 \times 250 \text{MVA}$	
	P(MW)	Q(MVar)	P(MW)	Q(MVar)	P(MW)	Q(MVar)
ACLine1	153.78	559.64	261.56	492.87	309.113	444.104
ACLine2	149.48	561.18	231.87	550.05	279.24	492.59
Load1	95.171	30.7	190.37	61.4	237.93	76.751
Load2	95.171	30.7	190.34	61.4	237.93	76.751
Load3	95.171	30.7	190.34	61.4	237.93	76.751
	V(kV)	$\delta(^{\circ})$	V(kV)	$\delta(^{\circ})$	V(kV)	$\delta(^{\circ})$
ACGridbus	418.086	0.87	441.48	1.453	434.47	1.765
ACGenbus	182.79	46.79	164.74	52.35	157.71	55.58
Load1bus	25.02	31.17	23.99	32.095	24.14	32.56
Load2bus	31.7	36.27	29.31	39.62	28.42	41.72
Load3bus	32.53	37.22	29.93	41.01	28.94	43.42

Table 2: Case Study 1: Power losses and Voltage deviation

Elements	$S_{Load} = 4 \times 100 \text{MVA}$		$S_{Load} = 4 \times 200 \text{MVA}$		$S_{Load} = 4 \times 250 \text{MVA}$	
	$P_{Loss}(MW)$	$Q_{Loss}(MVar)$	$P_{Loss}(MW)$	$Q_{Loss}(MVar)$	$P_{Loss}(MW)$	$Q_{Loss}(MVar)$
ACLine1	3x7.97	3x262.72	3x6.51	3x300.061	3x6.75	3x277.32
ACLine2	3x8.02	3x241.	3x9.06	3x241.52	3x8.4	3x236.432
	V(pu)	du(%)	V(pu)	du(%)	V(pu)	du(%)
ACGridbus	1.045	4.52	1.104	10.37	1.086	8.62
ACGenbus	1.38	38.48	1.25	24.79	1.195	19.48

7.1.2 Case Study 2: HVAC and Converted DC Network in operation

This case study involves both AC and DC line operating in parallel. The converted DC line uses same conductor parameters used under AC for Case study 1, with one line converted to DC and the second one remains in AC. The power and voltage flow results are summarized in table 3.

Table 3: Case Study 2: Power and Voltage flow results

Elements	$S_{Load} = 4 \times 100 \text{MVA}$		$S_{Load} = 4 \times 200 \text{MVA}$		$S_{Load} = 4 \times 250 \text{MVA}$	
	P(MW)	Q(MVar)	P(MW)	Q(MVar)	P(MW)	Q(MVar)
Grid	1614.74	49.91	1877.778	318.76	1960.6	604.32
Generator	-1041.6	714.36	-1027.32	703.89	982.96	671.55
Rect	2x631.2	0	2x621.203	0	2x590.44	0
Inv	2x520.8	0	2x513.66	0	2x491.48	0
DC Line	2x631.2	0	2x621.2	0	2x590.44	0
ACLine	257.22	676.79	445.03	445.03	541.76	165.36
Load1	95.17	30.7	190.34	61.4	237.93	76.75
Load2	95.17	30.7	190.34	61.4	237.93	76.75
Load3	95.17	30.7	190.34	61.4	237.93	76.75
	V(kV)	$\delta(^{\circ})$	V(kV)	$\delta(^{\circ})$	V(kV)	$\delta(^{\circ})$
DChubRec	2x435.1	0	2x433.778	0	2x429.81	0
DChub Inv	2x358.9	0	2x358.69	0	2x357.77	0
ACGridbus	132.00	0	132.00	0	132.00	0
ACGenbus	24.48	0	24.48	0	24.48	0
Load1bus	23.97	-	23.69	35.057	23.4	35.44
Load2bus	33.23	-42.62	29.64	50.47	25.23	57.26
Load3bus	36.85	-45.73	31.95	56.64	25.82	67.68

From Table 4, voltage deviation at AC bus on inverter side has dropped to values which is within admissible standards range (within 6% rules), although it was exceeding when both parallel line were operating in AC (reference Table 2). This is due to a high capacitance and charging current generated by both parallel AC. However, when one line is converted to DC the

capacitance and charging current on the remaining AC line dropped.

Table 4: Case Study2: Power Losses and Voltage deviation

Elements	$S_{Load} = 4 \times 100 \text{MVA}$		$S_{Load} = 4 \times 200 \text{MVA}$		$S_{Load} = 4 \times 250 \text{MVA}$	
	$P_{loss}(MW)$	$Q_{loss}(MVar)$	$P_{loss}(MW)$	$Q_{loss}(MVar)$	$P_{loss}(MW)$	$Q_{loss}(MVar)$
Rect	8x0	8x72.99	8x0	8x68.2	8x0	8x63.81
Inv	8x0	8x75.46	8x0	8x74.5	8x0	8x71.65
DC Line	2x111	0	2x108	0	2x99	0
ACLine	3x16.2	3x145.3	3x13.6	3x129	3x13.9	3x114.001
	V(pu)	du(%)	V(pu)	du(%)	V(pu)	du(%)
DcBusRec	1.029	2.94	1.0263	2.633	1.017	1.69
DcBus Inv	1.036	3.58	1.035	3.49	1.032	3.23
ACRebus	1.0003	0.0252	0.99	1.04	0.98	2.224
ACInvbus	0.9722	2.775	0.97	2.71	0.98	2.504

8 RESULTS ANALYSIS

The percentage (%) power upgraded or percentage (%) power loss decreased (figure 4 and 5) demonstrate how a converted DC line is performing with respective to the same line of same parameters, which is in parallel with and working in AC. It is clear there is more power being transferred by a converted DC line than when it was operating under AC and has a better percentage power upgrade. The I^2R losses for a DC line are lower than for a comparable HVAC lines because the reactance of the line $jX = j\omega L$ is not present in direct current system as $\omega = 0$, only the series resistance R of the transmission line causes losses. For the same line when it is converted to DC, it has resulted percentage (%) power losses (figure 5) being decreased, which could result on reduction on total cost of operation (TCO) whereby the objective of conductor optimization process would be met.

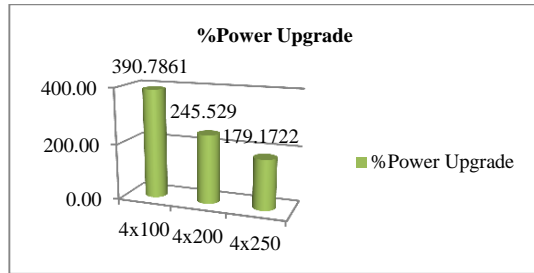


Figure 4: % Power transfer upgraded

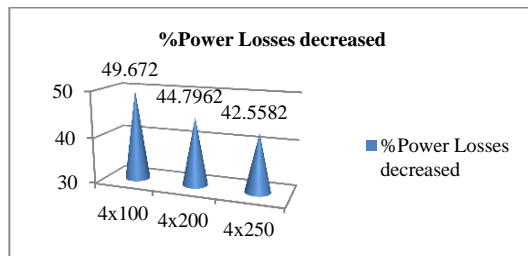


Figure 5: % Power losses decreased

9 CONCLUSION

From the case studies and results obtained, it is found that when HVAC line operates in parallel with a converted DC line, voltage deviation is within 6% rule at AC bus on generator side, this is due to a decrease in charging current produced by shunt admittance of AC line. This was not the case when both parallel lines were operating in AC (with AC Gen bus voltage deviation for case study 1 reaching 29%). There is power being upgraded, making a converted DC line to transfer more power at an upgraded power of 179%. Reducing percentage power losses to 42.56% contributes to a reduction in the total life cycle costs. The case studies facilitate interest for deeper investigations into converting actual long HVAC parallel line operating below their power transfer capability. Furthermore, it is encouraging for power system planners to look at this opportunity so that higher power capacities could be transferred into the existing systems and be able to meet consumer demands.

REFERENCES

- [1] I. Zamora, O. Abarrategui, A. Iraolagoitia, D.M. Larruskain, "Power transmission capacity upgrade of overhead lines," in *Larruskain*, p. 296.
- [2] Eskom Holdings, "Shift performance, grow sustainably," Eskom Holdings, Johannesburg, Divisional Report 2002/015527/06, 31 March 2012.
- [3] M.J Matabaro & G. Atkinson-Hope, "Efficiency of an Alternating Current Transmission Line Converted into a Direct Current System," in *Industrial & Commercial Use of Energy*, Newlands, Cape Town South Africa, 2013, pp. 311-316.
- [4] Julluri Namratha Manohar, Amarnath Jinka, and Vemuri Poornachandra Rao, "Optimization of Loss Minimization Using FACTS in," *Innovative Systems Design and Engineering*, vol. vol3, p. 49, 2002.
- [5] J.D. Glover & M.S Sama, *Power System analysis and design*, 3rd ed., Brooks/Cole, Ed. New York, USA: Pacific Grove, 2002.
- [6] A.C. Britten, R. Stephen, D. Muftic A. Singh, "Optimised conductor and Conductor Bundle Solutions for Long Distance HVDC Transmission," in *Inaugural IEEE PES 2005 Conference and Exposition in Africa*, Durban, South Africa, 11-15 July 2005, pp. 402-409.

A STUDY ON THE FEASIBILITY OF TAPPING POWER OFF AN OVERHEAD HVDC TRANSMISSION LINE

S.M. Mtakati, A.G. Roberts, W. Phipps and R.T. Harris

Faculty of Engineering and the Built Environment, Department of Electrical Engineering, Nelson Mandela Metropolitan University, Port Elizabeth 6031, South Africa

E-mail: MtakatSM@eskom.co.za, alan.roberts@nmmu.ac.za, william.phipps@nmmu.ac.za, raymond.harris@nmmu.ac.za

Abstract. HVDC transmission, when compared to HVAC transmission, suffers the disadvantage of providing no economical means of tapping power off to supply loads along its path. This paper presents an economical means of tapping small power off these lines. A parallel tapping station is designed to tap power off in two stages, first a high voltage ratio dc-dc converter lowers the high transmission line dc voltage to a lower dc voltage and then a voltage sourced inverter is used to invert the power into ac to supply isolated ac loads along the path of the line. The two stages were studied independently on PowerSim simulation tool. The complete interconnected system, rated to tap off 2.5MW, was simulated on DigSilent Power Factory where it was connected to a 500kV monopolar HVDC system. The tap circuit voltage and frequency can be locally controlled. It provides ac power of high quality and has a negligible effect on the overhead main transmission lines stability.

Keywords: HVDC transmission, tapping, dc-dc converter, voltage source inverter

1. INTRODUCTION

Over the years, HVDC transmission has been gaining widespread popularity from electricity utilities globally, mainly due to the rapid development of power electronics semiconductor equipment used in the conversion process. These developments allow for efficient and cost effective dc to ac (or vice versa) conversions. With the energy consumption of the world growing and generation sites largely remote, HVDC technology would be the most likely case to transmit this power to load sites, passing along its way many rural communities with no access to electricity. Supplying these communities with conventional ac transmission may not provide the most economical means of supplying the energy, thus a HVDC tapping circuit is developed to overcome this problem.

Previously, tapping power off HVDC overhead lines was proposed using line commutated converters which require an ac source to operate [1]. For application in an isolated load, with no ac source, expensive synchronous condensers would have to be used. Small power taps of this nature do not prove feasible. This problem can be overcome by using voltage sourced converters for the tapping station. The converter does not require an ac source to commute as commutation is self-controlled using pulse width modulation (PWM) [2]. The converter makes use of semiconductor devices with turn off capability such as gate turn off thyristors (GTO's), and insulated gate bipolar transistors (IGBT's).

Power can either be tapped off from a main overhead line by series connection or parallel connection. Fig. 1 illustrates the series and parallel

connections on the dc side of a HVDC network. A series tap should be rated at the same current rating as the main system; it also results in a voltage drop along itself and thus effectively reducing the systems efficiency [2]. Further, to create multiple tap's, series tapping would not prove feasible [3].

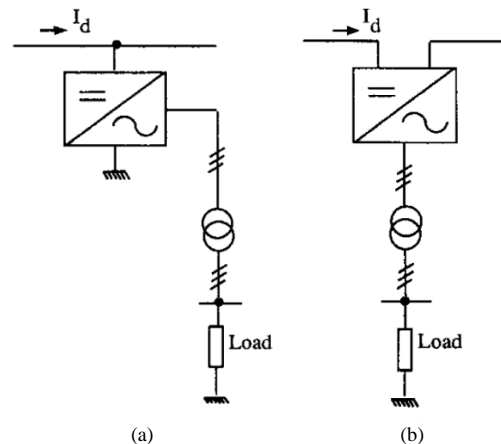


Fig. 1: Tap Methods (a) Parallel Tap (b) Series Tap [2]

A parallel connected tap on the dc side of a main network draws the rated current of the tap and is rated at the full dc system voltage.

In this paper, a 2.5MW parallel connected tapping circuit is developed, with power tapped off in two stages, first by lowering the high 500kV transmission voltage to a lower dc voltage, using a multi-level buck converter, and secondly by inverting the lowered dc voltage into a 22kV three phase ac voltage using a six pulse voltage sourced inverter. The circuit was designed to be cost effective and produce high quality power. Some simulation results are presented to show that the tapping circuit has a

negligible influence on the main overhead transmission line.

2. DESIGN OF THE PARALLEL CONNECTED TAPPING CIRCUIT

The circuit was designed for tapping 2.5MW from a 500kV dc scheme to supply an isolated load.

The parallel connected tapping circuit was designed to meet the following requirements:

- The circuit should locally control its own output voltage and frequency.
- The tapping circuit should have a negligible effect on the main HVDC transmission line.
- Power should be tapped off by the most economical means.

The switching devices used were high power IGBT modules, as they have greater reliability and fast power switching response [4]. In order to handle the applied voltage stress, the modules are required to be connected in series to form a valve. The voltage across the modules in a valve should be evenly distributed. This can be achieved by connecting an equalization resistor in parallel with each module in a valve [4].

The equalization resistor, R_{EQ} , may be calculated from (1);

$$R_{EQ} = \frac{\text{Module Voltage}}{I_{GES}} \quad (1)$$

Where, I_{GES} is the maximum leakage current of an individual module.

2.1 DC-DC Converter

To lower the high dc voltage, a high voltage ratio five-level buck dc-dc converter is proposed, shown in Fig. 2. Reducing the dc voltage is necessary to reduce the applied voltage on the inverter circuit and also the costs of the tapping station. The converter reduces the voltage across the switches, diodes and capacitors, lowers switching losses and has a reduced current ripple [5]. The IGBT switches are controlled by PWM with four triangular carriers phase shifted by 90° , allowing the converter to operate in four evenly spaced operating regions. The IGBT's are switched at 2 kHz to lower the switching losses.

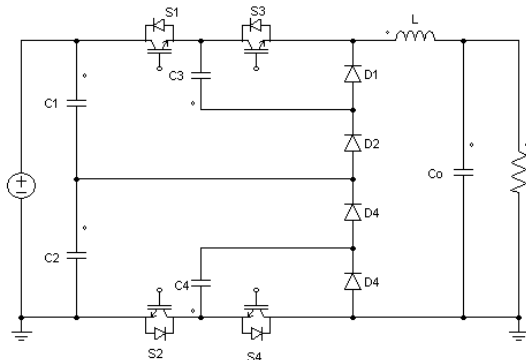


Fig. 2: Five Level Buck DC - DC Converter

The relationship between the input and output voltage of the converter can be expressed by (2);

$$V_o = DV_{in} \quad (2)$$

Where, V_o was chosen as 30kV to allow for voltage regulation and also switching losses in the circuit. The output power of the converter can be determined from (3).

$$P_{dc} = V_{dc}I_{dc} \quad (3)$$

The output of the converter is passed through a low pass filter to lower the output current and voltage ripple. The values of the inductor and capacitor can be obtained from (4) and (5).

$$L = \frac{V_i}{64 + f_s + \Delta i_L} \quad (4)$$

The size of the inductor is calculated at the maximum current ripple [5].

$$C = \frac{I_L}{4f_s \Delta V_c} \quad (5)$$

To determine the value of the capacitors, the maximum voltage ripple, the capacitor discharge time and instantaneous current ripple should be considered [5].

The circuit was simulated on PowerSim to evaluate its effectiveness in lowering the applied dc voltage. A constant 500kV dc source was simulated to represent the high transmission line voltage. A 360Ω load resistor, calculated from (6) to represent a 2.5MW load, was connected to the buck converter to draw the rated power of the tap.

$$P_o = \frac{V_o^2}{R_L} \quad (6)$$

When the simulation was run, the capacitors were initially uncharged. The five-level buck converter effectively reduces the high 500kV incoming voltage to 30.4kV, a lower output dc voltage containing some ripples before reaching steady state after 0.2s. The output current of the simulated circuit was measured as 84.5A. Fig. 3 and Fig. 4 illustrate the output voltage and current waveforms. The initial response of the semiconductor switches result in a voltage spike with an amplitude of 230kV lasting for 0.1s. The capacitors, C_1 and C_2 , arrangement limit the voltage rise.

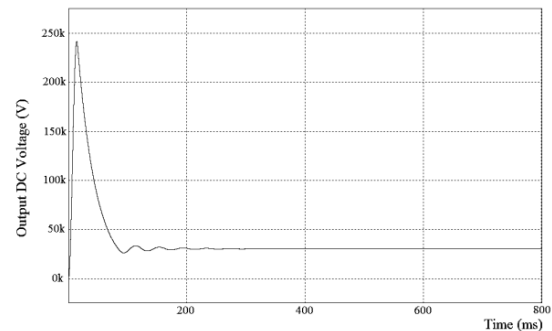


Fig. 3: Five Level Buck Converter Output Voltage Waveform

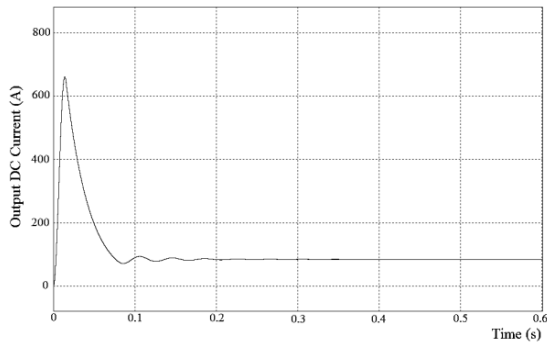


Fig. 4: Five Level Buck Converter Output Current Waveform

The circuit produces a low ripple output voltage and current. The ripple voltage in the steady state region lasts for a period of 0.5ms with an amplitude of 23V. The circuit, from simulation, operates at the desired output, producing real power equivalent to 2.57MW, calculated from (3).

2.2 Voltage Sourced Inverter (VSI)

An inverter is required to convert the lowered dc voltage from the dc-dc converter into a sinusoidal alternating voltage which should be a full wave three phase 50Hz ac voltage. A VSI has been chosen for this application as an off grid load will be supplied. A six pulse inverter provides the most economical means of converting the applied dc into ac, achieved by the operation of the switches. Some features of a VSI include independent control of active and reactive power, smaller filtering requirement and self-supporting commutation [6].

The six pulse inverter circuit is shown in Fig. 5; with a low pass filter circuit consisting of a series inductor and parallel connected capacitor bank. The converter transformer is not included in the design, instead a delta connected RL circuit representing the primary side of the transformer is modelled. The delta configuration eliminates the dc component on the inverter output ac voltage [3] and prohibits zero sequence components from entering the circuit. The system to be supplied will comprise mainly of single phase loads with very little inductive load. The power factor at which the ac is supplied has been selected to be 0.9 lagging. A $\pm 25\%$ unbalance among the phases was considered.

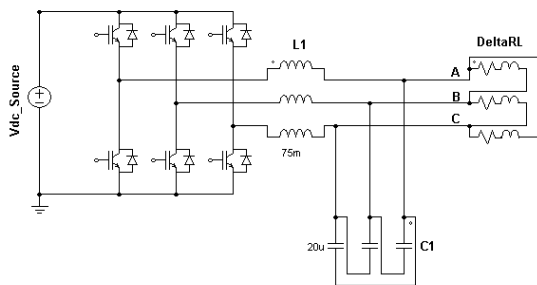


Fig. 5: Six Pulse Voltage Sourced Inverter

To obtain an output ac voltage the switching frequency is compared with a reference frequency. The reference frequency is generated from three generators phase shifted by 120° and compared with a triangular wave switching frequency operating at 1250Hz. The switching frequency was made odd in order to eliminate undesired even harmonic frequencies from occurring in the output. The output voltage can be controlled from the relationship of the amplitudes of the two signals.

The filter circuit is required to smoothen out sparks in the current waveform and eliminate certain harmonic frequency families in the output voltage waveform. The corner frequency of the filter may be calculated from (7) and should be designed to be less than one third the inverter switching frequency to eliminate the switching ripple in the output voltage [7].

$$f_c = \frac{1}{2\pi\sqrt{LC}} \quad (7)$$

To ensure the output voltage of the inverter remains stable for both balanced and unbalanced loads the capacitance should be maximized and the inductor minimized [8]. The value of the series inductor was chosen as 75mH and the capacitor as 20 μ F. The corner frequency was calculated as 130Hz.

The line output voltage expression can be expressed routinely by Fourier analysis;

$$V_{ab} = \frac{2\sqrt{3}}{\pi} V_{dc} \left(\sin\omega t - \frac{1}{5}\sin 5\omega t - \frac{1}{7}\sin 7\omega t \dots \right) \quad (8)$$

The neutral voltage;

$$V_{an} = \frac{4}{2\pi} V_{dc} \left(\sin\omega t + \frac{1}{5}\sin 5\omega t + \frac{1}{7}\sin 7\omega t \dots \right) \quad (9)$$

The line output current expression for a delta configuration is given as;

$$I_a = \frac{2\sqrt{3}}{\pi} I_{dc} \left(\sin\omega t + \frac{1}{5}\sin 5\omega t + \frac{1}{7}\sin 7\omega t \dots \right) \quad (10)$$

The output power of the tap can be calculated from the formula;

$$P_{ac} = \sqrt{3} V_L I_{ac} \cos \theta \quad (11)$$

Where, $\cos\theta$ is the power factor angle between the phase current and voltage.

Phase impedances for the 25% unbalance are shown below.

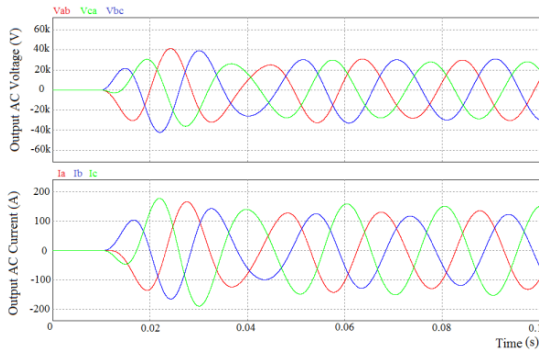
$$Z_a = 467 + j226\Omega$$

$$Z_b = 350 + j170\Omega$$

$$Z_c = 263 + j127\Omega$$

Phase a draws the rated power and set at +25% of phase b. Phase c was calculated to be -25% of phase b.

Powersim was used to simulate the inverter for both balanced and unbalanced load conditions. The ac output voltage and current results, when a $\pm 25\%$ unbalanced load was connected, are shown in Fig. 6.


 Fig. 6: Six Pulse Inverter VI Curve for $\pm 25\%$ Unbalanced Load

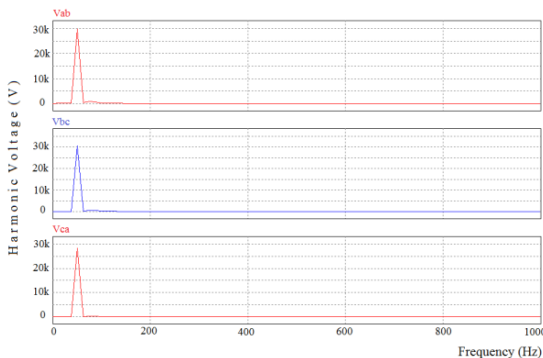
The voltages of the inverter under a balanced and unbalanced load are summarized in Table 1. The degree of unbalance is denoted as the ratio of the maximum difference among any three phase output voltages to the rated output, which is 22kV.

Table 1: Results of a Three Phase Inverter under Different Loads

Load Condition	V _{AB}	V _{BC}	V _{CA}	Degree of Unbalance
Balanced	21.8kV	21.8kV	22.5kV	3.2%
$\pm 25\%$ Unbalance	20.5kV	22.2kV	21.5kV	7.7%

From the results in Table 1, it is clear that the unbalance in the output voltage is caused primarily by the unbalanced load. The voltage remains stable as the zero sequence component of the voltage has been eliminated by the delta load configuration. The line ab voltage, under an unbalanced load, reduces to below the allowable $\pm 5\%$ voltage regulation. When this situation occurs, the modulation index should automatically be adjusted to maintain all line voltages within specified values. The inverter, however, under a balanced load also generates an unbalanced ac output. The unbalance is caused by the low pass ac filter circuit.

A harmonic analysis of the output line voltage under an unbalanced load was conducted. The results for all phases are shown in Fig. 7.


 Fig. 7: Voltage Frequency Spectrum for a $\pm 25\%$ Unbalanced Load

The results demonstrate that the output ac power is a single frequency component, thus meaning the ac low pass filter effectively eliminates harmonics from entering the ac system.

3. PARAMETERS OF THE MAIN HVDC TRANSMISSION LINE

The two stages of the parallel connected tap are integrated and connected to a main overhead HVDC transmission line. A monopolar 500kV transmission line model, available on DigSilent Power Factory, was used. Fig. 8 shows the monopolar HVDC system with the parallel connected tap circuit inserted at the middle of the dc transmission line.

The transmission line delivers 500MW of power over 500km between the rectifier and inverter. The system is controlled by two series connected six pulse converters on the either side. The converter transformers provide a 30° phase shift between the upper and lower converters on each side to eliminate some of the harmonics in the ac and dc voltages [9].

The converters are able to control the dc voltage and current by adjustment of the thyristors firing angle. The firing angle has been set to automatic, to follow the control characteristics of the converters. The rectifier controls the power being delivered and has been set to 500MW. The inverter side controls the voltage and has been set to maintain it at 0.99pu.

The HVDC system also contains harmonic filters to eliminate the resultant harmonics produced by the converters and also to ensure that the ac current lags behind the ac voltage [9]. The ac filters and capacitors are star connected while the smoothing reactor is connected in series with the line.

In order to be able to evaluate the effect the tapping station has on the main transmission line, some simulations were conducted using DigSilent Power Factory. These would form the basis of a comparison once the tapping station is connected.

An unbalanced three phase ac load flow simulation was run on DigSilent Power Factory before the tap was connected. The results of the simulations are presented in Table 2.

Table 2: Load Flow Simulation Results with No Tap is Connected

Converter	AC Voltage	DC Voltage	DC Current	DC Power
Rectifier	345kV	500kV	1kA	500MW
Inverter	230kV	495kV	1kA	495MW

The resulting voltage ratio between the rectifier and the inverter leads to a firing angle of $\alpha = 24.25^\circ$ on the rectifier side and a $\gamma = 22.74^\circ$ on the inverter side. The overlap angle on the inverter side is 11.03° .

A three phase short circuit was simulated on the inverter and rectifier side of the system, as shown in Fig. 9. A fault on either side of the ac system results in an increase in voltage on the ac side of the opposite end by 0.1pu. This increase in voltage is due to the stored energy in the filter capacitors discharging. A peak short circuit current of 12.4kA and 18.59kA results on the rectifier and inverter for a

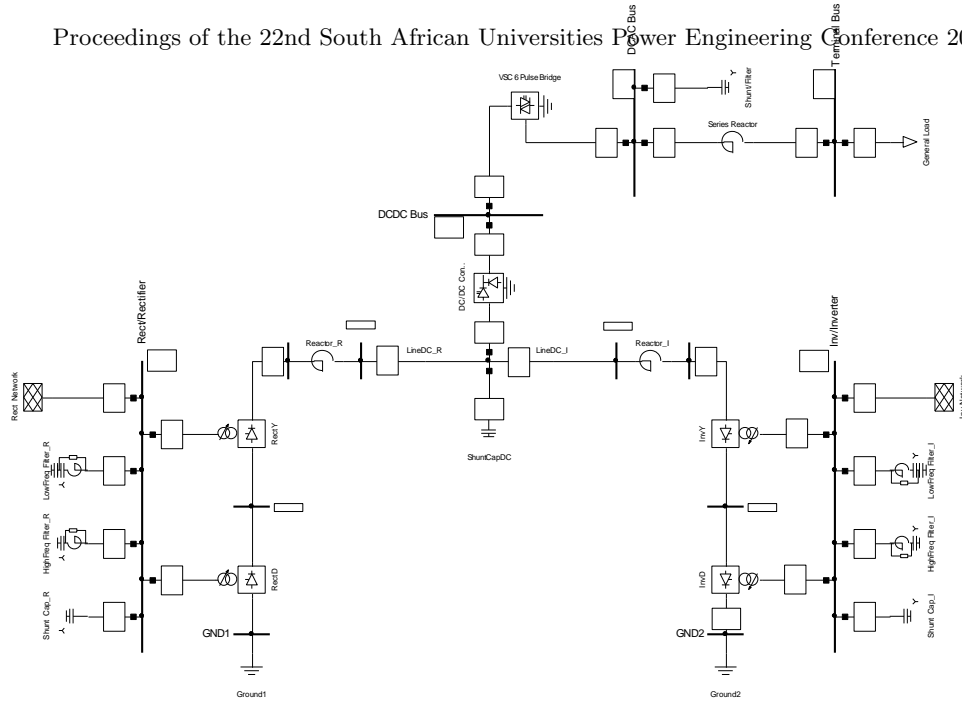


Fig. 8: Parallel Connected Tap Mid Way On an HVDC Transmission Line

fault on the ac side of the respective busbar. The short circuit power at both ends is 3000MVA.

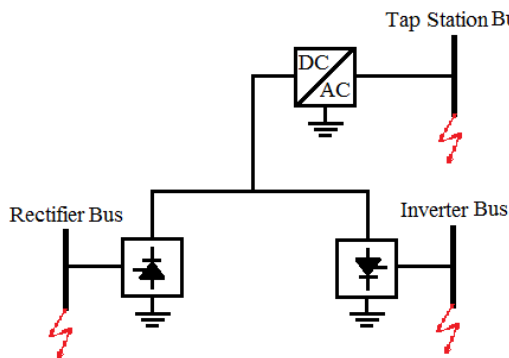


Fig. 9: Ac Fault Positions on HVDC System

4. HVDC SYSTEM WITH PARALLEL CONNECTED TAP

To simulate the influence a parallel connected tap has on a main HVDC system, the designed tap circuit was connected mid-way at 250km, the furthest from both ends to analyze the effect it would have on the main transmission system. The dc-dc five-level buck converter discussed in section 2.1 above could not be simulated on DigSilent Power Factory. A compact conventional buck converter was used instead, to lower the high transmission line dc voltage to a lower dc voltage. The two stages of the parallel connected tapping station were connected as shown in Fig. 8.

The tap circuit was simulated for both balanced and unbalanced load conditions. The unbalance was simulated with the same loads as done previously during the six pulse inverter design. The output results of the simulation are summarized in Table 3.

Table 3: Tapping Station Load Flow Results

Converter	AC Voltage	DC Voltage	Load Current	Output Power
Balanced	21.27kV	29.85kV	70A	2.33MW
Unbalanced	21.55kV	29.85kV	60A	1.86MW

For both balanced and unbalanced, as shown previously during inverter design, the voltage remains stable and within the recommended $\pm 5\%$ voltage level. The conventional buck converter reduces the high transmission line voltage to a lower dc voltage, applied to the inverter input terminals. The circuit operates with an efficiency of 90% with power losses across the series reactor and switching devices.

With the tap connected, it is of great interest to see what effect it has on the HVDC system. The results of the simulation for both balanced and unbalanced load conditions are presented in Table 4.

Table 4: Load Flow Simulation Results when Tap is Connected

Converter	AC Voltage	DC Voltage	DC Current	DC Power
BALANCED LOAD RESULTS				
Rectifier	345kV	500kV	1kA	500MW
Inverter	230kV	495kV	0.99kA	492.4MW
UNBALANCED LOAD RESULTS				
Rectifier	345kV	500kV	1kA	500MW
Inverter	230kV	495kV	1kA	493.2MW

The rectifier side of the system remained unaffected by the parallel connected tapping circuit. The firing angle α remained at 24.25° as the rectifier was not required to deliver additional power to the system. The inverter side gamma angle for a balanced and unbalanced load slightly increased to 22.77° and 22.76° , respectively. The gamma angle is set to keep the voltage at the inverter side constant at 0.99 p.u. The slight change means the parallel connected tapping station results in a negligible drop in the HVDC system voltage. The power delivered to the inverter decreases by the same power being drawn by the parallel connected tap.

A three phase short circuit fault, as simulated before the tap was connected, was placed on the inverter and rectifier buses, as shown in Fig. 9. The fault was also simulated on the tap circuit ac side bus. In addition, a

single phase to ground fault was also simulated at the tp station busbar, as it is the most frequently occurring fault on overhead power lines. The faults on the inverter and rectifier busbars both result in a 0.1 p.u voltage increase on the ac side of the tapping circuit, increasing due to the stored energy of the capacitor bank discharging. When the fault was applied on the inverter busbar, a peak short circuit current of 30.99 kA and an initial short circuit power of 5000MVA were experienced. The increase in fault levels is due to the additional load connected to the system, which reduces the source impedance seen by the inverter

A three phase short circuit fault on the ac side of the tapping station results in a 0.1 p.u voltage increase on both the rectifier and inverter ac busbars. A single phase to ground fault reduces the voltage on both ends. The voltage reduction is due to the degree of unbalance in the system, created by the single phase fault, which affects the controllers of the main ac system and, thus, the voltage.

5. CONCLUSION

The feasibility of a parallel connected tapping circuit to tap small amounts of power off an overhead HVDC transmission line has been investigated. Power was tapped off in two stages, first by lowering the high system voltage and then inverting it into ac.

The simulation experiments presented in this document show that tapping power off from an HVDC transmission line can be made possible by use of a parallel connected tapping circuit. As the power being drawn is less than 1% that of the main system, the circuit shows a negligible effect on the main system.

The proposed dc-dc five-level converter reduces the high transmission line dc voltage to a lower dc voltage, however during startup it has an initial peak of 230kV lasting for 0.1s. When setting up the protection of the tap, this initial peak should be considered. To reduce the effects of the peak on the six pulse inverter, a surge arrester should be connected in parallel with the inverter to provide overvoltage protection. The protective voltage level and energy rating of the surge arrester should be carefully selected.

For isolated loads, a VSI tap station provides the most economical means of providing power, owing to the development of high power IGBT's used in the conversion process. The tapping station remains stable for unbalanced single phase loads and allows for ease of control of the output voltage when a decrease in voltage is experienced.

Faults on the tapping circuit need to be isolated before they affect the main transmission line. Power flow on the main line should take priority over the tap.

Further study in the topic would include setting up the protection of the developed tapping circuit and perform time – domain simulations to better understand the controller's role in ensuring stability is maintained on the main HVDC system.

REFERENCES

- [1] M. R. Aghaebrahimi and R.W. Menzies, "Small Power Tapping from HVDC Transmission Systems," *IEEE Transactions on Power Delivery*, Vol. 12, No.4, pp. 1698-1703, 1997.
- [2] A. Ekstrom and P. Lamell, "HVDC tapping station: power tapping from a DC transmission line to a local AC network," *AC and DC Power Transmission International Conference*, pp. 126 - 131, 1991.
- [3] P. N. Ijumba and L. Chetty "Rural Electrification using Overhead HVDC Transmission," *Energize*, pp. 45 - 50, 2012.
- [4] M. Ranjbar et. al., "Theoretical and Practical Considerations Relating to Design High-Voltage IGBT Valve," *IEEE: Electrical Engineering (ICEE), 2011 19th Iranian Conference*, pp. 1 - 6, 2011.
- [5] L. F. Costa, S. A. Mussa and I. Barbi, "Multilevel buck dc-dc converter for high voltage application," *Industry Applications (INDUSCON), 2012 10th IEEE/IAS International Conference*, pp. 1 - 8, 2012.
- [6] R. Entriiken, *EPRI Power - Electronics Based Transmission Controllers Reference Book (The Gold Book): 2009 Progress Report*. Palo Alto, CA: Electric Power Research Institute, 2009.
- [7] K. Hatua, "Active Damping of Output LC Filter Resonance For Vector-Controlled VSI-Fed AC Motor Drives," *IEEE Transactions on Industrial Electronics*, vol. 59, pp. 334-342, 2012.
- [8] K. H. Ahmed S. J. Finney. and B. W. Williams, "Passive Filter Design for Three-Phase Inverter Interfacing in Distributed Generation," *Electrical Power Quality and Utilisation, Journal* Vol. 8, pp. 49-58, 2007.
- [9] J. D. Glover, M. S. Sarma and T. J. Overbye, *Power System, Analysis and Design*, 5th ed. Stamford, USA: Cengage Learning, 2012.

C. Nyamupangedengu

University of the Witwatersrand, Johannesburg, School of Electrical and Information Engineering, Private Bag 3, 2050, Johannesburg, South Africa.

Abstract: A nanocomposite dielectric is a material that is produced by uniform dispersion of suitable quantities of surface conditioned nano-sized fillers in the base dielectric such as epoxy and polyethylene. Through appropriate choice of combinations in filler and base material type, the properties of the resultant composite material can be tailor made to give specific performance parameters, a behaviour characteristic of smart technologies. Worldwide laboratory-based research has produced remarkably promising insulation characteristics improvements through nanocomposite technology. Major improvements have been reported in characteristics such as dielectric strength, electrical treeing endurance, surface discharge/tracking erosion and space charge retention in various types of electrical insulations. However, while notable achievements have been reported in the laboratory-based research field, the nanocomposite electrical insulation technology is still to make a breakthrough into commercial applications. While endeavours continue into proof of concept research in nanocomposite technology, more effort has to be directed at improving viability in industrial applications.

Key Words: Nanoparticle filler, nanocomposite, insulation, treeing partial discharges, dielectric strength, space charges, permittivity

1. INTRODUCTION

Electrical insulation is that which separates two points that are at different electrical potential; and this can be material (solid, liquid and gas) or vacuum. In most electrical equipment, insulation is the most vulnerable component and therefore the cause of most failures. In rotating machines 30-40% of the faults are attributed to insulation failures [1] while in power transformers and inductive reactors, it is in the order of 40% [2]. It is for this reason that a lot of efforts in high voltage engineering endeavours focus on improving the performance reliability of electrical insulation.

The need to transfer bulk power over long distances is becoming more prevalent in developing economies. In China, there are now transmission circuits operating at 1 million volts [3]. In Eskom and indeed the rest of the African region, ultra high voltage transmission voltages will soon be a reality. Like any other technology, miniaturisation is the fashion in electric power equipment. As an example in the increasingly growing business of off-shore wind power stations, space for inverter substations is very limited and therefore miniaturised high voltage equipment is imperative.

Space limitations, economic viability and stringent reliability requirements have caused engineers to continuously search for better electrical insulation techniques. Among other possibilities, micro-filler composites, function graded insulation and nano-filler composite insulation technologies are on the forefront as candidates for new generation electrical insulation.

1.1 Microfiller composite electrical insulation

By mixing host insulation with suitable microfiller particles, the resultant composite insulation can give remarkable functional properties. Silicon rubber composite insulation is such an example of major achievements in insulation development. Due to hydrophobicity properties, silicon composite insulation is now a popular product in outdoor high voltage applications, and especially in heavily polluted environments. Many power utilities such as Eskom have refurbishment programmes that include

coating ceramic outdoor insulation with Silicon rubber composite insulation to improve on pollution condition performance.

Silicon rubber composite insulation, being a hydrocarbon based material, has an inherent limitation; the vulnerability to electrical discharge induced degradation. Exposure of polymer matrices to localised intense energy through electrical discharges frees up carbon molecules that are electrically conductive and this becomes an agent for further degradation. It is for this reason that researchers have interest in identifying means of improving the electrical discharge degradation endurance of silicon based composite insulation [6].

1.2 Function graded insulation

High voltage insulation design in any context essentially entails manipulation and containment of electric fields to avoid insulation degradation and breakdown. The permittivity parameter of insulation plays an important role in the electric stress distribution profiles in electrical insulation systems. The principle of function graded electrical insulation entails causing the permittivity of the insulation to be a function of the geometrical profile of the insulation component. Research in the area of function graded insulation is being championed by the likes of Okubo et al [3].

At interfaces of two different insulations the electric field potential lines get closer together on transition from the medium of higher permittivity in accordance with equation 1.

$$E_2 = \frac{\epsilon_1}{\epsilon_2} E_1 \quad (1)$$

Where:

E_1, ϵ_1 and E_2, ϵ_2 are respectively the electric field strength and permittivity in insulation the two insulation layers.

If the ratio of the two permittivities is high, the electric field stress on the insulation boundary can be enhanced to cause surface discharge or insulation breakdown. Such a phenomenon is a design

challenge in high voltage components such as power cable accessories (terminations and joints), rotating machines stator bars and insulation spacers in gas insulated systems (GIS). Stress grading techniques are used to mitigate the stress enhancement problems but this may result in increased dielectric losses or physical dimensions of the apparatus. Function graded insulation technology has proven to be an effective mitigation where the permittivity at insulation boundaries is gradually transitioned instead of an abrupt change [3].

Function graded insulation technology has limitations in that it is still a new technology and that it is not easy to implement in large scale insulation manufacturing processes. Furthermore there are many more insulation parameters that cannot be manipulated through the function graded insulation technology.

Nanotechnology, when applied to electrical insulation, seems to be promising with regard to overcoming some challenges encountered in endeavours to improve insulation technology.

This paper presents a review of worldwide research work in nanocomposite dielectric technology and speculates on the future trends. The author's contribution in this research area is also highlighted.

2. THE PRINCIPLE OF NANOCOMPOSITE INSULATION TECHNOLOGY

When specific type of 'impurities' in the form of nano-dimensioned particles are homogeneously dispersed in host insulation matrix, such as epoxy or polyethylene, the resultant material is termed a nanocomposite dielectric. If appropriate nanoparticle type, size and geometry, particle surface conditioning for optimal compatibility with the host material are chosen, and that the nanoparticles are homogeneously dispersed, the resultant nanocomposite material can exhibit superior functional characteristics. The magic in nanodielectrics lies in the nanoparticles' ability to influence the behaviour of the host insulation because of the tremendously large interface area between the nanoparticles and the host insulation matrix.

2.1 The interfacial area

Due to the nanometric size, the interface area between the host insulation matrix and nanoparticles is incredibly big; orders of magnitude greater than if micro-sized fillers are used. As an example, spherical nanoparticles of 40 nm diameter when uniformly dispersed in the host epoxy at 5% loading by weight, the total interfacial area is about $3,5 \text{ km}^2/\text{m}^3$ of the nanometric composite [5]. In other words in 1 m^3 of such a nano-dielectric the total area through which the nanoparticles influence the behaviour of the host insulation is equivalent to the surface area of 3 Rugby fields [5]! The increase in interfacial area as a function of the filler size is as illustrated in Figure 1.

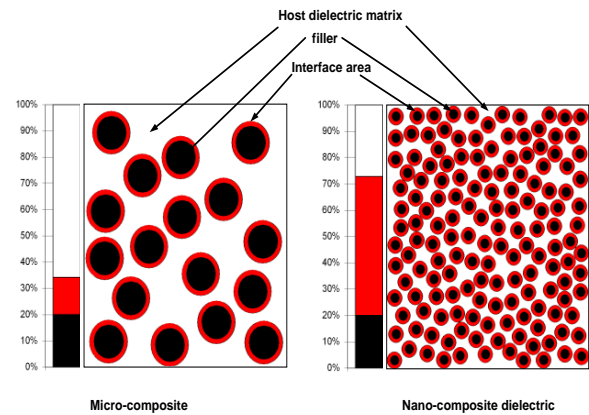


Figure 1: An illustration of the increase in interfacial area as a function of the filler size (reproduced with permission from Johannes Seiler [7]).

The ability of the nanofiller to influence the behaviour of the host insulation lies in the interfacial area. It is for this reason that the bulk of the research work in the development of nano-dielectrics lies in understanding the physiochemical phenomenon around the interfacial area. It is a fact that despite the hype worldwide in nano-dielectric research, the physics and chemistry across the interface between the nanofiller and host matrix is not yet sufficiently understood. A contributing factor in the slow progress is that there are so many combinations of filler type and host insulation and also many manufacturing methods such that it is difficult to establish consistent characterising techniques that can lead to generalized models.

It should however be noted that experts in nanodielectrics research such as Tanaka have been progressive enough to propose a model for the interfacial region [8]. In Tanaka's model, the interfacial region between the nano-filler and host insulation matrix has 3 categories; the inner, the middle and outer layer as illustrated in Figure 2. Each layer has a specific role in the functionality of the interfacial layer. More details in the physics of the layers are in [8] and [9].

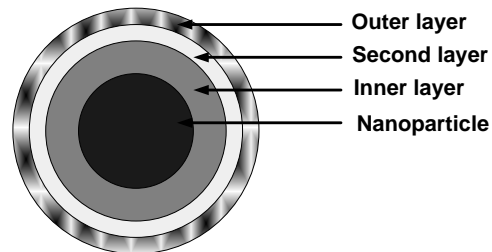


Figure 2: An illustration of Tanaka's interfacial model [8].

In relation to the interfacial model, it has been postulated that the effect of the nanoparticle in an insulation medium such as polyethylene is to realign the molecular bonds; thus altering the morphology around the particle as illustrated in Figure 3 [10].

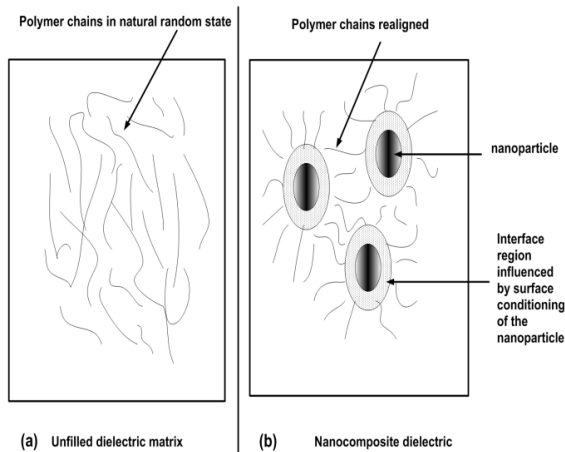


Figure 3: Influence of a nanoparticle on the morphology of molecules in the vicinity [10].

While efforts continue to be directed towards understanding the physiochemical phenomena of the interfacial area, remarkable characteristics of nanodielectrics have already been reported as outcomes of experimental investigations worldwide. As an example, by properly choosing the best combination of host insulation material and nanoparticle type and appropriate mix ratio and mixing process, the properties of the resultant nanocomposite can be made to specific requirements. A material can therefore be tailor made to give specific characteristics and this would be 'smart insulation' technology. As an example, by using material such as Boron Nitride nanoparticles, electrical insulation such as epoxy can be tuned to give very good electrical insulation characteristics while at the same time exhibiting very good thermal conducting properties, a phenomenon that is difficult in conventional insulation technology. Similarly loading suitable quantities of Boehmite nanoparticles in an insulation material can produce a fire retardant nanocomposite dielectric [11].

A summary of the state of the knowledge in nanocomposite worldwide research, according to the literature is summarised in Table 1.

3. ELECTRICAL TREEING PHENOMENON IN NANOCOMPOSITE DIELECTRICS

It can be argued that the litmus test of electrical insulation quality is in the ability to endure persistent high localised divergent electric stress. The failure mechanism under such high divergent stress is known as electrical treeing [18]. Once initiated electrical trees propagate into the insulation by means of partial discharges phenomena until a short circuit occurs across the insulation.

Many researchers have studied time-to-failure and the nature of treeing mechanisms as an important performance characterisation criterion for nanocomposite electrical insulation [19]. Although there are variations across wide ranging possible combinations of nanoparticle type, size and type of host insulation, it is now known that electrical treeing failure is greatly retarded in nanocomposites in

comparison to the unfilled insulation. It is generally agreed that electrical trees find it difficult to break through the interfacial regions of the nanoparticle and host insulation matrix.

Electrical treeing phenomena in nanodielectrics has mainly been studied using time-to-failure analyses, photographic images of the trees, as well as scanning electron microscope (SEM) images of the treeing channels. Although a lot of knowledge has been built up through these techniques, the electrical treeing phenomena in nanocomposites are not yet well understood. There are opportunities for further understanding electrical treeing mechanisms in nanodielectrics by using partial discharge (PD) detection techniques. The author is involved in research work that entails characterisation of electrical trees in nanocomposites using PD technology. In this section, the highlights of the findings in treeing PD characterisation in epoxy resin nanocomposite dielectrics are presented.

3.1 Distinct electrical tree PD magnitude regimes

Treeing PD measurement experiments have been conducted in shielded high voltage (HV) laboratories where sensitivities were in the order of 0.3 pC. Using the setup shown in Figure 4, a fixed test voltage is continuously applied on to the test sample. The measured PD quantities are logged at intervals throughout the sample life as the trees propagate from initial inception to complete failure.

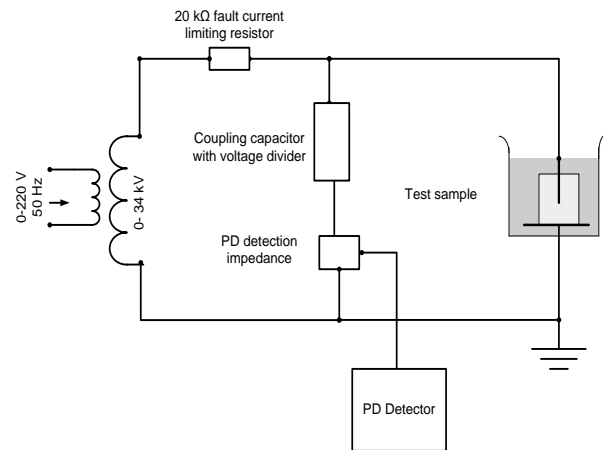


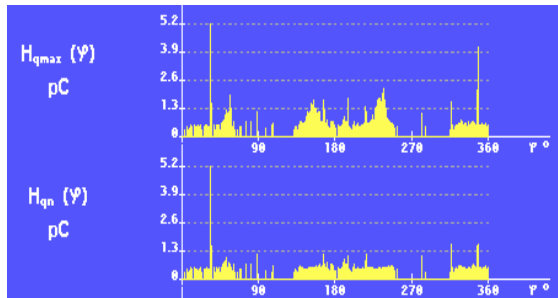
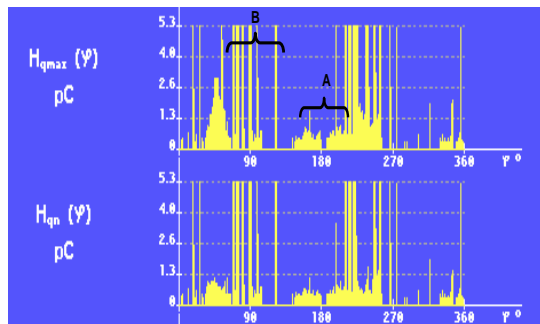
Figure 4: Electrical treeing PD measurement setup [20].

A distinctive feature of electrical tree magnitudes in the nanocomposites is that there are two groups of PD pulse types. The first group comprises of relatively very small (hardly exceeding 1.5 pC) and uniform magnitude pulses. The pulse repetition rates are more regular and the magnitude variation is consistent throughout the electrical tree life. It is presumed that these small regime pulses emanate from the small branch trees. An example of a typical phase-resolved-pattern image of the smaller electrical tree PD pulses measured in a MgO/Epoxy nanocomposite test sample is shown in Figure 5.

Table1: Examples of representative research results on nanodielectrics performance

Insulation performance parameters	Highlights of research findings
Dielectric strength (short term breakdown under uniform electric field)	TiO ₂ /Epoxy b/dwn voltage increases by up to 20% but only in 1-5% loading, at higher loading it decreases. Increases more at higher temperature [12,13]
Voltage endurance (long term breakdown under divergent high electric field stress)	Significant orders of magnitude improvement in SiO ₂ /XLPE and TiO ₂ /Epoxy [12,14]. There is a crossover phenomenon to be taken into account [5].
Surface discharge erosion/tracking	Less erosion on nano-filled Silicon rubber although conflicting results are still being reported [4]. However it's agreed that erosion resistance improves although dependent on compatibility of nanofillers and how well dispersed in host matrix [12]
Space charge retention	Less in XLPE nanocomposites than clean XLPE [12,15]
Thermal conductivity	Thermal conductivity is enhanced in Silica/Polyethylene nanocomposite [16]
Permittivity	Imaginary permittivity in XLPE/SiO ₂ much higher than in clean XLPE [15] A quantum change in permittivity to $\approx 10^{10}$ has been reported in nano-silver assembly in polymer matrix [17]

The second category of the electrical tree partial discharge pulses comprise of much bigger pulses; tens of orders of magnitude higher than the smaller regime. The bigger magnitude regime of electrical tree PD pulses have wide ranging variations in magnitude, are more erratic in repetition and can occur simultaneously with the smaller pulses as shown in Figure 6. It is postulated that the bigger magnitude electrical tree PDs are generated in the longer tree channels. The electrical trees in the nanocomposites are therefore bush/branch tree types.


 Figure 5: A typical $H_{qn}(\phi)$ for the electrical tree MgO/Epoxy nanocomposite [20].

 Figure. 6: A typical 2-minute record of $q_{max}(t)$ and $q_{mean}(t)$ for tree PDs in clean epoxy where showing the small PD magnitude regime, A and big PD magnitude regime B [20].

Distinguishing features of electrical tree PDs in nanodielectrics is that although the pulse magnitudes occur in two categories of small and big regimes, the bigger pulses are generally smaller in nanodielectrics than in unfilled host insulation. This observation may be interpreted as proving that the longer branches in nanodielectrics are shorter than those in clean insulation. Secondly, the prevalence of bigger pulses is less in nanodielectrics than in clean host insulation. It can therefore be postulated that the nanoparticles have an effect of hindering the growth of electrical trees in nanodielectrics as illustrated schematically in Figure 7. Discussions around this model in the nanodielectrics research fraternity has recently evolved and it is now generally agreed that the nature of how the nanoparticles hinder electrical tree progression is more in the tree channel width expansion restriction than elongation [21]. Further investigations around this hypothesis are ongoing.

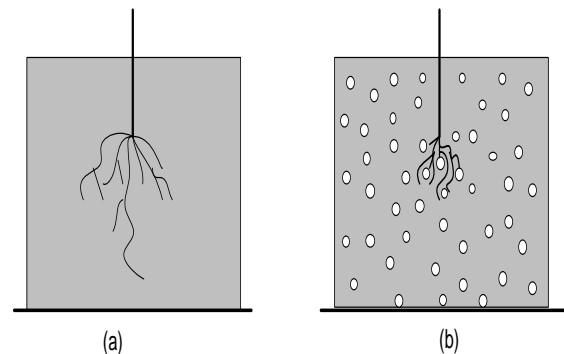


Figure. 7. An illustration of the electrical tree blocking effect of nanoparticles where (a) and (b) are the corresponding tree propagation models in clean and nanocomposite [5].

3.2 Time evolution of electrical trees PD in nanocomposite dielectrics

Partial discharge quantities such as average magnitude, maximum and minimum magnitudes as

well as the corresponding phase-resolved-patterns (PDPRP) were logged every second from initial inception to complete breakdown in various types of nanocomposite epoxy as well as unfilled epoxy. The test sample being used in these tests are needle plane configuration cast in the dielectric as illustrated in Figure 8.

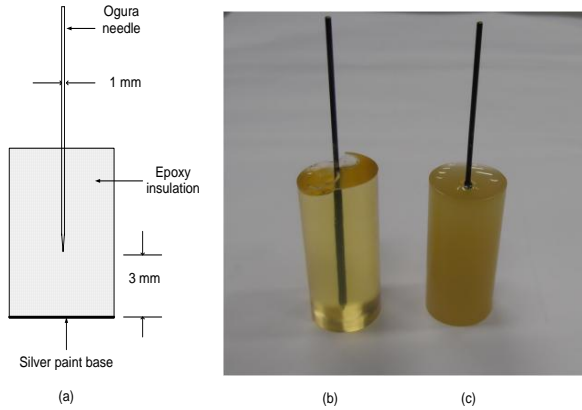


Figure. 8. Test samples; (a) is the schematic, (b) and (c) are the examples of clean epoxy and nanodielectric composite samples respectively [20].

Plots of PD magnitudes over the entire electrical tree lives have shown consistent trends although there are variations depending on the type of nanocomposite as well as the percentage loading levels. In essence there are periods (a couple of hours) where only small regime PD pulses are registered and periods where both small and large PD pulses are present. Most interestingly there are prolonged periods of complete evanescence of the PDs. The more of such instances the higher the probability that the sample will last much longer. In contrast, treeing PDs in unfilled epoxy show no features of prevalence of one PD regime over the other and no periods of sustained absence of partial discharges.

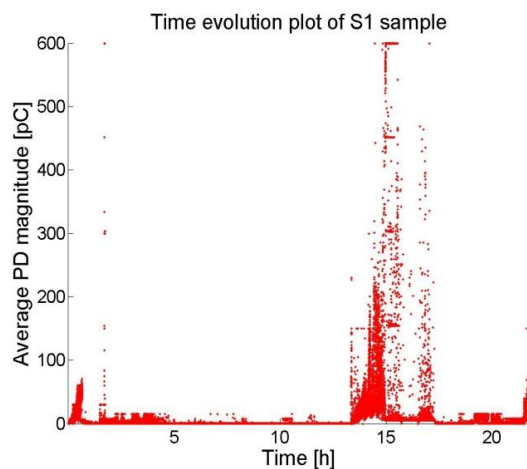


Figure. 9: An example of a plot of electrical treeing PD magnitude over the entire life span of a SiO_2 /Epoxy test sample.

It is postulated that the reason why in nanocomposites small regime electrical trees PDs are

predominant is that the electrical trees are bushier than the branch/bush in unfilled dielectrics. The nanoparticles prevent the growth of wider and longer tree branches. The reason why there are cases of prolonged extinction of PDs in nanocomposite dielectrics is that the PDs in the blocked tree channels cause pressure changes as well as depositing conductive chemical by-products that increase the PD inception voltage in the tree channels thus causing extinction of the PD activity. The situation may continue until new channels grow or the conditions change and lower the PD inception voltage. More details of the postulated PD evolution models are in reference [22].

4. THE POSSIBLE FUTURE OF NANOCOMPOSITE DIELECTRICS

In major international conferences such as IEEE Conference on Dielectrics and Electrical Phenomena (CEIDP), International Conference on High Voltage Engineering (ISH) and IEEE Electrical Insulation Conference (EIC), the subject of nanocomposites is a major attraction. It is an indication that there is a promising future in nanocomposite insulation technology. While nanotechnology applications in electrical insulation, is still largely at research level, in other material applications such as aviation, nanocomposites are already in the commercial domain; an example is the aerospace industry.

In the electric power industry, nanocomposite technology is still to cross the bridge between research and development (R&D) into commercial applications. The main challenge is in the cost and difficulties in ensuring consistency in the manufacturing processes [23]. It is of absolute importance that nanoparticles are homogeneously dispersed in the host insulation and while this can be achieved in the laboratory environments, albeit requiring due diligence, in the industrial environment the required precisions make the processes be unviable business cases. Research in nanocomposite insulation technology should therefore not only focus on proof of concept but on the ease with which the technology can be commercialised.

5. CONCLUSION

The possibilities of being able to tune properties of a material to meet specific electrical insulation performance requirements are quite exciting as this conforms to the concept of smart technologies. It would really be a major technological breakthrough if electric power equipment such as power transformers, generators, motors and power cables would be insulated with super electrical insulation that is also super thermally conductive. The impact on the capacity ratings and costs would be very significant. Nanocomposite insulation technology currently holds the hope for such futuristic smart insulation technology.

6. ACKNOWLEDGEMENTS

The authors would like to acknowledge with gratitude Eskom for their support of the High Voltage Engineering Research Group through TESP. They would also like to express gratitude to the Department of Trade and Industry (DTI) for THRIP funding and to thank the National Research Foundation (NRF) for direct funding.

REFERENCES

- [1] G. Paoletti and A. Golubev, 'Partial discharge theory and applications to electrical systems', *Proceedings of the Annual Pulp & Paper Industry Technical Conference*, Seattle, WA, June 1999.
- [2] A.K. Lokhanin, T.I. Morozova, G.Y. Shneider, V.V. Solokov and V.M. Chonogotsky, 'Internal insulation failure mechanisms of HV equipment under service conditions', *Cigré session 15-201*, Paris, 2002.
- [3] H. Okubo, "Enhancement of electrical insulation performance in power equipment based on dielectric material techniques", *IEEE Conference on Electrical Insulation and Dielectric Phenomena (CEIDP)*, 2011.
- [4] K.Y. Lau and M.A.M. Piah, "Polymer nanocomposites in high voltage electrical insulation perspective: A review", *Malaysian Polymer Journal*, Vol. 1, pp 58-69, 2011.
- [5] T. Tanaka, "Comprehensive understanding of treeing V-t characteristics of epoxy nanocomposites", *Proceedings of the 17th International Symposium on High Voltage Engineering (ISH)*, paper no. E-008, Hannover, Germany, August 2011.
- [6] C. Nyamupangedengu, and T. Andristch, "Nanocomposites – new generation electrical insulation", *Electricity + Control, Crown Publications*, pp 38-41, June 2012.
- [7] S. Johannes and J. Kindersberger, "Resistance to surface erosion of epoxy resin with silica and alumina nanofiller", proceedings of the 18th International Symposium on High Voltage Engineering (ISH2013), Seoul, South Korea, 2013.
- [8] T. Tanaka, M. Kozako, N. Fuse and Y. Ohki, "Proposal of a multi-core model for polymer nanocomposite dielectrics", *IEEE Transactions on Dielectrics and Electrical Insulation*, Vol. 12, No. 4, pp. 669-681, August 2005.
- [9] M. Roy, J.K. Nelson, R.K. MacCrone, L.S. Schadler, C.W. Reed, R. Keefe and W. Zenger, "Polymer nanocomposite dielectrics – The role of the Interface", *IEEE Transactions on Dielectrics and Electrical Insulation*, Vol. 12, No. 4, pp. 629-643, August 2005.
- [10] T. Andristch, "Epoxy Based Nanocomposites for High Voltage DC Applications – Synthesis, Dielectric Properties and Space Charge Dynamics." *PhD thesis, Delft University of Technology*, 2010, ISBN 978-90-5335-331-8
- [11] G. Groval, I. Aranberri, J. Ballesterro, M. Verelst and J. Dexpert-Ghys, "Synthesis and characterisation of thermoplastic composites filled with Y-Boehmite for fire resistance", *Journal of Fire and Materials*, Vol. 35, pp. 491-504, 2011.
- [12] T. Tanaka, G.C. Montanari, and Mulhaupt, "Polymer nanocomposites as dielectrics and electrical insulation-perspectives for processing technologies, material characterisation and future applications", *IEEE Transactions on Dielectrics and Electrical Insulation*, Vol. 11, No. 5, pp. 763-779, 2004.
- [13] M.M.S. Shirazi, H. Borsi and E. Gockenbach, "Effect of TO₂ nanofillers on electrical, thermal and mechanical parameters of epoxy resin", *IEEE International Symposium on Electrical Insulation (ISEI)*, San Juan, pp. 69-72, June 2012.
- [14] J.K. Nelson, "Overview of nanodielectrics: Insulating materials of the future", *Proceedings of the Electrical Insulation Conference and Manufacturing Expo.*, Nashville TN, pp229-235, October 2007.
- [15] Tanaka T, Bulinski A, Castellon J, Fréchette M, Gubanski S, Kindersberger J, Montanari GC, Nagao M, Morshuis P, Tanaka Y, Péliou S, Vaughan A, Ohki Y, Reed CW, Sutton S and Joon Han S, 'Dielectric Properties of XLPE/SiO₂ nanocomposites based on CIGRE WG D1.24 cooperative test results', *Proceedings of the Annual Report Conference on Electrical Insulation and Dielectric Phenomena*, Cancun, Mexico, 2011.
- [16] P.C. Irwin, Y. Cao, A. Bansal and L. Schadler, "Thermal and mechanical properties of polyimide nanocomposites", *IEEE Conference of Electrical Insulation and Dielectrics (CEIDP)*, pp 295-298, 2001.
- [17] Y. Cao, P.C. Irwin and K Younsi, "The future of nanodielectrics in the electric power industry", *IEEE Transactions on Dielectrics and Electrical Insulation*, Vol. 11, No. 5, pp. 797-807.
- [18] L. Dissado, "Understanding electrical trees in solids: From experiment to theory", *IEEE Transactions on Dielectrics and Electrical Insulation*, Vol. 9, No. 4, pp. 483-497, 2002.
- [19] M.G. Danikas and T. Tanaka, "Nanocomposite – A review of electrical treeing and breakdown", *IEEE Electrical Insulation Magazine*, Vol. 25, No. 4, pp. 19-25, 2009.
- [20] C. Nyamupangedengu, R. Kotchetov, PHF Morshuis & JJ Smit, "A study of electrical tree partial discharges in nanocomposite epoxy", *IEEE Annual Report Conference on Dielectrics and Electrical Insulation (CEIDP)*, Montreal Canada, 2012
- [21] Tokashitu Tanaka (Waseda University, Japan), *Personal Communication*, 2013.
- [22] D. Cornish and C. Nyamupangedengu, "Electrical Tree Partial Discharge Characterisation in Epoxy Nanocomposite", *International Symposium on High Voltage Engineering (ISH2013)*, Seoul, South Korea 2013.
- [23] Andrew Philips (EPRI, USA), *Personal Communication*, 2013

Lightning Safety Game

D T Sadie*, A G Dreyer* and E Trengove*

**School of Electrical & Information Engineering, University of the Witwatersrand, Private Bag 3, 2050, Johannesburg, South Africa*

Abstract. The purpose of this report is to document the investigation, design, implementation and testing of a lightning safety game. South Africa has three times the number of lightning deaths, per million per year, than developed countries [1][2]. The opportunity to make a lightning safety game to act as a learning medium presents itself. The educational game attempts to move away from the typically boring educational games by encouraging player engagement. The lightning safety game, a puzzle-based game, delivers the safety rules rather than the physics of lightning and the mechanisms of lightning injury. The educational game was tested against a presentation as an educational medium on 183 learners. The game achieved a variability of 6.54% while the presentation produced a value of 12.12%. This shows that the game on lightning safety appeals to a wider audience. This project provides a great foundation, with recommendations for future stages of this lightning safety game. The recommendations include: the game should include an analytical system; the game should be able to teach through the mechanics of the game, rather than through reading; additional levels should be developed to help drive the safety philosophy home.

Key words: Educational, Games, Lightning, Pair programming, Lightning safety, Serious games.

1. INTRODUCTION

The need for lightning education is ripe in South Africa. Research shows that there are 3 times the amount of people killed per million per year in South Africa as opposed to developed countries [1][2]. This combined with the growth of a digital culture among the youth, who spend hours a day in front of a computer, provides an ideal opportunity for an educational game. An investigation was carried out, where an educational lightning game was developed, implemented and tested as an effective educational medium. Before developing the game, the need for lightning education and what an educational game is, were investigated. The game is iteratively designed, developed and tested in three iterations. The first two iterations are prototypes, developed for requirement findings, and the third iteration is the final product of this project. This is discussed in section 4. Section 5 discusses the elaborate testing procedures that were conducted with 183 learners, to quantify whether the game works well as an educational medium or not. In order to quantify this, it was tested against a presentation, which delivered similar content. The results are presented in section 6. Finally, section 8 and 9 present the final analysis and future recommendation of the final product based on the game's performance and a peer review group.

1.1. Constraints

The project had the following constraints:

- Time allocated was 6 weeks.
- The project had to be completed in groups of 2 under the allocated budget.
- The game must be suitable for 10 year old learners.
- The game needed to be aesthetically pleasing and engineers had no drawing or animation experience.
- The game had to be developed on GameMaker: Studio™.

1.2. Assumptions

The assumptions made are that the learners who partake in the testing, have had no prior lightning education and are computer and English literate.

1.3. Success criteria

The following criteria need to be met for the project to be a success:

- Lightning safety education is the aim of the game and players must learn while they play.
- The game must run bug free and be aesthetically pleasing.
- Players must want to engage in the game.
- The test results of the game must match or surpass the results of the traditional teaching methods.

2. THE NEED FOR LIGHTNING EDUCATION IN SOUTH AFRICA

Unfortunately South Africa does not have official records of the number of deaths occurring from lightning. There are however on-line and print newspapers (lay press) with such records. These records give an under-exaggerated reading (there are probably many deaths in rural communities which are not reported) but it gives some insight into lightning deaths occurring in South Africa. The records show that at least 136 people were killed from January 2009 to January 2011[1]. Although this information is a few years old, it is the only record that can reveal the extent of the problem on lightning deaths in South Africa. There were nine boys, from King Edward VII School (KES), who were injured from lightning earlier this year (2013) [3], illustrating the relevance of this problem.

It is reported that 0.3 people per year per million die from lightning in Australia, Canada, Europe, Japan and the United States [2]. The lay press reveals that at least 1.01 deaths per year per million lightning fatalities occur in South Africa. This is more than 3 times that of developed countries [1]. There is thus room for improvement in South Africa.

The problem of lightning deaths in South Africa is compounded when considering injuries occurring from lightning. There are no records in the lay press of how many people are injured during a lightning strike [1]. It is said that as a general rule of thumb for every person killed ten people are injured [2][4]. The need for lightning awareness is evident in South Africa because

lightning storms are common. A lightning safety philosophy will now be presented.

2.1. Lightning safety philosophy

The mechanisms of how lightning injures a person is not important for the purposes of this game. It is more important to learn how to prevent lightning injury from occurring. A list of safety rules will now be given and these will be the rules that are incorporated into the game [1]:

- When thunder roars, go indoors. You are safer indoors in a sturdy building than outdoors.
- When outdoors, squat down to keep your height as low as possible.
- Do not lie on the ground in order to keep your contact with the ground as small as possible.
- If lightning strikes a house it will favour electrical wired paths to ground, so avoid touching metal objects like electric wires, fences, or plugged-in electrical appliances like a washing machine.
- Avoid being in contact with water even if you are indoors.
- Do not be on a land line when a lightning storm is occurring.
- Avoid touching or standing near tall objects like trees.
- According to the faraday principle [5], you are safe in a car, taxi or bus as long as you keep the windows closed.
- Rubber offers no protection.

3. SERIOUS GAMES

A serious game is a game that is designed to train and educate the audience rather than merely for the purpose of pure entertainment. Examples of serious games arise from industries such as advertising ('advergaming'), healthcare, training and education [6]. One of the latest examples of a serious game is 'Call of Duty: Black Ops 2'. The game owes plenty of its inspiration to real military weapons and prototype technologies. This game would fall under the category of a serious war game [7]. It qualifies as a serious game as it delivers a message (latest weapons and technologies used in the military) and it is entertaining [6][8]. Serious war games can deliver both aspects quite easily, however educational games, a subset of serious games, struggle with the second aspect in making the game entertaining. This subset of serious games will now be discussed.

3.1. Educational games

Educational games focus on simulation and development of players' skills. Early educational games are often criticised for their boring nature where players are fed vast amounts of information and rely on the players' memorisation skills [6][8]. Good examples of this are games called the 'Young Meteorologist' [9] and 'Leon's Lightning Safety Game' [10]. Both games have minimal user input and information about lightning safety is just thrown at the player. The 'Young Meteorologist' is basically just a streaming video and 'Leon's Lightning Safety Game' is a simple multiple-choice game.

Educational games need to move away from their boring nature. Boring games don't get completed and are certainly never visited a second time. More recent educational games focus on

player engagement, motivation and the role-playing capabilities of games [6]. This is where educational games need to be heading as they have the capability of being a very powerful tool in the educational world. The next sub-section shows how educational games can surpass traditional teaching methods

3.1.1. Why educational games can be a better learning medium

Traditional teaching methods, involve a teacher, throwing information at a learner. Games force the learner to engage with the material. The list below reveals the benefits that games offer opposed to the traditional teaching methods:

- Games have the ability to reach an incredibly wide demography of people [11], especially with the rise of app-based and mobile games [6].
- Games also allow for interaction and provide a perfect platform for exploratory, goal-based learning [12].
- Games are ideal as educational tools because they are able to mirror real-world systems. They are thus inherently good at showing the cause-and-effect relationship of an environment [8].
- Games challenge players at the edge of their growing realm of competence [13], but never overwhelm them. This is an incredibly powerful model for educational tools [7].
- In traditional teaching methods failure is often perceived to be punished. However failure is part of the learning process in games and rewards failure and repetition [6].
- Games have the capability to fun [8]. Good games have reward systems used to provide engaging and self-motivating ways of stimulating interest [12].

4. IMPLEMENTATION METHODOLOGY

The design decisions involved in the iterative development of the game will now be discussed. Figure 1 below, shows the software development cycle used for this project. It is derived from the waterfall model. The waterfall model places considerable emphasis on the analysis before the system is built. This prevents constructing a system that does not satisfy the user requirements [14].

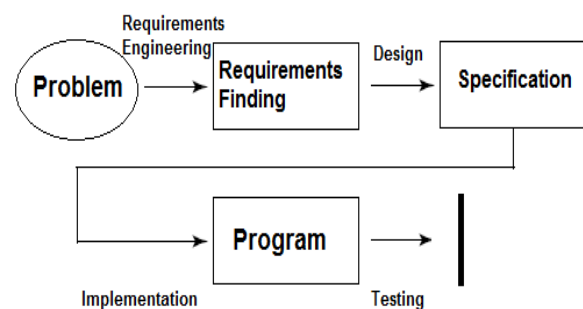


Figure 1: Software development cycle [14]

4.1. Work ethic

An agile methodology was adopted. Agile methods employ a small and incremental development style. At the end of each iteration there is a working system that delivers value to its users. Each iteration is then refactored, to improve the design and functionality, and so the next iteration is completed [14]. The agile method employed was Extreme Programming.

Extreme Programming has two programmers working together on one computer screen. One programs, and the other watches while trying to notice small slip-ups, giving advice and asking questions. At any point in time, the roles may shift. This practice is called pair programming [14]. The reason for choosing pair programming is the short time constraint on this project. Pair programming can perform concurrent tactical and strategic work which reduces the overall time to complete a task [15].

4.1.1. Paired programming reflection

There were a lot of bugs encountered, from both parties. Having someone on hand, to look at code with a clear mind at any point in time, was invaluable as most bugs were quickly fixed.

4.2. Advantages and disadvantages of GameMaker: Studio

Game Maker Language (GML) is the scripting language that is used in GameMaker: Studio. The language is heavily integrated into the IDE environment via a drag-and-drop interface. Objects in the game are given sprite-images in the form of standard image files. Functionality is provided by creating events for each object.

GameMaker: Studio does an excellent job of handling all of the interactions or interrupt based events. Keyboard, mouse or timer-based events are seamlessly integrated into objects by dragging the specific icon into the "event panel". Event specific parameters are easily modified by double-clicking on the event icon and changing a parameter in an input box.

The major shortfalls of GML and GameMaker: Studio are that the documentation is very limited and games are restricted to being 2-dimensional. Key examples are not given and functions are often poorly explained. This lack of documentation greatly increases the learning time and often experimentation is the only way of gaining an understanding of the language.

4.3. Concept development

The problem, at hand, has been thoroughly investigated in section 2 and 3. It is based on these findings that the game's concept is developed. The target audience for the game are children around the age of 10.

The game will have a simple user interface to accommodate any player having poor computer skills. Secondly, in order to force user interaction and engagement, the educational game will be a puzzle-based game. Puzzle-based games execute learning through failure. The game will reward failure with repetition [6].

4.3.1. Lightning behaviour

Firstly the lightning will be made to strike every object in the game. This removes the element of chance as players must learn if a scenario is safe or not. Secondly the game will not go into the lightning physics as these principles are complex and hard to understand for children. The game will simply teach the lightning safety philosophies discussed above in section 2.1. However there are some aspects of lightning physics running in the background. Each object in the game is given an invisible parameter and if a person is in this parameter (even if crouching), the lightning strike to that object kills/injures that person. This incorporates three mechanisms of lightning injury, namely an upward leader, touch potential and side flash [1]. If a person is standing or lying down outside the object's parameter, that person is injured through the final two mechanisms of

lightning injury, a direct strike (standing) and step potential (lying down) [1].

4.4. Requirements engineering and finding

The lightning safety philosophy discussed in section 2.1 forms the basis of the educational game. With no other information at hand, however, it is difficult to grasp the perception of the requirements of the perspective user. In such situations prototyping offers a lot of help. Prototyping techniques are particularly useful in situations where the user requirements are unclear. It is also useful for systems with a considerable emphasis on the user interface and shows a high degree of user interaction [14]. Two prototypes were used to conduct the requirement findings in the form of three interviews discussed in section 7. Based on these findings Iteration 3, the final product, was developed.

4.5. Iteration 1: Prototype 1

The prototype developed had one level to test whether the concept would work. The level has minimalistic user interface where the player could drag a person around (left click) and change the person's stance (right click). A screenshot of the prototype is presented in figure 2 below.

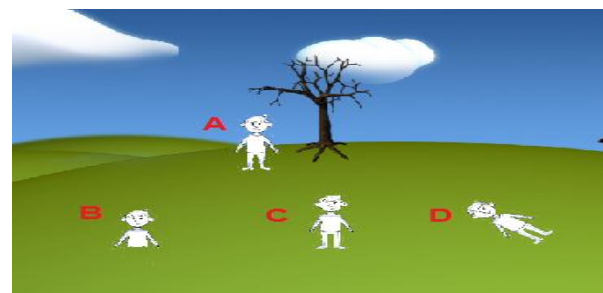


Figure 2: Prototype 1

To pass the level the player must move the person away from the tree and crouch. This is shown in the figure above from position 'A' to 'B'. Leaving the person in position 'A' (near the tree) or moving from 'A' to 'C'/'D' (remains standing / lies down) results in failure.

4.6. Iteration 2: Prototype 2

Following the testing and feedback on the prototype, the game was refined and a second prototype was developed. The game maintains the same concepts as iteration 1, however with aid of the requirement findings discussed in section 7 below, the game is made more aesthetically pleasing. This iteration also introduces a score and a timer to the game.

4.7. Iteration 3: Final product

Prototype 2 is then refined, based on findings in section 7, by making the game less abstract. This is done with the introduction of speech bubbles and an avatar that guides the player through the game. Once all the functionality and visuals of the refined Prototype 2 were working, it formed level 1 of the game. Four more levels were then created with the introduction of objects. People, in the game, can interact with the objects. For example level 2, shown in figure 3, introduces a taxi that the boy can get into.



Figure 3: Final product – snippet of Level 2

The image depicts part of level 2. It is the end of the level, after lightning has struck, and the boy has been left burnt. This level introduces the concept that one can be safe from lightning in a vehicle.

4.8. Instructive Game Elements



Figure 4: Instructive game elements

The bulk of the learning is achieved via screens before and after each stage. As can be seen in Figure 4, before a level begins, a hint screen informs the player of the situation, the new elements introduced and it provides tips on how best to complete the level. Should the player fail to save all the endangered children, dialogue boxes appear, giving hints as to why they were in danger. A post completion screen congratulates the user on completing a level and reinforces the lessons via text.

5. TESTING METHODOLOGY

Two different types of testing procedures took place. The first test determines how well the game is able to educate the learners about lightning safety as opposed to conventional teaching methods. For practical purposes the age range was extended from 10-13 years old to include a wider sample population. The second testing procedure determines how well the game functions and hence how it can be improved.

5.1. Testing the game as a learning tool

This test involved 183 learners from grade 4 to grade 7. Each grade was split into two groups randomly. The first group was given the presentation as its learning aid. The second group was given the game. Both groups were given 1 hour to complete the testing procedure. The testing process is depicted in figure 5 below.

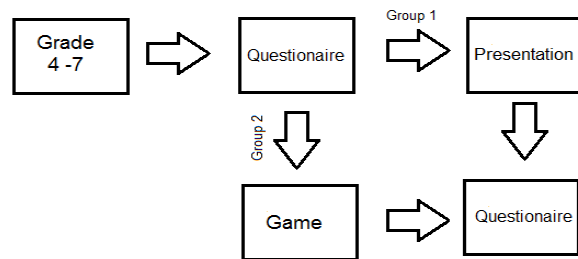


Figure 5: Game's educational ability's testing procedure

5.2. Testing the game's functionality

The testing of the game's functionality was done in the form of a peer review group. A group of second year digital arts students at the University of Witwatersrand were asked to play the game. After playing the game, each one filled out a survey. The survey collected information such as the participants' perceived level of knowledge on video games and lightning. The survey also recorded the participants' rating of the game in terms of fun factor, graphics and user interface. Finally the participants were given the opportunity to give open-ended feedback on whether the game portrayed the concepts of lightning well, what worked well in the game, what didn't work well and any additional comments and suggestions.

6. RESULTS

6.1. Questionnaire results

There was a great improvement in the results of the presentation and the game. Both the game and the oral presentation improved the mark by 20%. This show that the correct content on lightning safety was delivered. However, the game reduced the variability of the marks (standard deviation) to 6.56% as opposed to the presentation which had a variability of 12.65%. This illustrates that the game was able to produce higher marks more consistently than the presentation and hence provided a greater educational value.

6.2. Survey results

This section will present a summary of the results captured from the peer review group.

6.2.1. Game rating

The participants were asked to rate aspects of the game out of 10. On average the fun factor scored 6.25, the graphics scored 7.75 and the user interface scored 6.

6.2.2. Open-ended feedback

Portraying the concepts of lightning: All found the game to present the concepts of lightning safety sufficiently. However, the general consensus is that the concepts would not be readily retained. The aspects of stand/lie/crouch would be entrenched but the other safety measures would need to be further reinforced.

Favourable aspects of the game: The straight-forwardness, the visual elements and the ease of use were positively highlighted by the participants. A recurring answer was that the game was visually pleasing which engaged the learners and allowed the game play to be enjoyed.

Unfavourable aspects of the game: The instructive screens were deemed to have too much writing and all the participants felt that the target audience would not spend time reading the screens.

Other feedback and suggestions: Generally, it was felt the game needed to be refined and have extensive animations in order to capture the mind and imagination of a 10 year old learner. Instead of a 10 second timer, a "lighting button" which started the storm would give more meaning to the scoring system.

7. OBSERVATIONS AND REQUIREMENT FINDINGS

Observations were made while the learners played the game. Requirement findings were carried out in the form of three interviews. The interviews were done with a group of 10 year old learners, after prototype 1, and twice, after each prototype, with a teacher of that age group.

7.1. Requirement findings

The first interview (prototype 1) with the teacher revealed that a time limit should be introduced to rush the learners in each level. The second interview (prototype 2) highlighted the fact that learners wouldn't know why each level is passed or failed.

During the interview with the group of 10 year olds, it was discovered that, at this age, advanced games were already being played. This highlighted the need for the game to be as aesthetically pleasing as the budget and time allowed.

7.2. Observations

According to the observations made nobody read the messages before and after each level. All the educational value in these messages was then lost. It was also observed that some of the learners found it amusing when time ran out and the level was failed. This encouraged the learners to move faster in the following try. The final observation was that hardly anyone wanted to play the game for a second time.

8. CRITICAL ANALYSIS

Compared to the conventional teaching methods the game performed slightly better. The questionnaire did provide insight into the knowledge gaps of the learners and the knowledge gained from the game. But an analytical system would provide an even better insight, since the questionnaire limited the learners to a 33% chance of being right. It was also noted in section 6 and 7, that the message-based learning hindered the results because hardly any learners thoroughly read through the game. A way of educating the learners through gameplay should have been incorporated into the game. It was done, in the final version, by showing that crouching away from an object is the safest position. But this was because it was an on-going theme in the game. This needs to happen for the other safety rules, mentioned in section 2.1 as well. Also the problem with puzzle-based games is that once the puzzle, for a level is solved, nobody wants to repeat that level. Hence nobody wanted to play the game a second time.

One of the elements in the game that worked really well was the clock. In every game there should always be some elements that work against the player's success [14]. The clock acts well as a source of conflict in most levels. During the easier levels, which

the learners are able to complete quicker, the game loses this source of conflict and as a consequence player engagement.

9. FUTURE RECOMMENDATIONS

In order to accommodate the easier levels, where a player can finish faster than the time provided, a key will be employed to terminate the level. There will also be extra points given for every second the player beats the clock. Furthermore, puzzle-based games do not encourage players to play the game a second time. Also, additional levels could be developed to help drive the lightning safety philosophy home.

The implementation of an analytical system would benefit future iterations of the game. Being able to record how quickly a level was passed/failed and which levels were failed the most/least will provide invaluable insight into the learners-knowledge gaps in lightning safety. It would provide great insight in improving the game, to close these gaps, in future iterations.

The final recommendation is that the game needs to move away from message-based learning and towards game mechanics which offers greater educational value. The messaging in the speech bubbles during each level worked effectively. It is the messaging that occurs at the beginning and the end of each level that isn't read. More cleverly designed levels should be implemented that can use the existing concepts and deliver all the messages through the game play. For example, showing the players that lightning is more likely to hit the tallest object rather than a conductive object, was only presented in a tip shown before level 1. Levels should be designed to successfully communicate this fact with the players through the game mechanics.

10. CONCLUSION

The game proved to be a slightly more effective medium, for teaching lightning safety, than the presentation. There is plenty of room for improvement, but a strong foundation has been developed for future iterations of this lightning safety game. It is unfortunate that the game is only able to reach an English and a computer literate audience. In South Africa it is the rural community that is most at risk from lightning strikes [1]. Unfortunately a low percentage of children based in rural areas are both literate in English and computer. Hence this game will be more relevant in the suburban areas of South Africa. The positive results from presentations augur well for educating rural learners.

ACKNOWLEDGEMENTS

The authors would also like to thank Bennie Du Preez for his help with setting up the testing of the project, and Gill Rob and Marylyn Wood for providing an illustrator for the game's graphics.

REFERENCES

- [1] E. Trengrove, "*Lightning myths and beliefs in South Africa: their effect on personal safety*", University of Witwatersrand, Johannesburg, 2013.
- [2] R.L Holle, "*Annual Rates of Lightning Fatalities by Country*", Proceedings of the 20th International Lightning Detection Conference, Tucson, Arizona. 2008.

- [3] Lightning: 9 Jo`burg pupils in hospital
<http://www.news24.com/SouthAfrica/News/Lightning-9-Joburg-pupils-in-hospital-20130213>, last accessed 14 July 2013.
- [4] A. Kadir, M. Z. A. Cooper, and M.A.Gomes, “An Overview of the Global Statistics on Lightning Fatalities”, Proceedings of the 30th International Conference on Lightning Protection, Cagliari, Italy, 2010.
- [5] The Faraday Cage: What Is It? How Does It Work?
<http://www.gamry.com/assets/Application-Notes/Faraday-Cage.pdf>, last accessed 10 July 2013.
- [6] T. Susi, M. Johannesson, and P. Backlund. “Serious games an overview”. Skövde: University of Skövde (Technical Report HS-IKI-TR-07-001), 2007.
- [7] Call of Duty' video game could reshape real warfare.
<http://www.foxnews.com/tech/2012/11/21/call-duty-video-game-could-reshape-real-warfare/>, last accessed 11 July 2013.
- [8] B. Brathwaite and I. Schreiber, ”Challenges for game designers”. Course Technology, 2009.
- [9] Young Meteorologist
<http://www.gamesforchange.org/play/young-meteorologist-program/>, last accessed 11 July 2013.
- [10] Leon's Lightning Safety Game
www.lightningsafety.noaa.gov/teachers.htm. Last accessed 10 July 2013.
- [11] M.J. Mayo. “Games for science and engineering education”. Communications of the ACM,50(7):30–35, 2007.
- [12] B.R.C Marques. ”Video game as a medium for software education”, University of Witwatersrand, Johannesburg, 2012.
- [13] J.P. Gee. “What video games have to teach us about learning and literacy”. Computers in Entertainment (CIE), 1(1):20–20, 2003.
- [14] H. van Vliet, ”*Software Engineering: Principles and Practice*”, Wiley, 2007.
- [15] W.C. Wake, ”*Extreme Programming Explored*”, Addison Wesley, 2000.

DESIGN, CONSTRUCTION, TESTING AND COMMISSIONING OF A 20kA 10/350 μ S CURRENT IMPULSE GENERATOR

S. Muzoka, T. Gora, K.J. Nixon and I.R. Jandrell *

* Faculty of Engineering and the Built Environment, Private Bag 3, Wits 2050, South Africa
E-mails: sean.muzoka@students.wits.ac.za, tatenda.gora@students.wits.ac.za, ken.nixon@wits.ac.za, ian.jandrell@wits.ac.za

Abstract: Lightning protection is very essential in industry. Surge protective devices have been developed to protect power and communication systems from lightning surges. Before they are installed, it is important that the surge protective devices are tested. A 10/350 μ s current impulse generator is presented in this report, with the focus being on the design and construction of the triggering and dumping mechanisms and the control box. The design is aimed at satisfying the requirements of IEC61643-1 and IEC62305-1. An 18.8kA, 12/406 μ s current impulse was produced using a 14mm gap solenoid switch and a 1 Ω , 0.3 μ H wave-shaping bifilar resistor. This waveform is within the tolerances acceptable in the standard.

Key words: Current impulse generator, Surge protective device (SPD), Bifilar winding.

1. INTRODUCTION

The design, construction and commissioning of a 20kA 10/350 current impulse generator is documented in this report. The generator was required to be permanently configured and housed for use in the University of the Witwatersrand, Johannesburg high voltage laboratory. The generator was designed to meet the specifications highlighted for Class 1 current impulse tests in IEC 61643-1.

Included in this document is the discussion on the background of the current impulse generator, the charging circuit, wave-shaping components, triggering mechanism and the dumping safety mechanism

2. BACKGROUND

A large part of power systems engineering is the ability to supply uninterrupted and safe electricity. It has been observed that lightning is the largest cause of electrical outages on transmission systems [1–3]. Various mechanisms are put in place at different upstream levels to minimise these effects. One such method is the use of Surge Protection Devices (SPD). The use of Metal Oxide Varistors (MOV) as SPD has become common [4]. The arrester has the ability to clamp the voltage waveform to a range that can be handled by the downstream protection e.g. IDMT. In the real world the MOV may be contaminated by dust or moisture or manufacturing defects. This results in inhomogeneous surface of the arrester tube thus affecting the MOV performance. For this reason SPD need to be tested to ensure they function as per standard requirements.

One of the tests conducted on SPD's is the current impulse test. The current impulse test is described in IEC 61643-1. The parameters used for class 1 current impulse test are defined by the current peak value (I_{peak}), the charge (Q)

and the specific energy (W/R) [5]. The relationships between I_{peak} (kA), Q(As) and W/R(J/ Ω) are defined in equations (1) and (2).

$$Q = I_{peak} * a \quad (1)$$

$$W/R = I_{peak}^2 * b \quad (2)$$

where $a = 5 \times 10^{-4}$ s and $b = 2.5 \times 10^{-4}$ s.

The parameters of the current impulse test highlighted in [5] have a maximum current of 20kA. The designed generator will meet the below parameters and tolerances according to [5]:

- $I_{peak} = 20\text{kA} \pm 10\%$
- $Q = 10\text{As} \pm 20\%$
- $W/R = 100\text{kJ}/\Omega \pm 35\%$.

An impulse that is able to supply the above mentioned parameters is the 10/350 impulse introduced in IEC 62305-1 [6]. This definition is depicted in Figure. 1 where T_1 and T_2 are rise time and fall time, respectively.

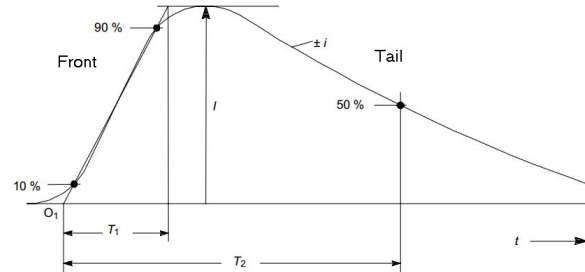


Figure 1: Definition of a short stroke current impulse [6]

The generator used to produce the 10/350 impulse would require a high amount of energy to be stored in the capacitor if the traditional design method is used. The

energy requirement can be reduced by using alternative designs. One such method is the crowbar mechanism as shown in Figure 2. This mechanism allows the

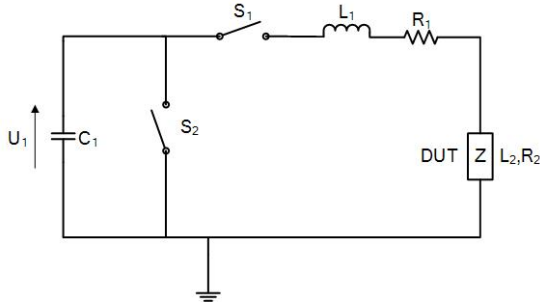


Figure 2: Simplified crowbar circuit

management of power through the use of the two switches S_1 and S_2 . Initially both switches are open. When C_1 charges to a voltage U_1 , the charging circuit is disconnected and the spark gap S_1 is then triggered. The circuit becomes a resonant LCR configuration and current builds up to a maximum value in $\frac{1}{4}$ of a cycle. Switch S_2 closes when the capacitor voltage U_1 has drops to zero as energy is transferred from capacitor C_1 to inductive energy L . The inductive current decays at a rate determined by the voltage drop across resistor R . If switch S_2 had been left open, current would decay in an oscillatory fashion. This design only needs adequate capacitive energy to create the front time, after that the transferred energy in the inductor produces the slow current decay [7].

3. SYSTEM DESIGN AND CONSTRUCTION

The circuit diagram of the generator is shown in Figure 3. The generator consists a capacitor bank with eight $62.5 \mu\text{F}$ capacitors supplied by Eskom. Each capacitor has a voltage rating of 20kV . Using the equation

$$E = CV^2 \quad (3)$$

where E is energy, C is capacitance and V is voltage, the energy calculated was 100kJ and was consistent with the energy requirements highlighted in [5]. This result was assuming that all eight capacitors will be connected in parallel, to give $500\mu\text{F}$ capacitance, and charged to 20kV . An impulse current can be mathematically modelled using equation (4).

$$I_{peak} = \frac{V}{\omega L} e^{\alpha t} \sin(\omega t) \quad (4)$$

where,

$$\alpha = \frac{R}{2L} \quad (5)$$

and

$$\omega = \sqrt{\frac{1}{LC} - \frac{R^2}{4L^2}} \quad (6)$$

Using equation (4)-(6) and MATLAB, the values of R_2 and L_1 that give a $10/350$ impulse were calculated to be 1Ω and $2\mu\text{H}$ respectively. The impulse simulated using the values of R_2 and L_1 is shown in Figure 4.

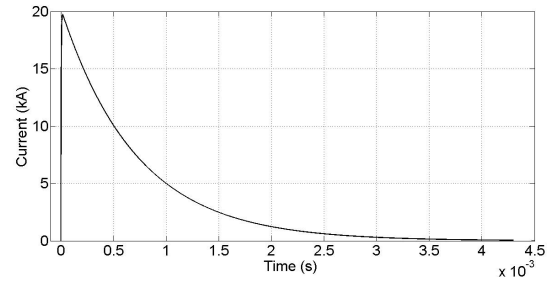


Figure 4: Simulated current impulse

3.1 Charging Circuit

The charging circuit for the generator is depicted in Figure 5. The time constant the charging circuit was designed for

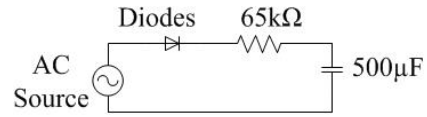


Figure 5: Charging Circuit

was calculated to be 32.5s using equation 7.

$$\tau = RC \quad (7)$$

A $65\text{k}\Omega$ water resistor was used as the charging resistor. The resistor was made by filling a 30cm perspex tube (3cm outer diameter and 0.3cm thickness) with distilled water and adding salt until the required resistance was obtained. Both ends of the perspex tube had brass electrodes. Water resistors are capable of handling high energy, usually with high power peaks [8] therefore making them useful for the charging process.

A chain of nine UX-F0B diodes in series was soldered together and used for rectifying AC to DC. The UX-F0B is a high voltage diode with the repetitive peak reverse voltage rated to be 8kV . By having nine diodes in series, the overall repetitive peak reverse voltage for the chain of diodes is 72kV . With a 72kV peak reverse voltage, the diodes are capable of stopping any reverse surges and spikes that occur during the charging process and could damage the AC supply considering the capacitors to be charged to 20kV . The diodes were bolt soldered together and immersed in a perspex tube with transformer oil to avoid corona around the soldered points and to cool the diodes during the charging process.

3.2 Wave Shaping Components

Instead of having separate resistor and inductor elements for wave shaping, a wire-wound resistor was made. The wire wound resistor was made of nichrome (alloy of 80% nickel and 20% chromium) resistance wire. The nichrome that was readily available had a resistivity of $1.09 \Omega\text{mm}^2/\text{m}$ and 2.6mm diameter. Using the equation (8), the length of

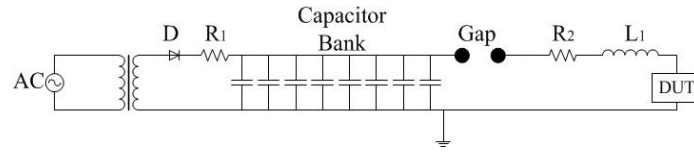


Figure 3: Circuit diagram for the designed current impulse generator

wire required to obtain a 1Ω resistor was calculated to be 4.87m.

$$l = \frac{\pi R D^2}{4\rho} \quad (8)$$

5m of wire was cut and wound around a 70cm long PVC tube to make a bifilar wire wound resistor. The PVC tube has a 7.5cm diameter and nine turns were wound (one turn of the winding has a pair of conductors going around the tube). Eye-hooks were used to fasten the wire and avoid the unwinding of the bifilar winding when an impulse current flows.

Figure 6 shows the winding methodology that was used for the bifilar winding. The bifilar winding that was made

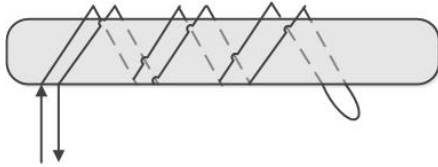


Figure 6: Bifilar winding structure used to build the commissioned one

had 4cm separation between adjacent windings. It had been earlier discovered that the less the distance between adjacent windings, the less the inductance of the winding and the more the heat produced when the 20 kA impulse is passed through it. The bifilar winding made was therefore a trade-off between the required inductance and being able to avoid the winding from overheating. The winding that was installed on the generator has 1Ω resistance and inductance of $0.3\mu\text{H}$. The winding was then immersed in transformer oil for cooling. Figure 7 shows the installed bifilar winding. It can be noted that the bifilar winding



Figure 7: Bifilar winding installed on the generator

made has less inductance than required in the design. The difference in inductance ($1.3\mu\text{H}$) is expected to be compensated by the busbar connections.

3.3 Triggering Mechanism

The trigger gap is designed to withstand very high transient energy transfer i.e. 100kJ in $360\mu\text{s}$. This translates to approximately 277MW. The stresses involved include magnetic attraction caused by high current flow in the cable carrying the impulse, heat produced by the arc on triggering electrodes and also jitter introduced by the physically under-damped triggering mechanism.

The electrode material used is red brass. The criteria for this choice is its relatively high melting point and low cost compared to aluminium and copper respectively. It is recommended that the metal be coated with tungsten carbide (Approx 3400°C melting point) to avoid damaging the electrode, however this facility is not readily available to us. An investigation is done on two types of mechanisms B and C shown in Figure. 8.

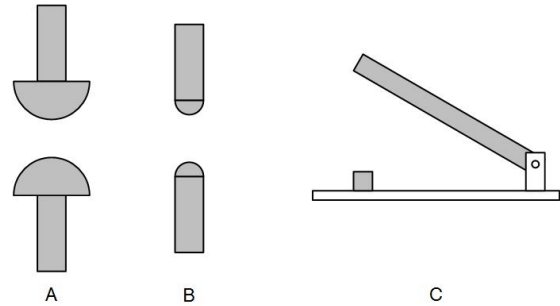


Figure 8: Investigated electrode configurations for the triggering mechanism

It was observed that configuration B in Figure. 9 performs well up to 15kA impulse current. Thereafter, the the two electrodes weld together upon triggering. To negate this effect, the electrodes were adjusted such that a 2mm gap is left when in closed configuration. This proved successful in avoiding the welding. However, the tips still deform after a number of switching sessions. Configuration C proved to produce perfect results up to the rated 20kA. It is postulated that this improved performance is due to the larger surface area compared to configuration B, resulting in faster dissipation of heat. Both these mechanisms are in commission on the generator. Configuration A is a possible solution that has a larger surface area but occupies less

space compared to configuration C. This option however was not investigated.

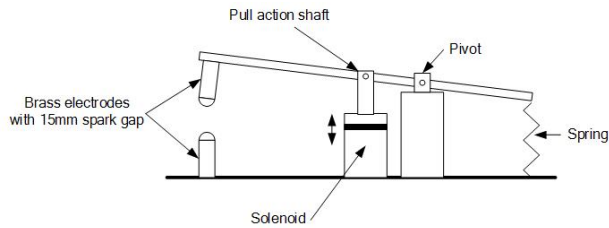


Figure 9: Triggering mechanism

3.4 Safety Dumping Mechanism

Dumping involves the complete discharging of the capacitors to allow the operator safe access into the enclosure. This subsystem consists of two components, a dump gap (switch) and a dump resistor.

Dump Resistor: Several options have been considered for the resistor on the basis of ability to dissipate very high energy. Ballast and water resistors are the most common, however the former is difficult to acquire due to cost and availability. For this application, a water resistor is used. Water resistors are desirable in this case for very low inductance and high power rating.

A common material used is perspex (methyl methacrylate). It is chosen for its resistance to sunlight, extreme cold, erratic temperatures [9]. Acrylic resins are inherently stable hence they do not deteriorate over time. The calculated dimensions are a length of 500mm with an inner diameter of 104mm and a thickness of 3mm are derived. Calculations show that with a 20kA impulse every 5 minutes, the resistor will heat up by an average of 2°C. NaCl solution is used as the conductive medium with a resistance of 45kΩ, this translates to a worst case current of approximately 0.5A and the caps are made of aluminium with the high voltage top side is rounded to reduce corona effects, see Figure. 10.

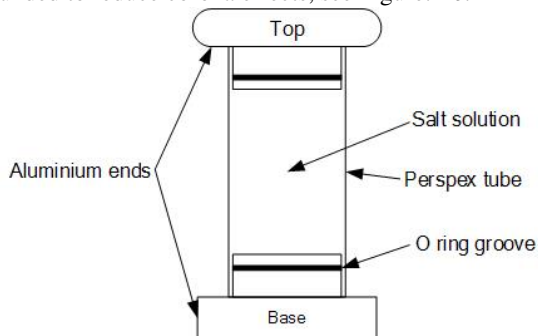


Figure 10: Water resistor

Dump Gap: The dump gap is placed in series with the dump resistor and the switching mechanism makes use of a pull action Mechetronix AC laminated solenoid 110V_{ac}

with a stroke of 35mm. The contacts were subjected to a worst case current of 0.5A which is relatively low, hence there was no need for fireproofing. The solenoid can carry a maximum of 300g, and the material of choice is brass for its high melting point compared to aluminium and its affordability compared to copper. Bullet shaped cylinders with a radius of 10mm and a length of 37mm shown in Figure. 8.

3.5 Control and Isolation

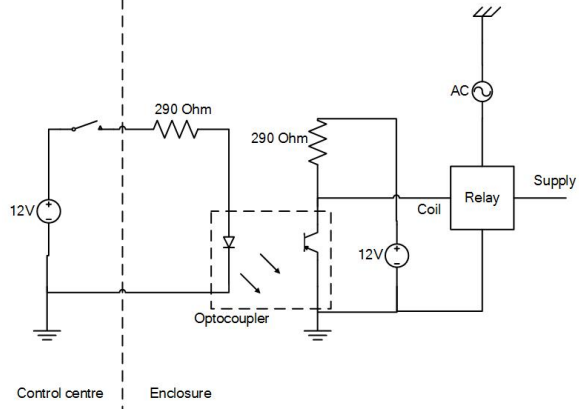


Figure 11: Isolated switching circuit

Remote control of the generator is a required safety measure. A control box was constructed for this purpose. Control electronics running at 12V_{dc} was interfaced with the various higher voltages i.e. 115V_{ac} and 220V_{ac} using 12V SPDT relays. To isolate the high voltage side from the control box, LITEON LTV847 opto-couplers were used. These have the highest available input-output isolation voltage of 5kV. The schematic is as shown in Figure. 11.

It is however noted that the isolation capabilities of the opto-couplers are below the required value of 20kV worst case scenario and therefore the circuit may fail in the case of a flashover.

3.6 Housing

The whole generator is housed in two 1.7m x 0.8m x 1.8m double door enclosures. Each enclosure houses four capacitors. A common grounding point was connected to both enclosures and it was ensured that there was continuity along all the walls of the enclosure. One of the enclosures was drilled and fitted with red and green warning lights to indicate whether it is safe or not to approach the generator.

To hold the charging resistor and diodes, two identical blocks were drilled and mounted on the outside of one of the housings. A 33kV rated bushing was mounted on both enclosures. Bolts and nuts moulded from nylon were used to hold the bushings in place. An aluminium busbar was then used to connect the two bushings. Investigation revealed that any substitute smaller than the installed bushing and the use of conventional bolts and nuts could potentially lead to a point to plane flash-over between

Table 1: Current impulse test results

Voltage [kV]	Peak Current [kA]	Error [%]	Rise time [μ s]	Error [%]	Time to half [μ s]	Error [%]
2	1.76	12	12	20	350	0
5	4.64	7.2	12	20	368	5.1
10	9.4	6	12	20	400	14.3
16	15.2	5	12	20	376	7.4
18	16.8	6.6	12	20	412	17.7
20	18.8	6	12	20	406	16

the bolts and the mounted busbar. In the housing, the four capacitors were connected in parallel using aluminium busbars 31mm wide and 6.2mm thick. The use of cables was avoided in an attempt to reduce the inductance of the whole system. The capacitors were connected to the bushing and ground points (wall of the housing) using aluminium strips 0.8mm thick and 50mm wide. To ensure a secure grounding connection of the capacitors, the paint was first scraped off the walls of the enclosure and the aluminium sheets were bolted to the wall.

Two holes were drilled on the floor of one of the enclosures so that the dump resistor and bifilar winding can be fastened there. A third hole was drilled and a terminal was set up on the floor of the enclosure. It is at this terminal that the device under test is connected to ground. A shelf 500mm by 600mm was also fitted to the inside wall of one of the enclosures. The purpose of the shelf is to provide a platform where the electronics and trigger would be set.

4. TESTING AND ANALYSIS

Before charging the capacitors, the triggering and safety dumping mechanisms were tested along with the lighting system. The green light switched on when the dump gap was closed and the red light switched on when the dump gap was open as per design.

The capacitors were charged to 1kV and the dump gap was closed. The capacitors began to discharge and took approximately 33 seconds for the voltage to fall to 100V. The capacitors were again charged to 2kV and the discharge process took approximately 40 seconds for the voltage to reach 100V. The dump resistor was inspected and there was no significant temperature change observed. With these tests, it was concluded that the dump resistor is functional. The longer rate of discharge allows the resistor to dissipate less power therefore it will be able to handle the energy of the capacitors without the water of the resistor boiling.

The trigger that was designed was tested. The capacitors were charged to 2kV and the trigger gap was closed. No testing device was connected so the capacitors discharged through the bifilar winding. A 1.76kA 12/350 impulse was obtained. Figure 12 shows the impulse obtained during the first test. Further tests were done and results are shown in Table 1. When the capacitors were charged to 15kV and the trigger was closed, the electrodes welded together due to the high temperature rise when the energy is transferred at contact. To continue testing whether the generator can produce the required peak current, the switch was replaced

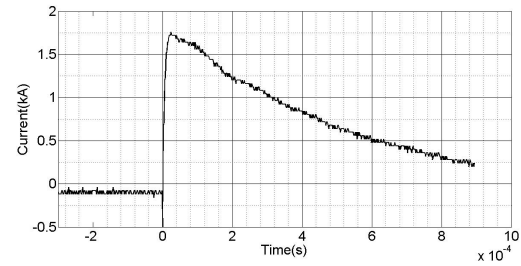


Figure 12: Current impulse obtained when capacitors are charged to 2kV

with an alternative switch that could withstand the high temperatures that occur during triggering.

During the final commissioning test, the capacitors were to be charged to 20kV. A flash-over was experienced during the charging process at approximately 18kV due to one of the live sheets being close to the grounded wall of the enclosure. The thin nature of the sheet and the sharp edge caused field enhancement around the sheet and therefore leading to the flash-over. The flash-over destroyed the grounding connections on the wall of the enclosures and, the electronics that had been set up. However, since the designed trigger was welding, the switch being used did not depend on the electronics to function. The grounding connections were replaced and the generator was charged to 20kV. Figure 13 shows the impulse produced at a charging voltage of 20kV. A peak current of 18.8kA was produced with a rise time of 12 μ s and a time to half of 406 μ s. The results show that the generator produces consistent 1:1 waveforms within the allowed tolerances. Even though the maximum current produced by the generator is 6% less than the required 20kA current, it still falls within the $\pm 10\%$ tolerance stated in [5] and is therefore acceptable to use for the class 1 current impulse test. The inability of the generator to generate 20kA is mainly attributed to the unaccounted for resistance of the whole set up. This includes the resistance of the busbars and the aluminium sheets used for the connections.

The area under the obtained impulse was integrated and the power obtained was divided by the equivalent impedance of the generator. It was calculated that the specific energy ($\frac{W}{R}$) produced by the generator is 111.7kJ/ Ω . The obtained specific energy deviates from the specific energy stated in the standard by 11.7%, which is still within the 35% tolerance as earlier stated.

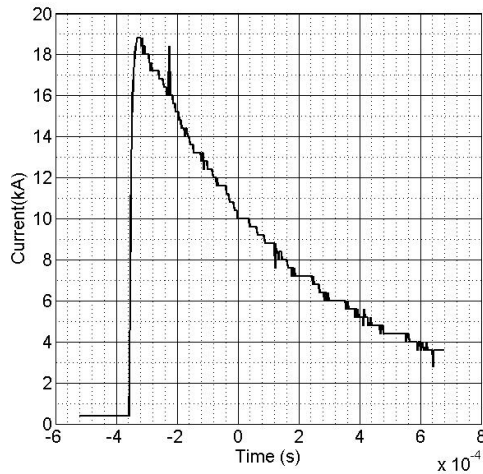


Figure 13: Impulse current at 20kV

5. RECOMMENDATIONS

The following recommendations are proposed for future work:

1. To improve the current magnitude of the impulse, the resistor winding has to be reduced. A new winding should be made of approximately 0.9Ω . The resistance of the busbars and any other connecting material will compensate for the difference in resistance.
2. A new bifilar winding with less inductance ($\approx 0.1 \mu\text{H}$) has to be wound. By having less inductance, the waveform is expected to have a more accurate rise and fall time.
3. The electrodes used for the trigger gap have to be made, preferably, in a circular manner. This allows for the surface area of contact to be bigger therefore reducing the amount of heat produced. The surfaces of the electrodes will require to be coated with a material that has a high melting point, like tungsten carbide that melts at 2780°C . The same has to be done for the electrodes used for the dump gap.
4. New and more rugged opto-couplers are to be used to isolate the electronics circuitry from the generator or any dependable method, like using infra-red transmission.
5. A damping mechanism has to be designed for the trigger switch to avoid jitter.

6. CONCLUSION

Consideration of mechanisms to minimise inductance so provides the main design attribute for designing a current impulse generator. To achieve minimal inductance on

discharging the capacitors a $45\text{k}\Omega$ high power water resistor is implemented. A bifilar winding configuration is used to obtain a low inductance wire with parameters 1Ω and $0.3\mu\text{H}$ resistor. Brass electrodes are used to trigger the spark gap. Negligible jitter is experienced and a 2mm gap when trigger is closed prevents the contacts from welding. The generator produces a 18.8kA , $12/406\mu\text{s}$ current impulse with specific energy of $111.7\text{kJ}/\Omega$ at 20kV . These results fall within the specified tolerances and recommendations are suggested to improve the accuracy and functionality.

ACKNOWLEDGMENT

The authors would like to thank Eskom for the support of the High Voltage Engineering Research Group through the TESP program. The would also like to thank CBI-electric for support, the department of Trade and Industry (DTI) for THRIP funding as well to the National Research Foundation for direct funding.

REFERENCES

- [1] N.K. Kishore P. Bhakta R.K. Sharan, *On the Development of an Impulse Current Generator*, International Conference on Electromagnetic Interference and Compatibility, pp 401-406, 1997.
- [2] R.A.W. Connor, R.A. Parkins, *Operational Statistics in Management of Large Distribution Systems*, Proc. IEEE, Vol. 113, pp 1823, 1956.
- [3] Report of Joint IEEE-EEI, *Committee on EHV line Voltages*, IEEE Trans. Vol PAS 86, pp 547, 1967
- [4] T. Haryono, K. T. Sirait, Tumiran, B. Hamsah *The Design of A High Amplitude Impulse Current Generator*, IEEE International Conference on High Voltage Engineering and Application, pp 339-343, November 9-13, 2008
- [5] IEC 61643-1, *Low-voltage surge protective devices- Part 1: Surge protective devices connected to low-voltage power distribution systems- Requirements and tests*, Ed 2, 2006.
- [6] IEC 62305-1, *Protection against lightning- Part 1: General principles*, Ed 2, 2011.
- [7] M. J. Maytum, *Impulse generators used for testing low-voltage equipment*, IEEE PES-SPDC: Impulse Generators, 2012.
- [8] Earthlink website.
<http://home.earthlink.net/~jimlux/hv/rwater.htm>, last accessed 24/10/2013.
- [9] W. F. Smith, J. Hashemi, *Foundations of Materials Science and Engineering*, Fourth Edition, McGraw-Hill, 2006.

INVESTIGATION INTO LIGHTNING SHIELDING FAILURE FOR HVDC LINES BASED ON INITIATION OF INDUCED LEADERS FROM THE POLE CONDUCTORS

GJ Strelec*,** and KJ Nixon**

**Eskom Research, Testing and Development, Sustainability Division, Rosherville, Lower Germiston Rd., Johannesburg, South Africa, Email: gavin.strelec@eskom.co.za*

*** School of Electrical and Information Engineering, Private Bag 3, Wits 2050, South Africa, Email: ken.nixon@wits.ac.za*

Abstract. There is international performance data on HVDC transmission lines, which suggests the positive pole is substantially more vulnerable to direct stroke penetration events. The mechanism appears to be related to the conditions for positive upward induced leader being more readily met due to the positive potential on the pole conductor. This discussion paper proposes an investigation into the physics and development of a model that will be used for simulations, and verified against performance data. The model is intended to inform the lightning shielding design for future HVDC lines.

Key Words. HVDC, Lightning, Shielding, Transmission lines, Back-flashover, Electro-Geometric Model, Leader Progression Model, Collection Volume method, Leader Inception Model

1. INTRODUCTION

There is an increasing worldwide need for the implementation of overhead HVDC transmission in traditional long distance, as well as some novel applications, such as right-of-way constraints. The substantial energy transport capacities of these lines, necessitates very high performance levels.

There is increasing international performance data indicating that the lightning shielding philosophy of HVDC lines is not adequately catered for in the present AC derived standards.

There have been attempts to refine traditional models to take into account the conditions associated with HVDC. It is proposed to investigate the physics of lightning stroke penetration in the HVDC case and assess whether the present models are adequate.

A model will be developed and utilized in simulations to assess validity by correlation between the predicted outage rate, and actual line performance data. The validity of experimental work will also be investigated.

2. BACKGROUND

The general experience in China on bipolar ± 500 kV HVDC lines, indicates that the positive pole experiences significantly more direct stroke penetration events leading to outages. In particular, for the ± 500 kV Jiang-Cheng line which is a part of the Three-Gorges project commissioned in 2004, eleven out of thirteen lightning shielding failure outages occurred on the positive pole [1]. This trend is consistent with experience on the ± 500 kV Tian-Guang and Gui-Guang lines [1].

In the period of 1994 and 1995, the Hydro Quebec ± 450 kV line from Radisson to Nicolet (1200km), experienced 12 lightning stroke penetration induced faults, i.e. 0.5 Fault/100km.year. 9 of these faults occurred on positive pole [2].

Another compelling example demonstrating the vulnerability of the positive pole is the 2 bipolar Nelson River ± 450 kV HVDC lines of Manitoba Hydro. The positive pole was affected by 4 out of 5 lightning penetration faults [2]. The positive poles of

the two parallel bipolar lines are operated on the inside pole conductors, separated by a mere 60m. This arrangement results in substantially better lightning shielding for the positive pole conductors compared to the more exposed outside negative pole conductors. This strongly suggests that the positive pole is far more susceptible to lightning penetration induced outages.

Statistically, this propensity of the positive pole to be subjected to direct strokes has been demonstrated on Eskom's Songo-Apollo HVDC scheme, where two separate mono-polar lines are utilised. 30% of faults between 1993 and 1999 were lightning induced [3], thereby having a significant impact on the line performance. The lines run along different routes, but only approximately 1km apart, and consequently altitude and local weather conditions are largely negligible in comparing the performance of the two poles. The incidence of faults is also influenced by the conductor surface gradient and hence operational voltage, which is noted when the line operates at full voltage with four stages in series at 533kV, as opposed to three stages at 400kV. This information however, requires further investigation. The positive pole is typically operated at +533kV and the negative pole at -400kV which has skewed the incidence of all types of faults since the lines are insulated to identical levels.

3. HYPOTHESIS

The positive pole on HVDC transmission lines is generally accepted to be more likely to experience shielding failure under approaching negative downward leader. This is due to the additive influence of the pole voltage on the cloud to ground potential, resulting in the conditions for the initiation of an upward induced leader being more readily met, as opposed to the negative pole or shield wire [2][6]. More than 80% of ground flashers are of negative polarity [4] and furthermore, for transmission lines in the conventional height range (i.e. as opposed to exceptionally tall structures for river crossings etc.), the majority of lightning exposure is to negative downward stepped leaders [6]. Consequently the positive pole is more affected by lightning strokes.

Shielding failure affecting the positive pole suggests more stringent protection must be applied to the positive pole. This could lead to asymmetrical bipolar structure configurations, or very conservative shielding designs, i.e. “negative shielding angles”, if there is an operational requirement for pole reversal.

The contribution of the pole voltage calculated according to the electro-geometric model increases the shielding failure rate by 4,84 times for a positive pole voltage of 500kV compared to when the line voltage is neglected [5] when considering negative downward leader [1]. The effect of negative pole voltage is not stated.

This results in a generally significant disparity in the lightning related performance of the poles. This disparity indicates that the lightning protection design must be more carefully approached in HVDC cases than for traditional HVAC.

Traditional methods of lightning protection system design evolved around HVAC lines. These models neglect the phase conductor voltage in the lightning attachment process for two significant reasons:

- On AC systems, the power frequency voltage has a mean value that approaches zero and therefore any voltage induced effects appear to be largely negated [6]
- The line voltage is negligibly small when compared to the tip potential of the descending leader [2]

The first reason is not applicable to HVDC, but the application of the second assumption in HVDC case is inaccurate.

The operational voltage should not be compared to the tip potential of the descending leader, but should be considered in the space potential (electric field gradient) that is required for the initiation of an induced upward leader [2]. The field intensification associated with the negative descending leader first induces positive streamers from ground objects which may further develop into a leader discharge if a critical electric field gradient is exceeded [6]. The effective conductor voltage, U_e , resulting in positive leader initiation is given by the following expression [2]:

$$U_e = V_{p-g} + E_g \cdot h + U_i \quad (1)$$

Where:

V_{p-g} : Pole to ground voltage

E_g : Ambient ground field due to cloud charge

h : Height above ground

U_i : Induced voltage at conductor position due to the descending leader charge

A significant portion of the electric field space potential required (around 30% for a positive 600kV pole) may be provided by the pole voltage [2]. From Equation 1, it can be seen that the negative pole voltage has a suppressing effect on the formation of induced leaders under negative lightning. The effect

of pole voltage is all but ignored in published models, except for an extension of the Rizk model in [6] in order to evaluate HVDC lightning performance.

The positive HVDC pole is also more vulnerable to back flashover events arising from strikes to the shield wire, as shown by the modeling of a ± 450 kV line in [6], where practically all flashovers due to negative stepped leaders affect the positive pole.

Performance data indicates that for AC transmission lines with maximum system voltages exceeding 300kV (EHV - Extra High Voltage), more than 90% of lightning related outages are due to shielding failure as opposed to back-flashover events, and that the ratio of shielding failure to back-flashover related outages for HVDC lines exceeds that of EHV AC lines [1].

Therefore lightning shielding failure is emphasized over back-flash incidents, in the performance of HVDC lines and is the focus of this investigation.

4. DISCUSSION

The research aims to address whether the lightning performance modeling criteria, in terms of shielding failure of HVDC lines, is sufficiently covered in the literature, and if published models are adequate in predicting the outage rate. Furthermore, the work will involve the development of a model and simulations in order to assess validity by comparison with performance data where feasible.

4.1 Literature review

The work commenced with a literature survey to develop an impression of the state of the art of lightning protection in respect of HVDC transmission lines.

There is substantial literature on lightning physics and the protection of structures, including transmission lines, and contributions to this field continue. Popular text books on overhead lines such as [6] and [8] do not consider particular lightning protection requirements for HVDC lines. In the EPRI series of HVDC reference books, only [6] covers lightning protection design for HVDC, and appears to be the only reference book with particular consideration of the HVDC case [2].

Recently, there have been several papers published around the performance of relatively new HVDC schemes and proposed models for HVDC lightning protection analysis [9], [10].

4.2 Modeling and validation

After review of the published models with specific focus on those that incorporate conditions particular to HVDC, the apparent validity of the models will be assessed. Simulations will be performed using appropriate electric field modeling tools and the model predicted outage rate compared to actual performance statistics.

This process will culminate in the adoption of a suitable model or possible development of a revised or extended version of an existing model that addresses the deficiencies.

Besides classical empirical methods and the electro-geometric model (EGM), there are a few popular models for evaluation of shielding failure [14]. The collection volume method (CVM), leader progression model (LPM), and the leader inception model (LIM).

The EGM was first applied to shielding design of 345kV AC transmission lines in the 1950's. The EGM defines the striking distance of the stepped downward leader in terms of the stroke amplitude in kA:

$$D_s = aI^b \quad (2)$$

Where:

D_s is the striking distance

I is the return stroke current in kilo amperes

Several researchers have proposed different values for a and b [14] uses the following, which gives shorter striking distances.

$$D_s = 8I^{0.65} \quad (3)$$

This equation was developed to include structure height dependence. This relationship is based on the assumption that the ground object only acquires an induced potential that is dependent on ambient ground electric field due to the cloud charge (see Equation 1). This approach has been widely applied to lightning shielding design for both HVAC and HVDC lines, however is not suitable for HVDC applications where the induced potential on the pole conductor is influenced by the pole voltage [2]. The EGM model must be modified to account for this effect.

There is still controversy in alternative models for lightning interception such as the LPM and LIM, where leader propagation plays an important role in the lightning attachment process [14].

Evaluation of the models by means of correlation with historical line performance is considered to be the only practical method of verification. At this stage it is not finalized which lines will be considered for the analysis.

Reliable performance data is accepted to be scarce internationally [2], despite that lightning faults have characteristic signatures with a steep wave front that is readily distinguished from other faults e.g. flashover due to fires under the line. Furthermore the sensitivity of historical performance information makes it difficult for utilities to share.

4.3 Experimental testing

Experimental testing depends on how effectively the lightning attachment process can be simulated, but for practical reasons requires the use of a scale model. The validity of such tests is often stated to be questionable [11], [12].

Some properties of both negative downward stepped leader and the upward connecting positive leaders were first investigated under simulated conditions [12].

Long air gap laboratory simulations are often used to simulate the conditions under which upward positive leaders are initiated, although these tests cannot fully replicate the conditions during natural lightning [13].

It is challenging to initiate flashovers by means of the leader mechanism in laboratory conditions even at impulse voltages in the megavolt range. There are possibilities around using slower wave-front (e.g. switching) to initiate leader breakdown. However the electric fields associated with switching do not adequately approximate the field produced by a negative downward leader. With switching the electric field rate of change varies from fast to slow whereas with natural lightning the rate of change is reversed from slow to fast as shown in Figure 1 [12].

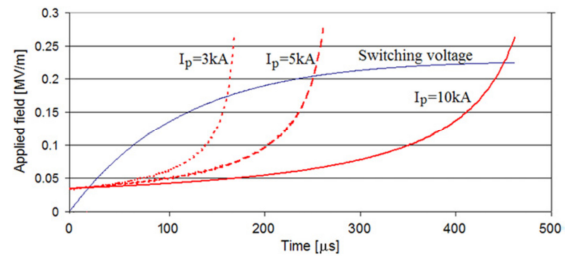


Fig. 1: Simulated electric field for switching vs. various peak return lightning stroke currents associated with downward descending leader [12].

The execution of large scale representative lighting related tests may provide limited benefit and require extensive resources that are costly and are not readily available.

Experimental work is not considered to be feasible at this stage.

5. CONCLUSION

It is clear from the literature that there is a dramatic performance disparity between the polarities on HVDC lines in respect of lightning. The positive pole voltage biases all negative lightning related events towards that pole.

Traditional lightning protection design methods and the published standards as applied to HVAC lines do not cater for ground objects energized at a HVDC voltage and are inadequate for design optimization and performance prediction. Traditional methods have been recently extended by some researchers [1][9], [10] to include the effect of the HVDC pole voltages, but there is no consensus on the approach at present.

Adequate lightning performance can be achieved by conservative shielding designs, but there is no guidance in standards on tower geometry in relation to environmental factors e.g. ground flash density and altitude, and line parameters such as operational voltage. There is only one published reference book

[6] that is based on the contribution of a single researcher, and requires further verification.

Laboratory experiments appear to have limited value in verification of lightning related models [11], [12] and the only practical means of verification may be correlation with actual line performance.

ACKNOWLEDGEMENTS

Thanks to Prof. Ken Nixon of Wits University for his encouragement and guidance in submitting this paper. Thanks also to Keri Pickster and Thavenesen Govender of Eskom, Power Delivery Engineering for their assistance and support.

REFERENCES

- [1] Hengxin HE, Junjia HE, Dandan Zhang, Li DING , Zhenglong JIANG, Cheng WANG, Huisheng YE “Experimental Study on Lightning Shielding Performance of 500 kV HVDC Transmission Lines”, IEEE 2009
- [2] Dr. Farouk A.M. Rizk “Lightning Exposure and Lightning Protection with Special Reference to High Altitudes, Review of State of the Art and Selection of Design Criteria”, Internal research report submitted to Trans Africa Projects in February 2012
- [3] AC Britten, “Unknown Category of Eskom Line Faults: Investigation into Light Pollution on Glass Disc Insulators as an Underlying Cause of Unexplained Flashovers”, Eskom Internal Research Report: TRR/CONS6/98, 1998
- [4] V.A. Rakov and M.A. Uman, “Lightning: Physics and Effects”, Book, Cambridge University Press, 2003
- [5] Hengxin HE, Junjia HE, Dandan Zhang, Li DING , Zhenglong JIANG, Cheng WANG, Huisheng YE, Abstract for “Experimental Study on Lightning Shielding Performance of 500 kV HVDC Transmission Lines”, IEEE 2009
- [6] Electric Power Research Institute, “EPRI HVDC Reference Book: Overhead Lines for HVDC Transmission, Electrical Performance of HVDC Transmission Lines”, Chapter 4, “Lightning Performance”, EPRI, Palo Alto, CA, 2008
- [7] F. Kiessling, P. Nefzger, J.F. Nolasco, U. Kaintzyk “Overhead Power Lines, Planning, Design, Construction”, Springer, 2002
- [8] Eskom Holdings Ltd, Eskom Power Series, “The Planning, Design and Construction of Overhead Power Lines”, 2005
- [9] M. You, B. H. Zhang, L. Y. Cheng, Z. Q. Bo, A.Klimek “LIGHTNING MODEL FOR HVDC TRANSMISSION LINES”
- [10] Mohamed Nayel, Zhao Jie, Jinliang He, “Analysis of Significant Parameters Affecting The Shielding Failure of HVDC-TL”, IEEE 2010
- [11] R. H. Golde , “ The validity of lightning tests and scale models”, Journal IEE, vol. 88, Part II, no. 2, pp. 67-68, 1941.
- [12] M. Becerra, V. Cooray, “Laboratory experiments cannot be utilized to justify the action of early streamer emission terminals”, Journal of Physics, March 2008
- [13] R. H. Golde , “ Lightning Protection”, London, Edward Arnold 1973
- [14] Institute of Electrical and Electronics Engineers, “IEEE Std 998-2012”

Proceedings of the 22nd South African Universities Power Engineering Conference 2014

EFFECT OF TEMPERATURE VARIATIONS ON WAVE PROPAGATION CHARACTERISTICS IN XLPE MV POWER CABLES

G D Mlangeni, M Sotsaka and C Nyamupangedengu

University of the Witwatersrand, Johannesburg, School of Electrical and Information Engineering, Private Bag 3, 2050, Johannesburg, South Africa.

Abstract: Medium voltage (MV) power cables are primarily designed to transfer power at 50 or 60 Hz, however, they are also being used for transmission of communication signals. Since power cables experience temperature variations due to load cycles, it is essential to understand how temperature affects transmission of communication signals. In this paper, the effect of temperature variations on wave propagation characteristics in an 8.25 m long 11 kV single-core cross-linked polyethylene (XLPE) MV power cable is determined using time domain reflectometry (TDR). To emulate temperature variations, 500 A from a 3 V/ 1667 A current injector is injected into the cable until its surface temperature is 58 °C. Using Matlab®, the cable wave propagation characteristics are extracted using Fast Fourier transforms (FFT) on the TDR measurements. The experimental results measured from 22 °C to 58 °C showed that the cable attenuation constant increased by an average 102 %, the phase constant decreased by 45 % and the propagation velocity increased by 1 % respectively. It is notable that the changes in parameters are nonlinear.

Key Words: Attenuation constant, phase constant, propagation velocity, time domain reflectometry, temperature.

1. INTRODUCTION

Power cable networks are critical electrical infrastructure to electrical utilities and other power systems. Cable failures are one of the primary causes of interruptions of electrical power delivery [1, 2]. Partial discharges and water-treeing are among the most common failure mechanisms associated with XLPE insulated cables [2, 3]. In order to pre-empt and prevent cable failures, effective diagnostic techniques, such as time domain reflectometry (TDR), are required to detect degraded cable sections. TDR is based on launching a high frequency pulse, with a short rise time, into the cable and observing the cable response, in the form of multiple reflections, on a high speed oscilloscope [4]. It is for this reason that the high frequency properties of the power cable and the degraded region should be well understood [3]. Furthermore, cable systems are subjected to internal and external influences such as temperature variations due to varying load cycles, and pressure from the surrounding environment, which may affect the accuracy of the diagnostic technique applied [5]. It is also important to study the effect of temperature variations on the propagation of high frequency signals in XLPE MV power cables, as cables are increasingly experiencing the dual function of power transfer, at 50 or 60 Hz, and communication signal transfer, at 2 - 50 MHz [6, 7].

The aim of the work presented in this paper is to determine the effect of temperature variations, due to load cycles, on wave propagation characteristics of XLPE MV power cables. Areas of applicability of this study are found in localisation of insulation degradation along power cables, partial discharge (PD) diagnostics [1-3] and high capacity data transmission over power networks [4]. Findings from [5, 8] and [9] show that the effect of temperature is to change the complex permittivity of semiconducting materials and therefore increase propagation velocity.

This paper is organised as follows, section 2 is the background and section 3 is the cable high frequency model. The simulation of the cable high frequency model and experimental work are presented in section 4 and 5 respectively. The discussion of

results is presented in section 6 and section 7 is conclusion.

2. BACKGROUND

2.1 Cable Diagnostics

Distribution cables are vital assets in electric power systems; however, they age and degrade over the period of operation and eventually fail [10]. Deterioration of cables result from defects such as water trees, which lead to electrical trees, contamination, protrusions and delamination of semi-conducting screens, to name a few. Cable accessories fail due to poor workmanship, moisture ingress and manufacturing defects [2]. Early detection of degraded sections is critical to the formulation and implementation of preventive maintenance schedules, and reduction in costs associated with the extended time taken to replace faulty cables [2, 11]. This is achieved through effective cable diagnostic techniques. The purpose of an effective and accurate diagnostic technique is to locate the degradation and yield information about the severity of the degradation [10]. This information is then used to answer important maintenance questions like whether to repair the degraded section; refurbish or completely replace the cable [2].

Dielectric spectroscopy method and TDR are some of the diagnostic techniques available. TDR provides more meaningful information about the broadband response of the cable [4]. The cable response is extracted and analysed using a mathematical tool applied on the TDR multiple reflections. Signal frequencies in the MHz range are required to detect defected areas to within 10 m [10]. Thus the high frequency characteristics of the cable and defect, where applicable, need to be well understood as the precision in localization of degraded sections, along the cable length, is dependent upon the frequency of the measuring signals [10].

Furthermore, cables experience varying temperatures while in operation. Thus the effects of temperature on wave propagation characteristics of the cable need to be studied to determine if, indeed temperature does affect wave propagation characteristics [8].

If temperature is found to affect wave propagation characteristics of the cable, then the temperature of the cable will need to be accounted for in the diagnostic techniques if they are to yield more accurate results [9].

2.2 Smart Grids and Power Line Communication

The use of wide spread power cable networks as a medium for communication signals, has been a subject of discussion in recent times [13, 14]; since these cables are capable of carrying high frequency signals relatively well in comparison to some commercial radio frequency (RF) coaxial cables [4, 13]. It is due to this capability that existing cable networks are being investigated as the alternative communication medium for smart grids [14]. Smart grid technology entails applying sensors, field automated devices and smart meters to the distribution power networks [14]. Using two way communication ability, these devices measure and control power grid conditions and communicate information to the consumers, operators and power utilities. Thus dynamic responses to changes in the grid will be possible [14]. This emphasizes the need for a robust and reliable communication network if smart grid technology is to be a viable technology of the future.

Power line communication (PLC) is emerging as one of the more promising communication technologies for smart grid technology. This is due to the existing power line and cable infrastructure and the fact that power utilities prefer to control their own networks [13, 14]. However, cable networks and power lines are subjected to internal and external influences which make them a harsh environment for communication signals. Varying impedance, considerable noise and high attenuation are among some of the major concerns for PLC [14, 15]. This again reiterates the need to investigate the effect of temperature on wave propagation characteristics in addition to the high frequency behaviour of the cable system. Attenuation and propagation velocity have been shown to increase in with increasing frequency as well as increasing temperature [11, 16].

Two main communication standards are used for PLC namely; Narrowband PLC (NPLC) and Broadband PLC (BPLC). NPLC operates in the frequency range 9 - 95 kHz (CENELEC-A norm) and provides up to 128kbps bit rate. BPLC operates in the frequency range of 1.8 - 28 MHz and provides up to 220Mbps [14].

Careful choice of modulation technique can increase data rates, thus third generation smart grid systems are based on orthogonal frequency-division multiplexing (OFDM). OFDM is one of many modulation techniques used for PLC and each is used depending on the advantages it offers to the target application. Code division multiple access (CDMA), for example, offers the advantage of using the system's inherent processing gain to meet radiation allowance limits while offering transfer rates of up to

1Mb/s [15]. This technique is thus greatly affected by the system attenuation.

3. HIGH FREQUENCY CABLE MODEL

3.1 Series Impedance Z

The cable used in this experiment is a single-phase, 120 mm² copper conductor, 6.35/11 kV XLPE MV power cable of 8.25 m length. The cable design is shown in Figure 1. This cable is used since it is a typical XLPE MV power cable, with ratings within the medium voltages 6.6 - 33 kV [17].

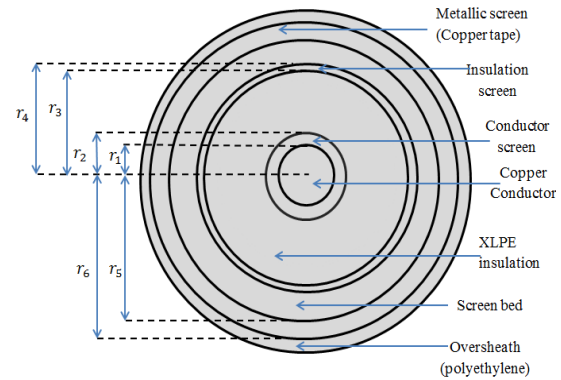


Figure 1: Design of the cable investigated [12]

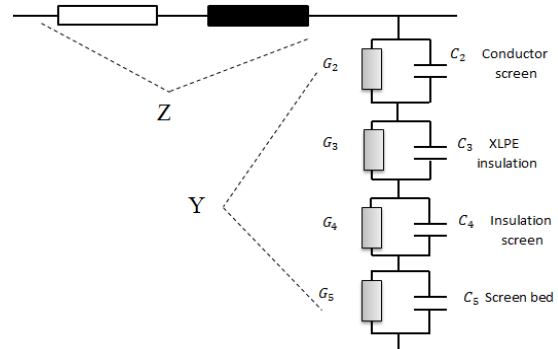


Figure 2: High frequency cable model [9]

The high frequency model of the cable is shown in Figure 2. In the model, the series impedance, Z , due to the copper conductor and copper-tape metallic screen is given by equation (1). In (1), the conductivity of the copper conductor, $\sigma_1(T)$, and conductivity of the copper-tape metallic screen, $\sigma_6(T)$, are given by equation (2), $r_1 = 6.75 \text{ mm}$ and $r_5 = 23 \text{ mm}$, $\mu_0 = 4\pi \times 10^{-7} \text{ H/m}$ is the permeability of free space and ω is the angular velocity (rad/s) [15].

$$Z = \frac{1}{2\pi r_1} \sqrt{\frac{j\omega\mu_0}{\sigma_1(T)}} + \frac{j\omega\mu_0}{2\pi} \ln\left(\frac{r_5}{r_1}\right) + \frac{1}{2\pi r_5} \sqrt{\frac{j\omega\mu_0}{\sigma_6(T)}} \quad (1)$$

$$\text{Where } \sigma_1(T) = \sigma_6(T) = \frac{1}{\rho(T)} = \frac{1}{\rho_0[1 + \alpha(T - T_0)]} \quad (2)$$

In (2), $\rho(T)$ is the resistivity at temperature T , $\rho_0 = 1.68 \times 10^{-8} \Omega \cdot \text{m}$ is the resistivity at room

temperature, $T_0 = 20^\circ\text{C}$, and $\alpha = 3.862 \times 10^{-3}^\circ\text{C}^{-1}$ is the temperature coefficient of resistivity [18].

3.2 Shunt Admittance Y

The shunt admittance, Y , due to the conductor screen, XLPE insulation, insulation screen and screen bed is given by equation (3) [8]. Equation (4) is the shunt admittance for a layer k , where $\epsilon_0 = (1/36\pi) \times 10^{-9}$ F/m is the dielectric permittivity of free space. In (4), $\epsilon_k^*(\omega)$ is the complex permittivity, G_k is the conductance and C_k is the capacitance for a layer k , in the shunt path of the cable model in Figure 2.

$$Y = \frac{1}{\sum \frac{1}{y_k}}, \quad k = 2, 3, 4, 5. \quad (3) \quad [8]$$

$$\text{Where } y_k = G_k + j\omega C_k = j\omega \frac{2\pi\epsilon_0\epsilon_k^*(\omega)}{\ln\left(\frac{r_k}{r_{k-1}}\right)} \quad (4) \quad [8]$$

Equation (5), is the cable propagation constant where, $\alpha(\omega)$ is attenuation constant (Np/m), $\beta(\omega)$ is the phase constant (rad/m) and (6) is the propagation velocity (m/s).

$$\gamma(\omega) = \sqrt{ZY} = \alpha(\omega) + j\beta(\omega) \quad (5) \quad [19]$$

$$v = \frac{\omega}{\beta(\omega)} \quad (6) \quad [16]$$

4. XLPE MV CABLE SIMULATION

4.1 Parameter Values Selection for Simulation

The cable model in Figure 2 is simulated in Matlab® using (1) to (6). Due to lack of a mathematical model which relates temperature to the complex permittivity of the semi-conducting screens and XLPE insulation in the shunt path of the model shown in Figure 2; the complex permittivity of the XLPE is assumed to be $\epsilon_3^* = 2.3 - j0.001$ at all temperatures and frequencies [12]. The complex permittivity values of the semiconducting screens and screen bed are obtained from the measurements done in [8, 19], at 25°C , 45°C and 65°C . Due to similarity in behaviour of the complex permittivity of the screen bed and conductor screen [8], the conductor screen permittivity is estimated to that of the screen bed.

4.2 Simulation Results

The simulated attenuation constant of the cable in Figure 3 increases by 14 % and 18 % when the temperature is increased from $25\text{--}45^\circ\text{C}$ and from $45\text{--}65^\circ\text{C}$ respectively. This translates to an average increase of 16 % from $25\text{--}65^\circ\text{C}$.

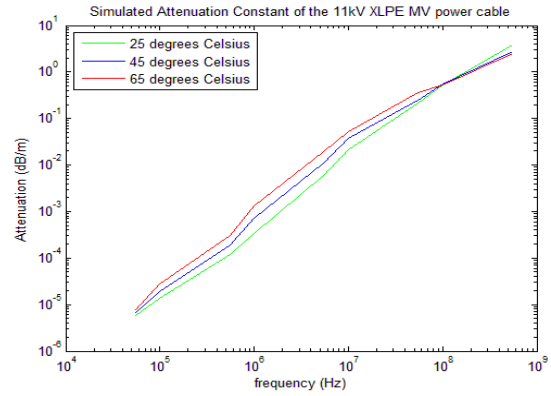


Figure 3: The simulated attenuation constant of the cable.

Figure 4 is the simulated phase constant of the cable, it decreases by 12 % and 15 % when the temperature is increased from $25\text{--}45^\circ\text{C}$ and $45\text{--}65^\circ\text{C}$ respectively, which is an average 14 % drop as temperature increases from $25\text{--}65^\circ\text{C}$.

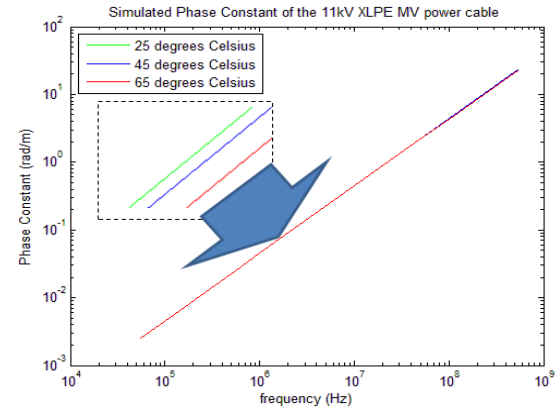


Figure 4: The simulated phase constant of the cable.

The simulated propagation velocity shown in Figure 5 is calculated using (6). There is an average increase of 0.9 % when the temperature is increased from $25\text{--}65^\circ\text{C}$.

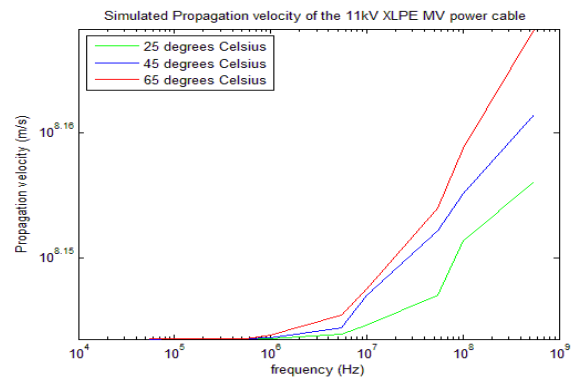


Figure 5: The simulated propagation velocity of the cable.

5. EXPERIMENTAL SETUP

5.1 Tan-Delta Measurement

To ensure that the cable used in the experiment is devoid of defects, tan-delta measurements up to the cable rated voltage were performed. For the tan-delta measurements, the voltage is increased from 2.2 kV with steps of 20 % of the rated voltage 11 kV. The results showed that the cable did not have any defects.

5.2 Cable Heating

To heat up the cable, 500 A from a 3 V/1667 A current injector was circulated through cable until its surface reached a steady state temperature of 58 °C. Since the temperature gradient between conductor and cable surface is 15 °C [20], when the cable surface is at 58 °C, the conductor is at 73 °C. After the temperature reached 58 °C, the cable was disconnected from the current injector and TDR measurements done as the cable cooled down. The cable temperature was monitored using a UNI-T UT33C digital thermometer.

5.3 TDR Measurement Setup

The TDR measurement setup in Figure 6 was used to extract the cable parameters given by equations (5), (6), (8) and (9). The connecting coaxial cables in Figure 6 are 50 Ω MIL-C-17F-RG058CU. The pulse generator produces a pulse with amplitude of 8.31 V, 22 ns pulse-width, 3.7 ns rise-time at an interval/period of 0.3 MHz. The pulse from the pulse generator was injected at one end of the cable while the other end was kept open-circuited. The output waveform measured on the oscilloscope is shown in Figure 7.

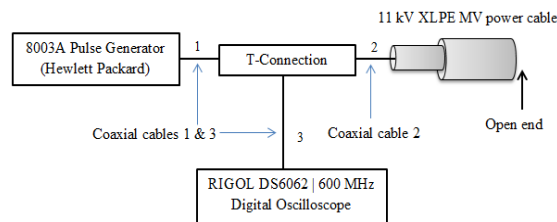


Figure 6: Schematic drawing of the TDR measuring setup [4]

5.4 Cable Parameter Extraction Method

The incident pulse from the pulse generator and reflected pulse from the open-circuited end of the cable are denoted *incident pulse 1* and *reflected pulse 1* in Figure 7 respectively. The impedance mismatch between the coaxial cable 2 and the power cable causes 60 % of *incident pulse 1* to be reflected. The reflected pulse is denoted *mismatch reflection*. This occurs because coaxial cable 2 has an impedance of 50 Ω and the XLPE cable have impedance between 21 – 34 Ω [13].

Since the power cable is considered as a linear system according to [4], then the ratio between the

Fast Fourier Transform (FFT) of the reflected pulse, V_{out} , and FFT of the incident pulse, V_{in} , gives the transfer function of the cable given by (7). In equation (7), l is the length of the cable and $\gamma(\omega)$ is the propagation constant given by (5). Therefore, from (7), the attenuation and phase constant can be deduced as given by (8) and (9) respectively.

$$H(\omega) = \frac{FFT(V_{out})}{FFT(V_{in})} = e^{-\gamma(\omega)2l} \quad (7) \quad [4]$$

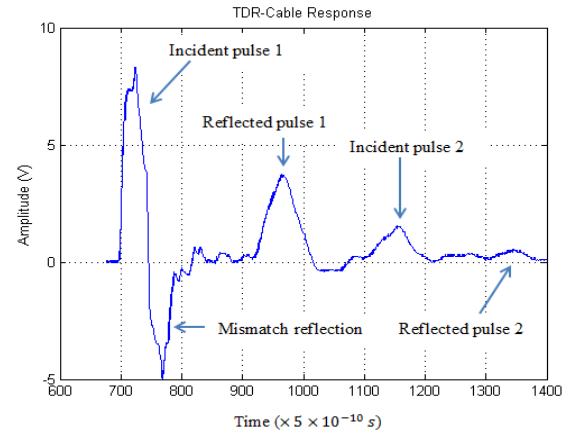


Figure 7: TDR response of the cable.

$$\alpha(\omega) = -\frac{1}{2l} \times \ln |H(\omega)| \quad (8) \quad [4]$$

$$\beta(\omega) = -\frac{1}{2l} \times \angle H(\omega) \quad (9) \quad [4]$$

Due to 60 % of *incident pulse 1* that is reflected, in this experiment, the *reflected pulse 2* and *incident pulse 2* shown in Figure 7 were used in (7). Before the signals V_{out} and V_{in} are Fourier Transformed, the pulses V_{out} and V_{in} , are padded with zeros up to the length $N = 2^n$, for $n=10$ before taking their FFT. For calculation in Matlab®, the oscilloscope sampling frequency of 2.0 GHz is used.

5.5 Laboratory Results

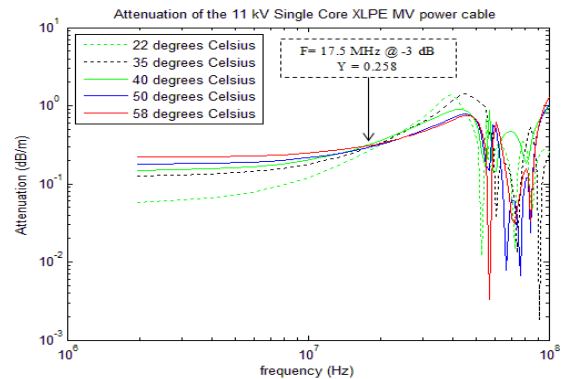


Figure 8: The measured attenuation constant of the cable.

To extract the cable attenuation constant shown in Figure 8, equation (8) is used. The attenuation constant of the cable increases by an average of 100 % when the temperature increases from 22-58 °C and the change is nonlinear.

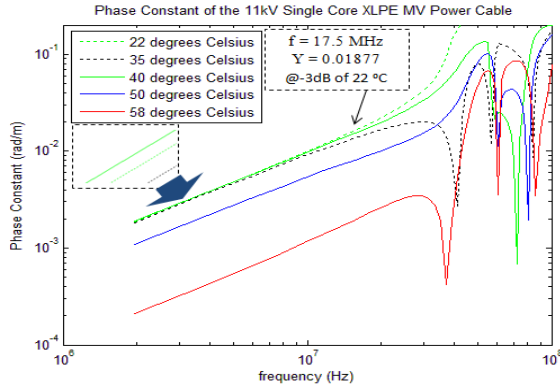


Figure 9: The measured phase constant of the cable.

In Figure 9, is the phase constant of the cable determined using (9). The phase constant decreases by an average 45 % as the temperature increases from 22-58 °C and the change is nonlinear.

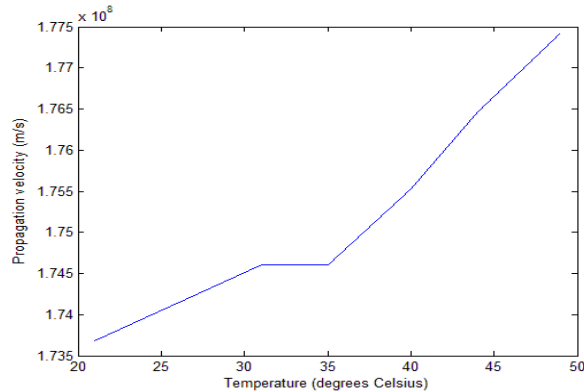


Figure 10: The measured propagation velocity of the cable.

The propagation velocity, V_p in Figure 10 is determined using (11), where T_r is the time difference between *incident pulse 2* and *reflected pulse 2* shown in Figure 7.

$$D = 0.5 V_p T_r \quad (11) \quad [21]$$

The propagation velocity increases by an average of 1 % as the temperature increases from 22-58 °C.

6. DISCUSSION

The effect of temperature variations on the attenuation constant, phase constant and the propagation velocity in a single-phase 11 kV, 8.25 m long XLPE power cable is observed in the simulations and measurement results presented in section 4 and 5 of this paper respectively. The

behavior of the attenuation constant, phase constant and propagation velocity from the measurements agree with the predicted behavior from the simulations. There is a significant increase in the measured attenuation as compared to the simulated.

The differences between the measured and simulated parameters are due to insufficient data for simulations. The complex permittivity of the XLPE insulation is assumed constant, in the simulations, since there is no mathematical model that relates it to temperature. An error due the use of a constant complex permittivity of the XLPE insulation was observed in an experiment conducted in [16] for determining the capacitance of a 7/12 kV XLPE power cable. In that experiment, the XLPE permittivity was set to a constant 2.3. This resulted in a 91 % and 89.85 % error on the predicted decrease of the cable capacitance when temperature is increased from 20-40 °C and from 40-60 °C respectively. However, when the permittivity of XLPE insulation was decreased by 1.4 % and 1.7 % for temperatures raised from 20-40 °C and from 40-60 °C respectively. This resulted in a 0.52 % and 1.19 % error on the decrease of the cable capacitance when temperature is increased from 20-40 °C and from 40-60 °C respectively. The above results show that the simulated model would inherently have errors in the estimation of the behaviour of cable, since the capacitance is part of the imaginary part of shunt admittance given by (3). In that regard, it should be noted that future work in this research should include characterization of the XLPE permittivity variations as a function of temperature.

The simulated model is not a complete representation of the actual cable, because from the literature found, the only measured complex permittivity was for screen bed and insulation screen. This shortage of data on the conductor screen complex permittivity, also contributes to the error in the simulated model. However, the simulated model provides the guideline on the expected results.

In the experiment conducted in [22], the propagation velocity of a 12 kV, 6.3 m long XLPE power cable is found to be 1.55×10^8 m/s at ambient temperature. In Figure 10, the propagation velocity at 22 °C is 1.737×10^8 m/s; this velocity is more by 10.77 % to the one measured in [22]. The deviation on the two velocities is expected, because according to [22], the propagation velocity increases with the length of the cable. The overall behaviour of the measured phase constant, attenuation constant and propagation velocity of the XLPE power cable as compared to the measured data in [16, 22], behaved as expected. At 17.5 MHz, the -3 dB point of the cable, a cross over phenomenon is observed; where beyond this point the effect of temperature is inverted. This behaviour is observed on both the measured and simulated attenuation constant; this could possibly be due to the screen bed. In [8], it is shown that the percentage contribution of the screen bed to attenuation increases with increasing frequency. However, at this point there is insufficient data to conclude that this

phenomenon is definitely due to the screen bed and therefore should be considered for future investigation.

7. CONCLUSION

A suitable high frequency model of the 11 kV, 8.25 m long XLPE power cable was simulated in Matlab® to predict the behaviour of the cable at different temperatures. TDR measurements were performed on the cable as it cooled down from a steady state temperature of 58 °C. Both the simulation and laboratory results revealed that the effect of temperature is to increase the attenuation constant and propagation velocity with an increase in temperature, however, the phase constant decreases with increasing temperature. The laboratory results show that attenuation constant doubles; phase constant decreases by an average of 45 %; and the propagation velocity increases by about 1 % as the temperature increases from 22-58 °C. Temperature affects wave propagation characteristic of XLPE MV power cables and needs to be accounted for in cable diagnostics and PLC communication channels design. Also a cross over point is observed in the attenuation constant. Further research of this phenomenon is required.

8. ACKNOWLEDGEMENTS

The authors would like to acknowledge with gratitude Eskom for their support of the High Voltage Engineering Research Group through TESP. They would also like to express gratitude to the Department of Trade and Industry (DTI) for THRIP funding and to thank the National Research Foundation (NRF) for direct funding.

REFERENCES

- [1] L. Bertling, R. Eriksson, R.N. Allan, L.A. Gustafsson and M. Ahlén. "Survey of causes of failures based on statistics and practice for improvements of preventive maintenance plans", *Proceeding of the 14th Power Systems Computation Conference PSCC'02*, Sevilla, Spain, Session 13, Paper 2, pp.1-7, June 2002.
- [2] G. Hartshorn, B. Lanz, and B. Broussard. "Medium voltage cable predictive diagnostics technique", *Petroleum and Chemical Industry Technical Conference*, Calgary, pp. 1-9, September 2007.
- [3] R. Papazyan, P. Pettersson and D. Pommerenke. "Wave propagation on power cables with special regard to metallic screen design", *IEEE Transaction on Dielectrics and Electrical Insulation*, Vol. 14, No. 2, April 2007.
- [4] G.M. Hashmi, R. Papazyan and M. Lehtonen. "Determining wave propagation characteristics of MV XLPE power cable using Time Domain Reflectometry technique", *International Conference on Electrical and Electronics Engineering*, Bursa, pp. I-159 – I-163, November 2009.
- [5] C. Fanggao, G.A. Saunders, R.N. Hampton, S.M. Moody and A.M. Clark. "The effect of hydrostatic pressure and temperature on the permittivity of crosslinked polyethylene", *Seventh International Conference on Dielectric Materials Measurements and Applications*, No. 430, pp. 267-270, September 1996.
- [6] N. Mallela and H. Shahnasser. "Broadband over power lines: Challenges ahead". http://www.co.it.pt/conftele2007/assets/papers/networking/paper_37.pdf.
- [7] S. Basu, S. Roy and P.K. Ray. "Broadband over power lines (BPL)", *International Conference on Power Systems*, Kharagpur, pp.1-4, December 2009.
- [8] G. Mugala. "High frequency characteristics of medium voltage XLPE power cables", Doctoral Thesis, The Royal Institute of Technology, (KTH), Stockholm, Sweden, 2005.
- [9] Y. Li, P.A.A.F. Wouters, P. Wagenaars, P.C.J.M. van der Wielen and E. Fred Steennis. "Temperature dependency of wave propagation velocity in MV power cable", *18th International Symposium on High Voltage Engineering*, Seoul, Korea pp. 1861-1866, August 2013.
- [10] R. Eriksson, R. Papazyan, G. Mugala. "Localization of insulation degradation in medium voltage distribution cables", *The 1st International Conference on Industrial and Information Systems*, Sri Lanka, pp. 167-172, August 2006.
- [11] T.M. Kuan, A.M. Ariffin, S. Sulaiman, Y.H.M. Thayoob. "Wave propagation characteristics of polymeric underground cables", *The 5th International Power Engineering and Optimization Conference*, Shah Alam, Selangor, Malaysia, pp. 410-415, June 2011.
- [12] J.R. Andrews. "Time Domain Reflectometry (TDR) Time Domain Transmission (TDT) measurement fundamentals". http://www.picosecond.com/objects/an15_tdr_tdt.pdf
- [13] H.A. Latchman and L.W. Yonge. "Power line local area networking", *IEEE Communications Magazine*, Vol. 41, No. 4, pp. 32-33, April 2003.
- [14] F. Aalamifar, H.S. Hassanein and G. Takahara. "Viability of powerline communication for the smart grid", *The 26th Biennial Symposium on Communications*, Kingston, ON, pp. 19-23, May 2012.
- [15] N. Pavlidou, A.J. Han Vinck, J. Yazdani and B. Honary. "Power line communications: State of the art and future trends", *IEEE Communications Magazine*, Vol. 41, No. 4, pp. 34-40, April 2003.
- [16] V. Dubickas and H. Edin. "On-line time domain reflectometry measurements of temperature variations of an XLPE power cable", *IEEE Conference on Electrical Insulation and Dielectric Phenomena*, Kansas City, MO, pp. 47-50, October 2006.
- [17] CBI-electric African cables. <http://www.cbi-electric.co.za/afcabweb/content/productrange.html>, Last accessed 23 October 2013.
- [18] R.A. Serway and J.W. Jewett. *Physics for Scientists and Engineers, with modern physics*, Thomson-Brooks/Cole, Belmont, CA, 6th edition, chapter 27, p. 837, 2004.
- [19] G. Mugala, R. Eriksson, U. Gäfvert and P. Pettersson. "Measurement technique for high frequency characterization of semiconducting materials in extruded cables", *IEEE Transactions on Dielectrics and Electrical Insulation*, pp. 471-480, Vol. 11, No. 3, June 2004.
- [20] G. Mazzatti and M. Marzinotto., *Extruded Cables for High-Voltage Direct-Current Transmission*, Advances in Research and Development, John Wiley & Sons, Inc., Hoboken, New Jersey, first edition, 2013.
- [21] I. Shim, J.J. Soraghan, W.H. Siew, F. McPherson, K. Sludden and P.F. Gale. "Partial discharge mapping in high voltage (HV) cable networks," *Electrical Insulation Conference and Electrical Manufacturing & Coil Winding Conference*, 1999. *Proceedings*, pp.497-500, 1999.
- [22] R. Villenfrance, J.T. Holboll and M. Henriksen. "Estimation of medium voltage cable parameters for PD-detection," *IEEE International Symposium on Electrical Insulation*, pp. 109-112, 7-10 June 1998.

THE CONVERGENCE OF HVDC CABLE AND VOLTAGE SOURCE CONVERTER TECHNOLOGIES: NEW SCOPE FOR HVDC TRANSMISSION

A. C. Britten*

* Affiliated to Electrical Engineering, School of Engineering, University of KwaZulu-Natal, King George V Avenue, Glenwood, Durban 4000, South Africa. E-mail: antony.britten@gmail.com.

Abstract: The popular view of HVDC power transmission is that it is dominated by long overhead lines and the technology of Line Commutated Conversion (LCC). However, there are a significant number of smaller HVDC schemes which use submarine cables, also with LCC as the transmission technology. This paper accordingly describes and reviews the convergence of Voltage Source Converter VSC and HVDC cable technologies, and thereby shows that a powerful new system, which does not experience commutation failure, has been created for the efficient transport of power from offshore and remote wind farm power sources, amongst other applications.

Keywords: HVDC, HVAC, VSC, transmission, cable, marine, terrestrial, long distance, cost, weak supply

1. INTRODUCTION

The purpose of this paper is to inform the readership of recent developments in the technology of voltage source converters and HVDC cable. It will be shown how these two technologies have converged during the last 10-15 years or so to create new possibilities for the wider use of dc transmission.

2. BACKGROUND AND SCOPE

From the time of the building first post-1950 HVDC schemes until the late 1990s, HVDC submarine cables have been relatively little used as the transmission path [1, pp 7-9], [2, p79]. The 18 schemes still in service from this period have all been based on Line Commutated Converter (LCC) technology. Since about 1998 until the time of writing (late 2013), there has been a steady and now accelerating growth in the commissioning of non-overhead line HVDC schemes based predominantly on the use of submarine cables, and in several cases, terrestrial cables. The use of Voltage Source Converter (VSC) technology has been one of the main catalysts for these developments. This growth has been made possible by the convergence of two key technologies and two well-identified strategic imperatives or drivers.

The two main drivers are, firstly, the need to make the transport of power generated by scattered and remote off-shore wind farms more technically efficient, and therefore fundamentally viable. The second driver is the urgent need to strengthen the integration of European

transmission and distribution networks to absorb and to transport the greatly increased amounts of renewable energy being generated. An additional driver, which to some extent is independent of the renewables issue, is the stabilising action provided by HVDC transmission to large, AC networks constrained by high fault levels, for example. This trend makes up what is already being called the “European HVDC Supergrid” [1].

The two enabling technologies which have emerged to augment this process are improvements and advances in VSC performance, and better HVDC cable technology. This chapter accordingly reviews the evolution, characteristics and application of improved cable technologies against the pressing need for methods to transport the power generated by off-shore wind farms (which are inherently weak ac networks.).

Although the application of the marine VSC-HVDC technology may not appear to be feasible in South Africa at this time, it is still necessary for local practitioners to become informed about its capabilities and features. The aim of this paper is to promote an increased degree of awareness of the technology.

3. THE PRESENT STATUS AND EXTENT OF THE TRANSMISSION OF POWER BY HVDC AND HVAC CABLES

One of the key advantages of the transmission of power by HVDC over HVAC transmission, whether by means of overhead lines or submarine cables, is its inherent ability to transport bulk power over long distances,

without requiring intermediate reactive compensation, as is the case with HVAC schemes. Consequently, the growth in the application of HVDC systems has been dominated by the building of high power, long distance schemes based on the use of Line Commutated Converter (LCC) technology. There is, in fact, a breakeven distance beyond which overhead HVDC systems become more economic than HVAC schemes. This distance is now acknowledged to be in the region of 600 km for overhead lines, and that it may continue to drop as the costs of converters stabilise or are further reduced [1, 2].

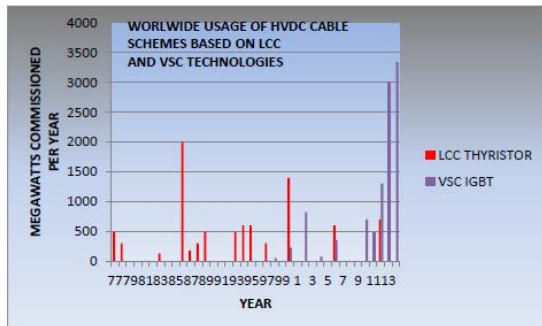


Figure 1: World-wide usage of HVDC cable technology

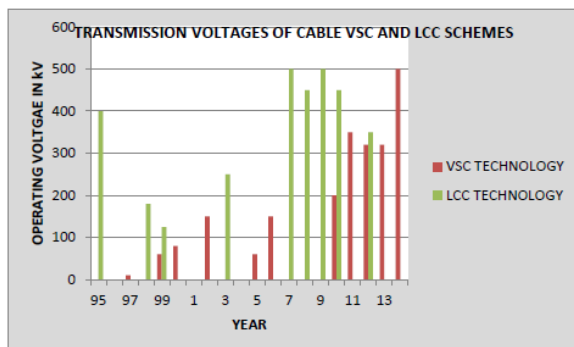


Figure 2: The growth of cable operating voltage in both converter technologies

The total installed capacity of all HVDC transmission schemes world-wide is in 2013 estimated to be 135 GW, of which some 21 GW comprises cable systems. This latter amount in turn comprises about 8.6 GW of LCC-based technology, and by 2015, about 12 GW of VSC-based technology. Cable-based HVDC systems thus make up about 15% of the total installed HVDC transmission capacity.

Perusal of the information in Figure 1 shows that, until about 1997, LCC with thyristor technology was the only method used in the transmission of cable HVDC power; with one exception, almost entirely by submarine cable

technology. It is evident from Figure 1, however, that before the introduction of VSC technology, HVDC was fairly extensively applied in some 18 schemes to shorter distance and lower power applications; this was done by making use of mass impregnated submarine cables and LCC technology [3]. The above-mentioned LCC cable schemes are far fewer in number than schemes making use of ac cable as the interconnection between conventional synchronous ac networks [1, 2].

The main impediment to the use of HVDC in the lower voltage applications was the relatively high costs and complexity of the HVDC technology compared with that of the mature HVAC systems. As will be explained, the various drawbacks in LCC technology, principally the need to apply it to a strong ac network (to effect commutation), were also factors which limited its usage.

HVAC transmission by means of cable is significantly constrained by the loading effect of the cable capacitance. Because the capacitive component of the total current drawn by the cable itself increases linearly with length, a critical distance is reached where the thermally rated load current will be equal to the capacitive current. Although inductive compensation is used to offset the capacitive current, there is a limit as to what can be achieved by means of this form of compensation; this limits the practicable length of ac cable lines to about 200 km as a rule of thumb. This leads to the existence of a breakeven distance beyond which it is not technically feasible to use HVAC cables, let alone economically feasible. An example of the limitation of real power delivered as a function of the transmission distance and the amount of reactive compensation is given in figure 3[1].

It is worth emphasising that the HVDC cable does not draw a continuously flowing charging current as is the case with ac. This means that the losses in the dc cable are generally lower than under ac. The series volt drop will also be lower.

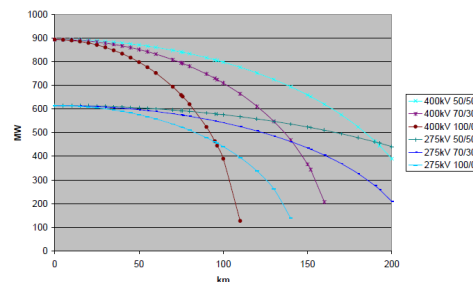


Figure 3: Power-distance profiles of HVAC cables as function of voltage and level of compensation

The schemes shown in figures 1 and 2 reveal, amongst other things, that the first VSC system was introduced in 1997, whereas dc systems using the LCC technology had been operational since 1956. It will be noticed further that the use of VSC technology has continued to grow in power and voltage ratings. The use of LCC technology with submarine cables has, on the other hand, begun to decline as can be seen in figure 1.

The cost of HVDC transmission by cable is inherently high, irrespective of whether VSC or LCC technology is being considered. It is of course to be pointed out that for the shorter transmission distances, where HVAC is certainly feasible, the HVAC- cabled scheme will still be cheaper than a similarly rated HVDC system, by a factor of about 2 to 3 [2]. For the longer distances where cable dc is the only choice, there are in fact still two options to consider, namely, the VSC or LCC technologies.

What then are the relative attributes of the main cable technologies used, namely, Mass Impregnated Paper and Extruded Cross-linked Polyethylene Insulation?

Table 1: Comparisons between VSC and LC

Technologies [2, 3, 4]

PARAMETER	VSC HVDC TECHNOLOGY	LCC HVDC TECHNOLOGY
General remarks	Power and voltage ratings will continue to increase, making multi-level VSC the only technology which can sustain the growth foreseen in offshore wind farms.	This is a mature, established technology with respect to cable applications, but it does have limitations; its future is seen to be at the 800 kV level, and not in off-shore applications.
Strength of AC network	VSC systems can operate and self-commutate into weak ac networks, or even passive networks; this technology is thus well suited wind farm and remote offshore generation.	LCC systems require connection a low source impedance synchronous voltage to effect commutation. LCC is thus not suitable for wind farm applications.
Semiconductors	Based on still-evolving IGBT technology; 600 kV, 3 GW ratings are considered by Cigré to be feasible, but are still a long way from being developed.	Based on mature thyristor technology in which a scheme rating of ± 800 kV, 7.2 GW over 2000 km has already been implemented.
Type of converter	As VSC is an evolving technology, which has niche applications, significant increases in ratings are likely to occur in the next five years.	The adequacy and reliability of the LCC technology is generally well proven.
Reactive power	VSC systems allow independent control of the active and reactive power, this allows a degree of voltage control (similar to the action of an SVC) to be applied to the ac system to which the VSC is connected.	LCC systems usually require capacitive compensation for correction of the lagging power factor at which they inherently operate.
Commutation failure	VSC systems are inherently self-commutating and do not undergo commutation failure, even when exposed to voltage dips.	Can be susceptible to commutation failure, particularly when exposed to voltage dips.
Multi-terminal operation	Multi-terminal operation is yet to be demonstrated, but it is considered to be feasible.	Multi-terminal operation is complex; only two such networks have ever been built.
Power losses	The total power loss for a pair of multi-level	The corresponding total loss at full power is

4. CABLE INSULATION DESIGN AND TECHNOLOGY

There is a fundamental difference between the dielectric design of the dc insulation of a cable and the design of an ac cable.

In an ac cable, the radial stress distribution is determined by the **capacitance** of the insulation layers. The relevant capacitances are not much sensitive to temperature; thus the stress distribution is not affected by the load current carried by the cable.

In a dc cable, the radial stress distribution is determined primarily by the **resistance** of the insulation and its temperature. The correct design has to take this interaction into account; herein lies some of the cable designer's art.

Figure 5, which refers to a 500 kV MI dc cable, shows that under full-load conditions, the maximum electric stress occurs at the insulation shield, namely, highlighted in Figure 5. In the steady-state no-load condition, the maximum temperature occurs nearer to the conductor screen. The design must be executed such that the stress limits are not exceeded during normal or abnormal operation, and that design limits are complied with.

Typical limits for the dc electric field are 30 kV/mm at the outer boundary of the insulation, at a temperature of 55 °C.

The elements of an XLPE cable are shown in figure 4.

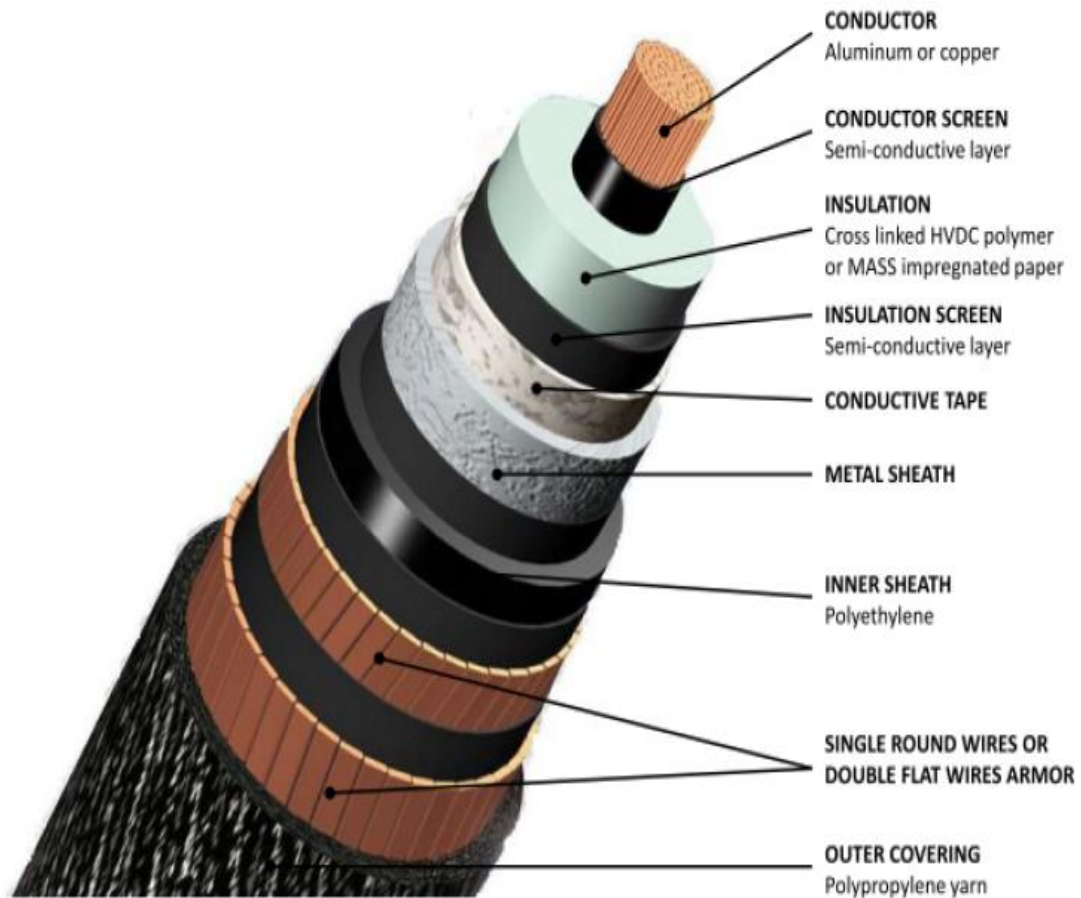


Figure 4: View of the elements of a single core XLPE cable designed for HVDC applications [5, 6]

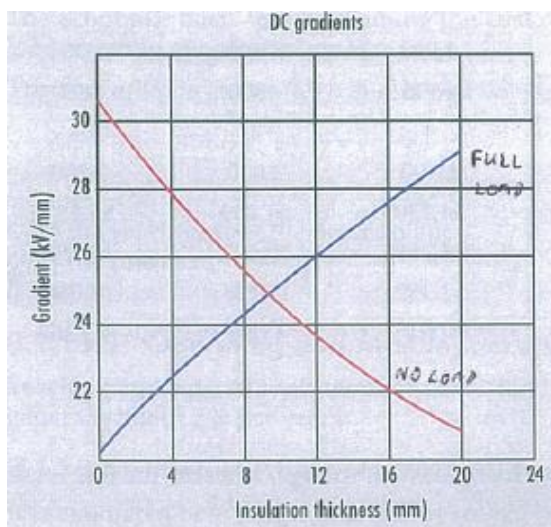


Figure 5: The effects of temperature on the distribution of The radial electric field stress in a 500 kV MI cable [6]

Four types of HVDC submarine cable are used today [3, 7, 8]. These are:

1. Self-contained, fluid-cables (SCFF).
2. Self-contained, mass impregnated cables (MI cables).
3. Self-contained, pre-impregnated gas-filled cables (SCGF cables).
4. Self-contained, solid dielectric cables (XLPE and EPR cables).

The insulation of the first three types makes use of the mature technology of paper tapes impregnated with a dielectric fluid. They differ from each other by the impregnant used, or by the type of fluid pressurising system employed. The essential differences between types (2) and (3) are to be found in the way in which the impregnation is done. The pre-impregnation method then requires the use of nitrogen under pressure to fill the gaps created between the tapes and the conductor. In the case of mass impregnation, the process is done on the entire cable core, after the tapes have been wound on the core. This is evidently the preferred form of insulation amongst the first three cable types mentioned. According to [2, 3],

about 80% of the length of marine cable installed is MI technology.

XLPE is a solid dielectric of high resistivity. It is this latter property which allows it to become polarised after a time; this causes the build-up of space charges in the insulation and consequent distortion of the electric stress distribution. According to [3], "This phenomenon manifests itself in a significant reduction in the dc and impulse electric strength of the insulation when the temperature increases, and a 30-40% decrease in the dc electric strength when the polarity is reversed." It is also stated in [3] that "Recent progress in the development of modified XLPE using special 'functional groups' [6] has been successful in solving the space charge problem." A few schemes which use the modified XLPE technology have now been built. It is understood that the highest voltage used so far with XLPE is 200 kV at 200 MW/cable. According to [1], 500 kV, 1 000 MW/cable (2 000 MW/bipole) XLPE cable schemes could be , which developed within "the next 5 years". To date, only MI cables have been used at the 500 kV, 1 000 MW/ bipole level.

The main reasons for the use of XLPE in preference to MI, for both submarine and land applications are:

Advantages of XLPE with respect MI:

- Its speed of fabrication and relative ease of fabrication.
- Relative lack of maintenance after installation.
- More robust mechanically
- Longer lengths between cable joints.
- A regards land applications, XLPE cables with aluminium conductor are lighter than copper-conducted submarine XLPE or MI types.
- For land applications, pre-moulded joints are available.

Disadvantages of XLPE with respect to MI:

- Susceptible to the phenomenon of space charge retention in the dielectric.
- Because LCC systems undergo polarity reversals, XLPE cables can generally only be used in VSC schemes (MI can be used in both).
- As the service history of XLPE is short, there may be some risks in predicting what its performance might ultimately be (the service history of MI is long and well-quantified).

5. CONCLUDING REMARKS

This paper has given a brief introduction to an important trend in HVDC technology; it is hoped that the material presented – incomplete though it is - has been interesting and informative.

It is furthermore hoped that the new insights hereby given into VCS-HVDC cable technology may stimulate investigations into possible and appropriate local applications of this technology.

Finally, it is suggested that developments in this technology should be closely tracked.

6. REFERENCES

- [1] Report on Offshore Transmission Technology. Prepared by the Regional Group North Sea for the NSCOGI (North Seas Countries' Offshore Grid Initiative). Published by the European Network of Transmission System Operators for Electricity ('entsoe' (sic)), Brussels, Belgium, 24.11.2011, (UPDATE 16.10.2012).
- [2] Andersen B., VSC HVDC Transmission, In: HVDC Power Transmission: Basic principles, planning and converter technology, Johannesburg, Crown Publications on behalf of Eskom Holdings SOC Ltd, 2 October 2012, Chapter 21.
- [3] EPRI Underground Transmission Systems Reference Book: 2006 edition. EPRI, Palo Alto, 2007.
- [4] Klüss J.V., HVDC historical advances: development review of high voltage dc transmission – Early stages to modern day application, Aalto ELEC, Department of Electrical Engineering, University of Aalto, Helsinki, 31 March 2011.
- [5] M.Satoru *et al.*, Development of XLPE cable under dc voltage. Paper B7.3, JiCable Conference, France, 1999.
- [6] HVDC: connecting to the future. Published by Alstom, 3, André-Malraux, 92309 Levallois-Perret Cedex, France, 2010.
- [7] CIGRE, Recommendations for mechanical tests on submarine cables, Electra no. 171, 1997.

- [8] JiCable Conference, Perpignan, France, 18 – 20 November, 2013.

INFLUENCE OF THE PERMITTIVITY AND RESISTIVITY ON THE ELECTRICAL STRESS IN MULTI-LAYER INSULATION SYSTEMS AT DIFFERENT FREQUENCIES.

T. Joubert* and J.J. Walker**

* Vaal University of Technology, Dept. of Power Engineering, Faculty of Engineering and Technology, Andries Potgieter Blv, Vanderbijlpark, South Africa E-mail: theresa@vut.ac.za

** Visiting Professor at VUT and Director – Walmet Technologies (Pty) Ltd, Vereeniging, South Africa E-mail: jerryw@vut.ac.za

Abstract: Field testing of insulation is normally done with the application of a DC voltage (Insulation Resistance) or very low frequency (VLF) due to the bulk of a test system that can test at rated frequency. It is therefore necessary to understand the behaviour of multi-layer insulation systems when a test is performed at a frequency lower than the rated frequency in order to do a sound evaluation of the condition of the insulation. This paper describes the mechanisms involved in the stress distribution in multi-layer insulation systems and will indicate the lowest test frequency that represents a test at rated frequency.

Keywords: Multi-layer insulation, cable accessories, permittivity, resistivity, conductivity, interfacial polarization, dielectric.

1. INTRODUCTION

Medium voltage cables and the accessories (joints and terminations) form a critical part of the power delivery system. As the systems ages the dielectric properties change such that it provides a very convenient way to monitor the degradation of the system insulation [1].

The final construction of medium voltage cable accessories consist of multi-layer insulation (XLPE, high permittivity stress relief material and an insulation tube) as found in heat shrink terminations. Figure 1 show the termination model used in this study.

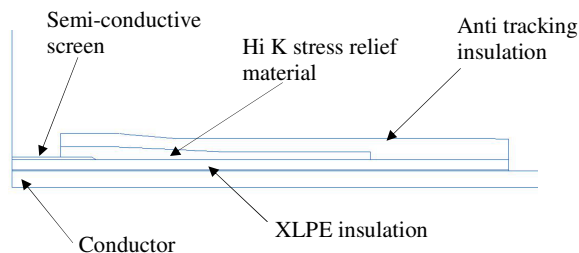


Figure 1 Termination model

This paper will report on the theoretical investigation using Quickfield™ finite element analysis software (FEA) for simulations on the voltage and stress distribution in medium voltage cable joints. The model of the termination used for this study was not drawn to exact scale but the dimensions used are only an approximation of the material thicknesses in a typical termination on a 95mm², 11 kV

cable. The problem was defined as an axis-symmetrical type and therefore only the top half of the termination in the length was drawn. The values for the electrical properties of the insulation materials used for the simulation are given in Table 1.

Table 1 Material Properties

Material	Permittivity (ϵ_r)	Conductivity (σ)
XLPE	2.5	1×10^{-14}
Heat Shrink Insulation	2.5	1×10^{-10}
Stress Control	22	1×10^{-11}

It is desirable that the applied voltage shall simulate the stresses that will occur during the normal operation of the cable, the test voltage is usually higher than the normal operating voltage [2]. The simulations were performed with an applied voltage of $2U_0$ and the instantaneous values of the voltages and stresses were determined, using the Transient AC Conduction solver of the software, at time intervals during one complete cycle for both 50 Hz and 0.1 Hz (VLF). The magnitudes of the voltages and stresses given below are therefore maximum values and not r.m.s values.

Figure 2 show the contours across the insulation layers in the termination where the voltage and stress profiles were simulated. The measurement of the voltage and stress

along the contours start at the high voltage electrode and extend through the XLPE, Hi K and insulation material into the air. The graphical results therefore also show the voltage and stress in the air around the termination. Voltage and stress values are shown in the different materials as a function of the distance from the high voltage electrode for all three locations. The voltages at the XLPE / Hi K and Hi K / Insulation interfaces are also shown as a function of time.

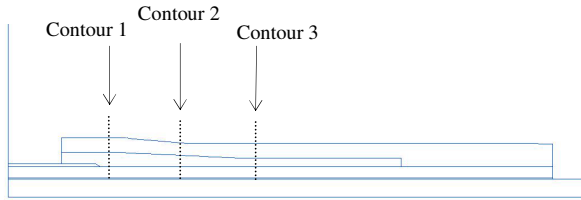


Figure 2 Measurement locations

2. RESULTS

The simulated values of voltages and stresses at contours 1 and 3 for the application of 50 Hz and 0.1 Hz voltage at contours 1 and 3 are given in this section.

2.1 Voltage profiles at 50 Hz

Figure 3 (a) and (b) show the 50 Hz voltage profiles at contours 1 and 3 respectively.

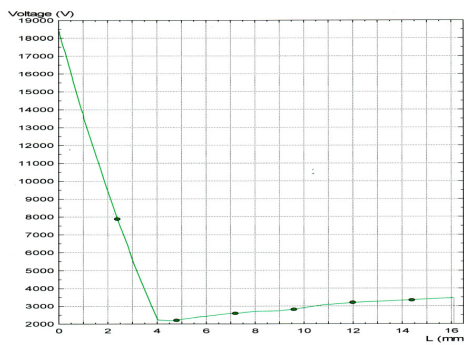


Figure 3 (a)

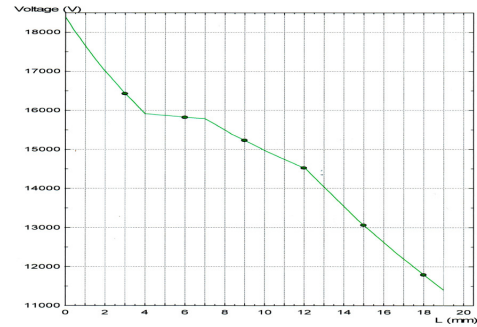


Figure 3 (b)

2.2 Voltage profiles at 0.1 Hz (VLF)

Figure 4 (a) and (b) show the 0.1 Hz voltage profiles at contours 1 and 3 respectively.

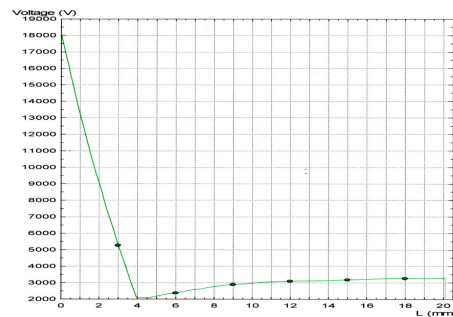


Figure 4 (a)

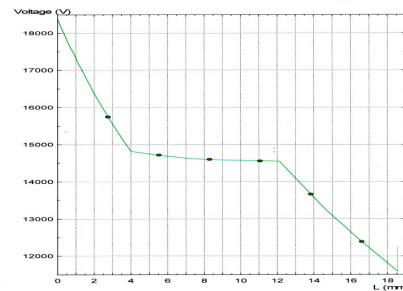


Figure 4 (b)

2.3 Stress profiles at 50 Hz

Figure 5 (a) and (b) show the 50 Hz stress profiles at contours 1 and 3 respectively.

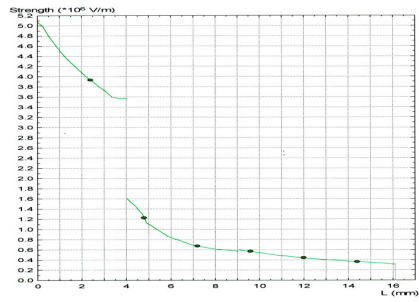


Figure 5 (a)

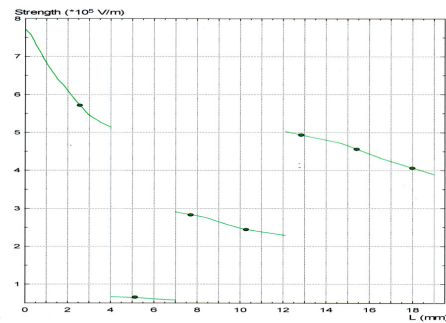


Figure 5 (b)

2.4 Stress profiles at 0.1 Hz

Figure 6 (a) and (b) show the 0.1 Hz stress profiles at contours 1 and 3 respectively.

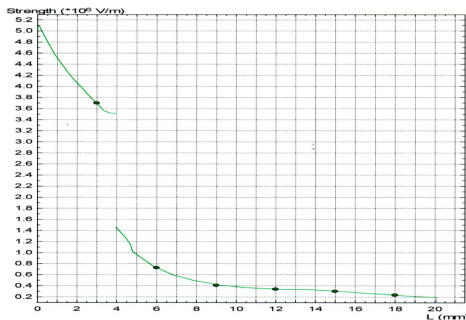


Figure 6 (a)

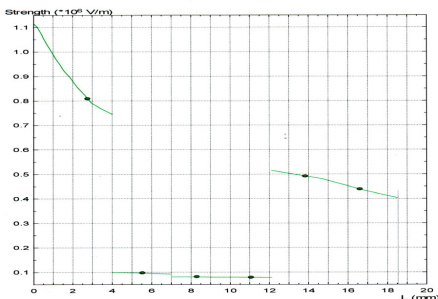


Figure 6 (b)

2.5 Voltage waves in XLPE and Hi K materials

Figure 7 (a) and (b) show the voltage waves in the XLPE and Hi K materials at 50 Hz and 0.1 Hz respectively.

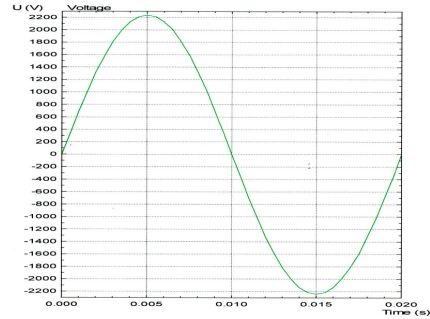


Figure 7 (a)

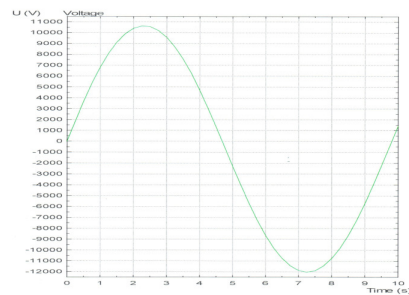


Figure 7 (b)

3. DISCUSSION

At contour 1, which is close to the semi-conductive material cut-back, the difference between the voltages and stresses measured at 50 Hz and VLF respectively is very small as most of the stress is still in the XLPE and the high permittivity material has minimal effect. This can clearly be seen in Figures 3 and 4.

When the voltages and stresses are calculated further away from the semi-con cut-back, the differences between the voltage and stress distribution in the termination become significant. It can be seen that the voltage across the XLPE insulation with VLF applied is larger than when 50 Hz voltage is applied. With an applied voltage at higher frequencies the permittivities of the materials determine the voltage and stress distribution. When low frequencies are applied the volume resistivity of the materials determines the voltage and stress distribution in the multi-layer insulation system.

Consider a two layer insulation model. When a direct voltage is applied across the combination the voltage distribution (at $t=0+$) will be:

$$V_1 = \frac{C_2}{C_1 + C_2} xV \quad (1)$$

and,

$$V_2 = \frac{C_1}{C_1 + C_2} xV \quad (2)$$

When the steady state is reached at $t=\infty$ the voltage distribution will be:

$$V_1 = \frac{R_1}{R_1 + R_2} xV \quad (3)$$

and,

$$V_2 = \frac{R_2}{R_1 + R_2} xV \quad (4)$$

Figure 7 also show a phase shift to occur in the high permittivity and anti-tracking insulation. This is explained by [3] as one of the processes that take place in multi-layer dielectrics being interfacial polarization, also known as space charge polarization. Interfacial polarization arises as a result of accumulation of charges locally as they drift through the material. With interfacial polarization large scale distortions of the field takes place as charges pile up in the volume or on the surface of the dielectric mainly due to change in conductivity that occurs at boundaries and imperfections such as cracks and defects [3]. During the transition period from high frequency to steady state DC the relaxation time for interfacial polarization can be as large as a few seconds in heterogeneous and semi-crystalline polymers [3].

It is further shown by [4] that as the frequency of the supply voltage is reduced and at a certain frequency the influence of the conductivity of the materials will become more dominant and other processes like interfacial relaxation has a bigger effect on the charge distribution. The frequency at which the volume resistivity of the materials starts playing a dominant role is approximately 10 Hz [1]. The frequency for sinusoidal test voltages where no phase shift will occur is a function of the conductivity and permittivity of the materials and will not be a constant for all terminations.

4. CONCLUSION

When high voltage commissioning tests and control tests after a repair is done on cables, it will always be done with the cables connected to the accessories and the accessories will therefore also be tested. Evaluation of the most appropriate test voltage, frequency and wave shape must not be done on the effect on the XLPE insulation only but

it should also consider the effect on the joints and terminations.

The ideal test frequency and wave shape should stress the cable and terminations the same as under normal operating conditions and based on the model used for the simulations only sinusoidal voltages at frequencies above 10 Hz will actually stress the cable termination similar to operating conditions.

The effect of the phase shifts of the stresses on the suitability of sinusoidal voltages below 10 Hz and especially at 0.1 Hz will form part of further studies.

References

- [1] J. Hernandez, N. Hampton, R. Harley and R. Hartlein: "Practical issues regarding the use of dielectric measurements to diagnose the service health of MV cables", JiCable, 2007.
- [2] SANS 10198-13, "The Selection, Handling and Installation of Electric Power Cables of Rating not exceeding 33 kV. Part 13: Testing, Commissioning and Fault Location", Edition 1, 1988.
- [3] G, Raju: "*Dielectrics in Electric Fields*", Marcel Dekker, chapter 4, 2003.
- [4] J.J. Walker: "Electrical Stress Distribution in Cable Accessories when Testing at Different Frequencies", *International Conference on High Voltage Engineering & Applications Proceedings*, New Orleans, pp. 152-156, October 2010.

ASPECTS OF THE ELECTROMAGNETIC ENVIRONMENT IN TRACTION SYSTEMS

J. Clay** and I. Hofsjer*

**University of the Witwatersrand, School of Electrical and Information Engineering, Johannesburg.*

***Transnet Freight Rail, Technology Management, Traction Technology, Johannesburg.*

Abstract: The electric railway environment has long been considered electromagnetically unfriendly and has been plagued by electromagnetic interference. Recently, it has been found that a substantial percentage of return current flows through the couplers of moving trains. This document aims to provide an understanding of the electromagnetic environment surrounding traction systems, through the process of a literature review, which will act as a foundation for further research into these coupling currents. Traction supply infrastructure, typically found in the South African environment, is described at a high level. The sources and mechanisms of transfer of electromagnetic interference are discussed. The problem of stray currents, particularly in Direct Current infrastructure, is documented, as well as methods of minimizing stray current originating from traction supply systems. Finally the path of return currents through the couplers is reviewed. The need for further in-depth research as to the causes and mechanisms resulting in this current through trains is concluded.

Key words: Electromagnetic Interference, Traction, Stray return current, Coupler current.

1. INTRODUCTION

The railway industry has developed from primitive beginnings of steam powered engines to the advanced electronically controlled induction traction motors found in today's modern locomotives. However, these great strides in technology have not come without cost. Electromagnetic Interference (EMI) in railway infrastructure has been one of the hurdles which we have faced due to our advances and one which we still face today. This interference plagues the railway signalling system and various methods to reduce electromagnetic interference have been employed to minimize their effects.

The question of alternative means of traction is raised, given these difficulties introduced by the use of the electric locomotive. The use of diesel locomotives would alleviate these EMI issues that electric locomotives introduce. Not only would the problem of EMI be solved, but the phenomena of corrosion in metallic and reinforced concrete structures in close proximity to the railway line would no longer be of concern. Further, the capital outlay would be considerably lower for diesel traction as the catenary infrastructure would no longer be required.

However, the efficiency of electric locomotives cannot be ignored [1]. Heavy haul railways which are consuming large amounts of power often prefer electric traction due to the substantially lower running costs.

It has recently been found that the current distribution, in the immediate vicinity of the train, across the return paths to the substation is not as predicted or assumed. Substantial current has been found to flow through the train itself.

In the past, this has not been a topic of concern as there have only been a few negative results noticed. However, the value of the information that could potentially be extracted from monitoring these current distributions has also not been explored. Thus, developing a model to describe the current distributions and the influences thereof can prove beneficial, and is the reasoning behind this research.

2. TRACTION SUPPLY INFRASTRUCTURE

Apart from a minority of exceptions such as three-phase electrification, two types of supply infrastructure are used in electric railway systems. These are single phase Alternating Current (AC) supply and Direct Current (DC) supply [2], [3].

The original advantage of DC infrastructure was that vehicle mounted equipment was minimal. DC traction motors could be powered directly from the supply voltage in series for slow speeds and parallel for high speeds [3].

The voltage levels for the AC infrastructure are typically 25 kV or 15 kV with the less common 50 kV also being used in some areas. The operating frequency is mainly 50 Hz or 60 Hz, which is dependent on the national grid supply frequency [2], [3]. Some of the older infrastructure operates on 16 $\frac{2}{3}$ Hz and 25 Hz in order to enable the operation of older locomotives which use DC traction motors and older on-board converter technologies [2], [3].

Higher voltage infrastructure has proved more economical for heavy-haul railways as a lower current is drawn for the same amount of power consumed. This lower current results in lower i^2R losses in the supply system.

DC voltage levels range from 500 V mostly found on tramway systems to the most common 3 kV [2].

The South African freight rail network consists mainly of 3 kV DC infrastructure, constituting more than 13 000 km of track. The DC substations can be found at an approximate spacing of 10 km as well as single-phase 25 kV AC at 50 Hz. Less common is the single-phase 50 kV AC at 50 Hz supply infrastructure which services the rail line between Sishen and Saldanha [1].

3. ELECTROMAGNETIC INTERFERENCE (EMI) IN TRACTION SYSTEMS

Neglecting electromagnetic interference in railways systems would prove to be dire to the point of halting operations due to the importance of the signalling systems and on-board electronics. It is thus very important to identify and understand the sources which can introduce a resonant phenomenon [4].

Electromagnetic interference can be defined as the appearance of any unwanted voltage or current or electromagnetic field which is generated by one system in another. The system generating the disturbance is referred to as the source, and the system affected, the receiver [5].

The railway environment is generally classified as electromagnetic interference unfriendly due to its amalgamation of power, information and communications [4]–[6].

R. Hill (1997), in his paper *Electromagnetic Compatibility – Disturbance Sources and Equipment Susceptibility* [5] presents the idea that EMI in railway traction systems can be categorised into three specific groups, these being:

- (i) Internal Interference:
 - This is interference in railway systems caused by railway systems themselves. An example of such would include interference in the safety signaling system caused by the traction power supply system.
- (ii) Outgoing Interference:
 - This is interference in external systems which is caused by railway systems. Stray or leakage currents (discussed further in section 5) causing corrosion or interference in electrical equipment is a prime example of outgoing interference.
- (iii) Incoming Interference:
 - This is interference received by railway systems caused by external systems. The transmission of utility power in proximity to the railway which can cause interference in the railway signaling systems.

In addition to the malfunctioning of railway systems, EMI can also pose a risk to safety. High step and touch potentials as a result of EMI, are a risk to personnel [5].

Modern locomotives which make use of switching electronics can cause over-voltages and power quality degradation [5], [7]–[9]. These can affect electrical equipment and cause premature failure due to insulation breakdown [7].

Electromagnetic Interference is a result of the coupling between the EMI source and the receiver. The principle coupling mechanisms are [6]:

- (i) Conductive (galvanic) Coupling:
 - Galvanic coupling is found when the source and receiver share a conductor. Signaling circuits are often plagued with EMI as they generally share the running rails, as a conductor, with the traction supply system.
- (ii) Inductive Coupling:
 - Changes in the magnetic flux caused by the source can induce $L \cdot di/dt$ voltages in the circuitry of the EMI receiver. Two parallel conductors are a prime example of equipment susceptible to inductive coupling.
- (iii) Capacitive Coupling:
 - Capacitive coupling can either be static where a high voltage conductor and a nearby metallic object form a capacitive potential divider, or dynamic, where the changes in the electric field result in $C \cdot dV/dt$ currents in the circuitry of the EMI receiver.
- (iv) Radiative Coupling:
 - EMI can result from high frequency effects such as arcing and/or fast current of voltage switching.

In order to address and/or minimize electromagnetic interference in the railway environment, the possible sources of internal and outgoing EMI should be identified. Such sources could include, however are not limited to [5]:

- (i) Rectifier Substations (discussed further in section 4):
 - Switching transients originating in the pulse rectifiers in DC traction substations introduce EMI into the traction supply. Further, an imbalance in the rectifier circuit, different magnitude in the incoming power supply phases or abnormal operating conditions can also lead to EMI being introduced into the system.
- (ii) Transformer Substations:
 - The three-phase transmission lines feeding the AC traction substations could be carriers of EMI which will be introduced into the traction supply system through the AC transformers. This EMI found on the three-phase transmission line can be a result of corona discharge or nearby conductors, or partial discharge or micro-arcs at metallic contacts or across insulator surfaces.
- (iii) Transmission of Traction Power:
 - Earth leakage or stray currents can be considered receivers of EMI, but their existence can also be the source or EMI. The insulators found in the traction supply infrastructure are also susceptible

to partial discharges across their surfaces which could result in EMI in neighboring systems.

(iv) Locomotives:

- Power electronic devices utilizing switching or high currents to convert power to traction motors can be the source of EMI. Further, EMI from arcing caused by pantograph jump, main circuit breaker operations, or the commutators of DC traction motors is also possible.

(v) Signaling or Track Side Equipment:

- Stereotypically, signaling and track side equipment are EMI receivers, however in some situations they can act as the source of EMI.

Zhezhelenko, et al. (2009) [7] wrote a paper which focused on the possible solutions of resonant modes found in single phase AC railways. The need to damp these resonant modes arose from the risk of electrical equipment failure due to high levels of harmonic distortion and voltage imbalance [7].

Three solutions to damp resonant modes are brought forward by Zhezhelenko, et al. [7]. The first solution is the installation of a first-order RC filter on either the locomotive or the substation. The surge impedance termination of a second-order RLC filter is provided as a second solution. Zhezhelenko, et al. proposed that this filter be installed at the open end of the traction section. The second-order filter has a lower filter resistor current and hence the electrical rating of filter components is reduced as well as the losses. The third solution suggested by Zhezhelenko, et al. is the combination of an active power filter and a passive RLC filter installed at the end of the traction feeder.

The resonant modes occur at frequencies defined by the length of the traction network, regardless of the locomotive position in this network. Zhezhelenko, et al. suggest that these frequencies decrease with increasing feeder lengths but lie typically in the range of 2 – 30 kHz [7].

S. Baranowski, et al. (2012) [4] provided a model and simulation of the transient noise created by a substation. Their measurements were performed with varying currents and analysed in the time and frequency domain [4]. One of their findings is that a nominal current directly affects the transient voltage levels at frequencies below 40 kHz but seemed to have no direct relationship at frequencies above 40 kHz [4].

In the paper by K. Yuuki, et al. (2010) [10] EMI is classified into two groups or frequencies as follows:

(i) Frequencies less than 10 kHz:

- These harmonics on the catenary line are usually caused by the high frequency switching of the power conversion units (inverters and converters) on board the locomotives.

(ii) Frequencies less than a few MHz:

- These frequencies are typically a result of common mode current. These currents can cause stray capacitances.

Yuuki, et al. suggest that for EMI with frequencies around 100 kHz, the common mode current is usually the dominant cause [10].

4. SUPPLY SYSTEM CONFIGURATION

The typical railway supply infrastructure consists of substations, connected to the national grid, which supply power to an overhead line or catenary system, with the running rails acting as the return conductor [2], [3], [6].

AC sections are separated by “neutral sections” or “dead sections” to avoid circulating AC currents, whilst DC sections are continuous with substations feeding the catenary in parallel [2]. This means that should a substation in a DC section fail, it can be isolated from the catenary, and the next substation will supply power to the section. However, if an AC substation fails, the section which that particular substation was supplying power to will remain unpowered until the problem is rectified. Figure 1 and Figure 2 describe the simplified equivalent models for the AC and DC traction supply systems respectively.

Alternative supply and return conductors such as a third rail supply are used however these are not as common as the above mentioned. This being said, it is common for a return conductor which is connected to the return rails to be connected at regular intervals [2], [3], [11].

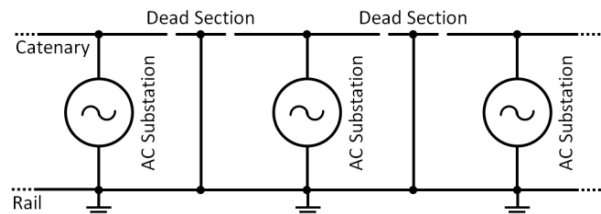


Figure 1: Diagram illustrating a simplified equivalent model of the AC traction system.

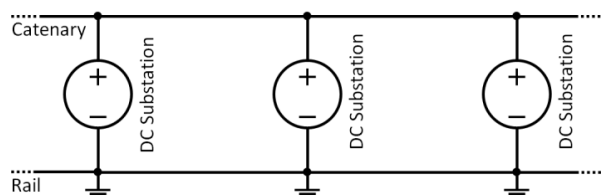


Figure 2: Diagram illustrating a simplified equivalent model of the DC traction system.

Expanding the model for the DC traction supply system, it must be noted that the DC traction power is rectified from the three-phase AC utility supply. This rectification is often performed through the use of six, twelve or twenty four pulse circuits [3]. As a result of this means of

rectification, regenerated power from the locomotives in braking cannot be transferred back onto the national grid or utility supply [3]. This can be seen graphically in Figure 3.

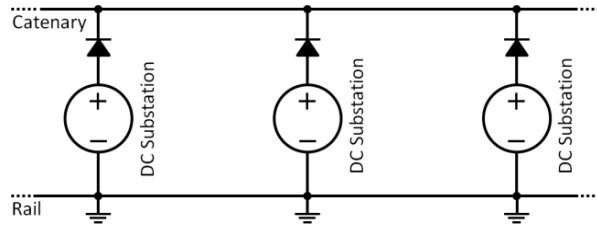


Figure 3: Diagram illustrating a simplified equivalent model of the one way DC traction system.

During rectification of the AC power to DC power, harmonics are introduced on the catenary supply due to these pulse circuits. In an effort to reduce these harmonics, series resonant filters are installed at the output of the rectifiers in the South African railways. The resonant frequencies of these filters is typically 600 Hz, 1200 Hz and in some cases 2400 Hz [1]. Figure 4 shows the equivalent circuit model of the typical harmonic filter installed at the outputs of the DC substations in South Africa.

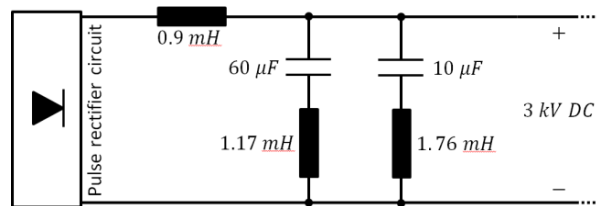


Figure 4: Diagram illustrating the equivalent circuit model of the typical harmonic filter at DC substations in South Africa adapted from [1].

5. STRAY RETURN CURRENTS

Stray return currents can cause damage to metallic objects in proximity to the railway as well as being environmentally undesirable. Stray currents can cause erosion of metallic objects such as water pipes through the mechanism of electrolysis [2], [3], [6], [8], [11]–[16]. Current will flow through the path of least impedance, whether it be the intended path or otherwise [13]. It is for this reason that stray currents must be mitigated as far as possible.

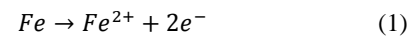
Stray return currents resulting from electric railway installations have been widely documented [2], [3], [6], [8], [11]–[16]. Despite this, it proves difficult to accurately model stray return currents as an equivalent electrical circuit due to the complexity of the phenomena, and that the model would be restricted to only very simple geometry [13], [16].

5.1 Stray Currents in DC Infrastructure

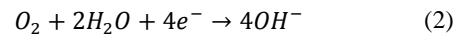
Stray current is closely related to the DC railway infrastructure. The DC railway typically uses the running rails as a return path for the current due to economic reasons. Because of this there is a resultant voltage drop on the running rails which alludes to stray current leaking onto the earth and imbedded structures in the earth [12]–[14]. These stray currents play a major role in the corrosion of rails and buried metallic structures in proximity of the railway. Additional to causing undesirable corrosion of metallic objects through the mechanism of electrolysis, these stray currents can also result in interference with signalling systems [12].

In order to form a brief understanding of the mechanism of corrosion, one must momentarily delve into the field of chemistry and the methods of conduction for different materials. In metallic conductors, the current flow is electronic meaning that charge is transferred through the flow of electrons. However, current flow in electrolytes, such as earth and concrete, is ionic. This means that for leakage current in DC systems to occur, an electron to ion transfer must occur as the current leaves the rails and enters the earth [14]. It must be stated that this electron to ion transfer occurs during direct current leakage such as that typically found in DC traction supply systems, and not during the induced effects found in AC traction supply systems.

When current leaves the rail to the earth, oxidation or an electron producing reaction occurs [14] and can be seen in equation (1) below. Should this reaction be frequent, it will become viable as corrosion.



In contrast, when the leakage current returns to the rail, an electron-consuming reaction occurs. Should this reaction take place in an oxygenated environment [14], which is typically the case, it can be described by equation (2).



An iron-reduction reaction is not thermodynamically preferred and so iron does not generally plate onto the rails when current returns to the rails.

From these chemical equations it is evident that corrosion will occur at instances where current leaves a metallic object into an electrolyte, however not when current enters a metallic object from an electrolyte.

In the paper compiled by M. Alamuti, et al. (2011) [12] four methods of decreasing the leakage or stray current to earth is suggested. The first is to decrease the rail resistance and hence the voltage drop across the running rails. The second is by increasing the rail-to-earth resistance and minimizing the opportunity for current to

leak into the earth. Thirdly, Alamuti, et al. suggest designing systems with a higher operating DC voltage and thus a lower return current for the same amount of power. Lastly, it is suggested that the traction substations be located closer to one another, however this greatly increases the construction costs of the railway [12]. These four methods of reducing leakage current in DC traction supply systems are echoed and supported by I. Cotton, et al. (2005) [14].

Closely related to the rail-to-earth resistivity, there exist various earthing schemes of the traction supply system. These include solid earthed, diode earthed, floating and thyristor earthed schemes [12], [14]. The various earthing schemes are graphically described in Figure 5.

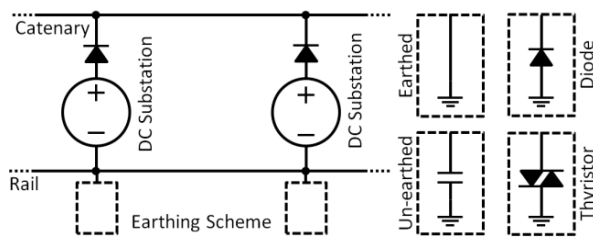


Figure 5: Diagram illustrating a simple equivalent model of the DC traction system

The first earthing scheme detailed is the unearthed scheme. In this scheme, the rails have no intentional connection to the earth thus creating a floating rail. This means that a high rail-to-earth impedance exists which limits stray current [12], [14].

As an opposite of the unearthed scheme is the directly earthed scheme which reduces the rail voltage, thus assisting in meeting safety requirements. Its main objective is to guarantee circuit continuity and also to ensure that personnel in the vicinity of the railway cannot be exposed to dangerously high voltages [12]. It is found that this scheme has many stray current problems [12].

Alamuti, et al. performed simulations which indicated that there is a strong correlation between the stray currents and the rail potentials in both earthed and unearthed schemes. This relationship was found to be linear [12]. This notion is also detailed by I. Cotton, et al. (2005) [14] in their paper *Stray Current Control in DC Mass Transit Systems* and R. Hill (1997) [6] in his paper *Electric Railway Traction – Electromagnetic Interference in Traction Systems*.

Considering an example of a locomotive drawing 1000 A, located 1000 m from the DC substation and the rails having a resistance of 20 mΩ/km. Through the use of Ohm's law it can be deduced that there will be a voltage drop of 20 V/km of track. Depending on whether the earthed or unearthed scheme is employed, this voltage can appear in one of two ways.

In the unearthed scheme, where the rails and the negative DC bus are "floating", this voltage drop of 20 V/km will be seen as a rail voltage of 10 V to remote earth at the locomotive and -10 V to remote earth at the DC substation.

However, in the earthed scheme, where the rails and the negative DC bus are connected to ground, this voltage drop of 20 V/km will be seen as a rail voltage of 20 V to remote earth at the locomotive and 0 V to remote earth at the DC substation.

The polarity of the potential between the rail and remote earth will determine direction in which the leakage current will flow.

If we assume that the voltage drop per meter is linear as per the papers of M. Alamuti, et al. (2011) and I. Cotton, et al. (2005), we will notice that voltage to remote earth midway between the substation and the locomotive will be 0 V for the unearthed scheme. This means that from the locomotive to midway, there will be a positive potential between rail and remote earth resulting in leakage current flowing from the rails and causing corrosion. From the midway to the substation, the a negative rail to remote earth potential will exist causing leakage current to flow back from earth into the rails. It should be noted that based on the chemical reactions detailed by equations (1) and (2), no corrosion of the rails will occur from midway to the substation.

However, in the earthed scheme, the rail remote earth potential is positive for the length of the track. This results in leakage current from the rails to the earth for the entire length between the locomotive and the substation, causing corrosion of the rails over the entire distance [14].

The third earthing scheme identified by Alamuti, et al. and Cotton, et al. is the diode-earthed scheme. Alamuti, et al. state that recent practical and theoretical studies have shown that in this scheme, high touch potentials as well as stray currents may exist simultaneously [12]. The negative busbar at the traction substation is connected to the earth through diodes in this scheme. The diodes act to limit rail voltage by providing a short circuit path to earth whenever the rail voltage exceeds the diode's threshold [12]. The use of stray current collection mats located beneath the track at regular intervals as well as beneath the substation is employed [12]. The diode-earthed scheme allows for current to flow back from the earth or current collector mats and prevents traction current flowing into the earth of current collection mats [12].

Finally, the thyristor-earthed scheme is highlighted by Alamuti, et al. In this fourth scheme a floating negative automatic earthing switch is created. This earthing switch consists of DC voltage and current monitoring circuits as well as two thyristors which provide bi-directional controlled current flow [12]. These are all located at the

traction substation. The scheme acts to limit the rail voltage by activating the corresponding thyristor. The activation of the thyristors is dependent on the polarity of the rail potential. The activated thyristor continues to allow current flow until the current reduces to zero or the polarity reverses across the thyristor [12].

The results of the simulations performed by Alamuti, et al. indicate that the corrosion hazard in unearthed schemes are approximately eight times that of solidly earthed schemes [12].

After comparing the results of their simulations, Alamuti, et al. concluded that the diode-earthed scheme results in the highest level of rail-to-earth voltage followed by the unearthed scheme and thyristor-earthed scheme. Unsurprisingly, this leaves the earthed scheme with the lowest rail-to-earth voltage [12].

Alamuti, et al. state that the most hazardous stray current resulting in corrosion of metallic objects initiates from a negative rail voltage [12] which is proved by equations (1) and (2) due to the direction of current flow. From their simulations, the unearthed scheme provides the best protection against stray currents and their effects. This is followed by thyristor-earthed, diode-earthed and solidly-earthed schemes respectively [12].

From their paper, it can be seen that a trade-off exists between the stray current levels causing corrosion and the rail voltage levels required to meet safety regulations [12]. This is verified by Hill in his paper detailing traction power supplies [3] and L. Ardizzone, et al. (2003) in their paper about electric traction and electrolytic corrosion [13].

Apart from the various earthing schemes to balance the trade-off between rail voltage and leakage currents, the solution of stray or leakage current collection systems is brought forward by I. Cotton, et al. (2005) [14], F. Fichera, et al. (2013) [15] and N. Dekker (1999) [16]. The concept behind the stray current collection systems is to “catch” any leakage current prior to causing corrosion damage to nearby metallic objects. This current catching infrastructure is often the reinforcements in the concrete track bed. The reinforcement is bonded along its length to provide a continuous path for current to the substation. In order to avoid corrosion of the reinforcement, the reinforcement is deliberately bonded to the DC negative bus at the substation.

5.2 Stray Currents in AC Infrastructure

Although more prevalent in DC infrastructure, stray currents also occur in AC infrastructure. A. Mariscotti, et al. (2005) as well as L. Ardizzone, et al. (2003) suggest that the important parameters which influence the amount of stray current are rail-to-earth conductance, earthed return conductors-to-earth conductance and earth resistivity [8], [13].

In their paper, Mariscotti, et al. suggest that the return current of traction systems can be characterized by a set of transfer functions which depend on frequency, geometrical arrangement of conductors, the earthing arrangement, distance between the locomotive and the measuring point, feeding arrangement, leakage to earth of the rails and earth conductivity [8], [9]. Further, in their analysis, the traction line is modelled as a Multiple Transmission Line (MTL) which achieves an accuracy level of within 20% in the frequency range of 50 Hz - 50 kHz [9].

Preliminary investigations by Mariscotti, et al. indicate that the dielectric constant of soil can vary capacitance terms, between overhead conductors and rails, by less than 10%. Larger variations are expected to be seen in rail-to-earth and rail-to-rail capacitance terms [8].

Conclusions made by Mariscotti, et al. suggest that the amount of stray current for the low frequency range is proportional to the conductance-to-earth of the return conductor [8].

In AC infrastructure, two alternative configurations to the simple configuration are employed to mitigate stray return currents. These are the use of Booster Transformers and Auto Transformers. The notion behind both these setups is that the transformer is rated at full traction current and acts as a 1:1 current transformer thus forcing the same magnitude of current in the return conductor as is flowing in the supply conductor [2], [3], [6], [11], [17]. This means that stray currents are “forced” to approximately zero. Grounding of the return conductor to the rails at regular intervals is often utilized in the booster transformer scheme. Figure 6 and Figure 7 show the equivalent circuit diagrams and current flow of the booster transformer and auto transformer respectively.

The principles of operation between the booster and auto transformer schemes are contrasting. The booster transformer scheme acts to balance current whilst the auto transformer scheme acts to balance voltages [3].

The booster and auto transformers are installed along the rail line. Booster Transformers are installed typically every 3 km and Auto Transformer every 8 to 10 km.

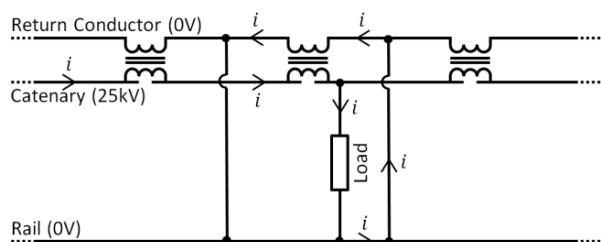


Figure 6: Diagram illustrating a simple equivalent model of a 25 kV AC traction system utilizing the booster transformer scheme.

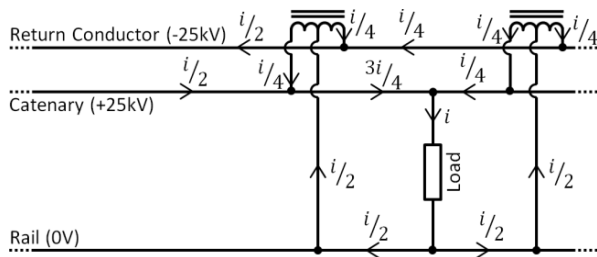


Figure 7: Diagram illustrating a simple equivalent model of a 2 x 25 kV AC traction system utilizing the auto transformer scheme.

6. ELECTRICAL CONTINUITY OF CONDUCTORS

The papers by P. Szacsavay (2011) [2], suggest that the most vulnerable part of the traction return circuit is not the rails but in fact the the bonding cables and connections [2]. These bonds are seen in Figure 6 and Figure 7 as the connection between the rail and the return conductor.

The rails are robust and sturdy when compared to the electrical bonds connecting sections of rails or connecting the rail to the return conductor. Not only are these cables more likely to become damaged, their connections to the rail can also become loose or may not be installed correctly.

Should one of these bonds be missing or faulty, the return current flows along the path of least impedance to the substation, which could consist of the next closest bond or in the form of stray currents.

Szacsavay also recommends that in DC traction systems with the rail as a return conductor, that both rails be used as the return path [2]. This will reduce the impedance of the return conductor and so minimize the voltage drop across the return conductor. Additionally, the second rail as a return conductor redundancy in the event that the electrical connection in the first rail is broken.

7. RETURN CURRENT DISTRIBUTION

Little research into the path of the return current through the train has been conducted, as it has mostly been considered as negligible or having little effect. However, the paper by J. Ekman, et al. (2009) [18] suggests that there is a significant percentage of current in the couplings of the train. The conductive characteristics of wagons and couplings allow for the train to act as an alternative path for return current. Because the current will divide among the available paths based on their impedance. This is illustrated in Figure 8.

Ekman et al. indicate that the current corrosion noticed in the bearings of wagons was as a direct result of this current found in the couplings [18].

Ekman et al. put forward the premise that, at locations where these current appear to be particular high in the

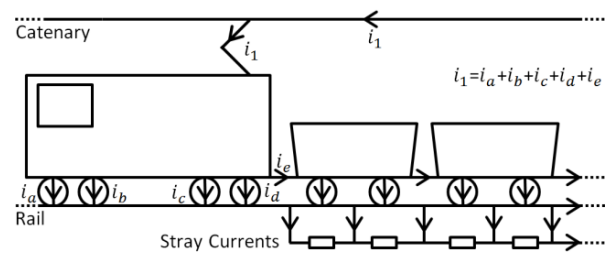


Figure 8: Diagram illustrating the possible return current paths immediately subsequent to the locomotive.

couplings, it could indicate failing, or defective, electrical equipment due to an observed difference in current magnitude resulting from the change in impedance of the return path such as a broken or missing bond.

Another notion that Ekman et al. conveys is that environmental variances could also affect the percentage of return current seen through the couplings of a train. Ekman et al. makes particular reference to changes in the water table [18].

Modern railway rolling stock, particularly some found in the South African environment have electronic systems on board. For example, some wagons have electronically controlled pneumatic braking systems. To achieve this, a signal cable must run the length of the train which provides both power to the electronics as well as transmits braking commands. Because this cable is connected and runs in close proximity to the couplers, current flowing through the couplers can have and has had a noticeable effect on the correct operation of these devices as a result of interference caused by this coupler current.

Ekman et al. proposes a solution to minimize the coupling currents by making the couplings of the electric locomotive electrically isolated from the locomotive itself [18]. This idea removes the conductive path through the coupling and forces return current directly into the rail. One must question whether this is a desirable situation as this offers a quick fix to the damages caused by the current through the couplings but does not address the root cause of the coupling currents.

Interestingly, through Ekman et al.'s experimental research, it was found that a high amount of current returns to the rails through the bearings and wheels of wagons towards end of the train as compared to the wagons closer to the locomotives [18]. This suggests that mutual inductance between the catenary line and the train as well as electrical impedances account for the current distribution through the train [18].

8. CONCLUSION

The importance of addressing Electromagnetic Interference has been described. Typical railway infrastructure has been discussed, as well as the problem of stray currents and methods of minimizing them.

The return current distribution through trains was described at a high level and the need for in-depth research to be conducted thereof explained. Research into the effects of seasonal or environmental changes to the differing levels of current through different locations of the train must be conducted. Further, the causes of return current distribution must be assessed in order to develop a model of these current distributions. This model will assist in realizing the importance of the information that can be extracted from these current distributions.

9. REFERENCES

- [1] B. Steyn, "Electromagnetic Compatibility of Power Electronic Locomotives and Railway Signalling Systems.pdf." Rand Afrikaans University, Johannesburg, pp. 1–262, 1995.
- [2] P. Szacsavay, "THE ELEPHANT and the FLEA LIVING with TRACTION RETURN," no. July, 2011.
- [3] R. J. Hill, "Electric railway traction, Part 3 Traction power supplies," *POWER Eng. J.*, no. December, pp. 275–286, 1994.
- [4] S. (University of L. Baranowski, H. (University of L. Ouaddi, V. (IFSTTAR/LEOST) Deniau, J. (IFSTTAR/LEOST) Rioult, and G. (Alstom T. Nottet, "Modelisation of EM field radiated by catenaries and due to the railway power system," 2012.
- [5] R. J. Hill, "Electric railway traction Part 6 Electromagnetic compatibility disturbance sources and equipment susceptibility," no. February, pp. 31–39, 1997.
- [6] R. J. Hill, "Electric railway traction Part 7 Electromagnetic interference in traction systems," no. December, 1997.
- [7] I. V Zhezhelenko, Y. L. Sayenko, A. V Gorpinich, V. V Nesterovych, and T. K. Baranenko, "Analysis of Resonant Modes in the Single-Phase Industrial AC Electrified Railway Systems," in *Electrical Power Quality and Utilization*, 2009, pp. 9–12.
- [8] A. Mariscotti, P. Pozzobon, and M. Vanti, "Distribution of the Traction Return Current in AT Electric Railway Systems," *IEEE Trans. Power Deliv.*, vol. 20, no. 3, pp. 2119–2128, 2005.
- [9] A. Mariscotti, "Distribution of the Traction Return Current in AC and DC Electric Railway Systems," *IEEE Trans. Power Deliv.*, vol. 18, no. 4, pp. 1422–1432, Oct. 2003.
- [10] K. Yuuki, H. Ueda, S. Shiraishi, S. Koizumi, and I. Yasuoka, "Study of EMI for Direct Drive Motor System in Railway Traction," in *The 2010 International Power Electronics Conference*, 2010, pp. 1609–1613.
- [11] C. Chou, Y. Hsiao, J. Wang, and Y. Hwang, "Distribution of earth leakage currents in railway systems with drain auto-transformers," *IEEE Trans. Power Deliv.*, vol. 16, no. 2, pp. 271–275, Apr. 2001.
- [12] H. Nouri, S. Jamali, and M. M. Alamuti, "Effects of earthing systems on stray current for corrosion and safety behaviour in practical metro systems," *IET Electr. Syst. Transp.*, vol. 1, no. 2, pp. 69–79, Jun. 2011.
- [13] L. Ardizzon, P. Pinato, and D. Zaninelli, "Electric traction and electrolytic corrosion: a software tool for stray currents calculation," pp. 550–555.
- [14] I. Cotton, C. Charalambous, P. Aylott, and P. Ernst, "Stray Current Control in DC Mass Transit Systems," vol. 54, no. 2, pp. 722–730, 2005.
- [15] F. Fichera, A. Mariscotti, I. S. Member, and A. Ogunsola, "Evaluating Stray Current from DC Electrified Transit Systems with Lumped Parameter and Multi-Layer Soil Models," no. July, pp. 1187–1192, 2013.
- [16] N. M. J. Dekker, "Stray Current Control - An Overview of Options," 1999.
- [17] H. Zhengqing, Z. Yuge, L. Shuping, and G. Shibin, "Modeling and Simulation for Traction Power Supply System of High-Speed Railway," Chengdu, 2011.
- [18] J. Ekman and A. Wisten, "Experimental Investigation of the Current Distribution in the Couplings of Moving Trains," *IEEE Trans. Power Deliv.*, vol. 24, no. 1, pp. 311–318, Jan. 2009.

THE SCOPE OF EPPEI-SPONSORED RESEARCH INTO HVDC AT UKZN: A PERSONAL VIEW

* A. C. Britten

* Affiliated to Electrical Engineering, School of Engineering, University of KwaZulu-Natal, King George V Avenue, Glenwood, Durban 4000, South Africa. antony.britten@gmail.com

Abstract: This paper presents the author's personal and considered suggestions for the technical content of the research programme of the HVDC Centre of Specialisation established at the University of KwaZulu-Natal. (It is being funded for five years by Eskom's EPPEI postgraduate education programme.) It is stressed in this short paper that the comments and suggestions made are intended to elicit informed feedback, and in this way to help the newly-appointed convenor of the Centre of Specialisation with the preparation of an overall technical plan. The author's former links with EPPEI and the "old" HVDC Centre (founded in 2000) are briefly described, so as to give some context and credence to his suggestions.

Keywords: HVDC, research, university, Eskom, strategic drivers, line commutated converter, voltage source converter, telecommunications, insulation

1. INTRODUCTION

The occasion of the 22 nd SAUPEC Conference gives an opportunity for the author, who recently retired from Eskom, to express a personal viewpoint on the scope and strategic direction of the HVDC Research Programme now being established at the University of KwaZulu Natal and funded by Eskom's EPPEI Initiative. In doing this, the author also offers some specific suggestions for the technical content of the programme, and identifies the relevant strategic drivers.

The objective of this paper is thus to enable the author to present his views, to stimulate discussion, and to receive informed comment and feedback. The author's wish and expectations are that this exercise will be helpful to the newly-appointed convenor of the HVDC Research Programme, also to the relevant staff at the University of the Witwatersrand in Johannesburg.

2. THE ESKOM EPPEI PROGRAMME [1]

The abbreviation "EPPEI" stands for the "Eskom Power Plant Engineering Institute". Its primary aim is to increase the technical strength and depth of Eskom's engineering resources, by offering junior specialists and engineers the opportunity to earn MSc and PhD degrees by means of full-time study at local universities.

The long-term aim of the EPPEI programme is to help develop the types of skills which Eskom needs, so as to sustain itself as a technical organisation, and to maintain the quality of its product.

The success of this initiative depends critically on the quality of the collaboration between Eskom and the universities. To help achieve this, the following Centres of Specialisation have been created:

- ENERGY EFFICIENCY (University of Cape Town)
- COMBUSTION ENGINEERING (University of the Witwatersrand)
- EMISSIONS CONTROL (North-West University)
- MATERIALS SCIENCE (University of Cape Town)
- ASSET MANAGEMENT (University of Pretoria)
- HIGH VOLTAGE ENGINEERING (HVAC) (University of the Witwatersrand)
- HIGH VOLTAGE ENGINEERING (HVDC) (University of the KwaZulu-Natal)
- RENEWABLE ENERGY (University of Stellenbosch)

Each Programme receives funding for five years. This funding is generous in that it allows senior academic staff to be recruited and retained. The indications so far are that the collaboration is in general going well at UKZN and Wits.

3. THE AUTHOR'S ASSOCIATION WITH EPPEI

The author took part as an Eskom employee in some of the early discussions which eventually resulted in the formation of EPPEI. He was responsible for preparing the first collation of research and investigative projects in the discipline of power station electrical engineering.

He has since contributed to the development of the electrical engineering research topics for transmission and distribution. He has also acted as the industrial mentor for a project on assessing the prospective improvements in the performance of electrostatic precipitators, to be brought about by the use of high frequency, low ripple power supplies.

4. BRIEF OVERVIEW OF THE HVDC RESEARCH CENTRE

The author assisted Professor Nelson Ijumba of UKZN and Mr Logan Pillay of Eskom in setting the technical direction of the HVDC laboratory. It was decided at an early stage in the life of the laboratory that it would concentrate on research into line design and performance topics. The development of a new HVDC programme, however, now makes it possible for the laboratory to re-consider its technical focus.

The author acted as the technical director of the HVDC Centre for several years.

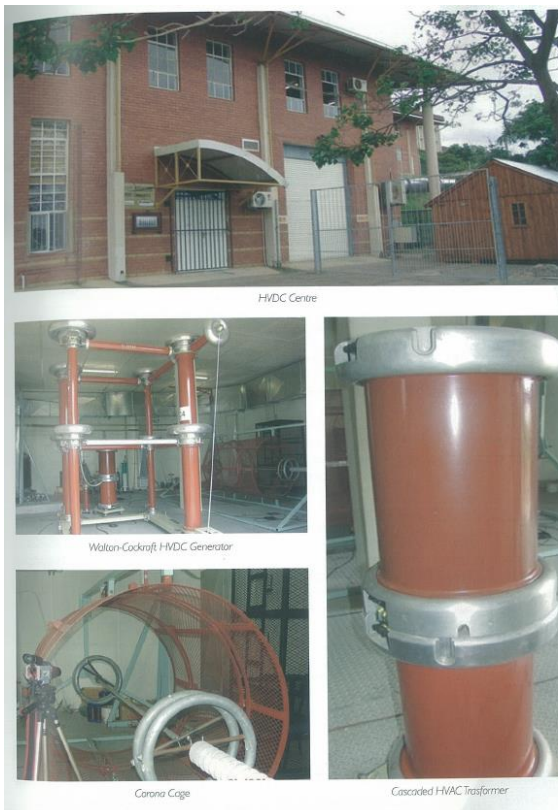


Figure 2: Views of the entrance to the laboratory and various items of equipment [1]

5. STRATEGIC DRIVERS FOR THE HVDC RESEARCH PROGRAMME

The strategic factors which can be said to be driving the EPPEI programme in HVDC are:

- The wide interest in (and curiosity about) HVDC generally, both here in South Africa and world-wide
- The possibility (however remote at this stage) of new long distance HVDC schemes being built in South and Southern Africa (See figure 1.)
- Generous financial support from Eskom

- Major technical developments in HVDC cable technologies, together with significant increases of size of voltage source converters
- The availability of motivated and capable university staff
- The need for Eskom and the South African Electricity Supply Industry to become an informed buyer and user of HVDC technology.

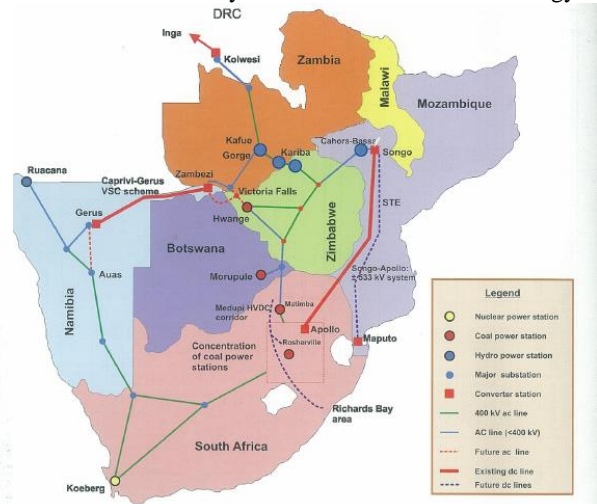


Figure 1: Existing (shown in red) and future (?) HVDC lines in the Southern Africa Grid [2]

6. SUGGESTED TECHNICAL THEMES AND TOPICS [2, 3]

The list of EPPEI research topics, given below, is long and diverse. It will therefore be necessary to rank and prioritise the projects.

The HVDC research themes are suggested to be [2, 3]:

- Long-distance transmission and the provision of telecommunications
- External insulation
- Corona and field effects
- Performance of lines and systems in Southern Africa
- Exploitation of VSC and HVDC cable technology
- Innovation

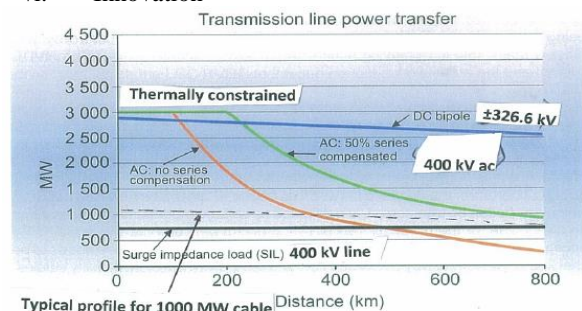


Figure 3: Conceptual profiles of the power transport capabilities of overhead dc lines, ac lines and dc cable

The projects suggested are:

1. Refinement of the design of long-distance HVDC schemes, **theme no (i)**
2. Provision of reliable telecommunications in HVDC systems operating in hostile environments (i)
3. Underlying reasons for, and implications of, anomalous flashovers across line insulators. (This deals with the physical mechanisms of insulator flashover under negative polarity) (ii)
4. Study of the physics of the speculated "fast flashover" mechanism of line insulation breakdown under negative dc polarity (ii)
5. Study of the physics of the conduction and flashover mechanisms of HVDC insulation in the presence of hot fire (ii)
6. Study of the mechanism of pollution flashovers on lightly polluted ceramic and non-ceramic insulators (ii)
7. Study of dc insulation strengths in the presence of live-line tools (ii)
8. Optimisation of line and tower designs in terms of corona and space charge parameters (iii)
9. Determination of air density corrections for corona on conductors (iii)
10. Explaining the physical mechanisms of shield wire corona and its avoidance (iii)
11. Study of the performance of HVDC lines in high lightning areas (iv)
12. Assessments of the performance of regional HVDC schemes (lines and converters); to concentrate on the causes of line faults. (This will be done collaboratively with the field staff concerned.). A specific proposal being made is that the performance of the Caprivi-Gerus 350 kV line should be assessed in this way, and the statistics compared with those of the Cahora Bassa and Inga-Shaba schemes (iv)
13. Study of electric and magnetic field coupling phenomena and interactions on hybrid ac/dc lines (i), (ii) and (iii)
14. Demonstrate the feasibility experimentally of converting a power line from ac operation to dc operation (i), (ii), (iii) and (iv)
15. Quantification and minimisation of line losses, for energy metering purposes (iv)
16. Investigate the feasibility of the possible role of VSC converter and dc cable technology as ultimately being an alternative technique to the use of conventional line commutation converter technology (v)
17. Consideration of the feasibility of the use of long undersea HVDC cables and VSC technology in the Southern African environment – where do the opportunities, if any, lie? (v)
18. Investigation into the feasibility of tapping off small amounts of power, by means of novel

techniques, at intermediate positions along the route of a specific HVDC line (vi).

7. CONCLUDING REMARKS

It is clear that the foregoing themes and topics will need to be analysed further before any specific research can be proposed. Thereafter, suitable topics will require alignment with the human and physical resources available.

It is to be hoped that the projects suggested will attract suitable MSc and PhD students, so as to ensure that the programme has a high impact, both locally and regionally.

It is pointed out finally that this paper does not consider the strategies that will have to be created in order to be able to implement the proposed research programme.

8. ACKNOWLEDGEMENTS

The pioneering spirit and vision shown by Nelson Ijumba and Logan Pillay in the establishment of the HVDC Centre at the Westville Campus of UKZN are hereby acknowledged.

Malcolm Fawkes of Eskom is thanked for the financial support received from the EPPEI Programme, and for the continued moral support given to the author in his new role.

9. REFERENCES

- [1] EPPEI handbook for 2012/13, published by the Eskom Academy of Learning, Dale road, Halfway House, Midrand.
- [2] S. Bisnath et al: *HVDC power transmission: basic principles, planning and converter technology*, Eskom Power Series, published by Crown Publications, first edition, Bedfordview, Johannesburg, October 2012.
- [3] L. E. Zafanella et al: *HVDC transmission line reference book*, EPRI TR-102764, Research project 2472-03, final report, published by EPRI, September, 1993.

Topic C

Power Systems

AN IMAGE PROCESSING METHODOLOGY FOR INSULATOR HYDROPHOBICITY CLASSIFICATION USING FLASH PHOTOGRAPHY

G. W. Blignault* and H.J. Vermeulen**

* Dept. of Electrical and Electronic Engineering, Stellenbosch University, Private Bag X1, Matieland, 7602, South Africa E-mail: 16089111@sun.ac.za

** Dept. of Electrical and Electronic Engineering, Stellenbosch University, Private Bag X1, Matieland, 7602, South Africa E-mail: vermeuln@sun.ac.za

Abstract: The hydrophobicity of an insulator material plays an important role in determining leakage current behaviour and is an important indicator of insulator ageing or degradation. Hydrophobicity classification is primarily performed through human evaluation using the Swedish Transmission Research Institute (STRI) classification guide. The subjective nature of this process can give rise to inconsistencies. This paper presents details of a research investigation aimed at the development of an image processing method or technique for use in automated classification of insulator hydrophobicity. A range of image processing methods, aimed at extracting unique visual features that correlate with hydrophobicity, are investigated. Results are presented for five sets of sample images of drop dispersion patterns representing different lighting and photography arrangements, each containing images of a range of hydrophobic behaviours. It is shown that good classification results can be obtained with two methodologies, namely an existing method named the Average of Normalized Entropies (ANE) and a new method developed in this study named Flash Spot Extraction (FSE).

Keywords: Image processing, insulator hydrophobicity, insulator ageing.

1. INTRODUCTION

Close relationships exist between surface leakage current behaviour and flashover phenomena associated with High Voltage (HV) insulators. The leakage current behaviour is in turn dependent on the hydrophobicity of the insulator surface. Increased hydrophobicity generally gives rise to better leakage current and flashover performance under wetted conditions [1, 2, 3]. Outdoor HV insulators are exposed to a range of ageing phenomena such as UV radiation, acidic conditions and other pollution compounds, abrasive effects from wind-borne particles, dry band arcing, etc. that degrade the electrical performance over time [2]. In this context, it has been found that hydrophobicity of an insulator surface is an important measure of the general health of the insulator, particularly with reference to ageing and the electrical performance under wet conditions [3, 4, 5, 6].

In practice, the hydrophobicity indicator is mainly derived by the comparison of sample images and classification reference images [7]. This is, by nature, a subjective human evaluation process that does not always produce consistent and repeatable results. Alternative less subjective hydrophobicity classification methodologies using computer-aided image processing techniques have been developed in recent years [8, 9, 10]. In practice, some of these methodologies have practical drawbacks such as the need for very specific image acquisition conditions [8]. Researchers have, however, shown that filtering techniques can be applied to greatly improve the performance of image processing methodologies to classify hydrophobicity [9, 10]. Thomazini *et al*, for instance, reported good results using

Haralick's descriptor homogeneity associated with the White Top-Hat filter for images acquired under natural lighting conditions [10].

This paper gives details of an investigation aimed at the development of an alternative image processing methodology that can determine the measure of hydrophobicity of an insulator using image acquisition techniques that involves flash photography rather than natural light.

2. HYDROPHOBICITY

2.1 Definition

The hydrophobicity of an insulator refers to the degree to which the insulator surface repels water. A hydrophobic surface will repel water, resulting in the formation of droplets on the insulator surface, while a hydrophilic surface will attract water, resulting in the formation of a continuous water layer or film. This property may also be described by the term wettability, which is defined as the ability of a surface to allow a larger surface area of liquid to cover it. A hydrophobic surface has a low level of wettability compared to the higher level of a hydrophilic surface.

2.2 STRI hydrophobicity classification

The Swedish Transmission Research Institute (STRI) hydrophobicity classification guide is a practical guide for use in the field [7]. The degree of the water repellence (hydrophobicity) of an insulator is divided into seven Hydrophobicity Classes (HC). HC1 is the most

water repellent class whereas HC7 represents a surface that is completely hydrophilic. This classification method requires physical inspection and manual subjective evaluation in order to categorise a surface into one of the seven classes. The criteria for classification depend on two factors, namely the contact angle θ_r of the majority of droplets and the total surface area that is wetted respectively. The latter factor involves evaluating the degree to which the liquid forms discrete drops rather than patches or rivulets [7]. Table I summarises the properties of each HC while Figure 1 shows typical examples of classes one to six.

Table I: Criteria for hydrophobicity classification (HC) [7].

HC	Description
1	Only discrete droplets are formed and $\theta_r \approx 80^\circ$ or larger for the majority of droplets.
2	Only discrete droplets are formed and $50^\circ < \theta_r < 80^\circ$ for the majority of droplets.
3	Only discrete droplets are formed and $20^\circ < \theta_r < 50^\circ$ for the majority of droplets. The droplets are usually no longer circular
4	Both discrete droplets and wetted traces from the water runoffs are formed and $\theta_r = 0^\circ$. Completely wetted areas $< 2 \text{ cm}^2$. Together they cover less than 90% of the tested area.
5	Some completely wetted areas $> 2 \text{ cm}^2$ are formed. Together they cover more than 90% of the tested area.
6	Wetted areas that cover more than 90% of the tested area are formed. Small unwetted areas (spots/traces) are still observed.
7	A continuous water film is formed over the whole tested area.

The wetting procedure specified by the STRI guide involves spraying a $50\text{--}100 \text{ cm}^2$ surface 1-2 times a second for 20-30 seconds from a distance of $25 \pm 10 \text{ cm}$ with a spray bottle that is capable of emitting a fine mist. The evaluation has to be performed within 10 seconds of wetting [7].

3. PHOTOGRAPHY ARRANGEMENT AND METHODOLOGY

3.1 Overview

The development of image processing methods for estimating hydrophobicity requires a representative range of sample images of drop dispersion patterns on flat insulator surfaces. These images are also needed in the case where the image processing algorithm under consideration requires calibration with images of drop distributions representing known hydrophobicity classes. A versatile sample set, representative of multiple camera and lighting configurations, were captured for use in

evaluating the performance of the image processing algorithms considered in the study.

3.2 Photographic test arrangement and insulator samples

The photography equipment used in the acquisition of the sample images include the following:

- Nikon D60 Digital camera
- Nikon 18 – 200mm 1:3.5-56 Lens
- Thule tripod
- Mounted tungsten spotlight

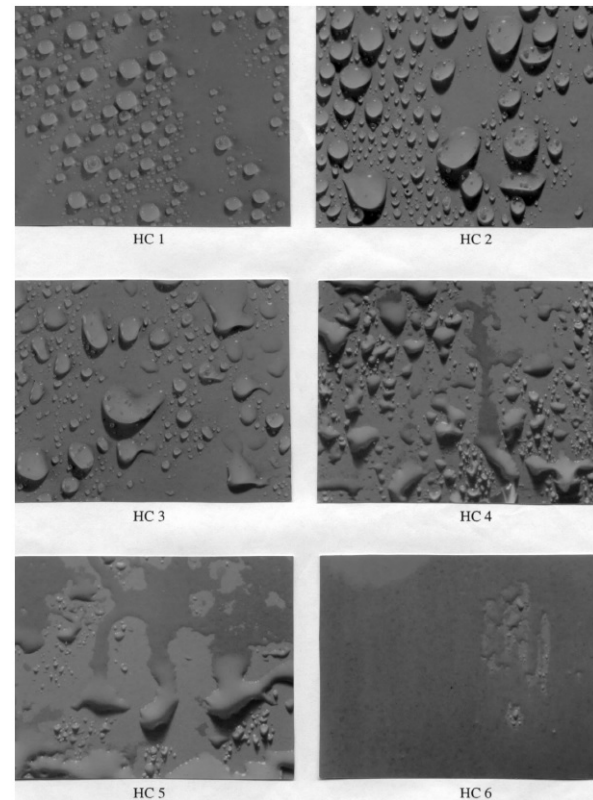


Figure 1: Typical examples of surfaces with HC from 1 to 6 [7].

Flat Silicone Rubber (SIR) samples with dimensions of $12\text{cm} \times 14.5\text{cm}$ were used for creating the images for the study. SIR is well suited for this purpose due to the high inherent initial hydrophobicity rating of the material, i.e. Hydrophobicity Class 1 (HC1). Because of this, systematically decreasing the hydrophobicity until HC7 is reached, and obtaining image samples of the drop dispersion pattern thereon at regular intervals would result in a sample group that covers the full range of hydrophobic behaviour from completely hydrophobic to completely hydrophilic.

3.3 Wetting method

A modified version of the wetting method recommended in the STRI guide was used for the purposes of the investigation with the view to improve the consistency and repeatability of the resulting images. The STRI

method does not specify configuration parameters such as the inclination angle of the insulator surface, which may result in different drop dispersion pattern behaviour under the same wetting conditions. This modified wetting method involves the following steps:

- The insulator is positioned at a $\pm 25^\circ$ inclination angle. Using a household spray bottle, the surface is misted by passing over it from left to right while spraying 1 to 2 times a second from a distance of 20cm. Care is taken to ensure that an even drop distribution forms as the drops grow larger with each misting sweep.
- The spraying process ceases as soon as the first drop starts to run.
- The insulator is then placed horizontally in order to stop the running.

The image of the drop distribution is taken within ten seconds of the wetting application.

3.4 Camera and lighting configurations

The images were acquired using a range of different photography and lighting configurations with the view to evaluate the performance of the image processing algorithms for different image acquisition conditions. The different image acquisition methods highlight different features, differ in terms of the consistency of the images, have different levels of detail or is better suited for certain processing methods than others. The configuration parameters considered include the following:

- The distance at which the image is captured.
- The angle of the camera to horizontal.
- The angle of insulator tilt.
- Various lighting conditions.
- Various pre-set or manual camera shooting modes.

A total of five sets of images were taken, each with a unique configuration of the above parameters. All images were taken with the insulator placed on a black surface to reduce reflections. The zoom setting of the camera was adjusted so that the entire insulator sample fits in the frame with the black border of the background visible around all edges. Table II summarises the configuration parameters for the different image sets.

Table II: Image set configuration parameters.

Parameter	Image set				
	1	2	3	4	5
Insulator inclination	0°	0°	0°	0°	10°
Camera orientation	90°	90°	90°	90°	25°
Shooting distance	1 m	1 m	30 cm	30 cm	30 cm
Lighting	Flash	No-ne	Flash in dark room	Flash	Spot-light

Camera mode	Ma-cro	Au-to	Macro	Macro	Ma-nual
-------------	--------	-------	-------	-------	---------

3.5 Pre-processing of digital images

The following pre-processing methodology was applied to all image sets before any image analysis:

- The black border of the background is cropped out of the image.
- Every image in a specific set is cropped to exactly the same size using MATLAB in order to ensure consistency in any area based calculations.

MATLAB offers a number of filtering algorithms that can be applied as part of the pre-processing methodology. Filtering can, however, result in loss of detail. Gaussian filtering, for instance, may result in softening of edges or the bleeding out of areas of high intensity. Some filtering algorithms enhance one feature while diminishing another. Because it was not initially clear which specific features in the images would have to be extracted and analysed, no filtering was applied as part of the pre-processing stage.

4. IMAGE PROCESSING METHODOLOGY

4.1 Problem evaluation methodology

The research problem gives rise to the following key questions:

- What physical properties do the hydrophobicity classification depends on?
- What image feature/s can be used to measure these properties?
- What image analysis methods can be implemented to extract these features?
- How successful are these feature extraction methods?
- How well do the results of a particular algorithm correlate with hydrophobicity class?

4.2 Feature extraction methods

The following four feature extraction methods were evaluated for the different image sets:

- Circular Hough-Transform.
- Edge detection.
- Average of Normalised Entropies (ANE) [8].
- Brightness thresholding.

For reference purposes, the existing ANE method [8] was applied to the image sets. The ANE results correlate well with hydrophobicity for image set 5, but to a lesser degree compared to the results published in the original study. This can be ascribed to the fact that the equipment and configuration used in this study differ from that of the original experiment. The other methodologies listed above performed unsatisfactorily for various reasons.

A new methodology, termed Flash Spot Extraction (FSE) was subsequently developed, and is discussed in detail in the following section.

5. FLASH SPOT EXTRACTION METHODOLOGY

5.1 Overview

This FSE methodology of feature extraction was specifically developed for extracting features associated with the use of flash photography. The feature vector investigated here is the reflections of the flash on the drop surfaces. The physical property responsible for this effect is the surface tension in the wetting agent. The flash reflections are due to the reflective nature of water. When flash photography is used, the brightness of the camera flash exceeds that of natural lighting conditions to such a degree that it can be ignored (this does not include very bright light sources such as spotlights). The camera automatically shortens the exposure time to counter the effects of higher gain. Since the flash intensity is relatively constant, the images that are captured using this configuration are likely to have similar gains regardless of the natural light conditions.

A drop with a higher surface tension, as in the case of a hydrophobic surface, has a higher change in gradient at the crest. Figure 3a illustrates how this will result in less of the flash-induced light to be reflected back to the camera lens. A drop with a lower surface tension has a smaller change in gradient at the crest. Figure 3b illustrates how this will result in more light reflected back to the camera lens. In the case of a highly hydrophilic insulator, pools form on the surface. The crests of these pools have large sections with very low changes in gradient. This results in large amounts of the light being reflected back to the camera lens.

A decrease in the hydrophobicity of the insulator surface gives rise to a decrease in the surface tension of the drops thereon. This can be simulated in practice by adding ethanol to the wetting agent, where increasing ethanol percentage produces decreasing surface tension [7]. Figure 4 and Figure 5 compare the sizes of the flash reflections for a wetting agent with high surface tension and a wetting agent with low surface tension respectively. High surface tension clearly produces relatively small flash spots while low surface tension produces large flash spots. The HC is therefore related to the total flash reflection area.

5.2 Flash spot feature extraction

The illumination intensities of the flash spots reflected from the drop surfaces are much brighter compared to that of the rest of the image. Since a greyscale image is represented as a matrix of grey level values, the grey level values associated with the flash spots will also be higher compared to that of the rest of the image. The total area associated with the flash spots in terms of the

number of pixels can be obtained, in principle, by applying a threshold operation to the image, where all values above a certain grey level are set to one and the rest to zero. Figure 6 shows an example of such a binary image, which is obtained by applying a threshold with a grey level value of 150 to the image shown in Figure 5.

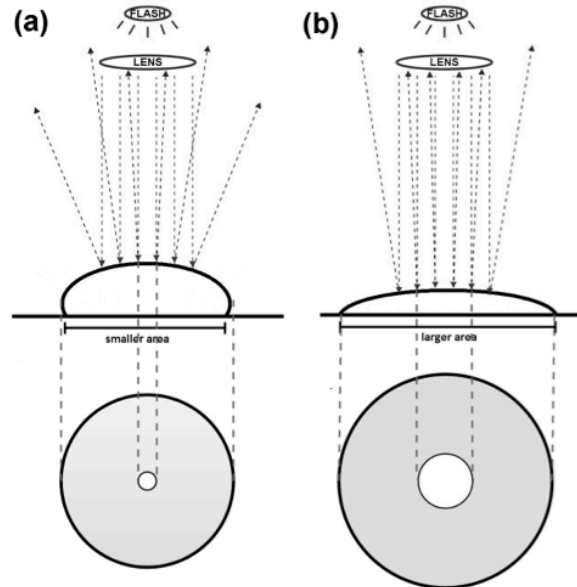


Figure 3: Light reflection from a flash source: (a) Side and top views of a drop with higher surface tension, (b) Side and top views of a drop with lower surface tension.

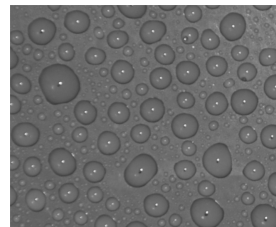


Figure 4: Set 1 sample close-up, 0% ethanol wetting agent.

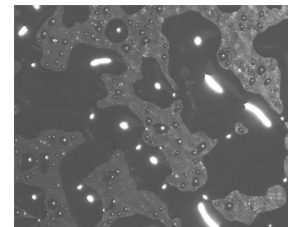


Figure 5: Set 1 sample close-up, 80% ethanol wetting agent.

In practice, the methodology outlined above is compromised by the fact that light is not only reflected from the droplets, but also from the insulator surface itself. Figure 5 and Figure 6 show significant reflections from the insulator surface, that increases the area above the cut-off intensity. It is therefore essential to remove the insulator surface reflection, or flash zone, in order to determine the correlation between total flash spot reflections and hydrophobicity.

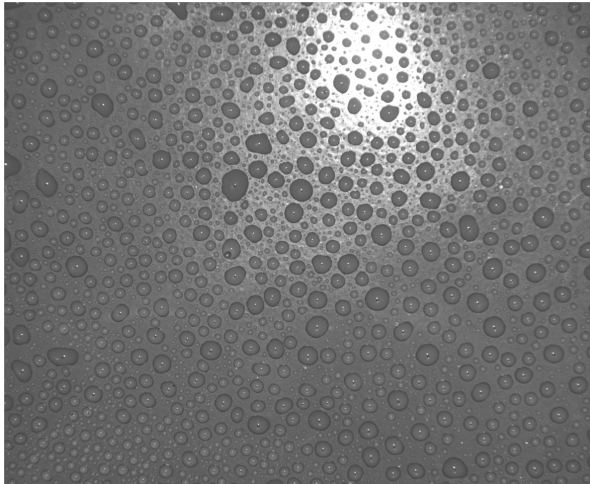


Figure 2: Set 1 sample, 0% ethanol wetting agent.

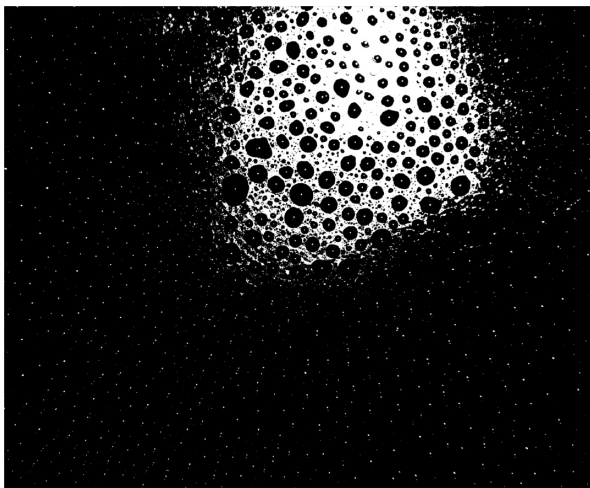


Figure 3: The image shown in Figure 5 thresholded to a grey level value of 150.

5.3 Flash zone elimination for a high hydrophobicity case

In the case of very high hydrophobicity, discrete drops form and the bulk of the flash zone is represented by one binary element. The rudimentary Flash Zone Elimination (FZE) process developed for such images can be summarised as follows:

- A threshold operation with a value of 150 is applied. Most of the flash spots saturate the maximum grey level (white = 255) in the image. A threshold value of 150 thus preserves most of the flash spots located in the flash zone, but also results in a small enough flash zone in most cases.
- Each cluster of pixels that are connected is indexed and labelled and the size and centroid of the cluster is stored in a structured array. This can be achieved with the Matlab functions *BWLABEL* and *REGIONPROPS*. The largest cluster will be the flash zone. Removal thereof from the images shown in Figure 6 yields the result shown in Figure 7. Although the flash spots in the flash zone are now isolated, the border of the flash zone can still be

observed. This is because of the slight ripple-like texture of the insulator, which brings about a region of patchy illumination around the primary flash zone cluster.

- A method named Low Level Masking (LLM) is applied to remove the border region. The largest cluster from the previous image, thresholded at 120, is extracted. It is placed on the higher level threshold image, yielding the result shown in Figure 8. Since the drops serve to isolate the flash spots from the insulator surface when thresholding, the low level mask covers up the border-noise from the flash zone seen in Figure 7.
- The low level mask is now removed from the image, resulting in a binary image with only flash spot elements, shown in Figure 9.

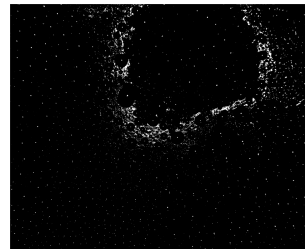


Figure 4: The image shown in Figure 6 with largest flash zone cluster removed.

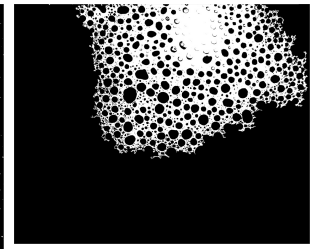


Figure 5: Lower threshold level mask of the image shown in figure 5.



Figure 6: The image shown in Figure 6 after flash zone elimination.

5.4 Flash zone elimination for the general case

The problem with the rudimentary FZE method discussed above is that it does not make allowance for when the flash zone is divided into more than one element due to the formation of pools or rivulets on the surface of the insulator. The odds of this happening are highest for hydrophilic insulators. Figure 10 and Figure 11 show a low hydrophobicity drops dispersion pattern along with the binary thresholded image thereof respectively. The

FZE methodology therefore needs to be adapted to automatically detect and remove multiple flash zone elements, while not incorrectly removing any large flash spot elements.

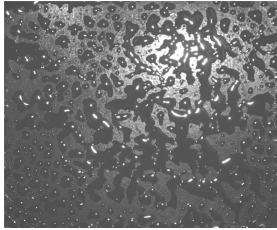


Figure 7: Set 1 sample, 80% ethanol wetting agent.

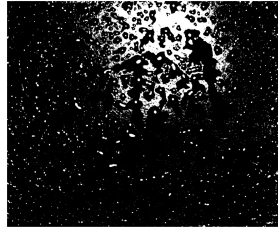


Figure 8: The image shown in Figure 10 thresholded to grey level value of 150.

Simply removing an arbitrary amount of the largest binary elements is not effective. This is because very large flash spots on wet pools may be mistaken for insulator reflection, or not enough flash zone elements are removed. The Flash Zone Elimination (FZE) process developed for this general case can be summarised as follows:

- The flash zone clusters are identified by noting that the flash spot clusters are solid, with no holes in them, while surface reflection clusters are perforated with blank holes caused by the presence of small drops or rough surface textures during thresholding. Checking the status of all of the clusters requires a lot of processing time, since there are thousands, so only the hundred largest clusters are checked and the surface reflection clusters identified are added to the low-level mask. Figure 12 shows the image obtained by applying this process to Figure 10.
- The high-level threshold image (Figure 11) is then masked and the mask removed (also through impure element detection).
- When performing calculations with the resulting binary elements, a cut-off value is defined that removes all clusters with a pixel count below a certain threshold value, due to the fact that they might be random reflection noise. A threshold value of 20 was selected for the images considered in this study.

The end result of the above FZE process on the hydrophilic drop distribution shown in Figure 10 is shown in Figure 13.

6. RESULTS AND RECOMMENDATIONS

The results of the flash spot extraction methodology described above show that the total flash pixel area increases with ethanol content, yielding an inverse correlation with hydrophobicity. This curve is shown in Figure 14. The deviation from the rising trend at 100% ethanol content is due to HC7 having no drops, just a featureless film of water. More samples are required between 80% and 100% to determine exactly at what level of extremely low hydrophobicity the flash spot extraction method no longer works. Presumably this will

only be the case for completely hydrophilic surfaces. Differentiating between HC classes between 0% and 20% ethanol is unsuccessful due to the small changes in flash spot size at those levels and further investigation is required.

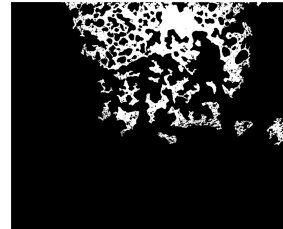


Figure 9: Low level flash zone cluster mask derived from Figure 10.

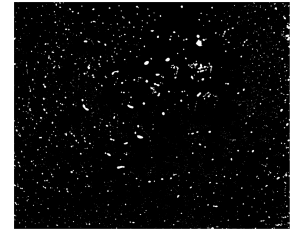


Figure 10: The image shown in Figure 11 after flash zone elimination.

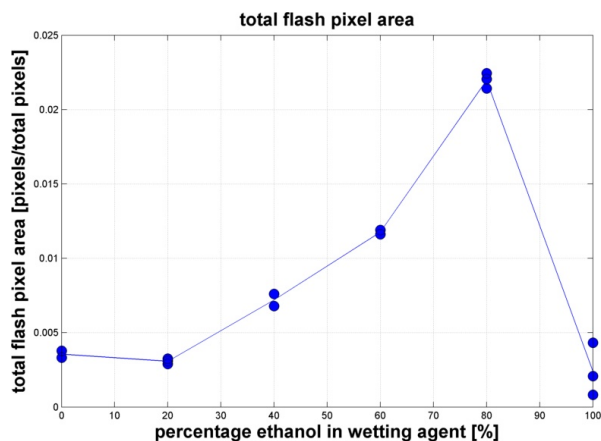


Figure 11: Calibration curve results after application of flash spot extraction on image set 1.

The methodologies implemented for flash spot extraction and flash zone elimination are new, and the performance of these methods may yet be improved through optimisation of the following aspects:

- The lower and higher level thresholding values are currently arbitrary. Automating the selection of these values could yield improved resolution in the flash zone.
- The cut-off value for random surface reflection noise is currently arbitrary; the effect of varying this value was tested, but further testing and observation on multiple sample sets would be needed to automatically determine the ideal value.

It is further recommended that the flash zone extraction method should be tested on more image sample sets allowing for the following considerations:

- Shooting distances.
- Natural lighting conditions (dark room, outdoor and indoor natural light).
- Flash intensity setting of the camera.

It is possible that a feature definition that combines the flash spot area and the density of flash spot clusters can improve the overall results. This requires further investigation.

ACKNOWLEDGEMENTS

The authors gratefully acknowledge the financial assistance of the Eskom Tertiary Education Support Programme and the contribution of Mr. P.J. Pieterse of the Stellenbosch University High Voltage Laboratory in procuring the insulator test samples.

REFERENCES

- [1] G Heger, HJ Vermeulen, JP Holtzhausen and WL Vosloo, "A Comparative Study of Insulator Materials Exposed to High Voltage AC and DC Surface Discharges", *IEEE Transactions on Dielectrics and Electrical Insulation*, Vol. 17, No. 2, April 2010.
- [2] AI Elombo, JP Holtzhausen, HJ Vermeulen, PJ Pieterse and WL Vosloo, "Comparative Evaluation of the leakage current and aging performance of HTV SR Insulators of Different Creepage Lengths when energized by AC, DC+ or DC- in a Severe Marine Environment", *IEEE Transactions on Dielectrics and Electrical Insulation*, Vol. 20, No. 2, pp. 421-428, 2013.
- [3] JG Wankowicz, SM Gubanski and WD Lampe, "Loss and recovery of hydrophobicity on RTV coating surfaces", *IEEE Transactions on Dielectrics and Electrical Insulation*, Vol. 1, No. 4, pp. 604-614, 1994.
- [4] N Yoshimura, S Kumaga and S Nishimura, "Electrical and Environmental Aging of Silicone Rubber Used in Outdoor Insulation", *IEEE Transactions on Dielectrics and Electrical Insulation*, Vol. 6, No. 5, pp. 632-650, 1999.
- [5] M Amin, M Akbar and S Amin, "Hydrophobicity of Silicone Rubber used for Outdoor Insulation (An Overview)", *Reviews on Advanced Material Science* 16(2007) 10-26.
- [6] B Venkatesulu, MJ Thomas and AM Raichur, "Accelerated Multistress Aging of Outdoor Polymeric", *Proceedings of the Annual Report Conference on Electrical Insulation Dielectric Phenomena*, Quebec, pp. 67-70, 2008.
- [7] S. G. 1, "Hydrophobicity Classification Guide", *Swedish Transmission Research Institute (STRI)*, 1992.
- [8] R Thottappillil and V Scuka M. Berg, "Hydrophobicity Estimation of HV Polymeric Insulating Materials Development of a Digital Image Processing Method," *IEEE Transactions on Dielectrics and Electrical Insulation*, Vol. 8, Issue 6, pp. 1098-1107, 2001.
- [9] D Thomazini, MV Gelfuso, RAC Altafim, "Hydrophobicity Classification of Polymeric Materials Based on Fractal Dimension", *Materials Research*, Vol. 11, No. 4, pp. 415-419, 2008.
- [10] D Thomazini, MV Gelfuso, RAC Altafim, "Classification of Polymers Insulators Hydrophobicity based on Digital Image Processing", *Materials Research*, Vol. 15, No. 3, pp. 365-371, 2012.

MODELLING IMPACT OF TRANSFORMER ASSET MANAGEMENT STRATEGIES ON COSTS USING SYSTEMS TYPOLOGIES AND PROBABILISTIC INFERENCES

B.O. Mkandawire, A.K. Saha and N.M. Ijumba

High Voltage Direct Current Centre, School of Engineering, University of KwaZulu-Natal, Durban 4000.
e-mail: 205521891@stu.ukzn.ac.za / burnemkanda@hotmail.com

Abstract. This paper models cost benefits of transformer asset management interventions based on systems theory and stochastic inferences. A triangulation methodology was used to collect non-censored time to failure data for power transformers. The data was processed using Least Squares Method to estimate statistical life parameters which were input into MATLAB simulation algorithms. There are two major contributions of the study. First, it applies systems methodology for quantitative modelling of risk – cost amplification and attenuation with their associated financial savings. Second, it shows quantitative benefits of refurbishment strategy. These savings/benefits are vital for planning and decision making. They form a basis for a paradigm shift in power asset management. Most published systems approaches lack quantitative capability that is demonstrated in this study.

Key Words. Systems thinking; risk–cost modelling; maintenance; renewal; transformer asset management.

1. INTRODUCTION

This paper applies systems thinking approach to formulate a quantitative risk–cost trending model. The model is used to determine cost benefits of risk amplification and attenuation that are caused by asset management interventions in asset management. Use of quantitative tools in the power sector has predominantly focused on financial techniques such as Net Present Value (NPV) and Internal Rate of Return (IRR) which tend to ignore impacts of technologies and strategies used in asset management [1]. The sector mostly uses qualitative and semi-quantitative management tools and a gap exists between these and fully quantitative risk analysis tools [2]; which this study attempts to fill.

Systems thinking is a conceptual framework and a body of knowledge that uses contextual and dynamic relationships in systems to determine cause and effects required to leverage change [3]. Systems thinking helps managers to see the holistic picture and cause and effects before problems are solved [3], [4], [5]. It has been used in insurance and management systems [6] in risk management in the space industry [7]; and in electric power sector [3], [8], [9]. The problem with most systems thinking approaches [4], [5], [6], [7] is that they have ended at the level of determining causation without quantitative capability. Some [3], [8] have combined analytical techniques with systems thinking but without system modeling equations. In a recent study, [9] applied stochastic techniques to develop a quantitative risk trending model, based on systems thinking, to determine impacts of technologies and strategies. In the trending model, [9] viewed a power asset management system as a system in state transition; hence applied Markov processes to develop the model.

Asset management involves whole life optimization of business impact associated with cost, risk and performance of the organization's physical assets or asset systems [10]. The model in [9] addresses the risk aspect of asset management as required by [10] but not the cost element. The current study adapts the component risk trending model in order to model

cost benefits of risk amplification and attenuation which can be used as imperatives for instituting incentive based schemes in asset management. A triangulation methodology was used to solicit primary data that was fitted in MATLAB algorithms to simulate cost benefits of life cycle management interventions. Statistical parameters were estimated using Least Squares Method (LSM) because the data was not censored/truncated [11]. Maximum Likelihood Estimation (MLE) would have been used if the data was censored [11].

2. ASSET MANAGEMENT MODELLING

Asset management modelling and simulation can be based on precepts that the grid consist of assets that are being maintained and refurbished [8]. This is shown in form of causal diagram in Fig. 1.

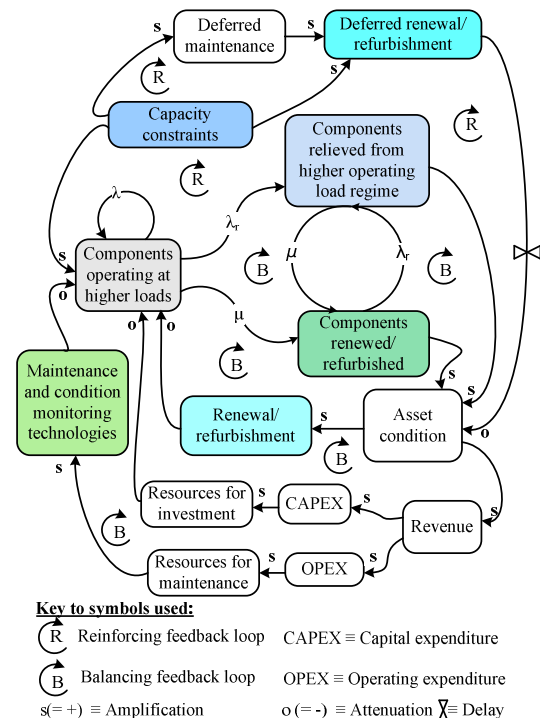


Fig.1: Systems view of renewal strategy

Causal diagrams are the best way to present a complex system [3], [4], [5], [6], [7], [8]. They act like Ishikawa (cause and effect) diagrams but with more detail on contextual relationship to enable asset managers see the holistic picture so as to leverage change.

In Fig. 1, λ is the rate at which components remain at higher operating load regime; λ_r is the rate at which they are relieved from higher operating load; and μ is the rate of refurbishment or repair [9]. Furthermore, dependent variables are at the arrowhead. An s (equals +) shows that when the independent variable increases, the value of the dependent variable will be more than what it was before input from the independent variable. An o (equals -) means when the independent variable increases, the value of the dependent variable will be less than what it was before input from the independent variable. Reinforcing loops are vicious circles whereas balancing loops tend to off-set adverse effects of the reinforcing loops [5]. In summary, and as advanced by [3], the diagram shows that operating intensity is the cause of deferred maintenance, deferred refurbishment, and component overload which in turn negatively affect asset condition. Improvement of asset condition increases revenue for capital expenditure (CAPEX) and operating expenditure (OPEX) which reduce stress on the system/components.

Systems theory characterizes systems by certain typologies such as emergency (small things make complete wholes) [5], [6], [7], interdependence [4], [5], [6], hierarchy, convergence and regulation/feedback [3], [4], [6], [7], [8], [9]. These typologies or classifications are constructs of causal diagrams as well as systems engineering modelling [3], [4], [5], [6], [7], [8], [9].

2.1 Cost modelling

A risk-cost model comprises two parts. The first part is the risk trending model and the second one is the cost model that is adapted and superimposed on the risk trending model.

2.2 Modelling component risk trends

A risk model is a function of number of critical components, ϕ ; total number of components, γ ; components already operating at high load regime, δ (for transformers, δ is determined by Hot Spot temperature (HST) [12]); components being admitted into high operating load regime, b ; components removed from high operating load regime, c ; and components renewed or refurbished, d given according to [9] as follows:

$$F = \frac{\phi}{\gamma} + \frac{\psi}{\phi} \{ \delta + [\zeta \lambda b] - [(\zeta - 1) \lambda c] - [(\zeta - 1) \mu d] \} | 1 < \zeta < 1/n, \phi > 0 \quad (1)$$

Where: λ is the failure rate; μ is the repair or renewal rate; ζ is the asset life phase determined by age bracket, n ; t is the technical life; and ψ is the

instantaneous failure rate expressed in terms of probability P as:

$$\psi_T(t) = \lim_{\Delta t \rightarrow 0} \frac{P[t \leq T \leq t + \Delta t]}{\Delta t} \quad (2)$$

$$\psi_T(t) = \int_0^t f_T(t) dt \approx \int_0^t f(t) dt \quad (3)$$

Where: $f(t)$ is probability density function (PDF); t and T are operating times, where $t \in T$.

There are three fundamental forms of maintenance cost models as provided by [13], and applied in [14]; and as advanced by [15], [16].

The first model presents maintenance cost as sum of planned and unplanned maintenance costs as follows [13], [14]:

$$Cost = \frac{8760}{m} \cdot \$_S + \frac{8760}{m} \cdot \$_F \cdot \left[1 - \exp \left[- \left(\frac{t - \gamma}{\eta} \right)^\beta \right] \right] \quad (4)$$

Where: 8760 is the number of hours in a year; m is the preventive replacement schedule; $\$_S$ is the cost of a preventive maintenance cycle; $\$_F$ is the cost of preventive maintenance when failure has occurred in each scheduled replacement; and the last term is the failure likelihood.

The second model presents total maintenance cost rate model, $C(\tau)$ (eq.5) based on renewal theory where survival likelihood, $P(L)$ (eq.6) fitted in the cost model is derived from the Inverse Power Law and the Arrhenius model, as follows [15]:

$$C(\tau) = [c_r N_r(\tau) + c_c N_c(\tau) + c_p] / \tau \quad (5)$$

Where: c_r , c_c and c_p are imperfect, corrective and preventive cost rates, respectively; τ is the interval time; N_r and N_c are number of components under repair and corrective maintenance, respectively.

$$P(L) = 1 - \exp \left[- \left(\frac{E}{E_o} \right)^{\alpha(n-bT)} \cdot \left(\frac{M}{M_o} \right)^{m\alpha} \cdot \left(\frac{L}{L_o} \right)^\alpha \cdot e^{aBT} \right] \quad (6)$$

Where: α is the Weibull shape parameter, E , M , T and L are respectively: electrical stress, mechanical stress, thermal stress and lifetime; E_o and M_o are respectively: scale parameter for the lower limit of electrical stress and scale parameter for the lower limit of mechanical stress; L_o is the lifetime corresponding to E_o and M_o ; n , m , B , b , a are respectively: voltage endurance coefficient, mechanical stress endurance coefficient, activation coefficient taking the reaction of materials under combined stress into account, $T = 1/\vartheta_o - 1/\vartheta$ where ϑ and ϑ_o are absolute and reference temperature, respectively.

The third model expresses cost per unit by the following [16]:

$$Cost = \left\{ \mathcal{E}_u \left[1 - e^{\left(\frac{t}{\eta} \right)^\beta} \right] + \mathcal{E}_p \cdot R(t) \right\} / \int_0^T R(t) \quad (7)$$

Where: \mathcal{L}_u is cost of unscheduled maintenance due to downtime and the term in parenthesis represents failure likelihood; \mathcal{L}_p is the cost of planned maintenance; t is operating time, whereas T is the total life time. $R(t)$ is the survival likelihood; and the integrand in the denominator stands for the total component population.

Eq. (4) assumes that preventive maintenance is constant regardless of number of components surviving which is not so in real life. Eq. (6) represents life of most electrical components well, but the coefficients and parameters are difficult to compute as they require a lot of statistical data to estimate; the data is usually too hard to obtain [8], [15]. Eq. (7) enables analysts to obtain modelling parameters with few data sets provided t , η and β are determined and is flexible; hence it is adapted by eliminating the denominator and superimposed on the risk trending model of [9].

2.3 Model parameter estimation

This section outlines parameter estimation method. The Weibull distribution can be used to model all types of distributions by altering the value of the shape parameter [13], [15], [16] hence it is applied in the study. For a two parameter Weibull, failure likelihood, $F(t)$ and survival probability $R(t)$ are related by (8) and (9) as follows:

$$F(t) = 1 - R(t) \quad (8)$$

$$R(t) = \exp \left[- \left(\frac{t}{\eta} \right)^\beta \right] \quad (9)$$

Where: β is the shape parameter; and η is the characteristic life, that is, time when 63% or $(1 - e^{-1})$ components will have failed.

Eq. (8) is related to the probability density function (PDF), $f(t)$ through (10) as follows:

$$f(t) = \frac{dF(t)}{dt} = \frac{d[1 - R(t)]}{dt} \quad (10)$$

Values of β and η for non-censored data of Table 1 are estimated using Least Squares Method (LSM) by taking double logarithm and processing (8) according to [9], [11], [17], [18] to obtain the parameter estimating model given by (11) and (12) as follows:

$$\hat{\beta} = \frac{\left\{ n \sum_{i=1}^n (\ln t_i) \left(\ln \left[\frac{1}{1 - i/n + 1} \right] \right) \right\} \left\{ \sum_{i=1}^n \ln \left[\frac{1}{1 - i/n + 1} \right] \right\} \sum_{i=1}^n \ln t_i}{\left\{ n \sum_{i=1}^n (\ln t_i)^2 \right\} - \left\{ \sum_{i=1}^n (\ln t_i) \right\}^2} \quad (11)$$

$$\hat{\eta} = e^{\left(\frac{\bar{y} - \bar{t}}{\hat{\beta}} \right)} \quad (12)$$

Where:

$$\bar{t} = \frac{1}{n} \sum_{i=1}^n \ln \left[\frac{1}{\left(1 - \frac{i}{n+1} \right)} \right] \quad (13)$$

And:

$$\bar{y} = \frac{1}{n} \sum_{i=1}^n \ln t_i \quad (14)$$

Where: i is the i th observation in the Bernard's approximation equation [17]; n is sample size; $\hat{\beta}$ and $\hat{\eta}$ are estimates of the β and η , respectively.

2.4 Modelling data

This section presents data that was applied to models in Section 2.2—2.3. Table 1 outlines time to failures of the active part of transmission transformers for a mean degree of polymerization (DP) of 184.

Table 1: Time to failures of 20 MVA transformers

Time to failure (x 10 ⁵ hrs)			
1.892	4.188	3.925	1.971
2.182	1.971	4.366	2.365
2.418	4.03	2.31	

Table 2 outlines costs of carrying out planned, unplanned and major overhaul maintenance. The major overhaul includes rewinding.

Table 2: Maintenance costs for 20MVA transformer

Cost (US\$)	Planned	Unplanned	Major overhaul
	17,466.7	30,000	123,529.4

3. RESULTS AND ANALYSIS

MATLAB algorithms were used for simulation and the results are presented and analyzed in this section.

Life of power transformers under good maintenance regimes generally goes to 35 - 60 years [15], [8]. However, for data used in this study (i.e. for $\beta=2.78$), at 60 years the probability density function (PDF) and cumulative density function (CDF) are truncated as shown in Fig. 2; meaning there is still life remaining in the asset population.

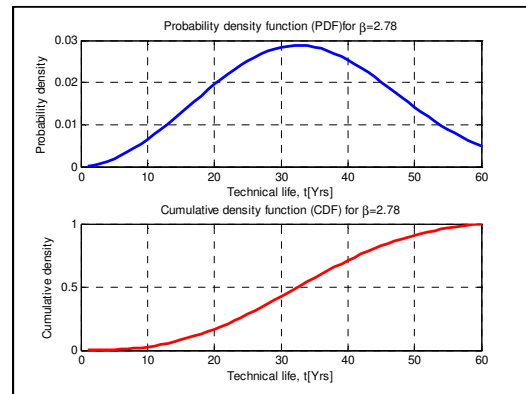


Fig. 2: Truncated PDF and CDF at 60 year life

The model presented here shows that the technical life may go to as long as 80 years, which is corroborated by [15] and [19]. Financial and capacity constraints force utilities to operate power assets that

were designed for a 30 year cycle to be replaced on a 100 year cycle [19].

Table 3 lists values of parameters computed using the LSM. Fig. 3 presents the hazard rates, PDF and CDF for the population of the power transformers. The β value of 2.78 shows an age related, increasing hazard rate as displayed on top of Fig. 3. The CDF shows that 63% of the transformers would have failed at 38.2 years which is the value of characteristic life, η .

Table 3: Weibull parameters computed by LSM

Parameter estimates	
$\hat{\beta}$	$\hat{\eta}$ [hours]
2.78	3.35×10^5

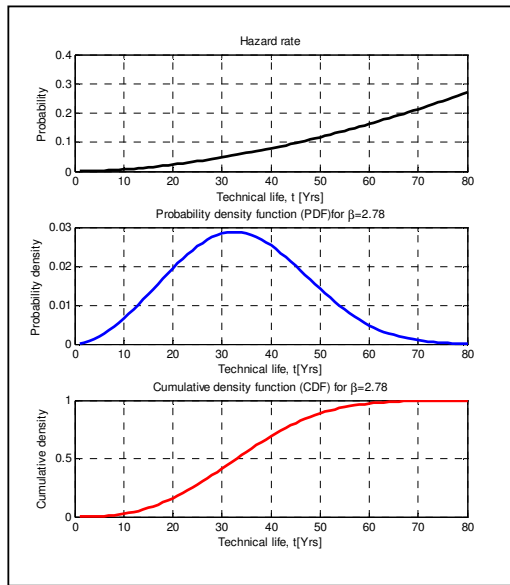


Fig. 3: Hazard rate, PDF and CDF

Fig. 4 shows costs of planned and unplanned maintenance as well as the total cost, but excluding major overhaul costs. If there are some major overhauls, the cost of planned maintenance becomes oscillatory as shown in Fig. 5.

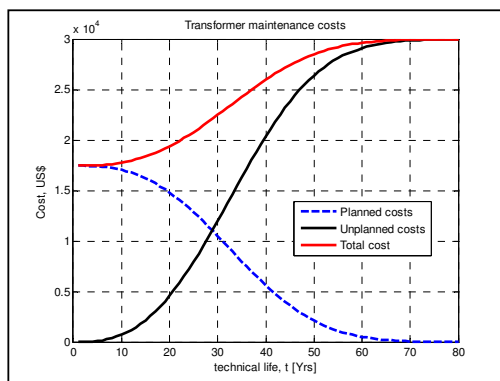


Fig. 4: Trends of maintenance costs

Fig. 5 presents costs of planned maintenance with major overhauls. Each peak in Fig. 5 is associated with a major overhaul. In practice, with proper

protection, there may be only one major overhaul due to a major breakdown.

It is worth noting that the abscissas of Figs 5, 6 and 7 are in 16 life phase groups (ζ) each composed of five years thus representing a technical life of 80 years.

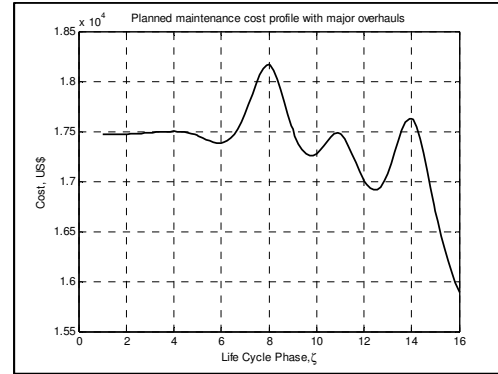


Fig. 5: Planned maintenance with overhauls

Fig. 6 shows trends of costs and savings realized due to major end-life asset management interventions such as renewal and application of technologies based on systemic risk trending model. Fig. 7 presents savings realized when major renewal interventions are carried out prior to mid-life and at mid-life. Cumulative savings are also presented.

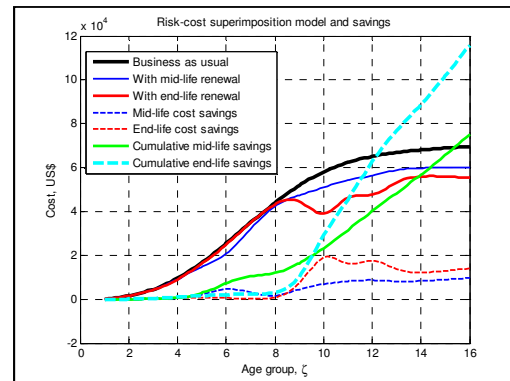


Fig. 6: Savings with major end-life interventions

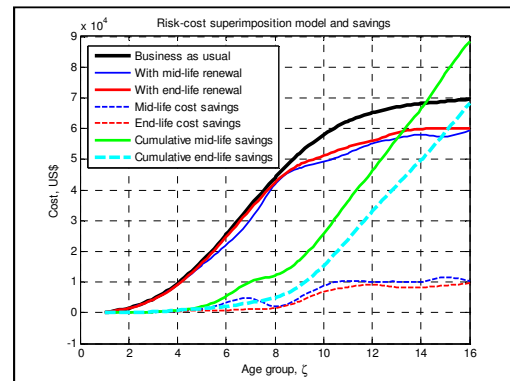


Fig. 7: Savings with major mid-life interventions

The savings in Figs 6 and 7 are what an asset manager needs in order to evaluate effectiveness and timing of strategies. Cumulative savings do not only add to profits, but also can be reinvested. The next

section discusses the results that have been presented in Section 3.

4. DISCUSSION

Different asset populations are characterized by different failure patterns depending on operating conditions as well as asset management strategies employed. Thus statistical life parameters such as the β and η that can be estimated will also vary accordingly. In this study, the parameters revealed that the components were characterized by age dependent, increasing hazard rate because β was 2.78. The scale parameter was 3.35×10^5 hours representing 38.2 service years.

The hazard rate, $h(t)$, stands for the conditional probability that the equipment will fail in a given interval of unit time given that it has survived up to that time interval. It is an important reliability parameter as it helps an asset manager make informed life cycle decisions like major maintenance and refurbishment. In Fig. 3, the hazard rate is plotted together with the PDF and the CDF to give comparative perspectives. From Fig. 3, it can be seen that the slope of the CDF and the PDF reaches point of inflection at 33 years where the hazard and failure rates begin to increase appreciably. At that point, more and more transformers will be overloaded and the cost of unplanned maintenance (Fig. 4) exceeds that of planned maintenance. That point would be inferred as the best time to carry out refurbishment/renewal. In the model in this study, it is 40% of the life span or 33 years. Technologies like Supervisory Control and Data Acquisition (SCADA) would be handy at that time so as to enable change of voltage taps to match the level of overload and to switch off any transformers that would be in danger of excessive overload. In addition, from Fig. 3, it is evident that at the early life the PDF is higher whereas the CDF is lower than that for the later stages of life meaning there are more surviving components than failed ones, an opportunity to optimize maintenance. This can also be seen from the right hand skewing of the sigmoid shape of the CDF curve. At late life stages, there will be fewer components that are greatly ageing; hence unplanned maintenance costs are high (see Fig. 4).

Fig. 4 assumes that there are no major breakdowns that require major overhaul. In contrast, Fig. 5 presents a case of planned maintenance costs where major overhauls result from major breakdowns. The graph is oscillatory. This is not common in power transformers as, with proper protection, a major overhaul would occur at most once in a lifetime and may involve rewinding. This would cost about US\$ 123,500 (see Table 2).

The ultimate aim of the component risk trending model based on systems thinking is to determine impacts of strategies and technologies. The best way to do that is to establish financial or cost benefits. Fig. 6 presents a model of costs with risk trends for

the following: business-as-usual, with minor mid-life refurbishment and with major end-life refurbishment together with the associated cost savings. Fig. 6 shows that end-life renewal realizes great financial benefits but they occur late in the asset life. If the major refurbishment was carried out earlier than end-life phase (prior to mid-life), the benefits would have been more rewarding as shown in Fig. 7. The model clearly indicates where the asset manager can leverage change or redesign systems in terms of timing and scope of renewal projects. Figs 6 and 7 demonstrate how the model advanced can also be used for instituting incentive or performance based schemes to asset managers through rewards for mitigating risks based on measurement of cost benefits. By simulation, asset managers can decide on the sensitivity analysis that suits their corporate objectives best.

It is worth noting that the above models (Figs 3-7) are meaningful if painstaking task of determining model parameters such as the shape and characteristic life has been done. That depends on whether data is censored (truncated) or non-censored. For non-censored data, the Least Squares Method (LSM) suffices, otherwise, other methods like Maximum Likelihood Estimation (MLE) or Method of Moments (MOM) should be applied. The fundamental question arises as to how to ensure that the data is not censored. In the current study, a network that had complete, reliable and traceable records of transformer failures was used to provide source of data for all transformers installed in a given period of time. The network chosen was for transmission transformers and small enough to ensure that all failure statistics were captured. In addition, the Degree of Polymerization (DP) of the cellulose insulation of 184 confirmed that the transformers were not taken out of service before the end of their life time as loss of strength of cellulose insulation occurs at a DP of 200 [12], [20].

The study shows that systems thinking gives causal typologies that can assist asset managers to forecast risk profiles of their assets and to plan the level of risk they are willing to take; and financial benefits to realize. With the systems approach advanced, quantitative measurements of costs and cost benefits are possible. The major problem with systems theory in management has been lack of measurement [4], [5], [6], [7], [8]; hence critics have argued that systems theory is a theory of everything hence not amenable [4]. This study has added costs to the quantitative risk trending capability of systems thinking approach by [9] thereby validating that systems thinking approach can be quantified. However, what can be viewed as both an advantage and a disadvantage of systems thinking is that it requires vast body of knowledge to develop models. In a learning organization, the disadvantage can be viewed as a strength as shown by [5].

5. CONCLUSION

In a complex asset management system such as the power infrastructure, a holistic view must be employed because problems in one system may be caused by snags in other systems and subsystems. The systems view pin points root causes that need to be addressed first. The major contribution of this study is that it uses systems methodology to provide a quantitative model for risk-cost amplification and attenuation with their associated financial savings that can be applied in planning and decision making. Furthermore, the model can show quantitative benefits of refurbishment which, unlike up-rating, does not add any capacity hence its financial benefits tend to be unappreciated. This is phenomenal as it overrides abstract/qualitative capabilities of most systems thinking approaches in published literature as demonstrated by the study. Application of the model can be extended to implementation of incentive based schemes such as rewards to asset managers and engineers for achieving commendable level of asset management performance; and in benchmarking. Further work will provide a comparative study between distribution and transmission transformers and will attempt to model life parameters for censored failure data.

ACKNOWLEDGEMENTS

The authors wish to express their gratitude to University of KwaZulu-Natal's High Voltage Direct Current Centre (HVDC) and Technology and Human Resources for Industry Programme (THRIP) of South Africa for supporting this study.

REFERENCES

- [1] I.E. Davidson, "Utility Asset Management in the Electrical Power Distribution Sector", *Inaugural IEEE PES 2005 Conference and Exposition in Africa*, Durban, South Africa, July, pp. 338-343, 2005.
- [2] Electric Power Research Institute, "Asset Management Toolkit Modules: An Approach for Risk-Informed, Performance-Focused Asset Management in the Power Delivery Industry", EPRI, Palo Alto, CA, Final Report No. 1011365, 2005.
- [3] B.O. Mkandawire, N.M. Ijumba and H. Whitehead, "Asset Management Optimisation Through Integrated Systems Thinking and N-1 Contingency Capability for Refurbishment", *IEEE Syst. J.*, Vol. 5, No. 3, pp. 321-331, 2011.
- [4] L. Skyttner, *General Systems Theory: Problems, Perspective, Practice*, 2nd ed. Singapore: World Scientific, 2006.
- [5] P. M. Senge, *The Fifth Discipline: The Art & Practice of the Learning Organisation*. London, U.K.: Century Business, 1993.
- [6] D. White, "Application of systems thinking to risk management: A review of the literature", *Manage. Dec.*, Vol. 33, No. 10, pp. 33-45, 1995.
- [7] N. G. Leveson, B. Barret, J. Carol, J. Cutcher Grschenfeld, N. Durac, and D. Zipkin, "Modelling, Analysing and Engineering NASA's Safety Culture", In Phase 1 Final Report, Feb. 2004-Feb., 2005.
- [8] J. Schneider, J. Gaul, C. Neumann, J. Hogräfer, W. Wellßow, M. Schwan, A. Schnetter, "Asset Management Techniques", *Intl. J. Elect. Power and Energy Syst.*, Vol. 28, No. 9, pp. 643-654, 2006.
- [9] B.O. Mkandawire, N.M. Ijumba and A.K. Saha, "Component Risk Trending Based on Systems Thinking Incorporating Markov and Weibull Inferences", *IEEE Syst. J.*, 2013 (In publication).
- [10] British Standard Institution, "Publicly Available Standard 55-1: Specification for Optimised Management of Physical Assets", BSI, London, 2008.
- [11] G.C. Stone and G. Van Heeswijk, "Parameter estimation for the Weibull distribution", *IEEE Trans. Elect. Insul.*, Vol. EI-12, No.4, 1977.
- [12] A.E.B. Abu-Elanien and M.M.A. Salama, "Asset management techniques for transformers", *J. Elect. Power Syst. Research*, Vol. 80, pp. 456-464, 2010.
- [13] P.D.T. O'Connor, *Practical Reliability Engineering*. Chichester: John Wiley & Sons. 1991, pp. 123-128, 311-327.
- [14] B.O. Mkandawire, N.M. Ijumba and H. Whitehead, "Markov and Weibull Analysis for HV Network Maintenance: Reliability Management, Preventive Maintenance", *Proc. 16th Intl. Symposium in High Voltage Engineering (ISH)*, South African Institute of Electrical Engineers (SAIEE), Cape Town, pp. 1605-1610, 2009.
- [15] X. Zhang and E. Gockenbach, "Age-dependent maintenance strategies of medium-voltage circuit breakers and transformers", *J. Elect. Power Syst. Research*, Vol. 81, pp.1709-1714, 2011.
- [16] D.J. Smith, *Maintainability and Risk: Practical Methods for Engineers*, 8th ed. London: Elsevier Butterworth-Heinemann, 2011.
- [17] M.A. Al-Fawzan, "Methods for estimating the Parameters of the Weibull Distribution," King Abdulaziz City for Science and Tech., Riyadh, Saudi Arabia, 2000.
- [18] S. Boonta, A. Sattayathan and P. Sattayathan, "Estimation of Weibull Parameters using a Randomised Neighbourhood Search for the Severity of Fire Accidents", *J. Mathematics and Statistics*, Vol. 9, No.1, pp. 12-17, 2013.
- [19] Electric Power Research Institute, "Third Power Delivery Asset Management Conference Proceedings: Decision Support and Information Technology", EPRI, Palo Alto, CA, Doc. # 1012497, 2007.
- [20] IEEE Std C57.91-2011 (Revision of IEEE Std C57.91-1995), "IEEE Guide for Loading Mineral-Oil-Immersed Transformers and Step-Voltage Regulators", IEEE, New York, March 2012.

Identification of Power System Oscillation Paths in Power System Networks

S Mvuyana^{*†}, J van Coller^{*} and T Modisane[†]

^{*} University of the Witwatersrand, School of Electrical and Information Engineering, South Africa

[†] Eskom Holdings SOC Limited, Group Technology Engineering, South Africa

Abstract – Power system oscillation modes have been studied mainly through eigenvalue analysis. Knowledge of the exact transmission paths travelled by oscillation modes of interest provides valuable information for selection of robust control signals and understanding the impact of various network contingencies on the specific modes. This paper presents a detailed study of network busbar voltage and line current oscillations with the specific aim of identifying the exact path which inter-area oscillation modes within the power system propagate. The technique presented in this paper is an extension of an already existing technique which is also used for the same application, two algorithms are used to identify the dominant inter-area oscillation paths and the results are presented.

Key Words: Voltage sensitivity, Current sensitivity, Inter-area oscillation, Participation Factor, Observability, Small Signal Stability (SSS), Dominant Inter-area Oscillation Path

1. INTRODUCTION

Small Signal Stability (SSS) of power systems is defined as the ability of a power system to remain stable after being subjected to a small disturbance. Disturbances acting on the system are considered small enough that linearization of the system equations is acceptable [1,2,3]. Modern day challenges imposed on transmission grid expansion by environmental, right of way and public opposition issues have resulted in SSS becoming a prominent challenge faced by power system engineers. Integration of large scale renewables and the growth of interconnections between grids have also resulted in degraded SSS performance [4].

Understanding the exact path which oscillation energy travels within a power system enables power system controllers to identify key transmission lines and busbars associated with the modes. This allows the grid operational SSS margins to be maintained within acceptable levels for all operating conditions.

The concept of ‘interaction paths’ in power systems is presented in reference [5] and its definition is stated as the main path along which generators, controllers and loads interact with one another allowing for the exchange of oscillation energy. Reference [6] presents an extension of the interaction path concept through the development of the ‘dominant inter-area oscillation path’. The most robust signals to be used in Wide Area Monitoring Systems (WAMS) can be easily determined through this type of analysis [7]. The main limitation as to why this analysis has not received much attention is because network parameters such as voltages and currents are also influenced by reactive power control equipment such as Automatic Voltage Regulators (AVRs) and Static Var Compensators (SVCs) [8]. Network busbar voltages are also influenced by nearby loads; hence the application of these techniques is best suited to transmission network busbars without large amounts of local generation or loads [8].

The aim of this paper is to demonstrate the application of the generalized dominant inter-area oscillation path concept by extending the analysis performed to consider the impact of generator torque changes on network variables of interest, namely busbar voltage and line current oscillations. The generalized dominant inter-area oscillation path is based on work presented in references [6,8]. Of particular interest within the analysis presented in this paper is the identification of inter-area oscillation mode interaction paths.

2. THEORETICAL BACKGROUND

2.1 Linearized Power System Model

Power systems can be represented by differential and algebraic equations, when subjected to a small disturbance the power system equations can be linearized about the operating point to yield an accurate solution [1]. The linearized power system model is given by:

$$\begin{aligned} \dot{x}_p &= A_p x_p + B_p u_p \\ y_p &= C_p x_p + D_p u_p \end{aligned} \quad (1)$$

- where A_p is the system state matrix, B_p is the system input matrix, C_p is system output matrix and D_p is the feed forward matrix, x_p is the system state vector, u_p is the system control vector and y_p is the system output vector [1,3,8].

State variables within power systems are mainly represented using generator machine states [1]. If the power system model analysed is treated as a minimal electromechanical model for an N machine network, the state space vector will be given by, [8]:

$$x_p = \begin{bmatrix} \Delta \delta \\ \Delta \omega \end{bmatrix} \quad (2)$$

- where $\Delta \delta$ and $\Delta \omega$ are the rotor load angle and rotor speed state variable vectors of all the machines in the

network. Assuming that $u_p = 0$ the power system model can be expressed as:

$$\begin{bmatrix} \Delta \dot{\delta} \\ \Delta \dot{\omega} \\ \Delta \dot{z} \end{bmatrix} = \begin{bmatrix} A_{11} & A_{12} & A_{13} \\ A_{21} & A_{22} & A_{23} \\ A_{31} & A_{32} & A_{33} \end{bmatrix} \begin{bmatrix} \Delta \delta \\ \Delta \omega \\ \Delta z \end{bmatrix} \quad (3)$$

- where Δz represents other state variables within the power system.

Eigenvalue analysis of the power system can be used to obtain the right hand side eigenvector of the network from:

$$A\phi = \lambda\phi \quad (4)$$

- where λ is the eigenvalue matrix of the power system, $\phi = [\phi_1 \cdots \phi_n]$ is the observability of the network (mode shape), and n is the number of state variables.

2.2 Network Sensitivities and Mode Shapes [6]

The system output matrix C_p is formed by obtaining network sensitivity with respect to a desired output variable.

The output variables of interest within a transmission network are the busbar voltage magnitude, busbar voltage angles, transmission line current magnitudes and transmission line current phase angles.

The sensitivities of the busbar voltage magnitudes with respect to the generator load angles can be expressed as:

$$C_{V\delta} = \begin{bmatrix} \frac{\partial V_1}{\partial \delta_1} & \frac{\partial V_1}{\partial \delta_2} & \cdots & \frac{\partial V_1}{\partial \delta_N} \\ \vdots & \vdots & \ddots & \vdots \\ \frac{\partial V_n}{\partial \delta_1} & \frac{\partial V_n}{\partial \delta_2} & \cdots & \frac{\partial V_n}{\partial \delta_N} \end{bmatrix} \quad (5)$$

The sensitivities of the busbar voltage magnitudes with respect to the generator speeds can also be expressed using a similar approach to that of Equation (5). Therefore the complete busbar voltage magnitude and phase angle sensitivities of the network can be expressed as:

$$\begin{aligned} C_V &= [C_{V\delta} \mid C_{V\omega}] \\ C_\theta &= [C_{\theta\delta} \mid C_{\theta\omega}] \end{aligned} \quad (6)$$

In a similar manner the line current magnitude and line current phase angle sensitivities matrices can be expressed as:

$$\begin{aligned} C_I &= [C_{I\delta} \mid C_{I\omega}] \\ C_\phi &= [C_{\phi\delta} \mid C_{\phi\omega}] \end{aligned} \quad (7)$$

In the application of the concept of the ‘dominant inter-area oscillation path’, the ‘network mode shape’ has to be formulated based on the use of transmission network variables of interest.

The ‘network mode shape’ of a power system is defined as: the product of the mode shape of the electromechanical oscillations and the transmission network sensitivity matrices. The network mode shape serves as an indication of how much each mode is distributed amongst the transmission network parameters. It gives the open loop observability of the network electromechanical oscillation modes, within various network parameters [9].

Network mode shapes of various network parameters are expressed as follows:

$$S_V = C_V\phi, \quad S_\theta = C_\theta\phi \quad (8)$$

$$S_I = C_I\phi, \quad S_\phi = C_\phi\phi \quad (9)$$

Equation (8) gives the network mode shape of the network busbar voltage magnitude (S_V) and the network mode shape of the voltage phase angle (S_θ). Similarly the current magnitude mode shape and phase angle mode shape are given by Equation (9).

2.3 Dominant Inter-area Path Mode Shape Properties [6,9]

For inter-area mode oscillations, the following observations are made based on the analysis carried out and presented in references [6,9]:

- (i) Voltage magnitude mode shape S_V and voltage phase angle S_θ indicates the modal observability of a signal
- (ii) The largest S_V or the smallest S_θ of networks indicates the center of the path. The center path can also be seen as the “inter-area mode center of inertia” or the inter-area pivot for the mode of interest
- (iii) Current magnitude mode shapes (S_I) indicates the percentage of the contents of the inter-area mode that is distributed among the transfer corridors of the network.
- (iv) Higher values of (S_I) indicate the most likely path which is to be travelled by the oscillation mode energy.
- (v) Current angle indicates the most likely direction of oscillation mode energy flow within the network.

2.4 Network Sensitivity Concept Extension

In the application of the network sensitivities presented in reference [6], the concept is limited to electrical network parameters that are deduced from network state variables. In most power plants machine load angle is usually not available as a parameter which can be explicitly measured or deduced from generator operating point.

Generator output power is a signal which is readily available and is closely related to the actual generator load angle, with the relationship given by Equation (10):

$$P_{OUT} = \frac{V_S V_R}{X_S} \sin \delta \quad (10)$$

- where V_S and V_R are the sending end and receiving end voltages respectively, X_S being the reactance between the sending and receiving end and δ the load angle between the sending and the receiving end.

The change in the electrical power output of a generator is governed by a change in the amount of torque applied via the steam inlet valve on the turbine end.

In per unit representation, the output power P_{OUT} and the torque τ applied to the generator are equivalent, hence torque changes are equal to power changes.

In the analysis of Equation (10), if we assume that $\frac{V_S V_R}{X_S}$ is a constant, then power output changes can

only be affected by varying the generator load angle δ and hence it can be seen that the output power is directly proportional to the generator load angle. Hence since the torque and load angle are directly proportional, it can be deduced that the sensitivities

$\frac{\partial V_k}{\partial \delta_i}$ (where $\frac{\partial V_k}{\partial \delta_i}$ is the voltage sensitivity of the k^{th}

busbar with respect to the load angle changes of the i^{th} machine) and $\frac{\partial V_k}{\partial \tau_i}$ (where $\frac{\partial V_k}{\partial \tau_i}$ is the voltage

sensitivity of the k^{th} busbar with respect to the torque changes of the i^{th} machine) are directly proportional to one another and that the relationship between the two is linear.

Thus based on the analysis of the network sensitivity relationships between $\frac{\partial V_k}{\partial \delta_i}$ and $\frac{\partial V_k}{\partial \tau_i}$ it can be seen

that system output matrix C_P can also be formed based in a similar manner to that presented in Equation (5).

Hence the $C_{V\tau}$ can be expressed in a similar manner to Equation (5), and is given in Equation (11)

$$C_{V\tau} = \begin{bmatrix} \frac{\partial V_1}{\partial \tau_1} & \frac{\partial V_1}{\partial \tau_2} & \dots & \frac{\partial V_1}{\partial \tau_N} \\ \vdots & \vdots & \ddots & \vdots \\ \frac{\partial V_n}{\partial \tau_1} & \frac{\partial V_n}{\partial \tau_2} & \dots & \frac{\partial V_n}{\partial \tau_N} \end{bmatrix} \quad (11)$$

- where N is the total number of generators in the network and n is the total number of busbars in the transmission network. In a similar manner the busbar voltage magnitude and phase angle sensitivities can be expressed by:

$$\begin{aligned} C_V &= [C_{V\tau} \mid C_{V\omega}] \\ C_\theta &= [C_{\theta\tau} \mid C_{\theta\omega}] \end{aligned} \quad (12)$$

Similarly the current magnitude and phase angle sensitivities with respect to the torque deviations can be expressed by:

$$\begin{aligned} C_I &= [C_{I\tau} \mid C_{I\omega}] \\ C_\theta &= [C_{\theta\tau} \mid C_{\theta\omega}] \end{aligned} \quad (13)$$

The extended sensitivity matrices can be used to obtain the network mode shapes in a similar manner as presented earlier. The network mode shape properties presented in section 2.3 are assumed to be valid for the extension presented.

3. MODEL BASED OSCILLATION PATH IDENTIFICATION

The identification of the dominant inter-area oscillation path for a known system model will be solved using the following two proposed algorithms:

- (i) Analysis of the network busbar voltages based on small deviations of generator parameters of interest.
- (ii) Analysis of the network busbar voltages based on the application of faults to various areas within the network to study the inter-area oscillation energy flow.

The first algorithm to be used is based on an algorithm presented in [9], the methodology to be used for the algorithm (i) is:

- a. Perform a load flow analysis of the network to obtain all the network parameter values
- b. Perform an eigenvalue analysis and identify inter-area modes with poor damping ratios.
- c. Solve for the matrices C_V , C_θ , C_I , and C_θ using Equations (12) and (13)
- d. From the eigenvalue analysis performed, obtain the mode shape of the inter-area mode of interest
- e. Compute the network mode shape corresponding to the inter-area mode of interest, S_{Vj} , $S_{\theta j}$, S_{Ij} , and $S_{\theta j}$ using Equations (8) and (9) (j refers to the j^{th} network mode)
- f. Arrange the current magnitude mode shapes in descending order, identify the lines and corresponding receiving and sending network busbar
- g. The lines having the highest content of the inter-area current magnitude network mode shape indicate the dominant inter-area oscillation path.
- h. Plot the results onto the network schematic to identify the path.
- i. Verify the characteristics of the path using the computed network voltage magnitude

mode shapes and network voltage angle mode shapes.

The second algorithm to be used for the study of the dominant inter-area oscillation path is based on the observations presented in references [5,7,6,10], which show that the dominant inter-area oscillation flow paths are deterministic. Thus faults within various parts of the network will result in a mode being excited to some extent because of the energy imbalance during fault conditions. Hence busbar variables of interest (current and voltage) within the network having a high content of the oscillation energy can be identified by performing harmonic spectrum analysis of the busbar currents and voltages.

The methodology to be used for this algorithm (ii) is:

- a. Perform a load flow analysis of the network to obtain all the network parameter values
- b. Perform an eigenvalue analysis and identify the inter-area modes with poor damping ratios.
- c. Apply faults to various parts of the network:
 - i. Apply faults to areas which supply power and obtain the respective network busbar voltage and current sensitivities matrices
 - ii. Apply faults to areas which receive power and obtain the respective network busbar voltage and current sensitivities matrices
 - iii. Apply a fault to a random busbar in the main transmission grid which serves as one of the connecting paths for the inter-area oscillation flow and obtain the respective

network busbar voltage and current sensitivities matrices

- d. From the eigenvalue analysis performed, obtain the mode shape of the inter-area mode of interest.
- e. Compute the network mode shape corresponding to the inter-area mode of interest, S_{Vj} , $S_{\theta j}$, S_{Ij} , and $S_{\theta j}$ using Equations (8) and (9) (j refers to the j^{th} network mode).
- f. Arrange the current magnitude mode shapes in descending order, to identify the lines and the corresponding receiving and sending network busbars.
- g. The lines having the highest content of the inter-area current magnitude network mode shape indicate the dominant inter-area oscillation path.
- h. Plot the results onto the network schematic to identify the path.
- i. Verify the characteristics of the path using the computed network voltage magnitude mode shapes and network voltage angle mode shapes.

3.1 Algorithm Demonstration Using a Simplified Network

The study system which was used to demonstrate the application of the proposed algorithms is the well-known two-area network example taken from references [1,2,11,12].

Figure 1 adapted from references [1,2,11,12] shows a simple two-area system with power flowing from area 1 to area 2.

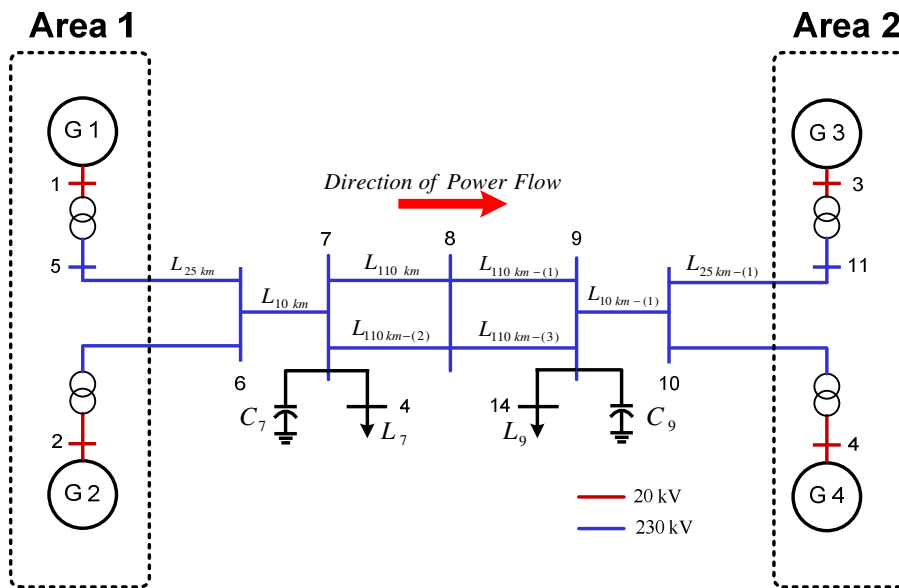


Figure 1: Simple two-area system adapted from references [1,2,11,12]

The data for the system is given in reference [1]. Eigenvalue analysis results of the power system are shown in Table 1 for a high gain thyristor exciter.

The Power system Stabilizer (PSS) was not considered in the analysis presented in this paper

Table 1: Eigenvalue analysis results for rotor oscillation modes (without PSS).

Load flow	Eigenvalue and (Frequency in Hz and Damping Ration)		
	Inter-area Mode	Area 1 Local Mode	Area 2 Local Mode
400MW	$+0.027 \pm j3.46$ ($\zeta = -0.00786, f = 0.551\text{Hz}$)	$-0.647 \pm j6.277$ ($\zeta = +0.102, f = 1.00\text{Hz}$)	$-0.659 \pm j6.473$ ($\zeta = +0.101, f = 1.04\text{Hz}$)
200MW	$-0.033 \pm j3.68$ ($\zeta = +0.008, f = 0.586$)	$-0.861 \pm j6.153$ ($\zeta = +0.139, f = 0.99$)	$-0.648 \pm j6.537$ ($\zeta = 0.099, f = 1.041$)

Based on the eigenvalue results given in Table 1, a single inter-area mode with poor damping was found, the busbar voltage and current sensitivity matrices were using Equations (12) and (13). The observability of the inter-area mode of concern was then used to calculate the network mode shape of the various busbar voltages and currents. It was found that the dominant inter-area oscillation path corridor is occurs along busbars 6-7-8-9-10.

Figure 2 (a) shows the normalized voltage magnitude mode shape and Figure 2 (b) the network voltage angle mode shape.

Artificial network busbars were added to the network in order to improve the resolution of the graph shown in Figure 2.

It can be seen in Figure 2 that the peak of the normalized voltage magnitude shifts to the left as the active power transferred from area 1 to area 2 is reduced, reference [8] states that this is a result of the AVR adjusting for different reactive power levels of the network.

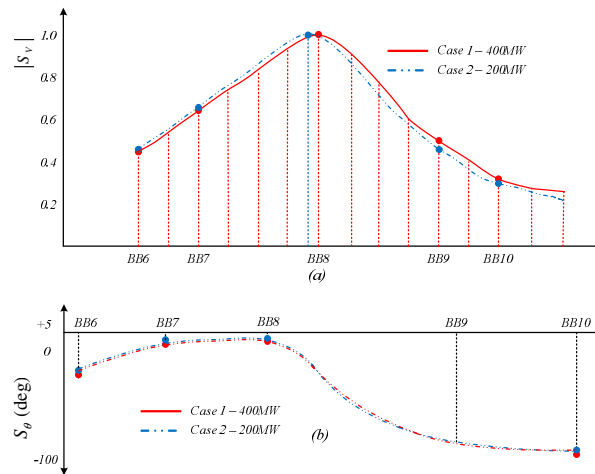


Figure 2: (a) Normalized network voltage mode shape (b) Voltage angle mode shape

It can be seen in Figure 2 (b) that busbar (8) serves as the pivot of the inter-area oscillation flow; this is based on the observation of the change of direction of the phase of the angle plot.

Both algorithms presented were used to identify the dominant inter-area oscillation path by calculating the normalized network voltage magnitude mode shape, and the normalized network current magnitude mode shape.

The normalized voltage and current magnitude results found using the two algorithms presented, were found to be identical. This is because; busbar voltages are primarily a function of the reactive power flow within the network, and normalized reactive power flow is a function of the various reactive power component responses, whether these responses are as a result of disturbances acting on the

network or calculated based on the influence of an individual generator on a busbar of concern in the network.

The voltage and current network mode shape angles values were not identical, but the graph shape for both cases was similar. The differences observed in the numerically computed solutions using algorithms (i) and (ii), arise as a result of the fact that the response of the network to a fault is governed by how long the fault acts on the network and the location of the fault within the network. These factors have an impact on the phase characteristics of the network because they directly influence the fault impedance and network stability.

Since the phase characteristics of the network obtained using algorithm (i) are based on the sensitivities of the network busbar voltage phase

angles and current phase angles to changes in generator torque or load angle parameters, the network responses based on these approaches will always be different to some extent from one another.

4. DISCUSSIONS & CONCLUSIONS

The use of algorithms to determine the dominant inter-area oscillation path using models is based on the assumption that sufficient data is available to model the network to an acceptable level and that the model behaviour has been verified.

The use of such techniques in the power system planning environment could help with identifying proposed network cases which are most prone to SSS restrictions. This would help to ensure that the full impact of introducing particular schemes and components into the network can be evaluated in much more detail as compared to using eigenvalue analysis which heavily relies on coherent generator grouping and cannot provide any further detailed information regarding inter-area oscillation modes.

This paper presented the application of two algorithms for the identification of dominant inter-area oscillation paths in power systems. The results obtained using the algorithms were confirmed using eigenvalue analysis and the observations were consistent with those presented in [1,11].

Dominant inter-area oscillation path identification also provides signals which have the highest inter-area oscillation content and hence these signals can be used to provide improved damping and optimal PMU placement within power systems. This analysis will also be carried out on the Eskom national grid in order to improve the SSS performance of the network as part of a larger research project.

ACKNOWLEDGEMENTS

I would like to acknowledge the Eskom Power Plant Engineering Institute (EPPEI) program for the opportunity and funding which they have provided for this research to be a success.

REFERENCES

- [1] P. Kundur, *Power System Stability and Control*, 1st ed., M.G Lauby N.J Balu, Ed. New York City, United States of America: McGraw-Hill, 1994.
- [2] G. Rogers, *Power System Oscillations*, 1st ed., M. Pai, Ed. Boston, London, Dordrecht, NETHERLANDS: Kluwer Academic Publishers Group, 2000.
- [3] Yonghua Song, Malcolm Irving Xi-Fan Wang, *Modern Power Systems Analysis*, 1st ed., Springer Science, Ed. New York, United States of America: Springer Science and Business Media, LLC, 2008.
- [4] Istvan Erlich Jose Rueda, "Impacts of large scale integration of wind power on power system small-signal stability," in *Electric Utility Deregulation and Restructuring and Power Technologies (DRPT), 2011 4th International Conference on*, Weihai, Shandong, 2011, pp. 673 - 681.
- [5] J.F Hauer, D.J. Trudnowski, and J.G. DeSteese, "A Perspective on WAMS Analysis Tools for Tracking of Oscillatory Dynamics," in *Power Engineering Society General Meeting, IEEE*, Tampa, FL, 2007, pp. 1 - 10.
- [6] L. Vanfretti and J.H. Chow, "Analysis of power system oscillations for developing synchrophasor data applications," in *Bulk Power System Dynamics and Control (iREP) - VIII (iREP), 2010 iREP Symposium*, Rio de Janeiro, 2010, pp. 1 - 17.
- [7] William A. Mittelstadt, Ken E. Martin, Jim W. Burns, and Harry Lee John F. Hauer, "Integrated Dynamic Information for the Western Power System: WAMS Analysis in 2005," in *Electric Power Engineering Handbook: Power System Stability and Control*, Leonard L. Grigsby, Ed. Boca Raton, FL, USA: Taylor & Francis Group, 2007, ch. 14, pp. 14-1 - 14-52.
- [8] L. Vanfretti and J.H. Chow, "Computation and analysis of power system voltage oscillations from interarea modes," in *Power & Energy Society General Meeting, 2009. PES '09. IEEE*, Calgary, AB, 2009, pp. 1 - 8.
- [9] Y. Chompoobutrgool and L. Vanfretti, "Identification of Power System Dominant Inter-Area Oscillation Paths," *IEEE Transactions on Power Systems*, vol. 20, no. 3, pp. 2798 - 2807, December 2012.
- [10] E. Z Zhou, "Power Oscillation flow Study of Electric Power Systems," *Electrical Power & Energy Systems, Elsevier Science Ltd*, vol. 17, no. 2, pp. 143 - 150, 1995.
- [11] G. Rogers, M. Klein P. Kundur, "A fundamental study of inter-area oscillations in Power Systems," *Transactions on Power Systems*, vol. 6, no. 3, pp. 914-921, August 1991.
- [12] M. Klein, G. Rogers, and M. Zywno P. Kundur, "Application of Power System Stabilizers for Enhancement of Overall System Stability," *IEEE Transactions of Power System*, vol. 4, no. 2, pp. 614-626, May 1989.
- [13] Juan J. Sanchez-Gasca, Haoxing Ren, and Shaopeng Wang Joe H. Chow, "Power System Damping Controller Designs using Multiple Input Signals," *IEEE Control Systems Magazine*, vol. 20, no. 4, pp. 82 - 90, August 2000.
- [14] Y. Chompoobutrgool and L. Vanfretti, "A fundamental study on damping control design using PMU signals from dominant inter-area oscillation paths," in *North American Power Symposium (NAPS)*, Champaign, IL, September 2012, pp. 1 - 6.

CAMEL NETWORK DEVELOPMENT PLAN

K Jikija* and P. Lazanas**

* University of Johannesburg, plazanas@uj.ac.za

** Transnet, Khayakazi.Jikija@transnet.net

Abstract. Network development is required in the Caramel Network which is situated in the North West and Gauteng provinces. Historical loading data, trending forecast indicated that growth in Arola Substation within Caramel Network will reach its maximum capacity in 2019. The project has been initiated as a result of overload of 121.55% experienced by Arola which is not within acceptable limits. Digsilent simulations on the existing and proposed network were made to comprehend technical disadvantages and advantages of having an overloaded system. The following were observed during simulation: loading, three phase and single phase to earth faults plus voltage drops. The following findings were made: by installing 2x 20MVA transformers the capacity is created in Arola substation. Installing new transformers automatically alter the relay settings of the network, hence new settings calculations have to be performed.

Keywords: Network developments, simulations, relay settings

1. INTRODUCTION

1.1 General Background

In this modern world, the dependence on the electricity is so much that it has become the part and parcel of our lives. The ever increasing use of electric power for domestic, commercial and industrial use necessitates expansion of the network from time to time in order to meet the demands of the customers and avoid overloading of the network. Transformers and other electrical equipment that are loaded above their ability to carry the current can be damaged or fail completely. The amount of damage depends on how heavily the equipment is overloaded. [1]

It is therefore essential to exercise utmost care when developing network, however decisions on the expansion of electricity are bogged down by high investment requirements and non-synchronised expansion between electricity generation and distribution. The expansion of a power system requires load studies, real and reactive power in various points of the electrical network.

High speed protection is important factor that need to be achieved on distribution network under fault conditions. Failing to clear faults on the network may result in unwanted conditions such as power instability, equipment damages due to high mechanical stresses during fault conditions

Therefore it is required that under fault conditions breakers should operate effectively to clear the fault completely.

Caramel Network is one of the largest Networks in the Grid. It consists of more than 10(ten) Substations feeding the Gauteng and North West

Areas. Due to the future load demand the some of the Substations experience overload.

The project will involve increasing substation capacity to cater for load growth in the area so as to ensure reliability and continuous supply.

1.2 Problem Definition

Growth in Arola substation will lead to future load demands, which will result to the substation reaching its maximum demand of 10 MVA in 2019.

2. POSSIBLE SOLUTIONS

2.1 Solution 1

Introduce a new substation that will assist existing substation by supplying the future customers

Advantages:

- i. Substations will be relieved from overload
- ii. Long term solution for future growth in the area

Disadvantages:

- i. High costs of building the new substation.
- ii. High costs of load shifting

Solution 2

Shift the load to the nearby substations from Arola to Doorn or Mooiriver rural or Elandsrand or Deelkraal Substations

Advantages:

- i. The Arola Substation will be relieved.

Disadvantages:

- ii. High costs of shifting the load
- iii. This is not a long term solution.

Solution 3

Install an additional 20MVA transformer and replace the existing 10 MVA with 20 MVA.

Advantages

- i. The system will be relieve the system
- ii. In case one transformer fails the other one will be able to feed (N-1).

Disadvantages

- i. There will be high cost of purchasing the transformers
- ii. There might be space issues

Cost comparison

Costing assumption used (%PPI escalation being used for the next 3 financial years: See table 1a

Table 1a

Options	Cost
1	R91,799,258.82
2	R1,809,287.30
3	R30,877,906.25

3. AIM

The preferred solution is option 3: Install an additional 20MVA transformer and replace the existing 10 MVA with 20 MVA.

4. SCOPE OF THE PROJECT

- i. Data Collection
 - All equipment specification
 - Literature review
- ii. Network Modelling using Digsilent
- iii. Load flow and results analysis
- iv. Perform and calculate faults currents and relay settings

All the necessary information about the networks was gathered at Eskom. This includes the cable types and sizes, transformer name plate information, Current transformer data, old relay settings. The network was modelled using Digsilent to perform simulations. The software enables to put all the required settings on the equipment.

5. OUTCOMES

Simulation of Option 01

The results in table 1b show the existing network with Arola loaded at 121.55% and Doorn at 95.90%.

Red colour represent overload, orange = above 80% or its rated and blue colour represents low voltage.

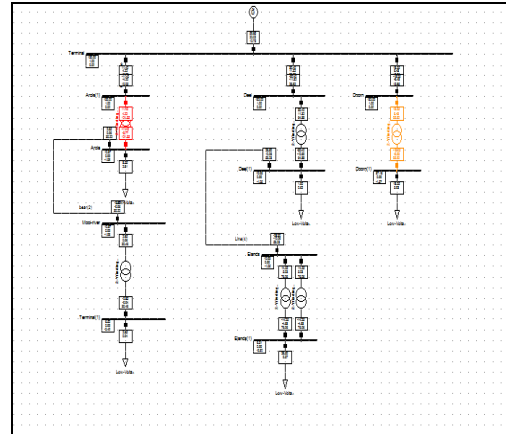


Figure 1: Existing network

Table 1b: Results existing network

Station	P(MW)	Q(MVar)	Loading%
Arola	11.40	4.22	121.55%
Deel	30.40	11.32	64.88%
Doorn	18.05	6.68	95.90%
Moorriver	9.76	3.43%	30.46%
Elands	14.25	5.03	76.06%

Figure 2 shows the results from shifting the load from Arola substation to the nearby substation. The network is not relieved

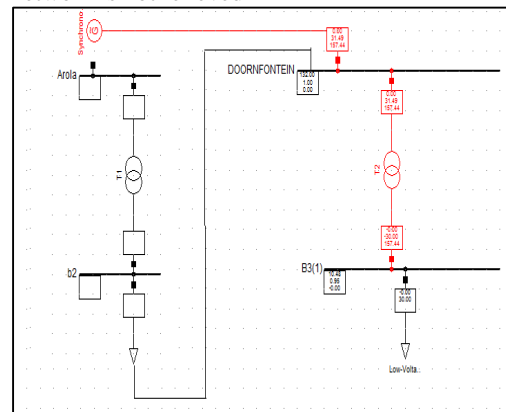


Figure 2: Shifting of load from Arola-Doorn

Table 2: Results of Arola-Doorn

Station Name	P(MW)	Q(MVar)	Loading%
Doorn	22.80	7.49	121.45
Arola	4.75	1.56	50.24

Figure 3 and table 3 below, show the results from shifting the load from Arola to Mooi-river. The network is not stable as Mooi-river has the challenges of overload and voltage drops.

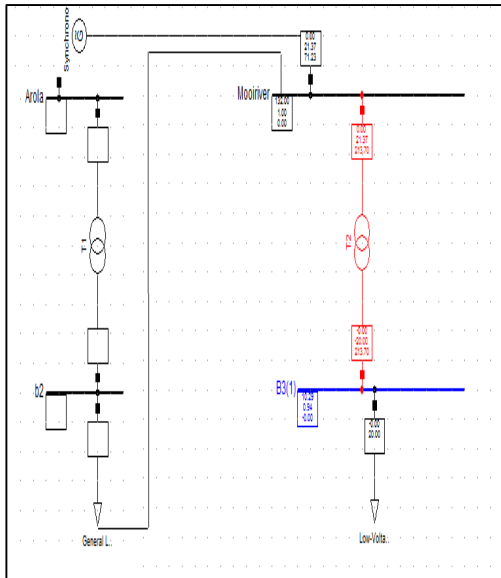


Figure 3: Arola-Mooi-river

Table 3: Results of shifting Arola-Moorriver

Station Name	P(MW)	Q(MVar)	Loading%
Mooi-river	7.6	2.50	80.63%

Shifting the load from Arola-Elandsrand results in Elandsrand experiencing overload of 88.26% as per Table 4.

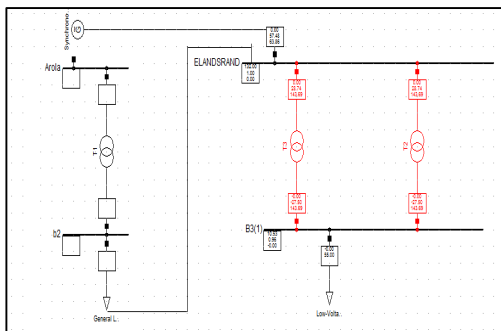


Figure 4: Arola-Elandsrand

Table 4: Results of Arola-Elandsrand

Station Name	P(MW)	Q(MVar)	Loading%
Elands	33.25	10.93	88.26

Table 5 shows the results after simulation of shifting the load from Arola-Deelkraal

Table 5: Results of Arola-Deelkraal

Station Name	P(MW)	Q(MVar)	Loading %
Deel	6.65	2.33	70.48
Arola	4.75	1.64	50.24

Results from simulating option 01: Shifting the load to the nearby substations does not solve the problem.

Simulation of option 02

Figure 5 and table 5a shows the results when an additional 10MVA is installed

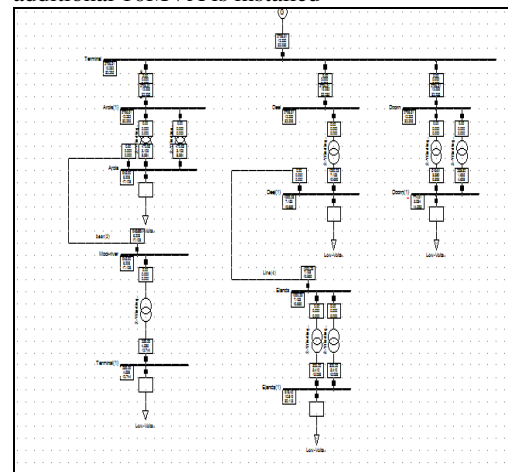


Figure 5: Install additional 10MVA transformer

Table 5a: Results

Station name	P(MW)	Q(Mvar)	Loading%
Arola(before)	9.50	3.12	121.45
Arola (after)	4.75	1.56	50.24

There is stability in the network, but the network will still experience loading challenges should one of the transformers fail.

Simulation of option 03:

10MVA replaced by 20MVA and additional 20MVA installed. This is shown in figure 6a and 6b

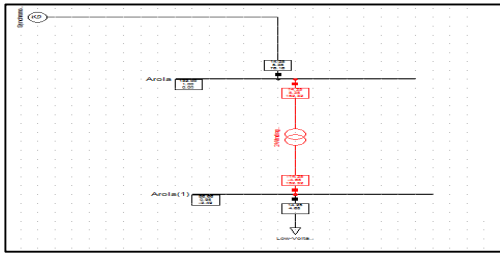


Figure 6a: Arela Substation before

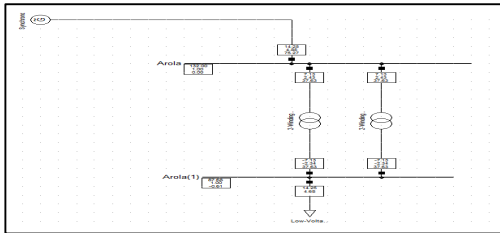


Figure 6b: Arela Substation after

Results of an improved network

Table 6a and 6b shows the results before and after the upgrade

Table 6a: Results of the Network before

Station	P(MW)	Q(Mvar)	Loading%
Arela	11.40	4.22	121.55%
Deel	30.40	11.32	64.88%
Doorn	18.05	6.68	95.90%
Moorriver	9.76	3.43%	30.46%
Elands	14.25	5.03	76.06%

Table 6b: Results of the Network after

Station name	P(MW)	Q(Mvar)	Loading%
Arela	5.70	1.94	30.11
Deel	30.40	11.32	64.88
Doorn	12.03	4.20	63.72
Moorriver	2.85	0.96	30.46
Elands	14.25	5.03	76.06%

The 10Mva at Arela installed at Doorn making it 30Mva, the results are shown in table 6c

Table 6c: Results of Doorn Substation on additional 10MVA transformer from Arela

Station name	P(MW)	Q(Mvar)	Loading%
Doorn (before)	18.05	6.68	95.90%
Doorn (after)	12.06	5.93	63.72

The results show the network or substation at its firm capacity;

From table 6a above it can be seen that the transformers are overloaded before the upgrade of the substation and after the upgrade all the transformers are operating on normal conditions.

Relay settings of the upgraded network

The relay grading and co-ordination calculations were done according to [3, 4] as shown in table 7b. The simulations were then done using the new calculated settings. Simulated values of the fault level are shown in table 7a

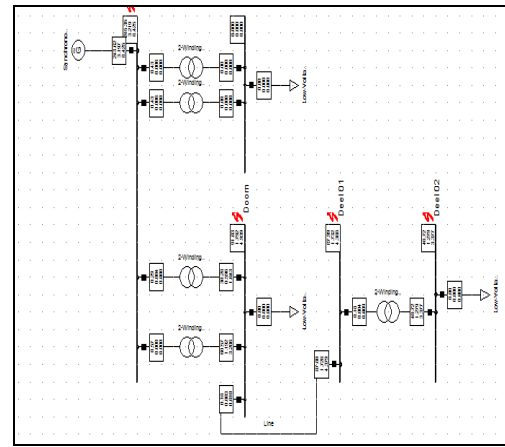


Figure 7: Upgraded network

Table 7a: Fault levels

3 Φ	Station name	Busbar name	If value(kA)	S fault value(MVA)
	Deelkraal 1	Deel 02	1.120	127.98
	Deelkraal 1	Deel 01	1.384	210.97
	Doorn	Doorn 02	1.423	216.82

1 Φ	Station name	Busbar name	If value(kA)
	Deelkraal	Deel 02	1.279
	Deelkraal	Deel 01	1.732
	Doorn	Doorn 02	1.793
	Doorn	Doorn-Supply	3.219

Table 7b: Grading of relays

	I_{max}(kA)	I_{min}	T_{min}
Relay A	1.120	-	0.25
Relay B	1.384	840	0.67
Relay C	1.423	948.66	1.089

4. John J. Grainger & William D. Stevenson, JR, "Power System Analysis", McGraw Hill. Inc, pp378, 1994

6. FINDINGS

The network is stable and reliable on installation of additional 20MVA transformer, Doorn main is also stable as the transformer shifted from Arola .The studies indicate that the network will operate under satisfactory conditions with the new changes in place.

7. RECOMMENDATIONS

Based on the above mentioned findings from the results obtained in Digsilent it is strongly recommended that the relay settings are set as per revised calculations.

Overloading of electrical equipment is unacceptable in electrical network. The main objectives of this paper were to evaluate the possible solutions of relieving the network and accommodate future developments.

Findings show that the network will be stable and reliable on installing of 2×20MVA transformers and revise the settings of protection relays.

ACKNOWLEDGEMENTS

I would like to thank Dr. P. Lazanas for guiding me throughout the year (power systems and projects). The role he played in my career enhanced my knowledge in the engineering field; I would like to also thank Mrs Hope Kunene for assisting and mentoring me with the project.

REFERENCES

1. Balabanian, N., and T.A. Bickart, "Power and Energy," in *The Electrical Engineering Handbook* R.C.Dorf(ed), pp 79,CRC Press, Boca Raton,FL,1993
2. V.K Mehta & Rohit Mehta, "Principles of Power systems" S Chand & Company, pp73, LTD 2004.
3. Chowdhury ,Bradul, "Power Distribution and Control," in *The Electrical handbook*, Jerry C. Whitaker(ed.), pp1003, CRC Press, Boca Raton, FL,1996

DEVELOPMENT OF AN INSTALLATION AND COMMISSIONING PROCESS FOR MV OPEN RACK HARMONIC FILTERS FOR DISTRIBUTION NETWORKS

A M Meru* and G Atkinson-Hope**

*Department. of Electrical, Electronic and Computer Engineering, Cape Peninsula University of Technology,
P O. Box 652, Cape Town, 8000, South Africa. E-mail: MeruA@cput.ac.za

** Technology Transfer and Industrial linkages, Centre for Power Systems Research, Cape Peninsula University
of Technology, P.O. Box 1906, Bellville, 7539, South Africa. E-mail: AtkinsonHopeG@cput.ac.za

Abstract. Harmonic filters are the most common means used for harmonic mitigation. The installation and commissioning process of harmonic filters is not well known. There is thus a need of research and documentation on this process which is in the know-how of very few specialists. The medium voltage open rack harmonic filter is the most common filter found in industry and mines and is an outdoor installation and consists of air core reactors, capacitor banks and in some instances resistors. During the installation and commissioning steps, certain aspects are considered and made necessary for the process to be completed. To meet the need, information was gathered by conducting interviews with specialists in the harmonic industry. A network is investigated and two types of harmonic filters are considered and the processes are discussed.

Key Words. Harmonic filter, installation, commissioning

1. INTRODUCTION

Harmonic filters have been used for mitigation for some decades now. Open rack harmonic filters are outdoor installations and are commonly used in the medium voltage industries and mines.

The shortcoming is that knowledge on the installation and commissioning of medium voltage open rack type harmonic filters is not well documented and the process is only known to a few specialists. The objective of this paper is to make the process known and prove its effectiveness through a network that was investigated

2. RESEARCH STATEMENT

The aim of this paper is to develop an installation and commissioning process for medium voltage open rack harmonic filters for typical real life scenarios.

3. INSTALLATION

The installation of filters for industrial application needs to take into account certain factors that have not been publicly documented. When evaluating what is needed in harmonic filter installation, the site and filter components are looked at.

3.1 Installation Drawings

Before doing an installation, drawings are prepared that show the physical placement of the filter components on a site, clearly indicating the dimensions of the components (their size) and their relationship to each other and the site boundaries.

3.2 Site construction

The choice of site where one or more harmonic filters are to be installed depends on certain factors. Such

factors can be from the number of filters, types of filters, proximity of the filter to power supply, data from component manufacturers and the space available. At such a site, the ground has to be level and gravel is spread all over the floor of the site. Gravel is a good insulator and caters for water logging at the site and is also used for covering the earth conductors connected to the earth mat.

Concrete plinths are constructed at the site for the filter components. The plinths are built so that the bases are not subjected to unnecessary physical stresses. A plinth is a concrete foundation of correct size and weight absorbing capability on which racks can be mounted.

The reactors position should not be near any metallic parts as there may be magnetic coupling. Since there are magnetic fields generated by the reactors, the concrete plinths are constructed without any metallic reinforcements. The reactors are mounted on stands with insulators to lift them above ground level.

The area occupied by each filter component has to adhere to the specifications supplied by the manufacturer. This also depends on the space limitations.

3.3 Site preparation and grounding connections

Grounding connection is the connection used to establish a ground point and consists of a grounding conductor, or a grounding electrode, and the earth that surrounds the electrode or some conductive body that serves instead of the earth [1].

A common ground is the point at site where all ground points meet with continuity to ground. The common ground is connected to the ground mat. The ground mat is a system of bare conductors, on or below the surface of the earth, connected to the ground or ground grid to provide protection from dangerous touch voltages. Plates and gratings of

suitable area are common forms of grounded mats [1].

3.4 Site fence

The site where the filter is installed must be fenced and is usually at a place without trees around. The fence prevents access into the site by human beings and animals that need to be kept away. The fence for the filter site is positioned adequately far away (about 2m) from the reactor positions so that magnetic coupling does not occur.

3.5 Filter installation

The installation of the harmonic filter is explained per filter component i.e. capacitors, reactors and resistors.

3.5.1 Capacitors

Capacitor banks are delivered from manufacturers either in pallets, open or closed crates or in containers. The client is required to verify the name plate on the capacitors upon delivery. Bushings are to be inspected for cracks as damage may occur in transportation.

A capacitor rack consists of a specific number of capacitors connected in series and parallel to obtain the expected voltage and Var size. The number of capacitors for a filter is given by manufacturers as per the design template specifications. The capacitors are connected in series and parallel in a rack. In such a rack, the capacitor elements will have bushings and interconnecting busbar.

When moving the capacitor banks, lifting lugs (see Figure 1) should be used for each rack. The lifting lugs are connected to each stack to make it balanced and have good lifting points to avoid sliding or skidding. It is insisted that no lifting should be done via bushings since they can easily be damaged.

Some elevating structures can be employed if necessary and should be requested depending on capacitor rack size can be supplied by manufacturers. In most cases the capacitor banks are delivered unassembled.

Figure 1 shows an already assembled capacitor rack being off loaded from a truck at an installation site using a crane. The lifting lugs are connected to the rack for easy connection to the crane. In such a case the capacitor rack was assembled before being delivered to the installation site.

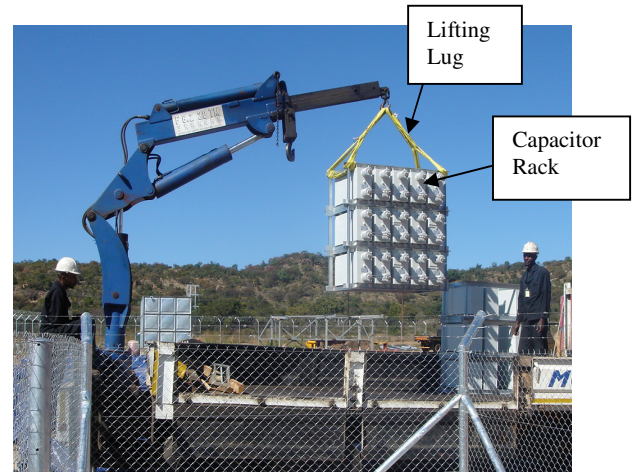


Figure 1: Crane removing capacitor rack from truck

The connection of the banks to the supply busbar is done with specifications given by capacitor manufacturers. Spring washers are used with unit nuts to tighten capacitor units to a busbar and are done according to torque strengths [2] provided by the manufacturer.

Table 1: Recommended torque for capacitor nuts

Wrench	Tightening torque Nm
M12	15-18
M14	30-34
M16	40-50

3.5.2 Reactors

The reactors are usually delivered in crates without insulators and bushings as they could be damaged during transportation. The manufacturer supplies drawings for the assembly of a reactor rack. The reactor specifications should be verified upon delivery to verify the reactor ordered. A typical harmonic filter reactors nameplate is shown in Figure 2.

HARMONIC FILTER REACTOR			
AREVA	Type 3xHFC-5700/186	Serial n° 08.9228-01	CENTRAL COIL
Rated Inductance	5.7 mH (±2.5%)	System Voltage	11 kV
Rated Impedance	1.79 Ω	Bill Between Terminals	95 kVp
Rated Frequency	50 Hz	Short-time Current/Duration	3.4 kA/ 1 s
Rated Current	174 A	Offset Peak Current	8.7 kAp
Design Current	186.2 A	Total Losses (75°C/in)	2.35 kW
Rated Power	54.2 kvar	Q-Factor/Frequency	> 82 / 250 Hz
Cooling	A.N.	Altitude	≤ 1400 m.a.s.l.
Installation	Outdoor	Ambient Temperature	45 °C
Temp. class	B (130 °C)	Standard	IEC-60289/88
N° Phases	1	Year	2008
Weight	3 x 152 kg	Instruction book n°	11622

Figure 2: Reactor Nameplate

Terminals are used for electrical connections to the coils while the insulators are used for insulation with the reactor stacks. Insulators separate the coils from each other as they are vertically mounted but there must be a way in which connections are made to the electrical system. Each phase has an electrical input and output terminal made of Copper Aluminium

(CuAl) plates that are used for the electrical connections (see figure 3).

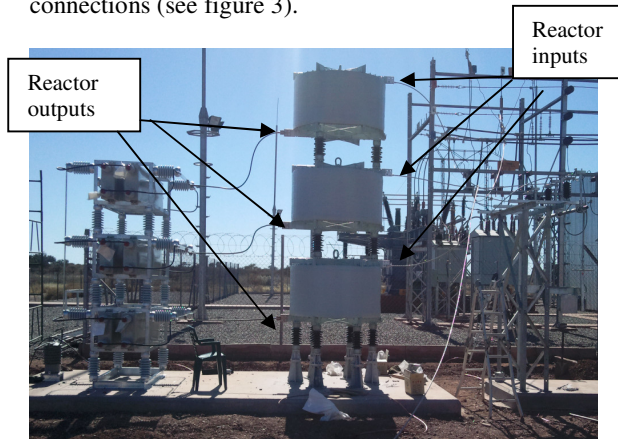


Figure 3: Reactors electrical input and output connections

When reactors are delivered by the manufacturers to the client, a technical sheet is supplied. The sheet will have data on the environmental conditions for installation, electrical data, construction data and support system.

The reactor terminals should be at the right position by placing the middle coil and tightening the bolts. The top reactor is mounted on the middle reactor just as the middle one is done on the bottom one.

After the installation, the terminals of the reactors are cleaned and layers of grease are applied to prevent corrosion. The installation engineers and technicians also make sure terminals are tightened using correct tightening torques not to damage the reactor terminals which are made from Aluminium. Nokian capacitors [3] have the recommended torques for the reactors seen in Table 2 with right wrench to be used.

Table 2: Recommended tightening torques for reactors

Joint	Screw/nut Material	Wrench	Tightening torque Nm
Insulators	AISI	M12	45-50
		M16	95-105
Others	AISI	M10	40-45
		M12	70-75
		M16	110-130

3.5.3 Resistors

Resistors are usually connected in parallel with the reactors for the 2nd order harmonic filters. Resistor banks are in most instances constructed before delivery to site. They come assembled with insulators and internal connections ready for installation.

For transportation purposes the resistor banks are mounted on wooden pallets and fastened with bolts to avoid any damage while on the move. Lifting lugs are supplied for loading and unloading. The client is requested to inspect the banks on arrival to check if

any damages occurred in transportation. Inspection includes verifying that all insulators are intact, all internal connections and bolts are tight after transportation and the insulators are clean and unpolluted. Since resistor banks are heavy, they are handled carefully using either cranes or forklifts [4]. Resistor banks are placed on prepared concrete foundations depending on their weight loading. This foundation is designed to withstand stresses during operation, such as wind, ice load, vibrations etc. The foundation must be of adequate distance away to give the required clearance from the reactor and capacitor banks respectively. Data of harmonic filter resistors on the electrical part, enclosure arrangement and design should be adhered as per the recommendations [5, 6].

During installation, the bushings on the resistor banks should be mounted and tightened. Lifting lugs are used to erect and place the resistor banks on its foundation. They are stacked units and porcelain is installed on the bottom of the metallic structure or steel bottom plate with the right bolts. The middle and top unit are installed in the same manner. The banks have to be properly grounded and the input and output connections are tightened.



Figure 4: Harmonic filter resistor assembled ready for installation

4. COMMISSIONING

The commissioning of the harmonic filter is dealt with per filter component.

4.1 Capacitors

With capacitors the tests and procedures below are conducted or followed depending on size of bank.

a) The capacitance is measured using capacitor meters. The readings are used to verify that the values are correct and the phases are balanced. If the values are not balanced, then each capacitor element is measured to note the one that is not operating as expected.

- b) Verifying that the capacitors are installed according to manufacturer diagrams.
- c) In some instances current transformers are used to measure current supplied to the capacitor banks. The continuity of such transformers is measured as some transformers may have defects of manufacture.
- d) In the control panels of some filters, some control programmes are designed for the operation. These are dependent on the client's needs so optional. They could be for alarms in case of overcurrent, power factor controllers, etc. These are verified by injecting currents in the control circuits where the current transformers measuring harmonic switch on the relays. The relays will switch off the circuits and ignite the alarms in cases where the harmonic content exceeds expected values.
- e) Tests can be done on the capacitor switches and control panel lights to make sure they operate as expected.
- f) The cables supplying the filters are checked to make sure that they conform to the rated values and also make sure the cables are not overheating or producing any "hissing" noises.
- g) Checks are conducted of bushings of the capacitor banks for any chips or cracks that might have occurred during transportation or installation. If any irregularities are found, the components are replaced immediately.
- h) The voltage and current in each phase is verified using power analysers to make sure they are balanced and within the ratings of equipment.
- i) 24hrs after commissioning of the banks, visual checks should be conducted to note if there is any

occurrence of overheating of electrical joints in the banks.

4.2 Reactors

Before commissioning the reactors, all joints are checked referring to the manufacturers specified torque values. Visual checks on the surfaces of the reactor are conducted. The continuity of all ground points is checked using meggers or resistance meters. It is important to verify that no loose objects such as tools and bolts are left on the reactors or between cylinders or near the reactors as they can induce some magnetism when the filter is switched on.

4.3 Resistors

With resistor banks, the resistance is measured at cold temperature and insulation resistance of resistor mid-point and resistor frame ensuring the value should be over 500 Mega-ohms under 500V DC. The values should take into consideration the ambient temperatures of the site for installation and compared with the suppliers readings. Other tests done in the commissioning of resistor banks are shown by Microelettrica Scientifica (M.S.) [7]. Resistance tests are such as insulation resistance tests and applied dielectric tests.

A flow chart on installation and commissioning of a harmonic filter is shown in figure 5 which is a continuation from the design stage (Flow chart A) of the filter which is not mentioned in this paper.

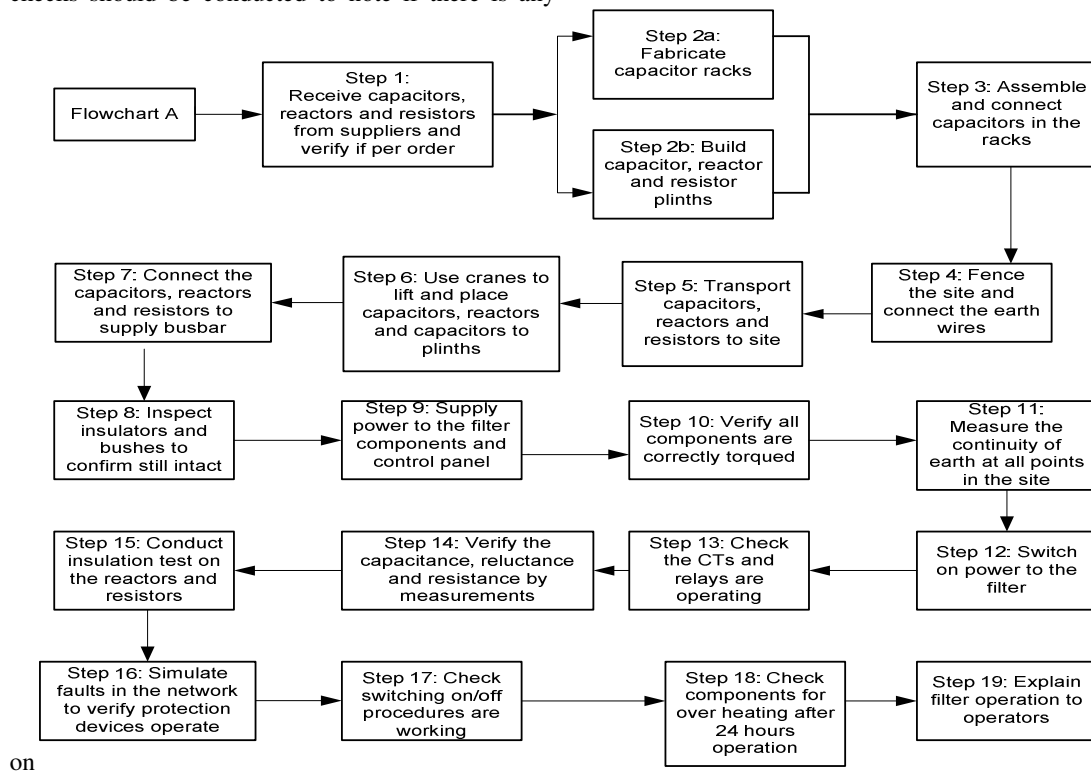


Figure 5: Flow chart on installation and commissioning of harmonic filter

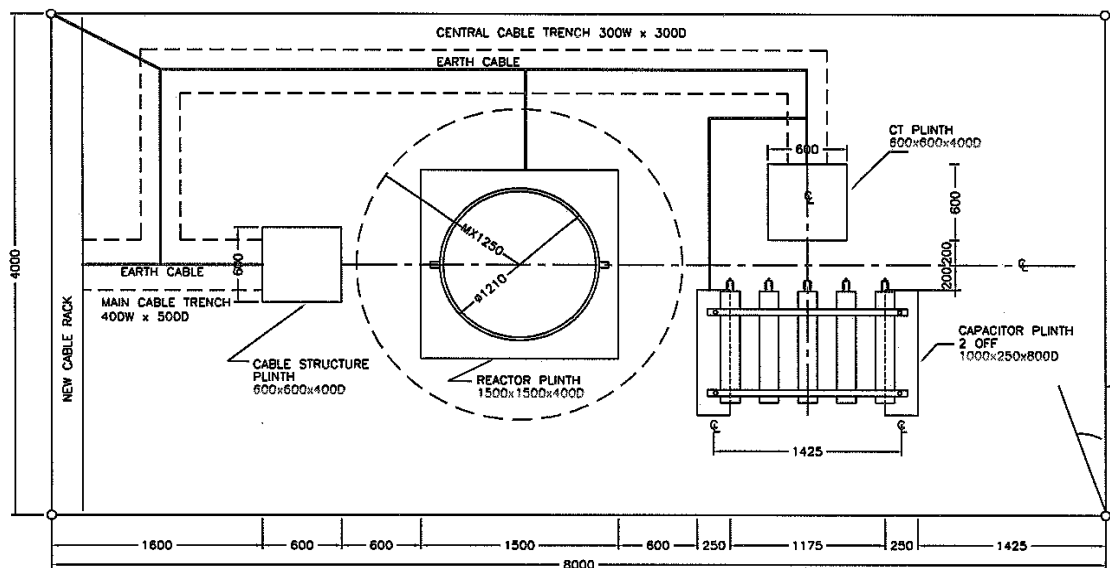


Fig.8: Top Plan view of harmonic filter components (Courtesy of RWW Engineering, South Africa)

The capacitors and reactors are then connected in star to the power supply from components the control panels (Figure 9).

The 5th harmonic filter to be installed at bus 5A in the case study network would have similar dimensions as the 4.5 MVar 5th harmonic filter shown in in figures 7, 8 and 9.

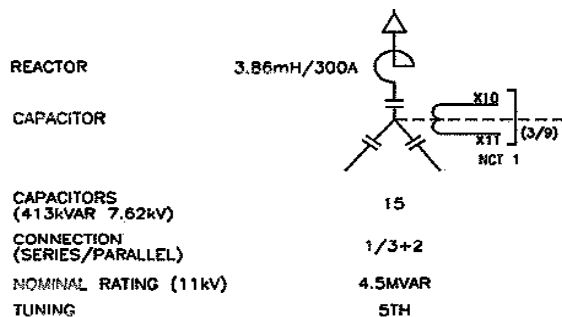


Fig.9: Capacitor and reactor star connection (Courtesy of RWW Engineering, South Africa)

The developed process in the flow chart in figure 5 can be implemented in the 5th harmonic filter at bus 5A in a real life scenario.

In the harmonic filter design, a 7.9 MVar second order harmonic filter was also designed at bus 4 using capacitors at buses 4A and 4B respectively. The filter would be installed in an area of 6000 mm by 8000 mm. The extra area recommended for this filter differs from the 5th harmonic as the resistor bank in this filter is now incorporated in the site. This also considers that the filter components are installed in a vertical layout.

6. CONCLUSION

The process for installation and commissioning of medium voltage open rack harmonic filters is a specialized field. Installation entails having a combination of electrical and civil engineering labour.

Time constraints should be considered as some components take time before delivery from manufacturers. Tests will be conducted on filter components such as cts, relays, cables, switches etc which are sensitive to any faults on the filter performance. Tests are emphasized to be conducted again 24 hours after commissioning of the filter.

ACKNOWLEDGEMENT

The Authors would like to thank staff at RWW Engineering (PTY) Ltd for the diagrams and photos of harmonic filters.

REFERENCES

- [1] Kruesi, W.R. et al 1978. IEEE Std. 100-1977. IEEE Standard dictionary of Electrical and Electronics terms, second edition, 22 May 1978.
- [2] Nokian Capacitors brochure, "High voltage capacitors and capacitor bank (U>1000V, Instructions for installation, operation and maintenance", Version O/MHe, pp. 10-17, 8th June 2001
- [3] Nokian Capacitors brochure, "Air core reactors, Instructions for installation, use and maintenance", Version 1.2KJy, pp. 5-9, 11th November 2002.
- [4] Installation & Maintenance Manual Damping Resistors, [http://www.msresistances.com/2-DA/Operation%20Manual%20%20\(DA\).pdf](http://www.msresistances.com/2-DA/Operation%20Manual%20%20(DA).pdf).
- [5] Microelettrica Scientifica (M.S.) Resistances. 2008. *Inspection & Test Plan (ITP)*, [http://www.msresistances.com/2-DA/ITP%20\(Draft\).pdf](http://www.msresistances.com/2-DA/ITP%20(Draft).pdf)
- [6] Filter Resistor Data Sheet Ref. R10. n.d., http://www.fortressresistors.com/wp-content/uploads/R10_00_FILTER_RESISTORS.pdf
- [7] Installation & Maintenance Manual Damping Resistors, [http://www.msresistances.com/2-DA/Operation%20Manual%20%20\(DA\).pdf](http://www.msresistances.com/2-DA/Operation%20Manual%20%20(DA).pdf)
- [8] E, Thunberg & L, Soder, "Norton Approach to distribution network modelling for harmonic studies". *IEEE Transactions on Power Delivery*, vol. 14, no. 1, January 1999.

Proceedings of the 22nd South African Universities Power Engineering Conference 2014
Improving the System Average Interruption Frequency Index (SAIFI) and the System Average Interruption Duration Index (SAIDI) on the ESKOM 11kV Bronze, Cuprite and Ferrous feeders, feeding from the Klevebank 88/44/11kV substation in the Sandton Diepsloot area.

Q E Louw* and P Lazanas**

*Ntamo Technologies (Pty) Ltd, quentin.louw@ntamotechnologies.co.za

** University of Johannesburg, plazanas@uj.ac.za

Abstract. ESKOM Gauteng Operating Unit's Plant and Network Performance division have been confronted with a high number of **System Average Interruption Frequency Index (SAIFI)** and **System Average Interruption Duration Index (SAIDI)** events over the past 36 months as measured in accordance with the requirements of specification [1]. NRS 048-6:2006 and [2]. IEEE Std 1366-2003 on the Eskom 11kV *Bronze, Cuprite and Ferrous* feeders, feeding from the *Klevebank 88/44/11kV* substation in the Sandton area. Reviewing the performance data from the [10]. Eskom performance system and using the [10]. DigSILENT Powerfactory network simulation tool has resulted in findings and recommendations of proposed new improved SAIFI and SAIDI quality of supply parameters

Key Words. SAIFI, SAIDI, Quality of Supply, Network Studies

1. INTRODUCTION

ESKOM Gauteng Operating Unit's Plant and Network Performance division situated at Simmerpan, Germiston have been confronted with a high number of **System Average Interruption Frequency Index (SAIFI)** and **System Average Interruption Duration Index (SAIDI)** events over the past 36 months as measured in accordance with the requirements of specification [1]. NRS 048-6:2006 (ELECTRICAL SUPPLY – QUALITY OF SUPPLY Part 6: Medium voltage network interruption performance measurement and reporting) and [2] IEEE STD 1366-2003: (IEEE Guide for Electric Power Distribution Reliability Indices) on the Eskom 11kV *Bronze, Cuprite and Ferrous* feeders, feeding from the *Klevebank 88/44/11kV* substation in the Sandton, Mnandi Diepsloot area.

The SAIFI and SAIDI interruption events are illustrated from figure 1.1 through to figure 1.6 for these particular networks and have been sustainably high indicating the plethora of interruptions.

Although Eskom have taken some corrective action towards improving the quality of supply parameters measured against the intended benchmarks, it has seemed challenging to establish and maintain long term improved solutions to address the underperforming indicators associated within these networks as a result of factors highlighted within the findings presented in this paper.

As stated in a paper presented by [3] Mr. Martin Cameron and Dr. Clinton Carter-Brown to 63rd AMEU convention in 2012 "The potential performance of a network, while influenced by operations, is mainly determined via the inherent design characteristics of the network e.g. lengths of feeders, number of customers supplied per feeder (which in turn is influenced by the development and land-use of an area e.g. urban, rural or agricultural, etc.), inter-connectivity between feeders and redundancy of installed equipment".

The paper further presents that "The fundamental flaw with the benchmarking-based approach is its ignorance of current network topology (which in itself is a function of past policies and design philosophies), and its influence on the inherent performance level capability of the distribution system".

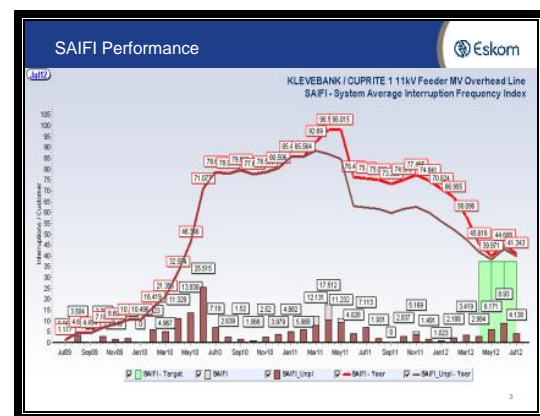


Figure 1.1 SAIFI Cuprite Feeder

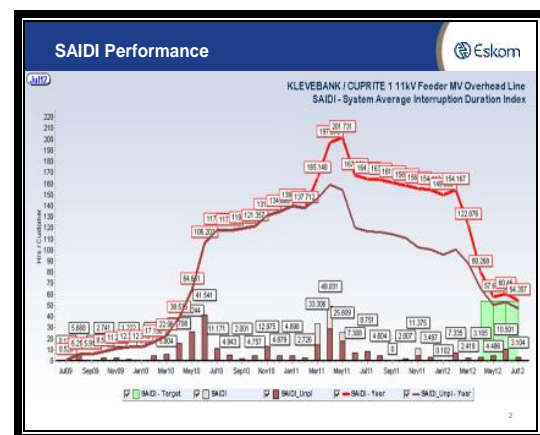


Figure 1.2 SAIDI Cuprite Feeder

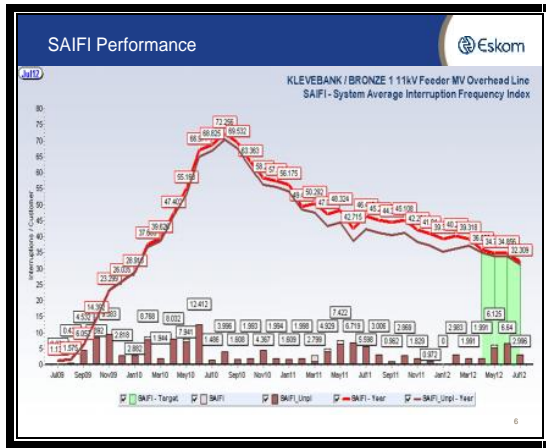


Figure 1.3 SAIFI Bronze Feeder

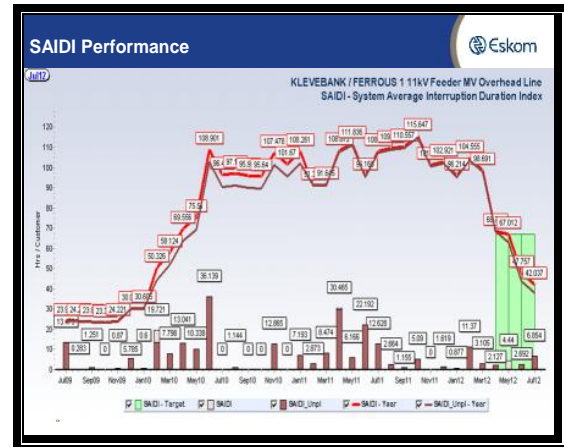


Figure 1.6 SAIDI Ferrous Feeder

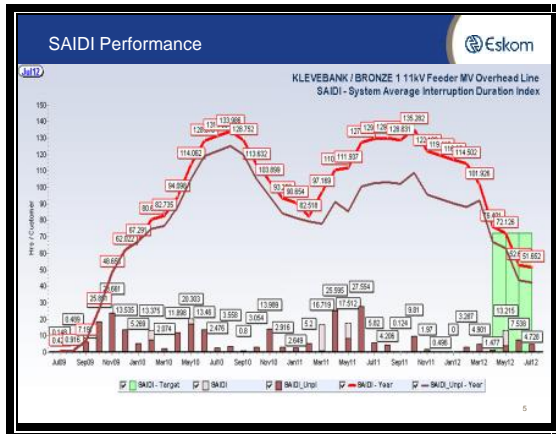


Figure 1.4 SAIDI Bronze Feeder

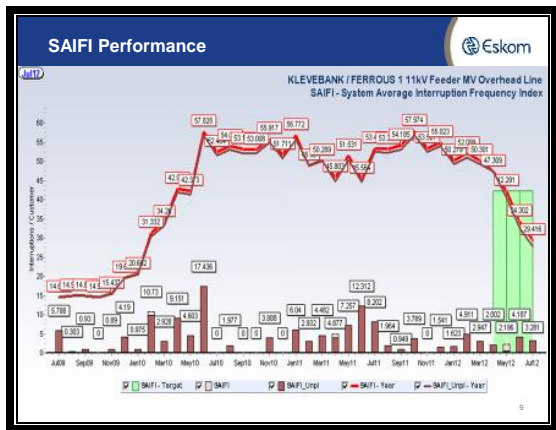


Figure 1.5 SAIFI Ferrous Feeder

1.1 Root cause analysis of interruptions.

The statistics presented in figure 1.7 to figure 1.9 illustrate the root cause analysis statistics captured within the [12] Eskom quality of supply performance monitoring software.

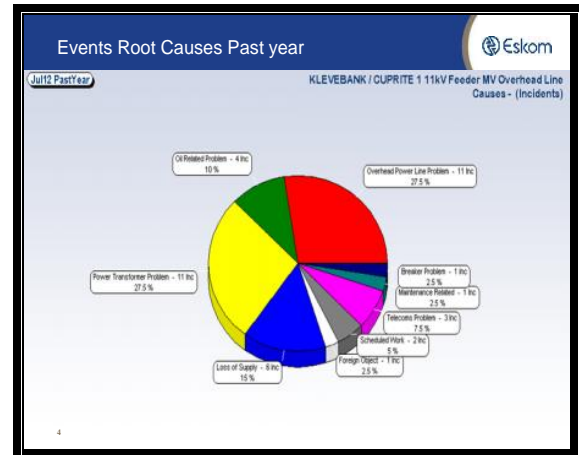


Figure 1.7 Root cause incidents – Cuprite Feeder

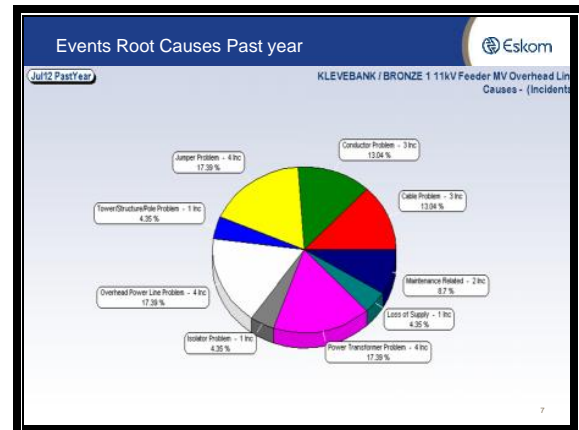


Figure 1.8 Root cause incidents – Bronze Feeder

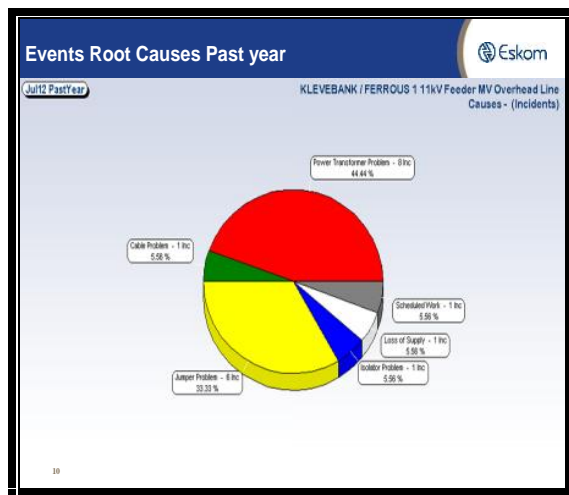


Figure 1.9 Root cause incidents – Ferrous Feeder

Figure 1.7 to 1.9 present statistics that the majority of root cause failures in all three networks occur as a result of infrastructure problems such as overhead lines, distribution transformers and cable.

2.0 METHODOLOGIES EMPLOYED

The following methodologies were employed to obtain results and findings:

- [13] Project Management principles (PMBOK)
- [11] DigSILENT Powerfactory network simulation software which included the formulation of:
 - Modelling of the networks
 - Load Flow Studies
 - Fault level calculations
- Comprehensive protection co-ordination setting analysis of all the networks involved.
- Field investigations to the various lines and Klevebank substation.
- Continuous quantitative measurement of the SAIDI and SAIFI indices over a period of time to monitor results.

3.0 MODELLING OF THE NETWORKS IN DigSILENT

Modeling the three networks in DigSILENT produced valuable results in terms of load flow values and faults levels.

From the field visits the in-situ settings from all the associated protection devices (i.e. transformer protection, feeder breaker protection and downstream auto-recloser protection) were obtained and modeled into a protection co-ordination study using the values obtained from the DigSILENT study. It was evident that the experiment yielded proof that large portions

of the poor quality of supply parameters were attributed to incorrect network infrastructure management in terms of protection setting applications and load flow management.

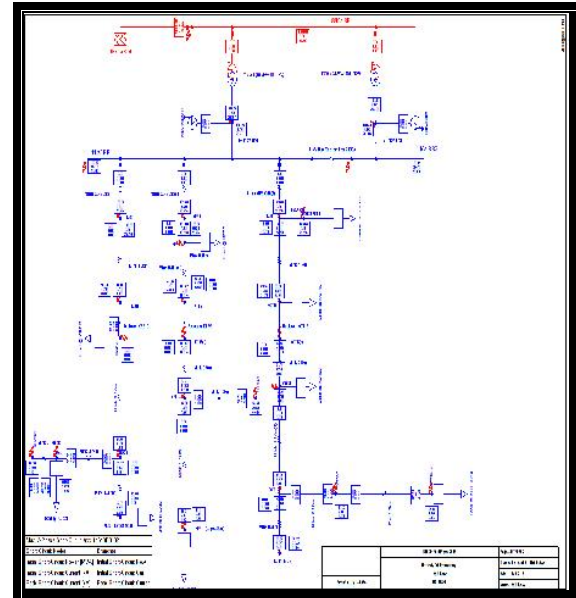


Figure 3.1: Typical DigSILENT Fault Modeling for one feeder

Node	Fault Level	Load Level
Busbar	9780A	*****
KBZ1	9640A	67.06%
KFR1	9640A	40.42%
KCT1	9640A	114.23%
Recloser (KBZ13)	4800A	18.77%
Recloser (KFR5)	7440A	27.38%
Recloser (KCT15)	4380A	113.49%
Cuprite End of line	1430A	65.93%
Bronze End of Line	2210A	18.77%
Ferrous End of line	2430A	27.38%

Table 3.1: Fault and Load levels produced from DigSILENT for the various feeders

In concluding the experiment certain results were obtained and these are published under the findings of this paper. One such a finding is the presentation of the protection setting co-ordination study within the *Bronze* feeder network which was highlighted during this experiment.

From figure 3.1 illustrated below it can be seen that the “Hi-Set” element in the protection settings of the substation feeder breaker at Klevebank substation would almost trip every time for a fault downstream of the substation not allowing the auto-reclosers downstream to co-ordinate correctly. This particular

problem is critical to the duration indices within the quality of supply parameters (SAIDI) as the feeder is not allowed to trip and auto-reclose due to the function of the implementation of the “Hi-Set” element which by nature is used for the isolation of high fault levels in the shortest possible time and more importantly with only 1 trip to lock-out.

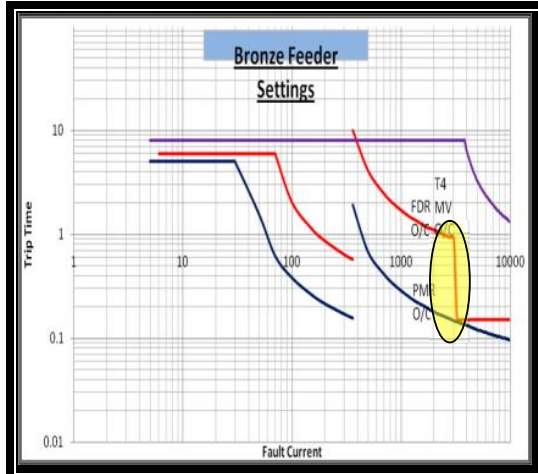


Figure 3.1 Hi-Set element on Substation feeder breaker

4.0 FINDINGS

The findings below are a culmination from the research into the problem as well as from results obtained in the various studies and experiments conducted.

The findings highlighted below needs to be seriously considered in order to take corrective action in improving the SAIDI and SAIFI indices within these particular networks.

These findings are:

- i. Eskom drawings display incorrect details.
- ii. Reclosers incorrectly positioned on setting drawings in relation to actual position and fault studies.
- iii. Cuprite feeder severely overloaded (116%).
- iv. Large Power User (LPU) should have dedicated feeder network from substation.
- v. Reclose dead time set at 2 seconds for 2 trips to lock-out
- vi. Overcurrent “Hi-Set” setting needs to be revisited (Typical as in figure 3.1 below).

5.0 RECOMMENDATIONS

The following recommendations need to be implemented to mitigate the current situation.

- i. Eskom drawings need to be corrected and updated.
- ii. Overcurrent “Hi-Set” needs to be set higher on all feeders.
- iii. Increase the dead time on the feeder breakers to 2 minutes (2 trips to Lock-Out).
- iv. Eskom needs to align with [1] NRS048-6 and [2] IEEE 1366-2003 with regards to the “dead time” settings which requires a minimum setting of 5 minutes.
- v. Additional reclosers to be installed on the networks to distribute the affected customers per incident during an interruption, in essence making the current networks shorter.
- vi. Cuprite feeder cable from substation to be upgraded from 185mm² to 240mm².
- vii. Re-conduct all backbone feeders from Mink to Hare conductor.
- viii. Install a dedicated feeder for Diepsloot mall which is defined as a large power user.
- ix. Bus section breaker needs to be “racked out” at all times as not to parallel transformers thereby minimising the associated fault levels in the network.
- x. Environmental and Socio economic issues need to be addressed.

6.0 CONCLUSION

The implementations of the above recommendations are crucial should Eskom wish to remedy the current situation.

Mitigating strategies must include implementing short term solutions such as simple setting changes and more detailed effort and planning in network infrastructure upgrades.

ACKNOWLEDGEMENTS

Sincere thanks to Marius Janse Van Vuuren and Magic Sibuya from the Eskom Simmerpan Settings department for assistance on the setting information and implementation and a very special thanks to Mr. Johan van Staden (Eskom Simmerpan –Plant and Performance) for the mentoring, coaching and guidance in the preparation of this paper and the completion of the project.

REFERENCES

- [1]. NRS 048-6:2006 (ELECTRICAL SUPPLY – QUALITY OF SUPPLY Part 6: Medium voltage network interruption performance measurement and reporting)
- [2]. IEEE Std 1366-2003: IEEE Guide for Electric Power Distribution Reliability Indices (IEEE Power Engineering Society: Sponsored by the Transmission and Distribution Committee: Revision of IEEE Std 1366-1998:Published by The Institute of Electrical and Electronic Engineers, Inc)
- [3]. A network reliability informed approach to prioritising investment for sustainability-63rd AMEU Convention 2012 (Mr. Martin Cameron, Eon Consulting and Dr. Clinton Carter-Brown, Eskom)
- [4]. Protective Relaying – Principles and Applications Third Edition (J.Lewis Blackburn; Thomas J. Domin CRC Press 2007)
- [5]. Practical Power System Protection (L.G Hewitson; Mark Brown; Ramesh Balakrishnan Newnes 2008)
- [6]. Power System Analysis (John.J Grainger; William D. Stevenson, JR McGraw-Hill, Inc International Edition 1994)
- [7]. Reticulation Protection Course – (Eskom A. J Hunt revised July 1992)
- [8]. Eskom Distribution Guide document 34-619 “Network Planning Guideline for Lines and Cables” Rev 1 (Published November 2010)
- [9]. DigSILENT Powerfactory version 14.0.524
- [10]. ESKOM Performance Management software (DB Focus_Oros software version 20)
- [11]. Project Management Techniques- College edition (Rory Burke: Burke publishing 2010)

COMPARISON OF LOW VOLTAGE RIDE THROUGH CAPABILITIES OF SYNCHRONOUS GENERATOR WITH STATCOM AND DFIG BASED WIND FARMS

W Appadoo* and S Chowdhury*

**University of Cape Town, Electrical Engineering Department, Rondebosch, Cape Town, SA.*

Abstract. Wind energy is a clean emission-free renewable energy resource available worldwide without incurring fuel costs, environmental pollution and supply import dependency. At many sites, wind power is already competitive with newly-built conventional energy technologies and in some cases much cheaper. However, for wind energy integration into a utility network, its operation requires compliance with a country's grid codes. A grid code covers all material technical aspects relating to connections to, and the operation and use of, a country's electricity transmission system. It lays down rules, which define the ways in which generating stations connecting to the system must operate in order to maintain grid stability. Specific requirements for wind power generation are changing as penetration increases and as wind power is assuming more and more power plant capabilities, i.e. assuming active control and delivering grid support services. In response to increasing demands from the network operators, for example to stay connected to the system during a fault event, the most recent wind turbine designs have been substantially improved. The majority of MW-size turbines being installed today are capable of meeting the most severe grid code requirements, with advanced features including fault-ride-through capability. This enables them to assist in keeping the power system stable when disruptions occur. All the grid codes demand that the Wind Power Plant must be able to produce reactive power at the point of common coupling (PCC). One solution is to use an external reactive power compensation. The work pursued in this paper involves the application of STATCOM which has been developed as a control strategy to implement ride through conditions on wind generators and their performance is analysed in comparison to DFIG built-in fault ride through characteristics (using crowbar protection).

Key Words. Fault-Ride-Through, STATCOM, Grid Code, Wind Energy, Synchronous Generator, DFIG.

ACRONYMS

LVRT – Low Voltage Ride Through
VSC – Voltage Side Converter
STATCOM - Static Synchronous Condenser
FACTS – Flexible Alternating Current Transmission System
WTG – Wind Turbine Generator
WECS – Wind Energy Conversion System

1. INTRODUCTION

Demand of cheap and clean electricity across the globe has resulted in deployment and grid-integration of wind farms in the range of 1 kW to 100 MW, located in areas rich in wind resource and at varying distances from the load centres. Wind energy penetration into utility network started increasing since the 1970s and by the end of 2012, global installed capacity of wind power stands at about 282.5 GW [1]. Apart from technical issues of grid-integration, research is also being done to investigate the participation of wind energy systems in enhancing grid performance through fault ride-through capabilities, providing voltage control and power quality improvement etc. The goal of a Fault Ride Through (FRT) or Low Voltage Ride Through (LVRT) system is to enable a wind farm to withstand a severe voltage dip at the connection point and still remain connected to the power system as long as the fault persists. During LVRT, the wind farm is expected to supply voltage support to mitigate the voltage dip at critical buses in order to prevent a drastic degradation of voltage quality during fault or other contingency causing the voltage dip. These ancillary service capabilities of wind farms for voltage support and LVRT are required as per South Africa's Grid Code's requirements [1] in order to ensure a secure and reliable power system operation

and must maximise their reactive power injections to the network. The maximisation of reactive current must continue for at least 150 ms after the fault clearance or until the grid voltage is recovered within the normal operation range. An ideal voltage source is imposed at the Point of Connection (POC) which has a zero voltage for 150 ms, followed by discrete voltage level changes until $t > 120$ s where the voltage should be 0.9 p.u [1,2]. This paper reports on results of the modelling and simulation studies carried out to demonstrate the compliance of a wind farm to meet the fault ride-through requirements of the National Grid Code in South Africa. The comparison between DFIG and Synchronous Generator (SG) operating during grid fault is proposed in this paper. The results are presented and discussed considering the performance of terminal voltages and the reactive power injections. Some limitations to control the terminal voltage during fault exist in the DFIG. However, it can operate without disconnecting from the network. The operation period of the crowbar system affects considerably the injection of reactive power considerably in the network. This protective device is essential to guarantee the safe operation during short circuits on the network [2].

2. LOW VOLTAGE RIDE THROUGH

2.1 Grid Code Requirements as per South African Requirements

South African Grid codes require that wind farms must withstand voltage dips to a certain percentage of the nominal voltage, down to 0% voltage drop in some cases, and for specified duration [3]. This is most commonly known as Fault Ride Through or Low Voltage Ride Through (LVRT). LVRT is usually described by a voltage v/s time graph, showing the minimum required protection characteristics of the wind farm as shown in Figure 1.

The operational requirements of a wind farm to provide LVRT is to supply additional reactive power to mitigate the voltage dip during a fault or contingency condition within the framework of the grid codes.

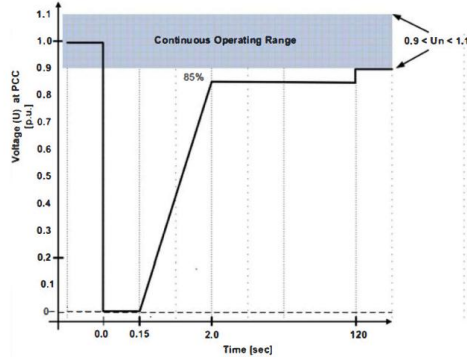


Figure 1: Characteristics of Fault Ride Through as per SA grid code [3]

It is important to discuss here the immediate impact of the voltage dip on the wind farm operation. During the voltage dip, the active power provided to the grid by the wind farm is instantaneously reduced at least temporarily to that lower than the mechanical power available at the rotor; hence the rotor speed of the wind generator increases. It is required for the LVRT capability of the wind farm, that the wind generators of the wind farm must not be disconnected from the grid during fault persistence, either due to over-speeding or under-voltage protections. After the clearing of the fault that led to the voltage dip, the voltage at the wind turbine bus increases. It is also required that the wind generators should resume their power supply to the network without losing stability. Upon voltage recovery, the wind turbines must not consume excessive reactive power when re-exciting the generator, as this may result in a further voltage dip

The required fault behavior of a wind generation system is characterized as follows [4]:

For system faults that last up to 140 ms the wind farm has to remain connected to the network [1,3,5].

- During system faults and voltage sags a wind farm has to supply maximum reactive current to the grid system without exceeding the transient rating of the plant [1,3].
- For system faults that last up to 140 ms upon the restoration of voltage to 90% of nominal a wind farm has to supply active power to at least 90% of its pre-fault value within 0.5 sec. For voltage dips of duration greater than 140 ms a wind farm has to supply active power to at least 90% of its pre-fault value within 1 sec of restoration of voltage to 90% of nominal [1,3].
- During voltage dips lasting more than 140ms the active power output of a wind farm has to be retained at least in proportion to the retained balanced supergrid voltage [6,7].

During the duration of voltage sag, active power provided by the wind generator is immediately reduced, which makes it lower than the mechanical power generated. Thus there is an increase in rotor speed of the generator. The ride through capacity will not trigger the wind turbine generator to disconnect during this period, in cases of over-speed or under-voltage. However, after the clearing of the fault or low voltage condition, the voltage of the turbine increases, enabling the WTG to resume the power supply to the network grid and recover stability. Control capabilities in various generators such as Synchronous, induction and doubly fed limits the risk of loss of stability [8].

2.2 STATCOM

Another way to enhance a wind power plant with ability to deliver or absorb reactive power from the grid is to use static synchronous compensation. STATCOM can be treated as a solid state synchronous condenser connected in shunt with the AC system. The output current of this controller is adjusted to control either the nodal voltage magnitude or reactive power injected at the bus. STATCOM is a new breed of reactive power compensators based on VSC. It has characteristics similar to a synchronous condenser, but it has no inertia and it is superior to the synchronous condenser in several ways. Lower investment cost, lower operating and maintenance costs and better dynamics are greater advantages of this technology [9]. In theory, the STATCOM can help mitigating the flicker due to variations of reactive power absorbed by wind farms. The reactive power required by the farm is evaluated and a controller drives the STATCOM inverter so as to generate the adequate quantity, permitting to reduce drastically reactive power flows towards the grid and therefore, the associated flicker. Unlike thyristor based solutions (TSC and SVC), VSC power electronic systems are based on IGBT (insulated gate bipolar transistor) technology, intrinsically faster than thyristors. Continuous progress in the semi-conductor industry now makes it possible to build and operate high power STATCOM (about a few tens of MVA), with a very good dynamic response i.e. time constants in the millisecond range [10]. STATCOM applications include the following [9]:

- Stabilization of weak system voltage
- reduce transmission losses
- enhance transmission capacity
- power oscillation damping
- improve power factor
- reduce harmonics
- flicker mitigation
- assist voltage after grid faults

STATCOM consists of one VSC with a capacitor on a DC side of the converter and one shunt connected transformer. Voltage source converter is usually built with thyristors with turn-off capability like gate turn-off (GTO) or today integrated gate commutated

thyristors (IGCT) or with Insulated gate bipolar transistors (IGBT) based converter. STATCOM configuration and its working principle is shown in Figures 2 and 3 respectively [9,11].

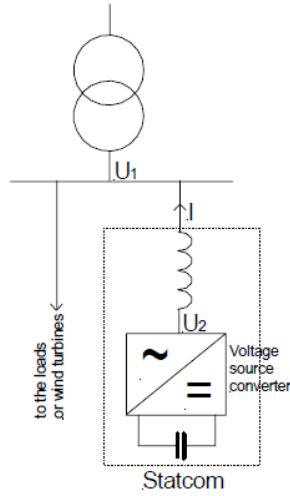


Figure 2: Showing working principle of STATCOM [4]

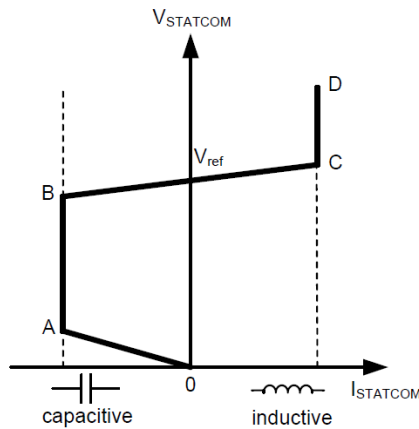


Figure 3: Schematic representation of working principle of STATCOM [9]

2.3 Synchronous generator v/s DFIG

Synchronous generators usually operate together, forming a large power system supplying electrical energy to the loads or consumers. They are built in large units, having their rating ranging from tens to hundreds of megawatts. Synchronous generators are known to be much more effective in terms of reactive power injection during grid fault and by consequence; the terminal voltage is kept in higher levels as compared to DFIG [11].

DFIG is a popular wind turbine system due to its high efficiency, reduced mechanical stress on the wind turbine, separately controllable active and reactive power and relatively low power rating of the connected converter. But due to the direct connection of the stator to the grid, the DFIG suffers from a great vulnerability to grid faults and requires additional protection of the rotor side power electronics. The crowbar's method of protection is

the most useful and convenient way for LVRT [2,11].

3. METHODOLOGY

In this section, an overview of how the research work meets the objectives of this paper as presented in section 1 is depicted. The methodology is as follows:

- Explanation of the overall methods used in conducting the research and simulations.
- Description of the design in terms of mathematical modeling and how relevant information and data were used to report to the objectives mentioned.

This section explains how specific tasks in this research were performed. The protection scheme simulations were performed on Matlab® 2012a Simulink® as per the block diagram, Figure 4.

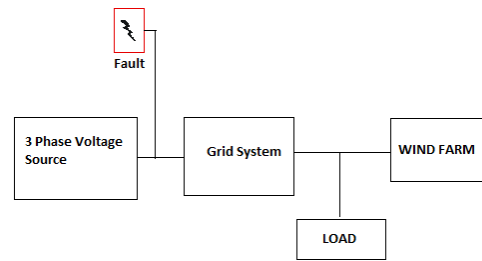


Figure 4 : Block representation of grid system including wind farm

The proposed simulated fault ride through system implementation consists of analyzing the aspects and comparing results from fault ride through conditions. Thus the research was divided into the following tasks:

- Mathematical modelling of the system involved
- Designing system on Matlab®/ Simulink® using blocks
- Case Study 1: Fault clearance at 0.1 s
- Case Study 2: Fault clearance at 0.2 s

Two types of machines were used to determine fault ride through and a comparison was made between the two scenarios. The comparison was used to analyse the fault ride through characteristics of both the machines and also determine the efficiency of the mechanism. The first mechanism uses a synchronous generator based wind energy conversion system with a STATCOM to achieve fault ride through in case of a fault or voltage sag. The second method involves a doubly fed induction generator based WECS with an integrated crowbar protection for fault ride through. The simulations are compared to determine how the synchronous generator based wind energy conversion system provides a better ride through control than the doubly fed induction generator based wind farm in terms of reactive power fed to the grid and thus give a stronger support to the grid voltage.

3.1 The Grid Model

The grid system is modelled using a symmetrical three-phase voltage source including an inductance

and resistance. It is defined as a controllable three-phase voltage source.

3.2 The STATCOM Model

The dynamic equations of the instantaneous values of the three-phase voltages across two-sides of STATCOM and the current flowing into it are given by equation (1) [12]:

$$\left(R_p + L_p \frac{d}{dt}\right) i_p = V_s - V_p \quad (1)$$

where,

R_p = ON state resistance of the switches including transformer leakage resistance

L_p = transformer leakage inductance and the switching losses are taken into account by the shunt dc-side resistance R_{dc}

The dynamic model is given by equation (2):

$$\begin{aligned} \frac{d}{dt} \begin{bmatrix} i_{pd} \\ i_{pq} \\ V_{dc} \end{bmatrix} = & \begin{bmatrix} -\frac{R_p}{L_p} i_{pd} + \omega i_{pq} \\ -\frac{R_p}{L_p} i_{pq} - \omega i_{pd} \\ \frac{3}{2CV_{dc}} [V_{sd} i_{pd} + V_{sq} i_{pq} - (i_{pd}^2 + i_{pq}^2) R_p] - \frac{V_{dc}}{CR_{dc}} \end{bmatrix} \\ & + \begin{bmatrix} \frac{1}{L_p} & 0 \\ 0 & \frac{1}{L_p} \\ 0 & 0 \end{bmatrix} \begin{bmatrix} V_{sd} - V_{pd} \\ V_{sq} - V_{pq} \end{bmatrix} \end{aligned} \quad (2)$$

3.3 The model's equations and equivalent circuit of a synchronous generator

The synchronous generator's equivalent circuit in the rotor reference frame is shown in Figures 5 and 6. The circuit describes the generator electrically below [12]:

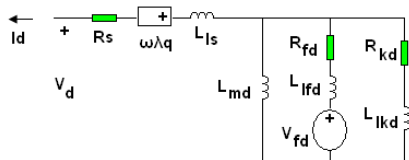


Figure 5: Synchronous generator equivalent circuit in rotor reference frame d-axis

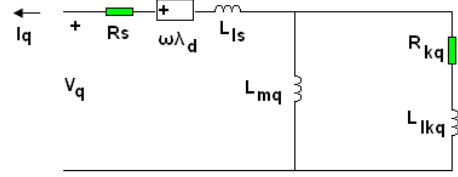


Figure 6: Synchronous generator equivalent circuit in rotor reference frame q-axis

The generator parameters used for the simulation are as shown in Table 1 below:

Table 1: Parameters for synchronous generator and DFIG

Frequency (Hz)	50
Rated Voltage (V)	400
Rated Complex Power (VA)	8100
Field current (A)	50
Inertia (kg.m ²)	0.0923
Number of pole pairs	2

4. RESULTS

This section presents the simulation results using the MATLAB® / SIMULINK software version 7.6. The paper is divided into different sections presenting the two different simulation case studies. Different output waveforms in the form of graphs from the various component technologies used in the model simulated are illustrated to show the performance output from the generator in relation to the function of the STATCOM. The output is then compared to that of the DFIG based generator system. The linear waveform of the r.m.s. output of voltage and current are also included to provide a clear illustration of the output. The simulation is carried out over a period of 1 s and the circuit is as follows:

1. 10 MW wind farm consisting of five 2 MW wind turbines based on synchronous generator is connected to a 25 kV distribution system, exports power to a 120 kV grid through a 30 km, 25 kV feeder.
2. 10 MW DFIG wind farm consisting of five 2 MW wind turbines connected to a 25 kV distribution system, exports power to a 120 kV grid through a 30 km, 25 kV feeder.

The performances of both generators during a three-phase short circuit at Bus 2 and Bus 3 for different fault clearance times (100 ms and 200 ms) are presented in the following figures.

4.1 Case 1: Fault Clearance in 0.1 s

Case 1: The graphs in Figures 7 to 10 in Figure show voltage profile for both synchronous generator and DFIG at Bus 2 and Bus 3. Figure 11 shows the reactive power compensation provided by Synchronous generator and DFIG wind farms.

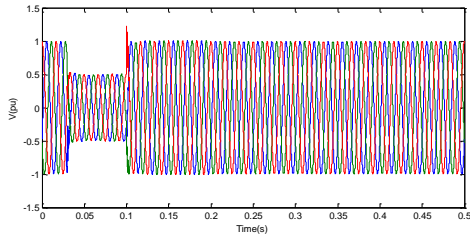


Figure 7: Voltage drop at bus 2 – synchronous generator

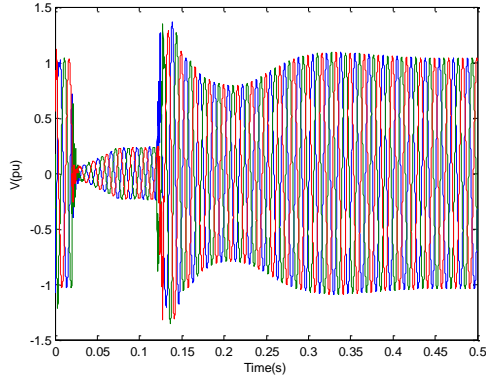


Figure 8: Voltage drop bus 2 – DFIG

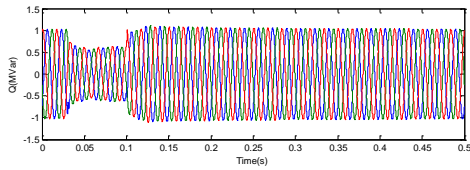


Figure 9: Voltage drop at bus 3 – synchronous generator

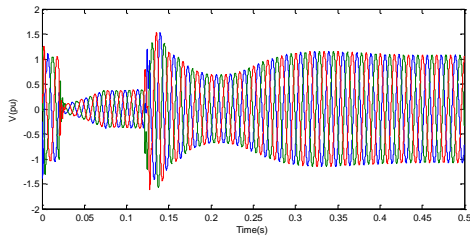


Figure 10: Voltage drop at bus 3 – DFIG

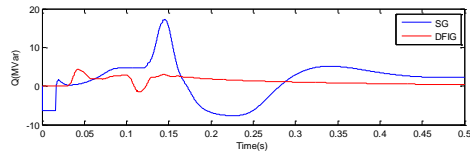


Figure 11: Reactive power compensation - comparison of synchronous generator and DFIG

4.2 Case 2 : Fault Clearance in 0.2s

Case 2: The graphs in Figures 12 to 15 show voltage profiles for both Synchronous generator and DFIG at Bus 2 and Bus 3. Figure 16 shows the reactive power compensation provided by Synchronous Generator and DFIG wind farms.

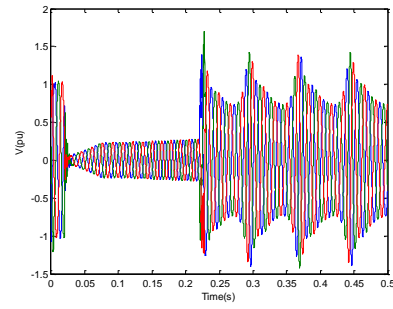


Figure 12: Voltage drop at bus 2 – DFIG

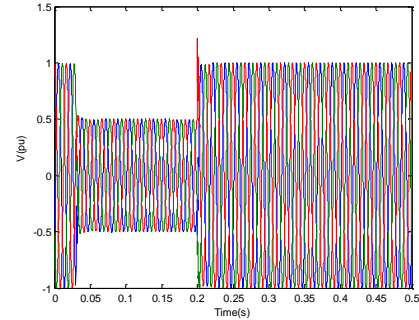


Figure 13: Voltage drop at bus 2 – synchronous generator

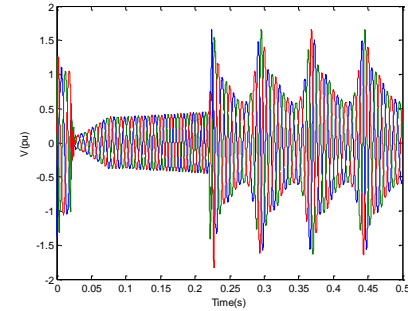


Figure 14: Voltage drop at bus 3 – DFIG

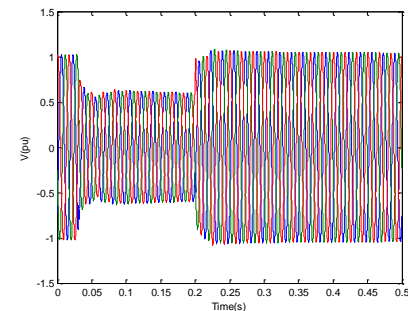


Figure 15: Voltage drop at bus 3 – Synchronous generator

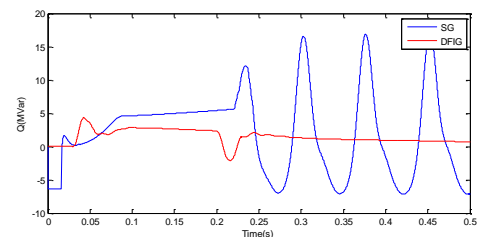


Figure 16: Reactive power compensation - comparison of synchronous generator and DFIG

The results show that for both the cases, the voltage during the fault at Bus 2 and Bus 3 are higher for the Synchronous generator wind farm than those for DFIG wind farm. This fact can be explained because the rotor side converter of the DFIG is blocked during the complete low voltage time and the rotor windings are connected to the crowbar system; only the grid side converter is capable to inject reactive power into the grid limiting the effectiveness of the voltage control. Reactive power is injected into the synchronous generator during the complete fault period, this fact enable higher voltage levels at the buses.

5. CONCLUSION

This paper compares the LVRT capabilities of synchronous generators and DFIG wind farms in relation to a fault initiated in a test network. The modelling and simulation was done to show the pre-, during- and post-fault voltage profile of a network with the integration of wind farms, one with synchronous generator with STATCOM and the other with DFIG. The results are presented to show how much the during-fault voltage can be supported by the two generator technologies. The results show that the synchronous generator with STATCOM performs better in terms of LVRT as compared to the DFIG. However, further research needs to be done in order to investigate the control mechanisms for these technologies to improve their LVRT performance. Also investigation needs to be done to correlate the LVRT performance of different wind generator technologies with their capacities, point of integration, distance from fault and the presence of other reactive power compensation devices in the network.

ACKNOWLEDGEMENTS

The authors gratefully acknowledge the support and infrastructure provided by Electrical Engineering Department, University of Cape Town, SA for carrying out this research work.

REFERENCES

- [1] "Grid Connection Code for Renewable Power Plants (RPPs) connected to the Electricity Transmission system (TS) or the Distribution System (DS) in South Africa", Document prepared by Eskom Transmission Division, RSA Grid Code Secretariat, Germiston, South Africa, Nov 2012.
- [2] L. Shi, N. Chen and Q. Lu, "Dynamic Characteristic Analysis of Doubly – Fed Induction Generator Low Voltage Ride Through", *International Conference on Future Energy, Environment, and Materials*, Vol. 16, Part C, pp. 1526 - 1534, May 2012.
- [3] G Wenming, W Yun, H Shuju and X Honghua, "A Survey on Recent Low Voltage Ride – Through Solutions of Large Scale Wind Farm", *Power and Energy Engineering Conference (APPEEC)*, Wuhan, China pp. 1 - 5, March 2011.
- [4] Pierre Bousseau, Floriane Fesquet, Régine Belhomme, Samuel Nguefeu, Thanh Chau Thai, "Solutions for the grid integration of wind farms – A survey", *European Wind Energy Association Publication*, Vol 9, Issue 1 – 2, p 13 – 25, April 2006.
- [5] Rajveer Mittal, K. S. Sandhu and D. K. Jain, "Low Voltage Ride-Through (Lvrt) Of Grid interfaced Wind Driven Pmsg", *ARPN Journal of Engineering and Applied Sciences*, Vol. 4, No. 5, July 2009.
- [6] I. Erlich, W. Winter and A. Disttrich, "Advanced grid requirements for the integration of wind turbines into the German transmission system", *Power Engineering Society General Meeting, IEEE*, p. 7, 18-22 June 2006.
- [7] X.P. Zhang, C. Rehtanz, B. Pal, "Flexible AC Transmission Systems: Modeling and Control", *Springer-Verlag Berlin Heidelberg*, 2006.
- [8] F. Iov and F. Blaabjerg, "Power electronics and control for wind power systems", *PEMWA, IEEE*, pp. 116, 24-26 June 2009.
- [9] P. Lipnick, T.M. Stanciu, "Reactive Power Control for Wind Power Plant with STATCOM", Master's Thesis, Institute of Energy Technology, Aalborg University Denmark, Year 2010.
- [10] Jarrad C. Wright, Paul M. Tuson, John M. Van Coller, "Studies for Wind Energy Facility Grid Code Compliance in South Africa", *Exposition in Africa (PowerAfrica)*, IEEE p1-7, 2012.
- [11] J. A. Fuentes, M. Canas, A. Molina, E. Gomez, F. Jimenez, "International review of grid connection requirements for wind turbines", *International Conference on Renewable and Power Quality, ICREPQ'07*, Sevilla, March 2007.
- [12] M. B. C. Salles, A. P. Grilo, and J. R. Cardoso, "Doubly Fed Induction Generator and Conventional Synchronous Generator Based Power Plants: Operation during Grid Fault", *International Conference on Renewable Energies and Power Quality, ICREPQ*, April 2011.

IMPACT OF PHASOR MEASUREMENT UNITS ON DISTRIBUTION SYSTEM STATE ESTIMATION

A. E. Kahunzire* and K. O. Awodele**

Department of Electrical Engineering, University of Cape Town, Rondebosch, 7701 Cape Town, South Africa. Email: [*akahunzire@gmail.com](mailto:akahunzire@gmail.com) [**kehinde.awodele@uct.ac.za](mailto:kehinde.awodele@uct.ac.za)

Abstract: As more Distributed Generation (DG) is connected to distribution networks, these networks are evolving from passive networks to active networks. Some of the new characteristics of active networks include bi-directional power flows, voltage profile issues, as well as unintentional islanding, to mention but a few. With these new characteristics, the present monitoring schemes characterized by slow and highly inaccurate measurements are no longer adequate. There is a need to develop a faster, more accurate real-time monitoring scheme, and one way of doing this is by installing Phasor Measurement Units on distribution networks. This paper investigates the impact that PMUs can have on distribution network monitoring. Specifically, it considers the role that appropriate PMU placement patterns have to play in improving distribution system state estimation. Finally, it investigates the effect of improved system monitoring on the reliability of distribution systems.

Keywords: Active Distribution Networks, Phasor Measurement Units, State Estimation, Reliability

1. INTRODUCTION

As governments all over the world seek to reduce their countries' carbon footprints, the installation of DG on distribution networks has gained momentum. This, together with technological developments and de-regulation of the electricity industry, points towards increased DG penetration on power networks in the coming years [1]. As more DG is installed, the traditional, passive distribution networks are gaining new characteristics and hence evolving into active distribution networks. These new characteristics include the following: Bi-directional power flows [2], unstable power supply especially where weather dependent sources such as wind and solar are used [3], unintentional islanding [4] [5], increased fault levels [6] and voltage profile issues [6]

Generally, the monitoring of transmission networks has been prioritised over that of distribution networks mainly because transmission networks carry more power and service more customers than distribution networks [2]. However, as more DG is connected to distribution networks, their behavior and efficiency is carrying more weight towards the efficiency of the entire electricity grid. For that reason, the current monitoring systems which include load forecasting based on historical data and some Remote Terminal Unit (RTU) based SCADA may prove inadequate in terms of accuracy and speed of data retrieval [7]. This calls for the deployment of faster and more accurate real-time monitoring devices. One such device is the Phasor Measurement Unit (PMU). This paper investigates the impact that PMUs can have on distribution network monitoring, specifically in the area of state estimation, and the impact of this on system reliability.

The paper is arranged as follows: Section 2 provides a brief introduction to PMUs, Section 3 introduces State Estimation, Section 4 talks about PMU placement, Section 5 outlines the methodology, Section 6 discusses the results while Section 7 presents the conclusions of the paper.

2. PHASOR MEASUREMENT UNITS (PMUS)

PMUs carry out synchronised, real-time measurements of voltage and current phasors on the power network at the nominal frequency of the network. They produce time-stamped phasor measurements by synchronising with a universal time reference, the coordinated universal time (UTC). This is provided by the Global Positioning System (GPS) technology [8]. Such measurements taken at a known time and recorded with a time-tag are called *synchrophasors*.

A *phasor* is a mathematical representation of a sinusoidal waveform in terms of its magnitude and phase angle with respect to a time reference [8]. Phasors translate signal equations from time domain to another co-ordinate system whose parameters are magnitude and angle [9].

The time domain sinusoid $x(t) = X \sin(\phi + \omega t)$ (1)

can be represented as:

$$x(t) = \left(\frac{X}{\sqrt{2}}\right) e^{j\phi} = \frac{X}{\sqrt{2}} (\cos\phi + j\sin\phi) \quad (2)$$

where X is the peak value of the sinusoid, ϕ is the phase displacement, and ω is the angular frequency, $\frac{X}{\sqrt{2}}$ is the rms value of the signal, and ϕ the phase angle at time $t=0$ [10].

Time and phasor representation of a sinusoid given in Figure 1 below.

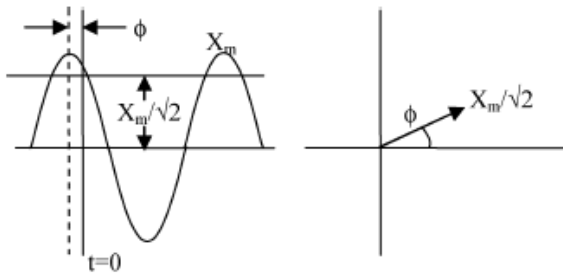


Figure 1. Time and phasor representation of a sinusoid [10]

2.1 Applications of PMUs in distribution networks

After great success in monitoring transmission systems, it is expected that PMUs can provide the same and more benefits on distribution networks. These benefits include but are not limited to the following: System monitoring [11], power quality analysis (harmonic distortion) [12], post-mortem fault analysis [8] [13], phase identification [13], system wide data collection [14], islanding detection and response [5], improved state estimation [3],[15]

Since the biggest issue facing distribution network monitoring is the insufficient monitoring devices due to the large number of nodes, state estimation will continue to play a central role in the monitoring of these networks, especially as they evolve into active networks. For this reason, the focus of this paper will be the role of PMUs in creating a faster, more accurate state estimation system for distribution networks.

3. STATE ESTIMATION

State Estimation is the process of using available system measurements to obtain voltages (magnitude and phase) at unmonitored buses by using specially developed formulas and algorithms [3]. State estimation takes into consideration the inaccuracy of measurement devices in order to reach a more realistic picture of the true system state at a given time. Measurements can include voltages, power flows and power injections. The system state that is obtained after state estimation is the voltage magnitude and phase at each bus on the system. Most state estimation procedures can be referred to as non-linear. This is because the available measurements are related to the states by non-linear relationships [16]. For example, power is related to voltage magnitude and phase by a non-linear relationship that contains squares and trigonometric functions like cosine and sine.

The basic non-linear state estimation problem can be defined as [17]:

$$z = h(x) + e \quad (3)$$

Where z is a measurement vector with m elements, $h(x)$ is a measurement function made up of non-linear relationships between the measurement vector and the state vector, x , and e is an error vector.

Such a state estimation can be solved by several methods such as the Weighted Least Squares (WLS) [17], Weighted Least Average Value (WLAV) and more recently the Kalman Filter [18] [19]. These methods incorporate what is known as a covariance matrix whose purpose is to attenuate the impact of inaccurate measurements while amplifying that of highly accurate ones.

The implementation of PMUs in state estimation gives rise to the concept of linear state estimation [20]. This is so because PMUs return voltage and current phasors, both of which are linearly related to the system states (bus voltage magnitude and phase). Because of this, the system states can be calculated via a simple non-iterative state estimation procedure. This is faster than the conventional non-linear method and is also more accurate since PMUs provide very accurate data. In situations where both conventional and PMU measurements are available, PMU data can be included into the state estimation via one of two methods. The first is referred to as a hybrid state estimator [8], where both measurements are used in an iterative state estimation procedure. The second includes the PMU data in a linear post-processing step, after the conventional state estimation has been run [20]. The linear post processing approach is adopted in this paper since it does not call for a complete overhaul of the existing state estimation architecture available to utilities [7].

Most work and research on state estimation have been carried out on transmission networks. In order to extend the state estimation algorithm to distribution networks, some distinctions between the two networks must be considered. Distribution networks, unlike transmission networks, have short lines so the voltage drops are much smaller and they are connected to unbalanced loads, i.e. the three phases are not balanced, and therefore state estimation must be done on a per phase basis [21]. Distribution System State Estimation (DSSE) also utilizes several different types of measurements such as pseudo, virtual and real measurements, all of which have different accuracies [22]. Though still an ongoing research topic, some valuable work has indeed been done on distribution system state estimation [3] [7] [19] [22] [23].

4. OPTIMAL PLACEMENT OF PMUS

Before the benefits of PMUs can be enjoyed on distribution networks, their placement pattern on the networks must first be established. A PMU placed on a node measures the voltage at that node and the current on all branches connected to that node i.e. a PMU placed at one bus makes that bus and all buses adjacent to it observable [24]. Ideally, to achieve full observability of a power network, PMUs would be placed on each node of the network. That way, current and voltage phasors at

each point on the network could directly be obtained i.e. the state of the network would be immediately available based solely on PMU data. There would thus be no need for state estimation. However, considering the high cost of a single PMU and the traffic constraints in communication channels, it is not feasible to carry this out [25].

There are several objectives to PMU placement on electricity networks. The main two are to achieve complete observability and to improve the accuracy of the state estimation process on a network. While most placement schemes on transmission networks aim at complete observability, this is not financially feasible on large distribution networks with several nodes. On distribution systems, the most common objective for PMU placement is to improve the performance of state estimation [7] [26] [27], and this has been chosen as the objective for this paper.

5. OUTLINE OF PRACTICAL WORK DONE

The focus of all practical work done was to investigate the impact of PMUs on the accuracy and speed of Distribution System State Estimation (DSSE). All code was written using MATLAB (Processor: 2.3 GHz Intel Core i5). Distribution system simulations were carried out in DiGSILENT PowerFactory.

As mentioned earlier, most research on state estimation has been carried out on transmission systems. For this reason, all code was first tested on a known transmission system (IEEE 14 bus system) shown in Figure 2 below.

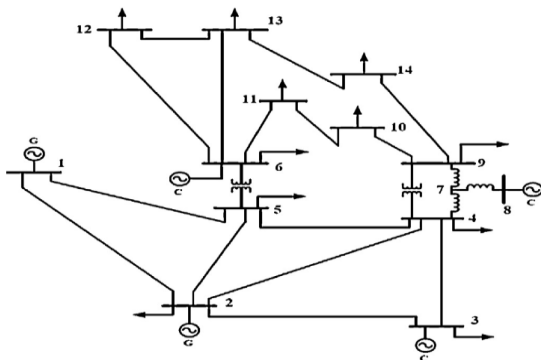


Figure 2. IEEE 14 bus test system [28]

Using this system, the performance of two state estimation methods was compared. The two methods were the Weighted Least Squares method as explained in [17] and an extension of the Kalman filter method known as the Iterated Kalman Filter as explained in [19]. The aspects investigated were the deviation indices for different accuracies of available system measurements (different entries into the covariance matrix, R). The state estimation in this case was done on a single-phase basis. The performance was rated based on its accuracy compared to 'true values' obtained from [29]. True

values means the actual system parameters which would be measured if the measurement devices used were 100 % accurate and these are usually obtained by carrying out a load flow on the system.

The code was then extended to include PMU data. This was done by first running a conventional iterative state estimation procedure. The solution of this, together with the available PMU data was then implemented in a linear post processing state estimation step as explained in [7] [20].

The placement pattern adopted in this procedure was based on two indices introduced in [7] namely: the Maximum Relative Voltage magnitude Deviation (MRVD) and the Maximum absolute Phase angle Deviation (MPD) whose formulae are given below:

$$MRVD = \max_i \left(\frac{abs(\hat{E}_i - E_i)}{E_i} \right) \quad (4)$$

where \hat{E}_i is the i_{th} estimated voltage while E_i is the i_{th} true voltage

$$MPD = \max_i (abs(\hat{\phi}_i - \phi_i)) \quad (5)$$

where $\hat{\phi}_i$ is the i_{th} estimated phase angle while ϕ_i is the i_{th} true angle

These two indices are generated by calculating the deviation between the estimated state vector and the true values.

$$Deviation = x_{estimate} - x_{true} \quad (6)$$

This calculates the deviations in both magnitude and phase at each bus. The MRVD and MPD are then obtained by searching through the deviations at each bus and returning the largest one. In other words these two indices point towards the buses at which the largest magnitude or phase deviation (inaccuracy) has occurred.

It is therefore reasonable to state that a sum of these two indices would give the 'total' deviation at each bus. PMUs were therefore placed at those buses which exhibited highest total deviation. Using this method, one could choose either a fixed number of PMUs or a fixed accuracy level and hence deploy as many PMUs as required to meet that accuracy. For this paper, the former was selected as the more cost-effective option for implementation by utilities. In order to increase the speed of the process, the buses made observable by the PMUs were removed from the state vector of the conventional state estimation. This was done because it would result into simpler matrices and hence reduce the computational time.

Once the code and algorithms were validated, the procedure was extended to implement a three phase

DSSE for the IEEE 13 bus test feeder shown in Figure 3 below.

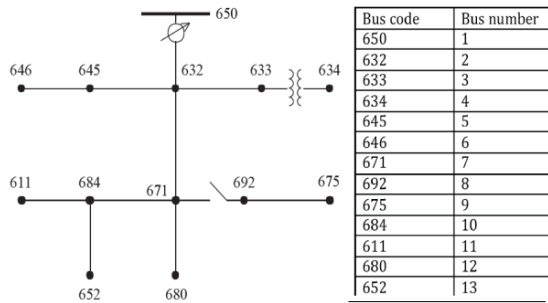


Figure 3. IEEE 13 bus distribution test feeder [30]

The true values were obtained by carrying out a load flow using the ladder iterative technique [31]. This method was chosen because the Newton-Raphson technique was found not to converge for distribution systems, perhaps due to the very sparse impedance matrix of distribution networks.

6. DISCUSSION OF RESULTS

6.1 Choice of State Estimation method

It was found that in all cases, the WLS converged faster than the IKF. In terms of accuracy, the performance of both methods was comparable, with the WLS method behaving slightly better than the IKF for most cases. However, when highly inaccurate measurements were used, the IKF performed slightly better. These results are summarised in Table 1 below.

Table 1: Comparison of state estimation methods

Case I: Fairly accurate conventional measurements		
	WLS	IKF
MRVD	0.0328	0.0339
MPD	1.5856	1.6525
Runtime (s)	0.02	0.12
Case II: Highly inaccurate power flow measurements		
MRVD	0.0167	0.0167
MPD	1.8478	1.6814
Runtime (s)	0.02	0.20

6.2 Inclusion of PMU data in state estimation

It was also shown that state estimation that included PMU data at the buses with highest error indeed improved the accuracy of the final result. Buses with the highest error were found to be 6, 12 and 14 for the IEEE 14 bus system. These could be monitored by PMUs at buses 6 and 9, and these made buses 5,6,7,8,9,10,11,12,13 and 14 observable. These results are summarised in Table 2 below.

The PMU placement algorithm is represented graphically in Figure 4 below. It was noted that for example 2 PMUs placed at 2 buses made 10 buses observable, and for this reason there was a significant improvement in the state estimation as seen in Figure 5 below.

Table 2: Maximum deviation indices with optimal placement of 2 PMUs

	MRVD	MPD
Before PMU data was used	0.0328	1.5855
After PMU data was used	0.0142	0.5410

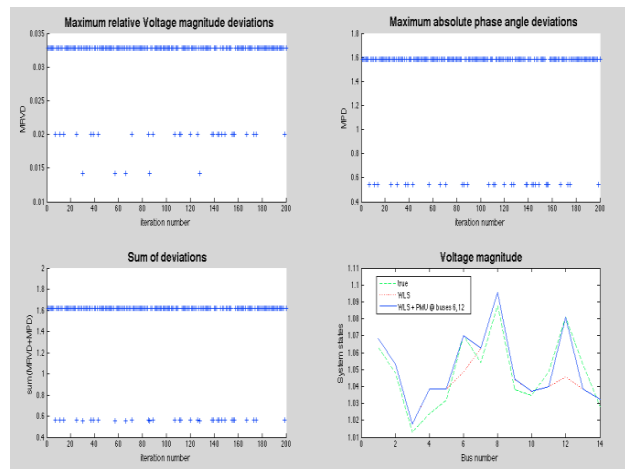


Figure 4. Illustration of PMU placement algorithm and resulting state estimation

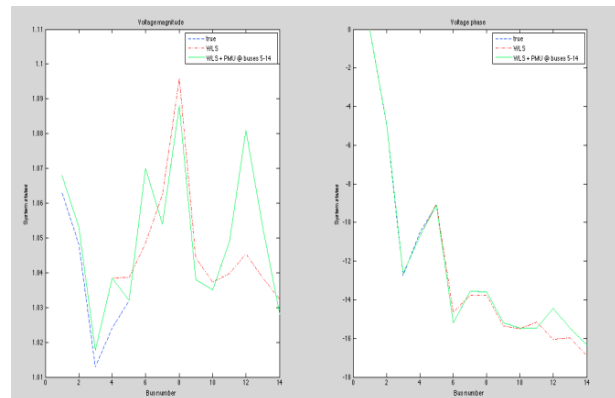


Figure 5. Final state estimation result considering all buses observable by deployed PMUs (true-blue, WLS-red, WLS+PMU-green)

Table 3: Computational time for full and reduced state vectors

	Computation time
Full state vector for conventional SE	0.04
Reduced state vector for conventional SE	0.02

Having eliminated the observable buses from the state vector of the conventional state estimation, the computation time reduced to about half the initial run time as shown in Table 3 above.

6.3 Three-phase DSSE

The validated WLS state estimation algorithm was extended to carry out a 3-phase DSSE. It was found that the gain matrix was ill-conditioned. It was suggested that the large number of injection measurements used was the cause of this [17]. Some alternative forms of the WLS procedure were suggested and tested, such as Orthogonal Factorisation and Method of Peters and Wilkinson. However, these too led to singular matrices. To solve the problem, the original WLS was used after the gain matrix was scaled, by adding a constant $1e10$ to every diagonal element in the gain matrix (the gain matrix was of order $1e9$). This returned reasonable results and these were used to carry out the tests.

The same procedure for PMU placement was run on the DSSE. Largest error was found at buses 2, 7 and 8. All three are directly connected to bus 7 and so one PMU was deployed there. This made buses 2, 7, 8, 10 and 12 observable. The resulting state estimation for Phase A of the system is represented graphically in Figure 6 below.

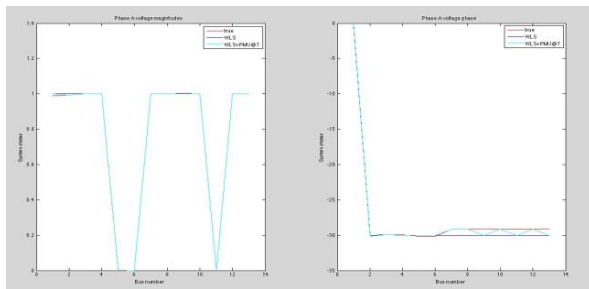


Figure 6. Phase A DSSE result with and without PMU data for IEEE 13-bus system (true-red, WLS-dark blue, WLS+PMU-light blue)

7. CONCLUSIONS

Considering all observations made during the investigations, it is found that PMUs can indeed improve the accuracy of distribution system state estimation. They also increase the speed of state estimation, providing a better tool to monitor dynamic, real time states of active distribution networks.

It has been proved that both the WLS and IKF methods work within acceptable accuracy to solve the state estimation problem. The IKF performed better than the WLS for less accurate measurements. However, the WLS converged faster than the IKF for all scenarios. The choice of estimation method could therefore depend on a number of factors such as computational time and accuracy of measurement devices.

The DSSE had to be carried out on a three phase basis due to the unbalanced nature of distribution networks. The gain matrix from the DSSE was found to be ill-conditioned and had to be scaled in order to find its inverse. In a real-world scenario, bus flow measurements can be included in the measurement set to reduce the dominance of injection measurements. This will lead to a better-conditioned gain matrix and hence eliminate the need for scaling [17].

It was also found that the Newton Raphson method of load flow did not converge for the distribution system. This was attributed to the very sparse impedance matrix that characterises radial distribution systems. Rather, a method known as the Ladder Iterative method was implemented and this converged.

8. ACKNOWLEDGEMENTS

The authors are grateful to the authority Electrical Engineering Department, University of Cape Town, South Africa for providing the infrastructure necessary for carrying out this research, and to ESKOM, through the Tertiary Education Support Programme (TESP) for financial support.

9. REFERENCES

- [1] C. T. Gaunt , Definition of DG-Characteristics of Distributed Generation.
- [2] V. Hamidi, K. S. Smith and R.C. Wilson , "Smart Grid Technology Review within the Transmission and Distribution Sector," Transmission and Distribution, Mott MacDonald Ltd, Glasgow,.
- [3] M. Powalko, K. Rudion, P. Komarnicki, J. Blumschein , "Observability of the Distribution System," in *CIREN 20th International Conference on Electricity Distribution*, Prague, June 2009.
- [4] S. P. Chowdhury, S. Chowdhury, and P. A. Crossley , "Islanding protection of active distribution networks with renewable distributed generators: A comprehensive survey," *Electric Power Systems Research*, vol. 79, pp. 984–992, 2009.
- [5] J. Mulhausen, J. Schaefer ,M. Mynam, A. Guzman, M. Donolo , "Anti-Islanding Today, Successful Islanding in the Future," in *Texas A&M Conference for Protective Relay Engineers*, 2010.
- [6] R.A.F. Currie, G.W. Ault, C.E.T. Foote, G.M. Burt, J.R. McDonald , "Fundamental Research Challenges for Active Management of Distribution Networks with high levels of Renewable Generation," Institute for Energy and the Environment, University of Strathclyde,.
- [7] J. Liu, J. Tang, F. Ponci, A.Monti, C. Muscas and P.A. Pegoraro , "Trade-Offs in PMU Deployment for State Estimation in Active Distribution Grids," *IEEE Transactions on Smart Grid*, vol. 3, no. 2, pp. 915-924, June 2012.
- [8] M. Rihan, M. Ahmad and M. S. Beg , "Phasor

- Measurement Units in the Indian Smart Grid," Department of Electrical Engineering, Aligarh Muslim University, Aligarh.
- [9] D. G. Hart, D. Uy, V. Gharpure, D. Novosel, D. Karlsson, M. Kaba, "PMUs – A new approach to power network monitoring," *ABB Review*, no. 1, 2001.
 - [10] B. Singh, N.K. Sharma, A.N. Tiwari, K.S. Verma, and S.N. Singh, "Applications of phasor measurement units (PMUs) in electric power system networks incorporated with FACTS controllers," *International Journal of Engineering, Science and Technology*, vol. 3, no. 3, pp. 64-82, 2011.
 - [11] American Transmission Company LLC (II), Phasor Measurement Unit Project, June 2012.
 - [12] A. Carta, N. Locci, C. Muscas and S. Sulis, "A Flexible GPS-Based System for Synchronized Phasor Measurement in Electric Distribution Networks," *IEEE TRANSACTIONS ON INSTRUMENTATION AND MEASUREMENT*, vol. 57, no. 11, November 2008.
 - [13] G. Hataway, B. Flerchinger and R. Moxley, "Synchrophasors for Distribution Applications," PowerSouth Energy Cooperative and Schweitzer Engineering Laboratories Inc., 2012.
 - [14] J. Thlusty, A. Kasembe, Z. Muller, J. Svec, T. Sykora, A. Popelka, E.V. Mgaya and O. Diallo, "The Monitoring of Power System Events on Transmission and Distribution Level by the use of Phasor Measurement Units (PMUs)," in *20th International Conference on Electricity Distribution*, Prague, 2009.
 - [15] G. N. Korres and N. M. Manousakis, "State estimation and bad data processing for systems including PMU and SCADA measurements," *Electrical Power Systems Research*, vol. 81, pp. 1514-1524, 2011.
 - [16] M. Hurtgen and J-C. Maun, "Advantages of power system state estimation using Phasor Measurement Units," in *16th Power Systems Computation Conference, July 14-18, 2008*, Glasgow, 2008, pp. 1-7.
 - [17] A. Abur and A. Gomez Exposito, *Power System State Estimation: Theory and Implementation*. New York, USA: Marcel Dekker, Inc, 2004.
 - [18] G. Welch and G. Bishop, "An Introduction to the Kalman Filter," Department of Computer Science, University of North Carolina at Chapel Hill, North Carolina, 2009.
 - [19] S. Sarri, M. Paolone, R. Cherkaoui, A. Borghetti, F. Napolitano and C.A. Nucci, "State Estimation of Active Distribution Networks: Comparison Between WLS and Iterated Kalman-Filter Algorithm Integrating PMUs," in *3rd IEEE PES Innovative Smart Grid Technologies Europe (ISGT Europe)*, Berlin, 2012.
 - [20] K. D. Jones, "Three-Phase Linear State Estimation with Phasor Measurements," Electrical Engineering, Virginia Polytechnic Institute & State University, Virginia, Masters Thesis 2011.
 - [21] S. Lefebvre, J. Provost, L. Lenoir, J.C. Rizzi, H. Delmos, A. Ajajal, "Distribution State Estimation for Smart Grids," in *IEEE Power and Energy Society General Meeting*, Vancouver, BC, 2013.
 - [22] N. Nusrat, M. Irving and G. Taylor, "Development of Distributed State Estimation Methods to Enable Smart Distribution Management Systems," in *IEEE International Symposium on Industrial Electronics*, Gdansk, 2011, pp. 1691-1696.
 - [23] C. Gómez-Quiles, A. Gómez-Exposito, and A. de la Villa Jaén, "State Estimation for Smart Distribution Substations," *IEEE Transactions on Smart Grid*, vol. 3, no. 2, pp. 986-995, June 2012.
 - [24] G. N. Korres and N. M. Manousakis, "A state estimator including conventional and synchronized phasor measurements," *Computers and Electrical Engineering*, vol. 38, pp. 294-305, 2012.
 - [25] X. Tai, D. Marelli, E. Rohr, F. Minyue, "Optimal PMU placement for power system state estimation with random component outages," *International journal of Electrical Power and Energy systems*, vol. 51, pp. 35-42, 2013.
 - [26] K. Zhu, L. Nordström and L. Ekstam, "Application and analysis of Optimum PMU Placement methods with application to State Estimation Accuracy," in *Power & Energy Society General Meeting*, Calgary, 2009, pp. 1-7.
 - [27] R. Singh, B. P. Pal and R. B. Vinter, "Measurement Placement in Distribution System State Estimation," *IEEE Transactions on Power Systems*, vol. 24, no. 2, May 2009.
 - [28] A. Mahari and H. Seyedi, "Optimal PMU placement for power system observability using BICA, considering measurement redundancy," *Electric Power Systems Research*, vol. 103, pp. 78-85, April 2013.
 - [29] M. T. Hagh and M. A. Jirdehi, "A Robust Method for State Estimation of Power System with UPFC," *Turkish Journal of Electrical Engineering and Computer Sciences*, vol. 18, no. 4, pp. 571-582, 2010.
 - [30] IEEE PES Distribution System Analysis Subcommittee's Distribution Test Feeder Working Group. IEEE PES Distribution Test feeders. [Online]. <http://ewh.ieee.org/soc/pes/dsacom/testfeeders/index.html>
 - [31] W. H. Kersting, *Distribution System Modelling and Analysis*, 2nd ed., Leo L. Grisby, Ed. Florida, USA: CRC Press, Taylor & Francis Group.

PROPOSED EVALUATION OF THE POTENTIAL RISK OF VOLTAGE COLLAPSE IN THE WESTERN CAPE NETWORK AS A RESULT OF GIC

A. Jakoet*, A. K. Saha** and ALL Jarvis**

* Eskom Power Plant Engineering Institute, University of KwaZulu-Natal, School of Electrical Engineering, Howard Campus, Durban, South Africa

Email: JakoetA@eskom.co.za

** University of KwaZulu-Natal, School of Electrical Engineering, Howard Campus, Durban, South Africa

Email: saha@ukzn.ac.za

Abstract. The purpose of this paper is to provide a literature review of a study on the evaluation of the impact of geo-magnetically induced currents (GICs) on the voltage stability of the Western Cape transmission system. The review covers the impact of GICs on large power systems, specifically power transformers, and provides a methodology to assess the risk of voltage collapse in large power systems. The reactive power absorbed by a transformer has been showed to be linearly related to the amount of DC current applied to the neutral of star-wound transformers according to previous literature. Methods for quantifying the additional absorbed reactive power by transformers due to GIC are also discussed. No results have as yet been obtained as the models are still required to be simulated and validated.

Key Words. Geo-magnetically induced currents; half-cycle saturation; voltage stability

1. INTRODUCTION

Eskom, South Africa's energy utility, produces most of its power in the Northern Province and Mpumalanga, close to the coal mines in the northern part of the country. The utility relies heavily on its network of 27 770 km of overhead transmission lines and 325 000 km of distribution lines to transmit power from the northern part of the country to the south, where there are fewer generating stations [1]. Eskom plans to expand its transmission network over the next ten years, by being able to transmit power at higher voltages and installing more transformers and transmission lines in strategic positions for network strengthening [2]. Higher transmission voltages result in higher levels of geo-magnetically induced currents (GICs) [3].

Today's electrical power networks are more at risk to the GICs than a few decades ago, as the number of assets (transformers and transmission lines) providing a path for GICs to flow has increased dramatically over the last five decades. These large networks act as antennae that are electromagnetically coupled to the usually dormant magnetic field of the earth. Fluctuating electrojet currents in the earth's ionosphere, caused by geo-magnetic disturbances (GMD) from the sun, disrupt the earth's magnetic field. According to Faraday's law of electromagnetic induction, a magnetic field changing with respect to time induces a voltage in a conductor. This is the driving force that allows GICs to flow up the neutral of grounded star-wound (Y) transformers and along transmission lines [4]. Fig. 1 provides an illustration of the phenomena of GICs and how it is formed as well as how it flows in an electrical power system (EPS).

The effects of GIC on power system components have been studied since the early 1990's [5]. GICs can cause power transformer half-cycle saturation, which leads to the generation of both even and odd harmonic currents the fundamental frequency (50 Hz) to be injected into the system. Harmonic currents can cause overloading of capacitor banks and static-VAR-compensators (SVCs) as

well as malfunctioning of protective relays [6]. Transformer saturation also causes a large amount of stray flux in the transformer members, tank walls and frames, which can lead to localised heating, causing insulation

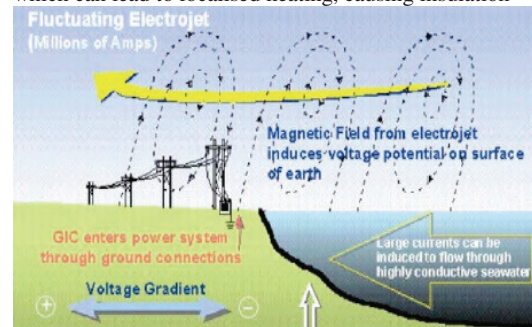


Fig.1: An illustration showing the phenomena of GICs [7]

damage and gassing resulting in shortened transformers life [8].

The power engineering community was brought to the realisation of the seriousness of this phenomenon following the blackout on 13 March 1989 in the Hydro-Quebec 735 kV power system in Canada, where 6 million people were left without power for more than 9 hours [9]. A large GMD caused a network wide saturation of some power transformers, causing an increase in reactive power demand and generation of harmonics. Harmonic currents caused the overloading of capacitor banks and SVCs. The loss of VAR support systems and the excess reactive power demand by transformers under saturation, caused voltage levels to dip and a cascading blackout was experienced. The effects on power transformers, high voltage DC (HVDC) transmission systems, relaying and protection systems were conducted over the years following the event, and a vast amount of literatures are available regarding the aforementioned [6,10,11,12,13].

The objective of this paper is to provide a review of the existing literature regarding the effect of GICs on power transformers and load flow studies in the presence thereof.

It further provides a methodology to quantify the additional reactive power absorbed by different transformers, in a selected part of the South African transmission system, under saturation because of GICs. Subsequently, a methodology to conduct a voltage stability study of the selected network is presented, considering different contingency analysis scenarios for its comprehensive evaluation.

2. EFFECTS OF GICs ON POWER TRANSFORMERS

Transformers form the backbone of an EPS as they step-up voltages for power transmission across a region and step-down voltages to different usable levels for the consumer. In the past, power transmission over longer distances was not possible due to the high power losses experienced. Resistive power losses in transmission lines are reduced when stepping up voltages for power transmission across long distances. Transformers can be used to vary the relative voltage of circuits, isolate them, or both.

Power transformers are designed to operate in the linear region of their saturation characteristic (B-H curve) so as to minimise the amount of copper used in its construction, thus minimising construction costs. Fig. 2 indicates the saturation characteristic of a specific ferromagnetic material used in transformer core construction.

The curves indicate the relationship between the magnetic field strength H , and the magnetic flux density B . The characteristic varies with different core material types. The B-H curve on the left includes hysteresis and eddy current losses, whereas the curve on the right ignores this phenomenon and can therefore be linearized as shown. The linear region of the curve is indicated by the red arrows in the figure.

During a GMD, GICs of frequencies between 0.001 Hz and 1 Hz with periods of 1 second to 1000 seconds can flow in or out of the neutrals of grounded Y transformers. These quasi-DC GICs cause half-cycle saturation of power transformers. Power transformer saturation is the root cause of EPS problems associated with GICs [5,14].

The application of DC to the neutral of power transformers causes a one directional DC flux in the core, which depends on the reluctance path, the magnitude of the GIC and the number of turns in the winding in which it flows [11]. This DC flux causes the AC flux in one half-cycle to rise above the knee-point voltage (V_{knee}). The result is that the core now operates in a very non-linear region of its B-H curve causing short duration, high magnitude and asymmetrical magnetization current peaks. This is illustrated in Fig. 3. An increase in leakage flux is observed which can result in overheating depending on transformer design and core construction.

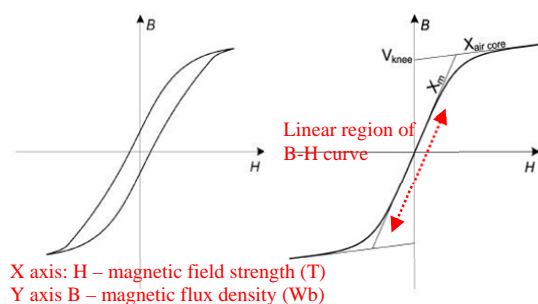


Fig. 2: A typical saturation characteristic of a ferromagnetic material used in transformer core construction [10]

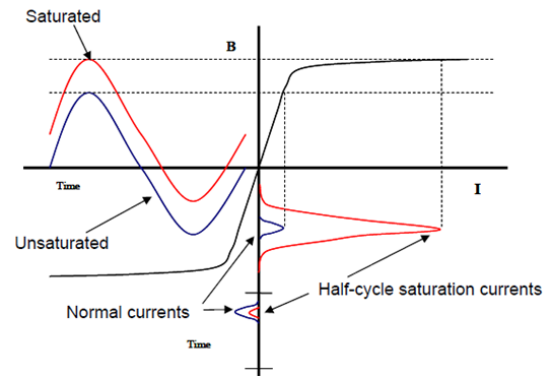


Fig. 3: Relationship between flux and current with and without DC-bias [4]

Due to the asymmetrical nature of the magnetization current during saturation, the exciting current of a half-cycle saturated transformer is rich in both even and odd harmonic components, which can lead to problems mentioned briefly, previously in this paper. The characteristics and harmonic profile of the magnetization current during DC-bias, shown in Fig. 4, and the associated reactive power consumption associated therewith, has been reported in [15], [16] and [17].

The relationship between the applied DC, the excitation current and VAR consumption are linearly related [15-17]. A decrease in harmonic amplitude of the excitation current is observed as the harmonic frequency increases [4].

A transformer's susceptibility to GICs is dependent on its core construction, as this relates to how many complete DC flux paths will be present in the core [18]. Single phase transformers are considered to be the most susceptible to GICs [19]. In a 3-phase three limb transformer, no complete DC flux path exists in the core, making this type of design the least susceptible to GICs. The 3-phase five limb transformers, 3-phase seven limb and 3-phase shell form are next, in order of increasing susceptibility. It should be noted, that field tests of applied dc to 3-phase three limb transformers indicated some signs that saturation has occurred [15], so the statement that a 3-phase three limb transformer is not susceptible to GICs could not be entirely true and needs to be investigated in the future. A possible explanation is that the transformer tank and structural members could perhaps supply a sufficient return-path permeability to allow main-leg saturation. The effects of GICs on the transformer tanks have been studied by [20] and include effects such as localised heating of the tank, corrosion and paint damage.

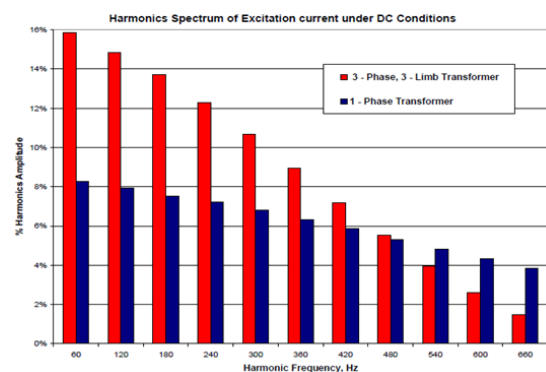


Fig. 4: Harmonic spectrum of excitation current under different GIC conditions [4]

In order to accurately model the transformer for GIC studies, its low frequency and saturation behaviour under DC-bias needs to be considered.

3. MODELLING OF GICS IN AN EPS

A methodology for conducting load flow studies of an EPS considering the effects of GIC is described in [21]. It involves modelling the geo-electrical field produced by a GMD to determine the induced earth surface potential that drives GICs and modelling this as a DC voltage source in the transmission line.

GICs can be considered as DC when compared to the 50 Hz or 60 Hz operating frequency of power transformers, hence the term quasi-DC. The reactance of the transmission lines, transformers and other devices required in the EPS (shunt capacitors and inductors) can thus be ignored when determining the magnitude and direction of GIC flow. Delta winding transformers are also ignored and series capacitors block the flow of GICs along that path. Important parameters that influence the magnitude and direction of GICs are the following [22]:

- i. The magnitude of the induced earth surface potential due to a GMD (modelled as a DC voltage source in the transmission line)
- ii. Resistance of the coils of grounded transformers
- iii. Resistance of the series winding of auto-transformers (including common winding if grounded)
- iv. Resistance of transmission lines
- v. Substation grounding resistance

The GIC distribution in the network can then be calculated. Hereafter, a method for determining the increased VAR requirements under different levels of GICs should be developed, subsequently, these VAR requirements should be modelled in a load flow program, including realistic loads, in order to provide suitable responses to voltage stability problems.

In more recent work in the field of calculation of GIC, Turnbull [23] improved the modelling of GIC in the United Kingdom. It is recommended, that in order to improve GIC modelling, specific substation transformer data is required [23]. Marti et al [24] and references therein, shows that GICs can be calculated using the excessive reactive power absorption of transformers when saturated.

4. RTDS MODELLING OF TRANSFORMERS TO DETERMINE MVAR CONSUMPTION

RTDS[®] Simulator (RTDS) is a power system simulator that solves electromagnetic transient simulations in real time. The system is used for high speed simulations, closed-loop testing of protection and control equipment and hardware in the loop (HIL) applications.

Transformers in a selected portion of the South African transmission system will be modelled in RTDS to determine its excess reactive power consumption in the saturation region of the B-H curve. The transformers will be injected with different magnitudes of GIC in its neutrals and the corresponding reactive power will be recorded. A curve of MVAR vs. GIC will be derived for each different transformer in the network being studied.

The Unified Magnetic Equivalent Circuit (UMEC) model, developed by Enright [25], will be used to model the

transformers behaviour in the saturated region. Unlike the classical transformer model, the UMEC considers magnetic coupling between windings of different phases, and coupling between windings of the same phase. The UMEC transformer model is based primarily on core geometry and uses the duality principle to solve magnetic circuits instead of electrical circuits as in the classical transformer model. Normalized core parameters are used in the model so that requirements of physical data are minimized [25]. Fig. 5 illustrates a 3-limb transformer and 5-limb transformer and the required core geometry ratios for the UMEC model. RTDS allows for the selection of a 3-phase, 3-limb or a 3-phase, 5-limb transformer from the configuration menu.

Selecting a 3-limb core requires the input of the ratio of core yoke length (L_y) to the core winding-limb length (L_w), as well as the ratio of core yoke area (A_y) to the core winding-limb area (A_w). Selecting a 5 limb core requires the ratio of core yoke length (L_y) to the core outer-limb length (L_o) and the ratio of core yoke area (A_y) to the core outer-limb area (A_o) in addition to the two ratios required for a 3-limb transformer. The name plate data of the specific transformer is also entered into the configuration menu and the saturation curve can be entered discretely as points on a curve, shown in Table 1. For a more detailed explanation of the UMEC model, see [25] and references therein.

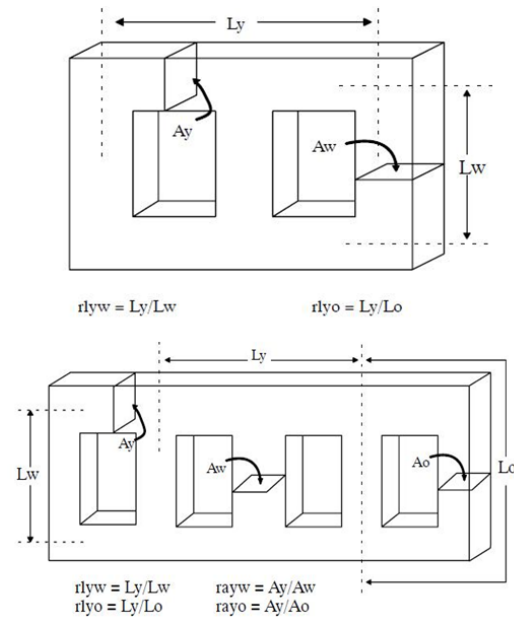


Fig. 5: Core structures of 3-limb and 5-limb transformers [26]

The network to be studied is shown in Fig. 7. The black squares represent substations and the red stars represent towns. High voltage transformers (132 kV and above) at the different substations will be modelled using the UMEC model in RTDS as shown in Fig. 8 to determine the reactive power consumption of transformers when subjected to different magnitudes of GIC.

The UMEC model is computationally intensive, therefore some banks of transformers would need to be lumped together to limit the computational power required. This will be assessed on an as needed basis in the detailed modelling, which is not presented in this paper.

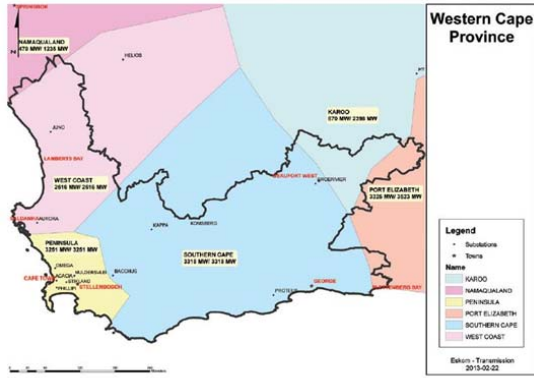


Figure 5.9 Western Cape Province with generation connection capacity limit (steady-state (N-1) limit MW / Stability limit MW)

Fig 7: Western Cape network to be studied indicating substations and towns [28]

Table 1: Saturation curve input in RTDS for UMEC transformer model

Variable Name	Description	Value
X1E	Point 1 - Current as a % of rated current	0
Y1E	Point 1 - Voltage in p.u.	0
X2E	Point 2 - Current as a % of rated current	0.1774
Y2E	Point 2 - Voltage in p.u.	0.324129
X3E	Point 3 - Current as a % of rated current	0.487637
Y3E	Point 3 - Voltage in p.u.	0.61284
X4E	Point 1 - Current as a % of rated current	0.980856
Y4E	Point 1 - Voltage in p.u.	0.825118
X5E	Point 1 - Current as a % of rated current	2
Y5E	Point 1 - Voltage in p.u.	1
X6E	Point 1 - Current as a % of rated current	3.09543
Y6E	Point 1 - Voltage in p.u.	1.08024
X7E	Point 1 - Current as a % of rated current	6.52348
Y7E	Point 1 - Voltage in p.u.	1.17334
X8E	Point 1 - Current as a % of rated current	20.357
Y8E	Point 1 - Voltage in p.u.	1.26115
X9E	Point 1 - Current as a % of rated current	60.215
Y9E	Point 1 - Voltage in p.u.	1.36094
X10E	Point 1 - Current as a % of rated current	124.388
Y10E	Point 1 - Voltage in p.u.	1.49469

Overbye et al [27] describes a linear relationship between the absorbed reactive power and the per-phase GIC flowing in the neutral of grounded Y transformers. An approximate equation to quantify the additional reactive power absorbed by the transformer is shown in Equation 1.

$$Q_{loss} = V_{kv} k I_{GIC} \quad (1)$$

Where:

Q_{loss} = additional reactive power absorbed by the transformer under GIC conditions

V_{kv} = the terminal voltage

k = a transformer specific constant

I_{GIC} = the per-phase GIC flowing in the neutral of the grounded Y transformer

In load flow calculations, bus voltages are usually expressed in per-unit (p.u), we thus include the transformers maximum nominal voltage in the transformer specific constant, denoted as K , which has a unit of Mvars/Amp. Equation 2 below indicates the form of the equation to be used for large system studies. V_{pu} is the per-unit voltage at the bus [27].

$$Q_{loss} = V_{pu} K \frac{V_{nom kV}}{V_{nom kV, assumed}} I_{GIC} \quad (2)$$

Literature provides some guidance for the values of K for a specific transformer core design, if they are not known [3,11,16].

The proposed values for K are listed below:

- Single phase core: $K = 1.18$
- Shell form core: $K = 0.33$
- 3-limb core: $K = 0.29$
- 5-limb core: $K = 0.66$

K values are to be derived for different transformers, in the network to be studied, using RTDS and the model shown in Fig. 8. These will be compared to that proposed in literature.

5. LOAD FLOW AND VOLTAGE STABILITY STUDIES CONSIDERING THE EFFECTS OF GIC

The South African EPS is currently very stressed and the system is run very tightly in order to meet demand while performing maintenance on an ageing fleet. As previously mentioned, South Africa has long transmission lines spanning from the north of the country to the south. Voltage stability problems are usually associated with very stressed power systems and long lines [28].

The main factor causing voltage instability problems in an EPS is the inability of the power system to meet the demand for reactive power. When performing voltage stability studies generator reactive power and voltage control limits, load characteristics, characteristics of reactive power and voltage control devices need to be considered. Voltage stability depends on how the variation of reactive power as well as real power in the load area affect the voltage at the load buses [28].

The additional reactive power loads drawn by transformers will be quantified based on a one in a hundred year severe solar storm. The additional reactive power load of the different transformers at substations will be modelled as constant reactive current loads in a load flow program such as DIGSILENT Power Factory. The impact to voltage stability will be assessed considering different "what if" scenarios, e.g. loss of a critical SVC or loss of a critical line.

An assessment of the impact of degraded **voltage** on nearby industry and nuclear plants will be made based on the voltage stability results obtained by the study. Safe operational voltage of nuclear plant equipment will be reviewed during the study to ensure that the network voltage remains within the safety limits during a GMD event.

6. CONCLUSION

The paper aims at providing a review of the existing literature regarding the effect of GICs on power transformers and load flow studies when GICs are present. It reported a methodology to quantify the additional reactive power absorbed by different transformers, in a selected part of the South African transmission system, under saturation because of GICs and a methodology to conduct a voltage stability study of the selected network. Contingency analysis for a comprehensive evaluation of voltage stability concerns is considered.

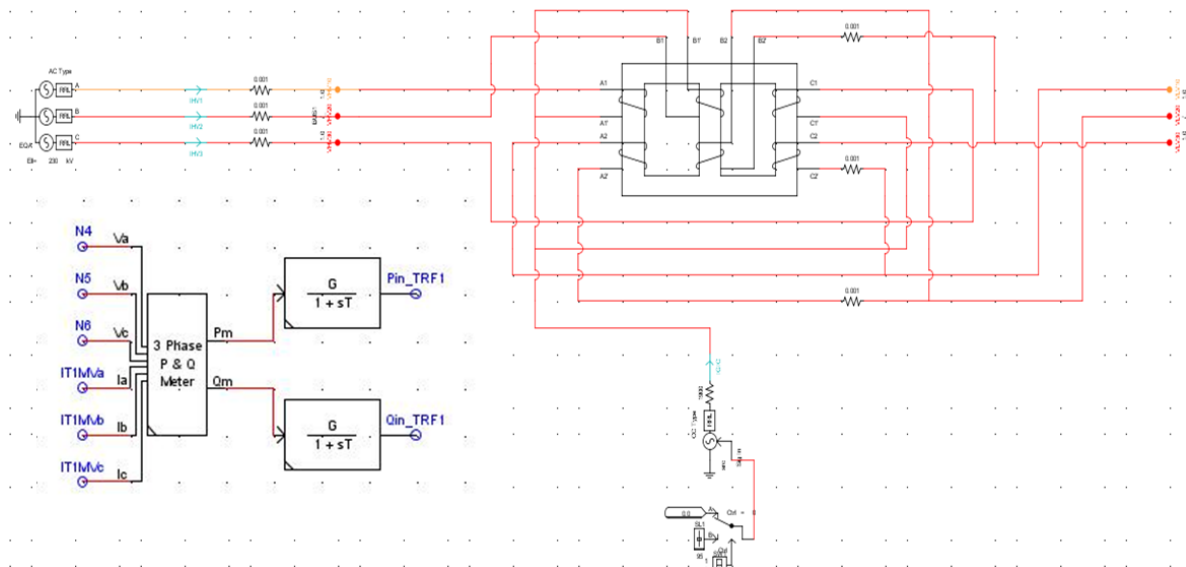


Fig. 8: RTDS UMEC transformer test model for GIC vs. MVAR consumption determination

This literature review provides a basis for the evaluation of the potential risk of voltage collapse in the Western Cape network as a result of GIC.

Power transformers in the network are simulated using the UMEC model to determine their reactive power consumption under different levels of DC applied to its neutral. Predicted GIC levels, from literature for the area to be studied, are to be used to determine the reactive power consumption of transformers for one in a hundred year solar storm. These reactive loads are then modelled in a load flow program so as to determine the impact on the voltage stability of the network. The impact on associated industry and nuclear power plant in the study area can then be assessed.

REFERENCES

- [1] Eskom, "How electricity is transmitted," [Online]. Available: <http://www.eskom.co.za/c/article/209/how-electricity-is-transmitted>
- [2] Eskom, "Transmission Ten-Year Development Plan," [Online]. Available: <http://www.eskom.co.za/Whatweredoing/TransmissionDevelopmentPlan/Documents/TransDevPlanBrochure2013-2022.pdf>
- [3] W.A. Radasky and J.G. Kappenman "Impacts of geomagnetic storms on EHV and UHV power grids," *Asia-Pacific Symposium on Electromagnetic Compatibility (APEMC)*, pp. 695-698, 2010
- [4] NERC, "2012 Special Reliability Assessment Interim Report: Effects of Geomagnetic Disturbances on the Bulk Power System," NERC, Tech. rep. 2012.
- [5] J.G. Kappenman and V.D. Albertson, "Bracing for the geomagnetic storms," *Spectrum, IEEE*, Vol. 27, No. 3, pp. 27-33, 1990.
- [6] R. J. Pijola, D. H. Boteler' and H. Nevanlinna, "The Effects Of Geomagnetic Disturbances On Electrical Systems At The Earth's Surface," *Advance Space Research*, Vol. 22, pp. II-21, 1998.
- [7] W.A. Radasky, "Overview of the impact of intense geomagnetic storms on the U.S. high voltage power grid," *IEEE International Symposium on Electromagnetic Compatibility (EMC)*, pp. 300-305, 2011.
- [8] C.T Gaunt and G. Coetzee, "Transformer failures in regions incorrectly considered to have low GIC-risk," *IEEE PowerTech, Lausanne Switzerland*, pp. 807-812, 2007.
- [9] L. Bolduc, P. Langlois,; D. Boteler, and R. Pirjola, , "A study of geoelectromagnetic disturbances in Quebec. I. General results," *IEEE Transactions on Power Delivery*, Vol. 13, No. 4, pp. 1251-1256, 1998.
- [10] J. Berge, R.K. Varma, and L. Marti, "Laboratory validation of the relationship between Geomagnetically Induced Current (GIC) and transformer absorbed reactive power," *IEEE Electrical Power and Energy Conference (EPEC)*, pp. 491-495, 2011.
- [11] R.S. Girgis, and K. Vedante, "Effects of GIC on power transformers and power systems," *IEEE PES Transmission and Distribution Conference and Exposition (T D)*, pp. 1-8, 2012.
- [12] M Lehtinen and R. Pirjola, "Currents produced in earthed conductor networks by geomagnetically-induced electric fields," *Annales Geophysicae*, Vol. 3, No.4, pp. 479-484, 1985
- [13] L. Trichtchenko and D.H. Boteler, "Effects of Recent Geomagnetic Storms on Power Systems," *7th International Symposium on Electromagnetic Compatibility and Electromagnetic Ecology*, pp. 265-268, 2007
- [14] T.S. Molinski, "Why utilities respect geomagnetically induced currents ," *Journal of Atmospheric and Solar-Terrestrial Physics* , Vol. 64, No. 16, pp. 1765-1778, 2002.
- [15] R. A. Walling and A.N. Khan, "Characteristics of transformer exciting-current during geomagnetic disturbances," , *IEEE Transactions on Power Delivery*, Vol. 6, No. 4, pp. 1707-1714, 1991..
- [16] X. Dong,; Y. Liu, and J.G. Kappenman, "Comparative analysis of exciting current harmonics and reactive power consumption from GIC saturated transformers," *IEEE Power Engineering Society Winter Meeting*, Vol. 1, pp. 318-322, 2001.
- [17] J. Yao, M. Liu, C. Li, and Q. Li, , "Harmonics and Reactive Power of Power Transformers with DC Bias," *Asia-Pacific Power and Energy Engineering Conference (APPEEC)*, pp. 1-4, 2010.
- [18] N. T. Takasu,; T. Oshi,; F. Miyawaki, S. Saito, and Y. Fujiwara, "An experimental analysis of DC excitation of transformers by geomagnetically induced currents," *IEEE Transactions on Power Delivery*, Vol. 9, No. 2, pp. 1173-1182, 1994.
- [19] A.P. Meliopoulos, S. Elias, N. Glytsis, G.J. Cokkinides, and M. Rabinowitz, "Comparison of SS-GIC and MHD-EMP-GIC effects on power systems," *IEEE Transactions on Power Delivery*, Vol. 9, No. 1, pp. 194-207, 1994.

- [20] B. Zhang,; L. Liu,; Y. Liu,; M. McVey, and R.M. Gardner, "Effect of geomagnetically induced current on the loss of transformer tank," *IET Electric Power Applications*, Vol. 4, No. 5, pp. 373-379, 2010.
- [21] V.D. Albertson, J.G. Kappenman; N. Mohan and G.A. Skarbakka, "Load-Flow Studies in the Presence of Geomagnetically-Induced Currents," *IEEE Transactions on Power Apparatus and Systems*, Vol.100, No. 2, pp. 594-607, 1981.
- [22] J. Berge and R.K. Varma, "A software simulator for Geomagnetically Induced Currents in electrical power systems," *Canadian Conference on Electrical and Computer Engineering (CCECE)*, pp. 695-700. 2009
- [23] K. Turnbull, "Modelling GIC in the UK," *A&G*, Vol. 51, pp. 5.25-5.26, 2010
- [24] L. Marti,; J. Berge, and. R.K. Varma, "Determination of Geomagnetically Induced Current Flow in a Transformer From Reactive Power Absorption", *IEEE Transactions on Power Delivery* , 2013
- [25] W. Enright,; N. Watson, and O. Nayak, "Three-phase five-limb unified magnetic equivalent circuit transformer models for PSCAD V3.," *International Conference on Power System Transients*, 1999.
- [26] RTDS Technologies, *Real Time Digital Simulator Power System Users Manual*. Canada, 2006.
- [27] T.J. Overbye, T.R. Hutchins, , K. Shetye,; J. Weber, and S. Dahman, "Integration of geomagnetic disturbance modeling into the power flow: A methodology for large-scale system studies," in *North American Power Symposium (NAPS)*, pp. 1-7, 2012.
- [28] Kundur,P, *Power System Stability and Control*, Mark G. Lauby Neal J. Balu, Ed. New York, USA: McGraw-Hill, 1994.
- [29] Eskom, "Generation Connection Capacity Assessment of the 2016 Transmission Network,"[Online] Available: http://www.eskom.co.za/Whatweredoing/GCCAReport/Documents/GCCA_2016REV1.pdf

THE USE OF DIGSILENT POWERFACTORY SOFTWARE FOR POWER SYSTEM EFFICIENCY CALCULATIONS UNDER DISTORTED CONDITIONS

H. Amushembe* and G. Atkinson-Hope**

* Centre of Power System Research, Dept. of Electrical Engineering, Cape Peninsula University of Technology, P.O. Box 682 Cape Town 8000, E-mail: 209103647@mycput.ac.za or amushembe@gmail.com

**Technology Transfer and Industrial Linkages, Centre of Power System Research, Dept. of Electrical Engineering, Cape Peninsula University of Technology, P.O. Box 682 Cape Town 8000, E-mail: atkinsonhopeg@cput.ac.za.

Abstract: There is an increase in electrical energy demand in the Southern African Region, thus saving energy has become a vital aspect for economic growth. One cause of high demand is that the power system equipment operates at low efficiency thus power losses increase. This prompted a need to evaluate efficiency in networks under distorted conditions to determine the impact of harmonics on efficiency. This study thus presents the use of DIgSILENT PowerFactory software, for efficiency calculation under distorted conditions. This method will assist the power quality engineers at utility and customer levels on how to calculate the efficiency of power system equipment and determine the power losses when harmonics distorts the current and voltage waveforms. The study looks at two case studies namely, Case 1: Non-sinusoidal network and Case 2: Non-sinusoidal network with power factor (PF) correction at Point of common coupling (PCC).

Key words: Efficiency, harmonics, distortion, power system, PCC.

1. INTRODUCTION

The main objective of the electric utility is to generate, transmit, transform and distribute electrical energy with the least possible losses. However, harmonics produced by non-linear loads such as adjustable speed drives, arc furnaces, cycloconverters, etc complicate this objective. These harmonics causes voltage and current waveform distortions, with adverse effects on the system efficiency [1]. Distortions result in additional current components flowing in the system that do not yield any net energy except that they cause losses in the power system elements they pass through. This requires the system to be built to a slightly larger capacity to deliver enough power to the load [2]. The response of the power system at each frequency determines the true impact of the nonlinear load on harmonic voltage distortion [2]. The traditional formula only calculates the electrical efficiency of a power system for power at fundamental frequency while harmonic distortions are ignored. The influence of the non-sinusoidal quantities on the efficiency of power system efficiency has thus received little attention. The literature does not say anything on how efficiency can be calculated in a network with

harmonic distortions. The aim of this study is to determine the electrical efficiency of the power system operating under non-sinusoidal conditions. This will be done with the aid of DIgSILENT Powerfactory, which is a computer aided engineering tool for the analysis of industrial, utility, and commercial electrical power systems [3].

2. RESEARCH STATEMENT

The aim of the study is to solve the problem of power losses in power systems. To determine how much distortions contribute to the total losses, which affect the efficiencies of the system. The main contributions of this study are: (a) a software-based methodology to overcome the shortcomings of DIgSILENT to determine efficiency in a power system; and (b) to apply the software-based methodology to different network case studies and calculate efficiency in three-phase networks with harmonic distortions. Two case studies of a 40 kV network are simulated using DIgSILENT software. The following procedures were carried out in sequence [3]:

- (i) Draw a one-line diagram of the network with defined parameters.

- (ii) Conduct a load flow analysis to obtain fundamental frequency results
- (iii) Perform a harmonic penetration study on the power system with an Adjustable Speed Drive (ASD) as a harmonic current source, to get power values at the 5th and 7th harmonic frequencies.
- (iv) Determine or calculate equipment efficiency as well as the efficiency of the whole system.
- (v) Perform Displacement Power Factor (DPF) correction at PCC.
- (vi) Determine or calculate equipment efficiency as well as the efficiency of the whole system with the PF capacitor.
- (vii) Perform impedance scan (ZScan) to check for resonance.

The software shortcoming is that, it does not calculate efficiency nor show the direction of harmonic power. The objective of this study is to use the power given by the software to calculate efficiency and losses under distorted conditions. The method once established can be implementable in actual systems.

3. THEORITICAL BACKGROUND

Harmonics are defined by [2] as the sinusoidal voltages or currents having frequencies that are integer multiples of the frequency at which the supply is designed to operate, usually 50 or 60 Hz. Efficiency of an entity (a device, component, or system) in electrical engineering is defined as useful power output divided by the total electrical power consumed (a fractional expression). It is typically denoted by "Eta" (η) and is determined by (1) [4].

$$Efficiency(\eta) = \frac{Useful\ power\ output}{Total\ power\ input} \quad (1)$$

A power system consists of transformers, capacitor banks, rotating machines and cables or lines as the main equipment [5]. Transformers are used to transform the voltage levels in the network from high to low levels and vice versa. The transformers endure an increase in losses due to excess heat when operating in a harmonic environment [5]. Power utilities and customers use capacitor banks to correct the DPF in an attempt to reduce power losses. However, in the presence of harmonics in the network, capacitor banks tend to cause resonance(s), which tend to amplify harmonics causing the voltage to exceed the rated voltage resulting in capacitor damage [6]. The following traditional way (2) of calculating power factor is based on assumptions that

all loads on the power system are linear. This power factor is called the displacement power factor (DPF).

$$DPF = \cos \theta = \frac{kW}{kVA} \quad (2)$$

This is however untrue when harmonic distortions caused by non-linear loads are present. In fact, a different term called true power factor (TPF) is used for power factor in non-sinusoidal networks [7]. The TPF is given by:

$$TPF = \frac{P_T}{S_T} = \frac{P_T}{V_{rms} I_{rms}} \quad (3)$$

Where P_T = total power including harmonic powers. In the case of rotating machines such as induction motors, the consumed power is increased to get the same work from the motor when supplied with non-sinusoidal voltage [8].

Since a harmonic produces extra power, it is only logical to think that the total power at a point would be the fundamental power plus the harmonic powers. That would yield to an equation such as (4):

$$P_T = P_1 + P_5 + P_7 + \dots P_h \quad (4)$$

Where h is the characteristic harmonic order of $6k \pm 1, k = 1, 2, 3, \dots n$

However, this is not necessary true as some harmonic powers may add, others may subtract.

4. ONE-LINE DIAGRAM

Fig. 1 illustrates a simplified radial distribution network [8] modelled to apply the developed methodology. The network has four busbars. The network consists of a symmetrical alternating current (AC) voltage source (VSRC), which is connected to Bus 1. Bus 1 is chosen as the reference busbar with a voltage of $40\angle 0^\circ$ kV with a system frequency of 60 Hz. A supply transformer (TS), modelled as a two winding transformer, is connected between Bus 1 and Bus 2, which steps down the voltage to 12 kV. The network line (Line1) is modelled as an overhead power line with a length of 90 km and is connected between Bus 2 and Bus 3. An end-user transformer (TRF1) is connected between Bus 3 and Bus 4, which steps down the voltage to 6 kV. Two loads are connected on Bus 4 with Load1 modelled as impedance model and SCR 1 modelled as current source; both loads have a DPF of 0.8 and have power ratings of 2.5 MVA

and 0.75 MVA, respectively. Table 1 below shows the parameters of the simulated network.

Table 1: Network Parameters

Elements	Value
(VRC1)	40 $\angle 0^\circ$ kV
TS	40/12 kV, S = 20 MVA, Z% = 15.1, X/R ratio = 15.1
Line1	Z = (1.1996+j27.7602) ohms (Ω); 20 MVA
TRF1	12/6 kV; S = 5 MVA, Z% = 12, X/R ratio = 12.14
Load1	S = 2.5 MVA; 0.8 DPF
SRC1	S = 0.75 MVA; 0.8 DPF

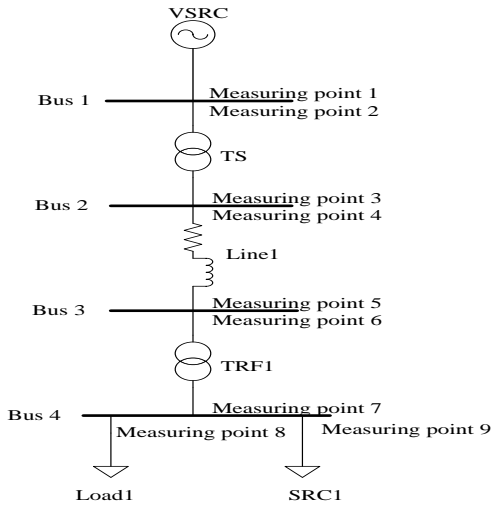


Fig. 1: Network modelled for simulation study.

5. SIMULATION CASE STUDIES

Two case studies were conducted to demonstrate effectiveness of the developed software-based methodology for determining the efficiency of the power system equipment, under balanced operating conditions.

In Case 1, load SRC1 is modelled as a harmonic source using a harmonic current injection method. The current injection according to [9] is widely used to carry out harmonic propagation studies in power systems. The harmonic source was modelled only with the 5th and 7th harmonic orders. The rest of the network elements modelling in case 1 are outlined below:

Line1: Line 1 is modelled as a passive element and all passive elements such as resistors, inductors and capacitors according to [9] are considered to behave linearly with frequency. They have the following characteristics,

$$R = \text{constant (Skin effect ignored)} \quad (5)$$

$$X_L(h) = jhX_L \quad (6)$$

$$X_C(h) = -j\frac{X_C}{h} \quad (7)$$

Where X_L and X_C are the rated inductive and capacitive reactances, respectively.

TS and TRF1: These are linear elements, whose harmonic impedance is derived as follows [9],

$$X_t = R\sqrt{h} + jX_t h \quad (8)$$

SRC1: This is represented by a harmonic current injection source. Table 2 below shows the published harmonic spectrum for SRC1 as adapted from [8], which was used to modelled SRC1:

Table 2: Published Harmonic Spectrum

Harmonic Order	k_h (%)	SPAi ($^\circ$)
5 th	18	110.51
7 th	12	82.08

In cases where there is no published spectrum for the current source, the value of injected current is determined by running a load flow at the fundamental frequency. The harmonic content is assumed to be inversely proportional to the harmonic number. Thus, the fifth harmonic is one-fifth, seventh is one-seventh and so on [2]. The values at the fundamental frequency, I_1 and ϕ_1 , are taken from a preceding load-flow calculation [10]. In case 2, all the modelling remain the same as in Case 1 only a DPF correction capacitor is added at Bus 4, which is the PCC to correct the DPF from 0.8 to 0.97. The following (5) is used to calculate the DPF capacitor value [9]:

$$Q_C = P(\tan \theta_1 - \tan \theta_2) \quad (9)$$

Where P is the active output power at measuring point 7, θ_1 is the DPF angle at measuring point 6, θ_2 is the new DPF angle and Q_C is the capacitor bank reactive power value given measured in var. The salient features of the method used to model the PF capacitor are that, capacitor banks are used for PF correction and are considered passive elements [9]:

$$X_C(h) = -j\frac{V_{LL}^2}{hQ_{3\phi}} \quad (10)$$

Where V_{LL}^2 is the line-line voltage obtained at the bus where the capacitor is to be connected, $Q_{3\phi}$ is the three phase reactive power.

Case 2: Non-sinusoidal network with PF capacitor
Using the results obtained from the load flow, and by applying (9), the capacitor value calculated is:

$$Q_c = 532209 \text{ var}$$

6. DIGSILENT GENERATED RESULTS

Table 3: Case 1: Measurement Point Powers (kW)

Measuring points	P ₁	P ₅	P ₇	P _T
Point 1	1111.9476	-0.0	-0.0	1111.9476
Point 2	1111.9476	-0.0	-0.0	1111.9476
Point 3	-1109.8799	0.0013	0.0007	-
Point 4	1109.8799	0.0230	0.0007	1109.8778
Point 5	-1074.3438	0.0230	0.0126	-
Point 6	1074.3438	-0.0230	-0.0126	1074.3082
Point 7	-1065.8130	0.0265	0.0138	-
Point 8	819.8602	0.6543	0.3564	820.8709
Point 9	245.9581	-0.6808	-0.3702	244.9071

Table 4: Case 2: Measurement Point Powers (kW)

Measuring points	P ₁	P ₅	P ₇	P _T
Point 1	1274.9725	-0.0	-0.0	1274.9725
Point 2	1274.9725	-0.0	-0.0	1274.9725
Point 3	-1272.9832	0.0027	0.0001	-
Point 4	1272.9831	-0.0027	-0.0001	1272.9803
Point 5	-1238.8553	0.0470	0.0020	-
Point 6	1238.8554	-0.0470	-0.0020	1238.8063
Point 7	-1230.6764	0.0541	0.0022	-
Point 8	946.6776	1.3360	0.0565	948.07
Point 9	284.0033	-1.3901	-0.0587	282.5545

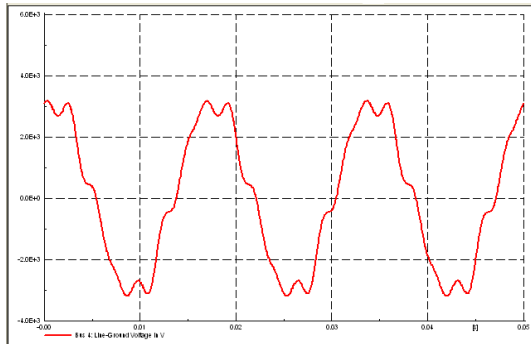


Fig. 2: Voltage waveform at Bus 4

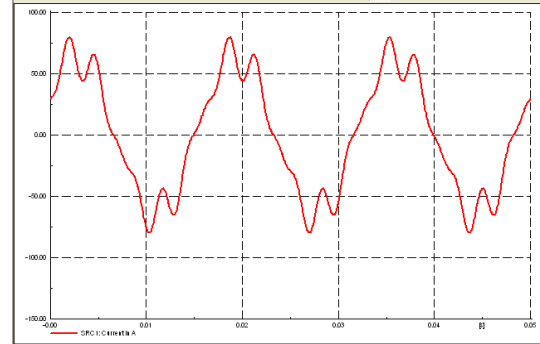


Fig. 3: Current waveform at harmonic source SRC1

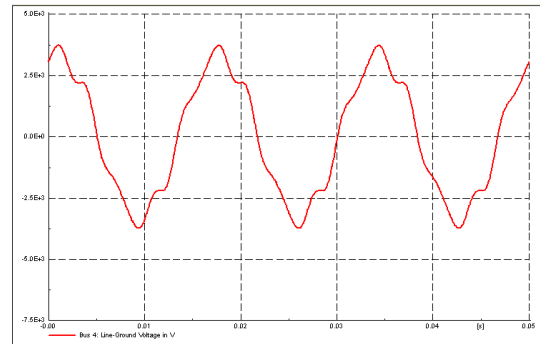


Fig. 4: Voltage waveform at Bus 4 with PF capacitor

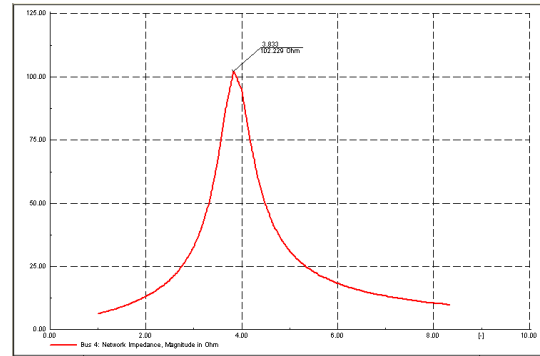


Fig. 5: ZScan at PCC (Bus 4)

In case 1, total voltage harmonic distortion (THD_v) is 12.5%, which is above the limit of 5% as set by IEEE 519 standards [11]. In case 2, the THD_v has slightly decreased to 12.1%, which is still above the limit. The ZScan in Fig. 5 shows resonance at harmonic order 3.853 and impedance of 102.229 Ω.

7. ANALYSIS OF RESULTS

Under load flow (P₁) power flowed away from source (VSRC) towards the loads. When harmonic load flow analysis was conducted using DigSILENT, the harmonic powers (P_h) are minus (-), meaning these flows are in

opposite direction. In addition, the P_h split from SRC1 into Load1 and TRF1 branch, satisfying the current divider rule. The values given in Tables 3 & 4 are entered into (4) with their signs to calculate P_T at a measurement point for example:

$$P_T = P_1 - P_5 - P_7 \quad (11)$$

$$P_T = -P_1 + P_5 + P_7 \quad (12)$$

7.1 Efficiency and losses of Transformers (Case 1)

For TS, input and output are points 2 & 3, for TRF1, points 6 & 7, respectively:

$$\begin{aligned} P_T@m.pt2 &= P_1@m.pt2 - P_5@m.pt2 \\ &\quad - P_7@m.pt2 \end{aligned} \quad (13)$$

$$= 1111.9476 \text{ kW}$$

$$\begin{aligned} P_T@m.pt3 &= P_1@m.pt3 - P_5@m.pt3 \\ &\quad - P_7@m.pt3 \end{aligned} \quad (14)$$

$$= 1109.8779 \text{ kW}$$

$$\begin{aligned} P_T@m.pt6 &= P_1@m.pt6 - P_5@m.pt6 \\ &\quad - P_7@m.pt6 \end{aligned} \quad (15)$$

$$= 1074.3289 \text{ kW}$$

$$\begin{aligned} P_T@m.pt7 &= P_1@m.pt7 - P_5@m.pt7 \\ &\quad - P_7@m.pt7 \end{aligned} \quad (16)$$

$$= 1065.7727 \text{ kW}$$

$$\begin{aligned} \eta_{TS} &= \frac{P_T@m.pt3}{P_T@m.pt2} \times 100 \quad (17) \\ &= \frac{1109.8779}{1111.9476} \times 100 = 99.81\% \end{aligned}$$

$$\begin{aligned} TS_{(losses)} &= P_T@m.pt2 - P_T@m.pt3 \quad (18) \\ &= 2.0697 \text{ kW} \end{aligned}$$

$$\begin{aligned} \eta_{TRF1} &= \frac{P_T@m.pt7}{P_T@m.pt6} \times 100 \quad (19) \\ &= \frac{1065.7727}{1074.3289} \times 100 = 99.21\% \end{aligned}$$

$$\begin{aligned} TRF1_{(losses)} &= P_T@m.pt6 - P_T@m.pt7 \quad (20) \\ &= 8.5355 \text{ kW} \end{aligned}$$

7.2 Efficiency of Line 1 (points 4 & 5)

$$\begin{aligned} P_T@m.pt4 &= P_1@m.pt4 - P_5@m.pt4 \\ &\quad - P_7@m.pt4 \end{aligned} \quad (21)$$

$$= 1109.8779 \text{ kW}$$

$$\begin{aligned} P_T@m.pt5 &= P_1@m.pt5 - P_5@m.pt5 \\ &\quad - P_7@m.pt5 \end{aligned} \quad (22)$$

$$= 1074.3082 \text{ kW}$$

$$\begin{aligned} \eta_{Line1} &= \frac{P_T@m.pt5}{P_T@m.pt4} \times 100 \quad (23) \\ &= \frac{1074.3082}{1109.8779} \times 100 = 96.80\% \end{aligned}$$

$$\begin{aligned} Line1_{(losses)} &= P_T@m.pt4 - P_T@m.pt5 \quad (24) \\ &= 35.5697 \text{ kW} \end{aligned}$$

7.3 Overall efficiency of network

The total output power of the network is calculated using (25) and (26), and the total input power is calculated using (27), used to calculate overall efficiency in (28).

$$\begin{aligned} P_TLoad1 &= P_1@pt8 + P_5@pt8 + P_7@pt8 \quad (25) \\ &= 820.8709 \text{ kW} \end{aligned}$$

$$\begin{aligned} P_TSRC1 &= P_1@pt9 - P_5@pt9 - P_7@pt9 \quad (26) \\ &= 244.9071 \text{ kW} \end{aligned}$$

$$\begin{aligned} P_TGrid &= P_1@pt1 - P_5@pt1 - P_7@pt1 \quad (27) \\ &= 1111.9476 \text{ kW} \end{aligned}$$

$$\begin{aligned} \eta_{(overall)} &= \frac{P_TLoad1 + P_TSRC1}{P_TGrid} \times 100 \quad (28) \\ &= \frac{820.8709 + 244.9071}{1111.9476} \times 100 = 95.85\% \end{aligned}$$

$$\begin{aligned} Overall_{(losses)} &= P_TGrid \\ &\quad - (P_TLoad1 + P_TSRC1) \quad (29) \\ &= 46.1696 \text{ kW} \end{aligned}$$

7.4 Case 2 Analysis

The same procedure as in Case 1 is followed and the results calculated are shown in Table 4:

Table 4: Case 2: Efficiency

Elements	(η %)	Losses (kW)
TS	99.84	1.9921
Line	97.32	34.174
TRF1	99.34	8.1863
Overall	96.52	44.3479

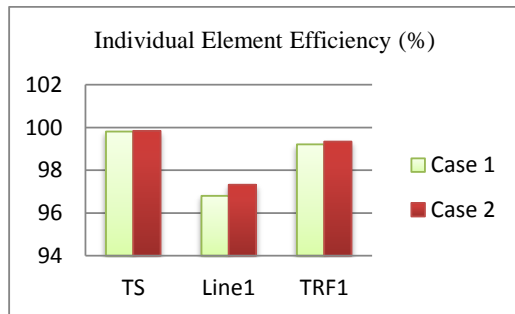


Fig. 6: Individual element efficiency

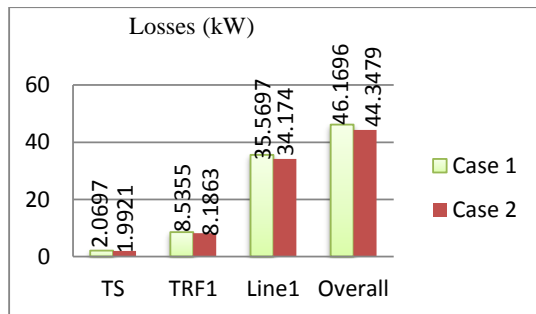


Fig. 7: Elements and network overall power losses

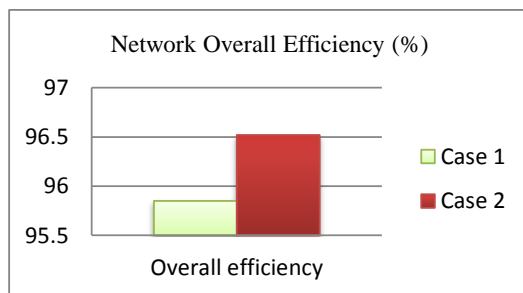


Fig. 8: Network Overall efficiency

The result shows that the efficiency increases when the PF is improved but the THD is still above the normal limit stipulated in IEEE 519 standards [11].

8. CONCLUSION

The efficiency does not vary much and has increased only a little even with improved DPF in case 2. Both the total output and total input power decreases when harmonic distortions are present. For example in (21) and (22) as $P_T@m.pt4$ decrease, $P_T@m.pt5$ decreases too, thus efficiency tend to be in the same range in both cases. This then leads to a conclusion that efficiency is not a good indication of harmonic effect, as it tends to stay the same under harmonic conditions. The losses are however significant and it is therefore important to focus on the losses instead when evaluating harmonic effects on power systems. The methodology developed using DIgSILENT has proved to be effective for efficiency studies but both load flow and harmonic penetration studies need to be independently ran.

REFERENCES

- [1] Ko, A., Swe, W. & Zeya, W. 2011. Analysis of Harmonic Distortion in Non-linear Loads. *The First International Conference on Interdisciplinary Research and Development, Thailand*, 31 May–1 June 2011:66.1–66.6
- [2] RC., Dugan, MF., McGranaghan, & HW., Beaty, *Electrical Power System Quality*, McGraw-Hill, 1996
- [3] DIgSILENT Power Factory, *Basic user's Manual*, DIgSILENT PowerFactory Version 12.1, DIgSILENT GmbH Gormaringen, Germany, 2001.
- [4] J Shepherd, AH., Morton & LF., Spence, *Higher Electrical Engineering*, Pitman, 1970.
- [5] Ortmeyer, T.H., Chakravarthi, K.R. & Mahmoud, A.A. 1985. The Effects of Power System Harmonics on Power System Equipment and Loads. *IEEE Transactions on Power Apparatus and System*, 104(9):2555-2563
- [6] GJ. Wakiley, *Power System Harmonics: Fundamental, Analysis and Filter Design*, Springer, 2001.
- [7] TE Grebe, "Application of Distribution System Capacitor Banks and Their Impact on Power Quality", *IEEE Transactions on Industry Applications*, Vol. 32, No. 3, pp. 714-719, 1996.
- [8] Atkinson-Hope, G., Folly, K.A., 'Decision Theory Process for Making a Mitigation Decision on Harmonic Resonance', *IEEE Transactions on Power Delivery*, vol. 19, No. 3, July 2004.
- [9] E Acha & M Madrigal, *POWER SYSTEM HARMONICS: Computer modelling and analysis*, John Wiley & Sons, 2001
- [10] DIgSILENT Power Factory, *Manual*, DIgSILENT PowerFactory Version 13.1, DIgSILENT GmbH Gormaringen, Germany, 2005, Step 1: D-7.
- [11] IEEE. 1990. *Power System Analysis*. IEEE Std 399-1990. ANSI 1990. ISBN 1-55937-044-0

ALLOCATING ENERGY WHEELING COST IN A DEREGULATED ENVIRONMENT

K T. Akindeji*

* *Durban University of Technology, Dept. of Electrical Power Engineering, 71 Steve Biko Road, Durban 4000, South Africa. E-mail: kayodea@dut.ac.za*

Abstract: Correct pricing of transmission services in a deregulated environment is vital to power systems operation, security, and development. This paper presents a viable and economic method of allocating energy wheeling cost for this purpose. The proposed method reflects the actual system operating condition, therefore allow the transmission provider to recoup the fixed and operating costs of the network. The paper includes test results on a 6-bus system and 24-bus model of Nigerian 330kV power network.

Keywords: Energy Wheeling, deregulation, power flow.

1. INTRODUCTION

The power industry has moved rapidly from regulated convectional setup to a deregulated environment [1]. The former existed as a monopoly, where the same company generates, transmits and distributes electrical energy. All electrical energy consumers were required to purchase their energy from the local monopolistic power company since there was no alternative. Some of the drawbacks to this arrangement are operational inefficiency, unreliable power supply, and wrong costing method. However, a number of countries have implemented or are implementing a free market power industry in recent years. It is strongly believed that deregulation will have profound important implications on technology within the electric power industry and the operation of industrial systems [2].

Deregulation changes how energy transaction and costing are carried out in power system operations. While the consumers are required to pay whatever price the regulated utility offers, deregulation allows for negotiation between the generating company (GENCO) and the distributing company (DISCO). With this change, customers have the option to purchase services and energy from different sources. Therefore, in a deregulated power system, transmission of electrical energy is treated as a separate business to create a fair competition among producers of electricity [1].

The general definition of wheeling is the transmission of electrical energy from a seller to a buyer through the transmission lines which maybe owned by a third party [3]. Pricing of transmission services plays a crucial role in determining whether providing transmission services is economically beneficial to both the wheeling utility and the wheeling customers. However, it is important to realize that pricing of transmission services, although a technical issue is not wholly an engineering problem. Engineering analysis which deals mainly with determining the feasibility and the cost of providing transmission services is only one of the many considerations in the overall process of pricing

transmission services. Market and political consideration could also play major roles in determining transmission prices.

Some existing pricing methods, such as postage stamp, contract path, boundary flow, line-by-line, megawatt mile, are considered to be more suitable for applications in vertically regulated utilities, where transmission access is not open [4]. Generally, pricing of any service or product without regard to political considerations, seeks to [5]:

- Increase customer value by providing a wider variety of services and price options;
- Promote economic efficiency by ensuring that the value of service and the cost of service are balanced;
- Change customer consumption patterns where appropriate to improve the utilization of existing resources;
- Encourage service use for application where it is the least cost option and discourage its use where it is not.

Pricing transmission services to account for the above might be difficult but becomes easy when necessary tools and data for evaluating the economic impacts of providing transmission services are obtainable. The proposed method is a hybrid of the megawatt-kilometre and the short-run marginal cost methods. The former recoups existing and reinforcement costs while the later covers the operating cost of the system. In section 2, the proposed method as well as its components are presented with explanations. Section 3 shows the applications of the proposed method on a 6-bus network and the 24-bus model of Nigerian 330kV power network. Discussions and conclusions follow in section 4.

2. PROPOSED METHOD

2.1 Short-run marginal cost (SRMC)

In the short-run marginal cost, the marginal operating cost of the power system due to a transmission transaction is calculated first. Marginal operating cost is

the cost of accommodating a marginal increase in the wheeling transaction. When the objective function is a cost function, the marginal costs are obtained for each node of the system with the aid of an optimal power flow (OPF) for small changes around an operating point. As the srmc method applies to the short run, investment costs remain constant and can hence be considered as fixed costs [6]. The srmc takes into account only the operating cost of the power system. This operating cost includes fuel cost, cost of transmission line losses as well as system constraints. In order to incorporate all these in any transaction, an OPF solution of the problem is required.

An OPF solution gives the active and reactive power generated and consumed at each bus and the nodal prices. The nodal prices are of special interest because they reflect the marginal generation and load at each bus. These prices are also called locational prices and are found to be the optimal prices, maximizing social welfare and taking transmission constraints into account. They can provide the right incentives to market players and to society [7].

The MATLAB Package (MATPOWER 3.2) was used to solve the OPF problem. The OPF was solved before and after the wheeling transaction. After these solutions were obtained, the SRMC for the wheeling transactions were found using equation (1).

$$srmc = \sum (BMC_i \times P_{i,transaction}) \quad (1)$$

where:

BMC_i = bus marginal cost of bus i

$P_{i,transaction}$ = net power injected at bus i due to the wheeling transaction. (Power generation at bus i after transaction - power generation at bus i before transaction).

The expression in parenthesis in equation (1) was computed in a tabular form for all generator buses and the sum calculated to give the wheeling cost of the transaction.

Optimal Power Flow (OPF) Formulation: The objective of the OPF is to minimize the operation cost for a given transaction such that the power flow equations are satisfied and no limit is violated. For a given power system network, the objective is to minimize the cost function subject to

$$F = \sum_{i=1}^n f_i(P_g) \quad (2)$$

where:

F = the optimal cost of generation

$f_i(P_g)$ = the fuel cost of the ith generator

n = total number of generators connected in the network. The cost is optimized with the following power system constraint;

$$P_g = P_d + P_l \quad (3)$$

where:

P_d = the total load of the system

P_l = the transmission losses of the system.

The power flow equation of the power network is given by

$$g(|v|, \delta) = \begin{vmatrix} P_i(|v|, \delta) - P_i^{Net} \\ Q_i(|v|, \delta) - Q_i^{Net} \\ P_m(|v|, \delta) - P_m^{Net} \end{vmatrix} = 0 \quad (4)$$

P_i and Q_i are respectively calculated real and reactive powers for PQ bus i; P_i^{Net} and Q_i^{Net} are respectively specified real and reactive powers for PQ bus i; P_m and P_m^{Net} are respectively calculated and specified real power for PV bus m. $|v|$ and δ are voltage magnitude and phase angles of different buses.

2.2 Megawatt-km (Mw-km)

Megawatt-km method requires two power flow calculations, one without the wheeling transaction and another one with the wheeling transaction. The Newton – Raphson technique (formulated in polar form) was used in this work. The first step is to establish the base case for the test systems. The Megawatt-km method requires that two power flow programmes be executed successively, this involves solving the power flow problem without considering any transaction and computing the voltage magnitude, voltage phase angle at each bus and the power flow on each transmission line. The next step is to include any available transaction one at a time. This requires that the generator and load bids be included at the appropriate buses. The Megawatt-km is calculated for every transmission line by multiplying the MW flow on it by its length in km for both power-flow cases. The wheeling cost is thus obtained as;

$$C_T = \left(\frac{EG}{8760} \right) \left(\frac{\sum (\Delta MW - km)}{\sum MW - km} \right) \quad (2)$$

where:

EG = existing transmission cost (fixed)

8760 = number of hours in a year

Three options exist for calculating the impact of the wheeling transaction on the power system network as follows [8].

(a) The negative and positive changes in power flow (Δ MW) on all lines are added together. The wheeling cost is correspondingly small and may have negative value. It might not be economical because of the small or negative value.

(b) The absolute value of changes in powers, $|\Delta \text{ MW}|$ are added to obtain the wheeling costs. This might not be fair because of the high cost.

(c) Negative Δ MW changes are ignored and only positive Δ MW are used in computing the sum of the changes in MW. The option described in (c) was used in this work in order to have an economical and fair wheeling cost.

2.3 The hybrid

The proposed method is a hybrid of the two methods explained above. Considering the fact that a wheeling cost should enable participants (buyers and sellers of electrical energy) to make efficient wheeling decisions based on operating costs, embedded capital, and power security [3].

The revenue collected through srmc method generally falls far short of the cost of transmission reinforcements but accounts for the operating cost. The mw-km on the other hand, consider only the costs of existing transmission facilities, and do not consider changes in production costs as a result of required changes in dispatch and or unit commitment due to the presence of the wheel.

3. TEST RESULTS

A 6-bus system and 24-bus model of Nigerian 330kV power network are used to demonstrate the applications of the proposed method. Four wheeling cost methods were investigated and analysed. The 6-bus network consists of six buses and 11 transmission lines. The one-line diagram is shown in Figure 1. The 24-bus model of Nigerian network is a relatively large system with 24 buses including 7 generators, 23 loads, and 39 lines. The one-line diagram of 24-bus model of Nigerian network is shown in Figure 2.

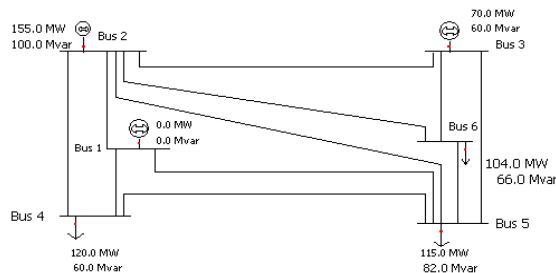


Figure 1: Single-line diagram of 6-Bus Network

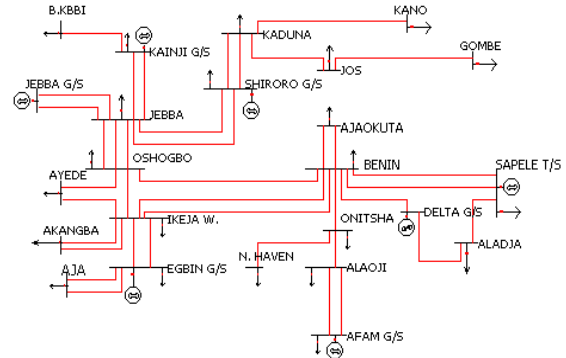


Figure 2: Single-line diagram of 24-bus model of Nigerian 330kv Network

3.1 Wheeling Cost Calculation for 6-Bus Network

Two wheeling transactions were simulated as follows and applied to all the methods;

Transaction T1: 10 MW Wheeled from Bus 2 (Seller) to Bus 6 (Buyer)

Transaction T2: 20 MW Wheeled from Bus 3 (Seller) to Bus 6 (Buyer)

Megawatt – kilometre: In this case, the power-flow analysis of the system was executed without the transaction, this is referred to as the base- case and again the power-flow was solved with the transaction. Tables 1 and 2 show the power flow results with transactions T1 and T2 respectively.

Table 1: Power flow result with transaction T1 on the 6-bus network

Fr om	To	L (km)	Base Case flow (MW)	T1 Branch flow (MW)	MW-km	Δ MW	Δ MW -km
1	2	4.00	19.10	18.80	75.20	-0.30	-1.20
1	4	3.20	56.50	56.50	180.8	0	0
1	5	8.64	47.20	48.20	416.5	1.00	8.64
2	3	5.12	16.20	19.10	97.79	2.90	14.85
2	4	6.40	75.60	76.20	487.7	0.60	3.84
2	5	10.1	32.30	33.50	337.7	1.20	12.10
2	6	13.92	47.40	52.40	729.4	5.00	69.60
3	5	14.40	28.90	28.10	404.6	-0.80	-11.52
3	6	5.60	57.20	60.80	340.5	3.60	20.16
4	5	8.32	5.50	6.10	50.75	0.60	4.99
5	6	6.72	1.90	0.20	1.34	-1.70	-11.42

Srmmc: The OPF was first solved without any transaction, the bus marginal cost and generation dispatched for each generator bus were recorded. The available transaction was included and the OPF was solved again. Tables 3 and 4 show the computation of the SRMC for the 6-bus network.

Table 2: Power flow result with transaction T2 on the 6-bus network

From	To	L (km)	Base Case flow (MW)	T2 Branch flow (MW)	MW-km	ΔMW	ΔMW-km
1	2	4.0	19.10	20.7	82.92	1.63	6.52
1	4	3.2	56.50	57.9	185.4	1.43	4.58
1	5	8.6	47.20	49.7	429.6	2.52	21.77
2	3	5.1	16.20	15	76.80	-1.2	-6.14
2	4	6.4	75.60	75.3	482.1	-0.27	-1.73
2	5	10.1	32.30	33.9	341.2	1.55	15.62
2	6	13.9	47.40	53.8	748.3	6.36	88.53
3	5	14.4	28.90	31.6	455.0	2.7	38.88
3	6	5.6	57.20	53.6	300.2	-3.6	-20.16
4	5	8.3	5.50	6.6	54.83	1.09	9.07
5	6	6.7	1.90	0.8	5.04	-1.15	-7.73

Table 3: Wheeling cost for T1 using SRMC Method on the 6-bus network.

B us	Genera- tion before Transa- ction (MW)	BMC before Transa- ction (₦/MW h)	Genera- tion after Transa- ction (MW)	BMC after Transa- ction (₦/MW h)	P _{i,trans} action (MW)	BMC _i * P _{i,transa} ction (₦/ h)
1	112.5	0.49	117.95	0.96	5.45	5.23
2	159.8	0.52	165.00	1.06	5.17	5.48
3	80.0	0.60	80.00	1.13	0	0
$srmc = \sum_{i=1}^n (BMC_i \times P_{i,transaction})$						10.71

3.2 Wheeling Cost Calculation for 24-bus model of Nigerian 330kv Network

Two wheeling transactions were simulated as follows and applied to all the methods;

Transaction T1: 50 MW Wheeled from KAINJI (Seller) to IKEJA WEST (Buyer)

Transaction T2: 70 MW Wheeled from AFAM (Seller) to NEW-HAVEN (Buyer)

Megawatt – kilometre: Also, the power flow analysis of the system was executed without the transaction, this is referred to as the base- case.

Table 4: Wheeling cost for T2 using SRMC Method on the 6-bus network.

B us	Genera- tion before Transa- ction (MW)	BMC before Transa- ction (₦/MW h)	Genera- tion after Transa- ction (MW)	BMC after Transa- ction (₦/MW h)	P _{i,trans} action (MW)	BMC _i * P _{i,transa} ction (₦/ h)
1	112.5	0.49	128.73	1.19	16.23	19.31
2	159.8	0.52	165.00	1.36	5.17	7.03
3	80.0	0.60	80.00	1.45	0	0
$srmc = \sum_{i=1}^n (BMC_i \times P_{i,transaction})$						26.34

Srmc: Through the use of the OPF, the srmc methodology was implemented as discussed earlier. The srmc of the wheeling transactions was estimated by solving the OPF for both the system with the transaction and the system without the transaction in place. After these solutions were obtained, the srmc was calculated.

4. DISCUSSION & CONCLUSION

4.1 6-Bus Network

Four methods of wheeling cost were investigated on the 6-bus network, postage stamp, contract path, Megawatt-kilometre and short-run marginal cost. Two wheeling transactions were also simulated and the wheeling cost of each transaction calculated using the four methods. The results are given in Table 5.

Table 5: Wheeling cost results for 6-bus network.

Transa- ction	Postage Stamp ₦/hr	Contract Path ₦/hr	Mw- km ₦/hr	SRMC ₦/hr	Proposed Method ₦/hr
T1	33.68	24.93	49.09	10.71	59.80
T2	67.35	17.28	38.01	26.34	64.35

The Megawatt-kilometre method gave the highest wheeling cost for transaction T1 while the postage stamp method gave the highest for transaction T2. The srmc was the least in transaction T1 and contract path the least in transaction T2. These results for the two transactions showed that the wheeling cost does not depend only on the magnitude of power wheeled but also on distance between the source and the sink, power flow in Megawatts and the cost of the transmission facilities.

Based on the proposed methodology in this work, that is the combination of Megawatt-kilometre and srmc (Megawatt-kilometre covers the extent of use of the

network while srmc covers operating cost), the wheeling cost for the two transactions are;

Wheeling Cost for T1 = 49.09 + 10.71 = 59.80 N/h

Wheeling Cost for T2 = 38.01 + 26.34 = 64.35 N/h

The wheeling cost for transaction T1 is quite higher than any of the four but that of transaction T2 is lower than the highest of the four. The result will also help the DISCO at bus 6 to decide which GENCO to enter into a bilateral contract with based on the cost of energy wheeling not considering other factors.

4.2 24-bus model of Nigerian 330kv Network

Two wheeling transactions were also simulated and the wheeling cost of each transaction calculated using the four methods. Table 6 gives the wheeling cost for the two transactions.

Table 6: Wheeling cost results for 24-bus network.

Transaction	Postage Stamp N/hr	Contract Path N/hr	Mw-km N/hr	SRMC N/hr	Proposed Method N/hr
T1	135.84	82.50	277.91	41.50	319.53
T2	190.64	161.00	110.92	57.28	168.59

The Megawatt-kilometre method gave the highest wheeling cost for transaction T1, this is due to the long distance (473km) between KAINJI and IKEJA WEST and the fact that the transaction increased the flow on the lines. The srmc gave the least accounting for the operating cost. For transactions T2, the Postage Stamp was the highest and the Megawatt gave the least, this was because of the short distance (257 km) and that the effect of the transaction on the power flow was negligible compared to that of transaction T1.

The contract path was also high because the power wheeled was the same as the maximum power along the contract path thereby making the ratio to be unity. Again these results, as in the 6-bus network have shown that the wheeling cost does not depend only on the magnitude of power wheeled but also on distance between the source and the sink, power flow in Megawatts and the cost of the transmission facilities. Based on the proposed method in this work, that is the combination of Megawatt-kilometre and srmc the wheeling cost for the two transactions are;

Wheeling Cost for T1 = 277.91 + 41.62 = 319.53 N/hour

Wheeling Cost for T2 = 110.92 + 58.67 = 168.59 N/hour

As obtained in the 6-bus network, the result shows that the wheeling cost from the proposed method for transaction T1 is higher than any of the four methods investigated but that of transaction T2 is lower. The result reflects the impact of distance that is the length of transmission lines in the cost of energy wheeling in any power system network.

The various impacts brought by the deregulation of the power industry led to the unbundling of the services once provided by the vertically integrated electric utilities. As a result, utilities that provide transmission services are separated from other functions in a typical power system. Therefore, accurate wheeling cost is essential for proper investment planning by the utility and the customers so as to maximize overall social welfare. This work investigated four wheeling cost methodologies, postage stamp, contract path, Megawatt-kilometre and short-run marginal cost. The report has been able to propose a viable and economic method of allocating energy wheeling cost to cover cost and provide incentive for investment in new infrastructure as and when necessary. Two of the wheeling cost methodologies, Megawatt-kilometre and short run marginal cost were combined to form a hybrid method of charging for wheeling transactions on power system networks.

5. REFERENCES

- [1] Y.R. Sood, N.P. Padhy and H.O. Gupta: "Wheeling of power under deregulated environment of power system – a bibliographical survey", *IEEE Transactions on Power System*, Vol. 17 No. 3, pp. 870-878, August 2002.
- [2] C. H. L. Lee and L. D. Swift: "Wheeling charge under a deregulated Environment", *IEEE Transactions on Industry Applications*, Vol. 37 No. 1, pp. 178-183, January 2001.
- [3] C.M. Caramanis, R.E. Bohn and F.C. Schweppe: "The cost of wheeling and optimal wheeling rates", *IEEE Transactions on Power Systems*, Vol. 1 No. 1, pp. 63–73, February 1986.
- [4] A.A. El-Keib and X. Ma: "Calculating short-run marginal costs of active and reactive power production", *IEEE Transactions on Power Systems*, Vol. 12 No. 2, pp. 559–565, May 1997.
- [5] D. Shirmohammadi, X.V. Filho, B. Gorenstin and - V.P. Pereira: "Some fundamental technical concepts about cost based transmission pricing", *IEEE Transactions on Power Systems*, Vol. 11 No. 2, pp. 1002–1008, May 1996.
- [6] H.V. Hitzeroth, D. Braisch, G.Herold and D. Povh: "Compensation, stability and losses in the presence of wheeling transactions with the use of FACTS devices", *IEEE Power Tech.99 Conference BPT99*, Budapest, Hungary, paper DPT99-397-12, August 1999.
- [7] T. Yong and R. Lasseter: "Optimal power flow formulation in market of retail wheeling", *IEEE Power Engineering Society, Winter Meeting*, New York, pp. 394-398, Jan. 31-Feb. 4, 1999.
- [8] H.H. Happ: "Cost of Wheeling Methodologies", *IEEE Transactions on Power Systems*, Vol. 9, No. 1, pp. 147-156, February 1994.

ASSESSMENT OF THE HARMONIC ENVIRONMENT OF A POWER STATION'S MV AUXILIARY POWER SYSTEM

M Makhetha*, J Van Coller* and M Manyage **

*University of the Witwatersrand, Faculty of Engineering and the Built Environment, Johannesburg SA.

**Eskom Holdings, Group Technology Division, Enterprise Park, Sunninghill, SA.

Abstract. The paper describes an approach when assessing the harmonic environment of a power station's MV auxiliary power system and includes the harmonic modelling of the harmonic emitting equipment such as VSDs.

Key Words. power stations, harmonic environment, variable speed drives (VSDs)

1. INTRODUCTION

When new power stations are designed or when old power stations are refurbished, greater use is usually made of power electronic equipment such as rectifiers and variable speed drives (VSDs). Depending on the type of power electronic equipment, low order or high order current harmonics are emitted into the power station's auxiliary power system. These harmonics can cause problems with equipment such as cables, transformers and motors as well as with control, protection and communication equipment.

Harmonic standards stipulate harmonic limits for distribution systems at the point of common coupling (PCC) and individual harmonic limits for individual current and voltage harmonic producing equipment. It is known that harmonics emitted from one area of the plant can be the cause of high harmonic levels in another area. Again it is possible to have large harmonic levels in specific areas of an industrial plant, but at the same time an acceptable total harmonic distortion (THD) and total current demand distortion (TDD) at the PCC. [1] Therefore harmonics must be assessed considering not only the effects at the PCC, but the effects at internal sections of the plant.

Previous Eskom power plant designs did not factor in the effects of harmonics and/or harmonic emitting equipment on plant auxiliary power systems. This has led to Eskom's power plants experiencing a number of costly equipment failures or malfunctions linked to or suspected to have been caused by harmonics in the station's auxiliary power systems.

The paper describes an approach when assessing the harmonic environment of a power station MV auxiliary power system and includes the harmonic modelling of the power station auxiliary system with harmonic emitting equipment such as VSDs in Eskom's power stations.

2. BACKGROUND THEORY

2.1 Non-Sinusoidal Load Currents

A load with purely resistive, inductive and capacitive characteristics will draw a sinusoidal current when supplied by a sinusoidal voltage. However, some types of loads and reticulation equipment do not draw a sinusoidal current when supplied by a sinusoidal voltage. A typical example is the three-phase, full-wave rectifier bridge shown on Figure 2.1 typically used in electronic power supplies. The current drawn from the system is used to charge the DC capacitor, and to maintain a constant voltage across this capacitor, current only flows when the diode is forward biased. i.e. when the DC voltage is less than the AC sinusoidal peak voltage. The resulting current waveform is therefore far from sinusoidal.

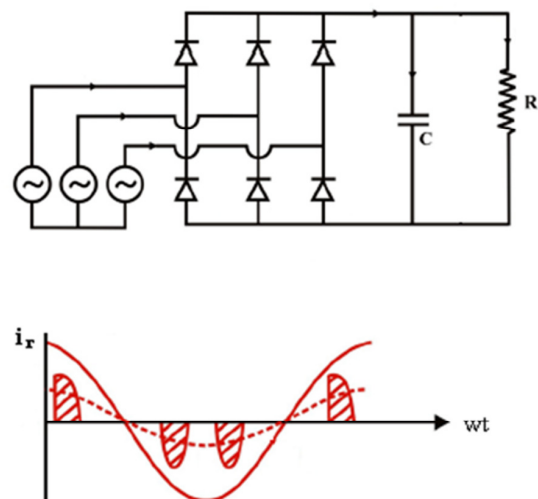


Figure 2.1: A three-phase, full-wave rectifier bridge and its associated current waveform when supplied by a sinusoidal voltage

Loads that draw non-sinusoidal currents when presented with a sinusoidal voltage may be categorised according to their primary cause, i.e.:

- Power electronics: electronic power supplies, light dimmers, variable speed drives, static-var compensators, etc.
- Electric arcs: arc furnaces, welders, electric discharge lamps, etc.
- Magnetic saturation: transformers, reactors, motor, etc.

Such loads are sometimes referred to as “non-linear” or “distorting” loads. [2]

2.2 Impact on the Voltage Quality

The non-sinusoidal currents drawn by a specific section of the plant, flow through the impedance of the supply network. The resulting voltage drop across this impedance will result in distortion of the voltage at other points in the supply network. In particular, the voltage distortion that arises at the point of common coupling (PCC) due to the non-sinusoidal currents drawn by one part of the plant will be seen by other parts of the plant connected to the network at this point.

2.3 Harmonic Measurement and Assessment

In order to describe the levels of voltage or current distortion in the network, a method based on the Fourier transform is used. [3] The Fourier transform decomposes a distorted waveform into sinusoidal harmonic components at various frequencies. The quality of the distorted waveform is therefore described by the magnitude of the harmonic components present. The power frequency in a power system e.g. 50 Hz/60 Hz has specific implications for applying Fourier analysis to power system studies. These aspects are described in detail below, as it is important to apply these correctly when undertaking harmonic measurements.

The term “harmonic” originates from acoustics, where it refers to the vibration of a string at a frequency that is a multiple of the basic (fundamental) frequency. In the case of electrical power systems, a harmonic is defined as a sinusoidal waveform component with a frequency (Hz) given by:

$$f_h = h \cdot f_o$$

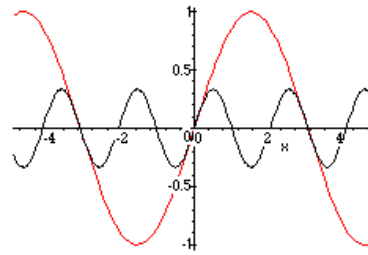
Where:

f_o = Power frequency of the power system

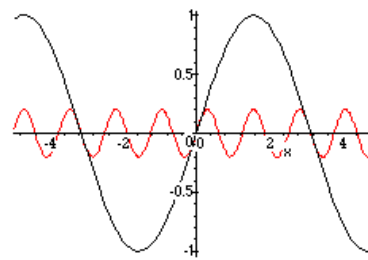
h = an integer called the harmonic order

In the case of a 50 Hz power system, a 250 Hz component in the waveform will therefore be termed the 5th harmonic (as h is equal to five). Figure 2.2

shows the power frequency sinusoid together with its third and fifth harmonic components respectively.



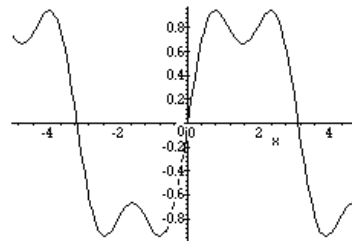
(a)



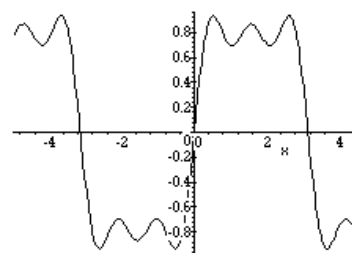
(b)

Figure 2.2: The fundamental sinusoid with its: (a) third harmonic and (b) fifth harmonic components.

According to Fourier theory, any stationary, periodic waveform can be obtained by the superposition of individual sinusoidal waveforms of given magnitude and phase angle. This process is illustrated in Figure 2.3, using waveforms in Figure 2.2.



(a)



(b)

Figure 2.3: Superposition of the fundamental sinusoid and its (a) third harmonic component only, (b) third and fifth harmonic components.

2.3.1 Fourier Transform Equations

Most frequency domain harmonic analysis algorithms are based either on the Discrete Fourier Transform (DFT) or Fast Fourier Transform (FFT) to obtain the voltage and current frequency spectra from discrete time samples.

A waveform $f(t)$ of period T angular frequency

$\omega = \frac{2\pi}{T}$, is expanded according to Fourier theory by

$$F(t) = \frac{a_0}{2} + \sum_{n=1}^{\infty} (a_n \cos n\omega t + b_n \sin n\omega t)$$

$$F(t) = \frac{a_0}{2} + \sum_{n=1}^{\infty} C_n \sin(n\omega t + \phi_n)$$

where:

$$b_n = \frac{2}{T} \int_0^T F(t) \sin n\omega t dt$$

$$a_n = \frac{2}{T} \int_0^T F(t) \cos n\omega t dt$$

$$\phi_n = \tan^{-1} \left(\frac{a_n}{b_n} \right)$$

In a power system, the DC component (a_0) is generally zero. The management of harmonic distortion therefore centres around limiting the magnitudes of the individual frequency components C_n .

2.3.2 Transducers and Harmonic Measurements

The measurement of power system harmonics requires some form of transducer to connect the instrument terminals to the circuit where the voltage or current must be measured, e.g. MV, HV or EHV busbar. Existing transducers are generally not designed with these measurements in mind and may be severely limited by their frequency response. Typical transducer bandwidths are shown below in Table 2.2. [4]

Transducer	Maximum frequency response
Magnetic voltage transformer (VT)	2.5 kHz
Capacitive voltage transformer (CVT)	Only accurate at 50 Hz
Current transformer (CT)	10 to 20 kHz
Resistive divider (laboratory standard)	1 MHz
Capacitive bushing divider (Note 1)	200 kHz

Table 2.1: Typical transducer bandwidths

Transformer tertiary windings are not an accurate means of measuring harmonics, as these reflect harmonic distortion levels on both the primary and secondary circuits of the transformer.

The following should be specifically taken into consideration when undertaking harmonic measurements:

- The burden on a transducer can affect the high frequency response, i.e. the response is reduced for heavy loading in the case of ferromagnetic transformers. In the case of CVT's, damping may assist in reducing the resonances introduced by the transducer.
- Other loads on the transducer e.g. measurement instruments or relays may generate harmonics, i.e. resulting in erroneous measurements.

2.4 Harmonic Indices

The most common harmonic index, which relates to the voltage waveform, is the total harmonic distortion (THD), which is defined as the root mean square (r.m.s) of the harmonics expressed as a percentage of the fundamental component, i.e.

$$THD = \frac{\sqrt{\sum_{n=2}^N V_n^2}}{V_1}$$

Where V_n is the single frequency r.m.s voltage at harmonic n , N is the maximum harmonic order to be considered and V_1 is the fundamental line to neutral r.m.s voltage.

Current distortion levels can also be characterised by a THD value but it can be misleading when the fundamental load current is low. A high THD value for input current may not be of significant concern if the load is light, since the magnitude of the harmonic current is low, even though its relative distortion to the fundamental frequency is high. To avoid such ambiguity a total demand distortion (TDD) factor is used instead, defined as;

$$TDD = \frac{\sqrt{\sum_{n=2}^N I_n^2}}{I_R}$$

2.5 Effects of Harmonic Distortion

Once the harmonic sources are clearly defined, they must be interpreted in terms of their effects on the rest of the system. Each element of the power system must be examined for its sensitivity to harmonics as a basis for recommendations on the allowable levels. The main effects of voltage and current harmonics within the power system are:

Possible amplification of harmonic levels resulting from series and parallel resonance

A reduction in the efficiency of the generation, transmission and utilisation of electric energy

Ageing of the insulation of electrical plant components with consequent shortening of their useful life

Malfunctioning of system or plant components

Among the possible external effects of harmonics are a degradation in communication system performance, excessive audible noise and harmonic induced voltage and currents.

2.5.1 Resonance

The presence of capacitors, such as those used in power factor correction, can result in local system resonances, which lead in turn to excessive currents and possibly subsequent damage to capacitors [5]

2.5.1.1 Parallel Resonance

Parallel resonance results in a high impedance at the resonant frequency being presented to the harmonic source. Since the majority of harmonic sources can be considered as current sources, this results in increased harmonic voltages and high harmonic currents in each leg of the parallel impedance.

Parallel resonances can occur in a variety of ways, the simplest being that where a capacitor is connected to the same busbar as the harmonic source. A parallel resonance can then occur between the system impedance and the capacitor. Assuming the system impedance to be entirely inductive, the resonant frequency is

$$f_p = f \sqrt{\left(\frac{S_s}{S_c} \right)}$$

Where f is the fundamental frequency (Hz), f_p is the parallel frequency (Hz), S_s is the short-circuit rating (Var) and S_c is the capacitor rating (Var).

2.5.1.2 Series Resonance

Series resonance is a typical problem with power factor correction installations, where harmonics associated with the distorted utility supply voltage flow from the utility HV busbar through a low impedance resonant circuit formed by the capacitor and the supply transformer. This can give rise to significant amplification of the harmonic source voltage. Load damping will have the effect of limiting the magnitude of the amplified voltage across the capacitor. [2]

3. POWER STATION RETICULATION MODEL AND HARMONIC SIMULATIONS

PowerFactory by DigSilent, a simulation tool for the analysis of transmission, distribution, and industrial electrical power systems was used to model and simulate plant conditions. In order to verify power station models, Kendal power station with known sources of harmonics was modelled and simulated to test simulation results against measured results and calculated results. When conducting harmonic measurements on MV reticulation system, it was detected that almost all harmonics emitted into the station's MV system were produced by the boiler feed pump drives, hence the focus of the paper is on harmonics emitted by MV drives.

Kendal power station is the largest power station in the country with installed generating capacity of 4 116 MW. The station has six 686 MW units, each equipped with three 8 300 MW, 6 000 rpm boiler feed pumps fed from load commutated inverters (LCIs). The basic configuration of the Kendal's boiler feed pump system is shown in the Figure 3.1.

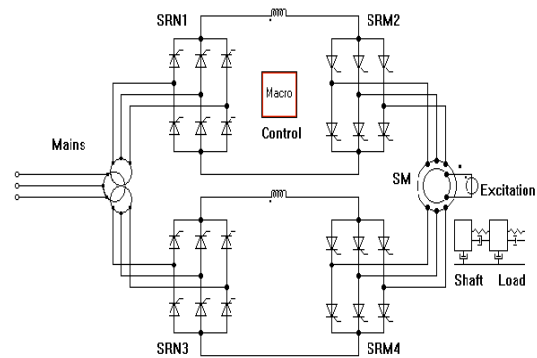


Figure 3.1: Kendal's 12-pulse boiler feed pump LCI feeding a synchronous motor

The 12-pulse line side rectifier is supplied with a three winding transformer (vector group Dd0y1) in order to eliminate the 5th and the 7th harmonics in the supply line current.

The 12-pulse machine-side inverter supplies the two three-phase stator windings of the high speed synchronous motor. This converter is load commutated and operates at variable voltage and frequency which depends on the motor speed.

The inductances in the d.c. circuits decouple both converters and smooth the d.c. current.

The two stator windings are displaced by 30° in order to eliminate the 5th and the 7th harmonics in the resultant air gap field and consequently the 6th rotor current harmonics as well as the pulsating-torque component of the 6th order.

The excitation system of the synchronous motor is supplied from a rotating field exciter combined with a rotating diode rectifier.

The control and protection devices are represented as a macro in Figure 3.1. [6]

3.1 Harmonic Measurements

Harmonic measurements were done using a Power Guide 4400 by Dranetz-BMI. Measurements conducted on Kendal's Unit 2 11kV boards had a similar harmonic spectrum to that of the harmonic spectrum measured on individual Unit 2 running boiler feed pump drives line, indicating that almost all harmonics on the 11kV reticulation system were generated by the boiler feed pump drives. The spectrum was again in line with the expected current spectrum of a 12 pulse rectifier given by a series containing mainly harmonics of order $12k \pm 1$.

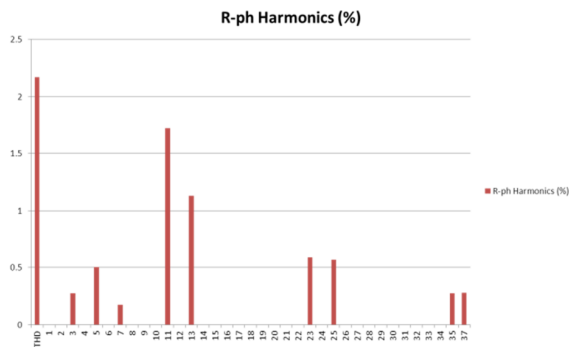


Figure 3.1.1: Red phase harmonic spectrum of Kendal's Unit 2 11kV board

3.2 Harmonic Simulations

Kendal power station's Unit 2 from the 400kV generator transformer terminals down to the 400V boards and auxiliary plant reticulation were modelled and simulated using the Power Factory program. The point of common coupling was considered as the Unit 2 11kV board and all measurements were made with reference to this board.

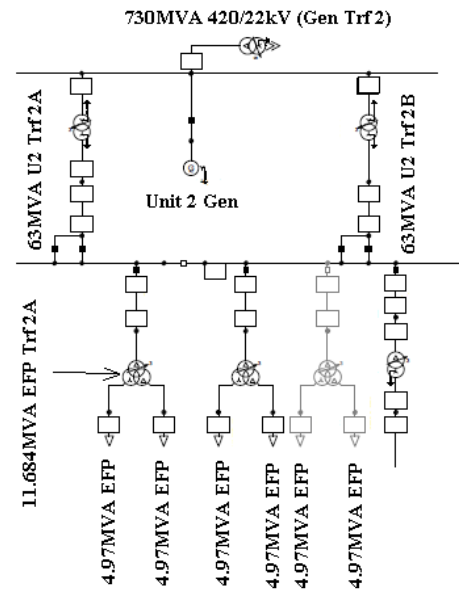


Figure 3.2.1: Part of Kendal Power Station's Unit 2 DigSilent Model

The correct modelling of synchronous generator is very important in all kinds of electrical power systems studies – especially for harmonic analysis. Kendal generators models had to be modelled with sub-transient, transient and synchronous parameters in order to conduct a harmonic study.

3.2.1 Frequency Sweep

In order to translate the injected harmonic currents into harmonic voltages, one needs to know the harmonic impedance of the system. DigSilent was used to perform a frequency sweep on the network and calculate the impedance at the 11kV board at different frequencies and results are displayed in Figure 3.2.1.1, showing possible harmonic parallel resonance at the 125th harmonic and series resonance at the 90th harmonic. Possible harmonic parallel and series resonance at Kendal's 11kV board does not pose a problem as there are no significant high order harmonics and again because the 125th and 90th harmonics do not fall within the series containing harmonics of order $12k \pm 1$.

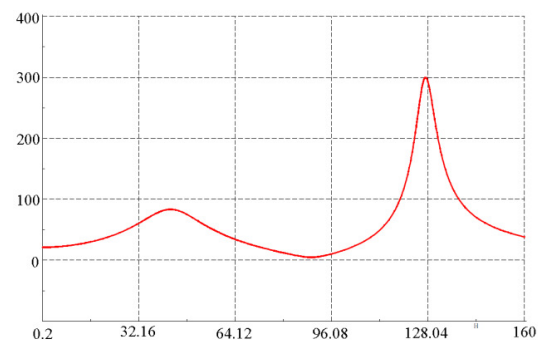


Figure 3.2.1: Unit 2 frequency sweep results

4. COMPARISON WITH OTHER INDUSTRIES

4.1 Effects of Power Factor correction Capacitors

Power Factor correction is applied to electric circuits as a means of minimising the inductive component of the current and thereby reducing the losses in the supply. The introduction of power factor correction capacitors is a widely recognised method of reducing an electrical load, thus minimising wasted energy and hence improving the efficiency of a plant and reducing the electricity bill.

A 4MVAR power factor correction capacitor was simulated on the Unit 2, 11kV board A to improve the power factor from 0.87 to 0.94 as shown on Figure 4.1.1.

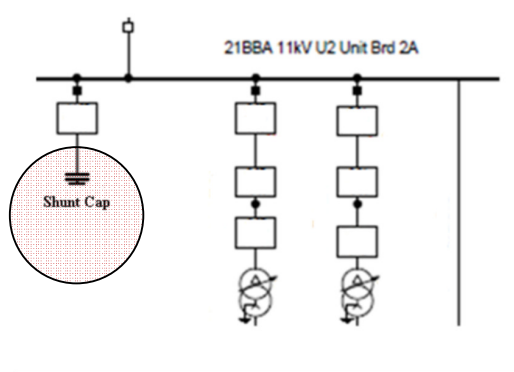
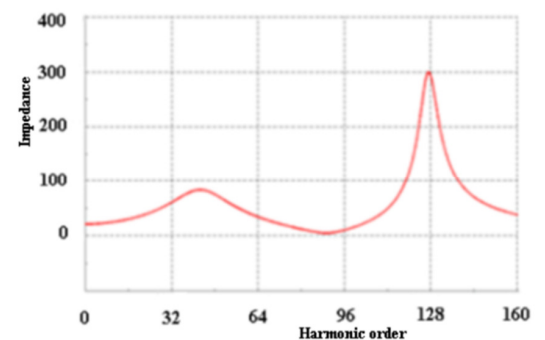
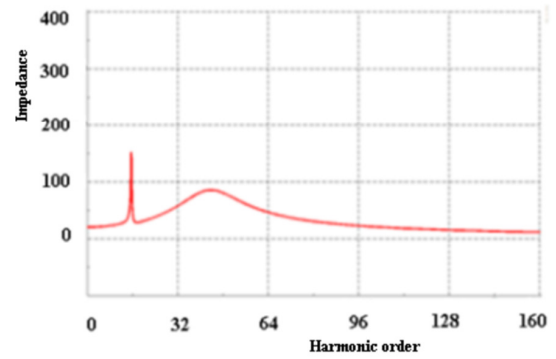


Figure 4.1.1: Power factor correction capacitor on Unit 2, 11kV board A

Results shown below in Figure 4.1.2 reveal a shift in expected or possible parallel resonance from the 120th harmonic to the 11th harmonic. This is of major concern as the 11th harmonic falls within the $12k \pm 1$ series presented by 12-pulse systems and having a significantly high harmonic component of about 1.7%.



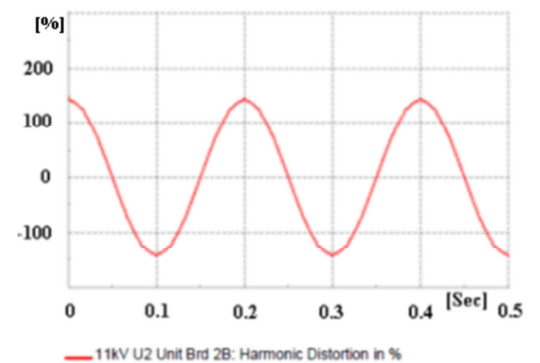
(a)



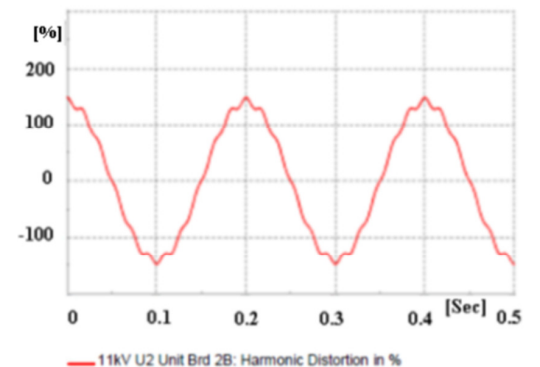
(b)

Figure 4.1.2: Frequency sweep results (a) Unit 2 11kV board without power factor correction capacitors, (b) with 4MVAR power factor correction capacitors

As explained in the background theory under parallel resonance, it was expected to have amplified voltage distortions due to parallel resonance at the 11th harmonic. This was verified by simulation results in Figure 4.1.3 below.



(a)



(b)

Figure 4.1.3: Voltage waveform at (a) Unit 2 11kV board without power factor correction capacitors, (b) with 4MVAR power factor correction capacitors

4.2 Effect of Long Cables

Lengths of cables supplying Kendal power station Unit 2 EFPs were increased from 11m to 2000m, in order to evaluate the effects of cable lengths on harmonics, this was done to compare the power station environment with other industries such as the mining industry which has long cables.

Simulation results revealed a shift in parallel resonance from 125th harmonic down to 75th harmonic as the EFP cable lengths were increased from 11m (Kendal's EFP cable lengths) to 2000m (typical lengths found in mines). The 125th harmonic parallel resonance does not pose any problem as there are no significant high order harmonics but results shows that further increment in cable length can result in possible parallel resonance being dropped down to frequencies with significant level of harmonics resulting in amplified voltage distortions or harmonics.

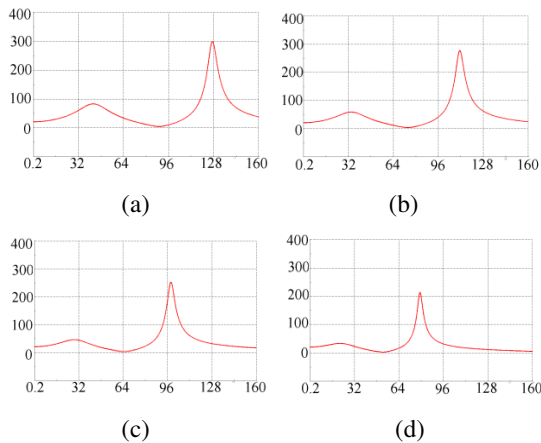


Figure 4.2.1: Frequency sweep results (a) U2 11kV board EFP supply cables on 11m, (b) EFP supply cables of 500m, (c) EFP supply cables of 1000m and (d) EFP supply cables of 2000m

5. CONCLUSIONS AND RECOMMENDATIONS

Power plants present an environment that is different from most industries i.e. short cables, being close to generators and hence high short circuit currents and without the need to correct power factors. These unique features also affect the manner in which harmonics propagate into their LV reticulation system.

Simulation results obtained in this paper under both Section 4.1 and 4.2 clearly shows that Kendal power station's configuration does not favour/support amplification of harmonics as compared to other industries with similar loads. This, supported by Eskom's MV drive philosophy of only installing drives with 12-pulse and higher, has aided in maintaining the harmonic environment of Kendal power station at values far below recommended/acceptable levels.

Future work on the subject should include the followings:

Similar study on a different power station to confirm whether a similar pattern of results can be achieved

Evaluation of the impact on the harmonic environment in power plants due to increased utilisation of VSDs in Eskom's power stations

Due to high transmission demand, the prospects of having HVDC converters close to power stations are high. Their impact on power station harmonic levels should be evaluated.

6. REFERENCES

- [1] R Feuntes and J Quezada, "Relevant Aspect for Harmonic Evaluation of Industrial Plant: a Scope from Real Cases"
- [2] R Koch, L Pittorino and G Botha, "Eskom power quality chapter 10, Harmonics, Interharmonic and Harmonic Filters".
- [3] J. Arrillaga, D.A. Bradley and P.S. Dodger, Power system harmonics, Edition 1, Chichester, UK, John Wiley and Sons, 1985.
- [4] R.G. Koch, 'The broadband modelling of electromagnetic voltage transformers using parameter estimation techniques', University of Stellenbosch, 1992.
- [5] N.W Ross, "Harmonic and ripple control carrier series resonance with P.F correction capacitors"
- [6] J. Arrillaga and N.R. Watson, Power system harmonics, Second Edition, Chichester, UK, John Wiley and Sons

7. ACKNOWLEDGEMENTS

I will like to thank the support of the Eskom Power Plant Engineering Institute (EPPEI), in particular for the financial assistance in making the project possible.

COMPARISON OF EVOLUTIONARY OPTIMIZATION TECHNIQUES ON ECONOMIC LOAD DISPATCH WITH TRANSMISSION LINE CONSTRAINTS

A Goudarzi* and AK Saha*

University of KwaZulu-Natal, School of Engineering, Durban, South Africa
Email:* 213570461@stu.ukzn.ac.za

Abstract. This paper presents an efficient and reliable comparison on two evolutionary techniques; genetic algorithm (GA) and particle swarm optimization (PSO) to find optimal solution for economic load dispatch (ELD) problem due to high attention of power industry and electricity market regulations on this issue. The problem handles two objective functions, namely total generation cost and power loss with considering the transmission line constraints. A simple Lagrangian multiplier method was applied to solve ELD by initializing, lambda as incremental cost rate. A binary GA method was utilized to find desired objective functions, and finally the PSO was formulated through a simplified social system to compare with other methods in terms of solution accuracy and computation time among the process of optimization. In order to obtain the comparison results and validate the aims of study, all the proposed methods are tested on a 26-bus test system, where the results testify robustness and effectiveness of GA in comparison with the other methods to find an optimal solution.

Key Words: ELD, GA, PSO, stochastic optimization process, evolutionary technique.

1. INTRODUCTION

In past few decades, optimal scheduling of power generation units through bulk interconnected power systems is getting more complicated due to emerging new topics into power sector such as changing of power industry policies and deregulation of power markets. In this regard, power system operators and planners are still looking for an efficient method to economically dispatch the power generation units in the system to meet the electricity demand and satisfy some of the most important power system constraints like equality, inequality and transmission line losses[1-2].

Several numbers of deterministic methods such as lambda-iteration, gradient method, quadratic programming (QP) and dynamic programming (DP) were applied previously to find an optimistic ELD solution. Deterministic methods are facing difficulty in finding local minimum because of some nonlinearity characteristics of generation units (ramp rate limits, prohibited zones and non-convex cost functions) in large-scale power systems [3]. Recently, several natural inspired stochastic methods like as tabu search (TS) [4], ant colony [5], simulated annealing (SA) [6], GA [7] and PSO [8] were developed, and shown to be more efficient and powerful in comparison to classical approaches in dealing and solving current issues in ELD with considerable reduction in total generation cost and transmission power losses.

Already, quite numbers of researches have been done in this area with different system considerations and analytical methods. In [9], Ongsakul et al. study introduced a well-established parallel tabu search algorithm to solve constrained economic dispatch problem through large-scale power system with ability to handle generating units with behavior of monotonically and non-monotonically increasing incremental cost function. Rahmat et al. [10] adopted two different optimization techniques (ant colony optimization (ACO) and differential evolution

method) together to crack the barriers to find the optimal scheduling of tested IEEE Reliability Test System (RTS), where the results shows proposed algorithm of the study is capable to acquire desired solution. In [6], authors combined and employed two evolutionary algorithm: system annealing (SA) method and GA; attempting to overcome the complexity of system constraints (equality and inequality). To ensure the feasibility of the proposed methodology, it was applied to 13 generators test system where results showed the practicability of idea. A fuzzy mutated evolutionary programming was developed for solving the combined emission economic dispatch in [11].

In this paper, two evolutionary techniques (GA and PSO) are utilized to solve ELD problem and determine the optimal scheduling of generators in order to reduce the total fuel cost and power loss. Thereafter, the proposed approaches of study are compared to ELD classical approach to validate accuracy and effectiveness of GA and PSO to find the optimum solution. The organization of this study is as follows: section 2 demonstrates the statement of methods. Section 3 provides a brief introduction to case study as well as the single line diagram of the test system, where the simulation results are discussed in the section 4. Subsequently, conclusion is given in the section 5.

2. STATEMENT OF METHODS

a. Economic Load Dispatch (ELD)

The main elements which have direct impact on generating power at minimum cost are operating efficiencies of generating units, fuel cost, and transmission line losses. The most effectual generating unit in the system does not warranty to reduce and minimize the total cost as it may be placed far away from the load point which is caused to have more transmission losses; also it is possible that the fuel cost can be high based on the geographical location of unit [12]. The aim of

economic dispatch problem is to minimize the total cost and meet the load demand of system simultaneously by determining the optimal amount of sharing between generating units. Therefore, the objective of ELD can be expressed as a minimization process:

$$\text{Min} \sum_{i=1}^{n_g} F_i(P_i) \quad (1)$$

$$F_i = \sum_{i=1}^{n_g} \alpha_i + \beta_i P_i + \gamma_i P_i^2 \quad (2)$$

Subject to equality constraint of power balance as:

$$\sum_{i=1}^{n_g} P_i = P_D + P_L \quad (3)$$

To have stable operation, all generating units are constrained to operate in lower and upper limits; accordingly the inequality constraint can be described as follows:

$$P_{i \min} \leq P_i \leq P_{i \max} \quad (4)$$

where:

$F_i(P_i)$: the fuel cost function of the i_{th} unit

P_i : power generated by the i_{th} unit

n_g : total number of dispatchable generating units

α_i , β_i and γ_i : the cost coefficients of i_{th} unit

P_D : total load demand

P_L : transmission power loss

$P_{i \min}$: minimum power output of i_{th} generating unit

$P_{i \max}$: maximum power output of i_{th} generating unit

The transmission line power loss has a major effect in ELD, especially when the generated power is transmitted over long distances of a bulk interconnected power network. Therefore, a general formula of transmission loss can be given as follows:

$$P_L = \sum_{i=1}^{n_g} \sum_{j=1}^{n_g} P_i B_{ij} P_j + \sum_{i=1}^{n_g} B_{0i} P_i + B_{00} \quad (5)$$

where:

B_{ij} : ij th element of the loss coefficient square matrix

B_{0i} : i th element of the loss coefficient vector

B_{00} : loss coefficient constant

B-coefficients can be estimated by Korn method through power flow solution, thus values of loss coefficients of square matrix, vector and constant can be found respectively by using the following equations [13]:

$$B_{ij} = \frac{r_{ij}}{V_i V_j} \sin(\delta_i - \delta_j) \quad (6)$$

$$\begin{bmatrix} \frac{Y_1}{\lambda} + B_{11} & B_{12} & \dots & B_{1N} \\ B_{21} & \frac{Y_2}{\lambda} + B_{22} & \dots & B_{2N} \\ \dots & \dots & \dots & \dots \\ B_{N1} & B_{N2} & \dots & \frac{Y_N}{\lambda} + B_{NN} \end{bmatrix} \begin{bmatrix} P_1 \\ P_2 \\ \dots \\ P_N \end{bmatrix} = \frac{1}{2} \begin{bmatrix} 1 - B_{01} - \frac{B_1}{\lambda} \\ 1 - B_{02} - \frac{B_2}{\lambda} \\ \dots \\ 1 - B_{0N} - \frac{B_N}{\lambda} \end{bmatrix} \quad (7)$$

where

r_{ij} : ij th element of Z_{bus}

V_i, V_j : voltages of i and j buses respectively

δ_i, δ_j : angles of i and j buses respectively

λ : incremental power cost

The process of ELD with determining B-coefficients and considering transmission line losses is provided in Figure 1.

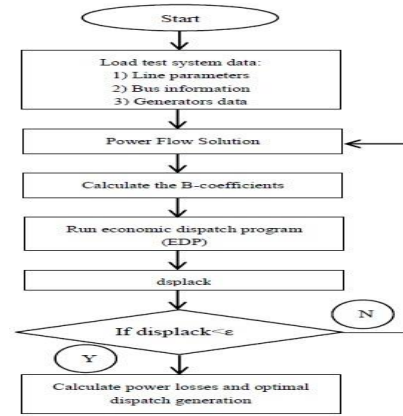


Figure 1: flow chart of proposed ELD Method

b. Genetic Algorithm (GA)

In the early of seventies, for the first time GA theory introduced by John Holland, and nowadays it is becoming one of a significant optimization tools in machine learning based on mechanics of nature and natural genetics which belongs to evolutionary techniques category [14-15]. In GA, the mechanism of biological and genetics selection are simulated artificially to obtain the optimal solution through combine evaluation of chromosomes as randomized inputs, and optimization process goes on by moving from an old population of individuals to new population. Genetic algorithms are considered as well-known optimizations techniques because of their restrictions on the solution space are not made during the process [16].

GA includes of a string representation of nodes in the search space, therefore the application of genetic operators is to generate new search nodes, in order to evaluate the search nodes a fitness function adopted with a probabilistic role to control the genetic operators. General fitness function of GA for ELD problem can be expressed as follows [22]:

$$F = \frac{1}{1 + K \left(\frac{\epsilon}{P_D} \right)} \quad (8)$$

subject to:

$$\varepsilon = \sum_{i=1}^{n_g} P_i - P_D - P_L \quad (9)$$

Where:

K : scaling constant

ε : power balance equation

GA has three main stream processes:

1. Initialization: create a random initial population.
2. Evaluation: evaluation of the fitness values of each nodes through the fitness function.
3. Genetic operation: operation process by itself can be divided into four sub-streams:
 - I. Mating: construction of a new string by connecting sub-strings.
 - II. Crossover: combines two individuals, or parents, to form a new individual or child, for the next generation. Crossover process can be simplified as [17]:

$$C_i^{gen+1} = a.C_i^{gen} + (1-a).C_j^{gen} \quad (10)$$

$$C_j^{gen+1} = (1-a).C_i^{gen} + a.C_j^{gen} \quad (11)$$
 - III. Mutation: generate a few random changes in the individuals thru the population, which provide generic diversity.
 - IV. Reproduction: reproduction options determine how the genetic algorithm creates children at each new generation.

Eventually, the process of GA according to all above mentioned steps can be simplified in Figure 2.

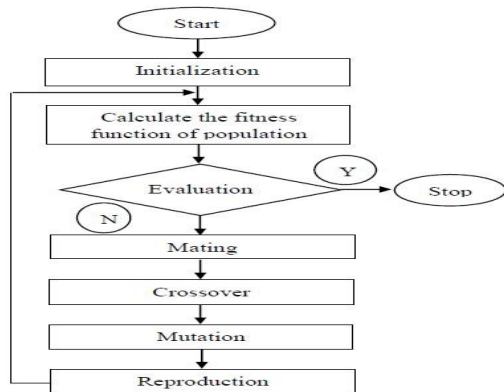


Figure 2: flow chart of GA method

c. Particle Swarm Optimization (PSO)

PSO is one of the algorithms based on swarm intelligence method, which was introduced for the first time by Kennedy and Eberhart in nineties [18]. PSO is emulated based on social behavior of animal groups like fish schooling or ant's colonies, whereas

it is a probabilistic, population-based evolutionary technique for problem solving. Like as other evolutionary techniques, PSO algorithm initialize by generating a population of individuals as “particles” randomly which evolve or change their positions among the time, and as it time goes on based on the experiences and neighboring of each particles, they modifies their position during the process of optimization by remembering the best position visited by themselves [19]. The behavior of this process can be simulated as a birds flock, each bird which is called ‘particle’ in population that is called ‘swarm’ is considered to fly over a long distance which is called ‘search space’ and looking for food among the suitable areas. To have an optimum searching process, such areas contain lower function values than the others previously visited. In this regard, each particle is treated as an index or point in the search space to fly towards the food (optimization target) based on its own best flying experience and the other particles [20]. PSO like as other evolutionarily algorithms have a fitness function that allocates the agent’s position into a fitness value. The position that has a lowest value in the whole iteration is called the global best (G_{best}), and the lowest fitness value would tracks by each agent is called local best (P_{best}). Therefore, the general formula for particle swarm optimization algorithm can be simplified as [21]:

$$v_i^{k+1} = \mu v_i^k + c_1 r_1 (pbest_i - x_i^k) + c_2 r_2 (gbest_i - x_i^k) \quad (12)$$

subject to:

$$x_i^{k+1} = x_i^k + v_i^{k+1} \quad (13)$$

$$\mu(i) = \mu_{max} - \left(\frac{\mu_{max} - \mu_{min}}{Max.Iter.} \right) * i \quad (14)$$

where:

c_1, c_2 : positive constants

r_1, r_2 : randomly generated numbers within [0,1]

μ : inertia weight

i : iteration index

x_i^k : position of individual i until iteration k

$pbest$: the best particle position based on its own experience

$gbest$: the best particle position based on overall swarm experience

In comparison with other optimization techniques PSO has some unique features such as:

- It is derivative-free algorithm unlike many conventional techniques which required gradient information for the starting point.
- It is flexible to be integrated with other evolutionary algorithm.
- Has less sensitivity with nature of objective function.
- It is easy to implement and coding with computer software.
- It has ability to escape local minima.

Figure 3 is described the algorithm of PSO based on simplified social system.

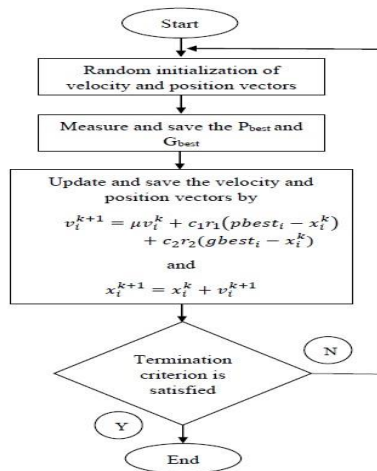


Figure 3: flow chart of PSO method

3. CASE STUDY

Results are obtained from 26-bus test system with six generating units with total load of 1263 MW[12]. Moreover, to have a precise investigation of all proposed methods, study considered four different load point (1263, 1303, 1343 and 1383 MW) with respect to capability of test system in case of load variation. In this study, the effect of transmission lines are considered and exact amount of power loss is determined after each single run. The generators cost coefficients and power limits are given in Table1, also the B-coefficients for the starting load point (1263 MW) are computed as follows.

Table 1: generators cost coefficients and power limits

Data	Q-Cost	P-Cost	F-Cost	Pmin	Pmax
Gen1	0.007	7	240	100	500
Gen2	0.0095	10	200	50	200
Gen3	0.009	8.5	220	80	300
Gen4	0.009	11	200	50	150
Gen5	0.008	10.5	220	50	200
Gen6	0.0075	12	190	50	120

B=

0.0017	0.0011	0.0006	-0.0001	-0.0007	-0.0002
0.0011	0.0013	0.0009	0.0006	-0.0005	-0.0001
0.0066	0.0009	0.0030	0.0001	-0.0010	-0.0005
-0.001	0.00006	0.00001	0.0024	-0.0005	-0.0007
-0.00054	-0.0005	-0.0010	-0.0005	0.0128	-0.0001
-0.0002	-0.0001	-0.0005	-0.0007	-0.0001	0.0149

4. SIMULATION RESULTS

To meet objectives of the study, all simulation cases were tested and analyzed on 26-bus test system. In addition, because of the probabilistic nature of the evolutionary techniques, study performed 100 single trials to observe the evolutionary optimization trend and compare their accuracy, convergence behavior and computation adequacy. One of the noticeable features of this study in comparison with other works which have been done in this area is, in order to satisfy transmission line constraints study considered

different B-coefficients values based on different load points during the optimization process of all cases until it reaches the convergence criteria. All the simulation cases were written in Matlab R2010a and executed on a personal computer with following specification: Intel® Core™ i5-3210M (3.1 GHz), 6.00 GB RAM (DDR3) and windows 8 operating system. Since all the evolutionary techniques are sensitive to the tuning of some parameters and weights, according to best knowledge of authors and many other studies, the following parameters are used for GA and PSO [22-23].

GA parameters are chosen as:

- Population size: 100, 1,000 and 10,000
- Generation size: 100
- Crossover probability: 0.8
- Mutation probability : 0.1
- Time limit: 200

PSO parameters are chosen as:

- Population size: 100, 1,000 and 10,000 particles
- Maximum number of iterations: 1,000
- C_1 and C_2 : 2
- Inertia weight : Min= 0.4 and Max= 0.9

The results are classified in four tables according to different load points and number of population size for each evolutionary technique. To have more accurate and efficient investigation through the comparison cases, study computed mean of total generation cost and power loss as well as their standard deviation among the probabilistic optimization process. The best and worst optimization results among all the simulation cases are shown in Figure 4 which helps to magnify the differences between analyzed methods. Table 2 Shows comparison cases for 1263 MW load demand, where Table 3, 4 and 5 shows the comparison cases for 1303, 1343 and 1383 MW, respectively. As it can be seen from Table 2 GA is more accurate and optimistic in comparison to PSO with respect to three population size, where amount of reduction in mean of total generation cost and mean of power loss is not really considerable through to the different population size for GA method, while by increasing the population size in PSO amount of reduction is absolutely noticeable. In case of deviation of values during 100 trials, it is observable that GA is steadier compared to PSO. This is because standard deviation of values (Mean cost and power loss) in GA is declining gradually while, in PSO, standard deviation is dramatically reduced when population size has been increased. One of the most notable aspects and issues in this comparison is computation time of optimization process, which is observable that PSO is thoroughly quicker than GA. All above mentioned analyses between GA and PSO is expandable to other simulation cases which are shown in Table 3, 4 and 5 with respect to value of their differences in total generation cost, power loss, standard deviation of values and elapsed time.

Table 2: comparison of simulation cases (1263MW)

1263 MW	ELD	GA			PSO		
No. of Run	1	100	1000	10000	100	1000	10000
Mean Cost	15447.72	15377.9752	15377.7378	15377.7322	15449.25	15411.17	15393.52
STD of Cost	0	0.18036112	0.00710594	0.00006197	164.2756	12.50721	0.936471
Mean P_{loss}	12.807	12.808854	12.80189	12.800934	12.89597	12.73188	12.37121
STD of P_{loss}	0	0.04767812	0.00705891	0.00068202	0.448424	0.391857	0.083376
Elapsed time	0.162923	1.560653	6.929873	57.136997	0.183078	0.867733	7.746028

Table 3: comparison of simulation cases (1303MW)

1303 MW	ELD	GA			PSO		
No. of Run	1	100	1000	10000	100	1000	10000
Mean Cost	15997.69	15927.9203	15927.7073	15927.7019	16018.56	15943.33	15929.42
STD of Cost	0	0.15016402	0.0035184	0.00010461	380.5635	9.572916	1.046884
Mean P_{loss}	14.0102	14.0051	14.003854	14.000726	14.07953	13.7496	13.53584
STD of P_{loss}	0	0.04399162	0.00711888	0.00071884	0.469105	0.347374	0.082595
Elapsed time	0.176584	2.042193	6.949571	57.811332	0.196558	0.867733	8.245335

Table 4: comparison of simulation cases (1343MW)

1303 MW	ELD	GA			PSO		
No. of Run	1	100	1000	10000	100	1000	10000
Mean Cost	15997.69	15927.9203	15927.7073	15927.7019	16018.56	15943.33	15929.42
STD of Cost	0	0.15016402	0.0035184	0.00010461	380.5635	9.572916	1.046884
Mean P_{loss}	14.0102	14.0051	14.003854	14.000726	14.07953	13.7496	13.53584
STD of P_{loss}	0	0.04399162	0.00711888	0.00071884	0.469105	0.347374	0.082595
Elapsed time	0.176584	2.042193	6.949571	57.811332	0.196558	0.867733	8.245335

Table 5: comparison of simulation cases (1383 MW)

1383 MW	ELD	GA			PSO		
No. of Run	1	100	1000	10000	100	1000	10000
Mean Cost	17119.51	17049.6988	17049.4637	17049.461	19725.51	17059.64	17049.37
STD of Cost	0	0.25256201	0.00241321	0.00005067	2652.674	6.856805	0.422491
Mean P_{loss}	17.1049	17.1034174	17.103126	17.099398	16.10276	16.69118	16.50353
STD of P_{loss}	0	0.01847282	0.00210442	0.00027761	0.665202	0.248909	0.030778
Elapsed time	0.18128	2.258982	6.897495	57.670118	0.1287	0.893247	8.342366

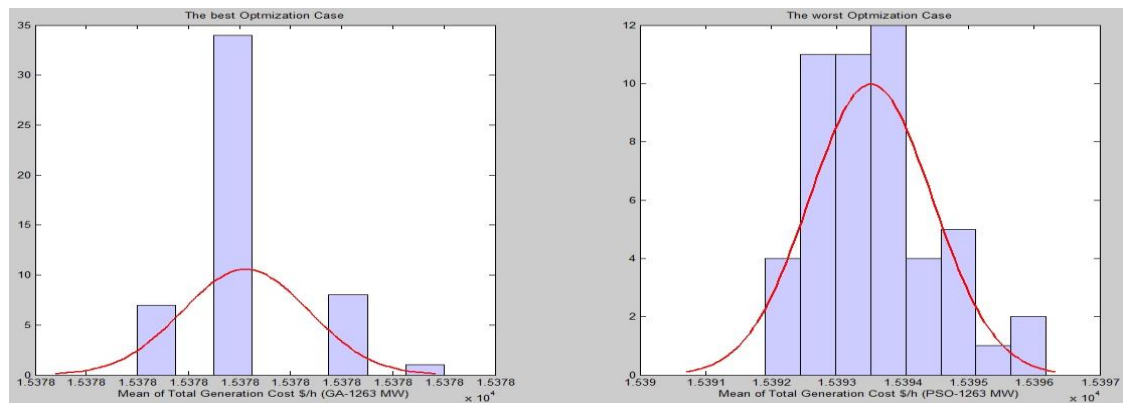


Figure 4: The best optimization case VS the worst optimization case

5. CONCLUSION

In this paper, both GA and PSO algorithm were presented and compared as an effective evolutionary techniques in solving ELD problem including the transmission lines constraint. The aim of economic dispatch problem is to minimize the total cost by optimal scheduling of generation units, while electricity demand is met. Simulation results show the efficiency and robustness of both techniques for this purpose. It can be seen that, in all scenarios, GA with 1,000 iterations achieves a better and faster result in terms of mean cost compared to PSO with 10,000 iterations. It can be also observed that increasing the number of GA iterations from 1,000 to 10,000 will not improve the result but will dramatically increase the computation time. PSO is as good as GA but, based on the findings of this study, it is advisable to use GA with 1,000 iterations to solve economic dispatch problem in bulk power systems.

REFERENCES

- [1] J.H.Park, Y.S.Kim, I.K.Eom, and K.Y.Lee, "Economic load dispatch for piecewise quadratic cost function using Hopfield neural network," *IEEE Trans. Power Syst.*, vol. 8, pp. 1030-1038, Aug. 1993.
- [2] A. J.Wood and B. F. Wollenberg, *Power Generation, Operation & Control*, 2 Ed. New York: John Wiley, 1984.
- [3] F. N. Lee and A. M. Breipohl, "Reserve constrained economic dispatch with prohibited zones", *IEEE Transactions on Power System*, Vol. 8, No. 1, pp. 246-254. , 1993.
- [4] W.-M. Lin, F.-S. Cheng and M.-T. Tsay, "An improved tabu search for economic dispatch with multiple minima," *IEEE Trans. Power Syst.*, vol.17, pp. 108 - 112, Feb, 2002.
- [5] T. Sum-im, "Economic dispatch by ant colony search algorithm", *IEEE Proceeding on cybernetics and intelligent systems*, Singapore, pp. 416-421, 2004.
- [6] K. P. Wong and Y. W. Wong, "Genetic and genetic/simulated-annealing approaches to economic dispatch," *Proc. Inst. Elect. Eng. Gen. Trans. Distrib.*, vol. 141, pp. 507-513, Sep. 1994.
- [7] D. C. Walters and G. B. Sheble, "Genetic algorithm solution of economic dispatch with valve point loading," *IEEE Trans. Power Syst.*, vol. 8, pp. 1325 - 1332, Aug. 1993.
- [8] H. Bai and B. Zhao, "A survey on application of swarm intelligence computation to electric power system", *Proceeding of the 6th world congress on intelligent control and automation*, Dalian, China, pp. 7587-7591, 2006.
- [9] W. Ongsakul, S. Dechanupaprittha and I. Ngamroo, "Parallel tabu search algorithm for constrained economic dispatch", *IEE Proceeding of Generation, Transmission and Distribution*, Vol. 151, Issue. 2, pp. 157-166, 2004.
- [10] N. A. Rahmat and I. Musirin, "Differential evolution ant colony optimization (DEACO) technique in solving economic load dispatch problem", *Power engineering and optimization conference (PEDCO)*, Malaysia, pp. 263-268, 2012.
- [11] T. S. Prasanna, and P. Somasundaram., "Fuzzy mutated evolutionary programming based algorithm for combined economic and emission dispatch", *IEEE TENCON Region 10 Conference*, pp. 1-5, 2008.
- [12] H Sa'adat, *Power System Analysis*, McGraw-Hill, 1999.
- [13] R. M. Kamel and B. Kermanshahi, "Optimal size and location of distributed generations for minimizing of power losses in a primary distribution network", *Transaction D: SCIENTIA IRANICA*, Vol. 16, No. 2, pp. 137-144, 2009.
- [14] J. H. Holland, *"Adaptation in Natural and Artificial Systems"*, University of Michigan Press, 1975.
- [15] W. M. Spears, K. A. De Jong, T. Baeck, and P. Bradzil, "An overview of evolutionary computation", *Proceedings of European conference on machine learning*, Springer-Verlag, Berlin, Vol. 667, pp. 442-459, 1993.
- [16] G. B. Sheble and K. Britting, "Refined Genetic Algorithm - Economic Dispatch Example", *IEEE Transactions on Power System*, Vol. 10, No. 1, pp. 117-124. , 1995.
- [17] T. Yalcinoz, H. Altum, and M. Uzam, "Economic dispatch solution using a genetic algorithm based on arithmetic crossover", *IEEE Power Tech Proceeding Conference*, Porto, Portugal, Vol 2, 2001.
- [18] J. Kennedy and R. Eberhart, "Particle swarm optimization," *Proc. IEEE Int. Conf. Neural Netw.*, Vol. 4, pp. 1942-1948, 1995.
- [19] K. Vaisakh, P. Praveena, S. R. M. Rao and K. Meah, "Solving dynamic economic dispatch problem with security constraints using bacterial foraging PSO-DE algorithm", *Electrical Power and Energy Systems*, Vol. 39, Issue. 1, pp. 56-67, 2012.
- [20] S. Sayah, and A. Hamouda, "A hybrid differential evolution algorithm based on particle swarm optimization non convex economic dispatch problems", *Applied Soft Computing*, Vol. 13, Issue. 4, pp. 1608-1619, 2013.
- [21] M. R. AlRashidi and M. E. El-Hawary, "Emission-economic optimization dispatch using a novel constraint handling particle swarm optimization strategy," *Electrical and Computer Engineering conference, Ottawa*. pp. 664-669, 2006.
- [22] N. Thenmozhi and D. Mary, "Economic emission load dispatch using hybrid genetic algorithm", *IEEE region 10 Conference*, India, Vol 3, pp. 476-479 2004.
- [23] R. C. Eberhart and Y. Shi, "Comparison between genetic algorithms and particle swarm optimization," *Proceedings of IEEE Int. Conference on Evolutionary Computation*, pp.611-616, May 1998.

COMPARISON OF DIFFERENT REACTIVE POWER COMPENSATION METHODS IN A POWER DISTRIBUTION SYSTEM

J. Nyangoma*, K. Awodele**

*Department of Electrical Engineering, University of Cape Town, Rondebosch 7701, Cape Town, South Africa. Email: *jnyangoma6@gmail.com **kehinde.awodele@uct.ac.za*

Abstract: This paper presents a comparative analysis between three reactive power compensation methods that are or can be implemented in distribution networks. Electricity distribution networks form the backbone by which electricity is effectively delivered to the consumers. Therefore a lot of precautionary measures have to be taken in order to ensure proper utilisation of distribution networks taking into account optimal economic operation, high system reliability as well as good quality of supply. Reactive power compensation in distribution networks is therefore fundamental in ensuring maximum transmission of power within the distribution networks. The three compensation methods investigated are shunt capacitors, Static Var Compensators and Distribution Static Synchronous Compensators. The test system used is the multi-phase IEEE 13 Node Test Feeder. This network is modelled using DIgSILENT PowerFactory software and all three options are simulated using this package. Load flow calculations are carried out and the results obtained are used to compare the impact of the three methods on the behaviour of the system. The methods are compared based on the improvement of the voltage profile, reduction in the total real power losses, power factor correction as well as the net present value of implementing the method. It was found that installation of the SVCs showed the best system performance overall with the highest net present value.

Keywords: reactive power compensation, load flow analysis, steady state operation, voltage profile, loss reduction, power factor

1. INTRODUCTION

Distribution systems are connected to a large number of consumer loads. Majority of these loads are seen to be non-unity power factor loads which draw a reactive component of current together with the active component. Additionally, most of these loads are either non-linear loads or unbalanced loads, resulting into power quality issues such as voltage waveform distortions due to the injection of harmonics, flow of excessive currents in the neutral conductor, poor power factor, voltage fluctuations and increased power losses across the network. As a result, electric utilities have to install compensation devices within their distribution networks that will ensure controlled flow of reactive power as well as achieve better power quality at minimal costs [1] [2].

This paper presents results got from simulating the IEEE 13 Node Test Feeder network and compares them with results already published by IEEE Distribution System Analysis Subcommittee. Once validated, the simulated test system is then used to investigate the impact of the three reactive power compensation methods on the performance of the system.

The rest of the paper is organised as follows: a brief description of the operation of each of the three compensation methods is presented in section 2. Section 3 covers the modelling of the IEEE 13 Node Test Feeder in DIgSILENT and NEPLAN as well as sizing and placement of the compensation devices on the network. Section 4 discusses in detail the steady state load flow results obtained for the three compensation methods as compared to the base case which does not have compensation. Section 5 presents the results for the Net

Present Value analysis and lastly, section 6 gives the conclusions.

2. REACTIVE POWER COMPENSATION PRINCIPLES

As the electricity demand continues to rapidly increase, electric utilities are posed with the challenge of meeting this demand reliably at a minimum cost. One of the ways through which electric utilities are achieving this objective is by employing various reactive power compensation technologies all over the power system. Electric loads require both active and reactive power components from the supply side. Since most of these loads are reactive loads, they tend to draw large amounts of reactive power. In order to relieve generating plants of the burden of having to supply reactive power from the source all the way to the consumer loads, compensation devices can be strategically placed very close to the loads to cater for the reactive power requirements of the loads. This in turn reduces the thermal capacity of the generators [3].

2.1 Shunt capacitors

The use of shunt capacitors originates from the early 19th century where they were first installed to carry out power factor correction [2]. Utilities use shunt capacitors to compensate for reactive power used by inductive loads like motors whose operation depends on magnetic fields in a way that the leading current drawn by the capacitors compensates for the lagging current drawn by the inductive load. As a result, the power factor of the system is improved resulting into a voltage increase at the point

where the capacitor is installed and what is more is that the reactive component of the current is reduced. This generally minimises the I^2R losses incurred along the distribution feeders leading to a fairly flat voltage profile. Furthermore, installation of shunt capacitors leads to a reduction in the total amount of current that would need to be transferred through the electrical equipment of the distribution network thereby releasing the system capacity of the power system.

2.2 Static Var Compensators-SVCs

SVCs consist of single phase shunt capacitors and reactors connected in parallel, which are controlled by a thyristor switching mechanism, to either generate or consume reactive power instantaneously as desired by the power network [4] [5]. Some of the common basic types of SVCs include: Saturated reactor (SR), Thyristor-controlled reactor (TCR), Thyristor-switched capacitor (TSC), Thyristor control transformer (TCT) and self- or line- commutated converter (SCC/LCC) [6]. However, the two most commonly used configurations are: the fixed capacitor (FC) with the thyristor controlled reactor (TCR) and the thyristor switched capacitor (TSC) with the thyristor controlled reactor (TCR). The thyristors are connected in an anti-parallel manner so as to allow for a bi-directional flow of current. It is also important to note that the fixed capacitor and TCR configuration helps in filtering out low order harmonics [7].

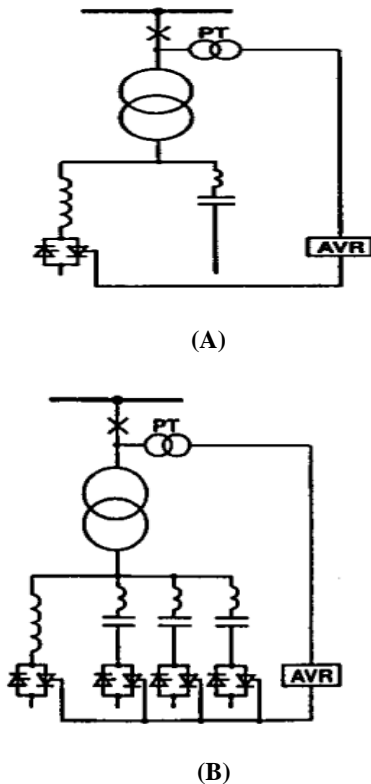


Figure 1: SVC with FC/TCR configuration (A), SVC with TSC/TCR configuration (B) [8]

2.3 Distribution Static Synchronous Compensators-DSTATCOMs

A DSTATCOM consists of self-commutated converters using either Insulated Gate Bipolar junction Transistors (IGBT) or Gate Turn off (GTO) thyristors, a DC voltage source (e.g. battery source), a voltage source converter (VSC) connected in shunt with a DC capacitor, coupling transformer; a step-up transformer (not usually required for the low voltage applications) and a controller [9]. From Figure 2 below, it can be observed that the AC side of the VSC is connected to the distribution bus through a coupling transformer. The DC side of the VSC is connected to a DC energy storage device which is a DC capacitor in this case, that carries the ripple current of the VSC and is the main storage device for reactive power production. The DC voltage source can be used to charge the capacitor. The DSTATCOM converts the DC input voltage stored in the charged DC capacitor into a set of three phase output voltages which are at the same frequency as the AC system. The amount of reactive power flow achieved is proportional to the difference between the VSC output voltage and system AC voltage. If the output voltage on the AC side of the VSC is equal to the system AC voltage, no reactive power can be delivered to the system. However, if the output voltage is greater than the system AC voltage, the DSTATCOM is operating in a capacitive mode (i.e. supplying reactive power) whilst if the output voltage is less than the system AC voltage, the DSTATCOM is operating in an inductive mode (i.e. absorbing reactive power) [9].

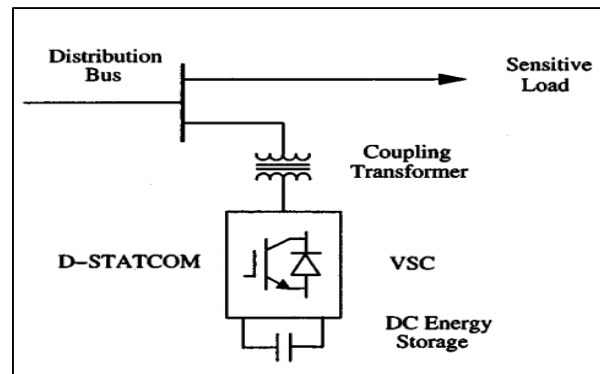


Figure 2: Schematic representation of a DSTATCOM [9]

3. MODELLING THE TEST SYSTEM

3.1 Simulation test system and software

The IEEE 13 Node Test Feeder was chosen as the test system for this work because it depicts the real world distribution systems, characterised by a varied range of complexities due to the nature of loads and sophisticated configurations for the different component models [10]. The original feeder was first simulated in both DIgSILENT PowerFactory and NEPLAN to obtain load flow results relatively close to those already published. Since the load flow results obtained for this system were

more or less perfect, the shunt capacitors which were included in the original setup (i.e. at buses 611 and 675), were taken out so as to get load flow results which show a need for reactive power compensation. The resultant modified test system was used as the base case. The lines, transformers, loads and all the other components on the network were modelled according to the specifications provided in the detailed data which can be downloaded from [11]. A one line diagram of this feeder is shown in Figure 3 below.

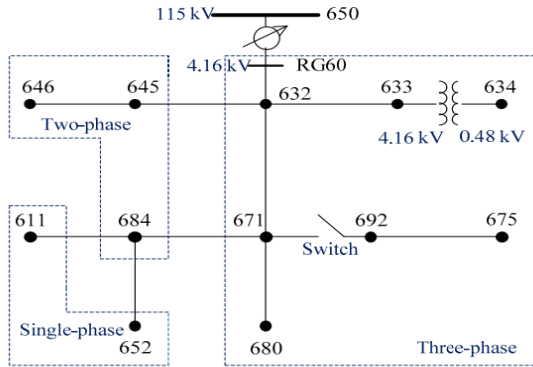


Figure 3: The IEEE 13 Node Test Feeder

3.2 Placement and sizing approach

DigSILENT PowerFactory was used to perform the load flow calculations and obtain results in terms of the voltage profile, power injections at each bus as well as sectional losses across each line section of the feeder. The candidate buses which require reactive power compensation were determined using a sensitivity analysis which incorporates a normalisation of voltages. The voltages at each of the buses obtained from the base case load flow are used to calculate the normalised voltages as follows:

$$Norm(i) = \frac{V(i)}{0.95} [12]$$

Where i is the bus number and $V(i)$ is the base case voltage magnitude obtained at bus i .

If a value less than 1.01 is obtained for the normalised voltage at any bus, then that bus qualifies as a candidate bus that requires placement of the compensation devices. The size of the compensation device placed at a candidate bus equals to the reactive component of the load attached to that bus. Table 4 in the Appendix shows the normalised voltages got for the buses connected to the radial feeder.

Load buses 671, 692, 675, 611 and 652 were selected as the candidate buses for placement of the compensation devices since the normalised voltages at each of these buses was less than 1.01. Buses 680 and 684 were left out because they did not have any loads attached to them and so the sizing approach would not apply.

4. DISCUSSION OF RESULTS

There were four test cases used to analyse and compare the impact of the three compensation methods. The criteria chosen to carry out this comparative analysis were voltage profile, power factor, real power losses and Net Present Value Analysis.

Results obtained from the simulation of the original feeder were first compared to already published results so as to validate the model to be used for any further tests in this research project.

4.1 Base case phase voltage magnitudes for the original feeder

In general, there was close agreement between the published results obtained in [11] and the two software packages, DigSILENT and NEPLAN. Figure 4 shows the comparison between the base case IEEE phase voltage magnitudes and those obtained in the software packages.

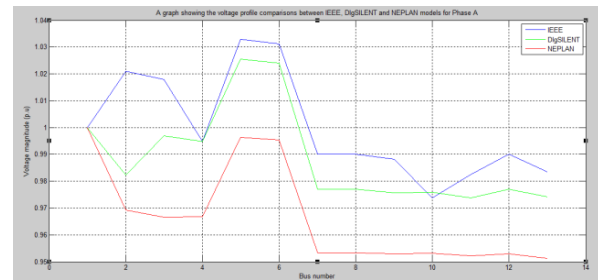


Figure 4: Voltage comparison between IEEE, DigSILENT and NEPLAN for Phase A

The highest deviation in phase A occurred at Node 632. The results obtained above can be attributed to the fact that the external grid model used was balanced and the phase voltages and angles could not be adjusted individually, as well as due to some simplifying assumptions that were made while simulating the test system. Despite the discrepancies between the results, all the voltage levels are seen to be within acceptable voltage limits of $\pm 5\%$ (i.e. between 0.95 and 1.05 p.u.).

4.2 Comparison between load flow results obtained for the modified IEEE feeder

Shunt capacitors, connected to buses 611 and 675 in the original feeder were removed so as to create the base case scenario. A load flow was carried out and results based on the selected criteria mentioned above were recorded. Thereafter, three test cases were considered namely:

- Case 1: installation of shunt capacitors
- Case 2: installation of static var compensators
- Case 3: installation of DSTATCOMs

4.2.1 Voltage profile

The graphs below illustrate the voltage profile for all the three phases, before and after the compensation devices were placed on the network.

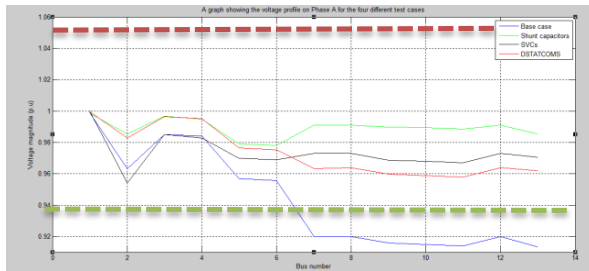


Figure 5: Voltage profile of Phase A showing all test cases

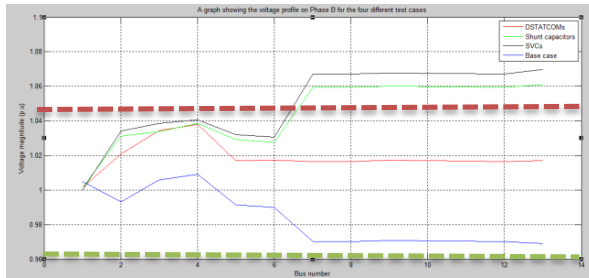


Figure 6: Voltage profile of Phase B showing all test cases

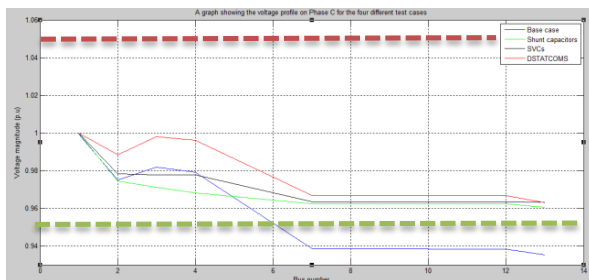


Figure 7: Voltage profile of Phase C showing all test cases

It is evident that the voltages at each of the buses noticeably improved after the compensation devices were added to the network with all the voltages falling within the satisfactory limits of 0.95 p.u (green dashed line) and 1.05 p.u (red dashed line) for Phases A and C. For Phase B however, the voltages were already within the acceptable limits even before compensation. This is because Phase B was the least loaded phase as compared to the other two phases, and so there was less current flowing through this phase resulting into lower voltage drops, hence higher voltages at the delivery end as seen at the buses. Overall, SVCs are seen to achieve the best voltage profile improvement, followed by the shunt capacitors and lastly, DSTATCOMs.

4.2.2 Total real power losses

Placement of the compensation devices on the network led to an overall reduction in the real power losses incurred across each line section along the feeder. This is because the compensation devices directly provide the reactive power requirements of the load which in turn reduces the total current that has to flow from the generating plant across the transmission network to the end users, leading to less I^2R losses. Installation of shunt capacitors resulted in a loss reduction of 320 kW, 300 kW

loss reduction with SVC installation and 100 kW with the installation of DSTATCOMs as seen in the figure below.

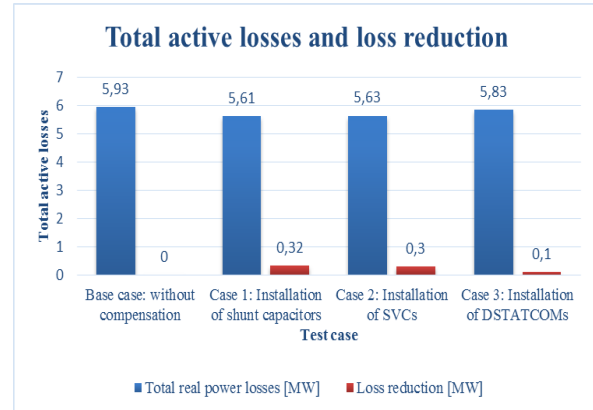


Figure 8: Total active losses and loss reduction for each test case

4.2.3 Power factor

The overall power factor of the network improved to 0.9813 when shunt capacitors were installed, 0.9825 for SVC installation and 0.98 for DSTATCOM installation. Additionally, a reduction in the total demand of the system (in MVA) results into the overall capacity of the system being released by 0.04 MVA for the shunt capacitors, 0.07 MVA for the SVCs and 0.01 MVA for the DSTATCOMs.

5. NET PRESENT VALUE (NPV) ANALYSIS

NPV analysis is used to determine if a project is cost effective in terms of the profits/savings realised in relation to the initial investment costs incurred. This is done by expressing future savings earned in terms of the current monetary value. A positive NPV signifies a viable project and the project with the highest NPV is the most profitable project.

The formula used to calculate the present value of future cash flows is given by:

$$PV = C_n \left(\frac{1+i}{1+d} \right)^n \text{ or } PV = C_n r^{-n} \quad [13]$$

where i is the inflation rate

d is the discount rate ; $r = \frac{1+d}{1+i}$

n is the number of years

C_n is the cash flow in n years' time (which in this case will be the cost savings)

The inflation rate, i was assumed to be 6.4 % (as of August 2013) [14] and the discount rate, d assumed to be 15 % (based on the fact that the World Bank recommends a net discount rate ($r-1$) to fall within the range of 8%-10% for investment in projects in developing countries [13]). All expected future cost savings were calculated by applying the above equation. The capital costs of installing each compensation devices are shown in the table 1 below [15]:

Table 1: Cost of installing each RPC device

RPC device	Total installation cost [R]
Shunt capacitors[1650 kVAR]	247 500
SVCs [2580 kVAR]	1 290 000
DSTATCOMs [600 kVAR]	360 000

The NPV analysis was carried out in two ways: firstly, based on if the compensation was a customer's initiative and secondly if it was the utility's initiative.

5.1 From customer's point of view

The cost savings calculated are the savings collectively realised by all the customers who have installed shunt capacitors as a result of a reduction in the total demand in MVA. The installation of SVCs and DSTATCOMs is not considered because the assumption is that customers would not be willing to install these devices due to their high costs. Using the tariff structure in [16], the monthly demand charge is given as R135 160 per MVA. The total annual demand charge is given by:

$$\text{Total demand charge for the first year} = \text{monthly demand charge} * \text{total demand per month} * 12 \text{ months}$$

Table 2: Total demand charge for the first year

Test case	Total demand charge [R]
Base case: without compensation	R 41 391 399
Network capacitors with shunt	R 41 326 522

The total cost savings in the first year are given by:

$$\text{Cost savings} = \text{Total demand charge without compensation} - \text{Total demand charge with shunt capacitors} \\ = \underline{\underline{\text{R } 64\,877}}$$

Assuming that this saving made is made every year for the life span of the compensation devices (i.e. 10 years), the NPV is obtained as follows:

$$\text{Total PV of the cost savings} = \frac{C_n}{r^0} + \frac{C_n}{r^1} + \frac{C_n}{r^2} + \dots + \frac{C_n}{r^9} ; \text{ where } C_n = \text{R}64\,877 \text{ is the same every year, } r=1.0808 \\ = \underline{\underline{\text{R } 468\,810}}$$

$$\text{Total PV of the cost} = \frac{C_n}{r^0} \text{ where } C_n = - \text{R } 247\,500 \text{ (capital cost shown in Table 4 above)} \\ = \frac{-247\,500}{1.0808^0} \\ = \underline{\underline{-\text{R } 247\,500}}$$

$$\text{Net present value} = \text{Total PV of the cost} + \text{Total PV of the cost savings} \\ = \underline{\underline{\text{R } 221\,310}}$$

The positive NPV got shows that the installation of capacitors is a viable project as the customers will earn significant savings.

5.2 From utility's point of view

The NPV analysis is done based on the cost savings that an electric utility would make as a result of a reduction in the total power losses due to installation of SVCs or DSTATCOMs.

The cost of losses per year are obtained using the formula adopted from [17]:

$$\text{Cost of network losses} = \text{Peak losses} * 8760 * \text{Loss Energy Cost} * \text{LLF}$$

Where Loss Energy cost is the cost per unit energy loss in R/kWh and is equivalent to R 0.223/ kWh

In this case, the peak losses in kW are assumed to be the total real power losses obtained from the load flow simulation results for each test case.

LLF is the loss load factor, defined as the ratio between the actual energy losses and peak load losses in a given time period. It can be obtained from the empirical formula [18]:

$$\text{LLF} = c * \text{LF} + (1-c) * \text{LF}^2$$

where $c=0.15$ for distribution and LF is the Load Factor.

From [19], a $\text{LF}=0.75$ was assumed based on the value given for a large industrial consumer.

$$\text{LLF} = (0.15 * 0.75) + (1-0.15) * 0.75^2$$

$$\underline{\underline{\text{LLF} = 0.5906}}$$

NPV analysis similar to that carried out for the shunt capacitors in subsection 5.1 above is adopted for the case of the SVCs and DSTATCOMs.

Table 3: NPV results for two RPC schemes

RPC device	NPV
SVCs [2580 kVAR]	R 1 372 097
DSTATCOMs [600 kVAR]	R 473 697

A positive NPV is obtained for both compensation schemes, implying that both schemes are viable. However, installation of SVCs yields a higher positive NPV, hence being a more profitable project for the electric utility.

6. CONCLUSIONS

This paper evaluated three reactive power compensation

methods that can be implemented in a power distribution system. From the load flow results obtained, all three methods achieved voltage profile improvement, reduction in real power losses and a slight improvement in the system's power factor, which are all benefits of reactive power compensation, with SVCs emerging as the best performing devices. The NPV analysis further justified that installing shunt capacitors from a customer's point of view is an economically viable project as cost savings are realised by the customer community, as a result of a reduction in the monthly demand charge imposed. From the utility's point of view, the cost of network losses reduced when either the SVCs or DSTATCOMs were installed on the network. However, installation of SVCs was more profitable as compared to installing DSTATCOMs since SVC installation lead to a higher NPV value.

7. ACKNOWLEDGEMENTS

The authors are grateful to the authority of Electrical Engineering Department, University of Cape Town, South Africa for providing the infrastructure necessary for carrying out this research, and to ESKOM, through the Tertiary Education Support Programme (TESP) for financial support.

REFERENCES

- [1] B. Singh, A. Chandra, K. Al-Haddad and D. Kothari, "Reactive power compensation and load balancing in electric power distribution systems," *Electrical Power and Energy Systems*, vol. 20, no. 6, pp. 375-381, 1998.
- [2] J. Dixon, L. Moran, J. Rodriguez and R. Domke, "Reactive Power Compensation Technologies, State-of-the-art Review," *Proceedings of the IEEE*, vol. 93, no. 12, pp. 2144-2164, 2005.
- [3] N. Muromba and D. Pudney, "Shunt capacitor banks increase capacity of distribution networks," EE Publishers, Gauteng, 2011.
- [4] X. Ziqiang and L. Yanqin, "Comparison of 3 kinds of Reactive Power Compensation Modes Based on Matlab/Simulink," in *Power and Energy Engineering Conference*, Wuhan, 2009.
- [5] Eskom, "Network planning guideline for shunt capacitors," Eskom, 2011.
- [6] M. Pikulski, "Controlled sources of reactive power used for improving voltage stability," in *Institute of Energy Technology, Aalborg University*, Aalborg, 2008.
- [7] M. A. Kamarposhti, M. Alinezhad, H. Lesani and N. Talebi, "Comparison of SVC, STATCOM, TCSC, and UPFC Controllers for Static Voltage Stability Evaluated by Continuation Power Flow Method," in *IEEE Electrical Power and Energy Conference*, Vancouver, 2008.
- [8] T. Petersson, *Reactive Power Compensation*, Karlstad, Sweden: ABB Power Systems, 1993.
- [9] T. Virk and A. Kaur, "Optimizing Power Supply by PWM Converter based Shunt connected Power Conditioners-Distribution Compensators," *International Journal of Engineering Research and applications (IJERA)*, vol. 3, no. 4, pp. 1682-1685, 2013.
- [10] J. O. Owuor, J. L. Munda and A. A. Jimoh, "The IEEE 34 Node Radial Test Feeder as a simulation testbench for Distributed Generation," in *IEEE Africon*, Livingstone , 2011.
- [11] P. D. S. A. S. IEEE, "IEEE PES-Power and Energy Society," IEEE PES-Power and Energy Society, 15 April 2010. [Online]. Available: <http://ewh.ieee.org/soc/pes/dsacom/testfeeders.html>. [Accessed 21 October 2013].
- [12] K. Prakash and M. Sydulu, "Particle Swarm Optimisation Based Capacitor Placement on Radial Distribution Systems," in *IEEE Power Engineering Society General Meeting*, Tampa, Florida, 2007.
- [13] C. Gaunt and K. Awodele, *Financial Evaluation of Projects*, Cape Town: University of Cape Town, EEE4089F Class notes, 2013.
- [14] J. Taborda, "Trading economics," Trading economics, 18 September 2013. [Online]. Available: <http://www.tradingeconomics.com/south-africa/inflation-cpi>. [Accessed 7 October 2013].
- [15] J. Kueck, B. Kirby, T. Rizy, F. Li and N. Fall, "Reactive Power from Distributed Energy," *The Electricity Journal*, vol. 19, no. 10, pp. 27-38, 2006.
- [16] C. Gaunt and K. Awodele, *Retail Electricity Tariffs*, Cape Town: University of Cape Town, EEE3044S notes, 2013.
- [17] Z. Stegmann and K. Awodele, "Comparison of compensation, distributed generation and transmission line upgrade options in meeting increased demand on a transmission line," in *Southern African Universities Power Engineering Conference*, Cape Town, 2009.
- [18] C. Gaunt and K. Awodele, *Loads, EEE 4089F Notes*, Cape Town: University of Cape Town, EEE4089F Notes, 2013.
- [19] J. Parmar, "Electrical Notes and Articles," Wordpress, 31 October 2011. [Online]. Available: <http://electricalnotes.wordpress.com/2011/10/31/demand-factor-diversity-factor-utilization-factor-load-factor/>. [Accessed 15 October 2013].

APPENDIX

Table 4: Normalised bus voltages for the IEEE 13 bus feeder

Bus	Phase A	Norm A	Phase B	Norm B	Phase C	Norm C
650	0,9989	1,0514	1,001	1,0537	0,995	1,0474
632	0,9631	1,014	1,02	1,0737	0,9751	1,0264
633	0,985	1,0368	1,0344	1,0888	0,982	1,0337
634	0,9842	1,036	1,038	1,0926	0,979	1,0305
645	0,9557	1,006	1,017	1,0705		
646	0,9989	1,0515	1,017	1,0705		
671	0,9198	0,9682	1,0165	1,07	0,9385	0,9879
692	0,9198	0,9682	1,0165	1,07	0,9384	0,9878
675	0,9133	0,9614	1,017	1,0705	0,9354	0,9846
684	0,9159	0,9641	1,017	1,0705		
611	0,9149	0,9630				
680	0,9198	0,9682	1,0165	1,07	0,9384	0,9878
652	0,9141	0,9622				

Topic D

Machines

DESIGN AND EVALUATION OF A 1 kW ROTARY TRANSFORMER

NL Zietsman , N Gule

University of Stellenbosch, Department of Electronic and Electrical Engineering, Engineering Faculty, Banghoek Road, Stellenbosch 7600.

Abstract. Some systems require power and signals to be transferred across a rotating interface. The current technology for achieving this connection makes use of slip rings and brushes. Mechanical contact between these two components leads to wear and shortens the lifespan of the assembly. The limited lifespan of slip rings makes them unsuitable for use in applications where regular maintenance is challenging due to inaccessibility. Such applications include wind turbines and spacecraft systems. A rotary transformer is designed that will provide magnetic coupling across a rotating interface, thus eliminating the physical contact and wear of components. The concept is researched thoroughly and a 1kW transformer is designed, built and tested. The rotary transformer is found to be a viable replacement of slip ring and brush assemblies.

Key Words. Rotary transformer; magnetic coupling; leakage inductance; magnetising inductance

1. INTRODUCTION

In many applications there is a need to transfer power and signals across a rotating interface. Slip ring and brush assemblies are the electromechanical devices conventionally used for this purpose. Due to the contact between the slip ring and brushes, these components experience wear and have a limited lifespan. Debris production is another problem resulting from the direct contact between the moving and stationary components. Regular maintenance is required in order to replace worn components and remove debris.

The modern technology in slip ring design has resulted in high efficiencies and extended life time of the components making them well suited for most applications. However, there are an increasing number of systems requiring longer lifetime of rotating contacts with decrease in debris production. These applications include spacecraft systems and wind turbines where inaccessibility and associated high cost of maintenance drives the design requirements. In order to address these problems an alternative method for contact across the rotating interface is needed: a rotary transformer. The concept of using a rotary transformer was first developed by Gibson in 1961 [1]. The principle allows for contactless energy transfer through magnetic coupling. The lack of mechanical contact removes the wear problem experienced in conventional slip ring assembly [1]. The concept has been applied in many high frequency applications such as an airborne radar power supply [2] and aerospace systems [3]. The rotating transformer has the same basic operation principles as a conventional transformer but the geometry and mechanical design differ considerably. In order to facilitate rotation, the primary and secondary sides are separated by an air gap. This configuration has to be designed to ensure minimal changes in electrical characteristics. Due to the rotating nature of the device, the mechanical design is more involved.

The major constraint that governs the design of

rotary transformers is the fact that it must be able to rotate freely without the rotation affecting the performance of the transformer. To achieve this, it is necessary to maintain a constant flux path at all angles of rotation. Two standard designs described by Landsman and shown in Figure 1 satisfy this condition: the axial transformer and the radial transformer [4], [5].

There are two main considerations in the design of a rotary transformer: the air gap and the spacing between the windings.

The air gap that is needed to facilitate the rotation leads to a more complicated mechanical design. The support structure of the transformer has to be designed to ensure that the integrity of the air gap is maintained throughout rotation. In the electrical design it is important to note that the air gap between the two halves of the transformer results in a low magnetising inductance. This low magnetising inductance causes a high magnetising current which needs to be accounted for during design.

Separation between the primary and secondary windings of the transformer results in alternative magnetic flux paths being produced through the air instead of inside the magnetic core material. This leakage flux causes an increase in leakage inductance of the transformer. This leakage inductance appears as a reactance in series with both the primary and secondary windings and results in a voltage drop across them [2]. High leakage inductance in a transformer is the primary cause of poor load regulation [6]. The leakage inductance can be calculated by using Equation (1) as described by [7]. This holds for both axial and radial rotary transformer configurations.

$$L_{lp} = \frac{4\pi(MLT)N_p^2}{a} \left(c + \frac{b_1 + b_2}{3} \right) (10^{-9}) \text{ Henrys} \quad (1)$$

Where: a = winding length

$b_{1,2}$ = winding depth of primary, secondary

c = spacing between windings

MLT = mean length of a turn

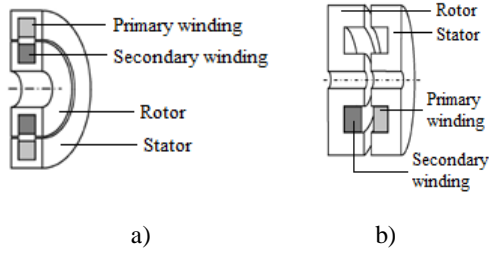


Figure 1: Rotary Transformer configurations: a) Axial and b) Radial

In this paper a 1 kW rotary transformer is designed, built and tested in order to determine its suitability as a replacement for slip rings in applications such as Doubly Fed Induction Generators (DFIG's) found in wind turbines.

2. DESIGN

The axial configuration, whereby the secondary side (rotor) is placed inside the primary side of the transformer (stator), is chosen for ease of construction. A design methodology is provided by Potter and Shirsavar in [4]. The method entails designing a standard transformer that meets the specifications and then adjusting the parameters to that of a rotary transformer. From the specifications of the transformer the area product, A_p , can be used to find the minimum core cross sectional area, A_c , based on the core's power handling capabilities. The area product is given by Equation (2).

$$A_p = A_c A_w = \frac{P_t (10^4)}{K_f K_u B_{ac} f} \quad (2)$$

Where: A_w = window area
 P_t = apparent power
 K_f = waveform coefficient – 4.44 for sine
 K_u = window utilisation factor
 B_{ac} = maximum flux density

This cross sectional area, A_c , is the minimum core area that will ensure the transformer will not saturate. Once the area, A_c , is calculated it is used in conjunction with Equations (3) – (5) to determine the transformer's dimensions. Figure 2 illustrates the axial configuration of the rotary transformer as well as the necessary dimensions of the design.

$$A_1 = \frac{\pi}{4} (D_1^2) \quad (3)$$

$$A_2 = \pi D_1 h_2 \quad (4)$$

$$A_3 = \frac{\pi}{4} [D_3^2 - (D_1 + 2g + 4w)^2] \quad (5)$$

Where: D_1 , D_2 and D_3 are the diameters as shown in Figure 2
 g and w are the air gap width and winding depth, respectively.

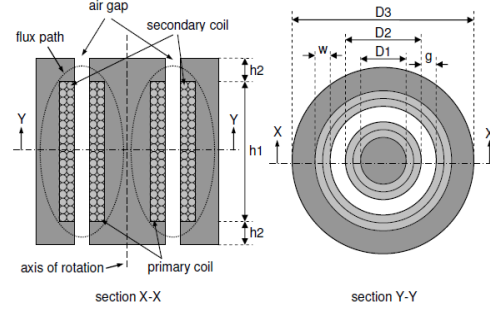


Figure 2: Dimensions for axial configuration [4].

The air gap width between the rotor and stator is chosen as 1 mm. Better performance is achieved when the air gap is smaller however a smaller air gap requires absolute precision during construction. A trade-off between size and difficulty of achieving the air gap size was done. The maximum flux density allowable in the core is chosen as 0.5 T and frequency of operation is chosen as 50Hz for ease of testing, however in applications such as DFIG's the frequency will be lower. The rated output voltage is chosen as 240 V. The higher rated voltage will lead to a corresponding lower current and therefore minimise the conduction losses. The current density allowable in the wire is chosen as 5 A/mm². Using this condition and the rated current of the transformer, the wire size is selected. A target efficiency of 90% is set, which is comparable to that of slip ring assemblies.

Faraday's Law provides a useful design expression as shown in Equation (3). The remaining parameters of the transformer can be determined by using substitution into Equation (3).

$$N_p = \frac{V_p (10^4)}{A_c B_{ac} K_f} \quad (3)$$

The rotary transformer is evaluated for low frequency applications. The core material is chosen as silicon steel laminations since it is the material that offers the lowest losses at low frequency operation. The final specifications of the transformer design are shown in Table 1. The primary and secondary number of turns are equal since the purpose of the transformer is not to step up or step down a voltage. The number of turns is 190.

Table 1: Design transformer parameters

Parameter	Designed Value
$P_o(\text{rated})$	1000 W
$V_o(\text{rated})$	240 V
$I_o(\text{rated})$	4.17 A
f	50Hz
N_p	190
N_s	190
B_{ac}	0.5 T
A_c	114 cm ²
η_{min}	90%

3. CONSTRUCTION

The design of the transformer and the support structure consist of three main parts: the shaft - around which the transformer rotates, the rotor and the stator. Both the rotor and the stator comprise of one half of the transformer's core along with the corresponding support structure. The core of the transformer is constructed using thin steel laminations. These laminations are shaped in such a way that they can be securely clipped into the rotor and stator housings. The shaft is stainless steel, while the support structures are machined out of aluminium. The aluminium is the ideal material since it is nonmagnetic and light-weight.

3.1 Rotor

There are two identical components that secure the laminations and make up the rotor. The component is designed with a ridge that corresponds to the cut made in the lamination in order to hold the rotor laminations in place. The rotor components must rotate with the shaft as one unit without any rotation of their own. A keyway and key are designed for this purpose. The key locks the rotor end piece onto the shaft, and a circlip is used to prevent the end piece sliding off the shaft.

The first step in the construction involved using the rotor laminations and rotor end pieces to construct the rotor around the shaft. The one rotor end piece is placed on the shaft using the key and circlip. The shaft is then secured upright in a jig. A piece of foam is measured and placed around the shaft as seen in Figure 3b), forming a cylinder. The laminations are then placed into this cylinder and clipped into the ridge on the bottom rotor end piece.

The ends of the rotor winding have to be taken out of the core assembly. In order to achieve this, laminations are cut and stuck to one another to form a channel in the core through which the winding ends can be fed. See Figure 3c). Thin strips of glass-reinforced epoxy are placed between the laminations in order to space them uniformly. The second rotor end piece is now placed on the shaft, securing the laminations. A layer of cloth and glass tape is wrapped around the rotor window as shown in Figure 3c) Epoxy resin is painted over the top and bottom of the laminations to secure the spacer strips. The winding is done next and the wire ends insulated and pull through the channel. The completed rotor assembly is shown in Figure 3d).

3.2 Stator

The stator is built inside the housing shown. The housing and its end piece are therefore designed with the ridge for the laminations to clip into. A hole is drilled into the exterior housing to allow for the stator winding ends to be accessed. A hole is required in the housing in order to place the rotor. A bearing is press fitted into the housing to facilitate rotation. Slots are machined into the sides of the stator housing in order to provide ventilation.

It is not possible to first place the laminations and then do the winding due to the c shape of the laminations. The choice is made to wind the coil first on a former, coat it with cloth and epoxy to harden it, and then construct the core around the winding. A similar channel as on the rotor is constructed through the laminations for the ends of the stator winding. Once all the stator laminations are placed, the assembly is secured using tape and the housing is slid over until the laminations clip into their securing ridge on the inside of the housing. This process is illustrated by Figure 4b). The rotor is then placed inside the stator as shown in Figure 4c). The end piece is placed and the transformer closed. The air gap between the rotor and stator is shown in Figure 4d).

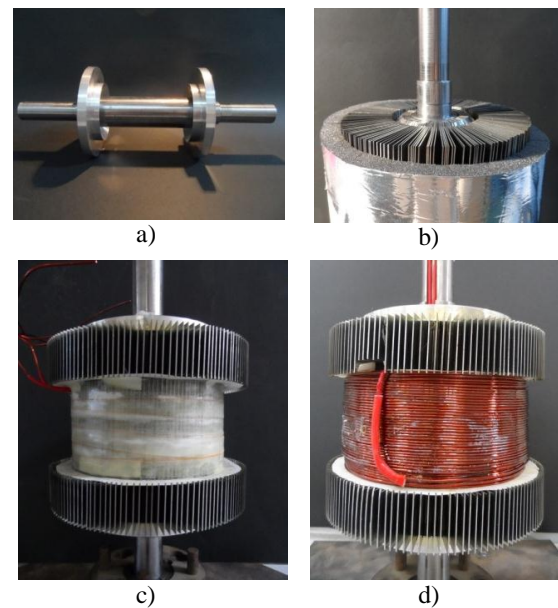


Figure 3: Construction of the rotor

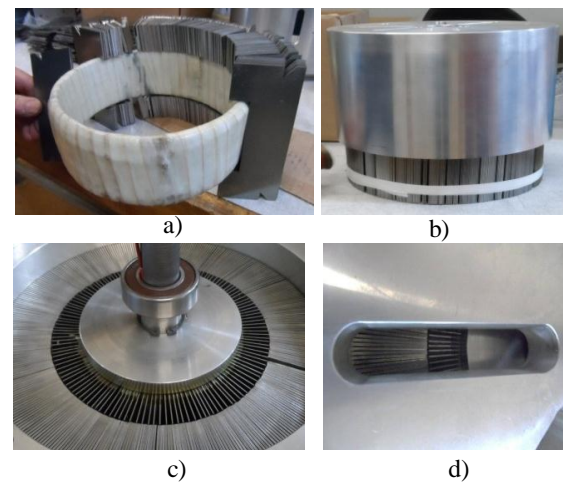


Figure 4: Construction of the rotor

4. ANALYSIS

The transformer's operation is tested using both standard transformer and specialised tests. All the tests are conducted for both stationary and rotating operation in order to compare the two and determine the effect of rotation. The main consideration for the rotational tests is that the rotor winding needs to be accessed. This is done by means of a Mercotac rotating conductor. These connectors make contact through a liquid metal molecularly bonded to the contact thus allowing for the rotation of one portion of the device. A 37 kW induction motor is used to drive the transformer for the rotational tests. The rotation of the transformer does not cause any torque on the shaft.

The electrical characteristics of the transformer are determined using the standard open and short circuit tests as well as a set of specialised inductance tests.

4.1 Open circuit tests

The open circuit test provides important information about the transformer. The chosen operating point can be verified to ensure that the transformer core material does not saturate. The shunt parameters and core losses of the transformer can also be determined.

The open circuit primary current waveform is distorted as shown in Figure 5 and shows signs of saturation. In order to measure the linear operating region of the transformer an open circuit characteristic graph, Figure 6, is plotted. From the graph it is clear that the rated voltage of 240 V is above the knee of the graph and leads to saturation in the core. A new rated operating voltage of 170 V is chosen and the open circuit test is conducted again. The open circuit primary current waveform at the new operating point is given by Figure 7.

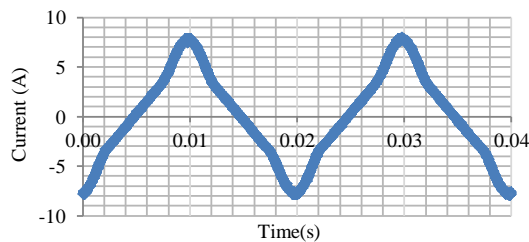


Figure 5: Primary open circuit current at 240 V operating point

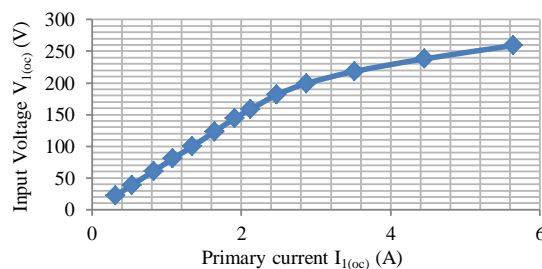


Figure 6: Open circuit characteristic curve

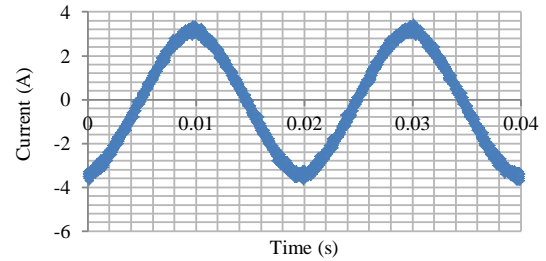


Figure 7: Primary open circuit current at new 170 V operating point.

The magnetising current of the transformer is high, at 2.7 A. In the conventional transformer the impedance of the exciting branch is large and so the voltage drop across the primary impedance is negligible. This assumption cannot be made with the rotating transformer since the magnetising reactance is low. For this reason, the simplified cantilever equivalent cannot be used. This has the effect that instead of the open circuit loss representing only core loss, it will contain a portion of conduction losses. The core loss is measured as 16.98 W and the conduction losses on no load are 8.01 W.

4.2 Short circuit test

The short circuit test is used to measure series parameters and conduction losses. The conduction losses of full load are 75 W.

4.3 Efficiency

From the measured losses, the transformer's efficiency is calculated as 90.91%.

4.3 Inductance tests

The magnetising and leakage inductances are of prime importance in a rotary transformer. The magnetising inductance of the transformer is 125 mH and the leakage inductance is 4.69 mH. These inductances are also tested during rotation. The values are taken at different angles of rotation and plotted as shown in Figure 8 and Figure 9. The magnetising inductance presented in Figure 8 varies with 1.35% during rotation which indicates that the air gap width is maintained throughout the rotation. The leakage inductance of the transformer varies significantly during rotation as shown in Figure 9. This indicates that the coupling between the windings is affected by rotation. The leakage inductance is shown to be at its highest value when the ends of the coils are aligned. During the construction of the rotor, the winding end is drawn over the width of the coil to take the end out of the core and onto the shaft. Parts of the magnetic laminations are also cut away on both the stator and the rotor to create gaps through which the winding ends can be drawn. This is the cause of the increased leakage inductance when the two ends are aligned. Over a full revolution the leakage inductance variation is 11.95%.

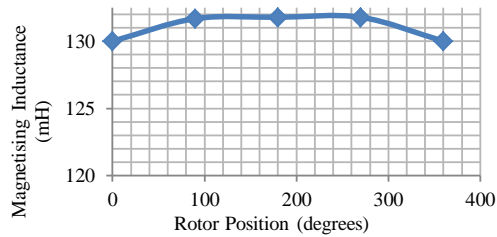


Figure 8: Magnetising inductance over full rotation

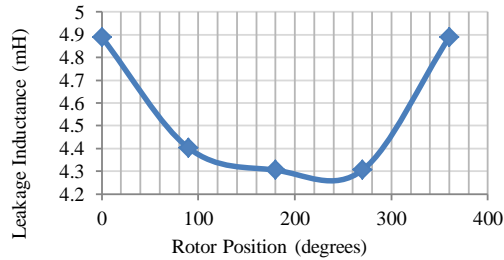


Figure 9: Leakage inductance over full rotation

5. CONCLUSION

The performance of the transformer is not significantly affected by the rotation. The transformer operates at an efficiency of 90.91% which meets the design requirements. This efficiency proves that the rotary transformer is a viable replacement for slip ring and brush assemblies. Further study on DFIG applications can be conducted with the design of a three phase rotary transformer to provide the contact between the converter and the rotor winding of a DFIG.

REFERENCES

- [1] "Rotary Transformers Developed To Replace Slip Rings and Brushes," *Of Current Interest*, pp. 469-470, June 1961.
- [2] Konstantinos D. Papastergiou D. Ewn Macpherson, "An Airborne Radar Power Supply With Contactless Transfer of Energy- Part 1: Rotating Transformer," *IEEE Transactions on Industrial Electronics*, vol. 54, no. 5, pp. 2874-2884, October 2007.
- [3] S.H. Marx R.W. Bounds, "A kilowatt Rotray Power Transformer," *IEEE Transactions on Aerospace and Electronic Systems*, vol. AES-7, no. 6, pp. 1157-1163, November 1971.
- [4] B.A. Potter S.A. Shirsavar, "Design, Implementations and Characterisation of a Contactless Power Transfer System for Rotating Applications," University of Reading, 2006.

- [5] E. Landsman, "Rotary Transformer Design," in *PCSC-70 Record*, 1970, pp. 139-152.
- [6] L.H. Dixon. (2003) Texas Instruments. [Online]. <http://www.ti.com/lit/ml/slup205/slup205.pdf>
- [7] Colonel WM. T. McLyman, *Transformer and Inductor Design Handbook*, 3rd ed. New York: Marcel Dekker Inc, 2004.
- [8] S.A. Shirsavar B.A. Potter, "Design, Implementation and Characterisation of a Contactless Power Transfer System for Rotating Applications," University of Reading, 2006.

INTERPRETATION AND SIGNIFICANCE OF SHAFT VOLTAGES IN ROTATING ELECTRICAL MACHINES

W. Doorsamy and W. A. Cronje

School of the Electrical and Information Engineering, Faculty of Engineering and the Built Environment, Private Bag 3, Wits 2050, South Africa

E-mail: wesley.doorsamy@students.wits.ac.za, willie.cronje@wits.ac.za

Abstract: This paper discusses the origins of shaft voltages in rotating electrical machines and describes the mechanisms which influence the features of this phenomenon. It is found that whilst extensive work has been conducted to suppress these circulating currents, more recent interpretations of the resulting signals have suggested immense potential in the area of condition monitoring and fault diagnostics. Deductions from an investigation show that these interpretations are valid. The investigation uses Finite Element Analysis (FEA) to predict magnetic field perturbations and affected shaft voltages resulting from fault conditions. The predicted fault condition behaviour is then experimentally validated, indicating definitive relationships between specific faults and frequency content of the machine's shaft signatures.

Keywords: Shaft voltages, rotating electrical machines, fault diagnostics, FEA.

1. INTRODUCTION

The measurement and analysis of shaft voltages in rotating electrical machinery, specifically synchronous generators, is continually growing as a method of condition monitoring. Progressive research conducted on the fault classification and non-invasive capabilities of the shaft voltage methodologies motivates such growth. Within the scope of fault diagnosis, the shaft voltage based technique provides the advantage of predictive capabilities in the form of incipient fault diagnosis.

Condition-based monitoring thrives on the technique's proficiency to diagnose early faults therefore allowing for remedial action before development of the fault mechanisms. An increase in efficiency is therefore inherent with avoidance of unplanned shut-downs and even catastrophic failure. This paper presents some of the mechanisms of shaft voltages and techniques which allow use of the phenomena in condition monitoring of rotating machinery. The significance of the circulating currents that create the shaft potentials and interpretation of the actual signals is discussed. Results of an investigation into the relation of specific faults to shaft signals are also presented together with simulation of a predictive model and experimental validation for shaft voltages in a synchronous generator.

2. INTERPRETATION OF SHAFT VOLTAGES

In electrical machines, stray voltages can occur on the rotating shafts due to external electromagnetic signal induction and interference. These signals are usually quite small in comparison to more significant voltages induced through shaft linkage of asymmetric magnetic fields [1]. Residual magnetism and switching power electronics have also been found to lead to induction of these stray voltages [2].

Shaft voltages and currents can have negative effects such as bearing and seal failure [3]. Hence, extensive work has been conducted in order to mitigate these effects such as the use of shaft grounding brushes [4].

2.1 Origins of shaft voltages

In a generator, the stray voltage observed across the rotating shaft, or the voltage difference between the shaft and ground plane is termed the shaft voltage [5]. As mentioned, electromagnetic interference (communication signals) do induce some effects however the significant causes of shaft voltages can be broadly classified into three general categories namely:

- Electromagnetic
- External Voltage Sources
- Electrostatic

The sources of the induced voltages under the category of electromagnetic origin are residual magnetism, magnetic asymmetries, axial shaft flux and homopolar flux. Together with sources of high residual magnetism such as rotor, bearings, housing etc., and a low-reluctance magnetic circuit, shaft voltages may be generated. Magnetic asymmetries, arising from acceptable manufacturing limitations and defects, commonly results in magnetic flux linkage which creates a shaft potential.

Examples of these manufacturing imperfections are segmented cores and acceptable eccentricity. Others may include weld recesses and key ways as depicted in Fig. 1. Another magnetic irregularity is caused through asymmetrical winding connections or faults which create an axial/ homopolar flux along the shaft thereby inducing current flow [6]. An example of asymmetrical flux is also illustrated in Fig. 1.

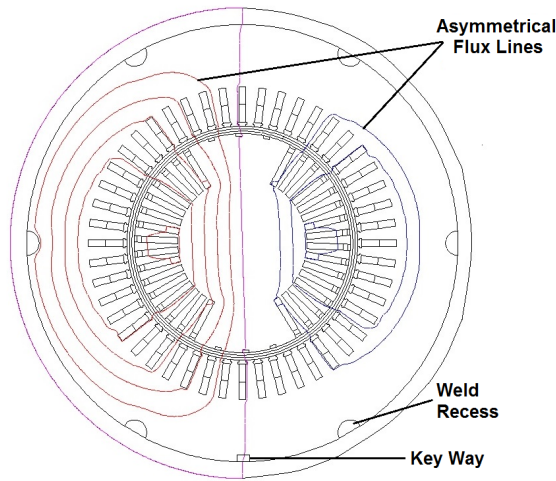


Figure 1: Cross-section of 2-pole synchronous generator with example of asymmetrical flux pattern and some products of the manufacturing process

External voltages applied through excitation sources also induce currents in the shaft through capacitive coupling. Excitation voltage harmonics (rectifier circuit output) are also transferred through this mechanism and are therefore evident in the shaft voltage.

Electrostatic sources are common in power generation applications and originate from capacitive charges that generate the high voltages. This occurs due to separation of charge when wet steam flows through turbine blades, consequently creating a shaft potential [7].

2.2 Significance of shaft grounding

For close to a century, shaft voltages and circulating currents have been found to negatively impact machines. Some of the main issues include bearing and seal damage. Numerous efforts to mitigate these effects such as use of insulated bearings and grounding brushes are still prevalent today. When the shaft potential reaches a certain level, electrical discharge occurs across the smaller spaces to ground.

Therefore components with reduced clearances, with respect to the shaft, are most susceptible to damage as a result of these discharges. It has also been reported that this mechanism is more prevalent in modern day machines with inherently reduced clearances.

There are no countermeasures to effectively completely eliminate such voltages. However, there are effective methods to diminish negative effects through techniques such as increasing stability and reliability of the ground grid. Proper bonding of all components to the ground grid is essential whilst maintaining a reliable grounding brush installation.

There are a various types of shaft grounding brushes available however not many of these brushes can be used for accurate shaft signal acquisition. The following are some examples of shaft grounding brushes [8]:

- Metal fibre brushes with silver alloy composite
- Conductive microfiber rings (carbon)
- Silver-gold composite shaft-riding brushes
- Copper-composite braid

The silver-gold composite shaft-riding brushes allow for continuous online shaft voltage monitoring and are used in the presented investigation.

2.3 Shaft Voltage Grounding and Measurement

Accurate measurement of shaft grounding current and shaft voltages is quite challenging due to accessibility to shaft sections and a reliable ground grid. Extensive work has been conducted in efforts to standardise shaft grounding systems as part of a best maintenance practice. Some of the earliest of standard guidelines, regarding shaft grounding, were published in [9].

The recommended practice for shaft voltage measurement is placement of brushes on the shaft extension of outboard-side i.e. excitation end. The driven end (turbine-side in power plant) has another brush connected to ground (may use a shunt resistor), across which a voltage measurement may be taken.

Figure 2 gives a cross-sectional side view of a generator and illustrates the concept for shaft voltage measurement where the brushes are placed on the inside of insulated bearings on either side of the shaft i.e. inboard and outboard. The inboard end is the driven end, whilst the outboard end usually consists of static field excitation.

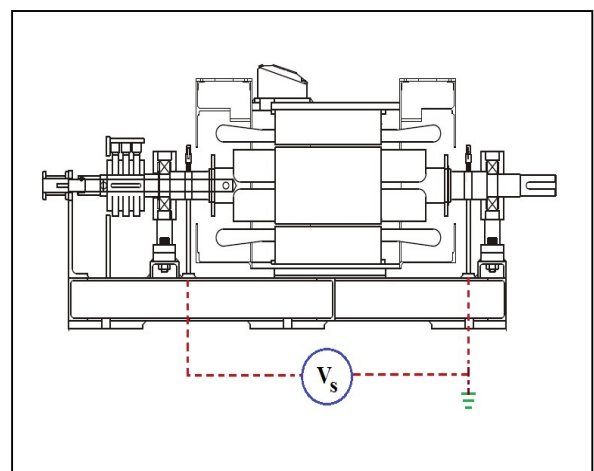


Figure 2: Cross-sectional side view of 2-pole synchronous generator with shaft brushes illustrating the concept for shaft voltage measurement

Through the nature of the origins of shaft voltage e.g. asymmetrical magnetic fields, the possibility of a valuable technique with which to discover incipient problems is made available. Recently, more work has been conducted on harnessing this inherent capability to diagnose faults [10], however efficient utilisation of the diagnostic powers of shaft voltages is heavily dependent on the measurement, processing and interpretation of the signal. Whilst there are a few systems available, a complete solution which incorporates shaft voltage monitoring in the definitive diagnosis of a wide scope of incipient faults is yet to be realised [11].

3. INVESTIGATION OF SHAFT VOLTAGE BASED CONDITION MONITORING IN GENERATORS

An investigation into the practicality of utilising shaft voltages in the diagnosis of faults was undertaken. The effects of specific faults on the shaft voltages were examined. Some of the previously mentioned origins of shaft potentials are validated through both simulation and experimental methods. The study utilises a miniature 2-pole synchronous generator driven by a 3-phase induction motor. A measurement system, consisting of a data acquisition system that utilises a commercial software (Matlab® and dSpace®), is connected to the generator. The generator model was firstly constructed in an FEA software package (Flux®) and various fault conditions were simulated. This was experimentally implemented and the accompanying effects were recorded.

3.1 FEA Model for Shaft Voltage Prediction

The first component of the investigation involves construction of a predictive model. This model is constructed using a finite element software application developed for solving 2-D and 3-D electromagnetic models. Analysis of the performance characteristics of the generator, specifically under fault conditions, provides initial indications of the affected frequency components of the shaft signals. This information also serves the purpose of optimising experimental procedures and providing a reference with which to validate measurements. The system model consists of coupling of the non-linear magnetic and electric circuits. Two major components of the model are the geometric component, a 2-D model of the actual machine as shown in Figure 1, and the physics component. Figure 3 illustrates the steps in the modelling and simulation process.

A 2-D model is deemed suitable for the purpose of this investigation as an axisymmetric model is adequate for implementation of all the concerned faults. However, for 2-D FEA, certain assumptions are intrinsic, such as the direction of the magnetic fields and flow of currents. Additionally, it is assumed that the stator and rotor are of equal length.

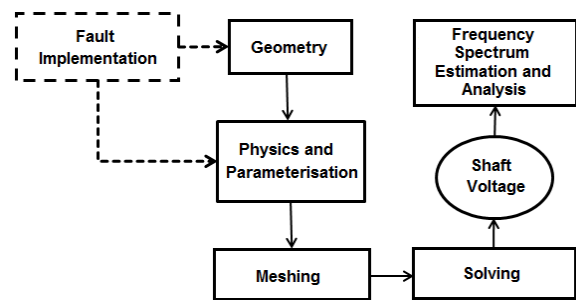


Figure 3: Flow diagram illustrating process sequence for construction of FEA simulation model of synchronous generator

A significant feature of the FEA model is the fault simulation capability. Selection of the faults for the investigated is based on evaluation of various possible faults that occur on a generator in application. The evaluation comprises of a number of criteria such as experimental practicability, frequency of occurrence, detectability and fault mechanisms i.e. tendency of the fault to further develop. Incipient winding, rectifier and static eccentricity faults, not easily detected through online methods, are considered in this investigation.

Obtaining the frequency content of the captured signals is fundamental to the presented method of condition monitoring as minor magnetic field perturbations are easily observed in the frequency domain. An algorithm inputs each of the signals and compares frequency spectra of the signals obtained under fault conditions to normal conditions.

An example of the shaft voltage signal obtained from the generator model under normal conditions, with corresponding periodogram, is given in Figure 4.

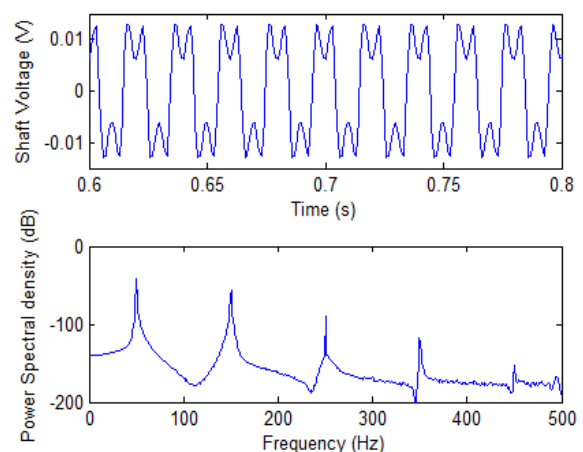


Figure 4: Example of simulated shaft voltage and corresponding PSD for generator model, under normal conditions

3.2 Shaft Voltages on Experimental Generator under Fault Conditions

In order to validate the predictive model experimentally, the investigation utilises a specialised miniature generator designed to mimic large turbo-generators. The generator is used in conjunction with various instrumentation and data capturing devices. An induction motor, controlled by a variable speed drive (VSD), is used to drive the generator. A block diagram of the experimental layout is given in Figure 5.

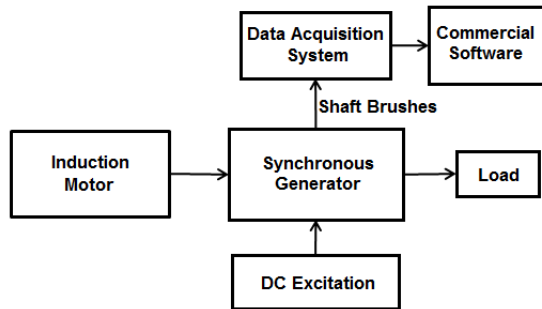


Figure 5: Block diagram of experimental configuration used for investigation of shaft voltage based condition monitoring in synchronous generator

The selected faults were implemented on the synchronous generator and the corresponding shaft voltages were recorded using the measurement system. The resulting signals were then processed as described in the previous section.

4. ANALYSIS OF RESULTS

Results from the signal processing algorithm yield a PSD periodogram for each of the signals. This allows for the calculation of the change a specific harmonic, between normal and fault conditions. In essence, this methodology allows for an incipient fault to be diagnosed by constantly monitoring variations in the harmonics known to be affected by such a fault. The technique therefore requires information linking a fault to a specific harmonic or multiple harmonics. In order to establish this information, iterative simulations and experimental measurements were conducted and the data analysed.

In-depth analyses of the results indicate the following:

- Experimental results concur with the predictive model results.
- Perturbations in the magnetic fields can be related to various faults and imperfections on a rotating electrical machine.
- There are definite relationships between faults and specific harmonics of a shaft signal. A summary of the affected harmonics for the faults examined is given in Table 1.

- The extent of a fault is not limited to a single harmonic and can affect multiple frequencies. This implies an overlapping effect on frequencies that can occur during multiple fault conditions.
- Varying fault levels i.e. extent of fault, produce quantifiable variations in the affected harmonic implying that the proposed technique can be utilised to quantify the extent of the fault.

The exact effects of incipient faults on shaft voltage waveforms (time domain) are difficult to determine, however specific harmonics of the power spectra for these waveforms are more substantial. This is indicated in the resulting change of the 300 Hz frequency component for an eccentricity fault, as shown in Figure 6. An eccentricity fault of 1mm (17 % of nominal air-gap length) was used in this case.

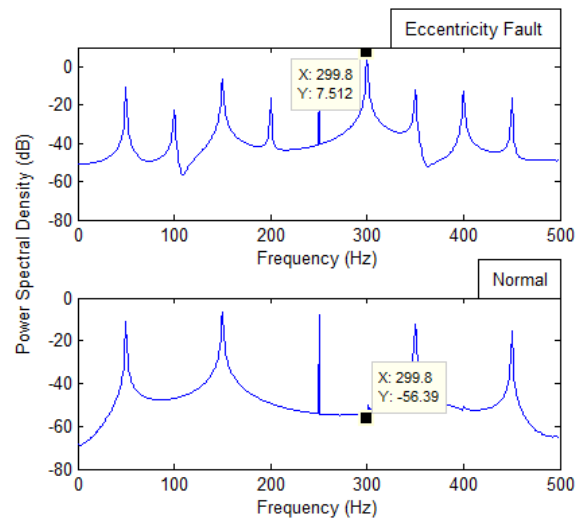


Figure 6: Comparison of Power Spectral Density plots for experimentally measured shaft signals of generator, under normal and static eccentricity conditions

Results obtained from a rectifier fault indicate a large degree of influence at 200 Hz and 250 Hz. This is due to the transmission of frequency content of the 50 Hz supply signal through the three phase rectifier to the rotor winding. Translation of the 50 Hz component onto the dynamic rotor winding i.e. 3000 rpm, provides the coupling of higher frequency components. Table 1 encapsulates the key fault-frequency relationships established during the investigation.

Table 1: Summary of investigated fault conditions and corresponding affected harmonics

Fault Condition	Affected Frequencies (Hz)
Rectifier Fault	200, 250
Rotor Winding Inter-turn Short	100, 300
Eccentricity	300

Simulations and experimental measurements of the field currents under rectifier fault conditions indicate the presence of these 50 Hz transients when compared to normal conditions. Static eccentricity introduces a considerable change in the 300 Hz component of the shaft signal.

Short-circuited turns on the excitation winding indicate a similar effect on the 6th harmonic and a distinguishable effect at 100 Hz. This is expected as shorted turns on the rotor windings generates a similar asymmetry in the rotating field due to weakened coupling, however it differs moderately from static eccentricity since the asymmetrical field is dynamic.

5. RECOMMENDATIONS FOR FUTURE WORK

Experimental data corresponds to the simulated results indicating the accuracy of the predictive model. Although there are prominently affected harmonics relating to a specific fault, additional even harmonics exhibit minor changes. Therefore it is necessary to investigate multiple or combinational fault conditions, in order to increase the certainty of a diagnosis. Furthermore, an overall improvement of the shaft voltage based condition monitoring technique is achievable through specification of confidence intervals for significant harmonics. It is also recommended that a more extensive range of faults be investigated to increase the integrity of the diagnosis. This is for the purpose of establishing a more comprehensive database of possible faults. Further investigation of the machine at different fault levels is also required to accurately quantify variations in the related frequency. This will allow for diagnosis of both the fault and extent thereof.

6. CONCLUSIONS

A description of shaft voltages in rotating electrical machines, specifically generators, was given. The origins and mechanisms of these voltages were also included. Traditionally, emphasis has been placed on mitigation of the phenomena through grounding brushes etc. However, more recently, extensive work is being conducted to correctly interpret these signals for use in the area of conditioning monitoring.

An investigation into this method for diagnosis of incipient faults on a synchronous generator has been presented. A predictive model was constructed and simulation of the generator model under normal and fault conditions were carried out using a finite element analysis package. Specific incipient fault conditions were selected and implemented in the model. Measurements on the actual generator were conducted using shaft brushes, under the same conditions. Measured data corresponds to the simulated results and indicate that specific faults induce distinguishable effects on the frequency content of power spectra of the shaft signals.

Results of this investigation indicate that incipient faults may be effectively diagnosed through analysis of frequency content of induced shaft voltages.

15. REFERENCES

- [1] P.I. Nippes: "Early warning of developing problems in rotating machinery as provided by monitoring shaft voltages and grounding currents", IEEE Transactions on Energy Conversion, Vol. 19, pp. 340 - 345, 2004.
- [2] GAMBICA/REMA Working Group: "Motor shaft voltages and bearing currents under PWM inverter operation", Technical Report No. 2, 2nd Edition, 2006.
- [3] M.J. Costello: "Shaft voltages and rotating machinery", IEEE Transactions on Industrial Applications, Vol. 29, No. 2, pp. 419 - 426, March 1993.
- [4] J.S. Sohre and P.I. Nippes: "Electromagnetic shaft currents in turbomachinery: An update, Parts 1 and 2", Amm. Plant Saf. , Vol. 23, pp. 185 - 202, 1981.
- [5] G. D'Antona, P. Pennacchi and C. Pensieri: "Turboalternator shaft voltage measurements", IEEE Applied Measurements for Power Systems (AMPS), pp. 1 - 4, September 2012.
- [6] R.J. Corkins: "The importance of grounding brushes to the safe operation of large turbine generators", IEEE Transactions on Energy Conversion, Vol. 3, No. 3, pp. 607 - 612, September 1988.
- [7] C. Ammann, K. Reichert, R. Joho and Z. Posedel: "Shaft voltages in generators with static excitation systems – problems and solutions", IEEE Transactions on Energy Conversion, Vol. 3, No. 2, pp. 409 - 419, June 1988.
- [8] E. P. R. I. Corporate: "Generator Stator Core Condition Monitoring by Tracking Shaft Voltage and Grounding Current", Electric Power Research Institute, California 1020275, 2010.
- [9] ANSI / IEEE: "IEEE Guide for Operation and Maintenance of Turbine Generators", IEEE 1972.
- [10] W. Yucai, L. Yonggang and L. Heming: "Diagnosis of turbine generator typical faults by shaft voltage", IEEE Industrial Applications Society Annual Meeting, pp. 1 - 6, October 2012.
- [11] P. Tavner, L. Ran, J. Penman and H. Sedding: "Condition monitoring of rotating electrical machines", vol. 56, IET Power and Energy Series, 2008, pp. 219–221.

Stator design for a 4kW axial flux permanent magnet generator

G.L. Clasen* and A.j. Grobler**

Abstract: There is a great need around the globe for the development of renewable energy technology. Axial flux machines are candidate technology in renewable energy applications. The nacelle casing of the 4kW axial flux permanent magnet generator (AFPMG) was constructed in 2012. This generator is designed for low speed applications for example in a direct drive wind turbine. The AFPMG which is developed makes use of the double stator; single rotor topology with the rotor placed between the two stators. The project was launched to complete the AFPMG so that the generator can be connected to a local wind turbine. The coils were manufactured and the AFPMG was assembled. The one stator had a short circuit and was therefore not tested. The second manufactured one was tested. The results from the test showed a poor voltage which prevents it from generating any significant power.

INTRODUCTION

The need for renewable energy is growing around the globe, especially with factors such as global warming and increasing electricity tariffs. In many rural areas there is no electricity grid nearby to supply the required electrical energy. Renewable energy sources such as solar and wind are typically used in these instances.

In the rural areas windmills are used to pump water from underground water sources. Most of the time a windmill pumps a small amount of water even if the wind is blowing at a reasonable speed. A wind turbine can be used in this application to supply power to a submersible water pump.

A generator has two main components, namely a rotor and a stator. The stator houses the windings that are wound around a magnetic or non-magnetic stator core. The rotor can consist of either windings that is wound around a permeable material or permanent magnets. When the rotor is rotated the magnetic field of the rotor induces an EMF in coils which is wound around the stator core.

Most generators and motors are manufactured in such a way that the flux of the machine flows in the radial direction in the air gap, these machines are called radial flux machines (RFM). The flux of the axial flux machine (AFM) moves in the axial direction through the air gap. The two topologies are shown in Figure 1.

A permanent magnet generator has permanent magnets on the rotor; therefore there are no slip rings that cause losses during operation and no maintenance is required to maintain the slip rings. Thus the permanent magnet generator requires little maintenance. The AFM can accommodate a large number of poles [1].

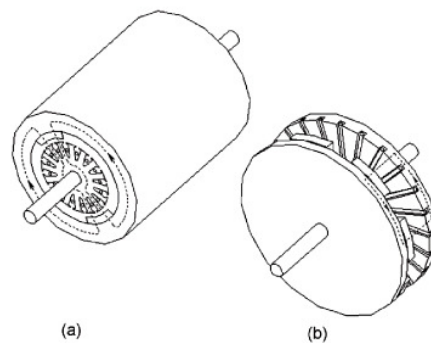


Figure 1 : RFM and AFM topologies [1]

The different topologies for AFM are shown in Figure 2. The double stator; single rotor topology which is used in this project is also known as the Kaman type. This figure shows that only the drum winding is implemented in the Kaman topology. The design for the magnets in the rotor for this project however has a unique.

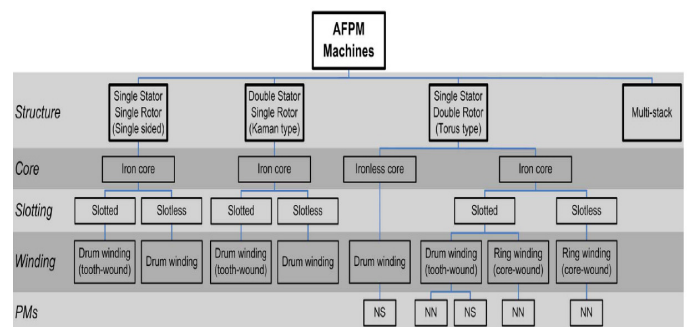


Figure 2 : AFM topologies [2]

The AFPM generator has been a subject for several projects at the North West University over the past few years. This project builds on these previous projects to prevent making the same mistakes as some of them during their design. In the previous projects the students used magnetic circuits to design the generator. One of these students also used Comsol Multiphysics® to design the generator.

CONCEPTUAL DESIGN

The generator is a double stator; single rotor topology. The layout of this topology which was used in the simulation is shown in Figure 3. In this figure it is important to note of the orientation of the magnets. The north pole of each magnet faces the north pole of the magnet next to it, thus forcing the flux into the air gap.

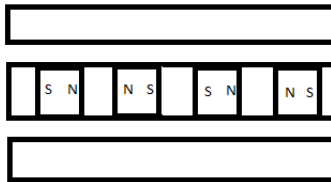


Figure 3 : Magnet layout of rotor

Figure 4 shows the flux lines to illustrate the paths which the flux flows in.

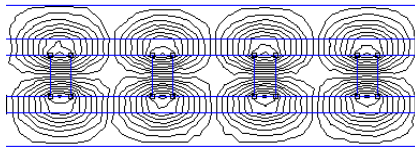


Figure 4 : Flux paths

A trade-off study is done to decide on a winding topology that will be used. There are four possible topologies that can be used and is listed in Table 1. The table contains four categories that were used to grade the respective topologies against each other. The last column contains the total score out of a possible ten points. The air gap was graded according to how small the air gap can be made between the core materials of the stator and the rotor respectively. It's obvious that a slotted machine will have a smaller air gap. The cogging torque is an important aspect for a wind turbine because it increases the cut-in wind speed. This is especially important for low wind speeds where the cogging torque may prevent the shaft from rotating. The ease of manufacturing category is also important to keep manufacturing costs low. In Figure 2 it was shown that only the drum winding is implemented in the Kaman topology. Due to the unique rotor layout it was decided to consider the ring winding for this project.

Table 1 : Concept design trade-off

Air gap	Cogging torque	Ease of manufacturing	Cost	Total
5	2	3	1	10

Topology					
Slotless drum winding	2	2	3	1	8
Slotted drum winding	5	0	1	0	6
Slotless ring winding	3	2	3	1	9
Slotted ring winding	5	0	1	0	6

The slotless Torus topology was chosen for the design of the generator. The trade-off in Table 1 indicated that this is the best suited topology to use. The two slotted topologies are shown in Figure 5 and Figure 6 respectively.



Figure 5 : Slotted drum winding

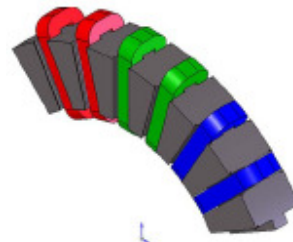


Figure 6 : Slotted ring winding

Another aspect of the AFPMG is whether it should be designed as a three-phase generator or if it should be designed as a single-phase generator. The advantages of three-phase generators above single-phase generators are [3]:

- Three-phase generators are smaller in size.
- Three-phase generators are more resistant to vibrations than single-phase generators.
- Voltage ripple is smaller in three-phase rectified DC.
- Three phase generators have a better power factor regulation.

The disadvantages of a three-phase design are:

Air gap (mm)	Number of turns per phase (200rpm)
4	3987
6	4558
8	6586
10	7975

ign is more complicated than a single-phase design.

- The air gap is larger, because less space is available.

The advantages of a single-phase are:

- Less complicated design
- Coils are easier to place

. DETAIL DESIGN

The simulation that is shown in this section was done in Comsol Multi-physics®. The simulation was done for a few variation in air gap dimension. Figure 7 shows the initial simulation for one phase.

In the initial design the following was assumed:

- 1) There is no leakage flux present in the system.
- 2) The magnetic material has no losses.

The line above the left magnet is used to integrate the flux density over the width of the stator core. This value is then multiplied by the length of the magnet. The magnets are then shifted in small increments to the left by means of a parametric sweep. The results from the parametric sweep give the flux the links the coil. These results are then exported to Excel® where the data is processed to give the voltage that is produced by a single coil over time.

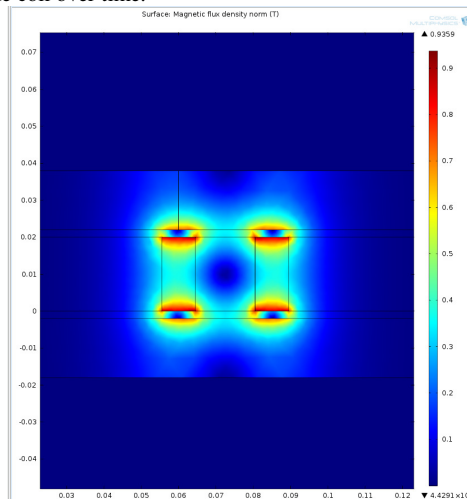


Figure 7 : Magnetic flux density (2mm air gap)

The initial design was for a rotation speed of 200rpm, but when the simulations was done it was seen that a rotation speed of 300rpm is required to yield a 50Hz waveform. An important aspect of the design is the air gap. The air gap should be as small as possible, since an increase in the air gap will increase the number of turns per phase to produce the specified output voltage. The specified voltage in this case is

- T 240V. The following table shows the results for the design h which assumed that there is no leakage flux present.

Table 2 : Initial simulation results

With the results from Table 2 it was assumed that an achievable air gap would be between 8mm and 10mm. A value of 5200 turns per phase was chosen for a rotation speed of 200rpm which results in a coil with 130 turns if 40 coils are used. One coil was wound on one of the stators and was tested after the machine was assembled. In fact thicker wire has to be used to be able to draw enough current to achieve the 4kW power rating. The simulation result for the 130 turn coil is shown in Figure 8. The output is 5.49V_{rms}.

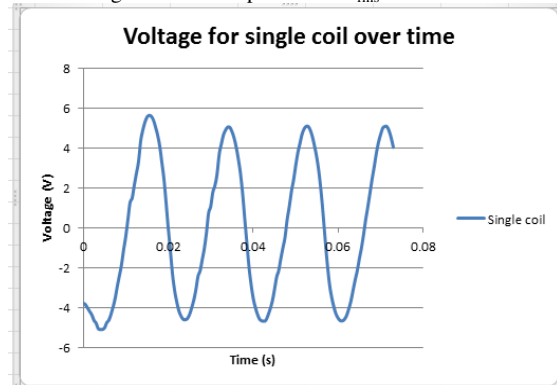


Figure 8 : Simulated voltage output for coil

The test results showed that ignoring leakage flux causes a significant under-approximation of the generated voltage. The result for the 200rpm test is shown in Figure 9. In this image it is shown that the generator generates 4.9V_{rms}.

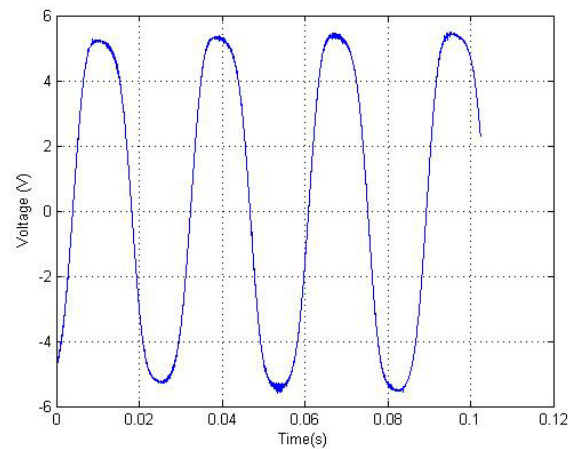


Figure 9 : Test result for 200rpm

The difference between the calculated voltage and measured voltage is due to the leakage flux. The additional flux is the leakage flux that was previously ignored. The next simulation that was done makes use of line integration from the top of the stator material to 1mm from the rotor core. This means that the flux that moves through most of the air gap is also linked to the coil. This value is again multiplied by the length of the magnet to achieve the total flux that links the coil. The results from the simulation are shown in Table 3. This simulation was done for a rotation speed of 300rpm. The table also contains the number of turns per phase when ignoring the leakage flux.

Now that the data from Table 3 is available it is necessary to determine which air gap is the smallest achievable air gap. It was determined that if there are 60 coils on a stator that the available width on the inside part of the stator is 6.15mm. When a large current density (6 A/mm^2) is assumed for the wire it will be possible to use the 0.63mm diameter wire. It was assumed that a packing factor of 0.61 is achievable which resulted that 96 turns per coil (3840 turns per phase) can be fitted in the given space of 8mm. Thus an air gap of 9mm is achievable. However I also assumed that the windings will not be thick everywhere and that an isolation material will also be used. Another half a millimetre was added to ensure that there is enough space between rotor and the two stators.

A three-phase simulation which is shown was done to determine the spacing between the coils of each phase. The blue lines indicate the centre of each coil and were spaced 15mm from each other.

Table 3 : Simulation results including leakage flux

Air gap size (mm)	Turns per phase excluding leakage flux	Turns per phase including leakage flux
2	1352	-
4	2047	2102
6	2876	2889
7	3352	3166
8	3976	3475
10	5086	4076
12	6202	5719
14	7251	7549
16	8563	8070
17	9082	8572
18	9424	8824

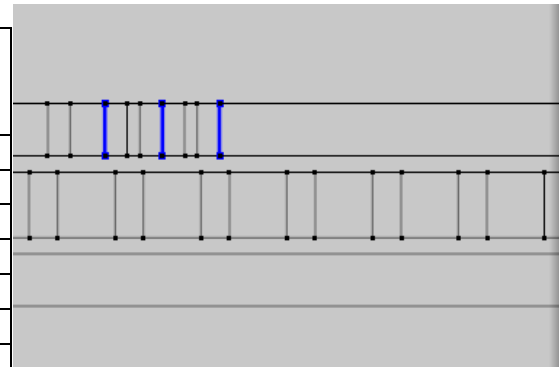


Figure 11 : Three-phase simulation

The result from this simulation is shown in Figure 11. The figure shows that the 240V output is achieved and that the phases are properly spaced.

Figure 10 shows the plot for the voltage induced for 3840 turns versus the air gap for both including and excluding the leakage flux.

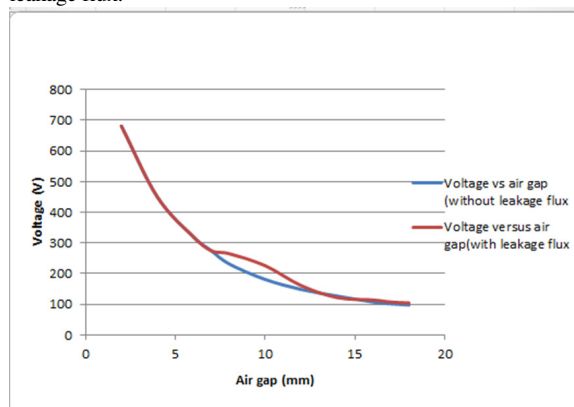
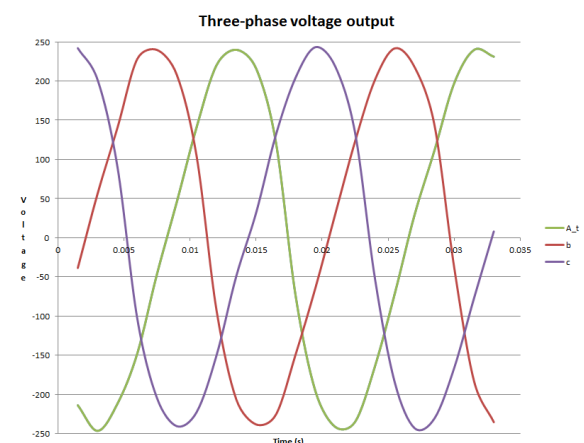


Figure 10 : Voltage versus air gap



The calculations that are done in this section are used to determine the amount of wire that will be needed to manufacture the coils of the stator. The calculations were

coded in MATLAB® to decrease the calculation time when variables are changed. The amount of turns that is required per phase in each stator is:

$$N=1920 \text{ turns}$$

. The length for a single turn is given as:

$$l = 0.311m$$

There are two stators and each stator has three phases; therefore the total number of turns that is needed is:

$$N_r = 3840$$

The length of copper wire that is needed to manufacture the coils is:

$$l_r = 3 \times 3840 \times 0.311$$

$$l_r = 4838.4m$$

The weight of copper wire per cubic meter is equal to 8960 kg. The diameter of wire that is needed for the stator is 0.63mm. This was determined by calculating the approximate current that will flow at full load. The amount of current was calculated as follows:

$$I = \frac{P_{out}}{\sqrt{3} \times V_{l-l} \times \eta \times \cos \theta}$$

$$I = \frac{4000}{\sqrt{3} \times 400 \times 0.9 \times 0.9}$$

$$I = 7.13A$$

The wire gauge was then determined to be 22 according to an American wire gauge (AWG) table. The volume of the copper wire is calculated in the code and is given as:

$$V = l_r \times \pi \times r^2$$

$$V = 1.9627 \times 10^{-4} m^3$$

The mass of the required amount of magnet wire is:

$$m_{cu} = 13.514kg$$

IMPLEMENTATION

The coils of the two stators were manufactured by Swift heat and Control. The company specializes in the development heat and control systems as well as toroidal transformers. The company has machines that are designed to wind this core topology. It was time-consuming to wound the coil that was used for testing.

The first stator was wound with 60 coils, with 96 turns each. The stator layout is shown in Figure 12. The coils consist out of three main colors which indicate the three phases of the generator. Then there is two color variations of each color, namely a dark one and a lighter one. The two variations in color indicate different directions in winding the coils. Each color is then connected in series with the rest of the coils with the same color. Each color therefore forms a phase.

The second stator was wound slightly different because it was wound with 30 coils which have 192 turns each. The coils are connected the same as in the previous paragraph. The resulting three phases are then each connected in series with the corresponding phase in the other stator.

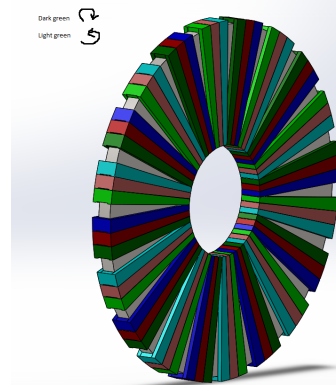


Figure 12 : Coil layout for stator 1

Figure 12 is the drawing that was sent to Swift Heat and Control.

Figure 13 shows the stator before it was vacuum pressure impregnated.



Figure 13 : First stator with coils

The second stator was not wound to the standard which was expected. The coils were wound unevenly which increased the air gap significantly. The layout of the coils was not wound correctly. The coils were shifted and rewound until the coils seemed that it would work. This stator is shown in Figure 14. In this figure it can be seen that the space between the different coil groups are not the same. The main problem areas are indicated with red arrows. This will have an effect on the output of the generator.

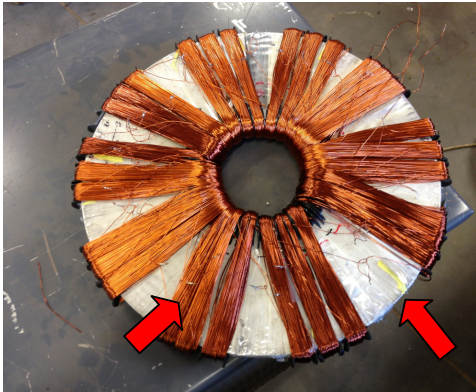


Figure 14 : The second stator after improvement

The white isolation material was tightly pulled against the stator by means of cotton rope. Figure 8 shows one of the stators after it was vacuum pressure impregnated (VPI). The stators were vacuum pressure impregnated by Mathinussen & Coutts.

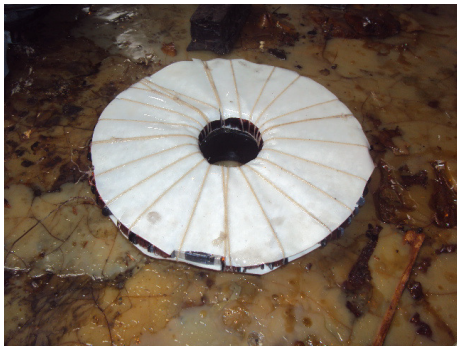


Figure 15 : Stator after vacuum pressure impregnation

The generator is now fully assembled, but test are required to check if the generator is capable of delivering 4kW.

TEST RESULTS

The first manufactured stator had a larger output voltage for each phase than the second manufactured stator, but during the no-load test it was noticed that two of the phases affect each other. A continuity test was conducted and it was determined that a short circuit occurred. The results for this stator are therefore not included.

In Figure 16 it is seen that the output of the three phases defer by a large margin. This is due to the poor spacing of the coils which was mentioned earlier.

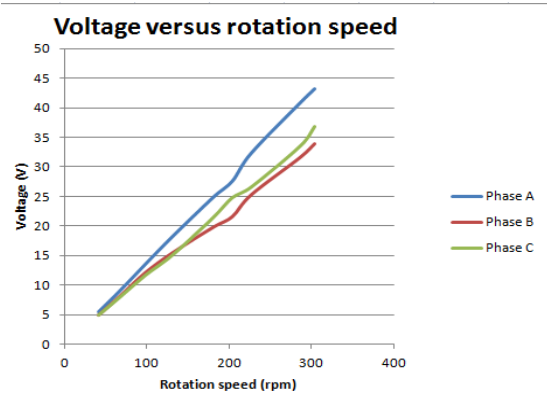


Figure 16 : Voltage versus speed characteristics

The no-load voltage of the three phases are shown in Figure 17. The output is lower then what it should have been. The reason for the lower output is the air gap that is 18.2mm. The stators were designed for a 9.5mm air gap.

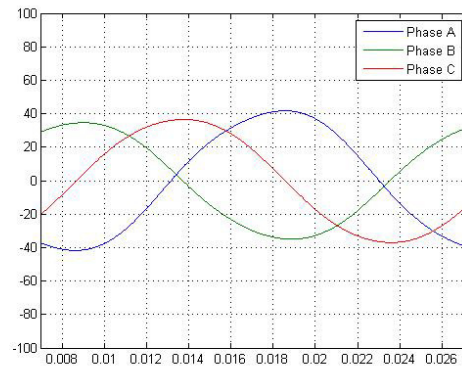


Figure 17 : No-load voltage output

The three-phases were connected in a star-connection and connected to a rectifier. A variable resistance was used to load the generator. The voltage regulation was so poor that only 15.2W could be dissipated.

CONCLUSION

The first important step in the design was to determine which topology was best suited for the project. The slotless Torus topology was chosen by means of a trade-off study. The second step was to decide between a three-phase and a single-phase design. The three-phase had superior advantages above the single-phase design and was therefore chosen for the design. A total of 3840 turns per phase were determined by assuming an air gap of 9.5mm. The final important step in the design was to determine the layout of all the coils to result in a balanced three-phase generator. The coils of the stators were manufactured and the stators were vacuum pressure impregnated. The two stators could not be loaded simultaneously, because the one had a short circuit. The voltage regulation was so poor that only 15.2W could be dissipated. If it was possible to redo the first stator and be

finished on time they could have been connected in series. The voltage regulation would have been better and the power output would have been much higher.

REFERENCES

- [1] J. Gieras, R.Wang and M.J.Kamper, Axial flux permanent magnet brushless machines, Dordrecht, The Netherlands: Kluwer Academic Publishers, 2008.
- [2] F. Capponi, G. D. Donato and F. Caricchi, "Recent advances in Axial-Flux Permanent-Magnet Machine Technology," IEEE transactions on industry applications, vol. 48, no. 6, pp. 2190-2205, 2012.
- [3] U.A. Bakshi and V.I. Bakshi. Electrical technology. Technical Publications Pune . 2003

GEAR RATIO SELECTION OF AN OUTER-STATOR MAGNETICALLY GEARED MACHINE

P.M. Tlali, S. Gerber and R-J. Wang

*Department of Electrical and Electronic Engineering
Stellenbosch University, Private Bag X1
Matieland 7602, South Africa
E-mail: 15894215@sun.ac.za*

Abstract: The selection of a gear ratio plays a critical role in the design of a magnetically geared electrical machine. It has been shown in literature that the gear ratio selection has a direct impact on the performance of the magnetically geared machine in terms of maximum torque limit, torque quality and core losses. Larger gear ratios are often preferred, which in turn requires greater difference in pole-pair numbers between the rotors of a gear. As a result, high pole-pair number on the low speed rotor is necessary. However, with a high number of pole-pairs, the inter-pole leakage flux tends to be more severe. In this paper, finite element analysis is used to investigate the effects of gear ratios on the performance of an outer-stator type magnetically geared machine. Relevant discussions are given and conclusions are drawn.

Key words: finite element analysis; geared electrical machines; gear ratio; permanent magnet.

1. INTRODUCTION

Geared electrical machines have proven to be more advantageous from the weight, size and output-per-cost perspectives than directly driven machines [1]. Mechanically geared machines are coupled together via shafts in order to achieve the conversion of low-speed / high-torque to low-torque / high-speed or vice-versa. However, the operation of a mechanical gear relies on the physical contact of teeth. Thus mechanical gears have inherent frictional losses and suffer from teeth wearing. Magnetic Gears (MGs) have increasingly received attention in recent years as an alternative technology.

Because of their contact-less operation, inherent overload protection, little or no maintenance, high torque density and efficiency [2, 3], MGs can potentially outperform their mechanical counterparts. Furthermore, they can easily be integrated into permanent magnet (PM) machines to form a more compact design. One notable type of such a magnetically geared machine (MGM), which was first presented in [4], incorporates a coaxial MG inside an outer-stator PM machine, as shown in Fig. 1.

There has been research focused on the influence of different design parameters on the performance of the MGs only. In [5], an investigation was done on the effects of the design parameters on the maximum torque capability of an MG. This study showed that amongst other parameters considered, the gear ratio has the major influence [5]. The same conclusion was proven to hold true for an axial field MG [6], where the optimum pole-pair number was also dependent on the air-gap length between the rotors. An in-depth simulation study on pole-pair combinations of MGs for wind turbine generators was made in [7]. It was concluded that the gear ratio affects both the magnitude

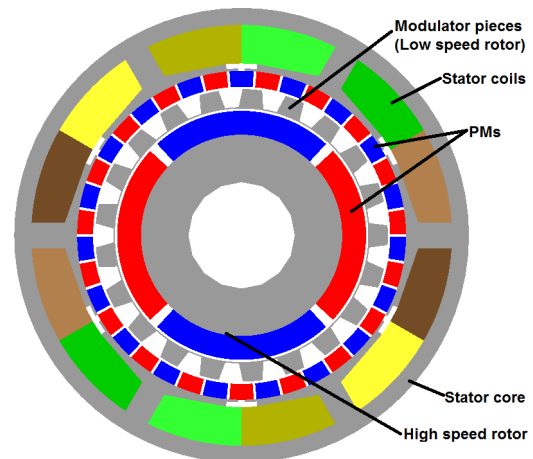


Figure 1: Outer-stator PM magnetically geared machine.

and the quality of torque. Although it was highlighted that there could be a practical limit to the number of pole-pairs used, higher gear ratios were found likely to have less ripples and larger torque capacity [7]. On the other hand, relatively little work has been reported on the impact of the gearing ratio and other design parameters on system torque and efficiency of combined MGMs. Similar to MGs, MGMs exhibit an increase in torque density as the gear ratio increases up to some optimal value [3, 8]. Evans and Zhu [9] conclude that the selection of such a best gear ratio is fundamental to optimal MGM design at a determined volume.

This paper investigates the effects of the gear ratio on the performance of an outer-stator MGM, shown in Fig. 1. Please note that all the designs in this paper are of the same outer radius and stack length. The mechanical layout

of the MGM under study and the relationship between its number of pole-pairs and gear ratios are explained in section 2. In section 3, the simulation setup for optimizing the considered machine and the imposed constraints are described. Section 4 discusses the effects of gear ratios on torque, core losses and some of the machine's component dimensions. Lastly, a conclusion is drawn from the presented results.

2. OUTER-STATOR TYPE MGM

This section briefly describes the main components of the outer-stator MGM and how they interact with each other to accomplish the overall working system. Moreover, the relation between the components' poles and their contribution to the gear ratio are elaborated on.

2.1 Machine configuration

The system layout of the MGM investigated in this paper is shown in Fig. 2. It comprises of the high speed PM rotor, low-speed ferromagnetic rotor (modulator) and the outer-stator with non-overlapping windings. Apart from carrying a balanced 3-phase winding, the stator core also supports PMs on its inner surface. These PMs, together with the modulator and high-speed rotor, form the MG part of this machine, while the stator and high speed rotor make up a PM machine.

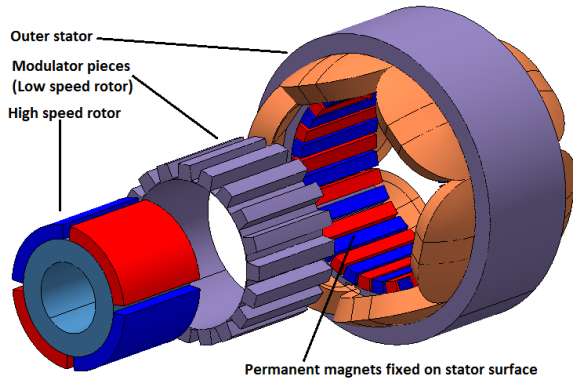


Figure 2: Structure of outer-stator magnetically geared machine.

In this MGM topology, both an MG and a PM machine are housed in a single volume sharing magnetic flux paths and mechanical structure. In this manner, high torque density can be achieved. Compared to the inner-stator type MGM designed in [10], the current topology has one less air-gap and thus a reduced mechanical construction complexity. On the other hand, the comparison study conducted in [11] found that the inner-stator MGM with three air-gaps is still better in both efficiency and torque density.

2.2 Torque transmission between the components

There exists two torque components within this type of MGM since it is a combination of two systems in one volume, that is, MG and PM machine. The first component, termed *magnetic torque*, results from the interaction of modulated fields from PMs on the high-speed rotor and field from the fixed PMs on the stator. The second one, called *electromagnetic torque*, is a result of the interaction between the field generated by the stator windings and the fundamental field of the high-speed rotor's PMs. Based on this, the high-speed rotor can be regarded as a coupling medium between the MG and PM machine. The modulator, being the input terminal, carries a large magnitude of magnetic torque. This value then gets scaled down onto the high-speed rotor according to the gear ratio as defined in the next section.

In order to achieve steady state operation, the magnetic torque needs to balance out with the electromagnetic torque experienced by the high speed rotor resulting in a zero net torque on the high speed rotor.

2.3 Relationship of gear ratio to number of poles

The basic principle of magnetic gearing operation derived and verified in [3, 12], boils down to two forms of gearing ratio G_r . The main difference between the two modes, illustrated by equations 2 and 3, is determined by whether the ferromagnetic pieces (modulator) or one of the rotors is fixed.

$$q_m = p_h + p_l \quad (1)$$

$$G_r = \frac{q_m}{p_h} \quad (2)$$

$$G_r = \frac{-p_l}{p_h} \quad (3)$$

In the above p_l , p_h and q_m are low-speed rotor pole-pairs, high-speed rotor pole-pairs and ferromagnetic pole-pieces, respectively. The second equation describes the case of MGM studied in this paper since the high number of PMs poles (p_l) are fixed on the inside surface of the stator core. That means the ferromagnetic modulator pieces will now form the low speed input rotor while the inner-most ring forms the high-speed rotor. It can be clearly seen from eqn. (2) that an increase in p_h decreases G_r whereas an increase in p_l increases G_r . Therefore, larger values of G_r can be obtained by maintaining greater difference between p_l and p_h . In synchronous PM machines, the value of p_h is equivalent to stator pole-pairs. Consequently, the selection of this variable has to abide by the stator pole/slot combination rules. This leaves p_l as a variable to be adjusted for different G_r values.

Conventionally, the balanced 3-phase stator can only have a number of slots which are multiples of 3. Likewise, both the stator and the rotor are limited to an even number

of poles. Several applicable stator pole/slot combinations for non-overlapping windings together with their resultant winding factors are listed in [13]. For the current study, the pole/slot combination was selected according to the criteria and procedure presented in [14]. Two stator pole/slot combinations, which can easily be accommodated within a small diameter of the proposed model are 4/6 and 6/9. Therefore, p_h will either be 2 or 3 throughout the entire investigation. The value of p_l is obtained by parameter sweeping through a certain range of numbers excluding those which give an integral G_r .

3. DESIGN OPTIMIZATION ENVIRONMENT

A dedicated design environment for MGs has been established, which consists of the following three components:

- SEMFEM - In-house developed FEM program.
- MagNet version - 7.1 from Infolytica Corporation.
- VisualDOC version - 7 from VR&D Inc.

Fig. 3 shows the process flow diagram used in the determination of maximum torque capacity at each G_r value. The combination of VisualDOC and SEMFEM is used to optimize the model for maximum torque per mass. This is done within the feasible search range as defined by the fixed dimensions and variable constraints shown in Tables 1 and 2, respectively.

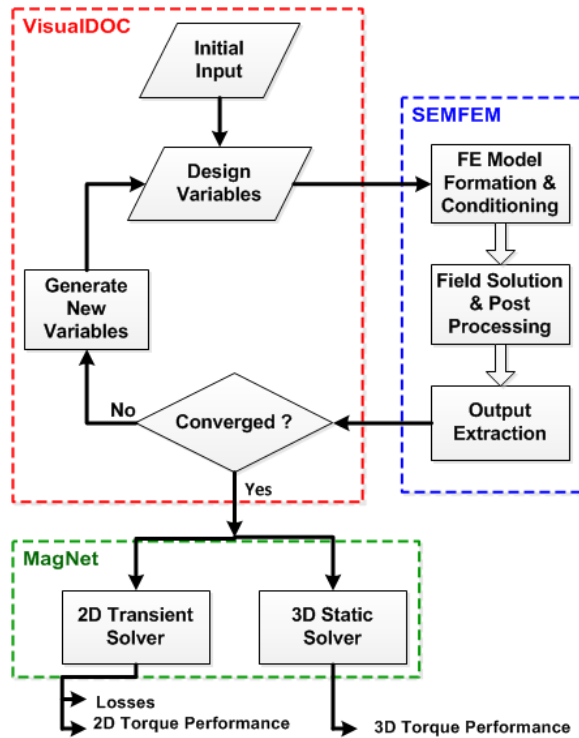


Figure 3: Flow diagram of the design optimization environment.

A gradient based optimization algorithm was used to solve the constrained problem formulated as:

$$\text{Maximize: } F(\mathbf{X}) = \text{Torque } (T_M) / \text{active mass} \quad (4)$$

$$\text{Subject to: } T_E \geq 0.8 \times T_M \quad (5)$$

$$t_{mh}/t_{ms} \leq 1.5 \quad (6)$$

where T_E is the electromagnetic torque, T_M is the magnetic torque on the high speed rotor, t_{mh} and t_{ms} are corresponding thickness of the rotor and stator magnets and, \mathbf{X} represents the variables in Table 2.

As illustrated in Fig. 3, VisualDOC iteratively directs inputs to and retrieves outputs from SEMFEM while also checking their compliance to the defined constraints. The task of SEMFEM is to perform the 2D FEM static simulation for each input set. To enhance the optimization time efficiency, VisualDOC has to be coupled with a fast FEM program. The choice of SEMFEM over MagNet for the above mentioned purpose is justified from Table 3, where the computational time is based on a desktop computer (Intel Core-i7 3.5GHz with 16GB RAM).

Table 1: Fixed geometric variables of the MGM.

Outer diameter of the machine (mm)	140
Stack length of the machine (mm)	50
Air-gaps (mm)	0.7

Table 2: List of design variables.

Description	min	max
Rotor yoke thickness (mm) t_y	8	15
rotor PM thickness (mm) t_{mh}	2.5	8
stator PM thickness (mm) t_{ms}	2.5	8
Rotor/stator PM thickness ratio t_{mh}/t_{ms}	0.667	1.5
PM span to pole-pitch ratio θ_s/θ_p	0.667	0.95
Modulator thickness (mm) t_{md}	6	
Modulator pole pitch ratio θ_{mi}/θ_{md}	0.45	0.7
Stator yoke thickness (mm) t_{sy}	4	-
Stator tooth thickness (mm) t_{st}	6	-
Stator tooth length (mm) l_{st}	10	-
Stator tooth base thickness (mm) t_{sb}	1.5	-
Slot pole to pitch ratio θ_{ss}/θ_{sp}	0.5	0.95
Slot open pitch ratio θ_{so}	0.1	0.5
Slot fill factor	0.3	0.55
Current density (A/mm ²)	1	5
Stator load-factor	0.8	-

Table 3: Computational time of different FEM packages.

Program	Simulation type	CPU Time (sec)
SEMFEM	2D-static	5
MagNet	2D-static	37
MagNet	3D-static	2700
MagNet	2D-transient	2040

Each optimum solution obtained from VisualDOC is then verified with MagNet's 3D static solver. Furthermore, a

2D FE transient simulation is carried out to analyze the transient behavior of that particular design.

The geometrical optimization variables in Table 2 are defined in Figs. 4-6. The modulator, situated between the two PMs sets, will be subjected to large attraction forces even for small imperfections in alignment. Hence, the minimum thickness constraint placed on this component is to ensure its mechanical integrity. The purpose of the thickness ratio between the two sets of PMs is to safeguard them against possible demagnetization, while the minimum PM thickness values take practical manufacturability into account.

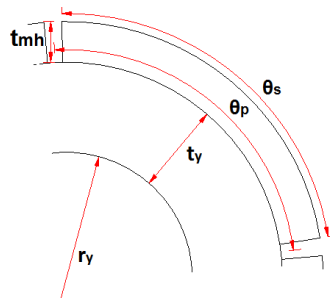


Figure 4: Portion of the MGM's high speed rotor showing design variables.

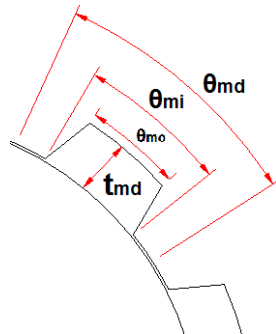


Figure 5: Portion of the MGM's modulator showing design variables.

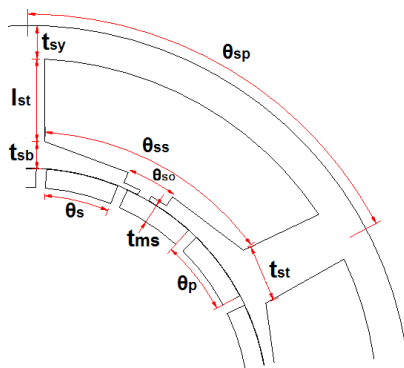


Figure 6: Portion of the MGM's stator showing design variables.

The stator load-factor is defined as the ratio of the stator electromagnetic- to gear's magnetic torques over the high speed rotor. It is constrained to avoid an under designed stator. The current density is limited to 5 A/mm² for all the designs since the machine is to be naturally air-cooled.

4. SIMULATION RESULTS

The performance of the MGM in terms of its maximum torque limit and quality, for a range of pole-pair combinations is assessed in this section.

4.1 Maximum torque capacity

The maximum torque capability of the machine as a function of the gear ratio is shown in Fig. 7. The graph includes both 2D and 3D FE simulated results for each of the 4/6 and 6/9 pole-slot combinations. The 3D FE results are around 20% less than those of 2D FE. This difference may be attributed to the 3D end effects which are ignored in the 2D FE solver.

It is important to note that all the graphs in Fig. 7 flatten as the gear ratio increases. The region where a graph's gradient declines significantly contains the preferred pole-pair combinations or the gear ratio values. This is because further increasing the gear ratio results in almost no gain in maximum torque.

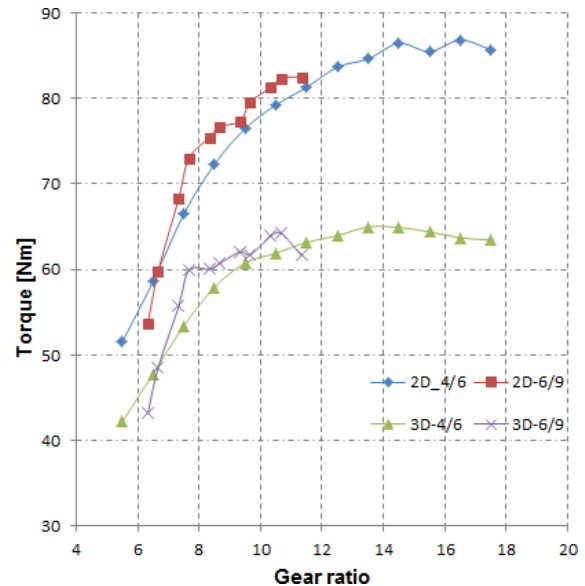


Figure 7: Maximum torque of the outer-stator MGM for different gear ratios.

Figure 8 confirms the stator load factor constraint as defined in section 3. The stator electromagnetic average torque is always around 80% of the maximum magnetic torque on high speed rotor at any instant. In other words, the stator can only be operated continuously up to 80% of the theoretic maximum load of the gear.

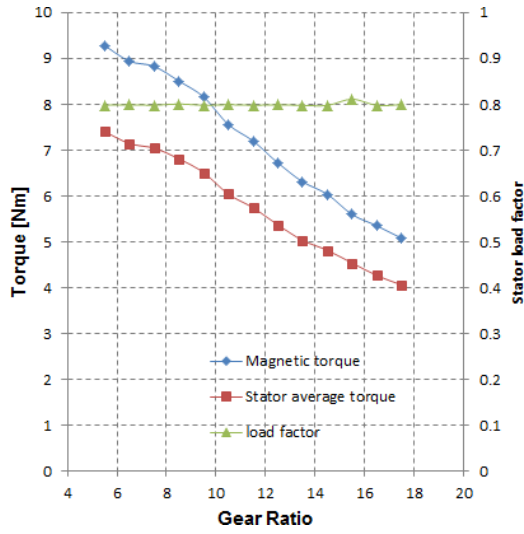


Figure 8: Comparison of electromagnetic and magnetic torques as seen by the high speed rotor showing a complied stator load factor.

4.2 Iron losses

The iron losses in this machine includes eddy current and hysteresis components, most of which are occurring in the stator core and modulator. These losses may be calculated by the following equation [15].

$$P_{iron} = P_h + P_e + P_{exc} = k_h f B_m^\alpha + k_e f^2 B_m^2 + k_{exc} f^{1.5} B_m^{1.5} \quad (7)$$

where B_m is the maximum flux density, f is the flux frequency, k_h , k_e , k_{exc} and α are the material specific loss coefficients which are normally provided by their manufacturers. The operating frequency in this type of MGM whereby the modulator is the mechanical input terminal is expressed in terms of the pole-pieces and input rotation speed as:

$$f = \frac{q_m n_{rpm}}{60} \quad (8)$$

where n_{rpm} is the rotation speed.

For a fixed input speed, the iron losses are a function of pole-pairs and flux density. Fig. 9 shows the plot of average core losses obtained from 2D FE transient analyses as a function of gear ratio.

For each of the two pole-slot combinations (4/6 and 6/9) considered, the iron loss graphs show a steady increase with the gear ratio. This proves that while the increase of G_r could be beneficial to the maximum achievable torque, the escalation of losses could degrade the machine's overall efficiency.

4.3 Cogging and ripple torque

The main source of the torque ripple is the cogging torque, which is caused by the interaction between the high speed

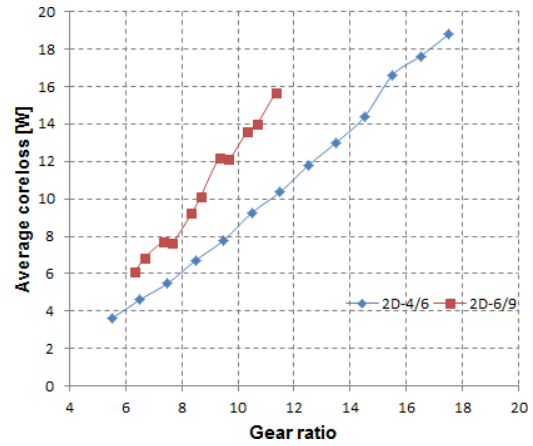


Figure 9: Average iron losses at different gear ratios.

rotor PMs and stator slots [16]. For MGMs, the cogging torque also depends on the least common multiple (LCM) between the rotors' pole-pair number and stator PMs. It is understood that the higher LCM value results in higher-order lower-amplitude of the cogging and ripple torques. The severity of this torque may be indicated by the so-called *cogging factor* f_c defined by eqn. (9), where p and q are number of pole pairs and slots respectively.

$$f_c = \frac{2pq}{\text{LCM}(p, q)} \quad (9)$$

In [7], the pole-pair combinations with whole, half and 1/3 gear ratios were found to have high cogging torque values. The pole/slot combinations selected for this study limits the gear ratio to either 1/2 or 1/3, hence relatively large cogging torque may be expected. Fig. 10 shows the computed cogging torques of the MGM.

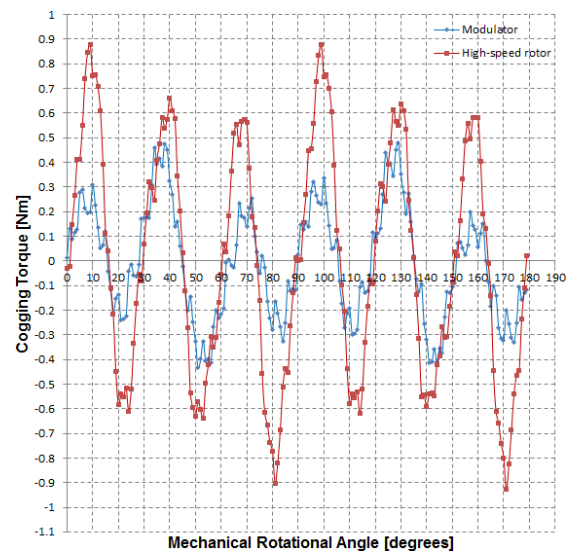


Figure 10: HS rotor and modulator cogging torque.

Fig. 10 further indicates that cogging torque on the high-speed rotor is larger compared to the one experienced by the modulator. This can be expected considering their pole-pairs numbers and respective LCM values.

4.4 Magnetic- and electromagnetic torques

The effect of the gear ratio on both the magnetic- and electromagnetic torques for a 4/6 pole/slot stator combination is shown in Fig. 11. As expected, the electromagnetic torque drops down while the magnetic torque rises as the gear ratio increases. The change in electromagnetic torque can be attributed to the reduction of the coil space area, which implies a reduction of electrical loading.

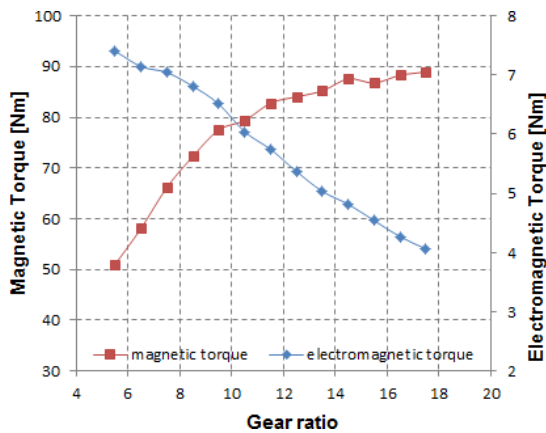


Figure 11: Electromagnetic and magnetic torques vs gear ratios.

Moreover, the change in coil space area is demonstrated by the decrease in stator radial length ($l_{st} + t_{sy} + t_{sb}$) shown in Fig. 12. The implication here is that as the gear ratio increases, the MG uses more space than the PM machine, which could compromise the balance between the two causing the under-design of a stator.

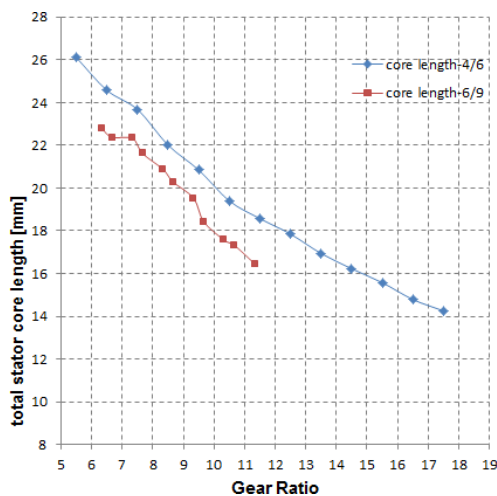


Figure 12: Stator radial length vs gear ratio

5. CONCLUSIONS

In this paper, the structural configuration of the outer-stator magnetically geared PM machine and its basic working principles, especially the torque transmission, have been explained. A dedicated design optimization platform for MGMs was then described. The optimization objective function was solved subject to the demagnetization and stator load factor constraints.

To determine the optimum gear ratio for the MGM with fixed diameter and stack length, the optimization analysis based on 2D static FE solver ran over a range of pole-pair combinations. Meanwhile each set of 2D FE optimized results were further verified in 3D FE analysis for comparison purposes, 2D FE transient simulation was also performed to analyze the core losses of the machine.

The presented simulation results show that the maximum torque of the MGM does reach an optimum value with an increase in the gear ratio. However, the rapid increase of frequency dependent losses with G_r could adversely affect the efficiency of the machine. Careful selection of the stator pole/slot combination could also assist in cogging torque minimization. In addition, the stator capacity is found to decline at larger number of pole-pair combinations.

ACKNOWLEDGMENT

This work was supported in part by ABB AB Corporate Research, Sweden and Stellenbosch University, South Africa

REFERENCES

- [1] H. Polinder, F. Van der Pijl, G.-J. de Vilder, and P. Tavner, "Comparison of direct-drive and geared generator concepts for wind turbines," in *Electric Machines and Drives, 2005 IEEE International Conference on*, 2005, pp. 543–550.
- [2] P. Rasmussen, T. O. Andersen, F. T. Joergensen, and O. Nielsen, "Development of a high performance magnetic gear," in *Industry Applications Conference, 2003. 38th IAS Annual Meeting. Conference Record of the*, vol. 3, 2003, pp. 1696–1702 vol.3.
- [3] K. Atallah, S. Calverley, and D. Howe, "Design, analysis and realisation of a high-performance magnetic gear," *Electric Power Applications, IEE Proceedings* -, vol. 151, no. 2, pp. 135–143, 2004.
- [4] K. Atallah, J. Rens, S. Mezani, and D. Howe, "A novel pseudo direct-drive brushless permanent magnet machine," *Magnetics, IEEE Transactions on*, vol. 44, no. 11, pp. 4349–4352, 2008.
- [5] D. J. Evans and Z. Zhu, "Influence of design parameters on magnetic gear's torque capability,"

- in *Electric Machines Drives Conference (IEMDC), 2011 IEEE International*, 2011, pp. 1403–1408.
- [6] T. Lubin, S. Mezani, and A. Rezzoug, “Simple analytical expressions for the force and torque of axial magnetic couplings,” *Energy Conversion, IEEE Transactions on*, vol. 27, no. 2, pp. 536–546, 2012.
 - [7] N. Frank and H. Toliyat, “Gearing ratios of a magnetic gear for wind turbines,” in *Electric Machines and Drives Conference, 2009. IEMDC '09. IEEE International*, 2009, pp. 1224–1230.
 - [8] K. Atallah and D. Howe, “A novel high-performance magnetic gear,” *Magnetics, IEEE Transactions on*, vol. 37, no. 4, pp. 2844–2846, 2001.
 - [9] D. J. Evans and Z. Zhu, “Optimal torque matching of a magnetic gear within a permanent magnet machine,” in *Electric Machines Drives Conference (IEMDC), 2011 IEEE International*, 2011, pp. 995–1000.
 - [10] K. Chau, D. Zhang, J. Jiang, C. Liu, and Y. Zhang, “Design of a magnetic-gear outer-rotor permanent-magnet brushless motor for electric vehicles,” *Magnetics, IEEE Transactions on*, vol. 43, no. 6, pp. 2504–2506, 2007.
 - [11] S. Gerber and R.-J. Wang, “Torque capability comparison of two magnetically geared PM machine topologies,” in *Industrial Technology (ICIT), 2013 IEEE International Conference on*, 2013, pp. 1915–1920.
 - [12] L. Yong, X. Jingwei, P. Kerong, and L. Yongping, “Principle and simulation analysis of a novel structure magnetic gear,” in *Electrical Machines and Systems, 2008. ICEMS 2008. International Conference on*, 2008, pp. 3845–3849.
 - [13] S. E. Skaar, Ø. Krøvel, and R. Nilssen, “Distribution, coil-span and winding factors for PM machines with concentrated windings,” in *Electrical Machines (ICEM), 2006 XVII International Conference on*, September 2006.
 - [14] S. Gerber and R.-J. Wang, “Design of a magnetically geared PM machine,” in *Power Engineering, Energy and Electrical Drives (POWERENG), 2013 Fourth International Conference on*, 2013, pp. 852–857.
 - [15] F. Deng, “An improved iron loss estimation for permanent magnet brushless machines,” in *Electric Machines and Drives Conference Record, 1997. IEEE International*, 1997, pp. WB2/3.1–WB2/3.3.
 - [16] L. Dosiek and P. Pillay, “Cogging torque reduction in permanent magnet machines,” *Industry Applications, IEEE Transactions on*, vol. 43, no. 6, pp. 1565–1571, 2007.

IMPLEMENTATION OF A MOVING BAND SOLVER FOR FINITE ELEMENT ANALYSIS OF ELECTRICAL MACHINES.

S. Gerber and R-J. Wang

*Department of Electrical and Electronic Engineering, Stellenbosch University, South Africa
E-mail: sgerber@sun.ac.za*

Abstract: The simulation of magnetically geared electrical machines using the finite element method is an especially demanding task when movement has to be considered. Several methods that facilitate movement exist and the most prominent ones are described in this paper. Based on the characteristics of these methods, the moving band is selected as the most appropriate for the simulation of magnetically geared machines. This method is implemented in an in-house finite element package and its performance is evaluated using two case studies. The accuracy as well as the computational efficiency of the moving band technique is compared to that of the air-gap element. For magnetically geared machines, the moving band is the preferred choice because of its low computational cost and acceptable accuracy.

Key words: moving band, air-gap element, finite element analysis, electrical machines

1. INTRODUCTION

Magnetically geared machines (MGMs) are a new class of electrical machine that integrates a conventional permanent magnet machine with a concentric magnetic gear. These machines are worth considering because of the exceptionally high torque density that they offer. Analyzing these machines using the finite element method is very demanding for two reasons: Firstly, the lack of periodicity often necessitates modeling of the full machine. Secondly, the machines have multiple air-gaps (typically two or three) which increase the problem complexity when movement has to be considered. An example of such a magnetically geared machine with an inner stator is shown in Figure 1.

In this paper, several different methods that facilitate movement in finite element meshes are briefly reviewed considering the requirements for simulating magnetically geared permanent magnet machines. Two of these methods, implemented in an in-house finite element code, are evaluated using two case studies which highlight the relative merits of each method.

2. MOVEMENT FACILITATING TECHNIQUES

The main methods used to facilitate movement in finite element analysis of electrical machines are the air-gap element (AGE), Lagrange multiplier method (LMM), mortar element method (MEM) and the moving band (MB). In this section, these methods will be reviewed briefly.

2.1 Air-gap element

The air-gap element [1] is a technique whereby the field in the entire air-gap region is calculated analytically using

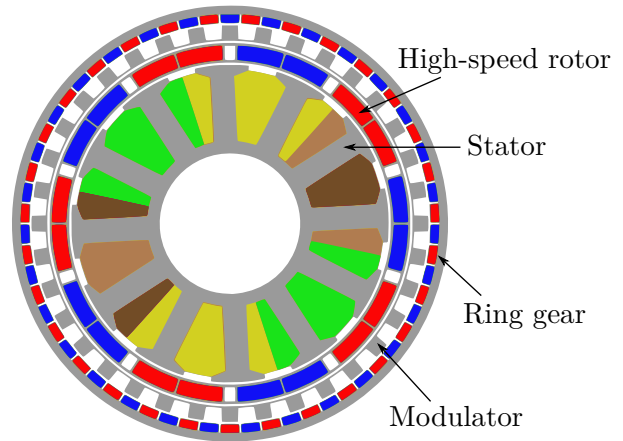


Figure 1: An example of a magnetically geared permanent magnet machine with an inner stator.

a Fourier series expansion of the vector potential. The field representation must satisfy the boundary conditions derived from the adjoining meshed regions. The vector potential in the air-gap takes the form

$$A(x, y) = \sum_i \alpha_i(x, y) u_i \quad (1)$$

where the α_i fulfill the role of a shape function and the u_i are the nodal values of the vector potential on the AGE boundary. Movement is accomplished by a simple recalculation of the α_i without any modification to the mesh structure, resulting in simple and efficient time-stepping [2].

Considering (1), it is clear that all the air-gap nodes are connected and thus, this method results in a dense block appearing in the final system matrix (see Figure 10) which can have a drastic impact on the computational time

required to obtain a solution. An advantages of the air-gap element technique is that the results can be very accurate because of the high order of the field representation in the air-gap region. Also, the Fourier series representation of the vector potential can be used directly to calculate the torque as described in [3].

2.2 Lagrange multiplier method

The sliding surface technique was first proposed in [4]. The idea is to split the model into two separate domains, Ω_a and Ω_b , and to ensure the continuity of the vector potential across the domain boundaries, an additional constraint

$$I_\lambda = \int_\Gamma \lambda(A_a - A_b)d\Gamma = 0 \quad (2)$$

is added to the standard finite element formulation. The solution to the coupled problem is obtained by minimizing

$$I(A_a, A_b, \lambda) = I_a + I_b + I_\lambda \quad (3)$$

with respect to the vector potentials of the two domains, A_a and A_b , and the Lagrange multipliers, λ . I_a and I_b are standard energy functionals,

$$I_a = \frac{1}{2} \int_{\Omega_a} \frac{1}{\mu} \left(\left[\frac{dA_a}{dx} \right]^2 + \left[\frac{dA_a}{dy} \right]^2 \right) d\Omega_a \quad (4)$$

$$I_b = \frac{1}{2} \int_{\Omega_b} \frac{1}{\mu} \left(\left[\frac{dA_b}{dx} \right]^2 + \left[\frac{dA_b}{dy} \right]^2 \right) d\Omega_b \quad (5)$$

The method also has the advantage that the structure of the mesh is maintained when moving, in other words, no remeshing is required. On the other hand, the method increases the system dimension by introducing an extra set of variables, the Lagrange multipliers.

2.3 Mortar element method

The mortar element method and the Lagrange multiplier method produce similar results [5], and can both be considered sliding surface techniques. In contrast to the LMM, the MEM deals with the interface between the two domains by considering one as the master and the other as the slave. The variables on the slave interface are functions of the variables on the master interface and so they can be eliminated. Thus, the methods differ in terms of the characteristics of the system matrices they produce. According to [5], the MEM produces a positive definite matrix whereas the LMM does not. This means that MEM systems can be solved by the Incomplete Choleski Conjugate Gradient (ICCG) method but LMM systems can not. On the other hand, MEM matrices have more nonzero entries than LMM matrices. It is concluded that the performance of MEM used together with ICCG quickly overtakes that of LMM with Gaussian elimination as the system dimension increases.

2.4 Moving band

This technique was first proposed in [6]. It has several advantages over the other techniques mentioned thus far. It employs no special elements or coupling techniques, it does not generate any dense blocks in the system matrix and it does not increase the system dimension. For these reasons, the moving band technique should be superior in terms of computational speed. However, there are difficulties with this method as well: Remeshing the air-gap region is inevitable and thus the numbering as well as the amount of nodes in the mesh does not stay constant. For this reason, the conditioning of the system matrix is not maintained and preconditioning routines must be rerun when the mesh changes. Also, because the elements in the air-gap are geometrically distorted to accommodate arbitrary movement, the results obtained using this method often have an oscillating error component.

2.5 General considerations

It is noted that the importance of having a sparse system matrix with a small profile depends on the method used to solve the system equation. In this study, a direct method (Lower-Upper factorisation) which is sensitive to the profile was used. Conjugate gradient methods may be less sensitive to the profile and could be considered in future.

Based on the above considerations, the moving band technique was selected as the most appropriate technique for modeling MGMs.

3. IMPLEMENTATION

In this section, the implementation of the moving band technique in an in-house Fortran finite element package call *SEMFEM* will be described.

A flowchart describing the working of the moving band solver is depicted in Figure 2. As shown in the figure, the first part of the solver consists of a single process which detects the number of air-gaps in the model and sets up the master data structures. The second part of the algorithm makes use of parallel processes where the number of time steps to be solved is divided among the number of threads. The parallelization is achieved using *OpenMP* [7]. Using this procedure, a significant speed-up can be achieved on multicore processors.

Two primary data structures are used in the solver. The first one stores the general mesh information, the second stores information on the moving bands. For every time-step, the bands have to be shifted which results in distortion of the elements and possibly reconnection of the air-gap nodes to avoid badly shaped elements. In periodic models where the full machine is not simulated, additional nodes also need to be added in order to maintain correct boundary conditions.

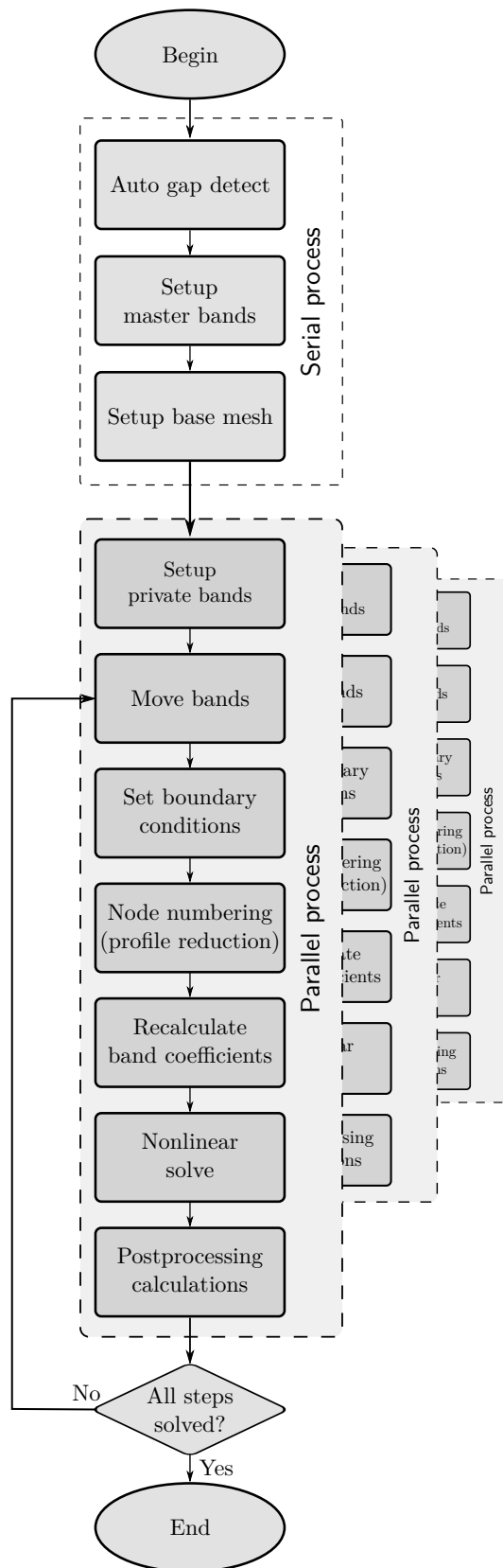


Figure 2: Flowchart of the moving band solver.

Once the bands have been correctly setup for a specific time instant, the information is appended to the base mesh to form a mesh specific to this time instant, complete with elements in the air-gap regions. The next step is to apply the appropriate boundary conditions to this mesh.

Because of the difference in the number of nodes and their numbering, a new mapping of nodes to unknowns is required for each time-step and similarly, profile reduction is executed for each time-step. It is noted that with the air-gap element technique previously implemented in *SEMFE*M, profile reduction was only performed once before proceeding to solving. However, the reduction in solution time due to the improved conditioning of the system matrix obtained with the moving band technique far outweighs the cost of the additional profile reductions, especially for multiple air-gaps with many nodes.

Prior to solving, the matrix coefficients related to the elements in the air-gap must be recalculated. The coefficients for the rest of the model are constant and are calculated only once, before starting the time-stepping procedure. The nonlinear problem is solved using the Newton-Raphson method.

Finally, the post-processing calculations of the torque, flux-linkage and copper loss are also performed in parallel.

4. VERIFICATION AND PERFORMANCE EVALUATION

In order to evaluate the accuracy and performance of the moving band solver, this section reports simulation results for two machines. The first machine is an interior permanent magnet (IPM) machine, shown in Figure 3. The second is the magnetically geared machine introduced in Figure 1. Both machines were simulated using air-gap elements as well as moving bands with a coarser and a finer mesh. The only difference between the air-gap element and the moving band models lies in the modeling of the air-gap regions. The meshes in the rest of the models were exactly the same. However, the underlying torque calculation method for the two movement methods also differ. For the air-gap element, the maxwell stress tensor method, as described in [3] is used. For the moving band method, the Coulomb virtual work method [8, 9] is used.

4.1 Interior permanent magnet machine

A time-stepped simulation consisting of 200 static solutions was performed for the IPM machine. Figure 4 shows a comparison of the torque calculated using the two movement handling methods for a relatively coarse mesh. It can be seen that the average torques are in good agreement, however, the torque calculated using the MB has a high frequency oscillation. This illustrates the superior accuracy of the AGE in coarse meshes. Typically when using the MB, the air-gap region would be meshed

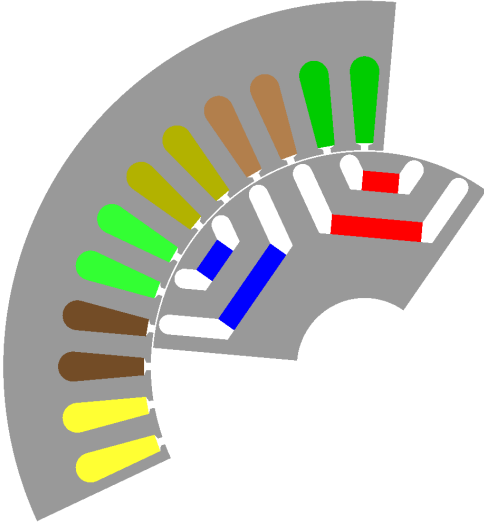


Figure 3: Single air-gap, periodic model of a synchronous PM reluctance machine.

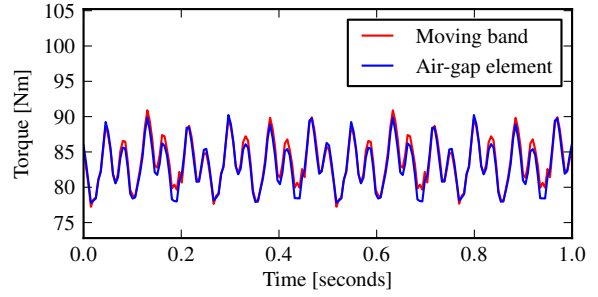


Figure 6: IPM machine: Torque comparison with a fine mesh.

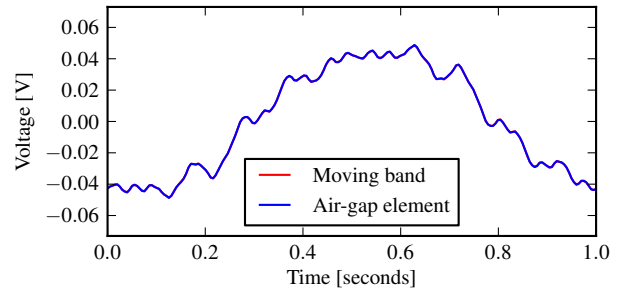


Figure 7: IPM machine: Voltage comparison with a fine mesh.

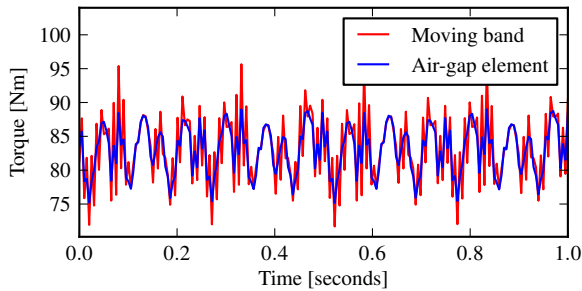


Figure 4: IPM machine: Torque comparison with a coarse mesh.

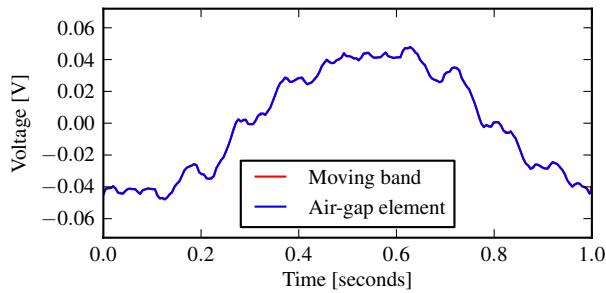


Figure 5: IPM machine: Voltage comparison with a coarse mesh.

finer than when using the AGE in order to improve the accuracy, with some added cost in computational time. However, such refinements are not considered in this paper. Figure 5 shows a comparison of the phase voltage for the coarse mesh. The results are in very good agreement.

The results for a simulation with a finer mesh are shown in Figures 6 and 7. Note that the calculated torques match very closely in this case. Once again, there is almost no difference in the calculated phase voltage.

4.2 Magnetically geared machine

The simulation of the MGM consisted of 50 time steps. Figure 8 shows a comparison of the calculated torques in each of the three air-gaps of the machine using the two movement methods. These results are for a relatively coarse mesh. Clearly, the results are in good agreement, although the moving band method's results for the outer air-gap does have a small oscillation. The phase voltages, shown in Figure 9, match very closely. Similar results have been achieved with a finer mesh, the only difference being a reduction in the torque ripple calculated using the MB.

4.3 Performance comparison

The simulations were run on an Intel i7 CPU with 4 cores (8 virtual cores). Both methods exploit the multi-core architecture to run calculations in parallel. The calculation times for the different simulations are given in Table 1. Note that in all cases the MB was significantly faster

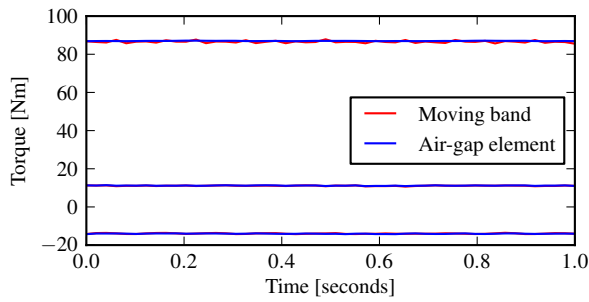


Figure 8: Torque comparison.

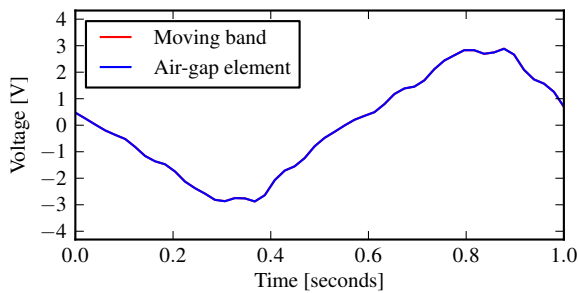


Figure 9: Voltage comparison.

than the AGE, but for the MGM a vast improvement in computational times is observed. The MB is roughly 20 times faster than the AGE for the MGM. Considering that the accuracy of the torque calculation for the MGM was also acceptable, the MB is definitely the preferred choice for the simulation of MGMs.

In order to explain why the MB band performs so much better than the AGE in the case of the MGM, Figure 10 illustrates the structure of the final system matrices obtained using the AGE and the MB. The contribution of the three air-gap elements are clearly present in the AGE matrix in the form of the three dense blocks. The profile of the AGE matrix is also higher than that of the MB matrix. The MB matrix can be solved efficiently using the direct method employed in *SEMFEM*.

Simulation case	Calculation times [seconds]	
	AGE	MB
IPM machine (2355 nodes)	19.7	9.4
IPM machine (7076 nodes)	108.5	68.9
MGM (9858 nodes)	971.8	37.4
MGM (28436 nodes)	7074	376.4

Table 1: Performance comparison of movement methods

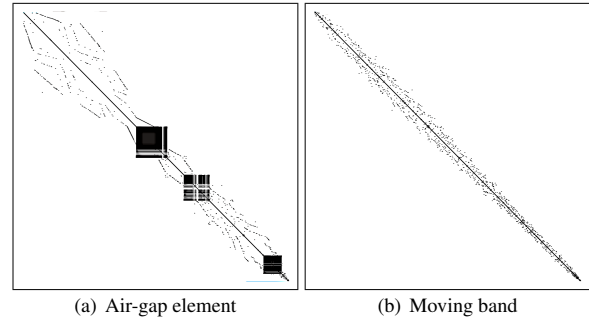


Figure 10: Matrices generated by FEM.

5. CONCLUSIONS

In this paper, the most prominent movement facilitating methods used in finite element analysis of electrical machines were briefly reviewed. The simulation of magnetically geared machines is very demanding when movement is considered. The difficulty is due to multiple air-gaps and lack of periodicity in the models. Considering these properties, the moving band method is a good choice when a direct method of solving the final system equation is employed. This is because it produces a highly sparse system matrix with the lowest bandwidth of all the methods considered. The method has been implemented in an in-house finite element package and good agreement with results obtained with air-gap elements have been demonstrated. For an example magnetically geared machine, the computational time when using the moving band is roughly 20 times less than when using the air-gap element. On the other hand, the superior accuracy of the air-gap element when using relatively coarse meshes have been demonstrated and it remains a valuable method, especially when the model size can be reduced by exploiting periodicity.

6. FUTURE WORK

Among the many techniques of solving the final system equation, the ICCG method [10] is a widely used method. The method has the advantage that it is not strongly affected by the bandwidth of the system matrix [11]. For this reason, the other methods considered in this paper may show a significant improvement in performance if this type of equation solver is used. These possibilities should be further investigated.

The problem of noisy results due to the distortion of the moving band elements can be avoided by using higher-order elements in the moving band, as demonstrated in [12]. If the accuracy of the first order implementation proves to be insufficient in some cases, it is recommended that higher-order hierarchic elements be used in the moving band.

ACKNOWLEDGEMENT

This work was supported in part by the National Research Foundation (NRF), Eskom Tertiary Education Support (TESP) and Stellenbosch University, all of South Africa.

REFERENCES

- [1] A. Abdel-Razek, J. Coulomb, M. Feliachi, and J. Sabonnadiere, "Conception of an air-gap element for the dynamic analysis of the electromagnetic field in electric machines," *IEEE Trans. Magn.*, vol. 18, no. 2, pp. 655–659, March 1982.
- [2] T. Flack and A. Volschenk, "Computational aspects of time-stepping finite element analysis using an air-gap element," *Proceedings of ICEM'94, Paris*, 1994.
- [3] A. Abdel-Razek, J. Coulomb, M. Feliachi, and J. Sabonnadiere, "The calculation of electromagnetic torque in saturated electric machines within combined numerical and analytical solutions of the field equations," *IEEE Trans. Magn.*, vol. 17, no. 6, pp. 3250–3252, November 1981.
- [4] D. Rodger, H. Lai, and P. Leonard, "Coupled elements for problems involving movement," *IEEE Trans. Magn.*, vol. 26, no. 2, pp. 548–550, March 1990.
- [5] O. Antunes, J. Bastos, N. Sadowski, A. Razek, L. Santandrea, F. Bouillault, and F. Rapetti, "Comparison between nonconforming movement methods," *IEEE Transactions on Magnetism*, vol. 42, no. 4, pp. 599–602, April 2006.
- [6] B. Davat, Z. Ren, and M. Lajoie-Mazenc, "The movement in field modeling," *IEEE Transactions on Magnetism*, vol. 21, no. 6, pp. 2296–2298, November 1985.
- [7] OpenMP Architecture Review Board, "OpenMP application program interface version 3.1," 2011. [Online]. Available: <http://www.openmp.org/mp-documents/OpenMP3.1.pdf>
- [8] J. Coulomb, "A methodology for the determination of global electromechanical quantities from a finite element analysis and its application to the evaluation of magnetic forces, torques and stiffness," *IEEE Transactions on Magnetism*, vol. 19, no. 6, pp. 2514–2519, 1983.
- [9] J. Coulomb and G. Meunier, "Finite element implementation of virtual work principle for magnetic or electric force and torque computation," *IEEE Transactions on Magnetism*, vol. 20, no. 5, pp. 1894–1896, 1984.
- [10] J. A. Meijerink and H. A. van der Vorst, "An iterative solution method for linear systems of which the coefficient matrix is a symmetric M-matrix," *Mathematics of Computation*, vol. 31, no. 137, pp. 148–162, 1977.
- [11] C. Trowbridge and J. Sykulski, "Some key developments in computational electromagnetics and their attribution," *IEEE Transactions on Magnetism*, vol. 42, no. 4, pp. 503–508, 2006.
- [12] O. Antunes, J. Bastos, and N. Sadowski, "Using high-order finite elements in problems with movement," *IEEE Transactions on Magnetism*, vol. 40, no. 2, pp. 529–532, 2004.

SIMULATION OF DELTA MODULATED PWM-FED BDCE CONTROLLED NINE PHASE INDUCTION MACHINE DRIVE.

L Gunda* and N Gule*

*Stellenbosch University, Department of Electrical and Electronic Engineering, Stellenbosch.

Abstract: The paper presents the simulation of a delta modulated Pulse Width Modulation (PWM)-fed Brush DC Equivalent (BDCE) controlled nine phase induction machine drive. The BDCE control method involves the decoupling of the stator current into a torque producing component and a field producing component. The BDCE controlled drive is simulated using both Matlab/Simulink and JMAG finite element analysis software for determination of the electro-mechanical characteristics of the induction machine. The control algorithm for the actual drive is to be implemented in software therefore the integrator in Matlab/Simulink is implemented using the trapezoidal integration algorithm instead of using the inbuilt integrator block. The simulation model produces eighteen PWM signals to trigger the nine full H-bridge inverters supplying the nine stator phases. The results of the delta modulated controller simulation compare closely with the results obtained using a hysteresis current controller on the same machine drive and show reduced current and torque ripples.

Key Words. BDCE control; hysteresis controller; Delta Modulation; modelling and simulation.

1. INTRODUCTION

Induction motors are the work horses of industry for variable speed applications and their control has been greatly researched on to optimise performance. The cage rotor induction motor in particular has got more attention because of mechanical robustness, simple construction, and less maintenance [1], [2]. There is also increasing research in the implementation of multiphase induction motors to reduce stator current per phase, machine noise, current and torque ripples [3].

Research has been done on control methods for these induction motors based on scalar control, vector control or field oriented control, direct torque control, Proportional-Integral (PI) control and fuzzy logic [9]. These methods have been well developed but coordinate transformations become complex when considering multi-phase machines especially for vector control and direct torque control. A relatively new control method, the Brush DC Equivalent (BDCE) control method, has been proposed in [10] for a six phase wound rotor induction machine and further work is presented on the method in [11] to implement it on a nine phase cage rotor induction machine. The BDCE control method does not involve any coordinate transformations but it uses stator phase windings as alternately flux or torque producing phases [10], [11] and hence is simpler to implement as the number of machine phases increases.

The performance of machine drives is mainly affected by the inverter switching mechanism and the current control method used which directly affects the harmonic performance of the machine. The current controllers mainly used in induction motor control are the hysteresis controller, the PI controller and the delta modulator, [9]-[15]. The hysteresis controller is implemented on the BDCE method described in [10] and [11]. The performance has been observed to be good though there are concerns about the amount of heat produced in the inverter at lower speeds.

In this paper, the simulation of the BDCE controlled nine phase induction machine drive using a delta modulated current controller is presented. The delta modulated PWM inverter fed induction machine drive is simulated using Matlab/Simulink to replace the hysteresis controller previously used in the model in [10]

and [11]. This model includes a full H-bridge circuit realised using discrete IGBT models to emulate the 6MBP25RA120 three-phase IPMs used in the inverter. The results are compared to the hysteresis controller results.

In section 2 the overall control strategy used in the BDCE control method is presented and in section 3 the development of the model of the induction machine drive is presented. The simulation results, their discussion and analysis are presented in section 4 and in section 5, the conclusions drawn from the simulations are given.

2. THE BDCE CONTROLLED NINE PHASE INDUCTION MACHINE DRIVE

The BDCE method introduced in [10] and further analyzed in [11] is based on the use of trapezoidal stator currents such that the stator phase can act alternately in time as either a flux or a torque producing phase. The machine phases are grouped into three groups which are 120 electrical degrees apart, and the phases within a group are 20 electrical degrees apart. The winding mechanism is such that at each instant, three neighboring phases act as either torque or field producing phases.

The stator currents produce a flux which induces voltages and currents in the rotor phases at slip speed and the rotor currents produce a rotor magneto-motive force (mmf) which tends to distort the air gap flux pattern. The torque producing stator current balances out this mmf giving a balanced mmf condition for flux decoupling. This condition ensures that the field producing phases produce a uniform flux density in the air gap. This implies that there is a fixed relationship between the torque current, I_t , and the angular slip frequency ω_{sl} , for balanced mmf control (or decouple control) and the relationship is given in equation (1) below.

$$k = \frac{\omega_{sl}}{I_t} \quad (1),$$

This relationship in (1) is used in the control system and k is the control gain used.

The trapezoidal stator wave used in the BDCE control method is constructed by optimizing the ratio of the number of field phases to the number of torque phases for the machine as described in [11]. Fig.1 below shows the trapezoidal waveform used in the BDCE control method. I_f is the field current and I_t is the torque current.

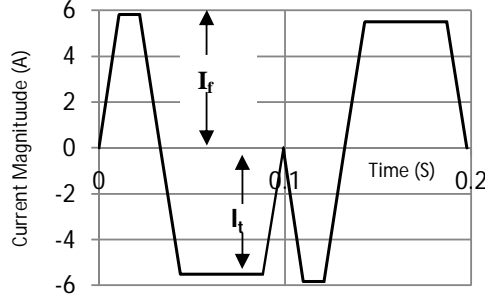


Fig.1: Trapezoidal current waveform used in BDCE control.

2.1 The control system

Fig.2 is the block implementation of the control system including the nine-phase inverter and motor.

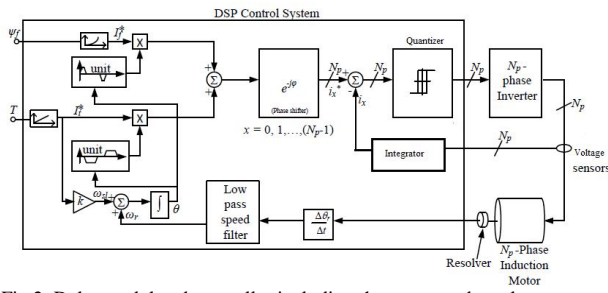


Fig.2: Delta modulated controller including the motor and resolver.

The control system comprises of a reference current generator block, a current controller, a nine phase inverter and a position resolver connected to the motor shaft. The resolver is used to determine the angular position of the rotor as the machine rotates. The time derivative of the angular position gives the rotor speed in revolutions per radian. From equation (1), the slip frequency ω_{sl} is determined by multiplying the torque current I_t and the gain constant k . The sum of the slip frequency and the rotor frequency gives the synchronous frequency which is used to determine the synchronous position of the rotor. The synchronous position is used in the look up table to determine the value of the stator phase current at each time instance.

The reference current is used in the current controller for the determination of the output state of the PWM signals as described later. Two major types of current controllers are used in the control system and these are the hysteresis current controller and the delta modulated current controller.

Current research shows that delta modulation is gaining popularity in motor control strategies because of its inherent filtering performance which eliminates lower order harmonics in the output voltage [12]- [16]. The delta modulated current controlled PWM-fed inverter

was first proposed in [12] and analyzed in [13], [16] and [17] forming the basis for its use in variable speed motor control. The delta modulator is shown in Fig.3.

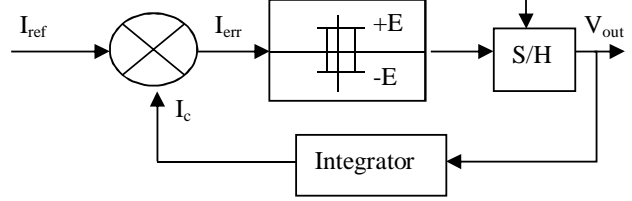


Fig.3: Delta modulated current controller

The main components of the delta modulator are the two level quantizer and the integrator. A carrier current waveform I_c is produced by integrating the hysteresis comparator output voltage V_{out} the integrator output is compared to the reference current I_{ref} to give an error signal I_{err} . The quantizer compares the error to the set hysteresis band value. When the error is above the hysteresis band value, the hysteresis comparator output is positive level $+E$ and when the error is below the hysteresis band value, the output is negative level $-E$. The two levels of the comparator output determine the state of the PWM output.

The control algorithm of the drive is implemented in a Digital Signal Processor (DSP) which is augmented by a Field Programmable Gate Array (FPGA) in both [10] and [11]. The FPGA receives the measured values from the machine and pre-processes them for use by the DSP. The DSP handles the control algorithm and passes its output to the FPGA which produces the PWM signal to control the inverter.

3. INDUCTION MACHINE MODEL

The induction machine drive has been fully modelled in [10] and [11] and in this presentation, only the calculation of machine parameters is presented. The stator circuit is designed from the per phase equivalent circuit shown in Fig.4. Equation (2) relates the supply voltage to the voltage drops in the circuit as presented in [10], [11], [19]-21].

$$\begin{aligned} V &= ir + v_L + e_m \\ &= ir + L \frac{di}{dt} + k\omega_s \end{aligned} \quad (2)$$

where V is the phase supply voltage, r is the stator resistance, i is the phase current, v_L is the voltage across the stator inductance, L is the stator inductance, k is the mutually induced voltage constant, ω_s is the motor synchronous frequency and e_m is the mutually induced voltage. Rearranging equation (2) gives equation (3) which is used to develop the motor phase model.

$$i = \frac{\int (v - ir - k\omega_s) dt}{L} \quad (3)$$

From equation (3) above, it is evident that the phase inductance L and the induced k are crucial parameters in the development of the phase model. The parameters can be calculated using flux linkage values obtained from JMAG finite element analysis software, using motor

parameter tables or can be measured on the induction machine under consideration. The equivalent circuit related to equation (3) is shown in Fig. 4 below.

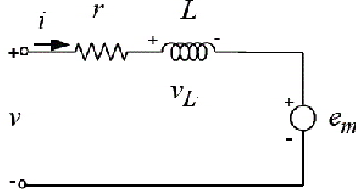


Fig.4: Stator phase equivalent circuit.

JMAG simulation software is used to simulate electrical, magnetic and mechanical performance of the machine. It uses finite element analysis to determine the performance and Williamson [18] gives details about the use of finite element analysis in modelling induction machines. The inductance L is calculated using the forward difference equation (4) which uses the change in flux linkage with the change in current through the phase coil.

$$L = \frac{\lambda(i+\Delta i) - \lambda(i)}{\Delta i} \quad (4),$$

where: λ is the instantaneous flux linkage, i is the instantaneous phase current and Δi is a small change in the current which causes a small change in flux linkage without affecting the balanced mmf condition [10],[11].

Equation (4) gives the general formula for calculating phase inductance using coil flux linkage. The phase current is split into a field and a torque producing phase and therefore the inductance for each phase is calculated separately depending on whether the phase is in the torque (L_t) or field (L_f) region of operation for a BDCE controlled drive.

Inductances can also be calculated using motor graphs given in [22]. The graphs use trend lines and hence estimated motor power factor is used in calculating the machine parameters. This requires prior knowledge of the motor power rating, number of poles and power factor. Fig.5 shows the resistance graph for a 4 pole induction machine as an example. A vertical line is drawn from the power axis until it crosses the parameter trend line. A per unit parameter value is read out from the graph. The base impedance is calculated using the phase voltage and current flowing in it. The reactance and resistance values are calculated using the impedance as shown in equation (5):

$$Z = \sqrt{R^2 + X^2} \quad (5),$$

where Z is the phase base Impedance, R is the base resistance and X is the base reactance. The per unit values extracted from the graph is multiplied with the base value to determine the actual machine parameter.

For practical measurements, an RLC meter is the easiest instrument to use. It gives the resistance, the capacitance and the inductance of the circuit connected to its terminals without any need for calculations or circuit manipulation.

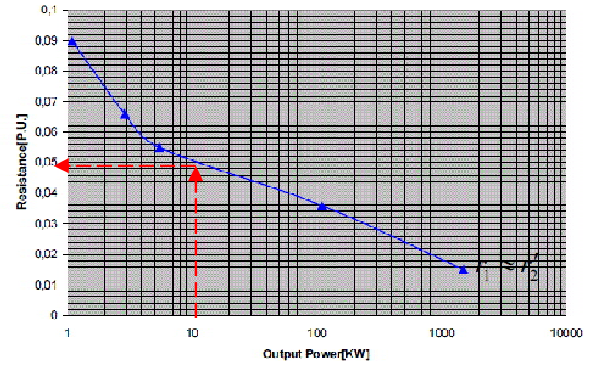


Fig.5: Parameter determination graphs of per unit resistance of 4 pole induction motors.

In [10], the induced voltage constant is calculated using the change in current with angular position using equation (6):

$$e_m = \sum_{j=a}^{j=i} L \frac{di}{d\theta} \cdot \frac{d\theta}{dt} = k * \omega_s ; [j \neq i] \quad (6),$$

where j represents a motor phase, e_m is the phase mutual induced voltage, L is the phase inductance, $\frac{di}{d\theta}$ is the rate of change of current, $\frac{d\theta}{dt}$ is the angular velocity, k is the induced voltage constant and ω_s is the angular rotational velocity of the motor. Once the constant k is known, the mutual induced voltage at any speed can be calculated using equation (6).

The developed torque is calculated using the machine transfer function and the torque. Equation (7) gives the equation used in the calculation.

$$\omega_r(s) = (T_e - T_L) * \frac{k_T}{Js + \beta} \quad (7).$$

$\omega_r(s)$ is the rotor speed in radians per second, T_e is the developed torque, T_L is the load torque, J is the machine motor moment of inertia, β is the motor frictional constant and k_T is the motor torque constant.

The machine parameter values obtained are used to develop the Matlab/Simulink model of the drive. In section 4, the simulation results of the induction machine drive are presented.

4. SIMULATION RESULTS

The induction machine under consideration is an 11kW, 4 pole, 9 phase, cage rotor induction machine. The rated field current I_f of the machine is 5.83A, torque current I_t is 5.5A, frequency f is 50Hz and flux density B is 0.7T. The induction motor has a rated torque of 70Nm at 1466 rpm speed. The motor has a moment of inertia J of 0.0724 kgm², a frictional constant β of 0.01 Nm/rad.s⁻¹ and a torque constant k_T of 12.8.

From the machine parameter graphs, the stator per unit resistance is estimated to be 0.052 and the leakage inductive reactance is estimated to be 0.15. For example, assuming 0.82 power factor, a 400V phase voltage and 11.66 A field current:

Base Impedance, $Z_b = 400/11.66 = 34.31\Omega$.

\Rightarrow Base Resistance, $R_b = 34.31 \times 0.82 = 28.13\Omega$

Base reactance $X_b = 34.31 \times 0.57 = 19.56\Omega$.

For the machine, $R = 28.13 \times 0.052 = 1.46\Omega$

$X_{Lf} = 19.56 \times 0.15 = 2.93\Omega$.

Since the operating frequency is 50Hz for the stator current, then: $L_f = \frac{X}{2\pi \times 50} = 0.00934 H$.

The same calculations are done for the torque phase where the current is 11 A. The results are tabulated in Table 1.

There is a marked difference between the inductances of the torque and the field phases calculated using flux linkage. This is because the slope of the current waveform is steeper during the field phase compared to the torque phase. The calculated inductance is therefore inversely proportional to the gradient of the current waveform when the induced voltage is used in the considered. Equations (4) and (8) show the relationships which explain the observation.

$$E = L \frac{di}{dt} \quad (8),$$

where E is the induced voltage. Practical measurements show one constant value since the inductance is calculated solely as a function of coil parameter. The values obtained using parameter graphs are close to those obtained using the other two methods, especially for the torque phases.

Fig. 6 shows the mutually induced voltage at rated slip speed of 34 revolutions per minute (rpm) as determined using JMAG. An average trend line of the mutually induced voltage constant k shown in Fig.7 is produced to enable the use of constant values of k per phase for calculating the mutually induced voltage per phase. The field phase constant k_f is 0.35 and the torque phase constant k_t is 0.11. The mutually induced voltage is calculated using equation (6) for any other speed using the constant k and the desired speed.

Table 1: Inductance values obtained using the three different methods

	Using Flux	Using Graphs	Practical measurement
L_t (mH)	9.13	9.90	7.513
L_f (mH)	6.50	9.34	

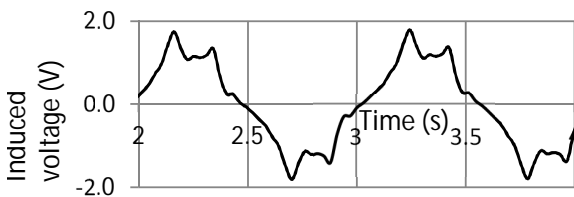


Fig.6: Mutually induced voltage and phase current as a function of time at slip speed

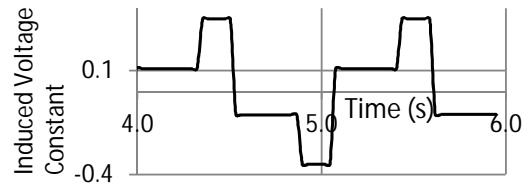


Fig.7: Average mutually induced voltage constant k against time as determined using JMAG.

A PI controller is used to control the speed response of the machine. The PI speed controller is designed for a settling time of 0.2 for fast step response. Its effect is observed in the speed response of the motor as well as on the developed torque.

The locked rotor simulation test is done with stator currents at half rated frequency of 25Hz to determine the maximum developed electromagnetic torque. Fig.8 shows the stator current waveform at rated slip frequency for a hysteresis controlled drive and Fig.9 shows the developed torque. A pull up torque of 85Nm which settles within the 0.2 seconds as determined by the PI controller settling time is observed.

The delta modulator implementation block is as shown in Fig.3. A sampling frequency of 10 kHz is used for the sample and hold circuit. The integrator block implementation is done using the trapezoidal integration algorithm represented by equation (9)

$$Iout_k = \frac{T_s}{2} * (In_k + In_{k-1}) + Iout_{k-1} \quad (9),$$

where $Iout_k$ is the current integrator output, T_s is the sampling period, In_k is the current input, In_{k-1} is the previous input and $Iout_{k-1}$ is the previous integrator output.

Fig.10 and Fig.11 show the locked rotor test results for a delta modulated current controlled drive. The developed torque is the same in magnitude as that developed using a hysteresis controller but it shows a smoother waveform showing the elimination of ripples due to the filtering effect of the delta modulator.

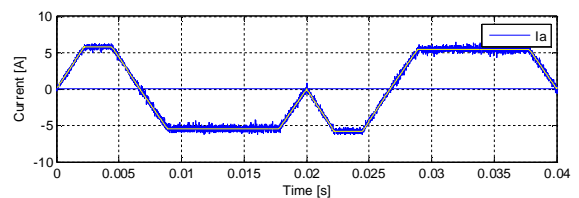


Fig.8. Locked rotor stator current waveform using hysteresis controller

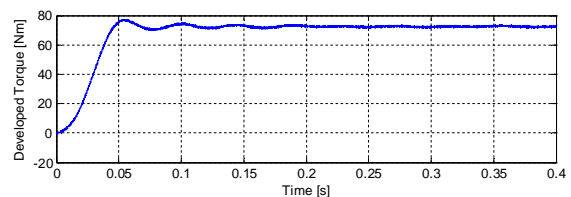


Fig.9: Developed torque using hysteresis controller.

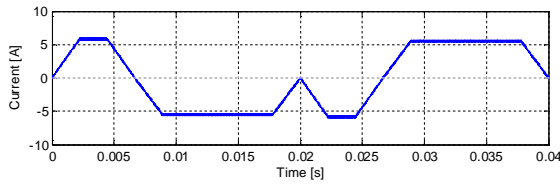


Fig.10. Locked rotor stator current using delta modulator.

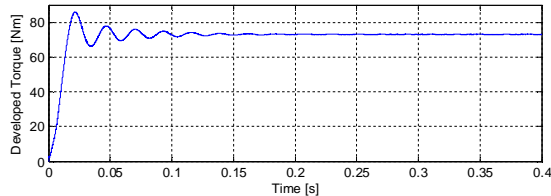


Fig.11: Developed torque using delta modulated controller

The results in Fig.12, Fig.13 and Fig.14 are for the light load (5Nm) test at 500 rpm speed command. The results show that an acceleration torque of about 20 Nm is required to accelerate the motor to the required speed and once the speed is reached, the torque falls to the load torque value. A larger deceleration torque is required because the motor is to be stopped in a shorter time which is half the acceleration time.

The developed torque rises to the rated value within 0.3 seconds as determined by the PI controller design.

Fig. 15, Fig. 16 and Fig. 17 show the response of the motor at rated load of 70 Nm. The rotor speed increases slowly as determined by the loading conditions. Equation (7) shows that the output of the speed calculator is negative when the developed torque is less than the load torque. This accounts for the negative going transition of the rotor speed at start up. It just shows that the machine is not yet rotating in the direction of the torque.

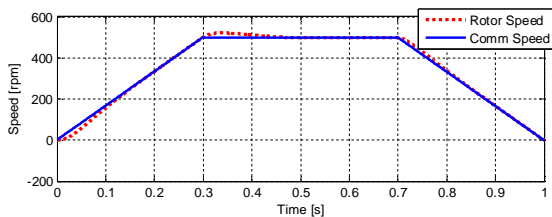


Fig.12: Command speed and rotor speed at light load

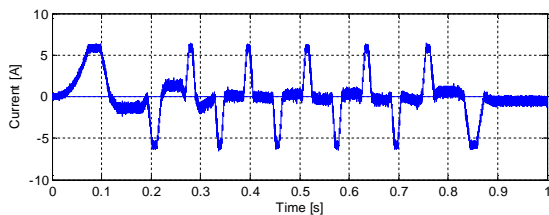
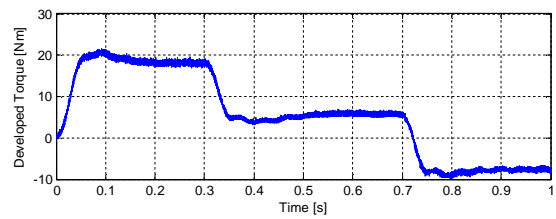


Fig.13: Stator current at light load



(c)
Fig.14: Developed torque at light load and 500 rpm command speed.

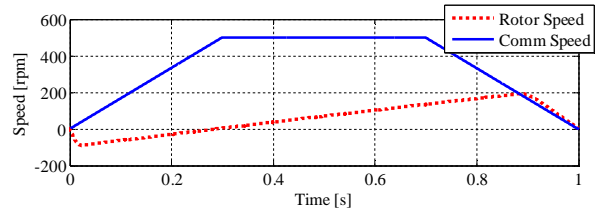


Fig.15: Command speed and rotor speed at full load.

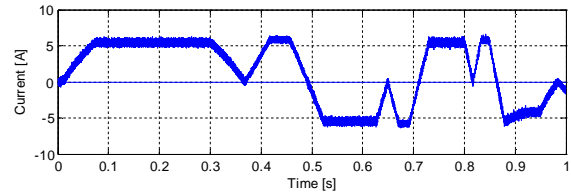


Fig.16: Stator current at full load and 500 rpm command speed.

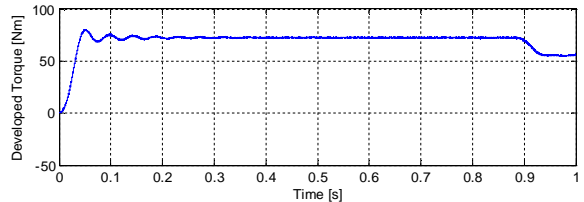


Fig.17: Developed torque at full load and 500 rpm speed.

The following conclusions can be drawn from the results discussed above.

5. CONCLUSIONS

The delta modulated PWM fed nine-phase BDCE controlled induction motor model has been developed and successfully simulated. Its static, transient and dynamic response has been simulated. The results show a response time that is acceptable according to the design requirements of the PI controller. They show that the motor torque can be directly controlled by controlling the torque current component of the stator current. Delta modulation shows that it effectively reduces torque ripple compared to the hysteresis controller as shown by comparing Fig.9 (a) to Fig. 11 (a) where a delta modulator was used. The results also show that the frequency of the stator current is a function of rotor speed as expected. The torque is proportional to the torque. The drive has acceptable response to speed and current commands and delta modulation gives less torque ripple. It can therefore be concluded from the simulations that the delta modulator can be used in the BDCE controlled drive and give acceptable performance.

REFERENCES

- [1] A.H. Bonnet and T. Albers. "Squirrel-Cage options for AC Induction Motors". *IEEE Transactions on Industry Applications*. Vol 37. No. 4. pp. 1197-1209, 2001.
- [2] R.C. Healey, S. Williamson and A. C. Smith. "Improved Cage Rotor Models for Vector Controlled Induction Motors". *IEEE Transactions on Industry Applications*. Vol 31. No. 4. pp. 812-822, 1995.
- [3] M Sowmiya, G Renukadevi and K Rajambal. "IFOC of a Nine Phase Induction Motor Drive". *International Journal of Engineering Science and Innovative Technology (IJESIT)*. Vol 2. No. 3. pp.72-78, 2013.
- [4] A Nanoty and A.R.Chudasama. "Design, Development of Six Phase Squirrel Cage Induction Motor and its Comparative with Equivalent Three Phase Squirrel Cage Induction Motor Using Circle Diagram". *International Journal of Emerging Technology and Advanced Engineering*. Vol. 3. No. 8. pp.731-737, 2013.
- [5] A Gautam and J. O. Ojo. "Variable speed multiphase induction machine using pole phase modulation principle". *IECON 2012 - 38th Annual Conference on IEEE Industrial Electronics Society*. pp. 3659-3665, 2012.
- [6] B. Kundrotas, S. Liasauskas, and R. Rinkeviciene. "Model of Multiphase Induction Motor". *ELECTRONICS AND ELECTRICAL ENGINEERING*. No. 5. pp. 111-114, 2011.
- [7] R Bojoi, A.Tenconi, F Profumo and F Farina. "Dual-Source Fed Multi-phase Induction Motor Drive for Fuel Cell Vehicles: Topology and Control". *Proceedings of Power Electronics Specialists Conference, (PESC '05)*. pp. 2676-2683, 2005.
- [8] G.K. Singh, V. Pant and Y.P. Singh. "Voltage source inverter driven multi-phase induction machine". *Computers and Electrical Engineering*. Vol. 29. pp. 813-834, 2003.
- [9] A Mishra and P Choudhary. "Speed control Of An Induction Motor by Using Indirect Vector Control Method". *Journal Of Emerging Technology and Advanced Engineering*. Vol 2. Issue 12, 2012.
- [10] Y. Ai, M. J. Kamper and A. D. Le Roux. "Novel Direct Flux and Direct Torque Control of Six-Phase Induction Machine With Nearly Square Air-Gap Flux Density". *IEEE Transactions on Industry Applications*, Vol. 43. No. 6: pp.1534-1543. 2007
- [11] N. Gule and M.J. Kamper "Multi-Phase Cage Rotor Induction Machine Drive with Direct implementation of Brush DC Operation". *IEEE Transactions on Industry Applications*, Vol. 43. No. 6: pp. 2014-2021.2012.
- [12] P.D. Ziogas. "The Delta Modulation Technique in Static PWM Inverters". *IEEE Transactions on Industry Applications*, Vol. 1A-17. No. 2. pp.199-204. 1981.
- [13] D. N. Trip, C. Gordan, M. I. Gordan, A. Schiop and R. Reiz. "Time Frequency Analysis of the Delta Modulation and PWM Control for the asynchronous Motors". *IEEE International Conference on "Computer as a Tool", (EUROCON)*, pp. 1586-1589, 2005.
- [14] Y. M. Chen, Y. C. Chen and H. C. Wu. "Improved Delta Modulation Control for PWM Inverters". *IEEE Conference on Industrial Technology (ICIT 2008)*, pp. 1-6. 2008.
- [15] J. W. Kimball, P. T. Krein and Y. Chen. "Hysteresis and Delta Modulation Control of Converters using Sensor less Current Mode". *IEEE Transactions on Power Electronics*, Vol. 21. No. 4. pp. 1154-1158, 2006.
- [16] V. S. Reddy and B. C. Babu. "Hysteresis Controller and delta Modulation- Two Viable schemes for Current Controlled Voltage Source Inverter". *IEEE International Conference on Technical Postgraduates (IEEE TECHPOS)*, 2009.
- [17] M. A. Rahman, J. E. Quaicoe, M. A. Choudhury. "Performance Analysis of Delta Modulation PWM Inverter". *IEEE Transactions on Power Electronics*. Vol. PE-2, No. 3, pp. 227-233, 1987
- [18] S. Williamson, L.H. Lim and M.J. Robinson "Finite Element methods for cage Induction Motor Analysis". *IEEE Transactions on Industry Applications*, Vol. 26. No. 6: pp. 1007-1017. 1990.
- [19] A. K. Ibrahim, M.I. Marei, H.S.El-Gohary, S.A.M. Shehata. "Modelling of Induction Motor Based on Winding Function Theory to Study Motor Under Stator/Rotor Internal Faults". *Proceedings of the 14th International Middle East Power Systems Conference (MEPCON'10)*, 2010.
- [20] A. A. Jimoh, P. J. Venter and E. K. Appiah. "Modelling and Analysis of Squirrel Cage Induction Motor with Leading Reactive Power Injection, Induction Motors - Modelling and Control, R. E.Araújo (Ed.),
- [21] T. A. Lipo, H.A. Toliyat and J.C. White. "Analysis of a concentrated winding Induction machine for Adjustable Speed drives Applications Part 1 (Motor Analysis)". *IEEE transactions on Energy Conversion*, Vol. 6. No. 4. pp. 679-683. 1991.
- [22] O.I. Okoro. "Dynamic and Thermal Modelling of Induction Machine with Non-linear Effects". *PhD Thesis, 2002. Kassel University Press, GmbH, Kassel*

TESTING AND CHARACTERIZING THE MOTOR AND DRIVE SYSTEM OF A SOLAR VEHICLE (OCTOBER 2013)

F Smal* and A J Grobler*

* North West University, Faculty of Engineering, School of Electrical, Electronic and Computer Engineering, Potchefstroom Campus (NWU PC)

Abstract. The motor and the drive system of a solar vehicle are essential parts of the car and play a major role in the performance. The scope of this project is to design a suitable test setup that can be used to characterize the 6kW brushless DC (BLDC) motor and drive system. This article discusses the mechanical and electrical designing of the test setup, the test procedure, the construction of the test setup and results. The results are used to determine the most effective operation region for different loading conditions. The conducted tests include the measurements of efficiency, parameters necessary to simulate the motor, and also the of the back electromotive (back-EMF) curves of the BLDC machine. These results will be used to characterize the system.

Key Words. Electric vehicle, brushless motors, DC machines, motor drives, current measurement, voltage measurement, efficiency, simulation.

1. INTRODUCTION

In 2012 the North West University (NWU) built a solar vehicle that competed in the South African Sasol Solar Challenge in September 2012. The team designed the vehicle but the equipment used in the vehicle was never properly tested or characterized. The motor that is currently installed in the solar vehicle of the NWU is 6kW. The reason for choosing a BLDC motor and drive to analyze is that according to [1], BLDC motors are more efficient at the nominal operating point of a solar vehicle (16-17 Nm torque and at a speed of 1050 r/min). The BLDC motor can be characterized as the modern kind of DC motor. The name comes from the fact that these motors have no brushes. This type of motor has entered the market quite recently (1950's – 1960's), as it had to wait for the development of more sophisticated electronic controls and sensors [2].

A feeling amongst the NWU solar team of 2012 was that the choice of motor was one of the main reasons for the below expected performance of the solar vehicle. The significance of this gesture would only be proven by testing the motor together with its drive and characterizing it.

A question that surfaced during the research of this project was why the team decided on a BLDC machine instead of any other type of motor. According to [3], the results of conducted tests clearly illustrate that between AC and BLDC motors, the latter has a higher operating efficiency at the operation region of a solar vehicle.

The University of Queensland also recons that the BLDC motor is the best choice of motor for high efficiency operation as in the case of the solar vehicle [4]. According to [4], a BLDC implemented by using an optimized Halbach magnet arrangement can reach efficiencies of up to 98.2%.

Two types of BLDC motors that have been very successful at the World Solar Challenge (WSC) are the axial flux Csiro motor (CM) and the radial flux Biel motor (BM) [1]. The choice of motor installed in the solar vehicle being tested is an axial flux permanent magnet (AFPM) motor. The reason for choosing the AFPM over the radial flux permanent

magnet (RFPM) motor is the fact that the AFPM has a better power-to-weight ratio meaning a smaller and lighter motor can be installed on the vehicle without sacrificing any power [1].

Other advantages regarding the AFPM motor include [4]:

- Drive transmissions are eliminated
- Better aerodynamic operation or performance due to the more streamline design
- No need to worry about dust entering transmission system
- No need to replace belts/chains that are broken – less maintenance.

The motor drive that is used to drive and control the motor is specifically designed by the same manufacturers than the motor. It is used to limit or govern the performance of the motor in some predetermined manner [5]. This device can manually start or stop the motor, put it in forward- or reverse motion, control the speed of the motor according to preset functions, regulate or limit the torque of the motor and also protect the motor against faults or overloading [6].

The scope of this project was to conduct the necessary tests to characterize the motor and drive system of the 2012 solar vehicle shown in Fig. 1.



Fig. 1. 2012 NWU solar vehicle that contains the motor and drive system to be tested and characterized.

The testing and characterization of a motor and drive system of a solar vehicle include taking of measurements and plotting it. It also includes the designing and construction of the complete test setup and the testing procedures. Various tests were conducted under different conditions in order to provide a wide range of data to characterize the overall performance of the motor and drive system of the solar vehicle. The results yield recommendations to the driver of the solar vehicle on the most efficient travelling speeds when driving at different loading conditions.

2. TEST SETUP

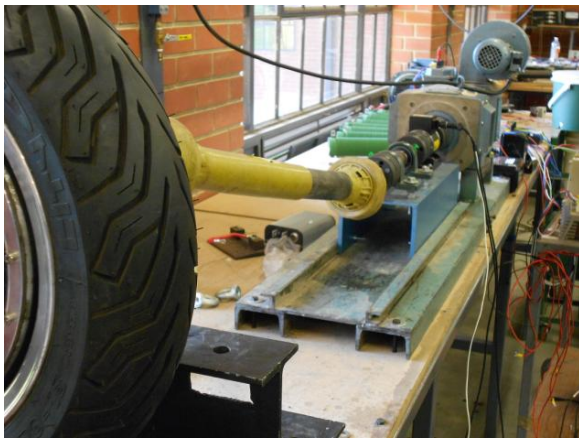


Fig. 2. Drive train of the test setup

The experimental test that was conducted was designed and conducted to determine the performance areas of the motor and drive system which would provide insight to the operator of the vehicle as to how to operate the vehicle at its optimal operation region. These tests include the measurement of the armature winding resistance and the back-EMF voltage constant which was used for the simulation of the system. The two other tests that was conducted was crucial to determine the performance curves of the system. The first was to operate the system at various constant loading levels while increasing the speed and the second was operating the system at full throttle and increasing the loading level gradually. The reasons for conducting these tests are discussed in section 4 of this paper.

The test setup was designed to connect the BLDC machine to the 7.5kW DC machine by means of torque- and speed measuring equipment. Implementing the test bench to satisfy the necessary safety regulations influenced the design of the test setup. The main components of the test setup are discussed in this section.

2.1 7.5kW DC machine

A 7.5kW DC machine was used as a motor to rotate the 6kW BLDC machine of the solar vehicle at a constant speed to measure the back-EMF by means

of a TiePie oscilloscope and as a generator to load the 6kW BLDC motor. The field and armature windings was supplied by DC power by making use of a three-phase power supply, variable transformers and three-phase rectifiers.

2.2 Torque and Speed Measuring Equipment

The torque on the drive train and the rotating speed of the setup was measured using a Magtrol TMB 311 in-line torque transducer. The transducer output a speed signal as pulses together with a torque measurement in a fractional voltage that must be converted to a torque value. The frequency of the pulses equals the rotational speed in r/min.

2.3 Compatibility of the test bench

As multiple motors and tests need to be connected on this test bench, the design must be compatible with motors of various shapes and sizes.

The problem was solved by making use of a power take-off (PTO) shaft.

2.4 Mounting the 6kW BLDC machine

The 6kW BLDC machine of the solar vehicle was mounted on the base plate of a 4kW axial flux permanent magnet generator by simply making small adjustments. The initial mounting was not stable enough, but was strengthened by means of pillow block bearing.

2.5 Complete Test Setup

The complete test setup with all the necessary adjustments made can be observed in Fig. 3.



Fig. 3. Complete test setup used to characterize the system

3. RESULTS

3.1 Armature winding resistance

The armature winding resistance of the 6kW BLDC machine was measured as 0.6Ω . As the winding is wye-connected, the measured must be divided by two. The armature winding resistance of a single winding is therefore:

$$R_a = \frac{R_{measured}}{2} = 0.3\Omega \quad (1)$$

3.2 Back-EMF Voltage Constant

The back-EMF curves of the BLDC machine was measured by rotating it at a constant rotational speed of around 600 r/min by operating the 7.5kW DC machine as a motor and controlling the speed by changing the armature voltage by changing the variable transformer output. An oscilloscope was used to measure the back-EMF on the three separate phases. The results are shown in Fig. 4.

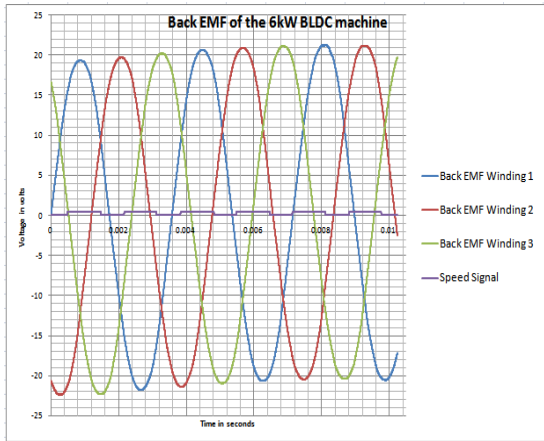


Fig. 4. Back-EMF waveforms generated by rotating the BLDC machine at a constant speed of 600 r/min.

The RMS value of the back-EMF voltage was measured at 15.586V and the speed was measured at 600 r/min. These two measured values resulted in a voltage constant of:

$$k_e = \frac{Voltage}{Speed} = \frac{15.586V}{595r/min} = 0.026 \quad (2)$$

4. PERFORMANCE CURVES OF THE MOTOR AND DRIVE SYSTEM

The performance curves of the motor and drive system were drawn by plotting the results of three different tests. These tests are:

- Test 1: Lightly loaded while the speed is increased
- Test 2: Loaded more heavily while the speed is increased
- Test 3: Throttle at full speed while the load is increased

From these three tests all the necessary information regarding the characterization of the performance of the motor and drive system of the solar vehicle are gathered.

The voltage waveforms that the controller supply to the 6kW BLDC motor were measured using 3 separate oscilloscope channels and combining the measurements on one graph. The oscilloscope measurement shown in Fig. 5 illustrate that the 6kW motor is indeed a BLDC motor as the three phases

are 120° electrically apart and range between zero voltage and maximum voltage.

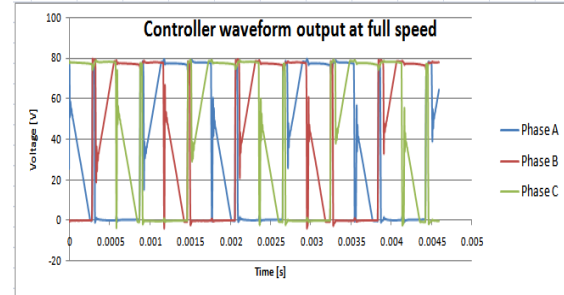


Fig. 5. Supply voltage of the 6kW BLDC motor.

The rms value of the waveforms was measured at 56V with a peak value of 79.3V. It is clear from Fig. 5 that at full speed, the duty cycle of the phases are 100% with 120° phase shift between the phases.

The results from the first test can be observed in Fig. 6:

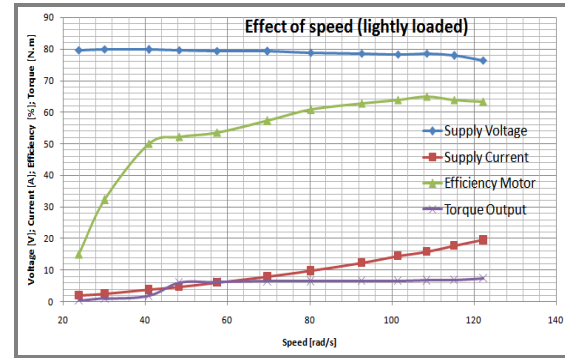


Fig. 6. Effect of speed under lightly loaded conditions.

This test was conducted with the field voltage of the generator set at 100V and the load reaching only 544W. Analyzing this test result, it is seen from Fig. 6 that as the speed is increased while the system is lightly loaded, the efficiency increases from 15% up to 65%. The reason for this increase in efficiency can be justified by the fact that the torque output of the motor is increased as the speed is increased. The low efficiency values during this test can be justified by the fact that the motor was very lightly loaded with the maximum load reaching only 544W. The increase in speed resulted in a slight load increase which directly affected the supply current and voltage. The DC supply voltage reduced from 79.6V to 76.3V with the supply current rising from 1.9A up to 19.5A to compensate for the increased load on the system which increases from 18W to 544W.

The results from the second test can be observed in Fig. 7:

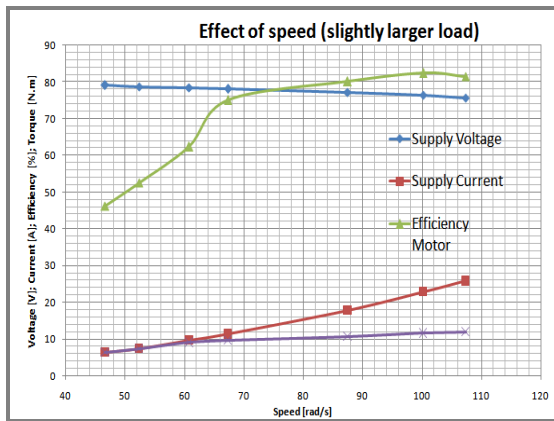


Fig. 7. Effect of speed (slightly larger load).

By studying the results of the second test illustrated in Fig. 7, the same conclusions can be made as to the first test. The test was conducted with the field voltage of the generator set at 250V. The efficiency increased from 46.19% at a load of 190W up to 82% at a load of almost 900W. These results further highlight the fact that the motor's efficiency increases as it becomes more heavily loaded. The DC supply voltage reduced from 79.1V to 75.75V with the supply current rising from 6.3A up to 25.8A to compensate for the increased load on the system which increased from 190W to 882W.

The approach that was followed for the third test is slightly different from the first two tests. For the first two tests the field voltage of the generator that controls the size of the load being applied to the motor was kept constant while the speed of the motor was increased. In this test the motor was run at full speed while the field voltage was increased to measure the response of the motor when the solar vehicle is being driven at full speed and the load is increased. This will happen when the solar vehicle is driving at full speed on a driving surface that has no incline and suddenly get exposed to a steep incline. The steepness of the driving surface will determine the size of the load that the driving system is exposed to. The results from the third test can be observed in Fig. 8:

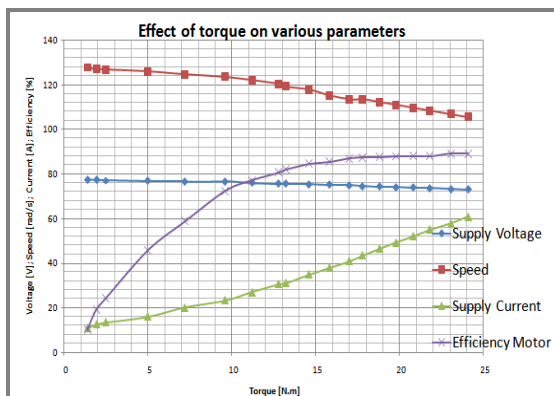


Fig. 8. Effect of torque on various parameters.

These results were found by rotating the 6kW BLDC motor at full speed (1220 r/min) while the

field voltage applied to the generator was increased from 0V up to 340V. At these high speeds the increase in field voltage resulted in the load power to increase from 0W to 5105W. This power range effectively covers 85% of the rated power range of the 6kW BLDC motor and therefore provides a wide range of data to be used in the characterization of the system.

The speed of the motor is represented in rad/s instead of r/min. The reason for this is to improve the legibility of the graph as the rad/s values are more in range with the other values that are also being displayed on the graph.

A clear observation from the graph is that the rotating speed of the motor decreases as the load is increased. The speed decreases from 1220r/min at a load of 0W to 1009r/min at a load of 5105W. The supply current needed to run the motor at full speed under no load was 11A but increased to a value of 60.76A at 5105W. The efficiency of the motor increased from a no-load value of 10.3% to a 5105W value of 89%.

The torque constant was also calculated from the test measurements and the average was determined as shown in eq.(3):

$$k_t = \frac{\text{Torque}}{\text{Current}} = 0.361 \quad (3)$$

The three tests that were conducted resulted in the following conclusion:

- When lightly loaded (downhill or flat road profile), the system operates at maximum efficiency at a speed of 95km/h.
- When loaded more heavily (slightly uphill), the system operates at maximum efficiency at a speed of 83km/h.
- When loaded close to full capacity, 5.1kW, the motor operates at an efficiency of 89% at a speed of 86km/h.

It must be noted that the drag of the vehicle has been completely neglected during the testing and characterizing of the system.

5. SIMULATIONS

5.1 Simulation Model

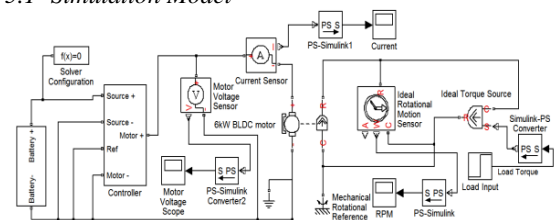


Fig. 9. Simulink® model of motor and drive system.

This model was used to simulate and predict the performance of the motor and drive system of the solar vehicle in future applications. The model receives the measured capacity of the battery pack, and the loading level that the operator wants to

simulate the motor at. The outputs of the model include the motor supply voltage and current, the rotational speed of the motor in r/min.

The battery pack is simulated by using a PWL (piecewise lookup) voltage source. The reason for this is to simulate the soft start of the motor as the driver steps on the throttle. The PWL voltage is programmed to reach its maximum supply voltage in a second, which is approximately the time the driver takes to fully step on the throttle.

The controller is simulated as an H-bridge supplied by a controlled PWM voltage source that is supplied from the battery pack. The expanded subsystem can be seen in Fig. 10

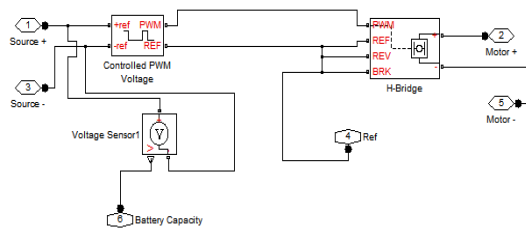


Fig. 10. Controller subsystem

5.2 No-load Simulation

For the no-load simulation the 1.4 Nm torque value that was measured during the tests was inserted into the simulation as the load input. The output scope of the no-load simulation is shown in Fig. 11.

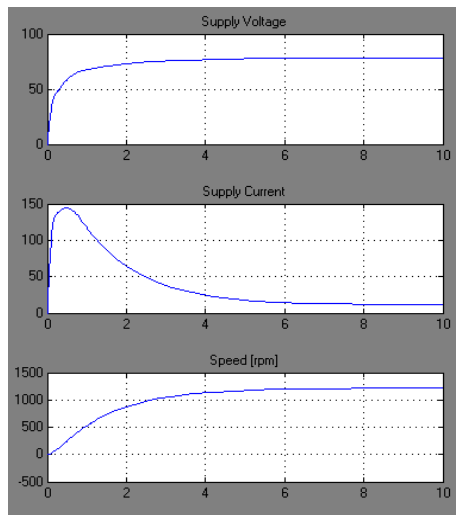


Fig. 11. No-load output scope of the simulation.

In Table 1 the no-load test measurements are compared to the no-load simulation results.

Table 1: No-load test vs. No-load simulation

Measurement	No-load test	No-load simulation
Torque	1.4 Nm	1.4 Nm
Supply Voltage	77.5V	78.17V
Supply Current	11.00A	11.33A
Motor Speed	1220 r/min	1218 r/min

It is clear that the measurements differ by less than 3% on the no-load test and simulations meaning that there is good correlation between the no-load test and the no-load simulations.

5.3 85% Load Simulations

For the 85% load test the 24.1Nm torque value that was measured during the tests was inserted into the simulation as the load input. The output scope of the 85% load simulation is shown in Fig. 12.

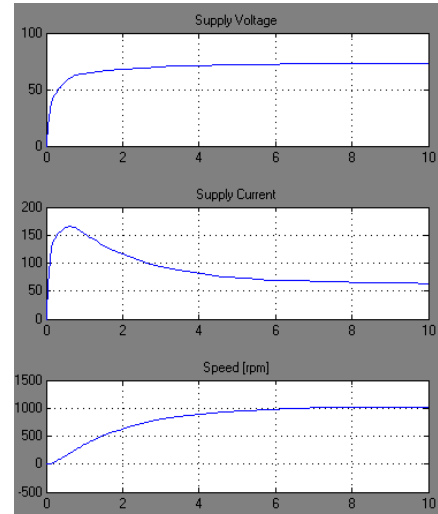


Fig. 12. 85% load output scope of the simulation.

In Table 2 the 85% load test measurements are compared to the 85% load simulation results.

Table 2: 85%-load test vs. 85%-load simulation

Measurement	85%-load test	85%-load simulation
Torque	24.1 Nm	24.1 Nm
Supply Voltage	73.09V	72.91V
Supply Current	60.76A	63.91A
Motor Speed	1009 r/min	1024 r/min

All values simulated are within 5% of the actual measured data confirming the correctness of the model. The small deviations between the measured and simulated values can be due to small human error in the taking of the measurements during the testing procedures or the battery capacity that reduces over the testing time. Another factor may be temperature as the system temperature increases as the testing time increases.

6. CONCLUSION

Characterizing the motor and drive system proved to be more challenging than thought at first. There were many factors that had restraining influence on the successful completion of this project, with mechanical issues on the designing of the test setup being the biggest. The initial problem was to design a test setup that must be compatible. The drive train

must be designed to fit various motor sizes and heights and the solution to this problem was the implementation of the PTO shaft onto the drive train. The inclusion of the PTO posed another problem which was the weight of the PTO hanging on the delicate shaft of the torque measuring equipment. This would cause damage to the torque meter but also results in inaccurate torque measurements. The inclusion of two 30mm pillow block bearings solved this problem.

Safety became a major concern once the testing phase of the project commenced as the fact that the motor was only bolted on one side made the motor and PTO shaft very unstable and caused a lot of vibrations on the shaft. The inclusion of I-beams and a 40mm pillow block bearing supporting the weight of the motor solved the safety concerns and the testing could continue.

The three performance tests that were conducted resulted in the following conclusions. In the case of the motor and drive system being lightly loaded, the driver must accelerate to a travelling speed of 95km/h to operate at a maximum efficiency of 63%. When the motor becomes more heavily loaded the driver must accelerate to a travelling speed of 83km/h to operate the system at a maximum efficiency of 82%. In the case of the motor operating near full capacity, the driver must operate the vehicle at a speed of 86km/h that will result in a maximum efficiency of 89%.

The simulations varied by less than 5% of the tested measurements indicating that the motor and drive system were tested and simulated very accurately and that the simulation model can be used for future predictions.

ACKNOWLEDGEMENTS

The author, F. Smal, would like to thank his project coordinator and supervisor, Dr. A.J. Grobler, for the continued guidance during the completion of this project. Without his help the project would not have been such a major success.

REFERENCES

- [1] A. I. Zaher, R. de Groot, S. Polinder, and H. Wieringa, "Comparison of an axial flux and a radial flux permanent magnet motor for solar race cars," in *XIX International Conference on Electrical Machines (ICEM)*, 2010, pp. 1-6.
- [2] Chang-liang Xia, *Permanent Magnet Brushless DC Motor Drives and Controls*. Singapore: John Wiley & Sons, Science Press Beijing, 2012.
- [3] Miyamasu, M.; Akatsu, K.; , "Efficiency comparison between Brushless dc motor and Brushless AC motor considering driving method and machine design," *IECON 2011 - 37th Annual Conference on IEEE Industrial Electronics Society* , vol., no., pp.1830-1835, 7-

10 Nov. 2011
doi: 10.1109/IECON.2011.6119584

- [4] A. J. Reghenzani, "A Motor Controller for the Solar Car Project," M.S. Thesis, The University of Queensland, Queensland, Australia, 1998
- [5] National Fire Protection Association (2008). ["Article 100 Definitions"](#). *NFPA 70 National Electrical Code*. 1 Batterymarch Park, Quincy, MA 02169: NFPA. pp. 24. <http://www.nfpa.org/aboutthecodes/AboutTheCodes.asp?DocNum=70&cookie%5Ftest=1>. Retrieved January 2008.
- [6] Siskind, Charles S. (1963). *Electrical Control Systems in Industry*. New York: McGraw-Hill, Inc.. [ISBN 0-07-057746-3](#).

TAN DELTA TESTING OF MV MOTOR STATOR COIL INSULATION

G Lebese*, G Sikhakhane*, Y Lekalakala* and J Van Coller*

** School of Electrical & Information Engineering, University of the Witwatersrand, Private Bag 3, 2050, Johannesburg, South Africa.*

Abstract. Tan delta testing is a widely applied off-line diagnostic test used to assess the condition of motor insulation. The difficulty in performing this test arises when testing medium to high voltage rotating machines such as ac motors and generators. This is due to the additional coatings such as the corona shield and the stress grading added to the stator bar and which influence the tan delta measurement and consequently give misleading results. To minimize the effect of these coatings, guard rings are recommended to be used. However, most test personnel in the industry do not apply guard rings for practical reasons. A laboratory experiment was conducted to investigate the effect of deviating slightly from the IEC 60894 standard as far as guard rings are concerned when performing tan delta testing on a medium voltage motor stator bar. The test was conducted at power frequency on a 4.2 kV rated stator bar using a Schering Bridge where four different materials were used to simulate the stator slot. It was found from the results that tinned copper wire is the best material for stator slot simulation. Using tinned copper wire as a measuring electrode, an error of 1 to 3 % was obtained when the stress grading was electrically isolated by guard rings. However, an error of 7 to 18% was attained when stress grading was not electrically isolated. From these results, it can be concluded that one should apply guard rings to electrically isolate the graded portion of the stator bar to avoid misleading results which are significantly influenced by the effect of the stress grading.

Key Words. Tan delta; stress grading; guard rings.

1. INTRODUCTION

Electrical failure in a motor is often due to insulation breakdown. The insulation system can deteriorate gradually and eventually fail and thus result in an electrical breakdown of the motor. These unexpected failures can be mitigated by consistently assessing the condition of the insulation system, which can be achieved by performing the tan delta test [1]. The tan delta test is one of the most commonly used diagnostic methods to evaluate the condition of the insulation system and can reveal whether the insulation system is in a good or a bad condition - thus allowing informed decision to be made on whether a repair needs to be undertaken [2]. This test is applicable to motors, generators, transformers, and cables; however, the interest of this paper is more on medium voltage (MV) ac motor testing.

Tan delta measurement of only the slot portion of the stator bar is difficult due to the additional coatings such as semi-conductive paint (corona shield) and the stress grading added to the insulation system to minimize partial discharges (PD) in the slot and surface discharges in the overhang region. Consequently, the performance and properties of these added materials under high voltage stress contribute significantly to the tan delta measurement. To minimize the effect of these coatings on the tan delta measurement, guarding techniques as recommended in standards must be utilized - i.e. applying guard rings to guard the stress graded region. However, in the industry, test personnel performing the test often do not comply with the standard as far as the guard rings are concerned. This is because guard rings are not easily installed in the closely packed overhang region of the machine. Consequently, the graded portions of the overhang will be included in the measurements, thereby increasing the probability of obtaining misleading results [3].

To address the above problem, a laboratory experiment was carried out to investigate what happens when deviating slightly from the IEC 60894 standard [8] as far as guard rings and other recommendations (such as electrode forms – wire, foil, etc.) are concerned, when performing tan delta tests on an MV motor stator bar. The obtained results were analysed to determine the effects of deviating from this standard.

This paper provides background on corona shield and stress grading coatings applied to MV motor stator bars. A brief background on tan delta measurement is also provided. The method used to conduct the experiment, which involved using a Schering bridge as the measuring instrument, is then discussed. The results obtained are then analysed. In addition, encountered problems in the course of the experiment and how they were resolved are briefly discussed.

2. BACKGROUND

2.1 Project Specifications

The tan delta tests were performed at power frequency (50 Hz) on a 4.2 kV rated motor stator bar first complying with the IEC 60894 [8] standard and then deviating from the standard by changing the guard ring specifications to see the effect on the overall results. The experiment used a Schering bridge as the measuring equipment.

The following assumptions are made.

- it was assumed that the stator bar to be tested was free of voids. This implied that no PD activity was present that might influence the tan delta results.
- the temperature of the stator bar remained constant throughout the experiment. This is

because the tan delta value is affected by temperature i.e. an increase in temperature will result in the increase in the tan delta value.

- it was assumed that there was no moisture in the insulation of the specimen to be tested; this is because the absorption of moisture by solid insulation has the effect of increasing the dielectric loss and reducing the insulation resistance; hence increasing losses which are picked up during the measurement (which is undesired).
- the constant power frequency of 50 Hz is assumed, this is due to the fact that any change in frequency affects the tan delta measurement.

2.2 Literature review

Figure 1 show a typical form-wound medium voltage (MV) stator bar which consists of ground-wall insulation, semi-conducting layer, and stress grading system on the overhang portions (which is not shown in the figure).

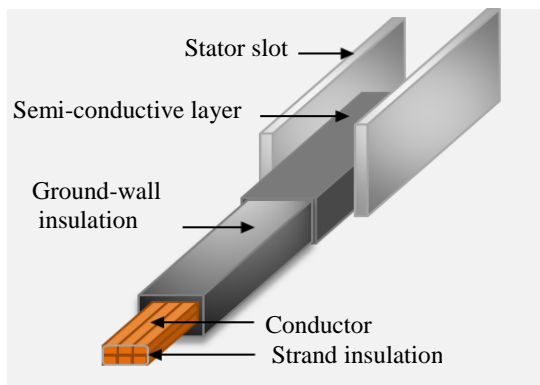


Figure 1: A typical medium voltage (MV) motor stator bar

Ground-wall insulation: This layer plays a vital role in isolating the conductor (at a high potential) from the stator core (at zero potential). The insulation is made of mica tapes wrapped around the conductor to form layers that achieve a certain thickness. These mica layers are then impregnated with epoxy to bind the tapes in a curing process. Voids are likely to occur during the curing process if not done well [4].

Semi-conductive layer: The primary purpose of the semi-conducting coating is to suppress partial discharge activity that may take place between the stator bar and the grounded stator slot. In the case where PD occurs in the gap, the PD activity will cause a hole that will wear down the ground wall insulation, thus leading to insulation failure [5]. These discharges are usually known as slot discharges. The partially conductive material is composed of carbon black loaded tape or paint. These coating are characterised by low resistance, and when in contact with the stator core, they are approximately at zero potential and hence the voltage across any air gap is zero. PD will not occur

since the electrical stress will not be greater than 3 kV/mm (the approximately breakdown strength of an airgap). It is also indicated in [5] that the semi-conductive materials have the resistance ranging from 0.1-10 k Ω . This resistance together with the resistance due to the voltage stress grading material (see Figure 2) contributes to the overall tan delta measurement, thus contributing to the tan delta measurement errors. to reduce the electric field

Stress grading layer: The stress grading layer is applied on the stator bar overhang to reduce the electric field where the bar exits the stator core. The grading materials usually contain silicon carbide (SiC) or zinc oxide (ZnO). The resistance of these materials decreases with the increase in electric field i.e. the SiC or ZnO is non-linear. The varying resistance makes the electric field more uniform along the semi-conductive layer. This leads to the reduction of the electric stress to less than 3 kV/mm (in air) thus limiting partial discharge (PD) activity that may occur [6].

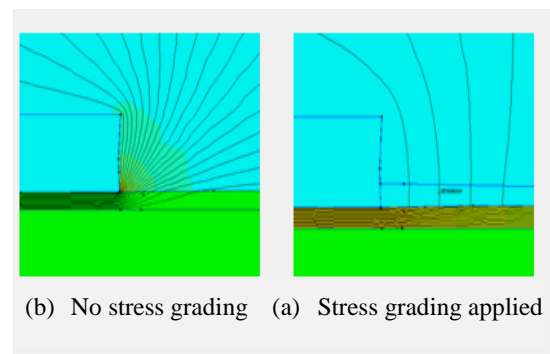


Figure 2: Stator bar overhang FEMM simulation.

Figure 2 (a) shows a simulated stator bar overhang without stress grading applied. It can be seen that the equipotential lines spread out around the edge of the earthed stator core. The electric field at this point is too high and this might lead to discharges in the surrounding air with potential degradation of the ground-wall insulation system and thus resulting in insulation breakdown. Figure 2 (b) shows the effect of applying stress grading on the overhang. It can be seen that when the stress grading coating is applied, the surface stress around the end of the earthed stator core is reduced. These simulations depict the advantage of using stress grading; however the disadvantage is that the stress grading greatly contributes to the tan delta measurements, thus leading to misleading results.

Stator bar electrical model: The circuit model for the stress grading portion of the stator bar is shown in Figure 3, where R_s is the specific surface resistivity of the semi-conductive material, R_1 to R_n are the stress grading non-linear resistors and C_1 to C_n are the modeled capacitances of the insulation. This model was used to interpret the results.

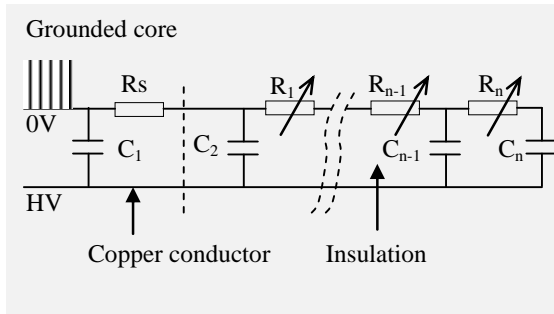


Figure 3: Electrical model of the bar overhang.

2.3 Tan delta

The ideal stator bar insulation shown in Figure 4 (a) can be modeled as an ideal capacitor. However, due to poor curing, voids, and contamination, the insulation can no longer be modeled as an ideal capacitor.

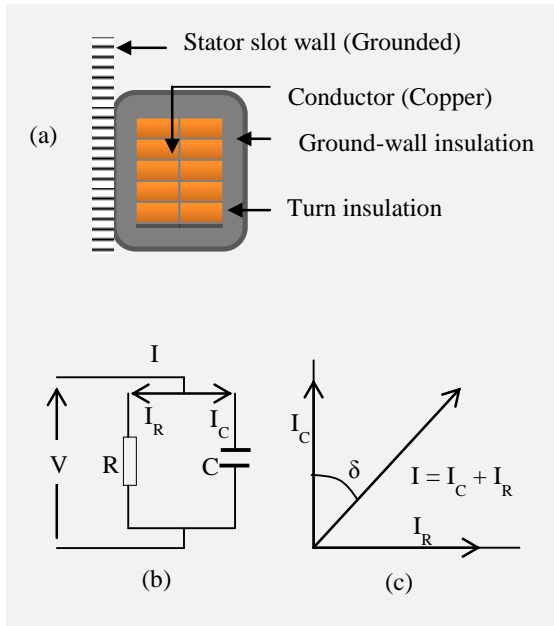


Figure 4: Stator bar ground-wall insulation model.

The insulation must now be modeled as a capacitor in parallel with a resistor as shown in Figure 4 (b) and the corresponding phasor diagram in figure 4 (c). It can be seen on the phasor diagram that the voltage does not lag the current by 90 degrees; it is now less than 90 degrees. This is due to the resistive component introduced in the insulation. The dielectric loss angle (δ , measured in radians) can be defined as the angle between I_C (capacitance current) and I (the resultant current). Hence the tangent of this loss angle or the ratio of current components I_R/I_C (I_R is the resistive current) is known as the tan delta as shown by Equation 1.

$$\tan(\delta) = I_R/I_C \quad (1)$$

The tan delta value can be used to assess the quality of the stator bar insulation. In defect - free stator bar

insulation, the dielectric loss angle δ is close to zero, whereas in defective insulation, the loss angle δ is large. Tan delta tip-up, is the difference between the tan delta measurements made at two different voltages. This is a good indicator of the condition of the insulation system.

3. THE EXPERIMENT

The tan delta measurement was performed adhering to safety standards on a new MV motor stator bar using a Schering Bridge to measure the dielectric loss. In order to perform the test, the location of the stress grading had to be known. However, a datasheet for the stator bar was unavailable which would have given information about where the stress grading was located on the bar. This issue was resolved by conducting a short experiment to locate the starting and ending point of the stress grading.

3.1 Experiment 1: Characterisation of the stator bar

The objective of this short experiment was to locate the starting and ending point of the stress grading on the overhang of the stator bar.

Setup: The circuit connection is shown in Figure 5. The apparatus used were: Step-Up transformer (220 V - 60 kV) controlled by a variac (0 - 260 V ac), voltage divider (ratio 1:1000), electrostatic voltmeter (Type 2065), and digital multimeter.

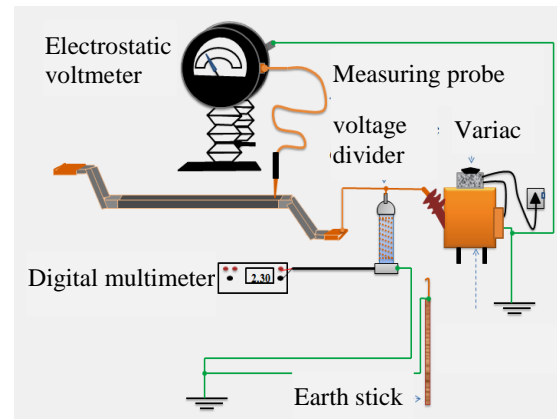


Figure 5: Surface voltage measurement setup.

Procedure and Results: The electrostatic voltmeter was used for the surface voltage measurement. The electrostatic voltmeter works on the principle of electrostatic force generated between two parallel discs, which in turn move the diaphragm that is linked to the voltage reading arrow. The probe was moved along the surface of the bar with a gap of ± 3 mm maintained between the probe and the bar surface [7]. The surface voltage readings from the electrostatic voltmeter were recorded as the probe was moved along the surface of the stator bar. From the analyzed results, it was found that the approximate location of the stress grading started at 65 cm (with a length of 2.5 cm) from the midpoint of the stator bar on either side.

3.2 Experiment 2: Tan delta measurement

The objective was to conduct the experiment adhering to the IEC 60894 standard and then to deviate slightly from the guard ring specifications. The guard ring arrangement is shown in Figure 6. The recommended and proposed guard ring specifications are shown in Table 1.

Setup: The circuit connection is shown in Figure 7. The apparatus used were: Step-Up transformer (220 V - 60 kV) controlled by a variac (0 – 260 V), 37.7 pF standard capacitor, voltage divider, multimeter for voltage increment readings and the Schering Bridge instrument. The thermometer was used to measure temperature for all experiments conducted. For safety purposes, the earth stick was used to discharge the capacitor after every experiment performed.

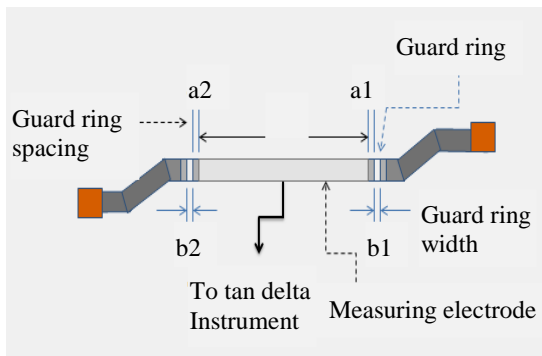


Figure 6: Guard rings arrangement

Table 1: Guard rings specifications.

	Guard ring width (mm)	Guard ring spacing (mm)
Standard	b_1 & b_2 10 min.	a_1 & a_2 4 max.
Deviation	b_1 & b_2 8 b_1 & b_2 1	a_1 & a_2 8 $a_1 = 4, a_2 = 8$ a_1 & a_2 70

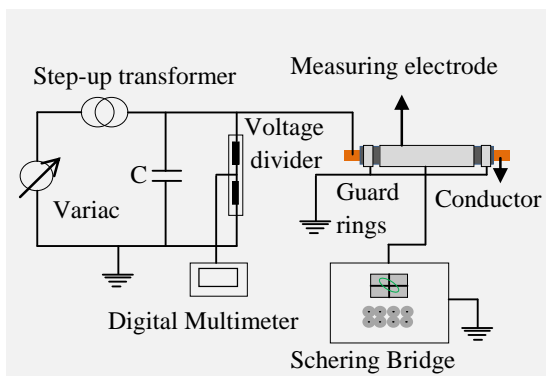


Figure 7: Tan delta measurement setup

Procedure: The setups shown in Figure 6 and 7 were configured. The experiment was performed using all four different measuring electrode forms i.e. aluminium foil, aluminium wire, tinned copper wire and steel plate sheaths. Aluminium foil and tinned

copper wire were also used as guard ring material. Table 1 presents the explored dimensions (width and spacing). The experiment was carried out as recommended in [8]. For each increment and under balanced conditions, the tan delta and capacitance readings were read off the Schering Bridge, and the process was repeated for each increment.

4. RESULTS AND INTERPRETATION

The data for the tan delta as a function of voltage for all four different measuring electrode forms (aluminum wire, aluminum foil, steel sheath plates and tinned copper wire) were recorded. Figure 8 shows the plots for these materials when the experiment was conducted according to the standard. It can be seen that tinned copper wire has the lowest tip-up and it also has a smooth tan delta trend compared to other materials. This might be due to the fact that copper is plated with tin to enhance its electrical properties, thus making a good electrical contact with the stator bar surface. For this reason, tinned copper results were deemed reliable.

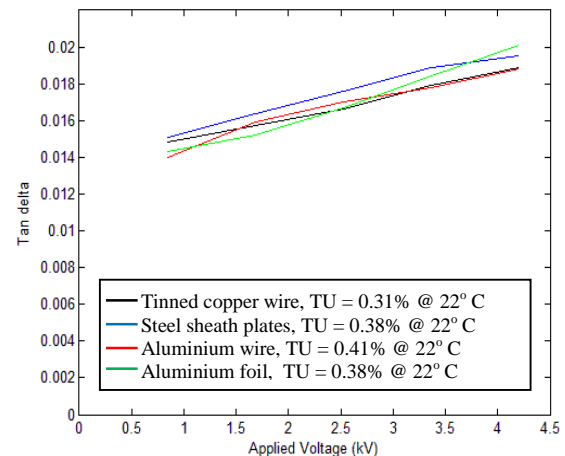


Figure 8: Tan delta plots for all different materials

Figure 9 shows the results when the experiment was performed adhering to and deviating from the guard ring specifications. The guard ring width was kept constant at 20 mm throughout the experiment and only the space between the guard rings and the measuring electrode was varied. It can be seen that when guard rings are not applied, the initial tan delta value and the overall tan delta trend (red line) are high with reference to the tan delta trend attained when complying with the test standard (black line). This was expected and it can be explained by using the model in Figure 3. In the model, it can be seen that the dielectric losses in the graded portion of the overhang together with the I^2R losses dissipated in the resistive grading material will be measured in addition to the dielectric losses in the slot portion, hence leading to high tan delta values. When the guard rings are applied but placed beyond the stress grading, the initial tan delta value and the overall tan delta trend (blue line) are high with reference to the standard plot (black line) but less than the red line.

This was also expected because the stress grading is included in the measurement but excluding the overhang portion of the stator bar after stress grading. When moving the guard rings closer to the stress grading (pink and green line), the tan delta is slightly higher with reference to the standard plot. This was expected as well since the currents that leaks from the guard rings due to poor electrical contact tends to flow towards the graded portion, hence leading to more losses induced and consequently giving high tan delta. Considering an assumption made that there is no PD activity taking place on the specimen, it is evident that the effect of stress grading is the main cause of the tip-ups observed in all the plots, irrespective of guard rings used i.e. there is no complete electrical isolation of the stress grading portion of the bar.

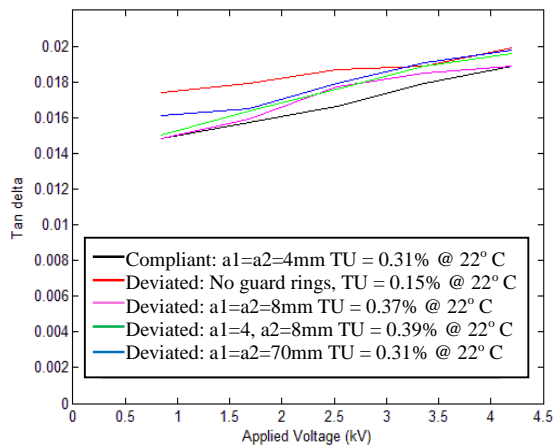


Figure 10: Tinned copper wire, 20 mm constant guard ring width with varied guard ring spacing

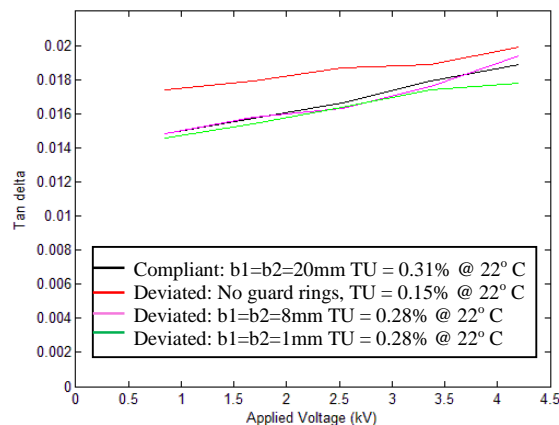


Figure 11: Tinned copper wire, 4 mm constant spacing with guard ring width varied.

Figure 11 shows the results when the spacing between the guard rings and a measuring electrode was kept constant at 4 mm and the guard ring widths were varied. It can be observed that when the guard rings were not applied (red line), the initial tan delta value was too high with reference to the plot (indicated by the black line) which is in accordance

to the standard. This was expected and this behavior can be explained using the same analogy that incorporates the model depicted in Figure 3. However, for guard ring widths of 8 mm and 1 mm represented by green and pink line respectively, are too close to the reference plot (black line). This can be elucidated by the fact that the spacing between the measuring electrode and the guard rings is kept constant and only the guard ring widths were varied. The currents flowing on the bar surface are intercepted at the same position, therefore the dielectric losses including the losses due to stress grading are approximately the same.

5. DISCUSSION

Considering the results presented in Figures 10 and 11, there are two common trends: The first one is that if guard rings are not applied when performing the test, a high percentage error in the range 14 to 18% is obtained and the tan delta as a function of voltage is high indicating that there are more dielectric losses in the stator bar insulation, which is incorrect and misleading because the high tan delta is due to the effect of the stress grading. The error is calculated by taking the first tan delta values of two plots to be compared as suggested in [9]. The other one is that if guard rings are applied but placed beyond the graded portion, the tan delta is a bit higher but reduced to an error range of 7 to 10 %. However, when guard rings are applied and placed before the stress grading to electrically isolate the graded portion, the error significantly drops to 1 to 3%.

6. CRITICAL ANALYSIS

Ideally the tan delta measurement on a new or healthy test specimen results in a horizontal tan delta versus voltage plot [10]. An increase in the tan delta with the increase in applied voltage implies the presence of voids and hence PD activity in the insulation. In addition, tan delta tip-up is due to the stress grading material added to the overhang of the stator bar. Guard rings when applied do not completely eliminate the non-linear behavior of the stress grading materials. This non-linear behavior leads to misleading results, and hence the measured results are prone to the particular percentage error due to this effect. It is worth noting that this is not the only source of error. Inconsistent contact on the measuring electrode and the guard rings will lead to incorrect measurements due to compromised guarding and unanticipated PD activity occurring between the measuring electrode and the stator bar, thus compromising the measurement accuracy. The sensitivity of the Schering Bridge was set to 5 instead of 6 (which is maximum) throughout the experiment since it was difficult to balance the bridge when the sensitivity was set to 6. At a sensitivity of 6, the ellipse was randomly moving up and down. For this reason, it was set back to 5 and thus, a better resolution and accurate results could have been achieved. In addition, the experiment was conducted in a room in which there was a lot of

movement and other experiments were being performed as well. This was undesired because the Schering bridge instrument is sensitive to movement and interferences. This might have slightly influenced the results. To resolve these issues Section 7 discusses how the results can be improved for future work.

7. RECOMMENDATION FOR FUTURE WORK

The following are recommended for future work.

- Perform the experiment in a controlled environment i.e. test room. This will allow the measurement to be performed under controlled temperature, humidity, and noise. In addition, interference from external sources will be minimized.
- Perform the experiment on different test samples i.e. aged, normal, and new stator bar to observe how the tan delta behaves on different test samples.
- Perform the experiment by varying the measuring electrode length and see the effect it has on the tan delta.

8. CONCLUSION

The background on the tan delta measurement and the effect of the stress grading has been outlined. It has been established that the stress grading material has a negative impact on the tan delta measurement results; however it plays a critical role as far as the surface discharge suppression is concerned.

Tan delta testing was performed on a MV motor stator bar using a Schering bridge instrument. It was found from the results that if guard rings are not used the error in the measurement ranges from 14 – 18 % and if guard rings are used but placed after the stress grading, the error ranges from 7 to 10%. However, if guard rings are used and placed before the stress grading, the error ranges from 1 to 3%. Therefore deviating from the standard by not using guard rings affects the results significantly.

REFERENCES

- [1] A. Haddad and D.F. Warne "Advances in High Voltage Engineering", "Polymer insulated power cable" J.C. Fothergill and R.N. Hampton, Chapter10, pp. 476, The institution of Engineering and Technology, London, United Kindom, 2007.
- [2] F.T. Emery," Principles of power factor testing of complete generator stator windings" IEEE International Symposium on Electrical Insulation, USA, pp.426-429, Sept 2004.
- [3] D. Train and L. Melia, "A new power factor and power factor tip-up measurement technique for stator bars and coils "Conference Record of the 1994 IEEE International Symposium on Electrical Insulation, Pittsburgh, PA USA, June 5-8, 1994.
- [4] S.S Dutta, "Water absorption and dielectric properties of Epoxy insulation," Norwegian University of Science and Technology, Department of Electrical Power Engineering, June, 2008.
- [5] G. C. Stone, E. A. Boulter, I. Culbert and H. Dhirani "*Electrical Insulation for Rotating Machines, Design, Evaluation , Aging, Testing and Repair* " IEEE press, John Wiley, 2004.
- [6] IEEE Std. 286-2000, IEEE Recommended Practice for the Measurement of Power Factor TIP-UP of Electric Machinery Stator Coil Insulation.
- [7] J. P. Mackevich, J. W. Hoffman, "Insulation Enhancement with Heat-Shrinkable Components Part III: Shielded Powder Cable", IEEE Electrical Insulation Magazine, pp. 31-40, 1991.
- [8] IEC/TR 60894 (1987-03), Guide for Test Procedure for the Measurement of Loss Tangent of Coils and Bars for Machine Windings.
- [9] F.T. Emery," Principles of power factor testing of complete generator stator windings" IEEE International Symposium on Electrical Insulation, USA, pp.426-429, Sept 2004.
- [10] IEEE Std. 286-2000, IEEE Recommended Practice for the Measurement of Power Factor TIP-UP of Electric Machinery Stator Coil Insulation.
- [11] F.T. Emery," Principles of power factor testing of complete generator stator windings" IEEE International Symposium on Electrical Insulation, USA, pp.426-429, Sept 2004.

THE EFFECT OF STRESS GRADING LENGTH ON TAN-DELTA AND CAPACITANCE MEASUREMENTS ON MV MOTOR COILS

Y.L Lekalakala* and J.M Van Coller**

* Eskom Power Plant Engineering Institute (EPPEI) – High Voltage (AC), School of Electrical and Information Engineering, Faculty of Engineering and the Built Environment, University of the Witwatersrand, Private Bag 3, Wits 2050, South Africa, E-mail: yvonne.lekalakala@eskom.co.za

** School of Electrical and Information Engineering, Faculty of Engineering and the Built Environment, University of the Witwatersrand, Private Bag 3, Wits 2050, South Africa, E-mail: john.vanoller@wits.ac.za

Abstract: End-user specifications for manufactured and refurbished MV motor stator bars and coils specify the maximum allowable measured values of the tan-delta and tan-delta tip-up. While the service provider is contractually obligated to meet these specified values, the test procedures required to perform such measurement are not always specified. Even when they are, factors in the design, manufacture, test and running of a rotating machine can affect the final values and these are not always specified nor fully understood.

This paper looks at the specification of tan-delta and capacitance measurements as well as their associated tip-up measurements. Specifically, it investigates the effect that the length of the stress-grading (for a particular type of stress grading) has on the final factory acceptance tip-up measurement; and consequently, the perceived quality of new winding insulation or the rate of deterioration of insulation in a motor that has been in service.

Keywords: tan-delta, dissipation factor, tip-up, stress grading, electrical insulation, stator winding, condition assessment, partial discharge.

1. INTRODUCTION

Insulation failure is widely documented as the number one electrical failure mode in rotating machines. The large mechanical, chemical and thermal stresses on the motor insulation affect the life expectancy of the insulation and hence also of the machine. As a result, manufacturers and end-users make use of a number of factory acceptance tests and ongoing routine tests to monitor the condition of the insulation to ensure that the winding will achieve its expected lifetime of 20 to 40 years [1, 7-9].

Some on-line tests that are employed include temperature monitoring, current signature analysis, vibration signature analysis and on-line partial discharge (PD) detection. Offline tests used to monitor insulation condition are Insulation Resistance (IR), Polarization Index (PI), DC and AC High Potential Tests, offline PD detection and the Dissipation-Factor test – also known as the Loss-Tangent or the Tan-Delta test [7].

2. TAN-DELTA AND CAPACITANCE MEASUREMENT

As offline ongoing routine tests, the tan-delta and capacitance measurements are an indirect way of measuring partial discharge activity or any other degradation processes or weaknesses in a high voltage winding. Since partial discharge activity could reveal insulation deterioration, an increase in PD activity with increasing voltage can be seen as an indicator of insulation weaknesses [1] and a maintenance intervention needs to be scheduled at the earliest opportunity.

2.1 Eskom Standard

The Eskom Standard on *Refurbishment of Power Station Electric Motors* requires that a motor pass all five of the criteria specified in *Table 1* for the tan-delta testing of MV motors:

Table 1: Eskom Tan Delta Acceptance Criteria for MV Electric Motors [2]

Individual phases and total winding	New Windings	Motors in use
0,2U _n Tan Delta value	< 0,0100	< 0,0400
1,0U _n Tan Delta value	< 0,0300	< 0,0800
Increments: 0,2U _n to U _n	< 0,0060	< 0,0100
tanδ tip-up: $\frac{0.6U_n - 0.2U_n}{2}$	< 0,0060	< 0,0100
Maximum capacitance change: $\frac{C_{max} - C_{min}}{2} \times 100\%$	< 3%	< 6%

Maximum value restrictions are placed on the initial tan-delta reading; incremental tan-delta values between voltages; the final tan-delta value; the tan-delta slope or tip-up; and the overall percentage change in capacitance.

As discussed in [1] and [3], tan-delta and capacitance measurements provide an insight into the condition of an insulation system:

Initial Value: The initial tan-delta value, measured at $0.2U_n$, where U_n is the rated coil line-to-line voltage, gives an indication of the cure state of a thermoset insulation system. This value can also be affected by overall moisture content of the insulation and contamination in the overhang region [3].

Tan-delta tip-up: The overall change in tan-delta with respect to change in voltage from initial test voltage $0.2U_n$ to rated voltage U_n , is an indication of total void content within a machine's insulation. In a new stator, this can be a measure of the quality of the manufacturing process. In a machine that has been in service, it can be a measure of degradation over time. Often, a sharp tip-up can be an indication of [3]

- Delamination
- Imperfect impregnation
- Incomplete cure
- Inadequate bonding
- Contamination

Capacitance tip-up: In ideal insulation, the insulation capacitance does not change as voltage changes. In real insulation, there are a small number of voids that occur as a result of the manufacturing process. Because there are relatively few voids in a healthy insulation system, the change in capacitance is negligible with the change in test voltage. In an unhealthy insulation system (with a significant number of voids), insulation capacitance changes as the test voltage increases. This is further discussed in Section 3.2 below.

Capacitance tip-up can be affected by [3]

- Voids within the insulation
- Contamination if the insulation
- Moisture content of the insulation

An insulation system that displays an overall percentage change in capacitance of less than 2% is considered healthy [4, 5].

2.2 IEEE Standard

It is worth noting that the Eskom Standard tan-delta tip-up definition:

$$\text{Tan-delta Tip-Up} = 0.8U_n - 0.2U_n \quad (1)$$

does not correspond to the *IEEE Std. 286* tan-delta tip-up definition [3].

The definition given in [2]:

$$\text{Tan-delta Tip-Up} = \frac{0.6U_n - 0.2U_n}{2} \quad (2)$$

is a calculation of initial tip-up and not overall tip-up. This might be as a precautionary way of eliminating the effect that stress grading in the overhang portion has on tip-up measurement at higher test voltages.

3. STRESS GRADING

The configuration for a typical MV rotating machine winding is shown in Figure 1(a).

The portion of the winding that fits into the slots of the laminated stator core is covered in a semi conductive coating (paint or tape layer) that ensures that the ground wall insulation of the winding and the grounded stator core are at the same potential. This avoids partial discharge activity between the stator bar insulation and the stator core [4, 11, 13].

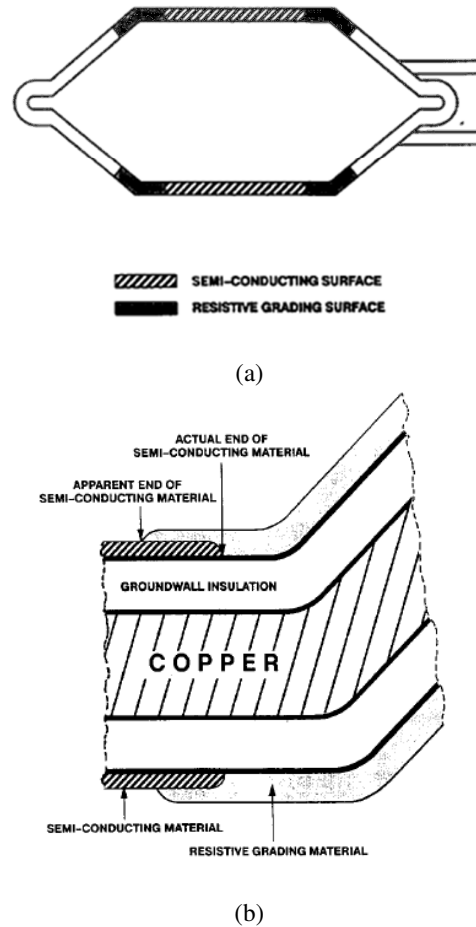


Figure 1 [10]

(a) Typical HV rotating machine winding

(b) Overlap of semi-conductive tape and stress grading

The portion of the bar or coil that extends outside the slot is additionally covered in a stress-control coating, similar to the semi-conductive coating – either a paint or tape layer. This coating overlaps the semi-conductive tape within the slot (Figure 1b) and extends to a length that is prescribed by the tape manufacturer. The stress-control coating – referred to in this paper as the “stress grading” – is infused with silicon carbide so that it adopts a non-linear relationship with voltage. As illustrated in Figure 2, it effectively linearizes the electric field distribution along

the coil surface as it extends beyond the slot and hence minimizes the risk of surface discharges in the overhang region.

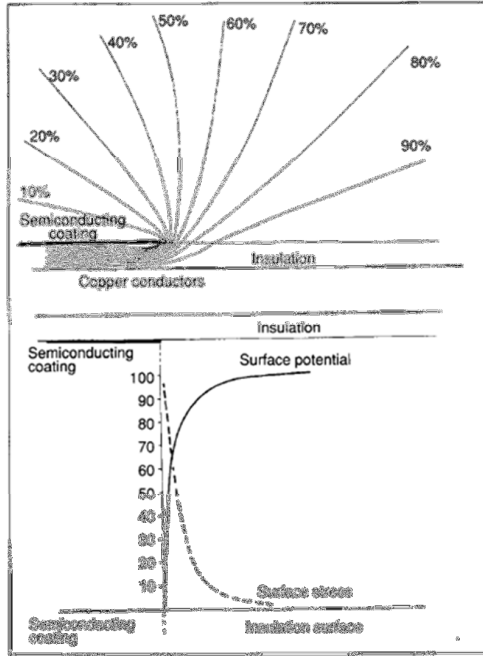


Figure 2: Potential and stress distribution along the insulation surface at the termination of the slot semi-conductive coating (with no stress grading present) [11]

3.1 The effect of the stress grading on the measured tan-delta tip-up

In a good insulation system, the change in tan-delta with increasing voltage (the tan-delta tip-up) is small. As the insulation system degrades and experiences delamination, an increase in void content and contamination, the change in tan-delta with increasing voltage also increases [3, 5]. The tip-up gives an indication that there is an increase in PD activity but cannot give an indication of the level, frequency, or location of the PD [3].

As discussed earlier, the non-linear nature of stress grading is such that at low voltages, its resistance is very high and no current flows through it. At high voltages however, the stress grading is designed to have a low resistance. As such, when a coil or bar is undergoing a tan-delta test, and the test voltage is increased incrementally, the resistance of the stress grading decreases. Capacitive charging currents start to flow through the decreased resistance and produce I^2R losses. Tan-delta measuring equipment picks up these losses and they increase the overall tip-up [3, 10]. It now becomes impossible to separate the PD contribution to the tan-delta tip-up from the contribution of the stress grading I^2R losses to the tan-delta tip-up.

3.2 The effect of the stress grading on the measured capacitance tip-up

When measuring the capacitance of a coil or bar, the initial capacitance measurement that is measured at $0.2U_n$, is the capacitance of the insulation containing voids. As the test voltage increases, the voids within the insulation get ionised and the voids become short circuited. Increasing the test voltage increases the number of voids becoming short circuited – effectively reducing the thickness of the insulation and hence increasing the overall capacitance [10]. The percentage change in overall capacitance (tip-up) estimates the void content of an insulation system [3].

4. LAB WORK

Two sets of experiments were carried out in order to determine the effect that the length of stress grading has on a) the tan-delta and capacitance tip-up measurements and b) the coil surface potential and field distribution in the overhang region.

The test sample consisted of five 11kV coils supplied by a local motor manufacturer. Each coil was constructed as per standard manufacturing procedure and set into a motorette in order to simulate the laminated stator core. The reference coil, Coil 1 was manufactured with 140 mm stress grading length as per design requirements for an 11kV winding. Coils 2 and 3 were manufactured with 150 mm and 160 mm respectively; while Coils 4 and 5 had shorter stress grading at 130 mm and 120 mm. The lap configuration used for application of stress grading was not considered for this paper as coils were manufactured identically and the focus was on changing lengths.

4.1 Tan-delta and capacitance measurement

IEEE 286 recommends the test setup in Figure 3 for the testing of individual coils. Guard rings are recommended in order to isolate the stress grading region in the overhang from the slot portion. This way a more accurate tan-delta tip-up is measured and a true sense of insulation condition is attained. A complete discussion on the different types of guard rings can be found in [4] and [10].

Two different tan-delta measurements were carried out on each of the five coils:

- With guard rings – to isolate the stress grading
- Without guard rings – to include the stress grading in order to assess the impact that the flow of capacitive charging currents in the stress grading has on the tan-delta measurement.

Test procedure: As discussed, each coil is set within a steel bracket in order to simulate the stator core as required in [4]. Guard rings are used to limit interference (current flow) in the overhang section as a result of the stress grading. The coil is pre-conditioned at $1.2U_n$ for

20s. Tan-delta and capacitance measurements are then taken at 0.2, 0.4, 0.6, 0.8, 1 and 1.2 U_n . The tan-delta tip-up is calculated as per Equation 1 and the capacitance percentage tip-up as per equation 3:

$$\text{Capacitance tip-up} = \frac{C_{\max} - C_{\min}}{C_{\min}} \times 100\% \quad (3)$$

The test is repeated without guard rings for each coil.

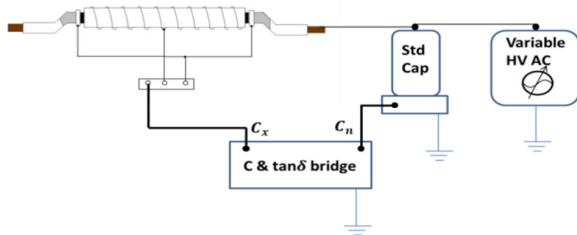


Figure 3: Test setup for tan-delta and capacitance measurement in individual bars and coils [4]

Comparisons of tan-delta and capacitance measurements for Coils 1, 3 and 5 (without guard rings) against a guarded Coil 1 are shown in Figure 4 and

Figure 5. The effect of the stress grading is immediately evident in the location of the three unguarded coils' curves. The deviation of measured values from each other (with Coil 1 as the reference) is notably small. Initial values, final values and tip-up values are all within 0.005 of each other. When compared to the guarded coil however, the stress grading contribution to overall tan-delta measurement is an average of 0.01.

Coils 1 and 3 display similar capacitance percentage tip-up values of 5.1% and 4.1% respectively; while Coil 5's shorter stress grading seems to have a greater impact on the change in capacitance: its capacitance percentage tip-up is much higher, at 17.6%.

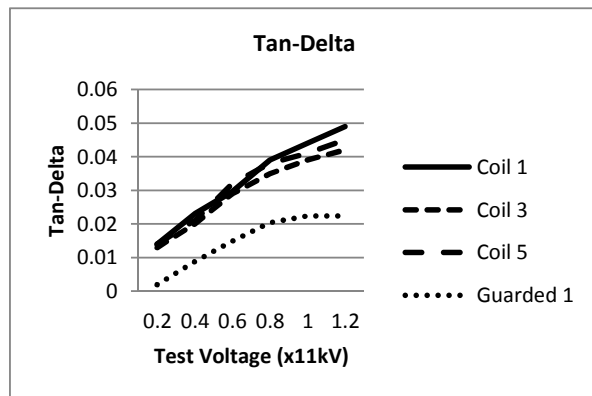


Figure 4: Tan-Delta measurement (without guard rings) for Coils 1, 3 and 5 compared to Coil 1 with guard rings

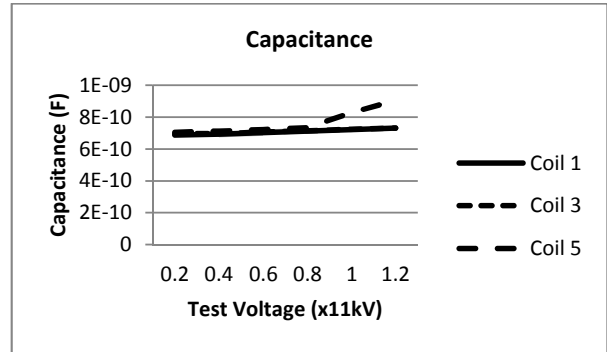


Figure 5: Capacitance measurement (without guard rings) for Coils 1, 3 and 5

4.2 Electrostatic Voltmeter Measurement

As a way of determining if the length of stress grading affects its linearization properties, three coils (1, 3 and 5) were compared. An electrostatic voltmeter was used to plot the surface potential along the coil's overhang – spanning the coils exit from the slot through to its nose.

Figure 6 illustrates the test setup and

Figure 7 illustrates the voltage distribution plot along the overhang surface of each of the three coils.

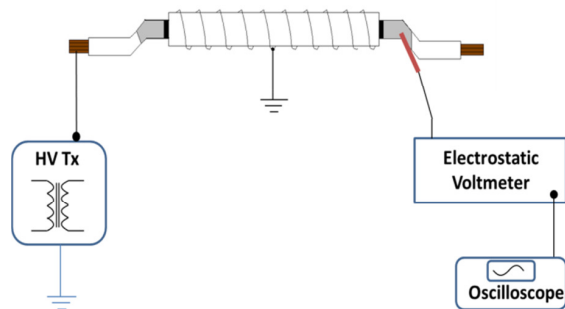


Figure 6: Test setup for surface potential measurement in individual bars and coils [6]

The effect that the length of stress grading has on each coil's surface potential can be seen clearly in

Figure 7. Coil 5, with 120 mm – the shortest length – stress grading, has the sharpest gradient. Coil 3 on the other hand, with 160 mm stress grading, grades the voltage significantly less aggressively. The increase in voltage is gradual over 50 mm while Coil 5's surface voltage climbs steeply within 30 mm.

Despite the relatively sharp change in surface potential, the electric field strength for all three coils is kept below Paschen's minimum value of approximately 3kV/mm required for partial discharge inception. The surface field along each coil is plotted in

Figure 8.

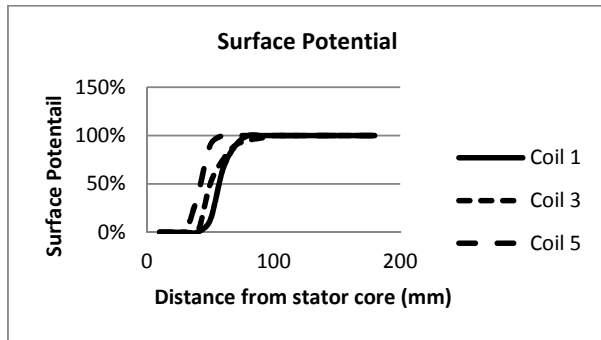


Figure 7: Stator coil surface potential for three coils with different stress grading lengths

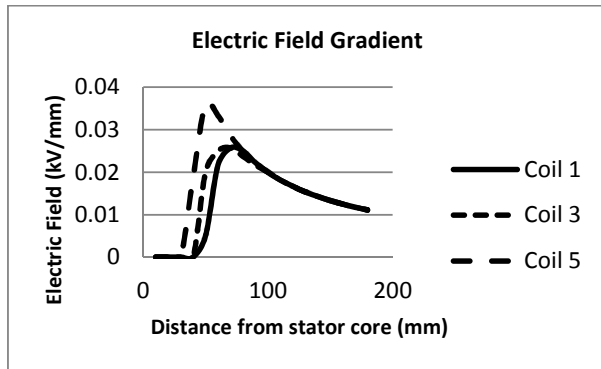


Figure 8: Stator coil surface electric field gradient for three coils with different stress grading lengths

5. DISCUSSION AND CONCLUSION

In [3], M Ferahani et al, conclude that “the influence of the electrical stress control coating on the dissipation factor measuring results is dependent upon the slot length and the conductivity of the applied field control elements.” The hypothesis for this study was that “the influence of the stress grading on the tan-delta value and capacitance value is also dependent upon the length of the stress grading material beyond the slot exit. Furthermore, longer stress grading will have a detrimental effect on the tan-delta measurement as the grading’s non-linear relationship with voltage will translate to a further decrease in resistance. This will allow a larger amount of capacitive current flow through the stress grading and this will produce higher I^2R losses. This will in turn translate to a higher tan-delta tip-up measurement which incorrectly suggests a compromised insulation system. Lastly, the length of grading should not have an effect on surface potential change since the stress grading is made of the same material and therefore has the same linearizing characteristics per unit length.

Tan-delta, capacitance and surface potential measurements of the five coil samples prove that the length of stress grading

- Does not have a marked effect on tan-delta measurement. The initial value, final value and tip-up measurements of all five coils were found to be within 0.005 of each other. Coil 3, with the longest grading, measured similarly to Coil 5, with the shortest grading. A difference of 40 mm between the two coils does not display significant impact on the measured result. This shows that it is the presence of stress grading, and not the length, that has an effect on the tan-delta measurement.
- Does not have a marked effect on capacitance percentage tip-up. All 5 coils measured fall within 1% of each other. Once again, it is the presence of stress grading over the changing length that dominates.
- Does have an effect on the surface voltage and electric field distribution in the overhang. The illustrated behaviour/trend suggests that the guidelines provided by stress grading tape manufacturers as far as application length as a function of coil rating should be adhered to. Optimal behaviour is acquired when the tape is applied to the machine at the length that it was designed for.

6. REFERENCES

- [1] G.C. Stone: “Recent important changes in IEEE motor and generator winding insulation diagnostic testing standards”, *IEEE Transactions on Industry Applications*, Vol. 41, No. 1, pp 91 – 100, January/February 2005
- [2] *Refurbishment of Power Station Electric Motors*, Eskom Standard GGS0389 Rev. 1, 2003
- [3] M. Ferahani et al: “Study of Capacitance and Dissipation Factor tip-up to evaluate the condition of Insulating Systems for HV rotating machines”, © Springer-Verlag 2006, DOI 10.1007/s00202-006-0011-9
- [4] *IEEE Recommended Practice for Measurement of Power Factor Tip-Up of Electric Machinery Stator Coil Insulation*, IEEE Std. 286-2000(R2006)
- [5] F.T. Emery: “Basics of Power Factor Measurement on High Voltage Stator Bars & Stator Windings”, *IEEE Electrical Insulation Magazine*, Vol. 20, No. 3, pp 40 – 45, 2004
- [6] Omranipour and S.U. Haq: “Evaluation of Grading System of Large Motors AC Stator Windings”, in *Conf. Rec. 2008 IEEE Int. Symp. Electrical Insulation*, Peterborough, ON, pp. 158-161, 2008
- [7] S. Grubic et al: “A Survey of Testing and Monitoring methods for Stator Insulation Systems in Induction Machines”, in *2008 Conf. Condition Monitoring and Diagnosis*, Beijing, China, April 2007 © IEEE. doi: [10.1109/CMD.2008.4580262](https://doi.org/10.1109/CMD.2008.4580262)

- [8] *IEEE Guide for Insulation Maintenance of large Alternating-Current Rotating Machinery (10 000 kVA and Larger)*, IEEE Std. 56-1997
- [9] G. Stone: "Short Seminar on Condition Monitoring for Rotating Machines", presented at *Rotating Machines Condition Monitoring Seminar*, Johannesburg, 2013
- [10] D. Train and L. Melia, "A New Power Factor and Power Factor Tip-Up Measurement Technique for Stator Bars and Coils," *Conf. Rec. 1994 IEEE Int. Symp. Electrical Insulation*, PA USA, pp 45 – 49 1994
- [11] A. Roberts: "Stress Grading for High Voltage Motor and Generator Coils," *IEEE Electr. Insul. Mag.*, Vol. 11, No. 4, pp 45 – 49, Jul/Aug 1995
- [12] F.T. Emery: "The Application of Conductive and Stress Grading Tapes to Vacuum Impregnated, High Voltage Stator Coils," *IEEE Electr. Insul. Mag.*, Vol. 12, No. 4, pp 15 – 22, Jul/Aug 1996
- [13] D.J. Conley and N. Frost: "Fundamentals of Semi-Conductive Systems for High Voltage Stress Grading," *Electr. Insul. Conf. and Electr. Manufacturing Expo, 2005. Proceedings*, pp 89-92, 2005

INVESTIGATION OF CORRELATION BETWEEN THERMAL AGEING PREDICTIONS AND MEASURED FURAN LEVELS FOR GENERATOR TRANSFORMERS

MT. Metebe*, J. van Coller** and R Cormack***

* School of Electrical and Information Engineering, University of the Witwatersrand, Johannesburg, 1 Jan Smuts Avenue, Johannesburg, 2001, Private Bag 3, Wits, 2050, South Africa E-mail: MetebeMT@eskom.co.za

** School of Electrical and Information Engineering, University of the Witwatersrand, Johannesburg, 1 Jan Smuts Avenue, Johannesburg, 2001, Private Bag 3, Wits, 2050, South Africa E-mail: John.VanColler@wits.ac.za

*** Eskom, Megawatt Park, Maxwell Drive, Extension 3, Sunninghill, Johannesburg 2000 South Africa E-mail: CormackR@eskom.co.za

Abstract: Furan level measurement is used for estimating the extent of the ageing of transformer cellulose insulation. Ageing of cellulose insulation reveals itself in a decrease in the length of the chains of molecules (degree of polymerisation) that provide the mechanical strength of the insulation. Based on the chemistry of ageing, equations have long existed describing the relationship between the rate of ageing of the insulation and the temperature of the insulation. This paper investigates whether it is possible to apply this equation (Arrhenius equation) to historical loading data for a transformer (or preferably historical temperature data) to estimate the progress of the ageing and then compare this prediction with the progress of ageing estimated from regularly measured furan levels.

Keywords: Arrhenius equation, paper degradation, Furan compound, paper DP, transformers.

1. INTRODUCTION

Transformers play a vital role in power systems and their failure is highly disruptive to the power system. Table 1 lists the financial impact of different types of transformer failures. The data in Table 1 was obtained from an international study of transformer failures over a five year period [1].

Cause of failure	Number	Total Paid
Insulation Failure	24	R 1,349,705,493
Design/Material/Workmanship	22	R 582,264,459
Unknown	15	R 267,986,205
Oil Contamination	4	R 106,527,303
Overloading	5	R 77,118,912
Fire/Explosion	3	R 72,411,939
Line Surge	4	R 44,637,219
Improper Maint/Operation	5	R 31,669,047
Flood	2	R 20,161,782
Loose Connection	6	R 19,680,525
Lightning	3	R 5,921,415
Moisture	1	R 1,575,000
Total	94	R 2,579,659,299

Table 1: Financial impact of different transformer failures (assuming \$1=R9)[1]

The remaining life of a transformer depends mainly on the condition of its insulation. Utilities around the world are concerned about the condition of the insulation used in their power transformers. Different techniques have been developed to improve the properties of the paper used as the main insulation in power transformers. It is also important to estimate the remaining life of the

insulation. In this paper we investigate if any correlation exists between thermal ageing predictions and measured furan levels for generator transformers.

Many power stations in Eskom and around the world were built many years ago and most of them are still using the transformers originally installed [3]. The failure rate increases with the increasing age of the transformers. Figure 1 below shows the rate of failure of transformers as they age [1].

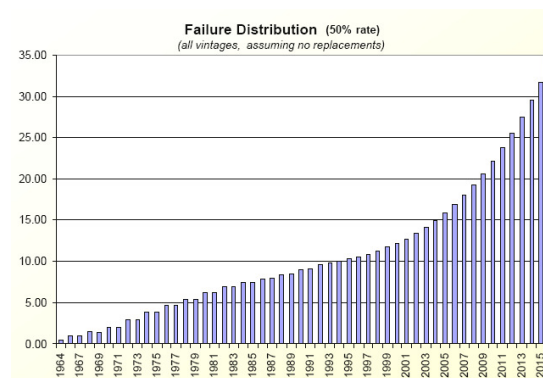


Figure 1: Failure distribution – all vintage [1]

2. MEASUREMENT OF THE DEGREE OF POLYMERIZATION (DP) OF PAPER INSULATION

Measurement of the Degree of Polymerisation (DP) is used to determine the extent of paper ageing within a transformer. DP is however only an average measure of the molecular weight distribution (distribution of the length of the chains (molecular weight) of molecules) and does not give detailed information about molecular weight changes occurring during degradation [4]. Ideally the measurement of DP should be done directly from a paper sample, which requires that the transformer be opened and hence be exposed to additional risks. Paper degradation occurs primarily by chain scission, which leads to a large number of different chemical by-products formed according to the temperature and local conditions [4]. The analysis of these by-products creates an indirect measurement of DP, which is the generally accepted method for determining the DP of the transformer paper. Some of these by-products are furanic compounds, gases, sludge and water. In a transformer where both paper and oil degrade simultaneously, it is important to distinguish between the by-products produced by paper degradation and by oil degradation. Thus is achieved for paper degradation if furanic compounds are monitored.

The dominant paper degradation compounds are [2]:

- 2-furfural (2-FAL)
- 2-acetylfuran (2-ACF)
- 2-furoic acid
- 5-methyl-2-furfural (5-MEF)
- 2-furfurylalcohol (2-FOL)
- 5-hydroxymethyl-2-furfural (5-HMF)

The concentration levels of these by-products can be used to assess the condition of the paper insulation in transformers [6]. In a normal degradation process the 2-FAL compound is produced the most and hence is usually used for the paper assessment [2]. The Cigre Technical Brochure [2] also explains that the 2-FAL compounds may primarily originate from the degradation of the hemicellulose rather than the cellulose. But at high temperatures between 100°C and 200°C the degradation mechanisms proposed show that 2-FAL should also be generated through the 5-HMF resulting from the degradation of the cellulose.

There are a number of factors that will affect the production of furanic compounds in the transformer. Some of these factors include the paper moisture level, the oil acidity and the paper temperature. The amount of paper used in a transformer will also have a significant impact on the furan levels and this must be appreciated when interpreting furan level results. Another factor that has a significant impact on the furan levels is the type of paper that is used in the transformer - different papers will have different proportions of cellulose, lignin and

pentosans. Table 2 below demonstrates the range of paper composition as measured by different authors [3, 4,8].

Cellulose	Lignin	Pentosans
90%	6-7%	3-4%
78-80%	2-6 %	10-20%
90%	3-7%	3-7%

Table 2: Paper composition as measured by different authors

Various equations have been proposed in the literature for converting measured furan levels to estimated DP levels. These equations should be used with caution because their accuracy will vary depending on the type and size of transformer. Models (equations) proposed by Cheim-Dupont, Chendong, Stebbins and De Pablo are listed below [7].

The **Cheim-Dupont model** is:

$$DP = \left(\frac{2FAL}{\lambda} \right)^{\frac{1}{\psi}} \quad (1)$$

- where,

λ – shortened expression – see reference [2] of [7]

d – type of paper (thermally upgraded or Kraft paper)

Ψ – hot spot gradient temperature

This model relates paper ageing to both hot-spot gradient temperature and paper type.

The **Chendong model** is:

$$DP = \frac{\log(2FAL) - 1.51}{-0.0035} \quad (2)$$

- where the 2FAL concentration is in ppm.

The Chendong model was developed using data collected from transformers insulated with Kraft paper and having free breathing conservators.

The **Stebbins model** is:

$$DP = \frac{\log(2FAL \times 0.88) - 4.51}{-0.0035} \quad (3)$$

- where the 2FAL concentration is in ppb.

The Stebbins model is a modification of the Chendong model, to allow it to be used with thermally upgraded paper.

The **De Pablo model** is:

$$DP = \frac{7100}{8.8 \times 2FAL} \quad (4)$$

- where the 2FAL concentration is in ppm.

This model was later modified by Pahlavanpour.

Modified De Pablo model:

$$DP = \frac{800}{[0.186 \times 2FAL] + 1} \quad (5)$$

- where the 2FAL concentration is in ppm.

3. THE PAPER DEGRADATION PROCESS

Paper degradation is affected by many factors, making the process complex. In a power transformer, paper degradation can be affected by transformer design, loading, temperature and paper type. Figure 3 below shows some of the factors leading to the degradation of the oil and paper used in an oil-filled power transformer. The degradation process involves chain scission (depolymerisation) and the release of by-products such as hydrogen, short chain hydrocarbons, carbon monoxide, carbon dioxide and water [3].

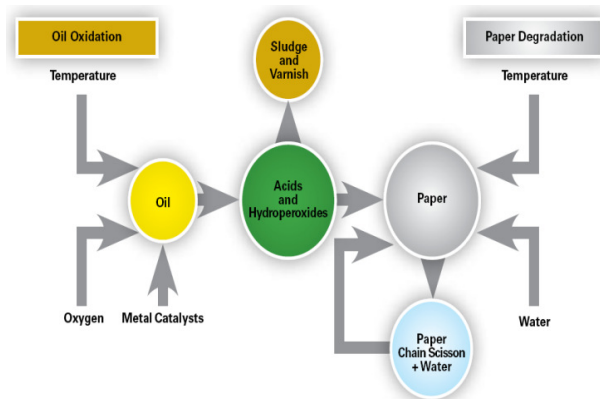


Figure 2: Paper degradation process [10]

In practice paper degradation consist of three simultaneously occurring sub-processes which are hydrolysis, oxidation and pyrolysis [8].

- Hydrolysis, which is a catalytically governed process where the rate of chain scissions depends on carboxylic acids dissociated in water. As both water and carboxylic acids are produced during ageing of cellulose this process is self-perpetuating.
- Oxidation, which could be catalysed by hydroxyl radicals ($HO\bullet$), which are produced by

decomposition of hydrogen peroxide, H_2O_2 and of organic hydroperoxides (ROOH).

- Pyrolysis which can take place without the presence of water and/or oxygen, or any other agent to initiate the decomposition. At normal operating or overload temperatures (i.e. $<140^\circ C$), pyrolysis is not likely to be present.

Degradation also releases larger molecules such as 2-furfuraldehyde (furfural) which can then be detected in the oil and can give an indication of the condition of the paper, because it can be distinguished from the oil degradation by-products [3, 4].

4. PREDICTION OF THE PAPER DP DURING AGEING

The complexity of the prediction of the paper DP is captured by reference [3]. The requirements of any prediction model are knowledge of the detailed chemical degradation processes of cellulose; information about the failure mechanisms within a transformer (for instance, from analysis of old or failed transformers); knowledge of the kinetics and mechanisms of the production of the chemical indicators resulting from paper degradation; and knowledge of the relationship between the concentration of the paper degradation by-products in the oil to the paper insulation condition (i.e. degree of polymerisation and strength of the paper) [3].

Besides the complexity and challenges posed by modelling paper degradation inside an oil-filled transformer, a model such as the Arrhenius equation can be used to estimate chain scission within the paper. The aging of paper, in an environment of constant temperature, moisture, and oxygen concentration, can be described using the Arrhenius equation [5]. The Arrhenius equation can have the following forms:

$$\frac{1}{\text{ageing}} = A \cdot e^{\left(\frac{-E}{RT}\right)} \cdot t \quad (6)$$

$$\frac{1}{DP_{\text{final}}} - \frac{1}{DP_{\text{initial}}} = A \cdot e^{\left(\frac{-E}{RT}\right)} \cdot t \quad (7)$$

- where A is the chemical environment constant (pre-exponential constant), E is the activation energy, R is the molar gas constant $8,314 \text{ J/mole/K}$ and T is the absolute temperature in Kelvin.

The Arrhenius equation assumes a constant temperature, thus it is necessary to use average temperature values calculated from the actual sampled values. Time duration (t) is the period between the initial DP and the final DP (duration between the sampled values). The chemical environment constant (A) values together with the 95%

confidence limits given in per hour are shown in Table 3. They are dependent on the type of paper used and the moisture level in the paper

Data set	Pre-exponential (h ⁻¹)	95% confidence limit (h ⁻¹)	
Upgraded paper	3.65×10^7	7.93×10^6	1.68×10^8
Dry Kraft paper	1.07×10^8	2.41×10^7	4.71×10^8
Kraft paper + 1% H ₂ O	3.50×10^8	8.41×10^7	1.46×10^9
Kraft paper + 2% H ₂ O	7.78×10^8	1.83×10^8	3.30×10^9
Kraft paper + 4% H ₂ O	3.47×10^9	7.66×10^8	1.57×10^{10}

Table 3: Chemical environment constant (A) in oil [3]

The activation energy (E) for the degradation of cellulose in oil, is quoted in the literature to be about 85 - 128 kJ/mole (for the thermal degradation reaction) [3, 5]. It should be noted that cutting, shredding, sieving and the size of the paper will have an influence on the activation energy. The activation enthalpy reportedly decreases and the activation entropy increases with increasing crystallinity of the paper [3]

In a real transformer, the temperature of the paper changes with the load and the environmental conditions. The Arrhenius equation does not take such changes into account. The environmental conditions will also determine whether hydrolysis or oxidation dominates the aging reaction. Nevertheless, the Arrhenius equation can be used to estimate the aging of the paper due to each process, assuming steady-state conditions

5. CORRELATION BETWEEN MEASURED AND PREDICTED DP

The Arrhenius equation assumes a constant temperature, but this will not apply in real situations where the generator transformer temperature varies with the dispatched power. Another issue is that the Arrhenius equation is non-linear. To address these issues, the following approach was adopted:

5.1 Assumption of constant temperature

The approach here was to replace the varying temperature curve with a stepped temperature curve where the step value represents the average value between regularly spaced time values. Figure 3 below shows the temperature profile of a typical generator transformer where the stepped curve has been generated from the actual varying temperature.

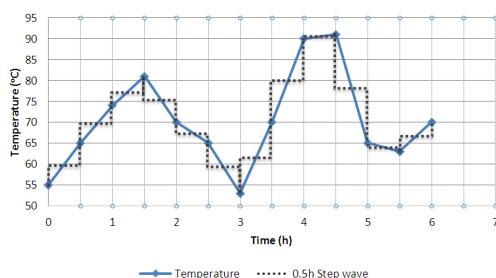


Figure 3: Transformer temperature profile

5.2 Non-linearity of the Arrhenius equation

The height of each step of the stepped temperature curve must not be too large. The choice of height of each step must take cognizance of the fact that a 6°C increase in temperature halves the paper life expectancy, so the step heights must be reduced to considerably less than 6 °C.

5.3 Measured and calculated DP

Even though it is crucial to know what is happening inside the transformer, it is to do repeated tests throughout its life. A Lethabo generator transformer, installed in 1986, had test data from 30 December 1991 to 25 April 2012 and it is this data that was used for this project. The available data was projected as shown below in Figure 4.



Figure 4: Three year projection demonstration

The assumptions mentioned earlier on the Arrhenius equation and factors affecting measured DP (like sample contamination) will have impact on the accuracy. Table 4 below show the results of the correlation between measured and calculated DP, also indicating the error percentage between them.

Date	Measured DP	Arrhenius Calculated DP	
		1 year projection	3 year projection
Oct 1997 Furans samples	680	494, 27% error	545, 20% error
Aug 1999 Paper samples	607, 683, 533 Avr: 608	456, 25%error	509, 16% error
Sep 2000 Furans samples	484	438, 10% error	488, 1% error

Table 4: Measured and calculated DPs

6. CONCLUSIONS

Even though further study is still needed, current results show that there is close correlation between Arrhenius paper degradation predictions and measured furans levels.

Thus using temperature data and the Arrhenius equation, long term average DP levels can be predicted.

7. REFERENCES

- [1] H. William and P.E. Bartley, "Analysis of Transformer Failures," International Association of Engineering Insurers 36th Annual Conference – Stockholm, 2003
- [2] "Furanic Compounds for Diagnosis," Cigre Brochure 494, 2012
- [3] A. M. Emsley and G. C. Stevens, "Review of chemical indicators of degradation of cellulosic electrical paper insulation in oil-filled transformer," IEE Proceedings – Science, Measurement and Technology, vol. 141, pp 324- 334, 1994
- [4] A. M. Emsley and G. C. Stevens, "Kinetics and mechanisms of the low-temperature degradation of cellulose," Cellulose 1:pp 26-56, 1994
- [5] N. Lelekakis, W. Guo, D. Martin and J. Wijaya, "A field study of aging in paper-oil insulation systems," IEEE Electrical Insulation Magazine, DEIS Feature article, 2012
- [6] O. Koreh, K. Luda'nyi, K. Ve'key, E. Ja'vorszky, E. Molna'r, K. Torkos and J. Borossay, "Determination of Furanic Compounds in insulating oil by High Performance Liquid Chromatography/Mass Spectrometry using atmospheric pressure chemical ionization," Rapid communications in mass spectrometry, Rapid Commun. Mass Spectrom. 12: pp1515–1519, 1998
- [7] N.S. Mtetwa, "Accuracy of furan analysis in estimating the degree of polymerization in power transformers,"
- [8] "Ageing of Cellulose in Mineral-Oil Insulated Transformer," Cigre Brochure 323, 2007
- [9] Doble 2005 regional seminar, "Failure Analysis for Power Transformers," Presentation P6, Doble 2005 Eskom transformer seminar
- [10] C.D.F Suez, "Paper degradation Assessing remaining transformer lifetime," BELAC Laborelec, 2012

A STUDY OF ROTOR TOPOLOGIES OF LINE-START PM MOTORS FOR COOLING FAN APPLICATIONS

Jéan-Pierre Els, Albert Sorgdrager and Rong-Jie Wang*

* Department of Electrical and Electronic Engineering, Stellenbosch University, Private Bag X1, Matieland 7602, South Africa E-mail: rwang@sun.ac.za

Abstract: The work presented in this paper deals with a study of different rotor topologies for line-start permanent magnet synchronous motors, which are compared and weighed up against each other to identify the best suited topology for fan type load applications. The design analysis and optimization of line-start permanent magnet machines are carried out by using a combination of finite element method and analytical models. The selected designs are optimized by formulating a cost function with key variables included. The optimization aims to optimize the permanent magnet weight with additional constraints to satisfy the required performance characteristics. The mass moment of inertia, the damping coefficient and the torque-speed curve of a practical cooling fan are experimentally determined, which are incorporated in the transient finite element analysis to evaluate the starting and synchronization capabilities of each candidate design. It is found that the rotor topology with asymmetrical magnet array delivers best overall performance.

Key words: Line-start motor; permanent magnet; induction motor; design optimization; finite element method; transient performance; cage winding.

1. INTRODUCTION

The energy consumption of the world is increasing at an alarming rate. Owing to the growing environmental concerns, the world increasingly focuses on energy saving programs [1]. Since electric motors are greatest energy consumption apparatuses, it is of critical importance to improve their energy efficiency. The induction motor (IM) constitutes, by far, the largest portion of electric motors both in terms of quantity and total power ratings among all electric motors [2].

Although significant amount of research and development effort has been dedicated to improve the performance of IMs, there is an inherent limit to their efficiency and power factor, especially at small power ratings. More efficient motor types gradually appear as alternatives. Amongst others, line-start permanent magnet synchronous machines (LSPMSMs) are increasingly receiving attention in recent years.

LSPMSMs have certain advantages over IMs such as higher efficiency and power factor within a wide load range. It is perceived that LSPMSMs could replace the IMs in many applications such as fans and pumps with better results. Due to the presence of a negative braking torque generated by the permanent magnets (PM) during start-up, LSPMSMs are not suitable for all applications. The magnitude of this braking torque is influenced by the back-EMF voltage induced by the PM in the stator coils [3].

This paper investigates the feasibility of an LSPMSM to replace an IM for fan-type loads. Selected LSPMSM candidate designs with different rotor topologies are each optimally designed and compared to identify the best suited topology for fan-type load applications.

2. DESIGN SPECIFICATIONS

In this section the design specifications of a LSPMSM is described. For this study a WEG 2.2kW 525V 4-pole three-phase premium efficiency induction motor (PEIM) is selected as a reference motor. The stator design of the PEIM will be applied to all the LSPMSM designs so that only the rotors need to be optimally designed. From a production perspective, it would be cost-effective if standard IMs can be easily modified to LSPMSMs. The basic design specifications and dimensions are listed in Tables 1 and 2 respectively. The winding layout of the PEIM stator is given in Fig. 1.

Table 1: Design specifications.

Description	Value
Power, kW	2.2
Line voltage, V	525
Rated speed, RPM	1500
Number of phases	3
Number of poles	4
Duty cycle	S1
Frame size	100L

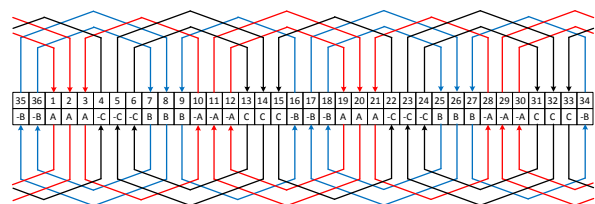


Figure 1: The winding layout of the induction motor stator.

Table 2: The dimensions of LSPMSM stator.

Description	Stator	Rotor
Outer diameter, mm	160	97.9
Inner diameter, mm	99.9	26.8
Stack length, mm	121	121
Wire diameter, mm	0.643	-
Winding type	lap	cage
Coil pitch	23/3	-
Phase connection	delta	-
Number of slots	36	28
Number of conductors per slot	82	-
Number of strands per conductor	2	-
Air-gap length, mm	0.5	-

2.1 Characteristics of fan-type loads

The load torque of a fan is proportional to the square of the fan rotation speed. This type of loads exhibit variable load torque characteristics. However most practical fans have to overcome a significant breakaway torque when starting [4]. Furthermore, the moment of inertia and damping coefficient of the load are also important factors. To start up a fan load, the transient torque profile of a LSPMSM should be designed in such a manner that the torque dip due to the PM breaking torque is higher than the required load torque. This is indicated in Fig. 2 with the black line representing the torque profile of the LSPMSM and the solid blue line the load torque profile of a fan-type load.

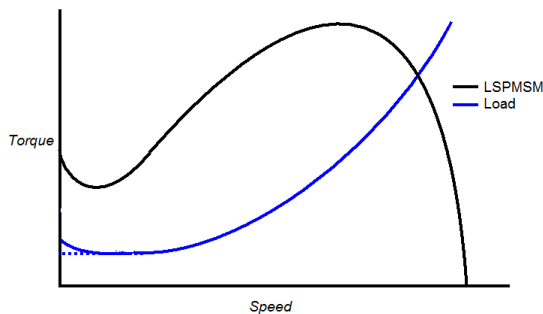


Figure 2: Torque-speed characteristics for fan-type load.

3. DESIGN AND OPTIMIZATION

This section presents the selected rotor topologies and the design optimization methodology and procedure of LSPMSMs.

3.1 Selected rotor topologies

The rotor topologies selected for the study are shown in Fig. 3. All four topologies are of embedded PMs as this allows more freedom of design with regards to the arrangements of PM array shapes [5]. In general, embedded LSPMSM rotor topologies have shown to provide better transient performance and stability over surface-mounted topologies but weaker steady-state

performance [6]. Round rotor slots are selected for all the designs simply for ease of manufacturing at a later stage. The cage bar material is aluminium.

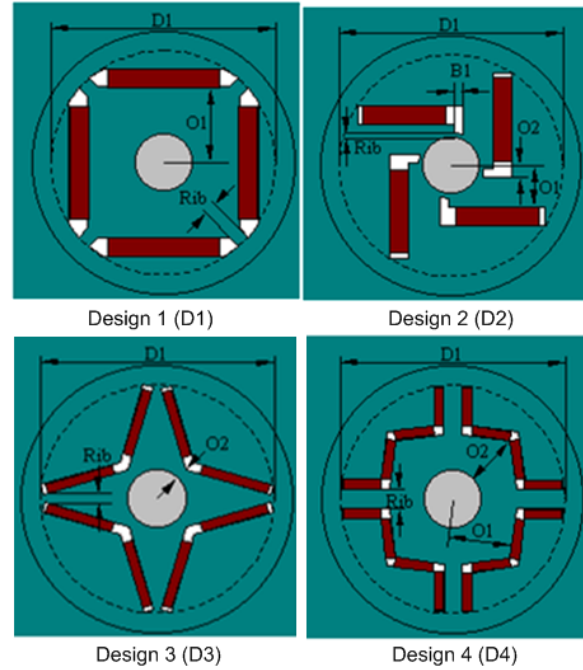


Figure 3: The selected LSPMSM rotor topologies showing key design variables.

3.2 Optimization procedure

The design of a LSPM motor is essentially a complicated multi-variable and multi-criteria optimization problem [7] as both steady-state and transient performance need to be taken into account. The basic design methodology employed here is to use a combination of both analytical and FEM performance calculations. The design optimization is performed for steady-state and full-load condition by using analytical method. To account for transient performance, the objective function is formulated to optimize for PM mass while subjected to the constraints such as output power, back-EMF, start-up torque and air-gap flux density. The rationale behind this is as follows:

- by optimizing the PM material required in the rotor the reactive power exchanged with the power supply will be minimized and a higher power factor can be gained at a lower line current [8]
- however, PM material in the rotor is also responsible for the braking torque during start-up process, which adversely affects the starting performance of a LSPMSM
- thus, a fine balance between the above two is the key for the design of a LSPMSM

All selected rotor topologies are individually optimized to ensure the best candidate designs are found. Once

an optimum design is identified, its start-up and synchronization characteristics will be validated by running a transient time-step FE analysis with the torque-speed curve of a practical fan. In the event that the design does not meet with the start-up or synchronization requirements, new design iterations need to be carried out until a satisfactory design is found. The flow chart of the LSPM motor design procedure is given in Fig. 4.

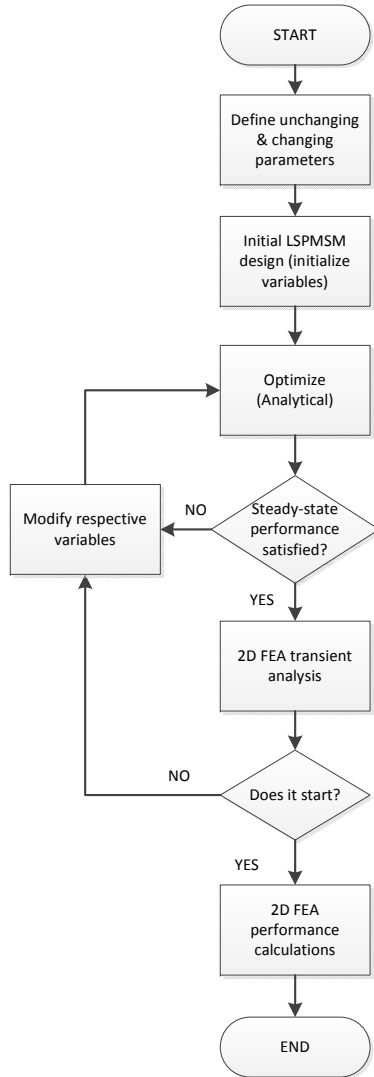


Figure 4: Flow chart of LSPM motor design procedure.

4. PERFORMANCE EVALUATION

In this section the steady-state and transient performance of the four optimized LSPMSMs will be evaluated and compared with each other. The LSPMSM with the best performance is then compared to the reference PEIM.

4.1 Steady-state performance

Table 3 summarizes the steady-state performance of the four optimal LSPMSM designs. It is clear that the second design (D2) shows the best steady-state performance of all. Although it has the highest back-EMF value of the four designs, it has the lowest braking torque component as well. This may be attributed to the higher d -axis inductance that also has a large impact on the braking torque (T_m) represented by the following equation:

$$T_m = \frac{3p}{\omega(1-s)} \left[\frac{R_1^2 + X_q^2(1-s)^2}{R_1^2 + X_q X_d(1-s)^2} \right] \left[\frac{R_1 E_o^2(1-s)^2}{R_1^2 + X_d X_q(1-s)^2} \right]$$

with p being the pole pairs, ω the electrical angular speed in rad/s, R_1 the stator resistance, X_q and X_d the dq axis inductances, and s the slip at a given instant [9]. Also interesting is that the second design (D2) utilizes the least amount of PM material.

Table 3: Optimized LSPMSMs: steady-state performance.

Description	D1	D2	D3	D4
Efficiency, %	95.8	95.98	95.8	95.7
Power factor	0.96	0.97	0.94	0.945
Total loss, W	96	94.2	97.6	98.4
Airgap flux density, T	0.44	0.61	0.48	0.49
Rated current, A	2.63	2.58	2.67	2.67
Braking torque, Nm	16.4	12.5	14.7	13.2
Back EMF, V	346.8	488.7	380.2	387
PM weight, kg	0.78	0.54	0.58	0.6

4.2 Transient performance

The transient performances of LSPMSMs are of particular interest as this type motor is known for its relatively poor transient performance [4]. The transient performance calculations of the four LSPMSM designs are carried out using a transient 2D FE software package. The experimentally determined fan load characteristics are incorporated into the simulation. Fig. 5 shows the flux plot of the Design 2 under full load at a certain time step. The detailed simulation results are included in Appendix A (Figs 6-15).

The transient performance of four designs are compared in Table 4. It is evident that the second design (D2) demonstrates the best transient performance as it reaches synchronization within the shortest time (also refer to Figs 6-9). It can also be seen in Figs 11-14 that the torque-speed trajectory of Design 2 shows less pole-slips repetitions and speed overshoots of all four designs. Better synchronization capability is also evident with a smaller locus around the synchronous speed.

Table 4: Optimized LSPMSMs: transient performance.

Description	D1	D2	D3	D4
Start-up time, s	2	1	1.4	1.25
Start-up current, A	32.5	29	30	32
Start-up torque, Nm	73	72.3	75.4	64

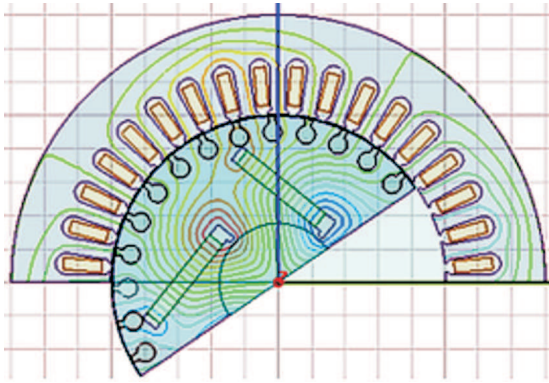


Figure 5: Flux plot of the LSPMSM (design 2) under full load.

4.3 Performance comparison: LSPMSM vs PEIM

Based on the comparison in Sections 4.1 and 4.2, Design 2 can be identified as the best design option of the four designs. The next step is to determine how the performances of Design 2 compare with these of a PEIM under the same load and operation conditions.

From Table 5 it is clear that the Design 2 has a higher efficiency, almost unity power factor, significantly lower steady-state losses and lower rated current. The LSPMSM (D2) also has larger start-up and breakdown torques. The synchronization time between the LSPMSM and PEIM is practically the same. However, the start-up current of LSPMSM is higher than that of PEIM.

Table 5: Performance comparison: LSPMSM vs. PEIM.

Description	LSPMSM (D2)	PEIM
Rated power, kW	2.2	2.2
Rated line current, A	2.61	3.16
Rated speed, RPM	1500	1457
Total loss, W	95	245
Efficiency, %	95.8	90.4
Power factor	0.97	0.88
Air-gap flux density, T	0.59	0.75
Air-gap length, mm	0.5	0.2
Start-up time, s	1	0.9
Start-up current, A	32.5	22.5
Start-up torque, Nm	75.14	51.81
Breakdown torque, Nm	83.95	64.7
Breakdown slip	0.56	0.36

As shown in Figs 12 and 15, for fan-type loads with relatively high inertia, the instantaneous speed-torque

trajectory for both LSPM motor and induction motor show signs of repetitive pole-slips profiles at starting. The synchronization process for both motors are satisfactory.

5. CONCLUSION

In this paper, LSPMSMs with different rotor topologies are optimally designed and compared for fan load applications. It clearly shows that Design 2 delivers the best overall performance among the selected designs. Furthermore, the steady-state and transient performances of both Design 2 and the PEIM are computed and compared by applying 2D transient FE analysis. The results show that the LSPMSM (D2) has higher efficiency and power factor compared to the PEIM at steady-state. Although the satisfactory transient starting performance of the LSPMSM is evident, the PEIM draws less starting current and exhibits a slightly better transient performance than the LSPMSM. The transient performance of the LSPMSM might be improved by investigating the cage design in the rotor. From the results provided in this paper it is clear that a LSPMSM can act as a direct replacement for PEIM for fan-load applications.

ACKNOWLEDGMENT

This work was supported in part by Eskom Tertiary Education Support Program (TESP), Sasol Technology Research and Development, and the National Research Foundation (NRF).

REFERENCES

- [1] T. Modeer, "Modeling and testing of line start permanent magnet motors," Master's thesis, KTH, Stockholm, Sweden, 2007.
- [2] I. Boldea, *The induction machine handbook*. New York, USA: CRC Press, 2002.
- [3] F. Kalluf, C. Pompermaier, and N. Ferreira da Luz, M.V. and Sadowski, "Braking torque analysis of the single phase line-start permanent magnet synchronous motor," in *Electrical Machines (ICEM), 2010 XIX International Conference on*, 2010, pp. 1–5.
- [4] C. Mutize and R.-J. Wang, "Performance comparison of an induction machine and line-start PM motor for cooling fan applications," in *21st Southern African Universities Power Engineering Conference (SAUPEC)*, 2013, pp. 122–126.
- [5] W. Kim, K. Kim, K. S.J., D. Kang, S. Go, H. Lee, Y. Chun, and J. Lee, "A study on the optimal rotor design of lspm considering the starting torque and efficiency," *Magnetics, IEEE Transactions on*, vol. 45, no. 3, pp. 1808–1811, 2009.
- [6] P. Hung, S. Mao, M. Tsai, and C. Liu, "Investigation of line start permanent magnet synchronous motors with interior-magnet rotors and surface-magnet rotors," in *Electrical Machines and Systems (ICEMS), International Conference on*, 2008, pp. 2888–2893.

- [7] W. Jazdzynski and M. Bajek, "Modeling and bi-criterial optimization of a line start permanent magnet synchronous machine to find an ie4 class high efficiency motor," in *Electrical Machines (ICEM), 2010 XIX International Conference on*, 2010, pp. 1–5.
- [8] D. Rodger, H. Lai, R. Hill-Cottingham, P. Coles, and F. Robinson, "A new high efficiency line start motor with high starting torque," in *Power Electronics, Machines and Drives (PEMD), 2006 IET International Conference*, 2006, pp. 551–555.
- [9] V. Honsinger, "Permanent magnet machines: asynchronous operation," *Power Apparatus and Systems, IEEE Transactions on*, vol. 99, no. 4, pp. 1503–1509, 1980.

APPENDIX

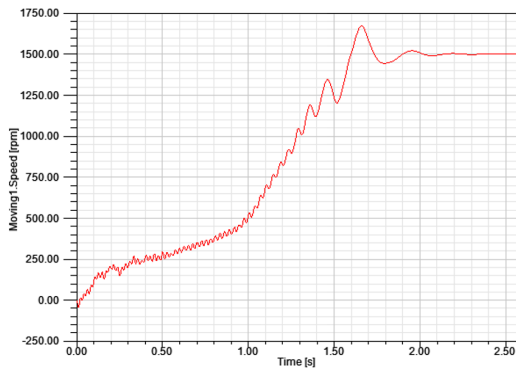


Figure 6: LSPM design 1: speed versus time curves.

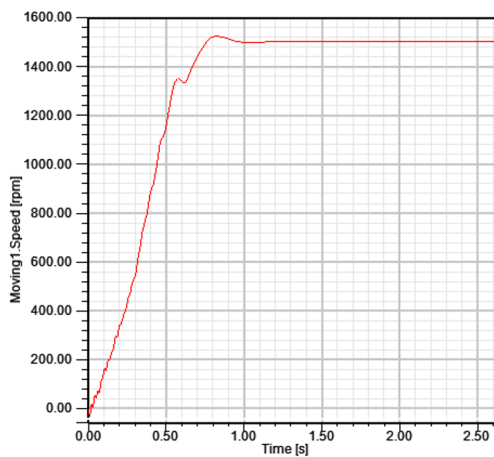


Figure 7: LSPM design 2: speed versus time curves.

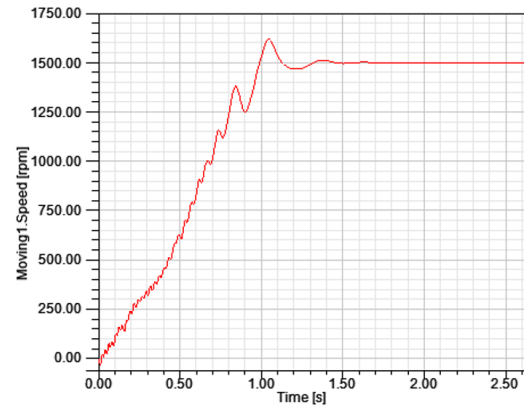


Figure 8: LSPM design 3: speed versus time curves.

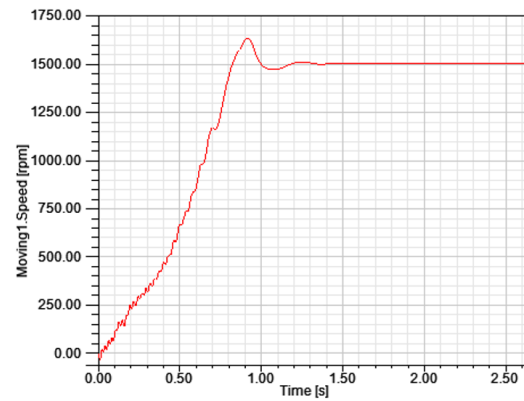


Figure 9: LSPM design 4: speed versus time curves.

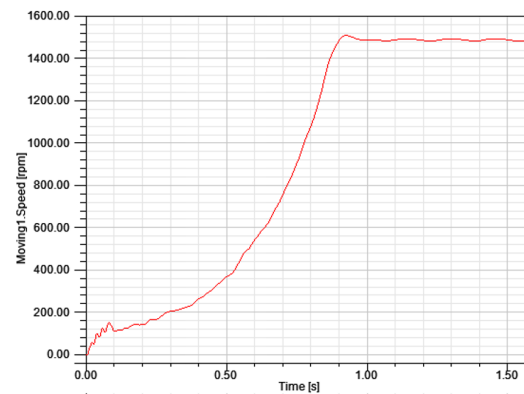


Figure 10: PEIM: speed versus time curves.

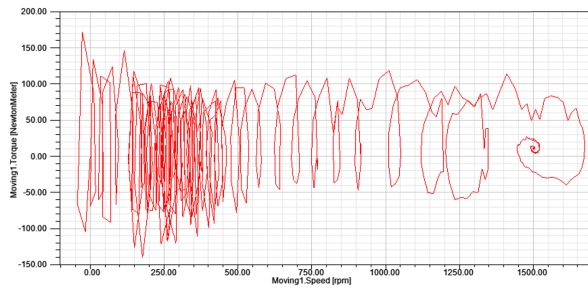


Figure 11: LSPM design 1: transient torque-speed trajectories.

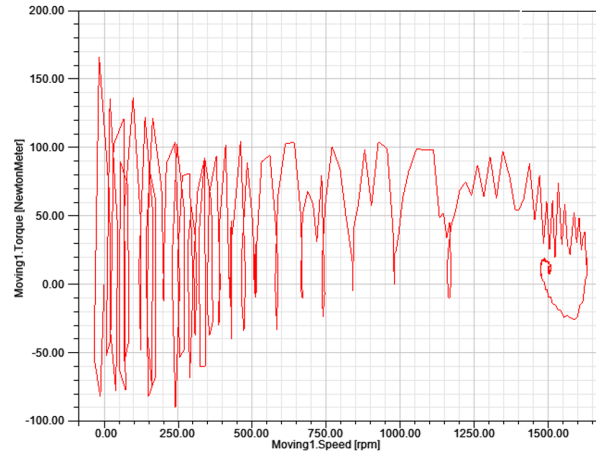


Figure 14: LSPM design 4: transient torque-speed trajectories.

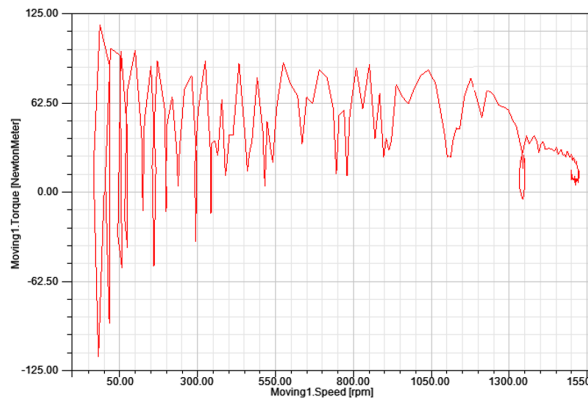


Figure 12: LSPM design 2: transient torque-speed trajectories.

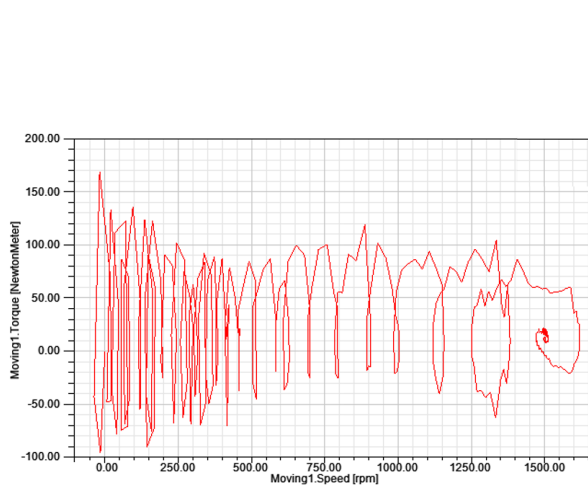


Figure 13: LSPM design 3: transient torque-speed trajectories.

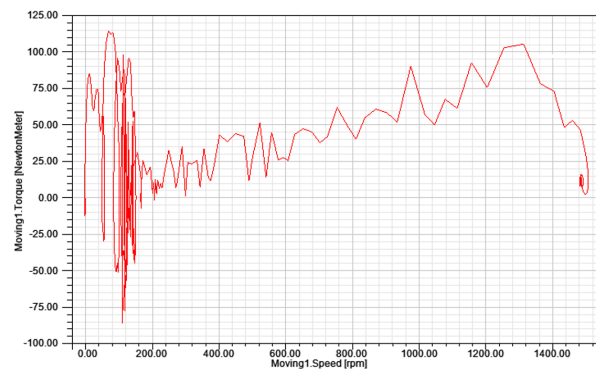


Figure 15: PEIM: transient torque-speed trajectories.

PERFORMANCE COMPARISON FOR MOTORING AND GENERATING MODES OF A RELUCTANCE SYNCHRONOUS MACHINE

J. du Plooy* and N. Gule*

**Stellenbosch University, Department of Electrical and Electronic Engineering, Cnr Banghoek Road and Joubert Street, Stellenbosch, 7600, South Africa*

Abstract. Iron losses result in performance differences in a reluctance synchronous machine (RSM). This paper explores these differences with regard to current magnitude, efficiency, and power factor between motoring and generating. FEM results are compared against a Simulink model of the machine as well as physical measurements. Results presented by this study indicate that the aforementioned performance indicators are indeed affected by the mode of operation of the RSM. These differences in performance are explained with references to iron loss.

Key Words. Iron loss, reluctance synchronous machine, generator, motor.

1 INTRODUCTION

The magnetic fields inside electrical AC machines during operation are complex and thus difficult to model accurately. Factors, such as saturation and iron loss, contribute additional nonlinear terms to the otherwise linear equations that describe the ideal machine. These nonlinear effects impact the performance of AC machines, specifically the reluctance synchronous machine (RSM), under different modes of operation. In some cases, these nonlinear effects can be beneficial to performance.

Research interest in RSMs has increased in recent years[1, 2]. The development of power semiconductor-based drives and digital electronics means RSMs can be operated in closed-loop control schemes. This has the implication that the magnetomotive force (MMF) within the stator of the machine can be placed accurately in relation to the rotor[3]. Also, RSMs under control by inverters do not require damping bars in the rotor, allowing the rotor to be designed for maximum saliency ratio and thus optimal performance[3]. These improvements in rotor saliency ratios put the RSM on par with, if not superior to, the induction machine in terms of power density[3].

From the literature available, it appears research focus is predominantly on the RSM's use as a motor with papers detailing the use and performance as a generator more limited[1, 4]. Of note, though, is a paper by Boldea et al.[5] in which iron losses are used to described differences in RSM performance between motoring and generating. In a paper by Tokunaga et al.[6], an RSM is used as a generator in a wind turbine, however, the study only presents specific FEM results. Given the majority of literature, it seems more interest is given to the switched reluctance machine (SRM) when it comes to the generator side of reluctance machines[7, 8].

This paper aims to investigate the difference in performance of an RSM between operation as a motor and generator. However, instead of autonomous generator operation as performed by Boldea et al.[5] and Mohamadein et al.[9], this study looks at an inverted-fed RSM. No literature has been found by the author in which this form of comparison between motoring and generating

of an RSM has been done.

2 THEORY OF OPERATION

The basic phenomenon behind the operation of an RSM is that of reluctance, hence the name. A metal bar placed arbitrarily inside a magnetic field will tend to align itself within the field in an attempt to create a path of minimum reluctance. If the magnetic field happens to rotate, the metal bar will rotate synchronously with the field. This is the basic functioning of an RSM.

The rotor of an RSM, however, is not as simple as a metal bar. Design of the rotor is aimed at minimising its reluctance in one direction while maximising it in another; this difference in reluctance (and thus inductance) between these axes is called the saliency ratio. The axis with minimum reluctance is the d-axis and the axis of maximum reluctance is the q-axis.

The equations that describe the RSM in the dq-axes are similar to those of the synchronous machine, except there is no flux-producing component on the rotor. As a result, the equations that describe the ideal operation of the RSM are

$$v_d = R_s i_d + \omega_e \lambda_q \quad (1)$$

$$v_q = R_s i_q - \omega_e \lambda_d \quad (2)$$

where, v is the voltage, R_s is the stator resistance, i is the stator current, ω_e is the electrical speed, and λ is the flux within the machine with subscripts denoting the dq-axes.

2.1 Core loss

A magnetic field alternating inside a magnetic material results in losses in the form of eddy currents and hysteresis. These losses are difficult to model accurately but can be approximated in the stator by incorporating an equivalent loss resistor[4]. The loss resistor is placed across the MMF-producing branches in the equivalent dq circuits as shown in Figure 1[10]. Since little flux variation is typically experienced by the rotor, modelling of rotor iron losses is nonessential.

The effect to the MMF-producing current vector i_m as a result of the core loss resistance R_c can

be explained with reference to Figure 1. The current path created by the loss resistance effectively allows the d-axis current i_{dm} to increase slightly compared to i_{ds} because of the speed-dependent voltage source. The opposite occurs with the q-axis current i_{qm} which is slightly reduced as a result of its reversed speed-dependent voltage source. These losses serve to alter the current vector that acts on the rotor from that current vector which is fed into the stator terminals. The equations that describe the dq stator currents with iron losses are given by

$$i_{ds} = i_{dm} + \frac{1}{R_c} \left[-\omega_e \lambda_q + \frac{d\lambda_d}{dt} \right], \quad (3)$$

$$i_{qs} = i_{qm} + \frac{1}{R_c} \left[\omega_e \lambda_d + \frac{d\lambda_q}{dt} \right]. \quad (4)$$

The core losses in an AC machine are not constant, but are dependent on the magnetic flux present[3]. The following equation, described by Kamper[3], gives the value of the iron loss resistance R_c as

$$R_c = \frac{3e_a^2}{P_c} \quad (5)$$

where P_c is the power lost in the iron and

$$e_a = \sqrt{\frac{e_d^2 + e_q^2}{2}}. \quad (6)$$

2.2 Performance difference between motoring and generating

The difference in performance of an RSM operating as a generator versus as a motor can be explained with the help of the phasor diagrams presented in Figure 2. The axes in the figure are in the rotor reference frame. In the ideal model

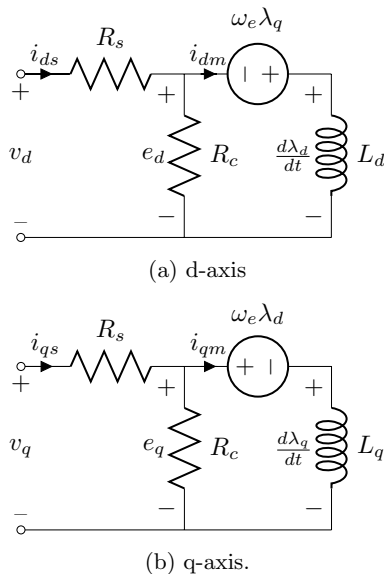


Figure 1: Electrical model of RSM incorporating stator core losses given by R_c .

of the RSM, where core losses are not considered ($R_c \rightarrow \infty$), the MMF current vector i_m is equal in magnitude and angle to the stator current vector i_s since no other current paths exist. However, when core losses are considered, additional currents are allowed to flow which disturb the torque-producing and magnetising currents, and i_m no longer equals i_s .

When operating as a motor, the stator current vector i_s is located in quadrant one as shown in Figure 2(a). In Figure 1, core loss currents, as a result of loss resistance R_c , allows additional current to flow in the magnetising branch of the d-axis circuit, thereby enhancing i_{dm} . Conversely, in the q-axis circuit, the core loss resistance allows currents to flow that reduce the torque-producing current i_{qm} . Figure 2(a) illustrates how these core loss currents affect the MMF current vector i_m that acts on the rotor, effectively reducing the current angle.

When generating, the stator current vector moves to the fourth quadrant as shown in Figure 2(b). Consequently, the stator d-axis current component i_{ds} remains positive while the stator q-axis current component i_{qs} becomes negative. This q-axis current reversal results in the reversal of the q-axis flux in the machine. As with the d-axis currents in motoring mode, the core loss resistance R_c results in additional q-axis torque-producing currents to flow. In addition, the negative q-axis flux results

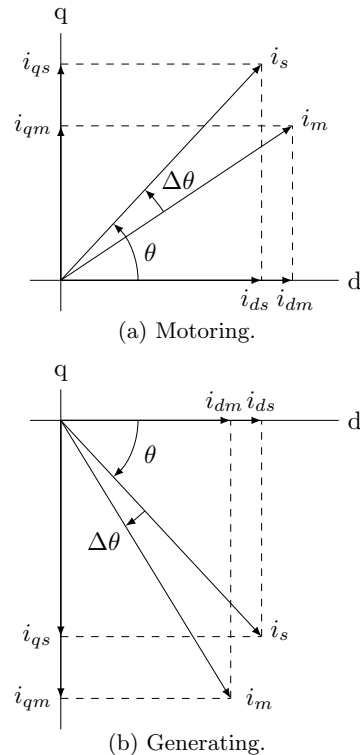


Figure 2: Phasor diagram depicting differences in stator and MMF current vectors in an RSM.

in the d-axis speed-dependent voltage source $\omega_e \lambda_{qm}$ to reverse polarity. This is the same effect that the q-axis torque-producing current experienced in motoring mode; it hinders the d-axis magnetising current. Figure 2(b) illustrates how the iron losses result in an effectively increased current angle of the MMF current vector i_m .

3 RSM USED AND SETUP

The RSM used in this study was part of research done by Kamper[3]. An optimised flux barrier rotor was designed and built inside a 5.5 kW induction machine (IM) stator. A summary of the most pertinent performance data of the RSM are presented in Table 1.

The measurement test bench comprises a 37 kW IM coupled to the RSM under test via a torque sensor. Both the IM and RSM are operated by their own inverter and control system combination. The systems controlling the switching of the inverters are PC/104-based computers, running a variant of the OpenSUSE Linux distribution with the Real-Time Application Interface (RTAI) kernel extension installed. This extension allows the systems to respond to interrupts in a deterministic manner. DC buses of the two inverters are joined to form a back-to-back configuration. Excess power produced by one machine but not consumed by the other via the DC bus during testing is dissipated in a large dumping resistor.

4 RESULTS

This section presents two categories of results: simulated and measured. Simulated results compare performance data from finite element method (FEM) modelling against the Simulink model of the RSM. For the measured results, FEM results are again used as comparison. Performance data considered are current magnitude, efficiency, and power factor. Implicit in the following figures is the current angle for generating that is negative in value.

4.1 Simulation

The RSM in this study is modelled in the FEM software package JMAG-Designer. JMAG is used

Table 1: Data relating to RSM used in study.

Attribute	Value
Rated current magnitude	39.4 A _{RMS}
Rated current angle	65°
Rated torque	60 Nm
Rated speed	1500 RPM
Rated power	9.2 kW
Rotor skewing	10°
Saliency ratio (L_d/L_q)	4.63
Stator resistance	0.15 Ω
Copper loss	700 W
Iron loss	291 W

both to simulate the performance of the RSM and to create a flux table that is used in the Simulink model of the machine.

To increase accuracy of the FEM simulations, rotor skewing is taken into consideration. To do so, three simulations are run per data point with the initial rotor position offset an amount for each simulation. The center of the rotor's length corresponds to an offset of 0° while offsets of $\pm 2.5^\circ$ correspond to the most opposite ends. The results from all three simulations are averaged together to represent the average effect across the length of the rotor.

A Simulink model from a previous study[2] is modified to include iron losses. A flux table of the RSM is extracted from JMAG and used to generate an inverse flux look up table (LUT). This inverse LUT is used in a 2D LUT in Simulink to model the effects of saturation and cross-magnetisation of the RSM.

Using equations (1)-(4), the following equations are derived to describe the flux present in the machine accounting for iron losses. The accompanying Simulink model is presented in Figure 3.

$$\frac{d\lambda_{dm}}{dt} = \frac{V_{ds} - R_s i_{dm}}{\frac{R_s}{R_c} + 1} + \omega_e \lambda_{qs} \quad (7)$$

$$\frac{d\lambda_{qm}}{dt} = \frac{V_{qs} - R_s i_{qm}}{\frac{R_s}{R_c} + 1} - \omega_e \lambda_{ds} \quad (8)$$

Simulink results beyond 78° are unobtainable as the model is not able to achieve rated torque beyond this value of current angle. This is a result of not a large enough maximum current magnitude being used in JMAG when generating the flux table for the Simulink model.

Figure 4 compares current magnitude required to produce 60 Nm of torque across a range of current angles. The iron loss reported by JMAG ranges from 86 W to 140 W, depending on current magnitude. However, performance data of the RSM presented in [3]

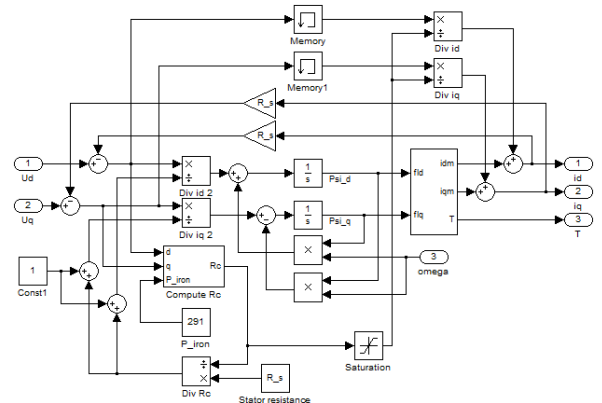


Figure 3: Simulink electrical model of RSM including modelling of iron loss and saturation.

report that iron losses are 291 W at 58.1 Nm torque, 22 A_{RMS} current magnitude, and 63.7° current angle. These rated values for the current differ from those of the RSM at the time of this study as the stator has been rewound as part of a prior study. It is not understood how iron losses are calculated in JMAG and thus the iron loss value cannot be confirmed. Also, the value reported by JMAG seems low for this machine. For this reason, the iron loss value of 291 W from [3] is used in the Simulink model. It is assumed that the maximum flux density in the machine has remained similar and that this value of iron loss remains accurate. This also helps to explain why the difference in current magnitudes between motoring and generating in Figure 4 is more pronounced in the Simulink results as opposed to the JMAG results.

The reason for the lower current magnitude when generating can be explained with reference to Figure 2 presented earlier. For the same stator current magnitude, but negative current angle, the current vector i_m is slightly larger in magnitude as well as in angle with respect to the rotor d-axis, in comparison to motoring. This has a beneficial impact on torque production[10] and as such, less current magnitude is required to obtain the same torque output for the same current angle when generating.

Figure 5 compares efficiency of the FEM and Simulink models between motoring and generating. At first sight, the Simulink results represent lower efficiencies than the JMAG model for both modes of operation. This goes back to the previous discussion; the iron loss for the Simulink model is assumed constant while JMAG's iron loss value is a lower and varying value. At 80°, JMAG's efficiency results drop off sharper than Simulink, again, this is due to the Simulink model employing a fixed iron loss value.

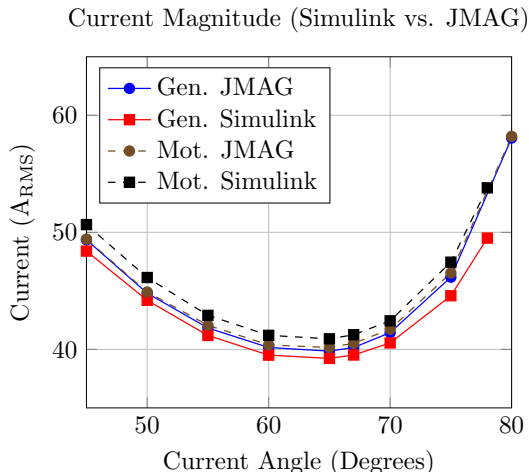


Figure 4: Simulink versus FEM current magnitude for generating versus motoring. Simulations are conducted at rated torque and speed conditions. Generator current angles are implicitly negative.

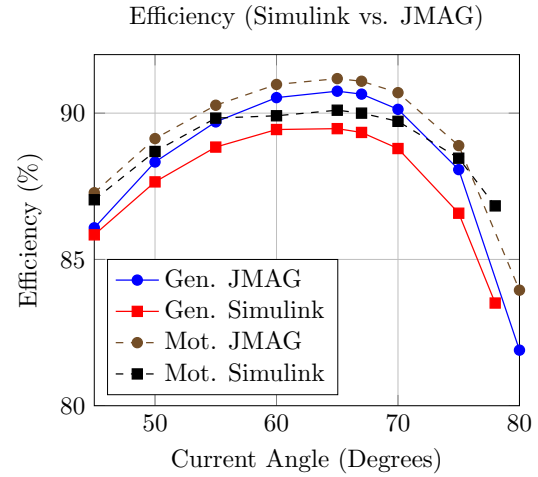


Figure 5: Simulink versus FEM efficiency for generating versus motoring. Simulations are conducted at rated torque and speed conditions. Generator current angles are implicitly negative.

Despite generating mode requiring typically less current in order to maintain output torque in Figure 4, its efficiency is generally lower than motoring in Figure 5. This result is interesting, unfortunately no explanation can be offered at present.

Comparison of power factors between the different modes and simulation models is presented in Figure 6. Despite the difference in iron loss between the models, their power factors compare well until larger current angles where the JMAG model begins to fall off faster than the Simulink model.

A more mathematical approach to the explanation of the difference in power factor is given by Boldea et al.[5]. The power factor equation is used as a potential description for the effects that losses, both copper and iron, have on the power factor. The equation for generating is given by

$$\cos \phi = \frac{T_e \omega_r / p - P_{\text{copper}} - P_{\text{iron}}}{|S|}. \quad (9)$$

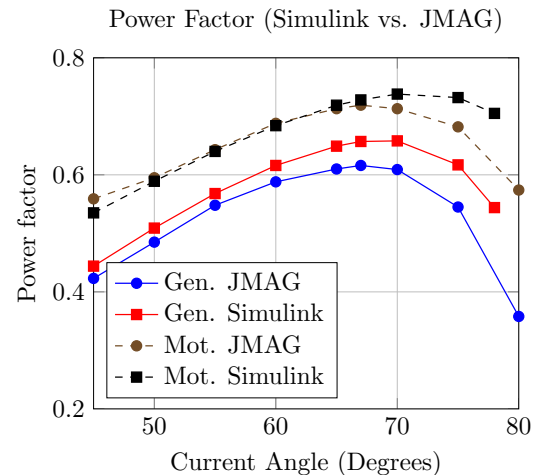


Figure 6: Simulink versus FEM power factor for generating versus motoring. Simulations are conducted at rated torque and speed conditions. Generator current angles are implicitly negative. Power factor when motoring is inductive and capacitive when generating.

The term $\frac{T\omega_r}{p}$ in the numerator of (9) represents the mechanical power that is input to the generator. ω_r is the mechanical speed, p the number of pole-pairs, and T the torque. Consequently, the copper and iron losses are subtracted from this input power to give the output electrical power. However, when motoring, the first term of the numerator represents the mechanical power output by the machine. The losses that were subtracted when generating must now be added since they need to be overcome by the input electrical power, represented by the numerator as a whole. This is a possible explanation for how losses enhance the power factor of an RSM operating as a motor while the same losses reduce the power factor when generating[5]. This explanation is given merit by the simulation results presented in Figure 6. The figure confirms power factor when generating is lower than motoring across all current angles for both the JMAG and the Simulink model.

4.2 Practical

As with the simulation graphs, the current magnitude, efficiency, and power factor graphs are presented again, but for measured versus FEM results. The IM provides input mechanical power to, as well as a load for, the RSM. The current magnitude of the RSM is adjusted to achieve rated torque at various current angles and the results recorded. In the event where a current reference cannot be set to achieve the desired torque, results either side torque value are recorded and the results interpolated.

Figure 7 compares current magnitude required by the RSM for motoring and generating. The measured generator current magnitude is less than motoring at low current angles, agreeing with results from Simulink and the qualitative explanation before.

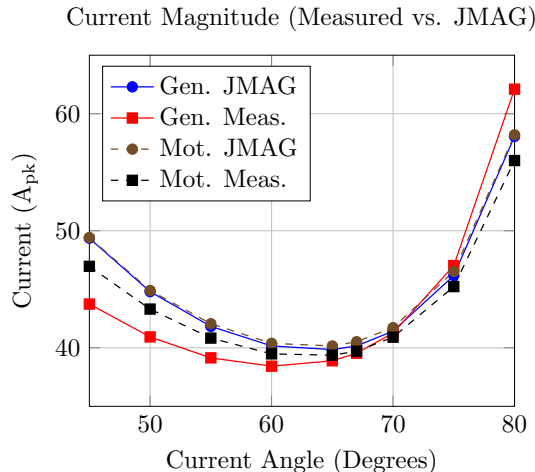


Figure 7: Measured versus FEM current magnitude for generating versus motoring. Simulations are conducted at rated torque and speed conditions. Generator current angles are implicitly negative.

However, as current angle increases, the current magnitude tends towards and surpasses the measured motoring current magnitude at 70°.

An explanation for this phenomenon is offered by Figure 2(b). When generating, the MMF current vector i_m has a slightly larger magnitude and angle between itself and the rotor d-axis than the stator current i_s . For this reason, at lower current current angles the MMF current vector is effectively larger in magnitude and closer in angle to the rated current angle, resulting in better performance. However, beyond a certain input current angle, the larger MMF current angle is no longer beneficial. It begins to degrade performance and requires increased stator current magnitude to maintain torque output. On the other hand, under motoring, the effectively reduced MMF current angle is beneficial for performance at higher current angles. This explains why the current magnitude when generating is greater than motoring at 80° for the measured results.

At lower current angles, the measured motoring and generator current magnitudes are overall less than the Simulink results presented earlier. It should be noted that the effects of saturation and iron loss are more pronounced in the physical measurements than in simulations. Higher-order flux harmonics in the stator caused by inverter switching exaggerate iron losses.

Figure 8 graphs the measured efficiency of the machine against FEM results. The efficiency results compare well with the exception of the measured generator efficiency. A sharper drop off is seen at 80° than the JMAG result as JMAG makes use of an iron loss table for the stator material. Flux density in the JMAG model could be exceeding that catered for in the table, resulting in slightly inaccurate results. JMAG efficiency results will inherently be favourable over measured results as windage and friction losses are not included.

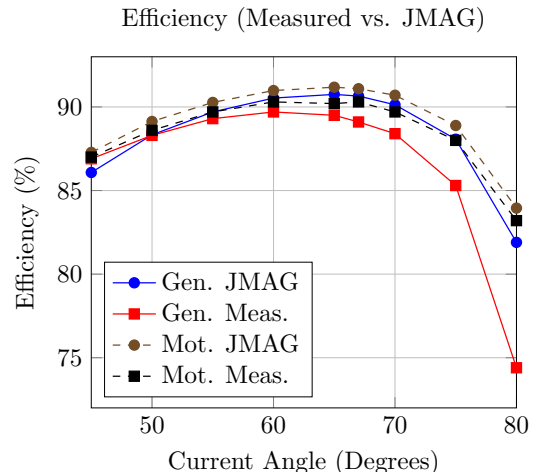


Figure 8: Measured versus FEM current magnitude for generating versus motoring. Simulations are conducted at rated torque and speed conditions. Generator current angles are implicitly negative.

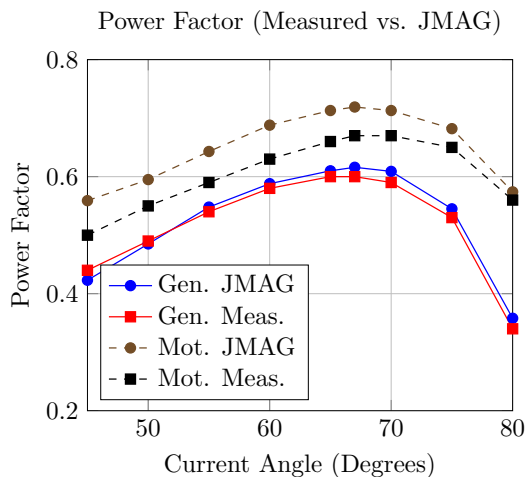


Figure 9: Measured versus FEM power factor for generating versus motoring. Measurements and simulations are conducted at rated torque and speed conditions. Generator current angles are implicitly negative. Power factor when motoring is inductive and capacitive when generating.

Figure 9 compares measured and FEM power factors. The results under generating match closely while under motoring results display a larger disparity. It is currently uncertain what may be the cause of this discrepancy. Nonetheless, the measured power factor still agrees with the theory where generating power factor is lower than motoring.

5 CONCLUSION

Saturation and iron losses in an RSM affect its performance depending on whether the machine is operating as a motor or generator. When motoring, iron losses help to improve power factor while the same losses reduce power factor when generating. In this study, the maximum power factor achieved for motoring is 0.67 but only 0.60 for generating, agreeing with the theory. Apart from power factor, iron losses also affect torque production for a specific current magnitude and angle. Despite the problematic power factor, RSMs still have a use in niche applications where synchronous operation or a cold rotor are beneficial.

REFERENCES

- [1] J. Malan and M.J. Kamper. Performance of a hybrid electric vehicle using reluctance synchronous machine technology. *IEEE Transactions on Industry Applications*, 2001.
- [2] H.W. de Kock. *Position Sensorless and Optimal Torque Control of Reluctance and Permanent Magnet Synchronous Machines*. PhD thesis, Stellenbosch University, 2009.
- [3] M.J. Kamper. *Design Optimisation of Cageless Flux Barrier Rotor Reluctance Synchronous Machine*. PhD thesis, Stellenbosch University, 1996.
- [4] R.E. Betz et al. Control of synchronous reluctance machines. Unpublished.
- [5] I. Boldea et al. High-performance reluctance generator. In *IEEE Proceedings Electric Power Applications*, volume 140, 1993.
- [6] S. Tokunaga and K. Kesmaru. FEM simulation of novel small wind turbine generation system with synchronous reluctance generator. In *2011 International Conference on Electrical Machines and Systems (ICEMS)*, 2011.
- [7] Y.J. Bao et al. Research on a novel switched reluctance generator for wind power generation. In *2011 4th Conference on Power Electronics Systems and Applications (PESA)*, 2011.
- [8] P. Asadi et al. Design and control characterization of switched reluctance generator for maximum output power. In *Twenty-First Annual IEEE Applied Power Electronics Conference and Exposition*, 2006.
- [9] A.L. Mohamadein et al. Steady-state performance of self-excited reluctance generators. *IEEE Proceedings Electric Power Applications*, 137(5), 1990.
- [10] L. Xu et al. Vector control of a synchronous reluctance motor including saturation and iron loss. *IEEE Transactions on Industry Applications*, 27(5), 1991.

DEVELOPMENT OF A SINGLE PHASE INDUCTION MOTOR VARIABLE SPEED DRIVE

A.J. McLaren* and P.J. Randewijk†

* E-mail: andrewjm.mclaren@gmail.com

† Universiteit Stellenbosch University, Private Bag X1 Matieland 7602, South Africa E-mail: pjranderw@sun.ac.za

Abstract: A three-phase drive to control the speed of a single-phase induction motor is developed. This drive is to be used in the application of speed control of residential pool pump motors. The split capacitor pool pump motor is equivalent to an unbalanced two-phase motor due to the difference in winding properties, resulting in different winding ratings. The developed drive is thus required to perform independent voltage control of each winding voltage. A space vector pulse width modulation (SVPWM) method capable of independent winding voltage control is developed. This method is simulated in VHDL-AMS using System Vision by Mentor Graphics and proven to enable independent winding current control while maintaining the required 90° phase shift in the current necessary for optimized torque generation.

Key words: Space Vector Pulse Width Modulation (SVPWM), Single-Phase Induction Motor (SPIM), Variable Speed Drive (VSD)

1. INTRODUCTION

The aim of of this project is the development of a single phase induction motor (SPIM) variable speed drive. This drive is to be used in the application of speed control of residential pool pump motors.

Speed control of a pool pump motor is desired, as reducing the operation speed of the pump reduces the energy consumption of the pump. The flow rate (q) of the pump is proportional to the speed (n) at which the pump is operated. For a swimming pool pump, the static head (h_s) of the pump is usually close to zero and can be ignored*. The total head (h) across the pump is thus only equal to the dynamic head (h_d) which in turn is equal to a constant (k), multiplied by the square of the flow rate. The output power or brake horsepower (BHP) of the pump, P_{BHP} is equal to the pressure across the pump (p) times the flow rate and can be calculated as follow,

$$P_{BHP} = pq \quad (1)$$

$$= (\rho gh)q \quad (2)$$

$$= \rho g k q^3 \quad (3)$$

with ρ the density of water and g the gravitational acceleration.

This implies that the power consumed by the pump (P) will be equal to the brake horsepower of the pump divided by the efficiency of pump (η_p) and the efficiency of the electrical motor (η_m),

$$P = \frac{P_{BHP}}{\eta_p \eta_m} \quad (4)$$

* This is also true for a swimming pool fitted with a closed-coupled roof mounted solar water heater. The static head only comes into to play at start-up to prime the system.

If we assume that the efficiency of the pump and that of the pump motor does not vary significantly with a variation in speed, the power consumption of a pump motor can be approximated by the following equation,

$$P = Kq^3 \quad (5)$$

with

$$K = \frac{\rho g k}{\eta_p \eta_m} \quad (6)$$

Thus with $q \propto n$, we can see that a reduction in speed of 30% would result in a power deduction of almost 66%. However to circulate a given quantity (or volume) of water in time (t) at a reduced speed of n' and thus a reduced flow rate of q' , the new time, t' , will need to be longer due to the reduced flow rate so that

$$t' = \frac{q}{q'} \cdot t \quad (7)$$

With energy (W), equal to

$$W = Pt, \quad (8)$$

it implies that the new energy consumption, W' , compared to the original energy consumption, W be proportional to the square of the new speed, n' , compared to the original speed, n :

$$\frac{W'}{W} = \left(\frac{n'}{n} \right)^2 \quad (9)$$

This implies that a reduction in speed of 30% equates to a reduction in energy consumption of 51% for the same m^3 of water to be filtered.

At present speed control of the single phase induction motor is not possible by merely varying the single phase voltage and frequency input to the motor, this is due to a running capacitor in series with the auxiliary winding that produces a 90° phase shift between the main and auxiliary winding currents. This capacitor is designed to produce the 90° phase shift only at 50 Hz. A two-phase drive is thus required to produce independent control of the main and auxiliary winding currents. The development of a space vector pulse width modulation (SVPWM) method for a SPIM is described in detail in this document. The developed method is capable of speed control as well as independent winding voltage control. The implementation and simulation of this method is further detailed in this document. Using the SVPWM method developed a single phase variable speed drive is simulated in VHDL-AMS using System Vision by Mentor Graphics. It must be noted that upon commencement of the project a literature study was conducted however a similar method, [1], was discovered after completion. This method however has a higher complexity to achieve a similar outcome.

2. SYSTEM REQUIREMENTS

The motor to be controlled in this project is a split-phase motor. These motors are explained in [2]. Split-phase motors consist of two windings which are displaced 90° electrical degrees in space, referred to as the main and auxiliary windings. These winding exhibit different electrical characteristics and thus have different ratings. It is thus important for the variable speed drive to operate within the constraints presented by the different winding tolerances. The constraints are as follows:

1. $V_{Main} = V_{rated}$, where V_{rated} is the rated single phase voltage
2. \vec{V}_{Aux} leads \vec{V}_{Main} by 90° 's
3. $I_{Aux} = KI_{Main}$ with $K = \frac{I_{AuxRated}}{I_{MainRated}}$, where $I_{AuxRated}$ and $I_{MainRated}$ are the magnitude of the respective winding currents while under normal permanent-split-capacitor operation.
4. Constant voltage frequency ratio(V/Hz) variable speed control.

3. TOPOLOGY

A modified three-phase inverter topology enables the full control of the auxiliary and main winding voltages, allowing the system to operate within the constraints specified in Section 2. The modified three-phase inverter topology is accomplished by connecting both the main and auxiliary winding to an inverter terminal while the second terminals of each winding are connected to the third inverter terminal, as can be seen in Figure 1. With this topology the winding voltages \vec{V}_A , \vec{V}_B and \vec{V}_C must be controlled to maintain a main winding voltage(\vec{V}_{Main}) and auxiliary winding voltage(\vec{V}_{Aux}) with a 90° relative phase shift. Variable speed is achieved by varying the magnitude and frequency of the voltages \vec{V}_{Main} and \vec{V}_{Aux} . [3]

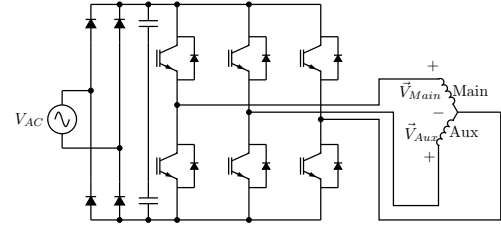


Figure 1: Modified Three-Phase Inverter Topology

4. TWO-PHASE SPACE VECTOR PWM METHOD

In order to control the switching pairs as seen in Figure 1 a SVPWM method is developed. The development of a SVPWM method for a SPIM is discussed in this section. This is done to achieve full control of the winding voltages. SVPWM is a method for deriving the switching times of PWM inverters [4]. The optimum switching times are derived from a known voltage reference vector to produce the desired space vector voltage. Space vector PWM is based on the Clarke transform [5] and is performed in the α - β plane. The methodology in this section is based on [6].

The Clarke Transform is a mathematical transform that allows any three-phase voltage or current to be converted to a two-phase plane (α - β plane) and is described in detail in [5]. By viewing the motor in the α - β plane where v_{Main} is α and v_{Aux} is β it is possible to reach the following equations to apply SVPWM for use on SPIM.

$$\alpha = v_{Main} = v_A - v_C \quad (10)$$

$$\beta = v_{Aux} = v_B - v_C \quad (11)$$

Using equations Equation 10 and Equation 11 it is possible to reach an modified Clarke transform for a two-phase output.

$$\begin{bmatrix} 0 \\ \alpha \\ \beta \end{bmatrix} = \begin{bmatrix} 1 & 1 & 1 \\ 1 & 0 & -1 \\ 0 & 1 & -1 \end{bmatrix} \begin{bmatrix} a \\ b \\ c \end{bmatrix} \quad (12)$$

Where 0, α and β correspond to the zero sequence, α and β quantities respectively; a, b and c correspond to the instantaneous values of the respective A, B, and C phases.

A three-phase inverter consists of 3 switching pairs and thus has 8 switching combinations. By applying these combinations to the clarke transform (Equation 12) above, six switching vectors of finite length are produced Figure 2. This calculation is expressed in tabular form in Table 1.

Table 1: Switching States and Corresponding Clarke

Switching State	Transform			Transformed	
	A	B	C	α	β
0	0	0	0	0	0
1	1	0	0	1	0
2	1	1	0	1	1
3	0	1	0	0	1
4	0	1	1	-1	0
5	0	0	1	-1	-1
6	1	0	1	0	-1
7	1	1	1	0	0

Thus it can be seen that the switching vectors have the following lengths:

$$|\vec{U}_1| = |\vec{U}_3| = |\vec{U}_4| = |\vec{U}_6| = U_d \quad (13)$$

$$|\vec{U}_2| = |\vec{U}_5| = \sqrt{2}U_d \quad (14)$$

where U_d is the DC bus voltage.

In order to generate a reference vector (\vec{U}_{ref}) the sum of all the switching vectors must equal \vec{U}_{ref} . However it can be seen that within each sector the minimum amount of switching states is achieved when states enclosing the sector and the two zero states are used. The switching sequence can be further optimized by ensuring that at each state change in the sequence only one switching transition occurs. The resulting switching sequences can be seen in Table 2. [6]

With \vec{U}_{ref} in sector I the respective duty cycle's can be calculated by using Figure 3 as a guideline. With $U_{ref\alpha}$ and $U_{ref\beta}$ known it is possible to calculate d_1 and d_2 .

Using geometry seen in Figure 3 the following can be

Table 2: Switching Sequences

Switching State	Switching Sequence
1	...0127210...
2	...0327230...
3	...0347430...
4	...0547450...
5	...0567650...
6	...01676710...

derived:

$$d_1 U_1 = U_{ref\alpha} - U_{ref\beta} \quad (15)$$

$$d_2 U_2 = \frac{U_{ref\beta}}{\sin 45} \quad (16)$$

from Equation 13 and 14 it follows that

$$d_1 = \frac{U_{ref\alpha} - U_{ref\beta}}{U_d} \quad (17)$$

$$d_2 = \frac{U_{ref\beta}}{\sqrt{2}U_d \sin 45} \quad (18)$$

If $d_1 + d_2 > 1$, then d_1 and d_2 must be scaled. The new values of d'_1 and d'_2 will then be as follows:

$$d'_1 = \frac{d_1}{d_1 + d_2} \quad (19)$$

$$d'_2 = \frac{d_2}{d_1 + d_2} \quad (20)$$

however if $d_1 + d_2 > 1$ the excess duty cycle type needs to be included in the zero state vectors, so that $d_1 + d_2 + d_0 = 1$. Using Table 2 it follows that the duty cycle of the phases are calculated as follows:

$$D_A = d_1 + d_2 + \frac{d_0}{2} \quad (21)$$

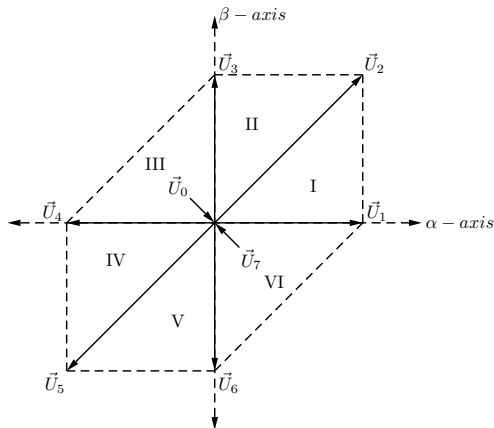


Figure 2: Switching Vectors and Sectors

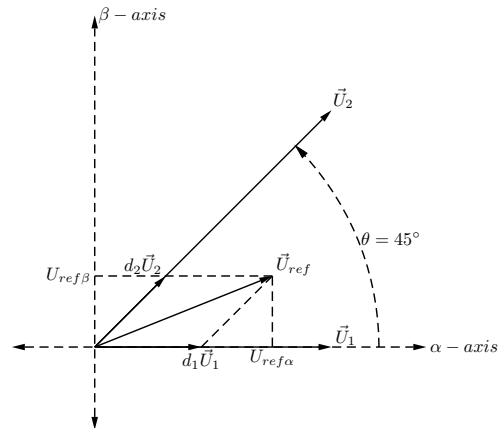


Figure 3: Sector I calculation of the Duty Cycles

Table 3: Switching Sector Duty Cycle Equations

Sector	Switching Vector Equ.	Duty Cycle Equ.
I	$d_1 = \frac{U_{ref\alpha} - U_{ref\beta}}{U_d}$ $d_2 = \frac{U_{ref\beta}}{\sqrt{2}U_d \sin 45}$	$D_A = d_1 + d_2 + \frac{d_0}{2}$ $D_B = d_2 + \frac{d_0}{2}$ $D_C = \frac{d_0}{2}$
II	$d_2 = \frac{U_{ref\alpha}}{\sqrt{2}U_d \sin 45}$ $d_3 = \frac{U_{ref\beta} - U_{ref\alpha}}{U_d}$	$D_B = d_3 + d_2 + \frac{d_0}{2}$ $D_A = d_2 + \frac{d_0}{2}$ $D_C = \frac{d_0}{2}$
III	$d_3 = \frac{U_{ref\beta}}{U_d}$ $d_4 = -\frac{U_{ref\alpha}}{U_d}$	$D_B = d_3 + d_4 + \frac{d_0}{2}$ $D_C = d_4 + \frac{d_0}{2}$ $D_A = \frac{d_0}{2}$
IV	$d_4 = \frac{-U_{ref\alpha} + U_{ref\beta}}{U_d}$ $d_5 = \frac{-U_{ref\beta}}{\sqrt{2}U_d \sin 45}$	$D_C = d_5 + d_4 + \frac{d_0}{2}$ $D_B = d_4 + \frac{d_0}{2}$ $D_A = \frac{d_0}{2}$
V	$d_5 = \frac{-U_{ref\alpha}}{\sqrt{2}U_d \sin 45}$ $d_6 = \frac{-U_{ref\beta} + U_{ref\alpha}}{U_d}$	$D_C = d_5 + d_6 + \frac{d_0}{2}$ $D_A = d_6 + \frac{d_0}{2}$ $D_B = \frac{d_0}{2}$
VI	$d_6 = -\frac{U_{ref\beta}}{U_d}$ $d_1 = \frac{U_{ref\alpha}}{U_d}$	$D_A = d_1 + d_6 + \frac{d_0}{2}$ $D_C = d_6 + \frac{d_0}{2}$ $D_B = \frac{d_0}{2}$

$$D_B = d_2 + \frac{d_0}{2} \quad (22)$$

$$D_C = \frac{d_0}{2} \quad (23)$$

The duty cycles of the respective phases can be similarly calculated for when \vec{U}_{ref} is located in the remaining sectors. The governing equations for each switching sectors' duty cycles can be seen in Table 3.

5. SIMPLE TWO-INDUCTOR MODEL

In order to simulate the two-phase SVPWM method a simple two-inductor model is used. The simple two-inductor model is an extremely simplistic two-phase motor model, that assumes the windings are purely inductive and experience no mutual inductance. The model is characterized by Equation 24.

$$\begin{bmatrix} \vec{V}_{Main} \\ \vec{V}_{Aux} \end{bmatrix} = \begin{bmatrix} j2\pi f L_{Main} & 0 \\ 0 & j2\pi f L_{Aux} \end{bmatrix} \begin{bmatrix} \vec{I}_{Main} \\ \vec{I}_{Aux} \end{bmatrix} \quad (24)$$

where f is the electrical frequency and assuming $L_{Aux} = K L_{Main}$ where K is as defined in Section 2.

The model parameters in Equation 24 can be calculated using basic AC circuit theory if the current through each winding is known during normal permanent-split-capacitor operation. The winding currents during normal

Table 4: SPIM winding current ratings and Two-Inductor model Parameters

Parameter	Value
I_{Main}	4.17A
I_{Aux}	2.49A
K	0.6
L_{Main}	0.17548H
L_{Aux}	0.10529H

permanent-split-capacitor operation at 50Hz 230V can be seen in Figure 4. It follows using Figure 4 and Equation 24 that the model parameters can be calculated as seen in Table 4.

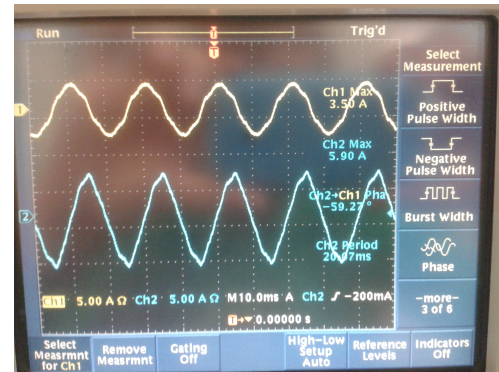


Figure 4: Auxiliary(channel 1) and Main(channel 2) winding currents during normal permanent-split-capacitor operation at 50Hz 230V [7]

6. SIMULATION

The SV method was simulated using System Vision by Mentor Graphics. The simple two-inductor model as discussed in Section 5 was used for these simulations. Using Equation 24 is clear that,

$$V_{Aux} = K^2 V_{Main} \quad (25)$$

thus,

$$U_{\alpha} = \frac{V_{rated}}{U_d} = \frac{320V}{320V} = 1 p.u. \quad (26)$$

however to remain within the area of operation seen in Figure 2, U_{α} must equal 0.94 p.u. Thus,

$$U_{\beta} = 0.6^2 U_{\alpha} = 0.3384 p.u. \quad (27)$$

must be set as such to meet the requirements set in Section 2.

From Figure 5 and 6 it is noted that the simulated system resulted in a similar duty cycle output as the ideal algorithm implemented in Matlab. Due to the unbalanced nature of the input values the switching points shift to reduce the range in which sector II and

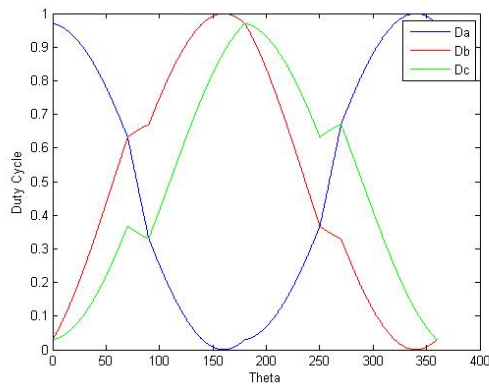


Figure 5: Duty Cycle output of Ideal Algorithm(Matlab)

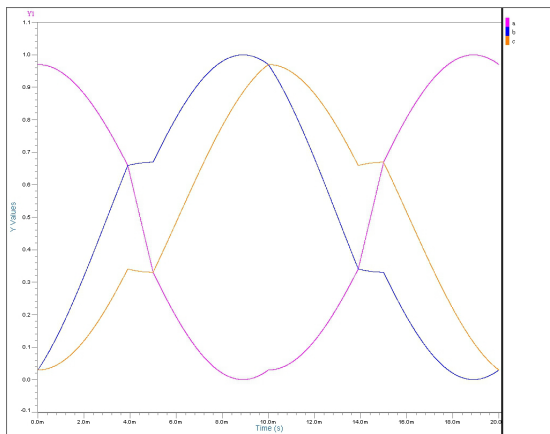


Figure 6: Duty Cycle output of Simulated System at 50Hz(System Vision)

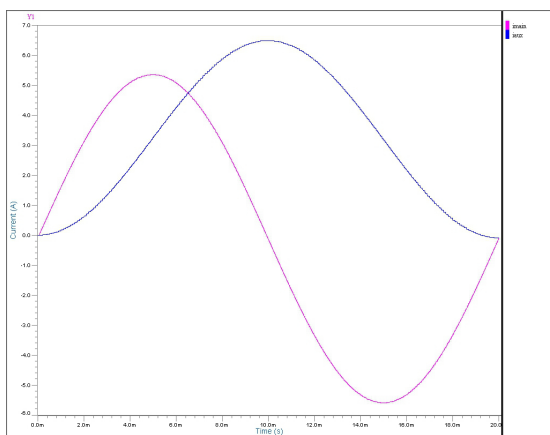


Figure 7: Current Waveforms of Simulated System at 50Hz(System vision)

sector V operate, starting now at approximately 70° 's and 250° 's respectively. Further once operating within these sectors D_B and D_C duty cycles becomes dependent on the U_β value only which at 70° 's has reached 94% of its

maximum value. This results in D_B and D_C duty cycles to experience a small increase and decrease which appears to be linear but is sinusoid in nature.

It can be seen from Figure 7 that the magnitude of the main and auxiliary winding currents 3.86A and 2.29A respectively, this is within 8% of their rated values of 4.17A and 2.49A respectively. Additionally as required to optimize the torque produced the winding currents are 90° 's out of phase with \tilde{I}_{Aux} leading \tilde{I}_{Main} . The SVPWM method presents an easy method to control the winding current by simply altering U_α and U_β , this allows for easy control of single phase induction motors with unbalanced windings.

7. CONCLUSION

The aim of this project is the development of a single phase induction motor variable speed drive. The project successfully developed and implemented a SVPWM method to control the duty cycles of the three-phase inverter for the single phase induction motor application. The SVPWM method developed allows for three control variables, the main and auxiliary voltage as well as the operation frequency. This method will allow for the independent control of the winding voltages while maintaining \tilde{V}_{Aux} at 90° 's leading \tilde{V}_{Main} . Further this method is capable of operating at varying speeds. This method was simulated using System Vision yielding promising results. The simulated system was capable of variable speed operation and the independent control of the winding currents. This is important as the windings exhibit different current ratings which must be adhered to.

REFERENCES

- [1] Vijit Kinnares and Chakrapong Charumit. Modulating functions of space vector pwm for three-leg vsi-fed unbalanced two-phase induction motors. *IEEE Transactions on Power Electronics*, 24(4):1135 – 1139, 2009.
- [2] A.E. Fitzgerald, Charles Kingsley Jr., and Stephen D. Umans. *Electric Machinery*, chapter 9. McGraw-Hill, 6 edition, 2003.
- [3] F. Blaabjerg, K. Skaug F. Lungeanu, and A. Aupke. Comparison of variable speed drives for single-phase induction motors. In *Proceedings of the Power Conversion Conference*, volume 3, pages 1328 – 1333, Osaka, 2002.
- [4] H. van der Broek, H.-C. Skundelny, and G. Stanke. Analysis and realization of a pulsewidth modulator based on voltage space vectors. *IEEE Transactions on Industry Applications*, 24(1):142 – 150, 1988.
- [5] E. Clarke. Problems solved by modified symmetrical components, part i. *General Electric Review*, 11(41):488 – 494, 1938.

- [6] P.J. Randewijk. An overview of space vector pwm. October 2013.
Class Notes, September 2011.
- [7] Ruan Botma. Automated pool pump controller,

SIMULATING SURGE PROPAGATION IN A ROTOR COIL FOR ROTOR SHORTED TURN DETECTION

T. Mashau¹, D. Tarrant² and J. Van Coller³

¹Eskom Holdings, PO Box 1091, Johannesburg, 2001, South Africa, E-mail: mashaut@eskom.co.za

²Rotek Industries SOC Limited, PO Box 40099, Cleveland, 2022, South Africa, E-mail: TarrantDC@eskom.co.za

³School of Electrical and Information Engineering, University of the Witwatersrand, Private Bag 3, Wits, 2050, South Africa, E-mail: John.VanColler@wits.ac.za

Abstract: Condition monitoring is important for turbo-generators. Due to their size and importance in power utilities, turbo-generators cannot be out of service due to failures. As a way to avoid this, extensive tests are done during planned outages. In this paper, a rotor winding is modeled to better understand the behaviour of the rotor windings when the Recurrent Surge Oscillograph (RSO) test is performed.

Key Words. Turbo-generators; shorted turns; RSO.

1. INTRODUCTION

For many years, exploratory tests have been performed on large turbo-generators. These are both off-line tests and on-line tests. One of the problems common to large turbo-generators is that of rotor winding inter-turn short-circuits. Inter-turn short circuits occur as a result of electrical breakdown of the inter-turn insulation, mechanical damage to inter-turn insulation or contamination in the rotor slot [1]. This paper will focus on a rotor winding and a Recurrent Surge Oscillograph (RSO) test system which was modelled as a way of better understanding the behaviour of the rotor windings when the test is conducted.

2. BACKGROUND

Shorted turns occur when the insulation between the copper turns in a rotor slot fails. When this occurs, the field ampere-turns is reduced as a result of the reduced number of effective rotor winding turns. This is represented mathematically by Equation 1 below:

$$F = NI \quad (1)$$

Where F is the MMF; N is the number of effective rotor turns and I is the field current [2]. In a case of shorted turns, this results in more field current required to maintain the same required rotor MMF compared with the full number of turns. This also causes an increase in the rotor winding temperature due to the increased field current. In extreme cases, this increase in temperature may damage the ground wall insulation which may eventually lead to a ground fault on the rotor. One other impact of the shorted turns is increased rotor vibration due to thermal effects. When a shorted turn occurs on one pole of the rotor, unequal heating of the rotor winding results between the poles. This may cause bowing of the rotor and hence increased vibration. Larger vibration occurs when the shorted turns are located in the Q-axis (on the shorter coils) and smaller vibration occurs when the shorted turns are

located in the D-axis (on the larger coils close to the pole faces) [1].

As a means of early detection of the rotor turn short-circuits, much work has been done around the world mostly focusing on online monitoring tools. A number of ways have been developed to detect rotor turn short-circuits by monitoring the flux. A reliable on-line rotor shorted-turns detector method that has been used for years is the stray flux probe method. This test uses a small probe mounted on the stator pointing towards the rotor body to detect the stray (leakage) flux of each rotor coil as it passes the probe. If there is a difference between the magnetic field patterns of one slot when compared to the corresponding slot on the opposite pole, it may be an indication of a shorted turn on the rotor [3].

Different devices and methods have been used to interpret the results from the online test such as the rotor shorted-turns monitor (RSTM) which uses a mathematical algorithm to process the signal from an air gap probe [4]. Artificial neural networks can be used for online detection of inter-turn faults on the rotor [5]. The problem with the above mentioned methods is that they require the machine to be online. The voltage drop test is another of the tests used to detect rotor inter-turn short-circuits. The purpose of the voltage drop test is to check for any problems with the insulation of the rotor (main or inter-turn). In this test, a voltage is applied between the ends of the winding. The applied voltage should be sufficient for at least a 2V drop across each coil and the current drawn should not exceed 10A. For evaluation, the voltage drop across each pole is measured and the results compared. The difference between the poles should not exceed 2%. The voltage drop across each full coil is measured, and the difference should not be more than 10% [6].

The greatest advantage of using this test for the detection of rotor inter-turn short-circuits is that it accurately locates the coil with the fault. The main disadvantages are that it takes a lot of time to measure across each coil and access to the coils is required - removal of the CRRs is required [1]. A winding resistance test is also used for the detection of shorted turns [7].

2.1 RSO Technique

Another method which has not received as much attention is the Recurrent Surge Oscillograph (RSO) test. The RSO test is one of the mandatory off-line tests performed on large turbo-generators to test for rotor winding inter-turn short-circuits. In this test a high frequency, low voltage pulse is injected into the rotor winding simultaneously from both ends of the winding, as depicted in Figure 1 below [8].

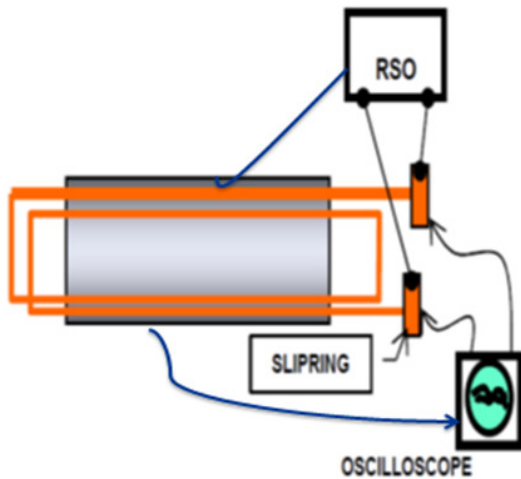


Fig 1: RSO Test Setup

The idea is to get two reflected waves as a result of the injected pulses. If the rotor winding has no shorted turns, both resulting waveforms are expected to be identical with the calculated difference between the waveforms expected to be zero. Figures 2 and 3 below show some actual test results:

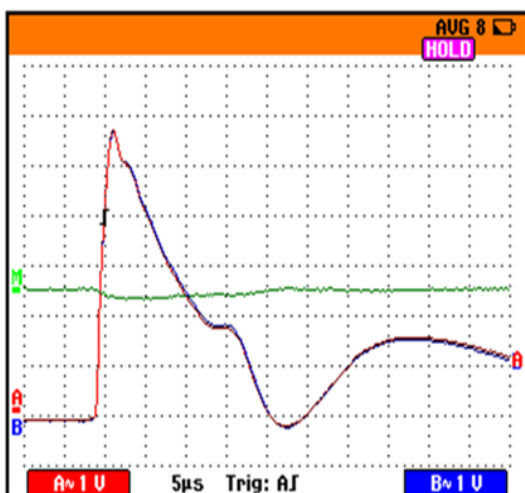


Fig 2: RSO test result without a shorted turn

In Figure 2 above; the two RSO winding traces are almost the same (the difference waveform is the green waveform), which denotes that there is no shorted turn.

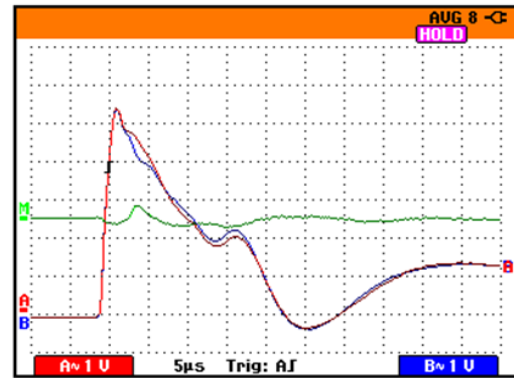


Fig 3: RSO test result with a shorted turn

In Figure 3 above there is a shorted turn in one of the rotor pole windings. The difference waveform is now increased in amplitude with distinct disturbances due to the presence of the inter-turn short circuit. The RSO works on the time-of-flight principle to detect a short-circuited turn in the rotor winding. Although it is successful in detecting a shorted turn it does not show the location of the fault. The aim of this paper is to better interpret the RSO test results as well as implement the time domain reflectometry principles to locate the slot with the shorted turn as a means of reducing repair time. The propagation of a surge along a transmission line is similar to the propagation of a pulse through a rotor winding [9]. The rotor winding is therefore modelled as a transmission line.

3. MODELLING

A rotor is made of a solid steel forging that is machined to form slots for the rotor coils. In the slots, the copper conductors are insulated with a resin impregnated fibre glass or some other type of epoxy-mica insulation depending on the machine design. In Figure 4 below a typical arrangement of conductors in a slot is displayed. The slot also holds the slot liner, packers as well as the slot wedges.

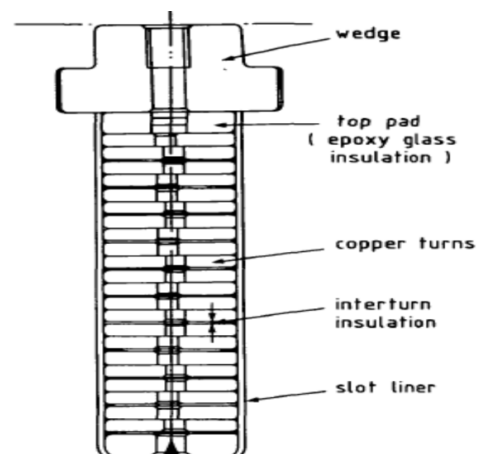


Fig 4: Rotor slot cross-section

The arrangement and geometry of the windings is different for each generator - this being due to the design of the generator which is dependent on the MVA rating, cooling method and type of insulation material used. Firstly the rotor winding is modelled

as a single-conductor transmission line and then it is modelled as a multiple-conductor transmission line (in both cases the rotor body is one of the return conductors). The transmission lines represent a coil with a specific number of turns. The simulations are done using MATLAB's Simulink and the simulated results are compared to real results on an actual rotor coil. A MATLAB Simulink model of a single-conductor transmission line with pulses being fed from both ends was implemented. The line represented a single turn rotor coil with the parameters calculated from first principles [10].

$$C = \frac{A\epsilon}{d} \quad (2)$$

Equation 2 above was used to calculate the capacitance between the conductor and the rotor body with reference to the rotor equivalent circuit in relation to a transmission line. Assumptions of the line lengths and insulation types were based on those relevant to rotors. The inductance of the line was also calculated based on Equation 3 below; where it is defined as the flux linkage of the coil per ampere of respective current [2].

$$L = \frac{\lambda}{I} \quad (3)$$

In the case of a multiple-conductor transmission line model, the exact slot geometry had to be considered so as to model the total number of conductors in the slot, the thickness of the insulation material and arrangement of conductors in the slot. To model a multiple-conductor line using a distributed parameter line model; the inductance and capacitance are modelled using an $N \times N$ matrix which was calculated based on the slot geometry. For this purpose, a finite-element modelling software package, FEMM, was used to obtain the matrices. This multiple-conductor transmission line model includes the coupling between the different conductors belonging to the different turns within the slot.

4. SIMULATION

4.1 Single-conductor transmission line model

The single-conductor transmission line model was excited with high frequency pulses fed into the line from both ends as well as from one end only. A shorted turn was then introduced. An impedance discontinuity is introduced at the location of the short circuit and hence additional reflections are expected in the measured waveforms. This was done in a form of a looped transmission line on the original single conductor line in MATLAB. The location of the fault was adjusted to view the impact of the resulting waveform. This was done to verify the relation of a line to a winding, since the location of an actual fault has an impact on the resulting waveform.

4.2 Multiple-conductor transmission line model

A three-conductor distributed parameter line was simulated to represent three turns in a coil. Hence three x three matrices had to be generated for the capacitance and inductance parameters [11].

5. SIMULATION RESULTS

The input pulse is shown below:

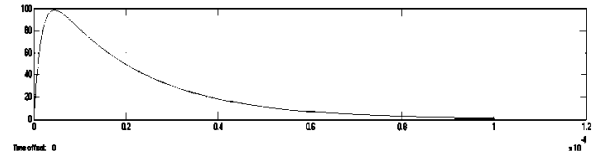


Fig 5: Input pulse

Single-conductor transmission line model

The waveform for a single-conductor transmission line model without a shorted turn is shown in Figure 6 below. The result shows the two waveforms from both ends of the line representing a winding undergoing testing.

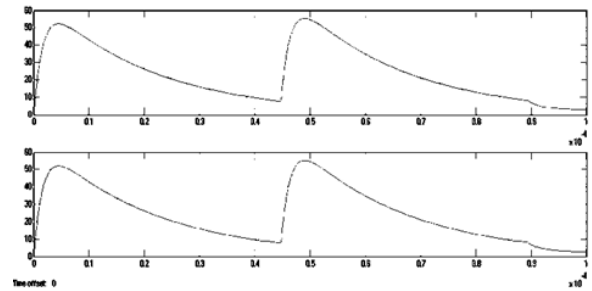


Fig 6: Single conductor transmission line model result without a shorted turn

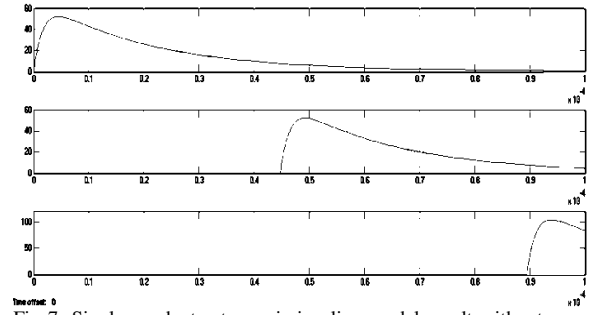


Fig 7: Single conductor transmission line model result without a shorted turn with a pulse from one end

Figure 6 above shows the result from a line being fed a high frequency pulse from both ends. As seen in the results are the transmitted (incident) and reflected waveform. In the following figure, figure 7; we see the impact with just the pulse being fed from one end. Propagation effects are clearly visible as the output is measured from different points on the model. The propagation delay can be seen between the successive points which is measured and calculated to be approximately 45 μs , which is equivalent to that seen in Figure 6 for the reflected signal. As we know from transmission line theory, that the propagation velocity is

$$v_p = \frac{1}{\sqrt{LC}} \quad (4)$$

and the delay is the reciprocal of the velocity.

$$T_d = \sqrt{LC} \quad (5)$$

The waveform for a single-conductor transmission line model with a shorted turn is shown below:

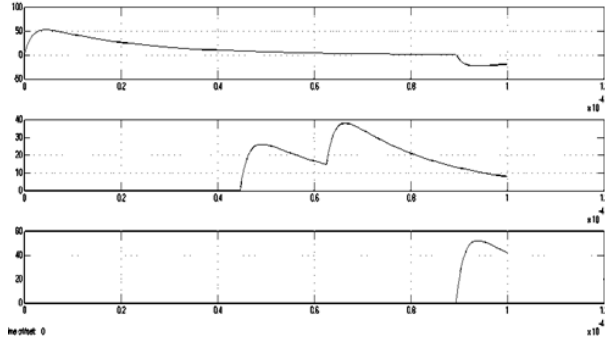


Fig 8: Single conductor transmission line model result with a shorted turn

While feeding a pulse from one end, the output waveform when there is a short in the line produces a reflection on the normal transmitted signal as well as an extra reflection on the normally reflected signal as seen in Figure 8's second waveform.

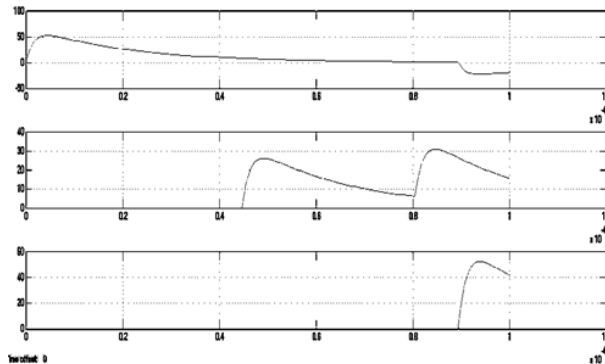


Fig 9: Single conductor transmission line model with a different location of the shorted turn

According to transmission line theory, when an electrical signal is transmitted down a transmission line, the electrical wave is transmitted without a disturbance as long as there are no impedance discontinuities along the line. The interruptions are caused by a mismatch in the impedance at some point along the line which then disturbs the normal transmission of the pulse along the line. This in turn causes the signal to be reflected back to the source; hence the term 'reflected signal'. The reflected signal is in the opposite direction to the transmitted signal and the amount of this reflected signal is a function of the change in impedance in the transmission line. The polarity of the reflected signal is dependent on the relationship between the downstream surge impedance and the upstream surge impedance. This is represented by the reflection coefficient as in Equation 5 below:

$$\rho = \frac{Z_R - Z_L}{Z_R + Z_L} \quad (6)$$

In Figure 9 above the location of the shorted turn along the line is changed. This results in a change in the output of the reflected signal. This is visible on the second waveform in Figure 9 as compared to the second waveform in Figure 8 above. This concludes that the discontinuity as seen on the reflected signal is dependent on the location of the impedance mismatch along the line which in turn means that one can locate the position of the mismatch.

Multiple-conductor transmission line model

Below in Figure 10 is the resulting waveform with a fault on the multiple conductor line. The location of the fault was then changed and the impact is also seen in Figure 11. From the waveforms below one can see the impact the discontinuity in the impedance has on the reflected signal as with the single conductor transmission line.

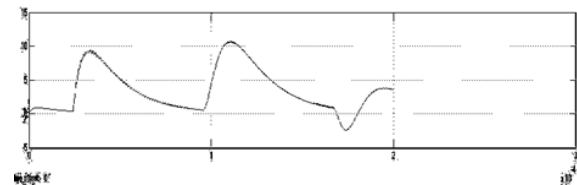


Fig 10: Multiple conductor transmission line model with a fault

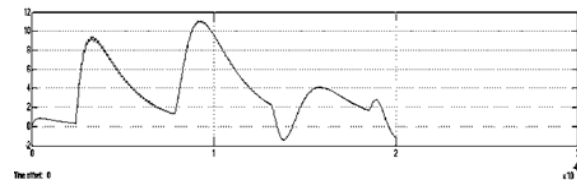


Fig 11: Multiple conductor line with a fault at a different location on the line

6. CONCLUSION

From the simulation and results above we can conclude that a single conductor transmission line model can be used to represent a winding that is subjected to the RSO test, where high frequency pulses are injected from both ends of the winding simultaneously to detect any inter-turn short circuits. With this knowledge and findings a multiple conductor transmission line was also modelled to represent the multiple conductors within the rotor slot and the results from surge propagation in normal and faulted conditions. It was clearly visible what an impedance mismatch can do to the resulting waveform also with reference to the location of the mismatch.

REFERENCES

- [1] G. Klempner and I. Kerszenbaum, Handbook of large turbo-generator operation and maintenance. Hoboken, NJ:IEEE Press, Feb.7,2008
- [2] P. C. Sen, Principles of electric machines and power electronics, John Wiley & sons Inc; 2nd edition 1996.

- [3] C. J. Beukman, F. A. Claassens, B. Lawrence, N. W. Smit and D. C. Tarrant, Power station electrical plant: generator basic engineering manual. July 2011.
- [4] R. Smith, "Monitoring for rotor shorted turns", IEE colloquium, Chester, April 1999, pp.811-820
- [5] D. W. Auckland, I. E. D. Pickup, R. Shuttleworth, Y. T. Wu, C. Zhou, "Novel approach to alternator field winding inter-turn fault detection", IEE Proc-Gener. Transm. Distrib, vol. 142. No.2. March 1995, pp.98-102
- [6] C. J. Beukman, F. A. Claassens, B. Lawrence, N. W. Smit and D. C. Tarrant, Power station electrical plant: generator systems, module 3. August 2009
- [7] Epri Report TR-1004951, "Optimised maintenance of generator rotors", 2004
- [8] I. Kerszenbaum C. Maughan, "Utilization of Repetitive Surge Oscillograph (RSO) in the Detection of Rotor Shorted-Turns in Large Turbine-Driven Generators", 2011 Electrical Insulation Conference, Annapolis, Maryland, 5 to 8 June 2011
- [9] B. C. Robinson, "The propagation of surge voltages through high-speed turbo-alternators with single conductor windings". October 1953 IEE Proceedings
- [10] D. J. Griffiths, Introduction to electrodynamics, Pearson; 3rd edition, Feb. 1, 1998
- [11] EMTP overhead transmission lines, www.dee.ufrj.br/ipst/EMTPTB.PDF.

DESIGN PROCEDURE OF A LINE-START PERMANENT MAGNET SYNCHRONOUS MACHINE

A.J Sorgdrager^{*/**}, A.J Grobler^{**} and R-J Wang^{*}

^{*} Department of Electrical and Electronic Engineering, Stellenbosch University, Stellenbosch, South Africa

^{**} School of Electrical, Electronic and Computer Engineering, North-West University, Potchefstroom, South Africa

Abstract: This paper presents a method for designing an LS-PMSM by dividing the design into sub-machine components. Each of the individual sub-machine components is then designed using several classical machine design principles. Once all the components have been designed they can be combined to form an LS-PMSM. The machine design is verified in two manners. Firstly the selected flux density values are compared with the FEM values to ensure they are in range of each other. Secondly the calculated asynchronous and synchronous performance is compared with the simulation results from a commercial design software package. Finally the proposed method is applied to the design of a prototype machine. The results show a good agreement with that obtained from commercial design package.

Key Words. LS-PSMS; permanent magnet synchronous motor; line-start; machine design.

1. INTRODUCTION

Induction machines (IM) are the backbone of the industry machine installation as they are robust, reliable and have relatively high efficiency. In a typical South African chemical plant the majority of electrical machines are IMs ranging between 2.2 kW and 22 kW. The majority of the machines in this power range are connected to pump and fan loads. Both of these load types are operated at a constant speed. As the price of electrical energy increases and stricter efficiency regulations are implemented in place, there is a need for more efficient electrical machines.

In 2008 the International Electro-technical Committee (IEC) standardized the efficiency classes for three-phase, line-fed general purpose machines to promote a market transformation [1]. The IE4 (Super-premium efficiency) is the highest of the four standards and was initially only intended to be informative. Many machine manufacturers saw no possibility of reaching these efficiency levels with IMs within the respective IEC frames [1]. This forced the manufacturers to investigate other technologies like permanent magnet synchronous machines (PMSM). The problem with a PMSM is that it is not self-starting thus limiting the possibility of acting as a direct replacement of an IM.

In 1971, Binns et. al. proposed a new type of self-starting synchronous machine that utilized both permanent magnets (PM) and a die-cast cage within a single stack of laminations [2]. The cage generates asynchronous torque during transient operation, which makes it possible for the machine to be started directly from the ac supply. This machine type is now known as a line-start permanent magnet synchronous machine (LS-PMSM).

In theory an LS-PMSM is a hybrid of a PMSM and an IM in a single rotor. During the transient period the asynchronous torque (T_{asy}) is the result of the interaction between the cage torque (T_c) and breaking torque (T_m) [3]. Both the breaking torque and the cage torque are dependent on different component in the

machine. T_m is generated by the PM and has a negative effect on the machine's start-up performance. The magnitude of this negative torque component is dependent on the PM volume [4, 5]. At steady state, the synchronous torque (T_{syn}) is mainly produced by the PM alignment torque. Depending on the rotor topology there can also be a reluctance torque component. The performance of the machine is greatly influenced by the interaction between the IM and PMSM topology [3,5]. Once the rotor is synchronized with the stator's rotating MMF, the rotor cage has no effect on torque production. This eliminates the cage rotor losses of the machine at steady state because there are no induced currents in the bars. Thus the efficiency of an LS-PMSM can be higher than that of an IM [3]. Figure 1 illustrates the torque components of a generic LS PMSM.

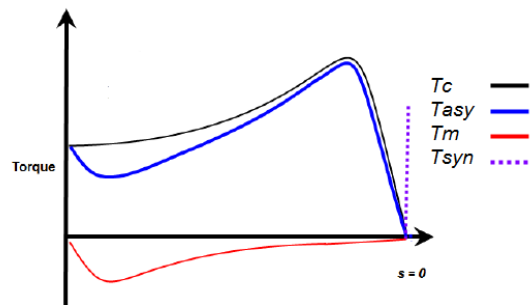


Figure 1: LS PMSM theoretical torque curves [3, 6]

Several comparison studies between IMs and LS PMSMs have been done during the last couple of years. In [7], it is concluded that an LS-PMSM has superior performance when compared to an IM with regards to pump, fan and compressor loads (constant speed with long operating cycle loads). Typically an LS-PMSM has higher efficiency, power factor and torque density and its operating temperature is lower than that of an IM due to the absence of rotor bar currents [1,7-9]. Although these machines' initial cost is higher than that of an IM, the cost of ownership is much less, making it a very suitable machine for certain applications. The drawback of this machine is however its starting torque and synchronisation capabilities, which place limits on its application capabilities.

This paper presents a design methodology for LS-PMSM, which utilizes classical machine design theory in combination with finite element method (FEM) analysis. The proposed method is applied to the design of a four-pole, low voltage LS-PMSM driving a fan-type load.

2. PROPOSED DESIGN METHOD

When designing an LS-PMSM there are two options available. The most popular one found in literature is a retro-fit design or IM rotor swop-out [6]. Since an LS-PMSM can operate with the same stator as an IM the IM rotor can be replaced with an LS-PMSM rotor [3, 4, 9, 10]. This option eliminates the need of machine sizing. The second option is to do a complete machine design. The method proposed in this paper can be used for both options. For the retro-fit option the stator must be characterised instead of designed but the same steps must be followed as some of the stator parameters are needed during the rotor design.

Figure 2 shows the low-level design flow diagram. The black dashed lines represents the need for changes in the design should the relevant parameters and flux density's not be met during the FEM verifications. Each of the four blocks is an independent sub-design for a component of the machine. As the rotor contains both an IM and a PMSM, they can be designed separately. Once both rotor designs are done they can be combined into one rotor. The PMSM is designed first as the magnetic braking torque must be known to design the cage torque curve. During the design of the PMSM the possible cage location must be kept in mind.

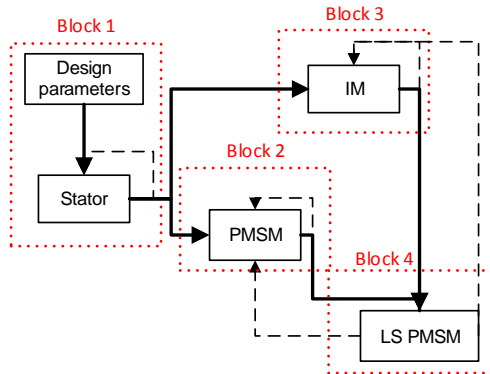


Figure 2: LS PMSM design processes

Figure 3 contains the design steps of Block 1. This block has a 2-step design: in the first step the machine is sized to determine rotor diameter (D_r) and active length (l). In the second step the winding factor (k_w), turns per coil (N_s) and the coil slot is determined. This design method was adapted and compiled from [10] and [11].

Once the stator design is complete the design must be verified to determine if the selected flux density values are achieved. This is done through static FEM analysis. The PMSM (Block 2) and IM (Block 3) design flow diagrams are shown in Figure 4 and 5,

respectively. Both Block 2 and 3 was compiled using [10 – 12].

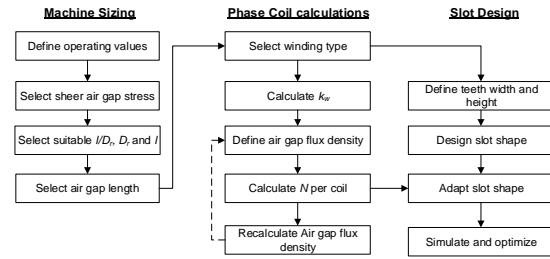


Figure 3: Design flow diagram of Block 1 [6]

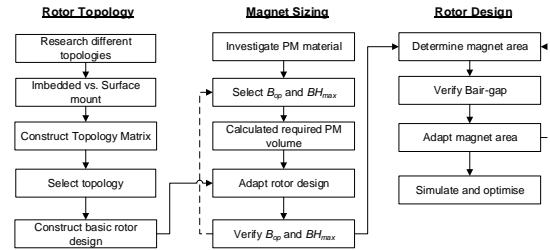


Figure 4: Design flow diagram of Block 2 [6].

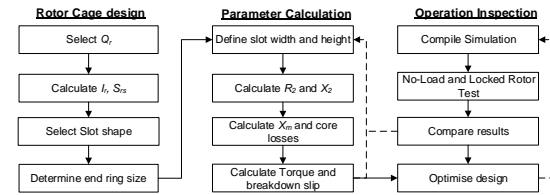


Figure 5: Design flow diagram of Block 3 [6].

Once both the PMSM and IM rotors sections have been designed and verified the two must be combined to form the LS-PMSM rotor. The performance of the LS-PMSM can then be compared to the two independent machines. Theoretically at steady state the LS-PMSM's performance will be similar to that of the PMSM and during transient operations to the IM although there will be difference due to the presence of T_m . For the static FEM simulations FEMM is used and for the performance comparison with the calculated model, Maxwell® RMxpert is used.

3. DESIGN AND VERIFICATION

In this section the afore-proposed method is implemented in the design of a prototype LS-PMSM machine.

3.1 Design Specifications

Table 1 contains the design specifications of the prototype machine. Besides the specifications in Table 1, the starting current of the machine is required to be similar to that of an IM with the same power rating. Furthermore the prototype must fit in a

132 size frame or smaller, enabling the machine to be used as a direct replacement for an existing IM.

Table 1: Prototype Machine Specifications

Specification	Value
Power (kW)	7.5
Phase	3
Line Voltage (V)	525
Line Current (A)	± 10
Number of Poles	4
Preferred Line Connection	Star
Rated Speed (RPM)	1500
Duty Cycle	S1

3.2 Machine Sizing

To determine l and D_r two options are available. The first option is to use the values of the IM counterpart and change either l or D_r while the second option varies both parameters. In both options (1) is used

$$\begin{aligned}
 T_{rated} &= \sigma r_r S_r \\
 T_{rated} &= \sigma r_r (2\pi r_r l) \\
 T_{rated} &= \frac{\sigma \pi D_r^2 l}{2} \\
 \sigma &= \frac{2T_{rated}}{\pi D_r^2 l}
 \end{aligned} \quad (1)$$

with T_{rated} being the rated torque of the machine and σ the tangential stress or sheer air-gap stress of the machine [10]. The tangential stress is the main torque producing component when it acts on the rotor surface. If σ is selected to be within limits as set out in [6] only the l and D_r is unknown. By fixing one of the two unknown and performing a variable sweep the other can be selected out of the graph. The selected value is then re-checked by fixing the selected value and performing a sweep again. A graph similar to Figure 6 can then be compiled. The l/D_r ratio must be checked to aid in final selection with the empirical ratio rule i.e.

$$\begin{aligned}
 X &\approx \frac{l}{D_r} \\
 X &= \frac{\pi}{2p} \sqrt[3]{p} \\
 X &= 1
 \end{aligned} \quad (2)$$

with p being the number of pole pairs [10]. The rotor diameter D_r must not be selected too small as this complicates the rotor design and limits the cross sectional area. The values of l and D_r for the design is 115 mm and 113.5 mm respectively. The air-gap (δ) length is selected as 0.5 mm.

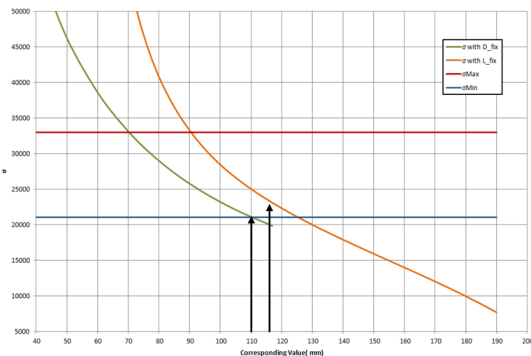


Figure 6: Variable sweep of LS PMSM design

3.3 Stator Design

Once the machine is sized the next step is to determine the winding factor (k_w), number of turns per coil phase (N_s) and the required slot area. To do this, the air gap flux density (B_δ) must be selected. For a PMSM the value of B_δ is usually between 0.85-1.05 T depending on the rotor topology, as for an IM the values is between 0.7-0.9 T [10]. By selecting the value as 0.85 T both machine's boundaries are respected.

In [6], a harmonic comparison study was done to select the winding layout. A 36 slot, overlapping double-layer layout was selected as it provided the best slot harmonics of the options. The coils are short pitched by one slot. Table 2 contains the winding configurations that were investigated with Q_s as the number of slots, q the number of slots per pole per phase, k_d the distribution factor, k_p the pitch factor and k_{sq} the skewing factor.

Table 2: Compilation of Various Winding Factors [6]

Q_s	q	k_d	k_p	k_{sq}	k_w
24	2	0.9659	1	0.9886	0.9549
24	2	0.9659	0.9659	0.9886	0.9223
36	3	0.9597	1	0.9949	0.9548
36	3	0.9597	0.9848	0.9949	0.9403
48	4	0.9576	1	0.9971	0.9548
48	4	0.9576	0.9914	0.9971	0.9466

As it is very difficult to skew the rotor bars and PM with respect to the stator it was decided to skew the stator slots by one slot pitch instead. This technique is not that common in mass produced IMs but is used in specific cases.

To calculate N_s , k_w is used in

$$\begin{aligned}
 N_s &= \frac{\sqrt{2} E_m}{\omega_e k_{w1} \Phi_m} \\
 N_s &= \frac{\sqrt{2} E_m}{\omega_e k_{w1} (\alpha_{pa} B_\delta \tau_p l')}
 \end{aligned} \quad (3)$$

with Φ_m being the PM flux [10]. Note the expansion of Φ_m in (3), where the air gap flux density B_δ and pole area is used. Table 3 contains the values and the definition of each symbol in (3). The pole arch coefficient is dependent on the rotor topology and seldom exceeds 0.85. The actual value can only be calculated once the final rotor has been designed.

Table 3: Values for Calculations of N_s

Symbol	Value	Description
E_m	303V	Phase voltage
ω_e	100 π rad/s	Electrical angular velocity
k_{w1}	0.9403	Winding factor
α_{ac}	0.8	Pole arch coefficient
B_δ	0.85 T	Air gap flux density
τ_p	0.089 m	Pole pitch
l'	0.115 m	Active length

Using the values listed in Table 3, N_s is calculated as 208. This value is rounded to 216 to provide 36 turns per slot. When substituting this value into (3), B_δ is recalculated as 0.868 T which is an acceptable increase of less than 3%.

The required slot size can be calculated using N_s , the wire's copper area and the fill factor (ff). The rated current is calculated as 10A. The stator coil current density (J_s) must be selected to calculate the required size of copper wire [10]. By selecting J_s as 6.5 A/mm² the required copper area per conductor is ± 1.6 mm² thus a SWG17 (1.422 mm \varnothing) can be used. However to gain a better fill factor, two SWG19 (1 mm \varnothing) is used. By doing so, J_s is re-calculated as 6.3 A/mm². Thus a single slot contains 72 conductors with a copper area of 60 mm². For the LS-PMSM the fill factor is selected as 0.5, thus the required slot area is 120 mm². To further aid in designing the slot shape the stator slot height (h_s) and tooth width (b_{st}) is calculated by selecting the flux density values in the teeth and back yoke as set in [6]. Table 4 contains the selected flux density values and calculated values of h_s and b_{st} . The tooth flux density is at its maximum on the d-axis and gradually decreases towards the q-axis. Thus the value in Table 4 is the peak value and not the average value.

As indicated in Figure 3, once h_t and b_{st} is calculated the slot shape must be selected and optimized. The final slot shapes parameters are listed in Table 5. Once the design is finalised the stator parameters (stator winding resistance (R_l) and the reactance (X_l)) can be calculated. R_l is calculated using the combined method of [10] and [13]. Table 6 contains R_l and the relevant performance factors (λ – not to be mistaken for flux linkage) used to calculate the stator leakage reactance. The leakage effects of skewing can only be incorporated once the initial inductance is calculated [10].

Table 4: Stator Slot Height and Width Parameters

	Yoke	Tooth
B (T)	1.4	1.7
h_t & b_{st} (mm)	35.5	4.5

Table 5: Stator slot dimensions

	mm
b_1	2.4
b_4	4.2
h_1	1.3
h_2	1.3
h_3	0.5
h_4	26.5

Table 6: Calculated Stator Parameters.

Parameter	Value
R_l	1.40544 Ω
Slot leakage (λ_{sq})	2.8836 Wb
End winding leakage (λ_{sw})	0.24197 Wb
Zig-zag leakage (λ_{sz})	0.1785 Wb
X_l without skewing	2.343 Ω
Skew leakage (L_{sq})	75.424 μ H
X_l	2.3668 Ω

To verify the stator design, the selected flux density values in both the stator yoke and teeth will be compared to the results from the FEM simulation model to check if they are in a good agreement. A simple surface-mounted PM rotor that generates $B_\delta = 0.85$ T may be used to verify the stator design as shown in Figure 7. A full pitch surface mount PMSM

is used as the flux density values of the PM is the flux density value of the air-gap. Thus by setting remanence value of the magnet to 0.85 T, the correct B_δ is obtained for verification. Model A is between two d-axes and Model B between two q-axes. The stator coils in both models are not excited. The simulation results of both models are listed in Table 7. The calculated value differs from that selected values in Table 4 as both the slot height and width was reduced during the slot optimization. M400-50A lamination material is used for the stator.

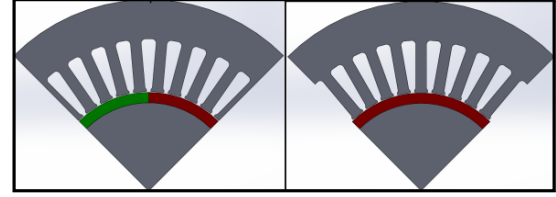


Figure 7: Stator verification models

Table 7: Stator Verification Information

		Stator Yoke Flux Density	
		FEM	Calculated
Model A	1.337 T	1.22 T	
Model B	1.383 T		
		Stator Teeth Flux Density	
		FEM	Calculated
Model A	1.206 T	1.3 T	
Model B	1.33 T		

From the table it can be seen that the calculated flux density values correlate with the FEM simulated ones.

3.4 Rotor Design

As indicated by Figure 2 the rotor design comprises of two parts. The PMSM rotor is designed first to simplify the design process as the PMs influence the space availability of the rotor the most. Furthermore the breaking torque must be known in order to design the cage to overcome it.

3.4.1 PMSM Rotor Component

Although many rotor topologies of PMSM exists, this study only considers four topologies namely surface mount magnets (SMM), slotted surface mount magnets (SSMM), imbedded radial flux magnets (IRFM) and imbedded circumferential flux magnets (ICFM) as shown in Figure 8.

Surface mounted topologies (SMM and SSMM) exhibit good steady-state performance, but suffer from poor transient operation capabilities [6]. Imbedded radial flux topology leads to high magnet consumption [6,14]. Thus the ICFM topology was selected as it provides the highest B_δ in comparison with the other 3 topologies for the same PM volume [14]. The key design consideration of ICFM topology is the large leakage flux through the shaft. This can be greatly reduced by using a non-magnetic shaft material.

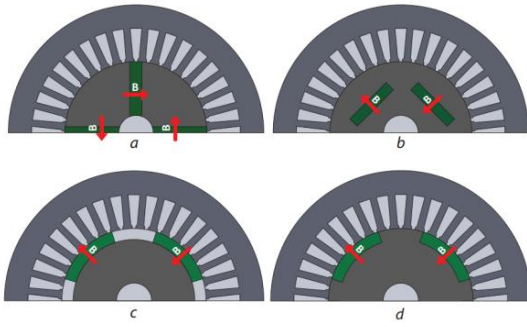


Figure 8: PM rotor topologies: a) ICFM; b) IRFM; c) SMM and d) SSMM [6, 14]

To determine the minimum PM volume to provide an airgap flux density of 0.85 T the assumption was made that there is no leakage flux in the rotor, thus $\Phi_m = \Phi_\delta$ and the PM volume (Vol_m) can be calculated with

$$Vol_m = \frac{Vol_\delta B_\delta^2}{\mu_0 (-H_m B_m)} \quad (3)$$

with Vol_δ the air gap volume and $H_m B_m$ the energy product of the operation point of the magnet [12]. By replacing $H_m B_m$ with the HB_{max} value of the selected PM grade, the magnet provided the maximum magnetic energy per material volume. As the active length of the machine is known only the height and thickness of the magnet must be selected. To provide adequate space for the cage the magnet height was selected as 26 mm. Table 8 contains the magnet thicknesses (t_m) as calculated with (3) for different PM grades.

Table 8: PM Thickness Sizing for Different Grades

Grade	N42	N40	N38	N35	N33	N30
t_m (mm)	3.1	3.24	3.78	3.9	4.2	4.57

All the magnets in Table 8 provide the same B_δ as ICFM utilizes flux concentration to form the poles [6]. It was decided to use a N33 grade PM and to increase the thickness to 6mm to accommodate for loss in magnetic energy due to leakage flux. Figure 9 indicates that the selected magnet volume provides the required energy (red line) at both rated (blue line) and operating (green line) temperature. The intersection points are the operation point of the magnets. The selected PM dimensions provided the required B_δ value.

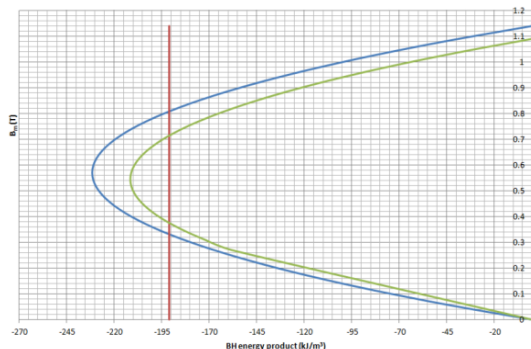


Figure 9: BH energy plot of the selected PM grade

The synchronous torque (T_{syn}) of the PMSM is the sum of electromagnetic torque (T_{em}) and reluctance torque (T_{rel}) components and is calculated using the general torque equation for a PMSM. The torque vs. load angle curve for the PMSM is indicated in Figure 10. The values used to plot Figure 10 is d -axis reactance, $X_d = 29.329 \Omega$, q -axis reactance, $X_q = 85.841 \Omega$ and back-EMF, $E_0 = 186.362$ V. These values were calculated as in [10] and [16].

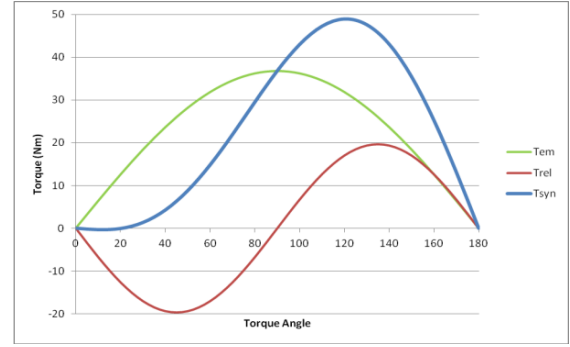


Figure 10: PMSM torque vs. load angle curve.

The breaking torque in an LS-PMSM was first investigated in 1980 by V.B Honsinger and published in his well-known paper [15]. T_m is calculated as a function of slip with (4). Figure 11 contains T_m 's plot with a peak value of ± 14 N.m at $s = 0.045$.

$$T_m = \frac{3p}{\omega(1-s)} \left[\frac{R_1^2 + X_q^2(1-s)^2}{R_1^2 + X_q X_d(1-s)^2} \right] \left[\frac{R_1 E_o^2(1-s)^2}{R_1^2 + X_q X_d(1-s)^2} \right] \quad (4)$$

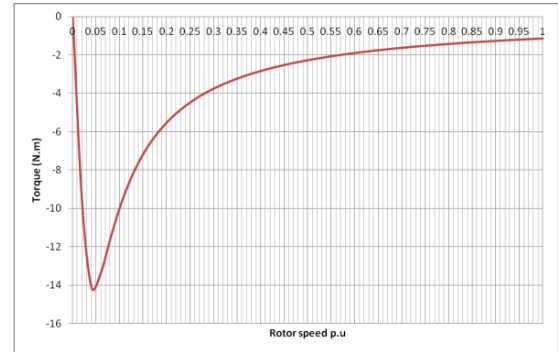


Figure 11: Breaking torque component of the PMSM in the LS PMSM prototype

3.4.2 IM Rotor Component

The first step in the IM design is to select the number of rotor slots (Q_r). As a slot is required above each PM to limit the leakage flux, Q_r must be divided by four. For the prototype rotor Q_r is selected as 24 with information gained from [10] and [11]. For ease of manufacturing round rotor slots will be used.

As with the stator the rotor yoke and tooth flux density must be selected to calculate the slot height and width. As the PM span the rotor yoke, the remanence value of the PM is used. This provided a yoke height of 26.63 mm. The maximum tooth flux density occurs on the d -axis and gradually decreases between each tooth towards the q -axis. By selecting the maximum value of 2.2 T the tooth width is

calculated as 7.425 mm. The next step is to determine the remaining dimensions of the round slot as in Figure 12. This is done with the aid of the slot performance factor (λ_{ru}) equation that directly influences the rotor inductance (L_2). By minimizing λ_{ru} , L_2 is also minimized. λ_{ru} is calculated with (5). The most influential dimension is the slot opening (b_1). Increasing the slot opening area will reduce the leakage flux whereas a deep slot will increase it. The values for b_1 and h_1 are selected as 2 mm and 1 mm respectively which results in $\lambda_{ru} = 3.078$. Along with λ_{ru} , the end ring performance factor (λ_{rer}), must be determined before L_2 can be calculated. The dimensions of the end rings were determined as 12 mm by 12 mm providing $\lambda_{rer} = 0.37007$.

$$\lambda_{ru} = 0.47 + 0.66 \frac{b_4}{b_1} + \frac{h_1}{b_1} \quad (5)$$

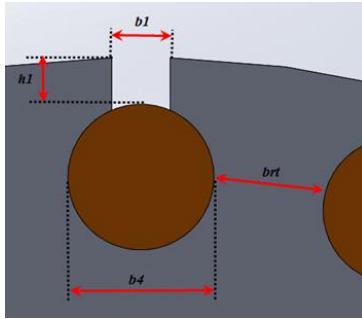


Figure 12: Rotor slot dimensions

To calculate R_2 , the rotor bar and end-ring resistance must be calculated, these values are calculated as 99 $\mu\Omega$ and 3.53 $\mu\Omega$ respectively as in [10, 11]. Once R_2 and L_2 is calculated in rotor reference frame these value must be transformed to the stator reference frame. The transformed values are $R_2' = 2.187 \Omega$ and $X_2' = 1.615 \Omega$ with X_2' being the rotor reactance in the stator reference frame.

With the aid of the machine parameters the starting and breakdown torque can be calculated. Both of these torque values are a function of the starting current. Table 9 contains the relevant torque and current values. The torque vs. slip curve will be provided in Section 5.

Table 9: Starting and Breakdown Parameters

Parameter	Symbol	Value
Starting Current	T_{start}	55.93 A
Starting Torque	T_{start}	130.67 N.m
Breakdown Torque	T_{bd}	153.59 N.m
T_{db} slip speed	s_{db}	0.511

3.4.3 LS-PMSM

Now that both the PMSM and IM rotor components have been designed the next step is to combine the two to form the design of LS-PMSM prototype rotor as shown in Figure 13. To ensure that a single lamination can be used two saturation zones are use between the PM and shaft as well as the PM and rotor bar. The original gap between the rotor bar and PM was 1.425 mm. However the PM leakage flux as determined from static FEM simulations was 18% of

the total PM flux. By increasing the shaft diameter with 1 mm the gap was reduced to 0.952 mm resulting in a 10% PM leakage flux which is acceptable according to the PM sizing done in 4.3.1.

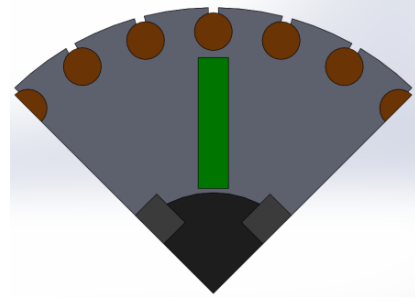


Figure 13: Quarter section of LS-PMSM Rotor

To verify the LS PMSM rotor the air gap flux, rotor yoke and teeth flux density will be used. For the FEM simulation the machine is driven a full load line current ($I_{line} = 10A$) at synchronous speed, Δf between the rotor and stator is zero. Table 10 shows the verification results. The tooth flux density is checked on the d -axis between two teeth.

Next, the air gap flux density of the machine is verified. The air gap flux density plot is taken over the pole arch and not the pole pitch as the flux only passes the air gap over the pole arch. If the flux over the pole is used a lower average flux density value will be obtained. The average flux density over the pole arch is calculated as 0.84 T which is acceptable. Thus the conclusion can be made that the simulation model is an accurate representation model of the LS PMSM machine.

Table 10: LSPMSM Rotor Verification Information

	Rotor Yoke Flux Density		
	FEM	Calculated	% Difference
Tooth 1	2.29 T	2.2 T	4
Tooth 2	2.082 T		6
	Rotor Teeth Flux Density		
	FEM	Calculated	% Difference
	1.208 T	1.17 T	3.2

4. PERFORMANCE PREDICTIONS AND SIMULATIONS

In this section the torque profile and the back-EMF properties of the prototype will be investigated. The calculated and simulation results of the asynchronous and synchronous torque components will be compared. This is done to ensure that the method used to design the prototype is correct. The back-EMF peak value is calculated and determined from the FEMM model. The peak back-EMF value is a key component in calculating the breaking torque of any LS-PMSM.

4.1 Asynchronous Torque Profile

In initial comparisons it was found that ignoring the skin effect on the rotor bars provided a significant

error in torque calculations. Once the effect was incorporated into the design the simulated and calculated torque curves are within acceptable range. Figures 14 provide a comparison between the cage torque with and without the skin effect while Figure 15 contains the revised T_{asy} curve and its components. The comparison between the calculated and simulated T_{asy} curves is given in Figure 16. The simulated results were obtained by using Maxwell® RMxpert.

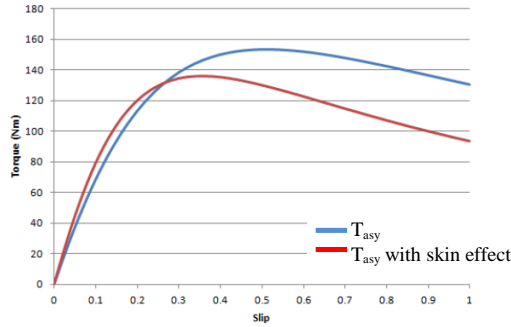


Figure 14: Cage torque with and without skin effect

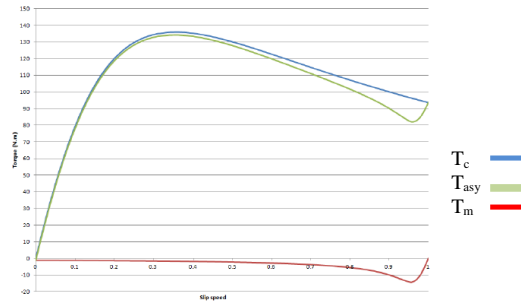


Figure 15: Torque vs. slip of different torque components (including skin effect)

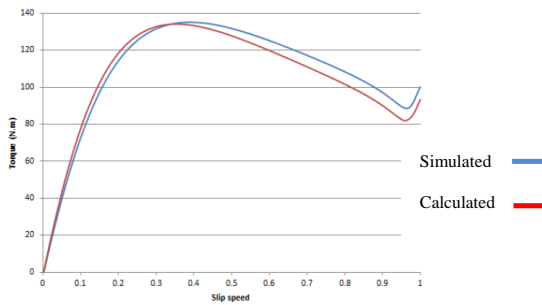


Figure 16: Simulated torque curve vs. calculated torque curve

Table 11: Simulation vs. Calculated Starting and Breakdown Results.

	Calculated	Simulated	% Difference
I_{start}	52.37 A	52.84 A	< 1 %
T_{start}	93.604 N.m	100.94 N.m	7.2 %
T_{bd}	136.01 N.m	135.20 N.m	0.5 %
s_{bd}	0.356	0.4	11%

Table 11 contains the breakdown and starting values for both the simulated and calculated machine.

4.2 Synchronous Torque Profile

The last comparison between the proposed model and the Maxwell RMxpert model is the torque versus load angle plot as indicated in Figure 17. The maximum

calculated torque is 48.9 N.m at $\delta = 120^\circ$ and the simulated maximum torque is 48.39 N.m at $\delta = 119^\circ$. Both the maximum torque and angle are within range of each other.

Table 12 contains the simulated and calculated parameters. The skin effect is included in the calculated parameters as the RMxpert simulation also incorporates the skin effect, thus providing an accurate resistance and inductance comparison.

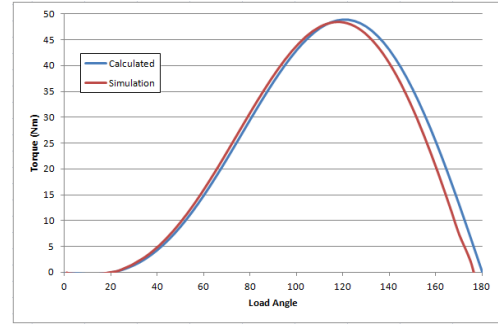


Figure 17: Load angle of simulated torque vs. calculated torque

Table 12: Parameter Comparison

	Proposed Method	Maxwell RMxpert	% Difference
R_l	1.428	1.423	< 1 %
R_2'	1.787	1.679	6 %
X_l	2.387	3.02	26 %
X_2'	1.6473	1.802	9.3 %

All the parameters except for X_l are within 10%, the effect of changing this value so that it is within 10% of the calculated value is investigated. By reducing the X_l the T_{start} and I_{start} increases. Thus the conclusion can be that the simulation package uses a different method to calculate the starting and breakdown values.

4.3 Back-EMF

The back-EMF of an LS-PMSM is a function of the PM flux linkage (λ_{pm}) with the stator coil phases with respect to the rotational speed of the rotor. The flux linkage of each phase is calculated in FEMM, by setting the phase current's value to zero. This simulates the rotor rotating at synchronous speed. To calculate the peak back-EMF value one of the phases must be aligned with the rotor d-axis. Once the flux linkage value of each phase is extracted the RMS back-EMF value is calculated as 186.167 V. This value correlates with the RMS phase back-EMF value calculated in ANSYS Maxwell® as 190.19 V.

5. CONCLUSION

The design method presented in this paper proved to present an adequate fit to the simulated results as indicated in Section 4. An efficient design approach for LS-PMSM has been presented in the paper. By dividing the LS-PMSM rotor design into two separate designs i.e. IM and PMSM, the final rotor's performance can be readily represented by using

classical electrical machine theory. To validate the proposed design approach, the calculated results are compared with the simulation results from both a FEM and a commercial design package. A good agreement is achieved.

During the initial design of the cage the skin effects was neglected, which caused a poor match between the calculated and simulated cage torque curves. Once the skin effect was incorporated the two torque curves correlated well. In future designs this effect must be incorporated in the design.

The calculated stator reactance differed greatly from the simulated value. Investigation into other calculation methods must be done and compared with the current method to refine the calculation of this parameter. Once this is done the proposed method in this paper can be seen as a viable design tool.

REFERENCES

- [1] T A de Almeida, F J Ferreira, and J A Fong, "Standards for efficiency of electrical motors," *IEEE Industry Applications Magazine*, vol. 17, no. 1, pp. 12-19, Jan/Feb 2011.
- [2] K.J Binns, W.R Barnard, "Novel design of self-starting synchronous motor", *Proceedings of the Institution of Electrical Engineering*, vol. 118, no 2 Feb 1971.
- [3] P W Hung, S H Mao, and M C Tsai, "Investigation of line start permanent magnet synchronous motors with interior-magnet rotors and surface-magnet rotors," *Electrical Machines and Systems*, pp. 2888 - 2893, October 2008.
- [4] A.H Isfahani, "Effects of magnetizing inductance on start-up and synchronization of line-start permanent-magnet synchronous motors," *IEEE Transaction on magnetics*, vol. 47, no. 4, pp. 823-829, April 2011.
- [5] F.J.K Kalluf, "Braking torque analysis of the single phase line-start permanent magnet synchronous motor," in *XIX International conference on electrical machines*, Rome, 2010.
- [6] A.J Sorgdrager, "Development of a line-start permanent-magnet synchronous machine", Master thesis, North-West University: Potchefstroom, 2013
- [7] A.H Isfahani, S Vaez-Zedeh "Line start permanent magnet synchronous motors: challenges and opportunities," *Elsevier: Energy*, vol. 34, pp. 1755-1763, April 2009.
- [8] C. Mutize, R-J. Wang, "Performanse comparison of an induction machine and line-start PM motor for cooling fan applications," in *Proceedings of the 21st Southern African Universities Power Engineering Conference, (SAUPEC)*, 2013, pp.122-126.
- [9] L Weili, Z Xiaochen, and C Skukang, "Study of solid rotor line-start PMSM operating performance," in *International Conference on Electrical Machines and Systems*, 2008, pp. 373-378.
- [10] J Pyrhonen, *Design of rotating electrical machines*, 1st ed. West Sussex, United Kingdom: John Wiley & Sons, Ltd, 2008.
- [11] I Boldea, *Electric machines*, 1st ed. USA: CRC Press, 2010.
- [12] A.E Fitzgerald, *Electrical machinery*, 6th ed. New Yourk, USA: Mc Graw Hill, 2003.
- [13] I Boldea, *The induction machine handbook*, 1st ed. New York, USA: CRC Press, 2002.
- [14] A.J Sorgdrager, A.J Grobler, "Influence of Magnet Size onf the Air-gap Flux Density of n Radial Flux PMSM." IEEE International Conference on Industrial Technology, Cape Town, 2013, 337-343.
- [15] V.B Honsinger, "Permanent magnet machines: Asynchronous operation," *IEEE Transactions on Power Apparatus and Systems*, vol. PAS-99, no. 4, pp. 1503-1509, July 1980.
- [16] D Henselman, *Brushless permanet magnet motor design*, 2nd ed. Orono, USA: Magna physics publishing, 2006.

Topic E

Energy and Energy Storage

Development of a Valve Regulated Lead Acid (VRLA) Battery Model to Aid in Battery Equalization Design

J.P A Almeida

University of the Witwatersrand, School of Electrical and Information Engineering, Private Bag 3, 2050, Johannesburg, South Africa.

Abstract. A multitude of battery models have been developed to predict the behaviour of different battery technologies with varying levels of detail. The model proposed in this paper focuses on the Voltage-Current (V-I) characteristics of Valve-Regulated Lead-Acid (VRLA) batteries to aid in the design of an equalisation strategy for series connected batteries in a system containing renewable energy sources. The model is based on Randle's model for electrochemical impedance, where a lumped equivalent electric circuit of the lead-acid battery predicts the behaviour of the battery as seen from its terminals. The parameters of the model are found to be multivariable functions of the battery's State-of-Charge (SoC), current and operating region (i.e. charging, discharging or rest). The experimental setup and parameterisation procedure, using non-linear least squares regression curve fitting techniques, is discussed and the parameterisation results for a 4.5 Ah 12 V VRLA gel battery at various discharge rates are presented. The model is then verified against experimental results through a Simscape (Matlab) simulation during the discharge and rest region, where the maximum run-time error was found to be less than 3% and an average run-time error of 0.407% was found.

Key Words. Valve-Regulated Lead-Acid, Equivalent Electric Circuit, Curve Fitting.

1. INTRODUCTION

Battery models are an essential tool to aid in the design of systems containing batteries as energy storage elements [14]. This ranges from the design of systems where multiple batteries form a single energy storage element within a larger system, down to the design of electric circuits and their interaction with each individual battery cell making up a battery bank [14]. A good battery model relates the terminal voltage, battery current, State-of-Charge (SoC), temperature and operational history of the battery at a suitable level of abstraction [9], [14]. Additionally, the model should be parameterized as easily as possible without permanently damaging the battery, while still yielding the required precision for a given application [9]. This paper discusses the development and parameterization of an equivalent electric circuit model for VRLA batteries, to predict their behavior when used in systems containing renewable energy sources and under the influence of a battery equalization strategy. Battery equalization aims to reduce the SoC mismatch between serially connected batteries, which arises due to differences in each individual cell's characteristics [4]. This is achieved by actively managing the energy flow into or out of each cell, preventing accelerated aging of individual cells and increasing the usable capacity of the series string [2].

There are a variety of existing battery models, including several electrochemical, mathematical and equivalent electric circuit models [12], [14]. Electrochemical battery models are in general more complex than their mathematical and equivalent electric circuit counterparts, due to the use of numerous chemical and mathematical equations [14]. This results in extended simulation times and powerful processing requirements. Additionally, most of the parameters used in these models are determined through physical measurement of internal components or chemical reactions during extensive experimentation, as the battery specific information required is often difficult to obtain from manufacturers. This parameterization process often

permanently damages the test battery. These models are primarily used to optimize the chemical and physical design of existing batteries. They are also restricted to the specific battery chemistries for which they were developed, reducing their versatility [14].

Mathematical models on the other hand are more suited to the design of larger systems utilizing battery banks as a single energy storage element [5], [12], [14]. They give general information such as a battery's estimated capacity and charge efficiency, but do not give detailed information about the behavior of individual cells. This limits their use in designing systems that depend on the properties of individual cells, such as battery equalization. These models often utilize empirical equations, which are parameterized from a manufacturer's datasheet to predict the general behavior of a battery under specific operating conditions. One such example is Perker's law, which is used to predict a battery's capacity under different discharge rates [12], [14].

Electric circuit modelling gives accuracy between that of electrochemical and mathematical models (approximately 1-5% error) [14]. These models normally consist of basic electric circuit elements arranged to give an accurate representation of a battery's behavior under different operating conditions [10]. They can either model discrete parts of a battery's internal structure or model the behavior as seen from the terminals [12]. The complexity of these models range from a simple voltage source with an internal resistance to circuits with multiple energy storage elements and multivariable dependencies on the battery's SoC, current, temperature and aging [9].

The paper is arranged as follows: Section 2 describes the requirements of the model to predict the behavior of VRLA batteries when used alongside an equalization strategy and renewable energy sources. Section 3 discusses the proposed model, explaining the significance of the various parameters. Section 4 and 5 describe the battery testing experimental setup and parameterization procedure. Finally Section 6

demonstrates the validity of the model by comparing simulation and experimental results.

2. MODEL REQUIREMENTS AND ASSUMPTIONS

The battery's model needs to accurately predict the electrical behavior of VRLA batteries under a variety of operating conditions. The majority of existing battery models focus on predicting battery behavior under constant charge and discharge. This is not applicable when used in systems containing renewable energy sources or a battery equalization strategy, as the operating conditions of each battery will change frequently [5]. From the model's intended application, a number of requirements can be determined.

Valid during Charge, Discharge and Rest periods as the model needs to predict the battery's behavior over both charge and discharge cycles, as well as during rest periods when the battery's current is approximately zero. Batteries used in systems containing renewable energy sources are often exposed to large variations in battery current due to the intermittent and/or periodic nature of the energy sources, resulting in multiple charge and discharge cycles at partial SoC and at different battery currents [3], [5]. Additionally, various equalization strategies are optimized to operate during the different periods, and therefore the model needs to predict the behavior of the battery under all these periods to allow an accurate means of comparison between different equalization strategies [2].

The model must incorporate the battery's dynamic response as electrochemical batteries are found to have a slow response time to sudden changes in operational characteristics, in the range of minutes to hours [9]. This attribute can be seen as the exponential change in a battery's voltage after a change in battery current. Both renewable energy sources and battery equalization will cause frequent variations in battery current, causing the battery to operate for a significant portion of time in a transient state [5]. Additionally, changes in operating conditions can occur before the battery reaches steady state, complicating the modelling procedure to prevent discontinuities arising during simulation [15].

The main objective in any portable device or system with limited energy, is to minimize energy loss and maximize battery runtime [14]. Energy dependency therefore becomes an important aspect of the model. For lead-acid batteries, this becomes particularly important during charging, especially near the end of charge, where charge efficiency decreases as only a portion of the charge energy is stored [1], [11], [12].

As most the operational characteristics of electrochemical batteries depend on SoC, it is also important to characterize the battery over the entire SoC range to ensure the model's accuracy is not reduced at the SoC extremes [5], [7], [12]. This is particularly important for battery equalization simulations as the importance of battery equalization increases at low and high SoC to prevent damage to

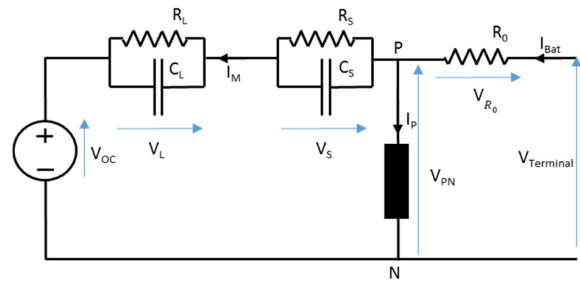


Fig.1. Proposed equivalent electric circuit model.

individual cells through overdischarge and overcharge [2–4].

Simple parameterization of the model's parameters should be easily performed from readily available measurements (current, voltage, temperature etc.), without permanently damaging or drastically affecting the battery's State-of-Health (SoH) [9]. This facilitates the initial parameterization of multiple test batteries, which can then still be used later, as well as the adaptation of the model's parameters as each battery ages.

Due to the complex behavior of electrochemical batteries being multivariable functions of SoC, current, voltage, temperature and SoH, some assumptions can be made to simplify the model without drastically reducing accuracy.

By operating batteries at a constant temperature, the effect of temperature can be minimized. Temperature mainly affects the available capacity of lead acid batteries during discharge (decreases capacity at lower temperatures), aging (SoH) and side reactions rates during charging (charge efficiency), which can be neglected for small capacity batteries without drastically reducing the model's accuracy [7], [14].

Although SoH affects the performance of batteries, the change in SoH is gradual (over numerous charge and discharge cycles). Therefore, the behavior of the battery can be assumed to remain constant over a small range of cycles, thereafter the battery can be re-parameterized to account for changes in SoH [14].

A frequently used battery is rarely left for days without use. Therefore, self-discharge (approximately 5% capacity/month for lead-acid batteries) can be neglected without encountering significant errors [7].

3. PROPOSED MODEL

The proposed equivalent electric circuit model, shown in Fig. 1, is based on Randle's model for electrochemical impedance [9]. The model aims to predict the behavior of a VRLA battery as seen from the terminals, rather than the individual internal parts of the battery (electrodes, electrolyte, electrode/electrolyte interface, connectors, etc.). This technique is suited to model batteries which may comprise of multiple cells connected internally within a sealed battery, as the user only has access to the positive and negative battery terminals.

The equivalent circuit is separated into two main parts: a main reaction branch consisting of a voltage source and number of RC networks (in this case two), and a parasitic branch, which accounts for the battery's behavior during charging. The number of RC networks is chosen according to the level of accuracy required for a given application, affecting the accuracy during transient conditions. In general, the model can have a high accuracy utilizing up to two RC networks, when parameterized for specific frequently occurring current and voltage waveforms [11], [12].

The voltage source (V_{oc}) represents the open circuit voltage (OCV) of the battery. For lead-acid batteries, a linear relationship between OCV and SoC exists [5], [7]. The relationship between OCV and SoC is determined by taking several steady-state OCV measurements at different SoC values. However, due to the long time constant of electrochemical batteries, this OCV measurement can take hours to perform, resulting in lengthy parameterization times. Techniques such as extrapolation of the battery's dynamic voltage response and voltage averaging during charge and discharge, can be utilized to quickly determine the OCV/SoC relationship [9].

The series resistance (R_0) takes into account the instantaneous terminal voltage change in response to a change in battery current. This term represents the Ohmic resistance of the internal battery connections, electrolyte, electrodes and separator [10].

The dynamic response of the battery is modelled by the two RC networks, which account for the slow exponential voltage change as a result of polarization (or over potential) within the battery. R_s and C_s are responsible for the short time constant, which is due to double-layer capacitance on the surface of the internal electrodes and electrochemical polarization. R_l and C_l are responsible for the long time constant of the exponential voltage change, due to concentration polarization (diffusion processes within the electrolyte) [10]. The circuit elements making up these RC networks depend on the battery's SoC, current and operational region [15]. The short time constant is the order of seconds and long time constant, in the order of minutes to hours, are given by (1) and (2) respectively [9];

$$\tau_{short} = R_s C_s \quad (1)$$

$$\tau_{long} = R_l C_l \quad (2)$$

The parasitic reaction branch models the behavior of the battery during charging. As the battery is charged, irreversible parasitic chemical reactions start occurring within the battery, such as gassing, resulting in energy losses. The behavior of this parasitic branch is highly non-linear, where I_p (parasitic current) is found to be a function of V_{PN} (main branch voltage) and electrolyte temperature (θ) [7], [11], [12]. From the Tafel gassing-current relationship, the relationship between I_p , V_{PN} and θ is:

$$I_p = V_{PN} G_{p0} e^{\left(\frac{V_{PN}}{V_{p0}} + A_{p0} \left(1 - \frac{\theta}{\theta_f}\right)\right)} \quad (3)$$

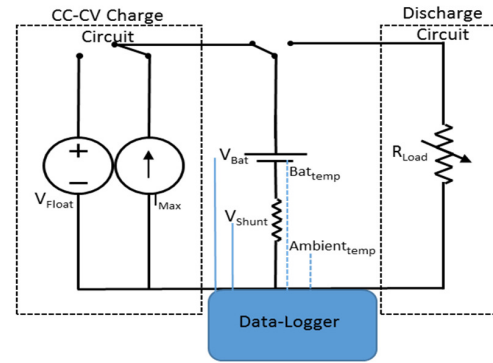


Fig.2. Battery testing experiment setup

where G_{p0} , V_{p0} , A_{p0} and θ_f (electrolyte freezing temperature) are constants to be determined for a particular battery. During discharge, $I_p \approx 0$ and increases during charging, particularly when the battery approaches 100% SoC. Only the main branch current (I_M) changes the SoC of the battery, and when the battery is fully charged, any remaining float current entering the battery is I_p . Various methods of calculating SoC are discussed in [13], but for this application the Coulomb counting method on I_M for determining SoC is utilized [5].

The electrical behavior of the equivalent circuit during discharge can be described by equation (4)-(6). From these equations and the response of the terminal voltage to current changes, the parameters of the proposed model can be calculated under a variety of operating conditions.

$$V_{Terminal} - V_{oc} + V_L + V_s + V_{R_0} = 0 \quad (4)$$

$$\tau_{short} \dot{V}_s + V_s - I_M R_s = 0 \quad (5)$$

$$\tau_{long} \dot{V}_l + V_l - I_M R_l = 0 \quad (6)$$

4. MODEL PARAMETERIZATION PROCEDURE

4.1 Experimental Setup

To extract all the parameters of the proposed model, a battery test system and experimental procedure, based on IEC and IEEE standards for testing VRLA batteries [6], [8], as well as previous systems to parameterize similar battery models is utilized [9], [10]. The experimental setup is shown in Fig. 2 and comprises of a test battery, data logger, charge circuit and discharge circuit. The charge circuit utilizes a DC Power Supply, which allows the user to set the maximum initial current and charging voltage, forming a Constant-Current Constant Voltage (CC-CV) two stage charging regime. The DC Power Supply is also used to supply a varying charging current when parameterizing a battery in the charge region.

The discharge circuit uses a power transistor, biased in it's linear region to act as a variable resistor. This circuit maintains a constant, user defined discharge current throughout an experiment.

The data logger records the battery terminal voltage, current and temperature (both ambient and the battery

via the negative terminal connector) at a minimum of 3 Hz. An adaptive logging regime is proposed in [9] to reduce the total data stored, while increasing the measurement frequency during rapid changes in terminal voltage. The battery current is determined by measuring the voltage across a 5 A, 12 mΩ shunt resistor placed in series with the battery. The test battery is placed in a sealed environment to regulate the ambient temperature surrounding the battery to room temperature ($\approx 22^\circ\text{C}$) during all experiments (as temperature is not considered in the model).

4.2 Test Procedure

To determine the dynamic properties of the test battery, the battery's voltage response to a number of different pulsed charge and discharge currents is analyzed. This ensures that all the parameters of the model, which are multivariable functions of SoC, battery current and operation region can be determined by analyzing the resultant terminal voltage [9].

The test procedure first ensures that the battery is fully charged (100% SoC) and that the terminal voltage and internal temperature has stabilized. The battery is charged at the maximum rated initial current or less until the battery reaches the standby charging voltage. Charging continues at this voltage until the current decreases and eventually stabilizes. The charge current is deemed stable when the same charging current is measured over a three hour interval [6], [8]. Once the battery is fully charged, it is disconnected from the charge circuit for between 1 and 24 hours in order for the battery's terminal voltage and temperature to stabilize.

The next phase of the test procedure involves discharging the battery via a number of constant current pulses ranging from 0.05 C to 5 C (where 1 C is the required continuous discharge current to fully discharge the battery in one hour) [7], [8], [12]. The pulse current magnitude is chosen according to the typical battery current for a specific application. The pulse width is selected to ensure that there are sufficient current pulses to determine the dynamic characteristics of the battery between 0-100% SoC (>10 pulses) [9]. The rest period is then determined to ensure sufficient time for the battery's terminal voltage and temperature to stabilize before the next pulse discharge commences (>30 minutes). The pulse discharge sequence continues until the end-of-discharge voltage is reached, which for VRLA ranges between 1.6 and 1.75 V/cell (9.6 V and 10.5 V for a 12 V VRLA battery) according to the battery's datasheet [7], [8]. Fig. 3a shows a typical discharge curve with a pulsed current.

Once the battery is fully discharged, it is left open circuit for between 1 and 24 hours to enable the battery's terminal voltage and temperature to stabilize.

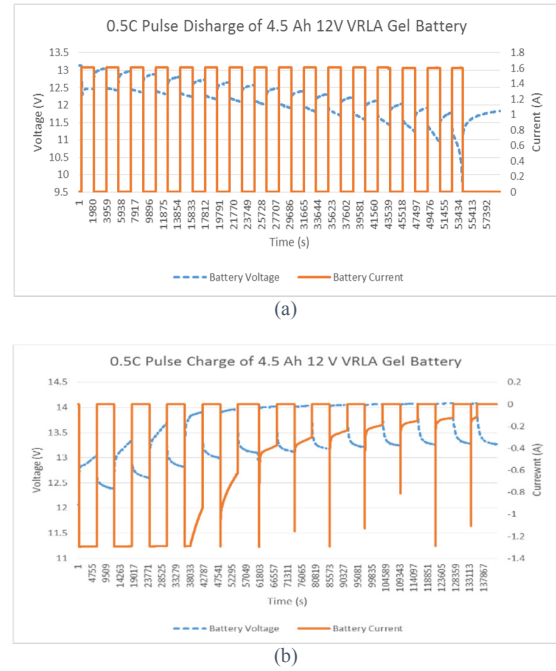


Fig. 3. Battery terminal voltage and current with pulse discharge current (a) and pulse charge current (b).

A pulsed charge, similar to the pulse discharge, is then applied where a number of constant charging current pulses are applied to the battery. The battery is pulsed charged until it reaches the standby charging voltage, hereafter the current pulses magnitude starts to decrease until the magnitude of the charging current has stabilized over 3 consecutive pulses. This process is shown in Fig. 3b.

5. MODEL PARAMETERIZATION

The proposed model is parameterized for a 4.5 Ah 12 V VRLA gel battery during the discharge and rest operation regions following the experimental test procedure discussed previously. The parameterization process utilizes the rest period after a current discharge pulse to determine the model parameters for a particular SoC in the rest region [9]. The subsequent discharge pulse is then used to determine the model parameters at the same SoC but in the discharge region [10]. This process determines all the parameters of the model in both regions, including the OCV via extrapolation over the entire SoC range.

The values of R_{0-rest} , R_{s-rest} , C_{s-rest} , R_{L-rest} , C_{L-rest} and V_{oc} are determined using non-linear regression curve fitting of the battery's terminal voltage in the rest region in Fig. 4. The voltage response is approximated to Equations (7) and the individual equivalent circuit parameters are determined from Equations (8)-(13).

The values of $R_{0-discharge}$, $R_{s-discharge}$, $C_{s-discharge}$, $R_{L-discharge}$ and $C_{L-discharge}$ are similarly determined using Equation (14) in the discharge region of Fig. 4. The circuit parameters are then determined from Equations (15)-(18).

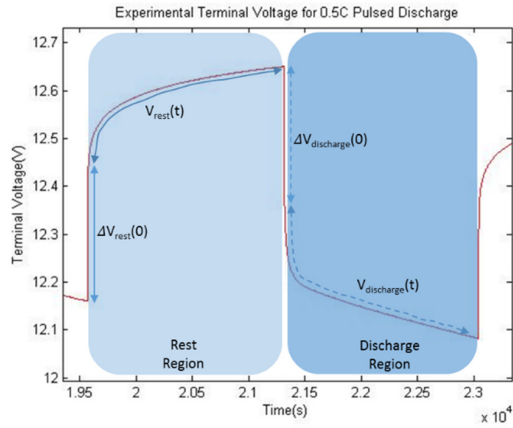


Fig. 4. Characterization during the rest and discharge region.

$$V_{rest}(t) = a \left(1 - e^{-\frac{t}{b}}\right) + c \left(1 - e^{-\frac{t}{d}}\right) + f \quad (7)$$

$$R_{s-rest} = \frac{a}{\Delta I_M} \quad (8)$$

$$C_{s-rest} = \frac{c}{R_{s-rest}} \quad (9)$$

$$R_{L-rest} = \frac{c}{\Delta I_M} \quad (10)$$

$$C_{L-rest} = \frac{d}{R_{L-rest}} \quad (11)$$

$$V_{oc} = \lim_{t \rightarrow \infty} V_{rest}(t) \quad (12)$$

$$R_0 = \frac{\Delta V_{rest}(0)}{\Delta I_M} \quad (13)$$

$$V_{discharge}(t) = ge^{-\frac{t}{h}} + je^{-\frac{t}{k}} - mt + n \quad (14)$$

$$R_{s-discharge} = \frac{g}{\Delta I_M} \quad (15)$$

$$C_{s-discharge} = \frac{h}{R_{s-discharge}} \quad (16)$$

$$R_{L-discharge} = \frac{j}{\Delta I_M} \quad (17)$$

$$C_{L-discharge} = \frac{k}{R_{L-discharge}} \quad (18)$$

Fig. 5 shows the extracted model parameters as functions of SoC, battery current and operation region (discharge and rest) for the 12 V test battery. V_{oc} is linearly related to SoC and independent of the discharge current. R_0 is approximately constant and independent of battery current and operation region above 20% SoC range, exponentially increases beyond this point [11], [12], [14]. R_s and R_L exhibit the same behavior as R_0 , with the additional dependency on discharge current and operation region (higher during discharge region and decreasing with an increase in battery current). C_s and C_L are both strongly influenced by the operation region, where they have vastly different functions of SoC. This highlights the fact that there is a significantly different voltage response time constant in the discharge and charge region, particularly affecting the long time constant which is reduced in the discharge region [15].

Although the model is only parameterized for discrete battery currents, it is possible to use interpolation to determine the model parameters' function of SoC and operation region for a range of battery currents [14].

6. MODEL VALIDATION AND DISCUSSION

To validate the model and extracted parameters for the 4.5 Ah test battery, a Simscape (Matlab) simulation

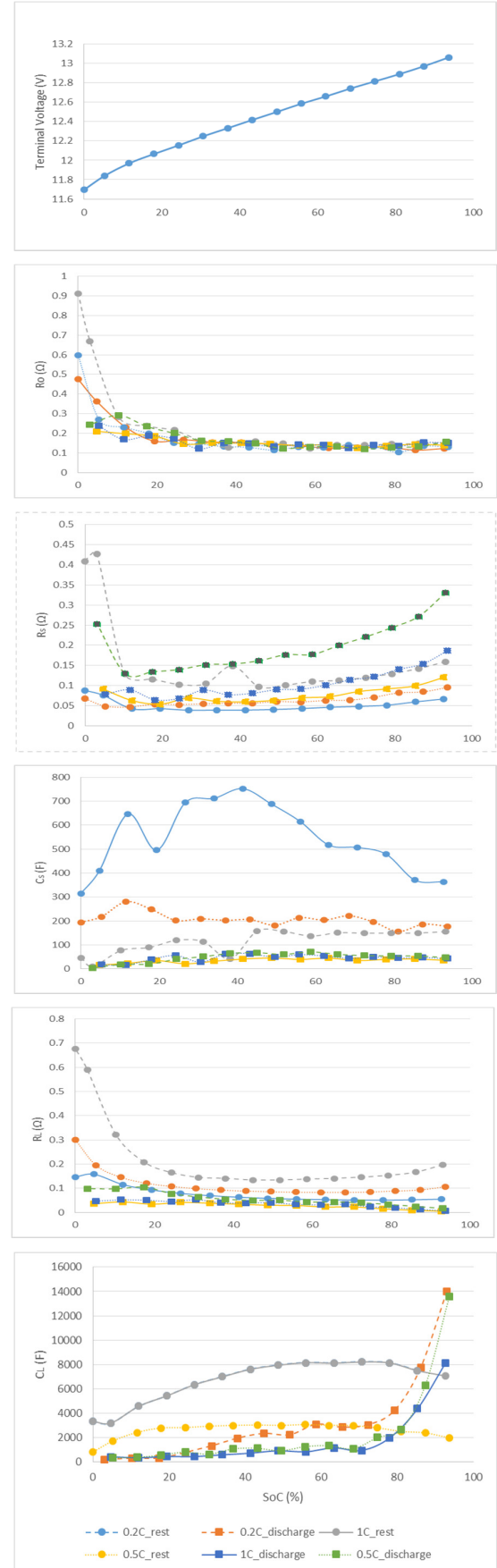


Fig. 5. Extracted parameters of the test battery

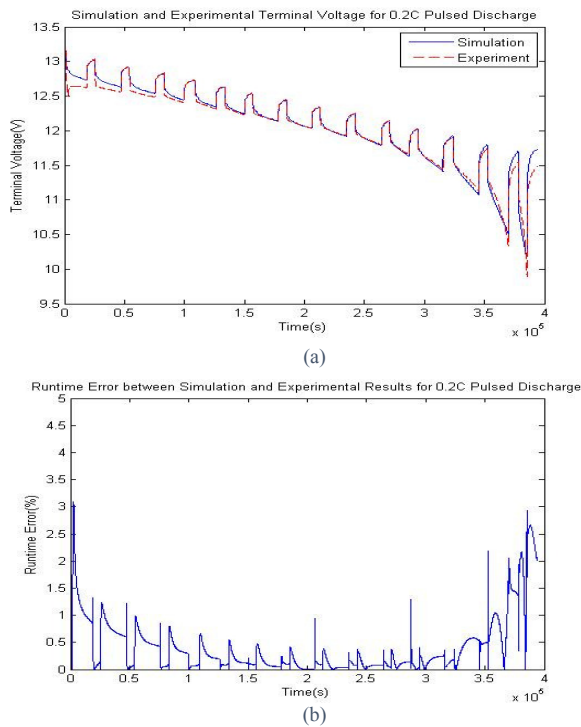


Fig. 6. Simulation and experimental results for 0.2 C pulsed discharge.

using custom developed blocks (to describe the models parameters' multivariable mathematical functions) was implemented. A comparison between the simulation and experimental results of the battery's terminal voltage for a 0.2 C pulsed discharge is shown in Fig. 6a. The run-time error, calculated by Equation (19), is shown in Fig. 6b. A maximum run-time error of 3% occurred during the *coup de fouet* region. The *coup de fouet* is the short duration voltage drop found as a fully charged lead-acid battery is initially discharged [13].

The mean run-time error was found to be 0.407%, but increased significantly below 20% SoC. This can be attributed to the exponential change in the model's parameters beyond 20% SoC. The use of more current pulses during parameterization could reduce this error by increasing the SoC resolution during parameterization. The run-time error can also be decreased by increasing the number of terms in the mathematic functions that approximate each parameters' curve in Fig. 5 during simulation [14].

$$Error(t) = \frac{|V_{Experiment}(t) - V_{Simulation}(t)|}{V_{Experiment}(t)} * 100 \quad (19)$$

Although the model attempts to account for the different operation regions, errors still occur as the battery changes from one region to the next (i.e. during the transitions from one rest to discharge), as shown in Fig. 7. The error decreases as the battery approaches steady state, indicating that the source of the error lies with the capacitive terms of RC networks, in contrast to the model proposed by [15].

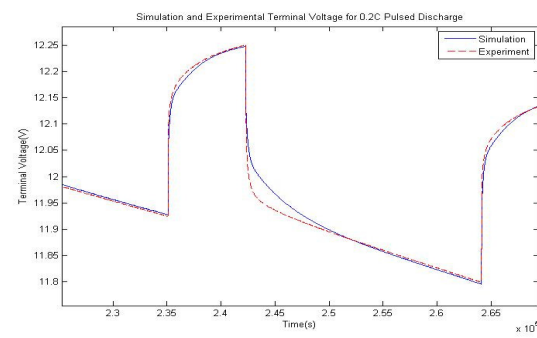


Fig. 7. Voltage difference during rest and discharge region

7. CONCLUSION

A dynamic equivalent electric circuit model for VRLA batteries has been developed based on the battery's terminal behavior. The operating conditions imposed by renewable energy sources and an equalization strategy was discussed to determine important aspects of the battery model. The model takes into account the influence of SoC, battery current and operation region to predict the steady state and dynamic battery terminal voltage. The experimental procedure and parameterization process was presented, which was then used to determine the parameters for a small capacity 12 V VRLA gel battery. Experimental results are then compared to a Simscape simulation where a maximum run-time error of 3% and a mean run-time error of 0.407% were achieved. Although there is close agreement between simulation and experimental results, significant errors occur at low SoC due to the exponential change in the model's parameters, as well as during the transition from one operating region to the next. This requires further investigation to determine the parameters' values with higher accuracy at low SoC as well as the cause of the error during operating region transitions.

REFERENCES

- [1] P. E. Pascoe and A. H. Anbuky, "A VRLA battery simulation model," *Energy Conversion and Management*, vol. 45, pp. 1015–1041, 2004.
- [2] M. A. G.-M. E. Romero-Cadaval M. I. Milanes-Montero J. Gallardo-Lozano, "Battery Equalisation Active Methods," *Journal of Power Sources*, vol. 246, pp. 934–949, 2014.
- [3] D. U. S. H. Wenzl R. Kaiser A. Jossen I. Baring-Gould J. Manwell P. Lundsager H. Bindner T. Cronin P. Norgard A. Ruddell A. Perujo K. Douglas C. Rodrigues A. Joyce S. Tselepis N. van der Borg F. Nieuwenhout N. Wilmot F. Mattera V. Svoboda, "Operating conditions of batteries in off-grid renewable energy systems," *Solar Energy*, vol. 81, pp. 1409–1425, 2007.
- [4] S. West and P. T. Krein, "Equalization of Valve-Regulated Lead-Acid Batteries: Issues and Life Test Results," in *Telecommunications Energy Conference*, 2000.
- [5] D. Guasch and S. Silvestre, "Dynamic Battery Model for Photovoltaic Applications," *Progress in Photovoltaics: Research and Applications*, vol. 11, pp. 193–206, 2003.
- [6] *Stationary lead-acid batteries Part 21: Valve regulated types —Methods of test*. Standards South Africa.
- [7] D. Berndt, "Valve-regulated lead-acid batteries," *Journal of Power Sources*, vol. 100, pp. 29–46, 2001.
- [8] *IEEE Guide for the Test and Evaluation of Lead-Acid Batteries Used in Photovoltaic (PV) Hybrid Power Systems*. IEEE-SA Standards Board.

- [9] S. Abu-Sharkh and D. Doerffel, "Rapid test and non-linear model characterisation of solid-state lithium-ion batteries," *Journal of Power Sources*, vol. 130, pp. 266–274, 2004.
- [10] K. M. R. B. Schweighofer and G. Brasseur, "Modelling of High Power Automotive Batteries by the Use of an Automated Test System," *IEEE Transactions on Instrumentation and Measurement*, vol. 52, pp. 1087–1091, 2003.
- [11] S. Barsali and M. Ceraolo, "Dynamical Models of Lead-Acid Batteries: Implementation Issues," *IEEE Transactions on Energy Conversion*, vol. 17, pp. 16–23, 2002.
- [12] M. Ceraolo, "New Dynamical Models of Lead-Acid Batteries," *IEEE Transactions on Power Systems*, vol. 15, pp. 1184–1190, 2000.
- [13] M. P. S. Piller and A. Jossen, "Methods for State-of-Charge determination and their applications," *Journal of Power Sources*, vol. 96, pp. 113–120, 2001.
- [14] M. Chen and G. A. Rincon-Mora, "Accurate Electrical Battery Model Capable of Predicting Runtime and I-V Performance," *IEEE Transactions on Energy Conversion*, vol. 21, pp. 504–511, 2006.
- [15] S. Mischie and D. Stoiciu, "A New Improved Model of a Lead Acid Battery." *Facta Universitatis*, 2007.

SIMULATION AND PERFORMANCE ANALYSIS OF DIFFERENT BATTERY MODELS FOR ENERGY STORAGE

L Ralikhwatha*, G Machinda* and S Chowdhury*

* University of Cape Town, Department of Electrical Engineering, Upper Campus, Rondebosch, Cape Town 7700

Abstract: Renewable energy generation form a part of the much needed alternative power generation; however maintain a balanced network system with various integrated renewable DGs can be a tormenting challenge. The intermittency nature of the renewable energies causes their output to continuously fluctuate and thereby posing a real challenge on keeping generation and load matched. The varying output power also has a negative impact on the overall network power quality. Storage systems have been used to reduce these fluctuations in renewable energy power systems and batteries play an important role in this regard. Batteries' importance to the new network system is credited to the developments that have been taking place in the batteries technologies. The study of these technologies can be done using their electrical circuit models that emulate their operations. In this paper, electrical circuit models are used to study a few of the most commonly used battery technologies and analyse their SOC with respect to batteries' parameters of influence.

Key Words. Storage, Renewable energy, State of charge (SOC).

1. INTRODUCTION

Renewable energy generation, wind and solar in particular, is growing significantly around the entire world [1]. Renewable energy generation has experienced a positive reception, predominantly because of its contribution towards reducing greenhouse gas (GHG) emissions. Literature has shown that in many nations around the world, policies with the objective of decreasing CO₂ emissions and/or raising the share of renewable energy have either been implemented or initiated, e.g. in the US, the EU and China policies have been formulated with the objective of reducing CO₂ emissions [2]. Apart from their contribution to emissions reduction, renewable energy generation form a part of the much needed alternative generation at a time when the current fossil fuels are expected to soon fail to sufficiently supply the current energy consumption rate for a longer period of time [3].

The network system is desired to be balance at any given time, i.e. supply meets demand, which can cause problems if not met; a common technical challenge trait for both PV and wind power generating systems [1]. Their output powers vary directly with weather changes, and independently from demand variations; hence the name intermittent sources. Both solar PV and wind are unable to supply base load power and they have difficulty matching the peak load [3]. These problems greatly affect the reliability of renewable energy sources such that it is virtually impossible to depend on them as sole energy suppliers.

However, if an efficient energy storage system is implemented, sustainability and reliability of the renewable energy generation systems can be enhanced [3] [4]. Batteries are proving to be the answer to this dilemma and therefore they have been increased research on battery technologies and their operations.

This paper performs an analysis on the performances of different electrical circuit battery models and gives conclusions based on the results obtained.

2. BATTERY CLASSIFICATION

Fig. 1 shows the battery classification block diagram.

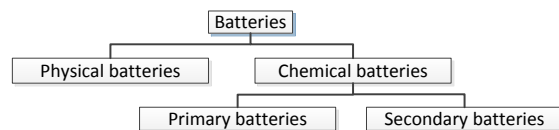


Fig. 1: Battery classification [5]

This research is based on chemical batteries, classified as secondary or primary batteries according to whether or not, respectively, they can be re-used (electrochemical reactions are reversible) after fully discharged [5].

2.1. Primary batteries

Primary batteries, also referred to as disposable batteries, cannot be re-used. This is because they are unable to reverse the electrochemical reactions once they are fully discharged; nevertheless, they are known for their high energy density. Common primary batteries include zinc carbon, alkaline, lithium and lithium-iodide batteries.

2.2. Secondary batteries

Unlike primary batteries, the secondary batteries are able to reverse their electrochemical reactions and thus enabling them to be re-used after they are fully discharged. The reversing of the electrochemical reactions is achieved by passing a reverse electric current through the cells, thus restoring the energy in the material of the electrodes. Secondary batteries are often referred to as rechargeable batteries. Common secondary batteries include the lead-acid, nickel-cadmium and lithium-ion batteries.

2.3. Secondary versus Primary batteries

Predominantly primary batteries were used as electrical energy source in many systems. However due to massive developments; primary batteries are becoming extinct more specifically in the industrial domain. The influences behind this is the fact that rechargeable batteries have recently seen vast improvements and now offer higher density, have improved charging methods and high readily available charge [6]. Another factor which plays a significant role is the cost. The one-time cost of a primary battery is approximately 30 times of a secondary battery [6]. In addition to that; when primary batteries are fully discharged they have to be newly replaced which cause inconveniences such as a cut off on the supply of power to users when power is required. Primary batteries are mostly used in portable applications because high reliability is not necessary in that domain. Such applications include hand watch, portable radios and etc.

Since primary batteries are not efficient in industrial systems, they cannot be used in implementation of renewable energy system. Thus our primary concern will be on secondary batteries. An overview of all secondary batteries with performance comparison will determine which battery is more efficient and viable for this application.

3. BATTERY ENERGY STORAGE SYSTEM

It is perceived that energy storage contributes significantly towards the full potential utilisation of renewable energy. Battery energy storage technology (BEST) is one of the advancing energy storage technologies. They are some of the most cost-effective energy storage technologies and they use chemicals to store the energy [7] [8].

Generally, energy storage techniques are classified according to the type of application (permanent or portable), storage duration (long-term or short-term) and type of production (maximum power required).

A battery energy storage system comprises of two main categories; the battery, and control and power conditioning system [9].

3.1. Battery Parameters

Battery models are derived on the factors which adversely affect the battery performance [44]. A number of battery technologies are under consideration for large scale energy storage. These technologies have been developing and advancing rapidly and therefore making the application of storage technologies more viable solutions for modern power application [9] [8]. Different models of varying complexity and accuracy have been developed by researchers in order to understand the dynamics of batteries. These models are derived on the factors which adversely affects their performance. These factors include internal resistance, discharge type, discharge mode, rate of discharge and charge, current flow and polarization, capacity and state of charge.

3.2. Control and power conditioning system

The control and power conditioning system is a vital integral part of the BEST. It is responsible for interfacing the battery with the load or utility (end user). It is also responsible for the regulation of the charging and discharging of the battery [9].

4. BATTERY TECHNOLOGIES

There are various battery technologies that have been developed for power system application; however, some of the developed technologies are more suitable for power system application, and these are discussed in this paper. The discussed technologies are then modelled in Simulink and the results presented in Section 6; but before this, the electrical circuit based battery models studied for this paper are discussed.

4.1. Electrical circuit-based battery models

Electrical circuit-based models are functions of various battery parameters stated in the previous section. However these models comprise of a combination of resistors, capacitors, inductors, voltage and current sources in an electrical circuit. The charging and discharging equations for these models depend on electrical components in the respective circuit. These models provide more relevant information, than their counterpart mathematical models, for integration with other electrical systems. There are several electrical circuit based battery model; however, only models that are more suitable for power system application are discussed.

Table 1: A general comparison of battery models

Characteristics	Battery Models		
	Electro-chemical	Mathematical	Electrical circuit based
Accuracy	High	Moderate	Medium
Complexity	High	Medium	Low
I-V relationship	Yes	No	Yes

The accuracy of electrical based models lies between that of electrochemical and mathematical based. Electrical models are easy to handle and are capable of computing battery parameters while on operation which offers good accuracy [10].

5. FACTORS AFFECTING BATTERY PERFORMANCE

The performances of a battery are dependent on various factors, listed in the sub-headings below; a short description for each of the factors is given.

5.1. The voltage level

The voltage level of the battery is a significant factor which draws relevant information about the cell such as the specific energy of the battery and the battery discharge characteristics. However the specific energy delivered by a typical battery is lower than the ideal specific energy of its active material due to I²R losses [11]. The energy of the battery in Watt-hours/gram is given by the equation below:

Watt-hours/gram = Voltage \times Ampere hours/gram

Where: Voltage is the voltage level of the battery in Volts (V).

5.2. Current drawn during discharge

The current drain during discharge is a measure of the depth of the discharge occurring in a battery during energy supply for a specific application. The significance of this factor is that it accounts to the service life of the battery. When the current drain is increased the battery life gets reduced due to the lower voltage limit caused by an increase of the IR losses of the battery [11].

5.3. Discharging mode

The current rate of the battery during discharge is dependent on the mode in which the battery is discharged at. There are three basic modes at which a typical battery can be discharged at; namely: constant current, constant resistance and constant power load [12].

A. Constant current

The current of the load remains constant during discharged and can be described using equation (3).

$$I = V/R \quad (3)$$

Constant resistance: The resistance of the load in this case is constant throughout the discharge of the battery but the current is directly proportional to the voltage limit of the battery. Equation (3) suitably describes the characteristic of this load.

Constant power: For this type of load, the power is continuously constant throughout the discharge of the battery and is described by equation (4) below.

$$P = V \times I \quad (4)$$

5.4. Battery age and storage condition

Batteries are sensitive devices which are most likely to rot in a very short period of time and deteriorate because of the chemical reactions that occur during storage. The charge retention of a battery is greatly affected by the storage conditions of the battery. The self-discharge rate of a battery proceeds at lower rates in reduced temperatures thus refrigerated storage extends the storage life of the battery. However storages at very low temperatures may cause a rapid self-discharge which may result in reduction of capacity [13].

5.5. Cell and battery design

The build-in structure of the battery strongly influences its performance features. This is due to the difference in electrode construction of different type of plates in a battery. However different types of batteries have different plate's construction method which effectively leads to better performance or poor performance to some. The plate's construction features include the physical dimensions, pitch, number of plates in each cell, the resistance of the lugs and the terminals. In addition to that, the amount of active

materials in the plates is a significant factor as well [14].

5.6. Service life

The battery service life is a function of many performance factors stated in this section. It is often impossible that all the factors affecting the performance of a typical battery occur simultaneously. However there are some which significantly affects the service life of the battery (i.e. temperature, current drain during discharge and etc.). The service life is importantly used to determine the efficiency of the battery during its operational life [11], [14], [13].

5.7. The charging methods

Because we are dealing with rechargeable batteries here, the mode or perhaps the charging technique of the cells has a great influence on the performance of the battery. If cells are undercharged they offer poor performance, if overcharged the performance is great but if cells are excessively overcharged the lifespan of the battery gets shortened. Improper charging causes sedimentation and gassing on the plates of the cells.

6. SIMULATIONS AND RESULTS

Simulations were conducted using MATLAB Simulink environment. Different cases are conducted to study the effect of the aforementioned factors on the battery performances. Different battery models are considered to perform this study.

6.1 Thevenin Diode-based model

Fig. 2 shows the implemented Thevenin diode based model, specifically for lead-acid batteries.

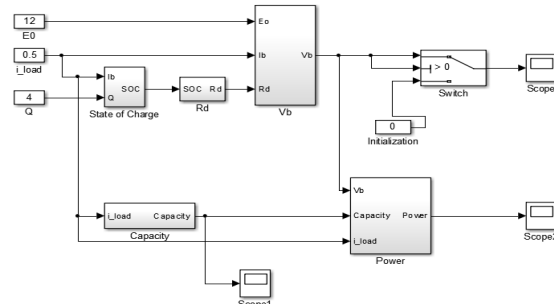


Fig. 2: Terminal voltage, Capacity and Power block diagram for the diode based battery model

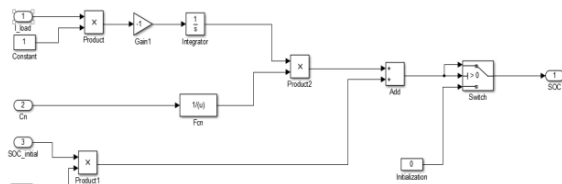


Fig. 3: The State of Charge Simulink implemented circuit

The voltage drop caused by the diode in forward bias was assumed to be a constant (0.6V). The discharge current denoted as I_b was changed in order to see the battery runtime and the available capacity in the battery at a specific state of charge (SOC); SOC is assumed to discharge from 100% to 0%. A nominal voltage of 12 volts with the capacity of 4 Ah is used.

Fig. 4 shows the obtained curves of the voltages with different discharge rates decreasing exponentially. The power distribution and the charge transfer at various discharge rates are plotted in Fig. 5 and Fig. 6 respectively. From Fig. 5 it is observed that the total extracted charge after the battery is empty is not equal to 4 Ah. In actual fact it is decreasing with an increase of the discharge rate. This model validates the idea that the discharge rate affects the shelf life of the battery since it will be decreasing when high rate of discharge is used.

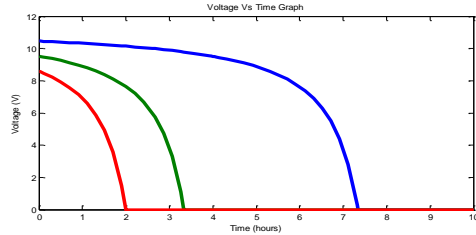


Fig. 4: Terminal Voltage at different discharge rate

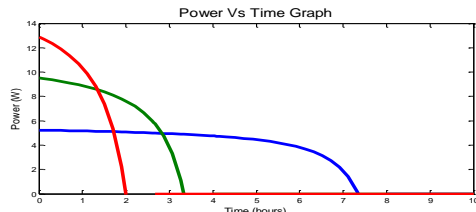


Fig. 5: Power distribution at different discharge rate

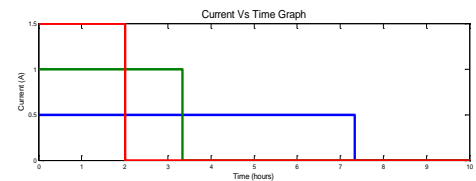


Fig. 6: Extracted charge at different charge rates

Table 1 below shows the SOC and the charge that can be extracted at different times using various constant currents.

Table 1: Comparison of battery performance results at different discharge rates

Time (hours)	Discharge/Charge current (A)					
	0.5 A		1 A		1.5 A	
	SOC (Dis-charge in %)	Extracted Charge (Ah)	SOC (dis-charge in %)	Extracted Charge (Ah)	SOC (Dis-charge in %)	Extracted Charge (Ah)
2.667	70	1	33.33	2.667	0	4
4	50	2	0	4	0	4
8	0	4	0	4	0	4

It is evident that when the discharge current is increased the time it takes the battery to be completely discharged for these cases decreases as well. However the charge that will be transferred at high constant is high for a short period of time. Discharging at 0.5 A constantly takes 8 hours to completely discharge the battery where else discharging at 1.5 A will take 2.667 hours.

6.2 Run-time based model

The main parameters include SOC, capacity, VOCV, Vb and the RC components. Fig. 7 and Fig. 8 show the components of the simulated run-time battery model.

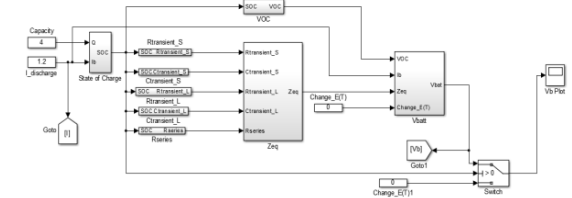


Fig. 7: Terminal voltage diagram for the runtime battery model

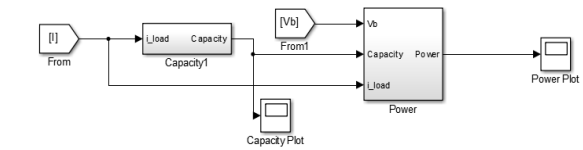


Fig. 8: Capacity and Power block diagram for the run time model

The capacity of this battery is a constant (4Ah) and the SOC characteristic curve at different charge rates (0.5, 1 and 1.5 A) is shown in Fig. 9 below.

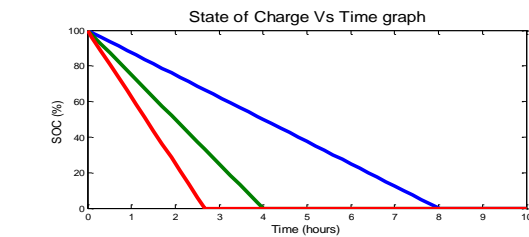


Fig. 9: SOC graphs of different discharge rates

The voltage at the terminals of the battery has been improved slightly from that computed in the previous cases. A plot showing a smooth exponential curve of the voltage is shown in Fig. 11 below. It is evident from the plot that as the discharge rate increases the smoothness of the curve starts fading away. This is an indication of that when the discharge rate increases the charge stored gets extracted more rapidly.

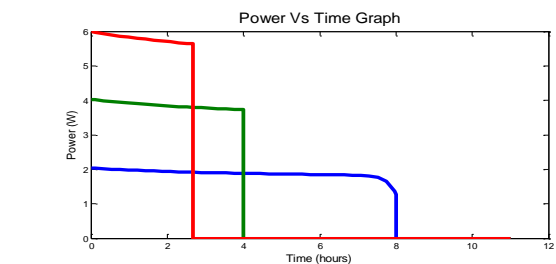


Fig. 10: Power distribution to the load

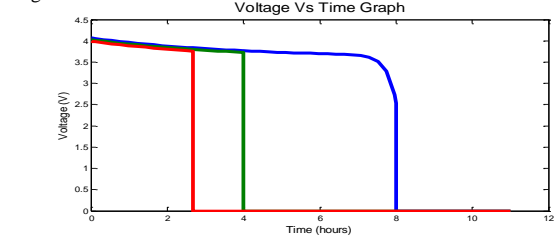


Fig. 11: Terminal voltage of the battery during discharge

The strength of this model is the ability to predict the run time of the battery. Since in this case the operating

temperature was assumed to be constant (20 °C to be more precise), the capacity lost during the discharge from 100% SOC to 0% taking approximately 10 hours is roughly 0.7%. This is illustrated in Fig. 6 above. However the downside about this estimate is that is entirely dependent on the temperature and the time for operation.

6.3 The Third Order Model

Fig. 12 below shows the implemented circuit for the third-order battery model.

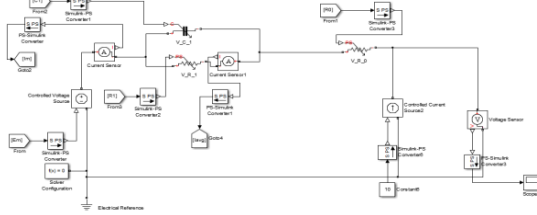


Fig. 12: Circuit diagram showing the main and the RC branch of the third-order model with the parasitic branch omitted

This third order model was proposed by [16]; it incorporates the temperature effect on the battery, the change in capacity during the discharge and charge process and the SOC. The SOC for this case is a function of the extracted charge and the capacity and the capacity is changing with the electrolyte temperature and the discharge current. However the discharge current and the electrolyte temperature were assumed to be constant for the purpose of this study. The electrolyte temperature was assumed to be 25°C (ambient temperature) and the discharge current was assumed to be (10A). The only case that was investigated for this section was the discharge process and the charging process was not investigated in order to further decrease the complexity of the model by omitting the parasitic branch since it is not essential during the discharging process. The initial extracted charge is assumed to be 0 Ah.

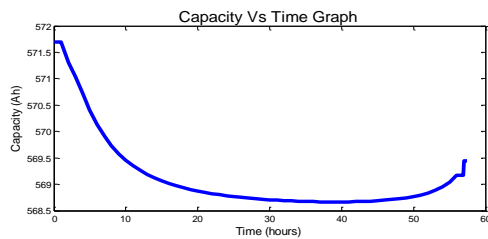


Fig. 13: Capacity of the battery against time during the discharge process

Capacity is another important parameter and it is taken as the changing parameter of the model in this case. Fig. 13 below shows the capacity of the battery as the SOC of the battery is decreasing and the electrolyte temperature and the discharge current values are kept constant. In the plot illustrated by Fig. 13, it is evident that there is a region where the curve is almost like a straight line (at approximately $t = 30$ hours). This is a region where the average current I_{avg} of which is the function of the capacity is equal to the discharge current. This can be seen by substituting $I_{avg} = \text{discharge current}$, the constant assumed electrolyte temperature. Hence the charge extracted in that point

is = the initial value (571.75) – the final value (568.75) = 3 Ah.

The effect of changing the temperature while the discharge current was kept constant or changing current while temperature was kept constant was observed and the obtained results are shown in Fig. 13.

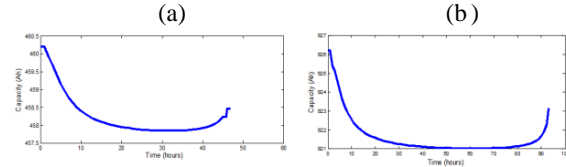


Fig. 14: Capacity plot of the third-order model for a discharge current 10A at (a) 100C and (b) 200C

The change in discharge current while the temperature was kept constant was investigated and the results were observed and the obtained results are shown in Fig. 15.

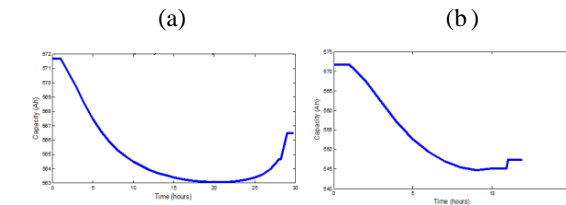


Fig. 15: Capacity plot of the third-order model for a discharge current of (a) 20A and (b) 50A, all at 200C

7. CONCLUSIONS AND RECOMMENDATIONS

The following conclusions are drawn based on the results obtained in the previous section.

7.1 Thevenin battery models

From simulations it is evident that the steady-state model provides completely irrelevant information about the discharge voltage of the battery because of its linear response with time. The internal resistance estimation based shows the exponential zone of the discharge characteristics but with constant discharge voltage afterwards. The diode based model shows a more closely matching characteristic curve of the build in battery model and also incorporates the voltage loss due to the voltage drop on the diode giving a more precise estimation about the capacity which is left in the battery. The drawback in this model is that it does not incorporate the loss of capacity due to self-discharge and temperature increase or decrease but is capable of modelling the loss in the capacity due to change in discharge rates of the load.

7.2 Runtime Battery Model

The dynamic model is a good demonstrative model for a lead-acid battery. It offers a good approximation of the characteristic discharge curves and provides precise estimation of the battery charge. Furthermore it provides information about the loss of capacity with the life cycle of the battery.

7.3 Third-Order Battery model

Despite this model's complexity drawback, it can be viewed as the perfect model to demonstrate batteries in a renewable energy system. This is because of its

capability to represent the change in temperature effect on the capacity of the battery. This model is also able to show the effect of a changing discharge rate in the capacity of the battery which can accurately show the consequence on the capacity of using solar panels or wind turbines as a renewable energy source.

The following recommendations are made based on the conclusions made.

- Lab Experiments Must Be Done To Improve Accuracy and Reliability

For complex models such as dynamic and third-order models; many assumptions were made which adversely affect their ability to present accurate results. It is recommended that for future research, experiments in the lab must be prepared using a renewable energy system for charging and using some form of load to investigate the performance of batteries in more depth.

- Future Work Recommendations

Many battery models are proposed for lead-acid batteries. This is because over the years lead-acid batteries have been well known for their low cost and hence were the most implemented for bulk energy storage. Improved types of batteries have been developed recently offering much more reliable and efficient performance. However because most models are proposed for lead-acid batteries; engineers and designers are unable to predict the response of new developed batteries when integrated with renewable energy systems.

It is recommended therefore that other battery types must be investigated and models must be developed based on them.

ACKNOWLEDGEMENTS

The authors gratefully acknowledge the research infrastructure and support provided by Electrical Engineering Department, University of Cape Town required for carrying out this research.

REFERENCES

- [1] M. Beaudin, H. Zareipour, A. Schellenberglobe and W. Rosehart, "Energy storage for mitigating the variability of renewable electricity sources: An updated review", *Energy for Sustainable Development*, Vol. 14, No. 4, pp. 302-314, 2010.
- [2] H.Lund and B.V. Mathiesen, "Energy system analysis of 100% renewable energy systems—The case of Denmark in years 2030 and 2050", *Energy*, Vol. 34, No. 5, pp. 524-531, 2009.
- [3] O. Adria: *Policy Recommendations for Energy Storage in Grids with a High Proportion of Renewable Energy*, PESS, pp. 1-3, 2010.
- [4] H. Ibrahim, A. Ilinca and J. Perron, "Energy storage systems—Characteristics and comparisons", *Renewable and Sustainable Energy Reviews*, Vol. 12, No. 5, pp. 1221-1250, 2008
- [5] Nipron, "Battery for NSP", *Power supply encyclopedia*, http://www.nipron.com/product_info/encyclopedia/5_3.htm, 2009.
- [6] I. Buchmann, *The cost of battery power*, <http://www.buchmann.ca/article20-page2.asp> (Accessed on the 28th of July 2013 at 14:03)
- [7] International Renewable Energy Agency (IRENA), *Electricity Storage and Renewables for Island Power: A Guide for Decision Makers*, 2012.
- [8] P.F. Ribeiro, B.K. Johnson, M.L. Crow, A. Arsoy, and Y. Liu, "Energy storage systems for advanced power applications", *Proceedings of the IEEE*, Vol. 89, No. 12, pp. 1744 – 1756, 2001.
- [9] K.C. Divya, J. Østergaard, "Battery energy storage technology for power systems: An overview", *Electric Power Systems Research*, Vol. 79, No. 4, pp. 511-520, 2009
- [10] S. Kai and S. Qifang, "Overview of the Types of Battery Models", *30th Chinese Control Conference*, Yantai, pp.3644-3648, 2011
- [11] D. Linden and T.B. Reddy, *3rd ed. Handbook of Batteries*, McGraw-Hill, 2001.
- [12] H.W. Beaty, *3rd ed. Handbook of Electric Power Calculations*, McGraw-Hill, 2001.
- [13] T.D. Jacobs and L.C. Saayman, "Sizing of DC systems for substation", ESKOM South Africa, 2009.
- [14] C.Van Zyl, M. Boltman, P. Van der Smit and T. Jacobs, "Advanced battery maintenance course", ESKOM South Africa, 2009.
- [15] S. Li and B. Ke, "Study of Battery Modelling using Mathematical and Circuit Oriented Approaches", *IEEE Power and Energy Society General Meeting*, pp.1-8, 2011.
- [16] M. Ceraolo, "New Dynamical Models of Lead-Acid Batteries", *IEEE Transactions On Power Systems*, Vol. 15, No. 4, pp. 1184 – 1190, 2000.

THE IMPACT OF DEMAND SIDE MANAGEMENT ON UTILITIES: ESKOM

M. Tabiri* and K. Awodele**

University of Cape Town, Department of Electrical Engineering, Rondebosch, Cape Town, South Africa. E-mail: *brmaa001@myuct.ac.za **kehinde.awodele@uct.ac.za

Abstract: Demand side management (DSM) is used by Eskom to achieve electrical energy demand reduction. The goals set by Eskom and the Department of Minerals and Energy for demand reduction are 12 % reduction by the end of the 2015 financial year and an accumulated savings of 3 422 MW by the end of 2017. Multi-criteria decision making can be used to select the best combination of DSM programs to achieve these goals. The analytic hierarchy process (AHP) was used to generate the combinations of DSM programs in each sector (residential, commercial and industrial) and determine the amount of savings required by each program in order to reach the goals. In the light of supply side issues such as the delay of Medupi power station, it is shown how DSM can be used to compensate for the unrealized expected capacity using the selected DSM programs.

Keywords: Analytic hierarchy process, demand side management, energy efficiency, load management

1. INTRODUCTION

The energy crisis is the centre of attention in South Africa today. Capacity that was once in over-supply is now depleted and supplying the current demand with the available capacity on the grid has become a difficult task. South Africa is a very energy-intensive country with a large, national power demand and a very high peak demand. Demand side management is a means of reducing the overall and peak demand and modifying the energy demand and usage of customers, with least costs, through energy-efficiency and load management programs that are implemented on the customer side of the meter [1]. Eskom has identified demand-side management (DSM) as a way of alleviating the crisis by lowering the national demand through focused demand-side management programs and projects. Demand-side management strategies can also be used to address environmental, social and economic concerns in addition to the energy crisis. There is a wide range of DSM programs available but their specifications in terms of factors such as cost and demand reduction potential vary. Multi-criteria decision making is a decision making process that allows the decision maker to assess programs based on a wide range of criteria to ensure that the selected set of programs is the optimal combination of programs with regard to all considered factors which will best serve the goals set.

For this study, the Analytic Hierarchy Method will be used to select the best demand side management programs to achieve Eskom and the Department of Minerals and Energy's goals.

2. ESKOM DSM PROGRAMS, GOALS AND RESULTS

Eskom's DSM programs focus on improving the efficiency of old equipment or replacing inefficient

equipment, installing energy saving technologies, improving the efficiency of electrical systems and instilling energy-consciousness in all customers. Eskom DSM has 9 main programs in which DSM activities are carried out. These are:

- Agriculture
- Compressed air
- Demand response
- Heat pumps
- Industrial process optimization
- HVAC
- Shower heads
- Solar water heaters (SWHs)
- Lighting

The Energy Efficiency Strategy drafted by the Department of Minerals and Energy has set a goal for a final energy demand reduction of 12 % by May 2014. This target was calculated by setting individual targets for each sector and weighting this target against the contribution of the specific sector to the total national energy demand as described by figure 1. This goal is to be implemented in each sector by the following targets:

- Residential Sector – 10% demand reduction by May 2014
- Commercial Sector – 15% demand reduction by May 2014
- Industrial Sector – 15% demand reduction by May 2014

This overall national target is based on a base case demand forecast on the assumption of a growth rate of 2.8 % per annum [3] as graphically shown in figure 2. The savings goal, 12 % reduction, is of the projected energy demand for 2014 which is 41 471 MW following the CSIR Mod model [4].

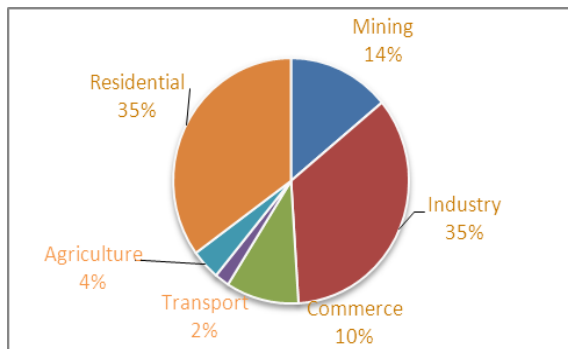


Figure 1: Energy demand for each sector [3]

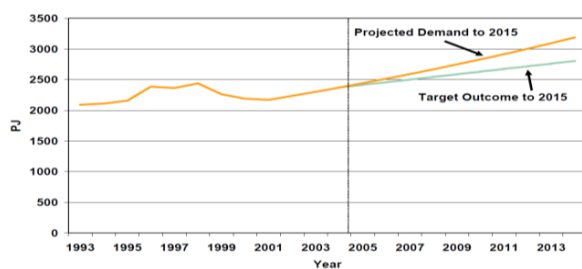


Figure 2: Projected energy demand in 2015 [1]

The IRP has also projected that by 2017 DSM should be contributing 3420 MW. In addition to demand reductions and energy savings goals, there are also social, economic and environmental goals that can be addressed through demand side management. These goals are described as follows:

- Improve the health of the nation by reducing atmospheric pollution causing respiratory-related diseases
- Increased job creation through the reduction of costs created by increased efficiency in commercial and industrial sectors and employment created in energy efficiency procurement and implementation activities
- Energy poverty alleviation by promoting low energy alternatives resulting in lower energy costs for households
- Reduce CO₂ emissions by improving energy efficiency in all sectors
- Improve industrial competitiveness and increasing profitability through the reduction of overhead energy costs

Currently the verified accumulated savings produced from DSM initiatives against Eskom's goals over the years are shown in figure 3. The accumulated savings up to 2013 is 3 586 MW and the projected energy demand for 2014 is 41 471 MW so the current percentage of savings achieved thus far is 8.65 %. In order to meet demand reduction goal a further 1 390 MW of reduction is needed over the next two financial years (ending March 2015). Eskom is looking to achieve total accumulated

demand savings of 3420 MW by 2017 through demand side management [4].

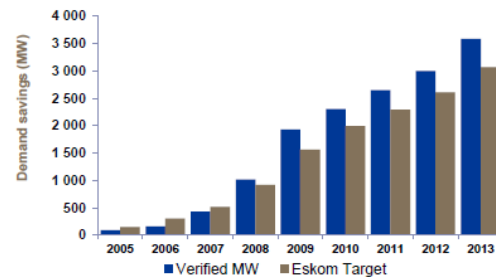


Figure 3: Verified accumulated demand savings over the years [6]

The evening peak demand and energy savings achieved over the last financial year are shown in table 1. This indicates that DSM initiatives are being implemented successfully and has the potential to achieve a lot more savings than expected.

Table 1: Total peak demand savings achieved [6, 7]

	Target 2012/13	Actual 2012/13	Actual 2011/12
Evening peak demand savings (MW)	459	595	365.4

3. THE ANALYTIC HIERARCHY PROCESS

The analytic hierarchy process is used to generate rankings of each of the alternatives based on a set of criteria. This process uses pair-wise comparisons of each of the alternatives with regard to each criterion. Alternatives are evaluated on a 1-9 scale which describes the relationship between the two programs being assessed with 1 being equal and 9 meaning one is very strongly better than the other. This will be done for all programs being assessed in each sector separately.

The criteria will first be evaluated against each other to generate the weightings of each criterion for the overall assessment of the alternatives. The alternatives will then be evaluated in pair-wise evaluations to determine to what extent one alternative is better than the other for each criterion.

The scores are then processed and rankings of the alternatives will be generated for each criterion and finally the overall ranking of the alternatives based on all of the criteria and their relative weightings will be generated. This will be done for the residential, commercial and industrial sector separately. The criteria being used to assess the programs are as follows:

1. Energy savings/peak demand reduction

In the case of energy efficiency interventions, the potential energy savings of the technology will be used to score this criterion. In the case of a load management intervention, the amount of the total peak demand that can be shifted to off-peak hours will be used to score this criterion.

2. Cost of implementation

This criterion is further broken down into cost to customer and cost to Eskom. Cost will be based either on the market price of the technology or the typical payback period for the intervention.

3. Financial benefits

Currently, DSM interventions are voluntary; consumers are not obliged to participate. In order to incentivize consumers into participating, the financial benefits they stand to gain through the DSM programmes must be evaluated.

4. Environmental impact

This criterion is further broken down in to CO₂ emission reduction and water conserved.

5. Job creation

This is a social criterion that must also be fulfilled as part of the larger context in which all activities exist. Job creation is one of the main social goals that the Department of Energy hopes to address through DSM interventions.

6. Useful lifetime

This criterion is a measure of either the life-span of an energy efficiency technology or the useful duration of a load management intervention.

The criteria were evaluated on the same 1-9 scale against each other to generate weightings to reflect their relative importance. The weightings for each sector are shown in tables 2, 3 and 4.

Table 2: Residential sector criteria weightings

Criterion	Weighting (%)
Cost	21.47
Ease of implementation	3.77
Energy savings/demand reduction	34.05
Environmental impact	8.09
Financial benefits to customer	19.51
Job creation	7.89
Useful life time	4.95

Table 3: Commercial sector criteria weightings

Criterion	Weighting (%)
Energy savings/Peak demand reduction	33.28
Cost	24.76
Financial benefit to customer	16.92
Environmental impact	8.65
Job creation	6.97
Useful lifetime	5.72
Ease of implementation	3.70

Table 4: Industrial sector criteria weightings

Criterion	Weighting (%)
Energy savings/Peak demand reduction	41.09
Cost	21.92
Financial benefit to customer	13.93
Environmental impact	6.32
Job creation	7.61
Useful lifetime	5.32
Ease of implementation	3.81

The programs to be assessed in each sector are as follows:

The Residential Sector

- Solar water heaters (SWHs) – R1
- Intelligent residential demand response – R2
- Customer awareness – R3
- Compact fluorescent lamp (CFLs) – R\$
- Aerated shower heads – R5
- TOU tariffs (Homeflex) – R6

The Commercial Sector

- Building management systems (BMS) – C1
- Heat pumps – C2
- Electronic control gears – C3
- HVAC – C4
- Variable speed drives (VSDs) – C5
- Compact fluorescent lamps (CFLs) – C6

The Industrial Sector

- Compressed air – I1
- Process optimization – I2
- Variable Speed Drives (VSDs) – I3
- Demand response – I4
- Energy efficient lighting (EE lighting) – I5
- Energy efficient motors (EE Motors) – I6

All weightings and evaluations are not exact but rather based on literature and expert opinion of professionals in

the engineering field. Alternatives are evaluated and scored relative to each other to ensure that the rankings are reflective of the strength of an alternative over another.

4. RESULTS

The results from the AHP assessment for the programs in each sector generated scores showing the performance of each alternative assessed. These scores were used to generate rankings in each of the sectors as described below:

4.1 The Residential Sector

The scoring and rankings generated from the AHP are shown in table 5.

Table 5: Residential sector program scores and ranking

Program	Score (total =100)	Rank
TOU tariffs	23.67	1
Intelligent residential demand response	22.75	2
Customer awareness	17.03	3
CFLs	15.66	4
SHWs	10.54	5
Aerated shower heads	10.35	6

4.2 The Commercial Sector

The scoring and ranking generated from the AHP is shown in table 6.

Table 6: Commercial sector scoring and ranking

Program	Score (total = 100)	Rank
Building management systems	27.7	1
CFLs	26.83	2
Variable speed drives	19.86	3
HVAC	11.56	4
ECGs	9.48	5
Heat pumps	4.57	6

4.3 The Industrial Sector

The scoring and ranking generated from the AHP is shown in table 7.

Table 7: Industrial sector scoring and ranking

Program	Score (total =100)	Rank
Demand response	30.43	1
EE motors	20.13	2
VSDs	15.59	3
Compressed air	13.00	4
EE lighting	12.69	5
Process optimization	8.15	6

5. CALCULATIONS AND ANALYSIS

The analytic hierarchy method results shows to what extent each program should contribute to the overall reduction goal. The scores of the programs all add up to 100, representing achieving the goal. The program with the highest score is the program that should have the greatest contribution towards achieving the goal in the sector and the program with the least should contribute the least. These scores will be used to determine the appropriate strategy to implement in the sector.

As mentioned previously, the total amount of savings needed to reach Eskom's goal is 1390 MW over 2 financial years. This must be distributed between the three sectors. Distribution of the savings will be done based on the demand of each sector which is shown below:

- Residential – 35%
- Commercial – 10%
- Industrial – 51%
- Other – 4%

Since this study focuses only on the residential, commercial and industrial sector, these demand figures will be scaled to a base of 96. This is done by this simple calculation:

$$\begin{aligned} \text{Residential} & \quad \frac{35}{96} \times 100 = 36.46\% \\ \text{Commercial} & \quad \frac{10}{96} \times 100 = 10.42\% \\ \text{Industrial} & \quad \frac{51}{96} \times 100 = 53.12\% \end{aligned}$$

So using these contributions, the distribution of the total demand savings is calculated as follows:

$$\begin{aligned} \text{Residential} & \quad \frac{36.46}{100} \times 1390 = 506.80 \text{ MW} \\ \text{Commercial} & \quad \frac{10.42}{100} \times 1390 = 144.80 \text{ MW} \\ \text{Industrial} & \quad \frac{53.12}{100} \times 1390 = 738.37 \text{ MW} \end{aligned}$$

The results from the AHP can be used in many ways to determine the combination of programs to be used and the demand reduction required of the programs. If all programs are used then the demand reduction required from each program can be calculated in proportion to the AHP scores. If the top 3 programs in each sector are selected then the demand reduction required by each program is as follows:

Residential Sector

- TOU tariffs **189.04 MW**
- Intelligent demand response **181.74 MW**
- Customer awareness **136.01 MW**

Commercial Sector

- Building management systems **53.91 MW**
- Variable speed drives **52.23 MW**

- CFLs **38.66 MW**

Industrial Sector

- Demand response **339.65 MW**
- Energy efficient motors **224.69 MW**
- CFLs **174.03 MW**

The AHP scores can also be used to determine the best combination of programs to achieve the overall demand reduction goal regardless of what sector the DSM programs were implemented in. This was done in Matlab which yielded the following best 4 combination of 9 programs as done in Eskom:

Table 8: Top 4 combinations of programs in any sector

Combination	Rank
R2, R3, R4, R6, I1, I3, I4, I5, I6	1
R2, R3, R6, I1, I2, I3, I4, I5, I6	2
R1, R2, R3, R6, I1, I3, IR, I5, I6	3
R1, R2, R3, R6, C1, C2, C6, I3, I5	4

According to the IRP it can be seen that the accumulated savings goal by 2017 is 3 420 MW after which no further savings are expected until 2030. The IRP was drafted in 2010 when it was believed that the new build program for Medupi was on track and all of the unplanned maintenance and damage was unforeseen. In light of those events DSM had to generate greater savings than planned to help keep the lights on and as a result it has already reached the accumulated savings goal as the accumulated savings till March 2013 is already 3 582 MW. The supply system is still currently under a lot of strain so it is not satisfactory to stop now that the originally intended target has been surpassed. Demand reduction through DSM must continue. The savings that can be expected over the next 5 years can be modelled as a function of the historical performance of DSM. This will give a trend that can be used to project into the future. The trend was calculated using Microsoft Excel. According to this trend the approximate demand savings that can be expected till 2017 are as follows in table 9:

Table 9: Projected accumulated savings over the next 5 years.

Year	Projected Accumulated Demand Savings (MW)
2014	3921.8
2015	4339.5
2016	4757.2
2017	5174.9
2018	5592.6

6. CONCLUSION

From the study conducted it can be seen that multi-criteria decision making is a very useful tool to evaluate programs against criteria to yield the best suite of programs to implement. It allows for a wide range of criteria to be assessed as it caters for technical, numeric criteria as well as non-technical criteria. In a country that is plagued by social concerns that can potentially be addressed by DSM, this is of particular use. The selection of weightings has a large influence on the results yet, it is a relatively subjective process in MCDM based on the concept of one criterion being more important than another by some factor. The difficulty in this is discerning the measure of importance and by whose judgment this lies as different evaluators may come to different conclusions about the importance of each criterion and its relative weighting.

7. RECOMMENDATIONS

The AHP is a very useful for determining how a set of programs can be used to achieve a goal, however, the result attained is specific to that goal and manipulating the results to make them applicable to greater goals as well leads to inaccuracies. A better method of determining which sectors have the most potential and should be focused on can be used instead of simply considering the demand of each sector. Perhaps a range of criteria could have again been used to determine this. In order for MCDM methods to be implemented in DSM effectively, all necessary criteria must be taken into consideration and the weightings assigned to these criteria need to be done in a way that it represents both the needs of Eskom and the needs of the country. There should be a group of evaluators, all with relevant expertise to ensure that there is minimal bias. Or a mathematical model based in fuzzy logic should be used to generate weighting. The DSM targets set in the IRP and by Eskom must be revised as the circumstances in South Africa have changed since they were set.

8. ACKNOWLEDGEMENTS

The authors are grateful to the authority of Electrical Engineering Department, University of Cape Town, South Africa for providing the infrastructure necessary for carrying out this research, and to ESKOM, through the Tertiary Education Support Programme (TESP) for financial support.

9. REFERENCES

- [1] H. Song, "Effective Electrical Energy Policies in terms of DSM," Korea Electric Power Corporation, Seoul, 2012.

- [2] J. D. Kendrick and D. Saaty, "Use Analytic Hierarchy Process," 2007.
- [3] Department of Minerals and Energy, "Draft Energy Efficiency Strategy of the Republic of South Africa," Department of Minerals and Energy, Pretoria, 2004.
- [4] Department of Energy, "INTEGRATED RESOURCE PLAN FOR 2010-2030," Department of Energy, Pretoria, 2011.
- [5] Eskom, "Integrated Demand Management," Cape Town, 2012.
- [6] Eskom, "Integrated Results Presentation," 31 March 2013. [Online]. Available: http://eskom.ensight-cdn.com/content/Results_presentation31March2013f.pdf. [Accessed 23 September 2013].
- [7] Eskom, "Energy efficiency and demand side management," 2012. [Online]. Available: http://financialresults.co.za/2012/eskom_ar2012/fact-sheets/007.php. [Accessed 22 July 2013].

ENERGY SAVINGS IN HIGHER EDUCATION INSTITUTIONS: SOLAR WATER HEATER IMPACT ANALYSIS

O.M. Popoola* and C. Burnier**

* Centre for Energy and Electric Power Electrical Engineering department, Tshwane University of Technology, Pretoria 0001, South Africa Email: walepopos@gmail.com **CORRESPONDING**

** ESIEE, Amiens, France and French South Africa technical Institute of Electronics Tshwane University of Technology, Pretoria 0001, South Africa

Abstract: The study focused on the impact of Solar Water Heater (SWH) at a higher institution of learning. Method of investigation includes energy audit and development of energy simulation model technique (correlation of consumption with weather; financial / economic analysis and environmental variables) to determine energy consumption or possible savings. The developed model technique analysis showed a high potential of energy and financial savings for higher education institutions especially those with residences using SWH renewable measure.

Keywords: Energy, Solar water heater, environmental variables, simulation model technique

1. INTRODUCTION

Countries are facing challenges with the increasing demand for electricity. This is also proportional to redundant gas emissions because we burn fossil fuels to create energy. The effect of all this extra carbon dioxide in the atmosphere is that the overall temperature of the planet is increasing (global warming). Whilst the average global temperature is increasing, on a day to day level the climate is changing in unpredictable ways (from floods and hurricanes to heat waves and drought). To try and reduce the risk of ever more extreme weather, we need to reduce the amount of fossil fuel we are burning and implement energy saving initiatives in the built environment and other facilities. High economic growth as well as a rapid expansion in the electric power consumer base has been experienced by South Africa. As a result, the demand for electricity has escalated but has not been matched by corresponding investment in generation [1]. Investment in renewable energy and energy efficiency is important so as to reduce the negative economic, social and environmental impacts of energy production and consumption in South Africa. Currently, renewable energy contributes relatively little to primary energy and even less to the consumption of commercial energy [2]. There are various sources of renewable energy e.g. from biomass, wind, solar and small-scale hydro, however in this part of the world solar is relatively available. The Southern African region, and in fact the whole of Africa, has sunshine all year round. The annual 24-hour global solar radiation average is about 220 W/m^2 for South Africa. Most areas in South Africa average more than 2500 hours of sunshine per year, and average solar-radiation levels range between 4.5 and 6.5 kWh/m^2 in one day. Solar energy, like all other renewable energies, is very safe and environmentally friendly. There are no emissions; the source of fuel is the

sun, unlike coal-powered stations [3]. There are various technologies hinged on solar usage, such as solar-photovoltaic, solar water heaters and etc.

Water-heating accounts for a third to half of the energy consumption in the average household. In South Africa, water heating is derived mainly from electricity, being the most common energy-carrier employed. The equivalent of a large coal-fired power station ($2000 \text{ MW}+$) is used to

provide hot water on tap to the domestic sector alone. Since the inception of the accelerated domestic electrification programme through grid extension in South Africa, a major distortion of the national load curve has emerged, with the early evening load peak growing significantly. Modelling indicates that the introduction of solar water-heating can ameliorate the situation substantially. Switching from electrical to solar water-heating can, therefore, have significant economic and environmental benefits [4].

The country's utility and policy makers have proposed domestic solar water heating as one of the most viable complementary solutions to the country's energy and environmental crises [1]. Economic benefits include reduction of energy bills, reduction on peak load at power utility, greenhouse gas (GHG) emissions and release of scarce capital to other pressing needs.

However, there are issues negating the use of SHW, such as high up-front-capital cost of the system and limited funding currently available; savings impact analysis; good economic and financial investigations in terms of investment- payback period. There are various schemes proposed by the government which are aimed at creating an expanded opportunity for attracting the much-needed sustainable financial stimulus into the DSM programme.

SWH is amongst the allowable technologies [3]. Commercial buildings and residential home owners' have not shown much interest due to the negating issues raised earlier. In order to assist and give a good perspective of SWH contribution there is the need to investigate both the savings impact and cost in respect of the high upfront capital involved in the implementation of SHW.

2. PROBLEM DESCRIPTION

Pollution levels and the energy prices are increasing on a daily basis. Furthermore, most of the energy sources in use actually would not last forever. Consequently, there is the need to find ways to reduce our energy consumption without cutting down on our standard of living. Also, the usage of renewable energy sources and its integration to the existing electrical sources in higher institution needs to be explored.

This study aims at evaluating the impact of SWH usage at an institution of higher learning, which will inevitably reduce its energy (electricity) consumption.

3. METHOD OF INVESTIGATION

Investigation methodology process includes audit of the hot water usage within the campus, analysis of bills, metering, and development of a simulation model technique for the analysis/evaluation of the energy impact and solar system design. To achieve the aim of the investigation, the following were applied:

3.1 Solar Water Heating Solution

For the model development, Matlab software application was used. The developed technique is expected to give an ample view of investment and payback period, energy and cost saving effects and etc. With this evaluation the usage of SWH may or not be justifiable. The synoptic schema of the working steps of the software using Matlab is shown in Fig: 1.

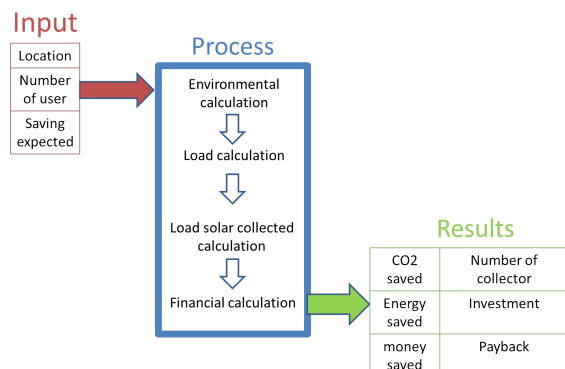


Fig. 1: SWH software process

The software analysis was undertaken in steps. Firstly, consideration of the environmental variables (latitude, declination, solar radiation, slope of the collectors, cold-water temperature and etc). Secondly, the expected water

heating load (KWh per year). Thirdly, calculation of the energy saved as result of the use of the collectors (taking into account the fraction of saving the user needs). Makes a synthesis about the financial part and gives the anticipated energy savings, the monetary savings, the initial investment, the number of collector needed and the payback period.

For the investigation, several inputs are needed. However for this simulation model or software application analysis, the following were taking into consideration: collector and tank model, electricity price, the outside temperature and days of the year. To achieve the outputs as shown in Fig 1, the following calculations were undertaken:

3.2 Environmental variables

The following variables were considered in the environment analysis portion of the SWH simulation model technique development and evaluation impact. This includes:

Cold water temperature: To determine the cold-water temperature, the equation below was used

$$T_{coldw} = \frac{T_{min}-T_{max}}{2} - \frac{T_{max}-T_{min}}{2} * h * \cos \left(2\pi * \frac{N-2}{12} \right) \quad (1)$$

Tmin and Tmax are the value of maximal and minimal cold water (corresponding to the soil temperature from 2m deep), in Pretoria these values are around 19.7 and 15.7 Celsius degrees; h indicate the location of the project, if it is in south or north hemisphere (1 if north or -1 if south hemisphere); N is the number of the month (between 1 and 12). From the formula it is possible to have average value of cold water for each month of the year. Fig 2 shows the estimates cold-water temperatures for Pretoria according with respect to number of days.

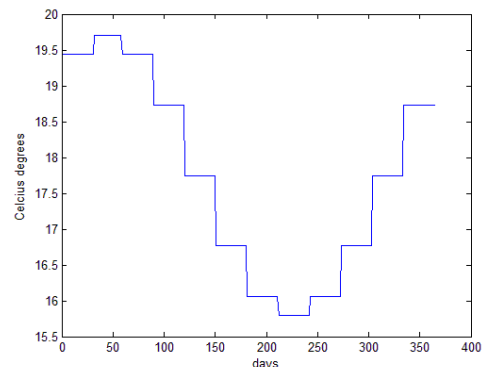


Fig. 2. Pretoria Cold water temperature for the year

Sky irradiance: The sky irradiance variable is an essential parameter used for calculating the energy collected by the solar panels. In order to calculate the sky irradiance, value basic concept of energy engineering was applied as shown by the evaluation below:

- **Declination:** Declination is the angular position of the sun at solar noon (corresponds to the moment when the sun is at its highest point in the sky).

$$\text{declination} = 23.45 * \sin\left(2 * \pi * \frac{284+n}{365}\right) \quad (2)$$

The declination for each day of the year (n is the day number) was analyzed using the developed Matlab simulation technique; result obtained as shown in Fig. 3 is from 23.45 at June 21st to -23.45 as at December 21st

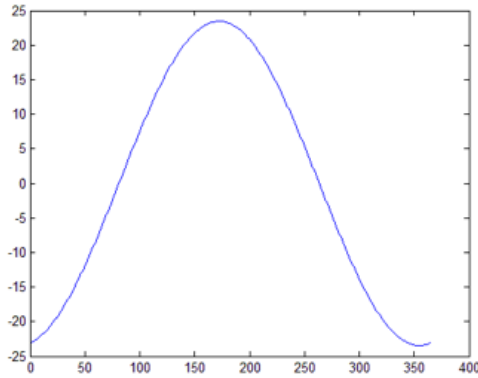


Fig. 3. Declination according to the day of the year

- **Sunset hour angle:** The sunset hour angle 'ws' is the solar hour angle corresponding to the time when the sun goes down. It is given by the following equation:

$$\cos(ws) = -\tan(\psi) * \tan(\sigma) \quad (3)$$

Takes 15 degrees per hours (positive in afternoon and negative in the morning) corresponds to 360 degrees per day. Fig.4 shows the sun set hour for Pretoria (latitude=25.732 S) according to days. For example on the 14th July the sunset is at 17h16 (note: this value is an average considering the sun at noon (12h00)).

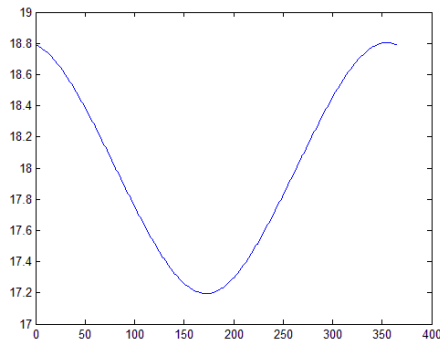


Fig. 4. Sunset hour for Pretoria

Extraterrestrial radiation: The extraterrestrial radiation is the solar radiation before it reaches the atmospheric land layer. The extraterrestrial radiation in a horizontal plane 'H0' can be evaluated for days of the year with the

following equation:

$$H_0 = \frac{24 * G_{sc}}{\pi} * \left(1 + 0.033 * \cos\left(2\pi * \frac{n}{365}\right)\right) * (\cos(\psi) * \cos(\sigma) * \sin(ws) + ws * \sin(\psi) * \sin(\sigma)) \quad (4)$$

Where ψ is the latitude, σ the declination, ws the sunset hour angle, and n the number of the day. G_{sc} correspond to the solar constant i.e. 1367 W/m². The value of H0 in this equation is dimensioned in Wh/m².

Solar radiation for an inclined plane: The solar radiation for an inclined plane has to be known so as to be able to evaluate the load of the solar panels and the amount of solar energy that can be accumulated. The formula of the solar radiation in an inclined plane is given by the equation below:

$$H_t = H \left(1 - \frac{H_d}{H}\right) * R_b + H_d * \frac{1 + \cos(\beta)}{2} + H * \rho * \frac{1 - \cos(\beta)}{2} \quad (5)$$

ρ = ground reflectivity expected to be equal to 0.2 if the yearly temperature is higher than 0 °C; and 0.7 if the temperature is lower than -5 °C. In this case the value for Pretoria is 0.2 as a result of the average yearly temperature being equal to 20 °C. H_b is the product of monthly average beam radiation: $H_b = H - H_d$; R_b is a geometric factor depending on the slope of the collector (β), the latitude (ψ), the declination (σ) and days:

$$R_b = \frac{\cos(\psi + \beta) \cos(\sigma) \cos(ws) + \sin(\psi + \beta) \sin(\sigma)}{\cos(\psi) \cos(\sigma) \cos(ws) + \sin(\psi) \sin(\sigma)} \quad (6)$$

The formula above is used for the southern hemisphere. As for the northern hemisphere, the sign before β in the cosine and sine function needs to be changed. ws is the sunset hour angle which is dependent on ψ and σ previous. H_d is the monthly average daily diffuse radiation calculated in two different cases using the global irradiation (H) and the clearness index (Kt).

If $ws < 81.4$ degrees:

$$H_d = \frac{1.3991 - 3.560 * Kt + 4.189 * Kt^2 - 2.137 * Kt^3}{H}$$

If $ws > 81.4$ degrees:

$$H_d = \frac{1.311 - 3.022 * Kt + 3.427 * Kt^2 - 1.821 * Kt^3}{H} \quad (7)$$

And β is the slope of panels. The slope of the surface will be fixed for each day and will be:

$$\beta = |\text{latitude} - \text{declination}| \quad (8)$$

Two cases were considered using the software, this include the collector as a tracking collector which can be programmed to the value above; or consider as a fixed collector using the mean value of 'beta'. For Pretoria TUT campus, test fixed collector was considered because tracking collector are rarely in use nowadays apart from the difficulty in estimating the initials.

Sky radiation: The value of the sky irradiance is needed to quantify radiative transfer exchanges between a body (solar collector) and the sky. The actual sky radiation

falls somewhere in-between the clear and the cloudy values. If c is the fraction of the sky covered by clouds, sky radiation may be approximated by:

$$L_{sky} = (1 - c)L_{clear} + c * L_{cloudy} \quad (9)$$

Where clear sky long-wave radiation (in the absence of clouds) is:

$$L_{clear} = 5.31 * 10^{-13} (T_a + 273.2)^6 \quad (10)$$

T_a is the ambient temperature in °C. For cloudy skies, the average temperature is assume to be $T_a - 5^\circ\text{C}$ and emit long wave radiation with an emittance of 0.96, that is, the irradiance of a sky cloudy is computed as:

$$L_{cloudy} = 0.96 * \sigma (T_a + 273.2 - 5)^4 \quad (11)$$

Where σ is the Stefan-Boltzmann constant assumed to be equal to $5.669 \times 10^{-8} \text{ (W/m}^2\text{)/K}^4$.

To find an approximate monthly value of ' c ' the formula below may be applied:

$$c = \frac{K_d - 0.165}{0.835}$$

K_d is calculated by using the average clearness index (' K_t ') and the Collares-Pereira and Rabl correlation:

$$K_d = \begin{cases} 1.188 - 2.272K_t + 9.473K_t^2 - 21.865K_t^3 + 14.648K_t^4 & \text{for } K_t \leq 0.17 \\ -0.54K_t + 0.632 & \text{for } 0.17 < K_t < 0.75 \\ 0.2 & \text{for } 0.75 \leq K_t < 0.80 \\ 0.2 & \text{for } K_t \geq 0.80 \end{cases} \quad (12)$$

3.3 Load collected

The energy collected per unit collector area per year is described by equation 13:

$$Q_{coll} = Fr(\tau_a)(1 - f_{dirt}) \left(G + \left(\frac{\epsilon}{\alpha} \right) * L \right) - Fr_{UL} * \Delta T \quad (13)$$

Where $Fr(\tau_a)$ and Fr_{UL} are collector characteristics explain below, G is the global incident solar radiation of the collector (taking the yearly average irradiation in an optimally inclined plane from Joint Research Centre – European Commission website, the ratio ϵ / α is set to 0.96 (ϵ is the long wave emissivity of the absorber), ΔT is the temperature differential between the working fluid entering the collectors and outside ambient temperature that is $T_s - T_a$. L is the relative long wave sky irradiance. It is defined by equation 14 as:

$$L = L_{sky} - \sigma (T_a + 273.2)^4 \quad (14)$$

Where L_{sky} is the long wave sky irradiance previously calculated and T_a the ambient temperature expressed in °C.

This model includes also the losses due to snow, dirt and piping. The dirt value is the losses due to snow; dirt can affect the irradiance level experienced by the collector. Therefore, $Fr(\tau_a)$ is multiplied by $(1 - f_{dirt})$, typical values range from zero to a few percent. In project location study (Pretoria, South Africa) it rarely snows, hence the value depends only on the dirt. This value is around 5%.

Hot water is stored in tanks and run through imperfectly insulated pipes giving rise to heat being lost to the environment. The load-collected value is affected by these losses as shown in equation 15:

$$Q_{coll}' = Q_{coll}(1 - f_{loss}) \quad (15)$$

The value f_{loss} is the losses in the pipes and the tank (if needed). This value varies between 1 to 12 %; difficult to estimate due to its dependency on several factors such as length of the pipes and water usage in the tank.

Collector panels: Three types of solar collector are considered in equation; these are glazed collectors, evacuated collectors and unglazed collector. The needed changes in the applicable equation are the collectors characteristics, namely Fr_{UL} and $Fr(\tau_a)$. There are generic values for these characteristics if not provided by the manufacturers.

Water pump load: To direct the heated water in the collector to the water tank or the existing water heating process, one or more water pumps is needed. The energy value of the water pump is based on this formula:

$$Q_{pump} = N_{coll} * P_{pump} * S \quad (16)$$

Where Q_{pump} is the energy needed to pump the water in a year. P_{pump} is the power by surface unity of the collector (this value is generally between 8 and 22 W/m²). S is the area taken by the collectors in m². And N_{coll} the number of working hours the solar collector is used. The value of N_{coll} can be approximated as

$$N_{coll} = \frac{Q_{coll}(1 - f_{loss})}{S * Fr(\tau_a) * H_t} * N_{clearness} \quad (17)$$

$N_{clearness}$ is the factor of the clearness index (computed in "Extraterrestrial radiation" part) number of hours in the days.

3.4 Load calculation

Load calculation is necessary for determining the water heating energy consumption without the solar system i.e baseline(reference point). This is used for evaluating how much energy and funds (money) will be saved.

From the sampling survey conducted in terms of human behavior and usage within the campus hostel, findings showed that consumption of hot water during a day is around 75 Liters per individual. The total hot water consumption is therefore the number of people in a building multiplied by the consumption [5].

At the university (TUT) most of the hot water consumption is at the hostels, hence the number of people is assumed to be the number of beds in each hostel. The energy required can be express as [6]

$$Q_{load} = C_p * \rho * V_l (T_h - T_s) \quad (18)$$

Where C_p is the heat capacitance of water (4,200 J/kg/ °C); ρ its density (1 kg/L); and T_s is the cold water temperature afterwards; Q_{load} is calculated for a year

period; “Th” is the hot water temperature in the tanks in most of case the average value is 60 °C.

Yearly load took into consideration the type of buildings as well as the purpose and activities in such buildings. For instance investigations at the hostels showed that the buildings were fully occupied during the week. However, as a result of the rest periods and holiday of between 2-3 months, the yearly average occupation per year is ~ 75 %.

3.5 Financial Evaluation

Using the various calculations highlighted above, the energy and cost savings will be substantiated as shown by the graph in terms of payback period and profitability. The energy saved is attributed to the use of solar water heating system/process. The money saved in relation to years is shown in Fig. 5.

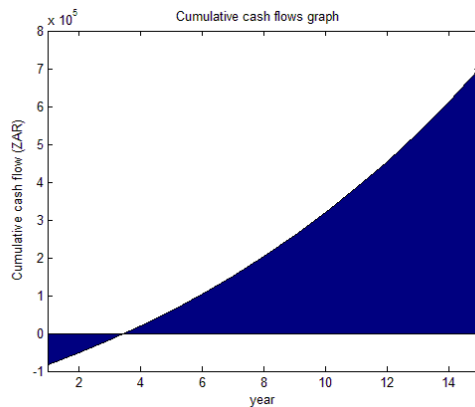


Fig. 5: Cumulative cash flow for Solar Water Heater

Fig. 5 is the result of the eco formula below using inputs such as the initial investment, the inflation and the electricity price.

$$eco = \frac{P_e}{(1 - inflation)^{year}} * Q_{coll} * year - P_{init} - maintenance \quad (19)$$

P_e is the electricity price given by the “energy saving software”; Q_{coll} is the energy calculated earlier; P_{init} is the initial price which corresponds to the price of collectors and the tank (if needed). Solar collector lifetime is around 25-30 years; however for the software analysis the value of 20 years was used. This is to take care of the possible maintenance cost according to the piping or the tanks. The maintenance is estimated by the initial price of the items divided by the lifetime per year (in a lower value), however the value of the initial price is based on this formulas:

$$Price_{init} = \begin{cases} price_{collector} * Nb_{collector} + tank_{nb} * Price_{tank} & \text{if } 0 < saving \leq 15\% \\ price_{collector} * nb_{collector} & \text{if } 15\% < saving < 70\% \end{cases} \quad (20)$$

The price of the water pump is included in the price of the solar collector. Only the power consumption of the water pump is considered in the financial part. That is the cost of power consumption by the water pump will be subtracted from the money saved as a result of the

installed SWH. For estimation of the inflation rate the mean value (5.47%) for the last 10 years in South Africa was (will be) applied. See <http://www.global-rates.co> for the last ten-year inflation rate.

4. SIMULATION TECHNIQUE APPLICATION

The aim of the developed model is to give an ample view of investment, energy and money saving, payback, baseline energy of the building, environmental variable-cold water temperature profile, solar irradiation on an inclined plane, number and slope of collector for better efficiency, energy required by the water pump and etc. These evaluations were carried out using the developed simulation technique model (see appendix 1 for extracts of the application), using the following course of actions:

4.1 Solar Water Heating- Process

The SHW process in Fig 1 was applied in the application development (Appendix 1) using the following inputted parameters [7, 8 and 9]:

- Location of installation: 25°43'56" South, 28°9'42" East; Elevation: 1310 m a.s.l.
- Type and size of solar collector: Xtreme Solar Collector- 12 pipe evacuated solar collector [with a surface area of 2.2256 m² (total cost ZAR 7439.28)]
- Type, size and cost of water storage tank: JoJo; 10000 liters capacity @ZAR 8366.00. The number of the tanks in the project deduction was based on the number of people using hot water and the fraction of energy/money saving expected. Other inputs include:

➤ *Water consumption:* From the audit exercise carried out at the campus, the total number of beds at the six residences is 1250. The average daily hot water usage per day was estimated to be 9500 liters (average of 7.6 liters).

➤ *Hot water electricity consumption per year :* The use of hot water corresponds to an electrical consumption, however in order to quantify the yearly water consumption, the holiday period in South Africa needs to be taken into account. Using the South Africa school calendar (www.kwathabeng.co.za/travel/south-africa/destinations.html?cal=school, 2011), there is around 94 days of vacation in a year which is about 25% of the number of days in year. As a result the use of residences is consequently around 75% in a year with an estimated annual water heating consumption of around 1279 MWh/year.

➤ *Energy consumption and energy saved:* The fraction of energy saving is set to 70% (maximum) so as to be able to reduce most of energy and money consumption.

➤ *Lifetime of project:* Lifetime of the existing project is fixed to 10 years.

4.2 Result

Using the SWH model, the energy required to heat water as 1535 MWh/year while the energy produced by the

solar water process is 1074 MWh/year. This shows that energy consumed with the SWH system is 461 MWh/year. Fig. 6 shows the cumulative cash flow graph analysis for SWH; payback period is 3 years 10 months as shown in the graph.

For maximum utilization of irradiance the slope of the collectors needs to be inclined at an around 25.2 degrees. To achieve the expected energy from the SHW, 329 collectors with correspondonding area of 732 m² is needed; i.e. 54 collectors of 120m² area need to be installed on each residential building roof. The impact cumulates to an emission reduction of 938 ton of CO₂. This translates into cumulative cost savings of 7.1million rand over a ten year period.

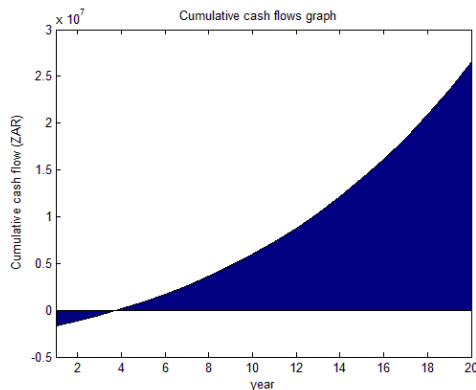


Fig. 6. Cumulative cash flows graph for the intended project implementation

5. Conclusion and Recommendation

This study was undertaken to evaluate the impact of SWH usage at an institution of higher learning, which is expected to assist policy makers in terms of energy management and control. To achieve this set goal, study of the existing water usage pattern usage and development of a simulation model technique for analyses and evaluation impact aimed at energy management initiatives was undertaken. From the result obtained it can be deduced that SHW implementation will bring about financial and environmental benefits that will alleviate the financial strain at higher institution. This will ultimately reduce the maintenance cost of the institution, more importantly the energy consumption and associated cost.

REFERENCES

1. P. Ijumba and A. B Sebitosi: "Evaluating the Impact of Consumer Behavior on the Performance of Domestic Solar Water Heating Systems in South Africa", *Journal of Energy in Southern Africa*, Vol. 21, No 1, 2010.
2. H. Winkler, H: "Renewable energy policy in South Africa: policy options for renewable electricity", *Energy Policy* Vol. 33, pp. 27-38, 2005.
3. Department of Energy: "White paper of Renewable energy: solar power" http://www.energy.gov.za/files/renewables_frame.html, 2012.
4. National Solar Water-Heating Programme (<http://www.energy.gov.za/files/esources/renewables/WaterHeating.pdf>).

5. J.A. Duffie, and W.A. Beckman: *Solar Engineering of Thermal Processes*, Wiley-Interscience, New York, 2nd Edition, 1991.
6. D. Redpath: "Thermosyphon heat-pipe evacuated tube solar waters for northern maritime climates", *Solar Energy*, Vol.86 No. 2, pp. 705-715, January 2012.
7. Retscreen® International: Solar Water Heating Project Analysis Chapter; retscreen.com and retscreen software.
8. W.L.O Fritz and D.C. Kallis: "Domestic load-profile measurements and analysis across a disparate consumer base", *Proceedings: 18th International conference on the Domestic Use of Energy Conference*, Cape Town, April 2009.
9. Electric Power Research Institute: *Engineering Methods for estimating the impacts of Demand – Side Management Programs: Fundamental equations for residential and commercial end uses*, Vol 2, Technical Report-100984, 1993

ACKNOWLEDGEMENTS

This work was supported by Eskom, South Africa and Centre for Energy and Electric Power, Tshwane University of Technology. Also Julien Masson (ESIEE, Amiens) that participated in the research work, as well as Prof J. Munda.

Appendix 1: SWH Matlab software (part 1) –Environment

```
function [Lsky,Kt,Rt,temp]=radiation
main campus
latitude=-25.736*pi/180; %latitude of pretoria tut
Gsc=1367; %solar constant in W/m2
teta=5.669*10^-8; %the Stefan-Boltzmann
constant (W/m2)/K^4
n = 1:1:365;

for i=1:1:365,
if i<=31
%applying monthly irradiation and
outside temperature into days %irradiation on horizontal plane
H(i)=7410; %the outside temperature in degree
(Wh/m2/day) temp(i)=22;
elseif i >= 31 && i <= 59
H(i)=6800;
temp(i)=22;
elseif i >= 59 && i <= 90
H(i)=6190;
temp(i)=23;
elseif i >= 90 && i <= 120
H(i)=5390;
temp(i)=18;
elseif i >= 120 && i <= 151
H(i)=4790;
temp(i)=17;
elseif i >= 151 && i <= 181
H(i)=4490;
temp(i)=15;
elseif i >= 181 && i <= 212
H(i)=4600;
temp(i)=15;
elseif i >= 212 && i <= 243
H(i)=5410;
temp(i)=18;
elseif i >= 243 && i <= 273
H(i)=6120;
temp(i)=23;
elseif i >= 273 && i <= 304
H(i)=6660;
temp(i)=24;
elseif i >= 304 && i <= 334
H(i)=7170;
temp(i)=22;
elseif i >= 334 && i <= 365
H(i)=7500;
temp(i)=23;
end
end
declination(n)=23.45*sin(2*pi*(284+n)/365)); %angular position of the
sun at solar noon
ws(n)=acos(-tan(latitude)*tan(declination(n)*pi/180)); %sunset hour angle
H0(n)=(24*Gsc/pi)*(1+0.033*cos(2*pi*(n/365))) * (cos(latitude)*cos(declination(n)*pi/180) + sin(latitude)*sin(declination(n)*pi/180)); %extraterrestrial radiation (Wh/m2/day)
Kt=H(n)/(H0(n)); %Monthly average clearness index
for i=1:1:365,
%Monthly average daily diffuse radiation
calculated in two cases
if (ws(i)>180/pi)<=82.4
Hd(i)=(1.391-3.560.*Kt(i)+4.189.*Kt(i).^2-2.137.*Kt(i).^3).*(H(i));
elseif (ws(i)>180/pi)>82.4
Hd(i)=(1.311-3.022.*Kt(i)+3.427.*Kt(i).^2-1.821.*Kt(i).^3).*(H(i));
end
end
beta(n)=abs(latitude-declination(n)*pi/180); %monthly slope of the
collector
betaal=mean(beta); %annual mean of the slope
Phi=latitude; %diffuse fraction index
Rd(n)=Hd(n)/H(n);
roger=0.2; %ground reflectivity
Rb(n)=(cos(Phi+betaal)*cos(declination(n)*pi/180)+sin(Phi+betaal)*sin(declination(n)*pi/180)).*(cos(Phi)+sin(Phi)*sin(declination(n)*pi/180)); %irradiance of a sky cloudy
%the fraction of the sky
covered by clouds
Lclear(n)=Rb(n)+Rd(n); %clear sky long-wave
radiation
Lcloudy(n)=0.96*teta*(temp(n)+273.2-5).^4; %irradiance of a sky cloudy
Lsky=(1-Lclear(n))*Lcloudy(n); %sky radiation
```


ANALYTICAL EVALUATION OF THE ENERGY LOSSES OF AN AIR SOURCE HEAT PUMP WATER HEATER: A RETROFIT TYPE

Stephen L. Tangwe¹, Michael Simon² and Edson L. Meyer²

* Atlantic International University, Florida United States of America

E-mail: stephenloh2001@yahoo.com

** Fort Hare Institute of Technology, University of Fort Hare, Alice, Eastern Cape, South Africa

Phone: +277406022086, Fax: +27 (0) 40 653 0665, E-mail: msimon@ufh.c.za

Abstract:

Air source heat pump (ASHP) water heater is a renewable and energy efficient device used for sanitary hot water production. The system comprises of two major blocks (storage tank and heat pump) connected by pipes. These blocks can either be compact as in the integrated model or split as in the retro-fit model. In this paper, the analysis of energy losses was performed using SIRAC residential split type heat pump of 1.2 kW input power to retrofit a 200 liters high pressure kwikhot storage tank without hot water being drawn off for the entire monitoring period. Likewise to experimentally determine the losses a data acquisition system (DAS) was designed and built to measure ambient temperature, relative humidity, outlet hot water temperature of the storage tank, inlet and outlet water temperatures of the ASHP. Two flow meters were also installed on the inlet water pipe of ASHP and on the outlet water pipe of the storage tank to the building. The results showed that heat gain to compensate standby losses could range from 1.8 kWh to 2.1 kWh with the corresponding electrical energy (EE) used by ASHP ranging from 0.55 kWh to 0.66 kWh. The standby losses depend primarily on volume of water heated (V), the temperature difference between the water from the outlet and inlet pipes of the ASHP ($T_h - T_c$) and ambient temperature (T_a) while the influence of the relative humidity (RH) is secondary.

Keywords: Air source heat pump, Data acquisition system, Renewable and energy efficient device

1. INTRODUCTION

Sanitary hot water production constitutes a significant percentage of monthly energy consumption in the residential sector worldwide. In South Africa, residential hot water heating can contribute to more than 50% of the monthly energy utilization [1]. A far-reaching research conducted to justify in terms of energy usage revealed that the hot water contribution in the domestic sector of South Africa is between 40% to 60% on an average monthly basis. Figure 1 shows that 45% of the total energy consumption in a typical South African residence are from hot water heating [2].

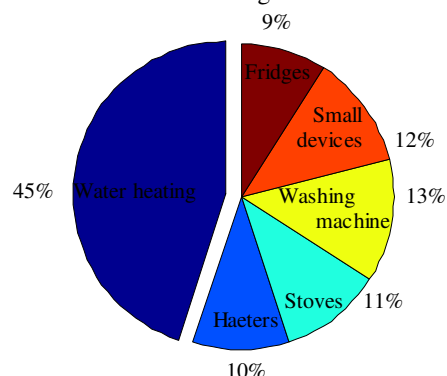


Figure 1: Percentage of energy consumption in a typical South African residence

It is worth mentioning that despite the daunting electrical energy consumed for hot water generation, not all the thermal energy gained by the hot water is effectively utilized. There are always standby losses which are responsible for 20% to 30% of the total thermal energy gained by hot water contained in a storage tank [3, 4]. Although, ASHP water heater coefficient of performance (COP) value can range from 2 to 4 [5,6], it is crucial to note that the COP depends on primary (volume of hot water heated, hot water set point temperature and mains supply cold water temperature) and secondary factors (ambient temperature and relative humidity). Clearly, the COP could be defined as the ratio of useful thermal energy gained when water is heated to set point temperature and the electrical energy used by the system during the vapour compression refrigerant cycle. A salient and better understanding of refrigeration cycle of heat pump water heater was given by Ashdown *et al.* (2004) and Sinha and Dysarkar, (2008) [7, 8]. Moreover, the performance can be severely affected by standby losses [9]. Heat pump water heaters also render an extra benefit of dehumidification and space cooling because they pull warm vapour from the air [10].

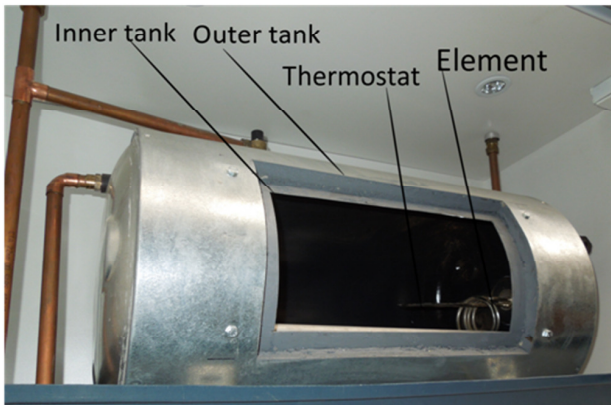


Figure 2: The geyser to be used as storage tank.

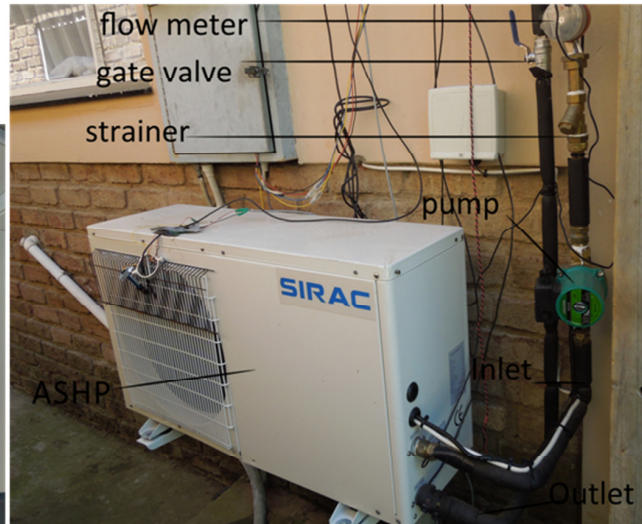


Figure 3: Illustration of the installed ASPH unit.

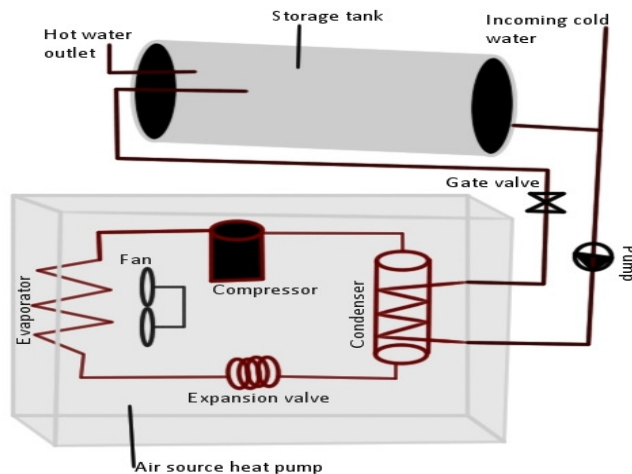


Figure 4: The schematic layout of the experimental setup

1.1. Brief description of the installation of a split type ASHP water heater

Figure 2 and 3 below shows the essential components of the system. It comprises of a 400 kPa, 200L high pressure geyser with its 4 kW element disabled, so that it now serves as a hot water storage tank and also an ASHP unit rated 1.2 kW. These primary components are connected by copper pipes incorporating water circulation pump, non-return gate valve and a mechanical close and open valve to complete the closed circuit.

The schematic shows all the functional components (evaporator, compressor, condenser, capillary tube, refrigerant fluid and fan) that make up the entire ASHP unit.

2. DESCRIPTION OF THE SENSORS USED IN THE EXPERIMENTAL SETUP

ASHP water heater was set to produce hot water at 55°C with a temperature differential of 5°C. This implied ASHP unit would start the vapour compression refrigerant cycle once hot water inside the storage tank was 5°C or more below the set point temperature. The system was allowed to operate in an uninterrupted mode and without any hot water drawn into the main building from the 18 th December 2012 to 01 st January 2013. The performance and thermal energy loss of the system was evaluated for eight consecutive days within the experimental duration. 12 bits S-TMB temperature sensors incorporating electronic input pulse adapters were used to measure water temperature into the inlet and water temperature from the outlet of the ASHP unit. 12 bits S-THB ambient temperature and relative humidity sensor was also used to measure ambient temperature and the relative humidity. The T-Minol 130 flow meters were installed on the inlet pipe in to ASHP and hot water outlet pipe from the storage tank to the building to measure the

water flow rates of the respective unit. A T-VER-B50B2 power and energy meter was also used to measure the power factor and energy consumption by the ASHP water heater. All these sensors are housed by hobo U30-NRC data logger except of the power consumption from the water circulation pump that was measured and logged by the power track analyzer.

3. METHODOLOGY

The methodology is divided into two; the data acquisition architectural design and the full schematic layout of the ASHP water heater including the meters installation and the data loggers. The losses are experimentally determined for each of the 24 hours period. This duration of the evaluation was only taking into consideration from the time that water had attained set point temperature (reference point) for the respective heating up cycles.

3.1. Data acquisition system

Figure 5 shows the data acquisition system designed and built for this study. All analogue signals sensed by their respective sensors and transducers were converted to digital signals by the input pulse adapters integrated with their connecting cables. The data were stored in hobo U30-NRC data logger and could only be downloaded for further analysis using the hoboware pro software.

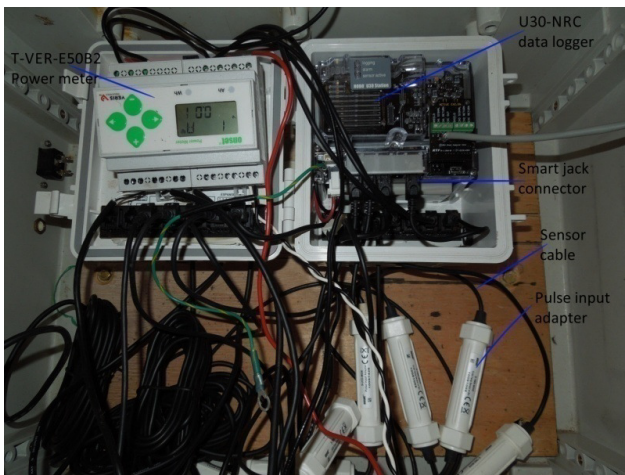


Figure 5: Shows the data acquisition system designed and built for the research

4. FULL SCHEMATIC OF THE COMPLETE SET UP

Figure 6 shows the complete setup for the study. This schematic was designed using the Simulink library of MATLAB. In the schematic all sensors (temperatures and relative humidity sensors) are represented by $f(u)$. The following labels are used for these sensors; temperature sensors (TS), ambient temperature (T_a) and relative humidity RH. The transducers mainly the flow meter and current transformer (CT) are also represented

by $f(u)$. In the setup, six TS, two flow meters and one ambient temperature and relative humidity sensor (RH and T_a) were installed and their reading recorded were stored in the U30 logger. The power meter T-VER E50B2 measured the real energy (Wh), reactive energy (VARh) and the current hour (Ah) of the ASHP water heater and was also stored in the logger as pulses or counts. The flow rate was also measured in counts and 1 count equal to 3.7854 L/min. The data loggers were configured to log every 1 minute throughout the duration of the experiment.

5. CALCULATIONS

The set of equations given in the equation 1- 4 shown below were used to calculate the active power (kW); electrical energy (kWh) and the thermal energy gained by hot water (kWh) respectively.

$$E_e = \frac{Wh}{1000} \quad (1)$$

$$E_e = p \times t \quad (2)$$

Where E_e = electrical energy in kWh and t = time in hour
 p = power in kW

$$E_t = mc(T_h - T_c) \Rightarrow E_t = Vc(TS5 - TS7) \quad (3)$$

Where E_t = thermal energy gain in kWh, $m = V$ = volume of water in litres heated by ASHP, c = specific heat capacity of water = 4.2 kJ/kg°C, $T_h = TS5$ = hot water temperature while $T_c = TS7$ = cold water temperature.

It is important to note that 1 pulse represents 1Wh and 1 VARh but 100 Ah as per the configuration setting in the T-VER-E50B2 power and energy meter.

The COP of the system is given by the empirical equation shown in equation 4 below

$$COP = \frac{E_t}{E_e} = \frac{\text{output useful thermal energy gain}}{\text{input electrical energy}} \quad (4)$$

6. RESULTS AND DISCUSSIONS

6.1. A comparative analysis of the performance and energy losses

Table 1 shows a detail analysis of the ASHP water heater coefficient of performance, energy factor; standby losses and conditions under which the following results were achieved. It is worth to note that for each run, the first row shows the condition in which water was heated to set point temperature before monitoring the heat losses for 24 hours. In each of the runs over 24 hours duration the ASHP unit only comes on once. This interval was recorded in the second row of each run. It can be

depicted that the average power of the system in each run was almost equal both when water was heated before the start of observation and when heated owing to standby losses within the 24 hours monitoring period. The COP in all the heating mode ranged from 2.95 to 3.4. This is in accordance with the studies of Levins (1982) and Bodwins (1997) ^[11, 12]. The standby heat losses also ranged from 1.8 kWh to 2.1 kWh. It can be shown that in all cases the average COP was greater than the energy factor (EF) of the system which ranged from 2.60 to 2.95. This could be accounted for by the electrical energy consumed by the power electronic circuit integrated into the ASHP water heater (0.09 kWh-0.1 kWh). Finally without loss of generality, the standby losses in the system were approximately equal to the heat gained to heat up water to set temperature before monitoring the losses for 24 hours ± 0.08 kWh.

6.2. Profile of electrical energy used and heat loss for a day

The figure 7 shows the profiles of electrical energy (red line graph) used by the ASHP water heater and the thermal heat gain (blue line graph) by hot water for the 5

th run (starting at 06:54 ,26 December 2012 and end at 07:26, 27 December 2012). From figure 7, the profiles of electrical and thermal energy for the 5 th run is divided into four zones; A, B, C and D. Zone A was where the water is first heated to set point temperature (referenced heating up cycle). The energy profiles were displayed in a five minutes interval and the total energy in each zone was the summation of the number of discrete energy values available in the specific zone. It can be clearly seen that the total energy of zone A was equal to that of zone B. Hence heat losses in the zone B were equal to heat gain in zone C. In zones B and D, no thermal energy was gained by water as ASHP was in an off mode but energy was consumed by system micro controller unit and each peak equal to 0.001 kWh. The subplot labelled A, B, C and D illustrates the electrical and thermal energy involved in the respective zones. It can also be observed that in the zones A and C where water was heated up by ASHP unit, the unit runs for about 5 minutes before continuous heating up of water begins. In the zones B and D the system was not heating up water, thus, no thermal energy was gained but electrical energy was consumed as the micro controller never turned off.

Table1: A comparison analysis of the system performance and energy losses of the 8 consecutive in the period 19 December 2012 to 1 January 2013

period	Heat up time HH:MM	¹ P _{av} kW	² E _e T kWh	³ E _t T kWh	⁴ COP	⁵ V L	⁶ T _c °C	⁷ T _h °C	⁸ T _a °C	⁹ RH %	¹⁰ E _c D kWh	¹¹ EF
1 run,19-20	05:54-06:27	1.44	0.62	1.97	3.15	204	30.1	53.9	18.7	94.8	0.72	2.76
	00:32-01:04	1.49	0.62	2.03	3.28	223	28.9	54.0	20.7	84.6	0.71	2.88
2 run,21-22	10:08-10:39	1.46	0.56	1.87	3.34	208	34.6	55.0	26.2	70.8	0.66	2.85
	06:39-07:10	1.48	0.57	1.82	3.20	208	31.3	54.6	23.8	80.6	0.65	2.79
3 run,23-24	03:14-03:47	1.46	0.63	1.95	3.10	227	31.3	53.8	19.5	83.7	0.71	2.76
	01:02-01:32	1.50	0.55	1.82	3.32	204	32.9	54.1	21.9	88.3	0.63	2.88
4 run,24-25	20:20-20:52	1.47	0.59	1.97	3.35	211	25.5	54.3	21.1	93.7	0.66	2.99
	13:36-14:08	1.49	0.59	1.85	3.10	215	30.9	54.6	24.6	66.0	0.68	2.73
5 run,26-27	06:54-07:26	1.47	0.58	1.89	3.23	219	35.7	54.3	20.4	94.7	0.70	2.78
	01:48-02:12	1.48	0.61	1.92	3.12	227	34.3	53.6	18.1	94.7	0.73	2.65
6 run,27-28	23:05-23:38	1.45	0.63	1.87	2.95	223	28.0	53.9	21.9	62.9	0.7	2.67
	19:36-20:08	1.44	0.60	1.88	3.13	211	23.9	53.7	21.7	69.6	0.66	2.87
7 run,29-30	16:20-16:42	1.56	0.47	1.49	3.19	162	38.9	55.9	33.8	41.5	0.51	2.94
	11:11-11:38	1.55	0.52	1.66	3.19	185	34.2	55.4	29.4	49.6	0.58	2.84
8 run,31-01	08:11-08:44	1.43	0.62	2.03	3.30	227	31.2	53.6	19.1	96.1	0.71	2.86
	01:50-02:25	1.46	0.66	2.14	3.25	234	28.9	52.9	16.4	98.7	0.76	2.80

¹Average power, ² Total electrical energy used , ³Total thermal energy gain , ⁴ Average COP , ⁵Total volume of water heated,⁶Initial cold water temperature,⁷Final hot water temperature, ⁸Average ambient temperature ,⁹Average relative humidity, ¹⁰Total electrical energy use in a complete 24 hours and ¹¹Energy factor

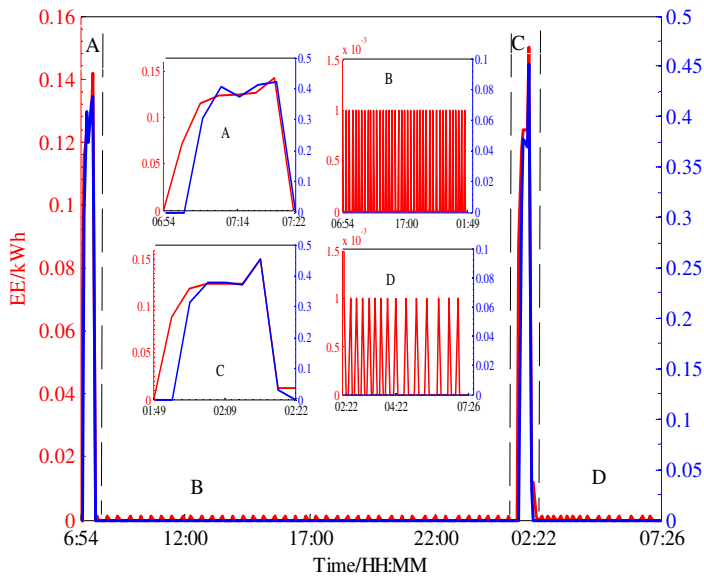


Figure 7: The energy profiles for the 5th run experiment

6.3. Temperatures and relative humidity variation

The figure 8 clearly shows temperature and relative humidity variation of the system in the 5th run whose energy profiles were shown in figure 7 above. The green, red and black lines represent the hot water temperature from the outlet of ASHP, water temperature into the inlet of the ASHP and the ambient temperature, respectively. The blue line represents the relative humidity and is on the opposite y axis. From figure 8 it can be deduced that at the start-up of the hot water heating process which is occurring in zone A, temperature of standing water at the respective inlet and outlet pipes of ASHP was equivalent to the ambient temperature (approximately 20°C). The heating up process lasted for 33 minutes before hot water could attain set point temperature and both the outlet and inlet ASHP water temperatures were 54°C and 46°C while the relative humidity was around 95 %. It can also be observed that once the hot water inside the tank attained the set point temperature, the rate of temperature drops in both pipes exhibited an exponential decay until they reached an equilibrium temperature with the ambient. This took place in the very early phase of the zone B and in the later phase of zone B temperature changes on both pipes are greatly affected by fluctuation in ambient temperature and relative humidity. As a final point, once the hot water inside the tank went below the 5°C differential, the ASHP water heater began the heating up process again where both cold and hot water in the inlet and outlet pipes of the ASHP began to rise. This occurred in zone C. The heat gain in zone C can be reasonably equated to the heat loss in zone B since heat loss in zone D can be neglected. The heat loss in zone D is very small since the losses were only taking place within the small volume of water inside the pipes and does not result in switching on the ASHP unit. It can be noted that at zone C, the peak is where the ASHP unit was again turned off and the inlet water, outlet water from ASHP and ambient temperatures were 46°C, 54°C,

and 18.1°C while relative humidity was 95 %. It can be noted that the point E shows an abnormality in the inlet and outlet water temperatures inside the pipes. This sudden rise of temperature is owing to increase in the ambient temperature and was maximum where ambient temperature was at its peak (28°C at about 14:30 on 26 December 2012).

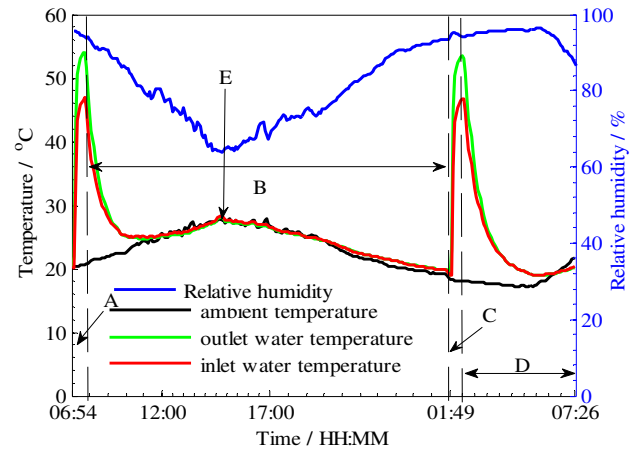


Figure 8: The 5th run temperatures and relative humidity profiles

6.4. Determination of input predictors contributing to heat gain to compensate standby losses

The four input variables; volume of water heated (V), the difference in the water temperature inside the inlet and outlet pipes of ASHP ($T_h - T_c$), ambient temperature (T_a) and relative humidity (RH) values obtained for specific heat gain to compensate standby losses were used to rank their importance to the output (heat loss) using the statistical function (reliefF test) in the MATLAB statistics tool. The result showed that the V was the most significant followed by the ($T_h - T_c$) and T_a . These three predictors were determined to be primary factors while the RH was secondary. The contributions by weight to the heat gain to compensate for standby losses for the four predictors were 0.5512, 0.0892, 0.0165 and -0.0292 as shown in figure 9 below.

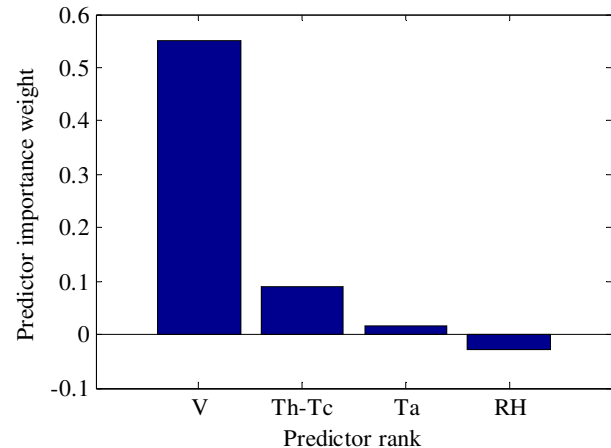


Figure 9: Shows the predictors weight ranking

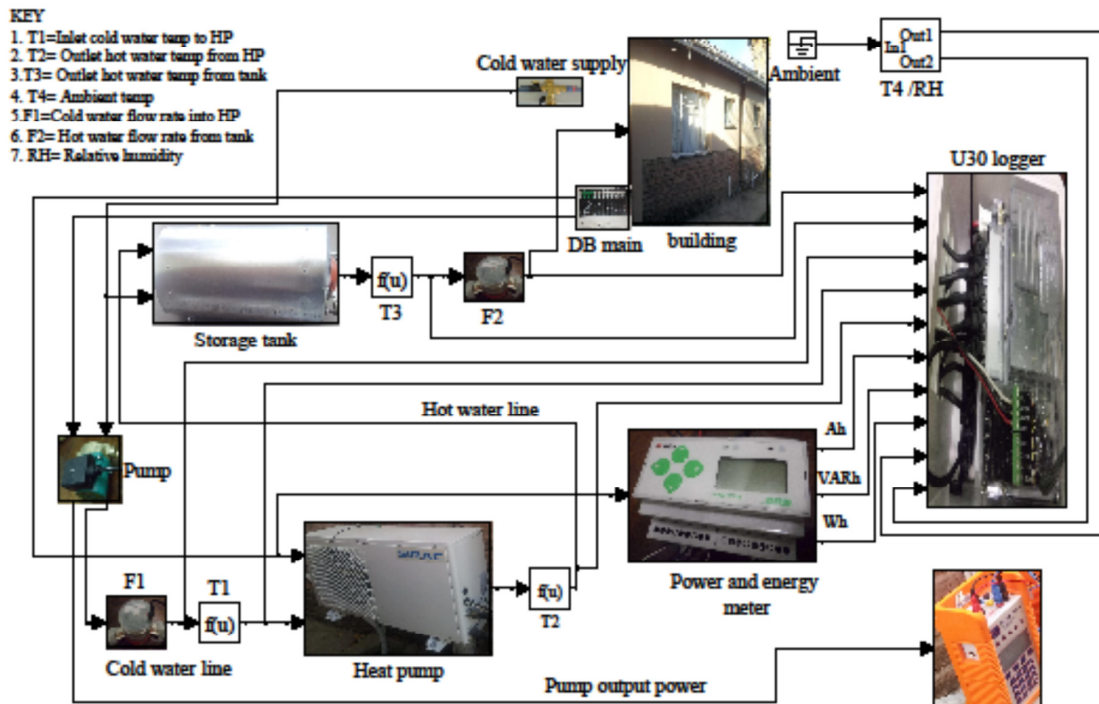


Figure 6: Shows the full schematic architectural layout used in the study.

7. CONCLUSION

The following observable conclusions can be drawn from this study;

Despite the average standby losses of 1.9 kWh which is in agreement with the South African Board standard (SABS) for measurement and verification rating for the storage tank, only 0.6 kWh of electrical energy was used by the ASHP due to its average COP of more than 3. In addition, considering the electrical energy and average COP of the second row of each run in table 1, the standby losses are approximately the product of these two quantities. Finally, standby losses depend primarily on volume of water heated by ASHP, the difference in the inlet and outlet water temperature from the ASHP and ambient temperature.

8. REFERENCES

- [1] Sustainable energy society South Africa. (www. Waterlite.co.za, 2013).
- [2] Van Tonder, J.C. and Holm, D. (2001). Measurement Based Quantification of storage water Heater losses and Benefit of Addition Thermal Insulation. Domestic use of Energy Conference. pp163-168.
- [3] Morrison, G.L., Anderson, T. and Behnia M.(2004). Seasonal performance rating of heat pump water heaters. Energy Conservation & Management. 76:147-152.
- [4] Douglas, J.(2008). Demonstrations Encourage Wider Use of Efficient Technologies. *EPRI Journal*, 15-17.
- [5]Baxter, V. D., Tomlinson, J. J., Murphy, R.W., Ashdown, B.G.and Lapsa, M. V. (2005) Residential Heat Pump Water Heater Development Status USA. Oak Ridge, TN: Oak Ridge National Laboratory.
- [6] Levins, W.P. 1982. Estimated Seasonal Performance of a Heat Pump Water Heater Including Effect of Climatic and In-House Location. Oak Ridge National Laboratory, Oak Ridge, TN
- [7] Bodzin, S. (1997), "Air-to-Water Heat Pumps for the Home", Home Energy Magazine Online, July/August 1997.
- [8] Meyer, J.P., and M. Tshimankinda (1998), "Domestic Hot Water Consumption in South African Townhouses", Energy Conversion and Management, 39:7, 679-684.
- [9] SIRAC; Sales and Technical training. Guateng Summer 2010 (www.sirac.co.za)
- [11] MATLAB and Simulink (Math work cooperation 2011b,Version 7.12)
- [12] Tangwe S L, M Simon and E Meyer. (2013) Experimental investigation to quantify the benefits of air source heat pump water heater in South Africa, International conference of applied energy.

ENERGY MONITORING DEVICE FOR SUSTAINABLE USER CENTRED SMART ENERGY SYSTEMS

D. Wolsky*, H. Hunt * and K. J. Nixon *

* School of Electrical & Information Engineering, University of the Witwatersrand, Private Bag 3, 2050, Johannesburg, South Africa. E-mail: david.wolsky@students.wits.ac.za

Abstract: Smart grids require monitoring of voltage, current and frequency values. In this project an investigation and evaluation into an consumer side energy monitoring system is conducted. A measurement board with five Cirrus Logic CS5480 energy ICs is controlled with a BeagleBone Black. SPI communications are used to transfer instructions and data between the ICs and the controller. GPIO pins, from the BeagleBone Black are used for chip selection. The measurement board uses opto-isolators and a DC-DC converter to isolate the live side of the board from the controller and its electronics. Lab and a practical application tests are conducted to evaluate the system. A Fluke power meter is used in the lab tests where a variac is used to change the voltage over a constant resistance. A Yokogawa power meter is used for monitoring a coffee machine in the practical application test. In both tests the voltage level on the energy monitoring device is lower than the other devices. The current exceeds that of the other measured currents. A time difference noted between the coffee machine measurements and is compensated for. The frequency measurements are very close to each other. Further recommendations of tests that need to be carried out, improvements to time stamp accuracy and functionality to the added to a configuration file are discussed.

Key words: Energy Monitor, BeagleBone Black, Open Source and Open Hardware, SUCSES- Sustainable User Centred Smart Energy Systems, Sub Second Power Measurements, Smart Appliances

1. INTRODUCTION

A step towards a stable balanced load and supply requires a better understanding of user and supply behaviour. To achieve this understanding energy monitoring systems can be used to log data from the consumer side of the network. This project investigates and evaluates a user side energy monitoring device that measures the current used by a load and the voltage and frequency of the supply. The first steps are already in place where recommendations are made to set timers to control when these devices should be switched off. However, with the introduction of renewable energy power supply a more advanced system could take advantage of excess power on the grid. For example, excess power could be used by smart systems connected to appliances and loads such as pool pumps or geysers.

This project is aimed to help provide open source hardware and software for equipment that can be used to gain a better understanding of existing user trends. This can help current manual and time based plans to balance energy demands better. In addition to this, steps are being made that can be incorporated into smart appliances as well as providing a tool for users to have a better understanding of how much power they use and when they use it.

There are two important aspects that play a role in making such a system: a measurement board that houses the energy measurement circuitry and a controller that sends instructions and retrieves data from the circuitry. The board must also ensure that there is isolation between the measurement side of the board that is connected to live and the electronics that are connected to the controller.

2. SYSTEM OVERVIEW

In this project a basic energy monitoring system is developed as a base for expansion to smart applications. A lightweight embedded devices is used to communicate with Energy Measurement ICs (Integrated Circuit). An overview of the flow of data through the system is shown in Figure 1. There are five measurement IC on the single phase measurement board. A potential divider is used to scale down the live line coming onto the board and current transformers are used to measure the current.

Opto-isolators are used to isolate the 'live' measurement side of the board from the controller side. The controller provides a 5V supply to the measurement ICs by using a DC-DC converter. The neutral line from the power utility is used as 'ground' on the measurement side of the board.

The controller communicates with the measurement IC using Serial Peripheral Interface (SPI). Typically four lines are required for this type of communication: a clock line, a chip select line, data in and data out lines. In this case each IC requires its own active-low, chip select line. General Purpose Input Output (GPIO) lines, from the controller, are used for the chip select as seen in Figure 1.

As measurements are taken from the ICs the controller keeps track of the time, to micro seconds accuracy. This accuracy is required so that when reviewing the measurements, from different ICs and different boards, at different locations, the data can all be synchronised. RMS voltage measurements are used to monitor the local supply. This can be used to model the source and local factors on the grid. RMS current and power measurements are taken

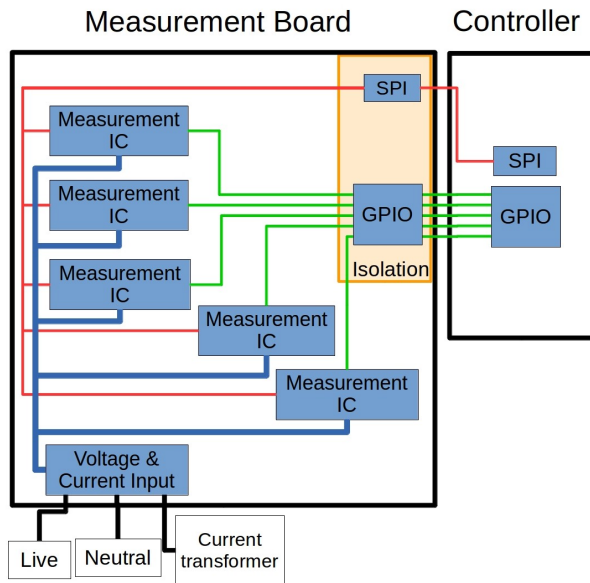


Figure 1: Overview of data flow through system

from the line going to the device under test which allows for modelling of the load. The power factor of the load is also measured. Finally a frequency measurement is used to monitor the load of the entire grid [1].

3. IMPLEMENTATION

A BeagleBone Black (BBB), running Angstrom Linux, is used as the controller of the energy monitoring board. Angstrom is the distribution that comes installed on the BeagleBone Black. C is the chosen programming language and the pre-installed GCC compiler is used [2].

The BBB expansion header P8 has two set of SPI modules [3]. SPI0 is used to avoid conflict with the HDMI pins. The SPI is not enabled by default and needs to be initialised [4]. The *ioclib* library is used to carry out data transfer with the measurement ICs.

The three channel Cirrus Logic (CS5480) is used as the measurement IC [5]. After initialising each IC, the data can be requested. The request takes place one at a time because SPI is being used. The controller cycles through the different measurement ICs using the active-low GPIO to signal which IC is required to receive instructions. To allow the user to use the system for different applications, a configuration file is read into the application on initialisation. This file contains the information about the number of ICs present on the board, the number of measurements required and a timing delay between measurements. Only sub-second delays are allowed as longer delays would typically use an averaging algorithm to get a greater accuracy over long interval measurements.

Once the measurements are retrieved they are processed

using the known potential dividers and current transformers ratios to work back to correctly scaled values. The values are then stored in a struct. A pointer to the struct allows the entire set of measurements to be passed between functions. A runtime debug mode is implemented so that, when in debug mode, each step of the program is printed to the terminal.

The measurements are then stored in a text file and GNU Plot is used to provide a visualisation of the measurements. The values are delimited by a space. Hourly and daily plots are generated using the CRON scheduler [6]. Due to limited network capability the time is manually set using the *date* functionality on the BBB. This time is logged just before each measurement is taken and stored in the text file. The data files and plots are copied from the device using the Secure Copy protocol (SCP). These could also be pushed up onto a website or stored on a removable micro SD card depending on the specific application.

A 5V, 2A power supply is used to supply the BBB. This in turn supplies 5V at 1A to the measurement board [5]. A lithium-ion battery is installed on the BBB to allow the controller to continue running in the event of a power failure. The battery does not keep the measurement board online. It is not the objective of this project to sample a power surge or to take measurement of the grid recovering for a fault, instead a simple error log is kept when measurements are not returned. The error log keeps track of any unsuccessful measurements or communications using the *STATUS0* register from the measurement ICs [5]. The error log is kept in a text file and in this way the display and data layers are kept separate.

4. TESTING METHODOLOGY

Two tests are carried out to evaluate the accuracy of the energy monitoring system. A variac is used for the variable voltage source and a 400Ω resistor is used as the load. Current clamps from both the energy monitoring system and a Fluke 39 Power Meter are placed over the line going to the load. A Magnetlab SCT-0400-020 current clamp is used to obtain current measurement on the energy monitoring device. Both devices measure the voltage across the resistor. Measurements are taken at voltage levels of 20, 50, 100, 150, 200 and 240 V_{rms}. Measurements are only logged at constant levels and not while the variac is being increased or decreased. The Fluke Power Meter measurements are manually logged while the energy monitoring system is run. The data from the energy monitoring system is saved on the controller and the Fluke measurements are added to the file at a later stage for plotting.

The practical test is carried out on a Jura Coffee machine. A Yokogawa CW240 Power Meter is used for this comparison with the energy monitoring system. Once again the Magnetlab SCT-0400-020 current clamp is used by the energy monitoring system. Six different practical tests are carried out using the coffee machine while the two systems log voltage, current, power and frequency. A

ristretto, espresso and normal coffee are made followed by a double of each of these. Both devices are left running for the full length of the test. Any system time offset that arises between the two sets of measurements are manually corrected. This offset results since the BBB is not connected to an online time server. Measurements on the energy monitoring device are logged every half a second, while the Yokogawa measurements are only logged every second. Requesting values from the energy monitoring ICs at shorter intervals is done through changing the delay value stored in the configuration file. The delay between measurements can be shortened to obtain more measurements. For long term measurement systems this will result in large data files being stored. To keep all the data some kind of compression system is required.

The coffee machine is used because it has a number of different processes with different loads. The power supply controlling the electronics will draw a small amount of power. The heating element and the coffee bean grinder will draw a larger amount of current at different rates. This range of different processes is useful to test different aspects of the measurement system.

5. RESULTS

The results of both the lab and practical tests are presented below.

5.1 Lab Tests

The different voltage levels are displayed in Figure 2. There is a greater difference in voltage at lower voltages than at higher voltages. At 20 V_{rms} , the energy monitoring system reflects an average voltage of $6.4\text{ V}_{\text{rms}}$ while at $240\text{ V}_{\text{rms}}$ an average voltage of $236\text{ V}_{\text{rms}}$ is measured. At this higher voltage there is a standard deviation of $2.4\text{ V}_{\text{rms}}$. The supply used for the test was from a power utility and not a clean and controlled voltage therefore there may be deviation even through the resolution of the Fluke Power Meter did not register changes.

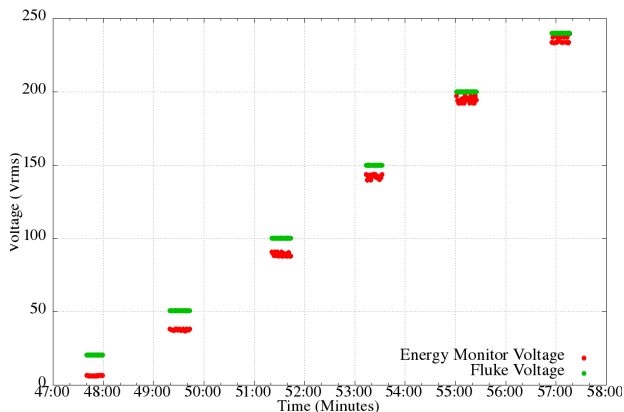


Figure 2: Voltage comparison of the energy monitoring device and the Fluke power meter

In Figure 3 the current measurements are shown. As mentioned before a $400\ \Omega$ resistor was used for this test and the current is seen to change with the voltage change. The energy monitoring system measures a lower current than the Fluke at smaller currents, while at the higher levels the energy monitoring shows a higher current measurement. These are at very small currents and the test should be repeated with a lower resistance.

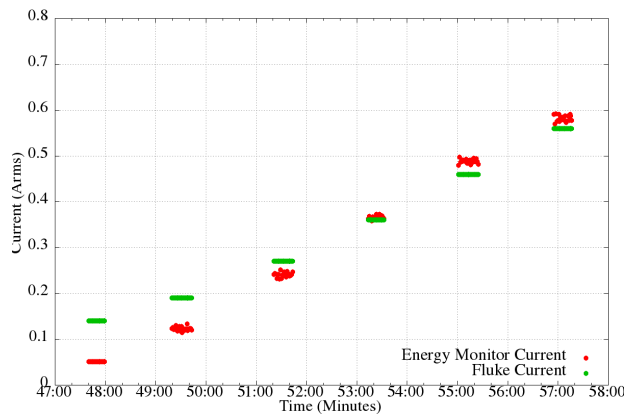


Figure 3: Current comparison of the energy monitoring device and the Fluke power meter

The power is calculated on the measurement IC using instantaneous current and voltage values averaged over a default number of samples [5]. The default value can be changed by writing a new value to the *SampleCount* register [5]. Errors in the current and voltage values combine and in this case results in an average of 8.9 W more power than that measured by the Fluke Power Meter, see Figure 4.

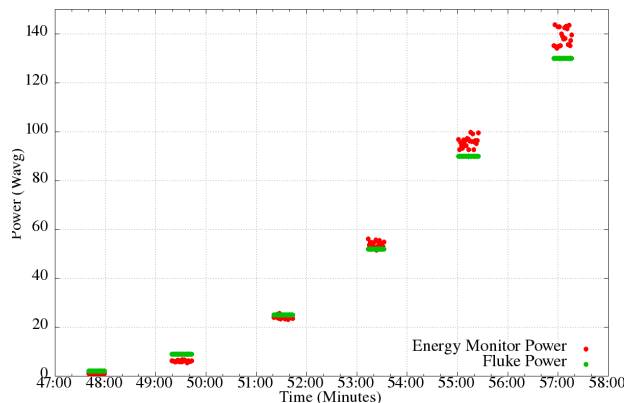


Figure 4: Power comparison of the energy monitoring device and the Fluke power meter

5.2 Practical Application Tests

As mentioned before six different coffees are made while both the energy monitoring system and the Yokogawa

power meter monitor are monitoring the current and voltage. The current waveforms are seen in Figure 5. An average difference of $0.7 A_{rms}$ is noticed between the energy monitoring and Yokogawa devices.

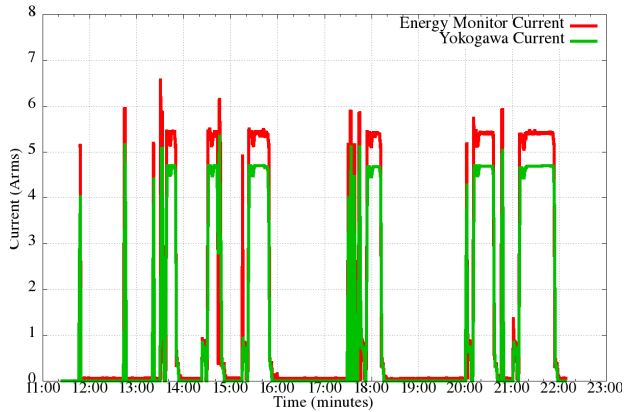


Figure 5: Practical application test using a coffee machine to compare currents of the energy monitoring system and the Yokogawa power meter

The voltage comparison between the energy monitoring and Yokogawa devices are shown in Figure 6. The smoother of the two graphs is the Yokogawa device and has an average of about $3 V_{rms}$ higher than the energy monitoring system.

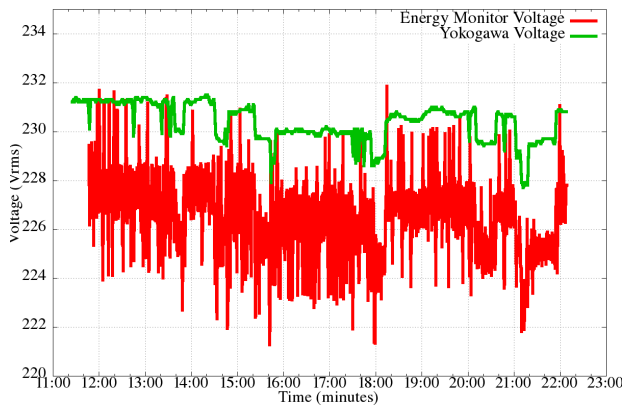


Figure 6: Practical application test using a coffee machine to compare voltages of the energy monitoring system and the Yokogawa power meter

Finally the frequency comparison is seen in Figure 7. There is clearly a strong correlation between the energy monitoring device frequency measurement and that of the Yokogawa.

6. DISCUSSION

The voltage and current measurement from the energy monitoring system differ both from the Fluke and

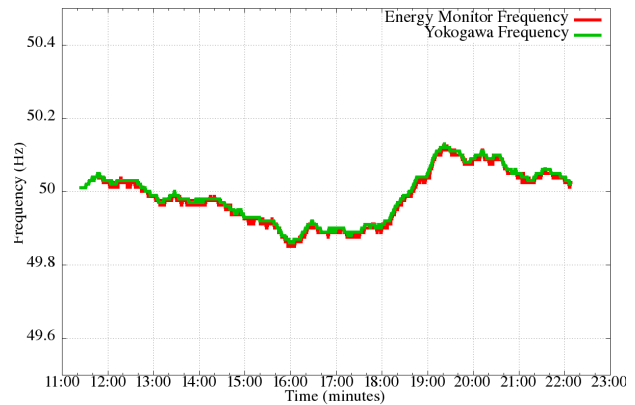


Figure 7: Practical application test using a coffee machine to compare frequencies of the energy monitoring system and the Yokogawa power meter

Yokogawa measurement devices. In both tests voltage values from the energy monitoring device are lower than other values. At lower voltages the difference is significantly greater. There are a number of reasons that the voltage could be different. The voltage divider used on the measurement board may not be the exact ratio used to convert the data from the measurement IC to usable values. A manual calibration can be carried out where the correction factor is adapted to better match the measured values. A system calibration from the measurement ICs can also be carried out [5]. The plots and the standard deviation of the voltage measurements suggests that there is a great deal of fluctuation in the measurement. This must however, be compared with devices that have as high a resolution as the energy monitoring device and that log values as fast. There are limitations to this due to the nature of the sine wave being sampled and RMS values being compared. Changing the number of instantaneous samples that are used to calculate the RMS values can be altered and the tests carried out again to see if using a bigger sample allows for less fluctuation.

The lab tests for the current measurements are carried out in the lower region of the current clamps and as a result the measurements may very well be in a non-linear region of the device. The practical tests are at higher currents and as a result the values seen are expected to be more reliable. The same methods of calibration can be carried out to achieve a greater accuracy.

7. FUTURE DEVELOPMENT

There are a number of tests that should still be carried out to complete the evaluation of the energy monitoring device. Some have been mentioned in the previous section but an important comparison that has not been discussed thus far is that of testing reactive power measurement of the load. This can provide information about the load being measured, especially if measurements are being taken from a power board or of an entire house instead of a single appliance. The coffee machine can be used for this test,

however other tests having known capacitive and inductive values must be carried out.

A real-time clock should be used if a reliable internet connection is not available. This can be housed on the measurement board in the isolated region. A line from the board to an available port on the BBB is then used to update the time where necessary. Delays are used to give process back to the processor on the BBB, after the delay finished the program is not given sufficient priority. This can result in the delay being longer than it should be. One way to avoid this would be to get the measurement IC to trigger the BBB when data is ready. Another method is to use a real time operating on the BBB, this would allow priority to be given to the application and less delay to be experienced.

Different measurement boards should be designed for different stages of testing. For simple and cost critical tests a single measurement IC with a cape for the BBB could be developed. At a larger scale three phase boards could be useful.

On the controller side it would be useful to be able to retrieve the entire set of instantaneous measurements used to calculate other measurements. If a specific characteristic is noticed, logging of data from other measurement IC can be suspended while faster measurements are taken from the IC of interest. This could also be used if a power/data saving mode is introduced. Logging data when there is no load present is both a waste of storage space and power. A sleep or low power mode on the BBB that is triggered by one of the ICs could reduce the power consumed by the system.

Having to recompile the software on the controller is not ideal as it requires additional software and source files to be present. Instead, the configuration file can be used to make changes to the system. Changing to different current clamps on different inputs to the system is currently not possible. If the configuration file contains the values of the current transformer ratios it can make changes to values being used for those calculations without having to recompile.

The use of the measurement board is currently limited to when the power supply for the BBB is connected. If running off the battery the measurements are not possible. Therefore, the logging of a power failure is potentially the same as if the measurement board is not connected correctly. If an additional battery, or potentially a battery housed cape is used on the BBB, there may be enough power to keep the measurement board active and to report that no voltage is being measured. If the power is off for an extended period of time and the battery is drained the software should save its data thus far and shut down safely. When the power comes back online the system, using *cron* should initialise and continue where it left off [6].

Finally neither temperature nor humidity are considered in either of the tests. If the measurement device is placed in a hot environment, such as a badly ventilated house or in

a ceiling near a geyser, the temperature could vary greatly. The effect of this should be tested to ensure that the device still operate with acceptable accuracy.

8. CONCLUSION

A stand alone, lightweight energy monitoring system is introduced and evaluated. In addition to being useful for consumers to monitor their power usage, the device can also be used to manage smart grids. An overview showing how the system operates and how the data flows between the system is given. A testing methodology of the lab tests and practical application tests is given, the results are presented and a discussion is conducted. In both tests the voltage level on the energy monitoring device is lower than the other devices. The current exceeds that of the other measurements higher currents. There is a strong correlation between frequency measurements from the two measurement devices. Different levels of accuracy are required for different applications. There are measures to be taken to achieve a better accuracy over a particular region of operation. Further recommendations of tests that need to be carried out, improvements to time stamp accuracy and functionality to be added to the configuration file are discussed.

9. ACKNOWLEDGEMENTS

The authors would like to thank Eskom for the support of the High Voltage Engineering Research Group through the TESP programme. They would also like to thank CBI-electric for support, the department of Trade and Industry (DTI) for THRIP funding as well as to the National Research Foundation (NRF) for direct funding.

REFERENCES

- [1] B. M. Weedy, B. J. Cory, N. Jenkins, J. B. Ekanayake, and G. Strbac. *Electric Power Systems*. USA: John Wiley & Sons, fifth ed., aug 2012.
- [2] G. Team. "GCC, the GNU Compiler Collection.", Nov 2012. URL <http://gcc.gnu.org/>. December 14, 2013.
- [3] G. Coley. "BeagleBone Black System Reference Manual." Reference manual, BeagleBoard, Oct 2013. Revision A6.
- [4] W. M. A. Traynor. "BeagleBone Black Enable SPIDEV.", Sep 2013. URL http://elinux.org/BeagleBone_Black_Enable_SPIDEV. December 14, 2013.
- [5] Cirrus Logic. "Three Channel Energy Measurement IC." Data Sheet DS980F3, Cirrus Logic, Inc., Mar 2013.
- [6] P. Vixie. "CRON(8) System Manager's Manual." Manual page, Debian, Apr 2012. 4th Berkeley Distribution.

BATTERY POWERED ELECTRIC VINEYARD TRACTORS: A FEASIBILITY STUDY

M M Guldenpfennig* and M J Kamper*

**Stellenbosch University, Department of Electrical and Electronic Engineering,
Private Bag X1, 7602 Matieland (Stellenbosch), South Africa*

Abstract. The agriculture sector is a very energy intensive sector when it comes to diesel fuel consumption involving vehicles that must drive for many hours on end. This is very costly and contributes to climate change and air pollution. Due to this farmers are seeking alternatives to diesel fuel to power their vehicles. This project focuses on the vineyard farming industry in the Western Cape in South Africa. More specifically it looks at the design and evaluation of a battery pack for an electric vineyard tractor. A standard diesel vineyard tractor is to be converted to an electric tractor by replacing the diesel engine with an electric motor drive system. This motor drive system is powered by the battery pack. Two battery technologies, lead-acid and lithium-ion, are considered for the battery pack. The energy content required from the battery pack is determined using different methods to ensure integrity of results. The battery pack is designed and the whole battery-powered vehicle system is simulated. It is found amongst others that the power of the power take-off for spray pumping drastically reduces the discharge travel distance of the electric vineyard tractor.

Key Words. Electric tractors, vineyard tractor, battery, feasibility.

1. INTRODUCTION

The agriculture sector is very energy intensive, especially when it comes to fossil fuel consumption. Whether it is planting, irrigation or harvesting, almost every aspect of their business involves vehicles that must drive for many hours on end.

In the Stellenbosch area the main agricultural activity that takes place is vineyard farming. These farms require tractors to irrigate, spray pesticides and herbicides, transport grapes and various other functions. This translates to massive spending on diesel fuel. Aside from the cost this also contributes to climate change and air pollution. Many farmers are becoming more environmentally conscious and are looking for alternatives to fossil fuels. An interesting solution that has presented itself is the possibility of an electric vineyard tractor. The idea is to replace the diesel engine that powers the tractor by an electric motor drive and a battery pack. A diagram of the proposed system is shown in Fig. 1. The battery pack powers the electric motor through the use of a power electronic converter. The electric motor drives the tractor wheels via the existing gearbox and differential. Some of the power also goes to the Power Take-Off (PTO) of the tractor as shown in Fig. 1. This is used to drive spray pumps and other equipment that the tractor may tow.

The problem that is being looked at is the design and evaluation of the battery pack that powers the whole drive system. Lead acid and lithium-ion battery technology are considered for this application. The energy that is required from the battery pack is one of the main variables that need to be investigated to do the design. There are also no readily available data on

the usage patterns of vineyard tractors. Modelling the entire system is also necessary for simulation and evaluation of the design. Models for the tractor and the batteries are developed to use in the evaluation of the design.

A very crucial piece of information that is required to run a simulation of the system is a driving cycle of a vineyard tractor. The driving cycle of a vehicle is typically a data set of velocity versus time. This data is readily available for conventional cars, but not for tractors. With the assistance of the Hartenberg Wine Estate at Stellenbosch a driving cycle was measured and compiled for a vineyard tractor.

One of the biggest questions in the design of the battery-pack is to know how much energy is required to power the tractor for a working day. Information on usage patterns and fuel consumption was gathered from viticulturists at various local vineyards. Using this data as well as the driving cycle data and tractor working duty cycle data an estimation of the energy requirement is done. This all is brought together in a case study where a battery pack is designed and simulated for a popular model tractor that is used in the area. The John Deere 5325N narrow tractor is investigated for the case study.

2. MODELLING

2.1 Tractor Modelling

The simulation model of the vineyard tractor is based on the dynamics of the vehicle. The aim is to determine the force required to drive the tractor. The modelling methods described here are adapted from work by Lowry and Larminie [1].

The total force required to drive the tractor, known as the total tractive effort, is given by

$$F_{te} = \mu_{RR} mg + ma + mg \sin \theta, \quad (1)$$

where m is the mass of the tractor. The first term of (1) is the force required to overcome the rolling resistance of the wheels. This is the friction force between the wheels and the road surface; μ_{RR} is the rolling resistance coefficient equal to $\mu_{RR} = 0.02$ for trac-

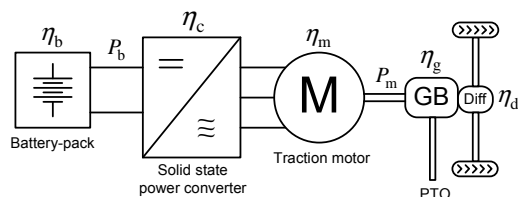


Fig. 1: Power system diagram of electric tractor.

tors travelling on gravel roads. The second term is the force required to accelerate the tractor. The third term is the hill climbing force. This is the force required to drive up an incline of angle θ . Note that in (1) the force due to aerodynamic drag is assumed to be negligible. From (1) the tractive effort power to drive the tractor is given by

$$P_{te} = F_{te} v, \quad (2)$$

where v is the instantaneous velocity of the tractor. The powers required to be delivered by the electric motor and the battery-pack are calculated by means of the subsystem efficiencies as given in Table 1. These powers and efficiencies are explained in Fig. 1. Hence, the electric motor and battery-pack output powers with the tractor in motoring mode are respectively calculated as

$$P_m = \frac{P_{te}/\eta_d + P_{PTO}}{\eta_g} \quad \text{and} \quad P_b = \frac{P_m}{\eta_m \eta_c}. \quad (3)$$

The efficiency of the differential, η_d , is assumed in the simulation as 100 %. The PTO-power is taken as either zero or else as a constant equal to the power consumed by the spraying pump.

Table 1: Assumed Subsystem Efficiencies.

Motor efficiency	η_m	90 %
Power electronic converter efficiency	η_c	95 %
Gearbox efficiency	η_g	80 %
Differential efficiency	η_d	100 %

2.2 Lead Acid Battery Modelling

The simulation model used for the lead-acid batteries is based on the simplified circuit diagram shown in Fig. 2. The internal resistance of the lead acid battery does not vary greatly depending on depth of discharge, and can generally be found from the manufacturer's data sheet. The open circuit voltage, e , however is a function of the depth of discharge of the battery. This function for a 12 volt lead-acid battery at simulation time step n is given by [1]

$$e_{n(\text{lead-acid})} = N_c [2.15 - D_{n-1} (2.15 - 2)], \quad (4)$$

where N_c is the number of battery cells and D_{n-1} the depth of discharge at time step $n-1$. The calculation of the depth of discharge using the modified Peukert model [2] is described in more detail in the Appendix. Knowing the battery-pack output power P_b from (3) and the battery-pack open circuit voltage e_n from (4), the discharge current at time step n can be calculated according to the circuit of Fig. 2 and solving the quadratic equation as

$$i_n = \frac{e_n - \sqrt{e_n^2 - 4R_i P_b}}{2R_i}. \quad (5)$$

2.3 Lithium-ion Battery Model

The performance of lithium-ion cells is affected by various factors. These include temperature, rate of

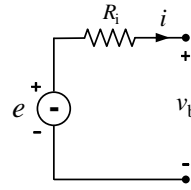


Fig. 2: Simplified battery equivalent circuit model.

discharge, and state of charge and age. This makes lithium-ion cells notoriously difficult to model. Once again we look at a simplified circuit model as shown in Fig. 2 to make modelling easier.

Unlike lead acid batteries the open circuit voltage and the internal resistance of lithium-ion cells vary non-linearly with depth of discharge. From [3] at time step n the open circuit voltage is given by

$$e_{n(\text{Li-ion})} = N_c [-1.031e^{-35D_n} + 3.685 + 0.2156D_n - 0.1178D_n^2 + 0.321D_n^3] \quad (6)$$

and the internal resistance by

$$R_{in(\text{Li-ion})} = N_c [0.1562e^{-24.37D_n} + 0.07446]. \quad (7)$$

The depth of discharge is calculated at each time step n by calculating the charge removed from the battery as explained in the Appendix. The battery current is calculated using (5) again.

3. DRIVING CYCLE

As explained earlier the tractor model requires details of the tractor and the velocity that it is travelling at to calculate the power required from the battery pack. It was thus necessary to collect data on the velocity driving cycle of the tractor for use in the electric tractor drive cycle simulation.

Due to lack of professional equipment a Samsung Galaxy S3 Mini and the My Tracks app from Google was used for this purpose. The app logs velocity, position, bearing and altitude information. The smartphone was mounted in the cab of a tractor at the Hartenberg Wine Estate when it went out to spray the vineyards. The velocity data was used to construct the driving cycle as shown in Fig. 3.

From Fig. 3 initially the velocity is quite high as the tractor travels to the vineyard block. After about 15 minutes it can clearly be seen that the tractor drives down a row of vines, slows and turns, and then repeats the drive.

The other part of the driving cycle that is important for this application is the incline that the tractor needs

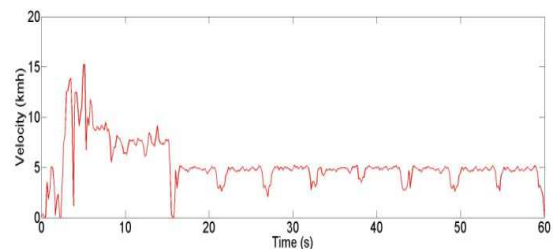


Fig. 3: Velocity versus time of a vineyard tractor.

to drive up. This is very applicable to vineyard tractors in the Stellenbosch area as many wine farms are located in mountainous areas. It was, however, not possible to gather data of the incline using the equipment available. To overcome this, two cases for incline driving cycle were considered. The first is a 0° incline everywhere to represent a completely flat terrain. The second scenario is a vineyard where the rows of vines lie on a constant incline of $\theta = 20^\circ$, used in (1). In this case the tractor climbs the incline as it drives up one row, and then goes down the incline in the next row.

4. BATTERY ENERGY REQUIREMENT

The next big challenge is to determine the amount of energy that is required from the battery pack. Three different methods are used in order to ensure the integrity of the results. From interviews at wine farms in the area it was found that the worst case working situation for vineyard tractors is when irrigation and herbicide and pesticide spraying needs to be done. During this type of operation the tractors drive out in the vineyards for up to 8 hours per day, powering a spray pump via the PTO. This is the working condition considered in the calculation of the energy required from the battery pack.

4.1 Average Fuel Consumption Method

The average fuel consumption of tractors used for spraying was obtained from interviews with viticulturists at wine farms in the area. The average figure for hourly fuel consumption was found to be 5 l/hr. This figure together with the energy density of diesel fuel was used to calculate the average power consumption from the diesel fuel. This was found to be 48 kW. The energy consumption for an 8-hour working day is thus 384 kWh.

The losses in the diesel engine next need to be considered. As the efficiency of diesel engines varies greatly depending on how they are being driven, three cases of efficiency are considered as given in Table 2. With these efficiencies the average diesel-engine power output is calculated, which is also the average power output of the electric motor P_m as given in Table 2. Assuming efficiencies as in Table 1, the average power output of the battery-pack is calculated according to (3). From this the required average energy output of the battery-pack for a working day is calculated as given in Table 2. This indicates, thus, a required energy output per day of between 90 – 180 kWh.

Table 2: Battery-pack Power and Energy Requirement of the Electric Tractor using the Average Fuel Consumption method.

Diesel engine efficiency (%)	20	30	40
Average power output P_m (kW)	9.6	14.4	19.2
Average battery power output P_b (kW)	11.2	16.8	22.5
Battery energy output required per working day (kWh)	90	134	180

4.2 Duty Cycle Method

The second method is to make use of the duty cycle of a tractor. This considers the engine speed and torque that the tractor operates at when in use. The Environmental Protection Agency (EPA) in the USA has done studies where this data was collected for agricultural tractors [4].

Using the EPA data of engine speed and torque the instantaneous power that is being output by the engine can be calculated. A plot of this is shown in Fig. 4. This instantaneous power divided by the electric motor and power converter efficiencies can be integrated over 8 hours to get the energy required from the battery pack for a working day. This calculation comes out as 243 kWh for a working day, which is substantially higher than the results of Table 1.

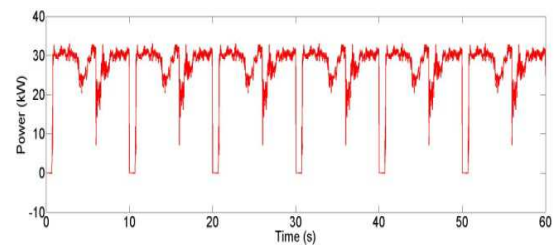


Fig. 4: Power (P_m) versus time using the duty cycle method.

4.3 Simulation Method

The third method used to estimate the energy output required from the battery pack is through simulation using the tractor and battery models of Section 2. The tractor model is used together with the driving cycles to determine the amount of energy required to drive the tractor. The constant PTO power drawn by the spray pump is also included in this simulation. The simulation result of the battery output power P_b versus time for a zero incline ($\theta = 0^\circ$) is shown in Fig. 5. Integrating this power over time we get a result of 206 kWh for a working day. This result matches well in between the results of the average fuel consumption and duty cycle methods.

The constant incline case must also be considered as this should yield a significantly higher energy requirement. The result of the instantaneous power simulation with $\theta = 20^\circ$ is shown in Fig. 6. The power requirement is significantly higher when the tractor has to climb up a hill. The energy required from the battery pack in this case was 258 kWh per working day, which is 24 % higher than with the zero incline case. Note, however, that regenerative power was not taken into account in this case.

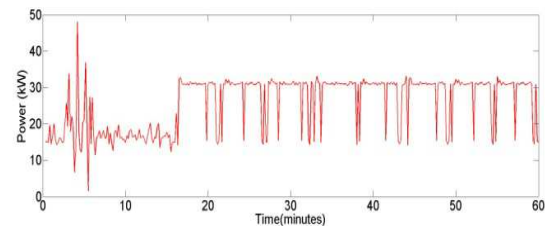


Fig. 5: Battery-pack output power (P_b) versus time for zero incline using the simulation method.

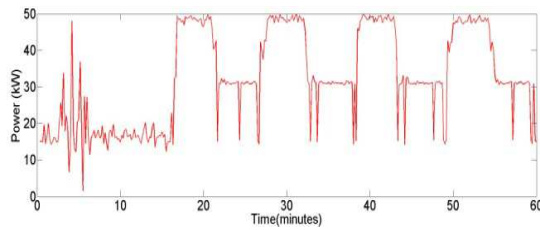


Fig. 6: Battery-pack output power (P_b) versus time for constant incline using the simulation method.

5. CASE STUDY

As a case study a battery pack is designed and evaluated for a vineyard tractor that is popular in the area. The John Deere 5325N shown in Fig. 7(a) is considered. The specifications of this tractor are given in Table 3. This is a narrow version of the 5325, made for use in vineyards and orchards. The PTO of the tractor is shown in Fig. 7(b).



(a)



(b)

Fig. 7: (a) John Deere 5325N vineyard tractor and (b) PTO for the spraying pump.

Table 3. John Deere 5325N Tractor Specifications.

John Deere 5325N	
Power	50 kW @ 2400 rpm
PTO	42 kW @ 2400 rpm
Torque	245 Nm @ 1400 rpm
Fuel Capacity	126.5 l
Weight	2735 kg

5.1 Electric Motor Design

Firstly the electric motor that is used to drive the tractor must be considered. This motor must match

the specifications of the diesel engine as closely as possible in order for the existing drive train to function properly.

The electric motor must be designed to produce 245 Nm of torque at 1400 rpm. It must also be able to deliver 50 kW of power at 2400 rpm. Hence, the proposed motor must be able to produce

$$P_{m(\text{rated})} = 2400(245)\pi/30 = 61.6 \text{ kW}$$

of rated power at rated speed.

Due to its relative high efficiency and its robustness a reluctance synchronous motor (RSM) is considered for this application. The torque density of totally enclosed RSMs varies between 14 – 20 kNm/m³ depending on the outer diameter of the motor stack [5]. A figure of 20 kNm/m³ is used, which translates to a volume of $0.245/20 = 0.0123 \text{ m}^3$.

The ratio of the length to diameter of the motor stack is chosen to be 2:1. A longer, narrow machine is chosen so as to intrude as little as possible in the space available for the battery pack. The design of the motor is summarised in Table 4. The calculation of the mass of the motor is done using the average density of copper and iron. This is to account for the iron and copper used in the construction, as well as any brackets and attachments that may be added.

Table 4. Summary of Electric Motor Design Parameters.

Stack length	397 mm
Stack diameter	199 mm
Stack volume	0.0123 m ³
Mass	100 kg
Rated Torque	245 Nm @ 1400 rpm

5.2 Battery Pack Design

The average of the daily energy required for a flat terrain and that for a constant incline terrain are used in the design. This is calculated from the simulation results in Section 4.3 as $W_b = (206+258)/2 = 232 \text{ kWh}$.

The specifications of the lithium-ion cells and lead-acid batteries considered in the design are given in the Appendix. The number of lithium-ion cells needed to meet the energy requirement of 232 kWh is

$$N_{c(\text{Li-ion})} = \frac{232 \text{ kWh}}{3.4 \text{ V} \times 100 \text{ Ah}} \approx 682 \text{ cells}.$$

Similarly the number of lead acid batteries is

$$N_{c(\text{Lead-acid})} = \frac{232 \text{ kWh}}{12 \text{ V} \times 110 \text{ Ah}} \approx 176 \text{ cells}.$$

These numbers are completely unfeasible due to size and mass constraints. The mass available for the battery pack is limited to the mass of what is removed from the tractor after the mass of the electric motor has been considered. The diesel engine is also structurally integral to the tractor, i.e. the front wheels are attached to the body by the engine. When considering the reinforcement that must be added to keep the tractor together, then only 480 kg mass is available

for the battery pack. This was found to be the main constraint in the design of the battery pack. Based on this constraint the number of lithium-ion cells is calculated as

$$N_{c(\text{Li-ion})} = \frac{480 \text{ kg}}{3.3 \text{ kg}} \approx 145 \text{ cells}.$$

The energy that can be supplied by a battery pack of this size is: $W_b = 145 \times 3.4 \text{ V} \times 100 \text{ Ah} = 49.3 \text{ kWh}$. The number of lead acid batteries that can be accommodated is

$$N_{c(\text{Lead-acid})} = \frac{480 \text{ kg}}{39 \text{ kg}} \approx 12 \text{ cells}.$$

Hence, the energy that can be supplied by the lead-acid battery pack is only $W_b = 12 \times 12 \text{ V} \times 110 \text{ Ah} = 15.8 \text{ kWh}$.

The final consideration that must be made is whether the battery packs are able to supply the maximum power of 50 kW to the tractor electric drive system. The maximum power that can be supplied by the lithium-ion battery pack is

$$P_{b(\text{Li-ion})\text{max}} = 145 \times 3.4 \text{ V} \times 150 \text{ A} \approx 74 \text{ kW}.$$

For the lead acid battery pack the maximum power that can be supplied is

$$P_{b(\text{Lead-acid})\text{max}} = 12 \times 12 \text{ V} \times 110 \text{ A} \approx 16 \text{ kW}.$$

At this stage it becomes apparent that the lead-acid batteries cannot supply enough power to meet the maximum power output of the motor. The lead-acid batteries can supply higher impulse currents, but these high currents cannot be sustained for the amount of time that the tractor requires the maximum power from the motor.

5.3 Depth of Discharge Simulation

The designed lithium-ion battery-pack is simulated to determine the theoretical maximum range of the tractor under different operating conditions. The zero incline and constant incline driving cycles are simulated for a spray tractor powering a spray pump via its PTO. A range simulation is then also done using these two driving cycles for a tractor with an unconnected PTO, however still carrying an extra mass of 1000 kg. This could be e.g. a tractor that is used to transport grapes, labourers or equipment. The results of these simulations are shown in Figs. 8 – 11.

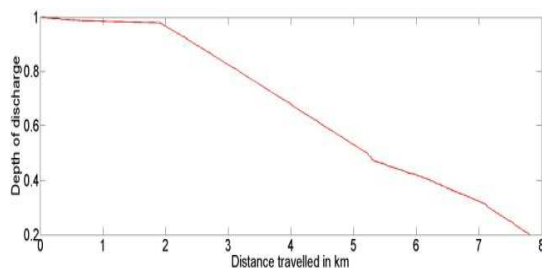


Fig. 8: Depth of discharge of Li-ion battery-pack versus distance travelled by electric tractor on a flat surface.

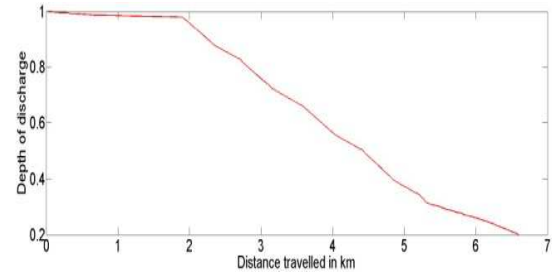


Fig. 9: Depth of discharge of Li-ion battery-pack versus distance travelled by electric tractor for a constant hill incline.

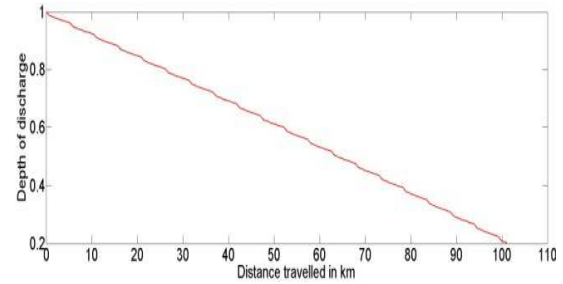


Fig. 10: Depth of discharge of Li-ion battery-pack versus distance travelled by electric tractor on a flat surface with no PTO power.

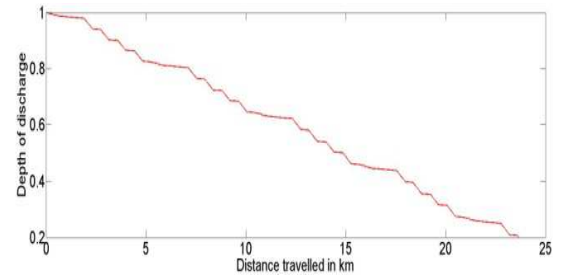


Fig. 11: Depth of discharge of Li-ion battery-pack versus distance travelled by electric tractor for a constant incline with no PTO power.

The simulation results of Figs. 8 - 11 show the drastic effect the PTO power has on the discharge-travel distance.

6. CONCLUSION

Conclusion 1:

It becomes apparent from the simulations of the system with the PTO power being drawn that with current battery technology the energy required for a spraying tractor cannot be met using only batteries.

There are a few options that can be considered to improve the range of the electric tractor as follows:

- Regenerative braking would increase the range, but not by the amount required.
- A hybrid electric tractor using solar panels or a gas turbine to recharge the battery-pack can be used. The space and weight constraints that are faced make this option difficult.
- A modular battery pack combined with battery changing stations in the vineyards can be used. This becomes difficult due to the large number of tractors that may be out at the same time that would call for an unrealistic number of battery packs.

- Overhead lines powering the tractors are an option. This would also become expensive and safety will have to be taken into account.

Although the energy density of lithium-ion batteries is increasing rapidly as shown in Fig. 12, and with some manufacturers claiming energy densities up to 400 kWh/kg, it still does not come close to the required energy density.

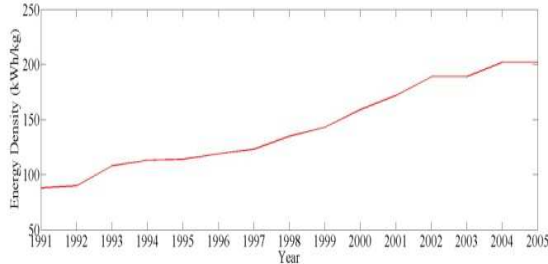


Fig. 12: Energy density development of lithium-ion batteries from 1991 to 2005.

Conclusion 2:

Ultimately the electric tractor appears to be feasible. The main problem that needs to be addressed is the large power of the PTO. The range of the tractor is greatly increased when the battery pack does not have to supply power to the PTO. A better way to look at this problem may be to consider more energy efficient ways of spraying. Alternatively the battery pack can be used only to drive the tractor and a dedicated power source can be used to power the spray pumps. This can be in the form of a high efficiency diesel engine or even possibly a gas turbine.

ACKNOWLEDGEMENTS

The authors acknowledge Mr Wilhelm Joubert from Hartenberg Wine Estate (Stellenbosch area) for assisting with the data collection and Mr Richard Haines, from the Department of Mechanical and Mechatronic Engineering at the Stellenbosch University, for giving insight into the working and efficiency of diesel engines.

APPENDIX

Specifications of batteries:

Table 5. Specifications of Li-ion Battery Cell.

Winston Battery Limited Lithium-ion battery WB-LYP100AHA	
Maximum cell voltage	4 V
Minimum cell voltage	2.8 V
Average cell voltage	3.4 V
Capacity	100 Ah
Maximum discharge current	150 A
Nominal Discharge current	50 A
Weight	3.3 kg
Dimensions	67 x 142 x 218 mm

Table 6. Specifications of Lead-acid Battery Cell.

Trojan 5SHP-Gel Lead acid battery	
Operating Voltage	12 V
Capacity	110 Ah
Maximum discharge current	110 A
Nominal Discharge current	22 A
Weight	39 kg
Dimensions	344 x 171 x 279 mm

Calculation of depth of discharge: Lead-acid

The depth of discharge of the lead acid battery pack for each time step is calculated using

$$D_n = \frac{CR_n}{C_p} \text{ with } C_p = I_n^k T_n \text{ and } k = \frac{\log T_2 - \log T_1}{\log I_1 - \log I_2}.$$

C_p is the Peukert capacity. All the current and time values are nominal values that can be found from the manufacturer data sheet. CR_n , which is the charge removed from the battery pack at time step n , is calculated by

$$CR_n = CR_{n-1} + \frac{\Delta t i_e^k}{3600} \text{ where } i_e = i_n \left(\frac{i_n}{I_n} \right)^{k-1},$$

where i_n is calculated from (5) using (4).

Calculation of depth of discharge: Lithium-ion

The depth of discharge of the lithium-ion battery pack for each time step is calculated by

$$D_n = D_{n-1} - \frac{i_n \Delta t}{3600 C_{cap}},$$

where i_n is calculated from (5) using (6) and (7). C_{cap} is the nominal capacity of a cell.

REFERENCES

- [1] J. Lowry and J. Larminie, *Electric Vehicle Technology Explained*, Chichester: Wiley & Sons Ltd., 2003.
- [2] S. Abu Sharkh and D. Doerfel, "A critical review of using Peukert equation for determining the remaining capacity of lead acid and lithium-ion batteries", *Journal of Power Sources*, vol. 155, pp. 395-400, 23 Jun. 2005.
- [3] O. Erdinc, B. Vural and M. Uzunoglu, "A dynamic lithium-ion battery model considering the effects of temperature and capacity fading", *Proceedings of International Conference on Clean Electrical Power*, Capri, 2009.
- [4] "United States Environmental Protection Agency", USA, Available at: <http://www.epa.gov/otaq/regs/nonroad/nrcycles.htm> (accessed 18 Oct. 2013).
- [5] M.J. Kamper, *Design Optimisation of Cageless Flux Barrier Rotor Reluctance Synchronous Machines*, PhD dissertation: Stellenbosch University, 1996.

DESIGN AND DEVELOPMENT OF A PROTOTYPE SUPER CAPACITOR POWERED ELECTRIC BICYCLE

K. Malan, M. Coutlakis and J. Braid*

* School of Electrical and Information Engineering, University of the Witwatersrand, Johannesburg

Abstract: The design and development of a prototype super-capacitor (super-cap) powered electric bicycle (E-bike) is presented. An existing, general-purpose bicycle was retro-fitted with a brushed DC motor driving the front wheel, fitted with a super-cap bank capable of storing 74 kJ, and comprising a bi-directional motor driver for acceleration and regenerative braking. It was envisaged that the designed E-bike would fulfil the role of a campus commuter, whereby members of the university's community could utilise such E-bikes to traverse a large campus. Consequently, the range of the E-bike was not as important as the rapid and frequent charge cycling requirements, hence the benefits of using super-capacitors as an energy storage medium was exploited. The developed prototype E-bike, carrying a 55 kg cyclist, had a satisfactory range (pedalling-free) and top speed of approximately 1100 m and 23 km/h respectively. Two weaknesses of the design that need future consideration are the unbalanced charging of the series-connected super-capacitors and the inadequate response time of passive thermal fuses under short-circuit conditions of the super-cap bank.

Key words: Electric bicycle, E-bike, super-capacitor, regenerative braking.

1. INTRODUCTION

1.1 What is an E-bike?

An E-bike is a bicycle incorporating an electric motor for additional propulsion, in combination with the users' pedalling [1]. In the case of a *pedal-assisted* E-bike, the electric motor augments the user whilst in the case of a *power-on-demand* E-bike, the electric motor only provides power when the user requires, whether pedalling or not. Irrespectively, all E-bikes have pedals and a lack thereof would result in it being classified as an electric scooter or other electric vehicle [2].

In some countries legislation limits the motor size and or the E-bike's maximum speed; for example in the USA, these are limited to 750 W and 32 km/h respectively [1].

1.2 The Concept of a Campus Commuter

A typical university campus is subject to a significant amount of pedestrian traffic. Often, lecture venues are located relatively far from established parking areas. The time and energy spent on foot, daily, to traverse a typical campus is not insignificant; to improve the quality of campus life, a *campus commuter* in the form of an E-bike, is proposed.

The envisaged idea is that a fleet of E-bikes and associated charging stations, would be owned and maintained by the university, and be provided as a service to its members. The communal E-bikes would be distributed around the campus, typically at the prominent lecture venues and large parking areas. At each point, a dedicated rapid-charger would be available, to replenish the E-bike quickly, before its next use by another user.

The focus of this paper is on the design, development and evaluation of a suitable prototype E-bike.

2. BACKGROUND

2.1 Existing E-bike Solutions

Performance specifications of existing commercial E-bikes are summarised in Table 1.

Table 1: Typical Performance of Commercial E-bikes

Performance	Typical value and reference
Speed	15 to 29 km/h [3], 32 km/h [1]
Range	13 to 31 km [3], 16 to 80 km [1]
Motor power	150 to 500 W [3]
Charge time	2 to 6 hours [1]
Usable life-time	≤ 400 charge cycles [1]

All the E-bikes encountered in the literature survey use batteries to store between 50 Wh and 500 Wh (corresponding to 180 kJ and 1800 kJ respectively) of energy [1, 3]. The hill climbing ability is directly related to the motor's output power; typical performance up a 4 % slope is 16 km/h, with an 80 kg user mounted [1].

Although E-bikes are more efficient than say petrol scooters, there are some associated environmental concerns, in particular lead pollution [4]. In China 95 % of E-bikes use lead-acid batteries [4]. Manufacturing and recycling of these batteries results in around 1 and 2 % of the lead being "lost" in the processes respectively [4], resulting in lead pollution. For this reason, E-bikes are not entirely green. This problem is worsened as the usable life-time of most batteries is limited to a finite number of charge-discharge cycles, typically between 300 [4] and 400 [1]. Consequently, during the life of the E-bike, the battery bank may need to be replaced up to five times [4], thus compounding the problem.

2.2 Batteries versus Super-Capacitors

The recent demand for electric vehicles has resulted in the rapid improvement in battery technology [5]. Fundamentally however, the life and performance of batteries is limited by their electro-chemical process used to store the energy [6].

Typically, super-capacitors have energy densities ($\approx 10 \text{ Wh/kg}$) an order of magnitude lower than batteries, however their power densities ($\approx 10 \text{ kW/kg}$) are an order of magnitude higher [7]. Super-capacitors are thus suited for rapid charge and discharge applications. In addition, the number of cycles in their useful life is far superior, typically exceeding one million, compared to a mere one thousand for batteries.

Prevalent amongst current electric vehicle energy storage systems is the hybrid combination of batteries and super-capacitors. In this configuration, the batteries are used as the primary energy source whilst the super-capacitors are used to supplement sudden power requests [8, 9]; essentially making the best use of both technologies.

Recent research into super-capacitors utilising graphene nanostructures has indicated the possibility of producing capacitors with increased energy densities, comparable to lead-acid batteries (45.8 Wh/kg), whilst still maintaining their significantly higher power densities [10].

2.3 A Typical Campus Route

At the authors' resident university, a typical worst case campus route from the main student parking area to the prominent lecture venues was profiled. The elevation-vs-distance data is plotted in Figure 1. The total distance of the route is approximately 1100 m and the change in elevation is approximately 50 m.

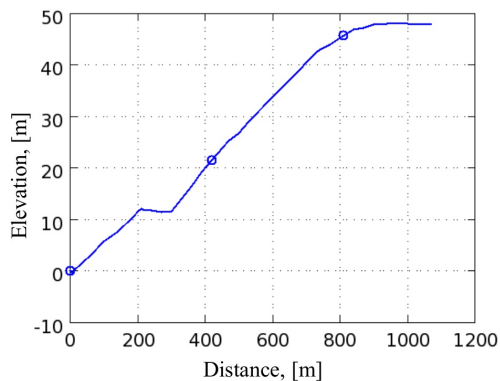


Figure 1: Elevation profile for worst case campus route.

From this profile, the steepest gradient en route is 6.0° whilst the average gradient is 2.6° ; the latter corresponding to an average slope of 4.5 %. From this data, the energy and power requirements of the E-bike are determined in section 4.1.

3. PROPOSED E-BIKE SOLUTION

3.1 Conceptual Design

For the campus commuter concept to be a success, the E-bike needs to fulfil certain fundamental requirements: it needs to be simple to use, rugged and reliable, safe, and offer a pleasant user experience. Since it can be assumed that the users would be familiar with riding a bicycle, an existing steel-tube chassis is chosen as a base from which to build up, naturally keeping the familiar pedals and brake levers. This allows the user to pedal-assist where necessary and offers a high degree of familiarisation. For safety reasons, the E-bike's performance needs to be limited in terms of its top speed, yet must be able to accelerate quickly enough to clear an intersection or cross a street. For the user's benefit, an interface displaying vital information (such as range remaining) is also required. Finally, to ensure that the campus E-bikes' availability are a maximum, the charging time needs to be kept to a minimum.

Since the alternative solution to the campus commuter concept would be a fleet of ordinary pedal-powered bicycles, this E-bike must offer to the user, better performance and a more pleasant experience than its contemporary.

3.2 Desired performance

The desired performance specifications for the E-bike are shown in Table 2. The range is as determined in section 2.3, the speed is based on the performance of the commercially available E-bikes in Table 1, and the acceleration is governed by that of a typical cyclist as given in [11].

Although not directly related to the desired performance of the E-bike, a charging time (from completely flat to full) deemed to be acceptable by the would-be users, has also been specified.

Table 2: Desired specifications for proposed E-bike.

Performance	Specification
Range	1100 m up a 4.5 % slope
Speed	20 km/h
Acceleration	$\geq 0.6 \text{ m/s}^2$
Charge Time	$\leq 1 \text{ minute}$

3.3 Assumptions Impacting the Design

In general, an 80 kg cyclist and a 25 kg E-bike are assumed and the specifications given in Table 2 must be satisfied or exceeded. The anticipated coefficients of drag and rolling resistance at the E-bike's top speed are assumed to be similar to that of a typical cyclist, as given in [12].

The user is anticipated to stop three times en route; erring on the conservative side, regenerative braking is neglected and the energy required to re-accelerate is assumed equal to the kinetic energy at travelling velocity. The E-bike is designed to operate in a *full assist* mode such that the user

need only pedal to extend their range i.e. pedalling is not essential for operation. Therefore, the energy required to satisfy the range stipulated in Table 2 must be sourced from the stored electrical energy.

4. DESIGN OF PROTOTYPE E-BIKE

A system level block diagram of the prototype E-bike is shown in Figure 2.

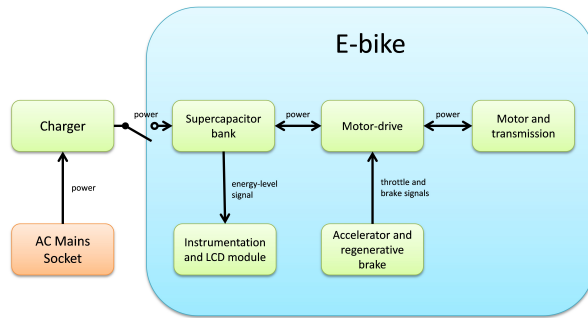


Figure 2: System level block diagram of the E-bike.

To aid familiarisation and safety, a fundamental decision was made to keep the existing system (pedal drive and mechanical brakes) de-coupled from the retro-fitted system (electric propulsion and regenerative braking): the rear wheel remains driven by the pedals and is mechanically braked by the left-side brake lever, whilst the front wheel is motorised and regenerative braking is actuated via the right-side brake lever.

4.1 Energy, Power and Acceleration

The potential energy (mechanical) required to overcome the height gain, the drag loss and that required for acceleration, are summed to 64 kJ. A typical 500 W permanent magnet brushed DC motor has an efficiency of 77 % [13], loosely assumed to remain constant across its operating range. The required motor driver would typically be 80 % efficient. This results in an energy requirement of 102 kJ (electrical).

For a 25 kg E-bike mounted with an 80 kg user, to climb a 4.5 % slope at 20 km/h, a power of 250 W (mechanical) is required. As a bench mark, a cyclist's acceleration from standstill is typically between 0.6 and 0.8 m/s² [11], requiring a wheel-surface contact force of at least 63 N for the 105 kg combination.

4.2 Choice of Energy Storage

Super-capacitors are generally used to supply or store peak power rather than as a form of primary energy storage [14]. However, their performance increase over the years, high cycling ability, low maintenance costs, fast possible recharge times and the prospect of future improvements has led some researchers to consider super-capacitors as primary energy sources in some applications, including a short range electric bus [15]. Since the energy densities of super-capacitors (5.4 Wh/kg [16]) are significantly lower

than that of batteries (140 Wh/kg for lithium-ion [17]), if the range requirement of the E-bike was any further than specified in Table 2, the use of super-capacitors as the primary energy storage medium would not be feasible.

Exploiting their rapid charging ability and high number of useful cycles, super-capacitors were selected since a practically sized 6 kg bank could store the required 102 kJ [16]. In addition, they are more readily available and perhaps safer than other alternatives, such as flywheels. With 95 % of the super-capacitor's stored energy being extractable, to satisfy the energy requirements of section 4.1 this brings the estimate to 107 kJ (electrical).

Using readily available 350 F, 2.7 V super-capacitors, a total of 87 pieces would be required, comprising three parallel strings of 29 each. At a cost of roughly R100 per piece, it was decided for demonstration purposes, to limit the super-cap bank to 58 capacitors (i.e. two strings of 29 each) with a storage potential of 74 kJ.

4.3 User Controls and Interface

An acceleration signal from the user is derived from a twist-grip actuator on the right-side of the handlebar, much like that of a motorcycle. When the right-side brake lever is squeezed by the user, a signal to initiate regenerative braking is triggered, and braking at a rate proportional to the amount of activation is undertaken.

The user interface comprises a handlebar-mounted unit that indicates the current level of charge, speed and distance, and estimated remaining range.

4.4 Motor Driver

A motor driver is required to allow bi-directional power flow between the super-cap bank and the motor. Power flow *to* the motor is controlled via the accelerator twist-grip whilst power flow *from* the motor is controlled via the regenerative brake lever. Although this task is usually simple in the case of a DC machine fed from a constant voltage, it is slightly more complicated with the super-cap bank's variable voltage.

4.5 Motor and Power Transmission

Since a 500 W DC machine (briefly mentioned earlier) that would satisfy the power requirements above was readily available, it was used in the prototype E-bike. From the nameplate, the machine produces 3.82 Nm of torque at its rated speed of 2500 rpm, when supplied with 36 V and drawing 18 A. A pair of sprockets was also available; a gear ratio of 15:1 would be required to reduce the speed and increase the torque to the specified values.

4.6 Rapid Charger

A charger is required to replenish the super-cap bank from the electrical mains supply. A custom designed charger was chosen in order to exploit the fast charging capability of the super-capacitors. The rated charging current of the super-capacitors is 20 A [16], therefore a constant current charging algorithm would be ideal.

5. IMPLEMENTATION OF PROTOTYPE

The prototype E-bike is pictured in Figure 3.



Figure 3: Implemented prototype E-bike.

5.1 Super-cap Bank and Charge Balancing

The prototype E-bike's super-cap bank comprises 58 capacitors, arranged in two parallel strings of 29 each. This configuration was chosen to avoid excessive current levels at the lower voltage range but also to avoid an excessive amount of series connections, to limit the number of balancing circuits should these need to be added in the future. The resulting voltage range from 16 V to 78 V means that 95 % of the 74 kJ of stored energy can be extracted from the super-cap bank.

The two strings of super-capacitors are soldered onto two PCBs and are vertically stacked to form a neat and compact super-cap bank. The complete bank is mounted inside a weather-proof box and mounted on a purpose-built aluminium carrier, overhead the rear wheel.

The tolerance in capacitance of each super-capacitor is typically about 15 %. This impacts the charging strategy in that, when charged by the same current in a series-connected string, some capacitors would be charged to higher voltages than others. Although various voltage balancing methods exist [18], the simplest method to prevent over-charging is to de-rate the maximum voltage of the bank. Therefore, the super-cap bank is charged to a maximum of 70 V.

To prevent catastrophic fault currents flowing should the super-cap bank be accidentally short-circuited, a 60 A thermal fuse was installed between the super-capacitor strings and the bank's connection terminals.

5.2 Motor and Power Transmission

The existing motor was mounted directly above the front wheel, supported by a steel sub-frame, connected to the wheel's axle and the chassis's front fork. The larger of the existing sprockets was mounted flush against the front wheel's hub. Finally, the motor and wheel were linked with an ASA25 type chain.

The sprockets available had a tooth ratio of approximately 6:1 which was far lower than the desired ratio of 15:1. Sourcing a larger ASA25 sprocket at short notice proved difficult, so to compensate for the reduced torque, the original 26" wheel was temporarily replaced with a smaller 16" wheel from a children's bicycle (noticeable in Figure 3). As a result, the effective gear ratio improved to approximately 10:1. The smaller front wheel resulted in the added benefit of making the E-bike easier to mount, and provided better traction by shifting more of the user's mass onto the front wheel.

5.3 Motor Driver Circuit

The permanent magnet brushed DC motor only requires two-quadrant operation: both driving and braking in the forward direction. A bi-directional Buck-Boost Cascade as described in [19] is very well suited to this application. The structure of this converter is shown in Figure 4. This topology can buck or boost in either direction and thus easily allows both acceleration and regenerative braking due to the bi-directional nature. The ability to step up or step down in either direction is extremely flexible. This capability allows the super-cap bank to be used over a large voltage range that extends above and below the motor's rated voltage, and also allows regenerative braking at any super-cap bank voltage and at any motor speed.

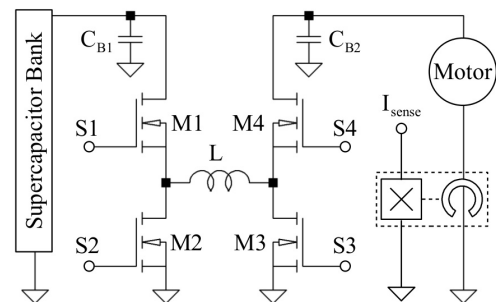


Figure 4: Topology of bi-directional motor driver.

In Figure 4, the MOSFET drive signals S1 to S4 are generated by bootstrap MOSFET driver ICs. MOSFETs M1 and M4 require gate drivers with 100 % duty cycle capability so simple floating fly-back supplies are used to power the bootstrap ICs. The motor current is sensed by a bi-directional Hall effect current sensor.

As suggested in [19], the accelerator and brake inputs provide a torque reference signal. Since the DC motor's torque is directly proportional to its armature current, the current is measured and controlled relative to the reference signals.

A PIC16F1827 microcontroller is used to control the motor driver since it has four PWM generators, sufficient analogue channels and is cheap. Closed loop control is necessary between the accelerator or brake input and the PWM signals due to the wide variation of the super-cap bank voltage. Initially, the microcontroller selects one of the four buck/boost operating modes according to the brake state and the voltages across the super-cap bank and motor.

The microcontroller implements a simple integration of error between the desired and measured motor currents, which is used to determine the duty cycle. A duty cycle of more than 100 % in buck operation or less than 0 % in boost operation is used to change between the converter modes.

A motor starting current of 40 A is allowed to provide sufficient starting torque. Maximum current is limited to the motor's rated current of 18 A once the motor terminal voltage has reached its rated 16 V.

Accelerator and Regenerative Brake:

The twist-grip accelerator is implemented by a single-turn potentiometer, axially connected to a knurled tube, that loosely fits over the existing handlebar. The grip's travel is limited by a grub screw and a torsion spring returns it to its zero position.

The regenerative brake makes use of the existing brake lever but replaces the cable with a micro-switch and linear potentiometer. The micro-switch is used to detect and initiate braking and signals the motor driver microcontroller to undertake the regenerative braking operation (which takes preference over the accelerating operation); the amount of braking being proportional to the linear potentiometer's output.

5.4 User Interface

The instrumentation consists of a 16 character, 4 line, alphanumeric LCD screen which displays the energy remaining in the super-cap bank, the speed of the E-bike and the distance travelled. All the computation and interfacing with the screen is achieved with a PIC16F690 microcontroller.

Using a potential divider, a voltage proportional to that of the super-cap bank is measured and the corresponding amount of energy is computed. A small magnet attached to one spoke of the front wheel provides a pulse per revolution signal via a reed switch mounted on the front fork. From the period between the pulses, the angular velocity of the wheel and hence speed of the E-bike is determined. Similarly, the distance travelled is computed from the number of pulses counted since the last reset. Although not implemented, the range remaining can be easily determined from the three functions above.

5.5 Rapid Charger

A Two-Switch Forward Converter [20] was chosen to charge the super-cap bank. This topology was chosen as it is often employed in arc-welding machines which perform a similar purpose of controlling a high output current [20]. Compared to other viable topologies, this one offers two advantages: it requires two fewer switches than the Full-Bridge Converter and does not require the input capacitors as in the Half-Bridge Converter.

Essentially the charger is designed as a constant current source that monitors the output voltage in order to prevent

over-charging the super-cap bank. The charger is intended to charge three parallel strings simultaneously, each at 20 A, and was therefore designed to output up to 60 A.

With the intention of powering the charger from a domestic AC outlet, the charger had a preset upper power limit that was implemented to avoid tripping the mains supply. The charger circuit is controlled with a dsPIC30F2011. Although it was fairly cheap, it had far superior capabilities when compared to the low-end devices. The transformer and inductor of the charging circuit were hand-wound onto ETD59 cores, using 2 mm copper wire to minimise Ohmic losses.

Rated at 3 kW, the charger is capable of replenishing the E-bike's super-cap bank in under 30 seconds, well within the requirement of Table 2.

6. EVALUATION AND RESULTS

6.1 Measured Performance

The prototype E-bike was evaluated on a level, oval-shaped course, by users of different masses; the results are shown in Table 3.

Table 3: Measured performance for the prototype E-bike.

Mass of user (kg)	55	65	100
Energy used (kJ)	54.3	53.8	55.0
Distance travelled (km)	1.09	1.03	0.90
Economy (km/MJ)	20.1	19.1	16.4
Max. speed (km/h)	22.6	20.8	18.4

Although not specifically tested with an 80 kg user, the results above show that the prototype E-bike satisfies the requirements for range and speed as specified in Table 2 very well. As one would expect, the performance diminishes as the specified mass of the user is exceeded.

The E-bike's static force at standstill, with the motor drawing its starting current of 40 A, was measured to be 147 N, by means of a spring scale anchored to the rear of the bicycle. For an 80 kg user, this equates to an acceleration of 1.4 m/s^2 - more than twice the specified value - and improves the E-bike's hill climbing ability to a slope of 14.4 %.

6.2 Evaluation along Campus Route

The E-bike was evaluated along the route described in section 2.3, by a 55 kg user. Although the capacity of the super-cap bank had been reduced from 107 kJ to 74 kJ during the design stage, the E-bike was re-charged en route (the markers in Figure 1 show these points) and required a total of 126 kJ to reach the destination; significantly more than the estimated 107 kJ and despite the significantly lighter user. For an 80 kg user, an additional 12 kJ of potential energy alone would be required, ignoring system inefficiencies.

The large discrepancy can be attributed to two assumptions that were under-estimated: Firstly, the motor's efficiency

of 77 % is a maximum when delivering rated power only; at lower speeds, such as when hill climbing, the lower back EMF internal to the machine results in higher currents being drawn, and hence higher losses, both within the machine itself and the motor driver circuitry. Secondly, the friction and windage losses in the motor and power transmission are amplified by the gear ratio and result in a significant braking torque, making any pedal assistance by the user, quite demanding.

6.3 Motor Driver Efficiency

The bi-directional Buck-Boost Cascade proved to be very well suited as a DC motor driver. It can provide a starting current of 40 A and the use of the duty cycle ratio to change between buck and boost modes is novel and effective.

To test the efficiency, the motor was replaced with a 2 Ω , 600 W resistive load. The controller was programmed to give a constant output current, across a range of super-cap bank voltages, such that the load power remained approximately constant at 500 W. The results reveal an average efficiency of about 92 %, especially near the transition from boost to buck, at circa 30 V. At lower voltages, the higher input current results in increased losses.

6.4 Recovery of Energy during Regenerative Braking

Since the motor driver is symmetrical, its regenerative braking efficiency should be similar to the above. However, the system efficiency during regenerative braking is lower than expected due to the significant friction and windage introduced by the motor and power transmission, as described in section 6.2.

After driving the E-bike up the first segment (between the first two markers) of the route in Figure 1, it was free-wheeled back to the start whilst braking and 6.8 kJ of energy was recovered. This segment corresponds to a change in potential energy of approximately 17 kJ, implying a regenerative braking system efficiency of 40 % under these test conditions.

6.5 Future Improvements to Prototype

The prototype E-bike has subsequently had an appropriate 15:1 ratio sprocket mounted onto the original 26" wheel, replacing the smaller temporary wheel.

Over-Current Protection: During an accidental short-circuit of the super-cap bank, the time response of the thermal fuse proved inadequate. It is highly recommended that active over-current protection be employed to allow for a faster response time under fault conditions.

Charge Balancing: To prevent the possible over-charging of individual super-capacitors, the super-cap bank voltage was de-rated from 78 V to 70 V. As a result of this trade-off, the possible extractable energy reduced from 95 % to 80 %. A charge balancing circuit, such as those described in [18] would allow the charging of the super-cap bank to its full potential without running the risk of over-charging.

Regenerative Brake Lever: Whilst this worked effectively, the lack of tactile feedback that a typical cyclist is accustomed to whilst squeezing the brake lever may result in the mechanical failure of the internal potentiometer when squeezed too hard. A spring-loaded lever with a mechanical end-stop is recommended to provide the tactile feedback and prevent over-extension respectively.

Rapid Charger Interface: The super-cap bank was charged directly from the rapid charger via polarised connectors. For the envisaged campus commuter concept, it is proposed that a split core transformer be used, with one half of the core located inside the E-bike's chassis and the corresponding other half mounted on the bicycle stand at the charging station.

Tracking and Management of E-bike Fleet: With the addition of a GPS and suitable communication module, the whereabouts of the campus' fleet could be tracked for management purposes. For security purposes, using the GPS data, the operational area of the E-bikes may be confined to campus use only, for example.

7. CONCLUSION

The concept of a campus commuter, comprising a fleet of E-bikes, has been presented. This paper focuses on the specification and design of such a power-on-demand E-bike. A prototype E-bike that satisfied the 1100 m range and 20 km/h top speed was developed and tested. The E-bike comprises a super-cap bank of 58, 350 F capacitors providing 74 kJ of energy storage, and a 500 W permanent magnet DC motor driving the front wheel. A bi-directional motor controller allows for motoring and regenerative braking. In addition, a 3 kW rapid charger was also designed allowing the super-cap bank to be fully charged in under 30 seconds; the benefit of using super-capacitors as the primary energy storage medium clearly being exploited. Despite under-estimating the system inefficiencies, the results from the prototype E-bike appear promising, making the campus commuter concept a feasible possibility.

REFERENCES

- [1] A. Meutze and Y. Tan, "Electric bicycles - a performance evaluation," *IEEE Industry Applications Magazine*, vol. 13, no. 4, pp. 12–21, Aug. 2007.
- [2] J. Weinert, A. Burke, and X. Wei, "Lead-acid and lithium-ion batteries for the Chinese electric bike market and implications on future technology advancement," *Journal of Power Sources*, vol. 172, pp. 938–945, May 2007.
- [3] H. Oman, W. Morchin, and F. Jamerson, "Electric-bicycle propulsion power," *WESCON '95*, pp. 555–560, Nov. 1995.
- [4] C. Cherry, J. Weinert, and Y. Xinmiao, "Comparative environmental impacts of electric bikes in China," *Transportation Research part D*, vol. 14, pp. 281–290, 2009.
- [5] J. Voelcker, "Lithium batteries take to the road," *IEEE Spectrum*, vol. 44, no. 9.

- [6] A. Mirhoseini and F. Koushanfar, "Hypoenergy. hybrid supercapacitor-battery power-supply optimization for energy efficiency," *Design, Automation and Test in Europe Conference and Exhibition*, pp. 1–4, Mar. 2011.
- [7] C. Goh and A. Cruden, "Automated high current cycling test system for supercapacitor characterisation," *International Symposium on Power Electronics, Electrical Drives, Automation and Motion*, pp. 748–753, Jun. 2012.
- [8] M. Bertoluzzo and G. Buja, "Propulsion systems for light electric vehicles," *IEEE Transactions on Industrial Informatics*, vol. 7, no. 3, pp. 428–435, Aug. 2011.
- [9] E. Lomonova, A. Vandenput, J. Rubacek, B. d'Herripon, and G. Roovers, "Development of an improved electrically assisted bicycle," *37th IAS Industry Applications Conference*, vol. 1, pp. 384–389, Oct. 2002.
- [10] J. Lin, J. Zhong, D. Bao, J. Reiber-kyle, W. Wang, V. Vullev, M. Ozkan, and C. Ozkan, "Electrochemical supercapacitor based on flexible pillar graphene nanostructures," *69th Annual Device Research Conference*, pp. 91–92, Jun. 2011.
- [11] W. Pein, "Bicyclist performance on a multiuse trail," *Transportation Research Record 1578*, vol. 1578, no. 970616, pp. 127–131, 1997.
- [12] S. Brand and N. Ertugrul, "Electric assisted bicycles and measurement of real-time performance characteristics for power management strategies," *AUPEC Power Engineering Conference*, pp. 1–6, Dec. 2007.
- [13] (2013) Unite Motor, Traction motor (Brushed PMDC). [Online]. Available: <http://www.unitemotor.com/en/cp036.htm>
- [14] D. Sousa, P. Costa, and J. Dente, "Electric bicycle using batteries and supercapacitors," *European Conference on Power Electronics and Applications*, pp. 1–10, Sep. 2007.
- [15] K. Zhiguo, C. Zhu, Y. Shiyan, and C. Shukang, "Study of bidirectional dc-dc converter for power management in electric bus with supercapacitors," *Vehicle Power and Propulsion Conference, IEEE VPPC '06*, pp. 1–5, 2006.
- [16] (2013) Ioxus Inc., Series: Multi-Pin. [Online]. Available: <http://www.ioxus.com/ultracapacitors/>
- [17] A. Burke, "Batteries and ultracapacitors for electric, hybrid, and fuel cell vehicles," *Proceedings of the IEEE*, vol. 95, no. 4, pp. 806–820, Apr. 2007.
- [18] D. Linzen, S. Buller, E. Karden, and R. D. Doncker, "Analysis and evaluation of charge-balancing circuits on performance, reliability and lifetime of supercapacitor systems," *IEEE Transactions on Industry Applications*, vol. 41, no. 5, pp. 1135–1141, September/October 2005.
- [19] F. Caricchi, F. Crescimbeni, F. G. Capponi, and L. Solero, "Study of bi-directional buck-boost converter topologies for application in electrical vehicle motor drives," *Presented at the Applied Power Electronics Conference and Exposition*, vol. 1, pp. 287–293.
- [20] H. Niilo and T. Vaimann, "Two switch forward inverter for parallel-series resonance alternating (psa) converter for supplying electric welding arc," *10th International Symposium on Topical Problems in the Field of Electrical and Power Engineering*, pp. 140–144, Jan. 2011.

Topic F

Renewables and Alternative Energy

RETROSPECTIVE ANALYSIS OF BIOFUEL PRODUCTION IN AFRICA

C. Nyamwena-Mukonza

* Chipu Nyamwena-Mukonza: Institute for Economics and research on innovation/Business school/Tshwane University of Technology, 159 Nana Street, Pretoria, chiponyam2@yahoo.com

Abstract:

The introduction of Biofuels in Africa has been hailed as offering income generation opportunities for small-scale farmers in Africa, increasing energy supply and as a mitigating measure for the global warming. The surge in biofuel production has also been necessitated by continuous increase in oil prices and the uncertainty surrounding the future of fossil fuels. Aggressive policies across nations have been crafted to support biofuels production. However since their introduction biofuels have provoked fierce debates in some circles, economic viability remains a controversy, and production has not matched reality or projected figures. This paper presents that the introduction of biofuels in Africa was a knee-jerk response to the energy crisis, oil importing countries find themselves in. Retrospective analysis is purposively employed on selected countries in Africa, to critically analyse the benefits accrued from biofuels since their introduction, drawing from the experiences from Zimbabwe Mozambique, and Madagascar

Keywords: Biofuels, Africa, production, economic viability

1. INTRODUCTION

In the last decade there has been global increase in biofuel production. The introduction of biofuels in Africa has been hailed as offering income generation opportunities for small-scale farmers in Africa, increasing energy supply and as a mitigating measure for the global warming. The surge in biofuel production has also been necessitated by continuous increase in oil prices and the uncertainty surrounding the future of fossil fuels. Aggressive policies across nations have been crafted to support biofuels production.

According to [1]Cotula et al (2007), this expansion is driven by government targets for biofuel substitution in energy budgets for transport, driven in turn by concerns about high oil prices, prospects for rural development, export opportunities and means to mitigate climate change. Biofuels for a long time will continue to be earmarked as a solution to the perils of Africa and projections are that productions are set to increase Africa The greatest challenges that Africa faces is that though biofuels are being propagated not much data and evidence has been made available to the public domain regarding their success.

This paper agrees with the findings of [2]Pesket et al (2007:1) who reckon that, *“Whilst some of the factors facilitating, and impacts of, biofuels can be tracked at global level, its distributional impacts are complex, and point to the need for country-by-country analysis of potential poverty impacts.”* However since their introduction biofuels have provoked fierce debates in some circles, economic viability remains a controversy, and production has not matched reality or projected figures.[2,1]Pesket,(2007) contends that the development of biofuels has generated vigorous debate on economic and environmental grounds. The intention of the paper is to provide a retrospective analysis on some of the projects that have been undertaken in Africa and to assess how they have advanced and what are some of the challenges.

This analytical account is done so as to draw lessons and provide solutions to upcoming projects. The paper contributes to the debate on the role of biofuels as climate change mitigations measure and its ability to improve the

livelihood of farmers. Retrospective analysis was done through extensive review of literature and content analysis of documents, reports and browsing of the internet.

1. Setting the scene for biofuels in Africa

Food and Agriculture Organisation [3](FAO, 2000) states that biofuels are organic primary and or secondary generation fuels derived from biomass which can be used for the purpose for the generation of thermal energy by combustion or by other technology. They comprise purpose grown energy crops as well as multi-purpose plantations and by products residues and wastes. The introduction and use of biofuels is not a new phenomenon, but what is new are the strides in technology development which have facilitated greater access to biofuels such as ethanol, biodiesel and biogas. Bioethanol is an alcohol derived from sugar or starch crops (e.g. sugar beet, sugar cane or corn) by fermentation. Ethanol can be used in either neat form in specially designed engines, or blended with petroleum fuel. Biodiesel is derived from vegetable oils (e.g. rapeseed oil, Jatropha, soy or palm oil) by reaction of the oil with methanol. Biodiesel can either be burnt directly in diesel engines or blended with diesel derived from fossil fuels.

2.1 Biofuels and Agro fuels

The term ‘agro fuels’ was first coined by social movements in Latin America to describe the liquid fuels derived from food and oil crops produced in large-scale plantation-style industrial production systems. These agro fuels are blended with petrol and diesel for use primarily by motor vehicles. Biofuels on the other hand, are the traditionally used wood, dung and other biological materials that are mainly used for heating and cooking [4](Biofuel watch 2011). A better understanding of this diversity will promote a more balanced and evidence-based debate [2.1] (Cotula et al , 2008).

For this reason in this paper the term biofuels will be adopted, as it is easy to relate to and more so it’s a common term and often used by many governments as well as when formulating policy documents and strategies. In Africa the crops that have been used for biofuel purposes are jatropha and sugarcane so as not to run into problems with food security problems. Jatropha

has been promoted as a crop that thrives well on marginal lands and does not need much water, a situation which is common in Africa.

2.2 Biofuel production in Africa

This section highlights some of the projects that have been implemented in Africa for Biofuel process. The purpose is to illustrate the length and the breadth of biofuel production within the argument that a number of the projects that have been implemented so far has been a case of too fast and too furious, meaning that voracious efforts and ambitious targets were set, yet reality to date does not match the expectation or those efforts that had been set. A number of projects have been implemented in Mozambique, Malawi, Zimbabwe, South Africa and other African countries.

3.0 Malawi

In Malawi a number of biofuel projects have been established, especially projects which have to do with jatropha production. As far ethanol production of the biodiesel is concerned it's not a new phenomenon it has been there since the early 1982 although the production volume has fluctuated significantly over the years, what might be new might be the stride in technology development.[5] (Amigun B. , 2011) reckons that Malawi has very favourable economic conditions for ethanol due to government policy to reduce the volume of imported fossil fuels. Of particular interest, is the Malawian firm Bio Energy Resources Limited (Berl) which has launched a \$8-million jatropha-based biodiesel production plant in Lilongwe district. This is a consortium led by Dutch investors, and the plant will process 250 t of jatropha seeds a day to produce 5 000 l of biodiesel. The main source of jatropha carcus seeds are the local smallholder farmers who are expected to sell to the local market the by-product seedcake for use as a bio-fertiliser.it is alleged that thousands of farmers have already benefitted from the investment and are being contracted to plant ten million trees jatropha trees that are providing raw materials for the production plant. It remains to be seen to what extent the project has benefited the small scale farmers and improve their livelihood.

3.1 Mozambique

In an attempt to support biofuels, the government of Mozambique enacted policies to support the production of biofuels. Firstly it was the, the National Rural Development Strategy of 2007 which had specific objectives regarding biofuel development. the Strategy aims 'to promote the production, consumption, transformation and export of fuels alternative to the traditional ones, namely biofuels produced from crops such as sugarcane, sweet sorghum, sunflower, ground nuts, jatropha, among others' [6](GoM 2008).

However the strategy had its own technicalities mainly with regards as to how the communities and the farmers were to be incorporated in these projects. In 2009, A National Policy and Strategy for Biofuels was adopted in 2009 (Resolution No. 22) specifically to provide strategic policy orientation for the sector [7](Nhantumbo et al 2008).The policy framework was thus developed after through consultations from different stakeholders and after assessment studies had been done, hence in one way or the other the policy framework attempted to address the concern raised. This together with other progressive laws of the countries such as the land act (which catered for the land rights of the people), the environment, and the forestry act provided a sufficient legal framework in which biofuels could be considered. [7.1]Nhantumbo et al (2008), reckons that land zoning was done prior to implementing biofuel projects, the results of the national land zoning are being used to direct the investments of potentially available lands.

Mozambique 's minister of energy, Salvador Namburete, stated publicly that "36 million hectares of land could be used for biofuels without threatening food production, while another 41million hectares of marginal lands would be suitable for raising jatropha". Mozambique fits the profile set by mainstream institutions seeking land to buy or lease a land-abundant country where taking blocks of under-utilized territory is theoretically assumed not to result in livelihood disruption or displacement and the dispossession of local people. The reality is different, as became apparent after the Central African Mining and Exploration Company (CAMEC) announced that it was to invest US\$510million in 30,000 hectares of land in Gaza province in 2008 under a 50-year renewable lease. While the land in question wasn't under large-scale commercial use, a study by[8] Dr Jun Borrás and colleagues identified three key agricultural economic activities by the local communities: livestock raising by cattle herders, charcoal production and subsistence farming. The land also showed great potential for food production. A major component of CAMEC's project was non-irrigated jatropha for biofuel production. But researchers pointed out that while jatropha plants may survive on dry lands, they are unlikely to be productive at a level that is commercially viable. In October 2009, CAMEC announced that it was discontinuing its investment in biofuel projects and shortly afterwards, the Mozambican government closed the operation and began the search for new investors to develop the land.

3.3 Zimbabwe

Zimbabwe revived the Biofuels programme in 2005, essentially as a response to the energy crisis the country was facing. Biofuels from sugarcane were not a new phenomenon as the country was once involved in Biofuels before and after Independence until 1991 when drought put an end to it.The introduction of biofuels is being championed on the premises that they are able to solve the twin problems of energy crisis and environmental crisis. Some have interpreted that the

introduction of biofuels in Zimbabwe was a clear show that the country can survive even if the international community has imposed sanctions. Such was the high moral, frenzy wave that even a ministerial task force was set up to deal with Biofuels. National Oil Company of Zimbabwe (NOCZIM) was mandated to head jatropha production across the scale, through smallholder's farmers. At the height of this euphoria the jatropha plant was named the plant of the year by the forestry commission in 2006. Several nursery beds of jatropha and contracted farmers were set up. To top it all, a state-of-the-art biofuel processing plant and, the first of its kind in Sub-Saharan Africa, was built in Mount Hampden Mashonaland West Province. The plant is said to be the brain child of the Reserve bank Governor Gideon Gono, and it has a 50% stake of the South Koreans. For a while it was thought that indeed Zimbabwe had found a solution to its perennial problems of energy, and what a cost cutting measure to its meager foreign currency. Mozambique had to send a delegation to tour the country, to witness the plant and the works of the miracle crop (jatropha) so that they can replicate it in their country. A visiting Brazilian delegation hailed the bio-diesel manufacturing plant in Mount Hampden describing it as a positive development that will result in huge agricultural production and value addition of farming produce.

Unfortunately, four years down the line there is nothing to show off from the plant and to make matters worse, Reserve Bank has since sold its 50% stake in the plant. NOZIM which was tasked to contract and buy jatropha has since abandoned the project leaving the farmers whom they had promised to give all the necessary support deserted. The authorities have acknowledged that the whole project was not properly planned hence the need to go back to the drawing board and the need to do thorough research. Feedstock availability has been sighted as the major problem at the plant.

With the aid of retrospection one would ask the following question; where else has jatropha produced miracle result, or where else had theory of jatropha matched reality? Much has been said about this miracle crop, but its economic viability is still a controversy. It has been touted as a crop that grows well in marginal lands, but one project in Mozambique, was abandoned after realising that the soils are not good enough. Critics of biofuels are scared of its threats to food security and environmental degradation.

Taking a critical look at other countries like Madagascar which is also complaining about its jatropha plantations, where a UK GEM Biofuels company had invested in Jatropha Plantation but they have not fared as was projected. An internal review has made it clear that despite having planted 55,737 hectares of Jatropha in Madagascar between 2007 and 2009, a lack of resources has resulted in significantly less success than had been hoped [9] (Biofuels Digest, April 2012). It is amply highlighted that Low intervention and maintenance following planting has resulted in a lower than anticipated number of plants reaching maturity and

producing oil-bearing seeds. The Board has commissioned external agronomic consultants to conduct a full review of both the Company's plantations in Madagascar and to assess the potential of its land bank for other crops. So jatropha whether by smallholder farmers or by plantations are not as rose tinted as they have been portrayed to be.

The introduction of ethanol on the market on the first of November 2011 saw other fuels dropping in price, indeed it was being hailed all over internationally. Partnership Mandatory blending of ethanol and unleaded petrol is expected to reduce the fuel import bill by at least five percent, [10] according to the Government. Zimbabwe imports all of its fuel mostly through Mozambique, Botswana and South Africa, with petrol retailing at about \$1, 49 a litre while diesel costs about \$1, 33 a litre. The Government increased the mandatory blending of anhydrous ethanol with unleaded petrol from five percent (E5) to 10 percent (E10) with effect from 15 October 2013. It further plans to increase the ethanol blend to 15 percent next month and 20 percent by March 2014. This is in terms of the Petroleum (Mandatory Blending of Anhydrous Ethanol with Unleaded) Regulations, Statutory Instrument 147A of 2013 published on 16 October 2013 in the Government Gazette.

Biofuels are also doing well in USA, with production of biofuels from corn in 2008 being attributed as one of the drivers of the increase food prices in 2008. In US the Environmental Protection Agency (EPA) has currently approved E15, but still it's not yet clear to what extent can it really damage the engine.

In Brazil flexi fuel cars have been developed, that are compatible to biofuels and the production and use of such vehicles has been on the rise in Brazil to date. So biofuels are not a completely failure, were they have been developed nicely with a comprehensive framework they have done well.

Therefore one stands to reason that the introduction of Biofuels in Zimbabwe was a question of too fast and to furious, so as solve the prevailing problems, without proper planning and infrastructure development in place as supporting mechanisms. Lack of institutional coordination has been observed across the ministries, especially with the energy and agriculture nexus. While there is a draft biofuels policy in place it's a necessary but not sufficient condition for the development of biofuels. Other mediating factors such as our infrastructure development policy, power asymmetries, safeguarding local rights of individuals are necessary to factor in when implementing Biofuels. There is need to explore public-public partnership's, rather than private-public partnership's as the have been met with scepticism and normally they have been characterised by lack of balance between the risks and the rewards between the partners. Lastly there is need to create an environment for sustainable business initiative. Biofuels are the future considering the depletion of fossil fuels, but these factors need to be taken care.

2. INSIGHTS FROM THE CASE STUDIES

Biofuels have been implemented for agriculture economic development, employment opportunities and low carbon fuels and the main beneficiaries targeted have been the small scale farmers. While it was a great move and noble to assist the farmer this way, this has not been the case, with the consolidation of land under foreign control, small-scale farmers have little hope of expanding their fields. The Industrial production for biofuels which has been promoted enhances the agricultural model which pushes small-scale farmers aside as 'inefficient' and 'insufficient' producers. On the other hand if plantation farming is the model, rural communities will once again become workers for foreign corporations which export the product and the profits. If contract farming is pursued as a means for producing biofuels, farmers become subservient labourers on their own land, often succumbing to debt, for they are burdened with all the climate and market risks. In addition small scale farmers are less able to access the carbon market because they lack expertise in implementing complex methodologies, ex-post payment systems mean there is a lack of up front funding for projects and investors are less interested in smaller projects with high risks and long-time scales. Small-scale methodologies with simpler requirements and processes for bundling projects have been developed to address some of these issues, but there is currently no small scale methodology for liquid biofuels, and only one large scale methodology based on use of waste cooking oil for biodiesel [11](CD4CDM, 2007).

Another challenge is that while jatropha is being promoted and up scaling of production is being intensified across the breadth of Africa Jatropha trees take about five years to attain average yields and can produce up to 30 years. The question then is will the land concessions be for 30 years?

The public private partnership model which is being used in some parts to promote biofuels production benefits the political elite in the country and marginalizes the poor. Small scale farmers are factored in under the disguise of out grower's schemes and are provided with inputs on contractual basis. Contract farming sounds like it leaves the farmers in command of their fields and production, but in fact, it does the opposite. Contracts are dictated, not negotiated, by the global corporations who demand rigorous standards; the kind and amount of fertiliser, of irrigation and much more, can be designated in the contract. The farmers agree to provide x amount of the crop at y time. If weather or pests reduce the yields, the farmers take all the risk, often still required to deliver equal value of cash that the crop would have provided, plunging them into debt. [12](Mushita and Thompson 2007: 93-96,).Contract farming can transform farmers into powerless labourers on their own land, retaining little or no role in decisions about production but simply executing what the global corporation requires.

4.1 Too fast and too furious

Biofuel projects that have been implemented in the most of the countries when they are being implemented, initially and on paper they look to god to be true. Most of them have a mission to become the leading supplier of biofuels in their respective countries, and helping the government in its endeavor to diversify and empower rural communities. In a review done by[5.1] (Amigun, 2008) biofuels equally satisfy as diversification strategy for alternative's sources of energy there is a lack of good understanding and application of key concepts of cost estimation, which is a key to successful project which impacts the project profitability and influences the technical solutions

Generic technological and non-technological constrictions have been identified as hindrances to biofuels adoption and development. Aside from the concerns as to whether it will become an invasive plant, questions have also been raised as to its oil-producing abilities. Also there appears to be no data as to whether or not it can produce enough oil under these drier conditions to be viable commercially, especially as current plans feature planting it in communal areas rather than commercial farms.

A fuel-from-Jatropha project in Nicaragua was stopped after it was proved to be uneconomic for smallholders. A Malawian USAID-sponsored study rejected Jatropha as a potential oil-producing plant for improving smallholder livelihoods for various reasons, including the fact that "the strength of the market for Jatropha products" was "unfounded".

The debates over biofuels include data and statistics which support arguments for both sides. Like GMOs, much of the confusion is the result of insufficient data over the long term. Given that jatropha helps to retain moisture in the soil, yet it is also an invasive plant, even outlawed as a noxious weed to other crops in some countries, [13](Nhantumbo,I,2008), what impact will widespread plantations have? Scientific studies report that generally using agro fuels instead of petroleum may reduce emissions of sulphur, carbon monoxide and volatile organic compounds, but may increase nitrous oxide and acetaldehyde emissions, depending on the materials used. [14] (Dufey in CBD 2008: 3) Scientists are being careful in their assessments, yet policy to promote quick profits tends to select the convenient data.

The issue of emerging markets has also contributed immensely to the expansion of biofuels. However in the accelerated-growth economies such as India and China there are already targets and mandates relating to biofuels which require vast amounts of feedstock. According to [15]Amezga and colleagues, (2007) they point out that several studies have suggested direct and indirect links between bioenergy production and, amongst others, deforestation and global food price rises [16](The Gallagher Review,2008).

These concerns have highlighted the need for effective assessment of bioenergy production in individual cases because, evidently, there are multiple variables determining the overall sustainability of each project or programme. Despite these potential positive benefits, biofuel expansion carries the threat of a number of possible negative consequences in both the socio-economic and ecological domains. Even the anticipated greenhouse gas benefits are not guaranteed under many scenarios. Developing countries have a number of unique sustainability concerns relating to biofuel expansion, especially as much of the pressure for biofuels comes from outside the countries concerned. Poverty, food insecurity and underdevelopment leads to a situation where potential development options such as biofuels can be hastily accepted without due concern to long term sustainability.

Some *Jatropha* projects such as GEM Biofuels in Madagascar plant *Jatropha* directly into degraded savannas or grasslands with relatively limited immediate impacts on current biodiversity. Other projects, such as ESVBio-Africa Limitada in Mozambique, plough the site before planting, effectively destroying most existing biodiversity.

A common feature in biofuel literature is the notion that biofuel feedstock, especially *Jatropha*, can be grown on degraded, waste, unproductive or marginal land. Even if grown in degraded areas there is limited data to substantiate if this will have positive biodiversity impacts or not; and the reality is that *Jatropha* will more likely be grown in good areas because this improves the economics of production.

There is a lack of coherent biofuel strategy in Africa despite the increase in the price of conventional fuel on daily basis and their rising demand mainly due to psychological fear of geopolitical uncertainties to the dwindling convertible currency earning and rising evidence of climate change [5,4](Amigun, 2008). In addition the contentious problems of biofuel commercialization in Africa relate to economic and political will, Economics competitiveness against mainly fossil fuel is a very common argument against biofuels.

3. CONCLUSION

This paper concludes that Africa has a lot of opportunities for Biofuel production both in terms of manpower, land and the need, but these need to be tapped/scaled-up by addressing supply side constraints and introducing domestic and external policies that support agricultural development.

Biofuels have been touted as a win-win situation for Africa by providing jobs, cleaner environment. Yet in truth since the introduction of biofuels to date they have been more of exploitative in nature, rendering most of the smallholder farmers landless. In describing some of the consequences of biofuel expansion there are likely to be complex trade-offs between different aspects of biofuel impacts. Obviously many of these impacts, such as the

biodiversity impact, cannot be accurately and rigorously expressed in monetary value terms. African countries face in the production and distribution of biofuels today is the reorienting of the current energy system toward a far greater reliance on technologies with low carbon dioxide emission. Economies of scale and technological advancement can lead to increase competitiveness of biofuels, [5.5](Amigun B., 2011) recognises that biofuel development, particularly in the context of African development, is a controversial issue that has recently attracted considerable interest among policymakers, development practitioners, donors and other key stakeholders.

6. REFERENCES

- [1] L.Cotula,N.Dyer,S.Vermeulen,S.2008.Fuelling exclusion? The biofuels boom and poor people's access to land, IIED, London. ISBN: 978-1-84369-702-2
- [2] L.Peskett,R. Slater,C.Stevens,and A.Dufey, A. 2007 'Biofuels, Agriculture and Poverty Reduction' Paper produced for the DFID Renewable Natural Resources
- [3] FAO (2008). Biofuels: Prospects, Risks and Opportunities. The State of Food and Agriculture. Food and Agriculture Organization of the United Nations. Rome, Italy.
- [4] Biofuel watch (2011). Bioenergy and waste incineration in the Renewables Obligation and DECC Consultation, Biofuelwatch, November 2011, http://www.biofuelwatch.org.uk/2011/rocs_introduction/
- [5] B.Amigun.2011.Commercialization of biofuels industry in Africa. A review. Renewable and sustainable energy reviews 690 -711
- [6] GoM, 2008, Mozambique Biofuels Assessment. Maputo, Ministry of Energy and Ministry of Agriculture, final report, 1 May.
- [7] I.Nhantumbo,and A.Salomão.2010, BIOFUELS, LAND ACCESS AND RURAL LIVELIHOODS IN MOZAMBIQUE, IIED, London. ISBN: 978-1-84369-744-2
- [8] Petromoc, 2008, Project Development Strategy. Petróleos de Moçambique. Maputo.
- [9] Biofuel Digest April 2012.Accessed on line: <http://www.biofuelsdigest.com/bdigest/2011/12/08/biofuels-digest-announces-line-up-for-2012-advanced-biofuels-renewable-chemicals-leadership-week/>
- [10]GoZ2007. National Biodiesel Production Programme. Ministry of Energy and Power Development. Zimbabwe.
- [11] Capacity Development for CDM Project published by Ecosecurities ISBN 978-87-550-3594-2
- [12] T.Mushita,C.Thompson C. 2008. Bio-fuels for Africa? Revised background paper (6 May 2008) prepared for National Consultative Workshop on Current Issues affecting Agro-Biodiversity for Civil

Society Positions to CBD-COP9, held at ZIPAM,
Norton, Zimbabwe, 28-30 April 2008

- [13] I.Nhantumbo. 2008, Bioenergy in Mozambique: not yet a small-scale business enterprise. WWF SARPO and WWF Sweden. Harare.
- [14] A.Dufey.2006. 'Biofuels production, trade and sustainable development: emerging issues.' International Institute for Environment and Development. London. Available at <http://www.iied.org/pubs/15504IIED.pdf>
- [15] Amezaga, J. M., G. von Maltitz and S. Boyes (Editors) ,(2010). "Assessing the Sustainability of Bioenergy Projects in Developing Countries: A framework for policy evaluation", Newcastle University, ISBN 978-9937-8219-1-9,179 pages.
- [16] The Gallagher Review of the indirect effects of Biofuels expansion .2008.Renewable fuels Agency

OVERVIEW OF ENERGY EFFICIENCY CHARACTERISATION AND MEASUREMENT OF A SOLAR-PV WATER PUMP FOR THE PURPOSE OF IDENTIFYING SYSTEM COMPONENT MATCHING PROBLEMS

T.A. Hoogenboezem* and D.C. Pentz*

* Group on Electronic Energy Processing (GEEP), Dept. of Electrical and Electronic Engineering Science, Corner of University Road and Kingsway Road, University of Johannesburg, Johannesburg 2006, South Africa E-mail: thean88@gmail.com

Abstract: Power (Watt) efficiency does not fully characterise a non-constant operating systems with varying operational conditions such as a solar-PV (solar photovoltaic) water pumping system. This is due to power measurements being taken only a specific intervals or instances that only characterise the operational cycle partially. The energy (Joules) efficiency can describe the operation of the system for a cycle of varying operational conditions. This energy efficiency can also be used to identify the specific operational instances where low efficiency operation occurs. Using the results obtained from energy efficiency characterisation system design can be optimised for better operational efficiencies within instances occurring more frequently. Solar-PV bare shaft unit water pumps and motors may be characterised and matched according to required efficiency design parameters. Also the design of a converter/inverter topology to drive the motor in the operational range established from characterisation may further improve overall efficiency.

Keywords: Energy Efficiency, Power Efficiency, Solar-PV Water Pumping, Component Matching of Solar-PV water Pumping Systems, Non-battery assisted solar-PV, Solar-PV Panel Modelling

1. INTRODUCTION

Most electrical, electronic and mechanical components, systems and solutions are sold with certain rated power efficiencies describing the performance of these systems. These performance indicators are reliable for systems operating under constant input and constant load conditions.

Due to the fluctuating input and load conditions of a solar-PV water pumping system without a battery bank, power efficiency may not fully characterise the operational cycle. This means that a power efficiency rating may only describe the operation at a single operational instance or various operational instances. However an efficiency rating is required that can describe the performance throughout the operational range.

Characterising the energy efficiency is important since a solar-PV (Photovoltaic) system only utilises a fraction of the available solar irradiation available from the solar-PV panel. This is after the 3 to 15 % of actual available solar irradiation has been utilised. The rest of the system is designed to operate optimally within this power range and the water pump does not utilise the full potential of the little energy available.

In this paper, a 120 W solar-PV water pump and controller is characterised and the energy efficiency of the system is determined. The purpose of this is to identify the need of proper component matching, picking a suitable pump to characterise and then matching it to a suitable motor, of water pump and motor when considering a solar-PV water pumping system. This consideration is more important when the system is not used in conjunction with a battery bank.

2. SOLAR-PV WATER PUMPING SYSTEM COMPONENTS AND TERMINOLOGY

In solar-PV water pumping systems, the following components are present:

- Solar-PV Panel
- Converter/Inverter/Controller/Maximum Power Point Tracker(MPPT)
- Motor
- Water Pump

The system setup is demonstrated in Figure 1 and the different components are briefly discussed thereafter.

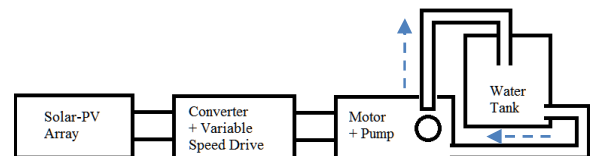


Figure 1: Solar-PV Water Pumping System Block Diagram

2.1. Solar-PV Panel

A solar-PV panel consists of solar-PV cells that are connected in series and parallel to supply the required voltage and current requirements of the system. However, solar-PV panels are mostly standardised for off the shelf applications supplied to the following specifications:

- Watt Rating
- Cell- and Panel Efficiency
- Open-Circuit Voltage
- Short-Circuit Current
- Dimensions
- I-V Characteristic Curves

Solar-PV panels may have low efficiency ratings. Silicon crystalline is the standard panel of choice due to availability and have efficiency ratings in the order of 5 to 15%. [1]

For this paper's experimental work a solar-PV panel was simulated. The specifications of the chosen panel are

discussed in section 4.2. The experimental work mostly focuses on the solar-PV water pump (converter, motor and pump). The exact specifications are described in section 4.1.

2.1.1. Solar Irradiation

The solar irradiation represents the intensity of the sun in Watt per Square meters (W/m^2). Solar irradiation may generally be expected to increase from morning to mid-afternoon and then to decrease from mid-afternoon to late afternoon. This is important for a non-battery assisted solar-PV water pumping system since the system may only operate when the panel supplies sufficient energy affecting the energy efficiency. The solar irradiation data obtained and used for this paper is discussed in sections 6 and 7.

2.1.2. Solar Insulation

The solar insulation is important since a solar-PV panel has an insulation layer on top of the silicon crystalline structure. The efficiency of the structure also requires consideration as well as the size of the panel that is being used. Figure 2 shows the basic structure of the solar insulation and the silicon structure. [2]



Figure 2: Solar-PV Cell Basic Structure

To properly characterise the solar insulation the circuit diagram demonstrated in Figure 3 was derived. This diagram is used to calculate the actual output power of the panel after the solar irradiation has been filtered through the insulation and the overall PV losses of the silicon crystalline structure.

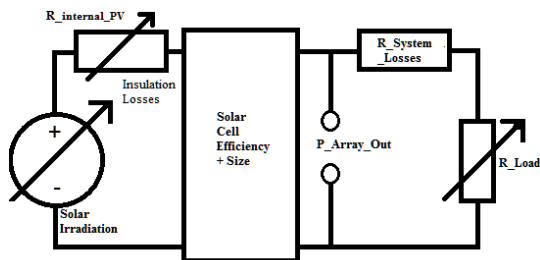


Figure 3: Block Diagram of Solar-PV Array to System Modelling [2]

Using equation (1), the output power of a solar-PV array may be calculated and this process is demonstrated by Figure 3.

$$P_A(t) = (\lambda_{SI}(t) \times A_E \times S_A) - I_{AO}^2(t) \times R_I(t) \quad (1)$$

Where:

P_A = Power array output (Watt)
 λ_{SI} = Solar irradiation ($W.m^2$)
 A_E = Array efficiency (%)
 S_A = Size of the array (m^2)
 I_{AO} = Array output current (A)

R_I = Internal Resistance (ohms)

t = Represents the time of day

2.2. Converter/Inverter/Controller/Maximum Power Point Tracker

Controlled dc-dc converters or dc-ac converters (inverters) are required depending on the type of motor being used. The maximum power point tracking (MPPT) is the algorithm used by the controller for a solar-PV application to control the converter operation to utilise the solar-PV panel optimally at the maximum power point for the present operational conditions.

The converter is not the main concern for this paper since the motor and pump components are evaluated. The efficiency of the motor and pump is expected to be much lower than the converter unit even though the converter operation may cause the low efficiency obtained.

2.3. Motor

AC- or DC- motors may be selected. In Table 2-1, Table 2-2, Table 2-3 the main differences of different motors, pertaining to solar PV water pumping applications, are summarized.

Table 2-1: Comparison between AC and DC Motors

	AC Motors	DC Motors
Size	Small	Big
Converter Topology	Complex	Simple
Permanent Magnets	In some types, such as permanent magnet synchronous motors	Mostly, Yes

Table 2-2: Comparison of AC Single and Three phase Motors

AC Motors	Single Phase	Three Phase
Start-Up Circuitry	Complex	Less Complex

Table 2-3: Comparison between Brushed and Brushless DC Motors

DC Motors	Brushed	Brushless
Brushes	Yes	No
Magnetic Sensors	No	Mostly, Yes
Control	Simple	Complex
Maintenance	Need to replace brushes regularly	Normal motor maintenance

2.4. Water Pump

Many different water pumps may be chosen for solar-PV water pumping applications. The different available choices for water pumps are compared in Table 2-4.

Table 2-4: Comparison of water pump [1], [3], [4], [5], [6]

	Positive Displacement Pumps			
Water Pump	Diaphragm	Piston	Helical (Grundfos)	Centrifugal
Head Range	Low to Moderate	Moderate	Very Good (Up to 300m)	Good
Flow Rate	Low	Average	Good (3 to 18 l/m)	Good
Power Level	Low (<500W)	Low to High		Medium to High (1kw<)
Voltage Required	12, 24, 48V, Low Voltage	High (220-380V) (Grundfos)		100-250V Medium Voltage

Life Time (Years=X)	1.3 3< X <6		X>3	
------------------------	----------------------	--	-----	--

3. ENERGY EFFICIENCY VERSUS POWER EFFICIENCY CHARACTERISATION

The power (W) input and output are frequently only measured for a specific instance of operation and used to calculate the power efficiency, making this measurement instantaneous. Energy on the other hand may characterise the full operational range or cycle of the system even under fluctuating operational input and load conditions.

The following equations would be used for calculating the power efficiency of a water pumping system. Electrical power input, [7]

$$P_I = V_I \times I_I \quad (2)$$

Where:

V_I = Input voltage to controller (V)

I_I = Input current to controller (A)

The power output of the pump may be calculated using equation (3), [7]

$$P_o = Q \times \rho \times h \times g \quad (3)$$

Where:

Q – is the flow rate in m^3/s

ρ – Density of liquid (water – 1000) (kg/m^3)

h – Pumping Head in meters

g – Gravitational constant ($9.81 m/s^2$)

The energy in Joules of the system may easily be calculated from the power of the various system components in equation (4).

$$Power(W) = \frac{Energy(J)}{Time(s)} \quad (4)$$

Thus the energy may be calculated by equation (5),

$$Energy(J) = \int_a^b Power(W) \times Time(s) dt \quad (5)$$

Now, with equation (2) to (5) the energy input and output of the system may be calculated that directly characterises the performance of the system for the full interval of operation. The energy efficiency may then be calculated using equation (6)

$$Energy\ Efficiency = \frac{Energy_{Input}}{Energy_{Output}} \times 100 \quad (6)$$

4. EXPERIMENTAL SETUP

The experimental setup is designed to measure the energy efficiency of the water pumping unit. By measuring the input power of the converter and the output flow rate of the water pump, the energy efficiency may be calculated.

4.1. Choice of Solar-PV Water Pump

The solar-PV water pump chosen for the controlled environment setup utilises a permanent magnet synchronous motor. The pump has been designed for solar-PV applications and specified for supplying water to livestock. The pump is rated at 120 W and has the following specifications listed in the Table 4-1.

Table 4-1: Solar-PV Water Pump Specifications

Factor	Specification
Q_Max (Flow Rate) (l/min)	33
Head Max (m)	25
Power (kW)	0.12
Volt (V)	24
Operation Specification	Continuous Duty
Thermal Protector	Yes

The water pumping unit is supplied with a converter unit with features such as battery operation support, a built-in implemented MPPT and protection from current surges. Due to legal and commercial protection, the supplier and specific pump/converter models have not been disclosed in this paper.

4.2. Choice of Solar-PV Panel

The solar-PV panel will be modelled in the experimental setup. A specific solar-PV panel was chosen to base the simulation on. The solar-PV panel that has been chosen is a 150 Watt panel with the specifications in Table 4-2. The internal resistances of the panel at different solar irradiations are demonstrated in Figure 4 as was used.

Table 4-2: Specifications of the Solar-PV module

Power	150W
Short-Circuit Current(I_{sc})	8.71A
Open-Circuit Voltage(V_{oc})	21.8V
Module Efficiency	15.13%

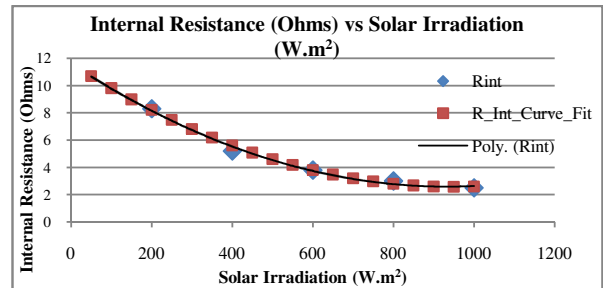


Figure 4: Graph of Solar Panel Internal Resistance (Ω) vs. Solar Irradiation (W/m^2)

4.3. Experimental Setup

A block diagram of the experimental setup is demonstrated in Figure 5. The controlled environment setup is required to allow for certain variables of the system to be varied. These variables include,

- Pump discharge pressure
- Input power
- Insulation resistance

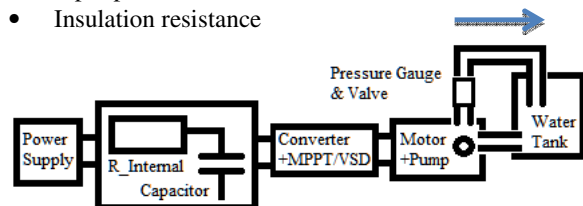


Figure 5: Solar-PV Water Pumping Experimental Setup

The internal resistance of the solar-PV array is simulated using the solar insulation data of the chosen panel from

section 4.2. The internal resistances for different solar irradiation levels have been calculated for the panel chosen in section 4.2. These internal resistances will then be emulated with a variable resistor demonstrated in Figure 5. The capacitor in Figure 5 provides a stable start-up current.

The valve is utilised to adjust the pump discharge pressure and the pressure gauge to monitor the pressure. The pump outlet is returned to the same tank. This is done to keep the inlet pressure to the pump constant. To measure the flow rate the “bucket test” was utilised. The bucket test procedure is performed by pumping the water outlet into a bucket floating on top of the water in the water tank. Thus the water level and pressure remains constant. The volume pumped into the bucket may be timed and the flow rate may be determined using equation (7).

$$\text{Flow Rate}_{\text{Bucket Test}} = \frac{\text{Volume (L)}}{\text{Time(s)}} \quad (7)$$

5. EXPERIMENTAL METHOD

To characterise the energy efficiency of a solar-PV panel all of the following characteristics need to be considered,

- Solar irradiation
- The direction the panel is facing
- The inclination of the panel mounting
- Solar insulation
- Internal resistance of the panel

The energy output of the solar-PV water pump is required to determine the energy efficiency of the system. The energy output is calculated from the flow rate, discharge pressure as well as the time intervals of pumping.

The solar irradiation was modelled as mentioned previously. The output flow rates were measured using the “bucket test”.

The power level was adjusted using a voltage source whilst adjusting the resistance of a series resistor which represents the internal resistance of a solar-PV panel connected in-between the power supply and the converter. Also, as specified in the previous section, a capacitor was added to allow for the controller to start-up under low input power conditions. This is required in a non-battery assisted solar-PV water pumping system since the power output of a solar-PV panel may fluctuate affecting the operation of the motor.

6. CHARACTERISATION OF WATER PUMP

The water pump was characterised by controlling the power level with a variable series resistor demonstrated in Figure 5. The resistor represents the internal resistances of the solar-PV panel as obtained from Figure 4. The power level was increased from low to high. At solar irradiation intervals the input power to the converter and the output flow rate of the pump were measured. These results were then used to plot characteristic curves that are demonstrated in section 7.

These plots are important to explain the results obtained for the energy efficiency measurements. The plots also indicate important aspects of the water pump unit (converter, motor and pump). These are discussed in the results and analysis section.

7. RESULTS AND ANALYSIS

In Figure 6 the flow rates (m^3/s) at different discharge pressures representing heads (m) can be seen. The flow rates increase as the solar irradiation increases and then decreases with increase in the discharge pressure from 0m to 17.5m.

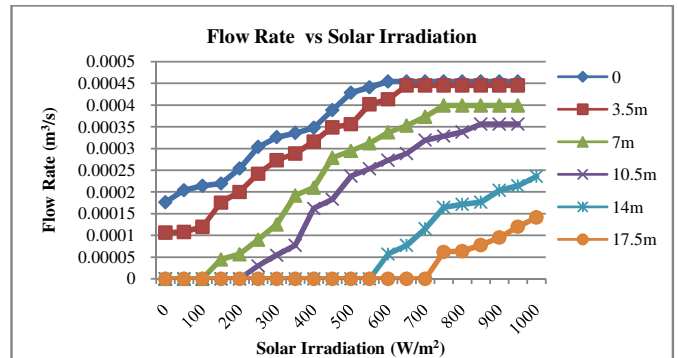


Figure 6: Solar-PV water pump flow rates at different discharge pressure versus the solar irradiation level

In Figure 7 the pointers indicate peaks on the different discharge pressures. These peaks occur at low solar irradiation, thus low power. They are caused by the power point tracker operating to adjust for maximum output power for the respective discharge pressures. The peaks shift to higher power points as the discharge pressure is increased. At the discharge pressures of 7m (C) to 14m (E) the results are as is expected.

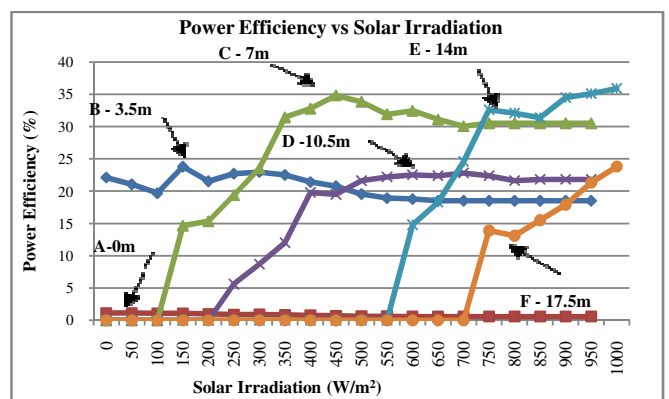


Figure 7: Solar-PV water pump power efficiencies at different heads of operation versus solar irradiation levels

The solar irradiation data demonstrated in Figure 8 was obtained from the JRC European commission on Solar Irradiation. This solar irradiation pattern was measured for a 15 degrees panel inclination, with the panel facing east. Figure 8 displays the annual direct nominal irradiation (DNI) for two cases the clear sky DNI (DNIc)

and the actual DNI. DNic(A) represents the solar irradiation with no obstruction and the DNI(B) represents the expected DNI due to weather conditions. [8]

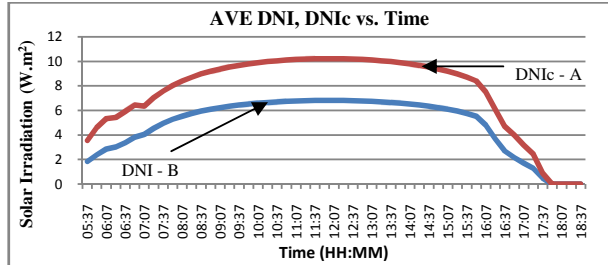


Figure 8: Solar Irradiation versus Time of day

Using Figure 8 the plot of DNI (B) for the annual daily actual solar-irradiation has been used to model the input solar irradiation to the solar-PV panel. The converter input power and the pump output flow rate has been used from Figure 6. From this data set the actual energy input to the converter was calculated. The corresponding pump output flow rates of the actual energy inputs were used to calculate the energy outputs. This data has been used to calculate the energy efficiencies given in Table 7-1.

In Figure 9 the energy that is available to the water pump at a head of 7m is indicated. The actual utilised energy is demonstrated matching up to each measurement point. These measured energy inputs with the energy outputs have been used to calculate the energy efficiency at a discharge pressure of 7m. The same outline plot is also present in Figure 11 and each corresponding energy efficiency plot outline is indicated in Figure 12.

$$\text{Energy Efficiency}_{7m} = 30.3\%$$

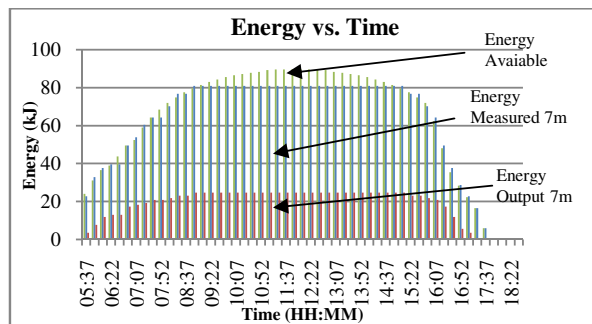


Figure 9: Energy Available, Energy Measured and Energy output at 7m versus Time of day

Using the same process the input and output energies are indicated in Figure 10 for discharge pressure 14m. There is an important difference to be noted from this result over Figure 9. This is that at a higher discharge pressure, the energy is only utilised at higher power levels. The efficiency is lower, but for the consideration of the total operational period the energy efficiency is less than calculated.

$$\text{Energy Efficiency}_{14m} = 23.1\%$$

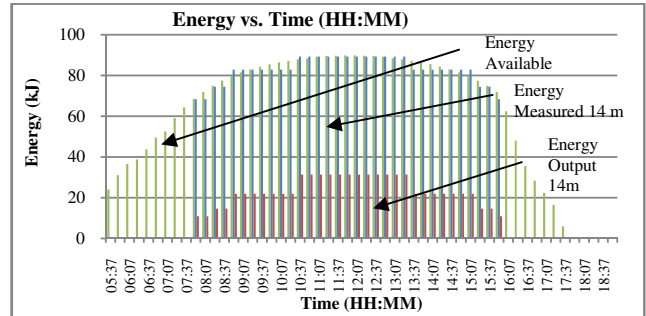


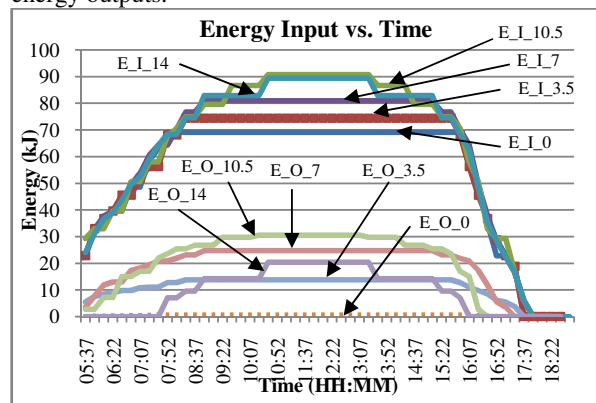
Figure 10: Energy Available, Energy Measured and Energy output at 14m versus Time of day

In Table 7-1 the energy efficiencies are given for pressure discharges that have been experimentally measured and calculated. It should be noted that the energy efficiency at 0m discharge pressure is the lowest even though the flow rate is the highest. This is because work equals displacement, at 0m there is no displacement so almost no work is done.

Table 7-1: Summary of Energy Efficiency at discharge pressure and Performance Analysis

Discharge Pressure (Meters)	Energy Efficiency (%)	Performance
0	2.5	Good Flow Rate, Bad Efficiency, No work
3.5	19.1	Better Efficiency, more work done
7	30.3	Best Efficiency, best operational discharge pressure in results
10.5	31.1	Decreasing efficiency, exceeding best discharge pressure
14	23.1	Efficiency decrease further exceeding best operational discharge pressure

The respective energy efficiencies in Table 7-1 have been calculated from the input and output plots in Figure 11. There are 10 plots on this figure, 5 energy inputs and 5 energy outputs.



E_I_# - Energy Input at Head #, E_O_# - Energy Output at Head #

Figure 11: Energy Input/output for 0m, 3.5m, 7m, 10.5m and 14m Head versus Time of day

In Figure 12 the energy efficiency plots of the five pressure discharges are demonstrated. The important features of these plots to note are in plot A, B, C and

partially D. There are peaks at low power levels and efficiency at full power is lower than these peaks. These peaks are expected due to the same pressure discharges in Figure 7 also exhibiting the peaks at low power levels. Plot D and E start shaping more as would be expected for the energy efficiency plot due to the same peaks not existing within their solar irradiation levels in Figure 12.

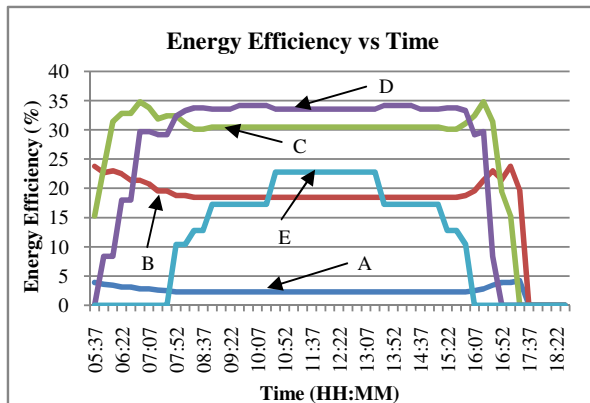


Figure 12: Energy Efficiency Plots of (A) 0m, (B) 3.5m, (C) 7m, (D) 10.5m and (E) 14m head versus the time of day

8. FUTURE WORK

Future work may be done on component matching of a solar-PV water pump. This may be done by selecting a small bare shaft pump and characterising it. Then picking a suitable motor operating within the same rotational speed range with a good efficiency rating the end product water pump may utilise more of the energy available. The same experiment as done in this paper may be used to test the new solar-PV water pump unit. A converter with a MPPT may also be designed and matched to the same system to attempt to utilise as many possible power levels of the solar irradiation period.

9. CONCLUSION

The energy efficiency of a solar-PV water pump has been calculated and compared with different pressure discharges. The effect these variables have on the unit's operational performance has also been analysed. It has been established that energy efficiency describes the operational cycle of the system better than power efficiency for a system with fluctuating input and load operating conditions. Since the energy efficiency may describe the full daily operational cycle of the system.

System component matching is a very important part of solar-PV system design for systems not operating under constant conditions. This is apparent from these results, but also raises questions on the specification of the optimum operating conditions of a system.

10. ACKNOWLEDGEMENTS

I would like to thank Prof. Daan van Wyk for his inputs on the study field of solar-PV water pumping based on

previous students that he supervised in the field. Then I would like to thank Mr. Andrew Joannou for his assistance in the interpretation and understanding of the project. Thank you to all my other colleagues in the GEEP research group for their inputs during presentations and discussions. I would also like to thank the NRF for their support towards the completion of this study.

11. REFERENCES

- [1] B. D. Vick and R. N. Clark, "Determining the Optimum Solar Water Pumping System for Domestic Use, Livestock Watering or Irrigation," in *American Solar Energy Society Solar Conference*, 8p. < <http://www.cprl.ars.usda.gov>, 2009.
- [2] M. A. Slonim and A. L. Tsaf, "Equivalent diagram of a solar cell, based on short-circuit and open-circuit tests," *Solar cells*, vol. 22, no. 4, pp. 255–262, 1987.
- [3] D. Fiaschi, R. Graniglia, and G. Manfreda, "Improving the effectiveness of solar pumping systems by using modular centrifugal pumps with variable rotational speed," *Solar energy*, vol. 79, no. 3, pp. 234–244, 2005.
- [4] B. Chowdhury, S. Ula, and K. Stokes, "Photovoltaic-powered water pumping-design, and implementation: case studies in Wyoming," *Energy Conversion, IEEE Transactions on*, vol. 8, no. 4, pp. 646–652, 1993.
- [5] B. D. Vick and R. N. Clark, "Experimental investigation of solar powered diaphragm and helical pumps," *Solar energy*, vol. 85, no. 5, pp. 945–954, 2011.
- [6] N. Lujara, J. Van Wyk, and P. Materu, "Modelling Photovoltaic Water Pumping Systems," *International Journal of Renewable Energy Engineering*, vol. 2, no. 3, pp. 200–213, 2000.
- [7] N. K. Lujara, "Computer Aided Design of Systems for Solar Powered Water Pumping By Photovoltaics," 1999.
- [8] "JRC Photovoltaic Geographical Information System." [Online]. Available: <http://re.jrc.ec.europa.eu/pvgis/>. [Accessed: Feb-2013].

IMPROVING SOLAR ENERGY GENERATION THROUGH THE USE OF THREE DIMENSIONAL PHOTOVOLTAICS TECHNOLOGY – LITERATURE REVIEW

O A Mafimidiwo, A K Saha

University of KwaZulu-Natal, School of Electrical Engineering, Howard Campus, Durban South Africa.

Abstract. This paper gives a general overview of a new technology in solar energy generation, called the three dimensional photovoltaic (3DPV) structure. The 3DPV technology is intended to improve on the regular method of flat solar panel technology. The different methods of 3DPV technology were briefly touched and the factors affecting optimum 3DPV were highlighted. Using the results of simulations on ground, this paper has shown that optimal 3D structures are not only about the material used such as simple box-like shapes or the tree shape but by using the genetic algorithm (GA) optimised shapes or other shapes using optimisation techniques with the ability for superior materials performance. These enable the 3DPV modules produce significantly more electrical energy than the conventional planar module assemblies. The simulation result on 3D photovoltaic structure was used in analysing 3DPV performance with height and the conclusions were drawn and presented in this paper.

Key Words. 3DPV technology; optimum; energy generation.

1. INTRODUCTION

According to B. Myers et al [1], 3DPV structures are found to absorb more light and generate more energy higher by a factor of 2-20 than flat PV panels of the same area footprint. This technology has been found to prove useful in space-constrained areas. Furthermore, the introduction of three-dimensionality in PV could allow 3D alternative fabrication routes, using cheaper and foldable substrates, resulting in consequent reduced installation costs. Research on 3DPV technology has revealed the need to determine what the optimal shape of a solar cell would be, if a 3D was to be considered indeed for it [1, 2]. Presumptuously, a 3DPV shape was then considered to be a box open at the top, made of double-sided solar cells by Marco Bernardi et al [2, 3]. This arrangement was referred to as an “openbox” as shown in Figure 1. The double-sided solar box (open at the top) was then considered to be able to allow light-trapping by multiple reflections. However, other factors such as light reflection, incident angle, position with respect to the sun, panel arrangement, etc., have also been reported to constitute complicated optimization problems by T. Suto as well as S. Suzumoto et al [4, 5].

There are various types of silicon solar cell and various factors such as the solar cell type, size, shape, efficiency etc., which could affect 3DPV generation. This means that to a large extent, the choice of solar cell made, affect the solar generated power output. The International Renewable Energy Agency (IRENA), gives an over-view and comparison of major PV technologies [6]. Various techniques and different optimisation methods are being used for solar energy generation through the use of 3DPV as analysed and reported in Table 1.

Suzumoto Seiji et al, [5] reported on an experiment carried out in Tokyo with (northern latitude 35.7°, east longitude 139.8°) by using various shapes of a particular type of silicon solar cells, to confirm that the shape of the solar cell affects the electrical output of a solar module to a large extent as shown in Table 2. Likewise Toshifumi Suto and Toshiaki Yachi in their report to the experiment performed on power-generation characteristics of an FPM by simulation, declared that 3DPV technology is an advanced PV system that comparatively generate higher amount of energy per installation area and is capable of maximising power generation than the planar module [4].

2. CONCEPT OF 3DPV GENERATION

The concept of three-dimensional (3D) photovoltaics is borne by M. Bernardi et al [1, 5] from the need to optimize the solar energy generated. Arbitrarily shaped 3D solar cells were considered for optimum energy generation in a particular day by exploring the 3D structure computationally, using a genetic algorithm. Optimization was carried out on the structures with a bounding-volume of area footprint (base area) 10 x 10 m² and height ranging from 2 to 10 m. This was necessarily carried out in order to produce energy of the best-performing GA structures capable of optimizing the generated power output.

For the “openbox” structure, optimal 3DPV shapes were examined using a GA combination and coding. The coded 3DPV structures were considered as triangular configurations in Cartesian space confined to a rectangular box volume whose face normals the north, south, east and west. The triangles represented the double sided flat panel solar cells which were able to develop their co-ordinates independently within the

GA to produce an optimised 3D structure [1, 7]. In the GA, candidates 3D structures were combined using three operation principles of selection, recombination and mutation. [1, 3, 7]

3, 3DPV POWER OPTIMISATION

The concept of 3DPV is to optimize the energy production in a day for arbitrarily shaped 3D solar cells confined to a given area footprint and total volume. Simulations carried out by Bryan Myers et al demonstrated that the performance of 3D photovoltaic structures scales linearly with height, leading to volumetric energy conversion, and provides power fairly evenly throughout the day than flat panels of the same area footprint. It stated further that the shapes optimized using a GA approach could allow for significant materials saving and also the use of materials within a wide reflectance range without degradation of the device performance. Furthermore, it was recorded that optimal 3D structures are not only about shapes, but that the design attributes such as reflectivity could be optimized using three-dimensionality

3.1 3DPV by FPM

In FPM, the PV modules are tree-shaped and are assembled in three-dimensional structures which were considered to enable more efficient conversion of limited amounts of solar energy using low-cost solar cells. This is illustrated in Figure 2 [3, 5], where configuration is based on Fibonacci numbers. In this method, the individual solar cells of the 3D PV module could be arranged in a leaf-like manner showing a 2/5 or 3/8 pattern for maximum power generation.

According to [4, 5], the leaves can most efficiently receive sunlight in this arrangement. Such a tree-type arrangement PV module is called Fibonacci number PV module FPM. The solar-powered tree (about 0.5 kW) installed at Tourism London, Ontario Canada, is funded by an Ontario Power Authority. The solar-powered tree is 7 meters (23 feet) tall and has 27 leaves, each producing power, as shown in Figure 2.

The use of Maximum Power Point Tracking, MPPT, was utilized in controlling the solar cells in each azimuth for maximized power generation [3, 8]. Like in the “openbox” method, in the FPM method, the effects of inter-cell shadowing as well as the influence of shadows cast by adjacent solar cells were accounted for in the angle of incidence of the incoming light [3]. The simulation report obtained on a particular day revealed that the power output of a double-stage FPM doubled that of a single-stage FPM and in both cases were much higher than the total output power of a planar PV module. From the report, it can then be deduced that the power output is a function of height of and it is improved upon with increasing installation height [9].

3.2 3DPV by Nanopillar-array Photovoltaics

There is yet another method of 3DPV power generation known as the three-dimensional nanopillar-array photovoltaics on low-cost and flexible substrates, as presented in Figure 3. According to [10], it was reported to be achieved by direct growth of highly regular, single-crystalline nanopillar arrays of optically active semiconductors on aluminium substrates which are then embedded in polycrystalline thin films of p-CdTe and configured as solar-cell modules, to enable high absorption of light and efficient collection of the carriers as in Figure 3 and Figure 4. According to [11], this was carried out by enabling highly versatile solar modules on both rigid and flexible substrates with enhanced carrier collection efficiency arising from the geometric configuration of the nanopillars.

3.3 Factors Considered to Affect/Determine Solar Power Optimization.

Findings from different 3DPV technologies available revealed that the followings are some factors discovered to affect achieving optimum solar power generation.

1. Light reflections [1-3]
2. Incident angle [1-3]
3. Position with respect to the sun [1-3]
4. Solar cell shape [1-3]
5. Solar cells spacing [1-3]
6. Solar panel arrangement [1-3, 12]
7. Cosine effects [3, 12]
8. Atmospheric attenuation between heliostat and receiver [3, 12]
9. Shading and blocking [3, 12]

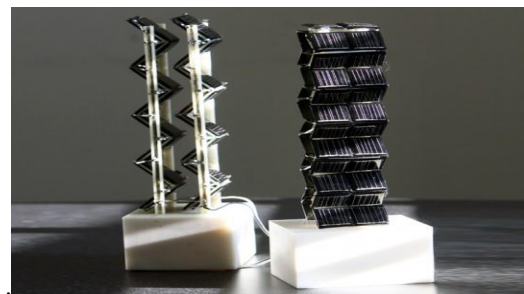


Figure 1: 3DPV Structures – “Openbox” [2]



Figure 2 The 0.5kW solar-powered tree at Tourism London, Wellington Rd, Ontario Canada [3]

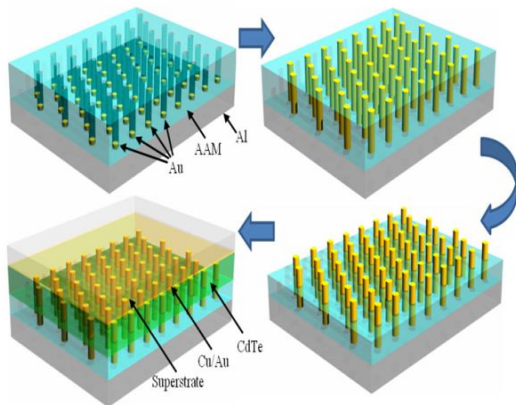


Figure 3: 3D Nanopillar-array Photovoltaics [10]

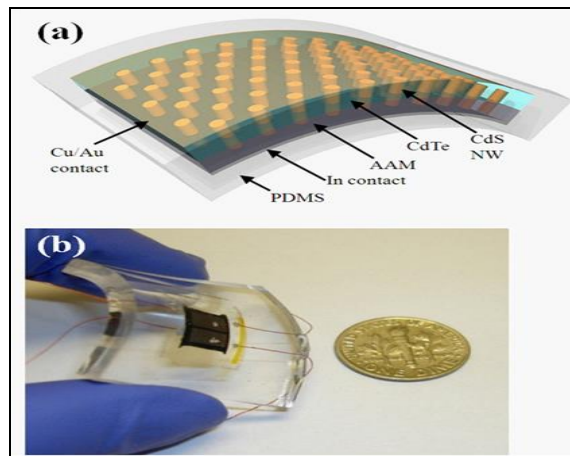


Figure 4: 3D Nanopillar-array PV – NPL/Thin film solar cell [10]

4. ENERGY GENERATION PERFORMANCE OF A 3DPV STRUCTURE USING GENETIC ALGORITHM OPTIMIZATION

The cubic 3DPV structures are considered for this exercise. Bryan Myers et al carried out optimization process on the structures with a bounding-volume of area footprint (base area) $10 \times 10 \text{ m}^2$ and height ranging from 2 to 10 m. This was reported to be necessary in order to produce energy of the best-performing GA structures capable of optimizing the generated power output [1]. Table 3 shows the energy generated in a day as a function of the height of the GA-optimized 3DPV solar cell, compared to that of a flat panel of the same area footprint. The energy generated by the 3D structures scaled linearly with height, thus leading to “volumetric” energy conversion. In addition, the power generated as a function of time during the day. Figure 3 showed a much more even distribution for 3DPV, due

to the availability of cells with different orientations within the structure. The increase in power with height was found dominant in the early morning and late afternoon. The intensity was found to be large in time and remained significant at all times during the day, even at midday. This steady supply of power throughout the day could be “built-in” to a 3D structure, which is in contrary to the power generated by a flat panel, which decayed rapidly around peak-time if not supported with the dual-axis tracking [1]

According to [2], the energy of the funnel shape was more than the energy from the open-box for all heights. The funnel shape and the open-box both generate more energy than the flat panel case but they both use more energy than that of the flat plate shape for a given energy. Hence M , the figure of Merit over the height range for both “openbox” and funnel shapes is less than 1 (i.e., $M < 1$). M is defined as the ratio of the energy produced in a day to the total area of active material used. It is a function of the solar materials used in relation to the structure’s height. As a standard, it is referenced and assumed to be 1 to the flat panel. For example, for a height of 10 m the open-box shape generates approximately 2.38 times as much energy as the flat panel but requires 9 times as much active material ($M = 0.26$). M for the open box decreased with height, on the other hand, the GA derived funnel shapes maintained a nearly constant M over this height range, with a cross-over to superior materials performance compared to the open-box at a height of $\approx 5 \text{ m}$, and 21% and 31% higher M at height 8 m and 10 m respectively. This revealed that the funnel shape is more ideal for 3DPV in terms of efficient materials’ use because it has successfully gone through GA optimization process.

Table 2 shows the energy generated in a day as a function of the height of the GA-optimized 3DPV solar cell, compared to that of a flat panel of the same area footprint [1, 2]. The energy generated by the 3D structures scaled linearly with height, thus leading to “volumetric” energy conversion. In addition, the power generated as a function of time during the day Table 3 showed a much more even distribution for 3DPV, due to the availability of cells with different orientations within the structure. The increase in power with height was found dominant in the early morning and late afternoon. The intensity was found to be large in time and remained significant at all times during the day, even at midday. This steady supply of power throughout the day could be “built-in” to a 3D structure, which is in contrary to the power generated by a flat panel, which decayed rapidly around peak-time if not supported with the dual-axis tracking [1]

Table 1: General comparison of different 3DPV Technologies

Source: Summary on Different Materials Analysed on the Output Power Characteristics of a Three-Dimensional Photovoltaic Module Using Different Technologies [1-3]

S/No.	Solar Cell Type	Electrical Characteristics	Technology Applied	Output Power Optimization Method	Reference
1.	Mono-crystalline Silicon, Type SCC3733 Size: 37x33mm ²	Nominal open-circuit voltage, $V_o = 6.7V$ Short-circuit current, $I_{sc} = 20 \text{ mA}$	Open cube (box) with double-sided solar cells. 3D architecture is used to capture light using multiple inter-cell reflections while preventing shading of the active material	Simulation followed by Optimization, using Genetic Algorithm (GA)	This is a function of height. Figure 1
2.	Single crystal silicon module of any shape Rectangular 210.5x49.5mm ² , Square 129.5x129.5mm ² Spherical 304x100mm ²	Rectangular, $V_o = 4.8V$ Square, $V_o = 4.8V$ Spherical, $V_o = 2.32V$ Rectangular, $I_{sc} = 0.353A$ Square, $I_{sc} = 0.53A$ or Spherical, $I_{sc} = 1.95A$	Fibonacci Photovoltaic Module (FPM) based on Fibonacci numbers Maximum Power Point Tracking (MPPT) strategy based on Fibonacci search algorithm	Simulation, followed by MPPT technique using the Fibonacci line search.	This is a function of height. Figure 2
3.	n-CdS Nanopillars and p-CdTe Polycrystalline		Single-crystalline n-CdS nanopillars, embedded in polycrystalline thin films of p-CdTe. 3D solar Nanopillar (SNOP) cells that enable high absorption of light and efficient collection of the carriers.	Simulation of the SNOP-cell performance (Efficiency) as a function of the NPL radius (while keeping the NPL pitch constant at 500 nm)	Function of high absorption of light and efficient collection of the carriers. Figures 3&4

Table 2: Specifications of different module.

Source: Output Power Characteristics of a Three-Dimensional Photovoltaic Module Using Fibonacci Number Composition - by Suzumoto Seiji et al, 2012 [5]

	Single crystal silicon Module		Spherical silicon Module
	Rectangle	Square	
Number of PV cell of each stage	8		
Form of PV cell	210.5mm ×49.5mm	129.5mm ×129.5mm	304mm ×100mm
The nominal Maximum output[W]	13	2	3.32
Open circuit voltage[V]	4.8	4.8	2.32
Short circuit current[A]	0.353	0.53	1.95
The output per area [W/mm2]	1.2×10 ⁻⁴		1.09×10 ⁻⁴
Azimuth direction	Rotated 135° (based on northern side)		
Installation site	Tokyo (northern latitude 35.7° east longitude139.8°)		

The energy generated by simple open-box shapes was compared with that of the funnel structures through a figure of merit M . From Table 3, the energy of the funnel shape outperforms the open-box at all heights. It was discovered that both structures (the box and the funnel) generated more energy than in the case of the flat panel. However, the open-box and the funnel shape used excess material for a given energy than that of the flat shape, where M was assumed to be 1.

Table 3 revealed that for a height of 10 m, the open-box shape generates approximately 2.38 as much

energy as the flat panel but requires 9 as much active material so, $M = 0.26$. This indicates that the figure of merit for the open box decreases with height, meaning that such a shape is not ideal for 3DPV in terms of efficient materials' use. On the other hand, at a height of 5 meters, the GA derived funnel shapes maintain a nearly constant figure of merit over this height range, with a cross-over to superior materials performance when compared to the open-box and 30% higher M at a height of 10 m [8].

Table 3: Energy produced in a day (E_{box} and E_{funnel}) relative to the flat panel (E_0) for the 3D open box and funnel structures, and corresponding figures of merit (M_{box} and M_{funnel}) for an area footprint of 10x10 m².

Height (m)	E_{Box}/E_0	E_{Funnel}/E_0	M_{Box}	M_{Funnel}	% Ratio of M_{Funnel} to M_{Box}
2	1.29	1.29	0.49	0.36	27% Drop
4	1.56	1.58	0.37	0.36	3% Drop
6	1.83	1.87	0.32	0.36	13% Gain
8	2.11	2.15	0.29	0.35	21% Gain
10	2.38	2.43	0.26	0.34	31% Gain

Source: Three-dimensional Photovoltaics by Bryan Myers et al, 2010

where:

E_{Box} = Energy of the funnel shape

E_0 = Energy of the funnel shape

E_{Funnel} = Energy of the funnel shape

M = Figure of Merit over the height range

It is the ratio of energy produced in a day to the total area of the active material used.

M_{Box} = Figure of Merit for the box

M_{Funnel} = Figure of Merit for the funnel

$E_{Funnel} > E_{Box}$ at all heights; & $(E_{Funnel}, E_{Box}) > E_{Flatpanel}$

Similar to what was obtained using "openbox" and funnel method, the FPM yields more power generation per installation area than a conventional planar module and both three-stage and two-stage FPM cylindrical modules exceed the power output of single planar PV modules [3].

5. BENEFITS OF 3DPV GENERATION

Two major reasons underlying the advantages of 3D technology are the presence of multiple orientations of the absorbers that enables effective capture of off-peak sunlight, and the re-capturing of the light reflected within the 3D structure (reflection regain), thus enabling greater generated power output [1, 2]. 3DPV structures disallow the absorption of reflected rays, which could have otherwise resulted in a loss of about half of the increase in energy production. Solar cells can be stacked in a vertical configuration, thereby

allowing for the effective capture of off-peak sunlight and reduced reflected energy rays. The decrease in the total power reflected to the environment has led to an appreciable increase in power generated. This is made possible by using the light reflected from the other solar cells. Also, 3DPV modules are equally foldable and more compact to handle. Furthermore, 3DPV technology favours land utilization for agricultural farm and/or estates development or any other land usage.

6. CHALLENGES IN 3DPV TECHNOLOGY

The technology is new and yet unpopular and requires more research work. More research work is expected to overcome the many challenges associated with 3DPV such as: design complexities in :

- ◆ Assembly of 3DPV architectures and
- ◆ Creation of 3D electrical connections and
- ◆ Corresponding power electronics.

The challenges notwithstanding, nonetheless, the benefits afore-mentioned suggest that three-dimensionality presents interesting opportunities in PV design and solar energy generation. Expectedly, 3DPV shall become cheaper to install and gradually replace the popular PV installation.

7. SUMMARY/ CONCLUSION

It has been established that 3DPV structures could provide substantially more energy in a day than the flat panels of the same area footprint. In addition,

- ◆ The “openbox” and the funnel-like shaped structures both generate more energy than the flat panel case, although, they use excess material for a given energy
- ◆ The energy generated by the GA structures remains consistently constant even for different heights. They were found to contain no holes running across the bounding volume, which would otherwise intercept most of the incoming sunlight. Hence, shapes optimized using a GA approach allow for significant materials saving and the possible use of materials within a wide reflectance range without degradation of the device performance.
- ◆ The energy of the funnel shape outperforms the open-box at all heights
- ◆ Shapes optimized using a GA approach may allow for significant materials saving

7.1. Further Work

The various 3DPV technologies discussed are at differing levels of development – and all have significant potentials for improvement. Continuous and sustained research, development and demonstration (RD&D) efforts are required over time in order to improve efficiency, accelerate cost reductions and the transfer of current mainstream technologies to the industry, develop and improve medium-term cell and system technologies, and design novel concepts and bring them to industrial use.

The next goal is to research further and make it a reality, the future of efficient and much less expensive PV materials through properly validated and executable 3DPV technology.

REFERENCES

- [1] B. Myers, M. Bernardi, and J. C. Grossman, "Three-dimensional photovoltaics," *Applied Physics Letters*, vol. 96, pp. 071902-071902-3, 2010.
- [2] M. Bernardi, N. Ferralis, J. H. Wan, R. Villalon, and J. C. Grossman, "Solar energy generation in three dimensions," *Energy & Environmental Science*, vol. 5, pp. 6880-6884, 2012.
- [3] A. Yuji and T. Yachi, "A novel photovoltaic module assembled three-dimensional," in *Photovoltaic Specialists Conference (PVSC), 2010 35th IEEE*, 2010, pp. 002811-002816.
- [4] T. Suto and T. Yachi, "Power-generation characteristics of an FPM by simulation with shadow-effect analysis," in *Photovoltaic Specialists Conference (PVSC), 2011 37th IEEE*, 2011, pp. 001881-001886.
- [5] S. Suzumoto, L. Tayo, and T. Yachi, "Output power characteristics of a three-dimensional photovoltaic module using fibonacci number composition," in *Telecommunications Energy Conference (INTELEC), 2012 IEEE 34th International*, 2012, pp. 1-7.
- [6] I. Secretariat. (May 2012, 2012). Renewable Energy Technologies: Cost Analysis Series. *Solar Photovoltaics [IRENA WORKING PAPER]*. 1(4/5), 52. Avail. <http://www.nrel.gov/gis/solar.html>
- [7] N. F. Marco Bernardi, Jim H. Wan, Rachelle Villalon and Jeffrey C. Grossman, "Solar Energy Generation in Three Dimensions," *Energy & Environmental Science*, pp. 1-5, 2012
- [8] "<A Novel Photovoltaic Module Assembled Three Dimensional (2).pdf>."
- [9] M. Gharghi, H. Bai, G. Stevens, and S. Sivoththaman, "Three-dimensional modeling and simulation of pn junction spherical silicon solar cells," *Electron Devices, IEEE Transactions on*, vol. 53, pp. 1355-1363, 2006.
- [10] Z. Fan, H. Razavi, J.-w. Do, A. Moriwaki, O. Ergen, Y.-L. Chueh, *et al.*, "Three-dimensional nanopillar-array photovoltaics on low-cost and flexible substrates," *Nature materials*, vol. 8, pp. 648-653, 2009.
- [11] Z. Fan, H. Razavi, J.-w. Do, A. Moriwaki, O. Ergen, Y.-L. Chueh, *et al.*, "Three-dimensional nanopillar-array photovoltaics on low-cost and flexible substrates," *Nat Mater*, vol. 8, pp. 648-653, 08//print 2009.
- [12] M. Ewert and O. N. Fuentes, "Modelling and simulation of a solar tower power plant."- Journal article. Available: http://scholar.google.co.za.ezproxy.ukzn.ac.za:2048/scholar?as_q=&as_epq=Modelling+and+simulation+of+a+solar+tower+power+plant&as_oq=&as_eq=&as_occt=t

VOLTAGE DIP MITIGATION WITH DISTRIBUTED GENERATION IN MICROGRIDS

N Mararakanye*, J Fadiran* and S Chowdhury*

**University of Cape Town, Electrical Department, Rondebosch, Cape Town, WC, ZA.*

Abstract. There has been a rising penetration of renewable sources in the form of distributed generation (DG) in the power system. Common renewable DG technologies include wind turbines, photovoltaic (PV) arrays and small hydropower (SHP) stations. DGs in a microgrid offer several advantages to a power system, one of which is voltage dip mitigation. A voltage dip is a short-term reduction in RMS voltage caused by faults, large motors starting, transformers energising and load switching. Voltage dips can cause serious problems for sensitive loads. Different DG technologies in a microgrid have different fault-ride-through capabilities and hence the voltage support needed during grid faults differ. In studying voltage dip mitigation with DGs in a microgrid, this paper compares the voltage dip mitigation capabilities of a doubly fed induction generator (DFIG), wind turbine system, PV arrays and a synchronous generator based SHP system. This comparison was achieved by using homogeneous microgrids, where each microgrid consisted of one type of DG technology, while the load flow parameters of all DG technologies were kept similar.

Key Words. Voltage Dip; Distributed Generation; Power System Quality.

1. INTRODUCTION

There are five main factors that continually stimulate the high rate integration of distribution generation in the generation of electrical power. These include the developments in distributed generation (DG) technologies, constraints on the construction of new transmission lines, heightened customer demand for reliable electricity, the liberation of electricity markets and lastly, concerns about climate change [2]. Approximately 65% of world's electricity is generated from fossil fuels. It is clear that electricity generation is one of the biggest contributors of carbon dioxide (CO₂) emissions and hence global warming. As a result, there has been an increase in the penetration and implementation of renewable energy sources in the form of distributed generation (DG) through microgrids. The electric power research institute (EPRI) defines distributed generation (DG) as generation from a few kilowatts up to 50 MW. Some argue that DG must be defined in terms of its location rather than its power rating. They therefore define DG as any generation connected directly to a distribution network [2, 5].

Voltage dips can cause serious problems for sensitive loads such as adjustable speed drives, process control equipment, computers and voltage-sensitive electronic equipment. And these form the basic devices of operating an industry. If one of these devices is interrupted, the entire industrial process might be affected and result in a shutdown of an industry. Following a shutdown, it might take hours or days to restart the industrial process and this has financial implications to the organization. Therefore, voltage dips need to be mitigated effectively.

Since different DG technologies in microgrids operate differently to generate electrical power, they also behave differently during grid faults. The ability of any electrical component to be able to operate during low grid voltage is called fault-ride-through (FRT) [5]. Depending on the technology in use, the FRT capability or the voltage support required during grid faults will be different [7]. It is important to know which DG technology can be used more effectively for application of voltage dip mitigation.

This project will focus on doubly fed induction generator (DFIG) wind turbine system; PV arrays and synchronous generator based small hydropower (SHP) system. With increasing penetration of DGs in the global electricity production and with several applications of DG being

mentioned, it is important to note that not all DG technologies are capable of effectively accomplishing each DG application. Since voltage dip is one of the most costly power quality issues, it is important to understand which of DG technologies have better capabilities in terms of mitigating voltage dips. This paper therefore aims to compare the voltage dip mitigation capabilities of wind turbines, PV arrays and SHP.

Although there are many types of DG technologies, this paper only focuses on voltage dip mitigation capability of wind turbine, PV arrays and SHPs. In addition, there are many causes of voltage dips; however, this study will use three-phase short circuit on the line to achieve voltage dips. Furthermore, voltage dips are more concerned with the voltage magnitude of the power system and therefore electrical parameters that do not characterize voltage dips, such as currents, active and reactive power and voltage angle will be ignored when extracting simulation results. This study will focus more on the generator models rather than plant models. Finally, this study does not include active voltage control techniques used in power systems, as these only exist in small scales. However, appropriate automatic voltage regulation was applied on generator models. This study forms part of a series of studies, and given sufficient investigation and results from simulation, a subsequent paper is underway for validation purposes through experimental results.

2. SYSTEM MODELING

2.1 Definition of a Voltage Dip

Voltage dip, also known as voltage sag, is defined by the international engineering consortium (IEC) electromechanical vocabulary, IEC 60050 [3], as any sudden and unexpected reduction of the voltage magnitude at any point in an electrical system, followed by voltage retrieval after a short period of time, from half a cycle to a few seconds. Fig. 1 below provides a basic visual explanation of voltage dip.

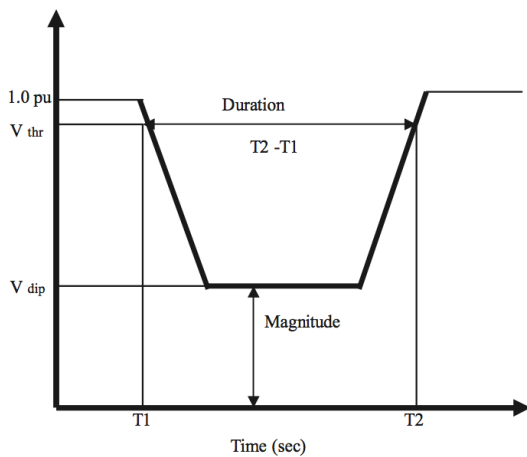


Fig. 1: Retained voltage and duration of a voltage dip [15].

It is important to notice that the IEC description of voltage dip does not provide a set of fixed durations and voltage magnitude that must be detected for a disturbance to be classified as a voltage dip. IEEE Std. 1159 [3] defines a voltage dip as sudden reduction of the supply voltage to a value between the ranges of 10% to 90% of nominal voltage followed by a voltage recovery after a short duration usually from $\frac{1}{2}$ cycle up to one minute. This is the formally accepted definition due to its specification of voltage magnitude and duration ranges. Some of the commonly used methods for mitigating voltage dips are listed below. The following subsection details a comparison different generators operation and implication on voltage support capabilities of different generators.

2.2 Doubly Fed Induction Generator

The DFIG is an induction machine with a wound rotor where the rotor and the stator are both connected to the electrical sources, hence the term ‘doubly-fed’. Its rotor has three phase windings, which are energized with three-phase currents. These rotor currents establish the rotor magnetic field whereas the stator currents set up the rotating stator magnetic fields. The rotor magnetic field interacts with the stator magnetic field to develop torque. The magnitude of the torque depends on the strength of the two fields (the stator field and the rotor field) and the angular displacement between the two fields. Mathematically, the torque is the vector product of the stator and rotor fields [17].

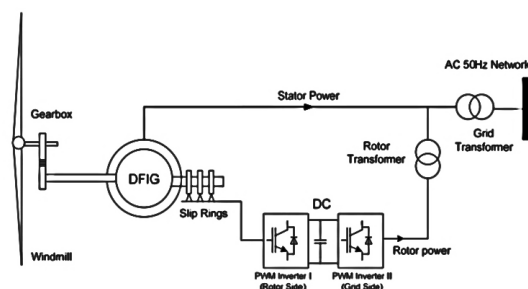


Fig. 2: Configuration of DFIG wind turbine system [19]

If a three-phase fault occurs on the grid, the stator terminal voltage goes to zero in a worst case. This will cause the stator rotating fields to freeze and stop rotating with respect to the stator winding. Thus the stator fields will be rotating at a rotor speed with respect to the rotor winding. Two current components of two frequencies are produced. Since the leakage inductance and the rotor winding resistance are usually small, the rotor current, which is a superposition of the two components, is consequently large. This large current becomes difficult to constrain with the RSC. In order for the RSC to be successful, a large rotor voltage is required [18].

2.3 Synchronous generator

In a synchronous generator, the rotor is mounted on the shaft driven by mechanical prime mover. The rotor winding carries a DC current that produces a constant magnetic field. The AC voltage is induced in a three-phase armature winding to produce electrical power. The electrical frequency depends upon the mechanical speed and the number of poles.

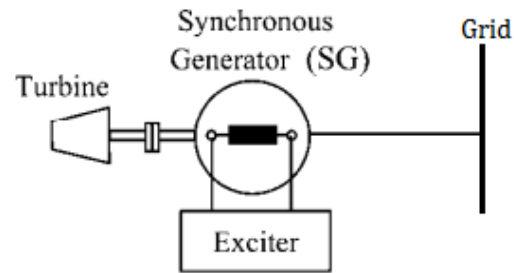


Fig. 3: Configuration of synchronous generator [40]

If a three-phase fault occurs on the grid, the rotor angle as well as the generator current will increase. The synchronous machine will generally deliver about six times the rated current for several cycles before decaying to between 400% and 200% of rated current. The external DC source continues supplying the voltage to the field windings of the generator and the prime mover continues to drive the rotor that produces the required induced voltage which in turn supplies a continuous fault current. As short circuit current continues flowing in the circuit, the machine’s impedance increases due to the increase in winding temperature. This helps the AC envelope to decay faster [16].

2.4 Photo Voltaic Inverters

The basic function of the inverter is to convert the DC power from the PV array into AC power, which can be connected to the grid. This is achieved by a set of solid state switches, MOSFETS or IGBTs. The other functions of PV inverter include maximum power point tracking (MPPT), grid disconnection and integration [20].

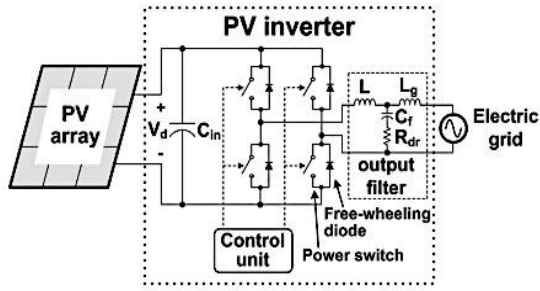


Fig. 4: Transformerless topology of PV inverter system [21]

Power electronic inverters do not have rotating mass components and therefore they do not develop inertia to carry fault current based on an electro-magnetic characteristic. Inverters have much faster decaying envelope for fault currents because the devices lack inductive characteristics [16]

3. METHODOLOGY

In order to observe the voltage dip mitigation capabilities of different DGs in the microgrid, various simulations need to be performed. The previous section outlined mitigation schemes, which are useful for this study. Using appropriate mathematical models developed by Power Factory, this study will use DIgSILENT Version 14.1 for simulation. In doing so, the microgrid and utility grid will be configured in DIgSILENT while providing motivations for the choices made in different stages of simulations.

3.1 Voltage dips magnitude at the PCC and load terminals.

To calculate the dip magnitude and the phase angle jump for the point of common coupling (PCC), the voltage divider model can be used to best achieve this. The model is shown in Fig. 3 and consists of the source impedance \bar{Z}_s at the PCC and the impedance \bar{Z}_f between the PCC and the fault [15].

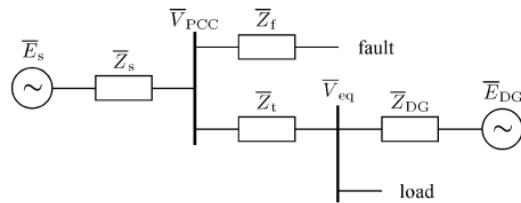


Fig. 5: Voltage divider model [15].

If the loads are initially constant, the voltage at the PCC is given by:

$$\bar{V}_{PCC} = \frac{\bar{Z}_f}{\bar{Z}_s + \bar{Z}_f} \bar{E}_s \quad (1)$$

This model can be extended to study the effects of DG units on voltage dips. In Fig. 5 another branch is added to the PCC which consists of the impedance \bar{Z}_t , representing the impedance between the PCC and the equipment terminals. The DG unit is represented by the voltage source \bar{E}_{DG} and impedance \bar{Z}_{DG} whereas the voltage at the equipment terminals which will strongly depend on the

behaviour of the connected DG units is represented by \bar{V}_{eq} . The voltage at the equipment terminal is given by Eqn. 2 [54].

$$\bar{V}_{eq} = \frac{\bar{Z}_{DG}}{\bar{Z}_t + \bar{Z}_{DG}} \bar{V}_{PCC} + \frac{\bar{Z}_t}{\bar{Z}_t + \bar{Z}_{DG}} \bar{E}_{DG} \quad (2)$$

3.2 System Model

The proposed power system, which will be used for simulation is shown in Fig. 4 below. The utility grid (inside green dotted block) is the IEEE 9 bus system obtained from [8] and it consists of three synchronous generators: CG-1 connected to Bus-1 at 22 kV, CG-2 connected to Bus-7 at 18 kV and CG-3 connected to Bus-8 at 13.8 kV. Bus-1 connected to CG-1 is the slack bus and its voltage is set to $1 \angle 0$ pu. Bus-7 and Bus-8 connected to CG-2 and CG-3 are the voltage controlled (PV) buses with the voltage magnitude of 1.025 pu. Each synchronous generator is connected to the grid through a step-up transformer that steps up each respective voltage to 230 kV. The six transmission lines transfer the electric power from the generators to the loads at Bus-3, Bus-4 and Bus-9.

The utility grid can be regarded as the base system for this study, because its topology is maintained through different case studies. Therefore, there is no need to focus on the simulation configuration of the utility grid since it will affect all the case studies in a similar way. However, all the utility grid parameters of the synchronous machines, transformers, transmission lines, buses and loads used in this study are available in the Appendix. Furthermore, the utility grid synchronous generators are modelled in the similar way as synchronous generators of SHPs.

The microgrid (inside blue dotted block in Fig. 6) network was obtained from [8] and modified to suit this study. It consists of five buses (MG_bus1 to MG_bus5) with MG_bus2 connected to three DG sources, MG_bus4 connected to one DG source and MG_bus5 connected to two DG sources. These DG sources will either be wind turbines, SHPs and PV arrays depending on the case study which will be discussed later in this chapter. The microgrid is operating in a grid-connected mode with the point of common coupling (PCC) being Bus-2. The microgrid has two step-down transformers (MG_TF1 and MG_TF2) that step down the 230 kV to 11 kV and 400 V respectively. The parameters of the microgrid components (DG sources, loads, transformers, lines and buses) used in this study are available in the Appendix.

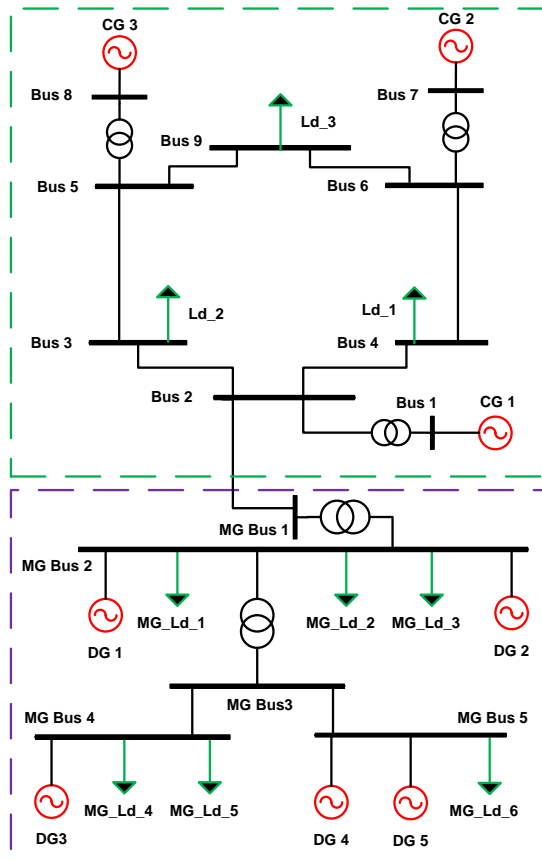


Fig. 6: The diagram showing the proposed Utility grid and microgrid networks for simulations.

4. RESULTS AND DISCUSSIONS

4.1 Case Studies

In studying voltage dip mitigation with distributed generation in a microgrid, the following case studies are considered. It is important to notice that for all case studies, this study is interested in the voltage magnitudes of the system buses and therefore these will be recorded for analysis

- (1) **Case 1: Utility grid operating without the microgrid.** In this case study, the utility grid is operating without the microgrid. This is done in order to observe the voltage magnitude of the utility grid buses when the system is initially operating at steady state conditions and when the three-phase short circuit is applied in the middle of line L2 (Bus 2-4). The following aspects are analysed:
 - The voltage magnitude of utility grid buses during normal operation.
 - The ability utility grid system to support its bus voltage levels during grid faults.
- (2) **Case 2: Microgrid operating in a grid connected mode but with DGs are out of service.** In this case study, the microgrid is connected to the utility grid but the DGs are out of service or not connected. This is done in order to observe the voltage magnitude of the utility grid and microgrid buses when the system is initially operating at steady state conditions and when the three-phase short circuit is applied in the middle of line L2. The following aspects are analysed:

- The change in utility grid buses when the microgrid is connected to the system during normal operation as compared to Case 1.
 - How does connecting the microgrid with DGs off service affects the voltage support capability affect the voltage support of the system during grid fault?
- (3) **Case 3: Homogeneous microgrid with SHPs is connected to the system.** In this case study, the homogeneous microgrid is completed by connecting five SHPs with the same load and other components as in Case 1 and Case 2. This is done in order to observe the voltage magnitude of the utility grid and microgrid buses when the system is initially operating at steady state conditions and when the three-phase short circuit is applied in the middle of line L2. The following aspects are analysed:
 - How will connecting SHPs to the microgrid change the bus voltage levels of both utility grid and microgrid as compared to Case 1 and Case 2?
 - How will the voltage support capability of the system during grid fault change as a result of connecting small hydo plants in the system as compared to Case 1 and Case 2?
 - (4) **Case 4: Homogeneous microgrid with PV system is connected.** In this case, SHPs in Case 3 are replaced by PV systems with other components of the microgrid remaining the same. The same observations and analysis as in Case 3 will be done. In addition, the obtained results will be compared with the results in Case 3.
 - (5) **Case 5: Homogeneous microgrid with DFIG wind turbine system is connected.** In this case, PV systems in Case 4 are replaced by DFIG wind turbine systems. The same observations and analysis as in Case 3 and Case 4 will be done.

4.2 Results

In this a three-phase fault will be used as a source of voltage dip. The fault is applied at 2 seconds and cleared at 2.3 seconds and thus the duration of fault is 0.3 seconds. The voltage magnitudes of both microgrid and utility grid buses are represented for different case studies assuming that the normal voltage range is between 0.95 pu and 1.05 pu. The voltage magnitudes are recorded before the fault at $t = 1$ seconds, during the fault at $t = 2.005$ seconds, as soon as the fault is cleared at $t = 2.305$ seconds and after the fault is cleared at $t = 8.0018$ seconds. In total, the simulation runs for 10 seconds. As already mentioned, the fault impedance $Z_f = 0.188 + j0.418 \Omega$ [8].

The following Fig. 7 shows the voltage profile at Bus-2 when the fault is applied and cleared on line L2 with the microgrid disconnected from the utility grid.

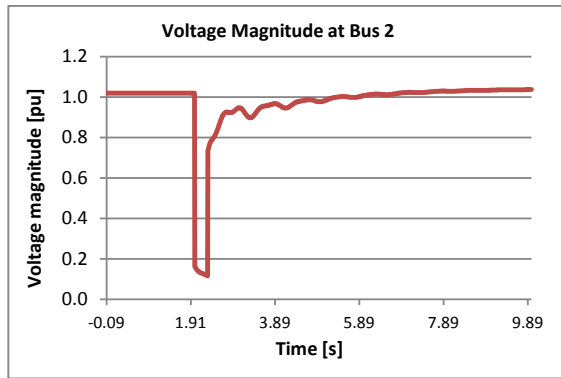


Fig. 7: Case 1, the voltage magnitude curve of Bus-2 during short circuit events.

The following Fig. 8 shows and compares the voltage profile at Bus-2 when the fault is applied and cleared on line L2 for all cases.

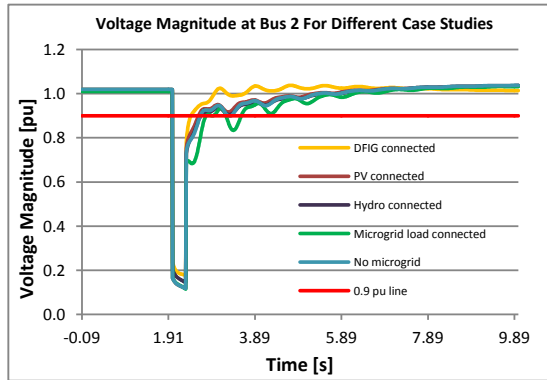


Fig. 8: Bus 2 voltage curves for different case studies.

From Fig. 8, the retained voltage when the SHPs are connected is 0.1441 pu, 0.1781 pu for DFIG system and 0.1180 pu for PV system which is the most severe. However, although the retained voltage of PV system is the most severe, it is not so when it comes to voltage dip duration. The voltage dip duration when the PV systems are connected is 0.5868 seconds, which is better than when synchronous generators are connected which is 0.6368 seconds. On the other hand, when DFIGs are connected, the voltage dip duration is 0.4168 seconds, which is the smallest.

From the results obtained, the DFIG wind turbine systems are better for voltage dip mitigation. This was seen in Case 5 and calculations made in the previous chapter. When DFIGs are in service, the retained voltage is the largest and the voltage dip duration is the shortest as compared to other DG technologies. However, this capability of DFIGs is not inherent but a design requirement. The model used for DFIG system in this study consisting of PWM converters, shunt capacitor and two transformers have many components contributing reactive power which were not taken into serious account in this study and hence affected the results. Therefore, it is only safe to say that DFIGs can be designed to be better for voltage dip mitigation rather than saying DFIGs are better for voltage dip mitigation.

Although the retained voltage when the synchronous generators are in service is better, the voltage dip duration is the longest as compared to the other DG technologies.

However, this duration is still better than when the DGs are out of service in Case 2. In addition, the voltage dip mitigation of the synchronous generators is inherent (not a design requirement) and therefore there is no additional cost in the voltage dip mitigation capability of synchronous generators as compared to other DG technologies.

When PV systems are in service, the voltage dip duration is shorter than for synchronous generators. However, the retained voltage is very poor. The retained voltages obtained when the DGs were out of service in Case 2 are better than the retained voltages obtained when PV arrays are in service. This makes PV arrays poor in terms of voltage dip mitigation. The PV arrays need reactive power controller if they are to inject little reactive power during faults.

5. CONCLUSION

The performance of homogeneous microgrids in voltage dip mitigation has been investigated. The best performing DFIGs can be further improved by designing configurations that better voltage dip mitigation capability, but this will add more costs to the design. On the other hand, synchronous generators maintain a very good retained voltage but the voltage dip duration is poor. PV systems offers very short voltage dip duration but the retained voltage is very poor. The above DG technologies have outperformed each other in terms of mitigated dip by retained voltage magnitude and dip duration. Future study should consider the overall performance in a power system restoration when operated as a mixture of micro sources in the form of a hybrid microgrids.

ACKNOWLEDGEMENTS

The authors are grateful to the authority of the Electrical Engineering Department of University of Cape Town, South Africa, for providing the support and infrastructure necessary for undertaking this research.

APPENDIX

Table 1: Utility grid load and generation

Bus	V_r [kV]	Load / Gen	
		P (MW)	Q (MVar)
1	22.0	slack	slack
2	230.0		
3	230.0	95	90
4	230.0	90	15
5	230.0		
6	230.0		
7	18.0	-50	0
8	13.8	-90	0
9	230.0	100	15

Table 2: Microgrid load and generation

MG Bus	V_r [kV]	Load / Gen					
		1		2		3	
		P	Q	P	Q	P	Q
1	230						
2	11	5	4	6	4.5	5.5	3.2
		20	3.5	14	2.5		
3	0.4						
4	0.4	7	2.4	9	2		
		8.5	2.3				
5	0.4	9	3.4				
		8.5	2.3	8.5	3		

Table 3: Utility grid line parameters

Line	Length [km]	R1 [ohms]	X1 [ohms]	B1 [μS]
2-3	50	3.148	17.6615	250
2-4	50	0.846	19.0845	250
3-5	200	8.992	61.7600	1000
4-6	200	10.58	80.0800	1000
6-9	100	8.993	28.6680	500
5-9	100	2.0631	29.9300	500

REFERENCES

- [1] A. Saidian, D.M. Mehrdad Heidari, "The Effect of Size of DG on Voltage Flicker and Voltage Sag in Closed-Loop Distribution System", IEEE Conference on industrial Electronics and application 5, pp. 68 – 72, 2010
- [2] G. Pepermans, J. Driesen, D. Haeseldonckx, R. Belmans, W. D'haeseleer, "DG: definition, benefits and issues", ELSEVIER, Energy policy 33, pp. 787-798, 2005
- [3] "Voltage sag mitigation", Endeavor energy power quality and reliability centre (EEPQRC), University of Wollongong, Technical note 11, August 2012
- [4] [O. Ipinnimo, S. Chowdhury, S.P. Chowdhury, J. Mitrab, "A review of voltage dip mitigation techniques with DG in electricity networks", ELSEVIER, Electric power systems Research 103, pp. 28- 36, 2013
- [5] O. Ipinnimo, S. Chowdhury, S.P. Chowdhury, "Voltage Dip Mitigation with DG Integration: A Comprehensive Review", Power Electronics, Drives and Energy Systems (PEDES) and 2010 Power India joint international conference, pp. 1- 10, 2010
- [6] K.J.P. Macken, M.H.J. Bollen, R.J.M. Belmans," Mitigation of voltage dips through DG systems", IEEE transactions, vol. 40, Issue 6, pp. 1686- 1693, 2004
- [7] O. Ipinnimo, S. Chowdhury, S.P. Chowdhury, "Voltage Dip Mitigation with DG Integration: A Comprehensive Review", Power Electronics, Drives and Energy Systems (PEDES) and 2010 Power India joint international conference, pp. 1- 10, 2010
- [8] O. Ipinnimo, S. Chowdhury, S.P. Chowdhury, "Effects of renewable DG (RDG) on voltage dip mitigation in microgrids", IEEE International development on Developments in Power Systems Protection (DPSP) conference, pp. 1- 6, 2012
- [9] A. Honrubia-Escribano, E. Gómez-Lázaro, A. Molina-García , J.A. Fuentes, "Influence of voltage dips on industrial equipment: Analysis and assessment", ELSEVIER, Electrical power and energy systems 41, pp. 87- 95, 2012
- [10] A. Moreno-Munoz, J.J.G. de-la-Rosa, M.A. Lopez-Rodriguez, J.M. Flores-Arias, F.J. Bellido-Outero, M. Ruiz-de-Adana, "Improvement of power quality using distributed generation", ELSEVIER, Electrical power and energy systems 32, pp. 1069- 1076, 2010
- [11] B. Renders, L. Vandevelde, L. Degrootea, K. Stockman, M.H.J. Bollen, "Distributed generation and the voltage profile on distribution feeders during voltage dips and the voltage profile on distribution feeders during voltage dips", ELSEVIER, Electric power system research 80, pp. 1452- 1458, 2010
- [12] M. Zangiabadi, R. Feuillet, H. Lesani, N. Hadj-Said, J. T. Kvaløy, "Assessing the performance and benefits of customer DG developers under uncertainties", ELSEVIER, Energy 36, pp. 1703 – 1712, 2011
- [13] D. Gallo, C. Landi, M. Luiso, "Accuracy Analysis of Algorithms Adopted in Voltage Dip Measurements", IEEE transactions on instrumentation and measurement, vol. 59, No. 10, October 2010
- [14] M. A. El- Gammal, A. Y. Abou- Ghazala, T.I. Shennawy, "Dynamic Voltage Restorer (DVR) for voltage sag mitigation", International Journal on Electrical Engineering and Informatics, vol. 3, No. 1, 2011
- [15] B. Renders, K. De Gussemme, W. R. Ryckaert, K. Stockman, L. Vandevelde, M. H. J. Bollen, "Distributed generation for mitigating voltage dips in low- voltage distribution grids", IEEE Transactions on power delivery, vol. 23, No. 3, pp. 1581- 1588, 2008
- [16] J. Keller, B. Kroposki, "Understanding Fault Characteristics of Inverter-Based Distributed Energy Resources", National renewable energy laboratory- Innovation for our energy future, January 2012
- [17] J. Fletcher, J. Yang, "Introduction to Doubly-Fed Induction Generator for Wind Power Applications" Paths to Sustainable Energy, Dr Artie Ng (Ed.), ISBN: 978-953-307-401-6, pp. 259- 278, 2010
- [18] D. Xiang, L. Ran, P. J. Tavner, S. Yang "Control of a Doubly Fed Induction Generator in a Wind Turbine During Grid Fault Ride-Through", IEEE transactions on energy conversion, vol. 21, No. 3, September 2006
- [19] K. Leban, "Doubly fed induction generator fault simulation", Thesis, Institute of Energy Technology, 2009
- [20] J. Worden, M. Zuercher - Martinson, "How inverters work", SolarPro, pp. 68- 85, May 2009
- [21] [45].E. Koutroulis, F. Blaabjerg, "Design optimization of grid- connected PV inverters", IEEE, 978-1-4244-8085-2, 2011

HARDWARE SOLAR POWER EMULATOR FOR EXPERIMENTAL MICRO-GRID STUDIES

*A. El-Haddad, *F. Bellim, *N. Horonga, *W. Cronje

** Faculty of Engineering and the Built Environment, Private Bag 3, Wits 2050, South Africa*

Abstract: A solar power emulator proves to be a useful tool in order to emulate the power output of a photovoltaic system. The solar power emulator is primarily designed to create a controlled environment to test the effects of PV systems on a micro-grid. The designed emulator is made up of two induction machines, rated at 2.2kW, as well as two quadrant and four quadrant inverters. Induction machines were used for the design, as opposed to electronics, in order to provide a system which allows for galvanic isolation between the infinite grid and the micro-grid. The control method used allows the output power of the system to emulate that of a photovoltaic system. The mechanical system slew rate is 1.07 kW/s which is sufficient in order to follow the power output of all weather conditions. This system offers an effective method for emulating the solar power output in a micro-grid for studying purposes.

Key words: emulator, induction machines, inverters, slew rate

1. INTRODUCTION

Electricity is a resource which is used by millions of South Africans every day [1]. As South Africa grows and develops, so does the need to produce more power for these developing areas. The national utility, Eskom, has struggled to keep up with these increased demands over the years and has thus been forced to implement load shedding techniques [2]. These techniques ensure that power station equipment is not damaged by operating at levels they have not been designed for [2]. It is clear that in the future, South Africa will have more renewable energy sources which will be connected to the grid. Therefore studies and tests are being performed to see how renewable energy sources such as solar and wind power can be integrated into micro-grids [3].

In order to understand the effects these renewable energy sources have on micro-grids, several tests under various different weather conditions have to be performed. By performing these tests using photo-voltaic panels, many factors are removed from the user's control. Tests can only be performed during periods of sunlight, and specific tests such as observing the effects when there is sudden cloud cover can only be conducted when this specific weather pattern occurs.

2. BACKGROUND

In order to understand the interaction of multiple sources of renewable energy in a micro-grid, one must observe and record the behaviour under various conditions. In order for these observations to be conducted at any time, independent of the wind or sun, it is useful to be able to emulate the renewable sources of energy. A set-up which is capable of emulating the electrical

characteristics of the renewable energy sources is shown in figure 1.

It can be seen from figure 2 that the system obtains the artificial renewable energy from a supply grid which can be modelled as infinite. This energy is then made to emulate the electrical characteristics of the renewable energy sources. The power is then fed into a micro-grid and the interactions are then observed. Due to the complexity of the system shown in figure 1, the objective of the investigation will be to investigate one instance of this system, which is the solar power emulator.

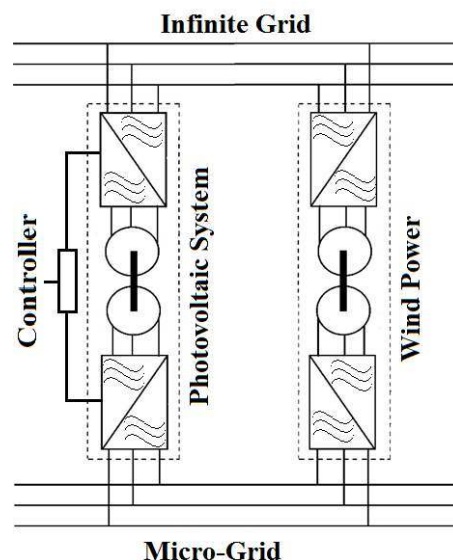


Figure 1: Emulating multiple renewable energy sources on a micro-grid.

2.1 Existing Solutions

There are currently a number of projects which are exploring ways in which to emulate solar power outputs. There are both software, hardware, and hybrid emulators. The photovoltaic power emulator is an example of an emulation system which is currently being used. The system is made up of inverters as well as specialized dc-dc converters [4]. The user is able to program the output characteristics and the system is able to evaluate the full range of power conditions [4]. A time dependant parameter can then define how long the power supply should emulate the loaded profile before the next profile in the sequence is loaded [4].

Other existing solutions include the RTDS simulator. This simulator is designed to simulate electrical power systems and to test physical equipment [5]. The design is customizable and has future expansion capabilities. The system can also combine modularity with Ethernet connections to provide the capability for different people to run several simulations concurrently [5]. The system is assembled in units called racks. Each rack is made up of several mounted cards. The cards are able to communicate with one another using a common backplane which allows information to be exchanged. The RTDS system also has a software component [5]. The software enables parameters to be modified as well as results to be analysed. The software also includes a multitude of power system, control system, and automation component models which are used to create simulation cases [5]. It is the software which determines the function of each processor card during simulation.

2.2 Proposed Design

A solar power emulation system is thus designed so that tests can be performed at any time of the day, and weather patterns from any chosen day can be preloaded onto the system. The emulation system provides control over weather, time frames, as well as geographical regions. The solar power emulation system provides a branch of a larger system which includes other renewable energies as well as actual testing at the micro-grid end. The emulation system uses two induction machines, rated at 2.2kW, as well as one 2 quadrant inverter, and one 4 quadrant inverter. The setup of the entire emulation system, automation, system relationships, measured results as well as a critique of the overall system will all be discussed. A block diagram of the entire system can be seen in figure 2.

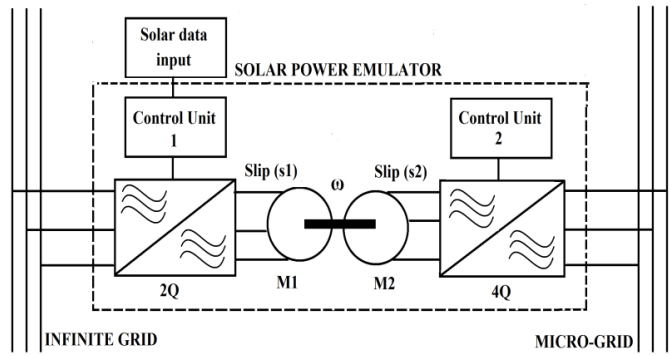


Figure 2: System block diagram of solar power emulator illustrating various components.

A flow diagram of the steps needed to convert the input insolation data sent from the laptop, into a three phase output power which is fed back into the grid can be seen in figure 3.

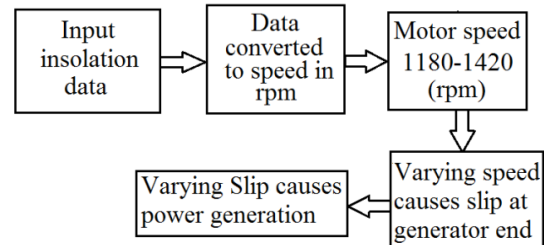


Figure 3: Flow diagram of system input to output.

2.3 Solar data input

The solar data insolation can be obtained from any source that has solar insolation data, provided that the sampling frequency between each data point is sufficient enough to see a clear change over the specified time frame. The data used for the test graph was obtained from the Genmin solar database located at the University of the Witwatersrand, Johannesburg. A day in April 2013 was chosen primarily based on the day having several variations with a combination of rapid cloud cover, rapid sunshine, as well as gradual sunset. Figure 4 shows the data input used for the test graph.

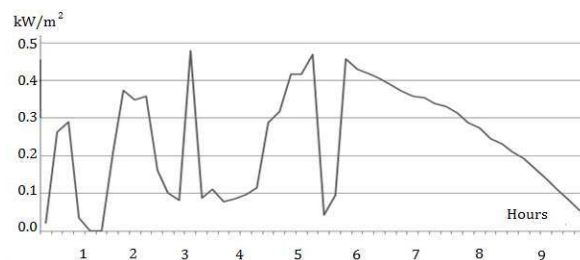


Figure 4: Recorded solar data used for testing in this study.

Due to the flexibility of the system, it is possible to input various signals which will result in a corresponding output power. The input signals are capable of representing the PV power output of any weather condition over specified periods of time.

3. SYSTEM SPECIFICATIONS

The emulation system which is to be designed and implemented should be able to accurately emulate the output power from a real solar panel. The output power cannot exceed 2.2kW since a 2.2kW rated induction machine is being used. The emulation system is thus emulating a 2.2kW output power equivalent solar panel.

3.1 Success Criteria

In order to determine if the project is a success, the following criteria must be met:

- The input signal sent correlates to the actual output power which is fed back into the grid.
- The delay between the input signal and output power is minimal (less than 2 seconds)
- The system can be easily integrated into a larger system with other renewable energy sources.

3.2 Assumptions

- The Eskom grid may be regarded as an infinite grid.
- The input signal does not change faster than the system slew rate of 1.07 kW/s.

3.3 Constraints

- The output power of the system is limited by the size of the induction machines.
- The lowest rating for the regenerative 4 quadrant inverter is 5.5kW, ideally a 2.2kW regenerative inverter should be used to reduce losses.

4. SYSTEM DESIGN

The emulator system is made up of several smaller parts which need to be considered when examining the overall system. These parts include both theoretical understanding as well as practical implementation. The subsections below discuss each relevant part.

4.1 Fundamental Principles

The principles behind the operation of the system include, torque, voltage frequency control (U/f), slip, as well as power factors. Each of these principles are important to the overall efficiency and accuracy of the system. The induction machines are set to operate under U/f control with linear output characteristics. This means that the total flux of the machine remains constant as the

voltage and frequency is increased or decreased proportionally. This technique is used on both machines.

An induction machine can run as a generator when the rotor speed is such that the resulting rotor electrical frequency, ω_r , is greater than the stator electrical frequency, ω_s . This gives the machine a negative slip which generates power. The slip of the machine may be calculated using (1).

$$s = \frac{\omega_s - \omega_r}{\omega_s} \quad (1)$$

Essentially the rotor speed of the induction machine must exceed the synchronous speed in order for the machine to perform the function of a generator. To obtain a rotor speed which is faster than the synchronous speed, an external force is required to rotate the rotor. This is precisely the function of the induction machine which acts as a prime mover. Since the two induction machines are mechanically linked, when the speed of the prime mover exceeds the synchronous speed of the induction generator, the induction generator produces an output power which is directly related to the slip (s2). The relationship between the slip and output power is further discussed in the following subsection.

The relationship between slip (s2) and output power can be seen in figure 5 and figure 6 respectively.

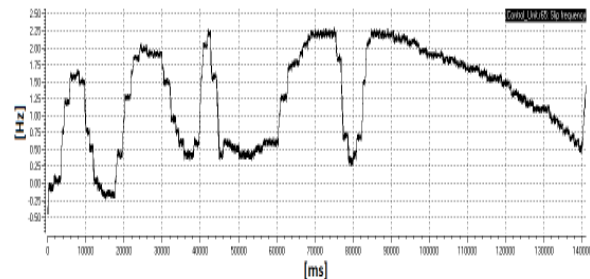


Figure 5: Varying slip according to varying input signal

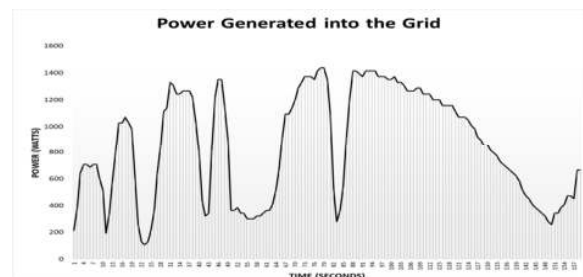


Figure 6: Varying power output according to varying slip. This is effectively power fed to the grid.

4.2 System Setup

Before the machines can be operated using the inverters, the inverters have to be preloaded with the induction machine ratings. These ratings include the rated speed, frequency, and current. This setup ensures that the system never exceeds rated values and is safe to use.

4.3 Range and Base Speed

Since maximum power output is required from the generator, the induction machines are operated at rated speeds. The maximum speed of the induction machine is 1420 rpm, therefore the speed of the prime mover is limited to a maximum of 1420 rpm, at which point maximum power output is achieved.

Since the generator slip is limited to a maximum of 2.25 Hz, there is a specific speed range in which the output power will be directly related to the slip (s_2). In order to determine the speed range of the system, the induction generator and the prime mover are set at rated speeds. The speed of the induction generator is then decreased until such a speed that the slip (s_2) is at a maximum of 2.25 Hz. It is at this speed that the base speed of the system will be determined. The speed at which maximum slip is reached is 1180 rpm. The speed of the generator is therefore constantly kept at a speed of 1180 rpm and the speed of the prime mover is varied from 1180 rpm to a maximum of 1420 rpm at which point a maximum slip is obtained and therefore a corresponding maximum power output.

The relationship between the speed and the slip can be seen in figure 7. As the speed of the generator is decreased, the slip of the generator increases proportionally until the point at which the slip reaches 2.25 Hz. Beyond this point it can be seen that a decrease in the generator speed results in a marginal change in the generator slip. The speed range of the prime mover is then determined to be between 1180 rpm and 1420 rpm. It is therefore required that the input signals should be manipulated such that the speed of the prime mover varies between 1180 rpm and 1420 rpm.

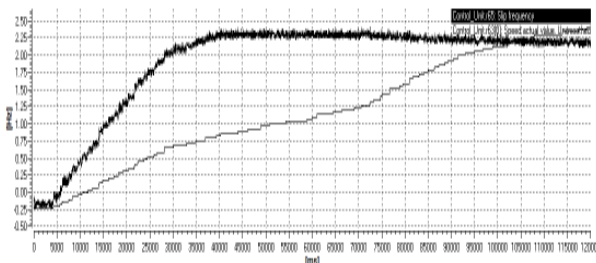


Figure 7: Relationship between speed and slip (s_2) in order to determine base speed.

4.4 System automation

In order to take advantage of the multiple functions offered by the Siemens Starter software, the AutoHotkey software was used in order to automate the system. This software was used since it is capable of operating in conjunction with the Siemens Starter software. The AutoHotkey software allows the speeds of the prime mover and induction generator to vary automatically, thus allowing a certain input signal to be replicated numerous times. The AutoHotkey software makes use of script files in order to automate the system.

It should be noted however that there are other methods of professional automation which may be used to automate the system. These methods of automation were not used since system automation was not a key aspect of the project. Professional methods of automation may also allow for improved functionality of the system due to possible closed loop control methods.

5. MEASUREMENTS AND RESULTS

Once the system has been configured tests were performed to determine the optimum speed at which the emulator system should operate. It was determined that as the speed tends towards the rated motor speed of 1420 rpm, the maximum power output of the system improves. Due to this trend, it was decided that the system should operate between 1180-1420 rpm. This speed range allows the slip (s_2) to vary between 0 and 2.25 Hz. The slip cannot exceed 2.25 Hz as the maximum slip range the four quadrant Siemens G120 PM250 inverter can operate at is 2.25 Hz [6].

Once the relevant slip (s_2) and speed ranges were confirmed, several tests to confirm that the system was able to accurately emulate the solar insolation data were performed. The solar data of a demo graph which was preloaded was run several times. Each time the data was run, a different measurement trace was taken using the built-in trace function available on the Siemens Starter software.

5.1 System relationships

The testing results show measurements taken at the generator end, as well as at the motor end. Due to the generator end being set at a constant base speed of 1180 rpm, the generator measurement traces are constant.

In order for the input signal to resemble the output power as closely as possible, several factors are required to have a one-to-one relationship. The factors which are directly proportional to one another in this configuration include, the output voltage, frequency, speed, slip and power factors.

6. MEASURED SYSTEM STEP RESPONSE

The step response of the system represents the maximum change in output power in the shortest period of time. From figure 8 it can be seen that the power varies from a minimum to a maximum over a period of 1.4 seconds.

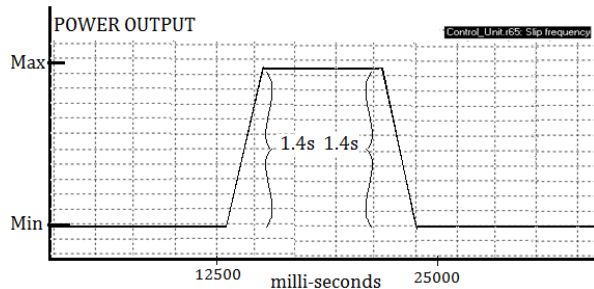


Figure 8: Step response of the system showing the slew rate between a minimum to a maximum power output.

In terms of sunshine, this would represent an instantaneous change from complete darkness to full sunshine which would result in rated power output from the PV system. In reality however, a change like this does not occur instantaneously and thus a slew rate of 1.4 s does not hinder the emulation process of the system. In terms of the input signal this would represent a slew rate of 1.07 kW/s. Therefore a change in the input signal of more than 1.07 kW/s will not be entirely processed by the system and thus the output power will not directly relate to the input signal

An analysis of the step response suggests that almost any input signal will result in an output which is directly related. In reality there will be no step inputs which will be required to be emulated. Given that the system is capable of handling a slew rate of up to 1.4s, it can be established that the system will be capable of handling any input signal.

8. TRADE OFFS

The efficiency of the system was improved by operating at higher speeds, however by doing so, the steps between each rpm increment was increased which led to a lower resolution which meant that the motor speed reading had more distinct steps when compared to the steps at lower speeds. A section showing this distinction can be seen in figure 9.

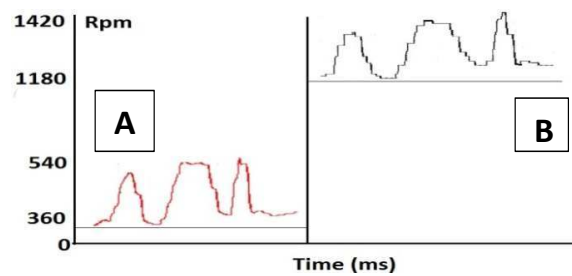


Figure 9: Comparison between graph A and B showing how the resolution varies as the operating range is varied.

The Siemens Starter software was used instead of using a micro controller to control the motor speed. The software was used as it had the advantage of providing useful readings such as torque, speed, and slip, when the trace function was activated. The disadvantage of using the software is that the readings obtained are software based and are not as accurate as the readings which can be obtained by connecting to the shaft encoder.

9. FUTURE IMPROVEMENTS

Due to the time limitations placed on the project, certain aspects of the solar power emulator may not have been optimised. These aspects are therefore suggested as possible improvements to be made to the system.

- A variable speed drive (VSD) controller can be integrated into the system so that the exact instantaneous speeds can be visible to the user at all times. Additionally the entire system will have improved power factors if the inverters and induction machines have identical power ratings.
- Since PV systems make use of inverters in order to obtain a grid compatible voltage, it is assumed that the output waveforms are similar to the output waveforms of the solar power emulator. Investigation should however be carried out in order to ensure that the output waveforms closely match.
- The existing setup of the solar power emulator makes use of two inverters which are independently controlled by two laptops. It is therefore required that the script files be manually activated at the same time in order to run an emulation. This method of initialising an emulation leaves room for faults due to human error. A method of networking the two inverters, by using a profi-bus connection, should be investigated in order to ensure a more accurate method of initialising the emulation process.

10. APPLICATION RECOMMENDATIONS

In order to investigate the effects of PV systems on micro-grids, a micro-grid as well as a PV system must be accessible. The issue with a PV system however, is that the output of the system is dependent on the availability of the sun. Therefore, analysis on the effects

of the PV system on a micro-grid may only be carried out when the correct conditions are present.

The solar power emulator may therefore be used as a means to provide a controlled environment in order to analyse the effects of a PV system on a micro-grid. The solar power emulator has the ability to emulate the power output characteristics of a PV system without being dependant on the natural resource itself. Furthermore the solar power emulator has the ability to emulate the power output which relates to any weather conditions throughout the year. These features of the solar power emulator allow for a controlled environment to be used for testing the effects of PV systems on a micro-grid.

The solar power emulator may also be used to assist in the sizing of grid-tied PV systems. Since grid-tied PV systems feed the output power directly to the grid, it is important to determine if the power fed to the grid is being used by the load or if it exceeds the requirements of the load. The solar power emulator may therefore be connected to the grid and the PV output from different weather conditions may be emulated. The grid may then be monitored over a period of time in order to determine if the PV output matches the load profile of the grid where the solar system will be installed. In doing so, the correct size of the PV system may be installed in order to provide an optimal solution.

11. CRITIQUE

Various aspects of the system can be critically analysed in order to determine the overall success of the project, these aspects are discussed below.

11.1 Power factor

Power factors for renewable energy sources being fed back into the Eskom grid are to be within 0.975 lagging and 0.975 leading [7]. The Siemens G120 inverters that form an integral part of the system cause the power factors to vary between 0.4 and 0.9 depending on the amount of power which is being generated at the time. The power factor output is thus not sufficient enough to be fed back to Eskom. In order to improve these power factors, power factor correction reactances can be employed, or alternatively, a larger motor rated at 5.5kW can be used at the generator side to ensure that there is no mis-match between the induction machine and the inverter being used.

11.2 Measured Power Output

The output power, measured with a three phase power meter, relating to the input signal, is shown in figure 10. A comparison between figure 4 and figure 10 shows that there is a direct relationship between the input signal and the output power. This comparison further verifies that the solar power emulator is capable of emulating any input signal over a selected period of time.

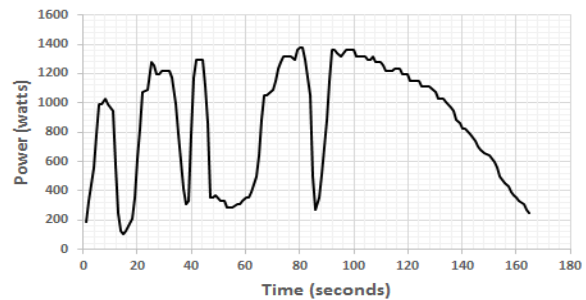


Figure 10: Actual measured power output corresponding to a recorded solar power input.

12. CONCLUSION

A solar power emulator was designed and implemented in order for experimental studies of a micro-grid to be performed without the dependency on weather patterns and seasonal changes. The solar power emulator has a slew rate of 1.07 kW/s, which is sufficient to follow most practical renewable energy transients. As weather conditions do not change instantaneously it is found that the slew rate of the system does not hinder the emulation process and the solar power emulator is therefore capable of accurately emulating the power output of a PV system. In order to replicate certain emulations, the system has been automated using an external software which may be used in conjunction with the Siemens Starter software. This method of automation was used since automation was not a key aspect of the project.

13. REFERENCES

- [1] Redpepper, "South Africa, Power to the People", October 2009.
URL: <http://www.redpepper.org.uk/south-africa-power-to-the-people/.html>, last accessed 20/10/2013
- [2] Load Shedding, "Load shedding" October 2013.
URL: <http://loadshedding.co.za/>, last accessed 21/10/2013
- [3] J. Kubby, D O'Leary, A Shakouri, "Renewable Energy Microgrid", Baskin School of Engineering, 2012.

[4] Magma Power, “Photovoltaic emulator”, URL:<http://www.magnapower.com/products/programmable-dc-power-supplies/photovoltaic-power-emulation>, last accessed 21/10/2013

[5] RTDS, URL: <http://www.rtds.com/index/index.html>, last accessed 11/11/2013

[6] Siemens, Sinamics “G120/G120D/ET Parameter manual”, 2010

[7] N.E.R.S.A. “Grid code requirements for wind turbines connected to distribution or transmission systems in South Africa” URL:

<http://www.nersa.org.za>, last accessed 22/10/2013

PERFORMANCE EVALUATION OF A SOLAR CAR'S PHOTOVOLTAIC ARRAY

R A Lotriet* and A J Grobler**

* North West University, School of Computer, Electric and Electronic Engineering, Potchefstroom Campus (NWU PC)

** North West University, School of Computer, Electric and Electronic Engineering, Potchefstroom Campus (NWU PC)

Abstract. The photovoltaic (PV) array of the North West University's solar car did not perform well during the 2012 Sasol Solar challenge. No test results or data were available that compares the power the PV array ought to generate and how much it was currently generating under the various irradiance conditions. Also, due to the race and other post events the solar car's PV array were damaged extensively. To evaluate the performance of the PV array, the best PV module on the array has been tested and simulated simultaneously. By comparing the simulated and tested results, the performance of the PV array has been benchmark and the different causes for under performances have been derived and solved. This article presents the results of the tests and simulations needed to benchmark the performance and to identify and solve the main causes to under performances. At the end of this article a comparative test has been conducted to illustrate the improvement on the PV cells, after improvements to the poor performances and other phenomena have been made.

Key Words. Solar car, photovoltaic cells, module, array, efficiency, modelling, tests, performance evaluation, improvements

1. INTRODUCTION

Photovoltaic (PV) cells are devices that the world has been waiting for, to harvest electrical energy from the most abundant resource available, the sun. PV technology dates back as far as 1958 where it was exclusively used in space to power satellites. Nowadays PV cells are being used in everyday appliances and have actually become a very common method to generate electrical energy [1].

PV cell are improving every day. The best commonly available PV cells on the market are silicon (Si) PV cells which is up to 30%-35% efficient, while other less common PV cells such as Gallium Arsenide (GaAs) and multi-junction cells have been reported to reach efficiencies of up to 44% [2]. One of the prestigious displays of PV technology is solar car race events where engineering teams showcase the advancements in PV technology.

During 2012, engineering students from the North-West University (NWU) manufactured a solar powered racing car with which they participated in the 2012 Sasol Solar Challenge and finished first in their division. However, no testing and analysis of the components were done after completion of the solar car construction. Without any proper tests on the PV array it was unclear whether or not the PV cells generated sufficient power and how efficient the cells truly are. This short coming ultimately caught up with the team. During the race the batteries depleted at a much faster rate than expected. This forced the team to drive at slower speeds and to even remove one of the vehicle's motors. The expected power generated by the array was 1044kW, but eventually it was found that the array only generated 700W, which is 33% less of what was expected. Since no evaluations prior to the race have been conducted no explanations could be given to why the array is generating 344W less of what was expected.

Another phenomenon that surfaced during the race was the effect of shadows casted over the array. The effect of even a brief shadow casted over one of the modules of the vehicle,

such as driving past a tree or street light, caused the current of the module to drop significantly resulting in almost 0W power generated by the partially shadowed module. This phenomenon influenced all solar teams and a thorough investigation needs to be conducted to provide a possible solution for this phenomenon's negative effect.

In Figure 1 the PV array of the solar car is illustrated.



Fig. 1. The NWU solar car containing 252 monocrystalline solar cells.

For the NWU's solar vehicle to be a formidable competitor in the 2015 WSC in Australia the PV array needs to be evaluated and optimised. By conducting proper simulations, tests and analysis on the PV array, the problem areas and short comings of the array can be identified. Solutions to the problem areas, such as the shadow effect also need to be addressed and analysed in order to evaluate whether or not the solution is feasible. Thus, in order to

conduct a detailed evaluation on the PV array's performance the PV array firstly needs to be modelled in Matlab® Simulink® so that it may be simulated. The simulations will be conducted simultaneously with the tests under the same ambient conditions and will serve as reference values to the tested results. After the evaluations between the tested and simulated results have been made, it will be possible to identify the different causes to the PV array's under performance. The research methodology followed can be seen in Figure 2.

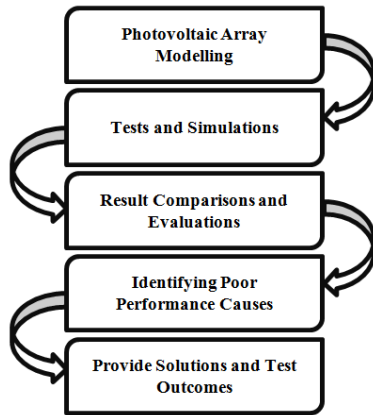


Fig. 2. Research Methodology

2. MODELLING THE PHOTOVOLTAIC ARRAY

2.1 Modelling the equivalent circuit of a photovoltaic cell

In order to design, model and simulate the PV array in Matlab® Simulink® the equivalent circuit of a PV cell must first be implemented as a cell. For this Simulink already has a predefined PV cell block. This block is based on the PV cell's equivalent circuit and can be used in simulations.

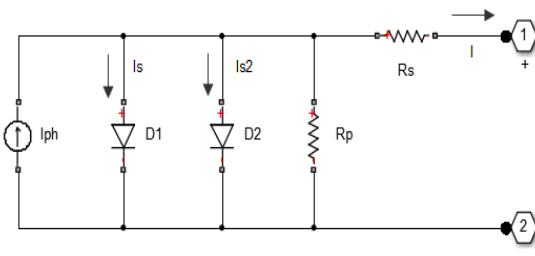


Fig. 3. Equivalent circuit of a PV cell [3]

Figure 3 illustrates the equivalent circuit of a PV cell which is modelled as a block component in Simulink. From the equivalent circuit in Figure 2 the following components are found in the circuit:

- I_{ph} – Measured photo generated current.
- $D_{1,2}$ – Diode 1 and 2, due to the p-n junctions of the PV cell.
- V_p – Voltage across the parallel resistor R_p .
- R_p – Parallel resistance.

- R_s – Series resistance.

To establish the accuracy of the PV cell, a single block has been adjusted according to the PV cell's datasheet and simulated at standard test conditions (STC). The requirements of these standard tests are established by the Underwriters Laboratory (UL) test protocol. Under these protocols, the manufacturer must test the PV modules at STC. STC has three main elements under which all PV modules are tested [2]:

1. Cell temperature: 25°C
2. Irradiance: 1000 W/m²
3. Air mass: A.M. 1.5

In Table 1 the simulated values are compared against the datasheet values.

Table 1 Simulated Values vs. Datasheet Values

Single PV cell		
Characteristic	Simulated Value	Datasheet Value
V_{oc} [V]	0.644	0.644
I_{sc} [A]	9.05	9.05
V_{pm} [V]	0.546	0.546
I_{pm} [A]	8.49	8.49
P_{pm} [W]	4.64	4.64

Since the simulated values correspond to the datasheet, as seen in Table 1, the PV cell block can be used to construct both a PV module and PV array model.

2.2 Simulink test model of the PV module

Figure 4 illustrates the simulation model for one PV module of the solar car. Since the solar car consists out of three equal PV modules only one PV module need to be modelled for the simulation outcomes. The model illustrated below is designed such that the simulation of the module will generate the characteristics of the solar PV module which includes:

Short-circuit current (I_{sc}): Which is the current value achieved when there is essentially no voltage is generated.

Open-circuit voltage (V_{oc}): This represents the voltage value at which the current is equal to zero.

Maximum power current (I_{PM}): The Maximum power current is the indicated current under which the PV module is delivering maximum power.

Maximum power voltage (V_{PM}): Similar to I_{MP} , the Maximum power voltage is the indicated voltage under which the PV module is delivering maximum power.

Maximum Power (P_{PM}): The maximum power generated at the optimal current-voltage relationship (I_{pm} and V_{pm}).

In addition, the simulation model also needs to provide the option to adjust the incoming irradiance as well as the cell temperature.

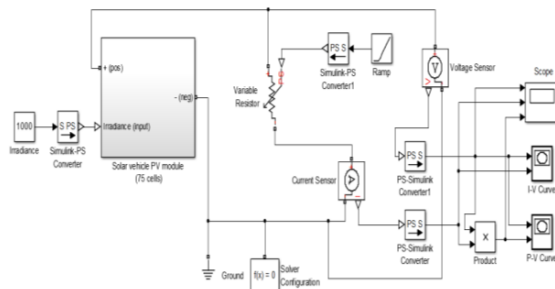


Fig. 4. Simulation system design for a PV module

The PV module is designed as a subsystem block consisting out of several levels of subsystems blocks which are connected in series to model 75 PV cells in series. The irradiance is modelled as a constant input to the PV module, while the temperature can be adjusted at the solar cells' input parameters.

In Table 2 the simulated datasheet for a PV module has been simulated under STC.

Table 2 Simulated Datasheet of the PV Module

PV Module					
η (%)	Pmax (W)	Voc (V)	Isc (A)	Vpm (V)	Ipm (A)
19.4	347.7	48.3	9.1	41.0	8.5

3. TESTING, SIMULATING AND EVALUATING THE PHOTOVOLTAIC ARRAY

The purpose of these tests is to provide a performance benchmark of the solar car's power generating ability. The solar car has a total of 225 PV cells and to test all of these cells will be unproductive. Thus, only the best PV module and its respective cells will be tested and simulated. These tests will clarify whether or not the PV cells are performing as specified in the datasheet.

The following characteristics need to be measured from the PV module and PV cells:

- Irradiance $I(t)$ [W/m^2]
- Cell/Module temperature T [$^{\circ}\text{C}$]
- Short-circuit current I_{sc} [A]
- Open-circuit voltage V_{oc} [V]
- Maximum power current I_{pm} [A]
- Maximum power voltage V_{pm} [V]
- Maximum power P_{pm} [W]
- Efficiency η [%]

3.1 Testing and Characterizing a PV module

It has been decided that only the best functioning PV module and its corresponding PV cells will be tested and evaluated., since the entire PV array consists out of three identical PV module, each consisting out of

75 serial PV cell. Fig. 5 depicts the PV module configurations on the solar car.

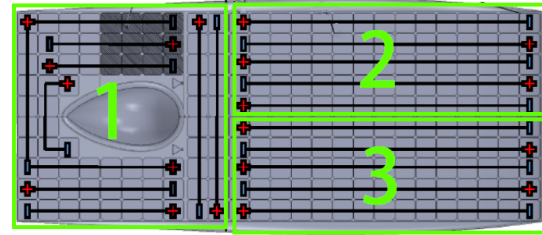


Fig. 5. Solar vehicle's PV layout with the three separate modules

PV module no. 2 has been identified as the best performing module. By only testing PV module 2 the test results will be clearer, since it would represent the best performance that the PV array is able to deliver.

Figures 6 and 7 illustrate the practical test setup to test the PV module. In Figure 6 all the equipment used to characterise the PV module are shown, which consists of a variable resistor, multimeter, thermometer and a solar power meter

3.1.1 Test setup

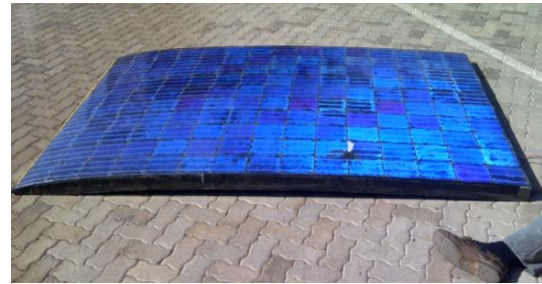


Fig. 6. Bonnet taken of the car to test PV module 2



Fig. 7. Test equipment used to test PV module 2.

3.1.2 Test results

The first tests conducted were to determine the PV module's performance under low irradiance and high irradiance conditions. The performance is evaluated by simulating the PV module under the same atmospheric conditions and then comparing the tested and simulated results. The simulated characteristics and respective curves have been simulated under same conditions at which they were physically tested.

A. Low Levels of Irradiance

Figure 8 depicts the tested I-V and P-V curves against its simulated counterparts.

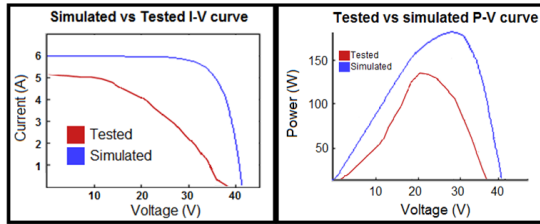


Fig. 8: I-V and P-V curves of the simulated and tested results of the PV module under low irradiance

By studying Figure 8, it can be seen that both tested and simulated I-V and P-V curves have similar shape. However, the measured values of the tested curves do not reach the same current, voltage and power values of that of the simulated curves, which indicates that in practice the PV module is under performing.

The efficiency of the PV module is the ratio of the PV module's power generated at its maximum point over the available solar power. The net area (A) of the module is measured as 1.792m^2 and the irradiance (I_t) during the measurements being $780\text{W}/\text{m}^2$. Hence, the efficiency is calculated as [4]

$$\eta = \frac{I_{mp} \times V_{mp}}{I(t) \times A} = \frac{120.2}{166.60} = 7.2\%$$

The tested and simulated PV characteristics of the PV module are illustrated in Table 3.

Note that the PV module has been tested and simulated under the same ambient conditions which is an irradiance of $780\text{ W}/\text{m}^2$ and a module temperature of 48°C

Table 3

Tested & Simulated PV Module Characteristics at Low Irradiance

	PV Module Characteristics under Low Levels of Irradiance					
	I_{sc} (A)	V_{oc} (V)	P_{pm} (W)	I_{pm} (A)	V_{pm} (V)	η (%)
Tested values	5.1	38.0	120.2	4.2	23.9	7.2
Simulink values	5.8	40.9	166.6	5.0	36.5	11.9

B. High Levels of Irradiance

In Figure 9 it can be seen that the measured curves have the same trend as the simulated curves. The simulated curves have higher values the tested values.

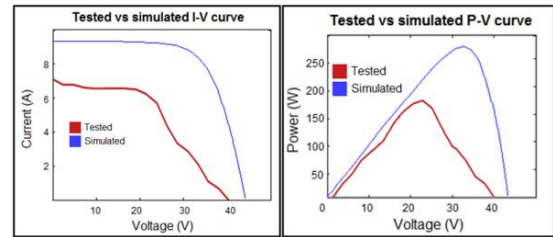


Fig.9: Tested and simulated I-V and P-V curves at high irradiance

This is also in the case for the PV module characteristics as seen in Table 4, with the efficiency calculated on the same manner as for low light conditions.

Again, note that the PV module has been tested and simulated under the same ambient conditions for high levels of irradiance, which is an irradiance of $1200\text{ W}/\text{m}^2$ and a module temperature of 55°C

Table 4

Tested & Simulated PV Module Characteristics at High Irradiance

	PV Module Characteristics at High Levels of Irradiance					
	I_{sc} (A)	V_{oc} (V)	P_{pm} (W)	I_{pm} (A)	V_{pm} (V)	η (%)
Tested values	7.1	35.2	176.0	6.9	25.3	8.2
Simulink values	9.0	42.1	279.0	7.8	35.4	13.0

The tested results are a cause for concern. This is a clear indication that the PV cells are not performing according to the specifications.

The results between the simulated characteristics (which depicts the values what the module should be able to generate) and the tested characteristics (which depicts the values what the module is physically generating) differs considerably with the measured values being 4.8% less efficient of the simulated values.

3.2 Testing and Characterizing the PV cells

Now all the individual PV cells will be tested and characterised.. The aim of these tests is to provide insight to the true characteristics under varying atmospheric conditions. It will also aid in the investigation of the different factors that influence the performance of the cells and ultimately the module's performance.

3.2.1 Test setup

To test and characterise the individual PV cells in the module, each cell will be disconnected from the other cells in the module. The irradiance and cell temperature will be measured first, after which the individual cell's solar characteristics will be testes and simulated under the same measured conditions.

Figure 10 shows the configuration of the series connected PV cells on the solar car.

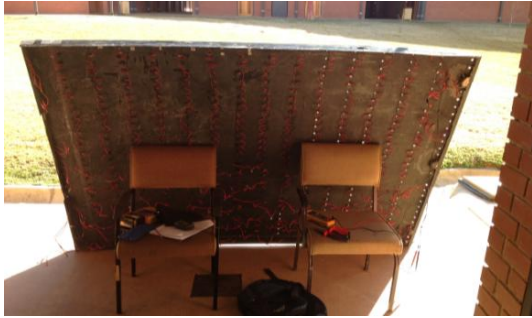


Fig. 10: Test station for testing and characterising the individual PV cells

The PV module consists of 75 individual PV cells. Each cell's characteristics along with its temperature and instantaneous irradiance were tested. It will not be productive to illustrate how each one of these values compares to its corresponding simulation. Instead it will be illustrated by what percentage each characteristic of the 75 PV cells deviates from the expected (i.e. simulated) results.

3.2.2 Test results

The analysis was done by implementing a deviation equation to determine the amount by which the respected PV cell deviated from its ideal results

$$\% \text{ Deviation} = 100 - \left(\frac{\text{actual value}}{\text{simulated value}} \times 100\% \right)$$

After all the characteristics' deviations for each individual cell have been calculated, each respective characteristic value from all the cells have been grouped and sorted together. The range in percentage by which deviation of the characteristics occurs is illustrated in a box and whisker plot shown in Figure 11. The boxes indicate the quartile and median ranges that represent the majority percentile deviation of the PV cells. As seen in Figure 13, the highest deviation percentage range comes from the current and power characteristics, with the maximum power point deviation reaching 81%. Even though the voltage characteristics are relatively low, there still isn't one value that deviates with 0%, i.e. generated its expected value.

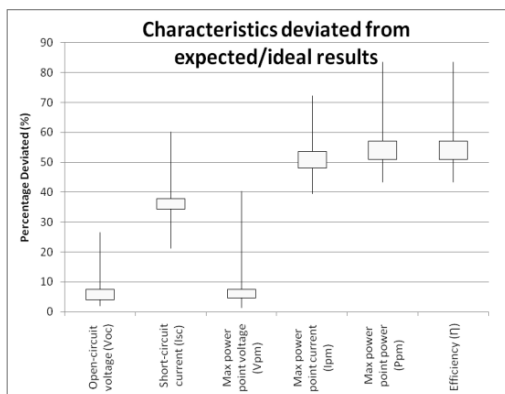


Fig. 11: Box plot showing the percentage deviation range of the PV cells' characteristics

4. PROVIDING SOLUTIONS TO CAUSES FOR POOR PERFORMANCES

There were four fundamental causes identified that impaired the solar car's generated power.

1. Effect of shaded PV cells
2. Mismatched Currents
3. Power losses due to excessive heat
4. Irradiance dissipation due to improper encapsulation

In this section viable solutions to these issues will be identified and presented.

4.1 Implementation of Bypass Diodes

The implementation of bypass diodes have proved to eliminate the degrading effects of mismatched currents and shaded PV cells. The net current in a PV module are limited to the PV cell generating the least current. In the same manner when a PV cell is shaded the net current drops significantly. This is because the current are forced to flow through the PV cell's diode path.

If the current is strong enough it will cause the PV cell to be destroyed due to the losses through the diode while being shaded. This phenomenon is illustrated in Figure 12.

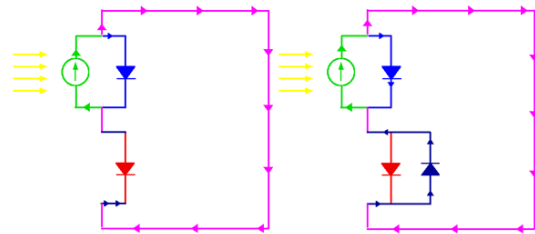


Fig. 12: Two series connected equivalent PV circuits, with the bottom circuit being shaded (left) and a bypass diode implemented (right)

Bypass diodes provide an alternative conduction path, which will rectify both mismatched currents and shaded PV cells. This will ultimately minimise current losses which will inherently lead to more generated power and higher efficiencies.

4.2 Rectifying Power Losses due to Excessive Heat

Figure 13 illustrates how a PV cell's power decreases as its heat increase.

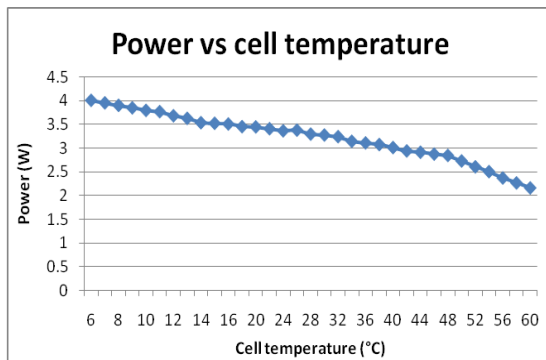


Fig. 13: Diagram showing how the output power decrease as heat increase

The main cause for the incremented heat is due to surface emissivity, ϵ . Emissivity is a body's ability to convert its radiated energy into thermal energy [5].

An efficient method to influence a surface's emissivity is by colour coating the surface. White, which reflects the majority of radiated light, has been identified as the optimal colour to reduce emissivity. Black, which is the solar car's current surface colour, has been found to increase emissivity, since it absorbs the majority of radiated light. Thus a test has been conducted by placing two similar PV cells on identical black and white surfaces.

The test results are displayed in a diagram in Figure 14.

The test showed that the PV cell on the white surface had a surface temperature of 40°C, against the black surface's 57°C.

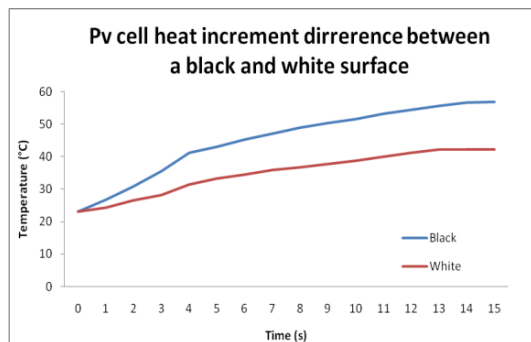


Fig. 14: Heat test of a PV cell on a white surface against a PV cell on a black surface.

4.3 Identifying a More Efficient Encapsulation Material

The solar car currently has a polymer encapsulation. To illustrate the impairing effect that the current encapsulation has on the PV array a test was conducted to evaluate the efficiency of the encapsulation.

For the test three PV cells were used. The first cell was left uncovered in order to provide an indication to the efficiency limit that the PV cell can deliver. The second PV cell was encapsulated with the standard polymer encapsulation. And the third was

encapsulated with Perspex which is almost ideally transparent.

The results are shown in Figure 15.

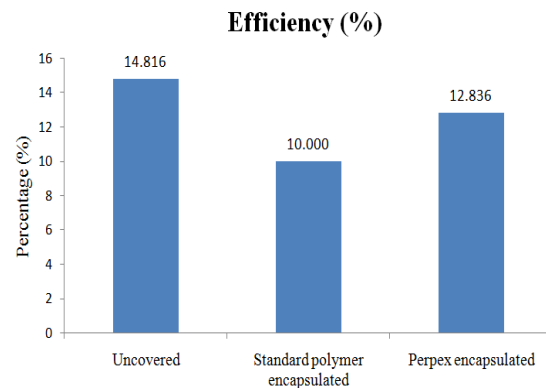


Fig. 15: Encapsulation tests showing the different efficiencies.

Figure 15 displays that polymer encapsulation is impairing the efficiency of up to 4.8%. And with Perspex being 2.8% more efficient gives a clear indication that there exists a better encapsulation option.

After thorough investigation a viable encapsulation choice was found.

Figure 16 shows the optical properties of ionomer encapsulation.

Optical Properties				
Property	Test Method	Test Conditions	Units	Value
Refractive Index	ASTM D542	23°C		1.49
Yellowness Index - 15mil / 0.38 mm	ASTM D313			0.3
Luminous Transmittance - 15mil / 0.38 mm	ASTM D1003		%	93.8

Fig. 16: Ionomer encapsulation optical properties [6]

The properties show that the encapsulation transmits 93.8% lamination, making it an almost ideal transparent material.

5. IMPROVEMENT IMPLEMENTATION

All the viable solutions discussed were simultaneously implemented on a series of three PV cells, which were ultimately tested and compared against the solar car's PV cells.

The improvements were not implemented directly on to the solar car. Instead a test setup with three of the same PV cells used on the solar car were constructed and connected in series. The solutions found were implemented on this circuit, i.e. the improved circuit and was measured and compared against the measured values on the solar car's PV cells found during the test phase under the same conditions.

Figure 17 displays the improved PV circuit against the unimproved (solar car) PV circuit.

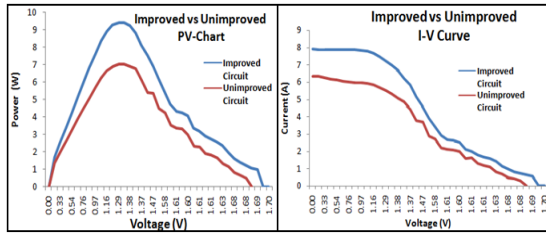


Fig. 17: Improved and unimproved P-V and I-V curves.

Finally the difference in the improved and unimproved PV characteristics can be seen in Table 5

Table 5 Improved and Unimproved PV circuit's Characteristics

Unimproved vs Improved PV cells		
Irradiance [W/m ²]	1045	
Temperature [°C]	34°	
	Unimproved	Improved
Cell temp [°C]	55	46
V _{oc} [V]	1.68	1.695
I _{sc} [A]	6.214	7.021
V _{pm} [V]	1.262	1.45
I _{pm} [A]	5.610	6.575
P _{pm} [W]	7.08	9.53
η [%]	9.46	12.38

The results showcase an improved efficiency of 11.48% against the unimproved 9.46%. Thus by implementing the suggested improvements will allow for more generated power from the PV array.

This ultimately indicates that the PV array's generated power can be increased from

$$(1045 \text{ W} / \text{m}^2)(6 \text{ m}^2)(0.0946) = 591 \text{ W}$$

Up to an improved output power value of

$$(1045 \text{ W} / \text{m}^2)(6 \text{ m}^2)(0.1238) = 776 \text{ W}$$

This is a significant improvement of 200W, which would undoubtedly gave the solar car a remarkable performance improvement and would have enabled the NWU solar car team to cover further distances throughout the race

4 CONCLUSION

In this paper the PV array of the solar car has been tested and evaluated. The aim was to benchmark the PV array's performance in order to investigate solutions to the poor performance causes. The photovoltaic (PV) array of the solar car was tested and analysed. The purpose of this project was to benchmark the performance of the PV array and to provide solutions to the causes for under performance

so that can achieve higher performances. The performance was evaluated by means of firstly identifying the best performing PV module and then to establish how far off it is performing from its specified performance. This was done by comparing the tested results against its corresponding ideal results under the same conditions. The ideal results were generated by means of designing, modelling and simulating the PV module with Simulink®. These evaluations ultimately provided a performance benchmark of the PV array. After the evaluations, the causes to the PV module's poor performance have been identified and viable solutions were presented. There were several causes identified, including mismatch currents, shaded PV cells, surface emissivity and infirm encapsulation effects. The solutions to these causes were tested and presented individually. The final outcomes to the solutions provided showed that the PV array's generated power can be significantly improved if these solutions are implemented on the solar car.

The NWU solar car has room for a lot of improvements. The current solar was the first solar car constructed by the NWU. By solely implementing the suggested solutions presented in this paper on the next solar car, the next car will undoubtedly have superior generated power than its predecessor.

ACKNOWLEDGMENTS

The author, R.A Lotriet, would like to thank his project coordinator and supervisor, Dr. A.J. Grobler, for the continued guidance during the completion of this project. Without his help the project would not have been such a major success.

REFERENCES

- [1] S. Aldous, et al. "How Solar Cells Work". 01 April 2000. Available: <http://science.howstuffworks.com/environmental/energy/solar-cell.htm> [Accessed: Jan. 24, 2013]
- [2] R. Mayfield. *Photovoltaic design and installation for dummies*. Wiley Publishing, Inc. Indianapolis Indiana, 11 River St. Hoboken, NJ 07030-5774. 2010. pp 110-115
- [3] .N. Tiwari and S. Dubey. *Fundamentals of Photovoltaic Modules and their Applications*. RSC Publishing. Cambridge, Milton Road, Science Park, CB 0WF, UK, 2010. pp 5-360
- [4] J.A. Gow, C.D. Manning. "Development of a Photovoltaic Array Model for Use in Power-Electronics Simulation Studies." *IEEE Proceedings of Electric Power Applications*, Vol. 146, No. 2, pp. 193–200, March 1999
- [5] HyperPhysics. "Stefan-Boltzmann Law" 2013. Internet: <http://hyperphysics.phy-astr.gsu.edu/hbase/thermo/stefan.html>. [Accessed: Aug 02, 2013]
- [6] DuPont™. "DuPont™ PV5400 Series". 2013. Internet: http://www2.dupont.com/Photovoltaics/en_US/assets/downloads/pdf/PV5400_Encapsulant.pdf [Accessed Aug. 03, 2013]

THE DEVELOPMENT OF A PASSIVELY CONTROLLED SEGMENTED VARIABLE PITCH SMALL-SCALE HORIZONTAL AXIS WIND TURBINE

S N Poole*, R Phillips**

*Mechanical Engineering Department, Faculty of Engineering, Built Environment and Information Technology,
Nelson Mandela Metropolitan University, Port Elizabeth, South Africa*

**SeanP@nmmu.ac.za*

***Russell.Phillips@nmmu.ac.za*

Abstract. Small scale wind turbines operating in an urban environment produce dismal daily yields of energy when compared to their rated maximum output [1, 2]. One of the factors contributing to their poor performance is the gusty wind conditions found in an urban environment coupled with the fact that the wind turbines are not designed for these conditions. A new concept of a Segmented Variable Pitch (SVP) wind turbine has been proposed and patented by NMMU which has a possibility to perform well in gusty and variable wind conditions.

This paper explains the concept of a SVP wind turbine in more detail and also shows analytical and practical results relating to this concept, as well as the potential benefits of the proposed concept.

The results of this research show that this concept has potential with promising results on aerofoil configurations as well as promising results on the scaled proof-of-concept models.

Key Words: wind turbine, blade pitching, renewable energy

1. INTRODUCTION

Since the design a wind turbine is largely based on the assumption of steady state conditions (hence the poor performance in gusty conditions) the design procedure and/or concept of a wind turbine operating in the urban environment needs to be reconsidered. To prove this concept of poor performance, a 3 metre diameter HAWT (Horizontal Axis Wind Turbine) was monitored (in relatively strong and gusty winds) to review the period of which the turbine operated at its designed TSR (Tip Speed Ratio). These results can be seen in Figure 2, which clearly show the small periods of when the turbine operates at the designed TSR.

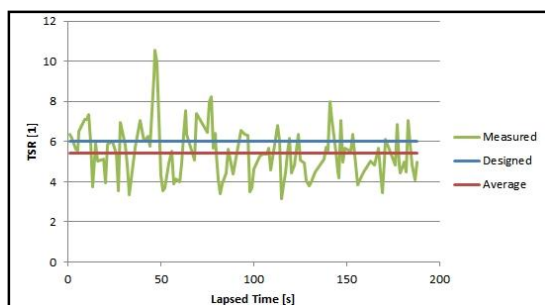


Figure 1: Operating TSR of a 3m HAWT in Gusty Wind Conditions

Therefore wind turbines which will operate in gusty (urban) environments should be designed for these conditions. This paper looks at the design of a SVP (Segmented Variable Pitch) wind turbine which has a possibility of working well in such conditions.

The concept of a SVP wind turbine has been proposed by Dr. Russell Phillips and patented by NMMU for this task of more effective wind power generation in the urban (gusty) environment. The concept of a SVP wind turbine is that of a turbine blade, segmented along the length, with each

segment rotating freely around its pitching axis, but held at a set angle of attack due to its aerodynamic configuration [See Figure 1]. This would allow the segments of the blade to passively adjust their pitch and therefore set their angle of attack relative to their relative wind angle, allowing the turbine blade to quickly adapt to any changes (gusts or lulls) in the wind.



Figure 2: Concept Rendering

2. AEROFOIL CONCEPTS

Three aerofoil configurations were chosen to compare the results relatively. The first aerofoil configuration is a NACA4412 profile [Figure 3]. This profile represents a common asymmetrical aerofoil which could be used in the design of a fixed blade wind turbine. The performance results from this aerofoil will be the benchmark for the results from the other aerofoil configurations, and will also be used to validate the wind tunnel results by comparing to XFOIL predicted results (A reliable analysis and design software for low Reynolds number aerofoil characterization [3-6]).

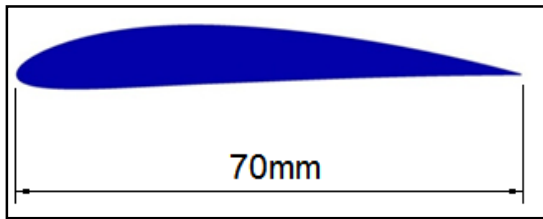


Figure 3: NACA 4412 Aerofoil

The second aerofoil configuration is that of a NACA0012 profile with a smaller NACA0012 profile acting as a stabilizing tail [Figure 4]. This tail aerofoil will control the angle of attack of the main aerofoil since the entire configuration is free to pivot around a pitching axis.

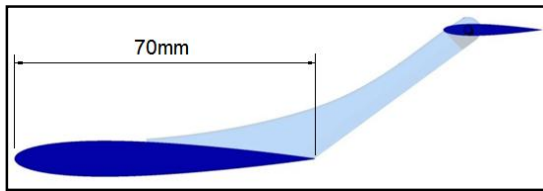


Figure 4: NACA 0012 Aerofoil Configuration

The third aerofoil configuration is an AOF139 profile which has a negative camber and positive pitching moment. If pivoted at the correct pitching axis location, this aerofoil will remain stable (w.r.t. pitch) and should maintain a set angle of attack.

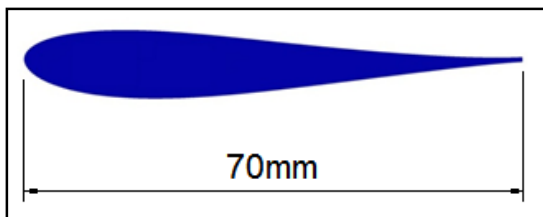


Figure 5: AOF139 Aerofoil

2.1 NACA4412 Results

Figure 6 below shows the wind tunnel results for the aerodynamic coefficients (at set angles of attack) and include the predicted XFOIL results. The correlations between the predicted and practical results are good and are shown to be similar.

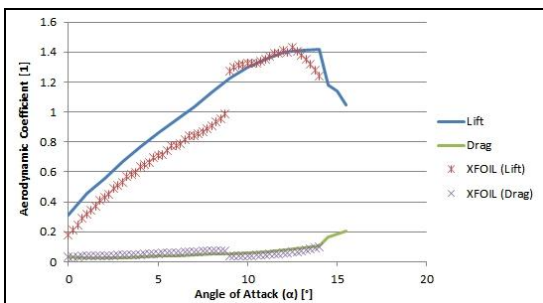


Figure 6: Tested NACA 4412 Aerodynamic Coefficients at Re=50 000

The lift to drag ratios of the NACA4412 aerofoil are shown below in Figure 7. The maximum lift to drag ratio is shown to be approximately 24.5 at an angle of attack of 6°.

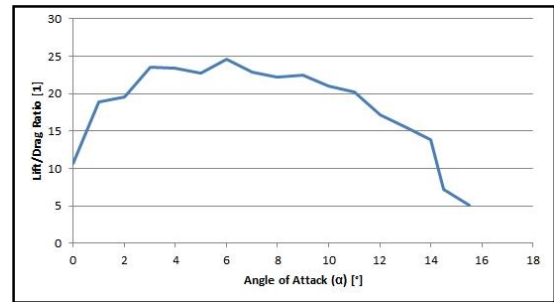


Figure 7: Tested NACA 4412 Lift to drag Ratios at Re=50 000

2.2 Tailed NACA0012 Results

The tailed NACA0012 aerofoil configuration [Figure 4] can be seen in Figure 8 as during the wind tunnel tests. During these tests the aerofoil configuration was neutrally balanced around the pivot axis and the system was allowed to pivot freely during the tests. The set angle of the tail aerofoil was adjusted for each set of data and this determined the angle of attack for the aerofoil configuration.

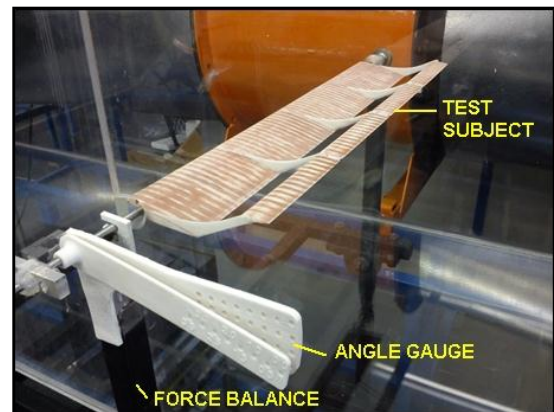


Figure 8: Test NACA 0012 Aerofoil Configuration in Wind Tunnel

The aerodynamic coefficients vs. angle of attack can be seen in Figure 9 below. The maximum lift coefficient is shown to be approximately 0.75 which is about half of that of the NACA4412 aerofoil at the same Reynolds number of 50 000.

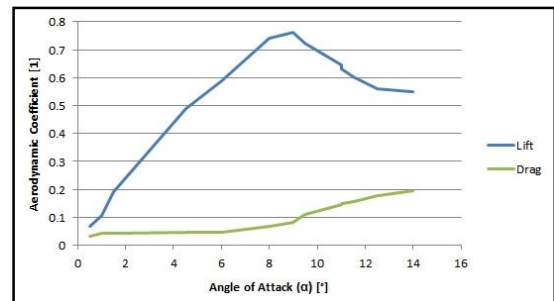


Figure 9: Tested NACA 0012 Configuration Aerodynamic Coefficients at Re=50 000

The maximum lift to drag ratio as shown below [Figure 10] is approximately 12.3.

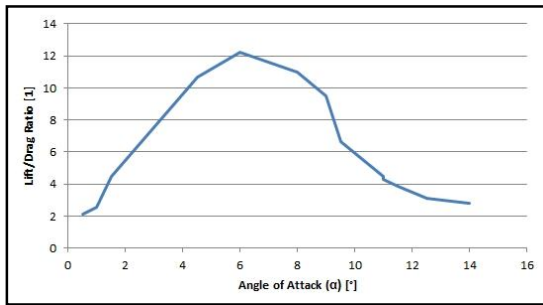


Figure 10: Tested NACA 0012 Configuration Lift/Drag Ratios at Re=50 000

The relationship between the tail aerofoil set angle and the angle of attack of the aerofoil configuration is shown in Figure 11. The relationship is shown to be linear but not similar and therefore it can be assumed (since the pivot point is through the aerodynamic centre of the main aerofoil) that the direction of the air flowing over the tail aerofoil is first effected by the main aerofoil.

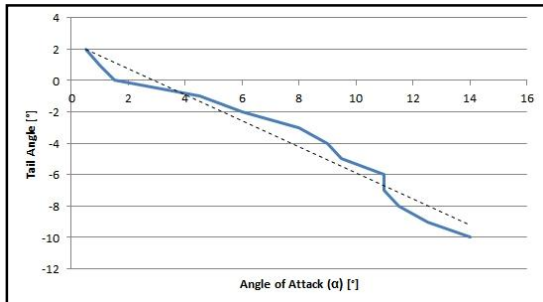


Figure 11: Tested NACA 0012 Tail Angle Vs. Angle of Attack at Re=50 000

2.3 AOF139 Results

The AOF139 aerofoil [Figure 5] can be seen in Figure 12 as during the wind tunnel tests at a defined angle of attack.

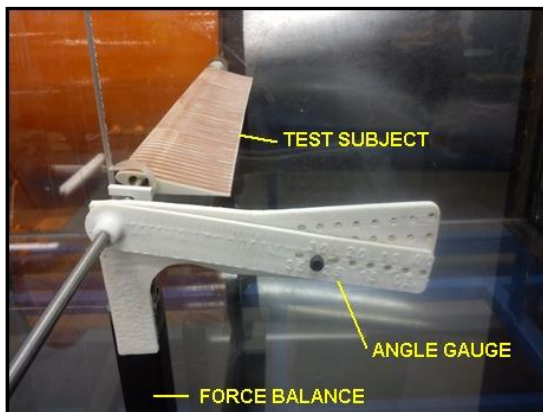


Figure 12: Test AOF139 Aerofoil in Wind Tunnel

The aerodynamic coefficients vs. angle of attack can be seen in Figure 13 and include the predicted XFOIL values. The correlations between the predicted and practical results are good and are shown to be similar. The maximum lift coefficient is shown to be approximately 0.7 which is about half of that of the NACA4412 aerofoil and similar to the

tailed NACA0012 aerofoil at the same Reynolds number of 50 000. However, using XFOIL to predict the maximum lift coefficients at a higher Reynolds number of 500 000 shows 1.32 for an AOF139 aerofoil which is 87% of the 1.51 predicted for a NACA4412 aerofoil, and so the predicted performance of this AOF139 aerofoil will be improved at higher Reynolds numbers. Figure 13 also shows four sets of data (black dots) which represent a “free to pivot” system. During these “free to pivot” system tests the aerofoil was neutrally balanced around the pivot axis and the system was allowed to pivot freely. The position of the pivot was adjusted relative to the aerofoil in the x-direction for each of the four sets of data and this determined the angle of attack for the aerofoil configuration (See Figure 15). It can be seen that three of these points (from the left) coincide with the measured results of the set angle of attack tests. This shows that the “free to pivot” aerofoil is stable (about the pitching axis) and produces similar results to the fixed angle tests as can be expected. Note that the point at 9.5° (on the right) does not correlate with the fixed angle results since the “free to pivot” aerofoil was not stable at this pivot position and therefore did not produce favourable results.

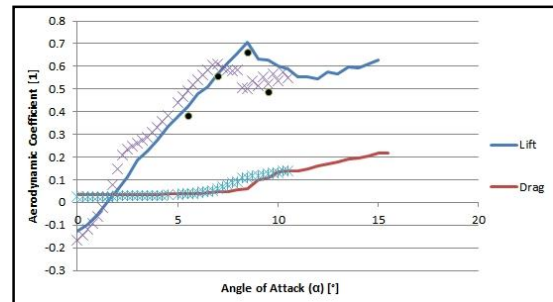


Figure 13: Tested AOF139 Aerodynamic Coefficients (Including 4 Unfixed Test Results) at Re=50 000

In Figure 14 below it can be seen that the lift to drag ratio is approximately 12.6 which is similar to that of the tailed NACA0012 configuration.

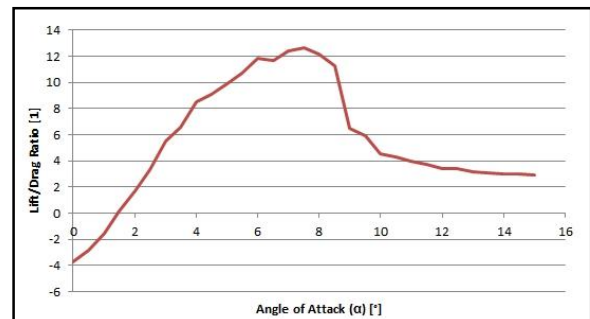


Figure 14: Tested AOF139 Lift/Drag Ratios at Re=50 000

Figure 15 shows the correlation between the angle of attack of the AOF139 aerofoil relative to the position of the pitching axis.

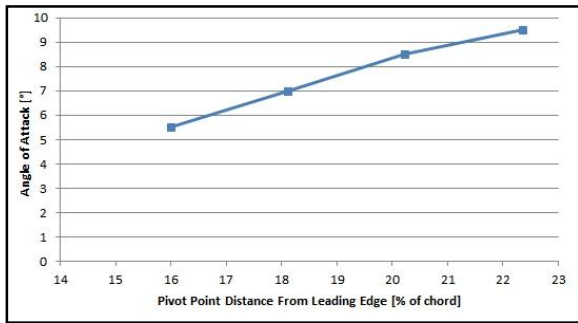


Figure 15: Tested AOF139 Angle of Attack vs. Pivot Point Position at $Re=50\,000$

3. SCALED MODELS

From the tests on the airfoil concepts it can be seen that the obvious advantage of the NACA4412 aerofoil over the other two concepts is its much higher lift to drag ratio. However, looking at the graph below [Figure 16] it can be noted that halving the lift to drag ratio has a non-proportional effect on the power coefficient and therefore the benefit of the concept of a SVP wind turbine could outweigh the disadvantage of the lower lift to drag ratios.

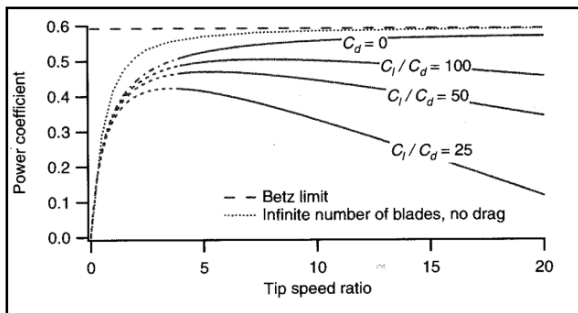


Figure 16: Lift/Drag Ratio Comparisons [7].

The AOF139 aerofoil was chosen over the tailed NACA0012 configuration for the following reasons;

- Simpler construction to manufacture
- Simpler construction to handle high centrifugal loads
- Better predicted performance at higher Reynolds numbers ($>100\,000$).

Figure 17 shows a rendering of the designed scaled model used for the tests. The design was based on Blade Element Momentum (BEM) theory and used the results from the wind tunnel tests to assist with the predicted aerofoil properties.

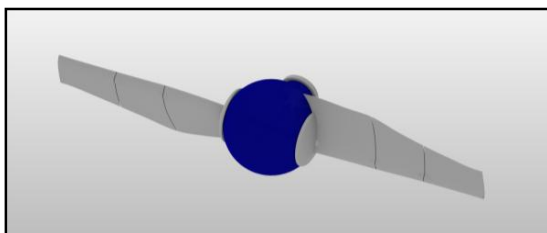


Figure 17: Rendering of Scaled Turbine Based on AOF139 Profile SVP Concept

The graph shown below [Figure 18] shows the results of the turbine blades fastened at different positions. Since the designed blade angle (0°) does not produce the maximum amount of power, this shows that this design is not optimal and needs to be refined. The maximum power coefficient is approximately 0.3 when fastened at -5° (decreased pitch).

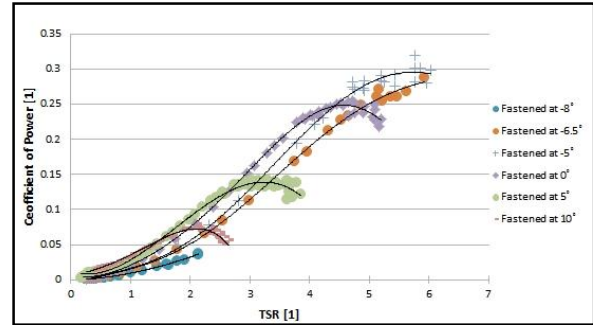


Figure 18: Segmented VP Turbine Blades "Fixed" at Various Positions (Wind velocity = 4.5m/s)

Figure 19 below shows the variable pitch results for two scenarios. The first scenario has all the segments free to rotate individually and produces a power coefficient of around 0.14. The second scenario has all 3 blade segments fastened to each other and allowed to rotate freely as a unit. This scenario only produces approximately a 0.08 power coefficient which is almost half of that of scenario one. Both of these scenarios do not reach the designed TSR of 5 (again showing the need for design refinement).

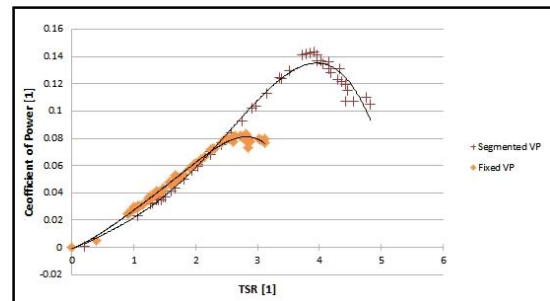


Figure 19: Variable Pitch Results (Wind velocity = 4.5m/s)

4. SIGNIFICANCE OF RESEARCH

As it is with any source of power production, one of the primary considerations is cost per energy yield. A SVP wind turbine has the potential to yield more energy (in gusty conditions) for its size, therefore potentially decreasing the cost per energy yield.

The concept of being able to control the angle of attack of each segment, while each segment 'adapts' to localized conditions, lends itself to various advantages over a fixed blade wind turbine.

These advantages could include the following:

- Higher power yield in gusty conditions.
- Variable "designed" Tip Speed Ratio (TSR)
- High starting torque.

- Same turbine can be used for different purposes such as direct mechanical water pumping (high torque-low TSR) as well as efficient electricity generation (low torque-high TSR).

5. CONCLUSION

This paper briefly shows the research results for the design of SVP turbine with the hope of producing more power in gusty conditions. The results of the aerofoil concept tests show that the AOF139 aerofoil looks like a more practical and better aerofoil concept of the two tested, although the stability of the two concepts were not quantified. The testing of the scaled model proved a predicted (since the blades were fixed) power coefficient of approximately 0.3, but this would require the design to be refined if this is to be achieved with the SVP concept. With this said, the recommended future development would be to adapt the BEM theory to include aerodynamically pitching aerofoils, as well as to gather more practical results for aerofoil concepts at higher Reynolds numbers.

ACKNOWLEDGEMENTS

My supervisor, Prof Russell Phillips, for his guidance and support, and financial backing.

My co-supervisor, Prof Theo van Niekerk, for his advice and guidance.

My wife, Jade, for her support, both financial and moral.

Gideon Gouws, for his advice and for his timely designing and constructing the wind tunnel at NMMU of which much of my research would not have been possible.

To my Lord and savior, for providing me the opportunity of coming back to university and completing my studies.

REFERENCES

- [1] Encraft: "Warwick Wind Trials Project" [ONLINE], 2008, Available at: <http://www.warwickwindtrials.org.uk/resources/Warwick+Wind+Trials+Final+Report+.pdf> [Accessed 06 January 2014].
- [2] J. Bull and G.D.J. Harper: *Small-Scale Wind Power Generation – A Practical Guide*, Crowood Press, first edition, 2010.
- [3] N.K. Borer: "Designing and Analysis of Low Reynolds Number Airfoils" [ONLINE], 2002, Available at: http://www.ace.gatech.edu/experiments2/6514/airfoils/fall02/borer_math6514_final_report.pdf [Accessed 06 January 2014].
- [4] M.D. Maughmer and J.G. Coder: "Comparisons of Theoretical Methods for Predicting Airfoil Aerodynamic Characteristics (Doc# RDECOM TR 10-D-106)" [ONLINE], Airfoils Incorporated, August 2010, Available at: <http://www.dtic.mil/cgi-bin/GetTRDoc?AD=ADA532502> [Accessed 06 January 2014].
- [5] M. Drela: "XFOIL: An Analysis and Design System for Low Reynolds Number Airfoils" [ONLINE], MIT Dept. of Aeronautics and Astronautics, Cambridge, Massachusetts, Available at: http://web.mit.edu/drela/Public/papers/xfoil_sv.pdf [Accessed 06 January 2014].
- [6] R.L. Hueners and C. Rasmussen: "XFOIL Project", California Polytechnic State University, Aerospace Engineering Dept, Available at: http://cdrasmus.files.wordpress.com/2010/10/xfoil_project_doc.pdf [Accessed 01 October 2014].
- [7] J.F. Manwell, J.G. McGowan and A.L. Rogers: *Wind Energy Explained - Theory, Design and Application*, John Wiley & Sons Ltd, United Kingdom, second edition, p 50, 2009.

DEVELOPMENT OF AN INTEGRATED LABORATORY TEST SETUP FOR HIGH TEMPERATURE PEM FUEL CELL PERFORMANCE STUDIES

C. de Beer*, P. Barendse*, P. Pillay*, B. Bulecks** and R. Rengaswamy**

* Department of Electrical Engineering, University of Cape Town, Rondebosch, Cape Town, South Africa, 7701. E-mail: c.debeer@uct.ac.za.

** Department of Chemical Engineering, Texas Tech University, Lubbock, Texas, United States, 79409

Abstract: South Africa is currently embarking on the deployment of renewable energy systems for integration with the national supply to boost power generation capacity. As part of the generation scheme, storage technologies will play an important role in the future infrastructure. High Temperature PEM fuel cells are a promising technology for small and medium scale as well as portable power applications. This paper presents the development of a flexible testing system that is able to perform a wide array of tests under a range of operating conditions on HTPEM fuel cells. The ability of the test rig to perform various diagnostics, accelerated life cycle tests and fault studies is presented.

Keywords: HTPEM, fuel cell, transients, degradation.

1. INTRODUCTION

The South African power generation and supply is mainly based on coal burning power stations. In order to reduce our dependence on coal and other fossil fuels, a number of projects that involve the construction of solar and wind generation plants are under way. In order to assist the generation base, storage technologies are implemented to assist with the peak loads. These include pumped storage facilities, compressed air storage, battery storage and fuel cells. To complement these systems, a fleet of electric vehicles can be integrated into the energy management plan. By using the storage of the vehicles, either batteries, fuel cells or a combination, the peak load capacity of the grid can be improved.

For base load applications, solid oxide fuel cells are the most commonly used technology and runs at a high operating temperature, 800°C to 1000°C [1], and as such can have high power densities and efficiencies. Due to the high temperatures, these systems require a significant amount of time for startup and are not suitable for portable power applications. For this market the proton exchange membrane (PEM) fuel cell is most commonly employed. These types of cells have high power density, quick startup times and good efficiencies. In order to increase performance, PEM fuel cells are currently under development that runs at slightly elevated temperatures, typically between 140°C and 180°C, referred to as high temperature PEM fuel cells. These high temperature PEM (HTPEM) fuel cells exhibit a number of advantages including faster response times, higher efficiencies and the ability to tolerate larger concentrations of impurities in the gas supplies [2].

In order to perform diagnostics and load analysis on the HTPEM fuel cells, a testing platform is required. A

number of commercial systems are available but are limited especially when very specific transient testing needs to be conducted for performance and diagnostic studies. One such scenario is the evaluation of performance during the change in gas composition and the resulting effect it has on the electrochemical equivalent circuit parameters. To address the issue, a custom test bed was developed that can perform a wide range of functions. This paper presents the development of a fully integrated HTPEM testing platform for conducting diagnostics, transient tests for both gas flow and electrical load as well as accelerated life cycle tests. The results from some of the tests are compared with a commercial test station to validate performance. In particular, the results from transient conditions are presented and provide insight into the fuel cell state of health.

2. FUEL CELL DIAGNOSTICS

An important tool in the design and optimization of fuel cell systems is the diagnostic methodologies that are used to gather data regarding cell performance, material properties and assessing its condition. Diagnostic procedures can be divided into intrusive and non-intrusive procedures. For the purpose of ensuring that cell performance is not negatively affected, non-invasive procedures are performed. These include polarization curve analysis, current interrupt, electrochemical impedance spectroscopy (EIS), gas cross-over and others [3].

2.1 Polarization Curve Analysis

A typical test bench can perform most of the non-intrusive procedures as these can be conducted quickly and successively at different operating conditions to

evaluate performance. The polarization curve is the most standard procedure and gives information on the activation losses, ohmic losses and diffusion through the triple-phase boundary. A typical polarization curve is presented in figure 1. From the data, the maximum power point can be calculated and optimization of the system control can be conducted. The curve is generated by increasing or decreasing the voltage or current of cell. At each increment the cell is allowed to stabilize before the measurement is recorded. A polarization curve does not deliver detailed information on individual component performance and it is difficult to diagnose a specific fault condition. It is also not possible to record a curve while the fuel cell is operational and delivering power to a load. As such, other methods are implemented in the test bench.

2.2 Electrochemical Impedance Spectroscopy

Electrochemical impedance spectroscopy (EIS) is conducted at a specific loading point and can thus be done while the fuel cell is in operation. The technique requires that a sinusoidal waveform be superimposed upon the DC load point, either voltage or current. The feedback is then measured and the magnitude and phase of the resulting impedance calculated. The frequency of the sine wave is varied, typically between 0.1Hz and 10kHz in order to produce a full spectrum Nyquist plot of the impedance. A graphical representation is presented in figure 1 at the operating point on the polarization curve. The magnitude of the sine wave is varied in order to maintain good signal to noise ratio while minimizing the disturbance on the fuel cell output. The resulting Nyquist plot is usually fitted to the impedance spectrum of an electrochemical equivalent circuit. By monitoring the values of the circuit elements, a number of tasks can be performed. This includes investigating the performance of individual cell components as well as fault diagnostics. Most laboratory setups make use of a frequency response analyzer (FRA) and a potentiostat module to perform EIS. More recently, it was shown how high performance electronic loads and controllers can perform the same tests without the use of the expensive FRA.

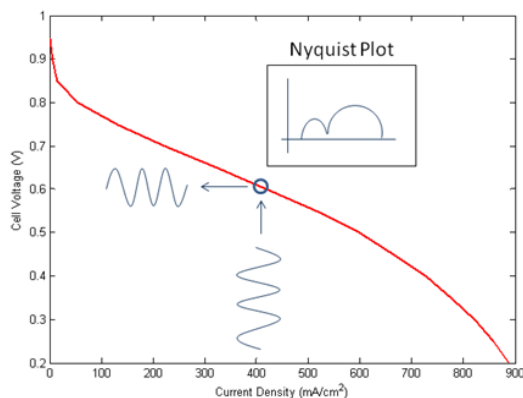


Figure 1: Polarization curve and EIS at a specific operating point.

2.3 Current Interrupt

A non-intrusive technique that can be performed by most test stations is the current interrupt (CI) technique. This method mainly gives information regarding the impedance of the fuel cell and requires that the fuel cell load be switched on and off. The voltage response is then recorded and time domain analysis is performed to determine a transfer function of the impedance of the system. A typical voltage response for a CI and the associated components is presented in figure 2. The fitted components of the impedance transfer function can be related to certain electrochemical parameters such as membrane ionic resistance, charge double layer capacitance and charge transfer resistance. Depending on the impedance model used and the fitting procedure, the technique can yield very good results when compared to the more complex methods such as EIS.

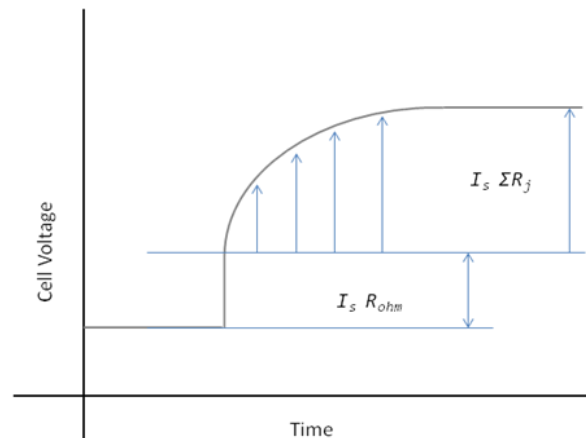


Figure 2: Typical voltage response from current interrupt.

3. EXPERIMENTAL SETUP

Two test stations will be presented and discussed; this includes the commercial test bench used as a benchmark and the in-house test station. Both experimental setups made use of a single cell assembly procured from Fuel Cell Technologies. The assembly housed commercial HTPeM membrane electrode assemblies with an active surface area of 45cm². The graphite bipolar plates were etched with quad serpentine flow fields.

3.1 Commercial Test Station

The commercial test station was procured from Scribner Associates and is shown in figure 3. This test station is primarily used for the evaluation of low temperature PEM fuel cells which requires humidification of the gas streams and less power to the heaters of the fuel cell assembly. To adapt the system for testing HTPeM fuel cells, the humidifier was bypassed. The cartridge heaters of the fuel cell assembly were controlled via an external controller. The test station included an embedded frequency response analyzer that performed the electrochemical impedance spectroscopy (EIS) tests. The

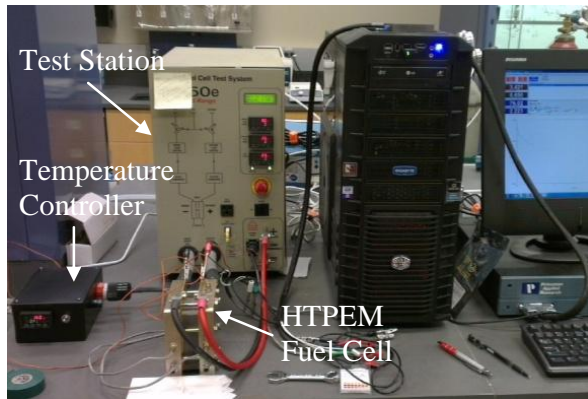


Figure 3: Commercial HTPEM test station.

system is able to perform EIS on a three electrode system if required.

Most commercial test benches can only perform the standard diagnostic tests as discussed in section 2. More advanced diagnostic tests such as impulse and step response analysis can only be done to a certain degree depending on the capability of the internal electronic load, mass flow controllers and data acquisition system. For the employed test bench, the maximum data acquisition rate was limited to 100samples/s and thus not suitable for impulse response analysis or the active load flow studies above 10Hz in frequency. Step changes in the flow rate of the anode and cathode gas streams could not be properly done due to the slow response times of the mass flow controllers.

3.2 Proposed Test Station

In order to address some of the shortcomings of the commercial test station, it was decided to develop an in-house test bed capable of performing a wide range of tests including transient analysis. A schematic diagram of the system is presented in figure 4.

The system was interfaced to a single supervisory PC that logged data and controlled the gas flows and the load connected to the fuel cell assembly. A high speed data acquisition card with a maximum sample frequency of 500kHz was used to record the current and voltage response of the cell. The gas flows were controlled using high precision mass flow controllers (MFC) with a response time of 2ms. The system was designed to allow for the poisoning of the anode gas stream with CO that commonly results from the reforming process. As such, the setup was constructed in a fume hood as shown in figure 5. CO sensors were placed inside the hood to monitor the concentration and ensure that it was within safety limits. The outlets of the H₂ and CO MFC were connected and the mixing controlled in the main control strategy on the supervisory PC. The cathode MFC was connected to the laboratory compressed air supply. The electronic load was supplied by Agilent and has a high current and voltage slew rate that enabled exact set point control during testing. The same temperature controller implemented in the commercial test bench was implemented in the proposed setup.

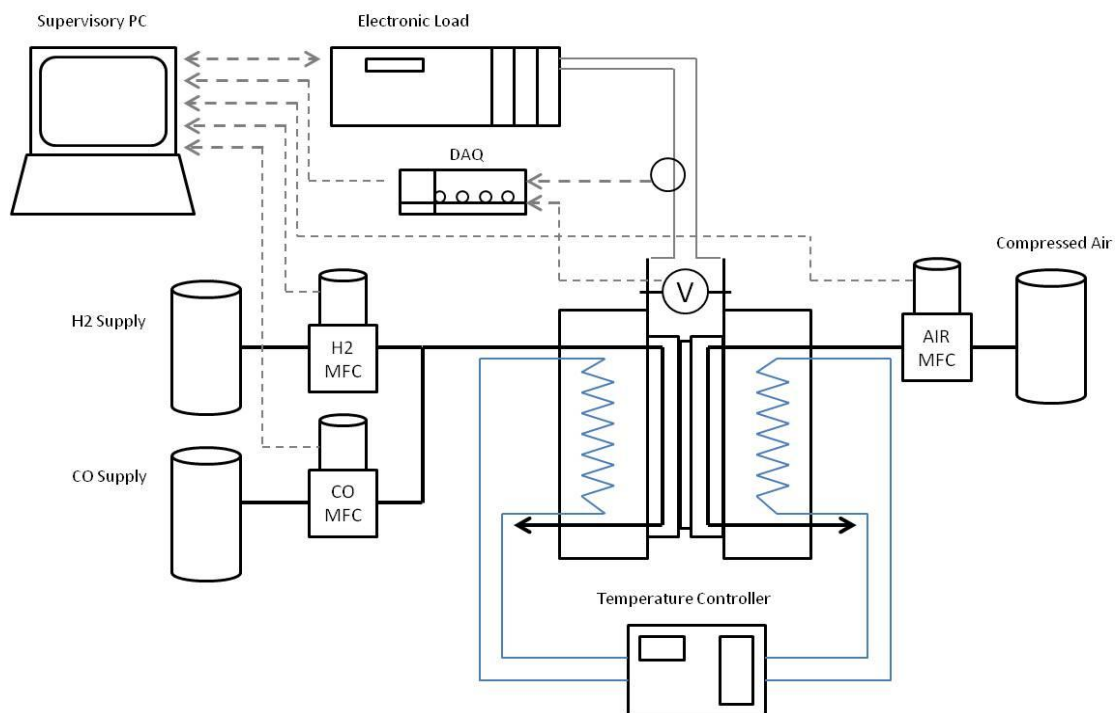


Figure 4: Schematic representation of proposed test setup.

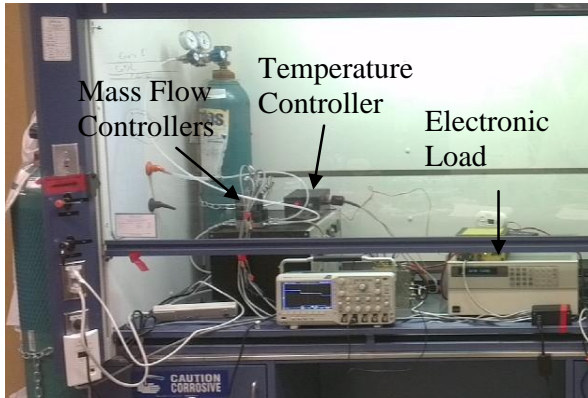


Figure 5: Laboratory implementation of integrated setup.

The control systems were implemented in MATLAB and executed via the real time workshop and data acquisition toolboxes. Individual control systems were implemented for each diagnostic test and called in the global test algorithm to ensure that the tests were carried out at a single operating point thereby maintaining consistency in the results. The EIS measurements were conducted in galvanostatic mode whereby a sinusoidal waveform was superimposed on the DC operating point of the current. A minimum of 5 cycles at each frequency set point was recorded and averaged to determine the magnitude and phase. The frequency was varied from 0.1Hz to 10kHz at 10 points per decade. The magnitude of the sinusoids was varied to deliver acceptable voltage response. Polarization curves were recorded from open circuit voltage (OCV) down to 0.45V in 0.05V intervals. At each set point, the current was allowed to reach steady state before measurements were recorded.

4. RESULTS AND DISCUSSION

Before testing commenced, the cells were run in as per the instructions of the manufacturer. This is done to condition the cell and clean the catalyst layers to ensure stable results. The current density was kept constant at 200mA/cm² and the voltage recorded. The stoichiometric ratio was kept constant at 2.4/4. The recorded voltage profile from one of the MEAs is shown in figure 6. It is clear that there is an initial drop in voltage followed by a steady rise. Various interpretations of the voltage during conditioning have been published [4], [5]. For low temperature PEM cells, the run in cycle allows the Nafion membrane to be sufficiently hydrated and ensure proper proton conduction. In HTPEM cells, the phosphoric acid in the membrane is allowed to properly distribute and reach steady state.

Following the run in procedure, polarization curves were recorded. The captured curves are presented in figure 7 for the commercial and constructed test stations. The resulting Nyquist plots at 400mA/cm² are presented in figure 8. There is a small discrepancy between the curves recorded for the commercial test bench and the constructed test bench. This is mainly due to the inherent

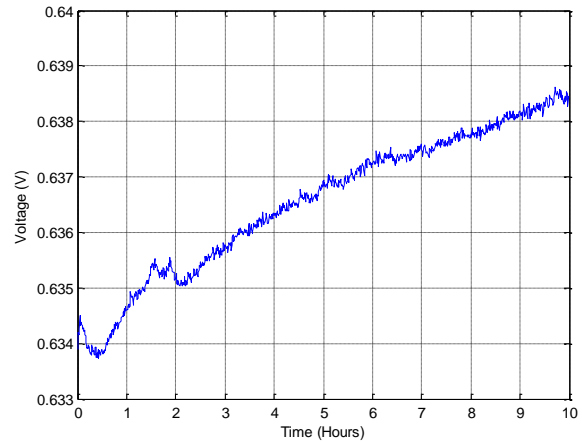


Figure 6: Cell voltage during run in procedure.

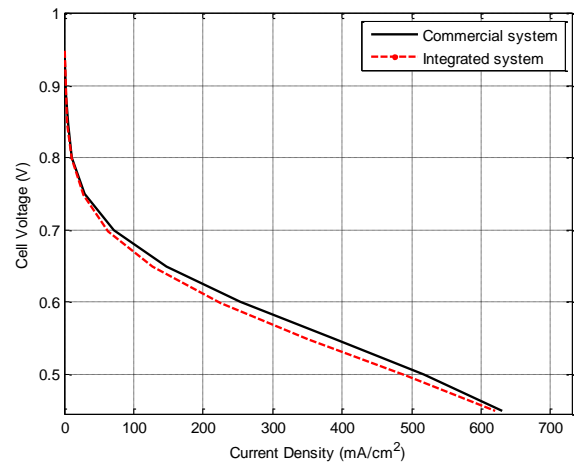


Figure 7: Polarization curves of commercial and integrated setups.

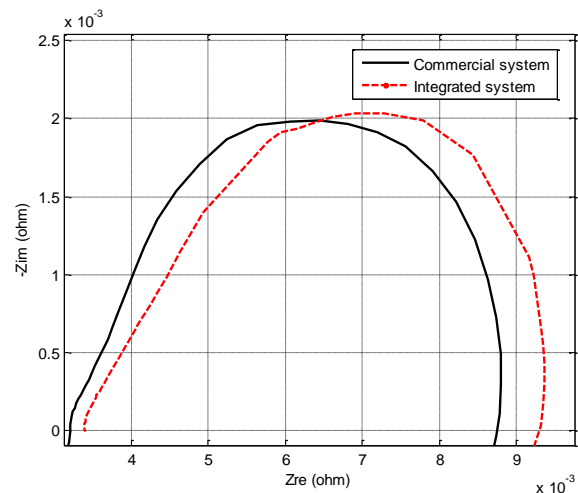


Figure 8: Nyquist plots of commercial and integrated setups.

differences between MEAs as a new MEA was tested on each setup. Small changes in ohmic resistance may be due to longer cables being used in the constructed test

bench. The small discrepancy does not influence the interpretation of the results and is acceptable.

The standard polarization curve and EIS tests provides insight into the testing capability of the commercial test bench. For more complex or transient testing methodologies, the constructed test bench was used as it incorporates a high performance electronic load and high speed data acquisition. The voltage response for a current step is shown in figure 9 and the magnified results at the transition in figure 10. The initial drop in voltage due to ohmic resistance of the cell and assembly is clearly visible followed by the exponential rise to steady state. These results can be interpreted in the same manner as the current interrupt test.

Following the load testing, transient testing of the gas flow rates was conducted on the constructed test bench. The voltage response for a stoichiometric change from 3/3 to 2/2 is presented in figure 11. The time constant for the flow dynamics is in the minute range when compared to the electrical dynamics that is in the millisecond range [6], [7]. As such, the sampling frequency of the data acquisition system must be set according to the test being conducted.

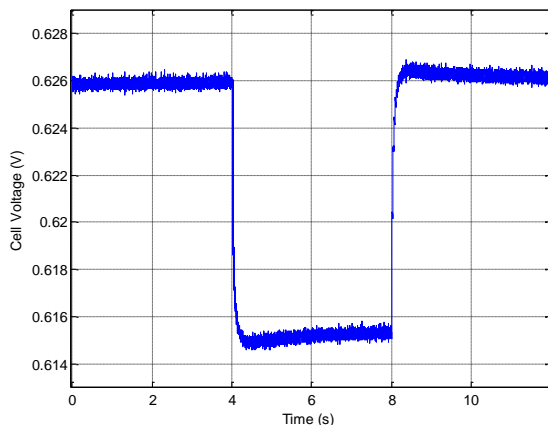


Figure 9: Voltage response for a current step.

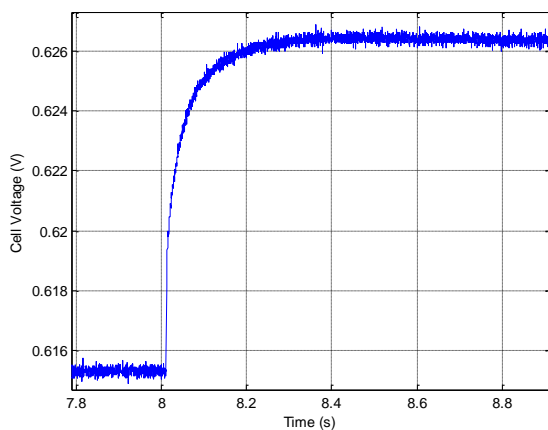


Figure 10: Magnified voltage response.

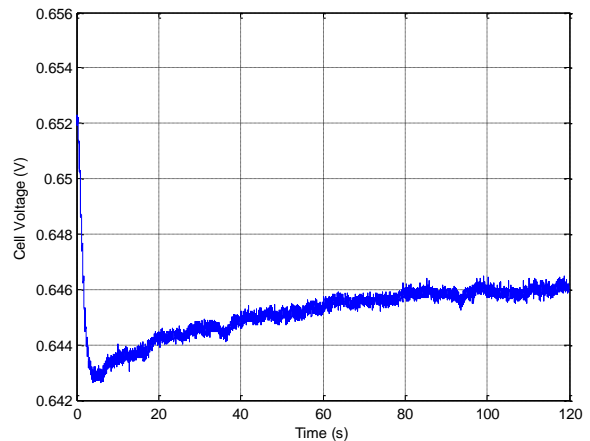


Figure 11: Voltage response during a hydrogen flow step change.

Many other tests can be conducted including step changes in CO concentration for performance degradation studies [8], [9].

5. CONCLUSION

This paper presents the development of an integrated test bench for fuel cell performance studies. The setup was specifically designed to accommodate the higher operating temperatures required by HTPEM fuel cells. The system performance compares well with that of a commercial system and has the ability to perform high speed transient testing and data acquisition. The test setup is able to perform high precision gas flow control and incorporates mixing strategies that allow for the evaluation of performance under non ideal operating conditions.

6. REFERENCES

- [1] F. Barbir, *PEM Fuel Cells – Theory and Practice*, Elsevier Academic Press, 2004.
- [2] J. Zhang, Z. Xie et al., “High temperature PEM fuel cells”, *Journal of Power Sources*, vol. 160 , No. 2, pp 872-891, May 2006.
- [3] H. Wang, X. Yuan, *PEM Fuel Cell Diagnostic Tools*, CRC Press, 2012.
- [4] M. Boaventura, A. Mendes, “Activation procedures characterization of MEA based on phosphoric acid doped PBI membranes”, *International Journal of Hydrogen Energy*, Vol. 35, pp. 11649 – 11660, 2010.
- [5] Thomas Tingelof, Jari K. Ihonen, “A rapid break-in procedure for PBI fuel cells”, *International Journal of Hydrogen Energy*, Vol. 3, pp. 6452 – 6456, 2009.

- [6] C. de Beer, P.S. Barendse and M.A. Khan, "Development of an HT PEM Fuel Cell Emulator Using a Multiphase Interleaved DC–DC Converter Topology", *IEEE Transactions on Power Electronics*, Vol.28, no.3, pp.1120-1131, March 2013.
- [7] J. Peng, J.Y. Shin, T.W. Song, "Transient response of high temperature PEM fuel cell", *Journal of Power Sources*, vol. 179, No. 1, pp. 220-231, May 2008.
- [8] C. de Beer, P.S. Barendse, P. Pillay, B. Bullecks and R. Rengaswamy, "Electrical Circuit Analysis of CO Poisoning in High Temperature PEM Fuel Cells for Rapid Fault Diagnostics", *IEEE Energy Conversion Congress and Expo(ECCE)*, Denver Colorado, 2013.
- [9] C. de Beer, P.S. Barendse, P. Pillay, B. Bullecks and R. Rengaswamy, "Degradation of High Temperature PEM Fuel Cells and the Impact on Electrical Performance", *IEEE International Conference on Industrial Technology (ICIT)*, Cape Town, 2013.

Topic G

Power Generation and Education

Delivering practical instruction to Power Engineering undergraduate students at an open distance learning institute

A.J. Swart* and P.T.A Mahlare**

* Dept. of Electrical, Electronic and Computer Engineering, Central University of Technology, Private Bag X20539, Bloemfontein, South Africa, 9300. Email: drjamesswart@gmail.com

** Dept. of Electrical and Mining Engineering, University of South Africa, Science Campus, PO Box 392, UNISA, 0003, South Africa. Email: mahlapta@unisa.ac.za

Abstract: Electrical Engineering 1 is a compulsory module for students enrolled for the undergraduate National Diploma in Electrical Engineering (Power) in South Africa. Many freshman students straight out of high school often struggle to pass this module at their first attempt. This may be due to the fact that students struggle to integrate theory with practice, not being able to “see” the theory at work in practical settings. The purpose of this paper is to highlight how this concern may be addressed within an open distance learning environment. Results show that the use of physical hardware kits enabled many more students to engage with practical instruction over a longer period of time, thereby helping them to integrate theory and practice.

Keywords: Electrical Engineering 1, ODL, practical kits, theory, practice

1. INTRODUCTION

“Eureka”! This word, ascribed to Archimedes when he stumbled upon a method to determine the purity of gold [1], well convey the cry of satisfaction when someone discovers something unique. Discovery is usually associated with research which brings much satisfaction when one’s findings or results are finally published for public scrutiny.

The purpose of this paper is to present results of research on how the practical instruction within a Power Engineering module was changed to address two concerns at an open distance learning (ODL) institute. Firstly, a low throughput rate was being experienced in this module. Many factors contribute to low throughput rates in engineering, including lack of student motivation, not aligning theory and practice and not exposing students to real world situations [2]. Secondly, practical instruction was being offered by a contracted university of technology in the form of a one day practical workshop. However, logistical problems along with poor student engagement forced academics at UNISA (the largest open distance learning (ODL) institute in Africa with over 400 000 students [3]) to consider other viable options. Physical hardware kits were subsequently selected as the alternative option in providing practical instruction to distance learning students enrolled for Electrical Engineering 1 (EE1) within a Power Engineering course.

A number of research articles have recently discussed the usefulness of physical hardware kits in helping engineering students to grasp theory principles relating to digital design [4], microprocessors [5], control systems [6], electronics [7], robotics [8] and optics [9]. However, little research exists in using hardware kits in Power Engineering modules offered by ODL institutes to integrate theory and practice. Furthermore,

engineering students often encounter difficulties in conceptualising theory due to a lack of direct physical hands-on experience [10].

The importance of integrating theory with practice is firstly established. The Power Engineering module is then introduced and contextualized, after which important outcomes of the EE1 module are presented. The research methodology follows with the results which are presented in a series of graphs and tables conveying quantitative data.

2. IMPORTANCE OF INTEGRATING THEORY AND PRACTICE

The importance of integrating theory and practice can be discerned by reviewing work done by Bloom, Gagne’, Piaget, Marton and Saljo, Haring et al, Biggs and Collis and Kolb. Added to this is the mandate from the Engineering Council of South Africa (ECSA) for engineering programmes to include practical instruction. Much of this discussion is adapted from research done by Swart and Sutherland [8] and Swart [9].

Bloom’s taxonomy (1954): Different categories of learning are explained which are often used to distinguish lower and higher levels of understanding [11]. First year level, or freshman, engineering students often engage more mentally in the lower types of learning when they acquire theoretical knowledge (verbs such as identify, describe, review and convert are used [12]). However, in practical instruction students must engage more physically with equipment and components (verbs such as determining, verifying, using, confirming, sketching, calculating and solving being used [12]).

Gagne’ (1962): An alternative framework for developing performance objectives was presented which

included verbal information, intellectual skills, cognitive strategies, motor skills, and attitudes [13]. Motor skills are those skills by which students execute movements and are vital in the effective use of electronic and electrical equipment in a practical environment based on verbal theoretical information which they receive.

Piaget (1972): The cognitive-development theory is based on the assumption that knowledge (assimilation describing how humans perceive and adapt to new information) is an interaction between the learner and the environment (accommodation describing how humans alter their pre-existing schemas to fit in the new information) [14]. Assimilation (theory knowledge) and accommodation (interaction with practical experimentation) must exist together in balance in order to ensure operative intelligence.

Marton and Saljo (1976): The constructs of surface and deep approaches to learning were explained [15]. Surface learning may be characterized by the simple acquisition of theoretical knowledge, which could be forgotten with the passing of time. However, deep learning may be characterized by students who attempt to relate theory with practice, thereby retaining and using it as time passes.

Haring et al (1978): The four levels proposed in the hierarchy of learning [16] include acquisition, fluency and proficiency, generalization, and adaptation [17]. The acquisition level emphasizes accuracy, and the learning process is characterized by demonstration, whereas fluency and proficiency result when practice is required for learning. Demonstration of theory is often accomplished by practical work which must be practiced regularly to ensure learning.

Biggs and Collis (1982): The SOLO (Structure of the Observed Learning Outcomes) taxonomy provides a systematic way of describing how a student's performance grows in complexity when mastering many academic tasks [18]. Five levels of learning are stipulated where levels two and three (termed the quantitative stage) require students to demonstrate an understanding of knowledge (theory) while the fourth and fifth levels (termed the qualitative stage) call on students to orchestrate action based on their acquired knowledge (practice). Biggs [19] further states that the quantitative stages of learning occur first (assimilating theory), after which learning must change qualitatively (applying of theory in practice).

Kolb (1984): The learning cycle aims to provide concrete experience, reflective observation, abstract conceptualization, and active experimentation [20]. Concrete experience occurs when students "see" theory at work, when they engage in active experimentation involving apparatus, tools and equipment.

ECSCA (2012): ECSCA released important knowledge areas and credits which need to be incorporated into relevant engineering courses which are accredited by them [21]. Specific knowledge areas and credits are shown in Table 1, which must be well distributed throughout all the modules offered within the new Diploma in Engineering qualification (National Qualification Framework Level 6). The engineering sciences and design areas are vital, where ECSCA expects students to acquire necessary hands-on skills and the ability to apply their knowledge and acquired skills to particular career or professional contexts.

Table 1: Knowledge areas and credits for the *new* Diploma in Engineering (NQF6 qualification)

Knowledge area	Minimum credit
Mathematical sciences (including Mathematics and Statistics)	35
Natural sciences (including Physics, Chemistry and Geology)	28
Engineering sciences (including the Engineering modules)	126
Engineering design (including the Capstone module)	28
Computing and IT (including Computer skills)	21
Complementary studies (including Language skills)	14
Work Integrated Learning (including Industrial training)	30
Redistribution in areas above	78
Total for the qualification	360

Currently at UNISA, the theory and practical instruction for each module is split into two modules, with the theory module comprising 10 credits and the practical module 2 credits. Students must pass both modules to be awarded 12 credits. This means that students need to pass approximately 20 theory ($20 \times 10 = 200$ credits) and 20 practical ($20 \times 2 = 40$ credits) modules. However, engineering students must also complete a year's work integrated learning (contributing 120 credits within the *current* National Diploma).

Students are encouraged to register for both modules at the beginning of the calendar year. However some students may pass the theory module and fail the practical module, or vice versa, and would then be required to re-register for the module which they failed. The theory and practical modules of Electrical Engineering 1 contain important principles which freshman engineering students need to grasp and apply.

3. IMPORTANT OUTCOMES

The Power Engineering module, EE1, is a compulsory offering within the National Diploma: Engineering:

Electrical, Mechanical and Industrial qualification. The theory module for EE1 encompasses the following syllabus, and can be completed within a 6 month period:

- 1) International system of measurements;
- 2) Introduction to electric systems;
- 3) Simple D.C. circuits analyses;
- 4) Capacitance and Capacitors;
- 5) Electromagnetism;
- 6) Simple magnetic circuits;
- 7) Inductance and Inductors;
- 8) A.C. voltage and current;
- 9) Single phase series circuits; and
- 10) Batteries.

The practical module for EE1 contains the following outcomes which students need to achieve:

- a) **Identify** the resistors supplied in the hardware kit, *determining* their colour code values and *verifying* them with a digital Multimeter;
- b) **Describe** the differences between series and parallel networks;
- c) *Use* a digital Multimeter to measure voltage and current and *confirm* Ohm's Law;
- d) **Review** the principles of voltage divider and current divider laws;
- e) *Sketch* the charging and discharging curves for a capacitor, as well as *calculate* time constants;
- f) **Convert** a delta circuit into an equivalent star circuit, or visa versa;
- g) *Solve* voltage divider and current divider problems for a combined series parallel circuit.

Verbs associated with practical instruction are shown in *italics*, and focus on higher levels of understanding according to Bloom's taxonomy. Verbs associated with simple theory assimilation are shown in **bold**, and encompass the lower levels of understanding from Bloom's taxonomy. The integration between theory and practice is described in Table 2, where attention is primarily focused on resistors and capacitors. The practical outcomes are readily achieved with the use of a physical hardware kit.

Table 2: Theory and practice integration

Syllabus section	Outcomes	Integration
1 / 3	a	Colour code resistor values verified by measurement
2	b / d / g	Series and parallel circuits constructed and evaluated
3 / 8	c	Verify the actual voltages and currents for network theorems
4	e	Measure the varying voltage across a capacitor
7 / 9	f	Conversion between two different circuit configurations

4. HARDWARE KITS

The physical hardware kit includes:

- A trainer (see Figure 1) encompassing various power supplies, a simple sine and triangular frequency generator, logic switches and probe, audio buzzer and TTL based signals;
- A breadboard (see Figure 1);
- An AC adaptor for 220V to 24V conversion; and
- Various resistors, capacitors and inductors.



Figure 1: AD2004 trainer and breadboard

These hardware kits are posted to student's immediately after the final student registration for the practical module has closed and the first student assignment has been received indicating that the student is active. Students also receive a detailed practical study guide covering 7 different experiments. The methodology which needs to be followed is described and empty tables are provided for specific results which students need to obtain from their measurements and observations. For EE1, students use all the resistors, capacitors, inductors, Multimeter, 12 V power supply and sine wave generator. The rest of the circuitry is included for students enrolled for Digital Systems 1 and Electronics 1, as they use the same hardware kit. This simplifies production, reduces overall costs and eases delivery issues of different hardware kits.

5. RESEARCH METHODOLOGY

A post-facto study is used where the target population is limited to all students enrolled for EE1 at UNISA between 2004 and 2012 (both theory and practical modules). This time period of interest encompasses the switch over period from practical workshops to hardware kits, and well illustrates the concern of low throughput rates and its associated improvement. A Pearson correlation is also performed to ascertain if student age, gender or language plays a role in the final student grades obtained for both the theory and practical modules within EE1. Quantitative analysis is used!

6. RESULTS

Figures 2 and 3 show the student profile and languages for the 2004-2012 time periods, which indicates that:

- The majority of students are male (80.7%);
- The dominate language is English (18.5%); and
- Many students are within the 21-25 year old age bracket (51%).

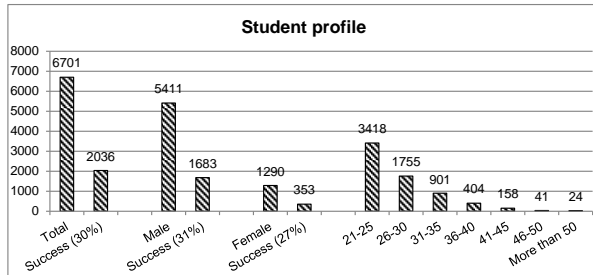


Figure 2: Student profile for 2004-2012

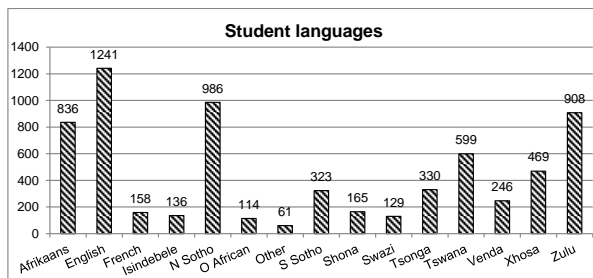


Figure 3: Student home languages

Figure 4 highlights the theory and practical module success rates, where the percentage of students who obtained more than 50% for their final mark is indicated. It is evident that student success in the practical module has been increasing for the past 4 years during which the hardware kit was used (from 62% to 75%), with more students achieving a final pass mark of 50% or more. A subsequent increase is noted for the theory module for the past three years, which has risen from 28% to almost 50%. However, more students seem to be achieving success in the practical module than in the theory module.

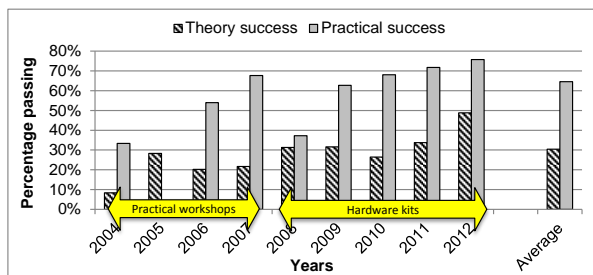


Figure 4: Percentage of students who achieved more than 50% for the theory and practical modules in EE1

Noteworthy too is the contrast between the periods in which practical workshops were offered to that in which

hardware kits were posted to students. Although an initial drop is observed in 2008 (maybe due to teething or implementation problems), student success rates did increase dramatically with the use of the hardware kits! The use of the practical workshops resulted in an average pass rate of 28%, whereas the period in which the hardware kits were used reveals a 33% average pass rate.

The results of the Pearson correlation are shown in Table 3. The results point to a statistically significant relationship between student age and the final grade marks. This suggests that older more experienced students are more likely to obtain higher final grade marks than younger less mature students. This may further suggest that older more experienced students have been engaging with life-long learning, enabling them to better succeed in their educational studies. A scatter plot of student ages to their final grade marks is shown in Figure 5.

A negative statistically significant relationship further exists between the student home languages and their final grade marks. This implies that students with specific home languages would score lower final grade marks than students with other languages. The pass rate success among languages is depicted in Figure 6, where the Shona speaking students enjoyed the highest success rate.

Table 3: Correlation between age, gender, language and the final student marks

Age correlation		Gender correlation		Language correlation	
Pearson	0.026	Pearson	-0.013	Pearson	-0.022
p-value	0.016	p-value	0.152	p-value	0.039

Note: *p<0.05; **p<0.01; ***p<0.001

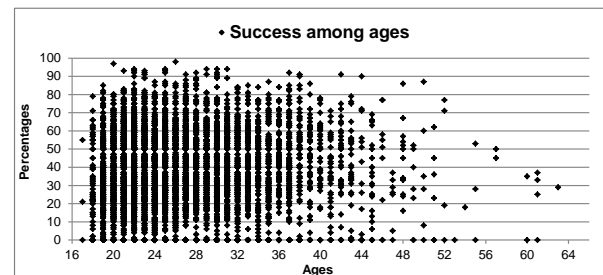


Figure 5: Ages of students with their respective final grades

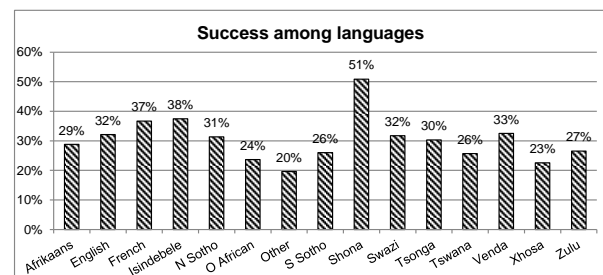


Figure 6: Languages of students with their respective pass rates

7. CONCLUSIONS

Being able to apply engineering “hands-on” is just as important as an understanding of its theoretical aspects [22]. The use of the physical hardware kit has enabled students to integrate theory and practice within the comfort of their own environment. This has helped to ease the logistical problems associated with practical workshops at contracted universities, and has further led to an increase in the number of students achieving 50% or more for the practical module. Delivering practical instruction within a Power Engineering module has therefore been achieved at an ODL institute.

8. REFERENCES

- [1] Oxford Dictionary, Available at: <http://www.oxforddictionaries.com/>. Accessed on 21 October. 2013.
- [2] U. Tschirner, S. Ramaswamy, and I. Harris, "Student Peer Teaching: An Innovative Approach to Instruction in Science and Engineering Education," *Journal of Science Education and Technology*, vol. 10, 2001.
- [3] University of South Africa, "Homepage" Available at: <http://www.unisa.ac.za/default.html>. Accessed on 21 October. 2013.
- [4] J. P. Oliver and F. Haim, "Lab at Home: Hardware Kits for a Digital Design Lab," *Education, IEEE Transactions on*, vol. 52, pp. 46-51, 2009.
- [5] N. Manjikian and S. Simmons, "Evolution and enhancements of a microprocessor systems course," *Education, IEEE Transactions on*, vol. 42, p. 19 pp., 1999.
- [6] W. Durfee, P. Li, and D. Waletzko, "Take-home lab kits for system dynamics and controls courses," in *American Control Conference*, 2004, pp. 1319-1322 vol.2.
- [7] M. Date, S. Patkar, M. Patil, N. Narendra, S. Shelke, A. Kamath, and D. Ghosh, "e-Prayog: A new paradigm for electronics laboratories," in *Technology Enhanced Education (ICTEE), 2012 IEEE International Conference on*, 2012, pp. 1-10.
- [8] S. Seiler, R. Sell, and D. Ptasiak, "Embedded System and Robotic Education in a Blended Learning Environment Utilizing Remote and Virtual Labs in the Cloud, Accompanied by 'Robotic HomeLab Kit'," *International Journal of Emerging Technologies in Learning*, vol. 7, pp. 26-33, 2012.
- [9] O. M. Jakšić, "Teaching optics: preuniversity level," in *19th Telecommunications forum TELFOR Serbia*, Belgrade, 2011.
- [10] N. Orion, "Model for the development and implementation of field trips as an integral part of the science curriculum," *School Science and Mathematics*, vol. 93, pp. 325-331, 1993.
- [11] B. S. Bloom, *Taxonomy of Educational Objectives*. New York: Longman's, Green and Company, 1954.
- [12] A. J. Swart, "Evaluation of Final Examination Papers in Engineering: A Case Study Using Bloom's Taxonomy," *IEEE Transactions on Education*, vol. 53, pp. 257-264, 2010.
- [13] R. Gagne, "Military training and principles of learning," *American Psychologist*, vol. 17, pp. 263-276, 1962.
- [14] J. Piaget, "Intellectual Evolution From Adolescence to Adulthood.," *Human Development*, vol. 15, pp. 1-12, 1972.
- [15] F. Marton and R. Säljö, "On qualitative differences in learning. I. Outcome and process.," *British Journal of Educational Psychology*, vol. 46, pp. 4-11, 1976.
- [16] N. Haring, T. Lovitt, M. Eaton, and V. Hansen, *The Fourth R*. Columbus, OH: Charles Merrill, 1978.
- [17] D. J. Hargreaves, "How undergraduate students learn," *European Journal of Engineering Education*, vol. 21, pp. 425-434, 1996.
- [18] J. B. Biggs and K. F. Collis, *Evaluating the quality of learning: The SOLO taxonomy*. New York: Academic Press, 1982.
- [19] J. Biggs, *Teaching for quality learning at university*, 2nd ed. Berkshire: Open University Press, 2003.
- [20] D. A. Kolb, *Learning Cycle and Learning Style Inventory*. London: Prentice Hall, 1984.
- [21] Engineering Council of South Africa, "Qualification Standard for Diploma in Engineering: NQF Level 6," in *E-02-PN*. vol. Standards and Procedures System, ECSA, Ed., 2012.
- [22] L. Anido, M. Llamas, and M. J. Fernandez, "Internet-based learning by doing," *Education, IEEE Transactions on*, vol. 44, p. 18 pp., 2001.

MULTIVARIATE ANALYSIS OF DATA AS A DECISION MAKING AND DESIGN PREDICTION TOOL: COAL ABRASIVENESS INDEX DETERMINATION

T F Ndlovu*, A F Mulaba-Bafubandi*, T N Mkhwanazi*

** Minerals Processing and Technology, Department of Extraction Metallurgy, Faculty of Engineering and the Built Environment, University of Johannesburg, PO Box 17011, Doornfontein, South Africa.*

Abstract: Abrasive index of coal is an important property of coal as far as power generating companies are concerned, as it has a bearing on the abrasive ability of the coal on the boiler liners. Since the abrasive index of coal is dependent on multiple properties of coal, a multivariate analysis approach was used to highlight the influence of each property towards the abrasive index value. The silica content of the coal showed the greatest influence towards the abrasive index value followed by the ash and pyrite contents which showed equal influence towards the abrasive index value. Since the difference in coal composition has a bearing on the AI value of coal, the AI value of coal from different geological locations was compared to test on the whether the difference in AI value is statistically significant. Coal from KwaZulu-Natal, Mpumalanga and Orange Free State showed statistically significant differences in AI values. This was a further confirmation that the composition of coal has a significant bearing on the AI value. The AI value can thus be predicted based on the Ash, Pyrite and Silica content of coal. Hence the conflict between the coal customers and the coal suppliers with regard to difference in AI values on the same coal sample can be solved by an analysis of the coal composition which will highlight the likely AI value of the coal sampled.

Keywords: Abrasive Index, Coal, Coal abrasiveness, Multivariate Analysis.

1. INTRODUCTION

Coal is mainly made up of organic and inorganic matter. Its burning characteristic is attributed mainly by its organic matter. Presently, about 77% of our country's primary energy needs are provided by coal and 95% of the country's electricity is coal-fired thermal generation, while Sasol's coal conversion technology provides half South African's liquid fuels requirements^[1]. The Metallurgy industry uses coal for iron and steel making as a fuel in a form coke for smelting metals^[2].

A conflict exists between Eskom and its collieries with regard to the Abrasive index value differences obtained between the customer's (Eskom) laboratory and the supplier's (Collieries) laboratory results. The abrasive index value of the coal is important to the customer i.e. the power generating company as it causes wear on the boiler liners which are used in the power generation process. The rapid wear increases the frequency of maintenance on the boilers which has a negative cost impact on the entire power generation process. Understanding the abrasive properties of specific coals is very important, allowing the frequency of maintenance work to be optimised and minimising the risk of failure requiring unscheduled outages of the boiler^[3]. It is also important to understand the nature and properties of the mineral matter inclusions in a coal that would contribute to abrasive wear hence; this will assist in prediction of wear based on the knowledge of mineral matter in a particular coal. Coals contain a wide variety of minerals,

but it is generally acknowledged that only those minerals that are harder than the components used to grind the coal contribute significantly to abrasion behaviour of coal particles. Evidence from previous studies indicates that the abrasion rate of mill grinding components is dependent on the ash content of the coal being ground. Studies also show that quartz and pyrite are the main components in coal responsible for wear. Clays, carbonates, sulphate, phosphate minerals and the carbonaceous coal matrix are all softer than the steel and therefore have little effect on wear^[3].

The process of size reduction presents huge problems to coal producers because coarse mineral matter, particularly quartz causes serious abrasion of pulverisation machinery^[4]. In material science abrasion is defined as the friction between two or more particles of different harnesses. The measurement of the abrasiveness of coal is often done based on the Yancey, Geer and Price Test^[4]. This test monitors the loss in weight of the metal blades which mechanically stir a sample of sized coal. The index that represents the number of milligrams of metal abraded from the metal blades per kg of coal used is known as the Abrasiveness Index (AI).

The management and control of the abrasion process requires a good understanding of the quantitative relationships that exist between AI and contributing factors. This is especially important in South Africa where coal quality issues have forced the power utility company Eskom to undertake some research into

variability of coals supplied by collieries. According to the state's Fossil Fuel Foundation (FFF) director and industry stalwart Rosemary Falcon this variation is known to affect the maintenance costs and power station performance. As a result Eskom ran a series of abrasion index (AI) tests for coals supplied by South Africa's collieries to gain a better understanding of coal quality issues. The tests present an opportunity to use the database to model the association between AI and contributing parameters based on empirical data.

Only a few such models have been proposed in the literature. This is mainly due to lack of models that show strong correlations with experimental data. By fitting a multivariate regression model to tested abrasion index data tests, a weighted ranking of parameters affecting AI could be produced and the relative weightings of each of the contributing parameters thus derived. The complex link between AI and contributing factors would thus be unravelled. The exercise hence would help develop mathematical models for predicting AI for any coal of known composition, for given test conditions.

2. LITERATURE

Coal

Coal is a fossil fuel, composed of lithified plant remains. It consists of macerals (organic matter), minerals (inorganic matter) and water. It is formed by the alterations of dead plant material that lived and died millions years ago. These swamps of dead plants were buried beneath layers of sediments. As the temperature rises, due to increasing depth or burial, the initial peat may be altered by the process of coalification through brown coal, which includes lignite and sub-bituminous coal, to black coals or hard coals that comprise bituminous coal, semi-anthracite and anthracite. Coal is known to be heterogeneous because they have other constituents such as moisture in addition to macerals and minerals. Coal is mostly recognisable due to its burning characteristics^[5] thus; coal can be used for many purposes. In South Africa the main use of coal is electricity power generation. Steel production is made from iron produced in blast furnaces which use coal, mainly in form of coke^[2]. Coal is also used to produce liquid fuels. Liquid fuels derived from coal are sulphur-free and have low levels of nitrogen oxides and particular matter. Sasol operates the world's only commercial, coal-based synfuels manufacturing facility at Secunda in South Africa, producing synthesis gas through coal gasification and natural gas reforming^[2].

Coal properties

Coal is classified into four main types: lignite or brown coal, bituminous coal, anthracite and graphite. Each type of coal has certain physical parameters. The chemical composition of coal has as strong influence on its combustibility. Chemical properties of coal include

moisture, volatile content, ash content, fixed carbon as well as oxygen, hydrogen and sulphur content.

South African coal geology

Coal is found in South Africa in 19 coalfields, located mainly in Kwazulu-Natal, Mpumalanga, Limpopo and the Free State, while lesser amounts in Gauteng, the North West Province and Eastern Cape^[1]. Coal reserves in South Africa are found in sediments of Permian age which generally occur as fairly thick, flat, shallow-lying coal seams.

South African coals rank from sub-bituminous to anthracite^[6] and are generally rich in inertinite, maceral and mineral matter. Bituminous coals of South Africa are found in the Mpumalanga region and anthracite coals are found in the KwaZulu-Natal region. South African coals are typically characterised by vitrinite reflectance meaning they range from 0.6-0.8%^[5]. This characterises South African coal as medium to low rank. Witbank of Mpumalanga contains extensive coal reserves and is the country's most productive coalfield with five major coal seams that occur in intervals within a sedimentary sequent, deposited during a 35 million year geological time period.

Electricity power generation

For the purpose of power generation, coal is pulverised in huge mills into a fine powder before it is blown into huge kettles, called boilers. Due to the heat in the boiler, the coal particles combust and burn to generate heat to turn water into steam. The steam from the boilers is used to turn the blades of a giant fan, called a turbine. The turbine turns a coil made of copper wire (the rotor) inside a magnet (the stator). Together they make up the generator. The generator produces an electric current, which is sent to the homes and factories of consumers via power lines^[7]. The presence of organic constituents also known as macerals in coals have rendered coals suitable to be used for power generation as well as a reductant in the metallurgy industry. Hard coal constituents cause problems during size reduction. Although there many problems encountered during coal comminution (size reduction), this study was based on coal abrasion encountered during size reduction. Coal constituents or rather minerals present in coals may impose hardness greater than that of grinding elements in the mill. These differences in hardness cause friction hence, abrasion wear. Due to abrasion wear, comminution is one of most expensive processes during power generation.

Abrasion

According to material science, abrasion is the friction between the coal and the machinery due to their difference in hardness. More precisely, abrasion is a tendency for a coal to wear away mill components^[6], a physical property that is measured using the abrasion index tester pot reported as AI (mg/kg)^[5].

Abrasiveness of coal, in addition to other coal constituents is a major effect to machinery wear in the

power generation plant, thus this property is of paramount importance when coal is used for power generation. According to the literature [9] South African mines supplying coal to Eskom's power stations measure the abrasiveness index (AI) value of their products and on the reception, the power stations also do the same but very often, values obtained differ. If the supplied coal does not meet or satisfy the agreed specifications not only will it damage the equipment, but also increase the maintenance costs hence, huge penalties are imposed. Eskom and its coal suppliers for power generation had agreed to support a research programme which would examine the effect of a number of variables on the abrasiveness index value for a particular coal [9].

Coal Abrasiveness Index (AI)

Coal abrasiveness of coal is measured by monitoring the loss in weight of the metal blades which mechanically stir a sample of sized coal. The index number of milligrams of metal abraded from the metal blades per kg of coal used. This loss mass and abrasion is done based on the test known as the Yancey, Geer and price Test [4]. Abrasion is not only the physical parameter that cause machinery wear during the size reduction stage (comminution). Physical properties such as coal's hardness, friability and grindability also contribute to machinery wear [5]. However this study was focused on the abrasion index and the variables that lead to coal abrasion such as pyrite, ash and silica content of coal.

Multivariate Analysis

Multivariate statistical Analysis involves an analysis of more than one independent variable towards one or more outcome variables. In design and analysis, the technique is used to perform trade studies across multiple dimensions while taking into account the effect of all variables on the response/s of interest. The information age has resulted in masses of data in every field being generated. Despite the quantum of data available, the ability to obtain a clear picture of what is going on and make intelligent decisions is a challenge. When available information is stored in database tables containing rows and columns, Multivariate Analysis can be used to process the information in a meaningful way. Multivariate Analysis methods are typically used for the following reasons:

- i. Research and development
- ii. Process optimisation and process control.
- iii. Quality control and quality assurance across a range of industries etc.

Multivariate analysis was applied to determine the effects and the contribution of different variables to coal abrasiveness index values from the coal used in power generation plants. These coal abrasive index variables which will be later discussed include coal composition such as silica (SiO₂), pyrite (FeS₂), and ash content and which are attributed to the geology of the source of the coal.

3. METHODOLOGY

STATISTICA Software was used for all the Multivariate Analysis Techniques used in the Project

Multiple regression analysis

The first step was to establish the independent variables and the dependent variables. In this case, the independent variables where: % moisture, % quartz, % ash, % pyrite, % limestone and the % remaining mineral matter in the coal. The dependent variable was the AI value. The aim being to check on the weight of each independent variable towards the AI value and also compute a regression equation that can be used to predict the AI value.

The computed regression with its Beta coefficients was analysed for each independent variable's P value. A p value less than 0.05 being an indication that most of the variation in the AI value was a result of the independent variable.

One way ANOVA

The technique was chosen to check on the significance of the effect of the geology of the source of coal on the AI value of coal. The first step was to check for multicollinearity between the variables. If the correlation is 0.6 or above, a composite variable (in which the highly correlated variables are summed or averaged), had to be made or one of the dependent variables is eliminated.

Secondly it was necessary to ensure that the observations in each group were equal or at least not more than 1.5 times larger than the smallest group.

The univariate p-value and the F-value were analysed to check for the statistical significance of the results. A p-value less than 0.05 was considered significant and an F value more than 10 was also considered significant as it meant that only less than 10% of the values lied in the residual group.

4. RESULTS AND DISCUSSION

Multiple regression analysis results

From table 1 it can be noted that the independent variables with p values less than 0.05 are indicated in red and are the only significant variables that have in effect towards the AI value. Hence the regression equation after standardisation becomes:

$$AI = 0.29Ash + 0.43Silica + 0.28Pyrite + 87.42$$

Regression Summary for Dependent Variable: Properties Influencing AI value						
R= .71559207 R²= .51207201 Adjusted R²= .50085528						
F(6,261)=45.653 p<0.0000 Std Error of estimate: 87.423						
	b*	Std Err. of b*	b	Std Err. of b	t(261)	p-value
N=268						
Intercept			-34.0205	21.07299	-1.61441	0.107646
% H ₂ O	-0.087963	0.053295	-10.3631	6.27883	-1.65048	0.100048
% Ash	0.287556	0.092273	6.9075	2.21653	3.11637	0.002035
% Free SiO ₂	0.430560	0.068238	31.4172	4.97916	6.30973	0.000000
% Pyrite	0.280911	0.047003	45.6858	7.64430	5.97645	0.000000
% CaCO ₃	-0.038163	0.047211	-2.3090	2.85645	-0.80835	0.419623
% Remaining Mineral Matter	-0.003670	0.061710	-0.0721	1.21297	-0.05948	0.952618

Table 1: showing that silica has the greatest influence (0.43) on the AI value.

This means these three variables are contributing factors to the abrasiveness index value. Since these variables are properties influencing coal AI value, we can use this equation as a way to predict the AI value at varying values of ash, quartz and pyrite.

ANOVA Results

Analysis of variance was used to test whether there is a significant difference in AI value in coals from different geologies i.e. three provinces. According to ANOVA the significant difference is shown by F value and p value. F value of more than 1 and a value $p < 0.05$ denotes significant difference among groups. From the univariate test of significance table 2, the F (9.03) and the $p < 0.05$ values indicate significant differences in coal geology from different regions/ provinces.

Univariate Tests of Significance for Abrasive Index (Organized AI Data2)					
Sigma-restricted parameterization					
Effective hypothesis decomposition					
Include cases: 1:268					
Effect	SS	Degr. of Freedom	MS	F	p
Intercept	2184996	1	2184996	151.2796	0.000000
Area Region	260768	2	130384	9.0272	0.000161
Error	3827509	265	14443		

Table 2: showing a significant F and P value of 9 and <0.05 respectively. Geology has an effective on the AI value of coal.

The analysis further confirms that the coal composition has an effect towards the AI value, hence if the coal composition of the coal is known; the AI value can be predicted using the multiple regression equation computed.

5. REFERENCES

- [1] Jeffreys, L.S. "Characterisation of the Coal Resources in South Africa", Journal of the Southern African Institute of Mining and Metallurgy, pp. 95. 2005
- [2] De Korte, G.J. "Coal preparation research in South Africa", The Journal of The Southern African Institute of Mining and Metallurgy, vol. 110, pp.361. 2010

- [3] J.J. Wells "The nature of mineral matter in a coal and the effects on erosive and abrasive behaviour". 2005
- [4] L Thomas "Coal Geology" p 109. 2002
- [5] Tlotleng, T. "Coal characteristics that Lead to Abrasion during Grinding", pp. 11-19. 2011
- [6] Falcon, L.M. and Falcon R.M.S. "The petrographic composition of South African coals in relation to friability, hardness and abrasion indices". Journal of The Southern African Institute of Mining and Metallurgy, 87 no 10, pp.323-336. 1987
- [7] <http://www.eskom.co.za/AboutElectricity/ElectricityTechnologies/Pages/CoalPower.aspx>
- [8] J. Kabuba and A.F. Mulaba-Bafubiandi "Comparing empirical model and Neural Networks for the determination of the coal abrasiveness Index" International Conference on Mining, Mineral Processing and Metallurgical Engineering (ICMMME'2013), Johannesburg (South Africa). 2013

INVESTIGATION OF FINES GENERATION BASED ON ROM COAL PHYSICAL AND CHEMICAL PROPERTIES.

R.S. Tshipa*, A.F. Mulaba-Bafubandi, N. Tshiongo-Makgwe*** and M. Bagopi******

**University of Johannesburg, Faculty of Engineering and the Built Environment, School of Mining, Metallurgy and Chemical Engineering, Department of Metallurgy, Minerals Processing and Technology Research Centre, South Africa, P. O. BOX 526, Wits 2050, South Africa, Email rstshipa@gmail.com*

***University of Johannesburg, Faculty of Engineering and the Built Environment, School of Mining, Metallurgy and Chemical Engineering, Department of Metallurgy, Minerals Processing and Technology Research Centre, South Africa, P. O. BOX 526, Wits 2050, South Africa, Email amulaba@uj.ac.za*

****University of Johannesburg, Faculty of Engineering and the Built Environment, School of Mining, Metallurgy and Chemical Engineering, Department of Metallurgy, Minerals Processing and Technology Research Centre, South Africa, P. O. BOX 526, Wits 2050, South Africa, Email ntshiongo@uj.ac.za*

*****Morupule Coal Mine, P. O. BOX 35, Palapye, Botswana, Email MBagopi@mcm.co.bw*

Abstract: Morupule Coal Mine (MCM) mines 3 sections with top customer being Botswana Power Cooperation (BPC). Recently it built a new power plant and that led to the expansion of MCM in order to meet the coal demands. Of recently the BPC product has been exceeding the allowable fines (-3.35mm) content in the final product leading to penalties. Since coal is made up of inorganics (mineral matter) and organic matter (macerals), both these were investigated to determine their content and their contribution to the overall physical and chemical behaviour of coal. For the inorganic matter, test carried out involved: trace element determination using the Scanning Electron Microscopy (SEM). And, for the organic matter coal petrology was used to examine for different lithotypes. Apart from the determining constituents of coal, the friability, hardness and distribution of particles in coal before processing was studied. All this various tests give an insight and explanation about the behaviour of coal that often result in fines generation. Of the tests carried out, it was found that the SM2-21 produces more fines because of its friability and the types of minerals present.

Key words: coal, fines generations, inorganic and organic matter, SEM analysis, lithotype examination, hardness, friability

1. INTRODUCTION

Morupule Coal Mine (MCM) is the only coal mining and producing company in Botswana. It was established in 1973 by Anglo American (Pty). In 2000, Debswana Mining Company took over the coal mine as a fully owned subsidiary. The mine produces two products; washed coal and thermal coal. The washed coal goes through a cleaning process based on the different densities between the coal and associated gangue. The thermal coal product goes through the comminution and sizing process. Thermal coal main customers for MCM are BPC, Botswana Ash and BCL.

In 2010 BPC built a new power station which necessitates more coal for production of electricity. This required MCM to expand so as to increase its total output and meet the demands for all its customers including BPC. The total annual production of Morupule was increased from 1 million tonne per annum to 3.2 million tonnes per annum. Although this was good for business it posed a challenge of strict quality assurance. BPC requires a product with maximum coal fines (-3.35mm) of 32%.

This is to allow easy handling of material. If thermal coal contains fines with a lot of moisture it is likely to stick to pipes, mills and other equipment reducing their capacity and leading to blockages and downtimes which are undesirable in power plants. MCM has been struggling

to meet the product specification and has experienced several penalties which are costly for the company. The research was initiated to identify underlying causes and potentially develop solutions to the problem, with the intention of reducing the penalties.

2. METHODOLOGY

The test works discussed in this project were carried out using a freshly mined coal sample. Each recorded a mass of ± 28 kg from the individual three sections mined; South Main 2-21, South Main 3 and West Main. The samples are identified as SM2-21, SM3 and WM for all the tests carried out from each section. For all the test work carried out, the samples were stored and prepared separately to avoid contamination.

Since coal is constituted of both organics and inorganics, different test had to be carried out in order to cover the variety of the coal composites and structure. This enabled a full understanding of the coal properties that lead to various fines generation rate. For this project, six different analytical techniques and examinations were carried out to emphasis the understanding of coal behaviour. Due to the fact that human error plays a role in the final results obtained, the different test works will also minimise the result inaccuracy. The results obtained from some of the tests were expected to relate to one another in several aspects.

2.1 Drop shatter test

Coal of various particles was screened using the following sieves; 100mm, 50mm, 45mm, 25mm, 18mm, 10mm, 8mm, 4mm and 2.25mm. The mass of each fraction was recorded. A 210 litre drum, lined with steel plate, was placed 2 meters below the stair case. Then the coal was dropped twice from a height to allow each coal particle to be subjected to impact upon heating the steel plate. The broken coal was then screened and the mass recorded. Data from the particle size distributions was then used to determine the friability of coal from the different mine sections [7].

2.2 Particle Size Distribution (PSD)

The test involved screening coal sample for 30 minutes from the three different mining sections and recording each size fraction. Sieves used were; 75mm, 63mm, 53mm, 45mm, 37.5mm, 31.5mm, 25mm, 12.5mm, 8mm, 6.3mm and 3.35mm. The amount of fines (<3.35mm) produced was expressed as a percentage of the total sample mass to determine their occurrence in each section.

2.3 Lithotype examination

Lithotypes are the macrostructures of coal that could be seen by a naked eye. Each lithotype is known to contain a certain macerals group. Therefore, identifying the lithotypes and comparing their bands thickness to coal samples obtained from other section may enable comparison of the three sections to a certain extent. To carry out this examination, coal samples of 130 to 200mm were examined in a geology laboratory [5].

2.4 Scanning Electron Microscope (SEM)

Coal ash was analysed with the Scanning Electron Microscope using backscattering technique so that the entire element lying beneath others are also analysed. Electron beams were scattered across the ash and fluorescent x-rays were generated. Energy of each x-ray photon characterises the element producing it. The Energy Dispersive Spectroscopy (EDS) microanalysis system permitted the spot elemental analysis and presented it as individual fractions.

2.5 Abrasiveness Index test

A sample of 4kg was used for each mine section. New blades were used which were conditioned by running them for 3 minutes in a coal sample. This was done until the blade mass did not change. After conditioning, they were cleaned with methylated spirit and brass brush to remove any coal sticking to them. They were connected into the blade arms, sample placed on top of them and the pot cover tightly closed. The test was run for 12000 ± 20 revolutions. After completion of the test, the blades were washed and their mass loss measured [4].

2.6 Vickers Hardness Test

Coal particles, approximately 5cm long, 3cm thick and 2.5cm wide, were cut along the bands and polished to obtain a smooth surface. Four samples were prepared for each section and individually placed on a stage. Using a magnification of 10, a flawless area was identified where an indentation by a load was to be made. A 10 kg load was used to test the hardness of the coal for 10 seconds [3]. Once the load was removed, the dimensions (i.e. sides) of the indentation were measured and the hardness automatically calculated. The test was performed randomly on the coal to avoid testing the same band of macerals or minerals for hardness giving biased results. A total of 16 tests were performed on each section.

3. RESULTS AND DISCUSSION

3.1 Drop shatter test

The drop shatter test is used to determine how easily the coal breaks once dropped at a given height. It depends on the length of the cleavages within the coal, the minerals filling the cleavage and the vitrain band.

SM3 coal was found to be more friable (43.24%) than the other two sections. Therefore it is expected that SM3 coal samples break easily and produce more fines. This could mean that SM3 coal has more fractures or even more vitrain bands. WM coal was found to be the least friable (23.07%), with SM2-21 coal at 37.77%. Therefore it is expected that WM coal will not break easily but that does not imply that samples from this section will not generate a lot of fines. The above observation had to be confirmed by the, lithotype examination, the SEM results and PSD test results. The brittle coal should be paid more attention to, to avoid unnecessary breakages that will contribute to generation of fines.

3.2 Lithotype examination

It was observed that SM3 coal has very little vitrain bands hence will not generate more fines even though is brittle. This is supported by the quoted literature "the brittle nature of vitrinite frequently results in a concentration of particle sizes smaller than 1mm" [2] On the contrary, more durain was found in comparison to other sections. Since durain is tough, the coal containing high amount of durain is expected to break generating big particles and less fines [2].

The SM2-21 coal has a lot of vitrain (vitrinite group maceral) compared to SM3 but less compared to WM. This type of coal is expected to generate fines but not in excess [2]. The clarain (inertinite group maceral) occupies one third of the sample. However the clarain is considered to be mechanically strong only in the absence of fusinite maceral group. It was observed that durain (liptinite group maceral) occupied almost half of the coal sample and it is tough. The WM coal has more vitrain

bands than the other two sections which means it can possibly contribute to excess fines generation. The high quantity of the vitrain bands in the sample explained the friability of this coal along the bands; leading to easy breakages and more fines production. WM was found to have more clarain than the other two sections therefore it contribute to the high fines production.

3.3 Scanning Electron Microscope analysis

Coal ash was analysed using the Energy Dispersive X-ray Spectrometry attached to the SEM equipment. Although some sulphide minerals may have lost the sulphur as an oxide during burning, main elements contained in the coal were still retained [6].

Table 1: Elements found in the ash of the MCM coal

	SM3	SM2-21	WM
CLAY + CARBONATE (CCM) MINERAL ELEMENTS			
Mg %	1.46	2.41	1.71
Al %	32.34	29.14	29.38
K %	0.44	*	0.74
Ca %	8.73	13.35	11.03
TOTAL CCM	42.97	44.90	42.86
SILICATES AND SULPHIDES MINERAL (SSM) ELEMENTS			
Si%	41.35	37.70	37.20
Fe%	5.59	6.58	10.96
TOTAL SSM	46.94	44.28	48.16

Table 1, SM2-21 coal, contains a higher amount of total clay and carbonate minerals (44.90%). According to the Moh's scale, clays and carbonates are very soft, scaled at 2-3. They also have very fine grains. Their presence in higher amount would contribute to a softer coal amenable to generating more fines during crushing. This is supported by the low quantity of hard mineral elements; iron (6.58%) for pyrite and silicon (37.70%) for quartz. Although the clay and carbonate elements for the WM and SM3 are almost equal, the silicates and sulphides elements content for WM is higher compared to the other sections. This explains the lack of fine generation due to the presence of hard minerals. The SM2-21 can then be easily crushed using less motor power. This confirms the friability of coal from the SM2-21 (though not more than that from WM). As SM3 coal has more SSM than coal from SM2-21 the blend of coal from these two seams may lower the risk of producing excess fines during coal processing at the plant. Seemingly it would be suggested to blend the WM coal with that from the SM3 coal. However factors (like the amount of fixed carbon of the two blended coal sections) that affect the coal quality may be looked at to avoid compromising the coal quality.

3.4 Abrasiveness Index test

The abrasiveness index of coal depends on the amount of pyrite and quartz minerals present in the coal. Much information is not known on the relationship between macerals and the abrasiveness of coal. Therefore there may be poor clarity of results although they have been repeated. The most important aspect of the results obtained is to see if they correspond with the SEM results and are reliable [4].

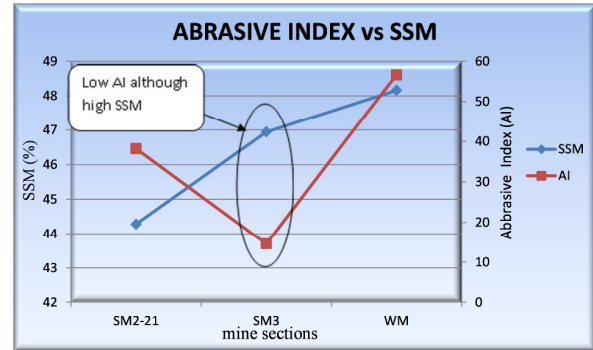


Figure 1: Abrasiveness of coal compared to the Sulphide and Silicate content

Figure 1 shows that WM coal is more abrasive than coal material from other sections. This is confirmed by its higher amount of sulphide and silicate elements. SM3 coal is the least abrasive coal although it has a slightly higher quantity of silicates and sulphides than SM2-21 coal.

3.5 Vickers hardness test

The test was performed using the Vickers Hardness test. The main reason being it is the best test to pick up slight differences on hardness of coal between the three mine sections [8-9].

WM is hard with 30.56kg/mm² compared to the other section and may not generate more fines when broken or crushed. This may be, because of the high quantity of the SSM elements with 48.16% and low friability of 23.07%. SM3 coal is less hard with 30.0 kg/mm² than the SM2-21 coal: 30.38kg/mm². Although results obtained from SEM analysis showed that SM3 coal more SSM compared to SM2-21 coal, expectations would be that the less hard the coal is the less SSM elements. This shows that the hardness of coal is dependent on other variables other than the SSM present in coal.

To minimise the production of fines, coal with more hardness should be blended with a less harder coal.

3.6 Particle Size Distribution

The test was performed using the different sieves. The size fraction of interest was -3.35mm because that is where the fines which have a limitation of 32% in the final product are found.

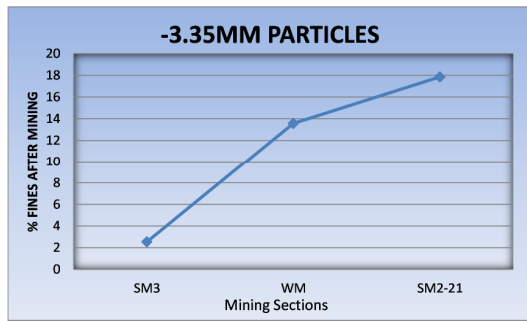


Figure 2: Fines content at the different mine sections

Results reported on Figure 2 shows that the coal from SM2-21 produces more fines, with 17.86% compared to the other two sections. This is supported by the friability of the SM2-21 coal (37.77% which is considered moderate) and high amounts of the clay and carbonates minerals (44.90%). WM coal produces moderate fines, 13.57%, although the figure is closer to that of SM2-21. Comparatively, SM3 coal produces the least fines amongst the three sections with 2.53%. Although it is more friable (highest with 43.24%) than the other sections it produces large particles when it breaks. See graphs below. BF denotes "Before Friability Test" and AF denotes "After Friability Test".

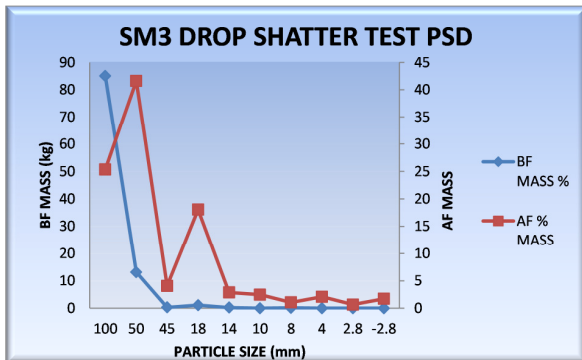


Figure 3: Friability of SM3

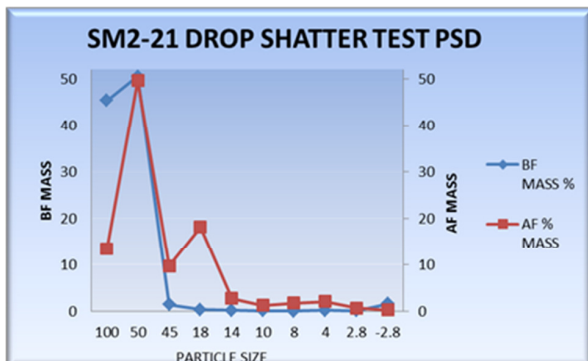


Figure 4: Friability of SM2-21

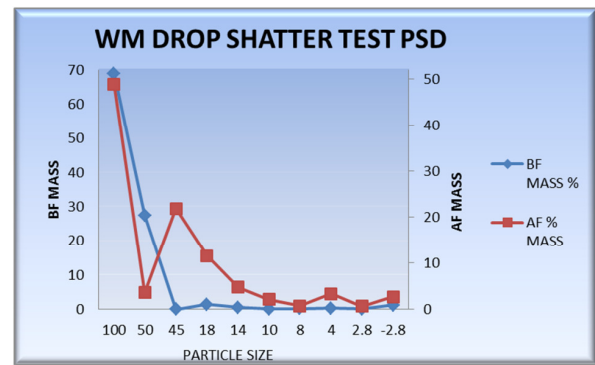


Figure 5: Friability of WM

Figure 3 shows that before the drop shatter test were performed 99.61% of particles were above 50mm in size. After dropping the coal from a height it generated 89.10% particles above 18mm. Therefore it breaks to yield medium to large particles with fines less than 2.38%. Graph 4 and 5 shows PSD of SM2-21 and WM which showed presence of 85.69-90.94% of particles greater than 18mm. To approach the problem, the product for BPC may be screened using the different sieves with following apertures; 18mm and 4mm. To avoid the reduction of mined volume, the undersize (-4mm) coal would be sold to briquetting companies or MCM may do it if the cost are well covered. This would be done on WM (13.57%) and SM2-21(17.86%) coals which showed the ability to produce more fines than SM3 coals (2.53%).

Although not specified as to how much fines are allowable in the freshly mined coal, the aim should be to obtain less 28-30% fines in the final product. This will allow room for any inefficiency that occurred during processing. The results discussed above seem lower than the acceptable fines for the BPC product. It should be kept in mind that the coal is not yet processed. Therefore the possible of obtaining excess fines is high.

3.7 Summary of results

Table 2: Summary of results excluding lithotype examination

	SM3	SM2-21	WM
Friability %	43.24	34.77	23.07
fines %	2.53	17.86	13.57
hardness kg/mm ²	30.00	30.38	30.56
SSM %	42.97	44.90	42.86
CCM %	46.94	44.28	48.16

Determination of coal's ability to produce fines based on lithotypes is difficult and unreliable. All the summary results are discussed briefly in the conclusion as a summary of the overall test work results obtained.

4. CONCLUSION

The problem that led to initiation of this research was the excess fines in the thermal coal product for BPC with the aim to determine the section that is a resultant. Based on Table 2, the SM2-21 section produces more fines than the other two sections, with 17.86%, before the coal processed. Therefore after processing it is likely to results in excess fines in the final thermal coal product. SM3 mine section produces fewer fines compared to the other two sections with 2.53%. The test results may also be interpreted that after processing the SM3 coal, the product particles are likely to be larger than 18mm. While the WM produced moderate fines when compared to SM2-21 and SM3, great attention should be paid to it. This is because most test results have a close call with SM2-21, therefore is a potential excess fines producer in the future.

5. RECOMMENDATIONS

This research was based on fines generation before the coal is processed at the plant. It is recommended to investigate fines generation along the processing route i.e. at the feeder breaker, at the conveyor belts transfer point and surge bin, at the crusher, at stockpile. Information obtained would be used to establish a mathematical model which will help predict the amount of fines to be produced based while ROM ore is processed at the plant. One would investigate the effect of blending of coal on quality of the product.

The type of crushers and their mode of operation should also be looked into and an alternative made where applicable, e.g. slow paced crushers that results on minimal impact [1].

6. ACKNOWLEDGEMENT

Permission from Morupule Coal Mine to carry out the research and present these results at SAUPEC is here acknowledged. R.S. Tshipa is thankful to the UJ laboratory staff for the technical assistance. Prof Mulaba and Dr Tshiongo-Makgwe, thank you for your support and patience.

7. REFERENCES

1. K. Alderman, "Impact of crusher type and pre-screening on fines generations", page 4, 7-8, 2009.
2. R.N.S. Falcon, & C.P. Suyman, *An introduction to coal petrography: Atlas of coal petrolographic constituents in the Bituminous coal of Southern Africa*, page 1-26, 1986.
3. N.H. Macmillian & D.G. Rickery, *Measurement of hardness in coal*, page 242-243, 1978.
4. M.T. Tlotleng, "Coal characteristics that lead to abrasion during grinding", page 14-20, 24-34, 2011.
5. R.C. Ward, *Coal geology and coal technology*, page 74-89, 1984.
6. T. Xiuyi, "Mineral matter in coal", page 1-5
7. ASTM, *Standard testing method of drop shatter test for coal 2010*, page 1-4, 1995.
8. [http://www.uk.ask.com/beauty/What-Is-the-Hardness-of-Coal\(2012/12/14\)](http://www.uk.ask.com/beauty/What-Is-the-Hardness-of-Coal(2012/12/14))
9. [www.askkids.com/resource/Hardness_of_Coal.html\(2012/12/14\)](http://www.askkids.com/resource/Hardness_of_Coal.html(2012/12/14))

PREDICTION OF CLEAN COAL PRODUCT USING MATHEMATICAL MODELS.

**University of Johannesburg, Faculty of Engineering and the Built Environment, School of Mining, Metallurgy and Chemical Engineering, Department of Metallurgy, Minerals Processing and Technology Research Centre, South Africa, P. O. BOX 526, Wits 2050, South Africa, Email rstshipa@gmail.com*

***University of Johannesburg, Faculty of Engineering and the Built Environment, School of Mining, Metallurgy and Chemical Engineering, Department of Metallurgy, Minerals Processing and Technology Research Centre, South Africa, P. O. BOX 526, Wits 2050, South Africa, Email amulaba@uj.ac.za*

****University of Johannesburg, Faculty of Engineering and the Built Environment, School of Mining, Metallurgy and Chemical Engineering, Department of Metallurgy, Minerals Processing and Technology Research Centre, South Africa, P. O. BOX 526, Wits 2050, South Africa, Email ntshiongo@uj.ac.za*

Abstract: Coal Process has challenges that can only be mitigated if a close attention is paid to the various process variable that contribute to the overall productivity of the Plant. Understanding how the input manipulative and disturbance variables affect the process output gives a better view of the process and the controls (models) that can be put in place to maximise plant performance with minimum cost. Information based on the raw plant data, real-time-monitor and washability data provides a clear picture on the system performance. From the information derived, it was found that the washability data provides a reliable model that can assist in predicting the product quality (feed ash) and the quantity (feed tons)

Key words: coal, washability data, mathematical models,

1. INTRODUCTION

The productivity of a plant depends on the variables presents and how they are controlled or manipulated in order to achieve the desired results with minimum production cost. This can be achieved by understand the behaviour of the process and modelling mathematical equations to predict the overall behaviour of the system if certain changes are introduced. In summary, engineers need to model processes if they are going to design or develop those processes. In the practices of engineering design, models are often applied to predict what will happen in a future situation. However, the predictions are used in ways that have far different consequences than simply anticipating the outcome of an experiment [4]. To obtain the response of a system in relation to the sum of the specific inputs, one superposes the separate responses of the system to each individual input. This principle is used to predict the response of a system to a complicated input by breaking down the input into a set of simpler inputs that produce known system responses.

2. METHODOLOGY

The aim was to develop the relationship between the variables that would build a model suitable for predictions. The individual input variables (Feed tons, Feed ash and Medium density) are superposed with output variables (Clean coal tons, Clean coal and Yield) to determine how they relate. Some of these variables can be controlled or manipulated eg feed rate and medium density while others are disturbances to the process eg; feed quality. The Feed ash (representing the mineral matter) either increases or reduces the coal density depending on its content in the coal. The medium density is regulated in accordance with the desired product based on the quality of feed ash content. If the

coal has a lot of mineral matter and the feed rate is high that means the sinks in the Wemco drum will become saturated or “stuffed up”. This deprives the floats to effectively separate from the sinks and increases residence time and recirculating load. Therefore regulating the feed rate based on the feed quality promotes good efficiency of the Separation system.

Information from the daily plant production was used to determine is a relationship exist between the input and output variable. The study will also be conducted using from the real-time-monitor and the washability data. The relationship will be taken a step further to develop a suitable control model that will be used to predict the clean coal tons and the ash content of the clean coal. This will assist the on making well informed decision before changing the process variables [3].

3. RESULTS AND DISCUSSION

3.1 Information based on the Raw Plant Data

According to project information based on the production report there is a definite relationship between feed tons and clean coal. This is supported by the R^2 of 0.9291, see Figure 1. Coal at this stage is liberated and sized as required for the Wash Plant input. The advantage here is that the ash, which represents the mineral matter, is reduced in content. This means the equation can be derived to forecast the clean coal production in terms of tones. However there is no relationship between the following input and output variables: feed tons and; 1) clean coal ash and 2) yield; feed ash and; 1) clean coal tons and 2) clean coal ash; medium density and; 1) clean coal tons and 2) clean coal ash.

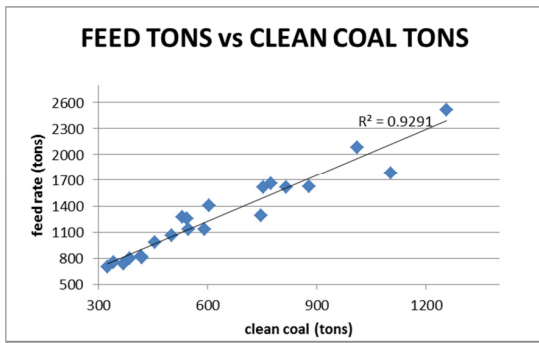


Figure 1: Feed tons Vs. Clean Coal tons

When the washability curves are used, a solid relationship between the medium density and: 1) clean coal ash and 2) clean coal tons is derived [2]. This, however, is dependent on the washability curves. This means in order to predict the yield of coal during a cleaning process, a float sink test has to be performed as often as possible to ensure accuracy of the model

3.2 Information based on the Real-Time-Monitor

The real-time-monitor filters information about the activities taking place at the field (both instrument and the equipment). This means the possibility of dealing with poor records is eliminated. However the quality of information from the instruments is dependent on their good maintenance ensuring their accuracy, for example calibration of weightometers. The relationships established using the direct reports was not definite. This goes for the chosen input and output variables.

Therefore with two sources of direct information not delivering expected result the separation and transportation process was investigated. The real time monitor software does not eliminate the process or operational errors. It shows the effect of various variable changes on the system / process e.g. how the continuous process affects delivery of the process and the final products. The software was used to determine the performance of the Density Medium Separation Circuit on the Clean Coal Production. Conversely, using the real time monitor system, it was found that as the Dense Medium System is fed continuously there is a high potential of recirculating load. This is supported by increasingly poor separation indicated by the ever decreasing value of R^2 as the washing time (production time) increases. See Figure 2 and 3. Note; each point was recorded at a time interval of 4 minutes.

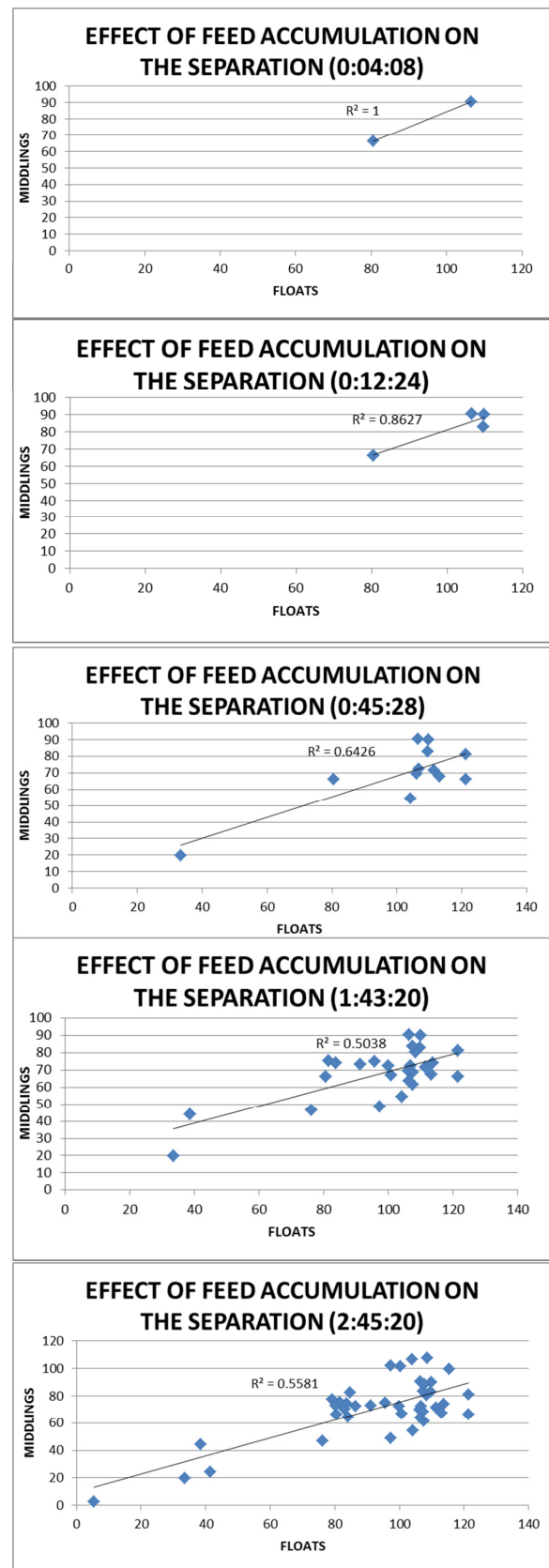


Figure 2: Effect of feed accumulation on the coal separation

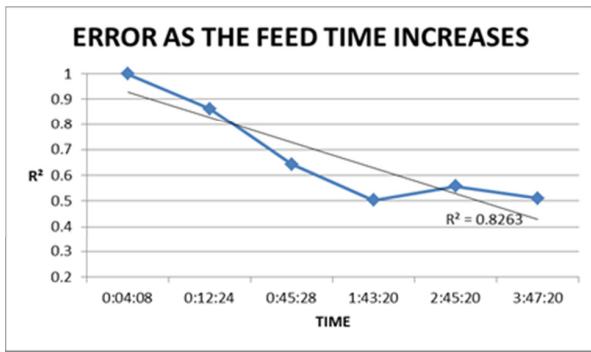


Figure 3: Relationship between the R^2 and the error populated during continuous Coal Washing process

1. From the graphs it was found that as the throughput for the plant increases the relationship between the variables weakens. This may be due to:

- Coal Particles misplacement: Feeding coal particles into the Dense Medium Drum at a high rate with inadequate residence time to allow effective separation can lead to misplacement of particles. Other factor that may lead to particle misplacement is the particle distribution. If there are lots of oversize materials in the drum, they will be easily lifted up even if they are floats (clean coal). If the undersize materials are high in quantity they will lead to high recirculation load. This poses a high potential of particle misplacement.

- Type of raw coal: Coal with a lot of gangue (high % ash) will sink and acquire a lot of residence time within the drum causing the separation efficiency to be low. A good indication that there is poor separation is the suspended static flow of the floats on the static panel. This has been observed repeatedly at the Plant.

- Density control: Coal feed containing a lot of ash requires that the medium density be dropped low to allow the low ash coal to float because of its low density. If the medium is left unregulated for various feed types a lot of material will be misplaced leading to a poor product.

2. The time record for the plant feed, sinks and floats is assumed to be the same. The time it takes for a sink or float particle to reach the weightometer is different. This is because the sinks are lifted by lifter bars that rotate at a certain speed then dropped into the launder. Thereafter transported by the extended launder to a drain screen and granulated to reduce the size particles. Then finally dropped onto a sinks conveyor where there will travel a certain distance before passing the weightometer.

Where else the floats are pushed by the medium out of the Wemco Drum and pass through the static panel onto a screen and finally the belt. In short the distance between the sinks discharge and the floats discharge point to the belt weightometer is different. The time at

which the tons report at the weightometer is different. The travel period was determined using coal samples painted red and a stop watch. At the first pass on the feed conveyor weightometer the timer was started and upon passing the last conveyor belt it was stopped. The times were as follows:

Table 1: Residence and transportation period for clean coal and middlings

Weightometer position	Period (seconds)
Feed conveyor	0 (start point)
Clean coal conveyor	57
Middlings conveyor	5.9

3.3 Information based on the Washability data

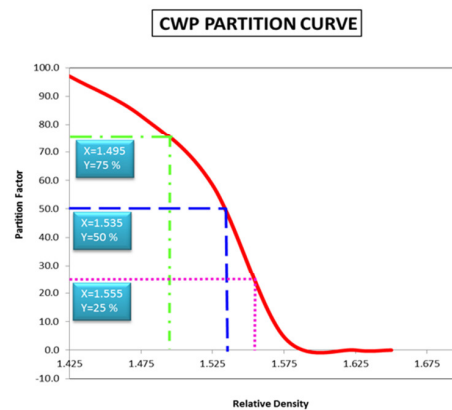


Figure 4: Partition curve for Coal Wash Plant (CWP)

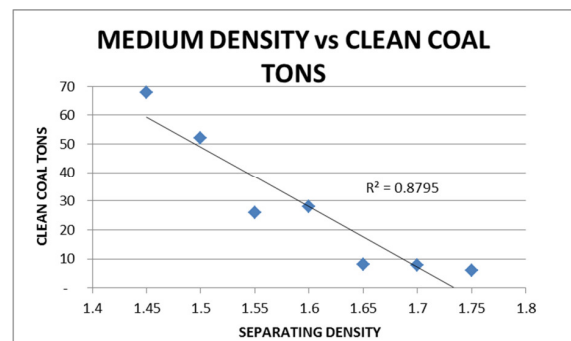


Figure 5: Washability data, Medium density and Clean coal tons

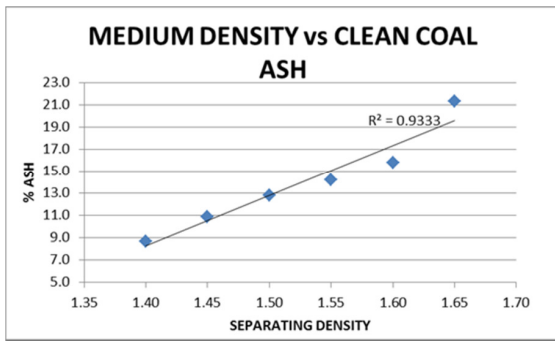


Figure 6: Washability data, Medium density vs. Clean coal ash

Figure 4 represent the separation effectiveness of the Coal Wash Plant. With the E_p of 0.03, the process can be rendered effective and can definitely perform far better if variables are well controlled. According to Figure 5 and 6 based on the medium density, there is a definite relationship between the ash content in the coal and the clean coal tons that can be attained based on the separation density. The equation developed at this stage (using washability results) wastested on raw plant information, i.e. feed tons but were erroneous. The results obtained were totally different from the true values. This meaning in order to predict the Clean coal tons production during a cleaning process it is more accurate to use the relationship derived from the information based on raw plant data. The equations for the clean coal ash are dependent on the washability data and can't be used for the daily plant inputs.

4. CONCLUSION

The information derived directly from the plant inputs (daily production reports) may be biased as it does not support some of the literature which was based on similar topics. The only information that can be relied on and is an equation developed to predict production based on the "Clean coal tons and Feed Coal tons". The information on the weightometers cannot be relied on because they are placed at different positions from the feed points [1]. Also the traveling distance for the sinks and floats is different: some report early at the weightometer than others. Likewise, various particles reside in the drum and exist at various time leading to inconsistencies and inaccuracies in the final output values. Washability curves can assist on prediction of the clean coal ash based on the various separation densities.

Because of the two reliable relationship obtained, the following equations were developed: **Since**

a) Feed

$$\begin{aligned} \frac{\partial W}{\partial t} &= [X(t) - X \cdot Zx(t)] + [Y(t) - Y \cdot Zx(t)] \\ &= X(t)[1 - Zx] + Y(t)[1 - Z] \quad (1) \end{aligned}$$

Where

$\frac{\partial W}{\partial t}$ is the feed tons over a certain period of time

$X(t)$ is the float tons

$Y(t)$ is the sink tons

Zx is the % float fines

Zy is the % sink fines

Therefore

b) Clean coal tonsis

$$\begin{aligned} \partial W &= [W - W \cdot q] \\ \frac{\partial [W - Wq]}{\partial t} &= X(t)[1 - Zx] + Y(t)[1 - Zy] \\ \frac{\partial [W - Wq]}{\partial t} - Y(t)[1 - Zy] &= X(t)[1 - Zx] \\ X(t) &= \frac{\left[\frac{\partial [W - Wq]}{\partial t} - Y(t)[1 - Zy] \right]}{[1 - Zx]} \quad (2) \end{aligned}$$

Where

q is the fines in the feed

c) Clean Coal ash

$$Xa = Wa - (Wa \cdot f) \quad (3)$$

Where

a is the ash content

f is the ash reduction factor (clean coal)

d) Clean Coal Yield

$$\eta = \frac{X(t)}{\partial W} \cdot \partial t \quad (4)$$

Where

η is Clean Coal yield based on the raw plant data. Taking into consideration the fact that yield is affected by the feed ash content, then

$$100Wa = Xa \cdot \eta + Ya \cdot (100 - \eta)$$

$$100Wa = Xa \cdot \eta + (100Ya - Ya \cdot \eta)$$

$$100Wa - 100Ya = Xa \cdot \eta - Ya \cdot \eta$$

$$\eta = \frac{100(Wa - Ya)}{Xa - Ya}$$

Since middlings ash is

$$Ya = Wa + (Wa \cdot g)$$

Where

g is the ash increase factor (middlings coal)

Then

$$\eta = \frac{100(Wa - (Wa + Wa \cdot g))}{(Wa - Wa \cdot f) - (Wa + Wa \cdot g)}$$

$$\eta = \frac{100(1 - (1 + g))}{(1 - f) - (1 + g)} \quad (5)$$

This equation is based on the washability data.

5. RECOMMENDATIONS

The following recommendations are based on the project findings. The clean coal tons model had the potential to be successful, however due to the unknown residual material in the drum (fines factor) the model output was affected. The input-output efficiency should be determined; this will give an insight of how much recirculation load is present in the system and how it affects the performance of the system. This can later be incorporated into the model for clean coal tons prediction as the sink and floats fine factor.

More washability tests should be carried out to assist in identifying the performance of the process. Also, the online analyser can be installed with washability software that will analyse the coal before being fed at the Wash plant. Since it was discovered that continuous operations does affect the separation process, the washability tests have to be performed at determined time interval so as to incorporate any deviations or changes into the already generated equations.

6. ACKNOWLEDGEMENT

Permission from Morupule Coal Mine to carry out the research and present these results at SAUPEC is here acknowledged. Prof Mulaba and Dr Tshiongo-Makgwe, thank you for your support and patience.

7. REFERENCES

- [1], M. Abzalov *Sampling Errors and Control of Assay Data in Applications and Experiences of Quality Control*, 2011, page. 622.
- [2] B.W. Bequette, *Process Control: Modelling, Design, and Simulation*, page 491, 2003
- [3] L. Thomas, *Coal Geology*, page 89-109, 2012
- [4] <http://www.sfu.ca/~vdabbagh/Chap1-odeling.pdf> (06/11/2013)

ASSESSING THE ACCURACY OF A PROTECTION CURRENT TRANSFORMER USED IN A WIDE AREA MONITORING SYSTEM

C.M. Mabotha, M.M. Mashaba and K.J Nixon

School of Electrical & Information Engineering, University of the Witwatersrand, Private Bag 3, 2050, Johannesburg, South Africa, E-mail: cm.mabotha@gmail.com, musa.mathews27@gmail.com, ken.nixon@wits.ac.za

Abstract: The purpose of this investigation is to assess the accuracy of the protection current transformer (CT) used in a Wide Area Monitoring System (WAMS). This is done through conducting steady state and dynamic response tests. At nominal frequency (60 Hz) and primary current ranging from 50 A to 100 A, the CT has maximum ratio and phase angle errors of 0.10 % and 0.397 ° respectively. At 50 Hz and same primary current range, it has maximum ratio and phase angle errors of 0.18 % and 0.40 ° respectively. At rated primary current (50 A) and frequency ranging from 47 Hz to 60 Hz, it has the maximum ratio and phase angle errors of 0.5 % and 0.3 ° respectively. It has maximum Total Vector Error (TVE) of 0.012585 % under both steady state and dynamic conditions. The tested CT is declared suitable for WAMS applications since its errors comply with the requirements for high accurate WAMS as per IEC 60044-1, IEEE C37.118-1 and ABB Group standards.

Keywords: WAMS, Phasor Measurement Unit, protection current transformer, phase angle error, ratio error, total vector error.

1. INTRODUCTION

The demands placed on a power utility have been increasing significantly over time and this has caused power systems to become larger and more complex [1, 2]. Due to the increasing complexity, systems such as a Wide Area Monitoring System (WAMS) are used for monitoring purposes. WAMS is a network system used to monitor the real time power operation status of the large and complex wide power network system using synchrophasor technology [3]. It consists of Phasor Measurement Units (PMUs) placed at different locations in a power network [4]. The PMUs are used to synchronously measure magnitudes, phase angles and rate of change of frequency of current and voltage signals from instrument transformers [4]. The instrument transformer that is of particular interest for this investigation is a protection current transformer (CT). The protection CT is mainly used to step down large primary currents to smaller secondary currents suitable for protection and measurement systems [5].

This paper entails the presentation of the steady state and dynamic accuracies of the protection CT used in the WAMS; the background on the WAMS and protection current transformer; existing and developed investigation test methods; test results; analysis and discussions of the test results; and recommendations for future work.

2. BACKGROUND

2.1 WAMS

The PMU accuracy is defined by Total Vector Error (TVE) which includes both magnitude and phase angle errors. The TVE is defined as follows [6]:

$$TVE = \sqrt{\frac{(X'_r - X_r)^2 + (X'_i - X_i)^2}{X_r^2 + X_i^2}} \quad (1)$$

Where:

X'_r = real part of the measured secondary current.

X_r = real part of the expected secondary current.

X'_i = imaginary part of the measured secondary current.

X_i = imaginary part of the expected secondary current (assumed to be zero due to purely resistive burden used)

The PMU is specified to have a maximum permissible Total Vector Error (TVE) of one percent [6]. However, this error does not include the propagation errors from the instrumentation transformers. Figure 1 below shows the connection between PMU and the instrument transformers [7].

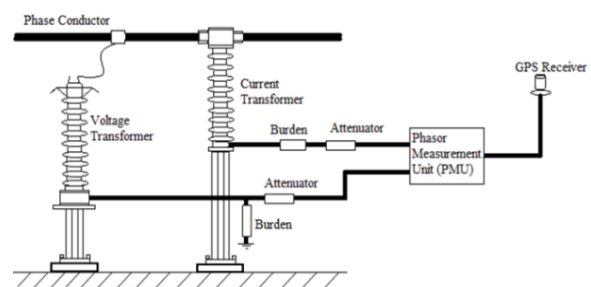


Figure 1: The connection of the instrument transformers and the PMU.

The instrument transformers are specified to have accuracies of between 0.2 % and 0.5 % for high accurate WAMS [8]. Therefore it is important to ensure that the errors of the instrument transformers meet the requirements for the WAMS applications under both steady state and dynamic conditions.

2.2 The protection CT

Mathematical model: The equivalent circuit of the CT can be used to describe its nonlinear mathematical model. Figures 2 and 3 below show a complete general equivalent circuit and phasor diagram of the CT with its quantities referred to the secondary side. The secondary current (i_2) is taken as the reference.

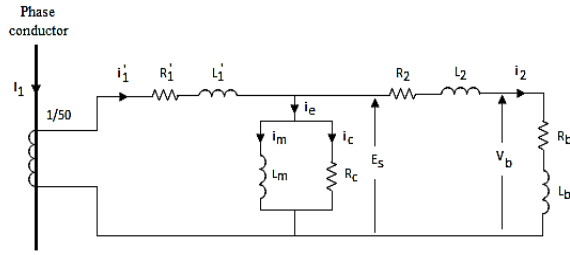


Figure 2: The equivalent circuit of the protection CT.

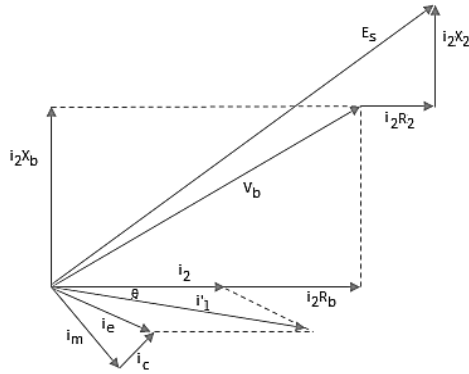


Figure 3: The phasor diagram of the protection CT.

Where:

- i_1' = primary current referred to secondary circuit.
- i_2 = secondary current.
- R_b = burden resistance.
- L_b = burden inductance (assumed to be zero in this case).
- R_2 = secondary coil resistance.
- L_2 = secondary coil inductance.
- R_1' = primary resistance referred to secondary circuit.
- L_1' = primary inductance referred to secondary circuit.
- V_b = secondary voltage or voltage across the burden.
- E_s = secondary induced e.m.f.
- i_m = magnetizing current.
- i_c = eddy current.
- i_e = excitation current.
- θ = phase angle between i_1' and i_2 .

Ideally, the product of the secondary current (i_2) and the rated turns ratio of the CT produces the exact value of the primary current (i_1). However, practically this is not the case because a certain amount of current (i_e) is drawn by the magnetising circuit which affects the accuracy of the CT. This is illustrated in Figure 2 above. The other factors that affect the accuracy of the CT include burden, temperature, physical configuration, saturation class, rating factor, and so forth [9].

Equations 2 and 3 below show the CT transfer function, assuming i_c equals zero, and induced/excitation voltage (E_s) respectively.

$$\frac{di_2}{dt} + \frac{R_2 + R_b}{L_2 + L_b + L_m} i_2 = \frac{L_m}{N(L_2 + L_b + L_m)} \frac{di_1}{dt} \quad (2)$$

$$E_s = 4.44 f N A B \quad (3)$$

Where:

N = number of turns in the secondary side of the CT.

f = frequency [Hz].

A = cross section area of the CT core [m^2].

B = magnetic field density [T].

Errors: The CT errors include ratio or current error and phase angle error. The ratio error is defined as the difference in magnitudes between the primary and secondary currents [10]. It is given by equation [11]:

$$\% \text{ ratio error} = \frac{\text{Actual ratio} - \text{rated ratio}}{\text{rated ratio}} \times 100 \% \quad (4)$$

The phase angle (pa) error is defined as the phase angle between the primary and secondary currents [10]. It is given by equations [11]:

$$pa \text{ error (deg.)} = 360^\circ f \Delta t \quad (5)$$

$$pa \text{ error (mins.)} = pa \text{ error (deg.)} * 60 \text{ mins.} \quad (6)$$

Where:

Δt = time difference between primary and secondary current waveforms (seconds).

Specifications: The current transformers, such as the one used for this investigation, are often used for the dual duty of measurement and protection [10]. The specifications of the tested protection CT are tabulated in Table 1 below.

Table 1: The specifications of the CT under test

Specifications	Values
Current Ratio	50/1
Rated Burden	2.5 VA
Nominal Frequency	60 Hz
Accuracy Class	1.0
Manufacturing Standard	IEC 60044-1
Basic Insulation Level (BIL)	0.66 kV

3. EXISTING SOLUTIONS

3.1 The current method

The current method is normally used to perform ratio tests but it can also be used to perform phase angle test. In this method, a known value of current is injected in the CT's primary circuit while measuring its corresponding secondary current [12]. The terminals of the secondary side are short circuited in this method.

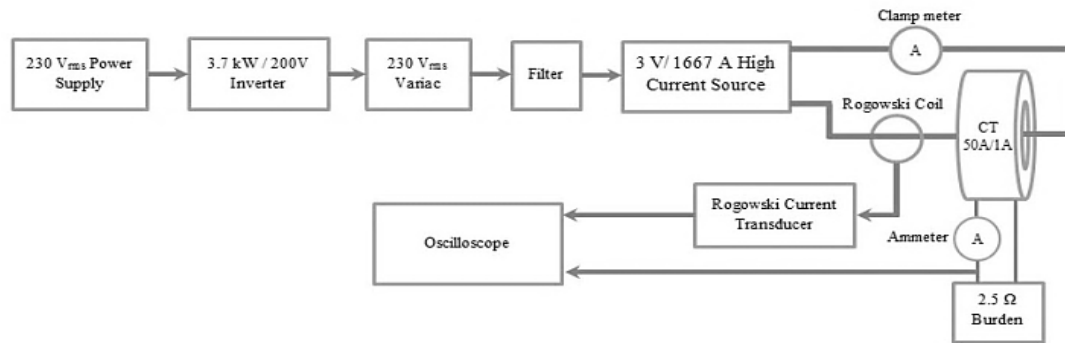


Figure 4: The test setup design.

3.2 The voltage method

The voltage method is normally used to perform phase angle test but it can also be used for ratio test. In this method, an oscilloscope is utilized to determine the time difference between the CT's primary and secondary voltage waveforms [12]. The ac voltage is supplied on the secondary circuit of the CT in this method.

4. DEVELOPED INVESTIGATION METHODS

4.1 Tests performed

Steady state test: The purpose of this test is to determine the actual steady state errors of the CT. These errors are then checked if they comply with the IEC 60044-1 standard. The other purpose is to determine the static characteristics of the CT.

Dynamic response test: In power systems, the frequency always oscillates around the rated frequency value. Hence, this test is conducted to observe how the CT performs under wide spectrum of frequencies due to system faults.

4.2 Test setup design

The test setup designed to perform both steady state and dynamic response tests is shown in Figure 4 above.

Single phase Inverter: This equipment is mainly used to vary the frequency of the CT primary current waveforms.

Variac: This equipment is used to control the magnitude of the CT primary current. It is advisable to connect a 10Ω potentiometer rated at 10 A between the variac and a filter if the variac used gives unstable readings.

Filter: This comprises of 150 μF capacitor bank. It is used to filter harmonics introduced by the inverter.

High current source: This equipment is used to generate the required currents for this investigation since the inverter can only inject a rated current of 18.5 A.

CT: This is the device under test.

Clamp meter: This device is used to measure the magnitude of the primary current of the CT.

Ammeter: This device is used to measure the magnitude of the secondary current of the CT.

Rogowski current transducer: This device is mainly used to obtain the primary current waveforms of the CT.

Oscilloscope: This device is used to measure the time difference between the primary and secondary current waveforms of the CT.

5. METHODOLOGY

Each test was performed five times to ensure reliable measurements.

5.1. Steady state test

For this test, the primary current is varied from 0 % to 200 % of the rated primary current of the CT in steps of five amperes, while the frequency is kept constant at either 50 Hz or 60 Hz. The choice of performing the test at 60 Hz is because it is the CT's nominal frequency from Table 1. Hence, the CT is expected to exhibit its best performance at this frequency. The frequency of 50 Hz is chosen because it is the rated value of the operational frequency of the power systems in South Africa [1, 13]. The magnitudes and time differences between the primary and secondary currents are measured for each step. These measured quantities are then used to determine the ratio and phase angle errors using (5) and (6) respectively.

5.2. Dynamic response test

For this test, the magnitude of the CT's primary current is kept constant at the rated value while its frequency is varied from 40 Hz to 60 Hz in steps of one Hertz. The magnitudes and time differences between the primary and secondary currents are also measured for each step. The measured quantities are again used to determine the ratio and phase angle errors using (5) and (6) respectively.

5.3. Time difference measurement

Since the time differences between the primary and secondary currents are always very small, the samples for each current or frequency step are saved as Comma Separated Values (CSV) files. A computer is then used to work out the time differences. The time differences are checked at the corresponding zero crossings of the primary and secondary waveforms and also at the corresponding peaks. Taking an average time difference from many samples leads to more accurate results [14].

6. EXPERIMENTAL RESULTS

6.1. Steady state

The static characteristics of the tested CT are tabulated in Table 2 below.

Table 2: The static characteristics of the tested CT

Characteristic	Value
Linearity	12.5 A – 406 A
Sensitivity	0.02 A / A
Hysteresis	0.05 %

Figures 5 and 6 below show the graphs of the ratio and phase angle of the CT as the functions of the primary current respectively.

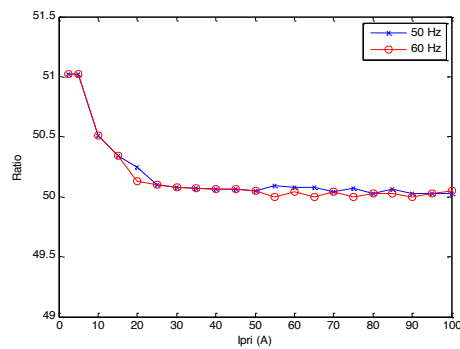


Figure 5: Ratio vs primary current graph of the CT.

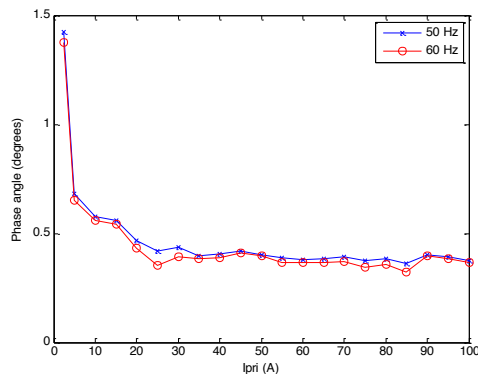


Figure 6: Phase angle vs primary current graph of the CT.

6.2. Dynamic response

Figures 7 and 8 below show the ratio and phase angle as the functions of frequency respectively.

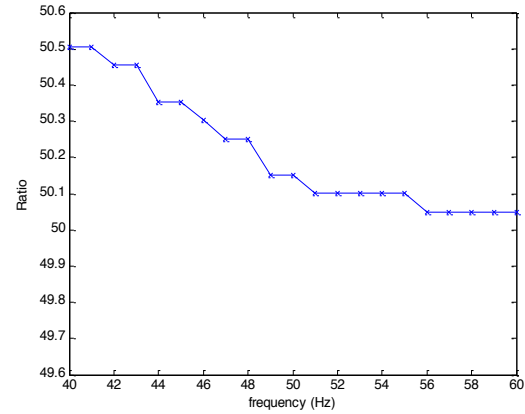


Figure 7: The ratio vs frequency graph of the CT.

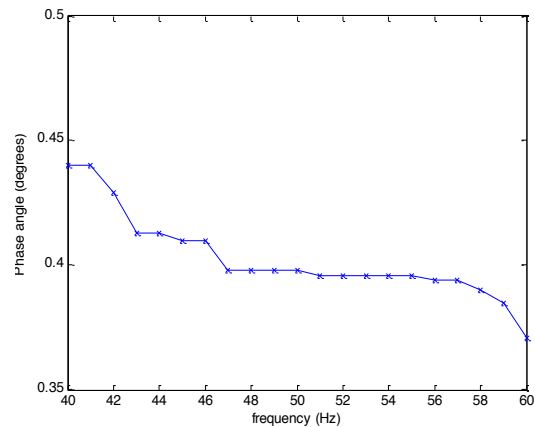


Figure 8: The phase angle vs frequency graph of the CT.

7. ANALYSIS AND DISCUSSION

7.1. Measurement errors

Table 3 below tabulates the list of measuring devices that were used and their typical errors [15-17].

Table 3: The measurement devices used

Measuring device	Part number	Error (%)
Clamp meter	Fluke336	± 2
Ammeter	Fluke76	± 1
Rogowski current transducer	CWT3	± 1

Based on these measurement errors, the measured CT's ratio and phase angle errors have tolerances of 2.236 % and 1 %, respectively.

7.2. Steady state

Tables 4 and 5 below tabulate the maximum permissible errors according to IEC 60044-1 standard and the measured values at certain primary current values of the CT [18].

Table 4: Ratio errors of the CT

$i_1 = 50 \text{ A}$	IEC 60044-1 ratio error (%)	Measured ratio error (%)
5 % i_1	± 3	2.04
20 % i_1	± 1.5	1.01
100 % i_1	± 1	0.10
120 % i_1	± 1	0.08

Table 5: Phase angle errors of the CT

$i_1 = 50 \text{ A}$	IEC 60044-1 phase angle error (minutes)	Measured phase angle error (minutes)
5 % i_1	± 180	82
20 % i_1	± 90	33
100 % i_1	± 60	24
120 % i_1	± 60	22

At nominal frequency and rated current ranging from 100% to 200%, the CT has maximum ratio and phase angle errors of 0.10% and 0.3974° respectively. At 50 Hz and same primary current range, it has maximum ratio and phase angle errors of 0.18% and 0.40° respectively. It can be observed from Figures 3 and 4 that at primary currents below 12.5 A, the CT operates in a nonlinear region. Hence the errors are bigger.

7.3. Dynamic response

At rated primary current and frequency ranging from 47Hz to 60Hz, the CT has the maximum ratio and phase angle errors of 0.50% and 0.3980° respectively. It can be observed from Figures 5 and 6 above that as frequency decreases the accuracy of the CT drops. From (3), it can be seen that the induced voltage in the CT's secondary circuit is directly proportional to the frequency. Therefore, as frequency drops, the induced voltage drops as well. This consequently causes the secondary current (i_2) to drop as well. The phase angle increases because the excitation current (i_e) increases such that the magnitude of primary current (i'_1) as referred to secondary side does not change. Also, the lines of flux generated by the primary current begin to appear as DC as the frequency decreases [19]. Hence, knee point of the CT drops and saturates quicker.

7.4. WAMS applications

The tested protection CT is found to have the TVE of 0.007 % at rated primary current for both 50Hz and

60Hz. It was discussed earlier in Section 2.1 that the instrument transformers should have accuracies between 0.2 % and 0.5 % for high accurate WAMS. Sections 7.2 and 7.3 have shown that the errors of the tested protection CT are within the required accuracy range. The errors are also far less than their maximum permissible values according to the IEC 60044-1 standard. Therefore the tested protection CT is declared suitable for WAMS applications due to these reasons.

8. RELIABILITY

Five experiments were conducted for each test and it was found that the test results were always consistent with each other. The CT and measurement devices give accurate results. The CT has very small errors as compared to its maximum permissible errors as per the IEC 60044-1 standard. Therefore based on the consistency and accuracy of the test results, the tested protection CT and the test setup are deemed reliable.

9. SAFETY AND PROTECTION

Since the test setup deals with very high currents, the personal protective equipment such as closed shoes with thick rubber need to be worn when conducting the experiments. The filtering capacitors need to be discharged after conducting the experiments. This is done by carefully shorting their terminals. The burden must always be connected firstly before injecting current in the primary side of the CT. This is because the CT can easily provide enough voltage and associated current that are dangerous to people's health if the secondary terminals are open circuited while primary current is flowing [20].

10. RECOMMENDATIONS FOR FUTURE WORK

It is recommended that at least three CTs of the same model should be tested to reach a fair conclusion as to whether or not that particular model of the CTs is suitable for WAMS applications. The CT analyzer can be used to obtain more accurate test results. As the protection CT ages it tends to lose its magnetic properties and hence its accuracy drops. Therefore the ageing of the CT must be determined to ensure accurate measurements at all times. An amplitude and frequency modulation tests may be conducted to monitor how the CT responds to the oscillating primary current waveforms.

11. CONCLUSION

This paper entailed the evaluation of the accuracy of a protection transformer used in WAMS. The background on both WAMS and the protection CT; existing CT test methods; tests performed as well as their test setup design; results and their analysis; recommendations for future work were discussed. The CT was found to meet the requirements for high accurate WAMS.

ACKNOWLEDGEMENTS

The authors would like to thank Eskom for the support of the High Voltage Engineering Research Group through the TESP programme. They would also like to thank CBI-electric for support, the department of Trade and Industry (DTI) for THRIP funding as well as to the National Research Foundation (NRF) for direct funding.

REFERENCES

- [1] M. Golshani, G.A. Taylor, I. Pisica and P. Ashton. *Investigation of Open Standards to Enable Interoperable Wide Area Monitoring for Transmission Systems*, Universities Power Engineering Conference (UPEC), 47th International, London, December 2012, pp. 1-6.
- [2] L. M. Putranto and N. Hoonchareon. *Wide Area Monitoring System Implementation in Securing Voltage Stability based on Phasor Measurement Unit Data*, Electrical Engineering/Electronics, Computer, Telecommunications and Information Technology (ECTI-CON), Krabi, 2013 10th International Conference, March 2013, pp 1-6.
- [3] K. Suresh. *Wide Area Monitoring Systems (WAMS) for Electricity Grids*. http://www.infrasure.com/quarterly/wide_area_monitoring_systems. Last Accessed October 2013
- [4] N. Pandit, K. Khandeparkar. *Design and Implementation of IEEE C37.118 based Phasor Data Concentrator & PMU Simulator for Wide Area Measurement System*. Indian Institute of Technology. <ftp://ftp.jaist.ac.jp/pub/sourceforge/i/ii/iitbpd/Tech%20Document.pdf>. Last Accessed July 2013.
- [5] R. Achary. *Operational features and optimisation of current transformers*. Transformers and Electricals Kerala Ltd. <http://www.telk.com/UserFiles/telk/ct.pdf>. Last Accessed November 2013.
- [6] *IEEE Std C37.118.1TM – 2011*, IEEE Standards for Synchrophasor Measurements for Power Systems, December 2011.
- [7] S. Jitlikhit. *Application of Phasor Measurement Units and Wide Area Monitoring System of EGAT's Network and Trend for Smart Grid*, Smart Grid and Diagnostic Presentation, December 2010.
- [8] ABB Group. *Wide Area Monitoring Systems Portfolio, applications and experiences*. <http://www.abb.com>. Last Accessed October 2013.
- [9] Kappa Electricals. *Protection Instrumentation Transformer*, <http://www.kappaelectricals.com/technical.html>, Last accessed 22 October 2013.
- [10] FECIME. *Current and Voltage Transformers*. <http://www.fecime.org>. Last Accessed October 2013.
- [11] ABB Group. *Instrument Transformers Application Guide*. <http://www.abb.com>. Last Accessed October 2013.
- [12] *IEEE Guide for Field Testing of Relaying Current Transformers*. ANSI/IEEE C57.13.1-1981 standard. <http://ieeexplore.ieee.org>. Last Accessed October 2013.
- [13] S. Jitlikhit. *Application of Phasor Measurement Units and Wide Area Monitoring System of EGAT's Network and Trend for Smart Grid*, Smart Grid and Diagnostic Presentation, December 2010.
- [14] B. Berry and A. Edwards; Personal Communication.
- [15] Pemuk. *Rogowski Current Waveform Transducer*, http://www.pemuk.com/Userfiles/CWT/cwt_1110.pdf, Last accessed 23 October 2013.
- [16] Fluke. <http://www.transcat.com/PDF/fluk336.pdf>, Last accessed 23 October 2013.
- [17] Fluke. <http://www.physics.purdue.edu/~jones105/phys536/labs/FLUKE76.pdf>, Last accessed 23 October 2013.
- [18] IEC 60044-1. *Instrument Transformers – Part 1: Current Transformer*, IEC Standard, February 2003.
- [19] G. Kalikiri. *Current transformer*. <http://gkreee.wordpress.com>. Last Accessed October 2013.
- [20] S. Laslo. *Current Transformers*. Bonneville Power Administration, Rev. 1.1, February 2012.

DEVELOPMENT OF ALTERNATIVE ELECTRICAL STRESS MONITORING TRANSDUCERS APPLICABLE TO MV/LV DISTRIBUTION TRANSFORMERS

F. A. Netshiongolwe¹, R. Cormack², J. M. van Coller¹

¹*Eskom Power Plant Engineering Institute (EPPEI)-High Voltage (HV), School of Electrical and Information Engineering, University of the Witwatersrand, Private Bag 3, Wits 2050, South Africa Email: netshifa@eskom.co.za, John.VanColler@wits.ac.za*

²*Eskom, PO Box 1091, Johannesburg, 2001, South Africa
Email: CormacR@eskom.co.za*

Abstract. This paper presents an alternative means of monitoring power frequency, harmonic frequency and surge currents and voltages and hence the associated electrical stresses on the medium voltage (MV) side of distribution transformers with a rating of 16 kVA up to 500 kVA. Limitations of conventional ferromagnetic core current transformers and voltage transformers are presented. The design of a wideband Rogowski coil current transducer with a three stage integrator is presented. The use of an electric field control screen, embedded in a 24 kV bushing, as a means of attaining capacitive voltage division is presented.

Keywords: bushing, capacitive voltage divider, electrical stress, measurement, Rogowski coils.

1. INTRODUCTION

Electrical stresses on the medium voltage (MV) side of distribution transformers rated 16 kVA up to 500 kVA remain unevaluated. Studies show that a run to failure maintenance strategy has been adopted as costs for monitoring of such transformers often outweighs purchase costs. Increased failures of pole-mount transformers in the Eskom Distribution network has resulted in annual replacement costs of over R71 894 000 [1]. Such costs coupled with the need to ensure quality of supply to consumers have resulted in the need to develop alternative cost effective monitoring techniques that will maximize transformer availability. The dawn of the Smart Grid concept in South Africa's distribution network will include improved restoration times, improved line monitoring and improved transformer monitoring [2]. Such goals can only be met with cost effective monitoring technology capable of relaying actual field information. This paper reviews monitoring techniques that can be employed on pole-mount transformers within the distribution networks. The use of capacitive voltage monitoring and Rogowski current coil monitoring in power systems is also reviewed. The design of a voltage and current monitoring bushing is described. The observed results are discussed and a conclusion is given.

2. BACKGROUND

2.1 Distribution transformer monitoring

Distribution transformers rated 16 kVA up to 500kVA are common in the South African network. Failures of such transformers are however also common. Traditional forms of condition monitoring, such as dissolved gas analysis (DGA), are not applied to such transformers due to cost considerations. The recent introduction of low voltage (LV) current and voltage monitoring (CVM) units has shown that

electrical stresses such as overloading, severe current unbalance and general overcurrent conditions are some of the causes of failures of such transformers [1]. The LV CVM units have been designed such that observable stresses produce alarms that are sent through to end users, affording them the opportunity to take corrective action. Alarms provided by LV CVM units have assisted end users in diagnosing some of the risks that may lead to premature transformer failure, which marked the evolution from reactive to proactive maintenance response.

The benefits that can be obtained by monitoring electrical stresses observed on the medium voltage (MV) side of such transformers have not been explored. Other electrical stresses that cause transformer failure such as harmonics and transients are presently not monitored. Limitations of observing stresses being monitored are often brought about by the lack of availability of cost effective MV electrical transducers. Figure 1 gives an overview of the proposed MV side monitoring system. This paper focusses on the construction of the electrical stress monitoring transducers that can be embedded in the MV transformer bushing with minimal intrusion to the transformer operation.

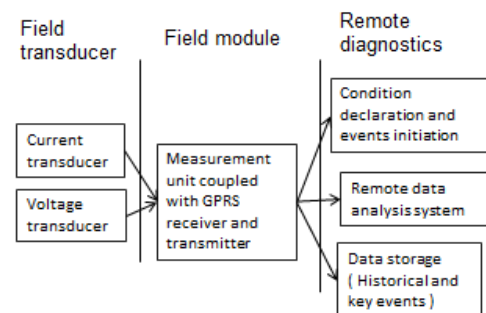


Figure 1: Proposed MV monitoring system

2.2 Current and voltage monitoring transducers.

Current and voltage monitoring has traditionally been performed using ferromagnetic current transformers (CTs) and ferromagnetic voltage transformers (VTs). Such CTs and VTs however have limited bandwidth, phase and magnitude errors, and exhibit nonlinearities such as saturation [3]. These limitations have resulted in the introduction of non-conventional current and voltage transducers. Non-conventional transducers such as the Rogowski coil and capacitive voltage transducers have successfully been used in monitoring current and voltage respectively. Figure 2 shows an example of a primary bar bushing with voltage and current sensing capabilities and various non-sensing bushings being considered for this study. Embedding current and voltage sensors into the non-sensing bushings in Figure 2 have the capability of providing end users with online operational data that can enhance the management of field assets.

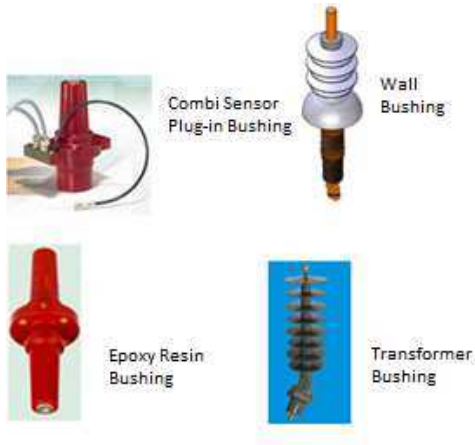


Figure 2: Combined current and voltage sensing and a variety of non-sensing bushings.

3. ROGOWSKI COIL CURRENT TRANSDUCER

Failures of pole-mount transformers due to harmonics, current surges and transients cannot be fully accounted for with existing current monitoring systems within South Africa's distribution network. CT's currently used for monitoring suffer from saturation effects and limited bandwidth. Rogowski current transducers depicted in Figure 3 have however been shown to have the following superior features [3, 4, 6]:

- High bandwidth (suitable for transients)
- Multiple primary current measurement ranges
- Non-intrusive to the primary circuit
- Modular in size

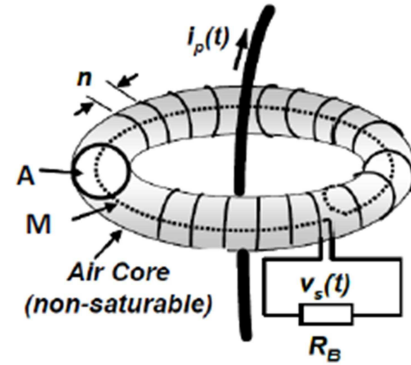


Figure 3 Rogowski coil current transducer [3]

3.1 Rogowski coil design

In this study, focus is on developing a Rogowski coil current transducer that can be embedded in a 24 kV transformer bushing and that has the capability of measuring power frequency currents, harmonic currents and transient currents. The output of the Rogowski current transducer is the induced coil voltage given by [3]:

$$V_c = -M \frac{di}{dt} = -\mu_0 n A \frac{di}{dt} \quad (1)$$

where:

- V_c = Coil output voltage, in V
- M = Mutual inductance, in H
- A = Coil cross sectional area, in m^2
- i = Primary current, in A
- n = Number of turns per meter
- t = Time, in s

Table 1 below shows the parameters of the Rogowski coil designed for this study. These parameters are determined based on the physical dimensions of the windings and lab measurements.

Table 1: Rogowski coil specification

Parameter	Parameter description	Value
d_w	Wire diameter	0.455 mm
R	Wire resistance	1.08 Ω
d_c	Coil diameter	7 mm
l	Coil length	286 mm
A	Coil area	38.48 mm^2
n	Number of turns per meter	1475/m
μ_0	Permeability of air	$4\pi \times 10^{-7}$ H/m
L	Inductance	29.2 μH
C	Coil capacitance	3.3 pF

3.2 Calculation of the primary current from the measured coil voltage

The induced coil voltage V_c is a function of the derivative of the primary current and thus it is necessary to integrate the induced voltage in order to determine the primary current. Based on Equation 1, the primary current is given by:

$$i = \frac{1}{M} \int V_c dt \quad (2)$$

The integration portion of Equation 2 can be achieved by implementing an electronic integrating circuit capable of wide bandwidth measurements. Passive integration on a correctly terminated Rogowski coil can be used for high frequency measurements; however op-amp integration is required for low frequency measurements [7, 8]. Figure 3 below shows a typical integration circuit suitable for this study. Petting [7], showed that by matching the time constants of the circuit in Figure 4, both low and high frequency integration could be achieved:

$$R_2 C_1 = R_3 C_2 \quad \frac{R_1}{R_2} \geq 1000 \quad \frac{L}{R_C} = R_4 C_2$$

In this case R_C represents the characteristic impedance of the cable joining the coil to the integration circuit. By choosing the integrating time constant of $R_1 C_1 = 10s$ with $R_C = 50 \Omega$, $R_1 = 1 M\Omega$, $\frac{R_1}{R_2} = 1000$ and $L = 29.2 \mu H$ (coil inductance) we get:

$$\begin{aligned} C_1 &= 10 \mu F & C_2 &= 1 \mu F \\ R_3 &= 805 k\Omega & R_4 &= 47 \Omega \end{aligned}$$

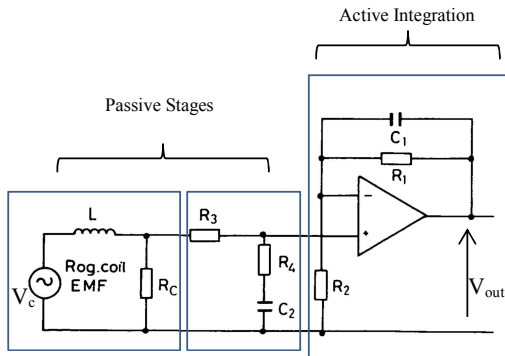


Figure 4: Three-stage integration Rogowski measuring circuit [7]

The circuit designed with the guidelines given above yields simulated results shown in Figure 6. The bandwidth based on the component value selection is of the order of 100 kHz. Other integrators that have higher bandwidth have been developed by Ray [8] and these will also be investigated in this study. Laboratory work still needs to be done to see if the results attained below can be replicated. The integrated voltage is ideally supposed to be in phase

with the primary current whilst this voltage is out of phase with the coil output voltage.

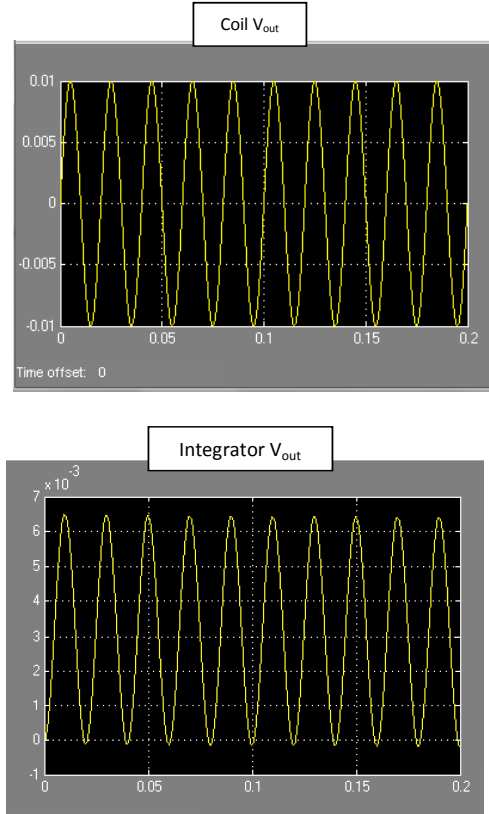


Figure 5: Simulated coil output voltage compared to integrated signal compared

4. CAPACITIVE VOLTAGE TRANSDUCER

High voltage measurements have traditionally been performed using capacitive voltage transformers. Recent developments have resulted in the use of capacitive voltage dividers in medium voltage switchgear and overhead lines [4, 5]. Solid insulation bushings used on transformers can either be ceramic, cycloaliphatic epoxy resin or silicone enclosed epoxy resin bushings for outdoor application. Silicone coated epoxy resin bushings will be considered for this study. Epoxy resin bushings often contain an embedded screen used for electric field control in the area where the bushing passes the earthed transformer tank. The presence of such a screen sets up capacitance between the conductor and the screen. The magnitude of such a capacitance is a function of the dimension of the screen relative to the MV conductor and the dielectric properties of the insulation that separates them.

A 24 kV screened bushing was considered for this research. Figure 6 and Table 3 below show a cutout view and the dimensions of the bushing to be used. The presence of the screen sets up a potential divider

shown in Figure 7 and this relates the conductor voltage V_{in} to the screen voltage V_{out} :

$$V_{out} = \frac{C_1}{C_1 + C_2} V_{in} \quad (3)$$

where:

C_1 = Capacitance between the conductor and the screen, in F

C_2 = Capacitance between the screen and the transformer tank as well as any external output (load) capacitance, in F

V_{in} = Conductor (input) voltage, in V

V_{out} = Screen (output) voltage, in V

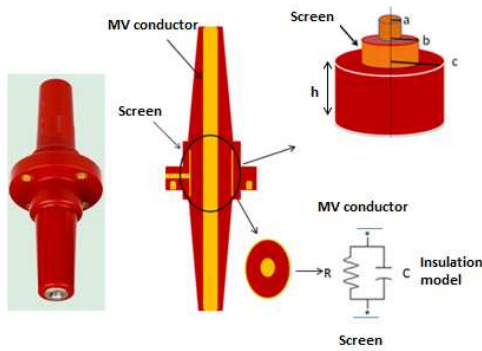


Figure 6: Cross-sectional view of a screened 24 kV epoxy resin bushing with emphasis on the position of the screen relative to the MV conductor.

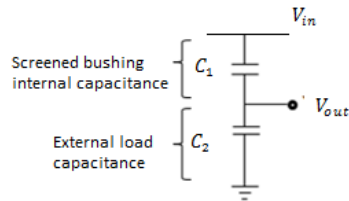


Figure 7: Embedded screen capacitive voltage transducer with the conductor-screen capacitance represented by C_1 and the screen-transformer tank capacitance as well as external load capacitance represented by C_2 .

Table 1: 24 kV bushing parameters

Parameter	Parameter description	Value
ϵ_0	Free space permittivity	8.854E-12 F/m
ϵ'_r	Relative permeability(Re)	3.8
ϵ''_r	Relative permeability (Im)	0.038
tan delta	Epoxy resin tan delta	0.01
a	Conductor radius	0.012 m
b	Screen radius	0.03 m
h	Screen height	0.06 m

The insulation capacitance between the conductor and the screen is given by [10]:

$$C = \frac{2\pi\epsilon_0\epsilon'_r h}{\ln \frac{b}{a}} \text{ [F/m]} \quad (1)$$

The corresponding resistance at angular frequency w is given by:

$$R = \frac{h \ln \frac{b}{a}}{w 2\pi\epsilon_0\epsilon_r} \text{ [\Omega/m]} \quad (2)$$

Table 3 tabulates the calculated resistance at a frequency of 50 Hz and also compares the calculated capacitance with the simulated capacitance which was obtained by varying the simulated supply voltage. The simulated capacitance in Table 2 was obtained using Finite Element Method Magnetics (FEMM) software and shows an acceptable error of 1.47 % when compared to the calculated value. Figure 7 shows the corresponding voltage equipotential plot with a simulated input of 24 kV. At power frequency, the resistance of the insulation is observed to be very high (G Ω) such that the electrical circuit can be represented by capacitance only. Figure 7 shows how the screen provides both line voltage sensing capabilities and electric field stress control at the interface between the live conductor and the earthed transformer tank.

Table 3: 24 kV bushing parameters

Methodology	Capacitance [pF]	Resistance[Ω], 50Hz
Calculated	13.6 pF	12.8 G Ω
FEMM simulation	13.8 pF	
Error	1.47%	

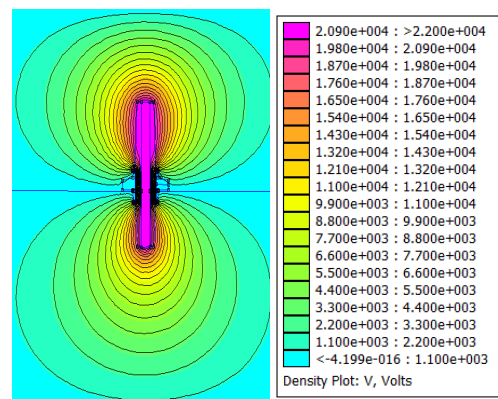


Figure 7: FEMM simulated plot of voltage equipotentials for the screened epoxy resin bushing at a supply voltage of 24 kV (phase to earth).

5. VOLTAGE MEASUREMENT RESULTS

The linearity of the 24 kV bushing capacitive voltage transducer was investigated at the power frequency

of 50 Hz with the supply voltage being varied from 1 kV up to 24 kV. Figure 8 shows the corresponding voltage measurement when an external load capacitance of 57.31 nF was used. One sample of readings with phase to earth voltage ranging from 1kV up to 24 kV was taken and the overall insulation capacitance observed with a fixed load capacitance of 57.13 nF was evaluated. The capacitances observed are shown in Figure 8, and these were then used to reconstruct other phase to earth voltages using measured results and Equation 3.

It should however be noted that the capacitance observed during voltage measurement is three times larger than the simulated and calculated values in Table 3. This variability still needs to be explored. The overall error of the phase to earth voltage reconstruction using the capacitance values obtained in Figure 8 is shown in Figure 9. Voltage measurements at 1 kV have been observed to have the largest error with the maximum error observed being 12.6%. All other voltage measurements were found to be within the 5 % error band. Phase to earth voltages above 13 kV were all reconstructed with the percentage error band being lower than 2%.

A second order polynomial equation was found to be best for relating the input supply voltage to the measured output voltage using the sample data used for the capacitance modeling above. Figure 9 below shows the error obtained whilst the polynomial equation is used to calculate the phase to earth voltage. The maximum error observed whilst calculating the output voltage from the measured voltage was 8.2 %. At phase to earth voltages of 2 kV upwards errors below 5 % were observed. Further analysis also showed that measurements from 12 kV upwards were observed to have a maximum 2% error.

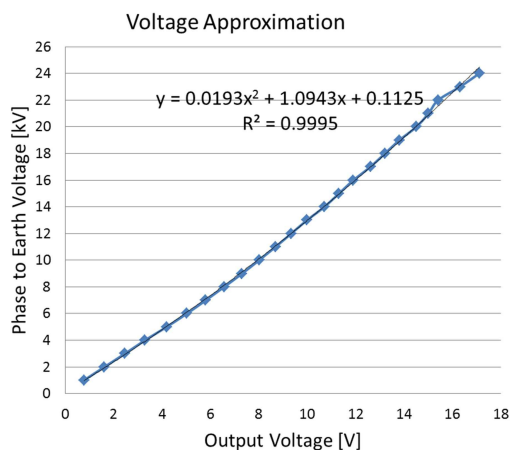


Figure 8: Measured capacitive voltage transducer output at a power frequency of 50 Hz and external load capacitance of 57.13 nF.

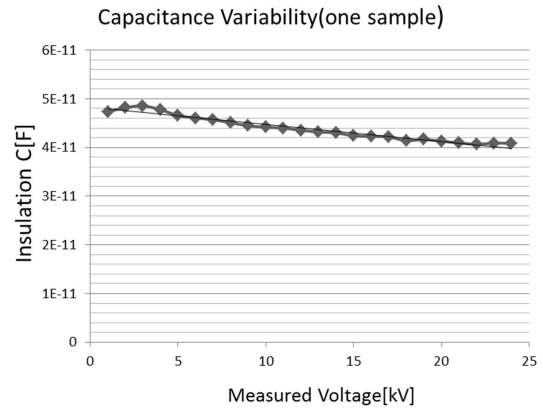


Figure 9: Capacitance variability of one measurement sample with external load capacitance of 57.13 nF.

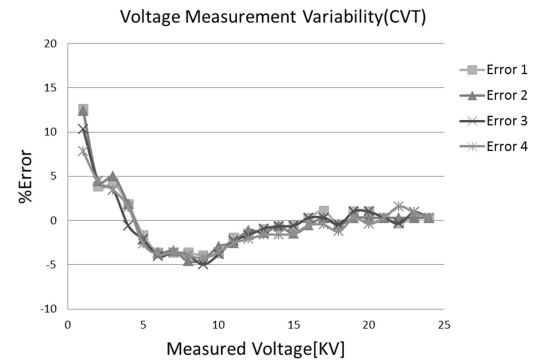


Figure 9: Phase to earth voltage measurement error at power frequency achieved with capacitive voltage division.

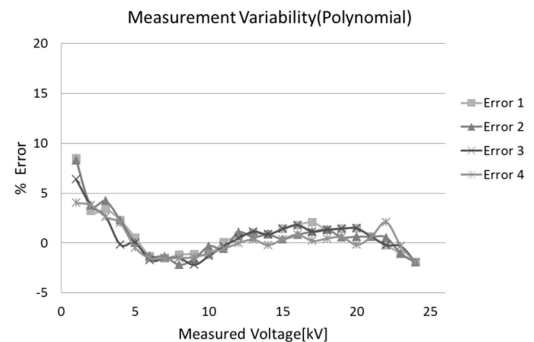


Figure 10: Phase to earth measurement error at power frequency achieved with polynomial curve fitting.

The largest error margin with both polynomial curve fitting and the capacitive voltage division method was seen to be at lower voltage measurements. Other results from 2 kV upwards agree with results observed from an earlier design of the KEVCY_R ABB combi unit sensor which had an error margin of 6% [10]. Further improvement on the error margins are possible, a more recent KEVCY_R ABB combi

sensor unit for indoor application has been optimized to meet error limits of 0.5 % at $\pm 20\%$ rated voltage and a 3% error margin over the full range of measurements.

6. CONCLUSION

The need for better management of distribution transformers has resulted in the need for developing voltage and current sensing transducers that can be embedded in transformer bushings. Both Rogowski coils and screened bushings provide plausible solutions with regard to dimension and overall sensing capabilities. The overall voltage sensitivity of the screened bushing was observed to have an error margin of 5 % for voltages above 1 kV. A polynomial equation approximation of the phase to earth voltage yielded better performance as compared to capacitive voltage division at 1 kV. More work still needs to be done to evaluate the bandwidth limitation of both the designed Rogowski coil transducer and the capacitive voltage transducer. Further work is also required in developing models that result in better accuracy within the rated operational voltage of the bushing (so that error compensation could be performed).

REFERENCES

- [1] R. Kleinhans. "Current and Voltage Monitors Combat Theft and Improve Supply Quality". *Energize Transmission and Distribution*, pp. 41-45, September 2011.
- [2] A. Khatri. "Evolution of Future Electrical Networks in Eskom". *AMEU 62nd Convention*, pp. 113-118. September 2010.
- [3] IEEE Standard C37.235-2007, IEEE Guide for the Application of Rogowski Coils Used for Protective Relaying Purposes.
- [4] R. Javora, M. Stefanka, P. Mahonen, T. Niemi, O. Rintamaki, "Protection in MV Networks using Electronic Instrument Transformers", *CIREN 20th International Conference on Electricity Distribution*, Prague, 8-11, June 2009.
- [5] R. Behzadi, M. Oskuoee, D. Mohammadi. "Integrated Electronic Metering Insulator for Medium Voltage Overhead Lines". *CIREN 19th International Conference of Electricity Distribution*, pp. 1-4, May 2007.
- [6] W.F. Ray and C.R. Hewson. "High Performance Rogowski Current Transducers". *Industry Applications Conference*, Vol.5, pp 3083 – 3090, 2000.
- [7] S.J. Petting and J. Siersema. "A Polyphase 500 kA current measurement system with Rogowski coils" *IEE Proc B*. Vol 130, No 5, pp 360-363. Sept 1983.
- [8] W.F. Ray and R.M. Davis: "High frequency improvements in wide bandwidth Rogowski transducers", *EPE 99 Conference Proc.*, Lauzanne. Sept 1999.
- [9] E. Kuffel, W.S. Zaengle, J. Kuffel. *High Voltage Engineering- Fundamentals*, Butterworth-Heinemann, second edition, chapter 4, pages 201-241, 2000.
- [10] ABB Group, Power Indoor Combi Sensor KEVCY_R, Last Accessed 13 Nov 2013. <http://www05.abb.com/>

Topic H

Power Electronics

COUPLING OF GATE DRIVER EMI IN A BOOST CONVERTER

G.N. Wooding*, A.S. de Beer** and J.D. van Wyk***

* Group on Electronic Energy Processing, Dept. of Electrical and Electronic Engineering, Corner of University Road and Kingsway Avenue, University of Johannesburg, Auckland Park 2006, South Africa E-mail: gnwooding@gmail.com

** Group on Electronic Energy Processing, Dept. of Electrical and Electronic Engineering, Corner of University Road and Kingsway Avenue, University of Johannesburg, Auckland Park 2006, South Africa E-mail: asdebeer@uj.ac.za

*** Group on Electronic Energy Processing, Dept. of Electrical and Electronic Engineering, Corner of University Road and Kingsway Avenue, University of Johannesburg, Auckland Park 2006, South Africa E-mail: daanvw@uj.ac.za

Abstract: One of the by-products in Switch Mode Power Supply (SMPS) operation is electrical noise. This can cause interference with other systems and is regulated by standards. It is therefore necessary to understand generation of Electromagnetic Interference (EMI) in SMPS's so that power supply designs can be made to comply with standards. In this paper the influence of the gate driver circuit in generating EMI in a boost converter is investigated. It is shown that a surprisingly large amount of total converter EMI is generated by the gate drive circuitry.

Keywords: Electromagnetic Interference, EMI, Gate Driver, Boost Converter

1 INTRODUCTION

With the ever increasing need for smaller power supplies with higher efficiencies, switched mode power supplies (SMPS) are becoming ever more prevalent. One of the problems with SMPS's is that they are one of the major generators of conducted electromagnetic interference (EMI) [1, 2].

Conducted EMI can be seen as the noise measured on the cables powering a device [3]. As mentioned in [3] conducted EMI can cause other susceptible devices connected to the same power source (ie mains network) to malfunction, therefore there are limits dictating how much EMI a specific device can generate. This makes understanding how different parts of a power supply generate EMI important.

The goal of this paper is to investigate how the gate driver signal contributes to the EMI. It is shown that a surprisingly large amount of total converter EMI is generated by the gate drive circuitry.

2 CONDUCTED EMI

2.1 Different Modes of Conduction

Conducted EMI can be split into two separate modes; the first is differential mode (DM) and the second common mode (CM).

As can be seen from Figure 1 the DM EMI current is defined as the EMI that flows in opposite directions down the two wires powering a device. While CM EMI current travels down these two wires in the same direction. It should also be noted in the CM case that the return path is created through capacitive coupling with the surroundings.

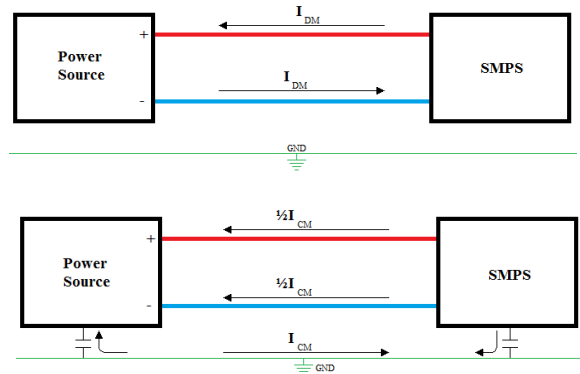


Figure 1: DM & CM Conduction Paths

2.2 Conducted EMI Measurement

Conducted EMI measurements are normally performed with the aid of a Line Impedance Stabilisation Network (LISN).

The setup presented in Figure 2 allows the total EMI on one of the wires to be measured. Presented in [4, 5] are a number of different techniques to separate CM and DM EMI during measurement. Although total EMI is generally used when trying to pass EMI standards, splitting the EMI into DM and CM allows greater insight into what is happening and where the EMI may be originating from. For this paper a power combiner was used.

A power combiner works by first combining the two signals obtained from the LISN, since the DM EMI travels in opposite directions down the two wires the DM EMI cancels itself out and the CM is measured. This is achieved using a 0° power combiner.

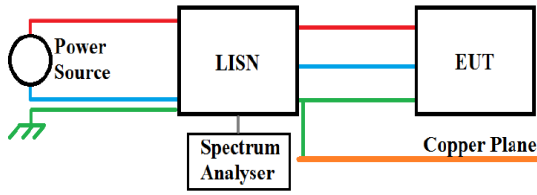


Figure 2: EMI Measurement Setup

Similarly DM is measured by using a 180° power combiner which causes the CM to be canceled out.

3 EXPERIMENTAL SETUP

3.1 Converter Specifications

- Power: 100W
- Input Voltage: 30V
- Output Voltage: 60V
- Operating Frequency: 100kHz

3.2 Gate Driver Circuit

In order to investigate the effects of the gate drive signal coupling through the parasitic capacitances inherent in the MOSFET, the driver circuit was powered from a 12V battery. Figure 3 indicates how the MOSFET driver circuit was setup.

The microcontroller used is a Microchip 18f1330 with a four times phase lock loop applied to the internal oscillator running at 8MHz. This allowed the microcontroller to perform operations at 32MHz.

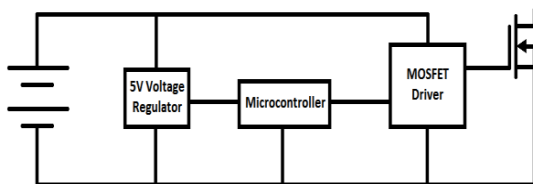


Figure 3: MOSFET Driver Circuit

3.3 Configuration 1- Driver only, Bus Connected

The first configuration can be seen in Figure 4. In this configuration only the driver is powered and the DC bus is connected but the main power supply is off. The 4.7μF capacitor on the DC bus output of the LISN was needed or the converter failed to operate correctly, it was there in all configurations. Reasons for this are explored in [6, 7]

This configuration allows us to observe the effects of applying a 100 kHz PWM signal to the gate of the MOSFET.

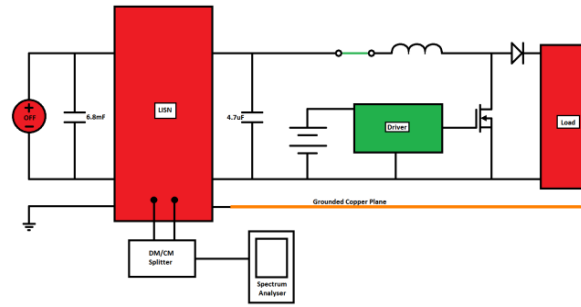


Figure 4: Configuration 1 - Driver only, Bus Connected

3.4 Configuration 2 Driver only, Bus Disconnected

The second configuration as shown in Figure 5 is similar to the first in that only the driver is powered. In this case however the DC bus is disconnected. Theoretically this should almost entirely eliminate the measured DM EMI since there is no clear path to the LISN for a DM current to flow.

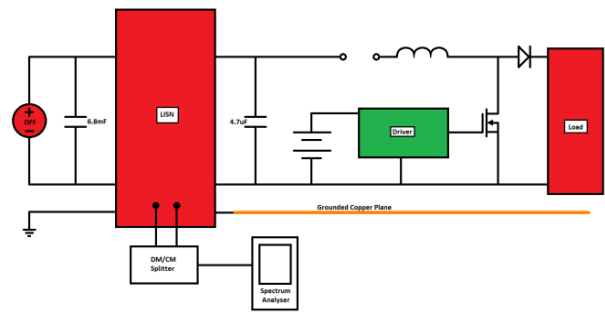


Figure 5: Configuration 2 - Driver only, Bus Disconnected

3.5 Configuration 3- Full Operation

The third configuration depicted in Figure 6 represents the scenario where the converter is operating under full load conditions with the DC bus power supply on. In this scenario the driver circuit is still powered by the battery therefore comparing these results with those obtained in configuration 1 can give an indication of what percentage of the full load EMI is caused by the driver.

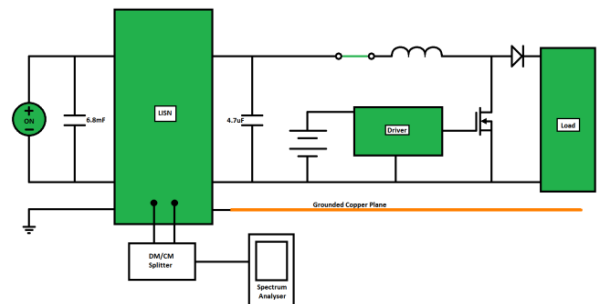


Figure 6: Configuration 3 - Full Operation

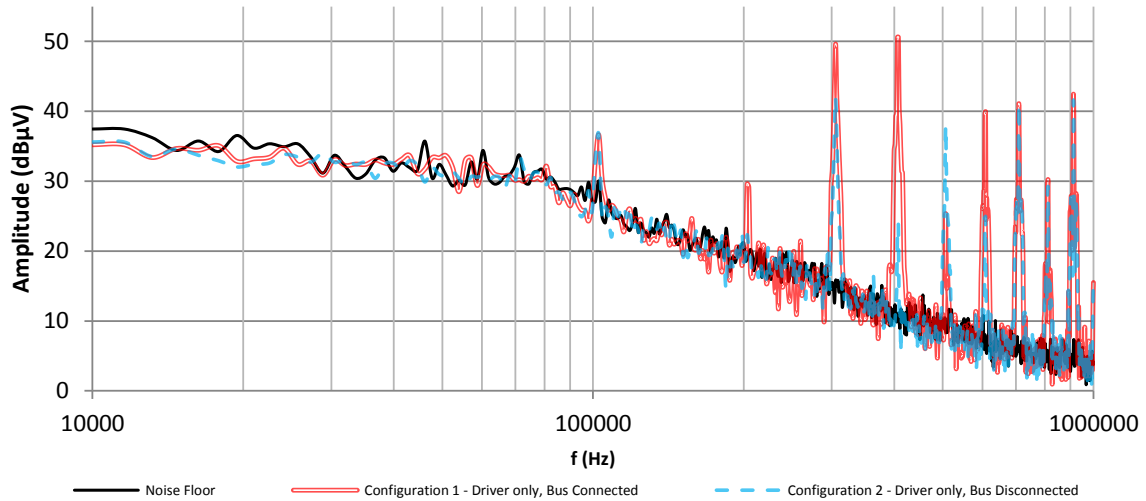


Figure 7: Comparison of DM EMI for Driver Only Configurations

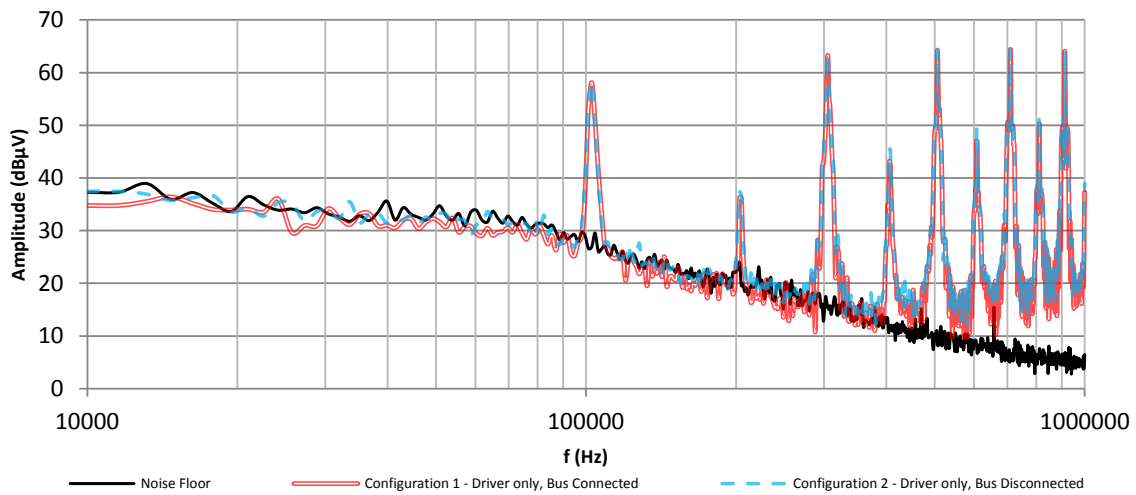


Figure 8: Comparison of CM EMI for Driver Only Configurations

4 RESULTS

4.1 No-load – Driver only

Figure 7 provides a comparison of the DM EMI generated for configurations 1 and 2. (Figures 4 & 5) It was expected that there would be almost no DM EMI present when configuration 2 was used (due to the lack of a clear DM path).

What actually was observed is drastically different. Firstly at the fundamental frequency (100 kHz) there is no difference between the two configurations. There is also no difference in the 7th to 10th harmonics.

Disconnecting the bus reduces the 2nd, 3rd, 4th and 6th harmonics with the greatest drop being observed at the 4th harmonic with a drop of more than 25dB.

What is very interesting however is that the 5th harmonic actually increases in magnitude by about 10dB when the bus is disconnected.

Therefore one has to assume that there is differential mode coupling even though the bus has been disconnected.

As can be seen from Figure 8 there is practically no difference in the measured CM EMI spectrum when the bus is disconnected from when it is connected.

4.2 Full-load

From Figure 9 it can be seen that there is quite a large increase in the DM EMI generated under full operating conditions which is expected since there are now large AC currents drawn through the inductor from the LISN.

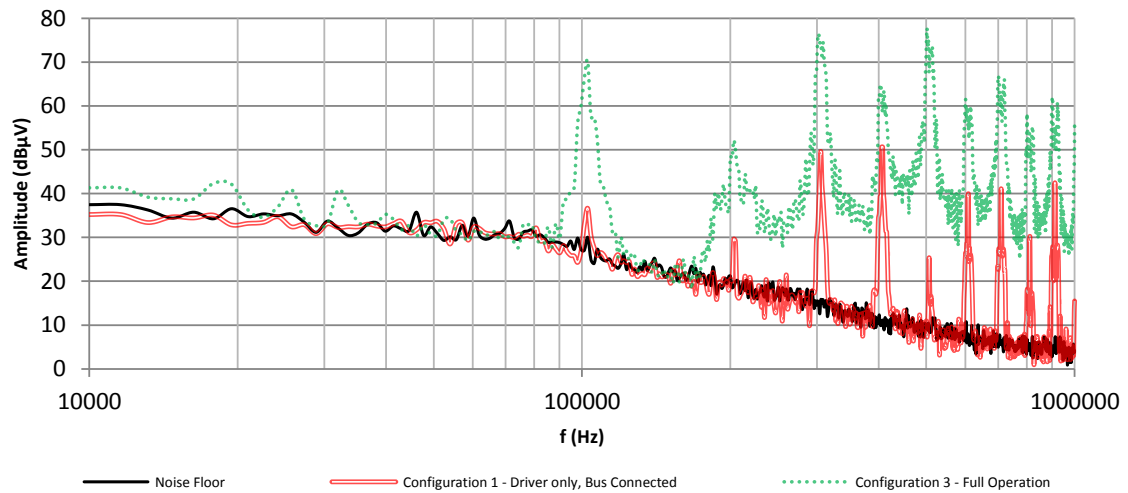


Figure 9: Comparison of DM EMI for Driver Only and Full Operation Configurations

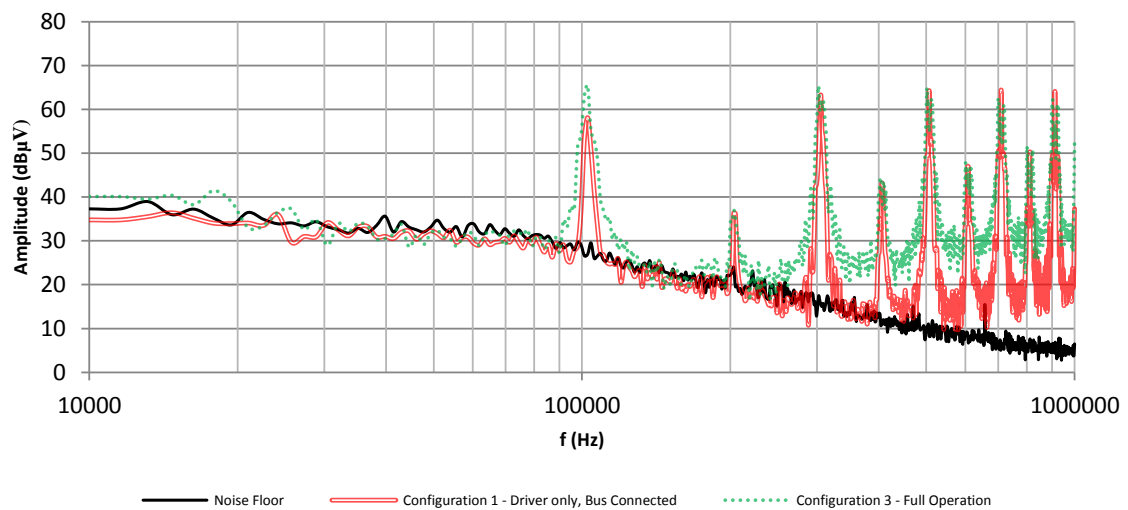


Figure 10: Comparison of CM EMI for Driver Only and Full Operation Configurations

In Figure 10 there is not much of a change in the CM at the harmonics.

This result is very significant since it implies that the gate drive circuitry is the major contributor to the CM EMI generated by this setup.

5 CONCLUSION

Powering the driver from a separate battery both DM and CM EMI were observed when only the driver was operated. This leads us to believe that the gate drive signal is coupling in both DM and CM.

Even when the main DC bus is disconnected DM and CM EMI is still observed with the CM EMI remaining unchanged. The fact that DM EMI is still measured means that the DM EMI current is flowing through unconventional paths which are not immediately apparent.

The lack of a change in CM EMI under these circumstances implies that disconnecting the DC bus has no effect on the CM coupling path either.

As expected, operating the converter under full load causes a significant increase in the DM EMI. What was not expected however is that there is not much change in the CM EMI spectrum. This implies that the gate drive circuitry is responsible for majority of the CM EMI in this setup.

Therefore the gate drive circuit contributes to the EMI more than was initially expected.

6 REFERENCES

- [1] R. Redl, P. Tenti and J.D. van Wyk, "Power electronics' polluting effects," *IEEE Spectrum*, vol. 34, no. 5, pp. 33-39, 1997.
- [2] R. Redl, "Electromagnetic environmental impact of power electronics equipment," *Proceedings of the IEEE*, vol. 89, no. 6, pp. 926 - 938, 2001.
- [3] T. Williams, *EMC for Product Designers*, 4th ed., Newnes, 2007, pp. 1-22, 131-140.
- [4] J. Stahl, D. Kuebrich, A. Bucher and T. Duerbaum, "Characterization of a modified LISN for effective separated measurements of common mode and differential mode EMI noise," in *IEEE Energy Conversion Congress and Exposition (ECCE)*, 2010.
- [5] G. Ting, D.Y. Chen and F.C. Lee, "Separation of the common-mode- and differential-mode-conducted EMI noise," *IEEE Transactions on Power Electronics*, vol. 11, no. 3, pp. 480 - 488, 1996.
- [6] A.S. de Beer, G.N. Wooding and J.D. van Wyk, "Problematic aspects when using a LISN for converter EMI characterisation," in *IEEE International Conference on Industrial Technology (ICIT)*, 2013.
- [7] J.C. Crebier, J. Roudet and J.L. Schanen, "Problems using LISN in EMI characterization," in *30th Annual IEEE Power Electronics Specialists Conference (PESC 99)*, 1999.

PERFORMANCE OF PASSIVE AC/DC FILTERS AND DC SMOOTHING REACTORS IN UHVDC POWER SYSTEMS

F M KASANGALA*, G ATKINSON-HOPE**

*Cape Peninsula University of Technology, Department of electrical Engineering, Centre for Power Systems Research, Keizersgracht and Tennant Street, Zonnebloem, PO Box 652, Cape Town 8000, South Africa.

** Cape Peninsula University of Technology, Department of electrical Engineering, Centre for Power Systems Research, Keizersgracht and Tennant Street, Zonnebloem, PO Box 652, Cape Town 8000, South Africa.

Abstract. The propagation of generated harmonics by power thyristor converters in HVDC transmission systems causes detrimental effects. Appropriate AC/DC filters and dc smoothing reactors application is essential in order to achieve desired performance criteria. In this paper, appropriate passive AC/DC filter types and configurations have been carefully selected and designed to mitigate DC harmonic voltages and AC distortion levels of a 4000 MW, 1500 km, ± 800 kV bipolar UHVDC power system, and meet specified AC filter performance requirements based on the IEEE Standard 519-1992 distortion limits. Two types of configurations of DC smoothing reactors have also been investigated. Results show that the utilised passive AC/DC filters effectively reduced the DC harmonic voltages below 0.1 kV and the exceeded distortion levels below the specified standard limits. The DC smoothing reactors adequately reduced the ripples in the DC voltage and current signals. The two series group per pole DC smoothing reactor configuration shows preferable effect on harmonic mitigation than the distributed one.

Key Words. DC smoothing reactors, Harmonic mitigation, passive AC/DC filters, UHVDC Power Systems.

1. INTRODUCTION

In high voltage direct-current (HVDC) transmission systems power thyristor converters acts as constant current harmonic sources on the AC side and as constant voltage harmonic sources on the DC side of the network [1]. The generation of harmonics by these power thyristor converters and their propagation throughout the network subject the network to detrimental effects such as voltage distortion, extra losses and overheating, and also influences telephone interferences with external services [1]. In practice, to prevent such undesirable occurrences adherence to a specified acceptable level of harmonic distortions at the converter terminals is required, and this is usually expressed in terms of harmonic voltages.

Because of high power and voltage levels associated with ultra-high voltage direct-current (UHVDC) transmission application the vitality of reducing the current harmonics generated on the AC side and the voltage harmonics produced on the DC side of the power thyristor converter has been achieved by means of a 12 pulse converter operation. This results in harmonic cancellations provided that a suitable 12-pulse converter arrangement is yielded; that is having in each pole two 6-pulse converters connected through two transformers of different configurations, star-star and star-delta windings [2]. However, this cancellation of harmonics is inadequate to meet requirements of approved standards. Therefore the consideration of the sole well known solution is essential, to make use of AC harmonic filters for limiting AC harmonic currents, while they provide reactive power compensation required by the power thyristor converters, and on the DC side to make use of DC smoothing reactors to smoothen out the DC current. DC harmonic filters are also required to reduce harmonic voltages on the DC circuit, particularly when the circuit includes overhead lines [2]. For effective performance of AC/DC filters and DC smoothing reactors, their selection and design are of utmost importance and must be of high interest.

In this paper, the performance impacts of AC/DC passive filters and DC smoothing reactors upon the DC harmonic voltages, AC harmonic voltage distortion levels and DC responses are assessed. Appropriate AC/DC filter types and configurations are carefully selected and designed for UHVDC applications to mitigate the DC harmonic voltages and the AC harmonic voltage distortion levels below specified standard limits. The size and configuration of DC smoothing reactors are selected to ensure sufficient

reduction of ripples in the DC waveforms. Their performance impacts upon the DC harmonic voltages and AC harmonic voltage distortion levels are assessed.

2. LITERATURE REVIEW

2.1 Harmonic Mitigation and Filter Selection

Harmonic mitigation is commonly achieved by the use of passive filters, which provide a shunt path of low impedance to harmonic frequencies [3]. In HVDC systems passive double-tuned filters are extensively used as AC/DC filters as opposed to single-tuned filters to mitigate the large percentage of harmonic distortions at lower harmonics of the 12-pulse characteristics [3,4]. Technically, the main reason for this is due to their advantage of subjecting only one reactor to full line impulse voltages [5]. There are two types of double-tuned filters, the conventional type as shown in figure 1 and the damped type [5]. The damped type includes damping resistance components which can be added in different ways depending on the desired filter performance thus resulting in various configurations [6]. As shown in figure 1 one resistor can be inserted either between point AB, AD, BD or CA, while two resistors can be added either between points BD and AB or AD and AB respectively. These resistors are added to avoid severe network resonance which results in severe overvoltage harmonics on the filters and other power system components when the power system reactance and filter impedance are conjugate [5]. This is achieved by limiting the high impedance at parallel resonance frequency to the selected resistance value thus avoiding rigorous amplification of harmonic voltage during resonance conditions [5]. On the DC side the inclusion of this damped resistor is mostly a prerequisite when the maximum permissible limit of the psophometric weighed disturbing current along the DC transmission pole and electrode lines is taken into account, for this is influenced by the resonance that occurs between the DC filter and the DC smoothing reactor at the 16th or 18th harmonic [6,7].

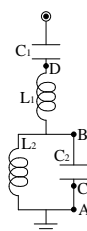


Fig. 1: Conventional double tuned filter

The need to eliminate the occurred resonances with the AC network at low order frequencies requires that a 3rd harmonic filter is designed. Though a triple-tuned filter is possible, an alternative solution to fulfill a specified harmonic performance requirement is to incorporate, in combination with a double-tuned filter, a single-tuned 3rd harmonic filter [3,7,8]. To avoid excessive losses in the series tuned filter at the fundamental frequency, a C-Type high pass damped filter shown in figure 2 (a) below is considered for reducing the effect of the resonance conditions at the lower 3rd order harmonic. This is due to the fact that C_4 and L_2 are series tuned and are chosen such that they resonate at the fundamental frequency [3]. For dissipation at fundamental frequency a damping resistor R_3 is incorporated in the series tuned circuit of the C-Type high pass damped filter as shown in figure 2 (b) below.

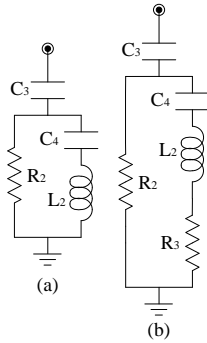


Fig. 2: C-Type high pass damped filters

2.2 AC Filter Performance Requirements

An HVDC system with 12-pulse converters, for harmonic cancellation, generates characteristic harmonic currents on the AC side of the order $12k \pm 1$, where k is a positive integer, while on the DC side the characteristic harmonic voltages generated are of the order $12k$ [2]. This results in the absence of the high magnitude lower harmonic orders of the 5th and 7th on the AC side and the 6th on the DC side. To measure the distortion levels of the resulting harmonic voltages on the AC side the following harmonic indices (equations (1) and (2)) are used.

$$HD_V = \frac{V_h}{V_1} \times 100 \quad (1)$$

$$THD_V = \frac{\sqrt{\sum_{h=2}^{50} V_h^2}}{V_1} \times 100 \quad (2)$$

There are various standards available upon which AC filter performance requirements can be based. The most commonly used is the IEEE Standards 519-1992. For a bus voltage of equal to or greater than 169 kV the individual harmonic voltage distortion (HD_V) level should not exceed 1%, while the total harmonic voltage distortion (THD_V) level must be limited to 1.5%.

2.3 Conventional Double-Tuned Filter Design

The conventional double-tuned filter of figure 1 above consists of a series resonance circuit and a parallel resonance circuit whose respective impedances are

$$Z_S(\omega) = j(L_1\omega - \frac{1}{C_1\omega}) \quad (3)$$

$$Z_P(\omega) = (\frac{1}{jL_2\omega} - jC_2\omega)^{-1} \quad (4)$$

ω is the angular frequency in radians. Therefore their resonance frequencies where their impedances are zero will be equal to

$$\omega_S = \frac{1}{\sqrt{L_1 C_1}} \quad (5)$$

$$\omega_P = \frac{1}{\sqrt{L_2 C_2}} \quad (6)$$

$$\omega^4 L_1 L_2 C_1 C_2 - \omega^2 (L_2 C_1 + L_1 C_2) + 1 = 0 \quad (7)$$

With the thevenin impedance of the conventional double tuned filter being the summation of the series resonance circuit impedance and the parallel resonance circuit impedance, and having this impedance equal to zero at the tuned frequencies ω_1 and ω_2 for respective circuits, using Vida's theory on the resulting simplified expression of equation (7) above the relationship between the resonance and the tuned frequencies can be expressed as follows

$$\omega_1 \omega_2 = \frac{1}{\sqrt{L_1 C_1}} \cdot \frac{1}{\sqrt{L_2 C_2}} = \omega_S \omega_P \quad (8)$$

Because the filter impedance at the parallel resonance frequency is very large the network characteristic should be taken into account and proper selection of the parallel frequency is recommended to avoid amplification of harmonic voltages at and near the parallel frequency [5]. ω_S can be calculated once ω_1 , ω_2 and ω_P are determined. Substituting equations (5) and (6) into (7) yields the following

$$\frac{\omega^4}{\omega_S^2 \omega_P^2} \left(\frac{C_1}{C_2} \cdot \frac{1}{\omega_P^2} + \frac{1}{\omega_S^2} + \frac{1}{\omega_P^2} \right) \omega^2 + 1 = 0 \quad (9)$$

ω_1 is one of the roots of equation (9) [5]. Replacing ω by ω_1 leads to the following equation

$$\frac{C_1}{C_2} = \frac{\omega_1^2 + \omega_2^2 - \omega_P^2}{\omega_S^2} - 1 \quad (10)$$

Using equations (5) and (6) also yield the following equations

$$L_1 = \frac{1}{\omega_S^2 C_1} \quad (11)$$

and

$$L_2 = \frac{1}{\omega_P^2 C_2} \quad (12)$$

The reactive power generated by the double-tuned filter is

$$Q_1 = \frac{V_1^2}{Z(\omega_f)} \quad (13)$$

The fundamental filter impedance $Z(\omega_f)$ can be calculated by summing equations (3) and (4) of the series and parallel resonance circuits. Substituting equation (13) into the summated equation of $Z(\omega_f)$ the parameter C_1 can be obtained by

$$C_1 = \left(\frac{\omega_f}{\omega_S^2} - \frac{1}{\omega_f} + \frac{\omega_f \omega_P^2 (\omega_1^2 + \omega_2^2 - \omega_P^2) - \omega_1^2 \omega_2^2}{\omega_1^2 \omega_2^2 (\omega_P^2 - \omega_0^2)} \right) \frac{Q_1}{V_1^2} \quad (14)$$

For damped double-tuned filters of various configurations, the resistance value is initially assumed [5,6]. The practical tuned frequencies of these filters may not be equal to the desired tuned frequencies ω_1 and ω_2 of the conventional double-tuned filters, and can rather be equal to the minimum impedance frequencies ω_{z1} and ω_{z2} or equal to the zero reactance frequencies ω_{x1} and ω_{x2} due to frequency deviations [5,6]. In this case the filter parameters are initially calculated with the tuned frequencies equal to ω_1 and ω_2 . If the permitted design errors between the practical and the desired tuned frequencies are exceeded an iterative method is used to recalculate the filter parameters until the errors are below the specified [5,6].

2.4 C-Type High Pass Damped Filter Design

The LRC parameters of the C-type high pass damped filter can be obtained by following the optimised approach presented in [9] as follows

$$C_4 = \frac{h_0^2 - 1}{m^2 - m\sqrt{m^2 - 1}} \times \frac{Q_1}{2\omega_f V_1^2} \quad (15)$$

$$L_2 = \frac{m^2 - m\sqrt{m^2 - 1}}{h_0^2 - 1} \times \frac{2V_1^2}{\omega_f Q_1} \quad (16)$$

If m is assumed to be approaching infinity the filter circuit of figure 2 (a) is reduced to a circuit without the resistance R_2 such that capacitors C_3 and C_4 , and reactor L_2 form a series single-tuned filter. C_5 is the added series C_3 and C_4 , and L_5 is equal to L_2 ; they can be calculated as follows

$$C_5 = \left(\frac{1}{C_3} + \frac{1}{C_4} \right)^{-1} = \frac{(h_0^2 - 1)Q_1}{h_0^2 \omega_f V_1^2} \quad (17)$$

$$L_5 = L_2 = \frac{V_1^2}{(h_0^2 - 1)\omega_f Q_1} \quad (18)$$

Reverting back to the C-Type high pass band filter of figure 2 (a), the damping resistor R_2 can be obtained using

$$R_2 = \frac{q V_1^2}{h_0 Q_1} \quad (19)$$

A damping resistor labelled R_3 is added in series with L_2 and C_4 to obtain the above circuit shown in figure 2 (b), and it can be calculated as follows

$$R_3 = \frac{\omega_f X_{L_5}}{Q_5} \quad (20)$$

By neglecting the resistance in the reactor and the dielectric power loss in the capacitor, C_3 is the filter reactive power compensation capacitor and is calculated as follows

$$C_3 = \frac{Q_1}{\omega_f V_1^2} \quad (21)$$

The impedance versus frequency response of a C-Type high pass damped filter can be obtained using the following equation

$$Z(\omega) = \left(\frac{1}{R_2} + \frac{1}{R_3 + j\omega L_2 - j\left(\frac{1}{\omega C_4}\right)^{-1}} \right)^{-1} + \frac{1}{j\omega C_3} \quad (22)$$

2.5 Configuration and Sizing of DC Smoothing Reactors

The sizing of DC smoothing reactors connected in series with the converters and before the DC filters depends on various requirements, but mainly upon the reduction of ripple in the DC current to prevent the current becoming discontinuous at light loads, and to also decrease harmonic voltages and currents in the DC line [10]. Inductors with values ranging from 270 mH to 1.5 H have been used for systems with DC lines. However, to avoid the use of large sizes of DC smoothing reactors their final sizes are selected based on the DC filter performance and the overhead line parameters [11]. Two types of configurations can be used for HVDC transmission systems, two series group per pole or a distributed DC smoothing reactor concept with reactor coils in the high voltage bus and the neutral bus [11]. The latter arrangement is more economical as a result of less insulation level requirement. Technically, the harmonic voltage drop across the neutral bus reactor significantly reduces the harmonic voltage stresses of the other converter equipment such as the converter transformers which are subject to increased voltage steps on the secondary winding due to commutation [8]. However, due to the induced voltage across the neutral bus reactor coils

the insulation level to ground on the valve side terminals is increased [8].

3. APPROACH AND METHODS

The following ± 800 kV bipolar UHVDC power system network was modelled in PSCAD EMTDC software tool. Two 12-pulse converters were used per each pole terminal to meet the high power and voltage levels associated with such a system. Total power of 4000 MW was transferred over a long transmission distance of 1500 km.

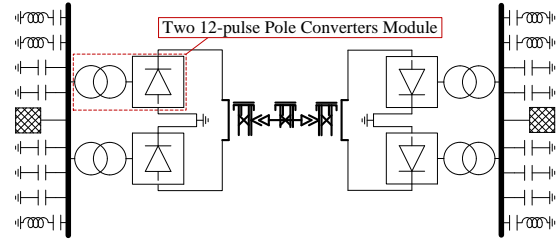


Figure 3: UHVDC power system network

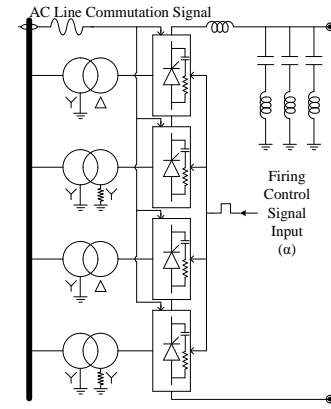


Figure 4: two 12-pulse pole converters

The following flow diagram of figure 5 shows steps taken for conducting the required studies. The variables manipulated were the respective addition of the AC/DC filters and DC smoothing reactors on the AC buses and DC terminals of the grid sourced ± 800 kV bipolar UHVDC power system network as shown in figures 3 and 4 above.

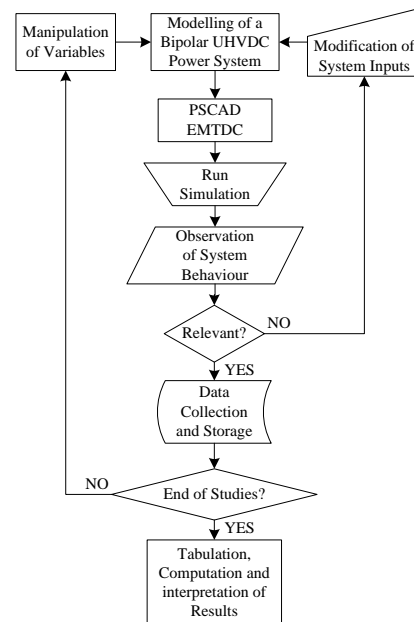


Figure 5: Steps for conducting studies

Figure 6 below shows simple steps taken in selecting and designing the AC/DC filters, and investigating their performance. However, the filter performance criteria based on the harmonic voltage distortion limits are applicable only for AC filters. The performance of DC filters was judged based on the effectiveness of the DC characteristic harmonic voltages reduction.

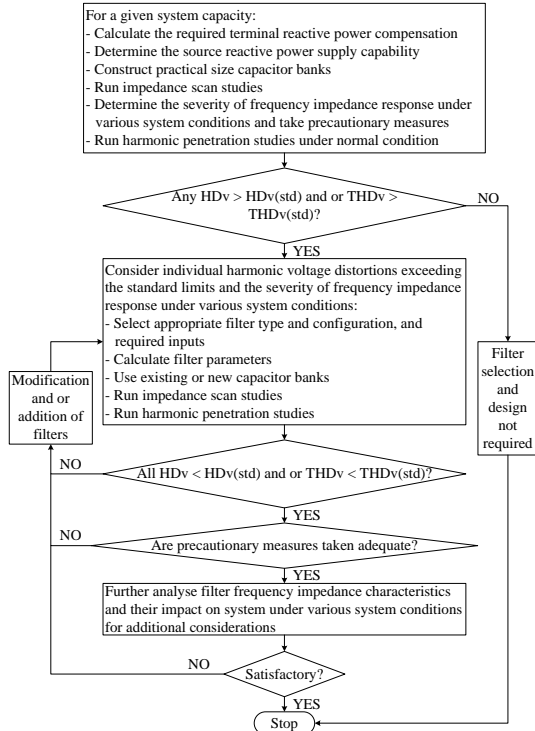


Figure 6: AC/DC filter selection and design procedures

Figure 7 below shows a specific scenario whereby a single-tuned filter was used to mitigate the 11th HD_V, which, among other harmonic orders, was found to be above the specified standard limit of 1%. However, the resulting impact was the amplification of the 13th HD_V above the specified standard limit due to parallel resonance with the source, and therefore the single-tuned filter performance can be undesirable, and this can be expected for any other system. Therefore in this case there will be a need to add a second single-tuned filter tuned at the 13th harmonic frequency. Though this process will provide adequate harmonic voltage mitigation, a double-tuned filter tuned at the 11th/13th harmonic frequencies is preferable for its considerable advantage(s) over two single-tuned filters application as an alternative solution.

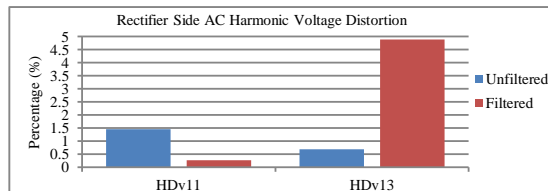


Figure 7: Impact of Mitigating a Single Order Voltage Distortion Using a Single-tuned Filter

Figure 8 below shows the impedance scans captured at the rectifier and inverter AC buses before and after insertion of AC filters. The rectifier and inverter AC sides damped double-tuned filters were both tuned at 11th/13th harmonics. The damping resistors were added between points AB (See figure 1), 400 Ω and 500 Ω for the rectifier and inverter sides AC filters respectively. Two C-Type high pass damped filters were installed at each AC terminal bus to

effectively reduce the high impedance at the 3rd harmonic frequency.

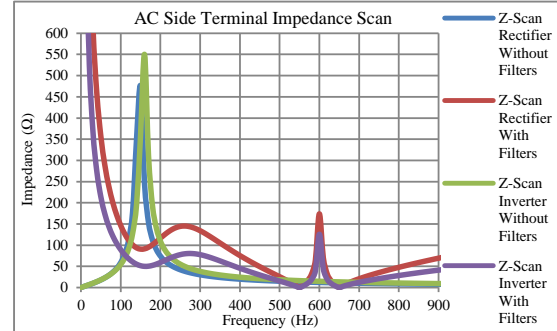


Figure 8: AC terminal impedance scans

Figure 9 below shows the individual impedance versus frequency responses of the damped double-tuned and C-type AC filters used at both the rectifier and inverter sides.

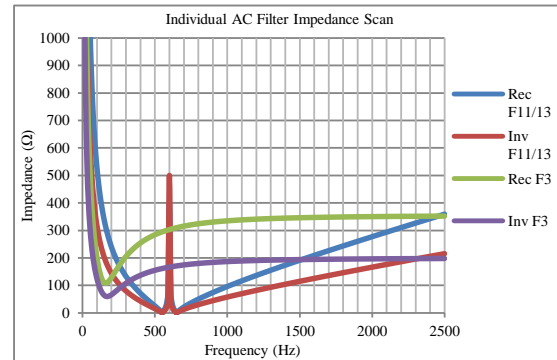


Figure 9: Individual AC Filter Impedance Scans

Three conventional double tuned DC filters were identically designed for both the rectifier and inverter sides, and were tuned at 12th/24th, 12th/36th and 12th/48th to effectively reduce the dominating 12th harmonic voltages. Figure 10 below shows their combined impedance versus frequency responses, while tables 1 and 2 tabulate the calculated AC/DC filter parameters.

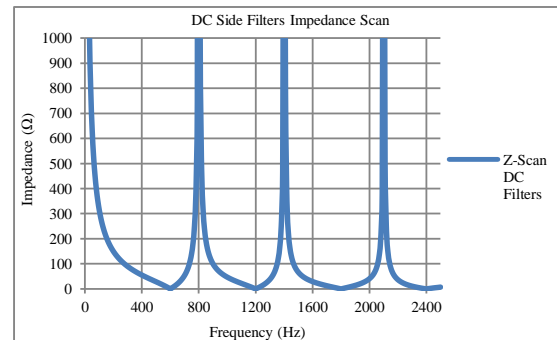


Figure 10: DC Filters impedance scan

Tuning Frequency (h)	L ₁ (mH)	L ₂ (mH)	C ₁ (μF)	C ₂ (μF)	R (Ω)
11 th /13 th (R)	24.284	0.6733	2.938	104.49	400
11 th /13 th (I)	14.571	0.404	4.897	174.15	500
12 th /24 th	16.286	9.107	1.652	5.051	-
12 th /36 th	8.821	15.653	1.652	2.412	-
12 th /48 th	6.071	20.506	1.652	1.505	-

Tuning Frequency (h)	L ₂ (mH)	C ₃ (μF)	C ₄ (μF)	R ₂ (Ω)	R ₃ (Ω)
3 rd (R)	424.4	2.98	23.87	711	88.88
3 rd (I)	220.5	4.97	45.96	400	46.18

Figure 11 below shows the effect of inserting DC smoothing reactors on the DC network before the DC filters upon their sizes for tolerable performance based on the DC instantaneous voltage waveform of a ± 800 kV bipolar UHVDC system. Such a design can result in larger DC smoothing reactor sizes in order to prevent voltage collapse as shown when DC reactors with inductances of 187.5 mH and 375 mH were used per pole terminal respectively, and also when further minimisation of ripple is required as shown being the case when a DC reactor of 1.5 H was used as opposed to 750 mH. This will further influence the insulation requirement and costs. Therefore, as a clear recommendation worthy of consideration, DC smoothing reactors of 150 mH were selected per pole terminal based on the DC filter performance. For the configuration with reactor coils in high voltage bus and the neutral bus the 150 mH were split into two halves of 75 mH to determine their performance impact.

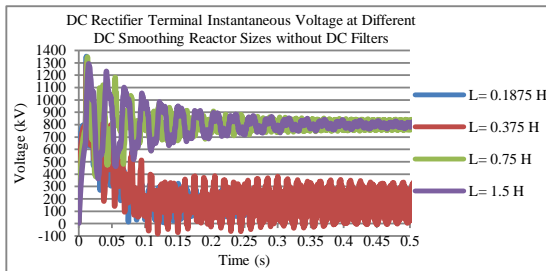


Figure 11: DC Instantaneous Voltage Waveforms

4. RESULTS

Relevant studies of the 1500 km, 4000 MW, ± 800 kV bipolar UHVDC power system were conducted in PSCAD EMTDC, and the following results were obtained. Figures 12 to 14 depict the individual and total harmonic voltage distortion levels computed at the rectifier and inverter sides AC terminal buses. Figure 15 shows the DC harmonic voltages at the rectifier and inverter sides DC terminals. Figures 16 and 17 are the DC instantaneous and average voltages and currents at the rectifier side DC terminal.

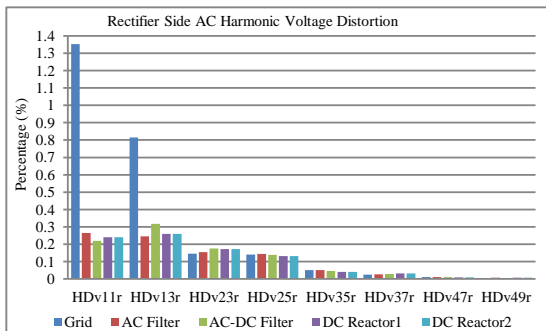


Figure 12: Rectifier Side AC Individual Harmonic Voltage Distortion Levels

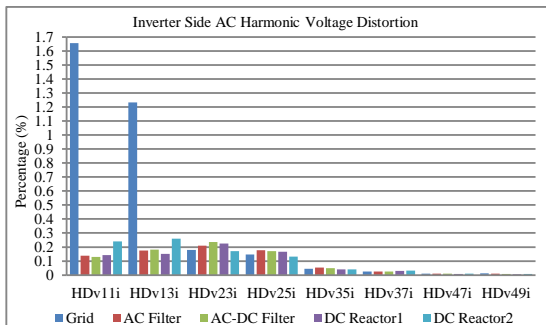


Figure 13: Inverter Side AC Individual Harmonic Voltage Distortion Levels

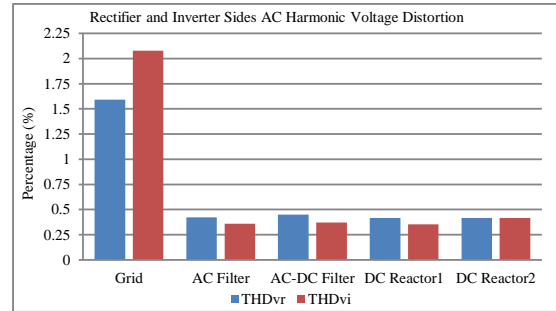


Figure 14: Rectifier and Inverter Sides AC Total Harmonic Voltage Distortion levels

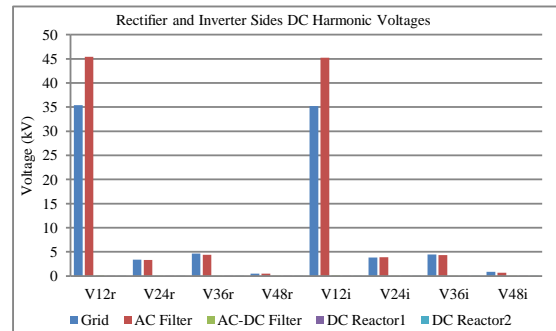


Figure 15: Rectifier and Inverter Sides DC Harmonic Voltages

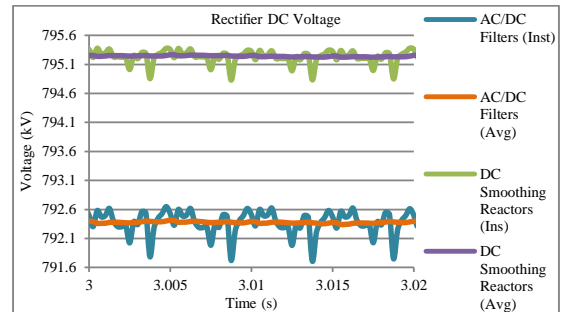


Figure 16: Rectifier Side DC Instantaneous and Average Voltages

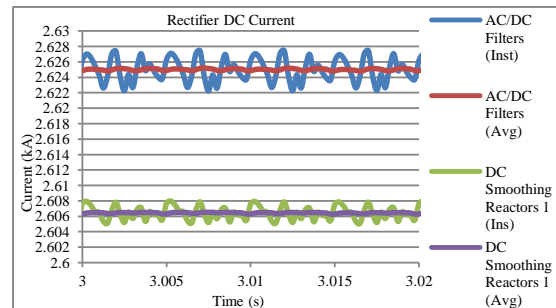


Figure 17: Rectifier Side DC Instantaneous and Average Currents

5. DISCUSSION

AC filters – Under a grid connected network the 11th HD_V level of 1.35% was found to exceed the 1% limit at the rectifier side as shown in figure 12. The exceeded harmonic voltage distortions were, at the inverter side, the 11th and the 13th as shown in figure 13 with their levels being 1.66% and 1.23% respectively. The THD_V levels were found to be 1.59% and 2.07% at the rectifier and inverter sides respectively as shown in figure 14 thus both exceeding the 1.5% limit. The higher levels of the harmonic voltage distortions at the inverter side occurred due to a larger capacitive reactance as a result of power losses in the DC lines thus minimising the receiving end power from the sending end, and also due to the fact that the inverter side grid source operated with a higher reactive

power supply capability. The smaller fault MVA at the inverter side also resulted in a larger source impedance, for the short circuit ratio (SCR) of 2.5 was equally chosen at both ends of the system. The AC damped double-tuned filters were inserted, and as can be seen in figures 12, 13 and 14 the AC filter performance requirements below the specified voltage distortion limits of 1% HD_V and 1.5% THD_V were achieved at both the rectifier and inverter sides. However, the dominating DC harmonic voltages of the 12th frequency order in figure 15 were increased by a large fraction, from about 35 kV to 45 kV, at both the rectifier and inverter sides with the rectifier side 12th harmonic voltages being slightly higher. It can be depicted in figures 12, 13 and 14 that better AC filter performance occurred at the inverter side. This holds true because, considering the need for power at the inverter side, larger size AC filter capacitors were used for MVar compensation to favour less reactive power to be supplied by the inverter side grid source.

DC filters – With respect to the AC filters performance, the addition of DC conventional double-tuned filters into the network decreased and increased simultaneously the HD_V levels as shown in figures 12 and 13, while increasing the THD_V levels as shown in figure 14 at both sides of the system. From 45 kV at the 12th frequency order, all the DC characteristic harmonic voltages were effectively reduced below 0.1 kV at both the rectifier and inverter sides as shown in figure 15. Though the exact same rectifier side DC filters were used at the inverter side, as shown in figure 15 better performance was achieved at the inverter side for the 12th harmonic voltage, while for the 24th, 36th and 48th better performance was achieved at the rectifier side.

DC smoothing reactor – In relation to the circuit with AC/DC filters in application, the use of both types of configurations of DC smoothing reactors had similar impact on the AC distortion levels at the rectifier side, and also on DC harmonic voltages as shown in figures 12, 14 and 15. While they provide equal performance of decreased THD at the rectifier side, they, however, increased and decreased the individual harmonic voltage distortion levels simultaneously depending on the frequency order. The first type configuration achieves reduced and or less amplification of harmonic voltage distortions (figure 13 shows reduced 11th and 13th) at the inverter side, while the second configuration shows increased harmonic voltage distortions, especially the THD_V as shown in figure 14. The filtering performance of DC smoothing reactors can be deduced to be better at the rectifier side for all the DC characteristic harmonic voltages, especially the lower orders due to effective reduction.

The use of both types of configurations of DC smoothing reactors had similar effects on the dynamic response signals at both the rectifier and inverter DC terminals. Figures 16 and 17 show the rectifier instantaneous and average DC voltages and currents waveforms. The ripple in the DC instantaneous voltage signal decreased and became less distorted at an increased peak voltage, while the average signal became much more constant of a value of 795.25 kV from 792.38 kV as shown in figure 16. The DC reactors reduced the ripple in the DC instantaneous current signal and shifted its peak below 2.61 kA, while reducing the more constant average DC current to 2.607 kA from 2.625 kA as shown in figure 17.

6. CONCLUSIONS

The aim of this paper has been to investigate the performance impacts of AC/DC passive filters and DC smoothing reactors upon the DC harmonic voltages, AC harmonic voltage distortion levels and DC responses.

The AC damped double-tuned filters performance requirements based on the IEEE standard 519-1992 distortion limits of 1% HD_V and 1.5% THD_V were met, while the dominating DC harmonic voltages of the 12th order were significantly amplified from 35 kV to 45 kV. The conventional double-tuned filters used on the DC side of the system effectively reduced all the DC characteristic harmonic voltages below 0.1 kV. The THD_V and various HD_V levels of the AC sides of the system were amplified. Both DC smoothing reactor configurations had similar impact upon the rectifier AC and DC sides, and equally decreased the THD_V level. The two series group per pole configuration seemed preferable at the inverter side. Both types of configurations of DC smoothing reactors had similar effects on the DC response signals of the rectifier and inverter sides. They adequately filtered the instantaneous and average voltages and currents, while increasing the voltages and decreasing the currents peaks.

ACKNOWLEDGEMENT

The principal author wishes to thank the Centre for Post-graduate Studies (CPGS) of the Cape Peninsula University of Technology (CPUT) and the Electrical Supply Commission (ESKOM) for funding the research project.

REFERENCES

- [1] J. Arrillaga. *High Voltage Direct Current Transmission*. 2nd ed. London: Institution of Electrical Engineers, 1998, pp. 56.
- [2] N. Mohan, T. M. Undeland & W. P. Robbins. *Power Electronics, Converters, Applications and Design*. USA: Wiley and Sons, 2003, pp. 460-471.
- [3] J. Arrillaga and N.R. Watson. *Power systems harmonics*. 2nd ed. West Sussex: John Wiley and Sons, 2003, pp. 219-250.
- [4] M. Joorabian, S. GH. Seifossadat and M. A. Zamani. "An algorithm to design harmonic filters based on power factor correction for HVDC systems," *IEEE International Conference on Industrial Technology*, India, Dec. 2006.
- [5] M. A. Zamani and M. Mohseni. "Damped-Type Double Tuned Filters Design for HVDC Systems," *9th International Conference on Electrical Power Quality and Utilisation*, Barcelona, Oct. 2007.
- [6] X. Yao. "algorithm for the parameters of double tuned filter," *IEEE International Conference on Harmonic and Quality of Power*, Greece, Oct. 1998.
- [7] B. Bergdahl and R. Dass. "AC-DC Harmonic Filters for Three Gorges-Changzhou ± 500 kV HVDC Project." Internet: [http://www.05.abb.com/global/scot/scot221.nsf/veritydisplay/b20a071fd73b9f8ac1256fda004aeabe/\\$file/icps01ac-dc.pdf](http://www.05.abb.com/global/scot/scot221.nsf/veritydisplay/b20a071fd73b9f8ac1256fda004aeabe/$file/icps01ac-dc.pdf) [Jul. 20, 2013].
- [8] D. Zhang, M. Haeusler. H. Rao, C. Shang and T. Shang. "Converter Station Design of the 800 kV UHVDC project Yunnan-guangdong." Internet: http://www.ptd.siemens.de/converter_stations_design_YG_zhang.pdf [Jun. 08, 2013].
- [9] Y. Xiao, J. Zhao and S. Moa. "Theory for the Design of C-Type Filter," *11th International Conference on Harmonics and Quality of Power*, New York, 2004, pp. 11-15.
- [10] K. R. Padiyar. *HVDC Power Transmission Systems Technology and System Interactions*. New Dehli: Wiley Eastern, 1990, pp.111-113.
- [11] H. Huang, V. Ramaswami and D. Kumar. "Design considerations of ultra-high voltage dc system." Internet: http://www.ptd.siemens.de/050714_Design_Considerations_UHVDC.pdf [Jan. 25, 2013].

CLASS D AUDIO AMPLIFIER THEORY INCLUDING A SIMPLE FEEDBACK LOOP EXAMPLE

S. Nienaber* and H.D.T. Mouton**

Faculty of Engineering, Stellenbosch University, Bosman Street, Stellenbosch, 7600, South Africa

* E-mail: 16082508@sun.ac.za

** E-mail: dtmouton@sun.ac.za

Abstract: The purpose of this document is to discuss the basic theory of a class-D amplifier. The distortion mechanisms at play will also be discussed and it will be illustrated how a controller can be implemented digitally to reduce the distortions. A more accurate small signal model will be given for PWM and the relevant NTF will also be discussed. The class-D amplifier will utilize voltage control across the audio band. Class-D amplifiers, however, have many uses beyond audio amplifiers and similar techniques can be used with high-precision drives and current regulation in converters.

Keywords: PWM, class-D, dead time, noise shaping, small signal model, quantization noise.

1. INTRODUCTION

Class-D audio amplifiers now dominate the market for applications in car audio systems, home-theatre systems, flat-screen television sets and personal computers. It also has recently been identified as the eleventh top technology of the past decade [1]. Class-D amplifiers have started to break ground in the high-end home audio market with performance approaching that of the best analog designs [2], [3].

Quantifying good audio performance in terms of measurable parameters is a difficult task which is shrouded by a certain degree of mysticism and “black magic”. However, discussions with highly experienced designers of some of the best audio products available on the market [4] led to the following specifications for what can be considered to be a state-of-the-art class-D amplifier:

- Low output impedance across the audio band ($< 1\text{m}\Omega$);
- Flat frequency response ($< 0.1\text{dB}$ from 10 Hz to 20 kHz);
- Low THD+N ($< 0.005\%$);
- THD+N must remain constant as a function of frequency.

It is possible to achieve these specifications using class-AB amplifier designs but they are very sophisticated and expensive [3].

The main advantage of class-D amplifiers is the fact that their efficiency is significantly higher than that of class-AB amplifiers. Higher efficiency leads to significant reductions in cost and weight. As a result class-D amplifiers have replaced their conventional class-AB counterparts in applications ranging from hearing aids to high-power PA amplifiers used in live audio.

Class-D amplifiers are widely used in mobile device applications where efficiency is of key importance. The requirements of mobile device amplifiers are remarkably

high [5], approaching those of the high-performance home-audio systems listed previously.

This paper discusses some of the fundamental issues plaguing the design of high-performance digitally controlled class-D amplifiers. It shows how imperfections in the digital pulse-width modulator and the output stage degrade the performance of the amplifier. It is then shown that a well-designed feedback loop can suppress these effects, thereby achieving the specifications listed previously.

The application of the techniques provided in this paper goes far beyond the realm of audio amplification. High-performance amplifiers are also used in precision motor drives used in the integrated circuit manufacturing sector. The same fundamental techniques have also been applied successfully to the control of high-power converters in [6].

2. THEORY

2.1 Basic operation of a class-D amplifier

The defining characteristic in class-D amplifiers lies in using the output stage devices as switches instead of operating them in their linear region. The basic open loop topology is illustrated in Fig. 1.

The archetype

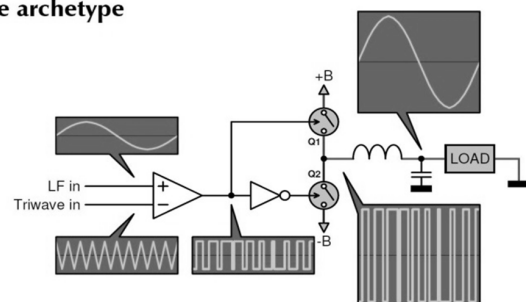


Figure 1: Basic operation of PWM [7]

The rough categories for class-D amplifiers are self-oscillating and PWM (Pulse Width Modulation/Modulator). This paper only focuses on PWM.

In Fig. 1, a sawtooth or triangular wave can be used as a carrier signal which will be compared to the input Low Frequency (LF) signal i.e. the audio signal. A sawtooth signal is used in this paper; however, they both operate in a similar fashion.

A comparator compares the two signals and if the input audio signal is greater than the carrier signal, the output of the comparator is +1; otherwise the output is -1.

This output waveform is a PWM signal and is sent to a driver circuit (power stage) that has two switches. The switches are switched alternatively and must never be on simultaneously. In the event that both switches are on, they will certainly create a short circuit across the DC source and the switches can be damaged. Dead time is inserted in the circuit to prevent this; however, this creates distortion in the output signal. The output signal is then filtered using the LPF (Low Pass Filter) with a cut off frequency of around 21 kHz (audio band).

PWM amplifiers in general can be categorised as analog controlled or digitally controlled. The focus here will be on a digitally controlled amplifier as the main advantage is that it is smaller to integrate into a system. The digital controller will closely emulate an analog controller due to the very high sampling frequency (98.304 MHz) used.

For a full audio application the relevant negative feedback loop is shown in Fig. 2. The digital compensator (Digital Loop Filter in figure 2) as well as the PWM will be implemented with an FPGA (Field Programmable Gate Array) for the time being although the final result of the project is to implement a single low cost chip that will incorporate these elements as well as the ADC (Analog to Digital Converter).

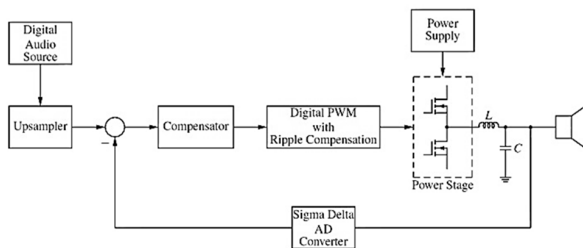


Figure 2: Simple feedback loop diagram [8]

Digital audio that was sampled at 44.1 kHz is used as the input to the system. An upsampler converts the audio to 98.304 MHz.

Experience has shown that the digital loop filter must ensure a gain of 50 dB is maintained over the entire audio band in order to suppress the quantization noise [9].

The output of the PWM is then fed to a power stage which can be either a half-bridge or a full-bridge topology and will contain high power fast switching MOSFETS. An output LPF removes all the high frequency components and passes only frequencies in the audio band to the speaker and ADC. The LPF will be realized with an inductor and capacitor.

2.2 Quantization noise

The sawtooth wave in the digital system is implemented as a counter and will therefore have discrete steps. This will create rounding errors which produce quantization noise as shown in Fig. 3.

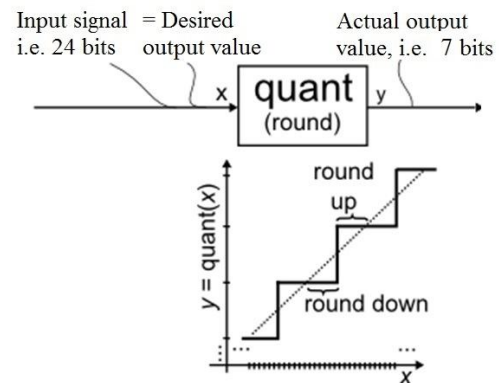


Figure 3: Quantization noise example [10]

For the moment, high resolution audio refers to 24 bit depth [11]. The input audio is sampled at 192 kHz. Therefore, it is desirable to use a 24 bit digital counter for PWM. However, using Eq. (1), it is found that the frequency at which the PWM must be clocked in the FPGA (for 24 bit audio sampled at 192 kHz (f_s)) is 3.221 THz!!

$$f_{PWM} = f_s \times 2^{Counter\ bits} \quad (1)$$

It is obviously impossible to clock an FPGA at this frequency. The PWM counter bits therefore needs to be much lower, for example, 7 bits. Clearly 7 bits is less than 24 bits but by using oversampling one can solve this problem. When oversampling, the dynamic range of the signal values can be reduced which in turn reduces the resolution requirements of the quantizer [12]. Therefore, the chosen switching frequency is 768 kHz and results in an FPGA PWM process that is clocked at 98.304 MHz.

In this paper, the ADC (as shown in the feedback path in Fig. 2) is not included in the feedback loop. In practise it will be included, possibly as a sigma-delta AD converter that will add its own quantization noise but this will be discussed in future work.

2.3 Dead time

Dead time is the dominant source of distortion for a class-D amplifier with a switching frequency above 150 kHz [13].

The effects of dead time in the frequency domain are shown in Fig. 4 for an input sinusoid of 1 kHz and a simulated dead time of 61.035 ns. The output stage voltage was ± 15 V in a half bridge configuration. The dead time inserts both even and odd harmonics especially in the audio band [14]. The amplitudes of these harmonics are very high. This will cause a large amount of distortion of the output. It is therefore important to design a controller that will suppress these components sufficiently.

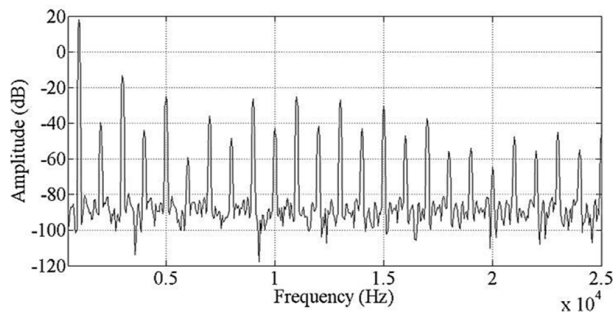


Figure 4: Dead time in the frequency domain

2.3 Noise shaping

The design of the digital loop compensator is very important and the main objective is to shape the previously mentioned quantization noise in such a way that the noise will be shifted outside the audio spectrum. This process is simply called noise shaping and an example of how noise can be shaped is shown in Fig. 5.

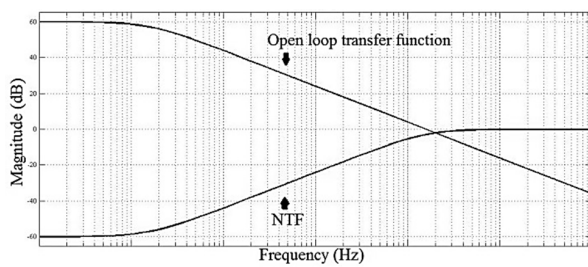


Figure 5: Noise shaping

From the figure it is clear that the desired signal transfer function must have a flat LPF response in the audio band to allow these signals to pass through without being distorted.

The NTF (Noise Transfer Function) (discussed later) must act like a High Pass Filter (HPF). It pushes the noise outside of the audio band where it is inaudible and will also be filtered by the output LPF. In most class-D applications, it will be necessary to have multiple integrators in the compensator. More integrators will

provide a sharper cut off as each integrator will provide a -20 decibel/decade roll off that will add up to a steeper slope in total.

2.4 Average model

To design controllers that are applicable to PWM loops, it is necessary to have a small signal model, which accurately portrays the behaviour of the PWM in the loop. In the past the average model was used to design controllers and determine the behaviour of PWM loops. In this section it is used to illustrate the basic NTF principles as it is a simple model.

Fig. 6 represents the PWM section as a simple gain of 1. In the figure $G_c(s)$ is the compensator, $Q(s)$ the quantization noise, V_d the output stage voltage and $G_p(s)$ represents the output LC filter and loudspeaker.

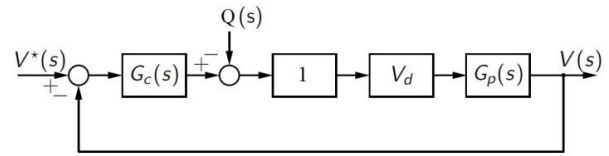


Figure 6: Average model

The noise transfer function $V(s)/Q(s)$ is then given as:

$$NTF = \frac{V_d G_p(s)}{1 + V_d G_p(s) G_c(s)} \quad (2)$$

In this paper, the feedback loop is closed before the output LC filter (G_p) and V_d is taken as 1 for noise transfer function simulation purposes. Therefore, $G_p(s)$ is simply taken as 1. The NTF obtained from the average model is not accurate and can indicate that a loop is unstable when in fact it is stable.

The average model is not accurate enough for our purposes and other models have been developed that are much more effective [15].

2.5 Small signal model and gain

A more accurate small signal model, which will lead to a more accurate NTF, is presented in Fig. 7.

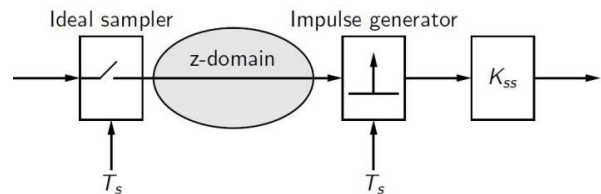


Figure 7: Small signal equivalent model [6]

The PWM is represented by an ideal sampler which will convert the input continuous time signal to a discrete time signal. The output behaves like an impulse generator

where the weight of the impulse is affected by the small signal gain (K_{ss}). K_{ss} is given by [16]:

$$K_{ss} = \frac{2f_s}{2f_s - \dot{f}(t_{sp})} \quad (3)$$

This small signal gain is dependent on the switching frequency of the PWM as well as the derivative of the input continuous signal i.e. the gradient of the continuous signal at the point where the continuous signal crosses the PWM counter. It must be remembered that the PWM counter and the sawtooth wave discussed in section 2.1 are one and the same.

2.6 Impulse Invariance Method

The small signal model in Fig. 7 indicates that if the loop is broken right after the PWM in Fig. 2 and an impulse is injected into the system, the impulse will travel around the loop and reach the output of the PWM again in a similar manner in which the PWM would have done without breaking the loop. Therefore, we need to use the impulse invariance method to transform the s-domain component in Eq.(5) to the z-domain thereby producing the discrete time equivalent.

Firstly, it is important to note that the first impulse into the system will be neglected. This is due to the assumption that there are delays in the feedback loop and a non-zero value of $g_z(0)$ will result in a delay free loop, which is inaccurate [16].

The impulse invariance method is then carried out by separating the transfer function into partial fractions using Eq. (4) [6]. Each section is then transformed using Eq. (6) [6]:

$$G(s) = \sum_{n=1}^N \frac{A_n}{s + p_n} \quad (4)$$

Where $G(s)$ is:

$$G(s) = K_{ss} V_d e^{-st_d} G_c(s) G_p(s) \quad (5)$$

$$\begin{aligned} G(z) &= T_s \sum_{k=1}^{\infty} g(kT_s - t_d) z^{-k} \\ &= T_s \sum_{n=1}^N A_n e^{p_n t_d} \frac{e^{-p_n T_s}}{z - e^{-p_n T_s}} \end{aligned} \quad (6)$$

2.7 Noise transfer function

The NTF is necessary to determine how well the compensator suppresses the quantization noise created by the PWM. It also confirms the effectiveness of the small signal equivalent model. We now have all the tools necessary to derive the NTF for Fig. 2.

Fig. 8 is used to provide the starting point for deriving the NTF. The compensator (G_c) and output LPF (G_p) are transfer functions in the s-domain. V_d represents the gain achieved by the power stages and e^{-st_d} is the combined transport delay in the loop.

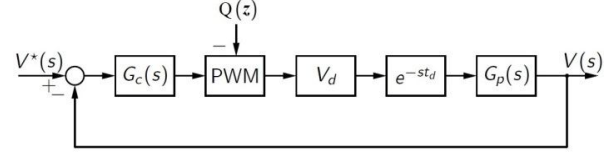


Figure 8: System block diagram

Inserting the small signal equivalent model in Fig. 8 yields Fig. 9.

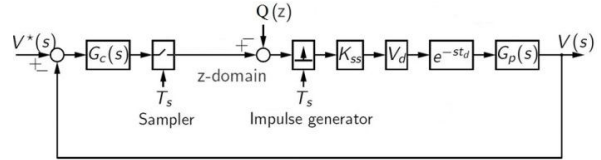


Figure 9: System block diagram including small signal model

Block diagram techniques can be used to simplify Fig. 9 which simplifies the analysis of the circuit and yields Fig. 10.

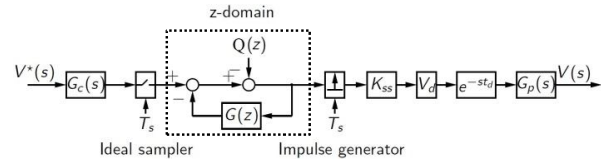


Figure 10: Final block diagram

The closed loop transfer function of the entire system is given by Eq. (7):

$$\begin{aligned} V(\omega) &= \left[K_{ss} V_d e^{-\omega t_d} \frac{G_c(\omega) G_p(\omega)}{1 + G(e^{\omega T_s})} \right] V^*(\omega) \\ &+ \left[K_{ss} V_d e^{-\omega t_d} \frac{G_p(\omega)}{1 + G(e^{\omega T_s})} \right] Q(\omega) \end{aligned} \quad (7)$$

Where $G(e^{\omega T_s}) = G(z)$ is given by equation 8:

$$G(z) = \text{INV}\{K_{ss} V_d e^{-st_d} G_c(s) G_p(s)\} \quad (8)$$

An expression for $G(z)$ can be obtained by using Eq. (5) and (6). This can then be used to design a controller which will behave as expected in the system i.e. predictable closed loop gain which leads to the expected stability of the controller.

The NTF for Fig. 10 is given by Eq. (9). This will be compared to Simulink simulation to confirm its accuracy.

$$NTF = \left[K_{SS} V_d e^{-\omega t_d} \frac{G_p(\omega)}{1 + G(e^{\omega T_s})} \right] \quad (9)$$

3. CONTROLLER

This section covers the design of the controller G_C . Stability can be more closely examined in the z-domain than in the s-domain and therefore, the controller was designed in the z-domain.

The bode plot of the controller is shown in Fig. 11.

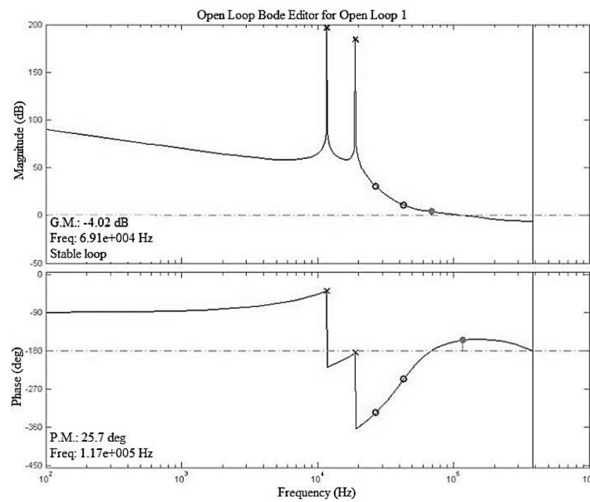


Figure 11: Controller bode plot

A gain of 50 dB across the audio band is reached with an open loop gain of 1.32.

The complex poles were placed in the audio band at 11.7 kHz and 17 kHz respectively. An additional integrator was also added. At the moment, the design is done manually but in future a script will optimise the design. To simplify the controller implementation in the FPGA, the poles were placed on the unit circle because they can be more easily expressed as a chain of integrators diagram.

Fig. 12 is the root locus diagram of the compensator. It is interesting to note that if the open loop gain should ever drop below 0.85, the system will be unstable. This is why the small signal gain is so important. To ensure that the closed loop system operates at the designed gain and never drops below 0.85, the compensator gain must be divided by the small signal gain to yield the designed gain of 1.32.

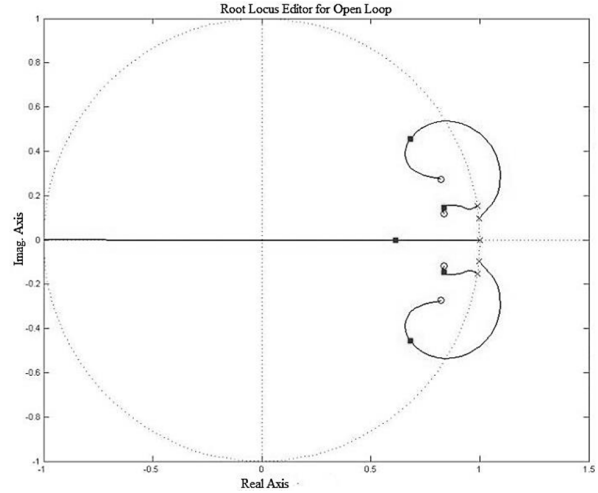


Figure 12: Root locus of compensator

4. RESULTS

A Simulink model of the system was created in MATLAB. Fig. 13 shows an FFT (Fast Fourier Transform) of the NTF. The Simulink data is represented by the thin line. The theoretical NTF given by equation 9 is represented by the thicker line. The noise floor of the theoretical model had to be lowered to that of the Simulink model using signal-to-noise calculations. This is due to the fact that the theoretical noise floor does not include the quantization noise of the PWM.

There is very good agreement between the theoretical model and that of the Simulink model. The poles from the compensator have been inverted and their nulls can clearly be seen. The trajectory of both lines also demonstrates the compensator's ability to shape the noise.

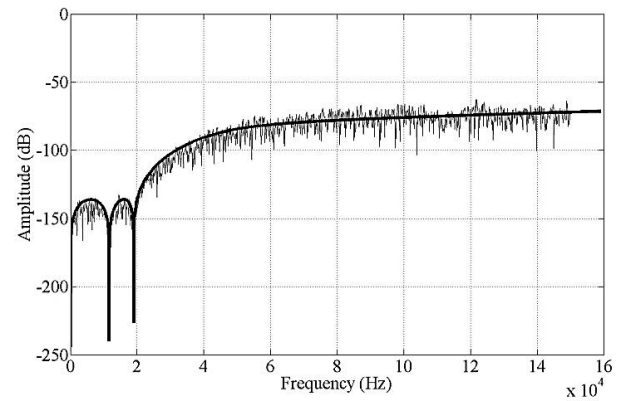


Figure 13: NTF results

To simplify the results, the feedback loop did not include the output LPF. Therefore, in the NTFs, $G_p(s)$ was replaced with a 1. The results presented for the NTFs were simulated and thus do not include any power stages or delays of any kind.

The effect of the compensator on the dead time is shown in Fig. 14. The dead time harmonics have been substantially reduced when compared to the original amplitudes given in Fig. 4.

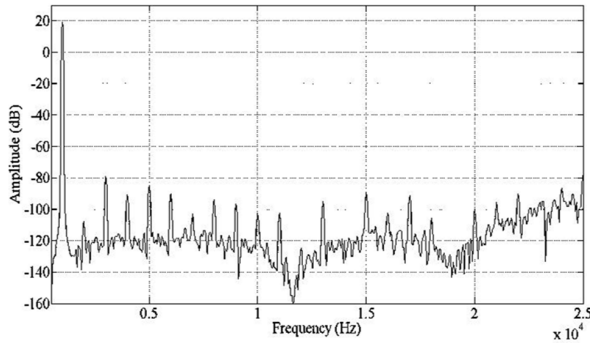


Figure 14: Reduced dead time harmonics

5. CONCLUSION

The distortion mechanisms and small signal model for a class-D amplifier have been discussed. The NTF that can be derived from the small signal model was presented and was shown to be an accurate mathematical representation of the PWM. A controller was also designed using the techniques provided which sufficiently suppressed the effects of the distortion mechanisms.

6. REFERENCES

- [1] G. Zorpette, "Top 11 technologies of the decade," in *IEEE Spectrum*, January 2011, pp. 58-59.
- [2] "Hypex Electronics," [Online]. Available: <http://www.hypex.nl/>. [Accessed 19 November 2013].
- [3] "Halcro," [Online]. Available: <http://www.halcro.com/>. [Accessed 19 November 2013].
- [4] B. Putzeys, Interviewee, Class-D Amplifier Technology. [Interview]. 19 11 2013.
- [5] A. Nagari, "Tutorial review: audio amplifiers in mobile platforms," *Analog Integrated Circuits and Signal Processing*, vol. 72, no. 3, pp. 511-520, September 2012.
- [6] H. Mouton, A. D. Beer, B. Putzeys, B. McGrath and G. Holmes, "Modeling and Design of Single-Edge Oversampled PWM Current Regulators Using Z-Domain Methods," in *IEEE ECCE Asia Downunder*, Melbourne, Australia, 2013.
- [7] H. Mouton, "State-of-the-art in Digital Class-D Audio Amplification," in *IEEE Meeting*, 2009.
- [8] H. Mouton and B. Putzeys, "Digital Control of a PWM Switching Amplifier," *AES 37th International Conference*, p. 2, 28-30 August 2009.
- [9] P. Kemp, H. Mouton and B. Putzeys, "High-Order Analog Control of a Clocked Class-D Audio Amplifier with Global Feedback Using Z-Domain Methods," in *131st Audio Engineering Society*, New York, 2011.
- [10] M. Nentwig, "DSPRelated," 9 December 2012. [Online]. Available: <http://www.dsprelated.com/showarticle/184.php>. [Accessed 28 March 2013].
- [11] Presonus, "Digital Audio Basics: Sample Rate and Bit Depth," [Online]. Available: <http://www.presonus.com/news/articles/sample-rate-and-bit-depth>. [Accessed 11 11 2013].
- [12] J. Proakis and D. Manolakis, "Chapter 6.6 Oversampling A/D and D/A Converters," in *Digital Signal Processing - Principles, Algorithms and Applications*; 4th edition, New Jearsey, Pearson Prentice Hall, 2007, p. 403.
- [13] I. Mosely, P. Mellor and C. Bingham, "Effect of Dead Time on Harmonic Distortion in Class-D Audio Power Amplifiers," *IEE Proc. Electronics Letters*, Vol. 35, No. 12., pp. 950-952, 15 April 1999.
- [14] F. Koeslag, H. d. T. Mouton, H. Beukes and P. Midya, "A detailed analysis of the effect of dead time on harmonic distortion in a class-D audio amplifier," in *AFRICON*, Windhoek, 2007.
- [15] J. Sun, D. M. Mitchell, M. F. Greuel, P. T. Krein and R. M. Bass, "Averaged Modeling of PWM Converters Operating in Discontinuous Conduction Mode," *Power Electronics, IEEE Transactions on* (Volume:16 , Issue: 4), pp. 482 - 492, July 2001.
- [16] L. Risbo, "Discrete-Time Modeling of Continuous-Time Pulse Width Modulator Loops," in *AES 27th International Conference*, Copenhagen, Denmark, 2005 September 2-4.

SOME ASPECTS ON INTEGRATED CURRENT SHUNTS FOR HIGH FREQUENCY SWITCHING POWER ELECTRONIC CONVERTERS

A.L.J. Joannou* D.C. Pentz* J.D. van Wyk*

* Group on Electronic Energy Processing (GEEP), Dept. of Electrical and Electronic Engineering Science, Corner of University Road and Kingsway Road, University of Johannesburg, Johannesburg 2006, South Africa E-mail: aljoannou@gmail.com

Abstract: Switched power electronic converters are now able to operate at very high frequencies due to the development in wide band gap high electron mobility transistors (HEMT) such as GaN and SiC power semi-conductor technologies. Measuring current at such high switching frequencies with rise and fall times of a few nanoseconds, requires specialised instruments and a good knowledge of measurement techniques. Current measurement technologies that are readily available are relatively expensive and can add unwanted parasitic impedances to the circuit. This paper investigates some aspects for a few current shunt options that can be integrated into a converter.

Keywords: Current measurement, high frequency, current shunt.

1 INTRODUCTION

The drive for smaller power electronic converters with a higher power density and high efficiency has forced the operating frequencies of converters to increase. The well-known advantage of the increase in switching frequency is that the energy storage elements reduce in magnitude and in essence physical size. Although size limitations still exist due to the magnetic energy storage elements, the overall reduction is still considerable. In the past, the limitation of the maximum switching frequency of these converters was the transistor losses associated with slow switching transients. With recent developments in wide band gap power semi-conductor technology, this is no longer the case.

Two of the most recent power semi-conductor technologies are Silicon Carbide (SiC) and Gallium Nitride (GaN) [1]. These wide band gap semi-conductors are power switching transistors which are theoretically able to switch at frequencies previously not achievable by Silicon (Si) devices [2]. They also have a higher power density compared to conventional silicon based semi-conductors [2]. The GaN transistors are said to be able to achieve even better characteristics than the SiC devices as discussed in [2] and [1]. These types of semi-conductor switches can now make the high frequency hard switching power electronic converters possible. This leaves power measurement of these high frequency converters as a potential problem. Although actual measurement probes are well developed, especially for voltage measurement, the high frequency switching operation of the circuit can cause stray flux to couple onto the measurement leads, causing considerable measurement error [3]. Voltage measurement terminals can be integrated into the main power circuit PCB which reduce the inductance of the measurement probe and hence the error for voltage measurements. Therefore HF switching voltage measurement can be performed

accurately. For sufficient power measurements, current also needs to be measured accurately.

Current measurement in power converters is well established, but these are bandwidth limited, have a response time delay and can become complex for high frequency accuracy and hence sensitive to interference. Current probes and a few other methods require that a loop be added to accommodate the current measurement device. This loop adds inductance to the circuit which will change the operating characteristics of the circuit. For this reason current probes and electromagnetic field based current measurement methods as in [4], [5] and [6] (e.g. hall-effect or Rogowski coils) are not discussed in this paper. The interest of this paper is mainly resistive shunts and in-circuit current measurement.

Ideally high frequency switching power electronic circuits should have as little parasitic inductance and capacitance as possible. This implies that current and voltage sensors should be carefully designed and characterised to ensure that the parasitic impedance they add is negligible whilst still maintaining accuracy in the measurement. This is especially important for new switching devices such as eGaN FETs [4].

2 CURRENT MEASUREMENT IN POWER ELECTRONIC CONVERTERS

Measuring current in power electronic circuits is important for several reasons, such as protection and control. Measuring current in RF devices in the past was not a concern, since the devices were either low power, or operated under sinusoidal conditions. Measuring the pulsed current waveforms in power electronic circuits requires current sensors with high bandwidth capability.

The bandwidth of any device corresponds to the 3dB knee frequency which also correlates to a 45 degree phase shift at that 3dB point. This large phase shift can cause inaccurate measurement and possibly failure in the

circuit. This is why it is important to realise that measurement specifications for non-sinusoidal switching power electronic circuits must be strict and that the 3dB rated frequency is not a true or sufficient figure of merit for comparison.

Current sensors, specifically in power electronic circuits, aim to achieve the following characteristics as listed in [5]:

- Compact size with a very low profile
- Ease of manufacture and low cost
- High bandwidth for high frequency operation
- Fast response with small/few or no parasitic elements introduced
- Reliable with good noise immunity
- High stability with varying temperature

The criteria listed above are used as guidelines while investigating the integrated current shunts discussed in this paper. The accuracy of a current sensor relies heavily on the impedance matching of the input and outputs of the device under test [6].

The possible voltage response which can be measured across the shunt will reveal characteristics of the shunt as well as the circuit in which the shunt is placed. Three main effects are:

1. Slow rise time will be due to inductance added by the shunt (or circuit inductance). Any stray circuit capacitance will then cause ringing and result in an overshoot
2. Skin effect will cause the initial voltage measured across the shunt to be higher, and once the current density is uniform, the voltage across the shunt will decrease reach a true steady state value
3. Coupling effects in the measurement if the measurement probe is not placed in a “field free” region.

Three different current shunt technologies are discussed next. These are single resistor current shunt, the lateral current shunt as well as the co-axial current shunt.

3 INTEGRATED CURRENT SHUNT MEASUREMENT DEVICES

It is again noted that the focus of this paper is specifically on current shunt measurement. Thus only shunts are considered. The shunts that are discussed in this paper are for low current applications (below 20 amperes). This low current will correspond to the voltage drop across the shunt resistor being comparable with the leakage flux that could induce measurement noise. Thus the shunt needs to be designed such that the desired signal can be differentiated from the measurement error.

3.1 Single surface mount (SMD) resistor measurement

The DC output current of power electronic converters is often measured by using a single SMD resistor as a current shunt. Using a single resistor as a shunt to

measure high frequency switching current will not yield an accurate representation of the actual current.

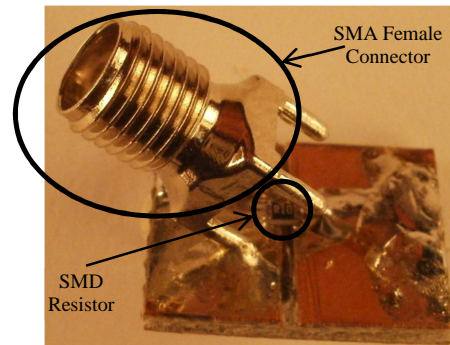
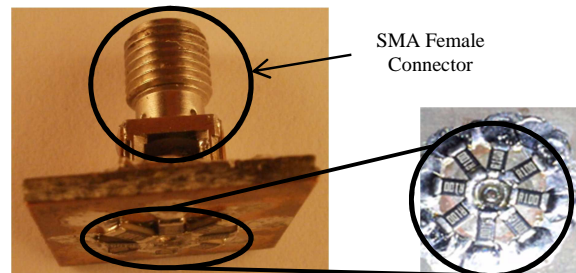


Figure 1: Single SMD resistor current shunt

The environment associated with the single resistor shunt falsifies the measurement. This is because the resistor can be physically small thus allowing one to neglect the electric energy stored, but the magnetic energy stored cannot be neglected because it can also not be defined. The magnetic energy is highly dependent on the associated surroundings of the resistor, how high it is from the PCB and components in close proximity to the resistor. These will all affect the magnetic energy around the resistor. Therefore the reliability of this type of shunt is expected to be low.

3.2 Lateral Shunt

A recent paper introduced an integrated lateral shunt idea [10]. The lateral shunt is claimed to be capable of measuring high frequency switching but is very prone to overshoot in the measurement [10]. This shunt resistor is constructed using thick film metallisation technology [8]. The advantage of this shunt design is its ultra-low profile and low cost. The actual resistance and the resistance measured may vary due to the contact resistance [5].



Radially arranged SMD Resistors

Figure 2: Lateral current shunt resistor

The advantage of this shunt over the single resistor is that it is electromagnetically defined due to its physical construction. The measurement lead is situated inside a field free environment [10].

The disadvantage of this shunt is that although it is electromagnetically defined, the presence of the

electromagnetic stored energy of the shunt still obscures the measurement. The shunt physically resembles a capacitor and will therefore store a large amount of electric energy.

This shunt will also experience time dependent conduction effects. This will greatly affect the wave shape of the measured voltage across the shunt. The way in which the current flows and stabilises itself uniformly through the shunt will affect the measured voltage. The current flows from the centre and uniformly spreads laterally through the resistor layer because of skin effect.

This current spreading takes time and the voltage measured across these resistors will decrease as a function of this skin effect. This was observed as an overshoot in [10]. This time dependent effect will be proven and shown later in this paper.

3.3 Co-axial current shunt

The co-axial shunt structure allows no external interference because of its co-axial structure which completely shields the measurement. The bandwidth and rise time of co-axial shunts are given by how fast the signal can propagate from one end of the shunt to the other and whether the shunt is physically short and thin so as to eliminate skin effects and time dependant effects associated with the stabilization of current density.

In this paper two co-axial shunts will be addressed: a commercial large co-axial shunt; and a miniaturised co-axial shunt that can easily be constructed and integrated into a power electronic converter. It will be shown that the miniaturised shunt performs better than the commercially available shunt and this is because of the length and physical dimensions of the shunt.

The commercial co-axial shunt used is a model 1M-2 by T&M Research Products. This co-axial shunt has a band pass of 200MHz and can measure a 2ns rise time according to [9].



Figure 3: T&M Research Products co-axial current shunt resistor

Simply miniaturising the shunt will reduce the area from which it can dissipate the thermal energy losses, hence lowering the power capability of the shunt. The shunt needs to be miniaturised so that it can be integrated into a PCB of a power electronic converter.

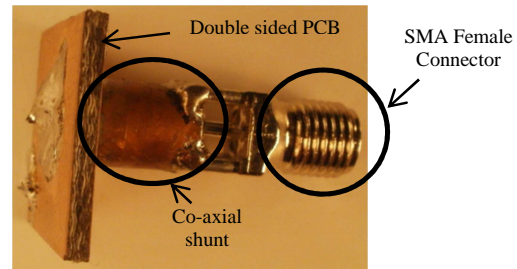


Figure 4: Miniature integrated co-axial current shunt integrated into double layered PCB

Since co-axial shunts generally have high bandwidth capability, a miniaturised co-axial shunt was designed and constructed. The problem with miniaturizing such a technology is the resistive material. Inspired by the lateral shunt, it was decided to use SMD resistors with thick film metallisation technology in a concentric fashion to create the tubular resistive part of the shunt.

4 EXPERIMENTAL WORK

In order to compare the different shunts, each shunt needs to be characterised in the same manner. The same DC response test was repeated on each shunt.

The frequency response of the shunts cannot be determined with a bode plot since bode plots only represent the system response to single sinusoidal frequencies. The intended application for this shunt is for non-sinusoidal converter current waveforms. Hence, an effective and informative test is to apply a step-current to the shunts, and observe their response. The measured rise time across the shunt gives an indication of the bandwidth of the shunt by using the following formula from [10]:

$$f_{BW} = \frac{0.35}{t_{rise}}$$

The problem with using this type of equation is that the shunt response might be limited by the circuit. For instance, if the circuit inductance is larger than the shunt inductance, the measured current rise time will not define the bandwidth of the shunt, rather that of the circuit.

Thus, the wave shape will be analysed to reveal additional information about the shunt performance, what is being measured and any time dependant effects or delays. This step-response test was performed on each of the shunts with the same experimental setup. An EPC 9001 development board, using eGaN FETs, was used.

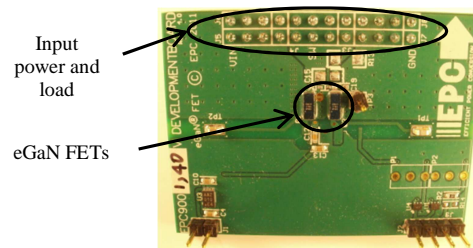


Figure 5: EPC9001 eGaN FET Development board

These eGaN FETs are able to switch within a few nanoseconds. It was assumed that the possible rise time achievable by the development board would be faster than the response of the shunts. The experimental setup layout inductance will affect the current step results. To minimise this effect all connections were made as short as possible and any loop formation is prevented. The current shunt under test was then placed in series with a constructed low inductance resistive load.

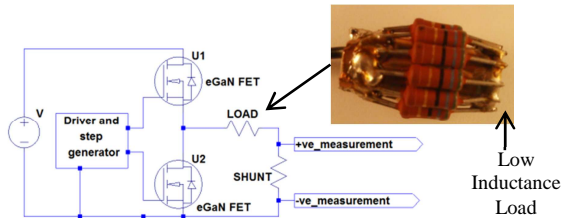


Figure 6: Equivalent circuit schematic of experimental setup and low inductance co-axial load

This load was constructed such that there is uniform current distribution through the load while still maintaining a low inductance. The voltage across the shunt under test was then measured and the waveform analysed. Another quick check is to also measure the voltage applied to the shunt and load. The current cannot rise faster than the voltage because of the unavoidable setup inductance. The measured voltage waveform however contains ringing. The origin of this ringing is a combination of stray flux coupling onto the voltage probe as well as ringing due to circuit inductance and capacitance.

4.1 DC response

Under DC conditions, the response each shunt is as expected. Ohms law holds and the current can easily be measured. The DC test was performed by passing a known DC current of 1A through the shunts respectively and then measuring the voltage across them. Since the application for these shunts is not for DC conditions, this simple DC test is sufficient. These shunts are intended to measure high frequency pulsed DC and switched AC. Therefore a more fitting experiment would be a step-response test.

4.2 Step response

The power circuit was then set up to induce a current step of a few nanoseconds rise time. The current through the resistive load and shunt was then measured using the shunt resistors. A Tektronix DPO7254 oscilloscope was used.

4.2.1 Single resistor

The resistance of the single resistor shunt is 0.1Ω with a power dissipation rating of $0.125W$. The step-response waveform of the voltage measured across the single resistor shunt is shown in Figure 7.

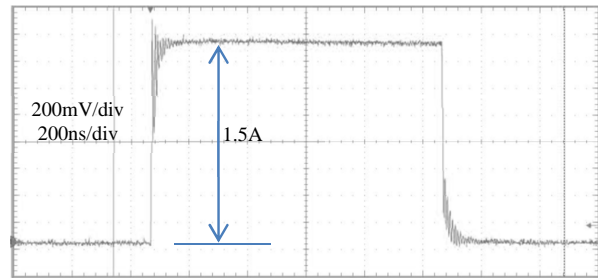


Figure 7: Voltage measured across the single SMD resistor shunt

The measured rise time across the single resistor is $3.65ns$. The voltage measured across the single resistor shunt in Figure 1, clearly contains an overshoot as well as ringing. This ringing can only occur because of a resonating electric and magnetic energy. This energy can cause the measurement to appear to rise faster than the actual current through the shunt (measurement noise). Although this setup should contain very little stored electric energy, the stored magnetic energy around the single resistor and the measurement terminal is highly undefined.

Another disadvantage of the single resistor shunt is its limited power and thermal capability. The chosen resistor needs to be small to avoid time dependant effects such as skin effect through the shunt. In order to measure higher currents, the actual resistor needs to be physically large and this will mean that the electromagnetic energy capacity of the measurement will be larger, which is undesired. A larger size resistor also implies that skin effect will occur. Therefore, the single resistor shunt cannot be used to accurately and reliably measure non-sinusoidal high frequency current.

4.2.2 Lateral Shunt

The resistance of the lateral shunt is $12.5m\Omega$ with a power rating of $2W$. The same step response test was applied to the lateral shunt. The voltage measured across the lateral shunt is shown in Figure 8.

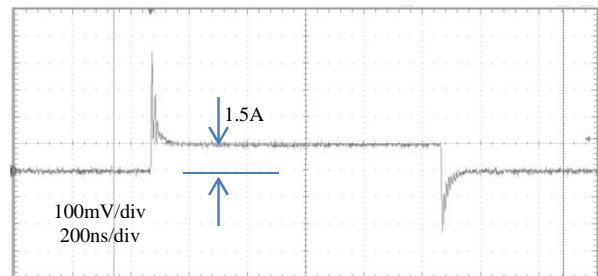


Figure 8: Voltage measured across the lateral shunt resistor

The highly noticeable overshoot in both the switch on and switch off transients already questions the ability of this shunt to measure current. Although there is overshoot, the ringing amplitude is low and therefore negligible. This is

very important because it indicates that the overshoot is due to a time dependant effect.

The way the current flows through the lateral shunt in accordance with the position from where the voltage is measured creates this overshoot. As current enters down the co-axial via it then spreads laterally. The current takes time to spread through the lateral resistor configuration. The potential across the resistor arrangement is initially high, since the current has not yet passed through the resistors, and as the current begins to flow through the resistors, the potential decreases until the current flows uniformly throughout the structure. The inverse happens for the switch off transient. This effect is seen as an overshoot in the measurement.

This is enough reason to suggest that the lateral shunt is not suitable for high frequency switching current measurement. The rise time of the waveform is 126.3ps. This value is not reliable since the waveform that is being measured is not the true representation of the current. A better characterisation of this type of shunt can be done using the methods described in [10].

4.2.3 Co-axial shunt

Neither the single resistor nor the lateral shunts are suitable for high frequency switching current measurement. A common shunt which is used to measure large currents is a coaxial shunt. This type of shunt has a high bandwidth and is also electromagnetically defined. The effects of the time domain characteristics of the co-axial shunt are dependant only on its dimensions. Even then, the response time can be determined. The resistance of the T&M shunt is 10m Ω with a power rating of 20W. The same step- response measurement was taken using a conventional co-axial shunt from T&M Research Products. The step response measurement is shown in Figure 9.

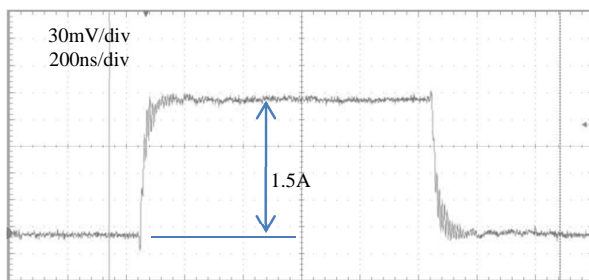


Figure 9: Voltage measured across the T&M co-axial shunt

This shunt is physically much larger than the previous shunts discussed. Yet, unlike both the lateral as well as the single resistor shunt, the co-axial shunt does not show overshoot in the measurement. This is because the measurement is taken in the field free region. This means that the measurement is effectively shielded from any stray electromagnetic fields which can interfere with the measurement. Some ringing is observed in the

measurement. This ringing is due to the complex circuit layout impedance and the load impedance.

The rise time was measured as 20ns. The datasheet for the 1M-2 co-axial model device states that this is a 2ns shunt [12]. So this must mean that the current is limited by the circuit and experimental setup.

Miniaturising the co-axial shunt should yield better results. This is because the current distribution through a physically smaller co-axial shunt will reach a uniform value much quicker. To prove this, a miniaturised shunt is discussed next.

4.2.4 Miniature co-axial shunt

A miniature co-axial shunt, in Figure 4, was constructed using SMD resistors. The resistors were used to create the co-axial resistive part of a co-axial shunt. The miniature co-axial shunt has a power rating of 1.5W and has a resistance of 16m Ω . The same step-response experiment was done with this particular shunt and the result is shown in Figure 10.

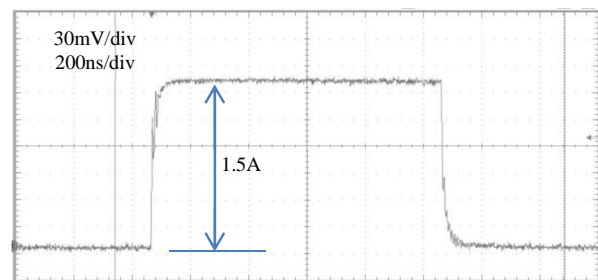


Figure 10: Voltage measured across the miniaturised co-axial shunt

Similar to the co-axial shunt, the miniaturized version also measures no overshoot in the measurement for the same reason. Initially, because of the discrete resistors, it was suspected that stray fields could penetrate the gaps between the discrete resistors and induce a voltage on the measurement lead in the field free region, but it is not the case. This is evidence that this shunt introduces a lower series inductance to the circuit. The rise time of this shunt was measured to be 14.45ns as in Figure 10.

The miniature coaxial shunt seems to have the best performance. The ringing noise in the measurement is reduced in the miniature shunt. This is simply because the current measurement lead is measured in a field free region.

5 FUTURE WORK

The results are not yet satisfactory due to the uncertainty and therefore require more work. Alternative methods of characterising the various current shunts are being investigated to verify the results presented in this paper.

Simulating the different shunts in a FEM package will also reveal any time dependant effects. The thermal aspects can also be simulated and will be investigated in an experimental setup as well. The equivalent circuit and

theoretical inherent parasitic elements of the various current shunts are also being considered. The equivalent-circuit impedance can also be used to verify the measured characteristics. Implementing the miniature integrated shunt into a HF and possibly RF switching power electronic converter circuit using GaN power transistors is also being looked into.

6 CONCLUSION

It is important to make current shunts that are electromagnetically small for integration in future high frequency switching power electronic converters. This means that the stored energy of the shunt should be small in both electric and magnetic energy. Simply making a shunt physically small does not mean that it is electromagnetically small. This is clearly shown with the lateral shunt design as well as with the single SMD resistor measurements presented in this paper.

The GaN based transistors are very small devices. The sizes of the integrated measurement instruments are much larger in comparison to the transistors as is shown in Figure 11. This means the measurements will always be prone to measurement noise as well as influence the circuit unless precautions are taken. Circuit layout and the insertion impedance of an integrated measurement device can and will alter the circuit drastically especially since the switching devices are so small and their fast switching ability.

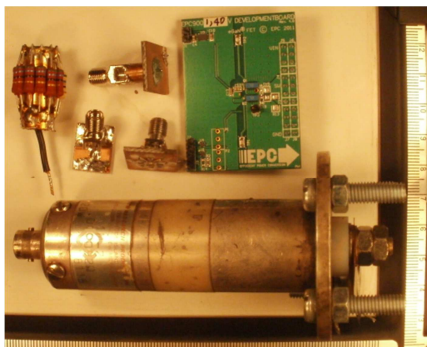


Figure 11: Image indicating relative size of components used

This paper shows that current measurement is a real challenge in future power electronic converters. The various current sensor methods discussed in this paper are low cost and can integrate easily into high frequency PCB designs. Current shunt measurement methods have been neglected in recent years mainly due to the development of alternative current measurement techniques such as hall sensor based technologies. As discovered in this paper, although most shunts have a good response at lower switching frequencies, the co-axial shunts have the best and most accurate performance. The co-axial current shunt design is low cost and easy to integrate into HF power electronic circuits. The co-axial current shunts also indicate that this type of integrated shunt is capable of measuring rise and fall times of a few nanoseconds.

7 REFERENCES

- [1] Nando Kaminski and Oliver Hilt, "SiC and GaN devices- competition or coexistence?," in *International Conference on Integrated Power Electronics Systems (CIPS)*, Nuremburg, 2012.
- [2] Alex Lidow, "Is it the end of the road for silicon in power conversion?," in *CIPS*, Nuremburg, 2010.
- [3] Howard Johnson and Martin Graham, *High-speed digital design a handbook of black magic*. New Jersey, United states of america: Prentice Hall, 1993.
- [4] E R Olson and R D Lorenz, "Integrating giant magnetoresistive current and thermal sensors in power electronic modules," in *IEEE-Applied power electronics conference and exposition (APEC)*, 2003, pp. 773-777.
- [5] Kuo-Hsing Cheng, Chia-Wei Su, and Hsin-Hsin Ko, "A high-accuracy and high-efficiency on-chip current sensing for current mode control CMOS DC-DC buck converter," in *IEEE-Electronics circuits and systems (ICECS)*, 2008, pp. 458-461.
- [6] Wolfgang Pfeiffer, "Ultra-high speed methods of measurement for the investigation of breakdown development in gasses," *IEEE transactions on instrumentation and emasurement*, vol. IM-26, no. 4, pp. 367-372, December 1977.
- [7] Alex Lidow. (2011) EPC Efficient Power Conversion. [Online]. <http://www.epc-co.com>
- [8] J A Ferreira, W A Cronje, and W A Relihan, "Integration of high frequency current shunts in power electronic circuits," in *IEEE Power electronics specialists conference (PESC)*, Toledo, Spain, 1992, pp. 1284-1290.
- [9] Yen-Chih Huang, Hsieh-Hung Hsieh, and Liang-Hung Lu, "A low noise amplifier with integrated current and power sensors for RF and BIST applications," in *IEEE-VLSI Test Symposium*, 2007, pp. 401-408.
- [10] A LJ Joannou and D C Pentz, "Miniature integrated co-axial current shunt for high frequency switching power electronics," in *South African Universities Power Engineering Conference (SAUPEC)*, Potchefstroom, 2013, pp. 140-145.
- [11] Chucheng Xiao, Lingyin Zhao, Tadashi Asada, W G Odendaal, and J D van Wyk, "An overview of integratable current sensor technologies," *IEEE-IAS*, 2003.
- [12] T&M Research Products. T&M RESEARCH PRODUCTS. [Online]. <http://www.tandmresearch.com/>
- [13] H Johnson and M Graham, *High-Speed Digital Design A Handbook of Black Magic*. New Jersey, United States of America: Prentice Hall, 1993.

REDUCTION IN EMI FOR AN LED BUCK CONVERTER

L.L.T. Lam* A.S. de Beer**

Group on Electronic Energy Processing (GEEP), Dept. of Electrical and Electronic Engineering Science, Corner of University Road and Kingsway Road, University of Johannesburg, Johannesburg 2006, South Africa E-mail: lusion2000@hotmail.com asdebeer@uj.ac.za***

Abstract: Light emitting diodes (LED) are becoming a popular choice in lighting because of its relatively low electrical power consumption. LEDs require converters to operate. In this conversion process two by-products are produced. Heat and electrical noise. Only the electrical noise will be discussed. This electrical noise is the electromagnetic interference (EMI) that causes interference with other electrical systems. A LED converter was chosen to reduce its EMI by changing the circuit board layout.

Keywords: LED converters, EMI, PCB layout

1. INTRODUCTION

The use of incandescent, florescent and halogen lights are slowly fading away. This is due to the high power consumption of these lights. LED lights are well known for their low power consumption properties [1]. The low power consumptions of LEDs encouraged the development of good LED power converters. The development of efficient converters allows for more control of the current to power the LEDs.

The physical size of LED converters have gradually reduced due to an increase in operating frequency. This has allowed the energy storage components on the converter to be smaller in size. This paper will focus on converters that use through-hole components. This is because using surface mount device (SMD) components already reduces the EMI [2]. But to see a more visible effect on the EMI, through-hole components were used. To keep the converter as small as possible, the arrangement of the components on the board needed to be considered. This was to keep the size of the LED converter to be as small as possible and to keep the EMI to a minimum.

LED converters are usually designed and built without inspecting the EMI. Add-on filters are typically installed after the devices are built if the devices generate EMI [3]. By adding filters onto devices, this makes the final product bulky. Therefore it is best to minimise the conducted EMI in the design phase before building. To reduce EMI, one technique is to localise all the high power switching at a specific area of the converter [4]. It also helps the reduction of the conducted EMI by keeping all the components as close as possible to one another [5].

The standard design of LED converters requires power switching to regulate current to power LEDs. The phenomena of conducted EMI occur during power switching. This noise mainly occur or have a larger affect during high frequency switching with fast rise and fall times. Therefore, all converters that require switching

will generate EMI. Only the conducted EMI will be discussed in this paper.

Two LED converters were tested. The first was a commercial LED converter used as a reference and the second converter, which was a rebuilt LED converter.

2. STANDARDS

Measuring EMI is important for power converters because these converters can interfere with other circuitry that are connected around them. To control this behaviour of conducted EMI, one can follow the CISPR 22 standard. The CISPR 22 standard is to monitor the amount of conducted EMI that a converter produce. Figure 1 shows the CISPR 22 standard where the class B line is of interest. Class B is the electromagnetic compatibility for generic standards or emission standard for residential, commercial and light-industrial environments [6].

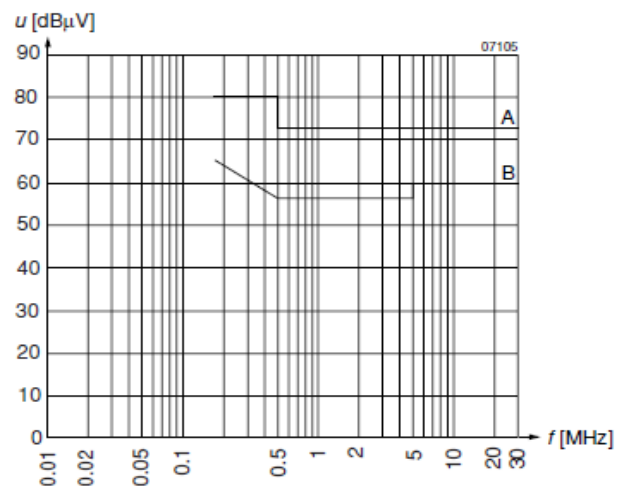


Figure 1: Disturbance voltage limits (quasi-peak) according to CISPR 11/EN55011 and CISPR 22/EN55022 [6].

Conducted EMI consists of two types or modes. These two types are the common mode (CM) noise and the differential mode (DM) noise, as demonstrated in Figure 2. CM noise is the conducted current that travels on all the power lines in the same direction. DM noise flows through the one power line and back along the other line [7]. The combination of the two types is called the total EMI. A common device used to measure EMI is a line impedance stabilisation network (LISN).

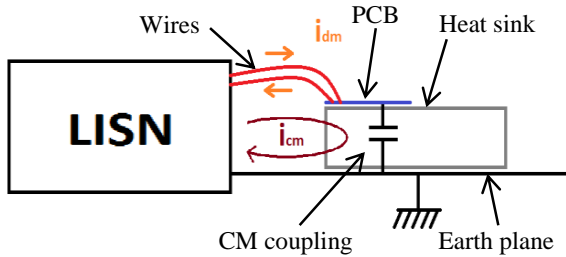


Figure 2: Experimental setup CM & DM noise paths.

The purpose of the experiment was to measure the change in EMI of the different layout LED converters. At the same time, the CISPR 22 standard was used as a guideline to ensure its compliance because all electrical devices need to comply with CISPR standards.

3. EMI REDUCTION

The objectives that were aimed for during the rebuilding of the LED converter are as follows:

- Keep printed circuit board (PCB) physical size as small as possible
- Maintain the same operation as the commercial LED converter
- Use the same components throughout the converter
- Reduce EMI from PCB layout

There are many techniques to reduce conducted EMI. One way is to arrange the components in the circuit so that the components are close to one another and to keep the track length to a minimum [8].

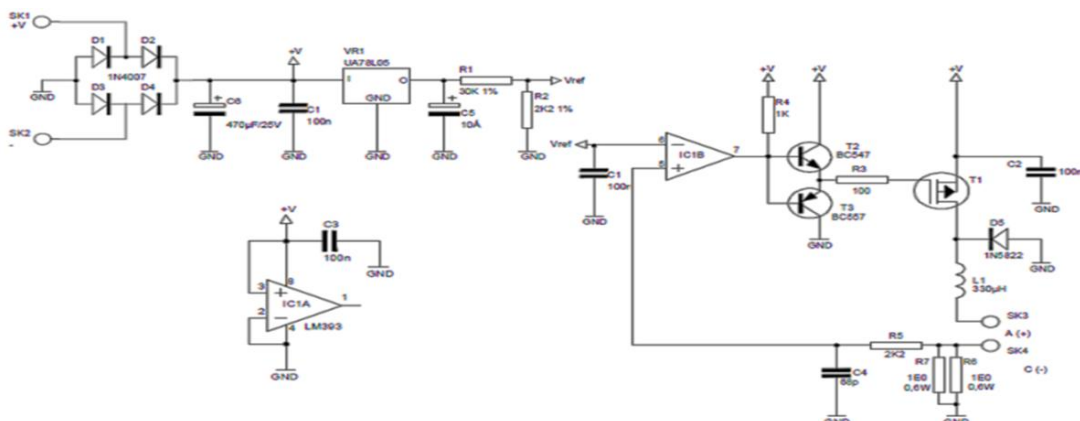


Figure 3: LED Converter Schematic [9]

As mentioned before, the technique of localising all the high power switching at an area of the converter can minimise EMI [4]. By localising all the high power switching parts of the circuit into a smaller area, reduces the amount of DM noise converted to CM noise. Additionally, the smaller area will reduce CM coupling.

To measure EMI accurately, one needs to place the equipment under test (EUT) in the same physical position every time the measurement is taken. Hence, when a different EUT is being measured, the EUT must be placed at exactly the same position as the one before. Even the leads or the wire leads must be in a fixed position. By doing so, this will minimise the undesirable change in results from the different EUT. The undesirable change is caused by the differences in CM coupling.

4. LED POWER CONVERTER

A commercial LED converter kit was chosen for testing as a reference to the new board that will be rebuilt. The chosen converter was a Velleman kit, as shown in Figure 4. This kit requires the user to build or solder the components onto the PCB.



Figure 4: Velleman LED converter [9]

4.1 LED Converter Specification

- Output: 350mA constant current
- Input voltage: 6 – 12 V AC / 9 – 18V DC
- Dimensions: 45x30x16mm

This buck converter kit contains a full wave rectifier (for AC input), a regulator which was used for a reference voltage for the comparator, a comparator for feedback and a transistor driver.

4.2 Operation

In reference to Figure 3, the way this converter operates is mainly dependent on the switching of the buck converter to maintain constant current. This converter can be powered by alternating current (AC) or direct current (DC). The full wave rectifier is used primarily for the AC input to convert the input to DC. The MOSFET that is used in the buck converter is a p-channel enhancement mode MOSFET. The load is attached on the output side of the buck converter and the comparator measures the output current for the feedback. The feedback is used to control the switching frequency.

The converter only operates when there is a load. If the current through the load is greater than a specific threshold of 350mA, the comparator output goes high and will start switching the p-type MOSFET.

4.3 Design Layout

There are a few features in the commercial board layout that needs to be kept in mind.

- Components on the PCB are placed vertically and horizontally.
- It is single-sided with no polygon pours/planes or copper pours/planes

4.4 LED Load

The circuit's load consists of 3 Cree LEDs mounted on insulated metallic substrate (IMS) PCB. These same LEDs were used throughout the experiment, as shown in Figure 5.

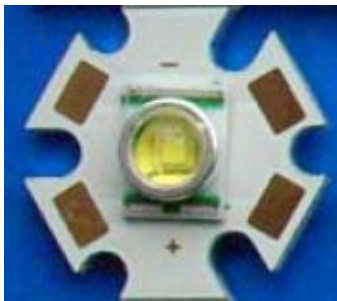


Figure 5: Cree LED [10]

5. LAYOUT DESIGN

5.1 New PCB Design Layout

In the new design, the two main changes to the commercial board are the component layout and track layout. The high power switching section of the circuit and the buck converter were placed close to one another. This is to reduce the inductance loop and current path of the high frequency switching. In addition, the high power track sizes were made wider than the rest of the circuit. The signal power switching section of the circuit was kept as close as possible together and the tracks were also kept close to each other.

Double-sided unplated Flame Retardant 4 (FR4) boards were used in the new design. This allows for a better layout compared to the single layer PCB (used in the commercial board) where there were no looping of tracks around the PCB.

Copper pours/planes were used on the new board design. The top layer copper pour was the ground plane and bottom layer copper pour was the positive supply voltage +VCC. There are pros and cons for using copper pours for this specific design, the pros are:

- Creation of a decoupling capacitor
- Even spread of current over the copper pour
- Reduction in the number of tracks

And cons are:

- Ground plane coupling onto earth plane increasing CM noise (shown in Figure 2)
- Change in circuit impedance due to the change in copper pours, leads to unfair comparison.

Copper pours were used while taking the coupling issue into consideration. The planes were therefore placed as far as possible from the earth plane.

5.2 New Design

This paper consider two LED converter boards, a commercial LED converter (Com.B) and a rebuilt LED converter (Reb.B)

The new design board in Figure 6 is the rebuilt board with all resistor and diode components positioned horizontally on the PCB. This made the physical PCB size of Reb.B slightly larger (40x48x20mm) than the commercial board. Nonetheless, the track and components layout on the Reb.B have been shortened and positioned closer respectively.

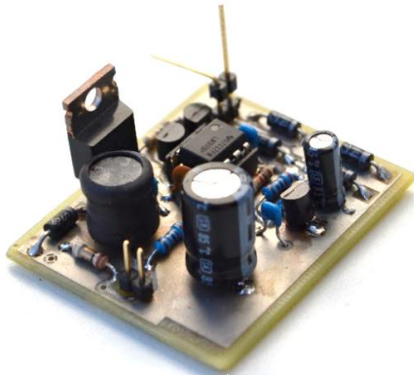


Figure 6: Rebuilt board (Reb.B)

6. EXPERIMENTAL WORK

6.1 Experimental Setup

The equipment that was used in this experiment included a DC power supply; a spectrum analyser; LISN and a CM and DM splitter. All measurements were taken over an earthed copper sheet.

Figure 7 shows how the experimental setup was connected. To measure the total EMI, the CM/DM splitter was removed and the spectrum analyser (SA) was connected to the LISN directly.

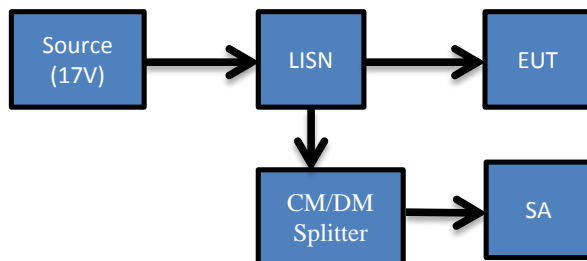


Figure 7: Setup block diagram

The voltage source was set to constant 17V DC because the buck converter will only start switching at a high input voltage. The specified input voltage for this LED converter is between 9 – 18V DC, therefore 17V DC was chosen and leaving 1V as safety factor. In addition, the 17V DC was chosen for the reason that it was noticed the EMI was at its maximum around 17V – 18V DC.

The spectrum analyser was set to the following:

- Resolution Bandwidth : 10kHz
- Video Bandwidth: 10kHz

- Sweep Time : 1.5s
- Trace Mode : Max Hold
- Noise Range : 10dB μ V – 85dB μ V
- Frequency : 100kHz – 30MHz

6.2 Equipment Under Test

EMI changes when a device is tested under different conditions. To get fair and accurate measurements, the LED converter that was under test was mounted onto the heat sink. The purpose of the heat sink was to cool down the LEDs that act as the load. The LED converters were tested one at a time and they were placed at the same position on the heat sink for consistency. The entire setup of the converter and heat sink were placed on a copper plane that was grounded to earth. The heat sink was placed at a fixed position for fair measurements. This setup is shown in Figure 8.

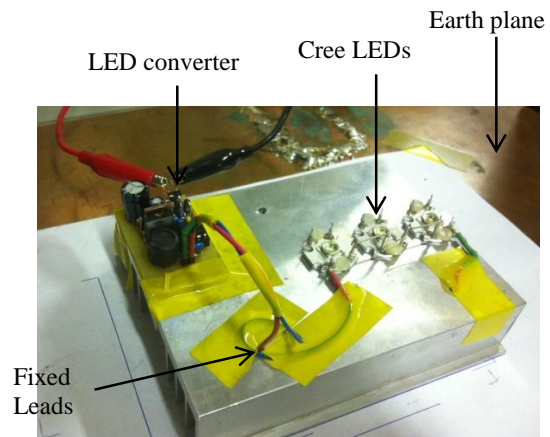


Figure 8: Converter and 3 Cree LEDs

7. RESULTS

Figure 9 shows the total EMI of the two LED converter boards that were tested. It can be seen that the Com.B and Reb.B have the same switching frequency of 250kHz. It was noticed that the total EMI of the Reb.B was below Com.B EMI.

Looking at the conducted EMI separately to the total EMI, the CM noise and the DM noise are analysed individually.

Figure 10 shows a greater degree of CM noise being reduced. An overall of 4.2dB μ V of CM noise was reduced from the Com.B to the Reb.B.

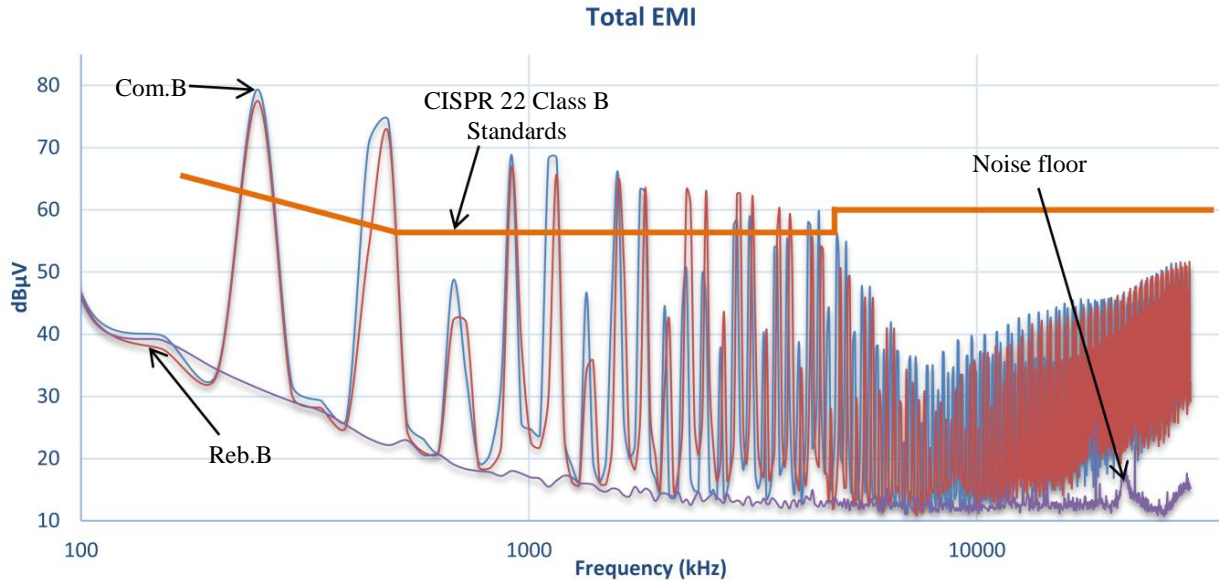


Figure 9: Total conducted EMI for the Com.B and Reb.B

These findings are significant, showing that by rearranging components on the PCB, can affect the CM noise. This was because the Reb.B had a better coupling from the board to the earth plane. Hence, less coupling improves CM noise.

In terms of the DM noise, Figure 11, the spectrum gives a good indication that the DM noise does not change for Com.B and Reb.B. This was understandable because the operation of the circuit has not changed and DM is mainly influenced by circuit operation.

In Figure 9, the CISPR 22 standards is compared to the total EMI. It is clear that the Com.B, commercial LED converter, was not within the CISPR 22 class B standard. Although the Reb.B was also not within standard, the results show that there was still a decrease in EMI compared to Com.B.

By measuring the lower frequency range between 100kHz to 4MHz, it was found that these LED converters CM noise was dominated by DM noise. CM noise was dominant at the higher frequency range from 4MHz to 30MHz.

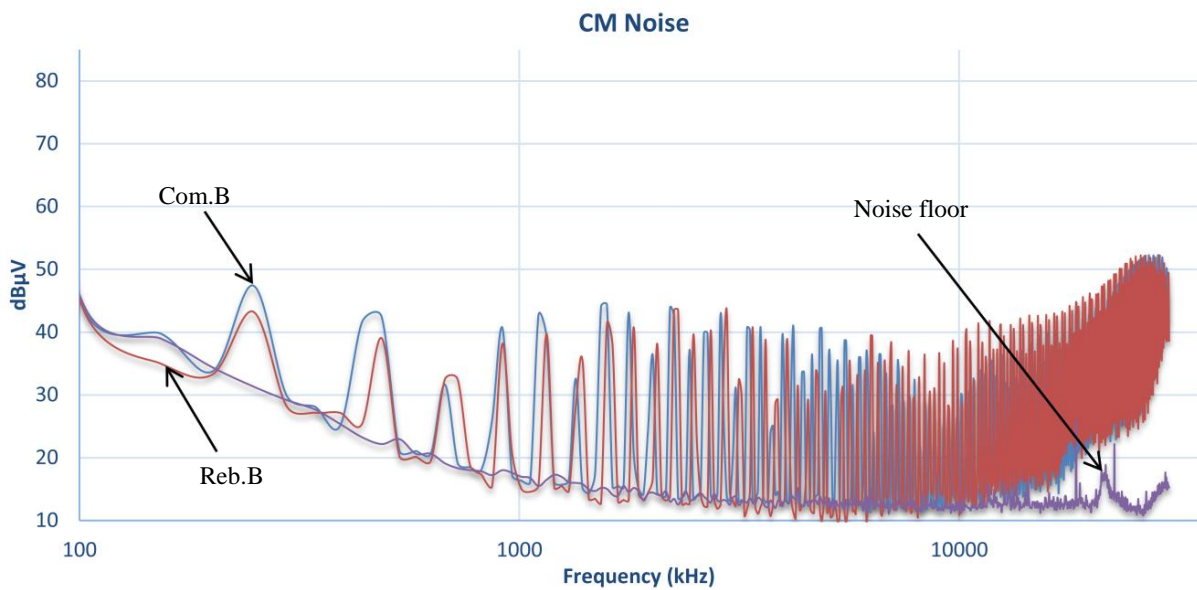


Figure 10: CM noise for the Com.B and Reb.B

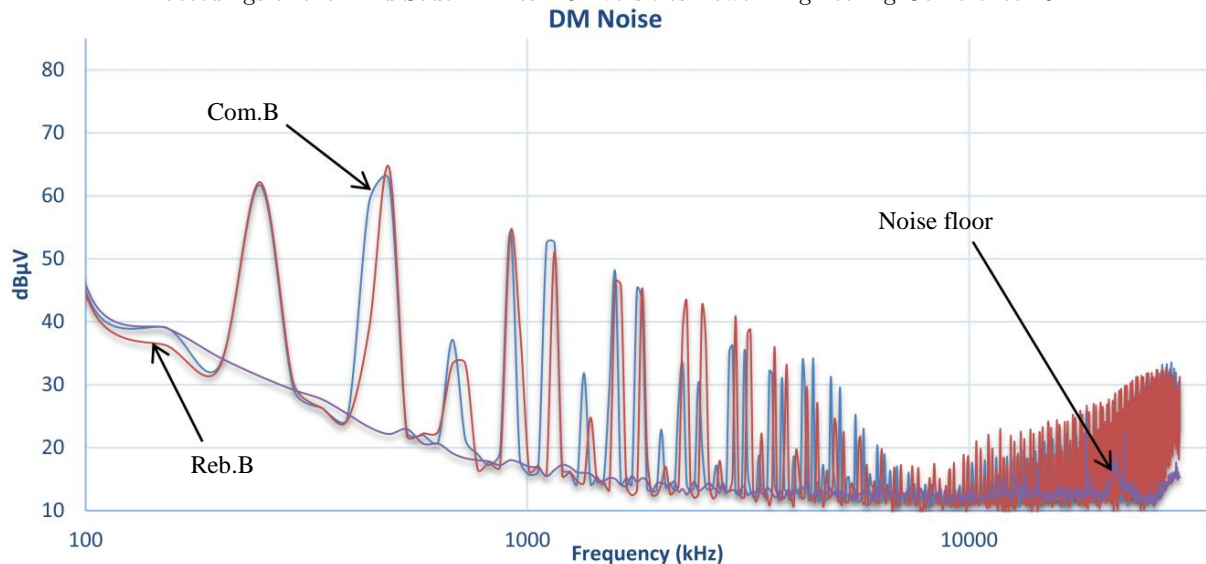


Figure 11: DM noise for the Com.B and Reb.B

8. CONCLUSION

Rearranging the component layout and minimising the track length on a PCB can reduce EMI. The total EMI was reduced to a level of 2dBμV for the changes that were implemented for the new design. The CM noise was reduced around 4.2dBμV. CM noise reduced the most compared to the DM noise.

It would therefore be beneficial to integrate this method while designing the circuit on a PCB to get minimal EMI from the circuit board. This can save time and costs if one needs to spend time to locate the origin of the EMI. This will also help the amount of additional bulky filters that would have been added onto the circuit to reduce EMI.

9. ACKNOWLEDGEMENT

I would like to thank Dr D.C. Pentz and A.L.J. Joannou from the University of Johannesburg for their assistance in measurements and guidance.

10. REFERENCE

- [1] Y. Uhm, I. Hong, G. Kim, B. Lee, and S. Park, "Design and implementation of power-aware LED light enabler with location-aware adaptive middleware and context-aware user pattern," *Consumer Electronics, IEEE Transactions on*, vol. 56, no. 1, pp. 231-239, February 2010.
- [2] B. Pejcinovic, V. Ceperic, A. Baric, "Design and Use of FR-4 CBCPW Lines In Test Fixtures for SMD Components," *Electronics, Circuits and Systems, 2007. ICECS 2007. 14th IEEE International Conference on*, vol., no., pp.375,378, 11-14 Dec. 2007.
- [3] H. W. Ott., *Noise reduction techniques in electronic systems, Second Edition*. New York: John Wiley and Sons, 1988 ch. 1, p. 5.
- [4] A. J. Sinclair, J. A. Ferreira, and J. D. Van Wyk. "A systematic study of EMI reduction by physical converter layout and suppressive circuits." In *Industrial Electronics, Control, and Instrumentation, 1993. Proceedings of the IECON'93., International Conference on*, pp. 1059-1064. IEEE, 1993.
- [5] A. Bhargava, D. Pommerenke, K. W. Kam, F. Centola, C. W. Lam, "DC-DC Buck Converter EMI Reduction Using PCB Layout Modification," *Electromagnetic Compatibility, IEEE Transactions on*, vol.53, no.3, pp.806,813, Aug. 2011.
- [6] Electromagnetic Compatibility, "Information technology equipment, Radio disturbance characteristics - Limits and methods of measurement," CISPR 22, 2008
- [7] T. Guo, D. Y. Chen, F. C. Lee, "Separation of the common-mode- and differential-mode-conducted EMI noise," *Power Electronics, IEEE Transactions on*, vol.11, no.3, pp.480,488, May 1996.
- [8] K. Mainali and R. Oruganti, "Conducted EMI mitigation techniques for switch-mode power converters: A survey," *Power Electronics, IEEE Transactions on*, vol. 25, no. 9. IEEE, pp. 2344–2356, 2010.
- [9] NV Velleman, *1W / 3W Power LED Driver Manual*, Velleman-kit, 2006.[Online]. http://www.velleman.eu/downloads/0/illustrated/illustrated_assembly_manual_k8071_rev1.pdf
- [10] Cree.Inc, "Cree MCE Mounted on a Star MCPCB," MCE4WT-xxxxxx-MCSTAR datacheet, Jan 2008 [Revised Nov. 2013] <http://docs-europe.electrocomponents.com/webdocs/10b0/0900766b810b034a.pdf>

HIGH BANDWIDTH HIGH POWER INVERTER FOR FACT DEVICES

M.Looi*

* Faculty of Engineering and the Built Environment, School of Electrical and Information Engineering, Private Bag 3, Wits 2050, South Africa E-mail: b.lacquet@ee.wits.ac.za

Abstract: This paper compares the performance of a 2 level and 3 level inverter, in terms of the frequency response and total harmonic distortion. The inverters are analysed using three techniques. The analytical model is based on the double Fourier series, the simulation model uses Simulink Simscape blocks, and the measured model is built using analog comparators and Mosfets. The models are tested at a lower power rating of 9W, compared to the expected power rating of 1 kW for flexible AC transmission systems. The analytical model is validated, as the Fourier series of the analytical model corresponds to the measured fast Fourier transform. The 3 level inverter has not yet been implemented, however from the comparison of the 2 and 3 level analytical model there is a 34.14% decrease in cut-off frequency of the filter. The building of a 3 level inverter, the increase to a 1 kW power rating and the expansion to a more voltage levels is left as future work.

Key words: Inverter, Double Fourier Series, Multilevel, Bandwidth

1. INTRODUCTION

Multilevel converters have become the enabling technology for many industrial applications, ranging from power systems, energy conversions and automotive applications [1] [2]. Multilevel converters falls under the category of power electronics and is implemented for the conversion of DC to AC voltages, with a advantage in power capabilities (the distribution of power amongst several semiconductor devices) and the quality of output waveform (in-terms of its spectral components) [3] [4].

The bandwidth of a converter is defined by output filter, which is used to eliminate the unwanted high frequency harmonics of the output. Multilevel converters have the potential to effectively increase the output bandwidth, by reducing the lower order harmonics, without increasing the individual switching frequency of the semiconductors. The operation of the semiconductors at a lower switching frequency allows the converter to be utilised at higher power levels.

The improvement in bandwidth is beneficial as it results in a decrease in output filter requirements, allowing the passive components of the converter to be smaller, more efficient and more cost effective. There are numerous applications where a high bandwidth output is necessary such as magnetic resonance imaging, audio amplifiers and Flexible AC Transmission Systems (FACTS) [5] [6] [7].

FACTS is an emerging technology, which allows the control of the flow power and to better utilise the transmission capacity, in terms of its thermal limits, within a power network [8]. FACTS devices can be incorporated in a variety of systems such as centralised generation, to distributed energy generation and to microgrids. FACTS devices require a higher bandwidth to improve the dynamic response to disturbances of various frequencies [9].

The drawbacks of a multilevel is the increase in complexity. With the increased number of semiconductors there is a increase in complexity in the modulation scheme and an increase in converter design parameters, both of which has an influence on the bandwidth performance of the converter. It is therefore a challenge to correlate the bandwidth performance and the design of a multilevel converter [10], and even Pulse Width Modulation converters [11] [12]. Some analysis techniques to determine the frequency response of a multilevel converter output include the fast Fourier transform and the double Fourier analysis [13].

This paper is an on going research, which aims to answer the following research question:

“Is multi-level technology the enabler for high-bandwidth high-power inverters for flexible AC transmission systems?”

To create a baseline with the simplest solution, a 2 level inverter and 3 level inverter are compared by their analytical, simulation and measurement results. In Section 2, the components of the inverters are discussed and the various methodologies for achieving the analytical, simulation and measurement results are described. In Section 3 the results are presented and discussed. Finally, the future work for the research is described.

2. SYSTEM DESIGN

A typical system for an inverter consists of the modulation, inverter and the output filter. The system is shown in Figure 1.



Figure 1: System Overview

The chosen modulation scheme is the dual edge natural pulse width modulation. This scheme is implemented with analog control, in the form of signal generators and comparators. This modulation scheme is chosen for its simplicity and commonly used to understand the mechanisms of PWM.

A full bridge, or H-bridge, inverter consisting of 4 semiconductor switches is used. This topology is for its capability of both 2 and 3 level voltage output. In FACT devices, the output filter is typically a second order low pass filter, which is implemented with passive components.

The various sub-systems for the analytical, simulation and measurements are implemented and tabulated in Table 1. It is also highlighted that the 3 level for the measurement setup has not been implemented.

Table 1: Sub-system Implementation

	Modulation	Inverter	Filter
Analytical	-	2, 3 Level	2 nd Order LPF
Simulated	2, 3 Level	2, 3 Level	2 nd Order LPF
Measured	2 Level	2 Level	-

2.1 Power Specifications

The specifications for the various sub-systems remain constant for all the analytical, simulation and measurement setup. In Table 2, the specification of the modulation scheme is described.

Table 2: Modulation Specifications

Parameter	Value
Modulation Depth	0.8
$f_{carrier}$	50 kHz
$f_{modulated}$	1 kHz

For the intended application as a FACT device, the inverter would require a DC voltage of 300 V with a power rating of 1 kW. This specification is achievable, however it may introduced complexity in terms of the inverters thermal limits and electromagnetic interference. Therefore, for baseline results a lower power rating is chosen at 9W and would be increased to the full rating of the FACT device. The comparison of the power ratings are highlighted in table 3.

Table 3: Comparison of FACT and testing power level

Parameter	FACT Device	Initial Testing
$V_{dc}(V)$	300	30
$P_o(W)$	1k	9

2.2 Analytical

The two level and three level inverters are analysed using technique known as Bennet's double Fourier series, which is introduced in general in [13] [14]. This analytical technique will later be applied to multilevel, which is described more specifically in [15] [16] [17]. The analysis provides a link between the multilevel design parameters, such as number of levels or switching frequency, to the output frequency spectrum. The benefits of the double Fourier series, is form of the results which separates the contribution of the modulated signal, the carrier signal, and the side-band harmonics which are by-products of the modulation.

The elementary square of the double Fourier series provides a convenient method to describe the modulation scheme in a form of a graphic. The elementary square helps identify the number of levels and the limits of integration for calculating the coefficients of the double Fourier series. The downfall, is the increase of mathematical effort with the increase in modulation complexity such as uniform modulation or increasing the number of levels to a multilevel inverter.

Figure 2 shows the elementary squares for both the 2 and 3 level inverter, with dual edge natural PWM and phase opposition PWM respectively.

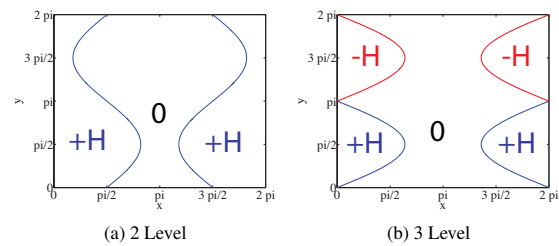


Figure 2: Elementary Square Diagrams

The time domain solution for the 2 level inverter is described in Equation 1. There are 4 terms in the equation, which represents the modulated signal, the carrier signal and the last two terms represent the sideband harmonics.

$$\begin{aligned}
 f(t) = & \frac{2HQ}{\pi} \sin(w_m t) \\
 & + \sum_{m=1}^{\infty} \frac{4H}{\pi m} J_0(mQ) \sin\left(m\frac{\pi}{2}\right) \cos(mw_c t) \\
 & + \sum_{m=1}^{\infty} \sum_{n=\pm 1, n=odd}^{\infty} \frac{4H}{\pi m} J_n(mQ) \cos\left(m\frac{\pi}{2}\right) \sin(mw_c t + nw_m t) \\
 & + \sum_{m=1}^{\infty} \sum_{n=-\pm 1, n=even}^{\infty} \frac{4H}{\pi m} J_n(mQ) \sin\left(m\frac{\pi}{2}\right) \cos(mw_c t + nw_m t)
 \end{aligned} \quad (1)$$

Equation 2 described the time domain solution for the 3 level inverter. The 3 level inverter has a smaller equation, as the carrier signal has no contribution.

$$\begin{aligned}
 f(t) = & MQ \sin(w_m t) \\
 & + \sum_{m=1}^{\infty} \sum_{n=\pm 1, n=odd}^{\infty} \frac{2H}{\pi m} J_n(mQ) \sin(mw_c t + nw_m t)
 \end{aligned} \quad (2)$$

Since these components are in terms of sines and cosines, it also represents the frequency response. A useful indication to validate the solution is to plot the time domain solution. Figure 3 is the time domain plot for the 2 level and Figure 4 for the 3 level.

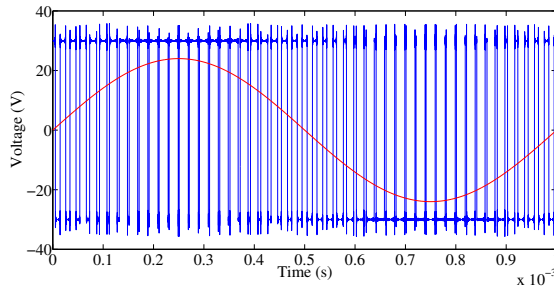


Figure 3: 2 Level Time Domain Plot

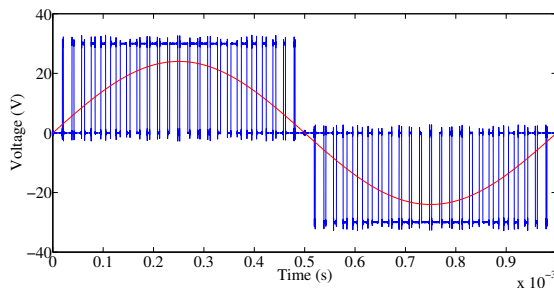


Figure 4: 3 Level Time Domain Plot

The analytical solution requires for the coefficient number

(m and n) to tend to ∞ . The computation restraint, made the computation of the 100th m and n coefficient. As seen in figure 3 and 4, a perfect square wave is not formed and higher frequencies is required. However, for the frequency representation the 100th m and n coefficient is adequate, as more emphasis is placed on the lower order harmonics.

2.3 Simulation

The simulation of the 2 and 3 Level is carried out with Matlab and Simulink. The Simscape toolbox is used, with Simpower System components. The solver for Simulink is set to discrete at a sampling frequency of 10MHz. A zero order hold simulink block is added to represent the lower sampling frequency of the digital oscilloscope. The switches of the semiconductors are left as ideal switches to reduce the complexity of the results.

2.4 Measurement

The components for the 2 Level inverter is tabulated in Table 4. The IR740 Mosfet power capability is rated for FACT devices, table 3. Two signal generators are used for the sinusoidal modulated signal and the triangular carrier signal.

Table 4: List of Components

Components	Part No
Modulator	
Comparator IC	LM311
Not Gate IC	HD74LS04P
Inverter	
Mosfet	IR740
Gate Driver	IR2113

The output waveforms are measured with a digital oscilloscope, which have a trade-off between the record detail, the sampling frequency, and the record length, the total duration of the waveform.

A Tektronix TDS 2002B with a 2.5k sample storage is used. A record length of 2.5ms is chosen to measure two and a half cycles of the 1kHz PWM signal, resulting in a sampling frequency of 1MHz.

To calculate the frequency response, the Fast Fourier Transform is performed on the time domain waveform using Matlab. The waveform is zero-padded to increase the resolution of the frequency to ensure more correct results.

3. RESULTS AND DISCUSSION

From Table 1, the results from the various sub-systems are presented and discussed.

3.1 Comparison of Analytical and Measured Results

The results of the analytical and measured results of the 2 level inverter is shown in Figure 5, where the

blue dots is the analytical and the solid red line is the measured. The magnitudes of the frequency response between the analytical and measured cannot be directly compared as one is a Fourier series and the other is the Fourier transform. However, as a general comparison, both frequency response have harmonics at the same frequencies. This indicates that the double Fourier is accurate for the 2 level inverter.

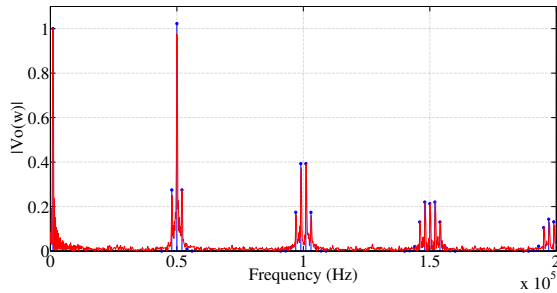


Figure 5: Analytical and Measured 2 Level

3.2 Comparison of Analytical and Simulation

The results of the analytical and simulation results of the 2 level inverter is shown in Figure 6, where the blue dots indicated the analytical and the green solid line represents the simulation frequency response. From the comparison, the analytical and simulation are in agreement in terms of the frequencies of the harmonics and the magnitude. This results indicate that the simulation model is as accurate as the analytical model.

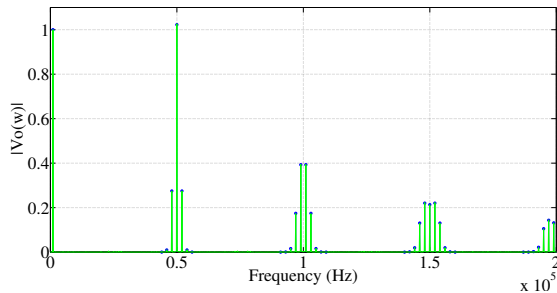


Figure 6: Analytical and Simulated 2 Level

3.3 Comparison 2 Level and 3 Level

The comparison of the 2 level analytical and 3 level analytical results is shown in Figure 7. The reduction in terms of the time domain solutions are highlighted in the frequency response. The 3 level inverter does contain greater sideband harmonics around the first carrier harmonic, however the first carrier harmonic is not present. This result does imply that the three level inverter has an improvement in bandwidth as the largest unwanted harmonic is no longer present. However, the total

harmonic distortion (THD) or other performance index can be used to better quantify the performance of the frequency response as a whole.

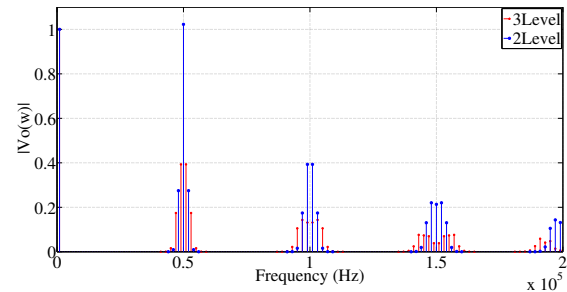


Figure 7: 2 Level vs 3 Level Comparison

3.4 Output Filter

The THD is used as the performance index to compare the performance between inverters. The THD of the output voltage is labelled as the THD before the filter, whilst THD after filter is the distortion calculated on the voltage across the load. The results are tabulated in Table 5.

Table 5: Reduction of Output Filter

	THD before Filter	$f_{cut}(Hz)$	THD after Filter
2 Level			
Analytical	145.31 %	8230	3 %
Simulated	146.16 %	8180	3 %
Measured	155.40 %	-	-
3 Level			
Analytical	76.69 %	11040	3 %
Simulated	77 %	11000	3 %

Reduction of Output Filter:

The reduction of output filter in terms of the cut-off frequency will result in a system which is smaller and more cost effective. More importantly, the highest frequency that the inverter can produce across the load will be increased, which is vital in a FACT device.

From the results there is a 89.47% decrease in THD of the voltage output from the filter. There is a reduction of 34.14 % in the cut off frequency of the filter. Similarly, the 3 level inverter can produce a signal up to frequencies of 11040Hz, which is 34.14% higher than the 2 level inverter. This signifies that a three level inverter has a higher bandwidth than a two level inverter.

Oscilloscope Sampling Effects:

For the simulation a zero-order hold sampling is added to simulate the effect of the digital scope. For the 2 level

before the filter, the THD increase to 148.99 % and 77.03 % for the 3 level. However, the THD after the filter and the f_{cut} remained the same. This indicates that the sampling of the oscilloscope at 1Mhz will introduce marginal aliasing error when measuring the THD before filter.

4. FUTURE WORK

The results of the analytical, simulated and measured inverters have been discussed. However, for the measured inverter, only the two level was built. A built three level inverter would provide a more definitive conclusion between the performance of a 2 and 3 level inverter. In addition, a second low pass filter must be built to test the reduction of output filter.

The inverters under test was only tested at a low power level of 9W. The power rating for the tested inverters must be increased to the 1kW specification to observe the unwanted effects that occur at higher power levels. This will provide a better understanding of the performance of the inverters that would be implemented as a FACT device.

From the results, the three level inverter provided more bandwidth than the two level inverter. To expand the result for multilevels, an inverter with 5 or more voltage level must be built. In addition, it would be beneficial to investigate and implement digital modulation. This would allow less components to be used once the multilevel are built and would allow for faster prototyping.

5. CONCLUSION

The baseline results for comparing a two and three level inverter has been presented. The analytical method, using the double Fourier series method, is compared to the simulation model, using Simulink, and to the measured model, built with analog comparators and Mosfets. The analytical and simulation model had a good correlation in terms of the frequency response. The analytical and measured model corresponded well and was only generally compared. From the analytical model, the 3 level inverter reduces the filter cut-off frequency allowing a increase in inverter bandwidth.

REFERENCES

- [1] S. Kouro, M. Malinowski, K. Gopakumar, J. Pou, L.G. Franquelo, Bin Wu, J. Rodriguez, M.A. Perez, and J.I. Leon. Recent advances and industrial applications of multilevel converters. *Industrial Electronics, IEEE Transactions on*, 57(8):2553–2580, Aug.
- [2] J. Rodriguez, L.G. Franquelo, S. Kouro, J.I. Leon, R.C. Portillo, M.A.M. Prats, and M.A. Perez. Multilevel converters: An enabling technology for high-power applications. *Proceedings of the IEEE*, 97(11):1786–1817, 2009.
- [3] M. Malinowski, K. Gopakumar, J. Rodriguez, and M.A. Perez. A survey on cascaded multilevel inverters. *Industrial Electronics, IEEE Transactions on*, 57(7):2197–2206, July.
- [4] J. Rodriguez, Jih-Sheng Lai, and Fang Zheng Peng. Multilevel inverters: a survey of topologies, controls, and applications. *Industrial Electronics, IEEE Transactions on*, 49(4):724–738, Aug.
- [5] O.M. Mueller and J.N. Park. Quasi-linear igt inverter topologies. In *Applied Power Electronics Conference and Exposition, 1994. APEC '94. Conference Proceedings 1994., Ninth Annual*, pages 253–259 vol.1, Feb.
- [6] J. Sabate, L. Garces, P. Szczesny, Qiming Li, and W.F. Wirth. High-bandwidth high-power gradient driver for magnetic resonance imaging with digital control. In *Applied Power Electronics Conference and Exposition, 2005. APEC 2005. Twentieth Annual IEEE*, volume 2, pages 1087–1091 Vol. 2, 2005.
- [7] Bhim Singh, K. Al-Haddad, and A. Chandra. A review of active filters for power quality improvement. *Industrial Electronics, IEEE Transactions on*, 46(5):960–971, 1999.
- [8] N.G. Hingorani. Flexible ac transmission. *Spectrum, IEEE*, 30(4):40–45, April.
- [9] R.E. Beighley, C.A. Gougler, and J.R. Johnson. Application of active harmonic filters for power quality improvement. In *Power Engineering Society Summer Meeting, 1999. IEEE*, volume 2, pages 1175–1180 vol.2, 1999.
- [10] G. Walker and G. Ledwich. Bandwidth considerations for multilevel converters. *Power Electronics, IEEE Transactions on*, 14(1):74–81, Jan.
- [11] L. Marco, A. Poveda, E. Alarcon, and D. Maksimovic. Bandwidth limits in pwm switching amplifiers. In *Circuits and Systems, 2006. ISCAS 2006. Proceedings. 2006 IEEE International Symposium on*, pages 4 pp.–5326, May.
- [12] F. Koeslag, H.D. Mouton, and J. Beukes. Analytical modeling of the effect of nonlinear switching transition curves on harmonic distortion in class d audio amplifiers. *Power Electronics, IEEE Transactions on*, 28(1):380–389, Jan.
- [13] WR Bennett. New results in the calculation of modulation products. *Bell Syst. Tech. J*, 12(228):19331, 1933.
- [14] S.R. Bowes and B.M. Bird. Novel approach to the analysis and synthesis of modulation processes in power converters. *Electrical Engineers, Proceedings of the Institution of*, 122(5):507–513, May.
- [15] B.P. McGrath and D.G. Holmes. An analytical technique for the determination of spectral components of multilevel carrier-based pwm methods. *Industrial Electronics, IEEE Transactions on*, 49(4):847–857, 2002.

- [16] B.P. McGrath and D.G. Holmes. Multicarrier pwm strategies for multilevel inverters. *Industrial Electronics, IEEE Transactions on*, 49(4):858–867, 2002.
- [17] G. Carrara, S. Gardella, M. Marchesoni, R. Salutari, and Giuseppe Sciutto. A new multilevel pwm method: a theoretical analysis. *Power Electronics, IEEE Transactions on*, 7(3):497–505, 1992.

A High-Frequency CMOS Based Driver for High-Power MOSFET Applications

A.J. Swart

Department of Electrical, Electronic and Computer Engineering, Central University of Technology, Private Bag X20539, Bloemfontein, South Africa, 9300. Email: drjamesswart@gmail.com

Abstract: Driving high-power MOSFETs at high frequencies requires a gate drive signal of more than 10 Vp-p. Generating high frequencies is usually accomplished via a frequency generator, such as a frequency synthesizer. However, the output signal voltage from these frequency synthesizers is often lower than 10 Vp-p, being 5.5 Vp-p in the case of the 74HC 4046. This requires some or other form of voltage amplification to successfully drive a high-power MOSFET. The purpose of this paper is to present a CMOS based driver, using a HEF 40106 HEX inverter, which was successfully used to raise a 6.78 MHz square wave signal from 5.5 Vp-p to above 10 Vp-p in order to drive a high-power MOSFET. Results indicate that this CMOS based driver exhibits a wide bandwidth, being able to amplify the 1st and 3rd harmonics of the square wave signal.

Keywords: CMOS driver, MOSFET, high-frequency, 4000 series, bandwidth

1. INTRODUCTION

The ability of high-power MOSFETs to act as a switch makes it an ideal switching device [1]. The technique of switching between maximum and zero voltage across a high-power MOSFET has easily been achieved in the past at frequencies below 1 MHz [2].

However, commercially available high-speed MOSFET drivers now have the ability to produce switching frequencies beyond 1 MHz, such as the TPS 2812, which was used by Xiarong et al. [3] in a driving circuit for ultrasonic transducers. It is only necessary to build a high speed, low power driver for the MOSFET driver when using the TPS 2812. However, a concern arises with this MOSFET driver in that its input circuit has a positive threshold of approximately 2/3 of VCC. The minimum gate voltage required to successfully switch a MOSFET is around 10 Vp-p [4]. This means that if VCC is 10 V, then the minimum input threshold voltage must be 6.67 Vp-p.

This 6.67 Vp-p becomes problematic when considering the output voltage of certain frequency generation devices, devices which are required to generate the switching frequencies in high-power MOSFET applications. For example, consider the 74HC 4046, a phase-lock loop device capable of generating frequencies up to 20 MHz (within the high-frequency range), but at a constant output voltage of 5.5 Vp-p [2]. This means that it will not be able to be connected straight into certain MOSFET drivers, such as the TPS 2812, without some or other form of voltage application that will increase the 5.5 Vp-p signal to more than 6.67 Vp-p.

The purpose of this paper is to present a CMOS based driver, using the HEF 40106, which was successfully used to raise a 6.78 MHz square wave signal from 5.5 Vp-p to above 10 Vp-p, in order to drive a high-power

MOSFET. The reason for piloting this frequency within the high-frequency range is because ICASA does not require a license for using this frequency [5]. This CMOS based driver may further be applied as a pre-amplifier to the TPS 2812 in order to raise any frequency below 6.78 MHz with a 5.5 Vp-p amplitude to above the 6.67 Vp-p threshold voltage required for successful switching.

Theory regarding gate charge, energy and power requirements for driving high-power MOSFETs is firstly presented. Various voltage amplification circuits are then presented, with focus being directed primarily to HEF 40106 HEX inverter. The simulation circuit is then introduced with its associated results.

2. GATE CHARGE, ENERGY AND POWER

MOSFET devices are not really inherently bound to frequency limitations within the high-frequency range due to the absence of minority carrier transport. Two limits to high-frequency operation do though exist, and include the transient time across the drift region and the rate of charging of the input gate capacitance [6].

Speed limitations of MOSFET devices are therefore due entirely to circuit capacitance and the inability of the device to charge and discharge this capacitance [7]. Important parameters to therefore consider are the parasitic capacitances of the MOSFET device [8]. Taylor [9] examined the gate control charge of a MOSFET device in the on position and expressed it as:

$$Q_{gate} = C_{iss} \cdot V_{gs} \quad \text{Coulomb} \quad (1)$$

Where $C_{iss} \equiv$ the input gate capacitance of the MOSFET in pF
 $V_{gs} \equiv$ the gate to source voltage V

Ciss is the sum of the real capacitance between the gate and source (C_{GS}) and the voltage dependant capacitance between the drain and the gate (C_{DG}). The value of V_{gs} is a function of the device and the voltage required to achieve full enhancement. The energy required for this gate charge can be expressed as [9]:

$$E_{gate} := 0.5 \cdot C_{iss} \cdot V_{gs}^2 \quad \text{Joules} \quad (2)$$

Subsequently, the power required for this gate charge can be expressed as [9]:

$$P_{gate} := 0.5 \cdot C_{iss} \cdot V_{gs}^2 \cdot freq \quad \text{Watts} \quad (3)$$

Where $f \equiv$ the input gate frequency in Hz

A portion of the gate drive power will further be dissipated in the internal resistance of the gate. These losses are negligible at frequencies around 100 kHz, but become significant at higher frequencies, especially when considering frequencies around 10 MHz. Contrasting the IRF140 with the IRF610 yields the results shown in Table 1 for a gate voltage of 12 Vp-p.

Table 1: Gate charge, energy and power required for 100 kHz and 6.78 MHz operation

100 kHz	IRF140	IRF610
Ciss (F)	1660 pF	140 pF
Gate charge (C)	1.992 nC	1.68 nC
Energy (J)	119.5 nJ	10.08 nJ
Power (W)	12 mW	1 mW
6.78 MHz	IRF140	IRF610
Ciss (F)	1660 pF	140 pF
Gate charge (C)	1.992 nC	1.68 nC
Energy (J)	119.5 nJ	10.08 nJ
Power (W)	810 mW	68 mW

Table 1 indicates that driving high-power MOSFETs at low frequencies requires only a small amount of power (1 mW versus 68 mW for the IRF610). This table further highlights that larger input gate capacitances requires higher input powers within the high-frequency range (810 mW versus 68 mW). This has subsequently resulted in the commercialisation of numerous MOSFET IC drivers that need supply only a few mW in the lower frequency ranges. However, higher frequency ranges would require a higher gate drive power and subsequently a slightly different MOSFET gate driver being able to source and sink larger amounts of current, while providing the correct gate voltage.

3. VOLTAGE AMPLIFICATION

Voltage amplification of square wave signals to drive high-power MOSFETs may be achieved in a variety of ways, including the use of:

- A voltage source in series with a resistance;
- Active pull down with passive pull up;
- A complimentary emitter follower; and
- CMOS based IC's such as the 4000 series;

A gate drive circuit may generally be represented by a voltage source in series with a resistance. A resistance may be inserted intentionally between the gate of the MOSFET and the voltage source so as to modify the switching speed or represent the impedance of the voltage source [10]. Different turn-on and turn-off times may be achieved by utilizing a diode in parallel with this series resistance as shown in Figure 1.

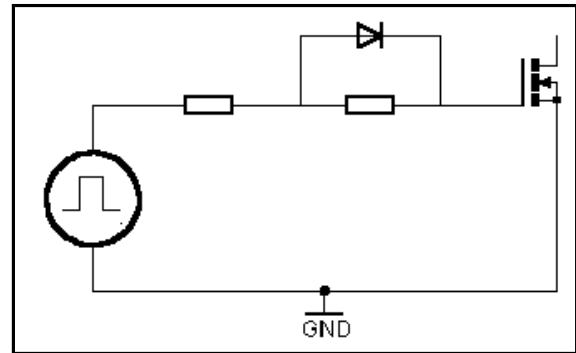


Figure 1: Asymmetric gate drives featuring a fast turn-on technique

However, asymmetry may be inherent in gate drive circuits, where an active pull down action but a passive pull up action (or visa versa) exists. Figure 2 illustrates gate drive circuits with inherent asymmetry.

To achieve switching speeds of the order of 100 ns or less requires a gate drive circuit with a low output impedance and the ability to source and sink relatively large currents [10]. A NPN and PNP transistor connected in a totem-pole configuration, as shown in Figure 3, is capable of sourcing and sinking large amounts of current, while providing a low output impedance [10].

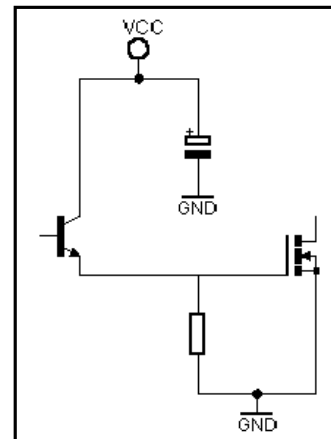


Figure 2: Gate drive circuits with inherent asymmetry

High-power MOSFETs may also be driven directly from CMOS IC's. The output characteristics of CMOS are approximately the same whether sourcing or sinking current. The main advantage is that the supply voltage may be set to 15 V, an acceptable voltage to switch the power MOSFET on and off. Lower output impedances and higher currents can be achieved by connecting a number of CMOS gates in parallel, as shown in Figure 4 [10].

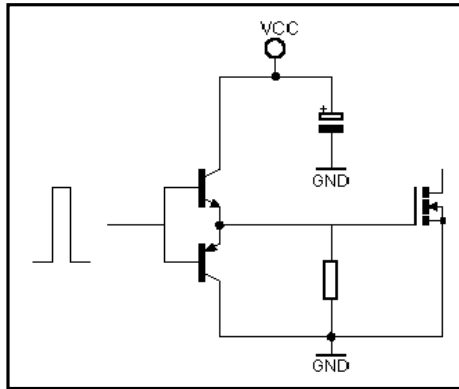


Figure 3: Complementary emitter follower, low impedance gate drive circuit

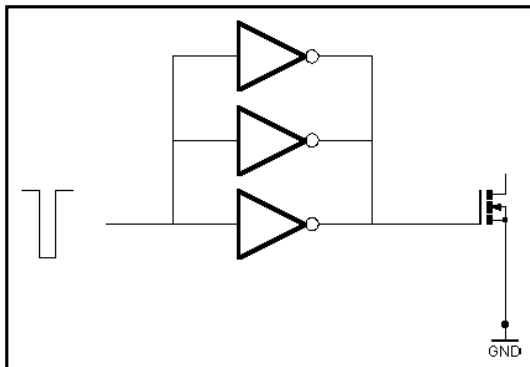


Figure 4: CMOS outputs paralleled to increase drive capability

This last gate drive circuit, incorporating multiple CMOS inverters in parallel was chosen for the voltage amplification stage. Reasons include the provision of a very low output impedance, the ability to source and sink large amounts of current and its wide operating bandwidth.

Voltage amplification of square wave signals requires the designer to take into consideration the harmonic content of the signal, and subsequently the bandwidth. Consider a 6.78 MHz square wave signal that would have harmonic content at 20.34 MHz (considering only the 3rd harmonic). This harmonic frequency would also have to be amplified, to ensure a more square wave signal than a sine wave signal at the output (see figure 5). This then requires that the voltage amplification stage possess a sufficient bandwidth to incorporate these harmonics, or else severe degradation of the square

wave signal will exist. The following equation is used to represent the 1st and 3rd harmonic waveform [11]:

$$f(t) := \frac{4}{\pi} \left(\sin(\omega t) + \frac{1}{3} \sin(3 \cdot \omega t) \right) \quad (4)$$

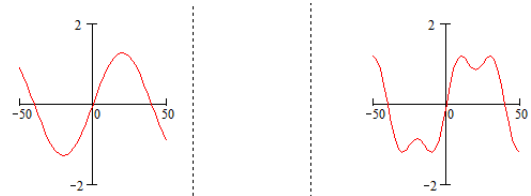


Figure 5: 1st harmonic only on the left, 1st and 3rd harmonic on the right

A CMOS based IC that incorporates such a wide bandwidth is the HEF 40106, a HEX inverting Schmitt trigger containing 6 separate invertors. Although logic ICs are not usually specified in terms of bandwidth (but rather in terms of propagation delay), there have been some researchers who have commented on their bandwidth characteristics [12, 13]. The datasheet for the HEF 40106 indicates that its transition time from low to high is typically around 60 ns when fed from a 5 V source. High to low transition time is typically also 60 ns. This means that 120 ns is required for a square wave signal to switch between zero, maximum and zero again. As the supply voltage increases, these transition times decrease, thus increasing the maximum allowable clock frequency.

A 5 V supply will cause the HEF 40106 to successfully accommodate an input frequency of around 8 MHz (120 ns time period). The Schmitt trigger action is mainly responsible for this transition time as well as for relatively high input noise immunity. The datasheet further indicates that the HEF 40106 requires a typical positive-going input voltage of 5.8 V to successfully switch the inverter, when run from a 10 V supply rail. This is just higher than the typical output voltage of certain frequency synthesizers which are often built around phase-lock loop (PLL) IC's. The 74HC 4046 is such a PLL IC capable of producing frequencies upwards of 20 MHz, but at an output voltage of 5.5 V.

The supply voltage to the first HEF 40106 must therefore be made lower to accommodate the 5.5 V from the frequency synthesizer. Using a voltage supply of 7.5 V allows a positive-going input voltage of below 5.5 V, therefore allowing the inverter to switch successfully and provide an output voltage of 7 V (0.5 V hysteresis voltage accounted for). This output voltage must now be fed into a second HEF 40106 operating at a supply voltage of 9.5 V to raise it to a higher voltage. A third HEF 40106, operating at a supply voltage of 11.5 V, is finally used to raise the signal to 11 V, providing the voltage required to drive the gate of the high-power MOSFET operating in the high-frequency range.

However, using just one of the six inverters available on the HEF 40106 will not provide sufficient drive to the following inverters in the circuit. Paralleling 3 inverters on the chip will result in a lower output impedance, thereby providing sufficient drive for the next set of inverters. This technique of paralleling inverters for a MOSFET driver was initially discussed by Grant and Gowar [10]. Figure 6 illustrates the circuit diagram comprising three individual HEX inverter Schmitt triggers which serve as the voltage amplification section to raise a voltage of 5.5 V to above 10 V. This same circuit comprises the simulation model, which was incorporated into National Instruments Multisim 11.0 simulation package.

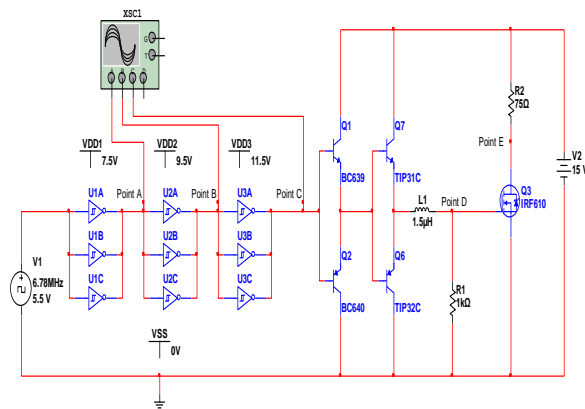


Figure 6: Simulation model

4. RESULTS

The voltage amplification section consists of 3 CMOS HEX inverters, where 3 inverters on each IC are parallel. The outputs of each of the CMOS HEF 40106 HEX inverters used in the experimental model, obtained from test points A through C, are shown in Figure 7. Point A represents a 7 V output signal, point B a 9 V output signal and point C a 11 V output signal, all at a high-frequency value of 6.78 MHz.

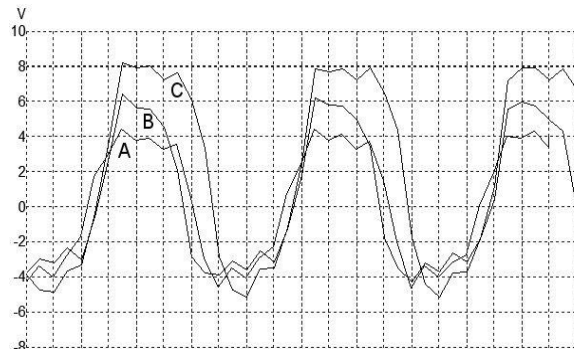


Figure 7: Outputs from the first three HEF 40106 CMOS inverters taken from the experimental model – time per division is 20 ns where Points A, B and C are indicated

The results of the experimental model were verified with a simulation model incorporated into the National Instruments Multisim 11.0 simulation package. The results of the simulation model are shown in Figure 8. Again voltage amplification is visible as the 6.78 MHz signal is raised from 5.5 V to 7 V, then to 9 V and then finally to 11 V. The simulation model does however present a sharper square wave signal than does the experimental model.

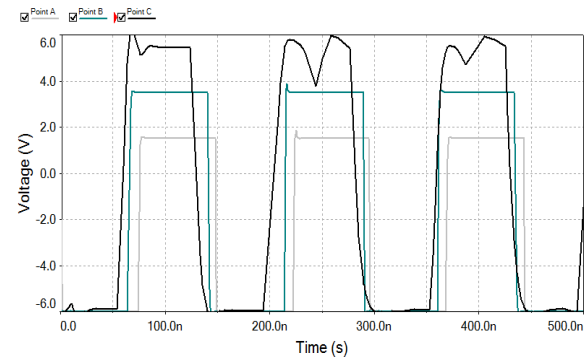


Figure 8: Outputs from the first three HEF 40106 CMOS inverters taken from the simulation model

The 11 V output signal from the final CMOS inverters were correlated to the mathematical equation (equation 4) for the 1st and 3rd harmonics of a square wave signal. This correlation is shown in Figure 9 which substantiates the wide bandwidth of the HEF 40106 as being able to accommodate harmonics up to 21 MHz.

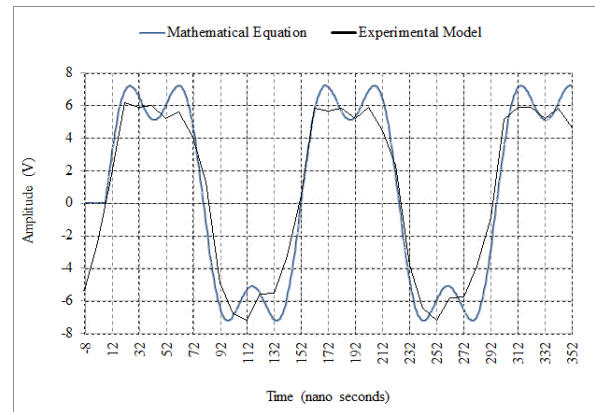


Figure 9: Correlation between the output waveform from the third HEF 40106 CMOS HEX inverter and the mathematical equation for the 1st and 3rd harmonics – Point C

The final output waveform of the voltage amplification stage was applied to a complementary emitter follower connected to the input of a high-power MOSFET. The input switching waveform of the MOSFET (IRF610) is shown in Figure 10, where successful switching was accomplished as depicted in Figure 11 (output voltage and current for the MOSFET device).

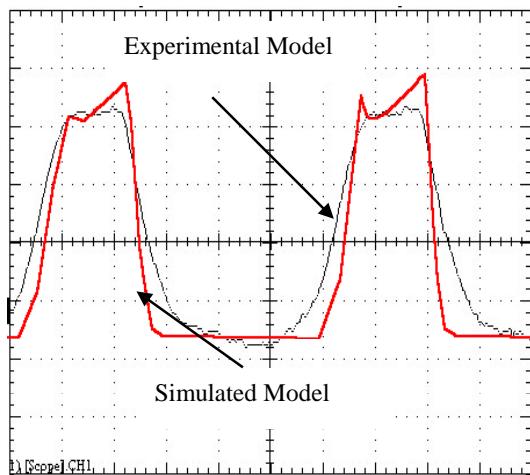


Figure 10: Final input switching waveforms from the high-power MOSFET [14] – Point D

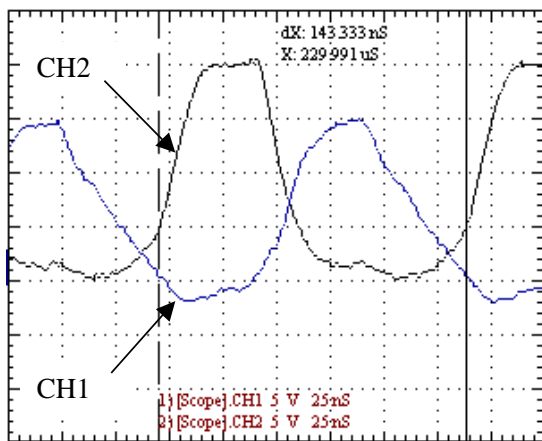


Figure 11: Output voltage (CH2) and current (CH1) for the high-power MOSFET [15] – Point E

5. CONCLUSIONS

The application of three HEF 40106 HEX inverters, each operating at a different supply voltage, has provided sufficient voltage amplification of the 6.78 MHz signal derived from a PLL IC (74HC 4046). Raising the 5.5 V signal to above 10 V has materialised where the 1st and 3rd harmonic of the square wave signal has been amplified. However, the final output signal was not a perfect square wave, but did indeed provide sufficient drive to turn the gate of the high power MOSFET completely on and off.

6. REFERENCES

- [1] O. H. Stielau, J. J. Schoeman, and J. D. Van Wyk, "A high-performance gate/base drive using a current source," *Industry Applications, IEEE Transactions on*, vol. 29, pp. 933-939, 1993.
- [2] A. J. Swart and H. C. Pienaar, "A high frequency Mosfet driver," in *SAUPEC 2004*, University of Stellenbosch, Stellenbosch, 2004.
- [3] G. Xiaorong, S. Xiaomei, P. Chaoyong, and G. Jianqiang, "Transmitting circuit design for ultrasonic transducer," in *Electronic and Mechanical Engineering and Information Technology (EMEIT), 2011 International Conference on*, 2011, pp. 1291-1293.
- [4] M. Brown, *Practical power supply design*. San Diego: Academic Press, 1990.
- [5] ICASA, "Electronic Communications Act," in *Notice 926 of 2008, Act No 36 of 2005*, ICASA, Ed.: Government, 2008.
- [6] B. J. Baliga, *Modern Power Devices*. New York: Wiley, 1987.
- [7] R. H. Crawford, *MOSFET In Circuit Design. Texas Instruments Electronics Series*. New York: McGraw-Hill, 1967.
- [8] L. Balogh, "Design And Application Guide For High Speed Mosfet Gate Drive Circuits..," vol. 2003, 2001.
- [9] B. E. Taylor, *Power MOSFET Design*. Chichester: Wiley, 1993.
- [10] A. D. Grant and J. Gowar, *POWER MOSFETS Theory and Applications*. New York: Wiley, 1989.
- [11] J. S. Beasley and G. M. Miller, *Modern electronic communication*, 9th ed. New Jersey: Pearson Prentice Hall, 2008.
- [12] G. Kumar, S. Sitaraman, J. Cho, S. J. Kim, V. Sundaram, J. Kim, and R. Tummala, "Power delivery network analysis of 3D double-side glass interposers for high bandwidth applications.," in *In Electronic Components and Technology Conference*, 2013, pp. 1100-1108.
- [13] M. Rodwell, Q. Lee, D. Mensa, J. Guthrie, Y. Betser, S. C. Martin, and S. Long, "Ultra high frequency integrated circuits using transferred substrate heterojunction bipolar transistors," in *Proceedings of the 1999 IEEE International Symposium on Circuits and Systems*, 1999, pp. 500-503.
- [14] A. J. Swart, H. C. Pienaar, and M. Case, "A Radio Frequency Mosfet driver," in *AFRICON 2004 international conference* Gaborone International Conference Centre, Gaborone, Botswana, 2004.
- [15] A. J. Swart, H. C. Pienaar, and M. J. Case, "A radio-frequency MOSFET driver," *SAIEE Africa Research Journal Incorporating the SAIEE Transactions*, vol. 97, pp. 243-247, September 2006.

Topic I

Condition Monitoring and Systems Automation

HOUSEHOLD ELECTRICITY AND WATER MONITOR AND CONTROL WITH CELLULAR COMMUNICATIONS AND WEB INTERFACE

R.I. Müller* and M.J. Booysen**

* Department of Mechanical and Mechatronic Engineering, Private Bag X1, Matieland 7602, South Africa. E-mail: regardtm@gmail.com

** Department Electrical and Electronic Engineering, Private Bag X1, Matieland 7602, South Africa. E-mail: mjbooyesen@sun.ac.za

Abstract: The availability and depletion of natural resources is increasingly pointed as the limiting factor for sustainability. A lot of focus is currently placed on the role and effect of fossil fuels as well as water conservation. One way to affect prudence with these scarce resources is to generally create timely awareness of consumption thereof, and also the related cost for the consumers. Existing metering solutions for electrical energy and water are often manually read by officials, and the information difficult to digest. Moreover, billing information, which serves as feedback, lags consumption by several weeks. Smart meters address many of these challenges by enabling electronic and real-time metering, but are still prohibitively expensive. In this paper, a low-cost power meter is discussed and also a novel low-cost water flow meter is developed to integrate into a household smart metering system. Electricity supply to appliances as well as the main water supply is controlled through relays and a valve. The whole system is connected to the Trintel SMART web platform by means of cellular communications from where end-users can manage their own energy and water usage. The results demonstrate that the smart metering system provides a functional, accurate and less expensive alternative to household metering. Further improvements on the system are also suggested.

Keywords: smart meter, M2M communications, cellular communications, power meter, orifice, water flow meter.

1. INTRODUCTION

Recent advances in technology have resulted in multi-functional devices, such as laptops, tablets, cell phones, etc., being ubiquitous and pervasive. These devices are already able to control most aspects of our lives. Concurrently, the global population is growing while natural resources are withering, increasing the already intense need to save and convert to a sustainable way of living. This growing global need for centralised control and optimisation also creates various opportunities.

One approach that offers various fringe benefits is that of smart metering. Driven mostly by the recent emergence of ubiquitous wireless networking, smart metering enables autonomous metering of utilities (e.g. electricity and water usage). Two key benefits of smart metering, both of which affect savings, are the low-latency and highly visualised method of data reporting. These two factors ensure that the consumer of the utility, who is usually also the payer thereof, is aware of consumption patterns, which leads to more responsible behaviour [1], [2]. The main enabler behind the reduction in latency with smart metering is that utility suppliers do not need to manually read the meters for billing purposes, but can autonomously capture and process all the data centrally, without having to send an official to every household to read the meter readings.

Significant inroads have been made towards achieving smart metering in the energy sector [3]. Trintel is a South

African company that specializes in providing wireless and machine-to-machine (M2M) solutions to customers through its self-developed SMART platform. They are currently in the testing phase of projects where customers have their household hot water cylinders (called geysers in South Africa) connected to several sensors and controlling devices which, through serial and cellular communications, provide real-time access to the SMART platform. The user can log on from any location to monitor and control the state of their hot water [2].

1.1 Contribution

This paper aims to prove the concept of enabling an end-user to monitor and control his/her household water and electricity supply on Trintel's Smart platform through cellular communications. The implementation of a low-cost power meter is discussed, and a novel low-cost water flow meter is developed for use in an integrated household smart metering system. Relays and a valve are incorporated into the electronic unit to respectively control the electricity supply to the individual electrical circuit breakers and the main water supply into the household. The results clearly demonstrate that the smart metering system functions accordingly, and provides a promising and inexpensive alternative approach to home metering.

The rest of this paper is organised as follows:

Section 2 discusses related work done in this field, Section 3 describes the design of the different components used in this system and Section 4 discusses the results after completing and testing the system. Section 5 concludes the paper.

2. RELATED WORK

The generic configuration and hierarchical architecture of an M2M network is described in [1] and [3]. Various smart metering solutions have been discussed in literature and some limited proof-of concept designs reported [2, 3]. However, no integrated solution exists that combines utilities, water and electricity, into a smart-metering platform with a highly visualised online platform.

A key challenge faced by smart water metering is the prohibitive cost and complexities associated with electronic water flow meters [4, 5]. Moreover, the design of a flow meter is cumbersome, and usually contains moving parts to accommodate the detectability of low flow rates. Off-the-shelf products in the range of this study are expensive and seldom adhere to all of the requirements simultaneously such as the flow medium, size, measurement range, ability to integrate with a microcontroller etc. For example, one suitable off-the-shelf product is the EH Promag 10P. This product functions as an electromagnetic flow measuring system, often used in chemical or process applications, to very accurately measure flow rates with little to no effect on the water flow. However, its price of approximately R 25 000 (US\$ 2 500), which eliminates it as an option for large scale household deployment, based on the criterion of affordability.

3. SYSTEM DESIGN

The proposed system can be seen in the system diagram in Figure 1. It shows all the major components and their relations to each other. The major components are discussed in the following sub-sections.

3.1 Processing

The microcontroller unit (MCU) serves as the centre of operations for this system. Most of the processing is performed by the MCU. Power meter and flow meter measurements are transmitted to the MCU to process and send to the web platform via the modem. The relays and effectively the valve are controlled by commands from the MCU. The MCU is programmed to interface with each of these components. The Arduino Mega 2560 is used as MCU platform.

3.2 Communication

The modem is the connection between the electronic unit and the online platform. It facilitates communication between the MCU and the SMART platform via GSM (Global System for Mobile Communications) networks which has extensive coverage in South Africa. AT commands

are used to send data over the network. The modem used is the Sierra Wireless Airlink GL6110. The Sierra Wireless AirVantage software is used to set up an asset model for the modem to interface with the SMART web platform.

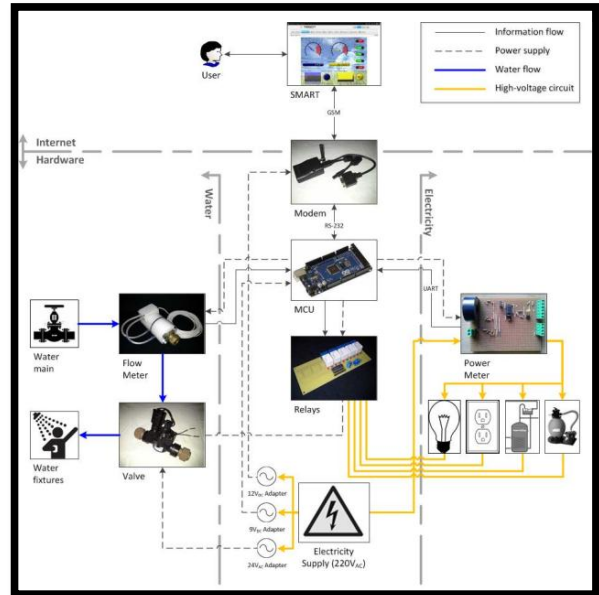


Figure 1: System diagram

3.3 Water

A device is required to accurately measure the flow rate and thereby also the volume of water flowing into a residence. In this paper, an orifice flow meter was designed as a prototype.

The orifice flow meter utilises the Venturi effect by placing an obstruction in the line of flow, which causes a measurable pressure drop. The pressure drop is measured with a differential pressure sensor to determine the flow rate, by applying Bernoulli's equation, which states that the pressure drop is a function of the square of the flow speed. Continuous flow rate measurements can be integrated over time to account for the volume of water that flows through the obstruction.

The design and accompanying calculations for this flow meter were based on the appropriate ISO standards [6]. The design was further based on ease of use and finding the most inexpensive way to manufacture such a device while still adhering to all the necessary requirements and regulations. The CAD (computer aided design) model can be seen in Figure 2a. This design was used to manufacture the final product seen in Figure 2b.

To enable the user to effectively control water supply into the residence, a simple solenoid valve is connected to the system. This valve may be switched wirelessly from the SMART Sight dashboard.

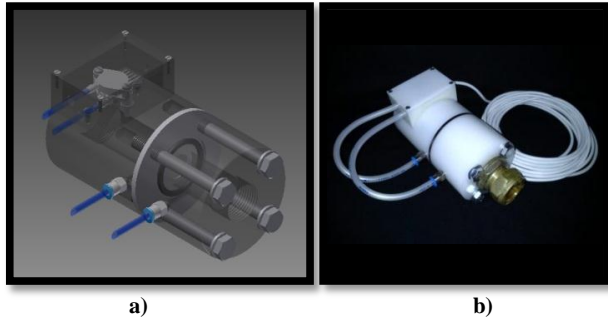


Figure 2: Orifice flow meter. a) CAD model. b) Manufactured flow meter.

3.4 Electricity

A device is required to accurately measure the billable kilowatt hours (*kWh*) of energy used by appliances in a residence for users and suppliers to keep track of energy consumption.

Off-the-shelf power meters were considered, such as the CRD5490 power meter from Cirrus Logic. These products were found to be expensive and in certain cases required specialist knowledge. Therefore, power meters were researched to produce an easy to design, affordable and safe-to-use product.

For this paper, only single phase electric power will be considered such as would be found in most residences. When measuring the amount of power that an appliance consumes, it is known that this refers to the real power component of its consumption for which the calculation is shown in Equation 1.

$$P = \frac{1}{2} \cdot V_p \cdot I_p \cdot \cos \theta$$

$$= V_{rms} \cdot I_{rms} \cdot \cos \theta \quad (1)$$

To find the amount of electrical energy used, the power is integrated over time, which in common practice would mean to average the power consumption over a period of time (often a quarter of an hour) and multiply this by the time as seen in Equation 2.

$$E = \int_0^t P(t) dt$$

$$= P \cdot t \quad (2)$$

The Cirrus Logic CS5490 integrated circuit (IC) was chosen for its power calculation capabilities. The power meter design, seen in Figure 3, was obtained from the CS5490 datasheet. For this design current measurements are made by using a current transformer (CT) and voltage measurements by using voltage dividing resistances from the household main live and neutral wires.

Burden resistance values were calculated by considering the maximum expected current.

The use of scaling resistors raised a question about the isolation of such a circuit, since it requires that the

resistors be connected between the live and neutral wire of a high voltage circuit. The power meter and essentially the whole electronic unit is therefore exposed to this high voltage circuit and potential high voltages differences between the local earth and neutral wires. This can be averted in future designs by using a voltage transformer instead of scaling resistances.

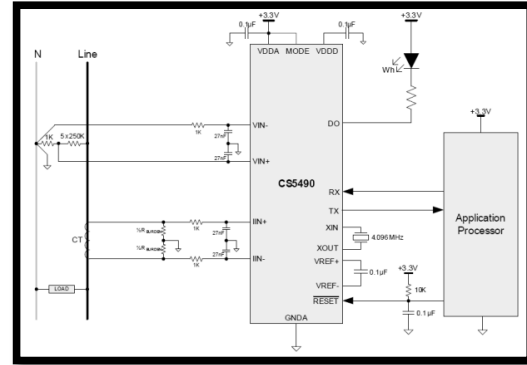


Figure 3: Power meter circuit design

The completed power meter can be seen in Figure 4.



Figure 4: Assembled power meter

To control the power supply to individual circuit breakers, relays are used. For this project solid state, printed circuit board (PCB) mounted relays were chosen with coil energising via change-over (CO) contacts and with the designation of single pole double throw (SPDT). These specific relays are rated at 250 V_{AC} and 10 A, and can be switched with 5 V_{DC}. This rating confines the use of these relays to single loads such as a kettle, heater, swimming pool pump etc. Future designs might include higher rated relays or solid state relays to switch larger loads.

The relay circuit board is connected to the MCU and each individual relay wirelessly controlled by the user from the SMART web platform.

3.5 SMART

The SMART platform is Trintel's own custom-developed M2M platform which gives their clients the ability to manage their wireless telemetry over the GSM network

through a web-based portal. By accumulating and reporting on diagnostic and statistical information from devices, SMART enables enhanced maintenance, cost control, service agreements and on-billing for their clients [8]. The SMART web-based tool that is used to monitor and control the system is called SMART Sight. This tool allows clients to create a graphical user interface (GUI) for end-users, such as the one displayed in Figure 5. The dashboard has numerous possibilities for displaying information and setting up controls in the form of gadgets placed on the dashboard.

SMART Sight was used to design the final dashboard seen in Figure 5. The layout was based on user-friendliness and optimum use of the space available in one window. To the left are all of the water flow information and controls, including the flow rate in l/min , the water usage in *litres*, the flow rate history and the high flow rate set point control. In the middle are the same gadgets for the power consumption and energy usage. To the right are the controls for all of the devices connected to the relays, in this instance the water valve, plugs, lights, hot water cylinder or geyser and the swimming pool pump. The information displayed on these gadgets is from real-time data received from the modem.

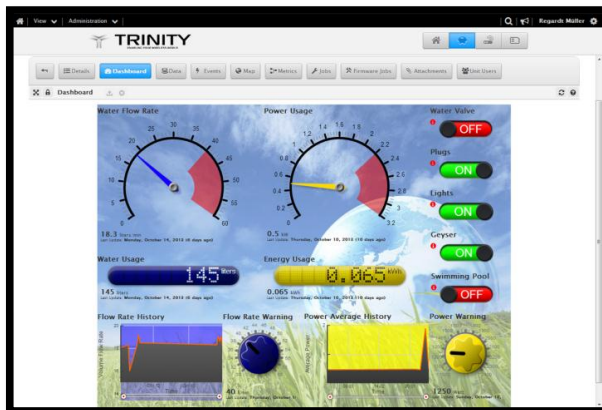


Figure 5: SMART Sight dashboard

4. RESULTS

The finished custom orifice flow meter was tested against a trusted product, the same Promag 10P named earlier [7]. From Figure 6 the water flow meter clearly matches the more complex and expensive product, providing a viable solution for household smart metering. However, future considerations should include using a Venturi flow meter design as well as refining the code for the flow meter on the MCU.

The power meter was calibrated by connecting it to a 2.2 kW heater with various settings and measuring actual readings with an oscilloscope. After calibration the power meter was tested against a commercially available power meter, the ACE9000 ISP.

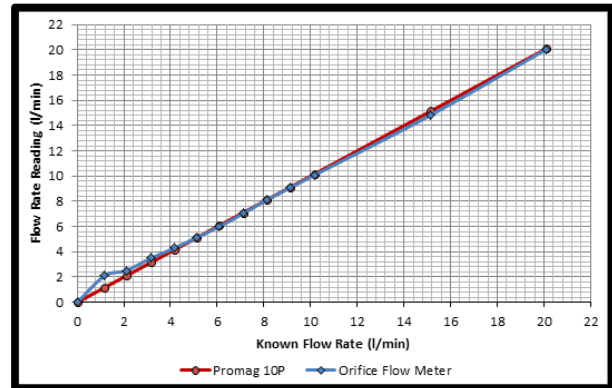


Figure 6: Flow rate reading comparison

The custom power meter kept track of the energy consumption, but eventually some inconsistencies did occur with the ACE9000 readings. The custom power meter gradually falls behind with the energy readings. After 1 kWh of energy was depleted from the ACE9000, the power meter's energy reading was approximately 6% off. This was attributed to inaccurate calibration and inaccurate (>1%) burden resistors, both of which should be easily rectifiable with further development. Overall, it is believed that the initial concept was proven to be realisable.

By integrating all of the above components, the concept of a smart household metering system was realised. The system efficiently and continuously monitors and displays electricity and water usage information to a user in a user friendly interface, and enables them to control consumption by being able to switch the electricity supply to certain appliances and the main water supply on/off.

The communication between the MCU and modem causes some errors. As stated earlier, the design of the flow meter can be improved. Improved isolation of the power meter from the main lines can be achieved.

5. CONCLUSION

The work in this paper presents the design of a smart household metering system. The system provides a low-cost alternative to existing solutions. The custom orifice flow meter has an estimated cost of 12% of the commercially available unit while the power meter parts amount up to no more than R 350 (US\$ 35).

The flow meter was manufactured and tested to measure flow rates to an accuracy of within 1% for flow rates between 4 l/min and 70 l/min . It is advised that Venturi meter be considered should the product be taken into mass production, for which this design could easily be adjusted.

Trintel's SMART platform was employed to provide a highly visualised online platform.

6. REFERENCES

- [1] M.J. Booysen, J.S. Gilmore, S. Zeadally, and G.-J. van Rooyen, "Machine-to-machine (M2M) Communications in Vehicular Networks," *KSII Transactions on Internet and Information Systems*, vol. 6, no. 2, pp. 529–546, Feb 2012. [Link](#).
- [2] M.J. Booysen, J.A.A. Engelbrecht, A. Molinaro, "Proof of concept: Large-scale monitor and control of household water heating in near real-time", International Conference of Applied Energy: (ICAE 2013), 1-4 July 2013, Pretoria, South Africa. [Link](#).
- [3] IEEE, 2013. *Machine-to-machine communications for home energy management system in smart grid*. [Online] Available at: <http://ieeexplore.ieee.org.ez.sun.ac.za/xpl/articleDetails.jsp?reload=true&tp=&arnumber=5741146> [Accessed 1 November 2013].
- [4] Baltimore Brew, 2013. *Totalling up the costs of "smart" water meters*. [Online] Available at: <http://www.baltimorebrew.com/2013/10/18/totaling-up-the-costs-of-smart-water-meters/> [Accessed 1 November 2013].
- [5] P.H. Sierck, 2011. *Smart Meter – What We Know: Measurement Challenges and Complexities*. [Online] Available at: http://hbelc.org/pdf/Resources/SmartMeter_Sierck.pdf [Accessed 1 November 2013].
- [6] ISO 5167-2, 2003. *Measurement of fluid flow by means of pressure differential devices inserted in circular-cross section conduits running full – Part 2: Orifice plates*, Geneva: ISO.
- [7] Endress+Hauser, 2010. *Promag 10P*. [Online] Available at: https://portal.endress.com/wa001/dla/5000000/0581/000/03/TI094DEN_1109.pdf [Accessed 27 September 2013].
- [8] Trinity Telecomms (Pty) Ltd., 2013. *SMART Sense Telemetry Management*. [Online] Available at: <http://www.trintel.co.za/content/4057/4023/smart-sense-solution> [Accessed 27 September 2013].

TRANSIENT RESPONSE OF EQUIPMENT TO FAST TRANSFER

C van Rensburg* and AJ Grobler*

*North-West University Potchefstroom Campus, School for Electrical, Electronic and Computer Engineering, 25 Borchard Street, Potchefstroom.

Abstract. Industries such as Sasol use high speed transfer devices to transfer equipment from a failing power supply to an alternative power supply, maintaining process continuity. The aim of this project is simulate and test the effect of fast transfers on different motors to determine whether transient current and torque caused by these transfers can damage the equipment.

1. INTRODUCTION

In Sasol, as in any other industry, process continuity is a crucial part of production. To maintain process continuity, high speed transfer devices (HSTD) are used. When an incoming supply voltage falls below a predetermined value, the transfer device disconnects the process equipment from the failing supply, and connects it to an alternative power supply. This transfer from one power supply to another is ideally done in such a short time that the process equipment does not experience a dip in supply voltage. [1]

Transfer schemes implemented in Sasol are initiated by an under voltage incidence. This incidence is when the supply voltage dips below a specified percentage of the normal supply voltage. [2]

Once the transfer has been initiated, the circuit breaker connecting the equipment to the failing power supply will be opened and the motors will start decelerating. The transfer device will then attempt to connect the load to an alternative power supply by closing another circuit breaker, called a tie breaker. This is shown in the Figure 1 and the discussion that follows.

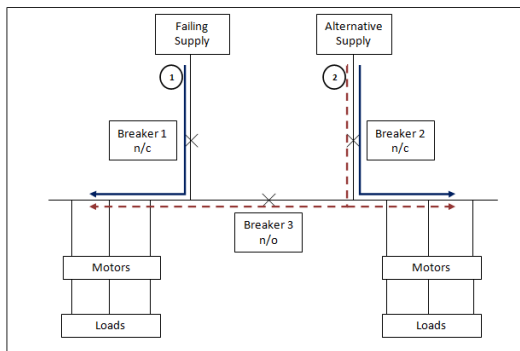


Figure 1: Basic bus transfer configuration

Path 1 shown by the solid line in **Error! Reference source not found.** shows how the two feeders supply their own sections of equipment under normal conditions. Breaker 1 will be opened when the power supply on the left starts to fail. The normally open tie breaker (Breaker 3) is then closed using one of the transfer methods listed below. When the tie breaker is closed, the transfer is completed and the section of equipment that was fed from the failing power supply will now be fed from the alternative power supply. This is shown by path 2, indicated with a dashed line.

A transfer system is often implemented with the assumption that the normal supply and the auxiliary supply are matched in voltage magnitude, phase angle, and frequency. Even though this is often true, there are cases where the two supplies are not matched. If this happens, the transfer system will have to monitor the two voltages for phase correlation before completing the transfer.

The fast transfer device has many advantages. These advantages include that system interruptions are minimized, effectively preventing loss in the form of unusable product. On the other hand, the effect of this device on the process equipment must be studied to determine whether or not the transfer could cause damaging transients in the equipment.

Since these transfer systems are a relatively new technology, very little research has been done on the effect that they can have on motors.

Of all the AC motors implemented by Sasol, it can be said that approximately 99% of these motors are induction motors. This is because cost of purchasing, maintaining, and repairing a synchronous motor is a lot higher than that of an induction motor. Also, an induction motor can be line-started, while a synchronous motor needs a drive. This article will show the effect of transfer systems on both induction and synchronous motors.

In this project research, simulations and experiments were used to investigate the effect of a fast transfer and a delayed in-phase transfer on process equipment, and determine if these transfer methods could cause damage to equipment. Recommendations

will be made about the implementation of these transfer methods.

2. TRANSFER METHODS

The basic operation of an automated transfer has been discussed in the introduction section. There are different methods of completing an automated transfer. These methods are defined by the amount of time that they take to complete after the circuit breaker of the failing supply is opened

2.1 Fast Transfer

After the circuit breaker between the failing power supply and the equipment is opened, a fast transfer is initiated in 40 to 100 milliseconds. The transfer is completed when the tie breaker is closed and connects the equipment to an alternative, power supply with normal voltage. The time taken to close the tie breaker also adds to the completion time of the transfer. [2]

A fast transfer, as implemented by Sasol, is referred to as a supervised fast transfer, because the transfer device monitors the magnitude, phase angle and frequency of the motor bus, normal supply and auxiliary supply.

Once the incoming breaker from the failing supply has been opened, a fault could occur that causes the equipment voltage and new supply voltage to be out of sync and would stop the tie breaker from closing. These faults include a difference in phase angle between the source and equipment voltage as a result of one of the following:

- The first breaker opens, and the equipment decelerates different than expected.
- The primary source and the auxiliary source are out of phase with each other.
- The fault that initiated the transfer causes a shift in phase angle on the motor bus.

If the breaker close has not yet been initiated after 100 milliseconds have lapsed, the next transfer method to be used is the delayed in-phase transfer. [2]

2.2 Delayed In-phase Transfer

A delayed in phase transfer takes 100 to 200 milliseconds for the closing of the tie breaker to be initiated. As the equipment decelerates, the HSTD monitors the voltage magnitude, phase and frequency of both the equipment and the alternative power supply. The device uses this information to predict the first time that the equipment and the supply would be in phase and send the command for the tie breaker to close at that same time. [2]

The disadvantage of the delayed in-phase transfer is that the residual motor voltage has dropped lower than with a fast transfer, also causing the speed to decrease more. This means that the equipment will

experience more reacceleration once the normal supply voltage is restored via the alternative supply.

2.3 Fixed Time Transfer

If 200 milliseconds have lapsed and transfer could not yet be initiated because there hasn't been a phase coincidence, the fixed time transfer is done. This transfer simply closes the tie breaker, regardless of whether or not the equipment and the supply are synchronized. The fixed time transfer operates on the assumption that the voltage has fallen below a certain value at which the transients of the breaker close and the normal voltage being restored, is low enough to not harm the motors. [2]

The fixed time transfer would cause for a large amount of reacceleration of the equipment, and could also cause some process interruption.

It is important to note that the fast transfer and the delayed in-phase transfer methods are classified as fast automated transfers, because they take into account the synchronization between the motor bus and alternative supply. The fixed time transfer, on the other hand, is classified as a slow transfer. [2]

For this project, a fast transfer was attempted. This meant completing the transfer in the shortest time possible without taking into account the phase correlation between the voltage of the failing supply and alternative supply.

3. SIMULATIONS

The effect of the fast transfer on different motors was simulated in Matlab® Simulink®. It is important to note that the load of the motor was approximated as a DC generator. Another important observation is that during the transfer, what the motor effectively experiences, is a power supply that is disconnected and reconnected in a short time. For this reason, the transfer was approximated with the use of a circuit breaker.

The simulations and tests were done on both a synchronous and induction motor. The actual motors were characterized and these parameters were used in the simulations.

3.1 Synchronous Motor

For the simulations and tests a 1.5 hp (1.1 kW) synchronous motor was used. The load of the motor was a 1.5 hp DC motor operated in generator mode.

Figure 2 shows the simulated speed, torque, rotor angle, and RMS stator current under no-load condition of the synchronous motor when a 150 ms transfer is done after 5 seconds.

The first part of the graph shows the starting transients, while the transfer transients start after 5 seconds.

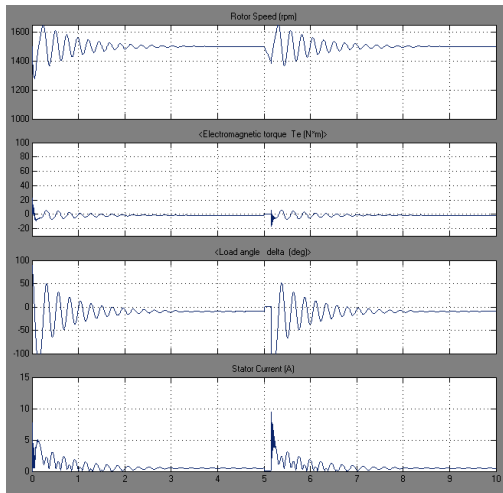


Figure 2: Synchronous motor simulation no-load

In Figure 2 it can be seen that the speed and torque transients during the transfer have approximately the same magnitude as the start up transients. The current, on the other hand, has a larger transient caused by the transfer than during start-up.

Figure 3 shows the speed, torque, rotor angle and stator current of the synchronous motor for a 150 ms transfer that takes place after 5 seconds. In this case, the synchronous motor is loaded by the dc motor driving a resistive load.

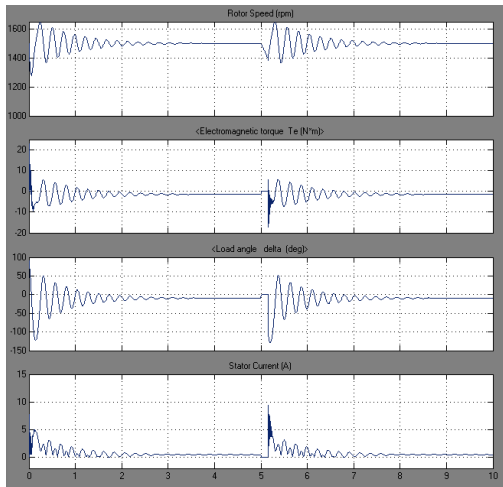


Figure 3: Synchronous motor simulation with load

In Figure 3 it can be seen that the torque transient is higher when the motor is loaded for both the starting and transfer transients. The magnitudes of the current transients are approximately the same.

It is important to note that in this case, the synchronous motor was able to recover after the transfer due the fact that the simulated motor has a damper winding. This damper winding allows the motor to act like an induction motor during starting and therefore also helps the motor to be synchronized again after transfer.

If the motor did not have a damper winding, the motor would not be able to be synchronized after the

transfer. This can be seen by lengthening the transfer time in the simulation.

Figure 4 shows the synchronous motor speed, torque, rotor angle and current for a 200 ms transfer that takes place after 5 seconds.

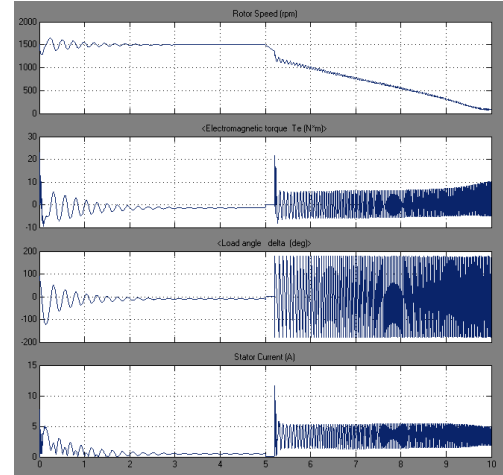


Figure 4: Synchronous motor out of synchronism

In Figure 4 it can be seen that the speed drops to zero after the transfer. During this time the current and torque is unstable. The variation in load angle shows that the motor is out of synchronism.

3.2 Induction Motor

For the simulations and tests a 2.2 kW induction motor was used. The load of the motor was a 7.5 kW DC motor operated in generator mode.

Figure 5 shows the speed, torque, rotor angle, and RMS stator current under no load condition of the synchronous motor when a 150 ms transfer is done after 5 seconds.

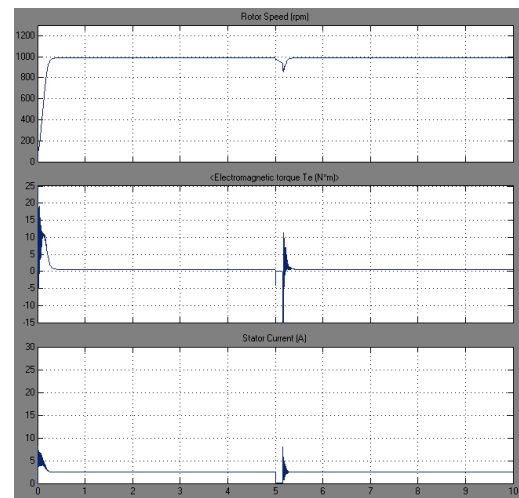


Figure 5: Induction motor simulation no load

In Figure 5 it can be seen that the motor loses some speed during the transfer, meaning that the motor has to be reaccelerated after the transfer. This

reacceleration causes torque and current transients that are higher than the starting transients.

Figure 6 shows the speed, torque, rotor angle and stator current of the induction motor for a 150 ms transfer that takes place after 5 seconds. In this case, the motor is loaded by the dc motor driving a resistive load.

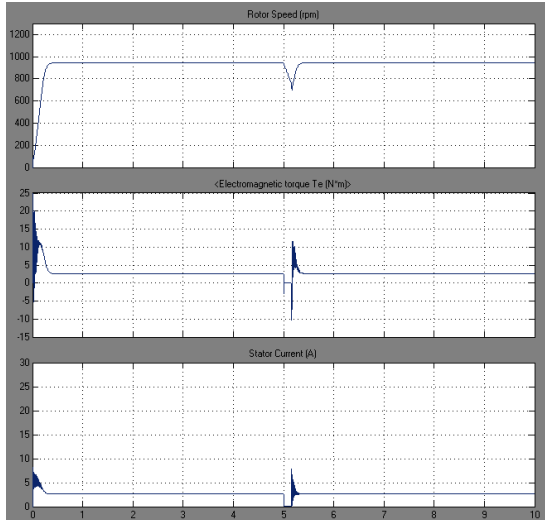


Figure 6: Induction motor simulation with load

In Figure 6 it can be seen that the motor loses more speed when it is loaded than under no load conditions. This means more reacceleration is required, but the torque and current transients remains approximately the same.

4. TEST PROCEDURE

To mimic the fast transfer done on the motor, an unequal repeating timer was used to magnetize the coil of a three phase contactor. This contactor was used to disconnect and reconnect the three phase supply to the motors. This transfer setup can be seen in Figure 7.



Figure 7: Transfer setup

It is important to note that the shortest off-time of the timer in Figure 7 is approximately 150 ms, making this the shortest possible transfer time for testing.

4.1 Synchronous Motor

The synchronous motor and dc machine test bench used for this project can be seen in Figure 8.



Figure 8: Synchronous motor and dc machine

Since the synchronous motor that was tested does not have a damper winding, it could not be started by simply using the variable ac source. To start the motor, it was therefore driven as a generator by a dc motor to run at its synchronous speed. The generated voltage of the synchronous generator, and the voltage from the source that was supposed to drive the motor once it was running, were both measured on a digital oscilloscope. The field voltage of the synchronous motor was increased to match the magnitudes of the two voltages. Once the two voltages were the same size and in phase, a circuit breaker was used to connect the source to the motor, effectively synchronizing it.

Once the motor was synchronized, the dc motor can be turned off and the synchronous machine would be running as a motor.

Once running, the timer and contactor transfer setup was used to disconnect and reconnect the three phase source of the motor in 150 ms.

From the tests it could be seen that the motor could not be synchronized after the transfer, as discussed in the previous section.

At this time the data from the tests on the synchronous motor are still being analyzed.

4.2 Induction Motor

The induction motor used for testing can be seen in Figure 9.



Figure 9: Induction motor

The dc machine test bench for the induction motor with the torque meter connected between the two machines is shown in Figure 10.



Figure 10: Induction motor test bench

Unlike the synchronous motor, the induction motor does not rely on exact synchronization to operate. This means that the motor could be started directly from the variable voltage source.

Once running, the timer and contactor transfer setup was used to disconnect and reconnect the three phase source of the motor.

Since the induction was able to recover from the transfer, the tests could be done for different transfer times, under no load and loaded conditions.

At this time the data from the tests on the induction motor are still being analyzed.

5. TEST RESULTS

This section will discuss the results measured when applying a fast transfer on different motors.

5.1 Synchronous Motor

Figure 11 shows the measurements of the armature voltage and current of the motor for a transfer of approximately 150 milliseconds.

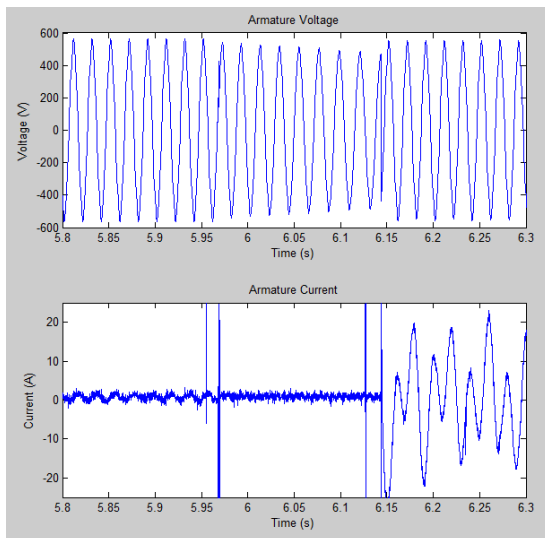


Figure 11: Synchronous motor test

From Figure 11 it can be seen that the synchronous motor was unable to recover to steady state conditions after the transfer. When the supply was reconnected after the transfer, the source voltage was

no longer in phase with the motor voltage. This is due to the deceleration of the synchronous motor, causing the frequency of the motor voltage to change. Since the motor could not be synchronized, the current in the motor became unstable.

The result of this test agrees with the results of the simulations done the synchronous motor. It is important to note that the test results show larger current transients after the transfer than the simulation results.

5.2 Induction Motor

The induction motor was firstly tested with no electrical load connected to the dc machine. Figure 12 shows the armature voltage and current as well as the speed and torque of the induction motor for a transfer that lasted approximately 150 milliseconds.

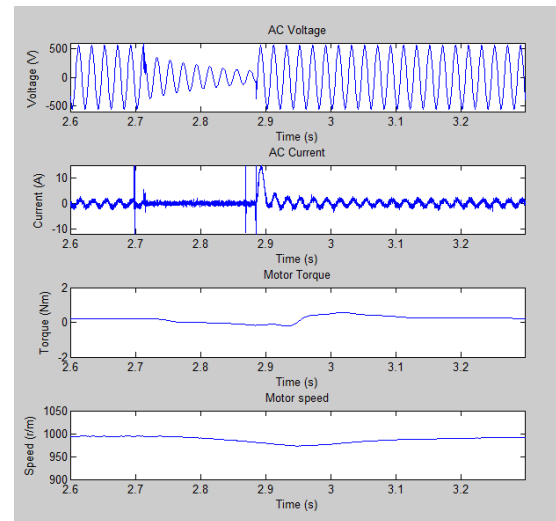


Figure 12: Induction motor test with no load

The waveforms in Figure 12 show that the voltage, current, torque and speed drop during the transfer. After the transfer, the motor is reaccelerated and the current transient reaches 9 A. The torque transient reaches 1 Nm, which is much higher than the steady state value of 0.2 Nm. During the transfer the speed drops to 975 r/m. It is important to note that some of the transients spikes may not be present due to the filtering effect of the measuring probes.

After the induction motor was tested with no load, a 13 Ω resistor was connected to the armature winding of the dc machine. Figure 13 shows the transients measured for the induction motor under loaded conditions for a 150 ms transfer.

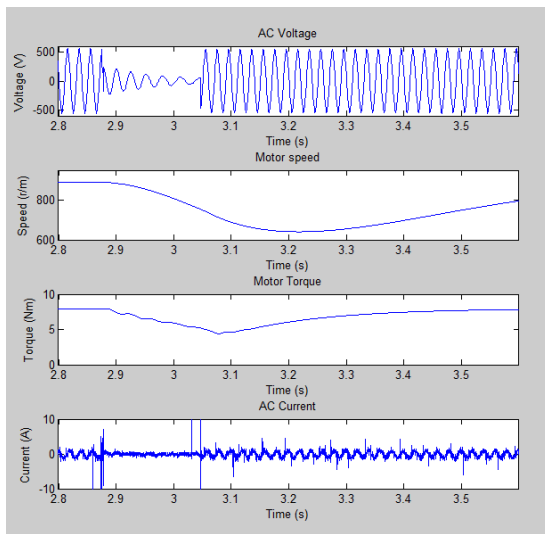


Figure 13: Induction motor test with load

The transfer in Figure 13 causes the speed to drop from 880 r/m to 620 r/m. The torque drops from 8 Nm to 5 Nm, but does not overshoot after the transfer. The current transient is approximately 4 A.

6. CONCLUSION

During the research phase of this project, it was found that there are different types of bus transfers that can be performed. The fast transfer and delayed in-phase transfers are considered to be fast bus transfers. When one of these can't be executed, a fixed time transfer is done.

In the simulations and tests for the synchronous motor, it was found that a motor without a damper winding needs to be exactly synchronized in order to operate. After attempting a 150 ms transfer, it was found that the motor is not synchronized when the circuit breaker is closed, and therefore can't recover from the loss in power supply. In this case the transients would be large enough to cause damage to the windings or couplings of the motor.

For the synchronous motor, it is thus recommended that a delayed in-phase transfer is done, where the motor voltage and bus voltage is monitored for the first phase coincidence. This would be the only way for a synchronous motor to recover from the transfer. If the transfer can be completed on this motor, the transients would be smaller than the starting transients, and would not damage the motor.

When the same simulations and tests were done for an induction motor, it was found that the motor can easily recover from a loss in power supply, since it does not rely on synchronism to operate. It was seen that the amount of deceleration in the motor is influenced by the time of the transfer and the load on the motor. The load of the motor did not, however, have a significant influence on the current and torque transients. Due to the fact that the transients did not

exceed the starting transients of the motor, it is unlikely that a transfer would be able to cause damage in the motor.

In general, the transients in the motors after a transfer is completed would be smaller than the starting transients of the motors. Since the motors were designed to handle these starting transients, it is unlikely that damage would occur. The largest risk for damage is when the synchronous motor is unable to recover from a transfer, causing high unstable current and torque transients.

7. REFERENCES

- [1] T.R. Beckwith and W.G. Hartmann, *MotorBus Transfer: Consideration and Methods*, 2nd ed.: IEEE Transactions on Industry Applications, 2006.
- [2] G. Engelbrecht, "Training: Basic Transfer Systems," Sasol Synfuels Electrical Engineering, 2012.
- [3] T.S. Sidhu, V. Balamourougan, M. Thakur, and B. Kasztenny, "A Modern Automatic Bus Transfer Scheme," *International Journal of Control, Automation and Systems*, vol. 3, no. 2, pp. 1-7.
- [4] B.S. Guru and H.R. Hiziroglu, *Electric Machinery and Transformers*, Kettering University Department of Electrical and Computer Engineering, Ed.: Oxford University Press, 2001, vol. 3.
- [5] McCulloch, "The Effects of Voltage Dips on Induction Motors," *Dip-Proofing Technologies Inc*, no. 1, pp. 1-2.
- [6] H. Hosseini, H. Abyaneh, F. Shahnia, H. Hatami, and S. Galvani, "Induction Motor Behaviour at Sudden Interruptions and Voltage Sag," in *The International Conference On Electrical Engineering 2008*, 2008, pp. 1-4.
- [7] R.F. McElveen and M.K. Toney, "Starting High Inertia Loads," *Industry Applications, IEEE Transactions*, vol. 37, no. 1, pp. 137,144, February 2001.

EFFICIENT LIGHTING DESIGN FOR BUILDINGS AND OFFICES: A CASE FOR THE CHANCELLOR OPPENHEIMER LIBRARY UNIVERSITY OF CAPE TOWN

R Boadzo*, S Chowdhury*

**University of Cape Town, Department of Electrical Engineering, Upper Campus, Rondebosch, Cape Town 7701*

Abstract. As the shift to more efficient lighting technologies becomes more apparent, the need for sizable research into LED technologies is of significant importance. This paper represents an analysis of the cost effectiveness of energy efficient lighting in today's buildings and offices. The Chancellor Oppenheimer Library at the University of Cape Town was chosen as a case study in which the investigation was carried out. The problems relating to environmental issues due to the use of non-efficient lighting schemes and carbon emissions was reviewed and efficient management schemes were proposed. It was recognised that energy efficient technologies in buildings and offices with the use of LED and CFL lighting systems have become more cost effective and necessary and thus various scenarios were investigated. Specific research was carried out on solid state light emitting diodes as they were notably the best overall option as, the efficiency of these lights were found to surpass all the competing technologies. Comparisons between different lighting technologies were made using the related literature as a basis.

1. INTRODUCTION

There is an enormous need for efficient lighting in buildings and offices in order to reduce energy costs and the associated carbon emissions [1]. In addition to this, the costs associated with the upgrade to newer and more efficient technologies such as LED lighting technologies are seen to be high over the past few years. Thus, there has been significant need for the bridging of the gaps between the transition from less efficient and high-energy consumption technologies to more efficient and less energy consuming technologies [2]. However, the cost of more efficient technologies such as LED technology is one of the reasons this transition is so difficult. Therefore, apart from attempting to research methods to reduce the costs of the actual technologies this study focuses on understanding and investigating the integration of new and old technologies by using the Chancellor Oppenheimer Library as a case study for this application.

The fundamental problems investigated in this case study relate to:

- (i) cost effectiveness of the lighting system used in the Chancellor Oppenheimer Library
- (ii) how efficient are the current lighting technologies in the Chancellor Oppenheimer Library in terms of cost effectiveness
- (iii) how the energy consumption and the lighting technologies can be upgraded at a suitable and reasonable cost
- (iv) whether it is plausible to use a combination of a number of technologies to reach reasonable energy efficiencies and energy consumption levels until the cost of LED lighting technologies reduces considerably

The lighting in the Chancellor Oppenheimer Library spans across the interior and exterior of the building, but this research focused only on the lighting used in the main library, specifically on levels four and five. Moreover, due to out-dated floor plans and electrical manuals available the newer areas now in existence

such as The Research Wing on these levels of the Chancellor Oppenheimer Library have not been included in this thesis.

This research takes note of the working hours of the lighting systems in the Chancellor Oppenheimer Library, however due to the addition over additional working hours caused by the examination periods this are seen as one of the reasons for variations in energy consumptions. Therefore for the purpose of this research it was assumed that the Chancellor Oppenheimer Library operating periods remained as normal during this period. In addition to this, it has been assumed that the working hours follow the South African calendar detailing the number of weekdays and weekends in the year 2013.

2. METHODOLOGY

2.1 Electrical Manuals

To start the research, The University of Cape Town's Property and Services manager was contacted in order to obtain information pertaining to the Chancellor Oppenheimer Library layout in addition to the electrical standards observed at the Chancellor Oppenheimer Library. The manual, which had the electrical schematic layouts of the building, were then obtained, which contained information about the lighting technologies working in the building. This included the types, and power ratings of the installed luminaires. Floor plans were also included in the manual and included information about the number of lights installed in the in the Chancellor Oppenheimer Library in addition to their specific locations.

2.2 Chancellor Oppenheimer Library Inspections

In order to verify that information obtained about the Chancellor Oppenheimer Library floor plans an inspection was conducted for reasons including the fact that the floor plans were not updated after each constructional addition to the building. A number of the lights in the Chancellor Oppenheimer Library had been retrofitted and in order to ascertain which one

had been changed a comprehensive video was taken with the help UCT libraries.

Energy consumption by the lights was reasonable; inspections were done around the building through observing the number of rooms which had their lights switched on at different times. These inspections also helped in estimating how long the lights were used in the meeting/study rooms. Building inspections together with the floor-plans were used to assess the residence's exposure to natural light.

2.3 Time of light usage

To closely approximate consumption figures of the proposed lighting systems, data gathered from the online and offline times of the luminaires in the Chancellor Oppenheimer Library is presented below.

Note that the annual usage is given by $T(\text{year}) = T(\text{day}) * T(\text{hours})$ assuming the Chancellor Oppenheimer Library is open from 6 January until 22 December for the year 2013 a non-leap year.

Table 1: Non leap year

Period	Days
Weekday	247
Weekend	101
Total Days	348

Table 2: Weekday lighting usage data

Location	Times	Online Time (Hours)	Offline Time (Hours)	Estimated annual time of usage T (year)[Hours]
Level 4	07:00-24:00	17	7	4199
Level 5	07:00-24:00	17	7	4199
Totals	-	34	14	8398

Table 3: Weekend lighting usage data

Location	Times	Online Time (Hours)	Offline Time (Hours)	Estimated annual time of usage T (year)[Hours]
Level 4	08:00-18:00	10	14	4199
Level 5	08:00-18:00	10	14	4199
Totals	-	20	28	8398

2.4 Scenario Building

Scenerio building enabled a more diverse approach to the modeling possibilities and are categorized below as follows:

- (i) Scenario 1: Setting up the Chancellor Oppenheimer Library using only Fluorescent Luminaire's
- (ii) Scenario 2: Setting up the Chancellor Oppenheimer Library using only LED luminaires only
- (iii) Scenario 3: Setting up the Chancellor Oppenheimer library using a combination of Fluorescent luminaires for the major lighting fixtures such as LBR Luminaire with prismatic diffuser (white foam) and implementing LED technology for down lights and wall-mounted bulkheads.
- (iv) Scenario 4: Setting up the Chancellor Oppenheimer Library using a combination of LED luminaires for the major lighting fixtures such as the LBR Luminaire with prismatic diffuser (white foam) and implementing Fluorescent luminaires for down lights and wall-mounted bulkheads.
- (v) Scenario 5: Setting up the Chancellor Oppenheimer Library using 50 % Fluorescent luminaires and 50% LED luminaires.

2.5 Modeling In Dialux EVO

After establishing the average time of light use in different areas of the Chancellor Oppenheimer Library, the light intensity tests carried out in order to assess the Libraries levels of illumination and to calculate the costs associated with these illumination levels added Dialux based simulation [3]. It was possible to use Dialux lighting to assess the cost effectiveness and energy efficiency status of the Libraries lighting system through comparing the costs and power ratings of the lighting technologies used in the Chancellor Oppenheimer Library with the costs and power ratings of other lighting technologies that could have been implemented in the Chancellor Oppenheimer Library.

For this approach where a 3-D model of a particular area was created and a lighting level for that area was selected in accordance to the standard lighting requirements. Each modelled area was then simulated using different lighting technologies to achieve the similar lighting levels [4]. The results were then compared in terms of the costs associated with each of the lighting technologies. In so doing, conclusions about the cost effectiveness of implementing a new lighting System for the Chancellor Oppenheimer Library's lighting system were drawn.

3. RESULTS

The simulation results shown in Fig.1, Fig.2 and Fig.3 were obtained from Dialux. The area to be modelled was constrained because the Chancellor Oppenheimer Library Building layout and electrical

manual were out of date at the time of inception this research project. Therefore, in order to produce results that are as accurate as possible the models only represent areas in the Chancellor Oppenheimer Library Level 4 and Level 5. However, the results obtained are more than good enough to generate sufficient results and draw conclusions from them. Due to lack of space and similarity of methodologies, the results for only Scenario 1 are shown in this paper.

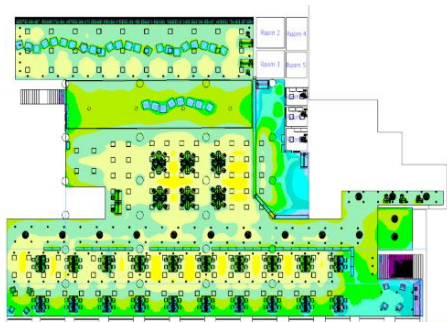
3.1 Scenario 1



Fig. 1: Screen shots 3-D model of level 4 of the Chancellor Oppenheimer Library (Scenario 1)



Fig. 2: Screen shots 3-D model of level 5 of the Chancellor Oppenheimer Library (Scenario 1)



Surface result object 1 / False colors/Perpendicular illuminance (adaptive)

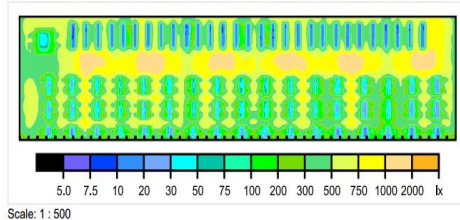


Fig. 3: False colour diagrams for Scenarios 1 for Levels 4 and 5

3.2 Luminous Efficiency

For the benefit of the study the differences between the different Scenarios the luminous efficiencies of each for in each scenario were calculated using the following formula adapted from Alibhai [5]. The comparisons of the luminous efficiencies for all the scenarios are calculated using the formula below:

$$\text{Luminous Efficiency} = \frac{(E(\text{average}) * (\text{Ground area})) * 100}{(\text{lumens})} \quad [1]$$

Table 4: Luminous efficiency parameters for Scenario 1 and 2

Scenario	Scenario 1 –level 4	Scenario 1-level 5	Scenario 2- level 4	Scenario 2- level 5
E (avg)(lx)	446	437	347	456
Total lumens (lx)	1174150	1194580	850530	1006180
Working area (m ²)	1557.10	870.16	1557.10	870.16
Luminous Efficiency (%)	59.15	31.83	63.53	39.44

Table 5: Luminous efficiency parameters for Scenario 3 and 4

Scenario	Scenario 3 –level 4	Scenario 3-level 5	Scenario 4- level 4	Scenario 4- level 5
E (avg)(lx)	334	491	372	365
Total lumens (lx)	850530	1172580	986950	928080
Working area (m ²)	1557.10	870.16	1557.10	870.16
Luminous Efficiency (%)	61.15	36.44	58.69	34.13

Table 6: Luminous efficiency parameters for Scenario 5

Scenario	Scenario 5 –level 4	Scenario 5-level 5
E (avg)(lx)	306	437
Total lumens (lx)	1006730	1100660
Working area (m ²)	1557.10	870.16
Luminous Efficiency (%)	47.33	35.02

Fig. 5: Graphical comparison annual consumptions

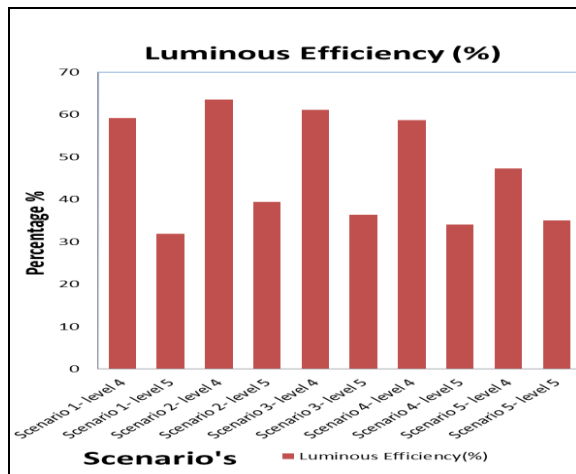


Fig. 4: Graphical comparison of luminous efficiencies

3.3 Annual Consumption

The annual consumption figures below were calculated using the data gathered from the lighting inspections done prior to this analysis.

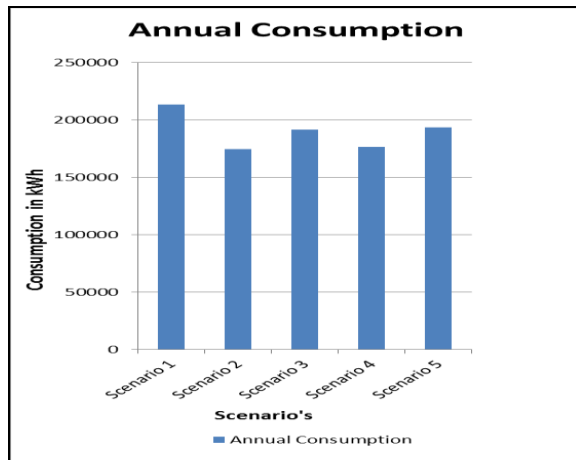


Fig. 5: Graphical comparison of annual energy consumption in kWh

3.4 Cumulative Annual Costs

In calculations for annual energy consumption for a number of luminaires differentiated between the years, an annual electricity price increase of 16% was accounted for and used in his calculations. Whilst Initial Electricity costing = R0.87 per kWh as per Eskom tariff plans remained constant throughout the calculation period (based on September 2012 figures).

Electricity costing (based on 2013 September figures) for the nth year is given by $0.87(1.16)^{n-1}$
 $ALC = L_n * L_c + L_e * 0.87(1.16)^{n-1} + R_c * R_n$

$$ALC = L_n * L_c + L_e * 0.87(1.16)^{n-1} + R_c * R_n$$

Where ALC = Annual luminaire cost
 L_n = total luminaire number
 L_c = Luminaire cost
 L_e = Annual luminaire energy consumption
 R_c = Replacement bulb costs
 R_n = Number of bulb replacement per year

[2]

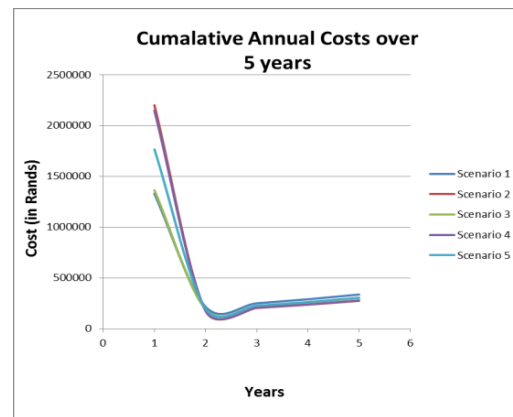


Fig. 6: Cumulative Annual Cost over 5 years

4. CONCLUSION

The simulation results that the current fluorescent lighting system currently in place in the Chancellor Oppenheimer Library is not the most efficient system nor does it have the best consumption figures which can be seen after analysing Scenario 1. Currently in Scenario 2 which modelled a complete replacement of the current fluorescent technology with LED luminaires. Scenario 1 as expected proved to be the most efficient option in terms of luminous efficiency and in addition displayed the best consumption figures between all five scenarios. With respect to the lighting distributions, which can be noted from the Isolines and false colours, diagrams the LED lighting only setup proved to display the most favourable characteristics as in this implementation the distributions of light throughout the modelled area will display the best distributions aesthetically.

Scenarios 3, 4 and 5 showed that the combinations between efficient lighting technologies have serious benefits compared to remaining with just one due cost constraints. From the graphs representing luminous efficiencies it can be noted that using LED lighting technologies for major lighting, such as the three or four tube recessed ceiling lighting and fluorescent lighting Down lights displayed the best luminous characterises. However from a strictly cost point of view this Scenario 3, had had the highest annual energy consumption figures of all three combination scenarios.

The cost, lifespan and consumption analysis in this thesis do not necessarily portray the most efficient

and preferred consumption scenario's as the best option, firstly due the fact that in a short period of time, here modeled as five years the true benefits of LED technologies cannot be seen. In addition to this, from a cost only point of view over a five-year period fluorescent lighting was the best option. However if one considers longer periods of time LED technology will regain some ground. However, it should also be noted that due to the short period under consideration the long-term benefits of the longer life span of the LED technology could not be adequately seen. In the long term due to the lower consumption benefits and the rising costs of energy in South Africa and globally LED technology implementations would reduce the consumption of energy from lighting considerably.

ACKNOWLEDGEMENTS

The authors gratefully acknowledge the support and infrastructure rendered by the Electrical Engineering Department of the University of Cape Town for carrying out this research work. The authors also gratefully acknowledge the support rendered by the staff members of UCT Libraries and UCT Properties and Services Department who helped the first author with his initial enquiries for obtaining the data required for this research work.

REFERENCES

- [1] N. Zografakis, K. Karyotakis and K. P. Tsagarakis, "Implementation conditions for energy saving technologies and practices in office buildings: Part 1. Lighting," *Renewable and Sustainable Energy Reviews*, Vol.16, pp.4165–4174, June 2012.
- [2] A. Jakoef and H.J. Vermeulen, "An investigation of the power consumption and quality of supply for lighting technologies used in industrial energy –efficient initiatives", 46th International Universities' power Engineering Conference (UPEC 2011), Soest, Germany, 2011.
- [3] N. Tshikuvhe, M. Nthonto, S. Chowdhury and S.P. Chowdhury, "Cost Effective Carbon Mitigation through Energy Efficiency: A Case for a University Student Residence Lighting in Cape Town", *Proc. of IEEE Africon 2013*, Mauritius, 2013.
- [4] C. Kaputu, "Building energy efficiency codes (BEEC) in the residential sector", http://active.cput.ac.za/energy/past_papers/DUE/2013/PDF/Papers/05%20-%20Kaputu%20C%20-%20Building.pdf (last accessed on September 2013)
- [5] Shabbir Alibhai, "Energy Efficient Lighting Design with Solid State LEDs", Senior UG Thesis, University of Cape Town, Cape Town, 2011.

POWER LINE COMMUNICATION CHANNEL MODELLING: ESTABLISHING THE CHANNEL CHARACTERISTICS

F. Zwane* and T. J.O. Afullo**

* University of KwaZulu-Natal, Department of Electrical, Electronic and Computer Engineering,
Private Bag X54001, Durban 4001, South Africa E-mail: 211560595@stu.ukzn.ac.za

** University of KwaZulu-Natal, Department of Electrical, Electronic and Computer Engineering,
Private Bag X54001, Durban 4001, South Africa E-mail: Afullot@ukzn.ac.za

Abstract: The Power Line Communications (PLC) channel is known to be a hostile and unpredictable channel. This calls for the development of an accurate channel transfer model that forms the basis for computer simulations which is crucial for proper PLC system design. In this paper, the attenuation coefficients are derived from both the calculations and measurements and then the prediction bounds for the same are determined. An analysis of measurement results for a single phase low voltage PLC network is done, from which a correlation of network constituent elements and topology to the channel characteristics is inferred.

Keywords: channel, attenuation, characteristic impedance, transfer function, frequency response, power line.

1. INTRODUCTION

True to its original purpose, the low voltage power line network is optimized for the transmission of high voltages at low frequencies contrary to data transmission which necessitates the transmission of low voltage at high frequencies. The communication signal passing through this network therefore encounters some hostile channel parameters. The most important parameters are noise, impedance mismatch and attenuation, which are frequency, time and location variant [1], which makes PLC modelling a non-trivial task. For broadband technology the frequency range of interest is 150 kHz to 34 MHz [2].

The signal attenuation in the channel is mainly determined by three factors; resistive losses of conductors due to skin effect, dielectric losses of insulation and coupling losses [3]. The geometry and materials used to manufacture the cable therefore significantly determine the characteristics of the channel. This is due to the fact that the attenuation constant coefficients are determined by these factors. Additionally, the characteristic impedance of the cable is also determined by the geometry and insulation of the cable accounting for the input impedance of the channel network.

The standing voltage and current waves produced by reflections account for the power losses and frequency variant input impedance. Loads connected to the PLC network that are not matched to the characteristic impedance of the given network cable present points of mismatch which in turn cause reflections thereby having a significant effect on the channel's response[4].

Even though channel characteristics have been studied by different authors [5-7], this paper sets to give more insight into the channel characterization task through analysing the measured frequency responses coupled with theoretical derivations. The attenuation constant

coefficients are shown to determine the average path loss of the channel and the position of the notches in the transfer function are seen to follow a certain trend.

2. THEORETICAL ANALYSIS OF CABLE AND MEASUREMENTS

From the two conductor transmission line model, the differential length Δx of the transmission line is described by the distributed parameters, R' , the resistance per unit length, L' , the inductance per unit length, G' , the conductance and C' , the capacitance per unit length. They are calculated as [8][9]:

$$R' = \sqrt{\frac{2f\mu_r\mu_o}{\pi r^2\sigma_c}} \left[\frac{\frac{D}{2r}}{\sqrt{\left(\frac{D}{2r}\right)^2 - 1}} \right] \quad (1)$$

$$L' = \frac{R'}{2\pi f} + \frac{\mu_r\mu_o}{\pi} \cosh^{-1}\left(\frac{D}{2r}\right) \quad (2)$$

$$C' = \frac{\pi\epsilon_r\epsilon_o}{\cosh^{-1}\left(\frac{D}{2r}\right)} \quad (3)$$

$$G' = 2\pi f C' \tan \delta \quad (4)$$

$$\delta = \frac{1}{\sqrt{2\pi f \sigma_c \mu_c}} \quad (5)$$

Where:

δ = the skin depth determining the dissipation factor

f = the wave frequency

ϵ_r = the dielectric constant
 $\epsilon_o = 8.85 \times 10^{-12}$ F/m

μ_r = relative magnetic permeability of the dielectric
 $\mu_0 = \pi \cdot 4 \times 10^{-7}$ H/m

σ_c = the relative conductivity of conducting material
 equal to 5.58×10^{-7} S/m

μ_c = the conductors relative permeability

r = the radius of the conductor

D = the separation between conductors.

The amplitude of an electromagnetic wave travelling through a transmission line, of distance l , decreases by a factor of $e^{-\gamma l}$. Where γ is the propagation constant calculated as [10]:

$$\gamma = \sqrt{(R' + j\omega L')(G' + j\omega C')} = \alpha + j\beta \quad (6)$$

Where:

α = the attenuation constant in Np/m

β = the phase constant in rad/m.

The attenuation coefficient is often expressed as [11]:

$$\alpha = a_0 + a_1 f^k \quad (7)$$

The characteristic impedance of the cable is calculated as [10]:

$$Z_0 = \sqrt{\frac{R' + j\omega L'}{G' + j\omega C'}} \quad (8)$$

The characteristic impedance and attenuation coefficients were measured using a calibrated Rohde & Schwarz ZVL vector network analyser. The input impedances of a short circuited end and open circuited end of a 3x2.5mm² cabtyre PVC cable were measured and the characteristic impedance was computed using the following equation [12]:

$$Z_0 = \sqrt{Z_{sc} Z_{oc}} \quad (9)$$

The propagation constant was computed using the expression in (10) [12]:

$$\gamma = 1/l \tanh^{-1} \sqrt{Z_{sc}/Z_{oc}} \quad (10)$$

Where:

Z_{sc} = the input impedance when the cable ended is short circuited

Z_{oc} = the input impedance when the cable ended is open circuited

l = the length of the measured cable

The characteristic impedance and attenuation constant measurement results are shown in Figure 1 and 2 respectively.

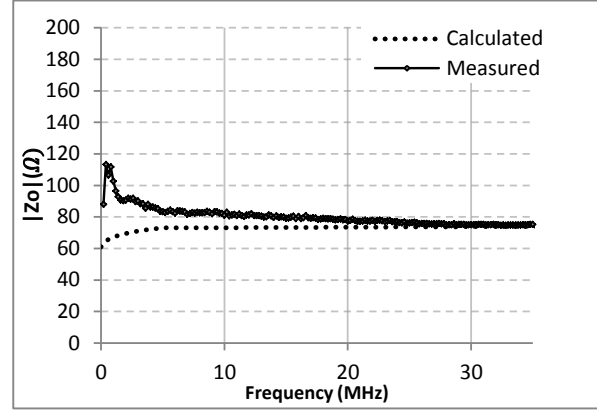


Figure 1: The characteristic impedance of the 3x2.5mm² cable

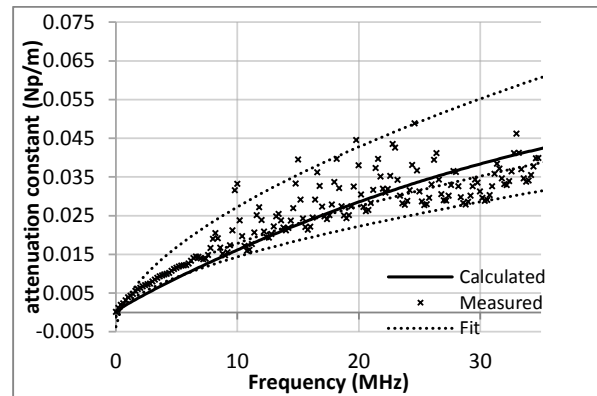


Figure 2: The attenuation constant of the 3x2.5mm² cable

From the measured attenuation constant, a fit is generated by the Least Absolute Residual (LAR) robust method, the maximum and minimum bounds are then determined and the coefficients are given in Table 1.

Coefficient	Calculated	Measured		
		Average	Maximum	Minimum
a_0	-0.00316	-0.001247	-0.00145	-0.00105
a_1	5.43E-6	1.438E-6	1.94E-6	1.582E-6
k	0.517	0.5893	0.5838	0.5948

Table 1: The measured fit and calculated attenuation constant coefficients

The Root Mean Square Error (RMSE) between the measured and calculated characteristic impedance values is 2.809 and the RMSE for the attenuation coefficients measurements fit and calculated values is 0.000702.

3. PLC CHANNEL MODEL AND MEASUREMENT RESULTS

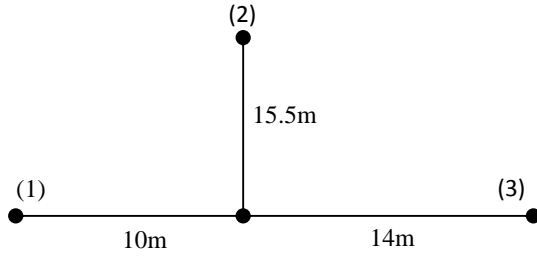


Figure 3: A single branch network

A deterministic approach by [13] is employed in calculating the transfer function of a single branch network as shown in Figure 3 by deriving its scattering matrix. The channel is broken down as shown in Figure 4 where Z_s is the source impedance, Z_L is the load impedance and Z_b is the load impedance at the branch end. Z_{in1} is the input impedance of the network looking into the load, Z_{in2} is the input impedance looking into the branch and Z_{in} is the input impedance looking into the single branch network.

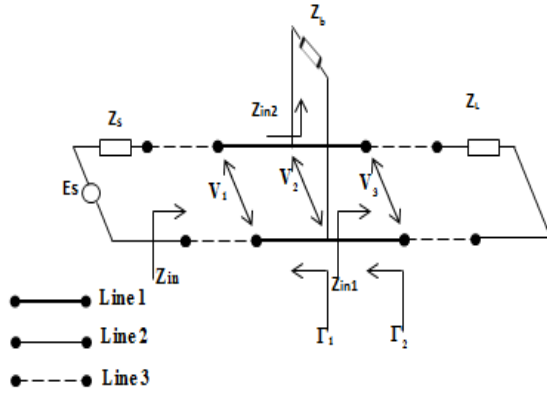


Figure4: Single-branch network

Γ_1 is the reflection coefficient at the node and Γ_2 is the reflection coefficient from the path end calculated respectively as[10]:

$$\Gamma_1 = \frac{Z_L - Z_0}{Z_L + Z_0} \quad (11)$$

$$\Gamma_2 = \frac{Z_{in1}||Z_{in2} - Z_0}{Z_{in1}||Z_{in2} + Z_0} \quad (12)$$

The parameters S_{11} and S_{21} are computed as [14]:

$$S_{11} = \frac{Z_{in} - 50}{Z_{in} + 50} \quad (13)$$

$$S_{21} = 2 \frac{V_3}{E_g} \quad (14)$$

The S_{21} parameter is indirectly calculated from [13]:

$$S_{21} = 2 \frac{V_3}{V_2} \cdot \frac{V_2}{V_1} \cdot \frac{V_1}{E_g} \quad (15)$$

$$\frac{V_1}{E_{g1}} = \frac{Z_{in}}{Z_{in} + Z_g} \quad (16)$$

Shifting in reference planes is applied according to [10] to obtain the ratios:

$$\frac{V_3}{V_2} = \frac{(1 + \Gamma_1) e^{-\gamma l_3}}{1 + \Gamma_1 e^{-\gamma l_3}} \quad (17)$$

$$\frac{V_2}{V_1} = \frac{(1 + \Gamma_2) e^{-\gamma l_1}}{1 + \Gamma_2 e^{-\gamma l_1}} \quad (18)$$

Measurement of the transfer function of a single branch network as shown in Figure 3 was done by the use of the vector network analyser, with point (1) at transmitter and (3) at receiver. The calculated transfer function for the same network, for open and short circuited branch terminations is as shown in Figures 4(a) and (b) compared to the measured transfer functions.

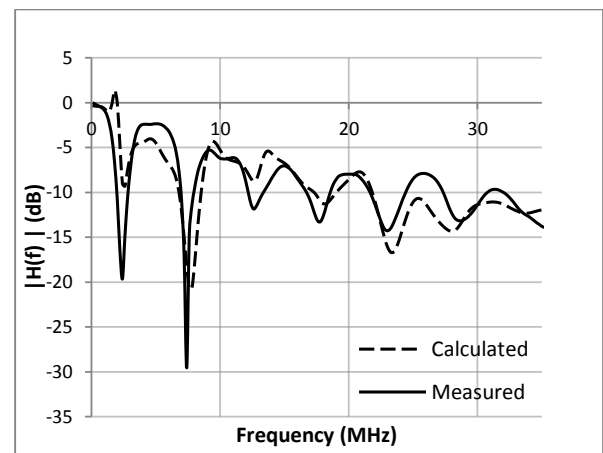


Figure 4(a): The single branch network frequency response for open circuited branch termination

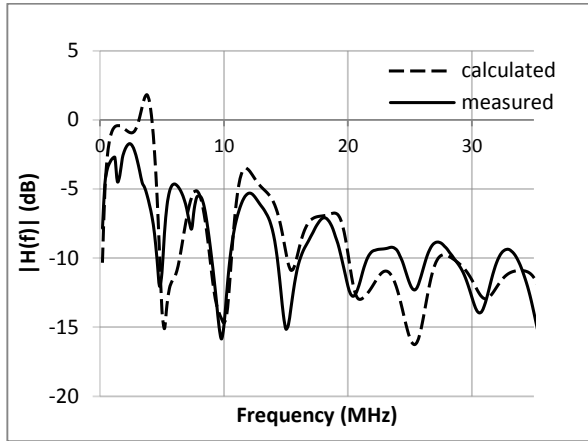


Figure 4(b): The single branch network frequency response for open and short circuited branch termination

The measured transfer function of the open circuited and short circuited branch terminations are shown in Figure 5. Also shown in the figure are the upper and lower bounds of the average path loss determined from the maximum and minimum bounds of measured attenuation constant obtained in Section 2.

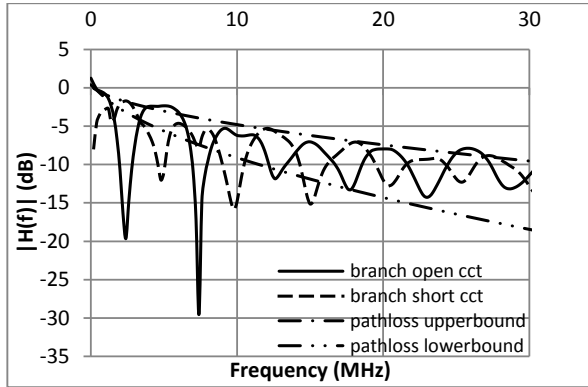


Figure 5: The transfer functions of the one branch network with open and short branch terminations.

The same network topology Figure 3 was used to take measurements for different branch lengths (15.5m, 10.5m, 7.5m). The frequency response acquired from the measurements is as in Figure 6.

4. DISCUSSION OF RESULTS

The measurement results differ marginally from the calculations from the analytical models as shown in Figures 1, 2, 4(a) and 4(b). When carefully studying the transfer function of the two variations in termination we conclude from Figure 5, that the attenuation profile of the transfer function follows the path loss determined by the attenuation constant bounds given in Table 1.

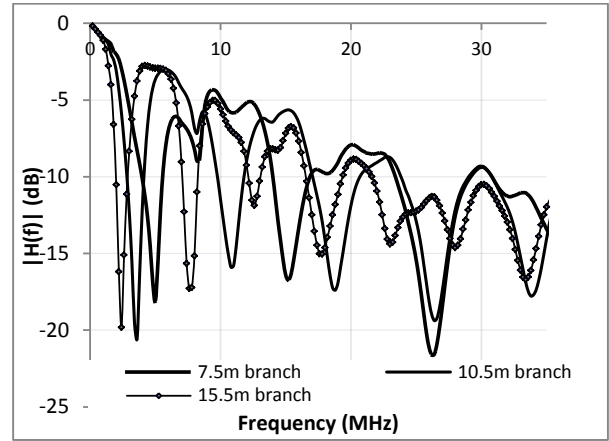


Figure 6: The transfer function for different branch lengths

Furthermore, there exists a trend in the notches, the separation between the notches is seen to be equal. We consider the electric length of the branch expressed in units of the wavelength λ , related to the propagation velocity v_p and signal frequency f by [15]:

$$\lambda = \frac{v_p}{f} \quad (19)$$

As the impedance of the channel is frequency dependent, for the open circuit end, the first notch will occur at a resonant frequency, relative to the length of the branch we shall refer to as d , and propagation velocity v_p as:

$$f_0 = v_p/4d \quad (20)$$

From the measurements the propagation velocity was estimated to be 1.488×10^8 . Given the first notch of the open circuit ended branch termination, solving for d will give 15.5m.

The subsequent notches will be at frequencies given by:

$$f_{ok} = \frac{v_p}{4d}(2k + 1), \quad k = 1, 2, \dots \quad (21)$$

For the short circuited branch termination the notch will occur first at zero and then at the frequencies:

$$f_{sk} = \frac{v_p}{4d}(2k), \quad k = 1, 2, \dots \quad (22)$$

Therefore if the branch length is known, we will be able to determine the notch positions and separation.

Moreover having a reference branch length, varying the length by a factor n will give a resulting first notch at frequency:

$$f'_0 = \frac{1}{n}f_0 \quad (23)$$

5. CONCLUSION

The transfer function of a single branch channel has been found to follow an average path loss determined by the attenuation constant coefficients. Expressions of the position of the notches have been established from the correlation of the signal frequency to the propagation velocity and length of the branch in a single branch network. More measurements need to be done to further determine the relation of channel response characteristic to different topologies of the power line communication channel and confirm the deductions made here.

6. REFERENCES

- [1] H. Philipps, "Modeling of power line communication channels," in Proc. 3rd Int. Symp. Power-Line Communications Applications, Lancaster, U.K., 1999, pp. 14–21.
- [2] R. Lehnert, H. Hrasnica, and A. Haidine, "Broadband Powerline Communications Network Design," Wiley, 2004.
- [3] A. Jero, "Applicability of Powerline Communications to Data Transfer of Online Condition Monitoring of Electrical Drives," Doctor Thesis, Lappeenranta University of Technology, ISBN 951-764-783-2.
- [4] D. Anastasiadou, T. Antonakopoulos, "Measurements-based method for impedance characterization of residential loads," Instrumentation and Measurement Technology Conference, 2004. IMTC 04. Proceedings of the 21st IEEE , vol.1, no., pp.669,674 Vol.1, 18-20 May 2004.
- [5] H. Philipps, "Performance measurements of power-line channels at high frequencies," in Proceedings of the International Symposium on Power Line Communications and its Applications (ISPLC), 1998, pp. 229-237.
- [6] D. Liu, E. Flint, B. Gaucher, and Y. Kwark, "Wide band AC power line characterization," IEEE Transactions on Consumer Electronics, vol. 45, no. 4, pp. 1087-1097, November 1999.
- [7] P. Mlynek, J. Misurec, M. Koutny, P. Silhavy, "Two-port Network Transfer Function for Power Line Topology Modeling," Radioengineering, Vol. 21, No. 1, April 2012, pp. 356-363.
- [8] I. C. Papaleonidopoulos, et al., "Evaluation of the TwoConductor HF Transmission-Line Model for Symmetrical Indoor Triple-Pole Cables," Measurement, Vol. 39, No. 8, 2006, pp. 719-728.
- [9] S. Ramo, J.R Whinnery and T. van Duzer, "Fields and Waves in Communication Electronics," John Wiley & Sons, New York, 1994, pp. 153–155, 180–186, 245–252.
- [10] D. M. Pozar, Microwave Engineering. New York: Wiley.
- [11] M. Zimmermann and K. Dostert; "A Multi-path Model for the Powerline Channel," IEEE Transaction On Communications, vol. 50, No. 4, pp. 553-559 April 2002.
- [12] S. Liao, Microwave Circuit Analysis and Amplifier Design, Prentice-Hall International, 1987.
- [13] H. Meng, S. Chen, Y.L. Guan, C. Law, P.L. So, E. Gunawan, T.T. Lie, "Modeling of Transfer Characteristics for the Broadband Power Line Communication Channel," IEEE Trans. Power Delivery, Vol. 19, No. 3, pp1057-1064 July 2004.
- [14] G. Gonzalez, Microwave Transistor Amplifiers. Englewood Cliffs, NJ: Prentice-Hall, 1997.
- [15] A. Smith, Radio Frequency Principles and Applications: The Generation, Propagation, and Reception of Signals and Noise. Wiley-IEEE Press, 1998

INVESTIGATING COMMON SCADA SECURITY VULNERABILITIES USING PENETRATION TESTING

S G Ralethe and K J Nixon *

** University of the Witwatersrand, Johannesburg, School of Electrical and Information Engineering, 1 Jan Smuts Avenue, Braamfontein, Johannesburg, South Africa*

Abstract. Supervisory Control and Data Acquisition (SCADA) systems were developed to assist in the management, control and monitor of critical infrastructure functions water and electricity supply. In the past, these systems had little connectivity to the Internet because they ran on dedicated networks and proprietary control protocols. As a result, SCADA systems were secure, and did not face challenging vulnerabilities associated with the Internet. The need for remote connectedness, in order to collect and analyse data from remote locations, resulted in SCADA systems being increasingly getting connected to the Internet. Therefore, SCADA systems are no longer immune to cyber-attacks. There are reported cases on cyber-attacks targeted at SCADA systems. This paper represent research that utilised penetration testing to investigate common SCADA security vulnerabilities. The investigation was conducted through experiments using virtual plant environment. The results revealed vulnerabilities which are considered as common by the Idaho National Laboratory and others which were not classified. Recommendations are provided on how to mitigate the vulnerabilities discovered during the study.

Key Words. SCADA systems; security vulnerabilities; penetration testing.

1. INTRODUCTION

Industrial control systems can be considered as part of the backbone of a large number of industries that are affecting almost every basic service required by the modern society. These control systems are usually large networked computer systems and are used to assist in the management, control and monitoring of critical infrastructure functions such as gas, water, waste, railway, electricity production and distribution, and traffic. Due to their prominent and increasing importance, these systems can be considered important asset whose safety and security must be protected. However, it is a difficult task to secure these systems.

With the recent growth in cyber-attacks targeted at computer networks and systems in the infrastructure of major nations, it is important to investigate and understand the vulnerabilities of these control systems in order to develop appropriate and effective mitigation techniques that will ensure the systems' security and protection. This is a necessity because the threat posed to these control systems has a greater impact and scale of attack than common computer vulnerabilities.

The increase in cyber-attacks on Supervisory Control and Data Acquisition (SCADA) systems has led to a rapid increase in research programs in the security analysis of SCADA systems. SCADA security is different from the traditional network security and as a result research on SCADA security cannot be approached from the perspective of currently available network security research. Therefore, it must be investigated as its own research area. Research programs in the security analysis of SCADA systems include vulnerability analysis, penetration testing, security assessment, etc. [1]. Penetration testing is utilised in this paper to investigate common SCADA security vulnerabilities, and it is discussed in the next section.

The investigation in this paper was conducted through experiments. The experiments were simulated using three computers under two different

scenarios. The experiments yielded vulnerabilities which are classified by the Idaho National Laboratory [2] as common to all SCADA systems and other vulnerabilities which were not classified. From the list of the vulnerabilities discovered during the experiments, recommendations are presented in this paper towards how to mitigate the discovered vulnerabilities.

The remainder of this paper is as follows. Section 2 present background information on SCADA system, SCADA vulnerabilities, Penetration testing and penetration testing tools. Section 3 discussed the research hypothesis addressed by this paper. Section 4 presents tools used to implement the virtual plant environment. The experiments and results are presented in section 5. The results are discussed in section 6, and recommendations are presented in section 7.

2. Background

2.1 SCADA System

2.1.1 Overview and Architecture

SCADA systems are the common computer systems used to monitor and control major infrastructure. Among the basic function of an SCADA system are its ability to provide data related to the operating state of the system and allow operators to remotely control the distributed system. According to [3], one of the benefits of using a SCADA system is that it allows the high-level management of industrial process by merging data from the many distributed portions of the process. This can help enhance the robustness and reliability of the system.

An SCADA system consist of a number of remote terminal units (RTUs) and/or Programmable Logic Controllers (PLCs), and the central host and the operator terminals. The RTUs collect field data and are connected back to a master station via a communication system [5]. For example, an SCADA can collect information regarding a leak on a pipe at the plant site, transfer the data about the leak back to

a central site, then alert the master station that a leak has occurred. The collected data is normally real-time and it allows for the optimization of the operation of the plant and process. The master station displays the acquired data and also allows an operator to perform remote control tasks [5].

In their early days, SCADA systems made use of Public Switched Network (PSN) for monitoring purposes. Today many systems are monitored using the infrastructure of the corporate Local Area Network/Wide Area Network (WAN). Wireless technologies are now being widely deployed for purposes of monitoring [3].

Even though SCADA systems are used in a varied of scale and purpose, they usually are designed based on a similar architecture. It is important to recognise the fundamental similarities in SCADA systems because that makes it possible for researchers to make use of general models of the class of all SCADA systems. The general model is composed of four major parts: the process to be controlled, the field devices (RTUs, PLCs) physically connected to it, the centralised control centre, and the network that connects the controller and field devices [6].

2.1.2 Security Vulnerabilities

[4] mentioned that, in the past, SCADA systems had little connectivity to the Internet because they ran on dedicated networks with proprietary control protocols and used hardware and software specific to the vendor. As a result, SCADA systems were secure, and did not face challenging vulnerabilities associated with the internet. Intrusion could only have been accomplished with physical access, so physical security measures were sufficient to repel computer-based attacks.

According to [7], the need for remote connectedness, in order to collect and analyse data from remote locations, resulted in SCADA systems being increasingly getting connected to the Internet and corporate networks. Therefore, SCADA systems are no longer immune to cyber-attacks, and such increased connectivity exposes SCADA systems to an enlarged attack surface [7].

[7] mentioned that when designing the networks for SCADA systems, little attention was paid to security aspects in order to maximise functionality. These design decisions implied that the security of the system was traded for performance, reliability and flexibility, and as a result penetrating the control network can be accomplished without physical access to the SCADA system by remote attackers exploiting vulnerabilities in the gateway between the corporate and SCADA systems [7].

According to [8], the Industrial Security Incident reported an increase in cyber-attacks during the period it collected incident reports. A popular attack on SCADA systems that further demonstrate the need for investing in the security of SCADA systems is the Stuxnet worm. This attack provides a good example of why protecting critical infrastructure is an

important part of national security. [9] mentioned that the Stuxnet worm was first identified in June 2010 and was likely targeted at SCADA systems in Iran.

Stuxnet worm infected field devices controlling centrifuges in a Natanz nuclear facility. According to [10], the Stuxnet worm was able to maliciously vary centrifuge speeds to force them outside normal operating conditions and sabotage the system. The attack inflicted by the Stuxnet worm is significant because it demonstrated the capabilities of cyber-attacks on critical infrastructure and showcased the potential they have in cyber warfare.

There are other reported cases of attacks and potential threats on SCADA systems worldwide. For example, the “Aurora Generator Test” [11] conducted in March 2007 simulated a remote cyber-attack on a generator control station which resulted in the partial destruction of a diesel-electric generator. Another example is the attempted distributed denial of service (DDoS) attack on an Israeli power plant [1].

According to [4], these attacks are not unique to SCADA systems as they can affect all networked computers regardless of where they are deployed. What makes the SCADA systems unique is that they are highly customised and most of them do not have the same configuration and functionality. As a result, it requires specific and detailed knowledge in order to attack SCADA systems.

Similarly, the vulnerabilities faced by regular computer systems hardware can also affect SCADA systems. These vulnerabilities include interruption, interception, and eavesdropping. Also, the communication links between SCADA hardware devices are susceptible to vulnerabilities faced by regular computers [4].

Although the vulnerabilities discussed above are associated with cyber-attacks via IP networks, there are reported cases of attacks via serial communication products. According to [12], the vulnerabilities were found in devices that are used for serial and network communications between servers and substations. An intruder could exploit the vulnerabilities by gaining physical access to a substation or by breaching the wireless radio network over which the communication passes to the server. Once an intruder has gained access to the network, they can send malformed message to the server to exploit the weakness [12].

In addition to the vulnerabilities mentioned above, there are other sources of security vulnerabilities associated with the web services of SCADA systems. These can be uncovered by performing penetration test on the SCADA system. Penetration testing is discussed in the next subsection.

2.2 Penetration Testing

2.2.1 Overview

Modern SCADA systems provide better access to plant information by means of web services. Web services provide a strategic mean for data exchange because of their simple interface. However, [13] noted that since web services are widely exposed, the existence of a security vulnerability in these services can be uncovered and exploited by hackers.

Most web services make use of relational database for persistent storage. Thus, security vulnerabilities such as SQL Injection are particularly relevant to web services of SCADA systems. According to [13], SQL Injection vulnerabilities are related directly to structure of the code of web services. SQL Injection attacks change SQL commands that are sent to the database. Improperly validated input parameters make it possible for SQL Injection [13].

Penetration testing is one of the well-known techniques used by web service developers to discover security vulnerabilities in their code. [13] mentioned that penetration testing takes a “black-box” approach in the sense that it stresses the application from an attacker’s point of view. In other words, penetration testing discovers vulnerabilities by simulating attacks from hackers on a target application [13].

According to [14], penetration testing can be divided into three phases: information gathering, attack generation, and response analysis. During information gathering, testers aim to gain information about the target application. This can be achieved by using techniques such as automated scanning, web crawlers, and social engineering. The information gathered is then used, together with domain knowledge about possible vulnerabilities, to generate an attack during the attack generation phase. The generation of attacks can be automated by using commercial or open-source tools. Under the response analysis phase, testers determine if an attack has succeeded, if so, testers then log information about the attack. The discovered vulnerabilities are then detailed in a report at the end of the penetration testing process. Developers can use this information to eliminate the vulnerabilities and improve the security of their software [14].

There are different reasons for carrying out a penetration test. One of the main reasons is to find vulnerabilities and fix them before an attacker does. Another reason for performing a penetration test is to give the IT department at the target company a chance to respond to an attack. Attackers are employing a variety of automated tools and launching network attacks looking for ways to penetrate systems. Penetration testing allows the IT department of a company to find holes in the system before somebody else does. In a sense, penetration testing provides IT management with a view of their network from a malicious point of view.

2.2.2 Penetration Testing Tools

There are a wide variety of tools that are used in penetration testing. According to [15], there are two

main types of penetration testing tools; reconnaissance or vulnerability testing tools and exploitation tools. However, [15] noted that penetration testing is more directly tied to the exploitation tools and the initial scanning and reconnaissance is often done using less intrusive tools. The difference between these two types is not clear cut. For this research, 3 different tools were used. The tools were chosen in line with the objectives of this study as outlined in section 3. The tools used for this research are: Metasploit, Nessus, and Nmap.

Metasploit is a framework for cyber exploitation. As a framework, it eases the effort to exploit known vulnerabilities in networks, operating systems and applications, and to develop new exploits for new or unknown vulnerabilities. Nessus is a tool designed to automate the testing and discovery of known security problems. Nmap is a port scanning tool. Port scanning is usually a part of the reconnaissance of a penetration test or an attack.

3. Research Hypothesis

The Vulnerability Analysis of Energy Delivery Control Systems report, prepared by Idaho National Laboratory [2], describes the common vulnerabilities on energy sector control systems, and provides recommendations for vendors and owners of those systems to identify and reduce those risks.

The report presents vulnerabilities at a high level to provide awareness of the common SCADA security vulnerability areas without divulging product-specific information. Vulnerabilities that could be used as part of an attack against an SCADA are consolidated into generic common SCADA vulnerabilities. The vulnerabilities were routinely discovered in NSTB (National SCADA Test Bed) assessments using a variety of typical attack methods to manipulate or disrupt system operations.

The 10 most significant cyber security risks identified by Idaho National Laboratory (2011) during NSTB software and production SCADA assessments are:

1. Unpatched published known vulnerabilities
2. Web Human-Machine Interface (HMI) vulnerabilities
3. Use of vulnerable remote display protocols
4. Improper access control (authorization)
5. Improper authentication
6. Buffer overflows in SCADA services
7. SCADA data and command message manipulation and injection
8. SQL injection
9. Use of standard IT protocols with clear-text authentication
10. Unprotected transport of application credentials

The common vulnerabilities in the report were found on two or more unique SCADA configurations. [2]

mentioned that even though SCADA functions, designs, and configurations vary among vendors, versions, and installations, their high-level vulnerabilities and defensive recommendations are similar. Therefore, the following hypothesis arises: Penetration testing on a given SCADA system, which was not part of the research covered by [2], will reveal vulnerabilities which are classified as common by the Idaho National Laboratory report, as well as other uncommon vulnerabilities.

4. Implementation

This section discusses the implementation of a virtual plant for experimental purpose. The design of the virtual plant environment consist of three aspects: SCADA software, OPC Server, and Simulated Process Model. The SCADA software and the Simulated Process model are linked together using an OPC interface. The conceptual design of the plant environment is illustrated in figure 1. This setup and implementation were adapted from [16]. The only difference is in the choice of the HMI software.

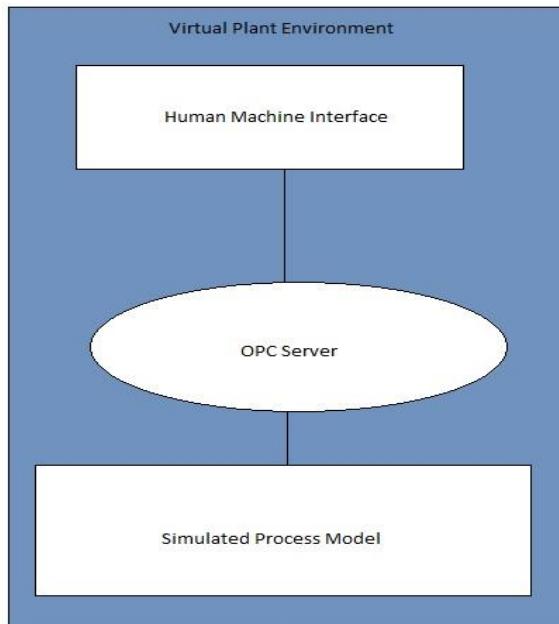


Fig. 1: Conceptual Design of the Virtual Plant Environment

An OLE (Object Linking and Embedding) for Process Control (OPC) is a standard mechanism that enables the communication and data exchanging between various types of devices and control applications. An OPC consist of an OPC Server and an OPC Client.

An OPC Server is a software application that acts as an API (Application Programming Interface) or protocol converter. It allows Windows programs to communicate with industrial hardware devices such as PLC, or any data source such as database or User Interface, and translate the data into the OPC Client [16].

An OPC Client is a software application used to access (for reading and/or writing) information provided by the OPC Server through the OPC standard. For this research, the OPC interface was implemented using KEPServerEX software. The other tools used in the design are Simulink, OPC Toolbox and SCADA software.

Simulink is a commercial tool for modelling, simulating and analysing multi-domain dynamic systems. Simulink is developed by the MathWorks, and comes as a package of MATLAB. OPC Toolbox software is a collection of functions that extend the capability of the MATLAB environment, and blocks that extend the Simulink simulation environment. KEPServerEx is a 32-bit Windows application that provides a means of bringing data and information from a wide range of industrial devices and systems into client applications on Windows PC.

For this research, the HMI used was the free version of ClearSCADA developed by Schneider Electric. According to [17], this free version has the same capabilities as the paid version, the difference being that the free version is only limited to 50 objects in a project.

5. Experimental Setup and Results

This research was carried out in terms of experiments that involve simulations. Three computers were: one running a SCADA system, one simulating a plant, and the other was used to run penetration tests targeted at the SCADA system. The SCADA system and the virtual plant were on the same network as well as the attacker PC.

Table 1 presents the results collected after running Nmap targeting the computer running the SCADA system.

Table 1: Nmap Results

PORT	STATE	SERVICE
23/tcp	open	telnet
513/tcp	open	tcpwrapped
514/tcp	open	tcpwrapped

Even though Nmap found three open ports, it was not able to identify the operating system of the computer running the SCADA system after three unsuccessful tries.

Table 2 presents results collected after running Nessus targeting the computer running the SCADA system.

Table 2: Nessus Results

Vulnerability	Risk Factor
Distributed Denial of Service	High
Information Disclosure	Medium
SQL Injection	High

SQL pg_dump	Medium
SMB Signing Disabled	Medium
SSL Certificate cannot be trusted	Medium
SSL Self-signed Certificate	Medium
SSL Certificate with wrong Hostname	Medium
SSL RC4 Cipher Suites Supported	Low

Table 3 presents results collected after running Metasploit, targeting the computer running the SCADA system

Table 3: Metasploit Results

Vulnerability	Risk Factor
Man-in-The-Middle attack	High
Weak Cryptography	Medium
Insecure renegotiation of TLS/SSL	Medium
IP Forwarding	Medium

6. Discussions

In the first run of experiments, Nmap was ran, targeting the computer running the SCADA system. Nmap is a port scanning tool and cannot exploit the vulnerabilities of the ports. During the run, Nmap identified open ports on the host which could be used by an attacker to gain improper access to the SCADA system and be able to manipulate SCADA data and command messages.

One of the open port was the one associated with telnet service. Telnet is a protocol that allows one computer to execute a text terminal on another. Tenet is not encrypted; passwords and all other data will be transmitted as clear text.

Nmap failed to identify the operating system of the host running the SCADA system. A possible explanation can be that, the host is running Microsoft's Windows 8 and the version of Nmap used did not have updated functionalities that can identify if the operating system is Microsoft's Windows 8.

The second run of experiments was conducted by using Nessus to target the computer running the SCADA system. The Nessus tool gives a detailed report on the vulnerabilities discovered and the effect of those vulnerabilities on the system. In this paper, only vulnerabilities with high risk factor are discussed.

The first vulnerability reported by Nessus was the denial of service vulnerability. Nessus report

revealed that the version of Apache HTTP Server running on the target computer was affected by a denial of service (DoS) vulnerability. By making a series of HTTP request with overlapping ranges in the *Range* or *Request-Range* request headers can result in memory and CPU exhaustion.

The other high risk factor vulnerability discovered by Nessus is associated with SQL injection. The scan discovered that *PostgreSQL* incorrectly checked permissions on functions called by a trigger. An attacker could attach a trigger to a table they owned and possibility escalate privileges. The scan also revealed that *PostgreSQL* incorrectly truncated SSL certificate name checks to 32 characters. If a host name was exactly 32 characters, this issue could be exploited by an attacker to spoof the SSL certificate.

The third run of experiments was conducted by using Metasploit to target the computer running the SCADA system. Only vulnerabilities with high risk factor are discussed. The vulnerability discovered was the Microsoft Windows Remote Desktop Protocol Server man-in-the-middle attack. The report from Metasploit penetration testing stated that the RDP client makes no effort to validate the identity of the server when setting up encryption. An attacker with the ability to intercept traffic from the RDP server can establish encryption with the client and server without being detected. A MiTM attack of this nature would allow the attacker to obtain any sensitive information transmitted, including authentication credentials.

7. Recommendations

This section brings forward recommendations for mitigating the vulnerabilities discovered by Nessus and Metasploit. The vulnerabilities covered here are those with high risk factor. The other vulnerabilities are not covered here because the strategies to mitigate are trivial, and in most cases can be fixed with clicking of buttons.

7.1 Distributed denial-of-service

[18] defines a distributed denial-of-service (DDoS) attack as an attack in which a multitude of compromised systems attack a single target, thereby causing denial of service for users of the target system. Furthermore, the incoming flood of messages to the target system essentially forces it to shut down, thereby denying service to the system to legitimate users. The aim here is to make the target system or network resource unavailable to its intended users by sending thousands of packets to the target system.

There are different forms of DDoS attacks. Therefore, it is important to consider these different forms when building a defence against DDoS attacks. The easiest, although costly, way of defence is to buy more bandwidth. However, modern DDoS attacks are getting large, and quite often can be much bigger than what finances will allow in terms of bandwidth.

Therefore, the method of increasing bandwidth might not be an effective one.

One critical piece of network that administrators can look to in order to mitigate DDoS attacks is the DNS server. It is not a good idea to leave the DNS server as an open resolver, and it should be locked down in order to save the organisation from being used as part of an attack.

7.2 SQL Injection

[19] defines SQL injection attack as a form of attack that comes from user input that has not been checked to see that it is valid. The objective of such an attack is to fool the database system into running malicious code that will reveal sensitive information or otherwise compromise the server. The specially crafted user data tricks the application into executing unintended commands or changing data [19].

By launching an SQL injection attack, an attacker can create, read, update, alter, or delete data stored in the back-end database. In its most common form, an SQL injection attack gives access to sensitive information such as identity numbers, credit card numbers or other financial data.

[19] mentioned that there are two main types of SQL injection attacks. First-order attacks are when the attacker receives the desired result immediately, either by direct response from the application they are interacting with or some other response mechanism, such as email. Second-order attacks occur when the attacker injects some data that will reside in the database, but the payload will not be immediately activated. This type of attack is commonly used to target SCADA systems [19].

SQL Injection can be effectively mitigated by informing the administrators to adopt an input validation technique to authenticate user input. Administrators should ensure that users with the permission to access the database have the least privileges. Administrators should use strongly typed parameterised query APIs with placeholder substitution markers, even when calling stored procedures. Lastly, administrators should show care when using stored procedures since they are generally safe from injection [20].

7.3 Man-in-the-Middle Attack

[21] defines man-in-the-middle (MitM) attack as an attack where the communication exchange between two users is surreptitiously monitored and possibly modified by a third, unauthorised, party. In addition, this third party will be performing this attack in real time. This is to say, stealing logs or reviewing captured traffic at a later time would not qualify as a MitM.

According to [23], MitM attack makes use of a technique called Address Resolution Protocol (ARP) spoofing to trick the computer of the first user into thinking that it is communicating with the computer of the second user. This technique allows the network traffic between the two computers to flow through

the attacker's system, which enables the attacker to inspect all the data that is sent between the victims.

A MitM attack can be performed in two different ways, according to [21]:

- The attacker is in control of a router along the normal point of traffic communication between the victim and the server the victim is communicating with
- The attacker is located on the same broadcast domain as the victim, or the attacker is located on the same broadcast domain as one of the routing devices used by the victim to route traffic

[21] mentioned that a MitM attack will exploit the weaknesses found in network communication protocols in order to convince a host that traffic should be routed through the attacker instead of through the normal router. What is happening here is that the attacker is advertising that they are the router and the client should update their routing records appropriately. This is, in essence, ARP spoofing. According to [21], the greatly simplified purpose of ARP is to enable IP address to MAC address translations for hosts. This is a requirement for facilitating the movement of packets from one host to another.

There are reported ways to prevent MitM attack. [23] mentioned that in practice, ARP spoofing is difficult to prevent with the conventional security tools that come with standard computers. However, users can make it difficult for people to view network traffic by using encrypted network connections provided by HTTPS or VPN technology.

According to [22], tools which use the advanced address resolution protocol and measures such as implementing dynamic host configuration protocol (DHCP) snooping on switches can limit or prevent ARP spoofing. This will in turn help prevent MitM attacks.

8. Conclusion

SCADA system security is an area of growing interest due to the security threats faced by SCADA systems. A research conducted by [2] on the security of SCADA systems revealed common SCADA vulnerabilities that are faced by all SCADA even though functions, designs, and configurations vary among vendors, versions, and installations. The research presented in this paper utilised penetration testing to investigate common SCADA vulnerabilities.

In the experiments, the attacker launched the attack at the host computer from within the company network. Even though there were no new vulnerabilities discovered during the experiments, this study demonstrated that the statement put forward by the Idaho National Laboratory can be verified. Also, the study demonstrated the ability of penetration testing

tools to discover vulnerabilities. The tools used in the research found different vulnerabilities. This highlighted the differences between the tools and further supported the idea of utilising multiple tools for this research. This can imply that the use of more tools will reveal new vulnerabilities and some of those might be among the ones classified by the Idaho National Laboratory.

ACKNOWLEDGEMENTS

I would like to thank my supervisor, Professor Ken Nixon, for all his invaluable input towards this research. I give thanks to the National Research Foundation for providing me with financial support.

REFERENCES

- [1] Wang Chunlei, Fang Lan & Dai Yiqi, "A Simulation Environment for SCADA Security Analysis and Assessment", *International Conference on Measuring Technology and Mechatronics Automation (ICMTMA)*, Washington DC, pp. 342-347, 2010.
- [2] Idaho National Laboratory, "Vulnerability Analysis of Energy Delivery Control Systems", last accessed 12 August 2013. URL <http://energy.gov/oe/downloads/vulnerability-analysis-energy-delivery-control-systems>
- [3] Daneels, A. & Salter, W., "What is SCADA?", *International Conference on Accelerator and Large Experimental Physics Control Systems*, Tokyo, 1999.
- [4] Chikuni, E. & Dondo, M., "Investigating the Security of Electrical Power Systems SCADA", *AFRICON*, Windhoek, pp1-7, 2007.
- [5] Bentley Systems, "The Fundamentals of SCADA", last accessed 15 August 2013. URL ftp://ftp2.bentley.com/dist/collateral/whitepaper/fundscada_whitepaper.pdf
- [6] Communication Technologies, "Supervisory Control and Data Acquisition (SCADA) Systems", last accessed 12 August 2013. URL www.comtechnologies.com
- [7] Queiroz, C., "Building a SCADA Security Testbed", *Third International Conference on Network and System Security*, Gold Coast, pp. 357-364, 2009
- [8] Byres, E. & Lowe, J., "The Myths and facts behind cyber security risk for industrial control systems", *Technical Report*, PA Consulting Group: London, 2004
- [9] Falliere, N., Murchu, L., & Chien, E., "W32.stuxnet dossier", *Technical Report*, Symantec Corporation: Mountain View, 2011
- [10] Farwell, J.P. & Rohozinski, R., "Stuxnet and the future of cyber war", *Survival*, 53(1), pp. 23-40, 2011
- [11] Meserve, J., "Staged Cyber Attack Reveals Vulnerability in Power Grid", last accessed 13 April 2013. URL <http://edition.cnn.com/2007/US/09/26/power.at.risk/index.html>
- [12] Zetter, k., "Researchers Uncover Holes that Open Power Stations to Hacking", last accessed 17 October 2013, URL <http://www.wired.com/threatlevel/2013/10/ics/>
- [13] Antunes, N. & Vieira, M., "Comparing the Effectiveness of Penetration Testing and Static Code Analysis on the Detection of SQL Injection in Web Services", *15th IEEE Pacific Rim International Symposium on Dependable Computing*, Shanghai, pp. 301-306, 2009
- [14] Halfond, W., Choudhary, S. & Orso, A., "Penetration Testing with Improved Input Vector Identification", *International Conference on Software Testing Verification and Validation*, Denver CO, pp. 346-355, 2009
- [15] Northcutt, S., "Penetration Testing: Assessing Your Overall Security Before Attackers Do", *Technical Report*, SANS Analyst Program, 2006
- [16] Eltayeb, M., "Implementation of a Virtual Plant Using SCADA/HMI Technologies", *Research Report*, University of Khartoum, 2009
- [17] Schneider Electric, "IGSS FREE50", last accessed 24 August 2013, URL <http://igss.schneider-electric.com/products/igss/download/free-scada.aspx>
- [18] Rouse, M., "Distributed Denial of Service", last accessed 30 September 2013, URL <http://searchsecurity.techtarget.com/definition/distributed-denial-of-service-attack>
- [19] Mackay, C., "SQL Injection Attacks and Some Tips on How to Prevent Them", last accessed 1 October 2013, URL <http://www.codeproject.com/Articles/9378/SQL-Injection-Attacks-and-Some-Tips-on-How-to-Prev>
- [20] Glynn, F., "SQL Injection Tutorial", last accessed 2 October 2013, URL <http://www.veracode.com/security/sql-injection>
- [21] Coates, M., "Man in The Middle Attack – Explained", last accessed 2 October 2013, URL <http://michael-coates.blogspot.com/2010/03/man-in-middle-attack-explained.html>
- [22] Hildayatullah, S., "Man in the middle attack prevention strategies", last accessed 2 October 2013, URL <http://searchsecurity.techtarget.in/tip/Man-in-the-middle-attack-prevention-strategies>
- [23] Hargrave, V., "What are Man-in-the-Middle Attacks", *Technical Report*, TrendMicro, 2012

IMPLEMENTATION OF A REMOTE MONITORING AND CONTROL SYSTEM USING A CELLULAR NETWORK

I Van Niekerk* and G Phillips**

**Nelson Mandela Metropolitan University, Advanced Mechatronics Technology Centre, Port Elizabeth, South Africa*

***Nelson Mandela Metropolitan University, Dep. Electrical Engineering, Port Elizabeth, South Africa*

Abstract. In this paper environmental data was measured and transmitted to a central server for remote monitoring, control and backup. The system demonstrated that it could measure soil information at various points and is able to send the sample with GPS co-ordinates to the central server via a cellular network. Using GPS co-ordinates data is sorted on the server and displayed on a website to enable precision agriculture to be applied to the field. A weather station measured weather conditions on the farm and updated the server on a regular basis using the cellular network. The aim of this paper is to show that modern industrial controllers and SCADA in collaboration with the existing cellular network infrastructure can be used in the agriculture industry to assist precision farming in South Africa.

Key Words. GSM Communication; Programmable Logic Controller; Supervisory Control and Data Acquisition; Precision Agriculture; GPS co-ordinates; Weather Station; Soil Measurement

1. INTRODUCTION

South Africa covers an area of 122 million hectare of which 18 million hectare is potential land for cultivation [1]. Eight percent of the potential arable land are under irrigation, which account for nearly half of the water requirements in South Africa [1]. South African farming does not fully utilize and integrate science and technology to enable precision agriculture; this leads to inefficient use of land resources for food production and with increasing population will lead to food and water shortage. There are virtually no remote monitoring and control sensing technology systems to support the farming industry to use environmental conditions in their decision-making. In the past manufacturing systems were standalone and hardly made use of communications [2]. With the development of the distributed control system, communication networks have become increasingly more important [2]. Networking control systems allows for more flexibility and higher efficiency with informed decision-making [2]. Traditional distributed control systems uses communication media like coaxial cable and twisted-pairs, but were limited in the distance of transmission. These media makes use of various modems and other hardware to cover these distances and contributes to high construction and maintenance cost. Furthermore, remote communications are generally unreliable and tend to breakdown. With the introduction of fiber-optic cable transmission distances became longer and more reliable, but construction costs very high [2].

2. CELLULAR TECHNOLOGY

The Global System of Mobile Communication (GSM) is the most popular standard for mobile phones and is an open standard making it compatible with almost any cellular network around the world [3]. Its wide spread coverage ensures availability to data all the time [3]. One of the services of GSM is the Short Message Service (SMS) in which end-to-end channel establishment is not needed [2]. This is a great service to use where real-time communication is not needed and the amount of data is not large.

Feedback of a control system can easily be supplied via this service to other industry control systems fitted with a GSM module or cellphone no matter what brand. This service will be used where application requires limited connectivity for feedback and limited control [2]. Many farms already have this technology installed on their water pivots for automatic irrigation. In the past farmer had to drive out to switch pivots on and off. Now they can send SMS from their mobile phones. Precision agriculture technology should make use of this service to communicate with other technologies already used in the industry. The control system communication network that uses GSM technology can cover anywhere in the world as long as there is GSM coverage in the area [2]. Another service that GSM offers is GPRS/3G series, which allows a device to connect to the internet. With this capability faster and more reliable communication is possible. The cost of this service is proportional to the amount of data exchanged. The cost to implement a data communication platform based on GSM in a large distributed control system is lower than traditional platforms [2]. Communications will play a vital role in precision agriculture, as it is the medium that will allow the farmer and his equipment access to the data anywhere on the farm and world. Therefore the medium chosen has to be robust and reliable [4].

3. HARDWARE ARCHITECTURE

The Siemens S7-1200 PLC was chosen as the field-computing-device because the product range offers a GSM communication module. There are also many other advantages using a PLC. These include quick reboot time, deterministic cycle, known sequence for programming execution, robust hardware and security [5]. Siemens offers a software package called Teleserver, which can be deployed on a server to manage S7-1200 PLC's using the internet connection and the GSM modules attached to the PLC's. The data is then available to the server in OPC (Open Platform Communications) format to any other software. Two field stations were built for this study. One field station will be used to monitor weather information and is assumed to be stationary,

referred to as the Weather Station. The other field station will be assumed moveable. This movement could either be with a human moving it around from point to point and doing measurements in the form of a handheld device or in the form of an AGV (Autonomous Guided Vehicle), which is doing the measurements autonomously. In this paper this unit will be referred to as the AGV Station.

3.1 Weather Station

The Weather Station architecture shown in Figure 1 is interfaced to standard industrial process instruments using standard industrial analogue signals to measure wind speed, wind direction, temperature, humidity and rainfall. An analogue module was attached to the PLC to enable communication between the PLC and sensors using analogue current and voltage signals. This ensures the system is a robust and a reliable solution. Process parametric scaling was achieved in programming.

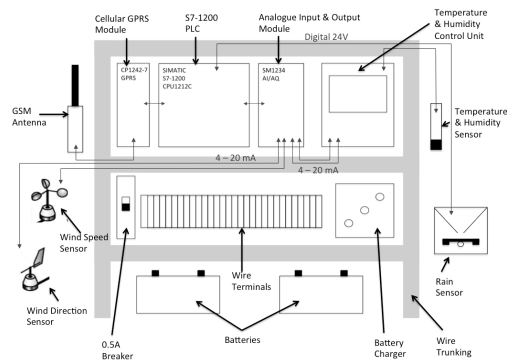


Fig. 1: Weather Station Architecture

3.2 AGV Station

Precision agriculture is all about managing the soil quality of each section of land according to the soil and crop needs. This is achieved using reliable data specific to that section of land. The AGV Station shown in Figure 2 needs to measure soil moisture and its own GPS co-ordinates in order to show that data can be collected autonomously and stored according to that position. This is vital in demonstrating that this technology can aid in precision agriculture.

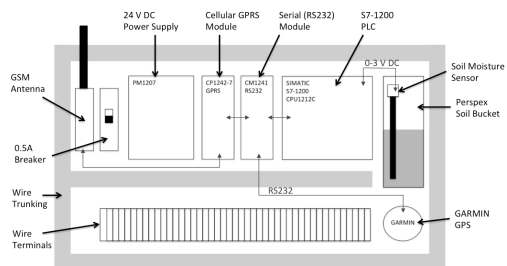


Fig. 2: AGV Station Architecture

Using a sensor the soil moisture is measured for irrigation purposes. This sensor uses standard analogue signals already used in the industrial sector, which insures reliability. The PLC has an analogue input on the CPU, which can measure 0 to 10V DC. The soil moisture sensor measures moisture content, which is represented in a 0 to 3 V DC signal, which the analogue card measure. Scaling was achieved in software programming. A Garmin GPS was used to determine where the unit is when taking a measurement so to pair this measurement with its own unique GPS co-ordinate before it is sent to a server for storage and display. This Garmin GPS uses a serial interface to communicate with the controller. A serial module was used to communicate with the Garmin GPS.

3.3 Server

A server had to be installed to collect the data from the field devices and make the data available to the farmer. This server has to be accessible by the field devices and the farmer. Figure 3 shows a router, 3G Internet modem and a personal computer that was used. In order for any device to reach a server it require the server's router's public IP address. The problem is every time the router reconnects to the Internet the Internet Service Provider (ISP) issues the router with a new public IP address. Reconnection happens when the router has lost power and regains power or if 3G signal was lost. There are two option to address this problem. One can buy a fixed IP address from the ISP or one can use a service called Dynamic Domain Name Service. Fixed IP addresses can be costly, but is preferred for its reliability. If a fixed IP is bought the service provider reserves that specific IP your device and every time the server's router reconnects to the ISP it gets issued with the exact same public IP address. This makes it easier for any device to reach the server, as its address never changes. With Dynamic DNS one registers an account with a DNS Server and gets issued with a unique Domain Name. When the router powers up it will connect to its ISP, which will issue it with its new public IP address. After the router is connected to the Internet it will send its new public IP address to the DNS Server, which pairs the public IP address with the unique Domain Name.

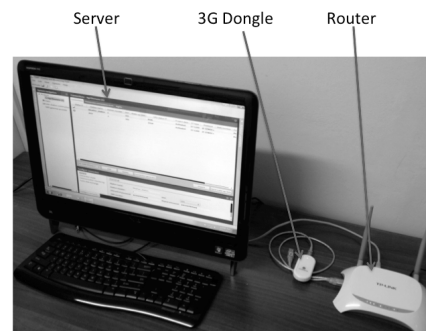


Fig. 3: The Server & Router

The client device (i.e. S7-1200) uses the unique fixed domain name to connect to the DNS where it gets routed to the router's public IP address, which the server knows. There are many free Dynamic DNS Services. For this paper Dynamic DNS was used to save cost. Now that the client devices can reach the server's router, the router needs to know where to forward the traffic. The router also needs to know when to allow traffic and when to block traffic. The server is given a fixed Local Area Network IP address, which the router reserves. Port forwarding is used to forward web traffic and Teleserver traffic to the server. All other traffic is blocked for security reasons.

4. SOFTWARE ARCHITECTURE

Two software packages were installed on the server. Teleserver was installed to manage the field PLC's and WinCC Advance was installed for data mining and storage. Other software packages were used to assist development of the system.

4.1 Teleserver

Telecontrol Server is installed on the server and is used to connect field stations to the control center. The software allows s7-1200 field devices to send data to the server to be accessed by any other software that support OPC (Open Platform Communication) installed on the server. OPC Scout is a software package that is used to view the OPC data on the server. This is a tool used to indicate what data Telecontrol Server is receiving and report the quality of this data. The data is sent over GPRS and the maximum number of field devices that can connect to the server is limited to five thousand field units. Telecontrol Server Basic is recommended for simple monitoring, for remote diagnostics and maintenance [4].

4.2 Industrial SCADA

WinCC Advanced is an industrial SCADA package used for developing visual displays, storing of data and is well known in the manufacturing industry.

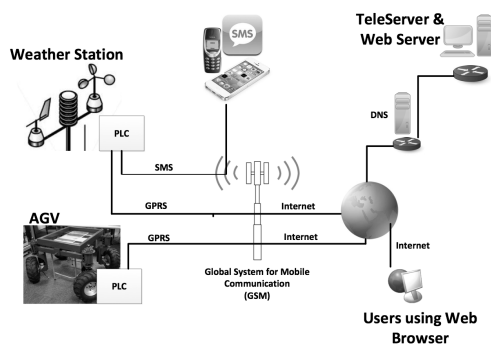


Fig. 4: Information Technology Architecture

WinCC supports the OPC format and is used in this project to access the data stored in OPC format by the Telecontrol software. Screens are developed for visualization and are published with the integrated web publisher software. The OPC Foundation was established to ensure interoperability in automation by creating and maintain open specifications that standardize the acquisition and control of process data to multi-vendor enterprise systems and between production devices [6]. Using OPC makes the data available for any other existing industrial device that supports OPC. The same server that Telecontrol and our industrial SCADA are installed on hosts the webpage. Figure 4 shows information technology architecture and how all these devices communicate with one another. For users to access the webpage they can type in the domain name allocated to the server's router, which is the same as what the PLC's are using to reach the server. The router will receive the traffic, but will see its web traffic on Port80. The router is setup to forward all Port80 traffic to the same server. The server will see its Port80 traffic and know the client is requesting the webpage hosted. All the security features in place for the SCADA locally are also automatically applied to the webpage. User accounts with different rights can be programmed and automatically applies these rights to the webpage. Each user can also be given different landing pages. This means when one user logs in, he gets routed to a different screen than another user would if they logged in. This way one service provider could actually host many different clients. All the clients share the server and services it offers, reducing cost and making this architecture even more viable without the clients seeing each other's data or pages. Figure 5 shows the main screen on the webpage displaying weather data and agriculture data. When clicking on the field blocks the output fields below change to display the soil content information relating to that specific spot.

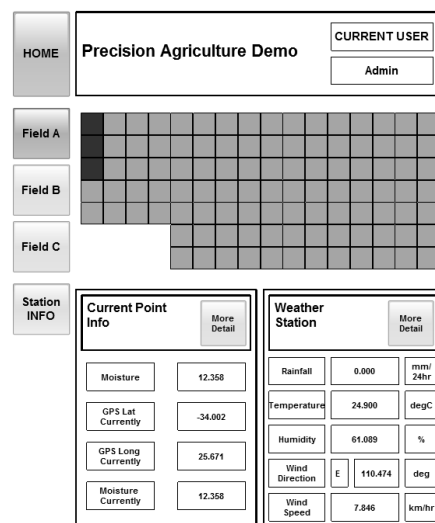


Fig. 5: Webpage Home Screen

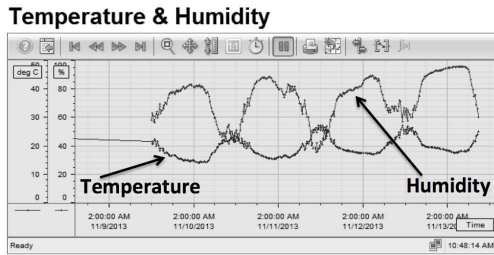


Fig. 6: Temperature vs. Humidity Archive

This was achieved by using the GPS co-ordinates that are paired to the sample data. All the data are also archived. The SCADA software monitors the data constantly and when ever there is a change, the value is archived. This data can be viewed in tables and graph form in the “More Detail” Screens as seen in Figure 6. Here we are comparing Temperature to Humidity. One can see as the temperature drops the humidity increases. The Teleserver monitors the connection to the PLC’s in the field and makes the data available in OPC format to the SCADA. For diagnostics purposes a screen was designed to make this data available to the farmer. In Figure 7 we see diagnostic information being displayed.

Weather Station Diagnostics	
GPRS Connected	CONNECTED
Signal Quality	GOOD
Device ID	K7 242-7KX
Firmware	2.1
Connection	CONNECTED
CPU State	RUN MODE
Protocol	CP 1242.7
CellTower ID	29353

Fig. 7: Temperature vs. Humidity Archived

4.3 Sensors & Scaling

Bolton defined [7] the term sensors as an element, which produces a signal relating to the quantity being measured. Most of the weather sensors used 4 to 20mA signals, which the analogue card converts into digital format. The analogue card converts 0 to 20mA signals into an integer format of 0 to 27648. Rescaling had to be done in the programming of the controllers in order for the sensors to be of value. These values will then represent the true weather values in its correct form. Figure 8 shows the modular program architecture. A sub procedure (FC) was created for each sensor to address individual scaling needs. Scaling was done cyclic on every scan cycle of the industrial controller. At the end of every scan the scaled value of each sensor was moved to the Global Data Block for storage. This Global DB is permanently available for any other communications platform that needs to collect weather data at any point in time. The Wind Direction sub program was

the only one that had to make use of local storage (FB with instance DB). Local storage had to be made available in order for the block to remember its north calibration setting. This calibration is done once after the controller is powered on. A program was written that enables one to point the device to north and send an SMS from an authorized phone to the weather station requesting a recalibration of the wind direction sensor to north. This value is then moved to retentive memory, which gets stored even if power is cut to the controller. An SMS is sent back to the installer to verify recalibration was successful. The direction block has been designed so that only one input has to be made high for one scan to calibrate north. This is done via the SMS request.

4.4 Protocol

The weather data shown in Table 1 is stored in one global DB to allow for access by any other communications blocks. “GPRS Send FC” sends this whole DB to the Server where the data is checked to ensure its quality and stored. This Send DB is a factory block that is pre programmed. It ensures the correct handshaking is done and that the server upon receiving checks the data quality. A positive edge to the send block triggers the sending of data from the data block. A counter is setup to count 60 seconds and trigger the sending of data periodically. This trigger time can be changed depending on the users application. The time taken for the data to get to the server depends on the amount of data sent and how busy the cellular network is at the time.

Table 1: Data Sent to Server

Name	Data Type	Byte Offset	Size
Rainfall	Real	0.0	4 bytes
Temperature	Real	4.0	4 bytes
Humidity	Real	8.0	4 bytes
Wind Direction	Real	12.0	4 bytes
Reserved	Real	16.0	4 bytes
Wind Speed	Real	20.0	4 bytes
Wind Direction	String	24.0	7 bytes

The user, using the SMS standard from any mobile cellular device, can also request weather information. A procedure was written so that the PLC constantly checks for an incoming SMS. If a new message is received, the data will be evaluated through string comparators. This will then be compared to preprogrammed functions. These preprogrammed functions are show in Table 2. The block will then respond to the users request by creating a string of maximum 160 characters with all the information the user requested. It then triggers this message to be sent using the users preprogrammed cellphone number.

Table 2: Programmed SMS Functions

Request Message from User to the Controller	Message from Controller to the User
't' or 'T'	'Current Temperature: +21.99 degC. Current Humidity: +51.23%'
'w' or 'W'	'Current Wind Speed: +21.13 km/h. Direction: W at +265.79 deg'
'r' or 'R'	'Last 24hr Rainfall: +0.00 mm'
'calW'	'Wind Direction Successfully Calibrated to North. Current Direction: N at +0.00 deg.'

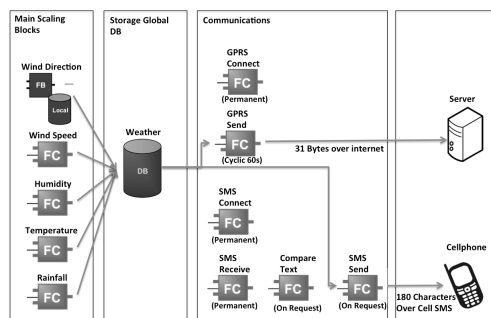


Fig. 8: Modular Program Architecture

5. INTEGRATION & TESTING

Two tests were done to check communications of both controllers, which can be seen in Table 3 and Table 4.

5.1 Weather Station Communication Test

In order to validate that communication using the Short Message Service, which is possible between the weather station controller and any mobile phone the following test was performed. Three different phones each from a different manufacturer using two different South African cellular communications companies was used to send the same message to the weather station controller. The controller would then need to reply by sending back the appropriate message and data the user has requested. Shown in Table 3 are these messages and the time taken for the controller and network to respond to the users request. The times taken to respond by the controller differ slightly, but this service is shared between many cellular users and can differ depending on how busy the network is. The small difference between the SMS data and the Website data is due to the delay in sample time. The Server only gets update every 60 seconds were as the SMS gets a value taken as soon as the request is received by the controller. Small changes will be notices because of the server update time.

Table 3: Testing Weather Station

Phone	Network Provider	SMS Sent	SMS Received	Time Taken till SMS Received	Current Value on Website
Model A	Company A	't'	'Current Temperature: +25.57 degC. Current Humidity: +61.03%'	17s	25.54
Model B	Company A		'Current Temperature: +25.54 degC. Current Humidity: +61.03%'	19s	25.56
Model C	Company B		'Current Temperature: +25.89 degC. Current Humidity: +61.03%'	22s	25.91
Model A	Company A	'w'	'Current Wind Speed: +12.60 km/h. Direction: E at +110.70 deg'	21s	12.75
Model B	Company A		'Current Wind Speed: +13.85 km/h. Direction: E at +110.70 deg'	14s	14.02
Model C	Company B		'Current Wind Speed: +14.62 km/h. Direction: E at +110.70 deg'	13s	14.54
Model A	Company A	'r'	'Last 24hr Rainfall: +0.00 mm'	15s	0.00
Model B	Company A		'Last 24hr Rainfall: +0.00 mm'	15s	0.00
Model C	Company B		'Last 24hr Rainfall: +0.00 mm'	13s	0.00

5.2 AGV Station Communication Test

The AGV Station has longitude and latitude GPS co-ordinates and soil moisture data it sends on request to the server. This is triggered either by the user doing the measurements by hand or by an autonomous guided vehicle. The Server will receive each soil measurement with its GPS co-ordinate and sort it according to specific block pre programmed. The farm will be divided into blocks. In order to test if this sorting is done correctly three blocks were programmed in the SCADA on the server and the AGV station was taken to that area and repeatedly used to take measurements of the soil. Each point had to be sent through on request to the server, sorted correctly and displayed on the website. In Table 4 we can see that this was done correctly. Although the user went to different spots the SCADA knew in which area that spot fell and stored the moisture level accordingly.

Table 4: Testing AGV Station

	GPS Longitude	GPS Latitude	Moisture on PLC	Block Allocation on Website	Moisture on Website
Point A	+25.6715	-34.001756	3.4	1	3.303
Point B	+25.67144	-34.001663	4.72	1	4.931
Point C	+25.67146	-34.0016	5.75	1	6.088
Point D	+25.67129	-34.001610	47.72	2	47.731
Point E	+25.67119	-34.001603	43.98	2	44.018
Point F	+25.67104	-34.00154	45.23	2	46.5
Point G	+25.67068	-34.00179	19.748	3	19.82
Point H	+25.67088	-34.001784	15.215	3	15.215
Point I	+25.67078	-34.00222	12.44	3	12.358

6. CONCLUSION

This project proves that industrial controllers and SCADA can be used to assist the automating of precision agriculture. It provides feedback quickly and is accessible from any cellular phone and computer. The system uses authentication to verify cellphone numbers and webpage logins, which makes it safe and secure. The data collected by the server is all stored in OPC format, which can easily be accessed by other software packages. Precision griculture is the future of farming and can only be applied if farmers and their equipment have up to date information pertaining to its environment and soil. This system does just that.

ACKNOWLEDGEMENTS

I would like to acknowledge and thank the following individuals and organizations without whom this project would not have been possible. To my mentors Mr. Grant Phillips from NMMU and Mr. Sakkie du Preez from Siemens thank you for all the guidance, support and patience. To the AMTC, and in particular Mr. Karl du Preez I thank for sponsorship with regard to the equipment used.

REFERENCES

- [1] H.J. Dennis and W.T. Nell, "Precision Irrigation in South Africa", Centre of Agriculture Management at the University of the Free State, Bloemfontein, South Africa
- [2] Chen Guiyou, "Distributed Supervisor System of Heat Supply Network Based on GSM Platform," *Intelligent Control and Automation*, vol. 2, 2006.
- [3] Rao, B. Srinivasa, "A proto-type for Home Automation using GSM technology," *Power, Control and Embedded Systems*, p. 4, Dec. 2010.
- [4] Siemens AG. (2013) TeleControl Basic for the control center. [Online]. Available: "http://www.automation.siemens.com/mcms/industrial-communication/en/industrial-remote-communication/telecontrol/telecontrol-basic/control-center/Pages/Default.aspx" <http://www.automation.siemens.com/mcms/industrial-communication/en/industrial-remote-communication/telecontrol/telecontrol-basic/control-center/Pages/Default.aspx>
- [5] H. De Schepper. (1999) PC based control vs. PLC. [Online]. Available: www.control.com/thread/941648158
- [6] OPC Foundation. (2003) About OPC Foundation. [Online]. Available: http://www.opcfoundation.org/01_about/April19_OPC-DISPLAY%20LAYOUT.pdf
- [7] W. Bolton, *Mechatronics Electronic control systems in mechanical engineering*, 2nd ed., Addison Wesley, Ed. New York, USA: Longman Publishing, 1999.

DESIGN AND IMPLEMENTATION OF A SUB-METRE ACCURACY POSITIONING SYSTEM USING A CONSUMER GRADE GPS RECEIVER

D. Hinch*, J. Penn*, K. J. Nixon*, G. J. Gibbon*

* School of Electrical and Information Engineering, University of the Witwatersrand, Johannesburg, Private Bag 3, Wits 2050, South Africa E-mail: damianhinch@gmail.com, 473226@students.wits.ac.za, ken.nixon@wits.ac.za, george.gibbon@wits.ac.za

Abstract: The purpose of this document is to describe the design, implementation and testing of a satellite positioning system that achieves sub-metre accuracy using a consumer-grade single-frequency GPS receiver. The three main techniques utilised are double differencing, Kalman filtering and elevation masking. The theory behind each of the three techniques is explained, following upon which testing is conducted. Two types of experimental procedures are utilised, the first serving to investigate the system's ability to calculate an absolute position and the second to test its ability to measure a displacement. The double differencing technique performs the best of the three main methods investigated, providing well under a metre accuracy in both sets of tests. This accuracy improvement technique is not standalone, as it requires data from an external source, and hence is not appropriate for use in all situations. The Kalman filter and elevation masking methods also both achieve accuracies under a metre in all tests and thus provides stand-alone alternatives to the double differencing approach. Recommendations are made with regard to the possible combination of the elevation mask approach with the other two main techniques and the over-arching conclusion is drawn that sub-metre positioning accuracies may be obtained using a consumer-grade single frequency GPS receiver in conjunction with the recommended methods.

Key words: BeagleBone Black, double differencing, elevation mask, GPS Opti-Sleuth, Kalman filter, Trignet

1. INTRODUCTION

The Global Positioning System (GPS) satellite constellation provides users with the ability to ascertain their position anywhere on the globe. Consumer-grade single frequency GPS receivers that are used without external correction systems typically have an accuracy of approximately 2.5m. More precise positioning is traditionally obtained via the use of geodetic-grade dual frequency receivers that may achieve sub-centimetre accuracy levels when used in conjunction with post-processing or external correction services. However, such systems are priced well out of the reach of the average user, typically costing between 100,000 and 300,000 ZAR [1].

In order to provide a cheaper solution that may be implemented in South Africa using a consumer-grade single frequency GPS receiver, Kalman filtering, elevation masking and Differential GPS (DGPS) double differencing techniques are utilised. These approaches improve the positioning accuracy of a consumer-grade single frequency GPS receiver to sub-metre levels. To effectively implement the techniques, a stable and modular software platform is needed that facilitates the reading of GPS receiver data outputs, applies the accuracy improving techniques and records all measurement results. Such a system, *GPS Opti-Sleuth*, is developed for use on a Linux computer and subsequently implemented on a *BeagleBone Black* (BBB).

A brief discussion of GPS accuracy errors and existing South African positioning correction infrastructure is

conducted. The design of the system is presented in terms of its hardware and software components, along with detailed explanations of the main investigated accuracy improvement methodologies. The results of fixed position and relative position testing procedures are presented and the performance of the implemented optimisation techniques are discussed in the context of the testing conditions. Recommendations for future improvements to the software application are made, accompanied by related general conclusions.

2. BACKGROUND

2.1 Single Frequency Psuedorange Observables

Each GPS satellite contains a highly accurate atomic clock, which is practically perfectly synchronised to an identical time across the GPS constellation. The satellites continually transmit a long time-code known as the 'coarse acquisition' or C/A signal [2]. GPS receivers can determine their distance from the transmitting satellite by comparing this code to their own internal clocks. The resulting distances, given in metres, are known as the C1 psuedorange observations. In addition to the code readings, the number of cycles of the C/A transmission signal carrier phase that have passed since transmission from the satellite are also measured. These are called the L1 psuedorange observables and they allow for the carrier-phase characteristics of the signal to be utilised in order to calculate the GPS receiver's position.

2.2 Clock Errors

Clock synchronization errors are invariably found to occur between the low-cost, low-accuracy quartz clocks utilised within GPS receivers and the high-cost, high-accuracy atomic clocks installed aboard the satellites. A minimum of four visible satellites are required in order to correct for clock errors. The first three are used to determine a position on the earth's surface via the process of trilateration. Once calculated, this position is compared to the measured distance from the located position to the fourth satellite. If this distance does not match up as expected, then a timing error correction is calculated for the GPS receiver clock that brings all four satellite distances to intersect at a single point on the earth's surface [3].

2.3 Atmospheric Errors

This ionosphere, which has a mean height of 350km, and the troposphere, which has a mean height of 15km, both have a profound effect on the propagation of satellite signals [4]. Any delay that may be applied to a satellite's transmissions introduces error into the calculation of the distance between it and the GPS receiver, negatively effecting the accuracy of the calculated position. The signal from each satellite passes through the ionosphere at an Ionospheric Pierce Point (IPP) where it is refracted due to the Total Electron Content (TEC) of the layer, which is continuously changing over time [5]. The weather conditions present in the troposphere can also have a significant effect on the propagation of satellite transmissions. The closer to the horizon a satellite is with reference to the GPS receiver, the greater the effect of local tropospheric conditions will be upon its transmissions.

2.4 Trignet Network

The National Geo-Spatial Information (NGI) Department has set up the *Trignet* network of base-stations equipped with high precision dual frequency GPS receivers. These are situated at known reference co-ordinates that are precisely surveyed in using the ITRF2008 reference frame [3]. This network was developed in order to provide users with DGPS facilities, which are made available free of charge. In addition to making each receiver's pseudorange observables available in real-time, the stations also compile precise and up-to-date ephemeris navigation data. At present all *Trignet* data may only be accessed via the internet, which limits the network's usability when operating in areas where internet connectivity is not available.

3. HARDWARE AND LIBRARIES

3.1 EVK-6T GPS Receiver Kit

The EVK-6T kit is a pre-assembled unit that contains a *uBlox* LEA-6T GPS receiver connected to USB and RS232 interfaces. This is used in conjunction with a

uBlox ANN-MS antenna, which attaches to the EVK-6T kit via a 5m cable, allowing for flexibility in physical placement. The receiver is capable of outputting raw satellite pseudorange and subframe data as well as NMEA messages, which is an operational requirement of *GPS Opti-Sleuth*. The off-the-shelf accuracy of the device is 2.5m.

3.2 BeagleBone Black Hardware Platform

One of the requirements of the system is portability, given the nature of common GPS usage. The BBB platform was chosen and a *ThreeFive* TFC 7" 800x480 touch screen was connected to the BBB to allow GUI interaction.

3.3 Software Libraries

RTKLib is an open-source GNSS library which provides support for a multitude of different navigation techniques. It supports the proprietary *u-blox* output and is used extensively throughout the design. The open-source *Orekit Space Dynamics* library was utilised for its tropospheric delay modelling functionality. The *Google Maps* API was used in order to display positioning results. *GPS Opti-Sleuth* was developed in the Java programming language, with the *Netbeans* GUI creator being employed in order to build a *Swing* interface for the software.

4. GPS OPTI-SLEUTH

An overview of the *GPS Opti-Sleuth* positioning software application may be seen in Figure 1. In the diagram, the coloured lines correspond to the external data that is fed into the system and the texture of the lines represents which libraries are used. For example, the double differencing method can be seen to make use of *Trignet* data as well as the *RTKLib* libraries.

4.1 GPS Opti-Sleuth Features

The creation of the stable, light-weight and portable *GPS Opti-Sleuth* software platform allows for the optimisation techniques discussed in Section 5. to be implemented and tested. The program manages coordinate conversions, provides display and comparison functionality, processes data outputs and contains a host of other essential features.

Position Calculation: Both a basic position, corrected only for clock error, and a variety of further refined positions are calculated within the software and presented to the user. In addition to the primary techniques - double differencing, Kalman filtering and elevation masking - a number of further methods are also utilised for the sake of comparative accuracy investigation.

Coordinate Conversions and Differencing: *GPS Opti-Sleuth* provides two modes of operation: 'Absolute' and 'Difference'. 'Absolute' mode shows the current position in DDMM.mmmmmmm (i.e. degrees, minutes

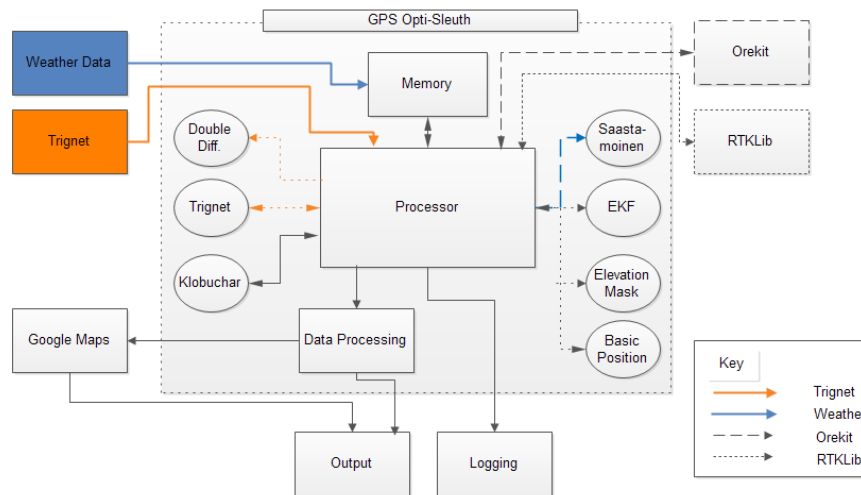


Figure 1: Block diagram of system design

and fractions of a minute to 7 decimal places). 'Difference' mode shows the difference between the current measurement and a fixed point input by the user, which makes this mode extremely useful for simultaneously comparing the performance of multiple accuracy improvement methods.

Data Logging, Aggregation and the Google Maps API: Readings from the GPS are processed, made accessible to any class in the program and continually logged for post-processing purposes. The main user output of the program is also logged, whilst normal program logging is performed using the logging services provided by Java.

GPS Opti-Sleuth performs data aggregation, whereby a set of single positioning or difference results may be aggregated and displayed to the user. This provides an averaged position that is more reliable than the results of each single iteration taken in isolation.

The *Google Maps* API was used to overlay the current position on satellite images of the globe. The *Google Earth* program was not used as it is not at all light-weight and runs very slowly on the BBB. Instead, *JavaScript* was used to create the map on an external server. The result is then displayed in the *Google-Chromium* web browser installed on the device.

Accessing Trignet Data: *GPS Opti-Sleuth* manages access to the *Trignet* servers in order to obtain required data. When using the double differencing method, the station data is streamed to the program for use in the differencing process. *Trignet .nav* files can also be retrieved from *Trignet's* FTP server via the software. *GPS Opti-Sleuth* can be run using either *Trignet's .nav* files or the *.nav* files produced by the device. In addition to this, downloading the latest *Trignet .nav* files also serves to updates the

Klobuchar coefficients required by the atmospheric delay modelling technique.

Session Persistence: The settings for *GPS Opti-Sleuth* are stored in a configuration file. This allows program settings to be changed without modifying variables in the source code. A settings screen is also provided in order to allow the user to change the settings easily without having to exit the program.

4.2 Software Maintainability and Extensibility

For *GPS Opti-Sleuth's* development the software engineering principle of 'high cohesion, low coupling' was adhered to. The graphic user interface can be modified without any significant changes being made to the program itself. This allow for the core functionality of the software to be easily ported to other devices which may feature different interface requirements.

5. ACCURACY IMPROVEMENT TECHNIQUES

Two main types of techniques were chosen for implementation, those that can perform entirely stand-alone and those that require external data from the *Trignet* system. In addition to the main methods selected for use, several further alternatives were also included in the software for investigation purposes.

5.1 Basic Position

GPS Opti-Sleuth continually logs the raw data outputs produced by the LEA-6T GPS receiver module. Each complete reading is converted into the RINEX format and processed in conjunction with a navigation file containing satellite ephemeris data in order to derive a basic position. The clock error elimination technique described in section 2.2 is applied to the psuedorange data as part of the

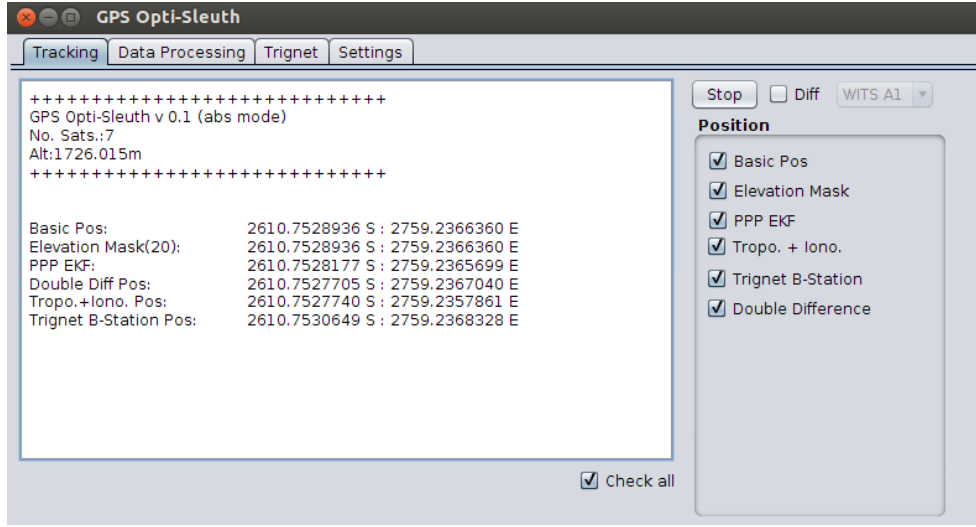


Figure 2: Block diagram of system design

position calculation process, serving to remove satellite and receiver clock errors from the resulting coordinate.

5.2 Elevation Mask

The elevation mask is the simplest optimisation technique employed in the software. It may be set such that the pseudorange data from any satellite that falls below a user-selected elevation angle is excluded from the basic position calculation. The closer to the horizon a satellite is located, the more atmosphere its transmissions must pass through and thus the greater the delay effects applied to its signal. An elevation mask level of 15° is commonly considered optimal and is the default value used in GPS Opti-Sleuth [6].

5.3 Kalman Filter

A major challenge encountered in the determination of accurate positions is the reduction of pseudorange noise [7]. Such noise can contribute to overall error and exacerbate position walk and scatter. A Kalman filter is a multiple input, multiple output digital filter that can optimally estimate the states of a system based upon its noisy outputs [8]. This allows for estimation of the true state of the system from the random-error containing pseudorange data. The inputs to the Kalman filter applied within GPS Opti-Sleuth are the uncorrected pseudorange data. The outputs are the filtered pseudoranges, which are utilised in the calculation of a corrected position.

5.4 Double Differencing

Unlike the techniques discussed above, this accuracy improvement technique relies upon pseudorange observable data streamed from the *Trignet* NTRIP server. The dual frequency measurements taken from any user-selected fixed base-station are utilised in conjunction with the

unprocessed LEA-6T GPS receiver's pseudorange data in order to minimise any remaining clock errors and reduce the effect of atmospheric and ephemeris errors via the process of double differencing, as follows [6]:

To obtain the code differential, the *Trignet* base-station and user GPS receiver pseudorange code measurements are compared for each visible satellite according to equation 1 below:

$$\rho_n = \rho + cdt - cdT + d_{ion} + d_{trop} + d_{ephem} + d_p \quad (1)$$

Where:

ρ_n = Measured pseudorange (m)
 ρ = True pseudorange (m)
 c = Speed of light (m/s)
 dt = Satellite clock error (s)
 dT = Receiver Clock Error (s)
 d_{ion} = Ionospheric Delay Error (m)
 d_{trop} = Tropospheric Delay Error (m)
 d_{ephem} = Satellite Ephemeris Error (m)
 d_p = Multipath, Thermal Noise and Receiver Channel Bias Errors (m)

First Difference: To obtain the first difference, subtract an equation of form (1) for the base-station receiver from a similar equation for the user GPS receiver, where both equations refer to the same satellite. This returns an equation of the form given below in equation 2 below:

$$\Delta\rho_M = \Delta\rho - \Delta dT + \Delta d_{ion} + \Delta d_{trop} + \Delta d_{ephem} + \Delta d_p \quad (2)$$

Here the satellite clock error term has disappeared. The

closer the user receiver is to the base-station, the closer d_{ion} , d_{trop} and d_{ephem} are to zero. This is due to the fact that the ionosphere, troposphere and ephemerides change very slowly with shifts in position.

Second Difference: Now subtract an equation of form (2) for a chosen satellite from a similar first difference observation for another satellite. This returns an equation of the form below:

$$\nabla\Delta\rho_M = \nabla\rho - \Delta dT + \nabla\Delta d_{ion} + \nabla\Delta d_{trop} + \nabla\Delta d_{ephem} + \nabla\Delta d_p \quad (3)$$

Here the receiver clock error term has disappeared. Assuming that the user receiver is located within a suitable radius of the base-station the tropospheric, ionospheric and ephemeris terms can now be considered approximately equal to zero and neglected, resulting in an equation of the reduced form in equation 4

$$\nabla\Delta\rho_M \cong \nabla\rho + \nabla\Delta d_p \quad (4)$$

The errors due to multipath, thermal noise and receiver interchannel biases may not be removed via this method as they are not common to both the base-station and user receiver. These corrected observations may now be used in order to calculate a more accurate position.

5.5 Alternative Techniques

In addition to these main methods, a number of further approaches were investigated, including the calculation of a *Trignet* spacial differential and use of both tropospheric (Saastamoinen) and ionospheric (Klobuchar) delay models

6. RESULTS

6.1 Fixed Position Testing

The Waterval trigonometric beacon located on Northcliff Hill in Johannesburg was utilised in order to evaluate the system's ability to determine a known point. As the beacon's position is accurately surveyed in, it allows for a comparison to be drawn between the real and *GPS Opti-Sleuth* calculated coordinates. The difference between the calculated and known points (in m) was calculated for each of the accuracy improvement techniques. The GPS receiver antenna was placed at the centre of the beacon and the system was set to run for 3.5 hours. The log files populated during this period were utilised in order to obtain an average of all the methods' recorded positions, as shown in table 1 below. The elevation mask was set to 15° for the duration of the experiment.

6.2 Relative Positioning Testing

In this experiment, the GPS receiver antenna was placed in an initial position and the software was run for 3.5 hours. Once complete, the antenna was moved distances of 1 and 2 metres away from this initial point in a straight

Table 1: Test 1 - Fixed location testing.

Method	Diff x (m)	Diff y (m)	Total Diff (m)
Dbl Diff	0.242	0.219	0.327
Kalman	0.276	0.259	0.379
Elevation	0.493	0.275	0.564
Basic	0.460	0.526	0.699
Atmosphr	0.346	0.663	0.748
Spatial	1.042	0.899	1.376

line and the testing procedure was repeated. Comparison of the real and calculated displacements could then be performed, providing indication of the system's ability to replicate the expected displacement. In order to ensure accurate displacement increments, a specialised testing rail was assembled for extremely precise GPS receiver antenna placement. This test was conducted twice in its entirety, yielding the results shown in tables 2 and 3 below. Again, the elevation mask was set to 15° throughout.

Table 2: Relative position testing 1

Method	Diff (m)
Kalman	0.191
Dbl Diff	0.418
Elevation	0.472
Basic	0.497
Atmosphr	0.620
Spatial	1.588

Table 3: Relative position testing 2

Method	Diff (m)
Dbl Diff	0.540
Elevation	0.733
Basic	0.763
Kalman	0.776
Atmosphr	1.124
Spatial	1.234

7. DISCUSSION OF RESULTS

7.1 Fixed Position Testing

The results from table 1 show that the double differencing method provides the best performance overall. However, it should be noted that this method cannot be reliably used in regions without an internet connection or at any point located further than 30km away from a *Trignet* reference station [9].

The Kalman filter and elevation mask methods both provide improvement on the basic position. Although this

enhancement is not as significant as that offered by the double differencing method, it is still sub-metre in both cases and should thus be considered successful in this experiment. All of the other techniques performed worse than the basic position, providing no improvement to the system's accuracy.

7.2 Relative Position Testing

The results shown in tables 2 and 3 correlate fairly well both with the results for the fixed position testing and with one another, indicating that the system features a relatively high level of repeatability. The double differencing method can be seen to perform better than the basic position in both tests, further validating the previous results.

The Kalman filter method performs extremely well in the first instance, but fails to improve upon the basic position in the second set of results. However, its failure is very marginal. In both tests, the elevation mask provides an improvement to the basic position, although this improvement is not as pronounced as that of the double differencing and Kalman filter methods. The alternative methods again failed to improve upon the basic position, further indicating the repeatability of the system.

8. RECOMMENDATIONS

8.1 Elevation Mask Combination

GPS Opti-Sleuth does not currently allow for the combination of any accuracy improvement methods and should be amended in order to facilitate the cascading of certain techniques. The nature of the elevation mask method makes it an excellent candidate for combination with other approaches, given that it serves purely to eliminate low elevation angle satellites from the position calculation process. As the elevation mask offered accuracy improvements in all testing iterations, it should be considered for combination with both the Kalman filter and double differencing techniques. This could lead to further refinement of positioning results and should at the very least be included in further incarnations of the software as an option that may be utilised at the user's discretion.

8.2 Alternative Methods

As all of the alternative methods investigated failed to yield positioning accuracy improvement in any of the tests, they should be discarded from future versions of the software.

9. CONCLUSION

The system achieved the desired sub-metre positioning results for all of the main investigated accuracy improvement techniques. The double differencing method performed best overall, dominating the results in all cases, excepting in the first of the relative tests. Thus this method should be utilised preferentially by users. However,

this technique requires both access to the internet-based *Trignet* system as well as reasonable proximity (<30km) to a reference station. Accordingly, it is prudent to provide users with the option of a fully standalone technique, in the form of the Kalman filter method. The *GPS Opti-Sleuth* software should be altered such that the elevation mask method may be used in combination with both the double differencing and Kalman filtering techniques. The alternative accuracy improvement methods investigated failed to offer any positioning accuracy improvement and should thus be discarded.

REFERENCES

- [1] UNAVCO. Permanent GNSS/GPS Stations - Budgets, <http://facility.unavco.org/kb/categories/GNSS+Permanent+Stations/>.
- [2] J.B. Tsui: "Fundamentals of Global Positioning System Receivers: A Software Approach", John Wiley and Sons, New York, 2000.
- [3] GPS Tutorial, "Trimble Navigation Limited", <http://www.trimble.com/gps-tutorial>, Last accessed July 10, 2013.
- [4] M. Ibrahim, N.D. Kaushika and F. de Mendonca. Short Paper on the Determination of Mean Ionospheric Height Related to Faraday Rotation Experiment, Journal of Atmospheric and Terrestrial Physics, Vol. 86, No. 4, pp. 713 715, 1974.
- [5] N. Yaacob, M. Abdullah and M. Ismail. GPS Total Electron Content (TEC) Prediction at Ionosphere Layer over the Equatorial Region, Trends In Telecommunications Technologies, C.J Bouras (Ed.), InTech, Croatia, pp. 458 508, 2010.
- [6] M.S. Grewel, L.R. Weill and A.P. Andrews. Global Positioning Systems, Inertial Navigation and Integration. John Wiley and Sons, New Jersey, second edition, 2007.
- [7] B.W. Tolman. GPS Precise Absolute Positioning via Kalman Filtering, ION GNSS 21st International Technical Meeting of the Satellite Division, Savannah, September 16 19, 2008.
- [8] R. Habash. GPS Kalman Filtering, University of Ottawa, <http://www.site.uottawa.ca>, Last accessed October 9, 2013.
- [9] "L.P.S. Fortes. Optimising the Use of GPS Multi-Reference Stations for Kinematic Positioning", Diss. University of Calgary, Alberta, 2002.

Index

- A**
- Afullo TJO, 505
- Akindeji KT, 200
- Almeida J, 316
- Amushembe H, 194
- Appadoo W, 176
- Atkinson-Hope G, 78, 164, 194, 453
- Awodele KO, 182, 218, 329
- B**
- Bagobi M, 425
- Barendse P, 409
- Bellim F, 390
- Berry BWD, 19
- Blignault GW, 140
- Boadzo R, 500
- Bokoro P, 69
- Booyesen MJ, 489
- Braid J, 358
- Britten AC, 117, 136
- Bullecks B, 409
- Burnier C, 335
- C**
- Chowdhury S, 31, 176, 323, 384, 500
- Clasen GL, 235
- Clay J, 128
- Cormack R, 279, 441
- Cornish DR, 57
- Coutlakis M, 358
- Cronje WA, 230, 390
- D**
- De Beer AS, 448, 471
- De Beer C, 409
- Doorsamy W, 230
- Dreyer AG, 95
- Du Plooy J, 290
- E**
- Edwards MA, 19
- El-Haddad A, 390
- Els JP, 284
- F**
- Fadiran J, 384

G

Gerber S, 242, 249

Gibbon GJ, 523

Gora T, 101

Goudarzi A, 212

Gouws R, 2, 44

Grobler AJ, 235, 261, 307, 397, 494

Gule N, 225, 255, 290

Guldenpfennig MM, 352

Gunda L, 255

H

Harris RT, 83

Heydenrych MG, 37

Hinch D, 523

Hofsajer I, 128

Hoogenboezem TA, 372

Horonga N, 390

Hove M, 69

Hunt HGP, 63, 347

I

Ijumba NM, 147

J

Jakoet A, 188

Jandrell IRJ, 69, 101

Jikija K, 159

Joannou ALJ, 465

Joubert T, 123

K

Kahunzire AE, 182

Kamper MJ, 352

Kasangala FM, 453

Kyere IK, 73

L

Lange JH, 63

Lam LLT, 471

Lazanas P, 159, 171

Lekalakala Y, 267, 273

Looi M, 477

Lorimer T, 13

Lotriet RA, 397

Louw QE, 171

M

Mabotha CM, 435

Machinda G, 323

Mafimidiwo OA, 378

Mahlare PTA, 416

Makhetha M, 205

Malan K, 358

Maneweld M, 31	Nyamgoma J, 218
Manyage M, 205	Nyamupangedengu C, 57, 89, 111
Mararakanye N, 384	Nyamwena-Mukonza C, 366
Mashaba MM, 435	
Mashau T, 302	O
McLaren AJ, 296	Oosthuysen NJ, 26
Meru AM, 165	
Metebe MT, 279	P
Meyer EL, 341	Penn J, 523
Mkandawire BO, 147	Pentz DC, 372, 465
Mkhwanazi TN, 421	Pieterse P, 9, 51
Mlangeni GD, 111	Pillay P, 409
Modisane T, 153	Phillips G, 37, 517
Mouton HDT, 459	Phillips R, 404
Mtakati SM, 83	Phipps W, 83
Mulaba-Bafubiandi AF, 421, 425, 430	Poole SN, 404
Müller RI, 489	Popoola OM, 335
Mushagala MJ, 78	
Muzoka S, 101	R
Mvuyana S, 153	Ralethe SG, 510
	Ralikhwatha L, 323
N	Randewijk PJ, 296
Ndlovu TF, 421	Reader HC, 9
Netshiongolwe FA, 441	Rengaswamy R, 409
Nienaber S, 459	Roberts AG, 83
Nixon KJ, 19, 63, 101, 107, 347, 435, 510, 523	Rowell, 13
Nthontho M, 31	

S

Sadie DT, 95

Saha AK, 147, 188, 212, 378

Sikhakhane G, 267

Simon M, 341

Smal F, 261

Sorgdrager A, 284, 307

Sotsaka M, 111

Strelec GJ, 107

Swart AJ, 416, 483

T

Tabiri M, 329

Tangwe SL, 341

Tarrant D, 302

Tlali PM, 242

Trengrove E, 95

Tshiongo-Makgwe N, 425, 430

Tshipa RS, 425, 430

V

Van Coller J, 153, 205, 267, 273, 279, 302, 441

Van Niekerk I, 517

Van Rensburg C, 494

Van Rooyen T, 44

Van Wyk JD, 448, 465

Vermeulen HJ, 140

W

Walker JJ, 26, 73, 123

Wang RJ, 242, 249, 284, 307

Wilken N J, 2

Wooding GN, 448

Wolsky D, 347

Z

Zietsman NL, 225

Zwane F, 510

ISBN 978-1-86840-619-7



9 781868 406197 >